Molecular Imaging and Targeted Therapy

Radiopharmaceuticals and Clinical Applications

Shankar Vallabhajosula

Second Edition

🦄 Springer

Molecular Imaging and Targeted Therapy

Shankar Vallabhajosula

Molecular Imaging and Targeted Therapy

Radiopharmaceuticals and Clinical Applications

Second Edition

Editorial Assistance
By
Brigitte Vallabhajosula, Ph.D.

Springer

Shankar Vallabhajosula
Professor Emeritus of Radiochemistry and Radiopharmacy in Radiology
Weill Cornell Medicine, Cornell University
New York, NY, USA

To my precious wife Shanthi,
For her belief and trust in me.

Foreword to the First Edition

Molecular imaging is a term that is now used frequently to describe much of what nuclear medicine has been involved in for almost 50 years. Since the early attempts to produce images representing the spatial distribution of specific tissue and organ functions such as the use of radioiodine to identify (and also to quantify) thyroid tissue function or the use radioiodine labeled human serum albumin (HSA) to identify the increased extracellular fluid in a brain tumor, nuclear medicine scientists and physicians have used the powerful tools, radioactive emission and decay and the tracer principle, for this purpose.

In the case of thyroid imaging with radioiodine, the radionuclide itself is the tracer that specifically recognizes (and is recognized by) the iodide transporter and the subsequent trapping and organification mechanism results in thyroid hormone synthesis. In the early efforts to localize brain tumors, the radioiodine was chemically bound to HSA, and as a result of its molecular size, radioiodinated HSA was useful to identify the increased extracellular fluid content of various brain tumors in contrast to normal cerebral cortex.

The number of applications of molecular imaging therefore depends upon the radionuclides available, their inherent biochemistry whereby the radionuclide itself might be a useful tracer [such as ^{131}I, ^{124}I, or ^{123}I as an iodide for assessment of thyroid function and imaging or ^{18}F as the fluoride to measure bone kinetics and skeletal imaging]. In addition, depending upon the chemistry of a particular element, the radiotracer may be useful to evaluate and image other molecular and physiologic processes if the radionuclide can either be incorporated into the native molecular structure of a compound [such as ^{197}Hg in a mercurial diuretic for renal imaging in the pre-^{99m}Tc era or ^{57}Co within the cyanocobalamin molecule to evaluate the intestinal absorption of vitamin B12] or bound to a messenger molecule without significantly interfering with recognition by the specific receptor [such as ^{111}In-DTPA-pentetreotide or ^{68}Ga-DOTATOC to somatostatin receptor subtypes].

To fully utilize these various radiotracers and radiolabeled molecules, the medical scientist and physician needs also to appreciate issues related to production and availability, type of radioactive decay and dosimetry, and the interaction of radiation and matter in order to efficiently detect the distributed signal or at least understand the inherent limitations and source of potential errors. Furthermore, by understanding existing instruments and radiotracers one may better design the next generation of strategies to help drive the field of molecular imaging.

Molecular Imaging: Radiopharmaceuticals for PET and SPECT is not a mere text on radiopharmaceuticals. In this volume, Shankar Vallabhajosula, Ph.D., has provided the reader with a single volume that describes and explains all of these components of radionuclide-based molecular imaging. Dr. Vallabhajosula shares his insight that molecular imaging is based on an understanding of the continuum of science from atomic structure and relationships, through chemistry and physiology, the physics of instrumentation, and the relationship of radiation and matter as well as the specific details of the radiopharmaceuticals themselves and the pharmaceutical principles including the practice of pharmacy. His description of his insight is further enriched by over 35 years of experience in nuclear medicine and all of its applications and his affection for the history and philosophy of science.

Molecular Imaging: Radiopharmaceuticals for PET and SPECT is a remarkable volume in that it comprehensively covers the entire scope of the basic sciences of nuclear medicine—and it does so in a highly readable style. It is further remarkable in that the entire text has been written by a single author, perhaps necessary to communicate, in addition to all of the scientific details, this over-riding view that all of the details are part of a continuum and that it is necessary to "see the forest as well as the trees" [to paraphrase an expression].

This is both a textbook on the subject and a history of the subject. It should be read by students and practitioners, medical doctors and scientists, radio-chemists, physicists, radiopharmacists, technologists, and research personnel. In addition, for those learning about molecular imaging using non-radionuclide (e.g., optical, MRI) based strategies, this book is an excellent introduction to important issues, lessons, and unifying principles for the entire field. The volume consists of 20 chapters and many excellent figures and tables. In addition to the science, it includes some brief history of the discoveries, the insights and developments that hopefully will sustain our memory of the science as well as of the scientists. Each chapter begins with a quote from a senior scientist. These quotes set a tone; recognition of, and respect for, the complexity of the physical and biological world—and man's ability to understand it.

Dr. Vallabhajosula has performed a highly important service for nuclear medicine and the medical imaging community by creating this volume that brings together the scientific foundation of our field and by sharing his passion for the subject. Hopefully, the material and this stimulating presentation will motivate some of the readers to contribute to further evolution of this adventure.

New York Presbyterian Hospital   Stanley J. Goldsmith, MD
and Weill Cornell Medical College
Cornell University,
New York, NY, USA

Stanford University Medical Center   Sanjiv Sam Gambhir, MD, PhD
Stanford, CA, USA

Foreword to the Second Edition

I am delighted to provide a "foreword" to this second edition of *Molecular Imaging and Targeted Therapy: Radiopharmaceuticals and Clinical Applications* by Dr. Shankar Vallabhajosula. The foreword to the highly successful first edition was contributed by Drs. Goldsmith and Gambhir, two giants in clinical nuclear medicine and molecular imaging. Sadly, Dr. Gambhir passed away far too early and was not able to contribute to the foreword to this new and updated edition, hence my authorship.

This is a remarkable effort by Dr. Vallabhajosula to cover, in a consistent manner, the entire spectrum of the field of nuclear medicine. So often, textbooks are written by multiple authors and the presentations, though expert, are not always well integrated. This book has the clear fingerprints of a true expert who has nearly five decades of experience in the field with relevant experiences in virtually all aspects of the discipline.

While the author is well known and respected in the fields of radiopharmacy and radiopharmaceuticals, he carefully covers the remarkable spectrum of technologies needed to deliver successful nuclear medicine imaging and treatments. From "A" toms to high "Z" materials to detect photons, Dr. Vallabhajosula has it covered. This is a great read for anyone interested in a comprehensive, but not exhaustive, review of nuclear medicines breadth with sufficient depth and referencing to guide further study. It is obvious that Dr. Vallabhajosula loves the field of nuclear medicine, and the manuscript reflects this love, and continued curiosity for the field. It should serve to bring new scientists into the field. The author's enthusiasm is apparent on each page and chapter.

It is an incredibly exciting time for nuclear medicine. While nuclear imaging and radiopharmaceutical therapy have been around for well over half a century, in my long experience in nuclear medicine, this is the most exciting time ever. There have been many patients, from newborns to seniors, positively impacted through nuclear medicine imaging. FDG PET/CT is now the preferred diagnostic and follow-up test in many patients with cancer; additionally it is now widely used to detect infection and inflammation. The explosion in PSMA targeting for diagnosis and therapy with newly approved diagnostic and therapeutic agents has brought renewed excitement to the field. There has also been substantial investment given the favorable results from targeted radiopharmaceutical therapies. The excitement with the newer alpha emitters is palpable and I am confident we are now moving from "improving survival" to "curing cancer." Expanding these methods more

broadly will be the future of our field with major investments from increasingly large, as well as small, innovative pharmaceutical companies. I believe radiopharmaceutical therapy is now the fifth arm of cancer therapy along with surgery, chemotherapy, external beam irradiation, and immunotherapy.

It is also a great time to use nuclear medicine techniques to interrogate brain health. With the recent approval of two antibody drugs to remove amyloid plaques from the brain and preserve cognition, the exciting opportunities in nuclear neurology are highlighted. The opportunities in brain imaging are massive. The projected growth in nuclear imaging of the brain, to guide treatments, will impact a huge population who could benefit from the procedures. In addition, fundamental studies of brain health with PET are pivotal for our understanding of the function of the brain, especially in aging, dementia, movement disorders, and psychiatric conditions.

An excellent review of cardiac imaging is provided as well. This is an area of great opportunity as we can now precisely measure cardiac blood flow and flow reserve, especially with PET. Similarly with nuclear methods we can now detect and guide treatment of amyloid cardiomyopathies, and detect previously undetectable inflammatory processes, and infections among other interrogations.

Dr. Vallabhajosula describes this book, in effect, as a "labor of love." Having been introduced to the field personally over four decades ago, falling in "love" with nuclear medicine is not a unique experience. I'm sure readers of this comprehensive yet approachable text will gain an increasing affection, possibly blossoming into a long-term relationship, or even "love" with nuclear medicine.

Department of Radiology   Richard L. Wahl, MD, FACR
Mallinckrodt Institute of Radiology,
Professor of Radiology and Radiation
Oncology, Washington University in
St Louis School of Medicine
St. Louis, MO, USA

Preface to the First Edition

Everything is determined, the beginning as well as the end, by forces over which we have no control. It is determined for the insect, as well as for the star. Human beings, vegetables, or cosmic dust, we all dance to a mysterious tune, intoned in the distance by an invisible piper.

Albert Einstein

In my life, the invisible piper has long been and will continue to be "science." Indeed, in 1967, during my second year in pharmacy school, while reading general books on science, I first learned that an unstable atom emits radiation, which might be used as a beacon or a signal for detecting the exact location of that atom. This initial introduction to atomic physics had a significant impact on my view of the universe and all that is within and has shaped my academic and scientific career in a way I could not have foreseen, then.

The discipline of nuclear medicine has tremendously enriched my professional and personal life and several people have been instrumental in shaping my destiny. Professor Walter Wolf, who ignited my research interests in the development of radiopharmaceuticals, Professor Henry Wagner, Jr., the ambassador of nuclear medicine, Professor Michael Phelps, the pioneer, and visionary of PET, in particular, have been my inspirational and intellectual gurus. Also, Professor Sanjiv Sam Gambhir, one of the founders of molecular imaging as a scientific discipline in diagnostic radiology, has been a continuous source of inspiration not only to me but to a whole new generation of young investigators. Words cannot express my gratitude to Professor Stanley J. Goldsmith, who for almost three decades has instigated many challenging discussions, supported me in all my scientific endeavors, and is now a part of my family.

Molecular imaging is a fascinating and important technology in radiology that grows more diverse every day. Imaging based on radioisotopes is the major theme of this book and emphasizes both the basic and clinical science of nuclear medicine, based exclusively on radiopharmaceuticals for PET and SPECT. This book grew out of many lectures and my own struggles to more fully understand this subject. My goal in writing this book was not to discuss, in depth, the chemistry of radiopharmaceuticals. Instead it was my intention to provide a broad view of clinical applications in molecular imaging and, thereby, make the readers better understand and appreciate the importance of radiopharmaceutical design and development in the optimization of molecular imaging technology. Finally, although Chapter 2, which provides a history of the atom, is not necessarily relevant to the practical and clinical applica-

tions of molecular imaging, it is my way of paying tribute to those extraordinary scientists who have systematically studied "nature" and demonstrated the reality of atoms.

It is impossible to acknowledge every technologist, scientist, and student, who has contributed to my understanding of nuclear medicine. However, I especially thank Ms. Helena Lipszyc not only for working with me on countless research projects, but most of all for her friendship. I also express my gratitude to Dr. Harry M. Lander, Associate Dean for Research at Weill Cornell Medical College, for encouraging me to write this book.

Also, I greatly appreciate the support of the editorial staff of Springer-Verlag and, especially, thank Ms. Dörthe Mencke-Bühler, Ms. Wilma McHugh, and Mr. Saravanan Thavamani. Finally, this book could not have been completed without the love, support and encouragement of my wife, Brigitte (affectionately called Shanthi), who has read every word of the manuscript and made countless corrections.

New York, NY, USA   Shankar Vallabhajosula, PhD
May 2009

Preface to the Second Edition

Look deep into nature, and then you will understand everything better.
Albert Einstein

The primary goal of targeted radionuclide therapy (TRT) is to fight cancer cells with more precision and with less side effects. TRT is based on therapeutic radiopharmaceuticals that are radiolabeled molecules consisting of a target-specific moiety, such as peptides, low molecular weight ligands, or monoclonal antibodies labeled with an appropriate alpha or beta emitting radionuclide designed to deliver therapeutic doses of ionizing radiation to specific disease sites. The continuing progress in biotechnologies over the last couple of decades opened avenues to a new management of many diseases, switching from a *population treatment approach* to the concept of *personalized medicine or precision medicine*. Theranostics in nuclear medicine is a molecular precision medicine approach to treating cancer, using similar (or same) molecules for both molecular imaging (based on PET or SPECT) and TRT.

The first edition of this book, published in 2009, focused primarily on the initial development of molecular imaging (MI) based on PET and SPECT radiopharmaceuticals. Since that time there has been tremendous interest and progress in the development of target-specific radiopharmaceuticals (TSRP) for radionuclide molecular imaging (RMI) and TRT.

The second edition was, specifically, designed to revise and update several chapters related to the development of FDA-approved PET and SPECT radiopharmaceuticals. In addition, six new chapters (Chaps. 17–22) were added to provide an extensive review of the basic concepts and clinical applications of therapeutic radiopharmaceuticals for TRT. While it is beyond the scope of this book to cover the entire field of radiopharmaceutical research and development in the last 15 years, the focus of this book is primarily to provide a broad overview of RMI and TRT, and to specifically describe the chemistry of radiopharmaceuticals in clinical use.

I want to thank all the nuclear medicine physicians, oncologists, scientists, and technologists at Weill Cornell Medicine and New York Presbyterian Hospital. Special thanks to Professor Stanley J. Goldsmith who, for almost four decades, has been my major research collaborator. I also want to give special thanks to several oncologists (Profs. Neil H. Bander, Scott T. Tagawa, John P. Leonard, and Morton Coleman) who believed in TRT, supported me, and collaborated with me for the last 25 years. I have no words to express my

New York, NY, USA   Shankar Vallabhajosula, PhD
February 2023

Contents

About the Author

Shankar Vallabhajosula attended high school in the small town of Bobbili, Andhra Pradesh, India. He graduated from Andhra University with a BS in Pharmacy and an MS in Pharmaceutical analysis. After migrating to the Unites States, Vallabhajosula obtained his PhD in 1980 in Biomedicinal Chemistry and Radiopharmacy from the University of Southern California. After receiving the doctorate, he first worked at Mount Sinai Medical Center in New York and since 1997 has been a Professor of Radiochemistry and Radiopharmacy in Radiology at Weill Cornell Medicine and New York Presbyterian Hospital. Dr. Vallabhajosula was the President, and Chief Scientific Officer at NCM USA Bronx LLC from 2018 through 2021. He is now Professor Emeritus in Radiochemistry and Radiopharmacy in the Department of Radiology at Weill Cornell Medicine, Cornell University, New York, NY.

Molecular Imaging and Targeted Radionuclide Therapy: Introduction

1

We really are not treating individuals yet; we are treating with therapies tailored for a population. By having the next generation of therapies customized for a given individual's genetic makeup we have the opportunity to truly move towards personalized medicine. (Sam Gambhir, May 2005)

1.1 Nuclear Medicine

Nuclear medicine can be defined quite simply as the use of radioactive materials for the diagnosis and treatment of patients, and the study of human disease [1]. Chemistry is the language of health and disease since the entire body is a collection and vast network of millions of interacting molecules. If the definition of the disease is molecular, the diagnosis is also molecular. Because the treatment of many diseases is chemical, it becomes increasingly appropriate that the chemistry be the basis of diagnosis and the planning and monitoring of a specific treatment. Nuclear medicine, therefore, is a medical specialty that is based on the examination of the regional chemistry of the living human body.

In the 1920s, George de Hevesy (Fig. 1.1) coined the term *radioindicator* or *radiotracer* and introduced the *tracer principle* in biomedical sciences. One of the most important characteristics of a true tracer is that it can facilitate the study of the components of a homeostatic system without disturbing their function. In the late 1920s, Hermann Blumgart and Soma

Fig. 1.1 George de Hevesy. The Nobel Prize in Chemistry, 1943

Weiss, two physicians at the Massachusetts General Hospital, injected solutions of radium-C (^{214}Bi) into the veins of healthy persons, and patients with heart disease to study the velocity of blood. Due to their pioneering work in nuclear medicine, Hevesy is regarded as the father of nuclear medicine, while Blumgart came to be known as the father of diagnostic nuclear medicine.

In the 1930s, the discovery of artificial radioactivity by Irene Curie and her husband Frederic Joliot, and the discovery of the cyclotron by Ernest Lawrence, opened the door to produce radiotracers of every element, thus enabling investigators to design radiotracers for the study of specific biochemical processes. Following the detection of radioactivity with the Geiger counter, it was discovered that thyroid accumulated ^{131}I as radioiodide. Consequently, it was soon realized that ^{131}I can be used to study abnormal thyroid metabolism in patients with goiter and hyperthyroidism. More specifically, in patients with thyroid cancer, distant metastases were identified by scanning the whole body with the Geiger counter. The names *radioisotope scanning* and *atomic medicine* were introduced to describe the medical field's use of radioisotopes for the purpose of diagnosis and therapy. The era of nuclear medicine, as a diagnostic specialty began following the discovery of the *gamma camera* based on the principle of scintillation counting, first introduced by Hal Anger in 1958. Since then, nuclear medicine has dramatically changed our view of looking at disease by providing images of regional radiotracer distributions and biochemical functions. Over the last four decades, several hundreds of radiopharmaceuticals have also been designed and developed to image the structure and function of many organs and tissues.

1.2   Molecular Medicine

At the present time, the precise definition of the *disease* is as difficult as defining what exactly *life* is. Defining disease at the cellular and molecular level, however, is much easier than defining disease at the level of an individual. Throughout the history of medicine, two main concepts of disease have been dominant [2]. The *ontological* concept views a disease as an entity that is independent, self-sufficient, and runs a regular course with a natural history of its own. The *physiological* concept defines disease as a deviation from normal physiology or biochemistry; the disease is a statistically defined deviation of one or more

functions from those of healthy people under circumstances that are as close as possible to that of a person of the same sex and age of the patient. The term *homeostasis* is used by physiologists to mean maintenance of static, or constant, conditions in the internal environment by means of positive and negative feedback of information. Approximately 56% of the adult human body is fluid. Most of the fluid is intracellular; however, one-third is extracellular, which is in constant motion throughout the body and contains the ions (sodium, chloride, and bicarbonate) and the nutrients (oxygen, glucose, fatty acids, and amino acids) needed by cells for the maintenance of life. Claude Bernard (1813–1878) described extracellular fluid as the internal environment of the body and hypothesized that the same biological processes that make life possible are also involved in disease. In other words, the laws of disease are the same as the laws of life. All the organs and tissues of the body perform functions that help maintain homeostasis. As long as the organs and tissues of the body perform functions that help maintain homeostasis, the cells of the body continue to live and function properly.

At birth, molecular blueprints collectively make up a person's *genome* or *genotype,* which is translated into cellular structure and function. A single *gene* defect can lead to biochemical abnormalities that produce many different clinical manifestations of disease (or *phenotypes*), a process referred to as *pleiotropism*. Several gene abnormalities can result in the same clinical manifestations of disease, a process called *genetic heterogeneity*. Thus, diseases can be defined as abnormal processes as well as abnormalities in molecular concentrations of different biological markers, signaling molecules, and receptors [3].

In 1839, Theodor Schwann discovered that all living organisms are made up of discrete cells. In 1858, Rudolph Virchow observed that a disease cannot be understood unless it is realized that the ultimate abnormality must lie in the cell [4]. Virchow correlated disease with cellular abnormalities as revealed by chemical stains and, thus, founded the field of cellular pathology. He also aptly defined pathology as physiology with obstacles.

Most diseases begin with a cell injury that occurs if the cell is unable to maintain homeostasis. Since the time of Virchow, gross pathology and histopathology have been a foundation of the diagnostic process and the classification of diseases. Traditionally, the four aspects of a disease process that form the core of pathology are etiology, pathogenesis, morphologic changes, and clinical significance [5]. The altered cellular and tissue biology, and all forms of loss of function of tissues and organs, are, ultimately, the result of cell injury and cell death. Therefore, knowledge of the structural and functional reactions of cells and tissues to injurious agents, including genetic defects, is the key for understanding the disease process. Disease may be considered a genetic or environmental reprogramming of cells to gain or lose specific functions that are characteristic of disease. Currently, diseases are defined and interpreted in molecular terms and not just with general descriptions of altered structure.

Pathology is evolving into a bridging discipline that involves both basic science and clinical practice. More specifically, pathology is devoted to the study of the structural and functional changes in cells, tissues, and organs that underlie diseases [5]. Molecular, genetic, microbiologic, immunologic, and morphologic techniques are also helping us to understand both, the ontological and physiological causes of disease. In molecular medicine, normal and disease states are defined at the cellular and molecular levels [6]. Therapeutic drugs are designed based on these definitions of disease and are being used to treat diseases by correcting abnormal cellular or molecular processes.

1.3 Molecular Imaging

In the past, much of biological and medical imaging was driven by anatomy-based imaging or structural imaging, such as computed tomography (CT) and magnetic resonance imaging (MRI). The field of nuclear medicine, by contrast, has focused on studying molecular events in living subjects, based on radiotracers, and is regarded as functional or physiologic imaging [7, 8]. This traditional distinction between structural and functional imaging has increasingly become blurred by CT, MRI, and other techniques that provide both functional and structural information [9].

Molecular imaging (MI) aims to integrate patient-specific and disease-specific molecular information derived from diagnostic imaging studies [10]. The goal of MI is the noninvasive localization and quantification of certain molecular events in vivo, including endogenous or exogenous gene expression, signal transduction, protein–protein interaction, and transcriptional regulation. Among a variety of possible target applications, the use of MI will lead to further insights into the molecular pathology of animal models of human diseases, as well as to the development of new molecular-targeted drugs and to the design and implementation of improved patient-tailored therapies.

Most, but not all, of the functional imaging studies performed in traditional nuclear medicine can be regarded as MI. The use of ^{123}I sodium iodide to assess thyroid function, and imaging somatostatin receptor (SSTR)-positive neuroendocrine tumors using ^{111}In-DTPA-Octreotide (OctreoScan®) or ^{68}Ga-DOTATATE (NetSpot) are clearly the best examples of MI. In contrast, ^{99m}Tc-DTPA and ^{99m}Tc-MAG3, which are used to study kidney function, are not appropriate examples of MI procedures.

Although MI is not necessarily new, what is new is "molecular and anatomic correlation." Positron emission tomography (PET) is a highly sensitive, noninvasive technology that is ideally suited for imaging cancer biology based on [^{18}F] Fluorodeoxyglucose (FDG), a glucose analog and substrate for the enzyme *hexokinase*. With the introduction of "hybrid imaging" techniques which combine, for example, FDG-PET and CT or FDG-PET and MRI, and thus providing anatomic and functional or molecular information in one image, a new era of MI has arrived. Clearly, this will have implications for the education of not only nuclear physicians, but also radiologists. More specifically, the former will need to learn cross-sectional anatomy and the latter the concepts of tracer techniques and functional imaging.

MI is also likely to lead to a further blurring of the distinction between diagnosis and treatment and to a paradigm shift to early diagnosis that will lead to image-guided, individualized molecular therapy. Further, biomarkers will be able to be imaged and quantified to provide early evidence of the efficacy of a specific treatment.

1.3.1   Definitions

In 2005, the Radiological Society of North America (RSNA) and the Society of Nuclear Medicine (SNM) jointly convened a workshop on MI [11]. At that time, the group developed the following definition of MI, successfully testing it against the existing variety of imaging tools available in humans and in animal experimental contexts:

> MI techniques directly or indirectly monitor and record the spatiotemporal distribution of molecular or cellular processes for biochemical, biologic, diagnostic, or therapeutic applications.

The members of the Molecular Imaging Center of Excellence (MICoE) Standard Definitions Task Force recently developed the following four standard definitions and terms that will serve as the foundation of all communications, advocacy, and education activities for MICoE and the Society of Nuclear Medicine (SNM) [12].

- MI is the visualization, characterization, and measurement of biological processes at the molecular and cellular levels in humans and other living systems. To elaborate, MI typically includes two- or three-dimensional imaging, as well as quantification over time. The techniques used include radiotracer imaging/nuclear medicine, MR imaging, MR spectroscopy, optical imaging (OI), and ultrasound.
- MI agents are "probes used to visualize, characterize, and measure biological processes in living systems. Both endogenous molecules and exogenous probes can be molecular imaging agents." MI instrumentation comprises tools that enable the visualization and quantification in space and over time of signals from MI agents.

- MI quantification is the determination of regional concentrations of MI agents and biological parameters. Further, MI quantification provides measurements of processes at the molecular and cellular levels. This quantification is a key element of MI data and image analysis, especially for inter- and intrasubject comparisons.
- MI has enormous relevance for patient care: it reveals the clinical biology of the disease process; it personalizes patient care by characterizing specific disease processes in different individuals; and it is useful in drug discovery and development, for example, for studying pharmacokinetics and pharmacodynamics.

MI aims to integrate patient-specific and disease-specific molecular information with traditional anatomical imaging readouts. The information provided by this field may ultimately lead to noninvasive or minimally invasive molecular diagnostic capabilities, better clinical risk stratification, more optimal selection of disease therapy, and improved assessment of treatment efficacy. Development of an MI strategy for a particular disease requires addressing four key questions [10]:

- Is there a molecular target relevant to the disease of interest?
- Once a target is selected, is there a high-affinity ligand (for example, a peptide, engineered antibody, or another small molecule) that will bind to the target?
- What is the appropriate MI system to provide the required spatial resolution, sensitivity, and depth penetration for the disease?
- For a given imaging system, can an agent be synthesized to detect the desired molecular target?

MI has the potential to improve the understanding of disease in several biological models and systems. MI targets should be able to define the disease status earlier than conventional imaging methods, identify the underlying molecular events in disease initiation and progression, distinguish between aggressive and indolent disease

states, and represent downstream targets in a well-characterized molecular network or pathway.

1.3.2 Molecular Imaging Technologies

A wide range of technologies are available for noninvasive in vivo MI studies [10, 13–17]. Various technical features of several MI technologies are summarized and compared in Table 1.1.

1.3.2.1 Magnetic Resonance Imaging

The primary advantage of MRI as an MI technique is its ability to provide soft tissue and functional information by exploiting proton density, perfusion, diffusion, and biochemical contrasts [18]. MRI offers two main advantages over nuclear imaging techniques: higher special resolution (<1 mm) and the ability to obtain anatomic, physiologic, and metabolic information in a single imaging session. In addition, MRI offers good depth penetration, like PET and CT [10]. MR scanners are frequently identified by their magnetic field strength expressed in tesla (1 T = 10,000 gauss). With higher T scanners, the magnet is stronger, both in general and within the bore of the machine. Most MR scanners are 1.5 T or 3.0 T, and more recently, up to 7.0 T. Increasing MRI field strength is designed to increase the signal-to-noise and contrast-to-noise ratio, which permits reduction in overall scan length and improvement in spatial resolution. The magnetic field strength for small-animal imaging systems is also increasing, with 9.4 T magnets becoming standard. These systems produce microscopic resolution (tens of micrometers range) images in small-animal models and allow for the analysis of physiologic and molecular markers [19]. A number of paramagnetic (e.g., gadolinium)- and super paramagnetic (e.g., iron oxide)-based MI agents have been tested for preclinical and clinical MI applications. The primary disadvantage of MRI is its inherently low sensitivity for the detection of targeted agents compared with nuclear imaging techniques.

1.3.2.2 Optical Imaging

One of the most successful MI modes for preclinical studies is optical imaging, which is based on the detection of light photons after their interaction with the tissue. The two major OI methods are bioluminescence imaging (BLI) and fluorescence imaging (FLI).

BLI requires the cellular expression of an enzyme known as *luciferase* that is responsible for making some insects, jellyfish, and bacteria glow [20]. The gene for this enzyme is incorporated into the DNA of cells in the animal models of disease. When an appropriate substrate (such as *D-luciferin*) interacts with the enzyme, a sub-

Table 1.1 Noninvasive in vivo molecular imaging modalities

Imaging modality	Form of energy used	Spatial resolution (mm)		Acquisition time/frame	Probe mass required	Sensitivity of detection	Depth of penetration
		Clinical	Animal	(s)	(ng)	Mol/l	(mm)
PET	Annihilation photons	3–8	1–3	1–300	1–100	10^{-11}–10^{-12}	>300
SPECT	γ-photons	5–12	1–4	60–2000	1–1000	10^{-10}–10^{-11}	>300
CT	X-rays	0.5–1	0.03–0.4	1–300	–	–	>300
MRI	Radiofrequency waves	0.2–0.1	0.025–0.1	50–3000	10^3–10^6	10^{-3}–10^{-5}	>300
Ultrasound	High-frequency sound waves	0.1–1.0	0.05–0.1	0.1–100	10^3–10^6	–	1–200
BLI	Visible to infrared light	–	3–10	10–300	10^3–10^6	10^{-13}–10^{-16}	1–10
FLI	Visible to infrared light	–	2–10	10–2000	10^3–10^6	10^{-9}–10^{-11}	1–20

tle glow of visible light (400–700 nm with energies of 1.5–3.0 eV) called *bioluminescence* (BL) is emitted. The detection of BL can be used to monitor the cellular and genetic activity of every cell that expresses the luciferase enzyme. The in vivo applications of BLI systems are most useful for small mouse models of disease since most of the organs of interest are found no more than 1–2 cm deep within the tissue. To obtain the best depth sensitivity, the camera system should be particularly sensitive to the red and near-infrared (NIR) portion of the BL emission spectrum (700–900 nm).

FLI is capable of imaging the surface distribution of FL signals. FL molecules may be genetically engineered into a mouse, for example by incorporating the gene for an FL protein as a reporter gene, or by using fluorophores or fluorescent particles known as *quantum dots* to label a biologically interesting molecule. FLI can be performed in both live and fixed cells and no substrate is required. *Fluorochromes* can be coupled to peptides and antibodies and fluorescence signals may be activatable or switched on and off by the presence or absence of specific molecules or molecular events, which can help to further reduce the background signal [21]. In contrast, the generation of BL is specific to cells that contain the luciferase reporter gene and is thus of limited use for studying genetically manipulated cells, transgenic mice, or infectious agents, such as bacteria or viruses. FLT images molecular processes in 3D, by studying the distribution of molecular probes tagged with fluorescent proteins, preferably emitting in the NIR for better tissue transmission.

Although the penetration of light through the tissue is a limitation for all optical imaging methods, attenuation and autofluorescence, however, are minimized in the near-infrared window, permitting deep tissue imaging up to 10 cm. The advantages of FI methods include improved relative sensitivity, high resolution (which may be in the submillimeter range when imaged endoscopically), and the availability of a variety of imaging reporters and signal amplification strategies. In addition, OI offers a convenient way to co-register surface anatomical information with molecular information.

1.3.2.3 Ultrasound Imaging

Molecular ultrasound imaging or targeted contrast-enhanced ultrasound (CEUS) offers high spatial resolution (<1 mm) and can provide excellent anatomical information for co-registration with molecular information. Ultrasound contrast agents are conjugated to ligands that bind with specific biomarkers in the areas of interest which can then be quantified using ultrasound technology. A number of targeted MI agents have been designed for ultrasound imaging (UI) using microbubbles, liposomes, or perfluorocarbon emulsions as scaffolds [22–24]. An important limitation of ultrasound for MI studies is the relatively large size of the imaging agent particles (<250 nm), which can restrict tissue penetration and, thus, limit application to vascular targets.

1.3.2.4 PET and SPECT

Nuclear imaging approaches, which include PET and SPECT, have the advantages of high intrinsic sensitivity and unlimited depth penetration. PET has the additional advantages of being fully quantitative and providing higher spatial resolution than SPECT. In addition, hundreds of radiotracers based on a wide variety of radionuclides decaying due to β^+ or γ emission have been developed and tested in animal models and clinical studies documenting their potential utility as MI probes. With these techniques, the mass of the MI radiotracers is so small (ng or μg) that the toxicity of the administered dose is never an issue. In a typical FDG-PET study, the mass of FDG administered is <20 μg. Similarly, with somatostatin receptors (SSTR) imaging, the mass of PET or SPECT radiotracer administered is <10 μg (<nmol); however, the spatial resolution of both these techniques is much less compared to that of CT and MRI. The fusion of molecular information of PET and SPECT with high-resolution anatomical detail from CT or MRI techniques, however, is playing an increasing role in routine clinical MI procedures. As of December 2021, the FDA has approved 20 PET/SPECT radiopharmaceuticals for routine clinical use (Table 1.2). This is a remarkable progress in the development of MI studies.

The [18F]FDG-PET scans based on glucose metabolism of tumor tissue have demonstrated

Table 1.2   FDA-approved PET and SPECT radiopharmaceuticals for MI studies

	Chemical Name	Trade Name	Indications	
1	^{82}Rb chloride	Cardiogen-82®, Rubi-fill®	To evaluate regional myocardial perfusion	1989
2	[^{18}F]Fludeoxyglucose (FDG)		To assess abnormal glucose metabolism in oncology To assess myocardial hibernation To identify foci of epileptic seizures	2000
3	[^{13}N]Ammonia		To evaluate regional myocardial perfusion	2000
4	[^{18}F]Sodium Fluoride		To delineate areas of altered osteogenesis	2000
5	[18F]Florbetapir	Amvid™	To estimate β-amyloid neuritic plaque density in patients with cognitive impairment	2012
6	[^{18}F]Florbetaben	Neuraceq™	To estimate β-amyloid neuritic plaque density in patients with cognitive impairment	2014
7	[^{18}F]Flutemetamol	Vizamyl™	To estimate β-amyloid neuritic plaque density in patients with cognitive impairment	2013
8	[^{18}F]Flortaucipir	Tauvid™	To estimate the density and distribution of aggregated tau neurofibrillary tangles (NFTs)	2020
9	[^{18}F]Piflufolastat	Pylarify®	To detect PSMA-positive lesions in prostate cancer	2021
10	[^{11}C]Choline		To help identify potential sites of prostate cancer recurrence	2012
11	[^{18}F]Fluoroestradiol	Cerianna™	For the detection of estrogen receptor-positive lesions in patients with breast cancer	2020
12	[^{18}F]Fluciclovine	Auximin™	Prostate cancer recurrence	2016
13	[^{18}F]Fluorodopa		To visualize dopaminergic nerve terminals in the striatum in patients with suspected parkinsonian syndromes (PS)	2020
14	^{68}Ga-DOTATATE	NETspot	For localization of SSTR-positive NETs	2016
15	^{64}Cu-DOTATATE	Detectnet	For localization of SSTR-positive NETs	2020
16	^{68}Ga-DOTATOC		For localization of SSTR-positive NETs	2019
17	^{68}Ga-PSMA-HBED-CC		PSMA-positive lesions in prostate cancer	2020
18	^{111}In-pentetreotide	Octreoscan™	For localization of SSTR-positive NETs.	1988
19	[^{123}I]Iobenguane	AdreView™	For the detection of primary or metastatic pheochromocytoma or neuroblastoma	2008
20	[^{123}I]Ioflupane	DaTscan™	For dopamine transporter visualization patients with suspected Parkinsonian syndromes (PS)	2011

not only extensive clinical utility in the detection of several types of cancers, but also in the monitoring and assessment of treatment responses (Fig. 1.2). ^{68}Ga-PSMA-PET/CT scans (Fig. 1.3) are becoming increasingly useful in the detection of metastatic lesions in patients with prostate cancer compared to the standard ^{99m}Tc-MDP bone scans. Somatostatin receptor (SSTR) imaging
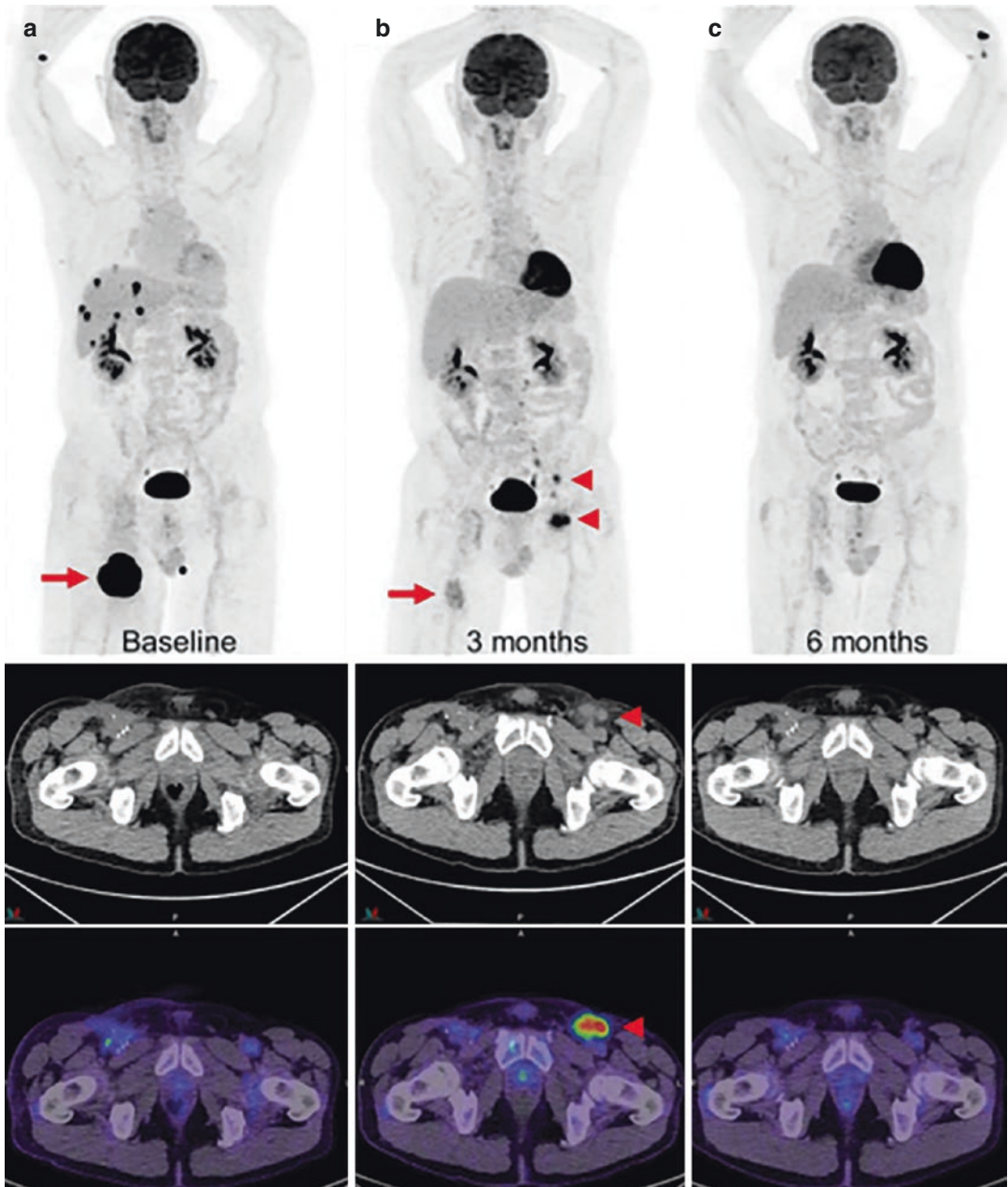
Fig. 1.2 [^{18}F]FDG-PET/CT: New lymph nodes in draining basin of regressing metastasis. (A and B) Metastatic melanoma (**a**, arrow) after 4 cycles of combination ipilimumab and nivolumab demonstrated marked regression of right thigh lesion and complete metabolic response of multiple liver and adrenal metastases (**b**, arrow); however, new FDG–avid lymph nodes were noted in left inguinal and iliac regions (**b**, arrowheads). (**c**) Biopsy of these lymph nodes shows reactive T cells that resolved on subsequent scan [25]
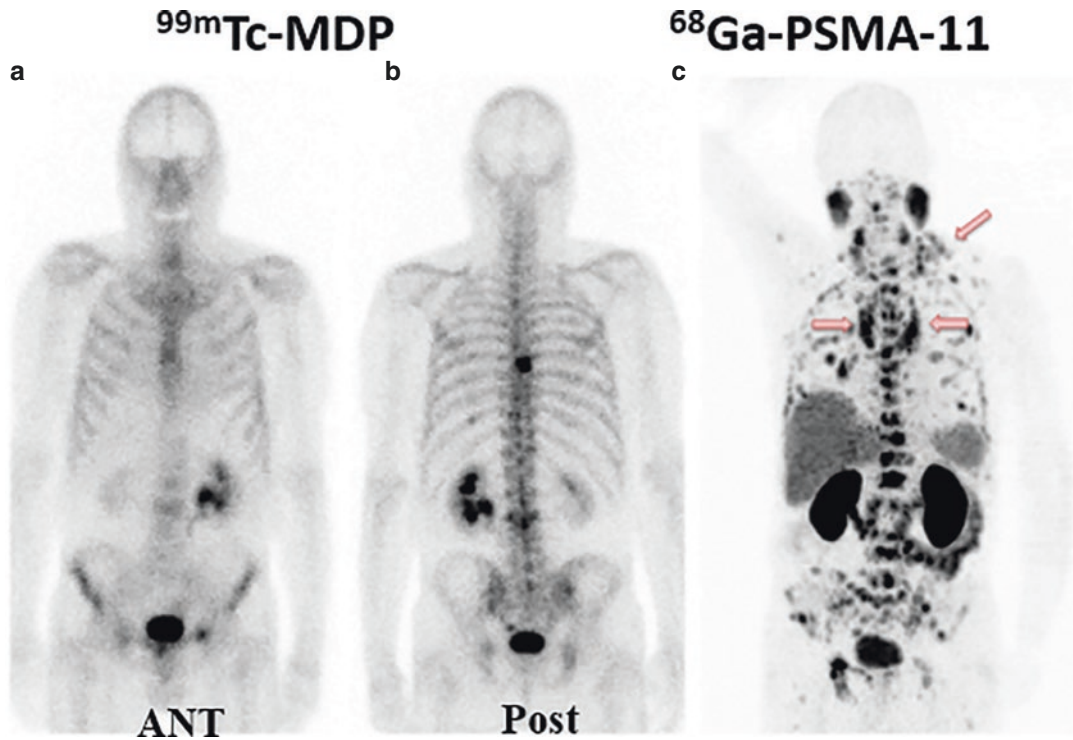
Fig. 1.3 ^{99m}Tc-MDP bone scan vs. ^{68}Ga-PSMA-PET: A 72-y-old patient with hormone and chemorefractory prostate cancer who underwent bone scintigraphy was referred for ^{223}Ra therapy. PSMA PET/CT (**c**) showed diffuse bone and bone marrow metastases, most not detectable by bone scan (**a**, **b**). Apart from bone metastases, there were many lymph node metastases, for example, mediastinal and left clavicular (pink arrows). PSA level at time of PET imaging was 630 ng/mL, ALP in reference range. Based PSMA scan, patient was not a candidate for 223Ra therapy, but underwent radioligand therapy with ^{177}Lu-PSMA-617 [26]

with ^{68}Ga-Dotatate illustrates the power and significance of PET/CT studies to assess the SSTR-positive lesions compared to SPECT imaging with Octreoscan™ (Fig. 1.4). In brain tumors, an amino acid analog, [^{11}C]methionine, and [^{18}F]fluorothymidine (FLT) provide more specific tumor identification than glucose metabolic images with FDG (Fig. 1.5). In the area of neuropsychiatric diseases, molecular imaging with PET and SPECT has shown significant potential in clinical diagnosis and disease management. While FDG-PET is useful for the differential diagnosis of Alzheimer's disease (AD) from other dementias, several PET radiopharmaceuticals, designed to image the amyloid burden and Tau protein in patients with AD, have been FDA approved and are in clinical use. (Fig. 1.6) After 3 decades of clinical investigations, [^{18}F]FDOPA is finally FDA approved and indicated to visualize dopaminergic nerve terminals in the striatum (Fig. 1.7) for the evaluation of adult patients with suspected Parkinsonian syndromes (PS).

1.3.2.5 Multimodality Molecular Imaging

Multimodality imaging has become an attractive strategy for in vivo imaging studies owing to its ability to provide accurate anatomical and functional information simultaneously [31–36]. The combination of CT and PET was introduced commercially in 2001, followed by CT and SPECT in 2004, and PET and MRI in 2008.

At present, a variety of different MI techniques have their advantages, disadvantages, and limitations. To overcome these shortcom-
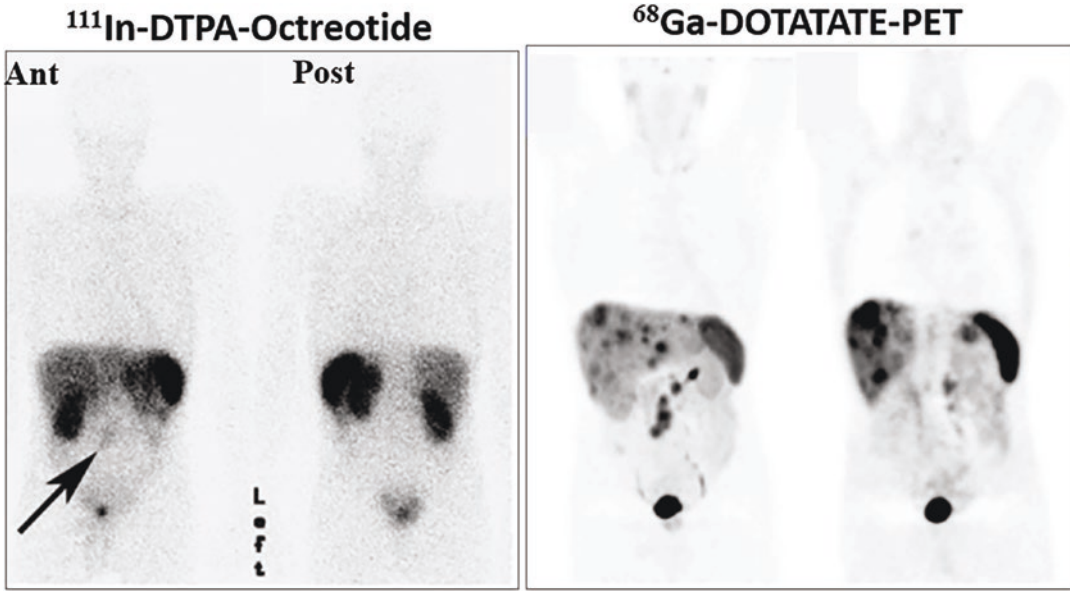
Fig. 1.4 Comparison of ⁶⁸Ga-Dotatate-PET with ¹¹¹In-DTPA-octreotide in a patient with low-grade metastatic midgut neuroendocrine tumor (NET). Anterior and posterior whole-body planar ¹¹¹In-DTPA-octreotide scintigraphy shows low-grade mesenteric metastases but no liver metastases. ⁶⁸Ga-DOTATATE PET shows multiple metastases in liver and mesentery [30]
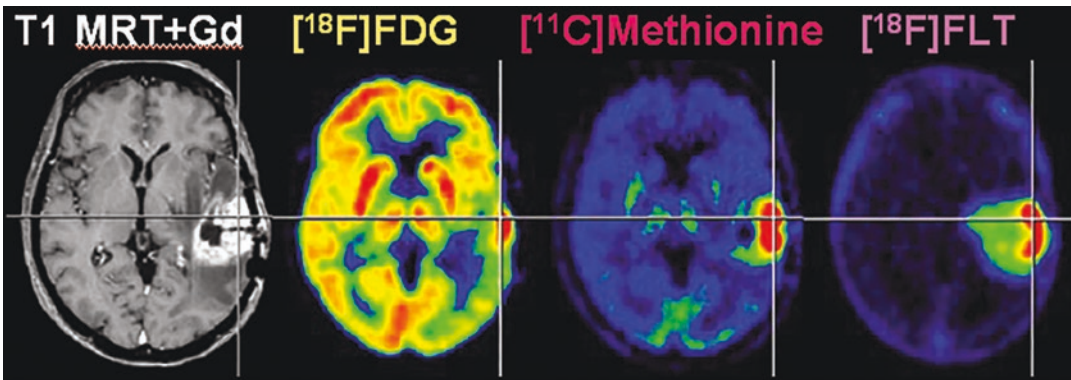
Fig. 1.5 Relative advantages of MR and PET imaging techniques to detect different biochemical processes in brain tumors (gliomas). MRI detects alterations of the blood–brain barrier and the extent of peritumoral edema, FDG-PET shows glucose metabolism, while increased cell proliferation can be imaged with specific tracers, such as [¹⁸F]FLT and [¹¹C]methionine [27]
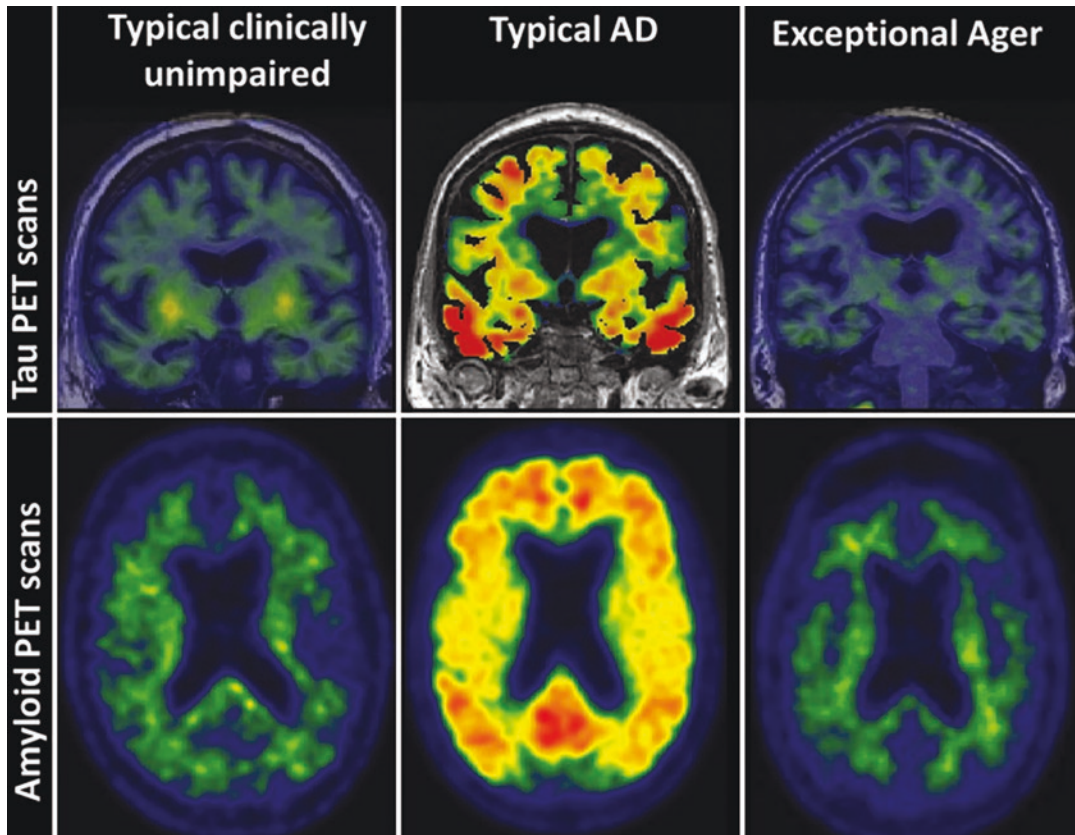
Fig. 1.6 Amyloid PET and Tau PET scans in a typical clinically unimpaired, typical AD, and an exceptional ager (>85-year-old APOE4 carrier) [28]
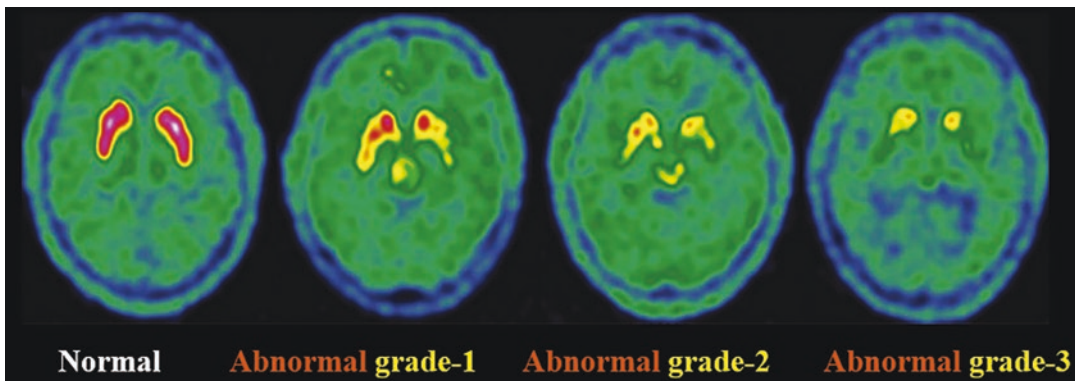
Fig. 1.7 [18F]FDOPA-PET Representative example of Benamer grades, adapted to FDOPA uptake in patients with parkinsonian syndromes. PET scans shown in the anterior commissure-posterior commissure plane and normalization of color scale on the basal ganglia [29]

ings, it may be beneficial to combine two or more detection techniques to create a new imaging mode, such as multimodal molecular imaging, to obtain a better result and more information regarding monitoring, diagnosis, and treatment [17, 37]. Several dual-purpose imaging agents were developed. For example, ^{64}Cu-labeled magnetic nanoparticles as a dual-modality PET/MR imaging agent were developed [38]. The first small-molecule-based $\alpha_v\beta_3$-targeted NIR-II/PET probe ^{68}Ga-SCH2 was evaluated in tumor-bearing mice. Excellent imaging properties such as good tumor uptake, high tumor contrast and specificity, tumor delineation, and image-guided surgery were achieved in the small-animal models [39]. The development of multimodality probes is challenging.

The use of multimodal imaging probes or biomarkers in a single molecule or particle to characterize the imaging subjects such as disease tissues certainly provides us with more accurate diagnosis and promotes therapeutic accuracy. A limited number of multimodal imaging probes are being used in preclinical and potential clinical investigations. The development of multimodal PET/MR and SPECT/MR imaging probes is an emerging research field and the challenges for designing multimodal probes have been addressed by many investigators to offer some future research directions for this novel interdisciplinary research field [37].

1.4   Radiation Therapy

Radiation therapy or radiotherapy is the medical use of high-energy electromagnetic waves or particles (such as X-rays, γ-rays, electron beams, or protons), generally as part of cancer treatments to control malignant cells. Radiation therapy works by damaging the DNA of cancerous cells. This damage is due to either direct or indirect ionization of the atoms which make up the DNA molecule. Indirect ionization happens as a result of the ionization of water, forming free radicals, which then damage the DNA. Charged particles such as

protons and α particles can cause direct damage to cancer cell DNA by causing double-stranded DNA breaks. Because cells have mechanisms for repairing single-strand DNA damage, double-stranded DNA breaks prove to be the most significant technique to cause cell death. Radiation therapy can be given in three ways:

- *External irradiation*: External beam radiation therapy (EBRT or XRT) or teletherapy can be carried out using a γ-beam from a radioactive cobalt-60 source, or high-energy X-rays from linear accelerators to direct electromagnetic rays from outside the body into the tumor. A person receiving external radiation is not radioactive and does not have to follow special safety precautions at home.

- *Internal radiation or brachytherapy*: A radioactive sealed source is put inside the body into or near the tumor. With some types of brachytherapy, radiation might be placed and left in the body to work or placed in the body for a period and then removed. Iridium-192 implants produced in wire form are introduced through a catheter to the target tumor area in the head and breast. Iridium-192 needles, or seeds of iodine-125 or palladium-103, are used for early-stage prostate cancer.

- *Systemic radiation or endoradiotherapy or radionuclide therapy (RNT):* Radioactive drugs (radiopharmaceuticals) given by mouth or injected directly into blood circulation (through a vein or an artery) are used to treat certain types of cancer. These drugs then travel throughout the body and deliver the radioactivity to both cancer cells and normal cells.

Both teletherapy and brachytherapy play a major role in the treatment of cancer in a specific region in the body, but they are not useful for the treatment of widespread metastases. Since 1936, when Dougherty and Lawrence first introduced ^{32}P for the treatment of leukemia, the use of radiopharmaceuticals for RNT, and to deliver therapeutic doses of ionizing radiation, has been

extensively investigated. The use of sodium [^{131}I] iodide, discovered in 1938 by Glenn Seaborg and John Livingood at the University of California, Berkeley, has been the success story in nuclear medicine. Iodine-131 has the advantage of emitting both γ-rays and β^- rays, the former enabling imaging for diagnosis and dosimetry and the latter being valuable for molecular radiotherapy of hyperthyroidism and thyroid cancer [40].

1.4.1   Targeted Radionuclide Therapy (TRT)

Traditional cytotoxic chemotherapy works primarily through the inhibition of cell division. In addition to cancer cells, other rapidly dividing cells (such as hair, gastrointestinal epithelium, bone marrow) are affected by these drugs. The primary goal of targeted therapy is to fight cancer cells with more precision and with less side effects. Targeted therapeutic agents are designed to block the proliferation of cancer cells by interfering with specific molecules required for tumor development and growth. Some of these molecules may be present in normal tissues, but they are often mutated or overexpressed in cancer cells. Drugs for targeted therapies are primarily small molecule drugs such as tyrosine kinase inhibitors (TKIs), interfering RNA molecules, microRNA, or monoclonal antibodies (mAbs) [41]. Targeted therapy is the foundation of precision medicine. Not all cancer patients are candidates for targeted therapy. The use of a targeted therapy may be restricted to patients whose tumor has an appropriate target for a particular target therapy drug.

The main objective of targeted radionuclide therapy (TRT) or TRNT is the ability to selectively deliver cytotoxic radiation to cancer cells that causes minimal toxicity to surrounding healthy tissues, using optimized vehicles that deliver a nuclear payload into the tumor cells [42–45]. In nuclear medicine, TRT is based on delivering therapeutic radionuclides to a specific target site. TRT is based on therapeutic radio-

pharmaceuticals that are radiolabeled molecules consisting of a target-specific moiety, such as peptides, low molecular weight ligands or antibody or antibody fragments, and particles, linked to an appropriate radionuclide designed to deliver therapeutic doses of ionizing radiation to specific disease sites [46, 47]. The goal of TRT is to kill tumor cells selectively by delivering high radiation doses to a specific target while minimizing damage to normal cells. In the last 5 years, there has been a great progress in the development of therapeutic radiopharmaceuticals using a wide variety of therapeutic radionuclides and target-specific molecules for treatment of cancers. Targeted therapy is predominantly molecular, in the sense that efficacy is dependent on a therapeutic advantage offered by interaction of the radiopharmaceutical with key molecular sites and receptors on the target tissue. Depending on the target-specific carrier molecule, TRT may also be called peptide receptor radionuclide therapy (PRRT), radioimmunotherapy (RIT), radioligand therapy (RLT), targeted alpha therapy (TAT), and targeted radionuclide therapy (TRNT).

The term unconjugated radiopharmaceutical has been generally defined as referring to those radionuclides that target-specific disease sites by virtue of chemical, biologic, or physical affinity of radioisotope itself, rather than by virtue of carrier agents to which they are tagged. Because of the untagged nature of their use, unconjugated radiopharmaceuticals are also referred as naked radiopharmaceuticals [46, 47]. During the last couple of decades, there has been significant increase in the application of conjugated radiopharmaceuticals for targeted radionuclide therapy (TRT), mainly due to the development of a range of new carrier molecules, which can transport the radionuclide to a molecular target at the disease site. The most important factors that influence tumor localization of conjugated radiopharmaceuticals include the chemical and biochemical nature of the carrier molecule transporting the radionuclide of choice to the targeted area. A

century ago, Paul Ehrlich postulated the notion that a magic bullet could be developed to selectively target disease. He envisioned that antibody molecules could act as magic bullets. The first demonstration of TRT was the use of ^{131}I-labeled polyclonal antibodies for the treatment of patients with melanoma. Several radiopharmaceuticals are now available for the treatment of different benign diseases and malignancies. The current forms of TRT using unconjugated or conjugated radiopharmaceuticals with specific examples are described in Table 1.3. Several review articles and book chapters have extensively discussed the development of radiopharmaceuticals for radionuclide therapy [42–44, 46–48]).

1.4.2　Personalized Medicine and Theranostics

Personalized medicine, or precision medicine, is a medical model that can separate people into different groups—with medical decisions, practices, interventions, and/or products being tailored to the individual patient based on their predicted response or risk of disease. The continuing progress in biotechnologies in the last couple of decades opened avenues to a new management of many diseases, switching from a "population treatment" approach to the concept of "personalized medicine" (Fig. 1.8).

The word theranostics is derived from the combination of the words, therapeutics, and diagnostics. The concept of "theranostics" was coined by the US consultant John Funkhouser, in a press release from the company Cardiovascular Diagnostics in August 1998, to describe a material that allows the combined diagnosis, treatment, and follow-up of a disease [49, 50]. Different imaging probes, such as PET/SPECT radiopharmaceuticals, MRI contrast agents (T_1 and T_2 agents), and fluorescent markers (organic dyes and inorganic quantum dots), and nuclear imaging agents, can be decorated onto therapeutic agents or therapeutic delivery vehicles to

Table 1.3 Radiopharmaceuticals approved for therapy

	Radiopharmaceutical	Trade name	Indicated for therapy in	Year
1	[131]I Sodium iodide		Thyroid cancer	1971
2	Strontium-89 chloride	Metastron	Bone pain palliation	1993
3	Samarium-153 lexidronam	Quadramet®	Bone pain palliation	1997
4	[90]Y Glass microspheres	TheraSphere™	Radiation treatment of unresectable hepatocellular carcinoma (HCC), neuroblastoma	2000, 2020
5	[111]In/[90]Y- ibritumomab tiuxetan	Zevalin®	Relapsed or refractory, low-grade, or follicular B-cell non-Hodgkin's lymphoma (NHL)	2002
6	^{131}I-tositumomab and tositumomab	BEXXAR	CD20-positive, relapsed or refractory, low-grade, follicular, or transformed NHL	2003
7	[223]Ra-dichloride	Xofigo®	Treatment of patients with CRPCa	2013
8	[90]Y Resin Microspheres	SirSpheres™	Radiation treatment of unresectable hepatocellular carcinoma (HCC)	2015
9	[^{131}I]Iobenguane	Azedra®	Treatment of iobenguane scan positive, unresectable, locally advanced or metastatic pheochromocytoma or paraganglioma	2018
10	^{177}Lu-Dotatate	Lutathera®	Treatment of SSTR-positive GEP-NETs.	2018
11	Lu 177 vipivotide tetraxetan (^{177}Lu-PSMA-617)	Pluvicto	Treatment of *patients with metastatic castration-resistant prostate cancer (mCRPC)*	2022
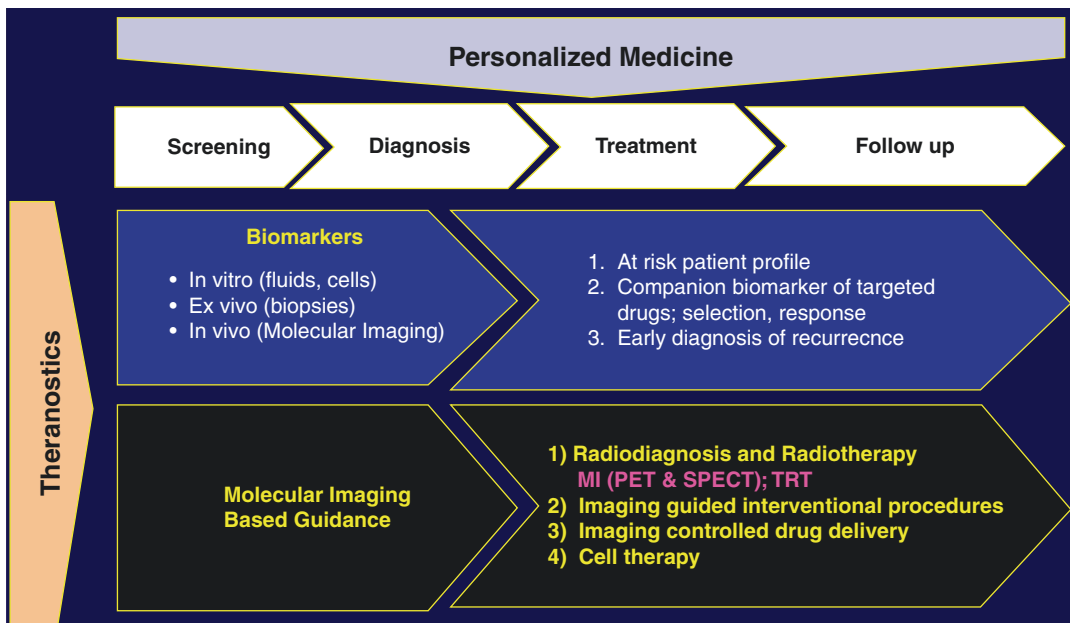
Fig. 1.8 Personalized medicine in nuclear medicine is theranostics based on molecular imaging and targeted radionuclide therapy (TRT)

facilitate their imaging and, in so doing, gain information about the trafficking pathway, kinetics of delivery, and therapeutic efficacy. This approach allows the selection of the subpopulation of patients most likely to benefit from a targeted therapy in accordance with their "molecular profile" at a given time-point or, conversely, those patients for whom the risk of adverse effects is higher.

The concept of theranostics integrates two distinct approaches that both encompass all steps of patients' management. In personalized medicine, diagnostic molecular imaging is often employed for selecting appropriate and optimal therapies based on the context of a patient's genetic content or other molecular, or cellular analysis. Having the ability to look at a patient on an individual basis will allow for a more accurate diagnosis and specific treatment plan. Theranostics in nuclear medicine is a personalized approach to treating cancer, using similar (or same) molecules for both imaging (diagnosis) and therapy. A target-specific biomolecule is designed in such a manner that it can be labeled with a γ or β^+ emit-

ting radionuclide for SPECT or PET imaging, and it can also be labeled with a therapeutic radionuclide decaying by β^-, α, or *EC* (emitting Auger electrons). One of the earliest examples of theranostics are the use of radioactive iodine (^{123}I and ^{131}I) for treatment of patients with hyperthyroidism and thyroid cancer. The past, present, and the future of theranostics in nuclear medicine were extensively discussed in many review articles [50–56]. Several theranostic radiopharmaceuticals of clinical importance are listed in Table 1.4.

The success of theranostics in the clinic has already been well established with the introduction of somatostatin analogs for PET/SPECT imaging and TRT or PRRT in patients with SSTR-positive NETs. For example, ^{68}Ga-Dotatate PET/CT scans in two patients (Fig. 1.9) with well-differentiated NETs who received 4 cycles of ^{177}Lu-Dotatate treatment. A patient with a pancreatic NET shows remission (A), while a patient with ileal NET did not respond (B) [52]. In a patient with extensive castration-resistant metastatic prostate cancer,

Table 1.4 Radiopharmaceuticals under clinical development in phase II/III trials

Radiopharmaceutical	Target	Disease/Indication
[18F]PSMA-1007	PSMA	Prostate cancer PET/CT
[18F]rhPSMA-7.3		
177Lu-PSMA-617	Prostate-specific membrane antigen (PSMA)	Therapy of metastatic castration-resistant prostate cancer (mCRPC)
225Ac-PSMA-617		
177Lu-PSMA-I&T		
225Ac-PSMA-I&T		
177Lu-RM2	GRPR	
177Lu-NeoBOMB1		
177Lu-EB-TATE	SSTR-2	Therapy of neuroendocrine tumors (NETs)
177Lu-Dotatoc (edotreotide) Solucin	SSTR-2	
177Lu-Satoreotide tetraxetan	SSTR-2	
177Lu-DOTA-JR11 (OPS201)	SSTR-2 antagonist	
68Ga-NODAGA-JR11 (OPS202)	SSTR-2 antagonist	
68Ga-DOTA-Exendin-4	Glucagon-like peptide-1 (GLP-1R)	PET/CT of NETs
68Ga and 177Lu-Pentixafor	CXCR4	Melanoma, multiple myeloma, small-cell lung cancer, NETs
68Ga-FAP analogs	Fibroblast activation protein (FAP)	Different tumors
90Y-FAP analogs		
111In/177Lu-3B-227	Neurotensin receptor (NTSR1)	Pancreatic adenocarcinomas
131I-IOMAB, Apamistamab	CD-45	Bone marrow ablation in leukemias
177Lu-lilotomab or (lilotomab satetraxetan)	CD37	B-cell lymphomas
131I-omburtamab (8H9) mAb	B7-H3 (CD 276)	Neuroblastoma, glioblastoma
89Zr/177Lu- HuMab-5B1 mAb	CA19-9	Pancreatic carcinomas, hepatocellular, gastric, colorectal, and breast carcinomas
89Zr or 18F anti-PD and PD-L1 mAb	Immune checkpoint inhibitors	PET/CT of different tumors

(Fig. 1.10) 68Ga-PSMA PET/CT scans revealed no response to 2 cycles of 177Lu-PSMA-617 beta therapy but, significant response to three cycles of 225Ac-PSMA-617 alpha therapy [57].

The future of theranostics is very promising and several investigational radiopharmaceuticals (Table 1.4) are in phase II/III clinical studies for both imaging and therapy. PET imaging of immune cell types in tumor microenvironment (TME) represents future direction of molecular imaging [54]. Examples include imaging of cancer-associated fibroblasts (FAP inhibitor or FAPI), CD8-positive T cells, and programmed death ligand 1 (PD-L1), which is found in antigen-presenting cells, including macrophages and myeloid-derived suppressor cells. The next major advance in theranostics will be the introduction of α therapy based on peptides and antibodies.
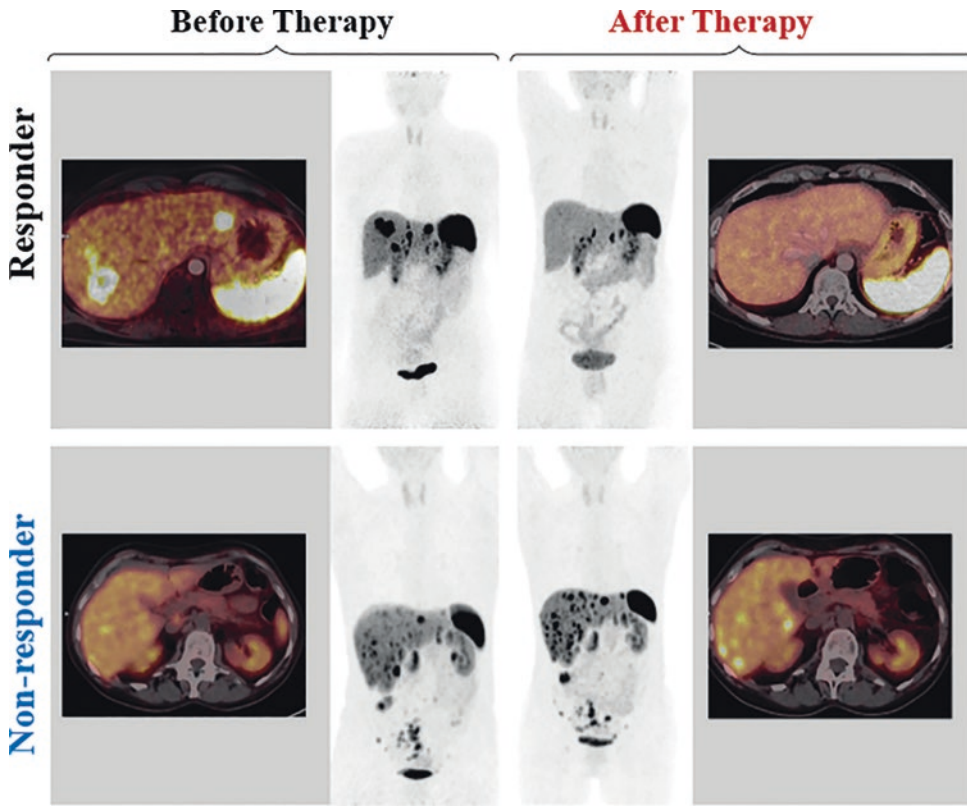
Fig. 1.9 ^{68}Ga-Dotatate PET/CT scans in patients with well-differentiated neuroendocrine tumors (NETs) undergoing ^{177}Lu-Dotatate treatment. After 4 cycles of therapy, PET scan shows remission in a responder (a patient with pancreatic NET), and progression in a nonresponder (a patient with ileal NET presenting with liver metastases and peritoneal carcinomatosis). Progression in nonresponder is evident even after 4 cycles of treatment [52]
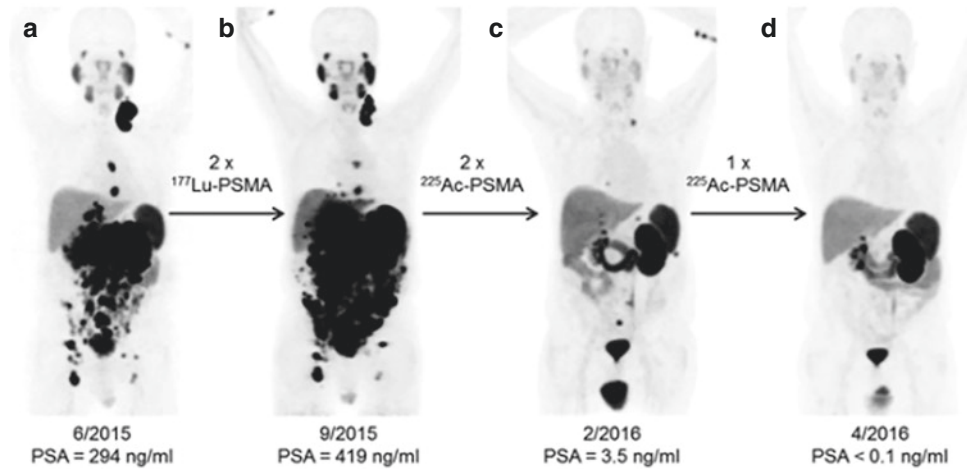
Fig. 1.10 ^{68}Ga-PSMA-11 PET/CT scans of a patient with metastatic castration-resistant prostate cancer (mCRP). In comparison with initial tumor spread (**a**), restaging after 2 cycles of β^- emitting ^{177}Lu-PSMA-617 presented progression (**b**). In contrast, restaging after second (**c**) and third (**d**) cycles of α emitting ^{225}Ac-PSMA-617 presented impressive response [57]

1.5   Summary

There is no best modality for MI, and one may have to use a combination of more than one imaging modality and molecular contrast strategy to answer the questions of interest. MRI and CT combine high-resolution morphological capabilities with physiological information, but require higher mass levels of contrast agents that may create toxicity problems. Further, MRI's morphological contrast resolution is high in soft tissue, while CT contrast resolution is best for bones and lungs. Ultrasound has the advantages of being widely available clinically, relatively inexpensive, and capable of acquiring real-time physiological information; however, the molecular probes needed for ultrasound are generally particles and, at this time, the technique is limited to only vascular targets.

The major advantage of PET and SPECT techniques is that the small probe mass and the radiolabeling strategies do not significantly perturb the biological processes under study. Further, PET has high molecular sensitivity and strong quantitative potential. SPECT can image multiple probes simultaneously provided they each emit distinct photon energies.

Theranostics in nuclear medicine has the potential to develop patient-specific radiation dosimetry strategies based on molecular imaging studies, and cell-killing radiation strategies to deliver the optimal therapeutic dose to the right patient at the right time. Also, a combination therapy approach of chemotherapy, immune modulation, and radiotheranostics may provide precise cancer therapy in both palliative and curative settings. Fruitful partnerships between industry and the academic centers will be essential to the successful growth of theranostics.

References

1. Wagner HN Jr. Nuclear medicine: what it is and what it does. In: Wagner Jr HN, Szabo Z, Buchanan JW, editors. Principles of nuclear medicine. Philadelphia: WB Saunders; 1995a.
2. Wagner HN Jr. The diagnostic process. In: Wagner Jr HN, Szabo Z, Buchanan JW, editors. Principles of nuclear medicine. Philadelphia: WB Saunders; 1995b.
3. Cotran RS, Kumar V, Collins T. Robbins pathologic basis of disease. 6th ed. Philadelphia: WB Saunders; 1999.
4. Virchow R. Disease, life and man. Stanford: Stanford University Press; 1958.
5. McCance KL, Huether SC. Pathophysiology. The biological basis for disease in adults and children. 3rd ed. Mosby, St Louis; 1998.
6. Wagner HN Jr. From molecular imaging to molecular medicine. J Nucl Med. 2006;47(8):13N–39N.
7. Massoud TF, Gambhir SS. Molecular imaging in living subjects: seeing fundamental biological processes in a new light. Genes Dev. 2003;17:545–80.
8. Reba RC. Molecular nuclear medicine. J Nucl Med. 1995;36(suppl):1S–30S.
9. Gabriel P, Miller KJC, Golding SJ, et al. Reinventing radiology in a digital and molecular age: summary of proceedings of the sixth biannual symposium of the international society for strategic studies in radiology (IS^{3}R), August 25–27, 2005. Radiology. 2007;244:633–8.
10. Jaffer FA, Weissleder R. Molecular imaging in the clinical arena. JAMA. 2005;293:855–62.
11. Thakur M, Lentle BC. Report of a summit on molecular imaging. AJR 2006;186:297–9.
12. Mankoff DA. A definition of molecular imaging. J Nucl Med. 2007;48(18N):21N.
13. Hoffman JM, Gambhir SS. Molecular imaging: the vision and opportunity for radiology in the future. Radiology. 2007;244:39–47.
14. Judenhofer MS, Wehrl HF, Newport DF, et al. Simultaneous PET-MRI: a new approach for functional and morphological imaging. Nat Med. 2008;14:459–65.
15. Levin CS. Primer on molecular imaging technology. Eur J Nucl Med Mol Imaging. 2005;32:S325–45.
16. Li Z, Tang H, Tu Y. Molecular and nonmolecular imaging of macrophages in atherosclerosis. Front Cardiovasc Med. 2021;8:670639.
17. Wu M, Shu J. Multimodal molecular imaging: current status and future directions. Contrast Media Mol Imaging. 2019;2018:1382183, 12 pages.
18. Tempany CM, McNeil BJ. Advances in biomedical imaging. JAMA. 2001;285:562–7.
19. Atri M. New technologies and directed agents for applications of cancer imaging. J Clin Oncol. 2006;24:3299–308.
20. Bhaumik S, Gambhir S. Optical imaging of renilla luciferase reporter gene expression in living mice. Proc Natl Acad Sci U S A. 2002;99:377–82.
21. Sevick-Muraca EM, Houston JP, Gurfinkel M. Fluorescence-enhanced, near infrared diagnostic imaging with contrast agents. Curr Opin Chem Biol. 2002;6:642–50.
22. Lanza GM, Wickline SA. Targeted ultrasonic contrast agents for molecular imaging and therapy. Curr Probl Cardiol. 2003;28:625–53.

23. Lindner JR. Microbubbles in medical imaging: current applications and future directions. Nat Rev Drug Discov. 2004;3:527–32.

24. Thumar V, Liu J-B, Eisenbrey J. Applications in Molecular Ultrasound Imaging: Present and Future. Advanced Ultrasound in Diagnosis and Therapy. 2019;03:062–075.

25. Iravani A, Hicks RJ. Imaging the cancer immune environment and its response to pharmacologic intervention, part 2: the role of novel pet agents. J Nucl Med. 2020;61:1553–59.

26. Ahmadzadehfar H, Azgomi K, Hauser S, et al. ^{68}Ga-PSMA-11 PET as a gatekeeper for the treatment of metastatic prostate cancer with [223]Ra: proof of concept. J Nucl Med. 2017;58:438–44.

27. Jacobs AH, Winkler A, Castro MG, et al. Human gene therapy and imaging in neurological diseases. Eur J Nucl Med Mol Imaging. 2005;32:S358–83.

28. Vemuri P. "Exceptional brain aging" without Alzheimer's disease: triggers, accelerators, and the net sum game. Alzheimers Res Ther. 2018;10:53.

29. Emsen B, Villafane G, David J-P, et al. Clinical impact of dual-tracer FDOPA and FDG PET/CT for the evaluation of patients with parkinsonian syndromes. Medicine. 2020;99:45. (e23060).

30. Srirajaskanthan R, Kayani I, Quigley AM, et al. The role of ^{68}Ga-DOTATATE PET in patients with neuroendocrine tumors and negative or equivocal findings on ^{111}In-DTPA-octreotide scintigraphy. J Nucl Med. 2010;51:875–82.

31. Catana C, Procissi D, Wu Y, et al. Simultaneous in vivo positron emission tomography and magnetic resonance imaging. Proc Natl Acad Sci U S A. 2008;105:3705–10.

32. Cherry SR. Multimodality in vivo imaging systems: twice the power or double the trouble? Annu Rev Biomed Eng. 2006;8:35–62.

33. Cherry SR, Louie AY, Jacobs RE. The integration of positron emission tomography with magnetic resonance imaging. Proc IEEE. 2008;96:416–38.

34. Culver J, Akers W, Achilefu S. Multimodality molecular imaging with combined optical and SPECT/PET modalities. J Nucl Med. 2008;49:169–72.

35. Insana MF, Wickline SA. Multimodality biomolecular imaging. Proc IEEE. 2008;96:378–81.

36. Townsend DT. Dual-modality imaging: combining anatomy and function. J Nucl Med. 2008;49:938–55.

37. Yang C-T, Ghosh KK, Padmanabhan P, et al. PET-MR and SPECT-MR multimodality probes: development and challenges. Theranostics. 2018;8(22):6210–32.

38. Glaus V, Rossin R, Welch MJ, Bao G. In vivo evaluation of ^{64}Cu-labeled magnetic nanoparticles as a dual-modality PET/MR imaging agent. Bioconjug Chem. 2010;21(4):715.

39. Sun Y, Zeng X, Xiao Y, et al. Novel dual-function near-infrared II fluorescence and PET probe for tumor delineation and image-guided surgery. Chem Sci. 2018;2018(9):2092–7.

40. McCready VR. Radioiodine – the success story of nuclear medicine. Eur J Nucl Med Mol Imaging. 2017;44:179–82.

41. Di Martino S, Rainone A, Troise A, et al. Overview of FDA-approved anticancer drugs used for targeted therapy. WCRJ. 2015;2(3):e553.

42. Dash A, Knapp FFR Jr, Pillai MRA. Targeted radionuclide therapy - an overview. Curr Radiopharm. 2013;6(3):1–29.

43. Fahey F, Zukotynski K, Capala J, Knight N. Targeted radionuclide therapy: proceedings of a joint workshop hosted by the national cancer institute and the society of nuclear medicine and molecular imaging. J Nucl Med. 2014;55:337–48.

44. Jadvar H. Targeted radionuclide therapy: an evolution toward precision cancer treatment. AJR. 2017;209:277–88.

45. Larson SM, Krenning EP. A pragmatic perspective on molecular targeted radionuclide therapy. J Nucl Med. 2005;46:1S–3S.

46. Sgouros G, Bodei L, McDevitt MR, Nedrow JR. Radiopharmaceutical therapy in cancer: clinical advances and challenges. Nat Rev/Drug Dis. 2020;19:589–608.

47. Vallabhajosula S. The chemistry of therapeutic radiopharmaceuticals. In: Aktolun C, Goldsmith SJ, editors. Nuclear medicine therapy: principles and clinical applications. New York: Springer; 2013. p. 2013.

48. Zukotynski K, Jadvar H, Capala J, Fahey F. Targeted radionuclide therapy: practical applications and future prospects. Biomark Cancer. 2016;8(S2):35.

49. Kelkar SS, Reineke TM. Theranostics: combining imaging and therapy. Bioconjug Chem. 2011;22(10):1879–903.

50. Langbein T, Weber WA, Eiber M. Future of theranostics: an outlook on precision oncology in nuclear medicine. J Nucl Med. 2019;60:13S–9S.

51. Herrmann K, Larson SM, Weber WA. Theranostic concepts: more than just a fashion trend—introduction and overview. J Nucl Med. 2017;58:1S–2S.

52. Herrmann K, Schwaiger M, Lewis JS, et al. Radiotheranostics: a roadmap for future development. Lancet Oncol. 2020;21:e146–56.

53. Marin JFG, Nunes RF, Coutinho AM, et al. Theranostics in nuclear medicine: emerging and re-emerging integrated imaging and therapies in the era of precision oncology. Radiographics. 2020;40:1715–40.

54. Weber WA, Czernin J, Anderson CJ, et al. The future of nuclear medicine, molecular imaging, and theranostics. J Nucl Med. 2020;61(12):263S–72S.

55. Vahidfar N, Eppard E, Farzanehfar S, et al. An impressive approach in nuclear medicine theranostics. PET Clin. 2021;16:327–40.

56. van de Donk PP, Kist de Ruijter L, et al. Molecular imaging biomarkers for immune checkpoint inhibitor therapy. Theranostics. 2020;10:1708–18.

57. Kratochwil C, Bruchertseifer F, Giesel FL, et al. 225Ac-PSMA-617 for PSMA-targeted alpha radiation therapy of metastatic castration-resistant prostate cancer. J Nucl Med. 2016;57:1941–44.

Science of Atomism: A Brief History

2

I... a Universe of Atoms, an Atom in the Universe (Richard P. Feynman)

2.1 Atomism

In natural philosophy, *atomism* is the theory that all the objects in the universe are composed of very small, indestructible elements—*atoms*. The notion of atomism first arose because of philosophic deduction. This idea of atomism is by no means self-evident. Since ancient times, philosophers in many cultures have been speculating on the nature of the fundamental substance or substances of which the universe is composed. These fundamental or basic substances are called *elements* in English, from a Latin word of unknown origin.

In India, during the sixth century BC, Kanada and Pakhuda Katyayana had propounded ideas about the atomic constitution (*Anu and Paramanu*) of the material world (Limouris 2006). Philosophy and science were not originally separate but, were born together as natural philosophy in Greece, at the beginning of the sixth century. In fact, the ancient Greeks were the first to propose that all matter in the universe was created from the following four elements: *water*, *earth*, *fire*, and *air*. They also believed that matter is continuous; there is no *vacuum* (space without any matter). The Greek philosopher Leucippus and his pupil Democritus (460–370 BC) (Fig. 2.1) conceived the idea of an *atom* as the smallest piece of a substance. The word atom comes from the Greek word *atomos* (ατομοσ) meaning "not cuttable" (unbreakable) and advocated that atoms are in continuous motion and are indestructible. The most famous Greek philosophers Plato (427–347 BC) and Aristotle (384–322 BC), however, completely rejected the idea of atomism. Nevertheless, the ideas of Democritus were further developed by the influential Greek Philosopher Epicurus almost a century later. One of the most important followers of the Epicurean philosophy was a Roman poet named Titus Lucretius Carus (96–55 BC), who explained the philosophy of atomism in a long poem entitled, *De rerun Natura* (On Natural Things). One copy of this poem survived the Dark and Middle Ages (it was discovered in 1417) and became a major source of the Greek theory of atomism. The French philosopher Pierre Gassendi (1592–1655) accepted atomism and spread this doctrine throughout Europe.
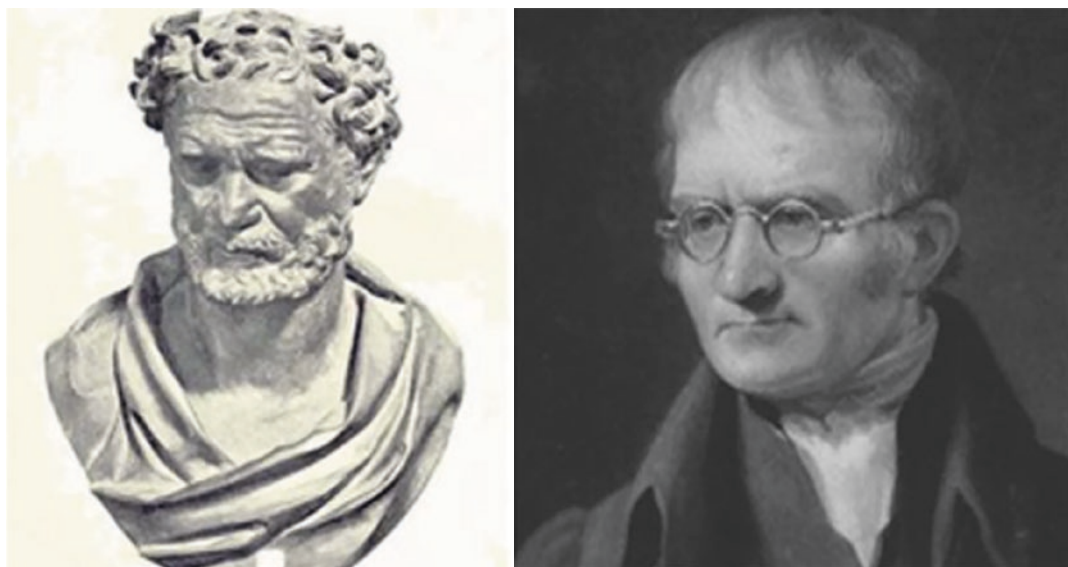
Fig. 2.1 Democritus, the Greek philosopher (on left), and John Dalton, an English chemist, and physicist (on right)

2.2   Chemical Elements

The British scientist Robert Boyle (1627–1691) was strongly influenced by Gassendi's writings and was probably the first person to perform experiments in connection with atomism. Boyle carefully measured and demonstrated an inverse relationship between the pressure and the volume of air (known as *Boyle's Law*), which clearly suggested that both atoms and vacuum are real. He, thus, revived the atomic hypothesis and called it the *Corpuscular Theory of Matter*. Newton also wrote in his *Opticks* that all matter is composed of solid and impenetrable particles—expressing a view similar to Democritus and Boyle.

Boyle was also the first chemist to recognize the significance of a *chemical element*. In his book, the *Skeptical Chemist*, published in 1661, he proposed that a substance was an element if it could not be broken into two or more simpler substances. In early 1700, the quantitative sciences of physics and chemistry were born, and 15 chemical elements came to be known. Following the discovery of important gases, such as carbon dioxide, nitrogen, hydrogen, and oxygen, the French chemist, Antoine Laurent de Lavoisier (1743–1794) in his remarkable book titled, *Traite*

elementaire de chemie, published in 1789, listed 33 substances as chemical elements under four major categories: *gases*, *nonmetals*, *metals*, and *earths*.

2.2.1   Chemical Laws

Lavoisier advocated the importance of accurate measurements in quantitative experiments of chemical reactions and discovered the *law of conservation of mass* which states that: mass is neither created nor destroyed. The principle of the constant composition of compounds, known as the *law of definite proportions*, was discovered by the Frenchman, Joseph Proust who showed that a given compound always contains exactly the same proportion of elements by mass. Proust's discovery stimulated John Dalton (Fig. 2.1) an English school teacher, who noted that a series of compounds can be formed by the combination of two elements in different ratios and, thus, discovered the *law of multiple proportions*. These chemical laws supported the hypothesis that each element consists of a certain type of atom and that compounds are formed from specific combinations of these atoms.

2.2.2   Atomic Theory

In 1808, John Dalton converted the atomic hypothesis into a quantitative theory. In his publication, *A New System of chemical philosophy*, Dalton stated that each element is made up of identical atoms and presented a theory of atoms. He prepared the first table of *atomic weights* for different elements and suggested that atoms of each element had individual weights and that these could be calculated relative to one another. Dalton made the simple assumption that one atom of hydrogen combined with one atom of oxygen makes a molecule of water. Many of the atomic masses proposed by Dalton were later proved to be incorrect but, the construction of a table of atomic weights of different elements was a major step forward.

In 1808, Joseph Louis Gay-Lussac made the remarkable observation that although all elements combine in definite proportions of weight, gases combine in definite proportions by volume. For example, he observed that two volumes of hydrogen combined with one volume of oxygen make one volume of water vapor. The explanation of the *law of combining volumes* was provided in 1811 by Amadeo Avogadro, an Italian physicist, who hypothesized that equal volumes of any gas at a given temperature and pressure always contain an equal number of the particles (atoms or molecules) of gas. Avogadro was the first to realize that certain gaseous elements, like hydrogen (H_2), nitrogen (N_2), and oxygen (O_2), under ordinary conditions contain two atoms each (also known as *diatomic molecule*). Avogadro's hypothesis was a brilliant guess and we now know, based on the *kinetic theory of gases*, that under normal conditions of temperature and pressure (NTP), 22.4 L of any gas contain exactly the same number of atoms or molecules. In chemistry, the concept of *mole* (as a unit of mass) is defined as gram atomic weight or molecular weight and 1 mol of any substance contains Avogadro's number (N_A) of atoms or molecules. Avogadro, however, never knew the exact value of this universal constant. Almost 100 years later the value of N_A was determined to be 6.022×10^{23}.

Based on Avogadro's hypothesis, Jons Jakob Berzelius, a Swedish chemist published more accurate atomic weights of many elements between 1814 and 1826. He also invented a simple set of symbols for elements along with a system for writing the chemical formulas of compounds, in order to replace the awkward symbolic representations of alchemists. By the end of the nineteenth century, not all chemists and physicists believed in the reality of atoms, however, they accepted that atomic weight is a very important property of an element.

In the late 1860s, two chemists, the Russian Dmitri Ivanovich Mendeleev, and the German Julius Lothar Meyer, arranged the elements in the order of increasing atomic weight in a tabular form, called the *periodic system of elements*, since elements with similar chemical properties recurred at regular, periodic, intervals.

The discovery of electricity eventually provided important clues and the experimental evidence necessary to demonstrate the existence of atoms.

2.3   Electricity and Magnetism

The phenomena of magnetism and electricity have been known since ancient times. A certain piece of iron ore or loadstone, first found near the town of Magnesia on the eastern shore of the Aegean Sea, was the basis for scientific investigation. The English physician William Gilbert (1544–1603), a contemporary of Galileo carefully studied the magnetic interactions and published the famous book, *De Magnete*, in which he concluded that the planet earth can be regarded as a giant magnet with geographical north and south poles; the magnetic south always pointing to the geographical north.

Since ancient times, people have also been aware that a piece of *amber*, when rubbed with fur will attract small bits of hair and other materials. Gilbert first introduced the term *electric* (*electrica* in Latin), after the Greek word *electron* for amber, and found that other substances such as glass, sulfur, wax, and gems also exhibit similar attractive property as amber. He also proposed

that electricity is some sort of fluid (an *effluvium*) that is produced or rubbed when bodies are rubbed together. Gilbert also recognized that despite their similarities, electricity, and magnetism are different phenomena, but are deeply related.

The French chemist Charles-Francois de Cisternay Du Fay, eventually, realized that there are two types of electricity (*vitreous and resinous*), which are very different from each other; unlike types of electricity attract each other while like types repel each other. In contrast, the American inventor Benjamin Franklin (1706–1790) concluded that electricity consists of a single type of fluid and that this fluid consists of extremely subtle particles. He referred to the deficiency of electricity as *negative* electricity and to an excess as *positive* electricity. The amount of electricity (positive or negative) in any body is called the electric *charge* of the body. Franklin also observed that electricity is not created or destroyed and, thus, was the first one to introduce the fundamental hypothesis of the conservation of electric charge.

During the second half of the eighteenth century, physicists in many countries were trying to understand the quantitative aspects of both electric and magnetic forces. For example, French physicist Charles Augustine de Coulomb developed the so-called *torsion balance* for measuring very weak forces and published his results on electric and magnetic forces during 1785–1791. More specifically, Coulomb discovered that the forces of electrical attraction and repulsion are directly proportional to the product of two charges and inversely proportional to the square of the distance between them. Subsequently, this law, known as *Coulomb's law*, helped to establish the unit for the electric charge. One *coulomb* of charge is defined as the amount of electric charge that passes a given point in one second in a wire that carries a one *ampere* current. Coulomb also found that the strength of the force of attraction or repulsion between the magnetic poles declines as the square of the distance between the poles increases. In 1687, Newton showed that the gravitational attraction between two bodies also followed the so-called *inverse square law*.

In 1786, the Italian physiologist Luigi Galvani accidentally discovered *electric current* while studying the phenomenon of muscular contraction in frog's legs. His friend, Alessandro Giusuppe Volta (1745–1827), a physicist, soon proved that electric current is purely an inorganic phenomenon (also known as *galvanism*) by demonstrating that electricity could be produced when two different metals were both dipped into a salt solution. Electricity, thus, was produced as a result of a chemical reaction. To produce a large electric current, Volta in 1800 constructed what is known as *Volta pile* using a number of alternating copper and iron or zinc disks, separated by layers of cloth soaked in a salt solution. Volta's invention of an electric battery had a significant impact on both chemistry and physics.

2.3.1 Electrolysis

While repeating Volta's experiments, William Nicholson, and Anthony Carlisle in England, accidentally observed that when terminals of wires from a battery are immersed in a tube of water, hydrogen gas is produced at the wire attached to a negative terminal and oxygen gas at the positive wire. Soon Humphrey Davy (1778–1829), a professor of chemistry at the Royal Institution in London, found that various salts could be decomposed by passing an electric current through molten salt solutions. He soon discovered a series of alkali and alkaline earth elements (Na, K, Ca, Mg, Sr, and Ba) based on the decomposition of molten salts or salt solutions. This was the discovery of chemical decomposition by means of an electric current or an *electrolysis*, as Michael Faraday, who had been Day's assistant and protégé called it in the 1830s.

The passage of an electric current through an electrolyte (salt solution) induces chemical changes and elements can appear at either electrode. If they are gases, they bubble off. Faraday introduced the term *ions* (Greek word meaning wanderer) to describe the chemical species passing through the solution. He also introduced the terms *anion* and *cation* for positive and negative ions and *anode* and *cathode* for positive and neg-

ative electrodes. Faraday carefully measured the mass of an element produced as a function of the amount of electricity and discovered two basic laws.

1. For a given solution, the amount of material deposited or liberated on the electrodes is proportional to the total amount of electricity.
2. The monovalent ions of different substances also carry an equal amount of electricity while multivalent ions carry correspondingly larger charges.

The Faraday laws, for the first time, suggested the existence of a universal unit of electric charge, known at that time only to be attached to the chemical species. He defined that one *Faraday* of electricity represents 96,500 C. A Faraday of electricity can be viewed as containing Avogadro's number of electrical units. This indivisible unit of electricity identified in electrolysis was given the name *electron* (ηλεκτρον), the Greek word for amber, by the Irish physicist and astronomer George Johnstone Stoney (1894). The Swedish chemist Savante August Arrhenius in his *theory of ionic dissociation* presented in 1887 proposed that Faraday's ions were actually atoms carrying positive and negative electric charge.

2.3.2   Electromagnetism

The credit for the discovery of *electromagnetism* belongs to Hans Christian Oersted, a professor of physics at the University of Copenhagen. In 1820, Oersted demonstrated that an electric current deflects a compass needle, thus showing an intimate connection between electricity and magnetism. A current carrying wire exerts a force on a compass needle. If the compass is continuously moved in the direction it is pointed, it will trace out a circle around the wire. Oersted also observed that a magnet will exert a force on a coil of wire (*solenoid*) carrying an electric current—the solenoid would act like a bar magnet, one end acting like the north pole and the other end as the south pole. Thus, the concept of electromagne-

tism as a unified force was realized. In 1820, Andre Marie Ampere, professor of mathematics at the Ecole Polytechnique in Paris, observed that parallel wires attract or repel each other if they carry electric currents flowing in the same or opposite directions, respectively. He concluded that all magnetism is electromagnetism and that the properties of a magnet (or loadstone) are due to tiny electric currents within the particles of the magnet.

In 1831, Faraday also observed that a magnet can induce an electric current in a wire and that the electric current in one coil can induce a current in another coil placed nearby. Before Faraday, the electric and magnetic forces (like gravity) were considered as acting across empty space between the interacting objects. Faraday was the first to propose the idea of a field of forces (or simply *field*) to explain how forces act over large distances. In the 1860s, the field concept of Faraday was developed into a quantitative mathematical formulation by James Clerk Maxwell, a British physicist. Maxwell showed that electric and magnetic fields do not exist independently, but only as a combined electromagnetic field with each of the components at right angles to each other. Using his equations Maxwell was also able to show that the electromagnetic field propagates through space as waves carrying away energy in the form of free electromagnetic radiation with a constant speed of 300,000 km s^{-1} or 3.0×10^{10} cm s^{-1}. In 1665, Newton showed that sunlight is not pure but consists of a band of colored light particles, which he called *spectrum* (from a Latin word meaning "ghost"). In contrast, the Dutch physicist, Huygens (1629–1695) revealed that light is composed of waves with different colors having different *wavelengths*. In 1801, Thomas Young, an English physicist, showed that the different colors of the spectrum have different wavelengths; red has longer wavelength (700 nm) than violet (400 nm). Since electromagnetic radiation travels with the same speed as light, in 1864, Maxwell was able to conclude that light is an electromagnetic radiation with certain wavelengths. His equations also suggested that there are many more varieties of electromagnetic radiations, differing only in their

wavelengths. Maxwell theory predicted that radiations of different wavelengths, which our eyes cannot see, can exist.

In 1800, even before Maxwell, the German–British astronomer, William Herschel discovered *infrared rays* by showing that the temperature of the dark area beyond red end of the spectrum is almost 1° higher than that of visible light. In 1801, the German chemist, John William Ritter discovered *ultraviolet rays* when he observed that a paper soaked in silver nitrate solution darkens more rapidly when exposed to the dark area beyond the violet end of spectrum.

Almost 20 years after Maxwell's prediction of the existence of electromagnetic radiations of different wavelengths, in 1888 the German physicist, Heinrich Rudolph Hertz, while setting up an oscillating electric current in a rectangular wire, accidentally discovered a new kind of radiation. These rays called *radiowaves* lay far beyond the infrared radiation and could have wavelengths of anywhere between a few centimeters to kilometers. Subsequently, electromagnetic radiations, such as *X-rays* and *γ rays*, far beyond the ultraviolet X-rays were discovered with wavelengths exceedingly smaller than that of visible light, thus confirming Maxwells' electromagnetic theory.

2.4 Thermodynamics

The scientific study of heat started with the construction of the first thermometer in an attempt to express the amount of heat in quantitative terms. In 1592, Galileo first invented an instrument known as *thermoscope* to measure the temperature; however, he did not introduce temperature scale. The first thermometer using mercury was built in Italy around 1650 by the *Accademia del Cimento*. In 1714, the German physicist Daniel Gabriel Fahrenheit assumed that the temperature of a mixture of ice and salt is zero degree, while the body temperature is set at 96 degrees. On this *Fahrenheit scale*, water has a freezing point of 32 degrees and a boiling point of 212 degress. In 1743, the Swedish astronomer Anders Celsius introduced a *Celsius*

or *centigrade scale* and showed that the freezing point of water is 0 °C and the boiling point is 100 °C. Both these scales are based on the assumption that the expansion coefficient of mercury is relatively constant.

While working on the mechanical properties and the compressibility of air and other gases, Boyle discovered that the volume of a gas at a constant temperature is inversely proportional to its pressure. Almost a century later, it was discovered that gases expand at higher temperature. In 1791, the expansion coefficient for air at constant pressure was measured by Volta and was found to be 1/273 on the Celsius scale. Around 1800, two French chemists Joseph Gay-Lussac and Jacques Charles observed that this expansion coefficient is the same for all gases regardless of the chemical nature of the gas. Similarly, the pressure of any gas at a constant volume increases at a constant rate, 1/273 of its initial volume at 0 °C for each degree of increase in temperature. Thus, at −273 °C, the pressure and volume of any gas are expected to drop to zero value.

2.4.1 Heat, Energy, and Temperature

Two different doctrines developed in the eighteenth century helped to explain the nature of heat and to establish units for the quantity of heat, separate from that of temperature. According to one theory heat is a substance with or without mass (or weight) while the other theory suggests that heat is a type of motion or vibration. The Scotch physician Joseph Black regarded heat as a substance and called it *calor*. He defined the unit of heat as the amount necessary to raise the temperature of 1 lb of water by 1 °F. In the Metric system, 1 cal is the amount of heat needed to raise 1 g of water by 1 °C. In 1799, Benjamin Thompson (also known as Count Rumford) presented some data which suggested that heat is a type of motion and not a material substance. In 1842, the ideas of Count Rumford were further developed by the German physician Julius Robert Meyer who tried to establish a relationship between heat production and mechanical work,

and in the process discovered the *law of conservation of energy*. In the 1840s, the Englishman James Prescott Joule performed many experiments to clearly measure the mechanical equivalent of heat and by 1875 he was able to show that 1 cal is equal to 4.15 J.

The concept of energy is rather difficult to explain precisely; however, energy can be defined as the capacity to do work or to produce heat. In 1738, Daniel Bernoulli was one of the first scientists to show, mathematically, that the pressure of a gas depends on the mass, the number of molecules in a given volume of gas, and the average velocity of the gas molecules. However, he could not explain the relationship between the velocity of molecules and the temperature of gas. The Charles and Gay-Lussac law clearly demonstrated that the pressure of a gas is dependent on the temperature. Subsequently, based on Joule's work on the mechanical equivalent of heat, Maxwell discovered a statistical law which governs the velocity distribution in a monoatomic gas. More specifically, he found that the number of molecules in a given velocity interval is proportional to the density of gas and depends only on the temperature of the gas, and the absolute mass of the gas molecules. His equations can be used to calculate the average kinetic energy of gas molecules at any temperature. The British scientist, William Thompson (also known as Baron or Lord Kelvin), suggested that the kinetic energy of gas molecules be used to establish a temperature scale. Maxwell's equation predicts that at $-273.16\ °C$, the average kinetic energy of gas molecules will have zero kinetic energy. Therefore, the temperature of $-273.16\ °C$ can be regarded as *absolute zero* based on the *Kelvin scale* of temperature.

2.4.2   Emission of Light

In the beginning of the nineteenth century, the German physicist, Joseph von Fraunhofer (1787–1826) repeated Newton's experiments on the solar spectrum, using prisms of much better quality. He also invented a device, known as *diffraction grating* (a plate of glass or metal on which fine and equally spaced scratches or grooves) which divided light into its component colors, and observed that the spectrum of colors is intersected by a large number of very thin separate black lines. Von Frauenhofer recognized that these lines correspond to emission lines in sparks and flames. The significance of these lines (the signals coming from atoms and molecular species) was discovered in the 1860s by two German scientists Robert Wilhelm von Bunsen and Gustav Robert Kirchhoff.

It is well known that metals, such as iron and tungsten become luminous or give off visible light when heated to sufficiently high temperatures. The color of light varies with the temperature of the metal, going from red to yellow to white as it becomes hotter and hotter, while other frequencies of electromagnetic radiation that are invisible are also emitted. At room temperature, most of the radiation emitted is in the infrared range of the spectrum. Thus, at a high temperature, the emitted radiation has a high frequency and rapidly becomes more intense. In contrast, if we look through a prism at the light emitted by a hot gas, we see a continuous spectrum from red to violet. In a Bunsen burner however, the gas becomes very hot and emits very little of bluish light only. Bunsen discovered that when pure sodium or potassium is introduced into the Bunsen flame, the corresponding spectra contain only yellow or red colors. With the use of a spectroscope, Bunsen and Kirchhoff quickly realized that the dark lines in the solar spectrum correspond to the emission lines of specific hot gaseous elements. The law that all substances absorb the same light frequencies which they can emit was discovered by Kirchhoff, in 1860. The spectral analysis was soon utilized to discover new elements, such as Ce, Rb, Tl, In, and Ga.

2.5   Major Discoveries

2.5.1   Cathode Rays

Faraday's electrolysis experiments demonstrated the existence of ions, charged atoms, and molecules. In order to detect the particles of electricity

that are not associated with atoms or molecules, investigations were initiated to pass an electric current through a good vacuum. In 1838, Faraday was the first to actually force an electric current through a vacuum, however, since the vacuum was not good enough the observations lacked any significance.

In 1858, the German glassblower Johann Heinrich Wilhelm Geissler and the German physicist Julius Plucker developed a glass tube with two electrodes with very good vacuum (known as *Geissler tubes*). When the electrodes were connected to a source of electric current, a greenish luminescence appeared on the glass tube near the cathode. It was soon realized that the position of the glow does not depend on the anode, the nature of the gas molecules in the tube, or the kind of metal used to make the cathode. Instead, something from the cathode appeared to be moving straight and hitting the glass before being collected by the anode. The German physicist Johann Wilhelm Hittorf suggested that objects placed in front of a cathode cast shadows. The German physicist Eugen Goldstein, however, maintained that the glow is associated with the current itself and in 1876 introduced a name for this mysterious phenomenon: *Cathodenstrahlen*, or *cathode rays*. In 1878, the British physicist William Crookes devised vacuum tubes that produced cathode rays which clearly moved in straight lines and which were better than the cathode rays produced in Geissler tubes. The investigations on the nature of cathode rays with the Hittorf and Crookes vacuum tubes ultimately led to the discovery of X-rays and electron.

2.5.2   X-Rays

In 1895, the German physicist Wilhelm Röntgen, while investigating the effects of cathode rays in a discharge tube, accidentally, discovered a new form of penetrating radiation, which he called *X-rays*. He observed that when cathode rays (negatively charged particles) strike the atoms of a glass vacuum tube, they produce penetrating rays that cause salt (barium platinocyanide) to glow. Soon thereafter, it was realized that X-rays are (1) more penetrating than the cathode rays and (2) not prone to deflection by a magnetic field and physicists started to discuss what these mysterious X-rays might be.

The true nature of X-rays was discovered in 1912 when the German physicist Max von Laue, using crystals as a type of three-dimensional grating, discovered that X-rays do not behave like particles, but instead have the wavelike characteristics of an electromagnetic radiation. An accelerated electric charge will radiate electromagnetic waves. As the fast-moving cathode rays approach the positive charge in the nucleus of glass atoms, electrons are brought to rest (accelerated) and the kinetic energy of the electrons is converted to electromagnetic waves. Radiation produced under these circumstances has been given the name *bremsstrahlung* (breaking radiation). It was also discovered, that when denser more massive atoms in a metal are used to stop the accelerated electrons, X-rays of higher energies can be generated. In 1911, the British physicist Charles Barkla noticed that each metal produced X-rays of a particular wavelength, called characteristic X-rays of a particular metal, and called the more penetrating beam *K* X-rays and, the less penetrating beam *L* X-rays. Subsequently, it was discovered that these characteristic X-rays emitted by metals are due to the deexcitation of electrons in the atomic shells.

2.5.3   Electron

Following the discovery of cathode rays and radiowaves, the Dutch physicist Hendrick Antoon Lorentz refined Maxwell's equations and developed a new theory, called *electron theory*. More specifically, Lorentz proposed that microscopic particles, each of which carry an electric charge, must be contained in all atoms and that these charged particles generate electric, and magnetic fields. He also proposed that oscillations of these charged particles inside the atoms are the source of light.

In 1895, the French physicist Jean Baptiste Perrin demonstrated that cathode rays, emitted from the cathode of a discharge tube, are negatively charged particles. In 1896, Lorentz deduced a value for the charge-to-mass ratio (e/m) for charged particles inside the atom. As a result of Lorentz's electron theory, it was presumed that a magnetic field would affect the electron oscillations and thereby the frequencies of the light emitted. In 1896, Pieter Zeeman observed such a broadening of the spectral lines by the magnetic field. Based on the Zeeman effect, Lorentz and Zeeman were, subsequently, able to estimate the e/m ratio and predict that the charge of the particles within the atom is negative.

In 1897, the British physicist Joseph John Thompson confirmed Perrin's observations and obtained a precise value for the e/m ratio of cathode rays. The ratio turned out to be over a thousand times greater than that of a hydrogen ion. Thompson also demonstrated that the cathode rays could be deflected by both magnetic and electric fields. He also discovered that cathode rays are negatively charged particles, which he initially called *corpuscles*. He later changed the name and called them electrons; the name first suggested by Johnstone G. Stoney in 1894. Thompson's measurement of an electron's mass and charge confirmed that cathode rays (electrons) are the same particles within the atom are also responsible for the emission of light by the atom. In 1911, the American physicist Robert Andrews Milikan succeeded in measuring quite accurately, the minimum electric charge that could be carried by a particle and found that if this charge were carried by an electron, it would have to be only 1/1837 as massive as a hydrogen atom.

In 1899, Philipp Lenard, while investigating the interaction of cathode rays with in metal plates, discovered that electrons are ejected when ultraviolet light strikes metal surfaces. He also discovered that the emission of electrons is dependent on the frequency of light but not on the intensity of light. This phenomenon, known as the photoelectric effect, was later explained by Albert Einstein and is based on the light quantum hypothesis proposed by Max Plank, in 1900.

2.5.4   Radioactivity

Henry Becquerel, professor of physics at the Ecole Polytechnique in Paris, heard about the discovery of X-rays and immediately thought of a possible connection between X-rays and fluorescence. He quickly initiated a series of experiments testing whether fluorescent substances emitted X-rays. In February 1896 he was exploring the possibility that sunlight might cause crystals to emit penetrating rays like the X-rays. As luck would have it, he used uranium–potassium bisulfate (uranium salts were known to be phosphorescent). These crystals were placed next to a photographic plate wrapped in dark paper. If sunlight causes the crystals to emit penetrating rays, then these rays might penetrate the dark paper and darken the plate. Since the weather was cloudy, Becquerel placed the unwrapped plates in the drawer of a cabinet leaving the crystals on the cabinet. Much to his surprise, a couple of days later, when he developed the plates, he found intense darkening of the plate, due to exposure to some intense radiation. Becquerel quickly concluded that invisible rays from uranium had penetrated the cabinet and the dark paper covering the plate and finally exposed the photographic plate. For a few years, these rays were known as "Becquerel rays" or *rayons uranique*. In 1898, Maria Sklodowska Curie and Pierre Curie (Fig. 2.3) discovered that the element thorium also emitted such rays. That year, the Curies coined the name *radioactivity* to describe the phenomenon of penetrating radiation emitted by uranium and thorium.

In the following years, other new radioactive phenomena were discovered. For example, in 1900 the French chemist, Paul Villard discovered an extremely penetrating form of radiation coming from radioactive sources. However, it was Ernest Rutherford (Fig. 2.2) at the Cavendish Laboratory in England who played a major role in the study of radioactivity. Rutherford and his colleagues identified three different components in the radiations from radioactive elements based on their behavior in electric and magnetic fields. He called them, *α-rays*, *β-rays*, and *γ-rays* and these components were eventually identified as being helium nuclei, electrons, and high-energy photons, respectively.
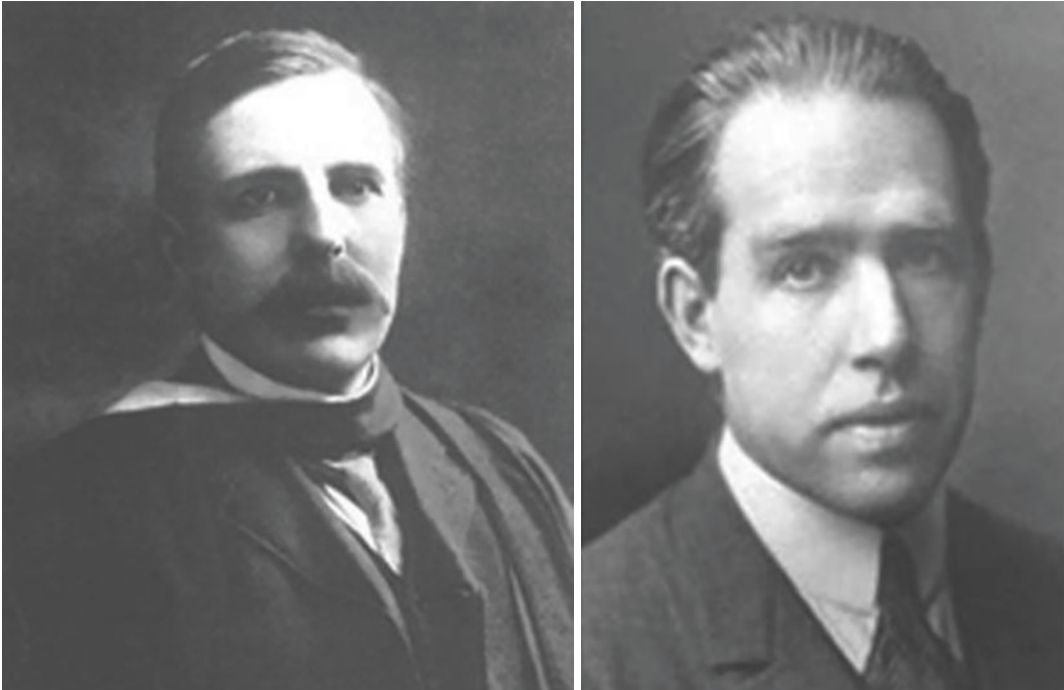
Fig. 2.2 Ernest Rutherford (on left), an English physicist, and the winner of the Nobel prize in chemistry. Niels Henrik David Bohr (on right), a Danish physicist, and the winner of the Nobel prize in physics

In 1903, Rutherford and Soddy sought to explain the cause and nature of radioactivity. They proposed a *disintegration theory*, which defined radioactivity as a change of one chemical element into another with the emission of alpha or beta particles. An unstable element reaches stability spontaneously by undergoing radioactive decay involving transmutation of elements and emission of energy; however, in the 1930s it was discovered that radioactive elements can also emit positively charged electrons or *positrons*.

2.5.5   Light Quantum

The classical theory of matter assumes that matter in general can absorb or emit any quantity of energy. It also predicts that the radiation profile of the emission spectrum has no maximum and goes to infinite intensity, at shorter wavelengths (or higher frequencies). This effect is called *ultraviolet catastrophe*. An ideal material body, known as the *black body*, is one that can absorb all radiations incident. Therefore, since it can absorb all radiations, it should also emit radiations of all frequencies. The experimental evidence, however, indicated that when a piece of metal is heated to incandescence, the profile of radiation emitted shows that the maximum (peak) shifts to shorter wavelengths as the temperature is increased. The question is why does the intensity of radiation drop gradually as the frequency of radiation increases? In 1901, the German physicist Max Planck's postulated that the energy of radiation can be absorbed or emitted by bodies only in specific packets or amounts and called of these small packets of energy a *quantum*. The energy (E) of each quantum is a product of the frequency of radiation (n) and a constant, h (known as Plank's constant). The value of h was determined to be 6.626×10^{-34} J. Hz^{-1}.

2.6   Reality of Atoms

2.6.1   Avogadro's Number

Avogadro's number is the calculated value of the number of atoms (or molecules) in a gram mole of any chemical substance. Although, as early as the seventeenth century, Boyle had attempted to estimate the size of atoms, it was not until 1865 that the first successful attempt was made by the Austrian physicist and schoolteacher Josef Loschmidt. Based on Avogadro's hypothesis, the atomic weights of several gaseous elements were accurately determined in 1860 by the Italian chemist Stanislao Cannizzaro. Subsequently, in 1865, using the new *Kinetic Molecular Theory*, developed by Maxwell and Clausius, Loschmidt found the number of atoms in 1 cm^3 of gaseous substance, under ordinary conditions of temperature and pressure, to be somewhere around 2.6×10^{19} atoms cm^{-3} (this is known as *Loschmidt's Constant*). Since 1 mol of any gas occupies 22.4 L at STP, the number of atoms in 1 mol is approximately equal to 5.8×10^{23} atoms.

2.6.2   Brownian Motion

In 1827, Robert Brown observed the random movement of pollen particles in a liquid. This phenomenon, known as *Brownian motion*, states that microscopic particles in a liquid are never at rest; they are in perpetual movement even under conditions of perfect external equilibrium or constant temperature. The only irrefutable explanation for this phenomenon ascribes the movements of the particles to the shocks produced by the atoms and molecules of the liquid themselves. A mathematical theory of this phenomenon was developed by Einstein, in 1905, and a theoretical estimate of Avogadro's number was given to be 6.2×10^{23} particles. The first experimental proof of this theory was provided by Jean Baptiste Jean Perrin in France around 1908. More specifically, Perrin determined that the number of atoms in 1 mol is approximately 6.8×10^{23}. The work of Einstein and Perrin provided some of the first concrete evidence for the existence of atoms. The current experimental value of $6.022\ 140\ 76 \times 10^{23}$ atoms per mole is the average for measurements using the best methods (Fig. 2.3).

Fig. 2.3 Antoine Henri Becquerel (on right), Pierre Curie (middle), and Marie Curie nèe Sklodowska (on right) received the Nobel Prize in Physics in 1903 for the discovery of spontaneous radioactivity and radiation phenomena

2.7 Atomic Structure

2.7.1 Nuclear Atom

Since 1890, various discoveries have shown that the atom is not indivisible (as Dalton supposed) but is really composed of parts. The discovery of *radioactivity*, the interaction of electricity with matter, and the discovery of free *electrons* have all contributed to the discovery of the subatomic structure of atoms. In 1910, Rutherford (Fig. 2.2) presented a model of an atomic structure, known as *nuclear atom*. According to this nuclear model, atoms consist of a massive, compact, positively charged core, or *nucleus*, surrounded by a diffuse cloud of relatively light, negatively charged electrons. In 1913, Moseley formulated the property of *atomic number* (*Z*), which is the number of positive charges in the nucleus. Moseley showed that the sequence of elements in the periodic table is, in fact, a sequence of elements that are arranged in order of their atomic numbers and not their atomic weight. In 1914, Rutherford named this positively charged particle in the nucleus, *proton* (from the Greek word "first"). A proton has an electrical charge exactly equal to that of an electron but, positive, and a mass 1836 times that of an electron. Incidentally, the nucleus of a hydrogen atom is known as the proton. In the electrically neutral atom, the number of orbiting electrons is sufficient to exactly balance the number of positive protons. In 1920s, Rutherford speculated that a neutral particle (one that is the same size as a proton) within the nucleus accounts for the total mass of the atom. Such a neutral particle was discovered by James Chadwick, in 1932. Heisenberg soon proposed that nuclei of different elements consist of protons and neutrons which are held together by strong exchange forces, known as nuclear forces. The total number of protons and neutrons within the nucleus is called the *mass number* (*A*), which is very close to the atomic weight of an element. The mass number (*A*) of ^{12}C nuclide is 12 and its atomic mass is considered as 12 atomic mass units (AMU or u). The atomic weight of natural carbon

is 12.011 since it is a mixture of ^{12}C (98.89%) and ^{13}C (1.11%) nuclides or isotopes.

2.7.2 Bohr's Model of Atom

The atom consists of an extremely dense, low positively charged nucleus surrounded by a cloud of electrons with small size and mass, with each electron carrying a single negative charge equal but opposite to that of a proton in the nucleus. Because the number of electrons and protons in an atom are the same, the whole atom is electrically neutral. The *atomic volume* (10^{-8} cm diameter) with the cloud of electrons is significantly much larger compared to the volume of the nucleus (10^{-13} cm diameter). Based on Rutherford's discovery of atomic nucleus and Plank's discovery of energy quantum ($E = hn$), Neils Bohr (Fig. 2.2) developed the first quantum model of an atom (Fig. 3.4 in Chap. 3), in 1913. According to this model, an electron in a hydrogen atom rotates around the nucleus at high speeds in closed *circular orbits* associated with a characteristic *quantum number* (*n*). The electron in general exists in a low energy orbit (*ground state*). The gain or loss of a quantum of energy occurs only when an electron moves from one orbital to one of greater or lesser energy. As a result, an atom can absorb or emit energy in discrete units or quanta.

In 1916, Arnold Sommerfeld suggested that the electron orbits can also be elliptical and at different degrees. Subsequently, the orbital *quantum number* (*l*) was introduced, which assumes the circular and elliptical orbits are in a single plane. When atoms are in a magnetic field, however, the orbits may be tipped and can be best represented in a three-dimensional spherical space around the nucleus. To account for this magnetic effect, a *magnetic quantum number* (*m*) was introduced. Subsequently, Wolfgang Pauli introduced the *spin quantum number* (*s*) to represent the direction of the electron spin (clockwise or anti-clockwise). The arrangement of electrons around the nucleus in an atom can be described based on the

four quantum numbers. A more detailed example of electron orbits based on quantum mechanics is provided in Chap. 7.

2.7.3   Isotopes

Dalton assumed that all the atoms of a given element have the same *atomic weight* or *atomic mass*. By 1914, it was realized that atoms of the same element can vary in weight but may have the same chemical properties. The word *isotope* was coined by Frederick Soddy to represent atoms of an element that have different weights but still can be placed in the same place in the periodic table. An isotope can be stable or unstable (radioactive). Some of the elements in nature such as Na, F, Al, and Bi have no isotopes, while 81 of the elements listed in the periodic table have at least one stable isotope. Further, all elements heavier than Bi are unstable; no stable isotope exists for these elements. In 1947, the American chemist Truman Paul Kohman suggested that the word *nuclide* is a more appropriate term to represent both the stable and unstable atoms (or radionuclide), of an element.

For any given element, the percentage of each isotope found in nature is called the isotope's *isotopic abundance*. Natural carbon exists in two stable isotopic forms (^{12}C and ^{13}C); the isotopic abundance of ^{12}C is 98.9% while the abundance of ^{13}C is very small—only 1.1%. Since the atomic mass of an element is expressed as an average of all the naturally occurring isotopes, the average atomic mass of carbon is 12.011. Similarly, the average atomic mass of copper is 63.545, since it has two stable isotopes: ^{63}Cu (69.2%) and ^{65}Cu (30.8%).

In nature, 92 elements (hydrogen to uranium) have been observed. Technetium and promethium, and all elements with atomic numbers greater than 82 have isotopes that are known to decompose through radioactive decay. Stable elements are 82, however, 252 isotopes (nuclides) are stable. In addition, >3000 nuclides are known to be radioactive.

2.7.4   Quantum Atom

At first Bohr's model appeared to be very promising but, by the mid-1920s, it became clear that Bohr's model needed refinement. The wave mechanics or quantum mechanics developed by Werner Heisenberg, Louis deBroglie, and Edwin Schrodinger finally provided a wave or quantum mechanical description of an atom. Quantum theory describes matter (electrons and electromagnetic radiation) as acting both as a particle and as a wave. This characteristic is called wave-particle duality. According to this model, the electron bound to the nucleus is similar to a standing or stationary wave, while the circumference of a particular orbit corresponds to a whole number of wavelengths. Schrodinger's famous wave equation ($Hy = Ey$) describes an electron in an atom, where y called the wave function, is a function of the coordinates (x, y, and z) of the electron's position in three-dimensional space and H represents a set of mathematical instructions called an *operator*. When this equation is analyzed, many solutions are found. Each solution consists of a wave function y that is characterized by a particular value of energy, E. A specific wave function for a given electron is often called an *orbital*. An orbital, however, is not a Bohr's orbit; the orbitals differ from each other in size, angular momentum, and magnetic properties. The wave function corresponding to the lowest energy of a hydrogen atom is called 1 *s* orbital. Quantum mechanics only provides the probability of an electron's position around the nucleus but, not the electron's motion around the nucleus. Also, each electron in an atom has a unique set of quantum numbers. *In a given atom, no two electrons can have the same set of four quantum numbers* (n, l, m_e, m_s). This is called the *Pauli Exclusion Principle*, which can also be stated as follows: *An orbital can hold only two electrons and they must have opposite spins*.

The atom's electron cloud—that is the arrangement of electrons around the nucleus in an atom—determines most of the atom's physical and chemical properties. The electrons in the out-

ermost shell, in particular, determine the chemical properties of an atom. Atoms bond with other atoms by donating or sharing electrons in order to fill their shells. It requires less energy to exist in this bonded state; atoms always seek to exist in the lowest energy state possible.

2.7.5 Discovery of Antimatter

In particle physics, *antimatter* is an extension of the concept of antiparticle to matter, where antimatter is composed of antiparticles (such as antielectron and antiproton) in the same way that normal matter is composed of particles (electrons and protons). In 1928, Paul Adrien Maurice Dirac, a physicist at Cambridge, combined relativity, and quantum mechanics in order to derive an equation that provides a complete description of the electron. Surprisingly, this theory not only described electrons but the particles we call *positrons* or antielectrons, as well. Dirac's theory predicted that when an electron encounters a positron, the two charges cancel each other out, and the pair annihilates, with the combined mass transforming into high-energy radiation of a pair of annihilation photons (511 keV). This conversion of mass into energy is the most dramatic expression of Einstein's celebrated equation $E = mc^2$. The theory also predicted that high-energy photons could rematerialize as matter and antimatter in a process known as the *pair production*. In 1932, positrons were first discovered by Carl D. Anderson, who gave the positron its name. More specifically, the positron was discovered by passing cosmic rays through a cloud chamber. In 1934, Irène Curie and Frédéric Joliot confirmed the existence of the positron by bombarding aluminum with alpha particles. This resulted in the artificial production of radionuclide ^{30}P, which quickly decayed to stable silicon by emitting positrons. Dirac, Anderson, Curie, and Joliot all received Nobel prizes for their pioneering discoveries. Subsequently in 1955, Emilio Segre and Owen Chamberlain discovered the antiproton using high-energy protons (6.5 billion eV) generated in a Bevatron accelerator at the Lawrence Berkeley Radiation Laboratory, in California.

2.8 The Elementary Particles

In particle physics, an elementary particle or a fundamental particle is a subatomic particle that is not composed of other particles. The notion that the atom is the ultimate building block of all matter in the universe is no longer valid. In the 1930s, it seemed that protons (with positive charge), neutrons (with no charge), and electrons (with negative charge) were the smallest objects into which matter could be divided. As a result, these three particles were regarded as the *elementary particles* or fundamental particles.

The Standard Model of particle physics is the theory classifying all known elementary particles, as well describing the three of the four known fundamental forces (electromagnetic, weak, and strong nuclear forces) in the universe. In particle physics, an *elementary particle* is a particle without a substructure; that is, it is not made up of smaller particles. The current accepted "Standard Model" of physics, which describes the interactions of particles and almost all forces in nature, recognizes 17 (seventeen) elementary particles. All elementary particles are either *fermions or bosons*; particles normally associated with matter (such as proton, neutron, and electron) are fermions, while elementary bosons (such as photon) are force carriers that function as the "glue" holding matter together. Among the bosons, only the photon is the most realistic elementary energy particle (Table 2.1).

In 1968, it was discovered that the proton contained much smaller, point-like objects and was, therefore, not an elementary particle. The objects in the proton were identified as up and down quarks. The up quark has a fractional negative positive charge ($+\frac{2}{3}e$), while the down quark has a fractional negative charge ($-\frac{1}{3}e$). Quarks are the fundamental constituents of protons and neutrons. Quarks are thought to have no internal structure, meaning that they exist as zero-dimensional points that take up no space. Individual quarks are never found in nature; however, quarks always bind together to form composite particles—the hadrons. The up quark and the down quark are generally stable, and they are

Table 2.1 Physical properties of elementary particles[a]

Particle	Charge	Mass (MeV/c^2)	Mass (kg)	Charge radius (m)	Spin	Mean lifetime
Photon (γ)	0	0	0	–	1	Stable
Electron (e^-, β^-)	−1	0.511	9.109×10^{-31}	–	1/2	Stable
Positron (e^+, β^+)	1	0.511	9.109×10^{-31}	–	1/2	Stable
Up Quark (u)	+2/3 e	2.2	–	10^{-18}	1/2	Stable in proton
Down Quark (d)	−1/3 e	4.7	–	10^{-18}	1/2	Stable in proton
Proton or uud (p^+ or H^+)	1	938.272	1.672×10^{-27}	$<10^{-15}$	1/2	$>10^{30}$ years
Neutron or ddu (n, n^0)	0	939.565	1.674×10^{-27}	$<10^{-15}$	1/2	879.6 s

[a] The above values are from Wikipedia
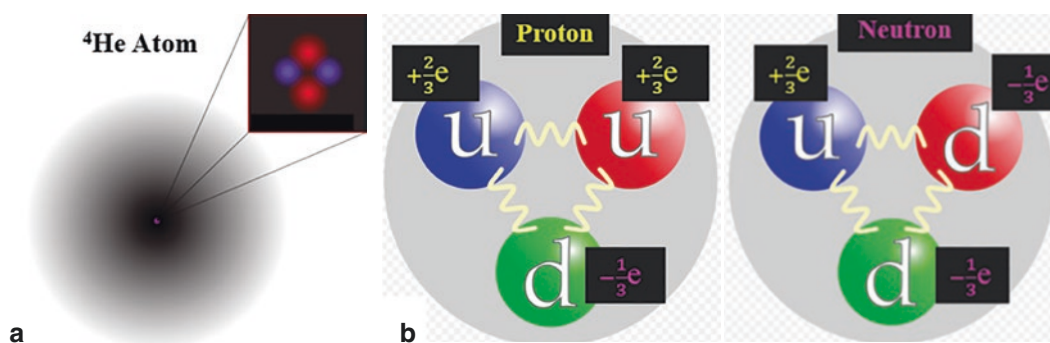
Fig. 2.4 Helium atom (**a**) with nucleus in the center with 2 protons and 2 neutrons. Proton (**b**) consists of 2 up quarks and 1 down quark, while neutron (**c**) consists of 2 down quarks and 1 up quark (b)

found in protons and neutrons. A proton is composed of two up quarks and, one down quark, while a neutron is composed of one up quark and two down quarks (Fig. 2.4). In the radioactive β^- process, a neutron "splits" into a proton, an electron, and an antineutrino. This process occurs when one of the down quarks in the neutron (udd) decays into an up quark by emitting a W^- boson, transforming the neutron into a proton (uud). The W^- boson then decays into an electron (e^-) and an electron antineutrino (ν_e).

Quarks are one of the primary building blocks of matter in the universe. The Nobel laureates Murray Gell-Mann and George Zweig first proposed the quark model, in 1964. It was also discovered that there are six *flavors* of quarks; the three positively charged quarks are called *up-type quarks* (*Up*, *Charm*, and *Top*) and the three negatively charged quarks are called *Down-type quarks* (*Down*, *Strange*, and *Bottom*). The more massive quarks produced in particle accelerators and cosmic rays are unstable and rapidly decay.

Because quarks cannot exist independently, the elementary particles in nature representing fermions are protons, neutrons, and electrons. It is the combination of these three subatomic particles that resulted in the formation of chemical elements, billions of years ago.

Further Reading

Asimov I. Atom. Journey across the subatomic cosmos. New York, NY: Truman Tally Books; 1992.

Gamow G. The great physicists from Galileo to Einstein. New York, NY: Dover; 1961.

Limouris GS. From the atomism of Democritus to the therapeutic nuclear medicine today. Eur J Nucl Med Mol Imaging. 2006;33:s65–8.

Pais A. Subtle is the Lord. The science and the life of Albert Einstein. Oxford: Clarendon; 1982.

Pais A. Niels Bohr's times, in physics, philosophy and polity. Oxford: Clarendon; 1991.

Segrè E. From X-rays to quarks. Modern physicists and their discoveries. New York, NY: Freeman; 1980.

Segrè E. From falling bodies to radiowaves. Classical physicists and their discoveries. New York, NY: Freeman; 1984.

Atoms and Radiation

3

Concerning matter, we have been all wrong. What we have called matter is ENERGY, whose vibration has been so lowered as to be perceptible to the senses. There is no matter. (Albert Einstein)

3.1 Matter and Energy

Everything in this universe is made up of *matter* and *energy*. Matter is anything that has *mass* (such as atoms and subatomic particles) and occupies space by having volume. In contrast, light and heat are forms of energy. The concept of mass is central to the discussion of matter and energy. The mass of an object depends on the quantity of matter in the object, while the mass of a body (material object) is directly associated with its weight. On earth, the weight of a body is the pull of the earth on the body, which is proportional to its mass and depends on the distance of the body from the center of the earth. Energy is the ability to produce change or the capacity to do work. Energy occurs in many forms such as electrical energy, mechanical energy, chemical energy, and nuclear energy. In addition, energy can also be *potential energy* (energy due to position) or *kinetic energy* (energy due to motion). The units for the quantities of mass and energy are shown in Table 3.1.

3.1.1 Mass–Energy Relationship

The most famous relationship Einstein derived from the postulates of special relativity—concerns mass (m) and energy or the rest energy (E_0).

$$E_0 = m_0 c^2 \tag{3.1}$$

Table 3.1 Primary and derived units of quantities based on Système Internationale (SI)

Quantity	Unit	Symbol	Equivalent
Mass	kilogram	kg	1 kg = 1000 g
Amount	Mole	mol	1 mol = Avogadro's constant, 6.02×10^{23} particles (atoms or molecules)
Length	Meter	m	Distance light travels in exactly 1/299,792,458 s.1.m = 100 cm = 1.0×10^{10} Å
Time	Second	s	Duration of 9,192,631,770 cycles of microwave radiation produced by Cs-133 atoms
Temperature	Kelvin	K	°C + 273.16
Current	Ampere	A	1 C s^{-1}
Energy	Joule	J	4.184 J = 1 cal
Electric potential	Volt	V	1 eV = 1.60269×10^{-19} J

In nonrelativistic physics, kinetic energy (KE) of an object of rest mass m_0 and speed v is given by

$$KE = \frac{1}{2} m_0 v^2 \qquad (3.2)$$

In relativistic physics, if the mass is moving, the total energy (E) is

$$E = mc^2 = \frac{m_0 c^2}{\sqrt{1 - v^2 / c^2}} \qquad (3.3)$$

The mass of a body moving at the speed v relative to an observer is larger than its mass when at rest relative to the observer by the factor, $\sqrt{1 - v^2 / c^2}$ where "c" is the velocity of light. Relativistic mass increases are significant only at speeds approaching that of light. For particulate radiation, relativistic effects are significant. Since mass and energy are not independent entities, according to the principle of conservation of mass energy, mass can be created or destroyed. When this happens, an equivalent amount of energy simultaneously vanishes or comes into being, and vice versa. Mass and energy are different aspects of the same thing. This mass–energy relationship is key for the estimation of nuclear binding energies and for the explanation of the liberation of enormous amounts of energy during the radioactive transformation of nuclides.

3.2   Radiation

The term *radiation* simply refers to *energy in transit*. There are two specific forms of radiation:

- Particulate radiation (nonpenetrating): mass (subatomic particles such as protons, neutrons, electrons) in motion carrying kinetic energy of particles
- Electromagnetic radiation: oscillating electric and magnetic fields carrying energy and traveling through space with a constant velocity

3.2.1   Electromagnetic Radiation

Visible light is the most familiar form of electromagnetic radiation. Ultraviolet, infrared, microwave, radio waves, X-rays, γ rays, and annihilation radiation are all different types of electromagnetic radiation. All types of electromagnetic radiations exhibit "wave-like" behavior in their interactions with matter. The wavelength (λ) and frequency (ν) of the oscillating fields of electromagnetic radiation (Fig. 3.1) are related by

$$\lambda \nu = c \qquad (3.4)$$

where c is the velocity of light in free space (2.998×10^8 m/s).

Maxwell was able to show that the speed "c" of electromagnetic waves in vacuum can be deduced mathematically by

$$c = \frac{1}{\sqrt{\varepsilon_0 \mu_0}} = 2.99 \times 10^8 \, \text{m / s} \qquad (3.5)$$

where ε_0 is the electric permittivity of free space (8.854×10^{-12} c^2/N m^2) and μ_0 is its magnetic permeability ($4\pi \times 10^{-7}$ T m/A).

According to quantum theory, electromagnetic radiation, however, behaves as discrete packets of energy (with no mass or charge), called quanta or photons. The energy of the photon is related to the frequency of the electromagnetic radiation by

$$E = h\nu \qquad (3.6)$$

where h is known as Planck's constant whose value is 6.626×10^{-34} J s.

De Broglie suggested that a photon, an energy particle, behaves in certain ways as though it has a wave nature. The wavelength of a photon is therefore specified by its momentum

$$\lambda = \frac{h}{\rho} \qquad (3.7)$$

where the momentum

$$\rho = \frac{h\nu}{c} \qquad (3.8)$$
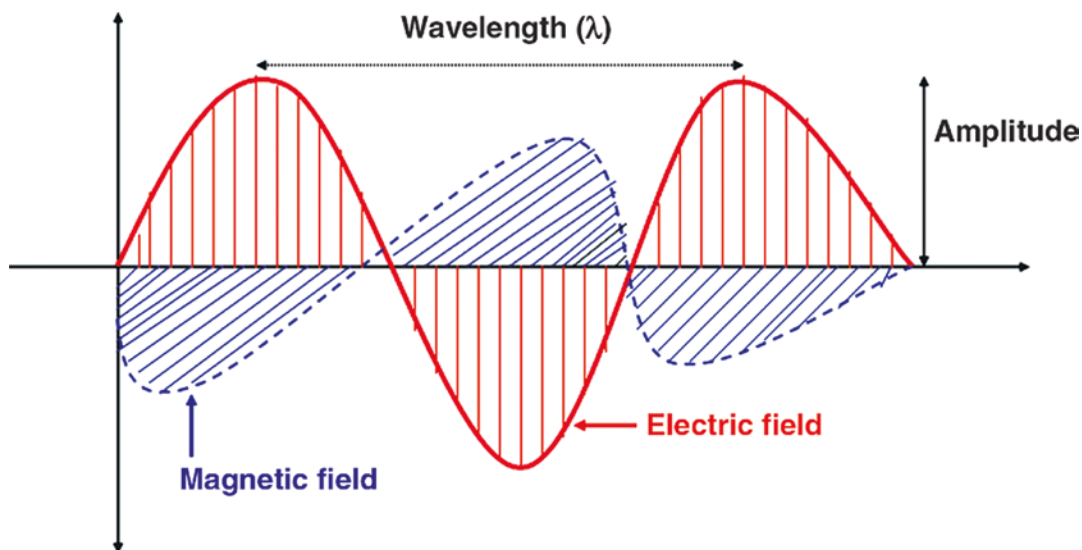
Fig. 3.1 The electric and magnetic fields in an electromagnetic wave are perpendicular to each other and to the direction of the wave
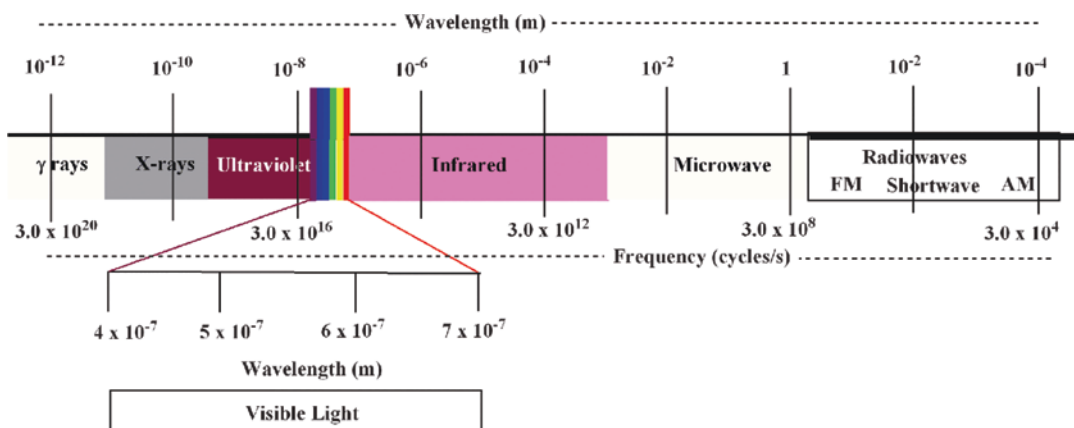
Fig. 3.2 The spectrum of electromagnetic radiation, the visible light (light waves) spans only a brief frequency interval from 4.3×10^{14} Hz for red light to approximately 7.4×10^{14} Hz for violet light

since

$$\lambda v = c \qquad (3.9)$$

Different types of electromagnetic radiation and their corresponding photon energies, wavelengths, and frequencies are shown in Fig. 3.2.

3.3   Classification of Matter

Based on the composition of matter as a basis for classification, matter may be regarded as a pure substance or as a mixture of substances.

There are two kinds of substances: *elements* and *compounds*. An element or a chemical element is a substance that cannot be broken down to simpler substances by ordinary chemical means. Compounds are substances consisting of two or more elements (sometimes also called molecules) combined in definite proportions by mass, having properties different from that of any of its constituent elements. A mixture consists of two or more substances and there are two kinds of mixtures: homogenous mixtures (also called solutions) and heterogeneous mixtures.

Fig. 3.3 The modern standard periodic table showing 18 groups

3.3.1   Chemical Element

All matter in nature is made up of pure substances, known as chemical elements. In the periodic table (Fig. 3.3), 118 chemical elements have been listed; 90 elements occur in nature and the rest of these elements have been produced artificially. Oxygen is the most abundant element in the earth's crust. Air is mostly a mixture of nitrogen (78%) and oxygen (21%). Since ancient times, the following ten elements have been known to be pure substances (carbon, sulfur, copper, silver, gold, iron, tin, mercury, tin, and antimony). The rest of the elements were discovered by man. In 1869, based on the chemical properties and relative atomic weights of approximately 70 natural elements, Mendeleyev, a Russian chemist, arranged the elements in a table of groups and periods, known as the periodic table. The long form of the modern periodic table with all the 118 elements is shown in Fig. 3.3.

3.4   Atoms

In 1804, John Dalton proposed the existence of atoms and attributed certain properties to the *atoms* based on experimental studies. Every chemical element is composed of individual particles, called atoms. An atom by definition is the smallest unit into which a chemical element can be broken down, without losing its chemical identity. Dalton assumed that all the atoms of a given element have the same *atomic weight* or *atomic mass*. By 1914, it was realized that atoms of the same element can vary in weight but may have the same chemical properties. The word *isotope* was coined by Frederick Soddy to represent atoms of an element that have different weights but, which can still be placed in the same position in the periodic table. An isotope can be stable or unstable (radioactive).

Some of the elements in nature such as Na, F, Al, and Bi have no isotopes, while 81 of the elements listed in the periodic table have at least one stable isotope. Natural carbon exists in two stable isotopic forms (^{12}C and ^{13}C) while tin has ten stable isotopes. All elements heavier than Bi are unstable; no stable isotope exists for these elements. In 1947, the American chemist Truman Paul Kohman suggested that the word *nuclide* is a more appropriate term to represent both, stable and unstable atoms (or radionuclide) of an element.

3.4.1   Atomic Structure

In 1910, Rutherford presented a model of an atomic structure known as *nuclear atom*. According to this nuclear model, atoms consist of a massive, compact, positively charged core, or *nucleus* surrounded by a diffuse cloud of relatively light, negatively charged electrons. In 1913, Moseley formulated the property of *atomic number* (*Z*), which is the number of positive charges in the nucleus. In 1914, Rutherford named this positively charged particle in the nucleus, *proton* (from the Greek word *first*). Proton has an electrical charge equal to that of an electron; however, a proton is positive and has a mass 1836 times that of the electron. In the electrically neutral atom, the number of orbiting electrons is sufficient to balance the number of positive protons. In the 1920s, Rutherford summarized that the existence of a neutral particle (the same size as a proton) within the nucleus accounts for the total mass of the atom. Such a neutral particle was, eventually, discovered in 1932 by James Chadwick. Subsequently, Heisenberg proposed that the nuclei of different elements consist of protons and neutrons which are held together by strong exchange forces known as nuclear forces. The total number of protons and neutrons within the nucleus is called the *mass number* (*A*), which is very close to the atomic weight of an element. The mass number (*A*) of ^{12}C nuclide is 12 and its atomic mass is considered as 12 atomic mass units (AMU or u). The atomic weight of natural carbon, however, is 12.011 since it is a mixture of ^{12}C (98.89%) and ^{13}C (1.11%) nuclides or isotopes. The mass–energy relationships of the fundamental subatomic particles are summarized in Table 3.2.

3.4.2   The Bohr Model of an Atom

The atom consists of an extremely dense, small positively charged nucleus surrounded by a cloud of electrons with small size and mass, each carrying a single negative charge equal but opposite to that of a proton in the nucleus. Because the number of electrons and protons in an atom is the same, the whole atom is electrically neutral. The *atomic volume* (10^{-8} cm diameter) with the cloud of electrons is significantly larger than the volume of the nucleus (10^{-13} cm diameter). Based on Rutherford's discovery of the atomic nucleus and Plank's discovery of the energy quantum ($E = hn$), Neils Bohr developed the first quantum model of an atom in 1913 (Fig. 3.4). According to this model, an electron in a hydrogen atom rotates around the nucleus at high speeds in closed *circular orbits* associated with a characteristic *quantum number* (*n*). The electron in general exists in
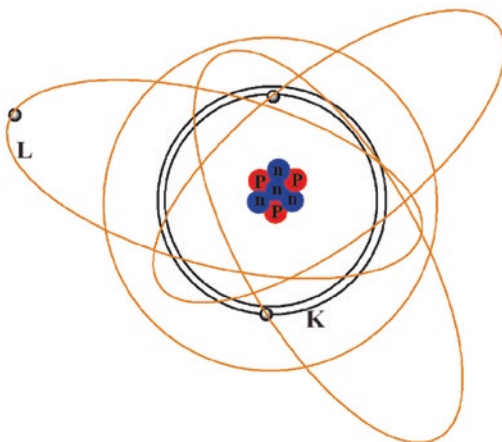
Fig. 3.4 Schematic representation of the Bohr and Sommerfeld model of atom showing circular (*K* shell) and elliptical (*L* shell) orbits

Table 3.2 Fundamental particles of matter

	Mass[a]		Energy[b]	Charge	
Particle	u	kg	MeV	Elementary	Coulombs (C)
Electron, e⁻	0.0005486	9.11×10^{-31}	0.511	−1	-1.602×10^{-19}
Positron, e⁺	0.0005486	9.11×10^{-31}	0.511	+1	$+1.602 \times 10^{-19}$
Proton, p/H⁺	1.007825	1.673×10^{-27}	938.78	+1	$+1.602 \times 10^{-19}$
Neutron, n°	1.008665	1.675×10^{-27}	939.56	0	–

[a] Mass is expressed in international mass unit (u), which is equal to 1/12th the mass of carbon-12 atom (1.66054×10^{-24} g)
[b] The energy given here is the rest mass energy of the particle

a low energy orbit (*ground state*). Gain or loss of a quantum of energy occurs only when an electron moves from one orbit to one of greater or lesser energy. As a result, an atom can absorb or emit energy in discrete units or quanta.

In 1916, Arnold Sommerfeld suggested that the electron orbits can be elliptical, and to different degrees. Consequently, the orbital *quantum number* (*l*) was introduced. The circular and elliptical orbits are assumed to be in a single plane. When atoms are in a magnetic field; however, the orbits may be tipped. These orbits can best be represented in a three-dimensional spherical space around the nucleus. To account for this magnetic effect, a *magnetic quantum number* (*m*) was introduced. Subsequently, Wolfgang Pauli introduced the *spin quantum number* (*s*) to represent the direction of electron spin (clockwise or anticlockwise).

The arrangement of electrons around the nucleus (Fig. 3.4) in an atom can be described based on the four quantum numbers. A more detailed representation of electron orbits based on quantum mechanics is described in the chemistry section Chap. 7.

3.4.2.1 Electron Binding Energy

When the atom is in a ground state, electrons in an atom occupy the innermost shells of an atom.

In the most stable configuration, electrons are most tightly bound to the nucleus. Electrons can move to higher energy or higher shells or can even be completely removed from the atom by providing energy to the electrons. The amount of energy required to remove an electron from a given shell (and to overcome the force of attraction of the nucleus), is called the *binding energy* of the shell. The binding energy is greatest for the innermost shell (*K* shell, $n = 1$) and increases as the atomic number (*Z*) increases (Fig. 3.5). The energy required for an electron to jump from a lower shell (*K* shell) to a higher shell (*L*, *M*, *N*, etc.) is exactly equal to the difference between the shells.

Calculations of the energy levels of electrons in an atom involve the following physical principles. Based on the electron rest mass (*m*), velocity (*v*) and radius of the orbit (*r*), the angular momentum (*mvr*) of the electron about the nucleus is given by

$$mvr = n\frac{h}{2\pi} \qquad (3.10)$$

where *n* is the principal quantum number and *h* is Planck's constant (6.626×10^{-34} J s).

The force experienced by an electron (mv^2/r) in its orbit is supplied by the Coulomb attraction between the electron (−*e*) and the nuclear charge
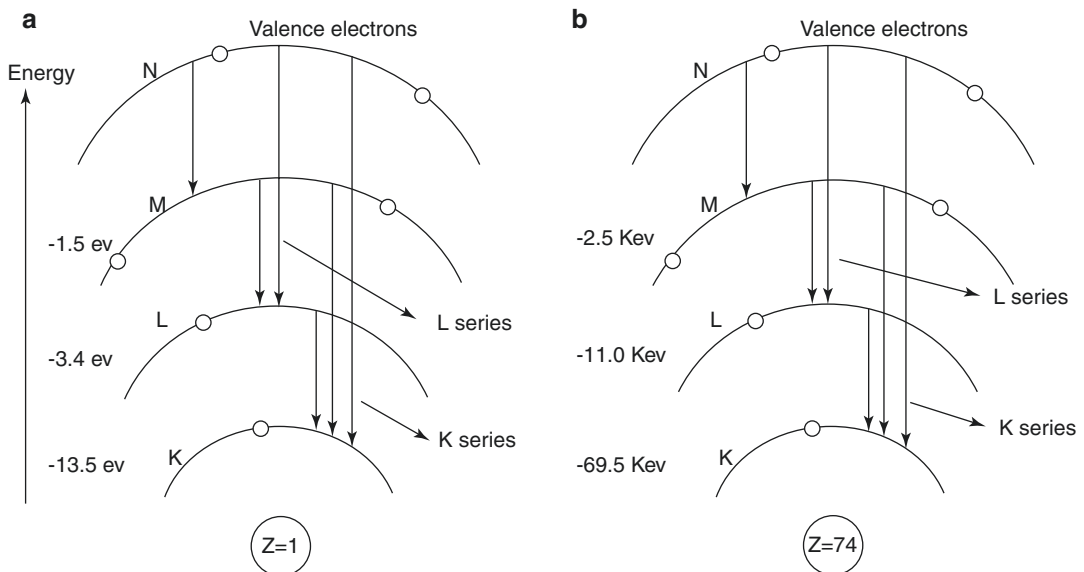
Fig. 3.5 The electron binding energy level diagram for hydrogen (**a**) and tungsten (**b**)

(+Ze), Therefore, the equation for the motion of electron is given by

$$\frac{mv^2}{r} = \frac{Ze^2}{4\pi\varepsilon_0 r^2} \qquad (3.11)$$

where ε_0 is the *permittivity of free space*, and $1/4\pi\varepsilon_0 = k_0 = 8.98755 \times 10^{-9}$ N m^2 C^{-2}.

The total energy of the electron in any orbit (nth orbit) is given by the sum of its kinetic and potential energy

$$KE = \frac{1}{2}mv^2 + PE = -\frac{e^2}{4\pi\varepsilon_0 r} \qquad (3.12)$$

$$E_n = \frac{k_0^2 Z^2 e^4 m}{2n^2 \left(\frac{h}{2\pi}\right)^2} = -\frac{13.6 Z^2}{n^2}\text{eV} \qquad (3.13)$$

The lowest energy occurs when $n = 1$. For a hydrogen atom, the ground state energy or the binding energy is -13.6 eV (Fig. 3.5). The energy required to remove an electron from its ground state is called the ionization potential, which is 13.6 eV. In comparison, for lead, the electron binding energy of a K shell electron is 88,005 eV.

3.5 Nuclear Structure

3.5.1 Composition and Nuclear Families

The size or the diameter of the atomic nucleus is very small compared to the diameter of an atom (10^{-13} cm versus 101^{-8} cm). The nucleus is composed of protons and neutrons and, collectively, these elementary particles are known as *nucle-*

ons. The mass of nucleons is almost 2000 times that of electron mass. Therefore, the density of the nucleus is very high compared to that of an atom.

For a given chemical element, the total number of protons (Z) and neutrons in the nucleus is known as the mass number (A), which is almost equal to the atomic weight (A_W). The difference between A and Z is the neutron number (n).

A nuclide with a life span of greater than 10^{-12} s is generally characterized by an exact nuclear composition, given by A, Z, and the arrangement of nucleons within the nucleus. Even though 118 chemical elements are known, more than 3000 nuclides have been discovered. The physical characteristics of the subatomic particles are summarized in Table 3.2.

Different combinations of protons and neutrons create different nuclear families. Atomic nuclei of the same element have the same number of protons (Z) but can have different numbers of neutrons (N) and different mass numbers (A). Such nuclides of an element are known as *isotopes* of that element. Nuclides with the same A, but different Z are called *isobars* while the nuclides with same N, but different A and Z are called *isotones*. *Nuclear isomers* are nuclides with the same A and Z, but different nuclear energies. Examples of different nuclear families are shown below (Fig. 3.6).

3.5.2 Nuclear Binding Energy

In physics and chemistry, *binding energy* is the smallest amount of energy required to remove a particle from a system of particles. At the nuclear

Fig. 3.6 Various nuclides or nuclear species are grouped into four major families having certain common characteristics. For example, isotopes of an element have the same number of protons (Z), but different mass number (A)

| Isotopes of Carbon | $^{11}_{6}C_5$ | $^{12}_{6}C_6$ | $^{13}_{6}C_7$ | $^{14}_{6}C_8$ |

| Isobars | $^{11}_{6}C_5$ | $^{11}_{5}B_6$ |

| Isotones | $^{14}_{6}C_8$ | $^{15}_{7}N_8$ |

| Isomers | $^{99m}_{43}Tc_{56}$ | $^{99}_{43}Tc_{56}$ |

level, the nuclear binding energy is the energy required to disassemble (to overcome the strong nuclear force) a nucleus of an atom into its component parts (protons and neutrons). Most of the binding energy, however, is nuclear binding energy, since energy required to remove electrons from an atom is relatively small. Mass defect or deficiency (Δm) is the difference between the mass of the atom and the sum of the masses of individual components. Binding energy (E_B) is the energy equivalent of Δm. For example, in the case of ^{12}C atom, the Δm is 0.09906 u, which is equal to 92.22 MeV. The binding energy per nucleon (E_B/A) for ^{12}C is 7.685 MeV. The binding energies of several nuclides as a function of mass number are shown in Fig. 3.7.

3.5.3   Nuclear Stability

Protons and neutrons within the nucleus are subject to two kinds of forces. Since like charges repel, electrical forces of repulsion exist between protons. In contrast, the strong exchange forces (the strong nuclear force), which can operate only at small distances (<3 fm), keep the protons and neutrons together in the nucleus. The shell model of the nucleus suggests that nucleons move in orbits about one another, while the liquid-drop model suggests that the nucleus is more like a drop of liquid.

Why are some combinations of protons and neutrons more stable than others? ^{12}C with six protons and six neutrons is stable forever, while ^{11}C with six protons and five neutrons is very unstable and decays with a half-life of only 20 min. In general, elements with a low atomic number ($Z < 10$) contain equal number of protons and neutrons and, therefore, are more stable. In contrast, as the atomic number Z increases, more and more neutrons are needed in the nucleus to keep the elements stable (Fig. 3.8). In general, nuclides with even number of protons and neutrons are more stable than nuclides with an odd number of protons and neutrons. The nuclear stability, therefore, depends on

- Neutron/proton ratio (n/p): Among the isotopes of every element, there is an optimal ratio favoring stability. The number of neutrons required to maintain stability is approximately 1.5 Z for heavy elements. All elements with $Z > 83$ and $A > 209$ are unstable and spontaneously decay or transform into more stable combinations of protons and neutrons.
- The binding energy/nucleon (E_B/A): The binding energy is greatest (>8 MeV) for nuclides with $A \approx 60$. It decreases slowly with increasing A, indicating the tendency toward instability for heavy elements.

Fig. 3.7 Binding energy per nucleon versus mass number (A) for several stable nuclides. One of the isotopes of iron (^{56}Fe) has the highest nuclear binding energy
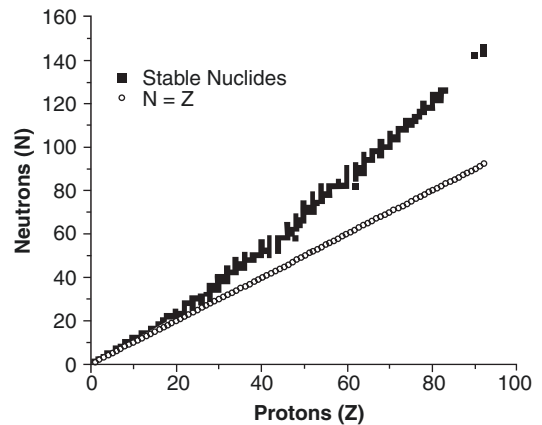
Fig. 3.8 Atomic number (Z) versus the neutron number (N) for the stable isotopes of elements. The neutron/proton ratio of unity represents a theoretical line of stability. The elements with higher Z, however, prefer $n/p > 1$ to achieve stability

The most stable arrangement of nucleons within the nucleus is called the ground state. *Excited states* are unstable and have higher energies. They also have a transient existence (10^{-12}s) and tend to transform into stable ground states. *Metastable states* exist longer ($>10^{-12}$s), but eventually, also transform to ground states.

3.6   Atomic and Nuclear Emissions

3.6.1   Emissions from Electron Shells

When atoms are excited, electrons in the inner shells gain energy and jump to higher energy outer shells, but with lower electron binding energies. When these electrons jump back to more stable lower orbits, energy is emitted in the form of electromagnetic radiation of all types (such as visible, UV, infrared, and radio waves), from atomic shells (Fig. 3.9). Also, electrons (*photoelectrons* or Auger electrons) are emitted from atoms under certain circumstances. The emission of photoelectrons following interaction of energetic photons is discussed in Chap. 5.

3.6.1.1 X-rays

In the photoelectric effect, photons of light transfer energy to the electrons in an atom. In the inverse photoelectric effect, the kinetic energy of an electron is converted into a photon. In 1895, Röntgen discovered that when cathode rays (negatively charged particles or electrons) strike the atoms of a glass vacuum tube, they produce penetrating X-rays that cause a salt (barium platinocyanide) to glow. Soon it was realized that X-rays are high energy electromagnetic (em) radiation. An accelerated electric charge will radiate em waves. As the fast-moving cathode rays approach the positive charge in the nuclei of atoms in the glass, electrons are brought to rest (accelerated), and the kinetic energy of electrons is converted to em waves. Radiation produced under these circumstances was given the name *bremsstrahlung* (breaking radiation). It was also realized that when denser, more massive atoms in a metal are used to stop accelerated electrons, X-rays of higher energies can be generated.

3.6.1.2 Characteristic X-rays

In 1911, the British physicist Charles Barkla noticed that each metal produces X-rays of a particular wavelength, depending on the metal (Fig. 3.9) and called the more penetrating beam *K* X-rays, and the less penetrating beam *L* X-rays. The wavelength of X-rays decreases (energy increases) as the atomic number of elements increased. Emissions from transitions >100 eV (0.1 keV) are called *characteristic or fluorescent X-rays*. Emission of characteristic X-rays occurs when orbital electrons move from an outer shell to fill an inner shell vacancy (such as $L \rightarrow K$ or $M \rightarrow K$ shell). The energy of the characteristic X-rays is the difference in binding energies of these shells. For example, de-excitation (e.g., $M \rightarrow K$ transition $= K_\beta$) of a tungsten atom results in the emission of characteristic X-rays of 67 keV, the difference in binding energy between *M* and *K* shells. The probability that the electron transition will result in the emission of characteristic X-rays is called *fluorescent yield* (ω), which is essentially zero for elements with low *Z* (<10) and increases as *Z* increases.

3.6.1.3 Auger Electrons

Just as in the production of characteristic X-rays, an electron from the outer shell drops down to fill the vacancy in a lower shell and energy is released. As an alternative to the emission of X-rays, the energy is transferred to another orbital electron, which is ejected from the atom (Fig. 3.9). The emission of electron from the inner shell is known as the *Auger effect (or Auger-Meitner effect)*, which in turn creates two vacancies in the shell. For example, the deexcitation (e.g., $M \rightarrow K$ transition $= K_\beta$) of a tungsten atom results in the emission of an Auger electron with 64.5 keV: the difference in binding energy between *M* and *K* shells minus the binding energy of another electron in *M* shell, which is ejected. Again, this vacancy is filled by outer electrons resulting in characteristic X-rays or Auger electrons. Elements with lower *Z* are more likely to eject Auger electrons, while elements with higher *Z* are more likely to emit characteristic X-rays.

3.6.2   Nuclear Emissions

3.6.2.1 Gamma Rays and Subatomic Particles

Like an excited atom, an excited nucleus can emit electromagnetic radiation in order to come to the ground state (Fig. 3.9). The photons emitted by the nuclei range in energy up to several MeV and are traditionally called *γ rays*. The energy of a γ photon corresponds to the energy difference between the various initial and final states in the transitions involved. Deexcitation of the excited nuclei may emit only γ rays (as in the case of nuclear isomers) or emit γ rays in addition to nonpenetrating radiation such as β-rays, α-rays,

protons, and neutrons during the radioactive decay process.

3.6.2.2 Internal Conversion

As an alternative to γ rays, an excited nucleus in some cases may return to its ground state by transferring the excitation energy to one of the orbital electrons, which is then ejected from the atom. This process of converting nuclear energy to eject an orbital electron (Fig. 3.9) is called *internal conversion*, which is analogous to the photoelectric effect. The KE of conversion electron is equal to the difference between the lost nuclear excitation energy and the binding energy of the electron from the ejected atomic shell.
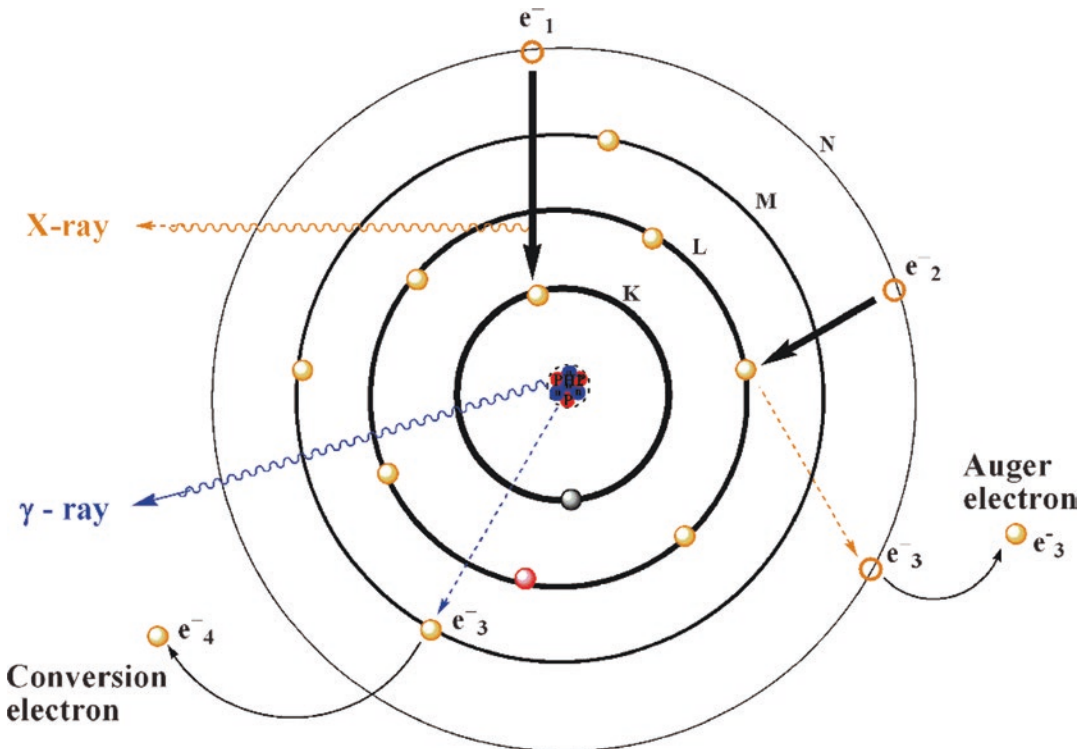
Fig. 3.9 Atomic emissions: When an electron from an outer higher energy shell moves in to fill a vacancy in a lower shell, the energy released may appear as electromagnetic radiations, such as X-rays or as an alternative, the atom may undergo Auger effect and may emit electrons, known as Auger electrons. In contrast, the energy from the nucleus may be emitted in the form of γ-rays or promote emission of conversion electrons

Further Reading

Beiser A. Concepts of modern physics. 5th ed. New York, NY: McGraw-Hill; 1995.

Bushberg JT, Seibert JA, Leidholdt EM Jr. The essential physics of medical imaging. 2nd ed. Philadelphia, PA: Lippincott; 2002.

Emsley J. The elements. 3rd ed. Oxford: Oxford University Press; 1998.

Saha G. Fundamentals of nuclear pharmacy. 5th ed. New York, NY: Springer; 2004.

Sorensom JA, Phelps ME. Physics in nuclear medicine. Philadelphia, PA: Saunders; 1987.

Turner JE. Atoms, radiation, and radiation protection. 2nd ed. New York, NY: Wiley; 1995.

Radioactivity

<div style="text-align: right">

4

</div>

My experiments proved that the radiation of uranium compounds … is an atomic property of the element of uranium. Its intensity is proportional to the quantity of uranium contained in the compound, and depends neither on conditions of chemical combination, nor on external circumstances, such as light or temperature. The radiation of thorium has an intensity of the same order as that of uranium, and is, as in the case of uranium, an atomic property of the element.

It was necessary at this point to find a new term to define this new property of matter manifested by the elements of uranium and thorium. I proposed the word **radioactivity** *which has since become generally adopted; the radioactive elements have been called radio elements.* (Marie Sklodowska Curie)

4.1 The Discovery

In 1895, Wilhelm Roentgen discovered X-rays because of the fluorescence they caused on a screen coated with barium platinum cyanide. He noticed that X-rays became fluorescent in the area where the cathode rays (electrons) interacted with the glass.

Two months later, Henry Becquerel, Professor of Physics at the Ecole Polytechnique in Paris, heard about the discovery of X-rays and immediately thought of a possible connection between X-rays and fluorescence. He quickly initiated a series of experiments to test whether fluorescent substances emitted X-rays. In February 1896 he was exploring the possibility that sunlight might cause crystals to emit penetrating rays like the X-rays. As luck would have it, he used uranium–potassium bisulfate (uranium salts were known to be phosphorescent). These crystals were placed next to a photographic plate that was wrapped in dark paper. If sunlight causes the crystals to emit penetrating rays, then these rays might penetrate the paper and darken the plate. Because the weather was cloudy, Becquerel placed the unwrapped plate in the drawer of a cabinet but left the crystals on the cabinet. When he developed the plate a couple of days later, to his surprise he found an intense darkening on it, caused by exposure to radiation. He immediately concluded that some invisible rays from the uranium had penetrated the cabinet and the dark paper covering the plate and finally exposed the photographic plate. For a few years, these rays were known as *Becquerel rays* or *rayons uranique*. Becquerel soon discovered that the rays from the uranium also ionized gases, thus making them conductors. A crude and simple gold leafed electroscope was used to measure the *activity* of this radiation.

In 1898, Maria Sklodowska Curie and Pierre Curie discovered that thorium also emitted such rays. That year, the phenomenon of penetrating radiation emitted by uranium and thorium was given the name radioactivity by the Curies. Marie observed that the uranium ore, **pitchblende** was much more active and discovered that the increased activity was due to the presence of two new radioactive elements, *polonium* and *radium*.

In 1900, the French chemist Paul Villard discovered a form of radioactive emission that was extremely penetrating and was not deflected by a magnetic field analogous to X-rays. This radiation was later given the name, gamma rays.

4.2   Nuclear Disintegration

Ernest Rutherford and his coworkers at the Cavendish Laboratory in England distinguished three components in the radiations from natural radioactive elements, which he called α rays, β⁻ rays, and γ rays. These components were eventually identified as helium nuclei, electrons, and high-energy photons, respectively (Fig. 4.1).

In 1902, Rutherford and Frederick Soddy explained the cause and nature of radioactivity. They proposed a *nuclear disintegration theory*, which states that radioactivity is actually the changing of one chemical element into another through the emission of α or β⁻ particles. According to their "Radioactive decay law,"

radioactivity is an "atomic" phenomenon, which is accompanied by "chemical" changes. The law of radioactive displacements, also known as Fajas' and Soddy's law, is a rule governing the transmutation of elements during radioactive decay. The law describes which chemical element is created during a particular type of radioactive decay. See Table 4.1, for specific examples.

The existence of isotopes was first suggested in 1913 by the radiochemist Frederick Soddy. He showed that mesothorium (later shown to be ^{228}Ra), radium (^{226}Ra), and thorium X (later shown to be ^{224}Ra) are impossible to separate. Soddy proposed that several types of atoms with different atomic weights (differing in radioactive properties, but same chemical properties) could occupy the same place in the table. The term "isotope," Greek for "at the same place," was suggested to Soddy by Margaret Todd, a Scottish physician and family friend, during a conversation in which Soddy explained his ideas to her. In 1921, the Nobel Prize in Chemistry was awarded to Frederick Soddy for his contributions to our
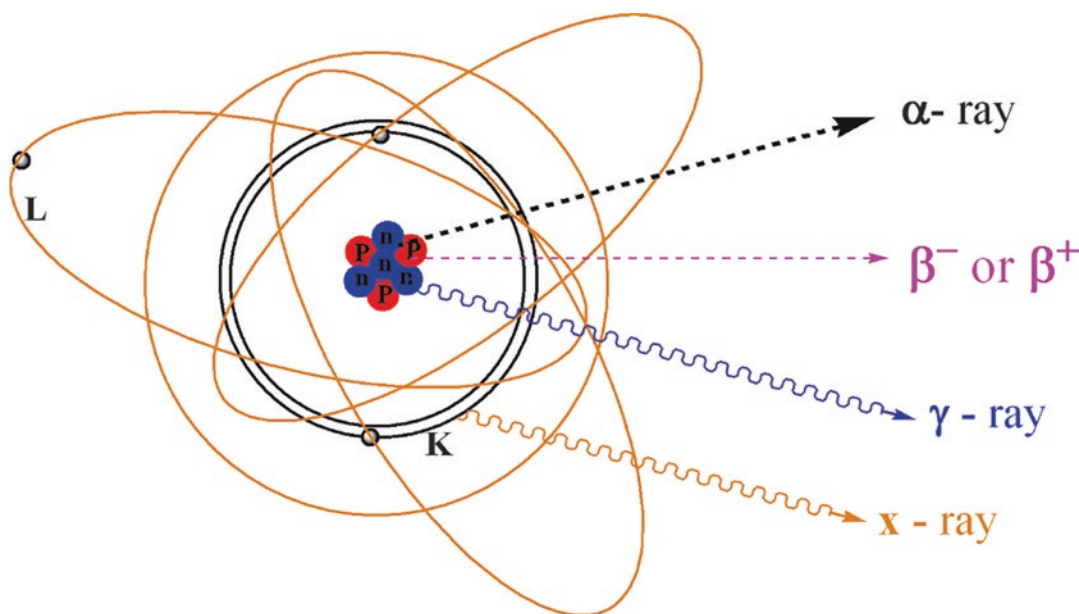
Fig. 4.1 The three components of radioactive emissions originating from the unstable nuclei of natural radionuclides of uranium and thorium: α, β⁻, and γ, as they were called by Rutherford. Subsequently, two other decay modes, EC and positron emission were identified. In contrast, characteristic X-rays originate from the inner shells of electronic orbits

Table 4.1 Elements with different isotopes showing differences in n/p ratios and the nuclear binding energy/nucleon

Element	Isotope			NBE/nucleon		% Decay abundance				
	Z	Isotope	n/p Ratio	MeV	Stability	α	β⁻	β⁺	EC	γ
Carbon	6	^{11}C	0.8333	7.645	Radioactive		–	99	1	*
		^{12}C	1.0	7.680	Stable (98.9%)		–	–	–	–
		^{13}C	1.1666	7.710	Stable (1.1%)		–	–	–	–
		^{14}C	1.3333	7.736	Radioactive		100	–	–	–
Fluorine	9	^{18}F	1.0	7.680	Radioactive		–	97	3	–
		^{19}F	1.1111	7.701	Stable (100%)		–	–	–	–
		^{20}F	1.2222	7.719	Radioactive		100	–	–	*
Copper	29	^{61}Cu	1.1035	7.699	Radioactive		–	100	–	*
		^{62}Cu	1.1379	7.705	Radioactive		–	98	2	–
		^{63}Cu	1.1724	7.711	Stable (69.17%)		–	–	–	–
		^{64}Cu	1.2069	7.717	Radioactive		39	19	41	*
		^{65}Cu	1.2414	7.722	Stable (30.83%)		–	–	–	–
		^{67}Cu	1.3103	7.733	Radioactive		100	–	–	*
Gallium	31	^{66}Ga	1.1290	7.704	Radioactive		–	56	43	*
		^{67}Ga	1.1613	7.709	Radioactive		–	–	100	*
		^{68}Ga	1.1935	7.715	Radioactive		–	90	10	*
		^{69}Ga	1.2258	7.720	Stable (60.1%)		–	–	–	–
		^{71}Ga	1.2903	7.730	Stable (39.9%)		–	–	–	–
		^{72}Ga	1.3226	7.735	Radioactive		100	–	–	*
Radium	88	^{223}Ra	1.5340	7.770	Radioactive		100			
		^{226}Ra	1.5682	7.774	Radioactive	100				
		^{228}Ra	1.5909	7.776	Radioactive	100				
Uranium	92	^{235}U	1.5543	7.564	Radioactive	100				
		^{238}U	1.5869	7.571	Radioactive	100				

knowledge of the chemistry of radioactive substances, and his investigations into the origin and nature of isotopes.

The first evidence for multiple isotopes of a stable (nonradioactive) element was found by J.J. Thomson in 1912. He observed that stable neon gas exists in two forms: Ne-20 (90.48%) and Ne-22 (9.25%). Subsequently, F.W. Aston discovered multiple stable isotopes for numerous elements using a mass spectrograph. Aston's whole-number rule for isotopic masses states that large deviations of elemental molar masses from integers are primarily due to the fact that the element is a mixture of isotopes. For example, the molar mass of chlorine gas (35.453) is a weighted average of the almost integral masses for the two isotopes ^{35}Cl (75.77%) and ^{37}Cl (24.23%). The Nobel Prize in Chemistry was awarded to Francis William Aston in 1922 for his discovery of isotopes, in a large number of stable elements, and for his enunciation of the whole-number rule.

Nuclear transmutation is a phenomenon in which an unstable atomic nucleus disintegrates in order to acquire a more stable state, by emitting subatomic particles, and/or electromagnetic radiation. This phenomenon is called *radioactivity* or *radioactive decay*. One of the most important points to understand is that the energy liberated during the radioactive decay comes from within the individual nuclei of a radioactive element without any external excitation, unlike in the case of atomic radiation.

In 1934, when Frèdèric and Irène Joliot-Curie bombarded aluminum (^{27}Al) with α particles, they observed that the product nuclide ^{30}P emits positrons (β⁺) identical to those found in cosmic rays by Carl Anderson in 1932. The Curies termed the phenomenon *artificial radioactivity*, because ^{30}P is a short-lived nuclide which does not exist in nature. Frèdèric and Irène Joliot-Curie received the Nobel prize in 1935 for the discovery of artificial radioactivity, while Carl Anderson received the Nobel prize in 1936 for the discovery of positrons.

In December 1938, the radiochemists, Otto Hahn and Fritz Strassmann bombarded uranium

with slow neutrons and observed that barium has been produced. The physicists, Lise Meitner and Otto Robert Frisch theorized and then proved that the uranium nucleus had been split into two lighter elements, with the emission of 2–3 neutrons and large amount of energy. They named the process *Fission*. Hahn was awarded the 1944 Nobel Prize in chemistry for the discovery of fission. With the discovery of nuclear fission, scientists realized that some unstable nuclides with high atomic numbers may also undergo *spontaneous fission*.

Following the discovery of the proton by Rutherford in 1919 and the neutron by Chadwick in 1932, it became clear that the neutron/proton ratio of any nuclide, and the nuclear binding energy per nucleon, NBE/nucleon (Chap. 3) are the two most important characteristics of any nuclide that would determine the stability of an element, and the kind of radioactive decay it undergoes in order to attain stability. ^{56}Fe is the most stable nuclide with 8.79 MeV NBE/nucleon. Table 4.1 shows several elements with different isotopes, showing differences in *n/p* ratios, and the nuclear binding energy/nucleon.

4.2.1 Types of Radioactive Decay

Three of the most common types of decay are *alpha* decay (α-decay), *beta* decay (β-decay), and *gamma* decay (γ-decay), all of which involve emitting one or more charged particles or electromagnetic radiation. The weak nuclear force is the mechanism that is responsible for β decay, while the other two are governed by the electromag-netic and strong nuclear forces. There are 28 naturally occurring chemical elements on Earth that are radioactive, consisting of 34 radionuclides (known as primordial nuclides). Another 50 or so shorter-lived radionuclides, such as ^{226}Ra and ^{227}Ac, found on Earth, are the products of decay chains that began with the primordial nuclides, or are the product of ongoing cosmogenic processes, such as the production of ^{14}C from stable ^{14}N in the atmosphere by cosmic rays.

The radioactive decay processes fall into two categories: one that involves a change in the mass number *A* of a radionuclide, and one in which both the parent and the daughter radionuclides have the same mass number (isobaric decay). The five major types of radioactive decay are shown in Table 4.2. The different radioactive decay modes are shown in the decay scheme diagram (Fig. 4.2).

4.2.1.1 Alpha (α) Decay

Alpha decay (Table 4.2) is generally seen in high atomic number elements such as ^{238}U, ^{230}Th, ^{226}Ra, and ^{225}Ac. The radionuclide ejects an α particle (two protons and two neutrons) and, because it loses two protons, it is converted into a nuclide with a lower atomic number. Alpha particles are *monoenergetic* and may have kinetic energies in the range of 4–9 MeV. Radionuclides emitting α particles may also emit γ photons. Nuclides with *A* > 210 are so large, they need to eject α particles to reduce their size and alter the *n/p* ratio to become relatively more stable.

$$^{226}_{88}\text{Ra} \rightarrow \,^{222}_{86}\text{Rn} + \,^{4}_{2}\alpha \qquad (4.1)$$
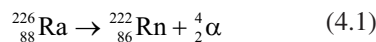
Table 4.2 Radioactive decay modes: nuclear transmutations

Decay mode	Reason for instability of parent nucleus	Transformation	Example	*n/p* ratio change
Alpha decay	Too large	$^{A}_{Z}X \rightarrow \,^{A-4}_{Z-2}Y + \,^{4}_{2}\alpha$	$^{226}_{88}\text{Ra} \rightarrow \,^{222}_{86}\text{Rn} + \,^{4}_{2}\alpha$	Increases
Beta decay	Neutron rich	$^{A}_{Z}X \rightarrow \,^{A}_{Z+1}Y + e^{-}$	$^{14}_{6}\text{C} \rightarrow \,^{14}_{7}\text{N} + e^{-} + v$	Decreases
Positron emission	Neutron deficient	$^{A}_{Z}X \rightarrow \,^{A}_{Z-1}Y + e^{+}$	$^{11}_{6}\text{C} \rightarrow \,^{11}_{5}\text{B} + e^{+} + v$	Increases
Electron capture	Neutron deficient	$^{A}_{Z}X + e^{-} \rightarrow \,^{A}_{Z-1}Y$	$^{111}_{49}\text{In} + e^{-} \rightarrow \,^{111}_{49}\text{Cd}$	Increases
Isomeric transition	Excess energy	$^{A}_{Z}X^{*} \rightarrow \,^{A}_{Z}Y + \gamma$	$^{99m}_{43}\text{Tc}^{*} \rightarrow \,^{99}_{43}\text{Tc} + \gamma$	No change
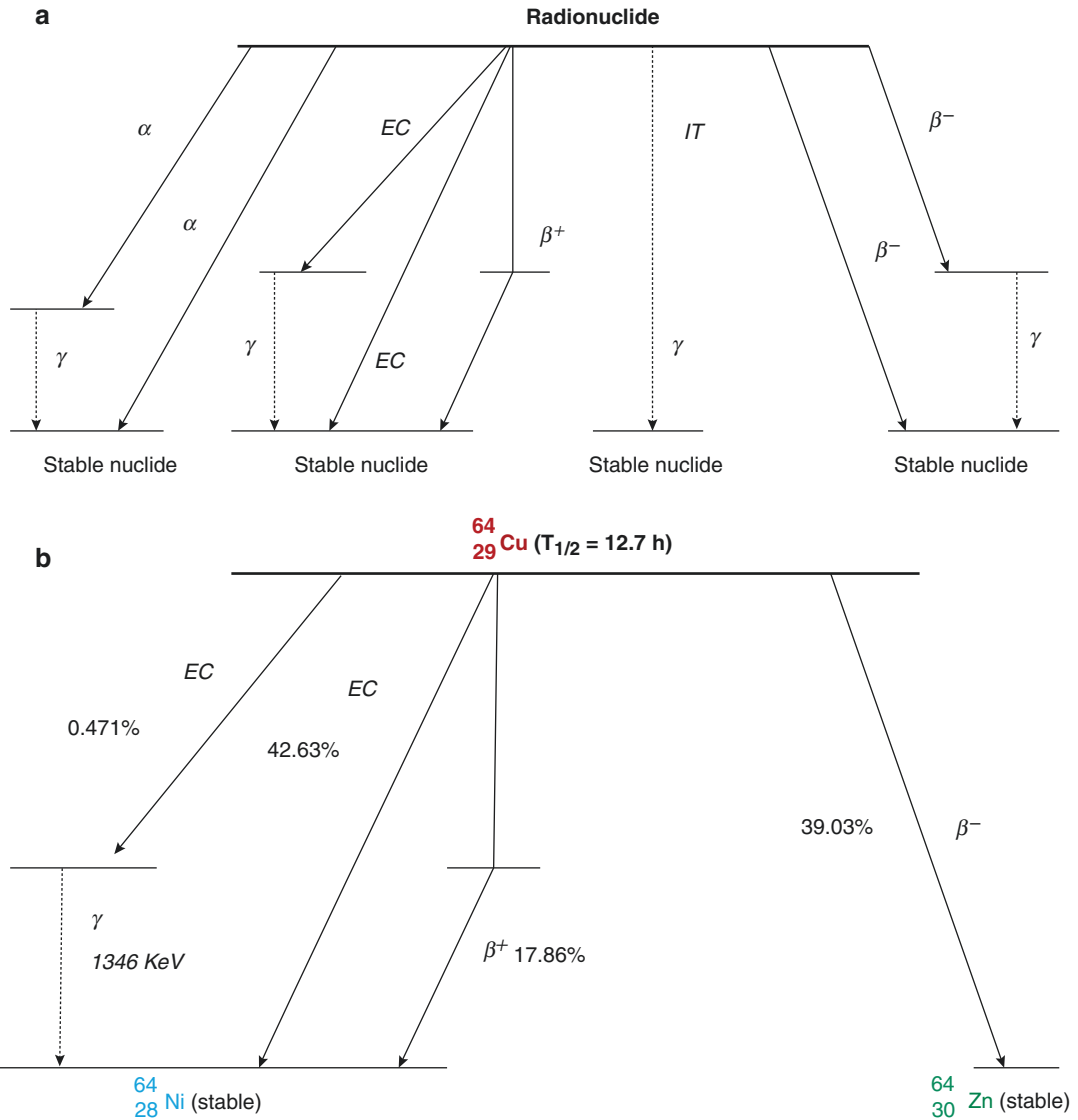
Fig. 4.2 The radioactive decay scheme diagram (**a**) shows the major decay modes. The parent radionuclide is shown above while the lines to the right represent β⁻ decay and the lines to the left represent α, β⁺, or EC decay modes. Gamma emission is represented by the perpen- dicular lines. The lines at the bottom represent the ground state energy of the stable nuclide. The decay scheme (**b**) of ⁶⁴Cu shows three different decay modes: α decay, β⁻ decay, and β⁺ decay

As shown in Eq. (4.1), ²²⁶Ra ($T_{1/2}$ = 1620 years) decays to ²²²Rn gas with the emission of a 4.78 MeV α particle and 0.186 MeV gamma photons. ²²²Rn ($T_{1/2}$ = 3.82 days) is also unstable and decays to unstable ²¹⁸Po. In fact, ²²⁶Ra (n/p = 1.5682) goes through a decay series (Sect. 4.2.2) to finally become stable ²⁰⁶Pb (n/p = 1.5122).

4.2.1.2 Beta (β⁻) Decay

In beta decay, neutron (n)-rich nuclides decay by emitting an electron or β⁻ rays. In an unstable nucleus, a neutron is converted into a proton (p), an electron, and an *antineutrino* (ν). Since only the electron and antineutrino are ejected, the daughter is the next element in the periodic table, with $Z + 1$ protons, compared to the parent.

$$n \rightarrow p + e^- + \overline{v} \qquad (4.2)$$

The electron and proton do not exist in the neutron; they, together with the neutrino, are created at the moment of decay. The kinetic energies of electrons ejected in the beta decay vary continuously from 0 to a maximum value of KE_{max} (E_β^{max}), characteristic of the radionuclide (Fig. 4.3a). In an attempt to explain the continuous spectrum of β particle energies, Wolfgang Pauli in 1930, proposed that a neutral particle with zero or a very small undetectable mass would carry off some of the energy equal to the difference between KE_{max} and the actual kinetic energy of the electron. This hypothetical particle was later called *neutrino* by Enrico Fermi and was eventually detected in the 1950s by Reines and Cowan. Typically, the average kinetic energy of the β particle ($\overline{E}_\beta$) is about one third of E_β^{max}. With certain β- emitting radionuclides, the daughter nuclide is in an excited state, which promptly reaches ground state by the emission of γ rays. For example, in case of ^{131}I, 81% of the daughter ^{131}Xe atoms are in an excited state and emit γ photons (364 keV). Since the emission of γ photons follows almost immediately after the beta emission, this sequential decay process is referred to as a β, γ decay.

4.2.1.3 Positron (β+) Decay

Nuclides that are deficient in neutrons are unstable and decrease the number of positive charges in the nucleus (i.e., protons) by decaying either through positron emission or *electron capture* (EC). These two decay modes are regarded as *inverse beta decay*. They are alternatives to reach the ground state when an unstable nucleus is neutron-deficient. Positron emission may be more common in elements with a lower atomic number, while electron capture is seen mostly in elements with high atomic numbers.

A positron is an *antiparticle* of an ordinary electron. In a proton-rich nuclide, a proton in the nucleus is transformed into a neutron, positron, and a neutrino (conversion of a proton into a neutron can only happen inside a nucleus).

$$p \rightarrow n + e^+ + v \qquad (4.3)$$

In 1928, Paul Adrien Maurice Dirac predicted the existence of an antielectron or positron. This prediction was unexpectedly confirmed in 1932 by the American physicist Carl Anderson, who detected high-energy positrons in cosmic radiation.

In 1934, Irene Curie and Frederick Joliot reported the discovery of artificial radioactivity. More specifically, when natural stable ^{27}Al was bombarded with alpha particles, ^{30}P ($T_{1/2} = 3$ min) was produced, following which positron emission decayed to stable ^{30}Si, as shown below.

$$^{27}_{13}Al + ^4_2\alpha \rightarrow ^{30}_{15}P + n \qquad (4.4)$$

$$^{30}_{15}P \rightarrow ^{30}_{14}Si + e^+ + v \qquad (4.5)$$
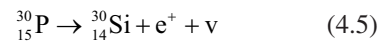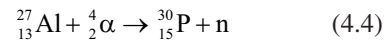
Positron emission leads to a daughter nucleus of a lower atomic number ($Z - 1$), leaving the mass number unchanged. Just as in β⁻ decay, the positron (β⁺) emission spectrum is continuous (Fig. 4.2), with positron energies ranging from 0 to E_β^{max}. The average energy of the positron is one-third of the maximum. The difference between the maximum energy and the actual energy of a positron is carried off by the neutrino. One of the consequences of positron emission is *annihilation radiation*, which is discussed in more detail in Chap. 5. Just as in β⁻ decay, the daughter nuclide may be in an excited state and as a result, the sequential β⁺, γ decay process involves emission of gamma photons from the daughter nucleus. ^{11}C, ^{18}F, ^{64}Cu, ^{68}Ga, and ^{124}I, used in developing molecular imaging radiopharmaceuticals for PET, are the most important radionuclides that decay by positron emission.

4.2.1.4 Electron Capture (EC)

The unstable neutron-deficient nuclides may also reach the ground state by decreasing the positive charge in the nucleus by a process in which an orbital electron, usually from a *K*-shell, is captured by the parent nucleus, resulting in the conversion of one of the protons into a neutron. Since the energy of the parent nuclide is high, a neutrino is also produced, taking away some of the transition energy.

$$p + e^- \rightarrow n + v \qquad (4.6)$$

a

b
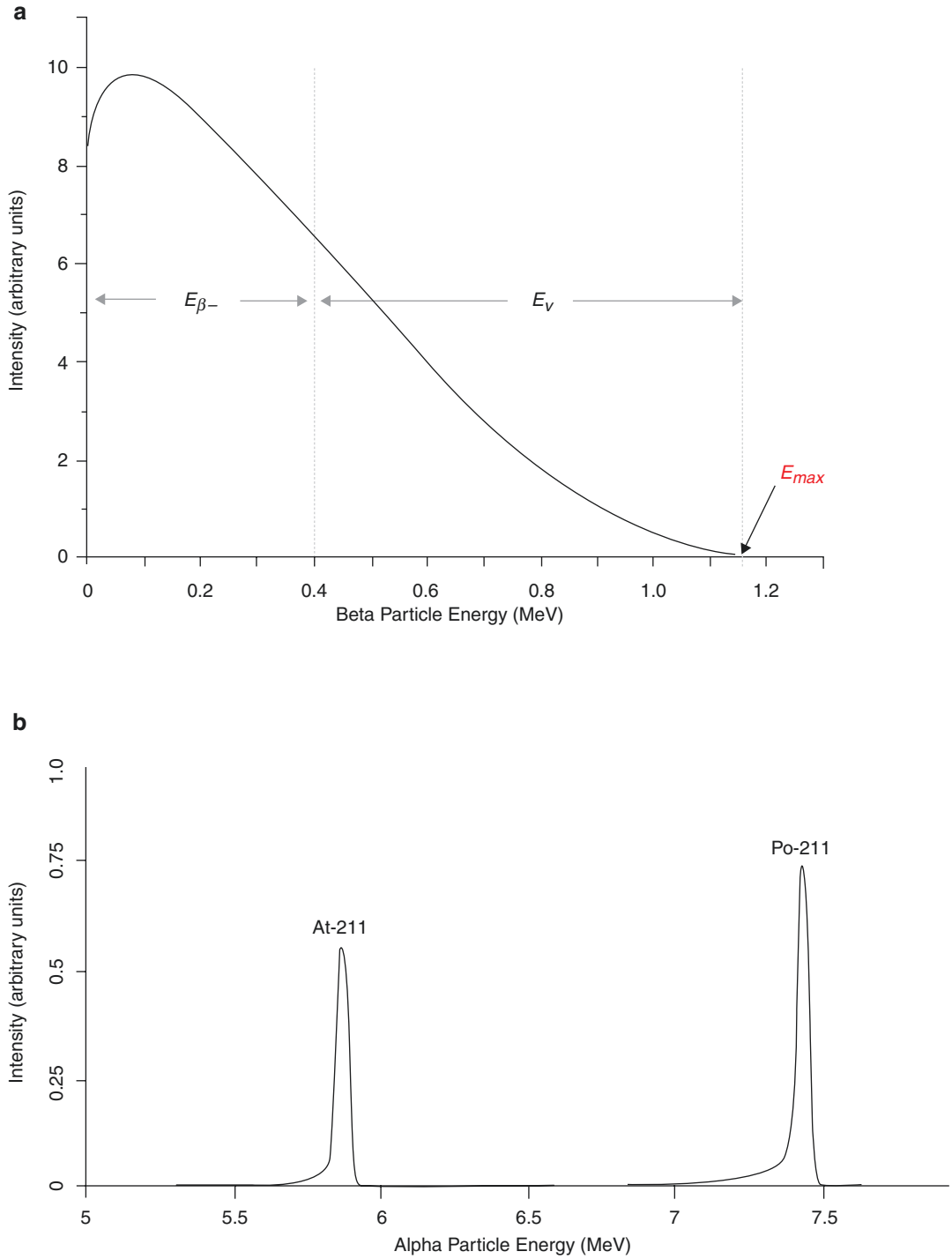
Fig. 4.3 The continuous β⁻ energy spectrum (**a**) showing the distribution of β⁻ particles (relative number versus energy) emitted by ^{14}C. The average energy is denoted by $\bar{E}_{\beta}$, while the maximum energy is denoted by E_{β}^{max}. The spectrum at the bottom (**b**) shows discrete kinetic energy of α particles ejected from the nucleus

The electron capture (*K*-capture) decay process leads to a daughter nucleus of a lower atomic number ($Z - 1$), leaving the mass number unchanged. As a vacancy is created in the *K*-shell of the daughter nuclide, characteristic X-rays and/or Auger electrons are ejected from the daughter nuclide. Sometimes, the daughter nuclide may also be in an excited state due to a change in the *n/p* ratio. As a result, gamma photons and conversion electrons are emitted from the daughter nuclide in a process known as EC, γ decay mode. ^{67}Ga, ^{111}In, and ^{123}I are the most important radionuclides with EC decay mode that are useful for developing molecular imaging radiopharmaceuticals for SPECT.

4.2.1.5 Isomeric Transition (IT)

When an unstable decay occurs by any of the decay modes described above, the daughter nucleus may be in an unstable long-lived *metastable* state. Transitions or decays of such metastable nuclides (exist for $>101^{-12}$ s) result in the emission of gamma photons (Fig. 4.2) and leave both *Z* and *A* unchanged. The two nuclides of an element that differ only in the energy content are called *isomers* (different from the concept of isomers in chemistry). The metastable states are called "isomeric states" (designated with letter *m* next to *A*), and the decay process is known as "isomeric transition." As an alternative, the nucleus of a metastable nucleus may transfer the energy to an orbital electron, which then is ejected from the atom, and such an electron is also known as a conversion electron. In contrast to beta decay, conversion electrons do not display a continuous energy spectrum, but show discrete energies. The most important radionuclide decaying by isomeric transition is ^{99m}Tc which is very useful for developing molecular imaging agents for use with SPECT.

4.2.1.6 Multiple Decay Mode

Certain radionuclides decay by a single decay mode while some decay by multiple decay modes. As mentioned earlier, neutron-deficient radionu-clides may decay by EC or by positron emission. However, for a radionuclide (such as ^{64}Cu) to emit both β$^-$ and β$^+$ particles, the *n/p* ratio must be very close to that of the stable isotope of that element (Table 4.2) and Fig. 4.2b. Every decay mode may also involve emission of γ photons.

4.2.2 Radioactive Decay Series

Often an unstable radionuclide, especially one with a high atomic number, cannot reach a stable ground state through a single decay process. In such a case, a *decay series* or *decay chain* (sequential series of transformations) occurs until a stable nuclide is formed. It is also known as a "*radioactive cascade*." The three main decay chains (or families) observed in nature, commonly are called the thorium series ($A = 4n$), the radium or uranium series ($A = 4n + 2$), and the actinium series ($A = 4n + 3$), representing three of these four classes, and ending in three different, stable isotopes of lead. The mass number of every isotope in these chains can be represented as $A = 4n$, $A = 4n + 2$, and $A = 4n + 3$, respectively. The long-lived starting isotopes of these three isotopes, respectively ^{232}Th, ^{238}U, and ^{235}U, have existed since the formation of the earth. In 1940s, it was discovered that the artificially produced radionuclide ^{237}Np exhibits a series decay mode ($A = 4n + 1$) in which the parent ^{237}Np after a series of transformations final forms the stable ^{209}B and ^{205}Tl isotopes.

In 1998, Marie and Pierre Curie discovered two new elements polonium (^{210}Po) and radium (^{226}Ra) in the uranium ore, pitchblende. The uranium decay series ($A = 4n + 2$) starts with ^{238}U and ends with stable ^{206}Pb (Fig. 4.4). During this process, eight alpha particles and six beta particles are emitted before reaching the ground state, after losing ten protons and 22 neutrons. Both ^{226}Ra and ^{210}Po are the intermediate radioactive decay products of ^{238}U. Radium-226 is 2.7 million times more radioactive than the same molar amount of natural uranium. The γ-ray energy spectrum of uranium ore (Fig. 4.5) shows several
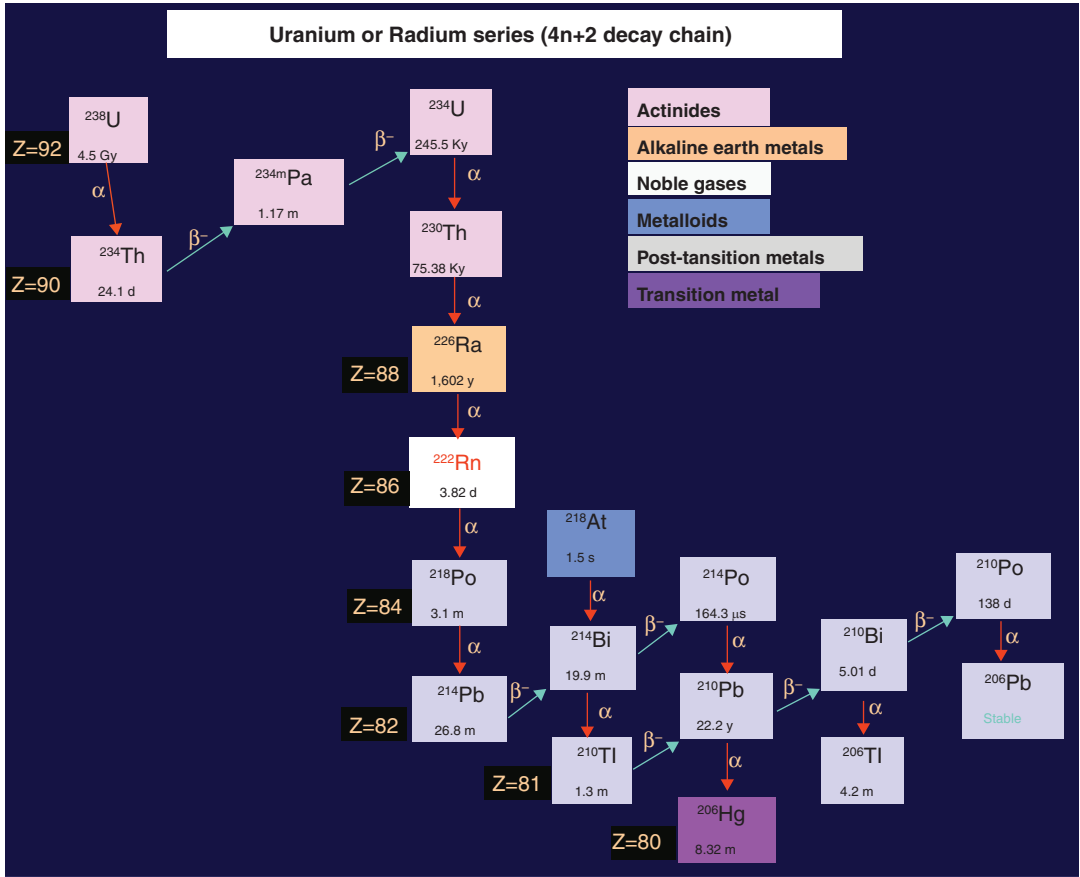
Fig. 4.4 U-238 decay chain ($4n + 2$) showing several decay products (such as ^{226}Ra and ^{210}Po) before it finally becomes stable ^{206}Pb

Fig. 4.5 The γ-ray energy spectrum of uranium ore shows several nuclides that are typical of the decay chain of ^{238}U and have been identified as ^{226}Ra, ^{214}Pb, and ^{214}Bi
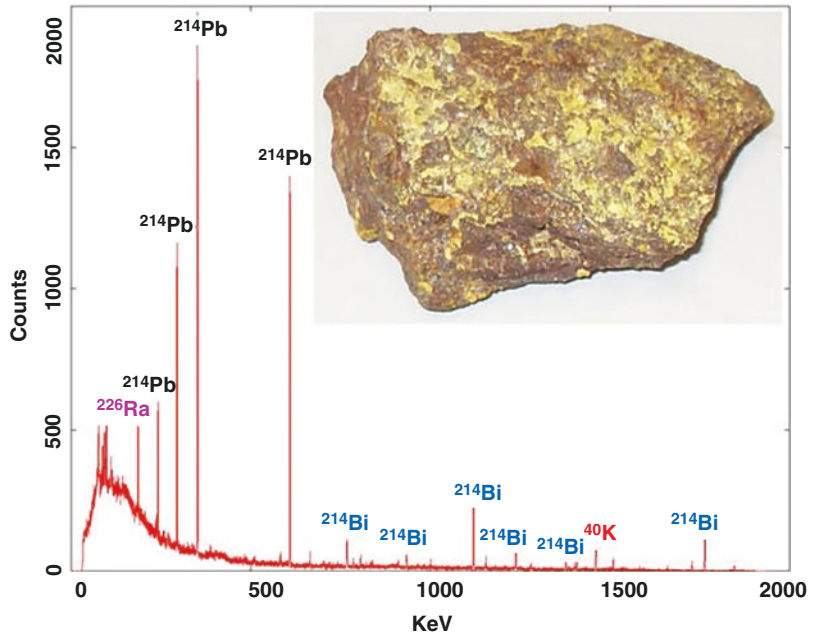
nuclides that are typical of the decay chain of ^{238}U and have been identified as ^{226}Ra, ^{214}Pb, and ^{214}Bi.

With some radionuclides, the decay series may involve only two or three decays before reaching a stable ground state. For example, the unstable ^{99}Mo reaches stable ^{99}Ru as shown below. The intermediate ^{99}Tc has a long half-life $(2.1 \times 10^5$ year).

$$\begin{array}{c} {}^{99}_{42}\text{Mo} \xrightarrow{\beta^-} {}^{99m}_{43}\text{Tc} \xrightarrow{\text{IT}} {}^{99}_{43}\text{Tc} \xrightarrow{\beta^-} {}^{99}_{44}\text{Ru} \end{array} \qquad (4.7)$$
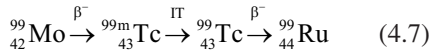
4.2.3   Nuclear Fission

Nuclear fission is the division or break-up of a heavy unstable nucleus into two lighter nuclei in order to reduce its size. Spontaneous fission may occur in heavy nuclides, but the probability is very low. For example, ^{235}U undergoes spontaneous fission with a very long half-life $(2 \times 10^{17}$ year).

In 1938, Otto Hahn, a German radiochemist, discovered that ^{235}U undergoes fission when struck by a slow neutron. It is not the impact of the neutron that induces fission. Instead, following absorption of the neutron, the ^{236}U nucleus is so unstable that almost at once it explodes into two lighter nuclei known as *fission fragments*. In addition, an enormous amount of energy ($\approx$200 MeV) and 2–3 high-energy neutrons, per nuclear fission, are also released. Lise Meitner, a nuclear physicist, coined the name *fission* to describe the splitting of a uranium atom into two lighter elements.

$$\begin{array}{c} {}^{235}_{92}\text{U} + \text{n} \rightarrow {}^{236}_{92}\text{U}^* \xrightarrow{\text{fission}} {}^{140}_{54}\text{Xe} + {}^{94}_{38}\text{Sr} + 2\text{n} + \text{Energy} \end{array} \qquad (4.8)$$

$$\begin{array}{c} {}^{235}_{92}\text{U} + \text{n} \rightarrow {}^{236}_{92}\text{U}^* \xrightarrow{\text{fission}} {}^{141}_{56}\text{Ba} + {}^{92}_{36}\text{Kr} + 3\text{n} + \text{Energy} \end{array} \qquad (4.9)$$
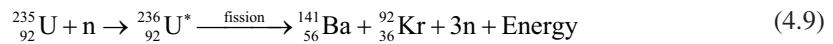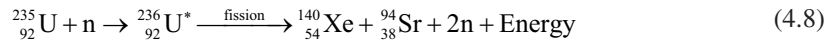
The above processes are only a couple of examples of the many fission fragments that ^{235}U can produce. In fact, over 200 different radioisotopes of 35 different elements have been observed among fission products. Most of these fragments are neutron rich and decay by beta decay.

4.3   Radioactive Decay Equations

4.3.1   Exponential Decay

Radioactive decay or transformation is a statistical process that obeys the laws of chance. No cause–effect relationship is involved in the decay of a radionuclide, only a certain probability per unit time.

The activity (A) of a sample of a radionuclide is the rate at which the nuclei of its constituent atoms (N) decay. Also, the activity or the disintegration rate of a radionuclide at any time is proportional to the total number of radioactive atoms present at that time. Mathematically, the rate of decay (A) is given by

$$A = -\frac{dN}{dt} \propto N \qquad (4.10)$$

$$A = -\frac{dN}{dt} \lambda N \qquad (4.11)$$

where N is the number of radioactive atoms and λ is the decay constant (or proportionality constant), which is defined as the probability of disintegration per unit time. The minus sign indicates that the number of atoms is decreasing with time. The above equation for the rate of decay is the rate law for a first order process. Upon integration, the formula for "radioactive decay" is given by

$$N = N_0 e^{-\lambda t} \qquad (4.12)$$

The formula for the time variation of activity or activity at any time t is given by

$$A_t = A_0 e^{-\lambda t} \qquad (4.13)$$

The above equations represent the *exponential decay* of any radionuclide in which λ is the *decay constant* of the radionuclide and the factor $e^{-\lambda t}$ is known as the *decay factor*, which is the fraction of original activity A_0 remaining after time t.

Fig. 4.6 The decay of radioactivity as a function of time (half-lives) plotted on a linear scale (**a**) and semilogarithmic scale (**b**)

The decay factor is an *exponential function* of time *t*. The exponential decay is characterized by the transformation of a constant fraction of the number of atoms or activity present per unit time interval. When the decay factor, number of atoms, or activity is plotted against time, it is a curve approaching zero on a linear plot but is a straight line in a semilogarithmic plot (Fig. 4.6).

4.3.2 Units of Activity

The SI unit of radioactivity is named after Becquerel

$$1 \text{ Becquerel} = 1 \text{ Bq} = 1 \text{ decay} / \text{s} \quad (4.14)$$

The traditional unit of activity is the Curie (Ci), which was originally defined as the activity of 1 g radium, ^{226}Ra. Curie is now defined as

$$1 \text{Curie} = 1\text{Ci} = 3.7 \times 10^{10} \text{ dps} = 37 \text{GBq} \quad (4.15)$$

$$1 \text{milliCurie} = 1\text{mCi} = 3.7 \times 10^{7} \text{ dps} = 37 \text{MBq} \quad (4.16)$$

$$1 \text{microCurie} = 1\mu Ci = 3.7 \times 10^{4} \text{ dps} = 37 \text{kBq} \quad (4.17)$$

4.3.3 Half-Life and Average Lifetime

Every radionuclide has a characteristic half-life ($T_{1/2}$), which is the time required for the activity to decay to 50% of its original value. That is, A_0 is reduced to $A_0/2$ in one half-life, $A_0/2^2$ in 2 half-lives, and $A_0/2^n$ in "*n*" half-lives. The activity *A*, of a radionuclide at any time *t*, is given by

$$A_t = \frac{A_0}{2^n} = \frac{A}{2^{(t/T_{1/2})}} \quad (4.18)$$

The half-life and the decay constant of a radionuclide are related

$$T_{1/2} = \frac{\ln(0.2)}{\lambda} = \frac{0.693}{\lambda} \quad (4.19)$$

In a given sample of radionuclide, not all atoms decay with the same half-life; some atoms may have a shorter and some atoms may have a longer life span than one half-life. The average, or mean life (τ) of a radionuclide is, therefore, defined as the average of all individual life times of the atoms in a sample of radionuclide experience. The mean life is related to the decay constant and half-life.

$$\tau = \frac{1}{\lambda} = \frac{T_{1/2}}{0.693} = 1.44 T_{1/2} \quad (4.20)$$

4.3.4　Specific Activity

The specific activity (SA) of a radioactive sample is defined as its activity per unit mass. The SA is the ratio of activity to the total mass of the element present. It has units of Ci g^{-1}, Ci $mmol^{-1}$, or GBq $mmol^{-1}$.

Many elements have several isotopes and some of the isotopes of an element can also be stable. The element carbon has four isotopes as shown below:

$$^{11}_{6}C, \ ^{12}_{6}C, \ ^{13}_{6}C, \ ^{14}_{6}C$$
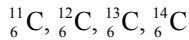
^{12}C and ^{13}C are stable and, in nature, most of the carbon is ^{12}C (99% abundance). ^{14}C ($T_{1/2}$ = 5760 years) decays by beta decay while ^{11}C ($T_{1/2}$ = 20 min) decays by positron emission. When stable isotopes of an element are present along with the radioactive isotope, then the stable isotopes are called *carrier*. When the radioactivity of the sample is said to be with the carrier, the SA of such a radioisotope is low, because the total mass of the element includes the mass of radioisotope and also that of the carrier. A radioactive sample that does not contain the carrier is called *carrier-free*. The highest possible SA of a radionuclide is its carrier-free SA (CFSA). It is also known as the theoretical SA, and may not necessarily be achieved practically by radionuclide production methods.

CFSA can be calculated since there is a well-defined activity–mass relationship based on the following mathematical relationships:

- Based on $T_{1/2}$, decay constant (λ) can be calculated as $\lambda = 0.693/T_{1/2}$
- Knowing the activity (Ci or GBq, etc.) and λ, the number of atoms (N) in a sample of radioactivity can be determined based on the activity law, $A = \lambda N$
- Based on N, the mass (gram or mole) of a radioisotope can be determined because 1 mol (gram atomic weight) of any element contains 6.022×10^{23} atoms (Avogadro's number).

For a number of radioisotopes, the carrier-free SA are shown in Table 4.3. The SA calculations for ^{11}C are shown below.

Carrier-Free Specific Activity (CFSA) of ^{11}C
1 mol of ^{11}C (11 g) contains 6.022×10^{23} atoms (N). λ Based on the equation. A = N. λ, the number of atoms in one Ci of C-11 can be calculated. since the $T_{1/2}$ of ^{11}C = 20 min,

$$\lambda = \frac{0.693}{20\,min \times 60s} = 5.775 \times 10^{-5}$$

Table 4.3 Radionuclides for PET and SPECT: Half-life and specific activity (SA)[a]

Radionuclides for PET			Radionuclides for SPECT		
Nuclide	$T_{1/2}$ (min)	SA (Ci μmol^{-1})	Nuclide	$T_{1/2}$ (min)	SA (Ci μmol^{-1})
^{82}Rb	1.20	150,400			
^{15}O	2.07	91,730			
^{122}I	3.62	51,912			
^{62}Cu	9.76	19,310			
^{13}N	10.0	18,900			
^{11}C	20.4	9220			
^{94m}Tc	52.0	3614	^{99m}Tc	360	522
^{68}Ga	68.3	2766			
^{77}Br	96.0	1960			
^{18}F	110	1708			
^{66}Ga	567	331	^{67}Ga	4320	40
^{64}Cu	768	245			
^{86}Y	884	213	^{111}In	4020	47
^{89}Zr	4709	39.9			
^{124}I	6048	31.0	^{123}I	780	237

[a] Maximum theoretical specific activity (SA)

Activity (Bq) in 1 mol:

$$Bq = 5.775 \times 10^{-5} \times 6.022 \times 10^{23} = 3.478 \times 10^{19}$$

since 1 Ci = 3.7×10^{10} Bq:

$$\frac{3.478 \times 10^{19}}{3.7 \times 10^{10}} = 9.4 \times 10^8 \, \text{Ci mol}^{-1}$$

since 1 GBq = 10^9 Bq:

$$\frac{3.497 \times 10^{19}}{10^9} = 3.478 \times 10^{10} \, \text{GBq mol}^{-1}$$

CFSA of ^{11}C = 9400 Ci μmol^{-1} or 9.4×10^3 Ci μmol^{-1}

A similar calculation shows that CFSA of ^{14}C = 6.205×10^{-5} Ci μmol^{-1}

4.3.5 Serial Radioactive Decay

When a sample of radioactivity consists of a pair of parent and daughter radionuclides, the parent activity (A_p) at any time t is given by Eq. (4.13). Because the daughter is continuously produced by the decay of the parent and at the same time the daughter activity is also decaying, estimating the daughter activity (A_d) at any time really depends on the decay constant or the $T_{\frac{1}{2}}$ of the daughter radionuclide. The *Bateman equation* describes the parent–daughter relationship and provides an estimate of A_d.

$$A_{d(t)} = A_{p(t_0)} \frac{\lambda_d}{\lambda_d - \lambda_p} \left(e^{-\lambda_p t} - e^{-\lambda_d t} \right) + A_{d(t_0)} e^{-\lambda_d t}$$

(4.21)

At equilibrium, the parent and daughter activities appear to decay with the same rate, even if the two nuclides have different half-lives. Two different equilibrium conditions, however, may exit, depending on how short-lived the daughter radionuclide is, compared to the parent. If the parent is short-lived compared to the daughter, then there is no equilibrium at all.

4.3.5.1 Secular Equilibrium

When the daughter radionuclide is very short-lived, compared to the parent ($T_{\frac{1}{2}d} \ll T_{\frac{1}{2}p}$), *secular equilibrium* is said to exist. The activity of the daughter builds up to that of the parent in about seven half-lives of the daughter. At equilibrium, $A_d = A_p$ (Fig. 4.7a). The activity of the daughter at any time, however, is given by

$$A_{d(t)} = A_{p(t_0)} \left(1 - e^{-\lambda d t} \right) \qquad (4.22)$$

Two important examples are ^{68}Ge ($T_{\frac{1}{2}}$ = 270 days) → ^{68}Ga ($T_{\frac{1}{2}}$ = 68 min) generator and ^{82}Sr ($T_{\frac{1}{2}}$ = 25 days) → ^{82}Rb ($T_{\frac{1}{2}}$ = 75 s) generator. The therapeutic radionuclide, ^{225}Ac ($T_{\frac{1}{2}}$ = 10 days), a decay product of ^{229}Th ($T_{\frac{1}{2}}$ = 7340 years) is generally obtained based on ^{229}Th → ^{225}Ac generator (also known as "thorium cow").
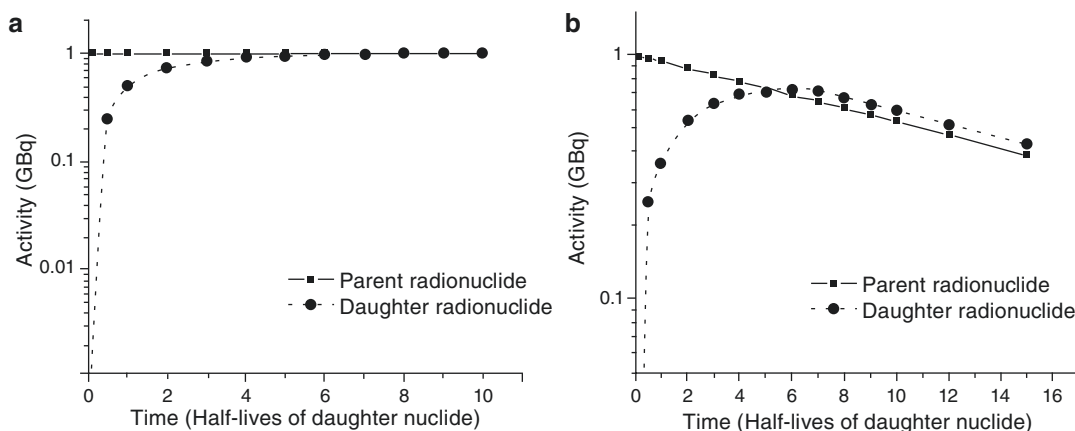
Fig. 4.7 In a parent–daughter decay, following the buildup of the daughter activity, the parent and daughter activities are said to be in secular equilibrium (**a**) or in transient equilibrium (**b**)

4.3.5.2 Transient Equilibrium

When the parent half-life is longer than the daughter half-life ($T_{\frac{1}{2}p} > T_{\frac{1}{2}d}$), the daughter activity increases while the parent activity slowly decreases. The daughter activity reaches a maximum and is slightly greater than that of the parent. Once the *transient equilibrium* is reached (~7 $T_{\frac{1}{2}}$ of daughter), both radionuclides appear to decay with the same rate, the decay rate of the parent (Fig. 4.7b). The daughter activity (A_d) at any time t is given by

$$A_{d(t)} = A_{p(t)} \frac{\lambda_d}{\lambda_d - \lambda_p} \qquad (4.23)$$

An example of transient equilibrium is ^{99}Mo ($T_{\frac{1}{2}} = 66$ h) $\rightarrow$ ^{99m}Tc ($T_{\frac{1}{2}} = 6$ h) generator.

Further Reading

Beiser A. Concepts of modern physics. 5th ed. New York, NY: McGraw-Hill; 1995.

Bushberg JT, Seibert JA, Leidholdt EM Jr. The essential physics of medical imaging. 2nd ed. Philadelphia, PA: Lippincott; 2002.

Emsley J. The elements. 3rd ed. Oxford: Oxford University Press; 1998.

Saha G. Fundamentals of nuclear pharmacy. 5th ed. New York, NY: Springer; 2004.

Sorenson JA, Phelps ME. Physics in nuclear medicine. Philadelphia, PA: Saunders; 1987.

Turner JE. Atoms, radiation, and radiation protection. 2nd ed. New York, NY: Wiley; 1995.

What we observe as material bodies and forces are nothing but shapes and variations in the structure of space. Particles are just schaumkommen (appearances). The world is given to me only once, not one existing and one perceived. Subject as well as object is only one. The barrier between them cannot be said to have broken down as a result of recent experience in the physical sciences, for this barrier does not exist. (Erwin Schrodinger)

5.1 Interaction of Radiation with Matter

Radiation emitted by radionuclides can be classified into electromagnetic (such as X-rays, γ-rays, annihilation photons) or particulate (such as β⁻, and β⁺) radiation. When we speak of the interaction of radiation with matter, we mean its interaction with the electrons, and nucleus of atoms. The interaction of radiation, in general, may be classified as *elastic* or *inelastic*. In an elastic interaction, the incident radiation is scattered in a different direction, but the total energy of the interacting particles is conserved. In contrast, in an inelastic interaction, a certain amount of energy is lost emitted X-rays.

Ionization occurs when an electron is ejected from an atom, producing an ion pair, a free electron, and a positive atom. High-energy photons (X-rays, γ-rays, and annihilation photons) and charged particles (β⁻, β⁺, H, and α or He^{2+}) are regarded as ionizing radiation. If an electron is not ejected from the atom but merely raised to higher energy levels or outer shells, the process is termed *excitation*, and the atom is said to be *excited*. In certain materials, when the electrons in the excited state drop to a lower energy state, with the emission of visible light, then that material is said to exhibit *luminescence*. If the production of light ceases within 10^{-8} s of the end of irradiation (or interaction), then the process is one of *fluorescence*; if it continues beyond this point, then the process is called *phosphorescence* (also known as *afterglow*).

5.1.1 Interactions of Charged Articles

5.1.1.1 Ionization

Charged particles (such as electrons β⁻, β⁺, and H⁺) passing an absorbing medium transfer some of the energy to electrons of the medium and are then deflected. Therefore, they cause⁺⁺ *ionization* and/or *excitation*. The probability of scattering increases with the atomic number Z of the absorbing medium and decreases rapidly with the increasing kinetic energy of the incident electron. In a close encounter, an orbital electron may be separated from the atom, thus causing ionization. The ejected electron may have sufficient energy to cause secondary ionization and eject an orbital electron, known as delta (δ) rays. The *specific ionization* (SI), the number of primary and secondary ion pairs produced per centimeter in air,

at standard temperature and pressure (STP), can be estimated on the basis of the velocity (v) of incident electron and the velocity of light (c) using the following equation:

$$SI = \frac{45}{\left(v/c\right)^2}$$ (5.1)

A less close encounter of the incident charged particle with an atom or molecule may result in an orbital electron being raised to an excited state, thus causing atomic or molecular excitation. The energy absorbed by the atom is dissipated in the subsequent atomic emission of electromagnetic radiation (such as infrared, visible, or UV).

5.1.1.2 Bremsstrahlung Radiation

When an incident β^- particle penetrates the electron cloud of an atom, it may interact with the nucleus and may be deflected with a reduced velocity. The energy lost by the incident electron will appear as electromagnetic radiation, known as bremsstrahlung (breaking radiation) (Fig. 5.1). The probability of bremsstrahlung varies with Z^2 of the absorbing medium.

5.1.1.3 Annihilation Radiation

A positron (β^+), after expending its kinetic energy in inelastic collisions, combines with an electron (β^-) of the absorbing medium. Both the particles are annihilated, and their mass appears as electro-magnetic radiation (usually two 511-keV photons), known as annihilation radiation (Fig. 5.1). This interaction of β^- and β^+ particles (matter and antimatter) is called *pair annihilation*.

5.1.1.4 Cerenkov Radiation

Particles normally cannot exceed the velocity of light in a vacuum (3.0×10^{10} cm s^{-1}). Light, however, travels at slower speeds in different materials or media. It is possible for β^- rays to travel at speeds much higher than that of light in a specific medium. When this occurs, visible light, known as *Cerenkov radiation*, is emitted. For example, the blue glow seen near the core of a swimming pool reactor is due to Cerenkov radiation.

5.1.2   Interaction of High-Energy Photons

The interaction of electromagnetic radiation with atoms, electrons, and nuclei of different materials is generally regarded as a collision involving transfer of their energy to matter without necessarily causing ionization directly. However, certain interactions do eject orbital electrons, produce ion pairs, and cause ionization effects. Therefore, high-energy photons, similar to charged particles, are regarded as ionizing radiation. However, unlike charged particles, high-energy photons being massless can penetrate
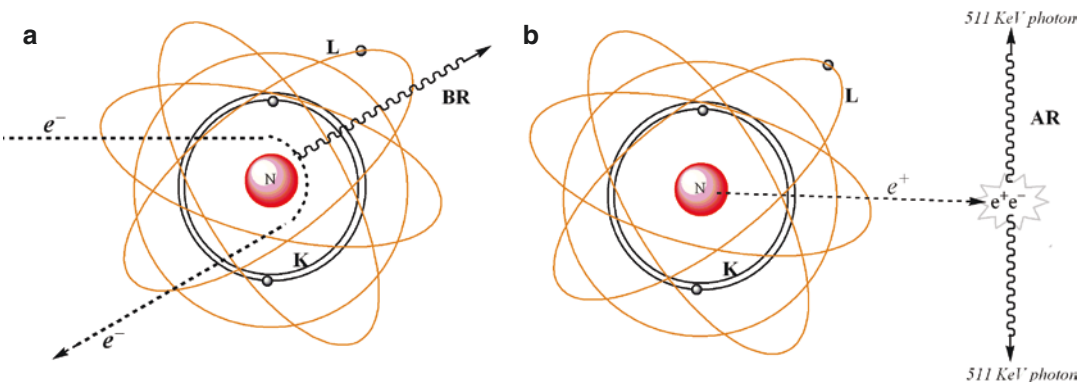
Fig. 5.1 Interaction of charged particles with matter. When high-energy electrons penetrate and approach the nucleus, they are decelerated and deflected (**a**). As a result, bremsstrahlung radiation (BR) is produced. The positron emitted from the atomic nucleus finally interacts with an electron and annihilates it (**b**). As a result, annihilation radiation (AR) is produced in which two photons with a minimum of 511 keV energy travel in opposite directions

soft-tissue thickness of >10 cm in vivo and are considered to be highly penetrating radiation.

The high-energy photons of X-rays, γ-rays, and annihilation radiation associated with radio-tracers in nuclear medicine undergo inelastic interactions by means of several mechanisms. The *photoelectric effect* and *Compton scattering* are important in radiation detection and measurement. Pair production and photodisintegration have a high-energy threshold (>1 MeV) and are not relevant to the photon energies normally encountered in nuclear medicine.

5.1.2.1 Photoelectric Effect

When a metal is exposed to electromagnetic radiation, electrons are ejected from the metal (Fig. 5.2). These electrons are called *photoelectrons*. Light with shorter wavelengths (such as UV) ejects electrons with greater speed. Thus, the kinetic energy of photoelectrons is dependent on the frequency; however, the number of electrons ejected depends on the intensity of the electromagnetic radiation. Different metals have different threshold values for the frequency. Depending on the Z of the element, electrons may be held more loosely or tightly. Einstein was able to show that photons with higher energy eject electrons with greater kinetic energy. This phenomenon of the photoelectric effect is very important for the interaction of radiation with matter and for developing radiation detectors. The photoelectric effect should obey the following relationship:

$$hv = KE_{max} + \varphi \tag{5.2}$$

Where

$$\varphi = hv_0 \tag{5.3}$$

Also, v_0 is the critical frequency below which no photoelectric effect occurs and φ (or ϕ) is the minimum energy (called the *work function* of the metal) needed for the electron to escape from a metal surface. The photoelectric effect is an atomic absorption process in which an atom totally absorbs the energy of the incident photon. It is an interaction of photons with orbital electrons in an atom, mostly the inner-shell electrons, in which the photon transfers all of its energy to the electron, which is then ejected. Some of the energy of the incident photon is used to overcome the binding energy of the electron, and the remaining energy is given to the photoelectron, as kinetic energy. Since the ejection of a photo-electron creates a vacancy in the inner shell, the
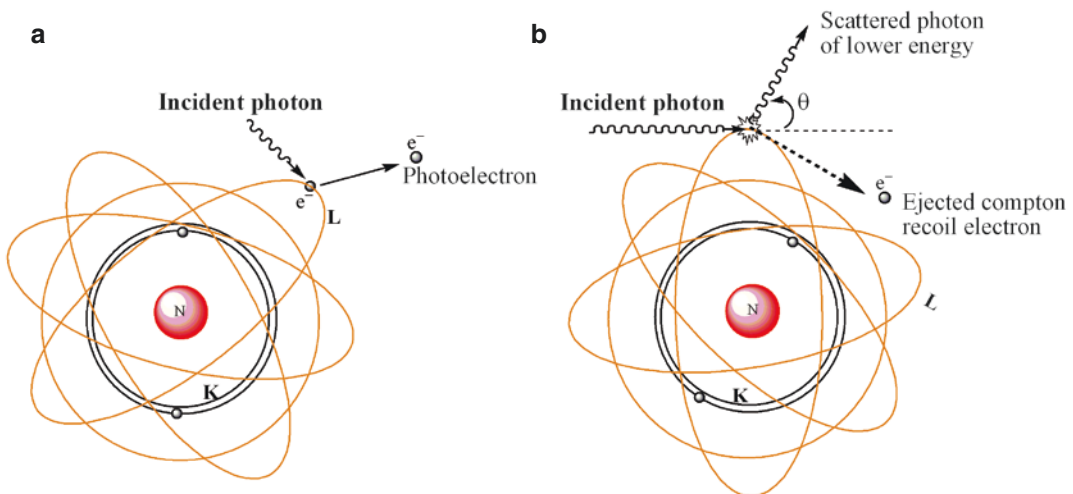
Fig. 5.2 Interaction of high-energy photons with matter. In the photoelectric effect (**a**), an incident photon transfers all its energy to an orbital electron, which leaves the atom and is known as a photoelectron. In Compton scattering (**b**), the incident photon transfers only part of its energy to an orbital electron, which is then ejected (recoil electron). The scattered photon is then deflected in a different angle (θ, the scattering angle)

photoelectric effect is usually accompanied by the emission of characteristic X-rays and/or Auger electrons.

The probability of a photoelectric interaction occurring at a particular shell depends on the energy of the incident photon and the binding energy of the shell (in other words, on *Z*). The probability is zero when the energy of the photon is less than the binding energy of the electron; it is greatest when the photon energy is equal to the binding energy of the electron and thereafter decreases rapidly with increasing photon energy. Following the injection of radiotracers, the photoelectric effect plays a minor role with soft tissue. In radiation detectors, such as scintillation detectors, however, the photoelectric effect is the predominant mode of interaction of photons.

5.1.2.2 Compton Scattering

Compton scattering is a collision between a photon and a loosely bound outer orbital electron. After the interaction, the *scattered photon* undergoes a change in direction and the recoil electron is ejected from the atom (Fig. 5.2). The scattered photon is deflected through an angle (θ_C) proportional to the amount of energy lost. The maximum energy loss occurs when the θ_C is 180° or when the photon is *backscattered*. For example, the annihilation photon (511 keV) after backscatter will have an energy of 170 keV. The energy lost by the scattered photon is divided between the small binding energy of the orbital electron and the kinetic energy of the recoil electron. The relative probability of Compton scattering increases slightly as the energy of the incident photon increases and as the effective atomic number (Z_{eff}) of the interacting medium decreases. Following administration of radiotracers, the most important and significant mode of interaction of photons with soft tissue is Compton scattering.

5.1.2.3 Pair Production

When a high-energy photon interacts with an electric field of a charged particle (atomic nucleus or even an electron), the incident photon may completely disappear and its energy is used to create a β^- and β^+ pair, known as *pair production*.

Since the rest mass (energy) of the electron is 511 keV, the incident photon must have a minimum energy of 1.022 MeV. The difference between the incident photon energy and 1.022 MeV is imparted to the electron pair as kinetic energy.

5.1.3 Attenuation

If we measure the intensity of the radiation before (I_0) and after it interacts with a given medium (I_x) of particular thickness *x*, we find that the intensity of the radiation after passing through the medium has reduced; the beam of radiation is said to have been attenuated. By the processes of absorption and scattering in a medium, a beam of radiation undergoes attenuation. The atoms in the medium act as targets, which, if hit, will attenuate a photon from the primary radiation beam. The probability of an interaction with a particular atom is low, but the very large number of atoms in a small volume of a solid increases the probability of attenuation, significantly. A parallel beam of monoenergetic electromagnetic radiation will undergo exponential attenuation as it passes through a uniform medium.

$$I_x = I_0 e^{-\mu x} \qquad (5.4)$$

where μ is the total *linear attenuation coefficient*, which can be defined as the fraction of photons removed from a beam of radiation per unit thickness of the attenuating medium. The parameter μ is a property of both the photon energy and the nature of the medium. It increases (i.e., photons become less penetrating) for low photon energies and low mass density. In a given thickness of medium, the number of atoms (*N*) may be the same for different materials, but the density (ρ) may vary. Therefore, the total mass attenuation coefficient μ/ρ is the fraction of photons removed from a beam of radiation of unit cross-sectional area by unit mass of the medium. For photons with <1 MeV energy, the parameters μ and μ/ρ are largely made up of components due to photoelectric absorption (τ) and Compton scattering (σ).

Other important parameters derived from *m* are half-value thickness (HVT) or half-value

Table 5.1 Linear attenuation coefficient and HVL values of photons for different materials

Material	Density (ρ) (g cm^{-3})	140-keV μ (cm^{-1})	Photon HVL	511-keV μ (cm^{-1})	Photon HVL
Water	1.0	0.15	4.62	0.095	7.29
Adipose tissue	0.95	0.142	4.88	0.090	7.70
Cortical bone	1.92	0.284	2.44	0.178	3.89
Pyrex glass	2.23	0.307	2.26	0.194	3.57
Lucite	1.19	0.173	4.01	0.112	6.19
NaI (Tl)	3.67	2.23	0.31	0.34	2.04
Bismuth germinate	7.13	~5.5		0.95	0.73
Lead	11.35	40.8	0.018	1.75	0.42
Tungsten				2.59	0.29

layer (HVL), tenth value layer (TVL), and the mean free path (MFP), which is the distance a photon (or a particle) travels before interacting. All these parameters are related mathematically as shown in the following equations:

$$\mu = 0.693 / \text{HVL} \qquad (5.5)$$

$$\text{MFP} = 1.44\,\text{HVL} \qquad (5.6)$$

With radiation, the three most important media of interest are the tissue, radiation detector material (the crystal), and the type of shielding (lead, tungsten). For various materials, the linear attenuation coefficient and HVL values for photons of two different energies, 140 and 511 keV, are shown in Table 5.1. For 511-keV photons, the primary interaction is Compton scattering; therefore, correction for attenuation and scattering is essential for PET imaging studies.

5.2 Radiation Detectors

Radiation detectors have been developed over the years on the basis of the two major consequences of interaction of radiation with matter: ionization and excitation. Radiation detectors are generally categorized as either ionization detectors or scintillation detectors.

5.2.1 Ionization Detectors

These detectors respond to radiation by means of ionization, which induces tiny electrical currents that can be detected and measured. The ioniza-

tion detectors can be either gas-filled (also known as *ionization chambers*) or *semiconductor detectors*.

5.2.1.1 Gas-Filled Detectors

Most gas-filled detectors are made up of a chamber, which contains a volume of gas (mostly air or an inert gas) between two electrodes with a voltage difference between them. Under normal circumstances, the gas is an insulator and no current flows between the electrodes. When the gas is ionized following an interaction with radiation, electrons are attracted to the anode and positive ionized atoms are attracted to the cathode, producing a small current. When gas-filled chambers operate at the saturation voltage (300–600 V), to ensure complete collection of ions at the electrodes, they are called *ionization chambers*. If the detector is calibrated to express the measured current as an exposure rate (R h^{-1}, mR h^{-1}), it is called a survey meter; if it collects the total charge over a period of time, it is called a *pocket dosimeter*; and, finally, if the measured current is used to assay the activity (mCi, MBq, etc.), it is called a *dose calibrator*.

Ionization chambers are quite inefficient as detectors for X-rays and γ-rays. Their response to photons changes with photon energy, but the energy discrimination, especially in the case of dose calibrators, is achieved only by the use of precalibrated amplifiers, one for each radionuclide of interest.

If an ionization chamber is maintained between 900 and 1200 V, the electrons generated by the interaction of radiation will accelerate and cause additional ionization. This process is

known as *gas amplification* of the charge, and the factor by which the ionization is amplified is called the *gas amplification factor* (GAF). A Geiger–Muler (GM) counter is a gas-filled detector designed to have GAF as high as 10^{10}. In a GM counter, the size of the electrical signal output is relatively constant and independent of the energy of radiation. Because of their high sensitivity, GM counters are mainly used as survey meters to detect ambient radiation levels and radioactive contamination.

5.2.1.2 Semiconductor Detectors

Semiconductor detectors are essentially solid-state analogs of gas-filled detectors [1]. Semiconductor materials, such as Si and Ge, when doped with Li, can function as solid ionization chambers, and are also called *solid-state detectors*. In order to create an ion pair in air, the energy needed is 34 eV per ionization. In contrast, the energy needed to create an ion pair is only 2.5 eV in Si(Li) and 3.0 eV in Ge(Li) detectors. When a small voltage is applied across a semiconductor detector, a high-energy photon will interact with the detector and liberate electrons leaving a positive hole in the lattice structure. Under an applied electric field, both the electron and the positive hole will move toward opposite electrodes inducing an electric current. Since the size of the electrical signal is relatively large and proportional to the radiation energy absorbed, semiconductor detectors are useful for energy-selective radiation counting.

Both, Ge- and Si-based semiconductors conduct a significant amount of thermally induced electrical current at room temperature. Therefore, it is necessary to operate and maintain these detectors at relatively low temperatures. High-purity germanium (HPGe), however, needs to be cooled to low temperatures, while others such as cadmium telluride (CdTe) and cadmium zinc telluride (CZT) operate at room temperature. Ge(Li) and Si(Li) detectors are relatively inefficient for detecting high-energy gamma photons. Both, CdTe and CZT have stopping powers similar to NaI(Tl) scintillation detectors. Even denser semiconductors, such as lead iodide (PbI) and thallium bromide (TlBr), are currently under development and may be useful for detecting high-energy photons. CdTe and CZT are also available as pixelated detector arrays with a typical intrinsic spatial resolution of 2.4 mm.

5.2.2 Scintillation Detectors

When high-energy photons interact with the atoms of a scintillation crystal, the electrons are raised from a *valence band* or an orbital to a forbidden, unfilled *conduction band* of a higher energy state. The excited atoms quickly return to the ground state emitting a visible light in a process known as *luminescence*. The number of electrons raised to a higher energy level, and the consequent number of visible light photons emitted by the crystal, depends on the energy of the incident photon. The photoelectric effect is the primary mode of interaction of photons with the atoms in the crystal. The visible light emitted by the crystal is usually in the ultraviolet range. For the crystal to emit light in the visible range (400–500 nm), an alkali halide crystal, with an impurity of (<1%), such as thallium iodide, must be *activated* (or *doped*). The scintillation photons produced by the luminescence are emitted *isotropically* (in all directions) from the point of interaction. The most important scintillators used in PET and SPECT scanners are the following:

- Sodium iodide doped with thallium iodide (NaI(Tl))
- Bismuth germinate, $Bi_4Ge_3O_{12}$ (BGO)
- Lutetium oxyorthosilicate doped with cerium, Lu_2SiO_5:Ce (LSO)
- Yttrium oxyorthosilicate doped with cerium, Y_2SiO_5:Ce (YSO)
- Gadolinium oxyorthosilicate doped with cerium, Gd_2SiO_5:Ce (GSO)
- Barium fluoride (BaF_2)
- Lutetium yttrium oxyorthosilicate (LYSO)

The physical properties of several scintillators are compared in Table 5.2. The most important properties of a detector are stopping power, light output, signal decay time, and the intrinsic energy resolution of the crystal. The following points

Table 5.2 Physical properties of scintillators

	NaI (Tl)	YSO	BaF2	LYSO	GSO	BGO	LSO
Density (g cm^{-2})	3.67	4.53	4.89	5.31	6.71	7.13	7.4
Effective Z	50.6	34.2	52.2	54	58.6	74.2	65.5
Light output (photons/keV)	38	46	2	30	10	6	29
Relative light output (%)	100	118	5	76	25	15	75
Wavelength, λ (nm)	410	420	220	420	440	480	420
Decay time (ns)	230	70	0.6	53	60	300	40
Attenuation, μ (cm^{-1}) at 511 keV	0.3411	0.3875	0.4545	–	0.6978	0.9496	0.8586
Attenuation length ($1/\mu$)	2.93	2.58	2.20	2.0	1.433	1.053	1.169
Photoelectric/Compton ratio	0.22	–	0.24	–	0.35	0.78	0.52

may be noted: (1) The stopping power is characterized by the MFP or attenuation length, which depends on the density (ρ) and effective atomic number (Z_{eff}) of the crystal. A crystal with shorter attenuation length will have higher efficiency and sensitivity. (2) A crystal with high light output (photons keV^{-1} absorbed) will have good energy resolution. (3) A short decay time of the crystal can help process each pulse separately at higher counting rates with minimum dead time. (4) A crystal with better energy resolution can reject scattered photons more effectively. The overall scanner spatial resolution, however, depends on several other factors.

With NaI(Tl) crystal, the detection efficiency for 140-keV photons is >90%, but for 511-keV photons, the efficiency drops to <10%. The intrinsic energy resolution of the crystal is more important for SPECT scanners, while the stopping power of the crystal is one of the main considerations in the choice of the crystal that can interact with 511-keV photons in PET scanners. With the current PET scanners, BGO and LSO are the preferred crystals, while NaI(Tl) is the only crystal that is used in all the major clinical SPECT scanners. A number of other scintillators such as CsI(Tl) and CsI(na) are also under evaluation. The technology of PET and SPECT scanners is continuously evolving and is dependent on many other factors besides scintillators.

5.2.2.1 Photodetectors

One of the common characteristics of all scintillators is that following interaction with high-energy photons they all produce a very weak signal of visible light, or a scintillation photon.

The purpose of a photodetector is to convert a scintillation photon with 3–4 eV energy into an electrical current. The probability of converting a photon into an electron is called *quantum efficiency*. The two categories of photodetectors used are photomultiplier tubes (PMTs) and semiconductor-based photodiodes.

A PMT is a vacuum tube that consists of an entrance window, *photocathode*, followed by a series of *dynodes* (electrodes), each of which is held at a greater voltage with a resistor chain. The scintillation photon strikes the photocathode and release photoelectrons, which are then accelerated to the first dynode and release even more electrons, which are then accelerated to the next dynode. After passing a series of dynodes, the number of electrons is amplified to >10^6, producing a sizeable current in the milliampere range at the anode. Despite their bulkiness, almost all commercial PET and SPECT scanners use PMTs because of their high gain or amplification, ruggedness, and stability. The quantum efficiency of the photocathode in PMTs is about 15–25%. In order to improve this efficiency, more advanced PMTs, known as position-sensitive (PS) PMTs and multichannel (MC) PMTs, are under development and evaluation.

A photodiode consists of a thin piece of doped silicon wafer (a couple of 100 μm thick). The principle of operation is the same as that of a semiconductor. The quantum efficiency (60–80%) of photodiodes is much better than that of PMTs, but the signal of the electrical current is very weak because photodiodes do not have internal amplification or gain. In order to improve the signal-to-noise ratio (SNR), a new type of

photodiode known as *avalanche photodiode* (APD) has been developed, which has an internal amplification; however, it is still not as good as that of PMTs.

5.2.2.2 Radiation Detector Performance

Spectroscopy is the study of the energy distribution of a radiation field. Most spectrometers are operated in the pulse mode and the amplitude of each pulse is proportional to the energy deposited by the interaction of the photon with the crystal. The amplitude, however, may not be proportional to the total energy of the incident photon. A *pulse height spectrum* (Figs. 5.3 and 5.4) represents the number of interactions or counts per minute (cpm) as a function of the energy of the photon, but it is not the same as the actual energy spectrum of the incident radiation. The performance characteristics of radiation detectors can be expressed quantitatively using parameters, such as *sensitivity* and *energy resolution*.

Sensitivity (or *efficiency*) is the detected count rate per unit of radioactivity. *Geometric sensitivity* of a detector is the fraction of emitted photons that reach the detector, whereas the *intrinsic sensitivity* or the *quantum detection efficiency* (QDE) is the fraction of those photons that reach the detector which are actually detected. For exam-

ple, 1 µCi of ^{99m}T has 2.2×10^6 disintegrations per minute (dpm), and each decaying atom produces one 140-keV photon. If the detector can detect 1.0×10^5 photons, then the sensitivity of the detector is 10%. As discussed previously, various physical characteristics of the crystal (Table 5.2) can affect the sensitivity of the scintillator.

Many radionuclides emit a number of photons (X-rays and γ-rays) of discrete energies. The electrical signal output from a detector–photodiode combination, however, appears as though it is coming from a range of energies due to the absorption and scattering of the incident photons. Energy resolution quantifies the ability of a specific crystal to differentiate or discriminate photons of different energies. It is expressed quantitatively as a percent of full width at half-maximum (FWHM = ΔE) of an energy spectrum (counts detected vs. energy (keV)) of a radionuclide with a specific photopeak energy (E_γ).

$$\text{FWHM}\left(\%\right) = \frac{\Delta E}{E_\gamma} \times 100 \qquad (5.7)$$

For energy-selective detection (as in Anger cameras), the FWHM determines the resolution of the detector. The sensitivity can be increased by increasing the value of ΔE, but that would degrade the resolution.
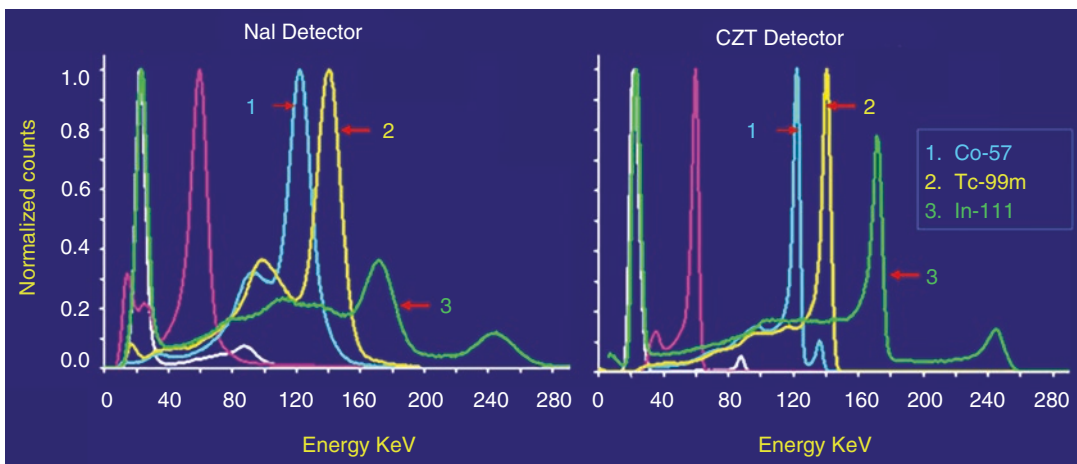
Fig. 5.3 Pulse height spectra of several radionuclides using NaI or CZT detector. The energy resolution with CZT detectors is much higher compared to that with NaI detector
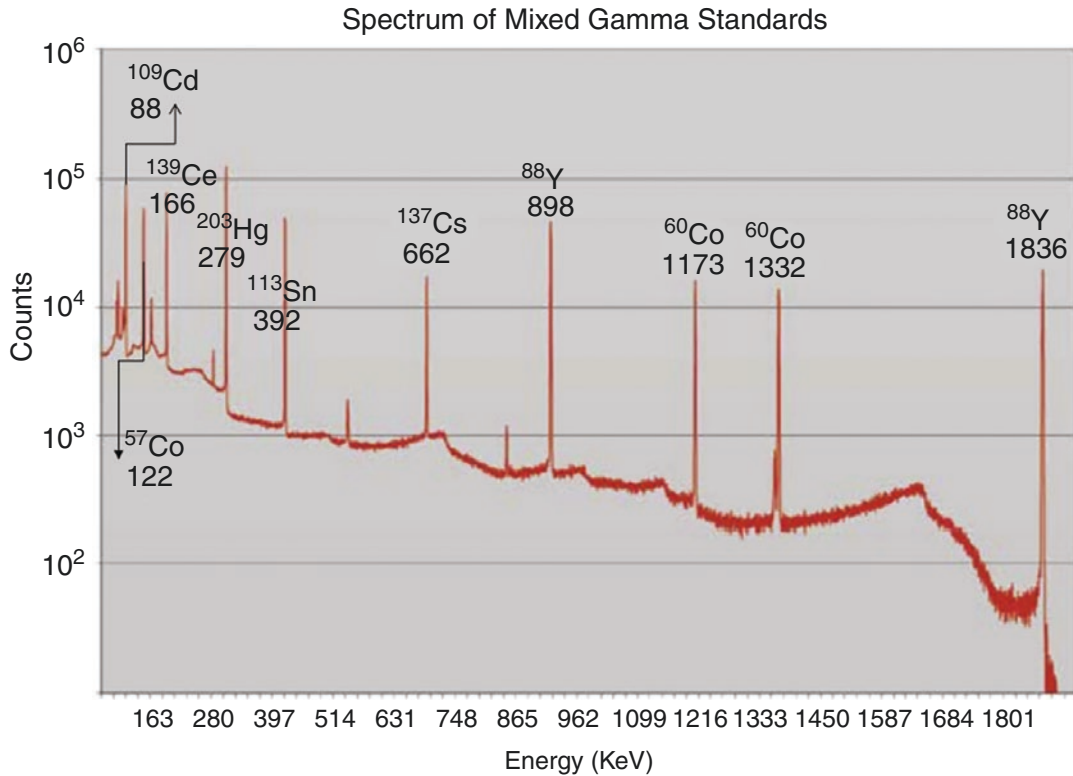
Fig. 5.4 Gamma spectrum of Analytics mixed standard using high-purity germanium (HPGe) detector. Analytic's mixed gamma standard utilizes the basic eight radionuclides which show minimal spectral interference

5.3 Radionuclide Imaging Systems

The purpose of radionuclide imaging is to obtain an image of the in vivo distribution of a radiotracer on the basis of the external detection of high-energy photons emitted by the radionuclide. In the 1940s, attempts were made to detect the distribution of radioactivity in vivo, but it was only in the 1950s, that in vivo radionuclide imaging became a practical clinical modality, due to the introduction of the rectilinear scanner, by Ben Cassen. In the 1950s, Hal Anger developed the first γ-ray camera using a single, large-area NaI(Tl) scintillation crystal coupled to PMTs. This camera, subsequently, called the *Anger scintillation camera*, has become the predominant molecular imaging device in nuclear medicine. Since then, many refinements and modifications have been made to improve the image quality of this camera.

Conventional Anger camera images compress the three-dimensional (3D) distribution of the radiotracer into a two-dimensional (2D) image. As a result, the contrast between areas of interest and the surrounding territory is often significantly reduced. In *planar imaging* systems, the radiation from a source (patient) is collected and the data are presented as though all photons are coming from a single plane. In a patient, images of a specific area of interest at one depth are obscured by images of structures above and below the area of interest. *Tomography* simply means an image of a slice. Tomographic images are 2D representations of structures lying within a selected plane or depth in a 3D object. *Computed tomography* (CT) techniques are based on rigorous mathematical algorithms initially developed by Radon, in 1917. The introduction of CT, in the 1970s, helped to implement CT techniques to the radionuclide imaging methods. X-ray CT is a transmission CT since X-rays from an external

source are transmitted through the patient to a detector. With radiotracers, high-energy photons are emitted from the patient; this technique is called *emission computed tomography* (ECT). While single photon emission computed tomography (SPECT) is based on radionuclides (such as ^{99m}Tc, ^{123}I, and ^{111}In) that directly emit single high-energy photons, positron emission tomography (PET) is based on positron-emitting radionuclides, and detection of high-energy (511 keV) photon pairs resulting from an annihilation process of positrons and electrons. The detection concepts used in the PET scanners make PET about 10–100 times more sensitive than SPECT and at the same time provide clinical PET images with higher spatial resolution.

PET and SPECT provide functional images of radiotracer distribution. In order to localize the tracer distribution, PET and SPECT are usually combined with structural imaging modalities that offer anatomical information with high spatial resolution, such as computed tomography (CT) and magnetic resonance imaging (MRI). These so-called hybrid-imaging modalities, PET/CT, PET/MRI, and SPECT/CT nowadays are standard in most nuclear medicine facilities. Also, CT and MRI are also used to improve the quantification of PET and SPECT. Several reviews described the technical developments of the hybrid scanners in greater detail [2–6].

5.3.1 SPECT/CT Scanner

Functional nuclear medicine imaging with SPECT/CT has been commercially available since the beginning of this century. Most of the SPECT systems available are based on the well-known Anger camera principle with NaI(Tl) as a scintillation material, parallel-hole collimators, and multiple photomultiplier tubes, which, from the centroid of the scintillation light, determine the position of an event. Recently, solid-state detectors using cadmium–zinc–telluride (CZT) became available and clinical SPECT cameras employing multiple pinhole collimators have been developed and introduced in the market. Quantitative studies with SPECT are still work in

progress; however, significant improvements have been made with CZT-based SPECT scanners. Most commercial SPECT/CT systems with dual-head or ring detectors (Fig 5.5), offered by General Electric (GE) Healthcare, Siemens Medical Solutions, Philips Healthcare, and Mediso Medical Systems all offer high-resolution diagnostic CT units as part of their SPECT/CT systems. Mediso even offers a complete SPECT/CT/PET with high-resolution LYSO detector technology as part of their AnyScan family of systems [2].

5.3.1.1 SPECT Based on NaI(Tl) Crystal

The principles of SPECT imaging with the commonly used scintillation camera based on the Anger camera design [7] consists of a single rectangular NaI(Tl) crystal (~50–60 cm in area) optically coupled to a large number of PMTs (typically 37–91). While the thickness may vary from 0.25 in. (~6 mm) to 1 in. (~25 mm), most cameras are made up of a 3/8 in. (~10 mm) crystal for optimum performance of radionuclides with energies between 120- and 200-keV photons. A *collimator* (usually made of lead) with holes (round, square, rectangular, or hexagonal) allows high-energy photons coming from the patient in a specific direction to enter and interact with the crystal. The walls, called *septa*, around the holes in the collimator absorb photons (~99% of photons reaching the collimator) that are traveling in an oblique angle to the axes of the holes. In other words, the collimator controls the direction of the photons entering the crystal. The thickness of the collimator and septa as well as the number of holes determines the overall sensitivity and resolution of the Anger camera. Most cameras have a wide choice of parallel-hole collimators such as "low-energy high sensitivity," "low-energy all purpose (LEAP)," "low-energy high resolution," medium-energy, high-energy, and ultrahigh-energy collimators, each designed to optimize a specific imaging study. With all parallel-hole collimators, the spatial resolution degrades rapidly as the distance (space) between the patient and the collimator increases. A pinhole collimator consists of a small hole (3–5 mm in diameter) in a piece of lead or tungsten and is

GE StarGuide SPECT/CT

Siemens Symbia Inteva SPECT/CT

Spectrum Dynamics D-SPECT

Spectrum Dynamics
Veriton SPECT/CT

Fig. 5.5 SPECT/CT systems in routine clinical use. GE Healthcare StarGuide, the most advanced SPECT/CT featuring advanced Cadmium Zinc Telluride (CZT) technology. Spectrum Dynamics CZT based digital systems include D-SPECT for cardiac applications and Veriton series for 360° total-body digital SPECT/CT. Siemens Healthineers Symbia Intevo dual-head SPECT/CT with high sensitivity

commonly used to produce magnified views of small objects. The magnification and sensitivity, however, decrease as an object is moved away from the pinhole. Following interaction of photons with the crystal, the emitted light photons induce electrical signals in the PMTs. In a NaI(Tl) crystal, approximately one visible photon is emitted for every 25 eV of energy deposited. For example, when a 140-keV photon deposits all of its energy in the crystal, it will generate 5600 visible light photons, of which only 20–25% may eject electrons from the photocathode and contribute to the signal from the PMT. The PMTs closest to the scintillation even in the crystal receive more light than those that are most distant and as a result produce a larger electrical signal. The relative amplitude of these pulses determines the location of the interaction in the crystal and the exact location of the origin of the photons coming from the patient. The electrical pulses from PMTs pass through preamplifiers and ADCs (analog-to-digital converter). The digital X, Y, and Z signals are corrected using correction circuits, followed by energy discrimination using SCAs (single-channel analyzers). The signals are finally converted into digital images in a computer. The measures of performance of a scintillation detector or camera alone are called *intrinsic* measurements, while the measures with the collimator are called *extrinsic* or system measurements; these measurements give the best indication or clinical performance.

With many of the Anger scintillation cameras, the intrinsic spatial resolution (R_i) for 140-keV photons of ^{99m}Tc is between 2.7 and 4.0 mm. With a parallel-hole collimator, however, the sys-

tem resolution (R_s) could dramatically decrease to 8–12 mm at a distance of 10–20 cm from the collimator surface. Also, the system resolution is not the same in the entire field of view.

5.3.1.2 SPECT Based on CZT Detector

Unlike the original SPECT technology based on Anger gamma camera, which relied on the pairing of scintillators to photomultiplier tubes, the commercial SPECT systems based on cadmium–zinc–telluride (CdZnTe or simply CZT) were introduced more than a decade ago [8, 9].

CZT is a semiconductor-based solid-state detector material with a density of 5.78 g cm^{-3} that generates signals from the collection of induced charge created by the ionizations from photoelectric interactions or Compton scattering. When the photons interact with the CZT in the semiconductor, the incident γ-rays create electron pairs, and an electrical signal is produced. The direct conversion of energy in the CZT detectors is characterized by good energy resolution (Fig. 5.3), and in clinical applications, the energy resolution is reported to be better than 6% at 140 keV. Unlike other detectors (e.g., germanium), CZT operates at room temperature due to the large size of the band gap in the CZT detector [10]. The high atomic number of CZT assists in efficient photoelectric absorption, leading to an improved system sensitivity compared with that of the sodium iodine (NaI) detector [11]. The major advantages of these new CZT modules are the small size of the CZT module and the absence of PMTs, which allows for a compact camera but still with multiple detectors. This means that it is possible to increase the overall system sensitivity significantly as compared with traditional SPECT systems. The improvement in sensitivity can be used to reduce the acquisition time of a given administered activity or decrease the amount of radioactivity dose injected.

The first clinical system, introduced in the market, was the D-SPECT (Spectrum Dynamics, Caesarea, Israel) and this was followed later by the Discovery NM 530c (GE Healthcare, Haifa, Israel). Both systems have a C-shaped gantry that contains multiple detectors. The number of detectors is, however, different between the systems.

The GE Discovery NM 530c has 19 stationary detectors equipped with pinhole collimators while the D-SPECT has ten CZT detectors where each is equipped with a parallel-hole square hole collimator, made of tungsten, and where each detector swivels around its own axis to acquire an optimized number of projection angles. The advantage of these SPECT scanners is the ability to perform fast dynamic SPECT with both these systems since all projections are acquired simultaneously. The first clinical CZT devices that were introduced were anatomically specific for cardiac examinations [12]. However, the general-purpose device continues to have the well-known design with a gantry and multiple detector heads. The first example of a general-purpose CZT device, coupled with a CT, was introduced by GE Healthcare (NM/CT 870 CZT DIGITAL SPECT/CT). Several clinical studies using this device have been reported, covering different aspects including the reduced radiation burden due to higher sensitivity, verification of dual-radionuclide imaging, and short time acquisition using Tc-99m and I-123 in myocardial blood flow tests [13]. Spectrum Dynamics (Shanghai, China) and GE Healthcare presented a different approach with their Veriton and StarGuide systems, respectively. While conventional SPECT devices have detector heads attached to a rotating gantry, and their tomography image acquisition is obtained by positioning the heads at different angles, the ring-shaped SPECT uses the same design as PET. The detectors are positioned in fixed positions (12 dedicated positions for both devices) around the ring, and the acquisition is obtained using these fixed positions.

5.3.1.3 Absolute Quantitation of SPECT Data

A major image-degrading process in SPECT is the scatter and resultant attenuation of photons as they traverse through the tissue before they reach the detector. Reliable attenuation and scatter compensation (ASC) is a pre-requisite for quantification tasks, such as quantifying biomarkers from SPECT images or performing SPECT-based dosimetry. Methods for absolute quantitation of SPECT images provide an estimate of the

activity uptakes in various organs and tissues in units of mBq or mCi/mL. Clinically valid semi-quantitative measure is the standard uptake value (SUV), also known as standardized uptake value or the dose uptake ratio (DUR). As the name suggests, it is a mathematically derived ratio of tissue radioactivity concentration at a point in time $C(T)$ and the injected dose of radioactivity per kilogram of the patient's body weight [14]. Because SPECT images generally are hampered by several physical and camera-specific effects, accurate and precise compensation methods are required. The most important effects such as photon attenuation in the patient, contribution of events from photons scattered in the patient and the collimator but accepted by the energy window, the effect of the collimator response function that degrades the image quality because of the relatively poor spatial resolution. All these effects can reduce the accuracy and precision in the activity concentration estimate. In addition to these compensation methods, a careful and consistent calibration is needed to translate counts in the image that corresponds to a location in the patent to activity, or activity concentration [3]. Based on xSPECT Quant™ technology and Symbia Intevo SPECT CT (Siemens Healthineers), the potential utility of quantitative SPECT was evaluated by the determination of standard uptake values (SUV_{max} and SUV_{mean}) with several SPECT radiopharmaceuticals [15]. While the results do show some clinical value, absolute quantitation in SPECT is still work in progress. In combination with iterative reconstruction methods with proper modeling of photon attenuation, scatter and collimator resolution degradation, SPECT/CT systems will be very useful for studies requiring patient-specific dosimetry or dose planning and longitudinal studies, especially when longer half-life radionuclides such as ^{89}Zr may not be ideal to develop targeted radiopharmaceuticals for PET.

5.3.2   PET Scanners

PET scanners were designed to obtain in vivo images of the distribution and uptake of radio-tracers on the basis of β^+ emitting radionuclides, and the ability to detect, and localize the positron-emitting nuclei by using coincidence counting to capture the paired annihilation of high-energy photons (511 keV) emitted following positron annihilation with an electron. The sensitivity of PET is the ability to detect low molecular mass of the radiopharmaceutical, which depends on the ability of the radiochemistry to produce labeled compounds with high specific activity (GBq or mCi/μmol). The power of the technique lies in the availability of more PET radionuclides than SPECT radionuclides and the wide range of available radiotracers that produce image contrast directly related to underlying physiology, metabolic pathways, or molecular targets. Using today's advanced PET scanners, radiotracers can readily be detected at trace mass levels (nanomolar concentrations or less) and using a dynamic sequence of images and the principles of tracer kinetic modeling, parameters related to the transport, metabolism, or binding of the tracer can be quantitatively derived [16].

One of the first positron imaging devices, the *positron camera* was developed in 1969 by Dr. Brownell and his team at Massachusetts General Hospital (MGH) in Boston [17]. That device consisted of only two planar arrays of crystals. Over the course of the last 50 years, coincidence detection of positron-emitting radionuclides has evolved from single pairs of detectors for planar imaging to current PET scanners with arrays of detector elements covering typically 25 cm or more, in axial length that contain on the order of 35,000 individual detector elements. Currently, the first total-body PET scanner, the EXPLORER, is which is 2 m in axial length and contains 560,000 individual detector elements [18, 19]. Developments have centered on improvements in the scintillator crystal and photodetector combination, the acquisition electronics and advances in data processing, reconstruction, and image analysis. Moreover, the introduction of digital PET offers the possibility to reduce radiation dose and scan times which may facilitate the implementation of PET to address unmet clinical needs [20]. In the last two decades, PET was successfully integrated, in 2000, with CT and subse-

quently with MRI, to create powerful hybrid-imaging systems that can interrogate structure, and function in the same imaging examination.

A typical PET scanner consists of many rings of scintillation detectors which surround the subject. The PET scanner uses the *annihilation coincidence detection* (ACD) method to obtain projection images of the radiotracer distribution. The images are first corrected for attenuation, scatter, etc., and then mathematically processed, as in the case of CT and SPECT, to obtain transverse images of several slices of the body in a given field of view (FOV). A number of reviews have been published, describing the historical development of the PET technology [16, 19–22].

5.3.2.1 Positron Annihilation and Coincidence Detection

A positron ejected by a radionuclide travels a very short distance in a tissue, dissipating its kinetic energy in collisions with electrons, and finally combines with an electron to form a positronium, a state which lasts for a very short time (10^{-10} s). The subsequent positron–electron annihilation results in the emission of two 511-keV photons, 180° apart. A PET scanner is designed to detect this pair of annihilation photons almost simultaneously on the basis of a process known as ACD, which establishes the trajectories of detected photons or lines of response (LOR). ACD only establishes the location of an annihilation event within the LOR; the exact location of a positron-emitting radionuclide, however, is determined mostly using the CT techniques, based on mathematical processing of millions of LOR to generate a computed tomogram of the PET tracer distribution. In a different approach, known as *time-of-flight* (TOF) method, measuring the difference in arrival time of the two annihilation photons at the opposite detectors helps to determine the exact location d of the annihilation event along the LOR.

Positron Range and Noncolinearity

Determining the exact LOR along which a positron-emitting radionuclide can be found is one of the major factors that determine the spatial resolution of a PET scanner. *Positron range* and *noncolinearity* are two effects that may lead to errors in determining the LOR.

Positron-emitting radionuclides differ in the kinetic energy of the emitted positrons. For example, the energy of positrons emitted by ^{18}F ($E_{max} = 0.63$ MeV) is almost one-fifth that of a positron emitted by ^{62}Cu ($E_{max} = 2.93$ MeV). The positron range (is similar to the beta particle range in tissue) is the direct distance traveled by the positron from the decaying atom to the exact location of the annihilation event. The positron range is a function of the kinetic energy of the positron (Fig. 5.6). The mean positron range may vary from a fraction of a millimeter to 4–6 mm, depending on the radionuclide. The error due to the positron range may be significant and, therefore, this range limits the ultimate resolution attainable by PET. It is very important to appreciate the fact that the SPECT technique inherently offers no limitation in spatial resolution due to photon energy, while the PET technique has a theoretical limit in terms of spatial resolution.

In contrast to the positron range, noncolinearity is independent of the positron-emitting radionuclide. The positron and electron are not exactly at rest when the annihilation occurs. As a result, the two annihilation photons differ in their momentum and are not emitted exactly at 180°
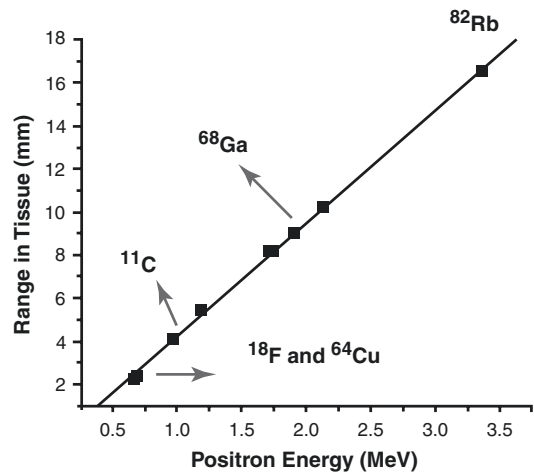
Fig. 5.6 The positron range in tissue as a function of positron energy

apart (they may be emitted with a distribution of angles around 180° (typically ±0.25°)). For a given PET scanner with diameter *D*, this blurring effect, due to noncolinearity (Δ_{nc}), can be estimated as follows:

$$\Delta_{nc} = 0.0022 \times D \,(\text{in mm}) \qquad (5.8)$$

With most clinical PET/scanners that have a ring diameter of ~80 cm, the blurring due to a noncolinearity error may be 1.76 mm. However, in MicroPET, this effect is somewhat less significant.

Coincidence Event Types

A *true coincidence* is the simultaneous interaction of a pair of photons (511 keV) resulting from the annihilation of a positron-electron pair (Fig. 5.7). A *random coincidence* occurs when two 511-keV photons from separate annihilation events, that occurred as a result of the decay of different atoms, strike the opposite detectors, simultaneously. In the tissue, the 511-keV photons undergo scatter and lose some energy. A *scatter coincidence* occurs when one or both of the 511-keV photons from a single annihilation event are scattered but, simultaneously detected, by the opposite detectors. The total number of events (true, random, and scatter) detected by the coincidence circuit in a PET scanner is referred to as *prompt coincidences*. Also, when 511-keV

photons or the scattered photons are detected, they are referred to as "singles." Since photons travel at the speed of light (30 cm ns^{-1}), the detection times of a pair of photons by the coincidence circuit can be between 2 and 3 ns. Typically, a coincidence timing window (τ) of 6–12 ns is used to account for statistical fluctuations in timing the detection events.

5.3.2.2 Pet Scanner Design

Since the early 1970s, several different PET detector configurations have been developed. In most dedicated PET scanners, pixilated or multi-crystal detectors are arranged in rings or polygonal arrays completely encircling the patient. In addition, two or three planar large-area detectors (as in Anger camera) are also used to configure the PET scanner. The majority of current clinical PET and MicroPET scanners, however, are based on the full-ring configuration (Fig. 5.8). Scintillation crystals coupled to PMTs are used as detectors. Compared to full-ring detectors, the efficiency of other detector configurations for coincidence detection is significantly poor (<30%). A PET scanner typically consists of several components:

- Detector consisting of a scintillator coupled to PMTs
- Collimator
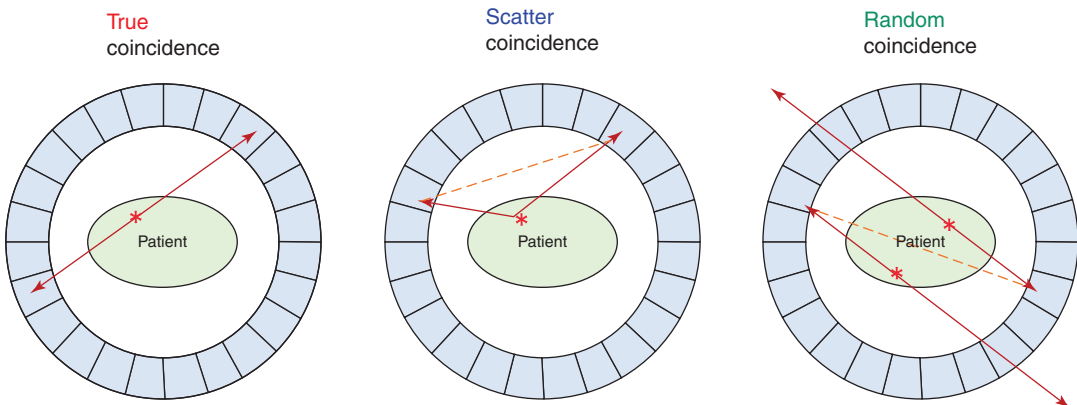
Fig. 5.7 In a PET scanner, the 511 keV photons from the patients are detected by coincidence counting. True counts are due to one annihilation and the photon path is straight in opposite directions. In random coincidence, photons from different annihilations will be detected, simultaneously. Scatter counts represent detection of scatter photons, simultaneously

Fig. 5.8 The typical PET scanner with ring detector configuration

- Signal processing electronics
- Coincidence circuit
- Data acquisition computer
- Reconstruction, display, and image analysis systems

The basic principles of a PET detector and collimation are discussed below. The electronics associated with the signal processing and the computer hardware needed for data acquisition,

image processing, etc. are highly technical, and are discussed in detail in many other publications [21, 23, 24].

PET Detector Crystals

There are several ways in which the choice of PET scintillating detector material affects image quality [5]. The denser the material, the higher its photoelectric fraction, or its ability to stop the incoming 511-keV radiation completely on the

first interaction. Also, high luminosity or light yield (expressed as the number of light photons emitted for each MeV of energy absorbed) is desirable for signal-to-noise considerations. Finally, the speed at which a detector emits light after absorbing a 511-keV γ-ray is directly proportional to its count rate capability, which is important in 3D acquisitions. The decay time is defined as the time needed for the detector's light output pulse to decrease to 36.7% of its maximum-amplitude value and a low decay time is virtually essential for TOF imaging. Table 5.2 shows the characteristics of several PET scintillator materials, such as BGO, LSO, and LYSO. Most commercial PET scanners use detectors, typically 18- to 25-mm-thick crystals of LYSO or BGO scintillators that result in detection efficiencies of 80–90%, and time-of-flight capabilities of ~400 ps or better with lutetium-based scintillators [16].

Block Detector

In early PET scanners, each scintillation crystal was coupled to a single PMT and the size of the crystal largely determined the spatial resolution of the PET scanner. Smaller crystals were needed to improve the resolution. Since the size of PMT is relatively large, it was difficult to couple one PMT for each of the small crystals. In the 1980s, a multicrystal, two-dimensional BGO *block detector* system was developed [21]. The majority of dedicated clinical PET scanners in use today are based on the block detector design. A schematic of the block detector is shown in Fig. 5.9.

A block of scintillation detectors is made by segmenting (cutting or channeling) a relatively large block of crystal. The size of the individual elements in a matrix (block) PET detector ranges from $4 \times 4 \times 20$ mm^3 of LSO to $6.3 \times 6.3 \times 30$ mm^3 of BGO [5]. The channels are filled with a light-reflective material to prevent conduction of light from each crystal element to the next in the block. The scintillator block is then coupled to four PMTs and requires a high voltage (1600–1800 V) supply. Most PET scanners consist of 144–288 block detectors and contain 10,000–20,000 detector elements. With block detectors, Anger logic must be employed to estimate the location of the photon's original impact, limiting further improvement of spatial resolution in PET imaging. Although this still allows for high spatial resolution of 4–5 mm at the center of the field of view (FOV), great improvements have been achieved in the way detectors interface with the scanner's front-end electronics [5].
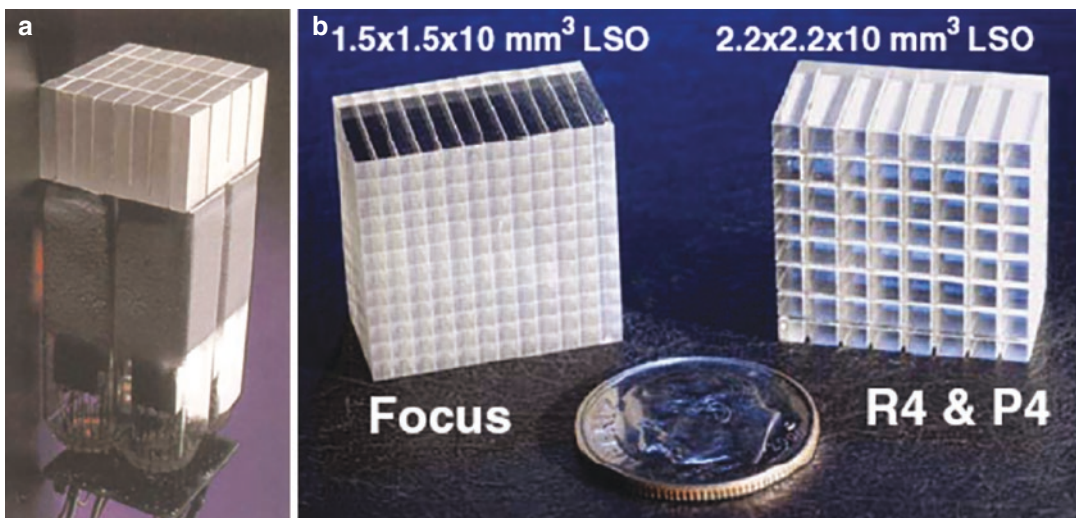
Fig. 5.9 The "block" detector (**a**), and Crystal arrays (**b**) used in the construction of MicroPET scanners [25]

Digital PET

Recent PET scanner designs feature smaller silicon digital photomultipliers (SiPM) or avalanche photodiodes [26]. The introduction of SiPMs as an alternative to standard PMTs used in analog PET scanners with block detectors. SiPMs, the basis for the so-called digital PET/CT systems, are smaller than standard PMTs (enabling higher spatial resolution) and provide up to 100% coverage of the crystal area, as well as high sensitivity, low noise, and fast timing resolution. Also, SiPMs in combination with optimized acquisition and reconstruction parameters improve the localization of the annihilation events, provide high-definition PET images, and offer higher sensitivity, and higher diagnostic performance [20]. This novel technology is actually used in different PET devices manufactured by different vendors, including Philips Healthcare (Vereos PET/CT), GE Healthcare (Discovery MI PET/CT), and Siemens Healthineers (Biograph Vision PET/CT system). The design of the digital system of different vendors, however, may have variations in the number of detector modules and the size of crystals. In principle, since each scintillation crystal is coupled to a single SiPM (1:1 coupling), there is an enhancement of the TOF and a reduction of the dead time, as well as an improvement in spatial, and timing resolution. Based on many clinical studies, it was concluded that Digital PET opens new perspectives in the quantification and characterization of small lesions, which are mostly undetectable using analog PET systems, potentially changing patient management, and improving outcomes in oncological, and nononcological diseases [20].

5.3.2.3 PET Data Acquisition

In order to obtain PET images of a radiotracer distribution, the data acquisition involves obtaining two different scans; a transmission and emission scan, while the patient is in the scanner. In addition, two other scans, called *blank scan* and *normalization scan*, are necessary to process, and reformat the PET projection data into a quantitative PET scan, with multiple slices.

Attenuation Correction Based on CT

Attenuation correction (AC) for the 511 keV photons originating from different parts of the body has been used in PET imaging ever since the introduction of the first PET scanners but, was originally based on radionuclide transmission rod sources circling around the patient to collect photon attenuation maps. With older PET scanners and several MicroPET devices, a transmission scan is first obtained by using external rod sources of radiation. The most common rod source is based on long-lived ^{68}Ge ($T_{1/2} = 270$ days), which decays by EC to ^{68}Ga, which in turn, decays by positron emission.

With the current PET/CT scanners, the most common method for attenuation correction is based on the CT scan. The maximum number of detector rows for the CT scanner component of a PET/CT is 128 although a CT scanner of 16 detector rows may be adequate for most clinical studies. A nondiagnostic CT scan can be used as a transmission scan. Since the CT scan is based on lower energy (~60-keV) X-ray photons, the CT scan can be performed either before or after the administration of a PET radiotracer. In addition, a CT scan for attenuation correction takes only 0.5–2 min.

A blank scan (with no object in the FOV) must be completely noise free and is generally performed for 1 h or, at least 10 times the duration for which the emission scan is obtained. The blank scan is obtained using a rod source or CT scan depending on the technique used for the attenuation correction (Fig. 5.10).

2D vs. 3D PET

There are two kinds of collimation used in PET: one to direct the photons to the detector and the other to select the detected events. Thick lead rings are used to define the external axial FOV, while thin lead or tungsten rings (1–5 mm thick) (usually referred to as septa) are employed to define the individual imaging planes. These septa can be positioned to define the slices during 2D PET studies, but can be retracted during 3D PET acquisition, to increase sensitivity.
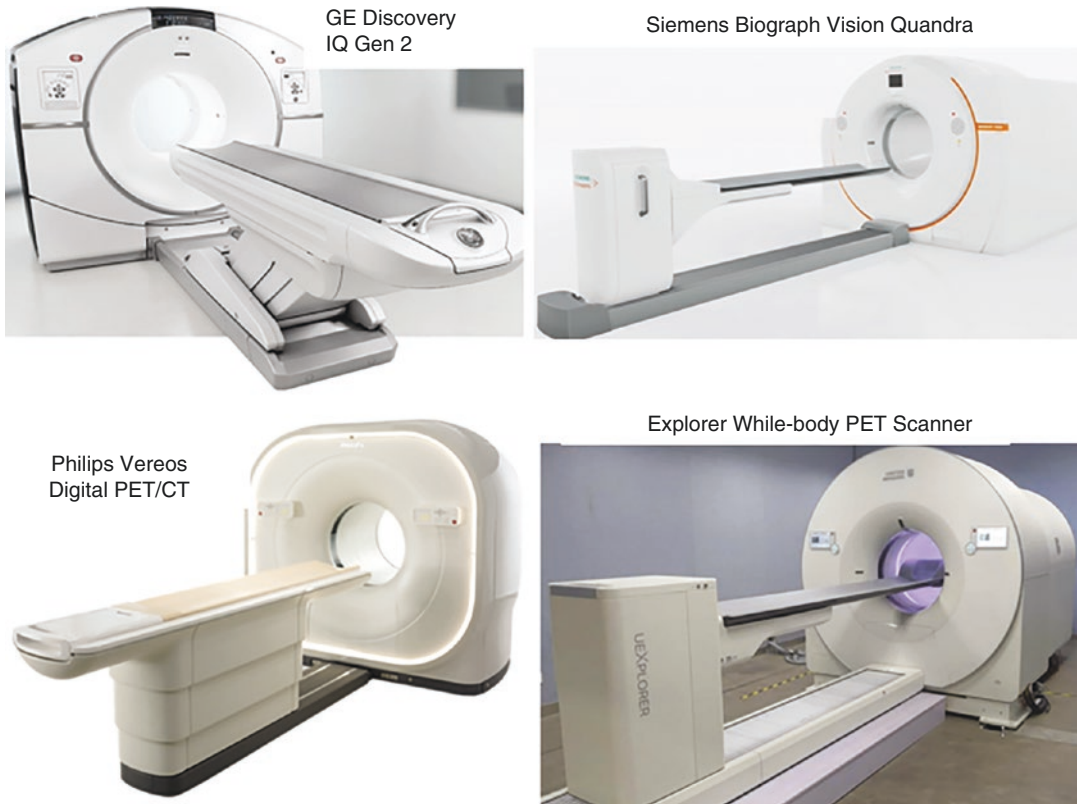
Fig. 5.10 PET/CT scanners: GE Discovery IQ Gen 2 is the next generation of our high-performance PET/CT system with faster scan times, with Motion-Free image clarity. Siemens Biograph Vision Quandra has a large axial PET field of view. To cover dynamically from vertex to thighs, Philips Vereos is the world's first and only fully digital, clinically proven, PET/CT scanner. The Explorer whole body PET scanner was developed by UC Davis scientists and approved by the FDA

The electronic circuit of ACD provides the *electronic collimation* by selecting only those counts that are simultaneously detected by the opposite detectors, during the coincidence timing window. Typically, electronic collimation selects only 1% of the singles as prompt events for further processing, while the remaining 99% are rejected. The use of newer detector materials with digital technology and techniques has allowed all modern PET and PET/CT systems to operate in 3D mode, with substantial improvements in photon sensitivity, compared with 2D PET. Therefore, a recent trend in PET imaging is 3D mode operation, without the interplane septa, which results in improved photon sensitivity by a factor of 4–6, as compared with the 2D mode [5].

PET Imaging Modes

Following the administration of a PET radiotracer into a subject, imaging can be performed in three different modes.

A *dynamic emission scan* is used to obtain PET images in order to study the time–activity distribution of a radiotracer in a specific tissue or organ of interest. Dynamic scans are performed using a series of imaging frames, which get longer as the study progresses. Measurement of blood flow and receptor imaging studies are often performed using dynamic scans. These studies, however, may require arterial or venous sampling to provide an *input function* to estimate quantitative parameters, based on pharmacokinetic modeling of radiotracer distribution.

A *static emission scan* is normally obtained only when the radiotracer distribution is fairly stable or reaches an equilibrium state. The static scan is acquired in a single frame and it is assumed that the tracer concentration in a given tissue is constant, except for the physical decay. Most PET scans are performed 1–2 h post-administration of the dose. *Whole-body emission scan* represents a series of static scans performed at different segments or portions of the whole body. The studies are performed in several bed positions by acquiring a static scan for a specific time and then moving the patient (the bed) by a distance that is less than the axial FOV. Most clinical PET scanners have a FOV of 15–20 cm. Typically, five to seven bed positions, each requiring 3–5 min, will complete a whole-body emission scan from head to midthighs in 15–35 min. The data collected at each bed position are subsequently reconstructed into a whole-body volume and can be reoriented into *transaxial*, *coronal*, and *sagittal* views.

Continuous bed motion (CBM) PET/CT scanner has been introduced by Siemens. Unlike the conventional scanning coverage where a technologist has to decide if an additional bed is needed or not, the CBM allows for a flexible selection of the start and finish locations for each body region in the PET scan coverage. It also allows a variable motion speed and consequently the collection of optimal photon counts for each region of the body, to optimize local sensitivity.

PET Scan Reconstruction Techniques

Most current PET/CT systems employ a fully 3D iterative PET reconstruction, which allows the incorporation of CT attenuation maps as well as corrections for scatter, random events, spatial system response, and dead time. An accelerated type of iterative reconstruction, 3D ordered subset expectation maximization, can be implemented on all systems to reduce reconstruction time. Despite such implementation, 3D iterative reconstruction can still pose significant limitations with respect to processing speed in standard workstations, particularly for cardiac PET imaging using dynamic and gated protocols. More detailed discussion on PET image data correction and PET image reconstruction is beyond the scope of this chapter.

5.3.3 Small-Animal Imaging Systems

Clinical imaging systems have relatively coarse spatial resolution that is insufficient for imaging structures in small animals, which requires high spatial resolution (on the order of 1–2 mm or better). To achieve this, scanners must use higher resolution detectors and achieve finer spatial sampling (e.g., using smaller detector elements) while maintaining as high a sensitivity as possible [27–30]. Molecular imaging can be obtained by imaging techniques such as optical imaging, nuclear imaging, magnetic resonance imaging (MRI), ultrasound imaging, and computed tomography (CT) (Table 5.1). Molecular imaging techniques such as PET and SPECT provide the 3D distribution of radiopharmaceuticals and have excellent sensitivity and high resolution with excellent tissue penetration depth as shown in Table 5.3.

Table 5.3 Small imaging techniques for drug discovery and development

Technique	Resolution	Depth	Sensitivity
	mm		Moles of label detected
CT	0.05	No limit	10^{-6}–10^{-3}
Ultrasound	0.05	mm	10^{-8}–10^{-6}
MRI	0.01–0.10	No limit	10^{-9}–10^{-6}
Optical	1.0	<10 cm	10^{-12}–10^{-11}
SPECT	1–2	No limit	10^{-14}–10^{-10}
PET	1–2	No limit	10^{-15}–10^{-12}

Table modified from Jang [28]

In the late 1990s, several groups began making significant progress in the development of high-resolution small-animal PET and SPECT scanners for the study of molecular imaging techniques in several rodent disease models [31–33]. For both clinical and animal scanners, for a given size of the detector and field of view (FOV), there is a tradeoff between the resolution and the sensitivity. For example, MicroPET scanners typically have at least 10 times greater sensitivity than the microSPECT scanners. Some of the commercial animal scanners are listed in Table 5.4. Among the existing imaging modalities PET and SPECT are particularly suited for molecular imaging because there are hundreds of potential molecular imaging targets and a variety of radiolabeled probes have been developed and are currently under development. While conventional imaging yields anatomical maps or a rendering of physiologic functions, molecular imaging provides additional information on the distribution and (in some cases) amount or activity of specific molecular markers in vivo and will, thus, expand the emphasis of radiological imaging beyond the anatomical and functional level, to a molecular one.

The first animal PET tomographs designed for imaging nonhuman subjects were the SHR-2000 developed by Hamamatsu (Japan) and the ECAT-713 developed by CTI PET Systems Inc. (Knoxville, TN). The first PET system developed specifically for rodent imaging was the RATPET scanner developed by Hammersmith Hospital in collaboration with CTI PET Systems Inc. The measured spatial resolution of this scanner was found to be 2.4 mm transaxially by 4.6 mm axially, giving a volumetric resolution of 0.026 cm^3. The 3D data acquisition of that system and the high detector efficiency provided a relatively high absolute sensitivity of 4.3%. Based on the UCLA MicroPET system, Concorde Microsystems Inc. introduced the commercial MicroPET systems for primates (P4) and rodents

(R4) based on a new generation of electronics designed to take full advantage of the fast decay time of the LSO detector. Since then, several other scintillator/PMT-based animal PET systems have been introduced. The Inveon, the last design of the MicroPET series, is a trimodality platform offering the largest axial extension (127 mm), up to threefold higher sensitivity (6.27%) in comparison to its predecessors There has been a significant improvement in the design of microSPECT systems for small-animal imaging studies. Because in microSPECT devices the required FOV is very small, it is possible to achieve a much higher resolution than with clinical SPECT scanners. A number of commercial systems are now available with a spatial resolution <2 mm. Some of these devices even report submillimeter resolution for specific organs and tissues that may accumulate significant amounts of radioactivity. For most of the animal SPECT scanners, the detection efficiency for high-energy photons (<200 keV) is <0.1%. As a result, it is necessary to inject radiotracers at dose levels that are hundreds of times more than the clinical doses. Many of these devices are based on a wide variety of detection instrumentation, including conventional scintillation cameras, pixelated detectors with PSPMTs or APDs, and semiconductor gamma cameras.

5.3.3.1 State-of-the-Art Preclinical PET Scanners

The remarkable improvements in system designs and overall performance introduced by the different vendors resulted in the current generation preclinical PET scanners surpassing the previous generations in many aspects. Today, high-end state-of-the-art technologies approach submillimeter spatial resolution, breaking a barrier that could open the door to more specific applications and more accurate quantification by eliminating the partial volume issue [27]. A brief summary of different commercial scanners is shown in Table 5.4 and Fig. 5.11.

Table 5.4 MicroPET scanner design characteristics and resolution

Scanner	Manufacturer	Scintillator	Crystal dimensions	Electronic	Radial FWHM (mm)	Volumetric resolution (mm^3)
MicroPET Focus 220	Siemens	LSO (12 × 12)	1.51 × 1.51 × 10	PSPMT	1.75 at 5 mm	5.35 at 5 mm
Inveon-DPET	Siemens	LSO (20 × 20)	1.51 × 1.51 × 10	PSPMT	1.63 at 5 mm	6.33 at 5 mm
Albira 3 rings	Bruker	LYSO	50 × 50 × 10	MAPMT	1.45 at center	5.55 at center
Albira	Brucker	Lyso	50 × 50 × 10	SiPMs	0.89 at center	<1 in the w-FOV
Vector	MILabs	NaI(Tl)	590 × 470 × 9.5	NA	0.6 at center	0.216 at center
PETbox4	UCLA	BGO	1.82 × 1.82.7	PSPMT	1.32 at center	3.4 at center
GNEXT	Sofie Biosciences	LYSO/BGO (8 × 8)/ (8 × 8)	1.01 × 1.01 × 61 1.01 × 1.55 × 8.9	NA	<1 at 5 mm	<1 at 5 mm
β-cubes	Molecules	LYSO	25 × 25 × 8	NA	1.06 at center	~1.0
Trans PET/CT X5	Raycan	LYSO (13 × 13)	1.9 × 1.9 × 13	NA	2.11 at center	5.71 at center
Nanoscan PET/CT	Mediso	LYSO (39 × 81)	1.12 × 1.12 × 13	PSPMT	1.03 at center	1.19 at center
IRIS	InviScan SAS	LYSO 27 × 26	1.6 × 1.6 × 12	NA	1.05 at 5 mm	1.38 at 5 mm

Siemens Inveon
PET/SPECT/CT

Brucker Albira SI
PET/SPECT/CT

Molecules
β cube PET
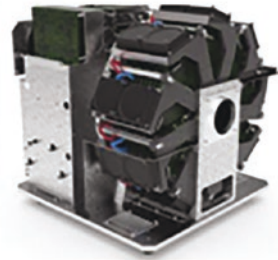
MILabs U-SPECT

MILabs U-PET

Mediso MultiScan™
LFER150 PET/CT

Ravcan Trans
PET/CT X5

Sofie GNexrPET/CT

Inviscan IRIS XL PET/CT

Fig. 5.11 Commercial PET, SPECT, and CT scanners for molecular imaging studies in small animals

References

1. Darambara DG, Todd-Pokropek A. Solid state detectors in nuclear medicine. Q J Nucl Med. 2002;46:3–7.
2. Ljungberg M, Pretorius H. SPECT/CT: an update on technological developments and clinical applications. Br J Radiol. 2018;90:20160402.
3. Ljungberg M. Absolute quantitation of SPECT studies. Semin Nucl Med. 2018;48:348–58.
4. Schillasi O, Orbano N. Digital PET/CT: a new intriguing for clinical nuclear medicine and personalized molecular imaging. Eur J Nucl Med Mol Imaging. 2019;46:1222–5.
5. Slomka PJ, Pan T, Germano G. Recent advances and future progress in PET instrumentation. Semin Nucl Med. 2016;46:5–19.
6. van der Meulen NP, Strobel K, Lima TVM. New radionuclides and technological advances in SPECT and PET scanners. Cancers. 2021;13:6183–98.
7. Anger HO. Scintillation camera. Rev Sci Instrum. 1958;29:27–33.
8. Erlandsson K, Kacperski K, van Gramberg D, Hutton BF. Performance evaluation of D-SPECT: a novel

SPECT system for nuclear cardiology. Phys Med Biol. 2009;54:2635–49. 6.

9. Gambhir SS, Berman DS, Ziffer J, et al. A novel high-sensitivity rapid-acquisition single-photon cardiac imaging camera. J Nucl Med. 2009;50:635–43.

10. Del Sordo S, Abbene L, Caroli E, et al. Progress in the development of CdTe and CdZnTe semiconductor radiation detectors for astrophysical and medical applications. Sensors. 2009;9:3491–526.

11. Ito T, Matsusaka Y, Onoguchi M, et al. Experimental evaluation of the GE NM/CT 870 CZT clinical SPECT system equipped with WEHR and MEHRS collimator. J Appl Clin Med Phys. 2021;22:165–77.

12. Ben-Haim S, Kennedy J, Keidar Z. Novel cadmium zinc telluride devices for myocardial perfusion imaging—Technological aspects and clinical applications. Semin Nucl Med. 2016;46:273–85.

13. Yamada Y, Nakano S, Gatate Y, et al. Feasibility of simultaneous ^{99m}Tc-tetrofosmin and ^{123}I-BMIPP dual-tracer imaging with cadmium-zinc-telluride detectors in patients undergoing primary coronary intervention for acute myocardial infarction. J Nucl Cardiol. 2021;28:187–95.

14. Weiss GJ, Korn RL. Interpretation of PET scans: do not take SUVs at face value. J Thorac Oncol. 2012;7:1744–6.

15. Lew C. Evaluating SPECT/CT quantification in clinical practice. Nuclear Medicine News & Stories. 2019. Siemens.com/NMNS.

16. Berg E, Cherry SR. Innovations in instrumentation for positron emission tomography. Semin Nucl Med. 2018;48:311–31.

17. Burnham CA, Brownell GL. A multi-crystal positron camera. IEEE Trans Nucl Sci. 1972;19(3):201–5.

18. Cherry SR, Badawi RD, Karp JS, et al. Total-body imaging: transforming the role of positron emission tomography. Sci Transl Med. 2017;9(381):eaaf6169.

19. Jones T, Townsend D. History and future technical innovation in positron emission tomography. J Med Imaging. 2017;4(1):011013, 1–17.

20. Lopez-Mora DA, Carri I, Flotats A, et al. Digital PET vs analog PET: clinical implications? Semin Nucl Med. 2022;52:302–11.

21. Nutt R. The history of positron emission tomography. Mol Imaging Biol. 2002;4(1):11–26.

22. Vandenberghe S, Moskal P, Karp JS. State of the art in total body PET. EJNMMI Phys. 2020;7:35.

23. Seo Y, Mari C, Hasegawa B. Technological development and advances in single-photon emission computed tomography/computed tomography. Semin Nucl Med. 2008;38:177–98.

24. Townsend DW. Positron emission tomography/computed tomography. Semin Nucl Med. 2008;38:152–66.

25. Levin CS. Primer on molecular imaging technology. Eur J Nucl Med Mol Imaging. 2005;32(suppl 2) S325–S345

26. van Dam HT, Seifert S, Schaart DR. The statistical distribution of the number of counted scintillation photons in digital silicon photomultipliers: model and validation. Phys Med Biol. 2012;57(15):4885.

27. Amirrashedia M, Zaidic H, Ay MR. Advances in preclinical PET instrumentation. PET Clin. 2020;15:403–26.

28. Jang B-S. MicroSPECT and MicroPET imaging of small animals for drug development. Toxicol Res. 2013;29(1):1–6.

29. Massoud TF, Gambhir SS. Integrating noninvasive molecular imaging into molecular medicine: an evolving paradigm. Trends Mol Med. 2007;13:183–91.

30. Vanderheyden JL. The use of imaging in preclinical drug development. Q J Nucl Med Mol Imaging. 2009;53:374–81.

31. Beekman FJ, van der Have F, Vastenhouw B, et al. U-SPECT-I: a novel system for submillimeter-resolution tomography with radiolabelled molecules in mice. J Nucl Med. 2005;46:1194–200.

32. Chatziioannou AF. PET scanners dedicated to molecular imaging of small animal models. Mol Imaging Biol. 2002;4(1):47–63.

33. Cherry SR. In vivo molecular and genomic imaging: new challenges for imaging physics. Phys Med Biol. 2004;49:R13–48.

Chemistry: Basic Principles

6

The internal machinery of life, the chemistry of parts is something beautiful. And it turns out that all life is interconnected with all other life.
(Richards Feynman)

6.1 Chemical Elements

In general, chemistry is the study of matter and energy, and the interaction between them. More specifically, chemistry is the study of matter, including its composition, properties, structure, the changes which matter undergoes, and the laws governing those changes. Chemical elements are the building blocks of all types of matter in the universe and, at present, 118 elements are known to exist. In nature, however, 94 elements have been discovered. Some elements are only present in trace amounts while some are manmade or artificially produced. From the point of view of chemistry, the smallest unit of an element is the atom, representing the chemical identity of that element. Among the elements that exist in nature, hydrogen is the lightest ($Z = 1$, $A = 1$) atom, while uranium is the heaviest atom ($Z = 92$, $A = 238$).

Chemical reactions take place between atoms of the same element or atoms of different elements to form molecules of compounds. Chemical interactions involve only the electrons in the outer orbits, while protons and neutrons of an atom do not participate in any chemical reac-

tions. The chemical properties of an element are determined only by the number of electrons in an atom, which is equal to the number of protons in the nucleus (Z).

6.1.1 Chemistry and Radioactivity

Radioactivity is a process which primarily involves the decay of the unstable nucleus of an element but, all the chemical reactions of an element involve the outermost orbital electrons. Atoms of different isotopes of an element, both stable and radioactive, will have a similar chemistry, regardless of the radioactive emissions from an unstable nucleus. Similarly, the chemistry of an atom does not, in any way, affect the radioactive decay characteristics of an atom. In nuclear medicine, *tracer principle* is based on the fact that the chemistry and physiological behavior of radioisotopes of an element is identical to the corresponding naturally occurring stable isotopes of that element. Because the mass of different isotopes of an element is slightly different, there may be some differences in the chemistry among the isotopes of an element. This effect known as *isotope effect* is only significant if the mass difference is substantial, as in the case of hydrogen isotopes, where the mass difference of the three isotopes is 200–300%. In contrast, the isotopes of iodine have only about 3% difference in their mass.

6.1.2   Periodic Table

The periodic table (Fig. 3.3) is a listing of the elements in the order of increasing atomic number (*Z*). More specifically, elements with similar chemical properties are aligned vertically in columns (called *groups* or *families*). It must be noted that in the modern periodic table, this order is based only on the atomic number and not the atomic weight. The horizontal series of elements are referred to as periods; the first two periods are short periods and consist of eight groups, while the remaining periods are called long periods, consisting of 18 groups. The position of an element in the periodic table explains the general chemical behavior of an element.

Most of the elements found in nature are metals and are shown in the periodic table as *alkali metals* (Group-1), *alkaline earth metals* (Group-2), and *transition metals* including lanthanides and actinides (Groups 3–12). Elements in groups 13–16 are regarded as metals or *metalloids*; elements in Group 17 are known as *halogens*; and elements in Group 18 are known as inert or *noble gases*. Some of the important elements and their radioisotopes, useful for PET and SPECT, are listed in Table 6.1.

6.1.2.1 Electronic Structure of Atom

The atom consists of an extremely dense, small, positively charged nucleus surrounded by a cloud of electrons with small size and mass, each carrying a single negative charge equal but opposite to that of a proton in the nucleus. Because the number of electrons and protons in an atom is the same, the whole atom is electrically neutral. The

Table 6.1   Important elements and their useful radioisotopes for imaging and therapy

Element	Atomic number	Stable isotope	Natural abundance (%)	Useful radioisotopes	Decay mode
Carbon	6	^{12}C	98.9	^{11}C	β^+
		^{13}C	1.10	^{14}C	β^-
Nitrogen	7	^{14}N	99.634	^{13}N	β^+
		^{15}N	0.366		
Oxygen	8	^{16}O	99.762	^{15}O	β^+
		^{17}O	0.038		
		^{18}O	0.200		
Fluorine	9	^{19}F	100	^{18}F	β^+
Copper	29	^{63}Cu	69.17	^{62}Cu	β^+
		^{63}Cu	30.83	^{64}Cu	β^+, β^-, EC
				^{67}Cu	β^-, γ
Gallium	31	^{69}Ga	60.1	^{66}Ga	β^+, EC, γ
		^{69}Ga	39.9	^{67}Ga	EC, γ
				^{68}Ga	β^+, EC, γ
Rubidium	37	^{85}Rb	72.165	^{82}Rb	β^+
		^{87}Rb	27.845		
Yttrium	39	^{89}Y	100	^{86}Y	β^+, EC, γ
				^{90}Y	β^-
Technetium	43	–	–	^{94}Tc	β^+
				^{99m}Tc	IT, γ
Indium	49	^{113}In	4.3	^{111}In	EC, γ
		^{115}In	95.7		
Iodine	53	^{127}I	100	^{123}I	EC, γ
				^{124}I	β^+, EC, γ
				^{131}I	β^-, γ
Lutetium	71	^{175}Lu	97.0	^{177}Lu	β^-, γ
Radium	86	–	–	^{223}Ra	A
Actinium	89	–	–	^{225}Ac	A

atomic volume (10^{-8} cm diameter) with the cloud of electrons is significantly larger than the volume of the nucleus (10^{-13} cm diameter). According to Bohr's model of atom, an electron in a hydrogen atom rotates around the nucleus at high speeds in closed circular orbits associated with a characteristic quantum number. The electron, in general, exists in a low energy orbit (*ground state*). Gain or loss of a quantum of energy occurs only when an electron moves from one orbital to another of greater or lesser energy. As a result, an atom can absorb or emit energy in discrete units or quanta.

6.1.2.2 Quantum Model of Atom

At first, Bohr's model appeared to be very promising. By the mid-1920s, however, it had become apparent that this model needed refinement. The wave mechanics or quantum mechanics developed by Werner Heisenberg, Louis de Broglie, and Edwin Schrodinger finally provided a wave or quantum mechanical description of an atom. According to this model, the electron bound to the nucleus is similar to a standing or stationary wave. The circumference of a particular orbit corresponds to a whole number of wavelengths. Schrodinger's famous wave equation ($H\psi = E\psi$) describes an electron in an atom, where ψ, called the wave function, is a function of the coordinates (x, y, and z) of the electron's position, in three-dimensional space, and H represents a set of mathematical instructions, called an *operator*. When this equation is analyzed, many solutions are found. Each solution consists of a wave function ψ, that is characterized by a particular value of energy, E. A specific wave function for a given electron is often called an *orbital* (an orbital is not a Bohr's orbit). The wave function corresponding to the lowest energy of an hydrogen atom is called $1s$ orbital. The theory of quantum mechanics only provides the probable position of the electrons around the nucleus but, not the electrons motions around the nucleus.

Schrodinger's equation for the hydrogen atom or other multielectron atoms has many solutions with many wave functions or orbitals characterized by a set of quantum numbers. In order to describe a given electron in atom, a set of four quantum numbers are needed. The values and the physical meaning of these quantum numbers can be described as follows:

The *principal quantum number* (n), which can have integral values (such as 1, 2, 3, 4 …), is related to the size and energy of the orbital. As n increases, the orbital size and the energy increases. The value of n, or the shell number, is represented by K, L, M, N, … (old terminology).

The *angular momentum quantum number* (l) relates to the ellipticity of the orbital or the angular momentum of an electron in a given orbital. It can have integral values of 0 to $n - 1$, and for each value of n, the value of l determines the shape of the orbital (such as s, p, d, f, …). These orbitals are also called subshells.

The *magnetic quantum number* (m_e), which can have integral values between l, and $-l$ including 0. The value of m_e relates to the orientation in space of the angular momentum associated with the orbital.

The *electron spin quantum number* (m_s), which has values of $+\frac{1}{2}$ and $-\frac{1}{2}$. The value of m_s represents the direction of the electron spin.

Each electron in an atom has a unique set of quantum numbers. *In a given atom, no two electrons can have the same set of four quantum numbers (n, l, m_e, m_s). This is called the Pauli Exclusion Principle*, which can also be stated as follows: *An orbital can hold only two electrons and they must have opposite spins*.

The electrons in atoms other than hydrogen and helium also occupy various energy levels or shells. The maximum number of electrons that can occupy a given energy level or shell (n) is $2n^2$. For example, if $n = 2$, then the total number of electrons in the second shell (L) is eight. The number of orbitals (l) in second shell is two since l can have values of 0 (called s) and 1 (called p). These two orbitals in the second shell are called $2s$ and $2p$. Since the number of electrons in each orbital is $2(2l + 1)$, a $2s$ orbital can hold two electrons while a $2p$ orbital can have six electrons. Further, because m_e can have values between l, and $-l$ including 0, the $2p$ orbital has three orientations in space ($2px$, $2py$, $2pz$), and each one of them, in turn, can only hold a maximum of two electrons (since m_s has only two values $+\frac{1}{2}$ and

Table 6.2 Electron configuration of some of the elements

	K	L		M			N				O				P					
Element	1s	2s	2p	3s	3p	3d	4s	4p	4d	4f	5s	5p	5d	5f	6s	6p	6d	6f	7s	7p
H	1																			
He	2																			
Li	2	1																		
C	2	2	2																	
N	2	2	3																	
O	2	2	4																	
F	2	2	5																	
Ne	2	2	6																	
Na	2	2	6	1																
K	2	2	6	2	6		1													
Cu	2	2	6	2	6	10	1													
Ga	2	2	6	2	6		2	1												
Kr	2	2	6	2	6	10	2	6												
Rb	2	2	6	2	6	10	2	6			1									
Y	2	2	6	2	6	10	2	6	1		2									
Tc	2	2	6	2	6	10	2	6	5		2									
In	2	2	6	2	6	10	2	6	10		2	1								
I	2	2	6	2	6	10	2	6	10		2	5								
Xe	2	2	6	2	6	10	2	6	10		2	6								
Lu	2	2	6	2	6	10	2	6	10	14	2	6	1		2					
U	2	2	6	2	6	10	2	6	10	14	2	6	10	3	2	6	1		2	

½). The electron configuration in different energy levels and the possible quantum numbers are shown in Table 6.2.

6.1.2.3 Arrangement of Electrons in Orbitals

Since the chemical properties of an element are determined by the electrons, it is important to understand how these electrons are arranged in the orbitals (Fig. 6.1). According to the *Aufbau principle*, as protons are added one by one to the atomic orbitals to build elements, electrons are added one by one to the nucleus to build up the elements. In the ground state, the lowest energy orbitals contain the electrons. The high-energy orbitals, however, are filled only after the lower-energy orbitals are filled. The various orbitals arranged in order of increasing energy are as follows:

1s, 2s, 2p, 3s, 3p, 4s, 4p, 5p, 6s, 4f, 5d, 6p, 7s, 5f, 6d.

It is important to note that the 3d orbital is not filled until after the 4s is filled, the 4d until after the 5s, the 4f until after the 6s, and the 5d until the 4f orbital is filled. The series of elements in which the d orbital is being filled are called *transition metals*.

In a group of elements ($Z = 57–70$) known as *lanthanides* (elements that are also transition elements), each of the elements differs from the other element only in the number of electrons in the 4f orbital, while the 5s, 5p, and 6s orbital are completely filled. Similarly, in *actinides* ($Z = 89–102$), 5f electrons are being filled, while the 6s, 6p, and 7s orbitals are completely filled.

Pauli's exclusion principle requires that only two electrons with opposite spin occupy any given subshell. *Hund's rule* states that the lowest energy configuration for an atom is the one having the maximum number of unpaired electrons in a particular set of degenerate orbitals (orbitals with the same energy level), such as p, d, and f. The electron configuration of several elements, shown in Table 6.5, clearly illustrates Hund's rule.

Valence Electrons and Stable Octet

The electrons in the outermost principal quantum level of an atom are known as *valence* electrons and the shell is frequently referred to as *valence shell*. These electrons are the most important elements in
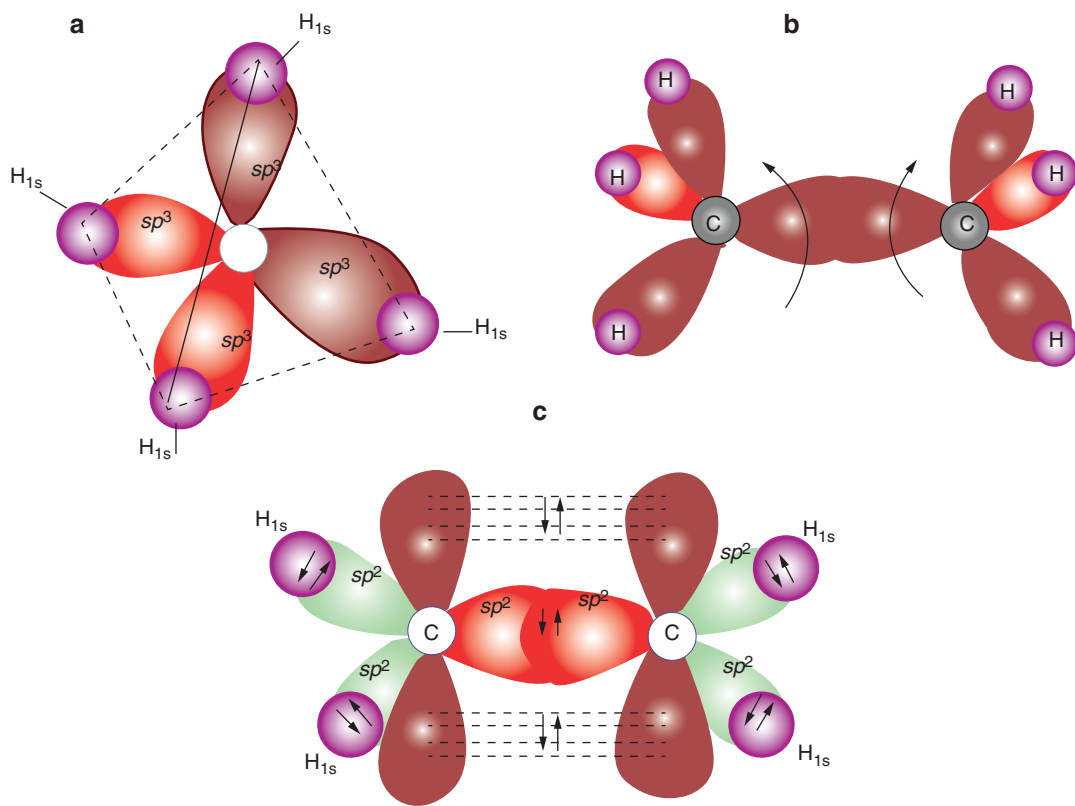
Fig. 6.1 The tetrahedral structure of methane (**a**) can be described in terms of carbon atom using a sp^3 hybrid set of orbitals to bond to the four hydrogen atoms. In case of acetylene, the carbon can be described as sp^2 hybridized (**c**), in which the C–C bond is formed by sharing an elec- tron pair between sp^2 orbitals, while the π bond is formed by sharing a pair of electrons between p orbitals. As a result, the free rotation of the two CH$_2$ group is prevented. However, with ethane (**b**) the free rotation of two CH$_3$ groups is possible

chemistry because they are involved in the formation of *chemical bonds*. The inner electrons are known as *core electrons* and generally do not participate in forming of chemical bonds. The elements listed in the same group of the periodic table (Chap. 3, Table 3.3) have the same electron configuration and, therefore, have similar chemical behavior.

The elements listed in Group-18 of the periodic table are known as noble or inert gases because they lack chemical reactivity; in general they form very few chemical compounds. The outer electron configuration for the inert gases (except for He) has eight electrons in the s and p orbitals. Based on this observation, the theory of chemical compound formation postulates that the stable electron configuration for the outer electron shell is eight electrons. More specifically, the *stable octet rule* postulates that compounds are formed between atoms of the same or different

elements as a result of the loss, gain, or sharing of electrons so that each atom attains a stable octet electron configuration.

The valency of an element is determined by the number of electrons in the outermost shell (Table 6.3) that can participate in a chemical reaction. For example, the valency of hydrogen and fluorine is 1, while the valency for nitrogen is 3 or 5, and 4 for carbon.

6.1.3 Chemical Bonding

John Dalton was probably the first to recognize that chemical compounds are a collection of atoms. Only in the twentieth century, however, was it realized that electrons participate in the bonding of one atom to another atom. The forces that hold the atoms together in compounds are called *chemical*

Table 6.3 Valence electrons of elements in the eight groups of the periodic table

	K	L			
	$1s$	$2s$	$2px$	$2py$	$2pz$
Element					
H	↑				
He	↑↓				
Li	↑↓	↑			
Be	↑↓	↑↓			
B	↑↓	↑↓	↑		
C	↑↓	↑↓	↑	↑	
N	↑↓	↑↓	↑	↑	↑
O	↑↓	↑↓	↑↓	↑	↑
F	↑↓	↑↓	↑↓	↑↓	↑
Ne	↑↓	↑↓	↑↓	↑↓	↑↓

bonds. The driving force behind the bond formation of any two atoms is the decreased overall energy state of the individual atoms.

6.1.3.1 Ionic or Electrovalent Bonds

Atoms are electrically neutral. An *ion* is an atom or a group of atoms that has a net positive (cation) or negative (anion) charge. The force of attraction between oppositely charged ions is called *ionic or electrovalent bond*. Ionic compounds are formed when a metal reacts with a nonmetal. Alkali and alkaline earth metals have one or two electrons in the outer shell. In order to reach a stable octet electron configuration, they can easily donate the valence electrons and become positively charged ions. Nonmetals, such as halogens, need only one electron to reach a stable octet configuration and so are willing to receive or gain an electron and form a negatively charged ion. The *ionic bond* is formed when an atom that looses electrons easily interacts with an atom that has a high affinity for electrons. *The ion pair has lower energy than the separated ions.* For a mole of Na^+ and Cl^- ions, the energy of interaction is -504 kJ mol^{-1}.

NaCl, NaF, NaI, CaO, and $CaCl_2$ are all known as ionic compounds or salts. When these compounds are dissolved in water, the ionic compound dissociates resulting in the regeneration of ions. Ionic compounds, however, are very sturdy materials; they have great thermal stability and high melting points. For example, NaCl crystal has a melting point of about 800 °C. Ionic compounds conduct electricity in the solid state as well as in the liquid state. Solutions of ionic compounds are known as *electrolytes*.

6.1.3.2 Covalent Bond

When atoms of the same element or different elements share a pair of electrons, a *covalent bond* is formed. The covalent bonding results from the mutual attraction of the two nuclei for the shared electron pair. The total energy of the molecule is less than that of the individual atoms. In the *diatomic* H_2 molecule, both hydrogen atoms share a pair of electrons so that the $1s$ orbital has the maximum of two electrons needed for stability. Sometimes it is necessary for two atoms to share more than one pair of electrons to reach stable octet configuration. Based on the number of pairs of electrons shared, covalent bonds may be called a *single bond*, *double bond*, or *triple bond*. In the O_2 molecule, the two oxygen atoms share two pairs of electrons while in the N_2 molecule, the two nitrogen atoms share three pairs of electrons. Also, molecules such as H_2O, NH_3, and CH_4 contain covalent bonds. Covalent bonds are most common between carbon atoms in organic compounds. Molecules containing covalent bonds are nonionic and are poor conductors of electricity because the pair of electrons is normally shared equally by each atom participating in the bond formation. When the electron sharing by the two atoms is unequal, *polar covalent bonds* are formed. For example, in the HF molecule, the electron pair is drawn more toward fluorine nucleus. As a result, the H atom has a fractional positive charge (δ^+) and the F atom has a fractional negative charge (δ^-).

Coordinate Covalent Bond

In a covalent bond, the pair of electrons required for sharing is donated equally by the two atoms. In contrast, in a *coordinate covalent bond*, the pair of electrons required for bond formation is provided by an atom to another atom, which can accommodate the pair in octet formation. These bonds are also called *semipolar bonds* because the donor atom has a partial positive charge, while the acceptor atom has a partial negative charge, just like in polar covalent bonds. Some donor atoms, such as N, O, and S, have a lone

pair of electrons, and these atoms form coordinate covalent bonds with metal ions to form metal complexes that can be cationic, anionic, or neutral, and which are very stable.

6.1.3.3 Hydrogen Bond

Molecules that contain hydrogen atoms bonded covalently to very *electronegative* atoms, such as F, O, and N, also form another chemical bond called a *hydrogen bond*. The strong electronegative atom has greater attraction for the pair of electrons and, as a result, acquires a partial negative charge (δ^-). Therefore, a hydrogen atom has a partial positive charge (δ^+). Now there is an electrostatic attraction between the partial opposite charges of the hydrogen atom of one molecule and the electronegative atom of another molecule. Such bonds between the partial opposite charges of hydrogen and the electronegative atoms are known as *hydrogen bonds*. Although hydrogen bonds are weak chemical bonds, they are important for the solvent properties of water and for the stability of the Deoxyribonucleic acid (DNA) structure.

6.1.3.4 Electronegativity

Different atoms have different affinities for the electrons that are being shared in a chemical bond. *Electronegativity* is a property, which describes the ability of an atom in a molecule to attract shared electrons. Linus Pauling developed a scale for electronegativity of different elements. In the periodic table of elements, electronegativity generally increases across a period and decreases down a group. For example, the value for Li is only 1.0 compared to a value of 4.0 for F (the most electronegative atom). In a chemical bond, the electronegativity difference between two identical atoms is zero and, therefore, no polarity occurs and covalent bonds are formed. When two atoms with widely differing electronegativities interact, ionic bonds are formed while unequal electron sharing results in polar covalent bonds.

6.1.3.5 Lewis Structures

In 1902, Gilbert Lewis conceived the octet rule. The Lewis structure of a molecule represents the arrangement of valence electrons among the atoms in a molecule. In a covalent bond formation, the pair of electrons found in the space between atoms are called *bonding pairs* while those pairs of electrons localized on an atom are called *lone pairs*.

In ionic compounds, such as NaCl, the Lewis structure shows all eight electrons on the Cl^- ion while the Na^+ ion has no valence electrons.

$$Na^+ + Cl^- \rightarrow \left[Na \right]^+ \left[:\overset{..}{\underset{..}{Cl}}: \right]^- \qquad (6.1)$$
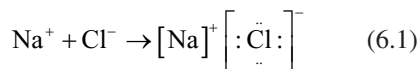
In molecules with covalent bonds, the Lewis structures show the bonding electron pairs in the place between the two sharing atoms.

$$H:H \quad :\overset{..}{\underset{..}{F}}::\overset{..}{\underset{..}{F}}: \qquad (6.2)$$
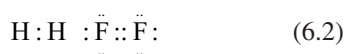
Sometimes more than one valid structure is possible for a given molecule. *Resonance* occurs when more than one Lewis structure can be written for a molecule and the electron structure represents an average of the resonance structures. For example, the nitrate ion is represented by a resonance structure. In reality, however, the electrons are delocalized or move around the entire molecule. Resonance is an exception to the general Lewis representation of electron configuration.

6.1.3.6 Formulas of Compounds

The formula of a compound indicates the numbers of atoms in the compound. An *empirical formula* represents the whole-number ratio of the various types of atoms in a compound. However, sometimes different compounds have the same ratio of moles of atoms of the same element. For example, the compounds acetylene (C_2H_2) and benzene (C_6H_6), each has 1:1 ratios of moles of carbon atoms to moles of hydrogen atoms. For both these compounds, the empirical formula is CH, and it will not be able to establish the identity of a given molecule. The *molecular formula*, however, is a formula which gives all the information that the empirical formula does, plus information about the number of atoms present in each molecule. For an unknown compound, the molecular formula can be determined from the empirical formula, if the molar mass is known.

In organic chemistry, a *structural formula* is very important to establish the real identity of a specific molecule or substance. For example, the molecular formula $C_6H_{12}O_6$ may represent several different sugar molecules. The structural formula provides a detailed orientation of different atoms of a molecule in a 3-dimensional space.

6.1.3.7 Stoichiometry

All chemical reactions are dependent on the mass of the reactants. Therefore, it is essential to measure the absolute quantities of materials consumed and produced in chemical reactions. This area of study is called *chemical stoichiometry*.

The modern system of atomic masses, instituted in 1961, is based on ^{12}C as the standard and was assigned a mass of exactly 12 *atomic mass units* (amu). The masses of all other atoms are given relative to this standard. Mass spectrometer is used to determine the exact mass of atoms. The atomic mass of every element is shown in the periodic table as atomic weight. It is important to note that the atomic weight of every element is the average mass of all stable isotopes of an element, present in nature. For example, the atomic weight of carbon is given as 12.01 amu since the natural carbon is a mixture of ^{12}C (98.89%) and ^{13}C (1.11%). Similarly, the atomic weight of copper is 63.55 since the natural copper is a mixture of 69.09% of ^{63}Cu (62.93 amu) and 30.91% of ^{65}Cu (64.93 amu).

The Mole

Mole (mol) is generally defined as the number equal to the number of carbon atoms in exactly 12 g of pure ^{12}C atoms. The number of atoms in 1 mol of ^{12}C was determined to be 6.022137×10^{23} (also known as *Avogadro's number*). Since the atomic mass of natural carbon is 12.011 amu, 12.011 g of a carbon element will have exactly 6.022137×10^{23} atoms. Thus, *m* the mass of 1 mol of an element is equal to its atomic mass, expressed in grams.

Molar Mass (Molecular Weight)

A chemical molecule, compound, or substance is also a collection of atoms. For example, a molecule of methane (CH_4) contains 1 atom of carbon and 4 atoms of hydrogen. The mass of 1 mol of CH_4 contains 1 mol of carbon (12.011 g) and 4 mol of atomic hydrogen (4 × 1.008 g), or 2 mol of H_2 molecule (2.016 g). Therefore, the *molar mass* of CH_4 gas is 16.043 g. The term *molecular weight* was traditionally used to describe the molar mass of a substance. Thus, 1 mol of any substance is equal to the molecular weight or molar mass of that substance, expressed in grams. In case of salts and ionic compounds, such as NaCl or K_2CO_3, the term *formula weight* is used instead of the term molar mass or molecular weight.

It is often useful to know a compound's composition in terms of masses of its elements. For example, the molar mass of glucose ($C_6H_{12}O_6$) is 181.122 g. In a glucose molecule, the mass percent (or weight percent) of carbon is 39.79%, of oxygen it is 53%, and of hydrogen it is 6.68%.

6.1.3.8 Solutions

Solutions are described in terms of the type of substance or *solute* that is dissolved in a medium known as the *solvent*. Both the solute and solvent may be solid, liquid, or gas. The solvent, however, is mostly chosen based on the chemical properties of the solute, compatibility, and physiologic conditions.

An *ionic solution* (also known as an *electrolyte*) is one that contains charged or ionic species, surrounded by solvent molecules. For example, in a NaCl solution, Na^+ and Cl^- ions are solvated by the water molecules that are dipolar. In *molecular solutions*, such as a glucose solution, the individual glucose molecule with covalent bonds retains its integrity and does not dissociate.

The amount or mass of a solute in a given solvent determines the strength or concentration of a solution.

Molarity and Normality

The term *molarity* (M) is defined as the number of moles of a substance (solute) per liter of a solvent and is a measure of the number of molecules per unit volume.

$$\text{Molarity}(M) = \text{moles}(m) / \text{volume}(v)$$

Different dilutions of a molar solution can also be expressed as millimolar (mM), micromolar (μM), etc. These concentration terms are very

important in chemical equations and reactions, since these terms specify the number of atoms or molecules in a given volume. For example, 1 M glucose solution contains 6.022×10^{23} molecules of glucose in 1 L, 6.022×10^{20} molecules in mL, and 6.022×10^{17} molecules in 1 μL.

In chemical reactions it is, sometimes, very important to know the number of reactive groups rather than the molecule itself. *Normality* (N) indicates the number of reactive groups (*equivalents*), such as proton (H^+), hydroxide (OH^-), or electron units per unit volume. For example, 1 M HCl is also equivalent to 1N HCl since HCl has only one acidic hydrogen ion (H^+). In contrast, 1 MH_2SO_4 is equivalent to 2 NH_2SO_4 solution since it has two H^+ ions.

Volume Percent

Solutions can be prepared using certain mass, g (*w*) dissolved in 100 g of a solvent or in 100 mL (*v*) of a solvent. Generally, solutions are prepared on the *w/v* basis. For example, the 0.9% NaCl solution (physiological saline) and the 5% dextrose solution are quite common in a clinic. It is important to recognize that in chemistry solutions prepared on *w/v* basis are not useful for balancing chemical reactions and must be expressed in terms of molar concentrations. For example, a 0.9% NaCl solution represents a 0.15 M solution of sodium chloride.

Radioactive Concentration

With radioactive solutions, it is quite common to express the concentration in units of activity/volume, such as mCi/ml or mBq/ml, etc. These radioactive concentration terms are mistakenly applied to SA, which really is an expression of activity per mass of the radionuclide or radiotracer.

6.2   Chemical Reactions

In a chemical reaction, one or more substances, called *reactants* or *reagents*, are allowed to react to form one or more other substances, called *products*. A chemical change involves reorganization of the atoms in the reactants to form the product (bonds have been broken and new ones have been formed). This process is represented by a *chemi-*

cal equation. For example, methane gas reacts with oxygen to produce carbon dioxide and water.

$$CH_4 + O_2 \rightarrow CO_2 + H_2O \qquad (6.3)$$
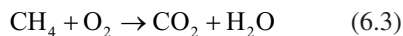
The law of conservation of mass dictates that in a chemical reaction, atoms are neither created nor destroyed. All atoms in the reactants must be accounted for among the products. To show the quantitative relationships, the chemical equation must be balanced. *Coefficients* are, therefore, used before the molecular formula of each compound to represent the number of moles of the reactant or the product. The above equation is not balanced and is not correct. A *balanced chemical equation* of the above reaction is written as follows:

$$CH_4 + 2O_2 \rightarrow CO_2 + 2H_2O \qquad (6.4)$$
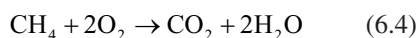
In the above reaction, 2 mol of oxygen interact with 1 mol of methane to produce 1 mol of carbon dioxide and 2 mol of water. Stoichiometric calculations of chemical reactions are very important for determining the number of reactants required to form a specific amount of a product.

6.2.1   Types of Chemical Reactions

In order to balance a chemical reaction, it is necessary to know the molecular and structural formulas of reactants and products. Also, one must be able to predict the products from the reactants. Simple chemical reactions are generally classified into five types. In a *Combination reaction*, two or more reactants combine to form one product. In a *decomposition reaction*, the reactant decomposes into its component elements or a simpler compound. Different elements have varying abilities to combine. In reactions involving several reactants, the possible product formation depends on the relative affinities, valency, and electronegativities of elements. *Substitution* (single or double) or *replacement reactions* involve the exchange of different elements based on their relative reactivities. In *combustion reactions*, compounds containing C, H, O, S, and N atoms involve burning with the liberation of energy and heat.

There are millions of reactions described in chemistry (both inorganic and organic). Most of these reactions occur among substances dissolved in water. Certain organic compounds are relatively nonpolar and do not dissolve in water. As a result, chemical reactions are performed in organic solvents. Both aqueous and nonaqueous chemical reactions can be categorized into three groups: *precipitation reactions*, *acid–base reactions*, and *oxidation–reduction reactions*.

1. *Precipitation reactions*: When two solutions are mixed, an insoluble substance (a solid)

sometimes forms and separates from the solution. Such a reaction is called a precipitation reaction and the solid that is formed is called a precipitate. For example, when a solution of barium chloride and a solution of sodium sulfate are mixed, a white, solid barium sulfate is formed, which can be separated from the sodium chloride solution simply by filtration. When ions combine to form a solid compound, the compound has to be neutral and not soluble in the solvent. The balanced equation can be written as a *molecular equation* or as a complete *ionic equation*.

$$BaCl_2 + Na_2SO_4 \rightarrow BaSO_4\,(s) + 2NaCl \tag{6.5}$$

$$Ba^{2+} + 2Cl^- + 2Na^+ + SO_4^{2-} \rightarrow BaSo_4\,(s) + 2Na^+ + 2Cl^- \tag{6.6}$$

2. *Acid–Base reactions*: Acids (from Latin word *acidus*) were first recognized as a class of substances that taste sour. In contrast, bases or *alkalis* are characterized by their bitter taste and slippery feel. In the 1880s, Savante Arrhenius proposed that in a solution, an acid is a substance that produces a proton, H^+ ions, while bases produce hydroxide OH^- ions. Since this concept applies only to aqueous solutions, Bronsted and Lowry, in 1923, defined an acid to be a proton donor, and a base to be a proton acceptor. In the 1920s, Lewis suggested a general definition for acid–base behavior in terms of electron pairs. An *acid is an electron pair acceptor* and a *base is an electron pair donor*.

3. Acids react with bases (and vice versa) to produce salts. Such a reaction is called a neutralization reaction, resulting in the formation of a salt and water, as shown in the examples below. The hydrolysis of salts in turn can regenerate H^+ ions.

$$HCl + KOH \rightarrow KCl + H_2O \tag{6.7}$$

$$H_2SO_4 + 2NaOH \rightarrow Na_2SO_4 + H_2O \tag{6.8}$$

Strong acids, such as HCl, H_2SO_4, and $HClO_4$ (per-chloric acid), dissociate completely in aqueous solution, forming hydronium, H_3O^+ ion. In solvents other than water, however, the

dissociation can only be partial. For example, hydrogen cyanide molecule may dissociate to form.

$$HCN \leftrightarrow H^+ + CN^- \tag{6.9}$$

$$NH_3 + H^+ \leftrightarrow NH_4^+ \tag{6.10}$$

Based on the Brønsted–Lowry definition, HCN is an acid since it can donate a proton and CN is a base since it can accept a proton. These two ions are called a *conjugate acid–base pair*. Similarly, ammonia is a base since it can accept a proton. A proton does not generally exist by itself; therefore, the Brønsted–Lowry equations usually show two sets of conjugate acid–base pairs and no protons, as shown in the example below.

$$HCN + NH_3 \rightarrow NH_4^+ + Cl^- \tag{6.11}$$

When HCl reacts with a CN^- ion, HCN is formed because a cyanide ion is a stronger base than a chloride ion and HCl is a stronger acid than HCN.

$$HCl + CN^- \rightarrow HCN + Cl^- \tag{6.12}$$

Arrhenius acids and bases deal with a H_3O^+ ion and a OH^- ion in aqueous solutions, while Brønsted–Lowry acids and bases deal with only protons or H+ ions in nonaqueous solvents. Lewis acids and bases deal with a pair of electrons in coordinate covalent bonds. A

Lewis base can be an electron-rich negative ion such as OH^- and HSO_4^-, or a molecule, such as NH_3, where the nitrogen atom has a lone pair of electrons to donate. Lewis acids include positive ions, such as H^+, Ag^+, and Al^{3+}, or a molecule, such as BF_3 and SO_3, with an atom that can accept a pair of electrons. The reaction between NH_3 and BF_3 forming NH_3BF_3 is a good example of an acid–base reaction, as shown below, there are covalent bonds between N and hydrogen and coordinate covalent bond between N and B atoms.

$$NH_3 + BF_3 \rightarrow H_3N : BF_3 \qquad (6.13)$$

4. *Oxidation–Reduction reactions*: Chemical reactions in which one or more electrons are transferred are called *oxidation–reduction reactions* or *redox reactions*. Many important reactions, such as combustion and oxidation of sugars and fats, involve redox reactions. *Oxidation* is the loss of electron(s) from the electron configuration of an atom or ion, while *reduction* is the gain of electron(s) by the electron configuration of an atom or ion. In some of these reactions, the transfer of electrons occurs in a literal sense to form ions, as in the case of NaCl formation, while in the combustion of methane by oxygen transfer occurs in a formal sense by covalent bond breaking and new bond formation. In the oxidation of methane, none of the reactants and products are ionic (as one would expect when electrons are transferred); however, the reaction is still assumed to involve transfer of electrons from carbon to oxygen.

$$2Na(s) + Cl_2(g) \rightarrow 2NaCl(s) \quad (6.14)$$

$$CH_4 + 2O_2 \rightarrow CO_2(g) + 2H_2O(g) \quad (6.15)$$
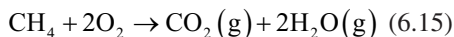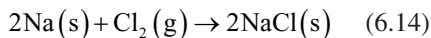
The concept of *oxidation states* or *oxidation numbers* provides a way to keep track of electrons in redox reactions. In the reaction of methane with oxygen, the carbon undergoes a change in oxidation state from −4 in CH_4 to +4 in CO_2. Such a change can be accounted for by a loss of eight electrons. Because each of the oxygen atoms has gained two electrons in CO_2 and H_2O molecules, the oxidation rate of oxygen changes from 0 in O_2 to −2 in CO_2 and H_2O molecules. Based on this example, the oxidation number is defined as the number of valence electrons in the free atom minus the number "controlled" by the atom in the compound. In any molecule with a covalent bond, the nonmetals with the highest attraction for shared electrons are F, O, N, and Cl. The relative electronegativity of these atoms is $F \gg O > N \approx Cl$.

$$\overset{-4}{CH_4} + 2\overset{0}{O_2} \longrightarrow \overset{+4}{C}\overset{-2}{O_2} + \overset{+1}{2H_2}\overset{-2}{O} \quad (6.16)$$
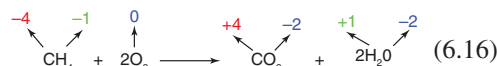
In the above reaction, carbon is *oxidized* as it loses electrons and the oxidation state is increased, while the oxygen is *reduced* because it gains electrons, and the oxidation state is decreased. In addition, because oxygen looses electrons, it is called the *reducing agent*, while methane is called the *oxidizing agent* since it gains electrons. It is important to remember that in a covalent bond, electrons are shared between the atoms. However, in redox reactions, the shared electrons are drawn more toward the more electronegative atoms and, therefore, the atom has a net gain of the shared electrons.

6.2.2   Chemical Equilibrium

Many chemical reactions proceed to completion until one of the reactants is completely consumed and the product formation is finished. For example, sodium metal and chlorine gas combine to form NaCl salt, which can decompose only when it is electrolyzed. On the other hand, many other reactions stop far short of completion since such reactions can be *reversible*. The products formed react to give back the original reactants, even as the reactants are forming more products. In fact, the system (the chemical reaction) has reached *chemical equilibrium*, when the concentration of all reactants and products remains constant with time.

When nitrogen and hydrogen gases react with each other at 500 °C and high pressure, ammonia is formed. Under the same conditions, ammonia is also decomposed. This situation, where two opposing reactions (forward and backward) occur at the same time, leads to a state known as chemical equilibrium.

$$3H_2 + N_2 \rightleftharpoons 2NH_3 \qquad (6.17)$$

Some reactions proceed slowly, while other reactions can proceed very fast. The *rate of a reaction* is defined as the change in the concentration of any of its reactants or products per unit time. The nature and concentration of reactants, temperature, presence of a catalyst, pressure, and the size of solid reactants all contribute to the changes in the rate of a chemical reaction.

Le Chatelier's principle states that if a stress (such as change in concentration, temperature, pressure, or addition of a catalyst) is applied to the system at equilibrium, then the equilibrium will shift in order to reduce that stress. The reaction may shift to the right (product formation) or to the left (product decomposition). Soon, however, the system will reach a new equilibrium at the new set of conditions. Le Chatelier's principle, however, cannot predict how much an equilibrium will shift under different conditions of stress.

Based on empirical data, Guldberg and Waage, in 1864, proposed the *law of mass action* as a general description of equilibrium condition. For a chemical reaction in general,

$$a\text{A} + b\text{B} \overset{k1,k2}{\leftrightarrow} c\text{C} + d\text{D} \qquad (6.18)$$
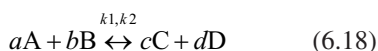
$$K_{eq} = \frac{[\text{C}]^c [\text{D}]^d}{[\text{A}]^a [\text{B}]^b} \qquad (6.19)$$

In the above equation, k_1 and k_2 are the forward and backward rate constants, while K_{eq}, is a constant called equilibrium constant. The square brackets indicate the concentration (in moles) of products and reactants at equilibrium and the

coefficients represent the number of moles in the balanced chemical equation. The value of K_{eq} for a given reaction system can be calculated from the observed concentrations of reactants and products at equilibrium. For example, in the synthesis of ammonia, described above, under the conditions specified, $K_{eq} = 6.0 \times 10^{-2}$ L^2 mol^{-2}. The higher the value of K_{eq}, the more likely the reaction will shift to the right with a net increase in the product concentration or formation. There is only one value for K_{eq} for a particular system, and at a particular temperature but, there are an infinite number of equilibrium positions.

6.2.2.1 Ionic Equilibria

Various salts, acids and bases, and their dissociated ions in solution also exist in equilibrium. The equation for the equilibrium constant is the same for any of the chemical reactions discussed above. Certain salts, such as NaCl and KCl, ionize completely in a solution. For very slightly soluble salts, the equilibrium constant is called *solubility product constant*, K_{sp}, because most of the salt concentration is relatively constant. For example, for very slightly soluble silver bromide (AgBr) salt,

$$K_{sp} = \left[\text{Ag}^+ \right]\left[\text{Br}^- \right] \qquad (6.20)$$

The ionic equilibrium constant may be K_a (*acidity constant*) if it represents the dissociation of an acid or K_b if it represents the dissociation of a base. A strong acid (or base) is a strong electrolyte that dissociates completely into its ions in aqueous solution. A weak acid (or base) is a weak electrolyte that dissociates only partially in aqueous solution. The stronger the acid or base, the higher the K_a or K_b value.

6.2.2.2 Dissociation of Water

Water is said to be amphoteric because it can behave as either an acid or a base. Pure water behaves like a weak electrolyte. As a result of the autoionization of a very small extent of water, H_3O^+ and OH^- exist in water at

25 °C. The concentration of each of these ions is 10^{-7} M.

$$H_2O \; \rightleftharpoons \; H_3O^+ + OH^- \tag{6.21}$$
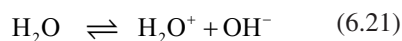
$$K_i = \frac{\left[H_3O^+\right]\left[OH^-\right]}{H_2O} = \frac{\left[1\times10^{-7}\,M\right]\left[1\times10^{-7}\,M\right]}{55.6M} \tag{6.22}$$

Since the water concentration is relatively unchanged, K_i of water is the ion product of water, $K_w = 1 \times 10^{-14}$ M². At neutrality, the concentration of H_3O^+ and OH^- ions is the same and is equal to 1×10^{-7} M.

The pH Scale

The acidity of a solution depends on the hydrogen (H^+) ion or hydronium (H_3O^+) ion concentration. Because the hydrogen ion concentration is typically very small, the *pH scale* provides a convenient way to represent the acidity of an aqueous solution.

$$pH = -\log\left[H^+\right] \tag{6.23}$$

Thus, for a solution in which

$$\left[H^+\right] = 1.0\times10^{-7}\,M \tag{6.24}$$

$$pH = -(-7.0) = 7.0 \tag{6.25}$$

The hydrogen ion concentration of an aqueous solution can be as high as 1.0 M and as low as 1×10^{-14} M. Therefore, the pH scale (Fig. 6.2) ranges from 0 to 14.
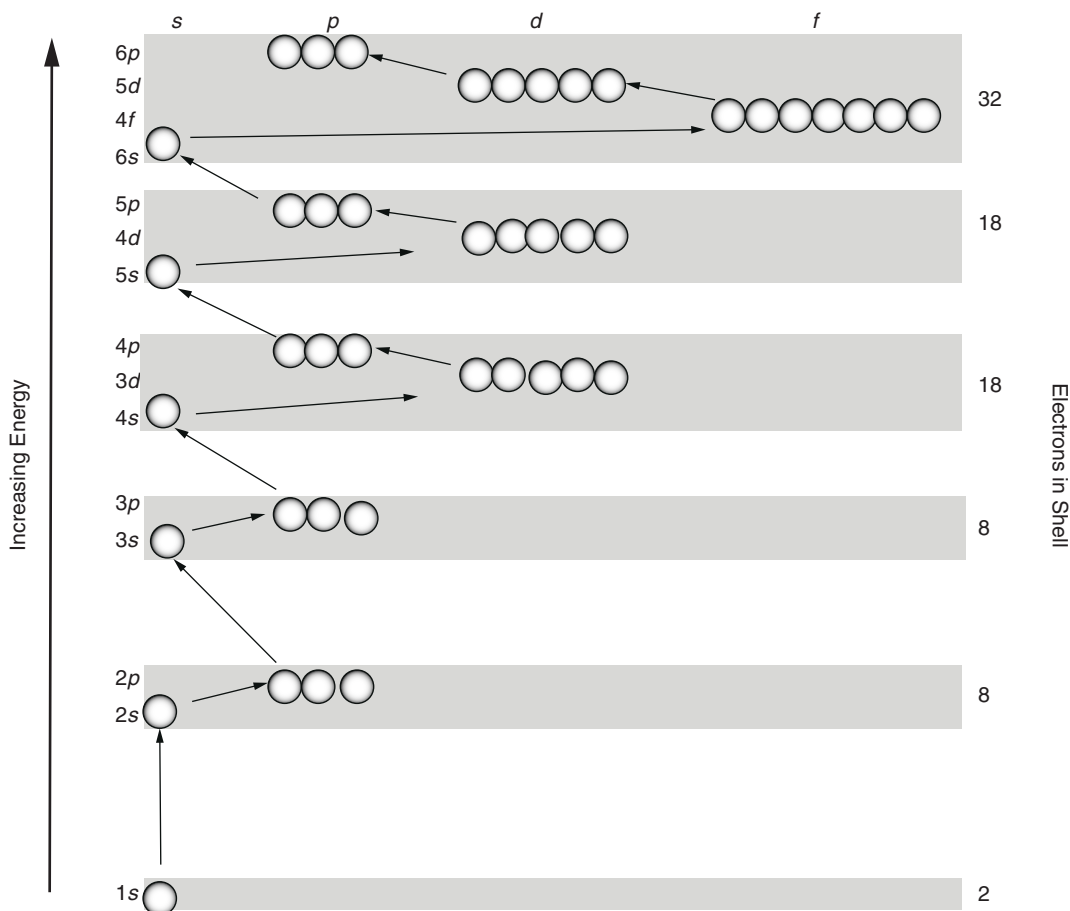
Fig. 6.2 Arrangement of electrons in orbitals. In the ground state, the lowest energy orbitals contain the electrons. The high-energy orbitals, however, are filled only after the lower-energy orbitals are filled

Buffer Systems

A buffer solution is defined as solution that resists pH changes when acid or base equivalents are added to it. The components of a buffer solution are a weak acid and its anion. Similarly, a buffer solution can be made from a weak base and its salt. The addition of any acid or base to a buffer is neutralized by ions in the buffer keeping the pH relatively unchanged.

Acetate, citrate, and phosphate buffers are some of the most common buffer systems used. The pH of a buffer system can be calculated based on pK_a of the weak acid used (based on the *Henderson–Hasselbalch equation*).

$$pH = pK_a + \frac{\left[A^-\right]}{\left[HA\right]} \quad (6.26)$$

For example, in the preparation of an acetate buffer, the concentrations of the acetic acid and acetate ion are the same and are equal to 0.2 M and K_a of the acetic acid is 1.8×10^{-5} M and the pH of the acetate buffer is 4.8.

$$CH_3COOH \leftrightarrow CH_3COO^- + H^+ \quad (6.27)$$
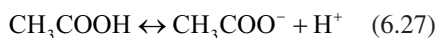
$$pH = 1.8 \times 10^{-5} M + \frac{\left[0.2M\right]}{\left[0.2M\right]} = 4.8 \quad (6.28)$$

There are several things that must considered before selecting an appropriate buffer for a specific purpose. First, it is important to make sure that the buffer does not chemically interfere with the chemical reaction. Buffer systems are most effective at pH values near the pK_a values. Further, buffers should be used at relative concentrations (>0.1 M) to have a high capacity of buffering. Finally, buffers are very important physiologically because the pH of blood is maintained in a narrow range of 7.3–7.5. Also, the enzyme activities within cells and in the plasma are pH dependent.

6.3 Organic Chemistry

Historically, the term organic chemistry has been associated with the study of compounds, obtained from plants and animals. In modern terms, the study of carbon-containing compounds and their properties is called organic chemistry. In addition to carbon and hydrogen, the elements most likely to be present in organic compounds are nonmetals, such as oxygen, nitrogen, phosphorous, sulfur, and the halogens.

The element carbon is in group IV (or group 14) of the periodic table. The chemical bonds between atoms of carbon and between carbon and the other elements are essentially covalent. With a valence of 4 and an electronegativity of 2.5, carbon can be expected to form nonpolar covalent bonds with other carbon and hydrogen atoms, and increasingly polar covalent bonds with O, N, and halides. With an atomic number of 6, the orbital electron configuration is $1s^2 2s^2 2p^2$. The carbon adopts a set of orbitals for bonding other than its native $2s$ and $2p$ orbitals. This modification of the native atomic orbitals, to form special orbitals for bonding, is called *hybridization* (Fig. 6.3). The four new orbitals, called sp^3, are identical in shape, each having a larger lobe and a smaller lobe. The four orbitals are oriented in space so that the larger lobes form a tetrahedral arrangement, as in the case of a methane (CH_4) molecule with bond angles of 109.5°. In a sp^2 hybridization, a set of three orbitals, arranged at 120-degree angles, can be obtained, as in the case of ethylene (CH_2CH_2) by combining one s orbital and $2p$ orbitals. For each bond, the shared electron pair occupies the region between the atoms. This type of covalent bond is called a *sigma (s) bond*. The parallel p orbitals share an electron pair in the space above and below the sigma bond to form a *pi (p) bond*. In a sp hybridization, two hybrid orbitals form two sigma bonds, arranged at 180°, oriented in opposite directions, as in the case of the carbon dioxide molecule (CO_2). The p orbitals can also form two pi bonds, perpendicular to each other. A combination of sigma and pi bonds can also facilitate the formation of a triple bond between two carbon atoms, as in the case of acetylene (C_2H_2). It is important to realize that this hybridization of orbitals in a carbon atom determines the shape and the 3-dimensional organization of atoms in organic compounds.

Acidic   Normal   Basic

0	1	2	3	4	5	6	7	8	9	10	11	12	13	14

1   10^{-1} 10^{-3} 10^{-5} 10^{-7} 10^{-9} 10^{-1} 10^{-14} M

H^+ concentration
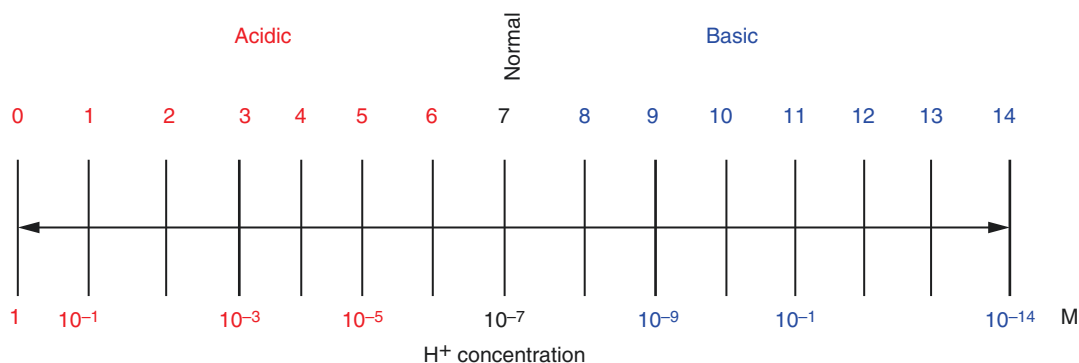
Fig. 6.3 The pH is a log scale based on 10

6.3.1 Hydrocarbons

Compounds composed of only carbon and hydrogen are called *hydrocarbons*. Compounds, in which carbon–carbon bonds are all single bonds, are called *saturated hydrocarbons* and, if the carbon–carbon bonds involve multiple bonds, they are called *unsaturated hydrocarbons*. Hydrocarbons can be classified into four fundamental series: *alkanes*, *alkenes*, *alkynes*, and *aromatic* hydrocarbons.

The simplest member of saturated hydrocarbons or alkanes is *methane* (CH_4), followed by *ethane* (CH_3CH_3), and *propane* ($CH_3CH_2CH_3$). Alkanes in which the carbon atoms form long "strings" or chains are called *normal*, *straight-chain*, or *unbranched* hydrocarbons, which can be represented by the general formula, C_nH_{2n+2}. The four-carbon butane and the subsequent members of alkanes exhibit *structural isomerism*. For example, butane can exist as a straight-chain molecule (*n-butane*) or as a branched chain structure (*isobutane*). Besides forming chains, carbon atoms can also form rings, known as cyclic alkanes (C_nH_{2n}), *such as cyclopropane* and *cyclohexane*.

Alkene series of unsaturated hydrocarbons are also known as *olefins* and have at least one double bond in the carbon chain (C_nH_{2n}) of each molecule. The simplest olefin is a *diene*, called *ethylene* (CH_2CH_2). Because of the restricted rotation of methylene (–CH_2) groups around double-bonded carbon atoms, alkenes exhibit *cis–trans isomerism*. For example, there are two stereoisomers of 2-butene (Fig. 6.4). Identical substituents on the same side of the double bond are called *cis* and those on the opposite side are called *trans*. In a series of alkanes, if only one saturated carbon separates the double bond, then it is called *conjugated*, however, if more than one saturated carbon separates the double bond, then the alkene is said to be *unconjugated*.

Alkynes are unsaturated hydrocarbons containing at least one triple carbon–carbon bond and have the general formula, C_nH_{2n-2}. The simplest alkyne is *ethyne* (C_2H_2), commonly called *acetylene*.

A special class of cyclic unsaturated hydrocarbons is known as the aromatic hydrocarbons. A six-carbon conjugated olefin, cyclohexatriene, an aromatic hydrocarbon, also known as *benzene* (C_6H_6), has a planar ring structure. Benzene exhibits resonance, since all the three double bonds in benzene are equivalent. The delocalization of π electrons is usually indicated by a circle inside the ring. Benzene is the simplest aromatic molecule. More complex aromatic molecules, such as naphthalene, anthracene, phenanthrene, and 3,4-benzpyrene, consist of a number of "fused" benzene rings.
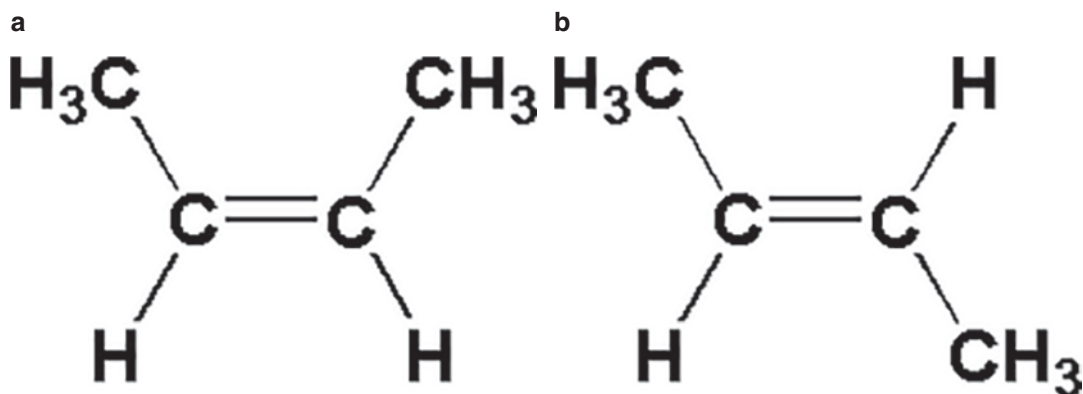
Fig. 6.4 The two stereoisomers of 2-butene: *cis*-2-butene (**a**) and *trans*-2-butene (**b**)

6.3.1.1 Reactions of Hydrocarbons

Combustion Reaction

Chemically, alkanes are relatively strong and fairly unreactive. Because of their limited reactivity, saturated hydrocarbons are called *paraffins* (meaning little affinity). At high temperatures, however, they react with oxygen, and these combustion reactions are the basis for their use as fuels.

Substitution Reaction

Alkanes can also undergo substitution reactions primarily where the more electronegative halogen atoms replace hydrogen atoms. For example, chlorine reacts with methane forming *chloromethane*, *dichloromethane*. Substituted methanes containing chlorine and fluorine are known as *freons* which are very unreactive and can be used as coolant fluids. Alkanes can also be converted to alkenes by *dehydrogenation* reactions in which hydrogen atoms are removed.

Benzene being unsaturated is expected to be very reactive but, actually, it is quite unreactive. The relative lack of reactivity of aromatic hydrocarbons is attributed to the delocalized double bonds. Because of its great stability, the benzene ring persists in most reactions. Substitution reactions are characteristic of alkanes. However, benzene also undergoes substitution reactions in which the hydrogen atoms are replaced by other atoms and functional groups, such as chlorine atom, nitro group ($-NO_2$), methyl group ($-CH_3$), and even a phenyl ($-C_6H_5$) group. These substitution reactions occur as a result of the attack of an *electrophilic* or electron-seeking ion on the π electrons of the benzene ring.

When the aromatic ring already contains a substituent, its reactivity will be greater or less than that of benzene itself. Electron releasing groups (such as $-OH$, $-OCH_3$, $-NH_2$) can be *activating* the benzene ring while electron withdrawing groups (such as $-F$, $-NO_2$, $-COOH$) can be *deactivating* the benzene ring. For example, both phenylalanine and tyrosine amino acids contain the benzene ring. However, iodination (or radio-iodination) of tyrosine is chemically easier since the hydroxyl ($-OH$) group already present on the benzene ring activates the electrophilic attack of iodine (Fig. 6.5). A benzene ring can have more than one substituent attached to the ring. If two identical substituents are attached to the ring, they are referred to as *ortho* (*o*), *meta* (*m*), or *para* (*p*), depending on their relative position.

Addition Reactions

Because alkenes and alkynes are unsaturated, their most important reactions are addition reactions. In these reactions, π bonds, which are weaker than the σ bonds, are broken, and new σ bonds are formed with the atoms being added. For example, *hydrogenation reactions* involve addition of hydrogen atoms to carbon atoms with double bonds in the presence of catalysts such as
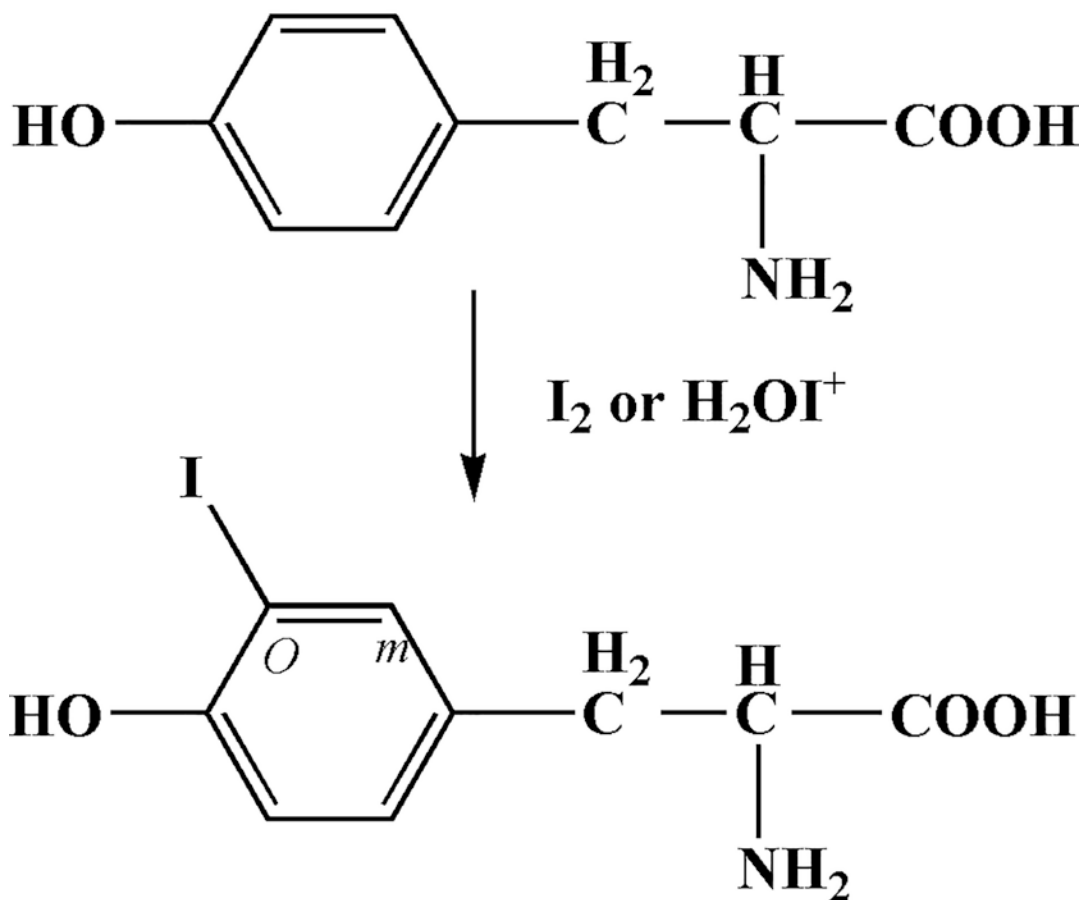
Tyrosine

Fig. 6.5 Iodination of tyrosine is chemically easier since the hydroxyl (–OH) group already present on the benzene ring activates the electrophilic attack of iodine

platinum, palladium, and nickel, which help break the strong covalent bonds of molecular hydrogen.

$$H_2C = CHCH_3 + H_2 \xrightarrow{\text{catalyst}} CH_3CH_2CH_3 \quad (6.29)$$
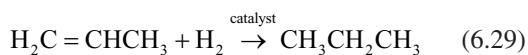
Halogenation of olefins involves the addition of halogen atoms to the carbon atoms with double bonds. Unlike the unsaturated hydrocarbons, benzene does not undergo rapid addition reactions.

6.3.1.2 Hydrocarbon Derivatives

The millions of organic compounds, other than hydrocarbons, can all be regarded as derivatives of hydrocarbons, where one or more of the hydrogen atoms on the parent molecule is replaced by another type of atom or groups of atoms, known as *radicals* and *functional groups*. A radical is a hydrocarbon with one hydrogen atom less and is reactive. For example, methyl (–CH_3) and ethyl (–CH_2CH_3) are often called radicals (Table 6.4) and usually denoted as "R" in formulas. If the

Table 6.4 The most common alkyl and phenyl substituents and their names

Structure	Name
$-CH_3$	Methyl
$-CH_2CH_3$	Ethyl
$-CH_2CH_2CH_3$	Propyl
$-CH_2CH_2CH_2CH_3$	Butyl
$CH_3\overset{|}{C}HCH_3$	Isopropyl
$-\overset{\overset{H}{|}}{\underset{\underset{H}{|}}{C}}-\overset{\overset{H}{|}}{\underset{\underset{CH_3}{|}}{C}}-CH_3$	Isobutyl
$-\overset{\overset{CH_3}{|}}{\underset{\underset{CH_3}{|}}{C}}-CH_3$	*tert*-Butyl
(phenyl ring structure)	Phenyl

radical is derived from an alkane, the radical is called *alkyl radical*; if it is derived from an aromatic hydrocarbon, it is called *aryl radical*, and if it is derived from benzene, it is called *phenyl radical*. Specific groups of atoms responsible for the characteristic properties of the organic compounds are called *functional groups*. The most common functional groups are listed in Table 6.5.

Alcohols are characterized by the presence of the hydroxyl (–OH) group. Alcohols are classified as primary, secondary, and tertiary, depending on whether one, two, or three radical groups attached to the carbon atom where the hydroxyl group is attached. Some common alcohols are methyl alcohol (methanol), ethyl alcohol (ethanol), glycerol, and phenol. Methanol is highly toxic while ethanol is the alcohol found in many beverages, such as beer, wine, and whiskey. The fermentation of glucose by yeast generates ethanol from grains (barley, corn) and grapes. Some of the important polyhydroxy alcohols are ethylene glycol and glycerol, which are two and three carbon alcohols. Alcohols are good solvents

of organic compounds since the hydroxyl groups of alcohols contain polar C–O and O–H bonds, which help to form hydrogen bonds. As the number of carbon atoms in an alcohol increase, its water solubility decreases. A chemical reaction that removes a water molecule between two alcohol molecules results in the formation of an *ether*. Diethyl ether ($CH_3CH_2OCH_2CH_3$), or simply ether, is used as a solvent and as an anesthetic.

Aldehydes and *ketones* contain the carbonyl (–C=O) group. In an aldehyde, the *carbonyl* group is attached to at least one hydrogen atom while in ketones, the carbonyl group is attached to carbon atoms. Aldehydes have very strong odors. Formaldehyde (HCHO) or formalin is generally used in pathology to store tissue specimens. Vanillin is responsible for the pleasant odor in vanilla beans, while butyraldehyde is responsible for the unpleasant odor in rancid butter. The most common ketone is *acetone*, commonly used as a solvent for hydrophobic molecules and as a nail polish remover. Methylethylketone or MEK is a solvent used in the chromatography of ^{99m}Tc pertechnetate. Alcohols and aldehydes or ketones can be interconverted by oxidation and reduction reactions.

Carboxylic acids are characterized by the presence of the carboxyl (–COOH) group and are also known as the organic acids with a general formula of RCOOH. The simplest and most common acid is acetic acid (found in vinegar), while citric acid is found in all citrus fruits. Unlike inorganic acids, organic acids are weak acids in aqueous solution. Reaction with a strong base such as NaOH converts them into carboxylate anion or sodium salt form, which increases water solubility. Carboxylic acids can be synthesized by oxidizing primary alcohols. For example, ethanol can be oxidized to acetic acid, using potassium permanganate.

A carboxylic acid reacts with an alcohol to form an ester and a water molecule.

$$CH_3COOH + HOCH_2CH_3 \rightarrow CH_3COOCH_2CH_3 + H_2O \qquad (6.30)$$

The reaction of CO_2 gas with organic magnesium halides (*Grignard* reagent) also results in the formation of carboxylic acids (Fig. 6.6). This

method is commonly used to prepare ^{11}C labeled organic acids, such as palmitic acid. Carboxylic acids can be converted to very reactive acid chlo-

Table 6.5 The common functional groups

Class	Functional group	General formula	Example
Halohydrocarbons	–X (F, Cl, Br, I)	R–X	CH_3I
			Methyl iodide
Alcohols	–OH	R-OH	CH_3CH_2OH
			Ethanol
Ethers	–O–	R–O–R′	CH_3OCH_3
			Dimethyl ether
Aldehydes	$-\overset{\overset{O}{\|}}{C}-H$	$R-\overset{\overset{O}{\|}}{C}-H$	HCHO
			Formaldehyde
Ketones	$-\overset{\overset{O}{\|}}{C}-$	$R-\overset{\overset{O}{\|}}{C}-R′$	CH_3COCH_3
			Acetone
Carboxylic acids	$-\overset{\overset{O}{\|}}{C}-$	$R-\overset{\overset{O}{\|}}{C}-OH$	CH_3COOH
			Acetic acid
Esters	$-\overset{\overset{O}{\|}}{C}-O-$	$R-\overset{\overset{O}{\|}}{C}-O-R′$	$CH_3COOCH_2CH_3$
			Ethyl acetate
Amines	$-NH_2$	$R-NH_2$	CH_3NH_2
			Methylamine

a

$$CH_3(CH_2)_{13}CH_2MgBr \xrightarrow[H^+, \ H_2O]{CO_2} CH_3(CH_2)_{13}CH_2COOH$$

Magnesium halide
(Grignard reagent)

Palmitic acid

b

$$CH_3\overset{\overset{O}{\|}}{C}-OH \xrightarrow{SOCl_2} CH_3\overset{\overset{O}{\|}}{C}-Cl \xrightarrow{CH_3CH_2OH} CH_3\overset{\overset{O}{\|}}{C}-O-CH_2CH_3$$

Acetic acid   Acetyl chloride   Ethyl acetate
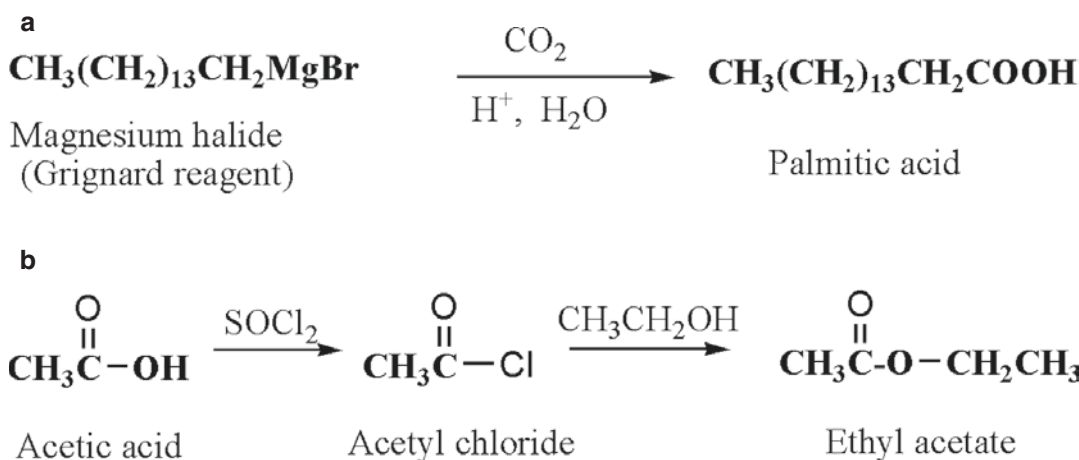
Fig. 6.6 The reaction (**a**) of CO_2 gas with *Grignard* reagent to form carboxylic acid (**palmitic acid**). In reaction (**b**), a carboxylic acid (**acetic acid**) is converted to very reactive acid chloride by the reaction of the acid with thionyl chloride ($SOCl_2$). The reaction of acid chloride with an alcohol will result in the formation of an *ester*

rides by the reaction of the acids with thionyl chloride ($SOCl_2$). The reaction of acid chloride with an alcohol will result in the formation of an *ester* (Fig. 6.6).

Naturally occurring esters are fats and triglycerides and often have a sweet, fruity odor. For example, *n*-amyl acetate smells like bananas and *n*-octyl acetate smells like oranges. One of the very important *esters is acetylsalicylic acid* (aspi-

rin) formed from the reaction of salicylic acid and acetic acid.

Amines can be considered derivatives of ammonia (NH_3), in which one or more hydrogen atoms have been replaced by organic radicals. Amines can be classified as the primary amines (RNH_2), secondary amines (R_2NH), and tertiary amines (R_3N). Many amines have unpleasant "fishlike" odors. *Putrescine* and cadaverin are

responsible for the odor associated with decaying animal and human tissues. Also, amines are the bases of organic chemistry. Like ammonia, amines react as *Bronsted* bases by reacting with water and acids to form positively charged ammonium species (RNH^+_3), which are soluble in water. Amines react with acid chlorides to form amides that contain an amide group (–CONH), commonly found in peptides and proteins (Fig. 6.8). Amines also react with aldehydes and ketones to give *Schiff* bases.

6.4 Biochemistry

Biochemistry is the study of the chemistry of living systems. The *essential elements* for human life are known to include 30 elements. However, only six of these elements contribute to 99% of the body mass. The most abundant elements are oxygen 65%, carbon (18%), and hydrogen (10%). Certain transition elements, such as iron, zinc, copper, cobalt, and iodine, are present in *trace amounts*. Life is organized around the functions of the cell, the smallest unit of life, and the building block of all tissues and organs. The main thrust of biochemistry is to understand how cells operate at the molecular level. The *nucleus*, which contains the *chromosomes* and DNA, is separated from the *cytoplasm* (the cell fluid) by a membrane and the cell, in turn, is separated from the extracellular fluid by the cell membrane. A number of subcellular structures carry out various cell func-

tions. For example, *mitochondria* process nutrients and produce the energy, the enzymes in *lysosomes* digest the proteins, and the *ribosomes* synthesize the proteins based on mRNA. The four major categories of natural chemical compounds present in living systems are proteins, carbohydrates, lipids, and nucleic acids.

6.4.1 Proteins

Proteins make up about 15% of our body mass and perform many functions. *Fibrous proteins* provide structural integrity and strength to many tissues, such as muscle and cartilage, while *globular proteins* are the "worker molecules" in various processes, such as transport of oxygen and nutrients. Globular proteins also act as catalysts for thousands of chemical reactions and participate in the body's regulatory systems. Chemically, proteins are a class of natural polymers and the basic building blocks are α-*amino acids*, molecules containing both, a basic amino group and an acid carboxyl group.

6.4.1.1 Amino Acids
Amino acids are the basic structural units of proteins, peptide hormones, and peptide antibiotics. The 20 natural amino acids most commonly found in proteins are grouped as polar and nonpolar classes or as neutral, basic, and acidic amino acids. The α-amino acids have the general formula (Fig. 6.7), where "R" represents a vari-
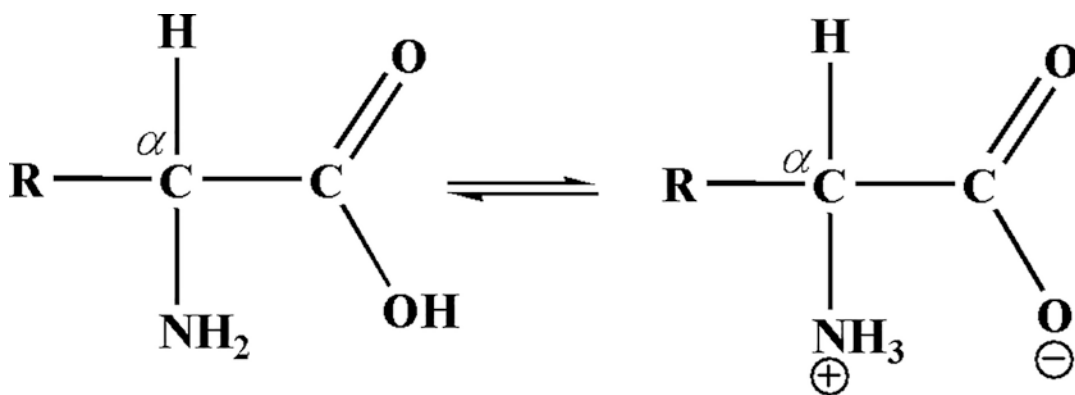
Fig. 6.7 The building blocks of all proteins are the α-amino acids, where R may represent H, CH_3, or a more complex substituent. At the physiological pH, there may be equilibrium between the neutral and charged species

able, organic polar (hydrophilic), or nonpolar (hydrophobic) side chain. They are called α-amino acids because the amino group is attached to the α-carbon, the one next to the carboxyl group. At the pH in biological fluids, the amino acids exist in a dipolar ionic form (known as *zwitterions*), where the proton from a carboxyl group is transferred to the amino group. Most of the amino acids are neutral. The basic amino acids (*lysine*, *arginine*, and *histidine*) have two amino groups, while the acidic amino acids (*aspartic acid* and *glutamic acid*) have two carboxyl groups. The amino acids, *cysteine* and *methionine*, contain organic sulfur atoms. The thiol group (–SH), similar to the hydroxyl group, can be oxidized in cysteine to a disulfide form, *cystine*. Methionine has a thioether linkage and serves as a biosynthetic intermediate in supplying the methyl group methylation reactions, in vivo. The amino acid, tyrosine, is important for radioiodination reactions, while lysine and arginine are useful to attach bifunctional chelating agents for labeling peptides and proteins with radiometals.

Stereochemistry of Amino Acids

When a carbon atom is attached to four different groups, it is called an *asymmetric* carbon atom. The compounds containing asymmetric carbon atoms, like mirror images, are said to be non-superimposable. The mirror image, *optical isomers* are called *enantiomers* (L and D forms). The amino acids in the solution can also rotate the plane-polarized light to the right (designated as D for dextrorotatory) or to the left (designated as L for levorotatory). Interestingly, L-amino acids are often dextrorotatory, while D-amino acids are levorotatory. The physical properties of L- and D-amino acids are identical. In biological systems, however, the reactivity of these two forms is quite different. For example, only the L-amino acids are mostly found in proteins. It is also important to recognize that the stereochemical requirements for biological activity are essential in the design of radiolabeled amino acids as molecular imaging agents.

Peptide Linkage

A condensation reaction between the amino group of one amino acid with the carboxy group of another amino acid will result in the formation of a dipeptide with reduced polarity. The structure, CONH, is called a *peptide linkage* (also called an *amide*). Such peptide bonds (Fig. 6.8) between several amino acids lengthen the polymer chain to produce a polypeptide, and eventually a protein. A naturally occurring tripeptide, glutathione is derived from only three amino acids (glu–cys–gly), while insulin with a molecular weight of 5700 is made up of 51 amino acids. Polypeptides with molecular weights of approximately 6000 or higher are generally called proteins. The sequence and the number of amino acids in a polypeptide determine the biological function of the molecule. With the 20 natural amino acids, which can be assembled in any order, there is essentially an infinite (10^{18}) variety of possible sequences of protein molecules.

6.4.1.2 Protein Structure and Function

The order, or sequence of amino acids in the protein chain, is called the *primary structure*, which determines the biological property. The arrangement of the chain of the long molecule is called the *secondary structure*, determined to a large extent by the hydrogen bonding within the chain
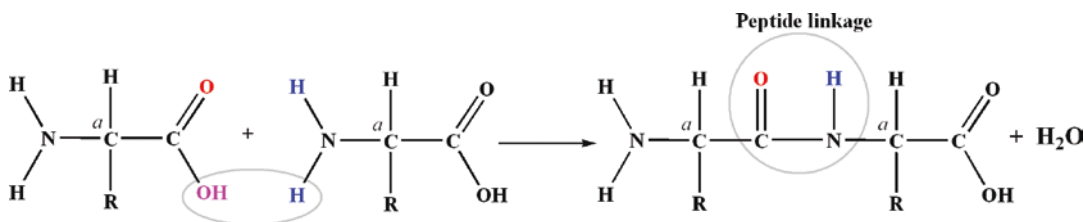
Fig. 6.8 A condensation reaction between two amino acids results in the formation of a peptide bond and one water molecule

coils, forming a spiral structure called an α-helix, which gives the protein elasticity. Proteins having no structural functions are *globular*. The overall shape of the protein, long and narrow or globular, is called its *tertiary structure*. The amino acid cysteine plays a special role in stabilizing the tertiary structure of proteins because of disulfide linkage. The process of breaking down the three-dimensional structure of proteins is called *denaturation*. Proteins have a wide range of specific functions in the body such as structure, movement, transport, catalysis, energy transformation, control, and buffering. Receptor protein molecules on the cell membrane are highly specific and bind to hormones, neurotransmitters, and specific molecules to initiate specific functions within the cell. Nearly all chemical reactions in living systems are catalyzed by enzymes, which are almost always proteins. Expression of genetic information is also under the control of proteins.

6.4.2 Carbohydrates

Carbohydrates or sugars are characterized by structures in which each carbon atom has an oxygen atom attached to it. All the carbon atoms in the molecule, except one, have hydroxyl groups

attached to them. The remaining one carbon atom has the oxygen in the form of an aldehyde (sugar is called *aldose*) or ketone (sugar is called *ketose*). For example, glucose is an aldose, while fructose is a ketose. Carbohydrates, such as starch and cellulose, are polymers composed of monomers called *monosaccharides* or *simple sugars*. Specific examples of pentoses (containing five-carbon atoms), D-*ribose*, D-*arabinose*, and hexoses (containing six-carbon atoms), and D-*glucose* and D-*fructose* (found in honey and fruit) are shown in Fig. 6.9.

6.4.2.1 Stereochemistry of Sugars

The number of optical isomers each sugar may have depends on the number of *chiral* centers or asymmetric carbon atoms. It turns out that there are 2^n possible different stereochemical forms, where n represents the number of chiral centers. For example, glyceraldehyde has one chiral center and two optical isomers: D and L forms (Fig. 6.10). On the other hand, glucose has four chiral centers and 16 optical isomers that differ in their ability to rotate plane-polarized light. The mirror-image forms of a pair of enantiomers will rotate the plane-polarized light in opposite directions to the same extent but, have identical properties. If we invert the stereochemistry of one of
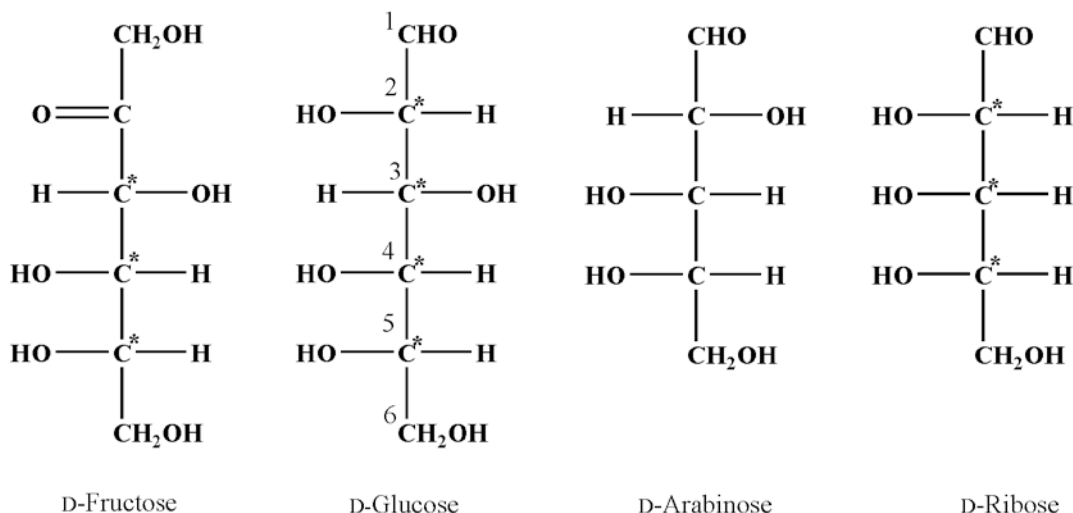
Fig. 6.9 Most important carbohydrates, such as starch and cellulose, are polymers composed of monomers called *monosaccharides*, or simple sugars; *pentoses* (such as arabinose and ribose) contain five-carbon atoms, while *hexoses* (such as fructose and glucose) contain six-carbon atoms
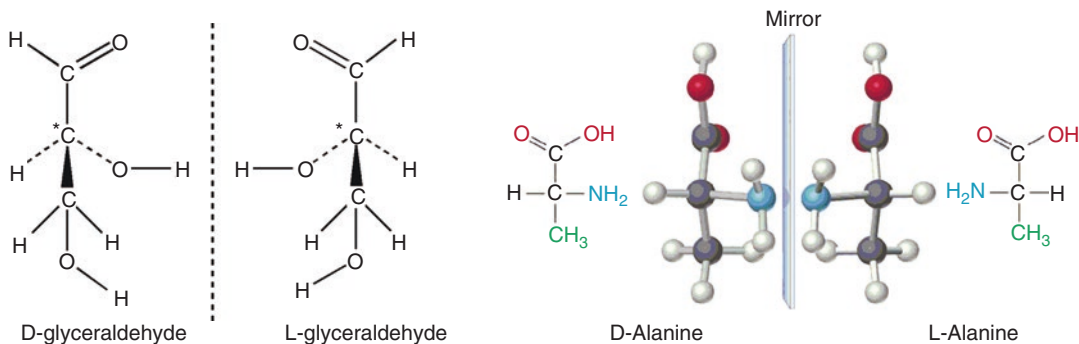
Fig. 6.10 A carbon atom with four different groups (also known as asymmetric carbon) bonded to it in a tetrahedral arrangement gives rise to a pair of *optical isomers* that are *nonsuperimposable*. The D, L forms are based on glyceraldehyde. Similar optical isomers also exist with amino acids

the chiral centers, the chemical properties also change. Compounds like glucose and mannose that differ by the inversion of only one optical center are called *diastereomers*.

The absolute configuration, designated by D- or L-, depends on the sugar's relationship to glyceraldehyde. In some sugar, if the terminus most remote from the carbonyl group has the D-configuration of glyceraldehyde, then that sugar is also called D-form. For example, the 5-carbon in D-glucose and D-fructose has the same configuration as the D-glyceraldehyde. However, in terms of optical rotation, glucose D-glucose is dextrorotatory (D or (+)), while D-fructose is levorotatory (L or (−)).

Simple sugars in solution, usually *cyclize*, or form a ring structure due to the creation of a new bond between the oxygen atom of the terminal hydroxyl group and the carbon of the aldehyde or ketone group. The cyclization of glucose resulting in the formation of a *hemiacetal* will have two different rings, designated as α and β forms, which differ in the orientation of the hydroxy group and hydrogen atom on 1-carbon, as shown in Fig. 6.11.

Polysaccharides

More complex carbohydrates are formed by combining simple sugars. For example, sucrose, common table sugar, is a *disaccharide* formed from glucose and fructose by elimination of water to form a C–O–C bond between the rings, which is called a *glycoside linkage*. Another

disaccharide is lactose of milk sugar, which is a combination of glucose and galactose. Most of the carbohydrates in nature are polymers of repeating sugar units, called *polysaccharides* such as *starch*, *cellulose*, and *glycogen*. They are polymers of glucose (300–3000 units) that yield only glucose upon hydrolysis. These polymers differ from each other in the nature of glycoside linkage, the amount of branching, and molecular weight.

Sugar Derivatives

Carboxylic acid derivatives of glucose are quite common. If the C-1 aldehyde group is oxidized to a carboxyl group, the acid formed is called *gluconic acid*. On the other hand, if the C-6 hydroxy group is oxidized to a carboxyl group, *glucuronic acid* results. In vivo, the nonpolar drug metabolites are converted to polar metabolites by linking glucuronic acid, via a hydroxyl group. Such metabolites are called *glucuronides*. One of the most popular analogs of glucose, used in nuclear medicine, is glucoheptanoic acid, which is a C-7 homologue of glucose.

6.4.3 Lipids

Lipids have widely variable chemical structures but, a common nonpolar nature. They are defined as water-insoluble substances. The lipids found in the human body can be divided into four different classes according to their molecular struc-

α- **D- glucose**　　　　　　　　　　β- **D- glucose**
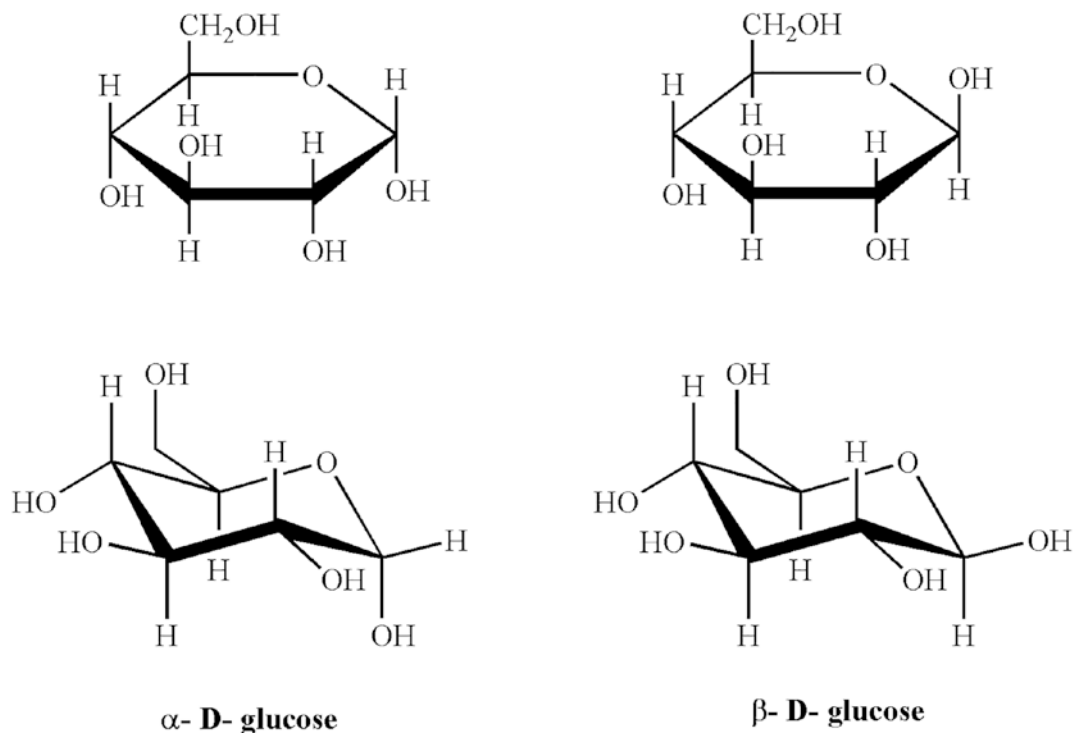
Fig. 6.11 The cyclization of glucose. Two different rings are possible; the two different forms designated as α and β differ in the orientation of H and OH groups on C-1. The structural arrangement of atoms can be shown in the cyclohexane ring form (*top*) or the chair cyclohexane ring form (*bottom*)

ture: *fats*, *phospholipids*, *waxes*, and *steroids*. Fats and phospholipids are derived from trihydroxy alcohol, *glycerol* and *fatty acids*, while waxes are derived from monohydroxy alcohol and fatty acids. Steroids are derived from C_{30} compounds or *triterpenes*.

6.4.3.1 Fats

The most common fats in meats and the milk butterfat are esters made when glycerol reacts with long-chain carboxylic acids or *fatty acids*. Fats that are esters of glycerol are called triglycerides where the fatty acids may be saturated or unsaturated. Naturally occurring fatty acids (Table 6.6) are monocarboxylic acids that are unbranched and contain an even number of carbon atoms.

In a process called *saponification*, fats are heated in the presence of an alkali (such as NaOH and KOH) to hydrolyze the ester and produce glycerol and salts of fatty acids (also known as *soaps*). The sparingly soluble salts of fatty acids, when dispersed in water, form *micelles* that are aggregates of fatty acid anions, which have nonpolar tails in the interior, while the polar anionic heads point outward to interact with the water molecules.

6.4.3.2 Phospholipids

Phospholipids are also esters of glycerol. However, unlike fats, phospholipids contain only two fatty acids, while the third ester linkage involves a phosphate group. The simplest form is phosphatidic acid, a major constituent of membranes. This molecule has a central asymmetric atom and can have a L or D configuration. It is the L-phosphatidic acid form which occurs naturally. Further, substitution on the phosphate group by molecules such as choline, ethanolamine, and inositol will produce phospholipids derivatives, which are constituents of specialized membranes. One of the important phospholipids is L-*phosphatidylcholine* (*lecithin*).

Table 6.6 Common fatty acids

Fatty acid	Molecular formula	Structural formula
Saturated fatty acids		
Butyric acid	$C_4H_8O_2$	$CH_3(CH_2)_2–COOH$
Caproic acid	$C_6H_{12}O_2$	$CH_3(CH_2)_4–COOH$
Lauric acid	$C_{12}H_{24}O_2$	$CH_3(CH_2)_{10}–COOH$
Palmitic acid	$C_{16}H_{32}O_2$	$CH_3(CH_2)_{14}–COOH$
Stearic acid	$C_{18}H_{36}O_2$	$CH_3(CH_2)_{16}–COOH$
Arachidic acid	$C_{20}H_{40}O_2$	$CH_3(CH_2)_{18}–COOH$
Unsaturated fatty acids		
Oleic acid	$C_{18}H_{34}O_2$	$CH_3(CH_2)_7CH=CH(CH_2)_7–COOH$
Linoleic acid	$C_{18}H_{32}O_2$	$CH_3(CH_2)_4CH=CH–CH_2–CH=CH(CH_2)_7–COOH$
Linolenic acid	$C_{18}H_{30}O_2$	$CH_3CH_2CH=CH–CH_2–CH=CH–CH_2–CH=CH(CH_2)_7–COOH$
Arachidonic acid	$C_{20}H_{30}O_2$	$CH_3(CH_2)_4CH=CH–CH_2–CH=CH–CH_2–CH=CH–CH_2–$ $CH=CH(CH_2)_3–COOH$
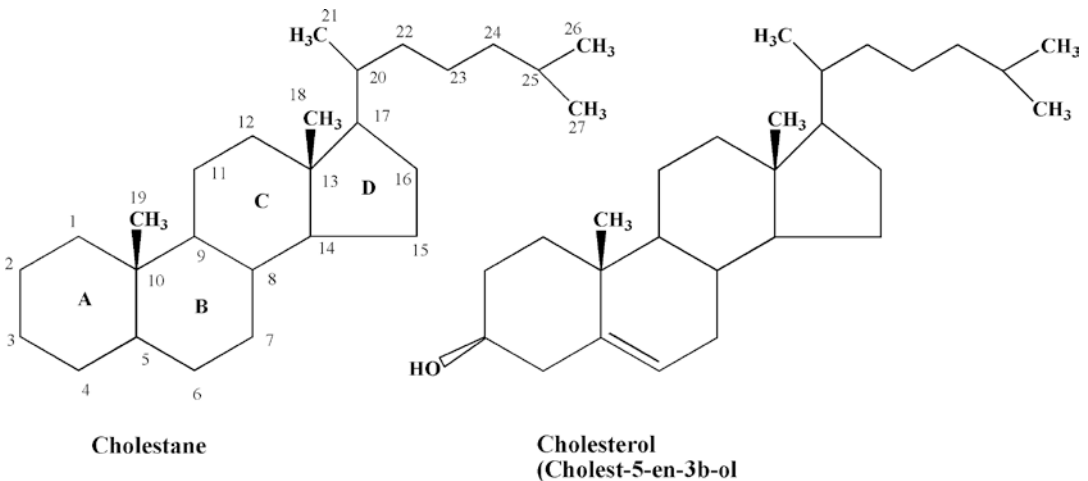
Fig. 6.12 The structure of steroids can be illustrated based on a completely saturated 27 carbon compound, cholestane while cholesterol is an unsaturated steroid alcohol, derived from cholestane

The phospholipids have two distinct parts: the long nonpolar tail and the polar substituted phosphate head. Because of this dual nature, phospholipids tend to form bilayers in aqueous solution, similar to micelles, described above. The bilayers of larger phospholipids can close to form *vesicles*. According to *the fluid mosaic model* of cell membranes, small uncharged molecules (such as H_2O, O_2, CO_2) can diffuse through the membrane, while other molecules pass through special *channels* and *transporters* provided by special proteins embedded in the cell membranes.

6.4.3.3 Steroids

Steroids are a class of lipids that have a characteristic ring structure consisting of four fused rings. Steroids include four major groups: cholesterol, adrenocorticoid hormones (such as cortisol and aldosterone), sex hormones (such as testosterone and estradiol), and bile acids. The simplest completely saturated compound is cholestane, which consists of 27 carbons, 17 of which constitute the ring system (Fig. 6.12), and three substituent groups; two methyl groups attached at C 10 and 13 and 8-carbon alkyl group at C 18 of the ring.

The biosynthesis of cholesterol starts with *lanosterol*, a 30-carbon steroid, first made from the triterpene, *squalene*. The liver synthesizes cholesterol and also disposes of it by transforming it into bile. In plasma, most of the cholesterol is conjugated to fatty acids by an ester linkage to the 3-hydroxyl group. Cholesterol also serves as a *precursor* for the formation of bile acids, steroid hormones, and vitamin D. The 21-carbon adrenocorticoid hormones are synthesized in the adrenal gland. *Aldosterone* is involved in the regulation of water and the electrolyte balance in body fluids, while *cortisol* is primarily involved in the regulation of protein and carbohydrate metabolism. The 19-carbon male sex hormone (*androgens*) *testosterone* is synthesized in the testes and adrenal cortex, but subsequently reduced to dihydrotestosterone in the prostate gland. There are two types of female sex hor-

mones; 21-carbon progesterone is produced by the corpus luteum and placenta, while the 18-carbon estrogens (17β-estradiol and estrone) are produced in the ovaries. Only in estrogens is the A ring benzene-like or aromatic. Steroids are relatively nonpolar and in plasma they are solubilized by binding to transport proteins. The structures of steroid sex hormones are shown in Fig. 6.13.

6.4.4   Nucleic Acids

The ability of cells to maintain a high degree of order depends on the hereditary or genetic information that is stored in a polymer called *deoxyribonucleic acid* (DNA). Within the nucleus of all mammalian cells, a full complement of genetic information is stored, and the entire DNA is
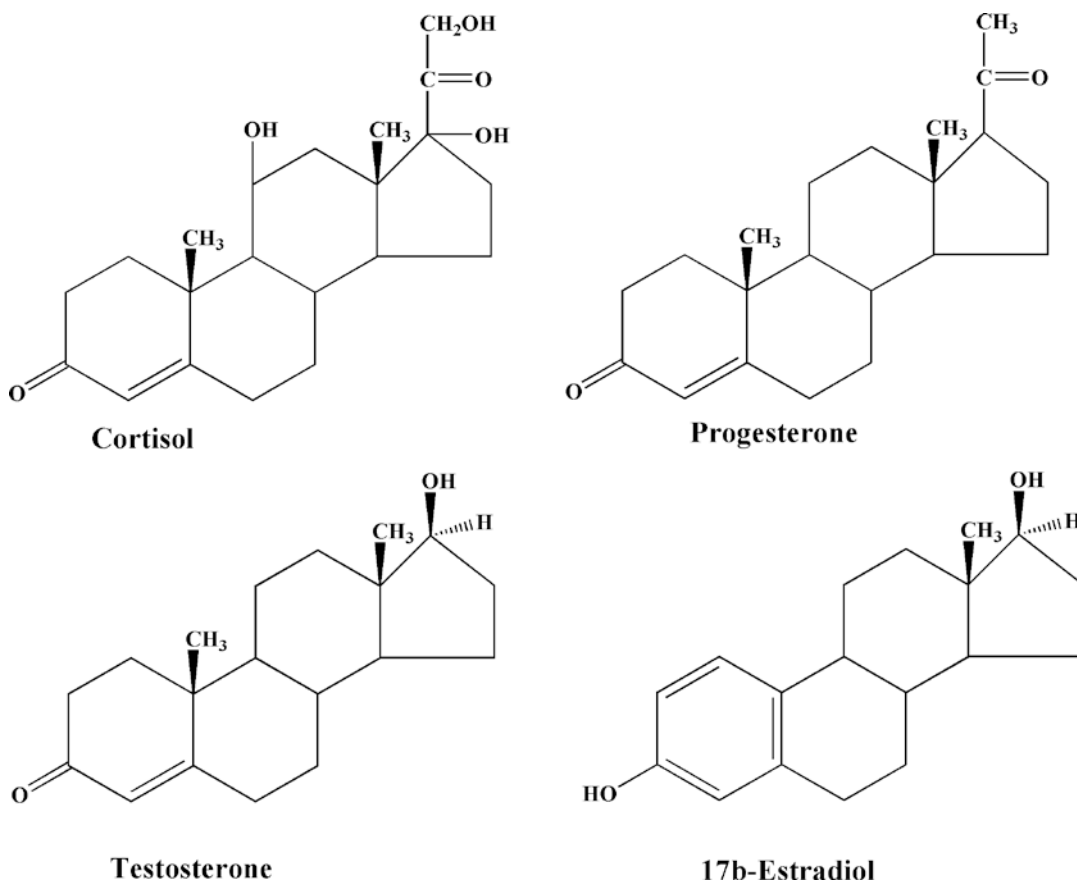
Fig. 6.13   The most common steroids hormones

packaged into 23 pairs of *chromosomes*. A chromosome is formed from a single enormously long DNA molecule that consists of many small subsets called *genes* that represent a specific combination of DNA sequence, designed for a specific cellular function.

The chromosomes can undergo *self-replication* that permits DNA to make copies of itself. More specifically, as the cell divides and transfers the DNA (23 pairs of chromosomes) to daughter cells, which inherit every property and characteristic of the original cell. There are approximately 30,000 genes per human genome and the genes control every aspect of cellular function, primarily through protein synthesis. The sequence of amino acids in a particular protein or enzyme is encoded in a specific gene. The central dogma of molecular biology is that the overall process of information transfer in the cell involves the *transcription* of DNA into *ribonucleic acids* (RNA) molecules, which are much smaller than DNA and found in the cytoplasm. Subsequently, RNA is responsible for generating specific proteins on ribosomes by a process known as *translation*.

A major characteristic of DNA is its ability to encode an enormous quantity of biological information. Only a few picograms (10^{-12} g) of DNA are sufficient to direct synthesis of as many as 100,000 distinct proteins within a cell. This supreme coding effectiveness of DNA is due to its unique chemical structure.

6.4.4.1 DNA Structure

DNA was first discovered in 1869 by the chemist Friedrich Miescher who extracted a white substance from the cell nuclei of human pus and called it *nuclein*. Since nuclein is slightly acidic, it is known as nucleic acid. In the 1920s, the biochemist P.A. Levine identified that there are two sorts of nucleic acids: DNA and RNA. Both DNA and RNA are *polynucleotide molecules* formed by the polymerization of nucleotides. Each nucleotide molecule is composed of three basic elements: a phosphate group, a five-carbon sugar, *deoxyribose* (in DNA) or *ribose* (in RNA), and one of the five types of nitrogen-containing organic bases (Fig. 6.14). Three of the bases,

cytosine (C), *thymine* (T), and *uracil* (U), are called *pyrimidines*, while the other two bases, *adenine* (A) and *guanine* (G), are called *purines*. Of the five bases, thymine is present only in DNA, while uracil is present only in RNA. The base and the sugar combine to form a unit called *nucleoside* by the elimination of one water molecule. The nucleoside in turn reacts with a phosphate group to form a unit called, nucleotide (Fig. 6.15), which is an ester. The nucleotides become connected through condensation reactions that eliminate water to give a polymer, which may contain billions of nucleotides in a single DNA molecule with a molecular weight as high as several billion grams per mole. In contrast, RNA molecules are small with molecular weights of 20,000–40,000.

The presence of 5′-phosphate and the 3′-hydroxyl groups in the deoxyribose molecule allows the DNA to form a long chain of polynucleotides by the joining of nucleotides by phosphodiester bonds (Fig. 6.16). Any linear strand of DNA will always have a free 5′-phosphate group at one end and a free 3′-hydroxyl group at the other end. Therefore, the DNA molecule has an intrinsic directionality (5′–3′ direction).

Although some forms of cellular DNA exist as single-stranded structures, the most widespread DNA structure, discovered by Watson and Crick in 1953, represents DNA as a double helix containing two polynucleotide strands that are complementary mirror images of each other. The "backbone" of the DNA molecule is composed of deoxyribose sugars joined by phosphodiester bonds to phosphate group, while the bases are linked in the middle of the molecule by hydrogen bonds. The relationship between bases in the double helix is described as complementarity since adenine always bonds with thymine, and guanine always bonds with cytosine. As a consequence, the double-stranded DNA contains equal amounts of purines and pyrimidines. An important structural characteristic of the double-stranded DNA is that its strands are antiparallel meaning that the two strands are aligned in opposite directions. During cell division, the two strands of DNA unwind, and new complementary strands are generated.

Cytosine   Uracil   Thymine

Adenine   Guanine
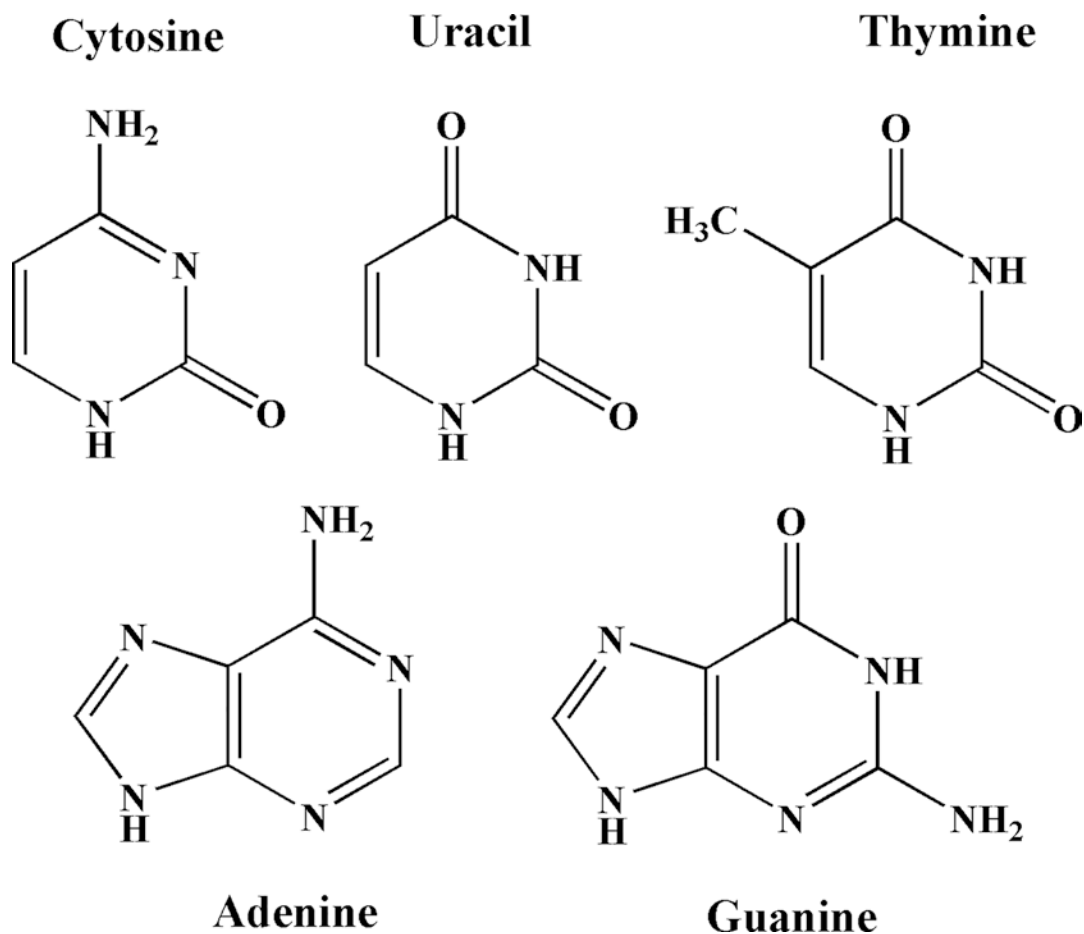
Fig. 6.14 The organic bases found in DNA and RNA. Thymidine is present only in DNA, while uracil is present only in RNA

Deoxyribosenucleotide
Thymine + Deoxyribose + Phosphate

Ribosenucleotide
Uracil + Ribose + Phosphate
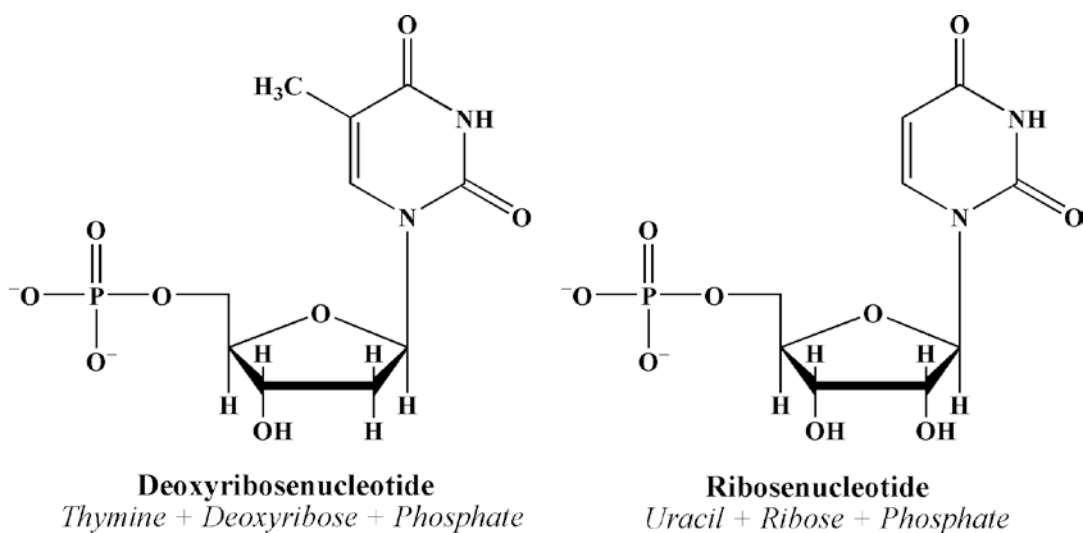
Fig. 6.15 The monomers of *nucleic acids* (DNA and RNA) are called *nucleotides*, which are composed of an organic base, a five-carbon sugar, and a phosphoric acid molecule
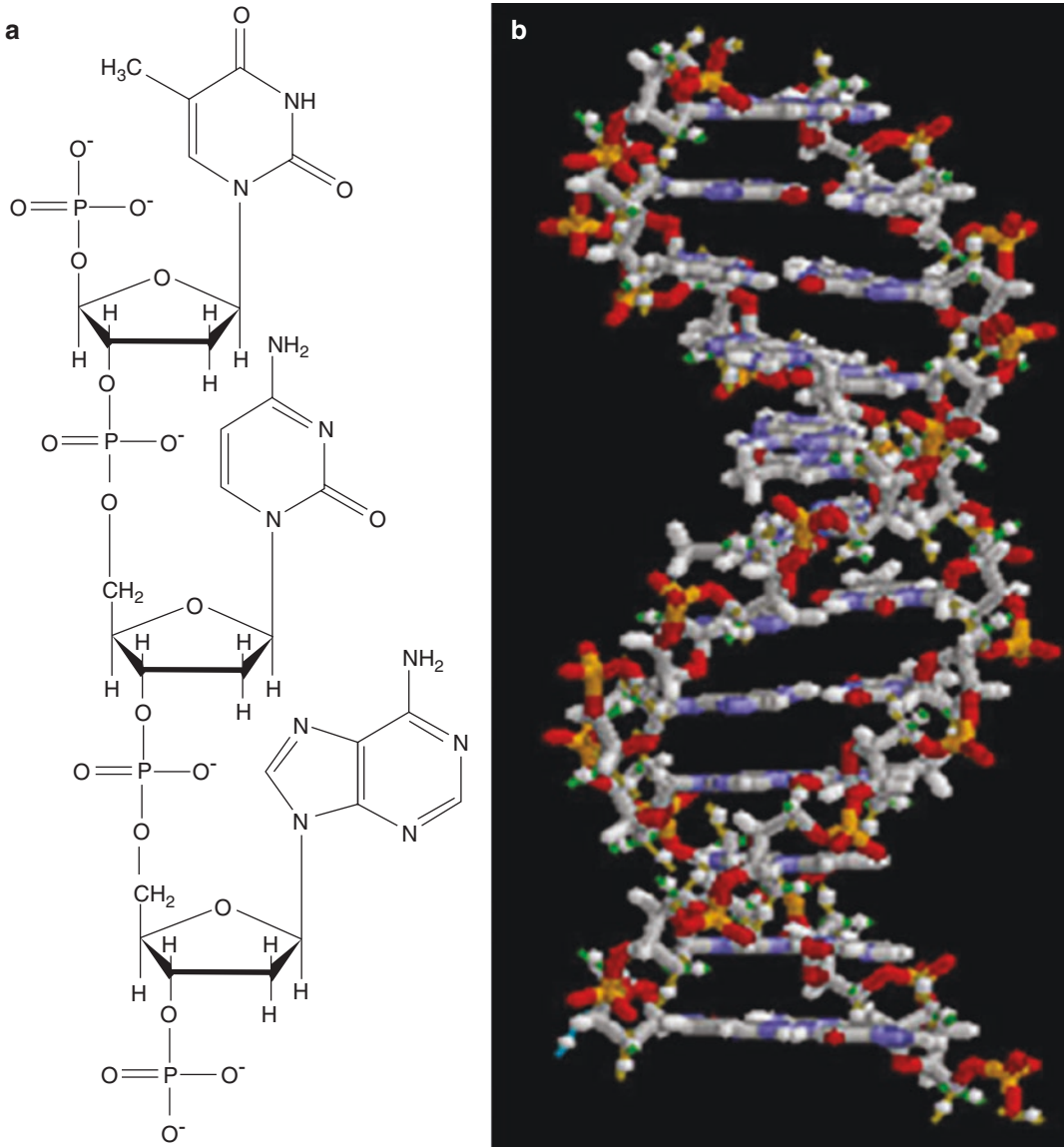
Fig. 6.16 In a DNA molecule (**a**), the nucleotides become connected through condensation reactions to form a polymer, which may contain a billion units. DNA molecule, however, is a double-helical structure (**b**) with complementary bases on the two strands that are connected by the bases, which form hydrogen bonds to each other

6.4.4.2 Protein Synthesis

A given segment of DNA is called *gene*, which contains the code, the specific sequence of amino acids for a specific protein. The code is specific for each amino acid and consists of a set of three bases called a *codon* (Table 6.6). Gene expression involves the synthesis of a specific protein. This process is initiated by building a special RNA molecule, called *messenger RNA* (mRNA), in the nucleus from an appropriate gene. mRNA migrates into the cytoplasm where the protein is synthesized. Small RNA fragments, called *transfer RNA* (tRNA), containing only 75–80 nucleotides, decode the genetic message from the mRNA, using a complementary triplet of bases called an *anticodon*. mRNA builds the protein

with the assistance of a ribosome. The tRNA molecule brings an appropriate amino acid to the mRNA. Soon after the codon and anticodon match, another tRNA, with its specific amino acid, moves to the second codon position. Once the two amino acids join together by peptide linkage, tRNA breaks away from its position. The process is repeated until the synthesis of protein is completed. The number of protein molecules synthesized by each cell, however, depends on the degree of gene expression that is warranted by the cell and the number of RNA molecules within the cytoplasm.

Further Reading

Billinghurst MW, Fritzberg AR. Chemistry for nuclear medicine. Chicago, IL: Yearbook Medical; 1981.
Zumdahl SS. Chemical principles. 3rd ed. Boston, MA: Houghton Mifflin; 1998.

Almost all aspects of life are engineered at the molecular level, and without understanding molecules we can only have a very sketchy understanding of life itself. (Francis Harry Compton Crick)

7.1 Introduction

The cell is the basic unit of life in all forms of living organisms, from the smallest bacterium to the most complex animal. On the basis of microscopic and biochemical differences, living cells are divided into two major classes: *prokaryotes*, which include bacteria, blue–green algae, and rickettsiae, and *eukaryotes*, which include yeasts, and plant and animal cells. Eukaryotic cells are far more complex internally than their bacterial ancestors and the cells are organized into compartments or *organelles*, each delineated by a membrane. The DNA of the cell is packaged with protein into compact units called *chromosomes* that are located within a separate organelle, the *nucleus*. In addition, all eukaryotic cells have an internal skeleton, the *cytoskeleton* of protein filaments that gives the cell its shape, and its ability to arrange its organelles and provides the machinery for the movement.

The entire human body contains about 100 trillion cells, which are generated by repeated division from a single precursor cell. As proliferation continues, some of the cells become *differentiated* from others, adopting a different structure, chemistry, and function. In the human body, more than 200 distinct *cell types* are assembled into a variety of types of tissues, such as epithelia, connective tissue, muscle, and nervous tissue. Each organ in the body is an aggregate of many different cells held together by intercellular supporting structures. Although the many cells of the body often differ markedly from one another, all of them have certain common basic characteristics. Each cell is a complex structure whose purpose is to maintain an intracellular environment favorable for complex metabolic reactions, to reproduce it when necessary, and to protect itself from the hazards of its surrounding environment.

7.2 Cell Structure and Function

The different substances that make up the cell are collectively called *protoplasm*, which is composed mainly of water, electrolytes, proteins, lipids, and carbohydrates. The two major parts of the cell (Fig. 7.1) are the *nucleus* and the *cytoplasm*. The nucleus is separated from the cytoplasm by a nuclear membrane, while the cytoplasm is separated from the extracellular fluid (ECF) by a cell membrane. The major organelles in the cell are of three general types: organelles derived from membranes, organelles involved in gene expression, and organelles involved in energy produc-
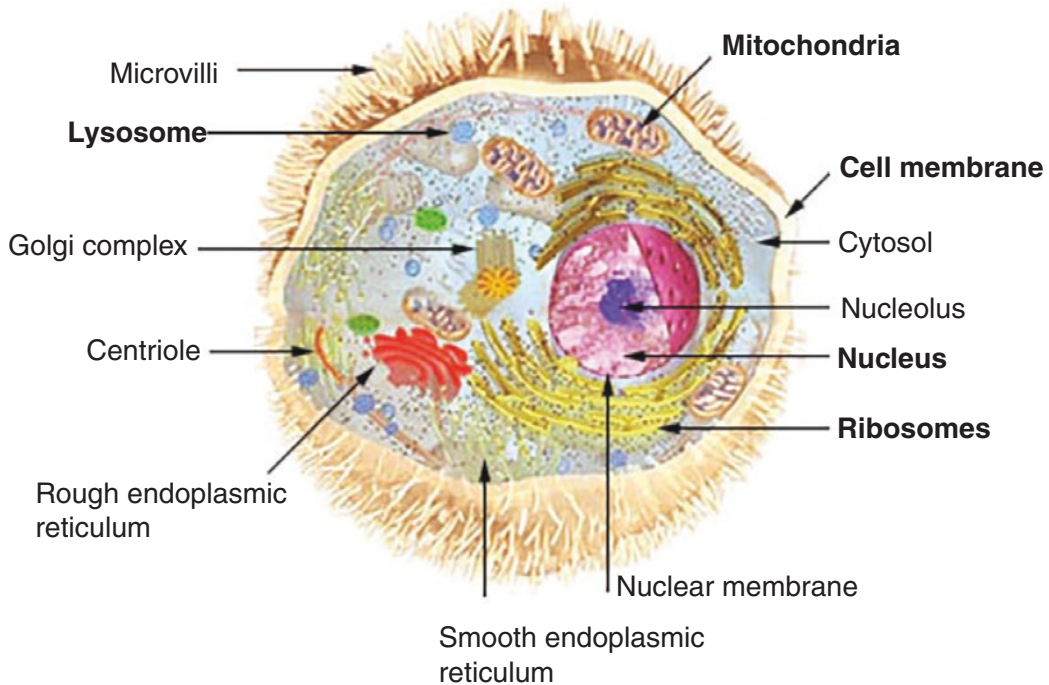
Fig. 7.1 A schematic drawing of an animal cell clearly depicting an intricate network of interconnecting, intracellular membrane structures such as the mitochondria, the nucleus, lysosomes, and the endoplasmic rough and smooth reticulum (facstaff.gpc.edu/~jaliff/anacell.htm)

tion. The important subcellular structures of the cell and their functions are summarized in Table 7.1.

7.2.1   The Plasma Membrane

The plasma membrane encloses the cell, defines its boundaries, and maintains the essential difference between the cytosol and the extracellular environment. The cell membrane is an organized sea of lipid in a fluid state, a nonaqueous dynamic compartment of cells. The cell membranes are assembled from four major components: a lipid bilayer, membrane proteins, sugar residues, and a network of supporting fibers.

The basic structure of a cell membrane is a lipid bilayer of phospholipid molecules. The fatty acid portions of both the molecules are hydrophobic and occupy the center of the membrane, while the hydrophilic phosphate portions form the two surfaces in contact with intracellular fluid (ICF) and ECF. This lipid bilayer of 7–10 nm thickness is a major barrier impermeable to water-soluble molecules, such as ions, glucose, and urea. The three major classes of membrane lipid molecules are phospholipids (phosphatidylcholine, phosphatidylserine, phosphatidylethanolamine, sphingomyelin), cholesterol, and glycolipids. The lipid composition of different biological membranes varies depending on a specific function of the cell or cell membrane, as summarized in Table 7.2.

The cell surface often has a loose carbohydrate coat called *glycocalyx*. The sugar residues generally occur in combination with proteins (glycoproteins, proteoglycans) or lipids (glycolipids). The oligosaccharide side chains are generally negatively charged and provide the cell with an overall negative surface charge. While some carbohydrates act as receptors for binding hormones, like insulin, others may be involved in immune reactions and cell–cell adhesion events.

Table 7.1 Cell structures (compartments) and their function

Cell structure	Major functions
Plasma membrane	Cell morphology and movement, transport of ions and molecules, cell-to-cell recognition, cell surface receptors
Endoplasmic reticulum	Formation of compartments and vesicles, membrane synthesis, synthesis of proteins and lipids, detoxification reactions
Lysosomes	Digestion of worn-out mitochondria and cell debris, hydrolysis of proteins, carbohydrates, lipids, and nucleic acids
Peroxisomes	Oxidative reactions involving molecular oxygen, utilization of hydrogen peroxide (H_2O_2)
Golgi complex	Modification and sorting of proteins for incorporation into organelles and for export, forms secretory vesicles
Microbodies	Isolation of particular chemical activities from the rest of the cell body
Mitochondria	Cellular respiration, oxidation of carbohydrates, proteins, and lipids, synthesis of urea and heme
Nucleus	DNA synthesis and repair, RNA synthesis, control center of the cell, directs protein synthesis and reproduction
Chromosomes	Contain hereditary information in the form of genes
Nucleolus	RNA processing; assembling ribosomes
Ribosomes	Sites of protein synthesis in cytoplasm
Cytoplasm	Metabolism of carbohydrates, lipids, amino acids, and nucleotides
Cytoskeleton	Structural support, cell movement, cell morphology

Table 7.2 The specific functions of the cell membrane components

Component	Composition	Function	How it works	Example
Lipid	Phospholipid bilayer	Permeability barrier	Polar molecules excluded	Glucose
Transmembrane protein	Channels	Passive transport	Creates a tunnel	Na^+, K^+ ions
	Carrier or transporters	Facilitated diffusion	Carrier "flip-flops"	Glucose transport
	Receptors	Transmits information into cell	Following receptor binding, induce activity in the cell	Peptide hormones, Neurotransmitters
Cell surface markers	Glycoprotein (GP)	"Self"-recognition	Shape of GP is characteristic of a cell or tissue	Major histocompatibility complex recognized by immune system
	Glycolipid	Tissue recognition	Shape of carbohydrate chain is characteristic of tissue	A, B, O blood group markers
Interior Protein network	Clathrins	Anchor certain proteins to specific sites	Form network above the membrane to which proteins are anchored	Localization of LDL receptor within coated pits
	Spectrin	Determines cell shape	Forms supporting scaffold by binding to both membrane and cytoskeleton	Red blood cell

The proteins of the membrane are responsible for most membrane functions, such as transport channels, pumps, carriers or transporters, specific receptors, enzymes, cell identity, and cell adhesion. The membrane proteins can be associated with the lipid bilayer in various ways, depending on the function of the protein. The polypeptide chain may extend across the lipid bilayer (transmembrane proteins) or simply be attached to one or the other side of the membrane.

7.2.2   Cytoplasm and Its Organelles

Cytoplasm or *cytosol* is an aqueous solution that fills the cytoplasmic matrix, the space between the nuclear envelope and the cell membrane. The cytosol contains many dissolved proteins, electrolytes, glucose, certain lipid compounds, and thousands of enzymes. In addition, glycogen granules, neutral fat globules, ribosomes, and secretory granules are dispersed throughout the cytosol. Many chemical reactions of metabolism occur in the cytosol where substrates and cofactors interact with various enzymes. The various organelles (Table 7.1) suspended in the cytosol are either surrounded by membranes (nucleus, mitochondria, and lysosomes) or derived from membranous structures (endoplasmic reticulum, Golgi apparatus). Within the cell, these membranes interact as an endomembrane system by being in contact, giving rise to one another, or passing tiny membrane-bound sacs called *vesicles* to one another. All biological membranes are phospholipid bilayers with embedded proteins. The chemical composition of lipids and proteins in membranes varies depending on a specific function of an organelle or a specific cell in a tissue or an organ.

7.2.2.1   The Endoplasmic Reticulum

The cytoplasm contains an interconnecting network of tubular and flat membranous vesicular structures called the *endoplasmic reticulum* (ER). Like the cell membrane, walls of the ER are composed of a lipid bilayer containing many proteins and enzymes. The regions of the ER rich in ribosomes are termed rough or granular ER, while the regions of the ER with relatively few ribosomes are called smooth or agranular ER. *Ribosomes* are large molecular aggregates of protein and ribonucleic acid (RNA) that are involved in the manufacture of various proteins by translating the messenger RNA (mRNA) copies of genes. Subsequently, the newly synthesized proteins (hormones and enzymes) are incorporated into other organelles (Golgi complex, lysosomes) or transported or exported to other target areas outside the cell. Enzymes anchored within the smooth ER catalyze the synthesis of a variety of lipids and carbohydrates. Many of these enzyme systems are involved in the biosynthesis of steroid hormones and in the detoxification of a variety of substances.

7.2.2.2   The Golgi Complex

The *Golgi complex* or apparatus is a network of flattened, smooth membranes, and vesicles. It is the delivery system of the cell. It collects, packages, modifies, and distributes molecules within the cell or secretes the molecules to the external environment. Within the Golgi bodies, the proteins and lipids synthesized by the ER are converted to glycoproteins and glycolipids and collected in membranous folds or vesicles called cisternae, which subsequently moves to various locations within the cell. In a highly secretory cell, the vesicles diffuse to the cell membrane and then fuse with it and empty their contents to the exterior by a mechanism called *exocytosis*. The Golgi apparatus is also involved in the formation of intracellular organelles, such as lysosomes and peroxisomes.

7.2.2.3   Lysosomes

Lysosomes are small vesicles (0.2–0.5 μm), formed by the Golgi complex and have a single limiting membrane. Lysosomes maintain an acidic matrix (pH 5 and below) and contain a group of glycoprotein digestive enzymes (hydrolases) that catalyze the rapid breakdown of proteins, nucleic acids, lipids, and carbohydrates into small basic building molecules. The enzyme content within lysosomes varies and depends on the specific needs of an individual tissue. Through a process of endocytosis, a number of cells either remove extracellular particles (phagocytosis), such as microorganisms, or engulf ECF with the unwanted substances (pinocytosis). Subsequently, the lysosomes fuse with the endocytotic vesicles and form secondary lysosomes or digestive vacuoles. Products of lysosomal digestion are either reutilized by the cell or removed from the cell by exocytosis. Throughout the lives of cells, lysosomes break down the organelles and recycle their component proteins and other molecules at

a fairly constant rate. However, in metabolically inactive cells, the hydrolases digest the lysosomal membrane and release the enzymes resulting in the digestion of the entire cell. By contrast, metabolically inactive bacteria do not die, since they do not possess lysosomes. Programmed cell death (apoptosis) or selective cell death is one of the principal mechanisms involved in the removal of unwanted cells and tissues in the body. In this process, lysosomes release the hydrolytic enzymes into the cytoplasm to digest the entire cell.

7.2.2.4 Peroxisomes

Peroxisomes are small membrane-bound vesicles or microbodies (0.2–0.5 μm), derived from the ER or Golgi apparatus. Many of the enzymes within the peroxisomes are oxidative enzymes that generate or utilize hydrogen peroxide (H_2O_2). Some enzymes produce hydrogen peroxide by oxidizing D-amino acids, uric acid, and various 2-hydroxy acids using molecular oxygen, while other enzymes, such as catalase, convert hydrogen peroxide to water and oxygen. Peroxisomes are also involved in the oxidative metabolism of long-chain fatty acids and different tissues contain different complements of enzymes depending on the cellular conditions.

7.2.2.5 Mitochondria

Mitochondria are tubular or sausage-shaped organelles (1–3 μm). They are composed mainly of two lipid bilayer-protein membranes. The outer membrane is smooth and derived from the ER. The inner membrane contains many infoldings or shelves called *cristae* which partition the mitochondrion into an inner matrix called *mitosol* and an outer compartment. The outer membrane is relatively permeable but the inner membrane is highly selective and contains different transporters. The inner membrane contains various proteins and enzymes necessary for oxidative metabolism, while the matrix contains dissolved enzymes necessary to extract energy from nutrients. Mitochondria contain a specific DNA. However, the genes that encode the enzymes for oxidative phos-

phorylation and mitochondrial division have been transferred to the chromosomes in the nucleus. The cell does not produce brand new mitochondria each time the cell divides. Instead, mitochondria are self-replicative. Each mitochondrion divides into two and these are partitioned between the new cells. The mitochondrial reproduction, however, is not autonomous and is controlled by the cellular genome. The total number of mitochondria per cell depends on the specific energy requirements of the cell and may vary from less than 100 to up to several thousand. Mitochondria are called the "power-houses" of the cell, where oxidative phosphorylation of various substrates derived from glucose and fatty acid enter the Krebs cycle to generate ATP molecules.

7.2.2.6 Ribosomes

Ribosomes are large complexes of RNA and protein molecules and are normally attached to the outer surfaces of endoplasmic reticulum. The major function of ribosomes is to synthesize proteins. Each ribosome is composed of one large and one small subunit, with a mass of several million daltons.

7.2.3   Cytoskeleton

The cytoplasm contains a network of protein fibers called cytoskeleton that provides a shape to the cell and anchors various organelles suspended in cytosol. The fibers of the cytoskeleton are made up of different proteins of different sizes and shapes, such as actin (actin filaments), tubulin (microtubules), vimentin, and keratin (intermediate filaments). The exact composition of the cytoskeleton varies depending on the cell type and function. Centrioles are small organelles that occur in pairs within the cytoplasm, usually located near the nuclear envelope, and are involved in the organization of microtubules. Each centriole is composed of nine triplets of microtubules (long hollow cylinders of about 25 nm length) and plays a major role during cell division.

7.2.4   Nucleus

The nucleus is the largest membrane-bound organelle in the cell and occupies about 10% of the total cell volume. The nucleus is composed of a double membrane called *nuclear envelope* that encloses the fluid-filled interior called *nucleoplasm*. The outer membrane is contiguous with the ER. The nuclear envelope has numerous pores called nuclear pores which are about 90 Å in diameter and 50–80 nm apart and permit certain molecules to pass into and out of the nucleus.

The primary functions of the nucleus are cell division and the control of the phenotypic expression of genetic information that directs all of the activities of a living cell. The cellular DNA is located in the nucleus as DNA–histone protein complex known as *chromatin* that is organized into *chromosomes*. The total genetic information stored in the chromosomes of an organism is said to constitute its *genome*. The human genome consists of 24 chromosomes (22 different chromosomes and two different sex chromosomes) and contains about 3×10^9 nucleotide pairs. The smallest unit of DNA that encodes a protein product is called a gene and consists of an ordered sequence of nucleotides located in a particular position on a particular chromosome. There are approximately 30,000 genes per human genome and only a small fraction (15%) of the genome is being actively expressed in any specific cell type. The genetic information is transcribed into RNA, which subsequently is translated into a specific protein on the ribosome. The nucleus contains a subcompartment called *nucleolus* that contains large amounts of RNA and protein. The main function of nucleolus is to form granular subunits of ribosomes, which are transported into the cytoplasm where they play an essential role in the formation of cellular proteins.

7.3   Cell Reproduction

All the cells in the human body are derived from a single cell, the fertilized egg, which undergoes trillions of cell divisions in order to become a new individual human being. Cells reproduce by duplicating their contents and then dividing into two equal halves. The reproduction of a somatic cell involves two sequential phases: *mitosis* (the process of nuclear division) and *cytokinesis* (cell division). In gametes, the nuclear division occurs through a process called *meiosis*. The life cycle of the cell is the period of time from one cell division to the next. The duration of the *cell cycle*, however, varies greatly from one cell type to another and is controlled by the DNA-genetic system.

7.3.1   The Cell Cycle

In all somatic cells, the cell cycle (Fig. 7.2) is broadly divided into the *M phase* (or *mitosis*) and the *interphase* (growth phase). In most cells, the M phase takes only a small fraction of the total cycle, when the cell actually divides. The cell is in *interphase* during the rest of the time, which is subcategorized into three phases: G_1, S, and G_2. During the G_1 phase, most cells continue to grow, until they are committed to divide. If they are not ready to go into the S-phase, they may remain for a long time in a resting state known as G_0, before they are ready to resume proliferation. During the G_2 phase, cells synthesize RNA and proteins and continue to grow until they enter into the M-phase.

The reproduction of the cell really begins in the nucleus itself, where the synthesis and replication of the total cellular genome occur during the S-phase. Every somatic cell is in a diploid phase, where the nucleus contains 23 pairs of chromosomes. Following replication, the nucleus has a total of 46 pairs of chromosomes. The chromosome pairs are attached at a point called *centromere* and are called *chromatids*.

7.3.1.1 Mitosis and Cytokinesis

One of the first events of mitosis takes place in the cytoplasm. A pair of *centrioles* is duplicated just before DNA replication. Toward the end of interphase, the two pairs of centrioles move to the opposite poles of the cell. A complex of *microtu-*

Fig. 7.2 The cell division cycle is generally represented by four successive phases (G1, Synthesis, G2, and Mitosis)
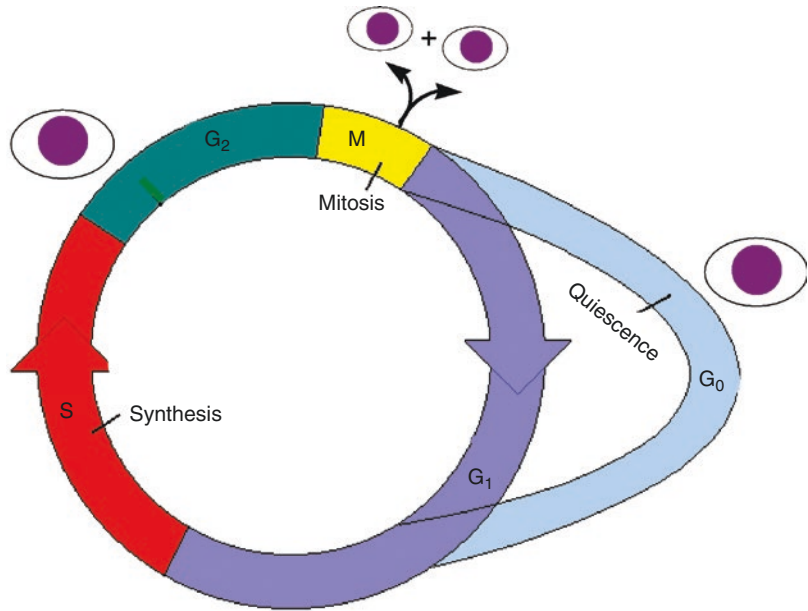
bules (spindle) pushes the centrioles farther apart creating the so-called mitotic apparatus. It is very important to note that mitochondria in the cytoplasm are also replicated before mitosis starts, as they have their own DNA. On the basis of specific events during nuclear division, mitosis is subcategorized into four phases. During the *prophase*, the nuclear envelope breaks down, chromosome condensation continues further, and the centromere of the chromatids is attached to opposite poles of the spindle. During the early *metaphase*, the spindle fibers pull the centromeres to the center forming an equatorial plate. At the end of the metaphase, the centromeres divide the chromatids into equal halves. During the *anaphase*, the sister chromatids are pulled apart, physically separated, and drawn to opposite poles, thus completing the accurate division of the replicated genome. By the end of the anaphase, 23 identical pairs of chromosomes are on the opposite sides of the cell. The *telophase*, the mitotic apparatus is disassembled, the nuclear envelope is reestablished around each group of 23 chromosomes, the nucleolus reappears, and finally the chromosomes begin to uncoil into a more extended form to permit expression of rRNA genes. Cytokinesis is the physical division

of the cytoplasm and the cell into two daughter cells, which inherit the genome as well as the mitochondria.

7.3.2   Rates of Cell Division

For many mammalian cells, the standard cell cycle is generally quite long and may be 12–24 h for fast-growing tissues. Many adult cells, such as nerve cells, lens of the eye, and muscle cells lose their ability to reproduce. Certain epithelial cells of the intestine, lungs, and skin divide continuously and rapidly in less than 10 h. The early embryonic cells do not grow but divide very rapidly with a cell cycle time of less than an hour. In general, the mitosis requires less than an hour, while most of the cell cycle time is spent during the G_1 or G_0 phase. It is possible to estimate the duration of the S-phase by using tracers, such as ^{3}H-thymidine or bromodeoxyuridine (BrdU).

Control system regulating the cell division: The essential processes of cell reproduction such as the DNA replication and the sequence of cell cycle events are governed by a cell cycle control system that is based on two key families of proteins: cyclin-dependent protein *kinases* (Cdk),

and activating proteins called *cyclins*. These two protein complexes regulate the normal cell cycle at the end of the G_1 and G_2 phases. The key component of the control system is a protein kinase known as *M-phase-promoting factor* (MPF), whose activation by phosphorylation drives the cell into mitosis. The mechanisms that the control cell division of mammalian cells in various tissues and organs depend on the social control genes and protein growth factors, as survival of the entire organism is the key, not the proliferation of individual cells. Growth factors, such as *platelet-derived growth factor* (PDGF), *fibroblast growth factor* (FGF), and *interleukin-2*, regulate cell proliferation through a complex network of intracellular signaling cascades, which ultimately regulate gene transcription and the activation of cell cycle control system.

7.4   Cell Transformation and Differentiation

The zygote and blastomeres resulting from the first couple of cleavage divisions are *totipotent*, meaning that they are capable of forming any cell in the body. As the development progresses, certain decisions are made that narrow the developmental options of cells. At the decision point where cells become committed, a restriction event has occurred. The commitment of cells during cleavage to become either inner cell mass or *trophoblast* and the segregation of embryonic cells into the three germ layers are the early restriction events in the mammalian embryo. When a cell has passed its last decision point, its fate is fixed, and it is said to be *determined*. A cell is determined, if it has undergone a self-perpetuating change of internal character that distinguishes it and its progeny from other cells in the embryo and commits them to a specialized course of development. The determined cell may pass through many developmental stages but can-

not move onto another developmental track. For example, a muscle cell cannot become a nerve cell. Restriction and determination signify the progressive limitation of the development capacities in the embryo. Differentiation refers to the actual morphological or functional expression of the portion of genome that remains available to a determined cell or group of cells, and characterizes the phenotypic specialization of cells. Therefore, differentiation is the process of acquiring specific new characteristics resulting in observable changes in cellular function. By contrast, cells within a developing embryo display the least amount of differentiation. In the adult, undifferentiated cells are known as *pluripotent cells*, which are precursor cells or *stem cells* that are not totally committed to a specific function.

The three germ layers *ectoderm*, *mesoderm*, and *endoderm* have different fates. The endoderm forms a tube, the *primordium* of the digestive tract. It gives rise to the pharynx, esophagus, stomach, intestines, and several other associated organs such as liver, pancreas, and lungs. While the endoderm forms the epithelial components of these structures, the supporting muscular and fibrous elements arise from the mesoderm. In general, the mesoderm gives rise to the muscles and connective tissues of the body. The mesoderm first gives rise to *mesenchyme* and ultimately to cartilage, bone, fibrous tissue, and the dermis (the inner layer of the skin). In addition, the tubules of the urogenital system, vascular system, and the blood cells also develop from the mesoderm. The ectoderm forms the epidermis and the entire nervous system. In a process known as *neurulation*, a central portion of the ectoderm creates a neural tube that pinches off from the rest of the ectoderm and will form the brain and spinal cord. Some of the ectodermal cells develop into a *neural crest* and form all of the peripheral nervous system as well as the pigment cells of the skin.

Cells differentiate through several mechanisms. A cell and its progeny may contain suf-

ficient intrinsic information to determine their phenotypic character. Cell differentiation generally depends on changes in gene expression rather than on gene loss, as the genome of a differentiated cell has the entire DNA content of the undifferentiated parent cell. In order to regulate the expression of genes, the most important point of control is the initiation of RNA transcription. These gene regulatory proteins can switch the transcription of individual genes on or off by recognizing short stretches of the DNA double helix of defined sequence and thereby determining which of the thousands of genes in a cell will be transcribed. Each cell may have a specific combination or different combinations of gene regulatory proteins. According to environmental models, cells respond to external signals and differentiate accordingly. For example, after exposure to 5-azacytidine, fibroblasts from a standard tissue culture line differentiate into skeletal muscle, cartilage, or adipose tissue.

7.5   Normal Growth

7.5.1   Cell Types

The human body is an ordered clone of cells, all containing the same genome but specialized in different ways. There are approximately 200 different cell types that represent, for the most part, discrete and distinctly different categories based on histological and morphological characteristics and cellular function. Recent subtler techniques involving immunohistology and mRNA expression are even revealing new subdivisions of cell types within the traditional classification. The different cell types, such as the neuron and lymphocyte, have the same genome, but the structural and functional differences are so extreme

that it is difficult to imagine that they came from the same cell.

Different cell types synthesize different sets of proteins. However, many processes are common to all cells and have many proteins in common. However, some proteins are unique in the specialized cells, in which they function, and cannot be detected anywhere else. The genome of a cell contains in its DNA sequence, the information to make many thousands of different proteins and RNA molecules. A cell typically expresses only a fraction of these genes and the different types of cells in a human body arise because different sets of genes are expressed. Moreover, cells can change the pattern of genes they express in response to signals from other cells or environment. Different cells perform different functions. The most important cellular functions are movement, conductivity, metabolic absorption, secretion, excretion, respiration, and reproduction.

7.5.2   Tissue Types

In the human body, specialized cells of one or more types are organized into cooperative assemblies called *tissues* that perform one or more unique functions. Different types of tissues combine to form organs, which in turn are integrated to perform complex functions.

The major types of tissues are epithelial, muscle, connective, nerve, blood, and lymphoid tissues that are further divided into many subtypes (Table 7.3). All cells are in contact with a network of extracellular macromolecules, known as *extracellular matrix*, that holds cells and tissues together and provides an organized latticework within which cells can migrate and interact with one another.

Table 7.3 Tissue types

Tissue	Tissue type	Location	Function
Epithelial	Simple squamous	Lines major organs	Absorption, filtration, and secretion
	Simple cuboidal	Lines tubules and ducts of glands	Absorption and secretion
	Simple columnar	Lines GI tract	Secretion and absorption
	Stratified Squamous	Lines interior of mouth, tongue, and vagina	Protection
	Transitional	Lines urinary bladder	Permits stretching
Connective	Loose connective Dense connective	Deep layers of skin, blood vessels, and organs Tendons, and ligaments	Support, and elasticity Attaches structures together, and provides strength
	Elastic connective	Lungs, arteries, trachea, and vocal cords	Provides elasticity
	Reticular connective	Spleen, liver, and lymph nodes	Provides internal scaffold for soft organs
	Cartilage	Ends of long bones, trachea, and tip of nose	Provides flexibility and support
	Bone	Bones	Protection, support, and muscle attachment
	Vascular connective tissue	Within blood vessels	Transport of gases, and blood clotting
	Adipose tissue	Deep layers of skin, surrounds heart, and kidney	Support, protection, and heat conservation
Muscle	Smooth muscle	GI tract, uterus, blood vessels, and u. bladder	Propulsion of materials
	Cardiac muscle	Heart	Contraction
	Skeletal muscle	Attached to bones	Movement
Neural	Different types of Neurons	Brain and spinal cord	Conduction of electrical impulse, and neurotransmission

7.6   Cell-to-Cell Communication

Cells in the human body are programmed to communicate with each other and to respond to a specific set of signals in order to regulate their growth, replication, development, and organization into tissues, and coordinate their overall biochemical behavior. Cells communicate with one another in three ways: (a) through physical contact with one another by forming cells junctions, (b) by secreting chemical signaling, molecules that help communication at a distance, and (c) by cellular receptors which bind to specific signaling molecules and respond by generating intracellular messengers.

7.6.1   Cell–Cell Interaction

Cells in tissues are in physical contact with neighboring cells and extracellular matrix at spe-

cialized contact sites, called cell junctions (communicating, occluding, and anchoring), which allow transport of molecules between cells or provide a barrier to passage of molecules between cells. Gap or communicating junctions are composed of clusters of channel proteins that create an intercellular gap (1.5 nm wide) to allow small molecules to pass directly from cell to cell. Cells connected by gap junctions are electrically and chemically coupled, since the cells share ions and small molecules. Occluding or tight junctions exist primarily in epithelial sheets. The tight junctions form a continuous, impermeable, or semipermeable barrier to diffusion and play an important part in maintaining the concentration differences of small hydrophilic molecules across epithelial sheets and restrict the diffusion of membrane transport proteins. Anchoring junctions such as *adherens*, *desmosomes*, and *hemidesmosomes* are most abundant in tissues that are subjected to severe mechanical stress and

connect the cytoskeletal elements (actin or intermediate filaments) of a cell to those of another cell or to the extracellular matrix. To form an anchoring junction, cells must first adhere. Such a selective cell adhesion or tissue-specific recognition process is mediated by two distinct classes of cell–cell adhesion molecules (CAMs). Cadherins, the transmembrane glycoproteins, mediate Ca^{2+}-dependent cell–cell adhesion, while the neural cell adhesion molecule (N-CAM) mediates the Ca^{2+}-independent cell–cell adhesion systems.

A substantial part of the tissue volume is the extracellular space that is filled by an extracellular matrix which is composed of proteins and polysaccharides that are secreted locally by the cells in the matrix. The extracellular matrix not only binds the cells together but, also, influences their development, polarity, and behavior. The two main classes of macromolecules that make up the matrix are glycosaminoglycans (GAGs) and fibrous proteins.

7.6.2 Cell Signaling and Cellular Receptors

Cells communicate by means of hundreds of types of intercellular signaling molecules that include amino acids, peptides, proteins, steroids, nucleotides, fatty acid derivatives, and dissolved gases. The four primary modes of chemical signaling are *endocrine*, *paracrine*, *autocrine*, and *synaptic*. Endocrine signaling involves specialized endocrine cells that secrete the signaling molecules (hormones) into the blood stream, which are transported to distant target cells distributed throughout the body in order to produce a response in different cells and tissues. In paracrine signaling, the signal molecules that a cell secretes may act as local mediators, affecting only the neighboring cells. In autocrine signaling, the signal molecules secreted by a cell act on the same cell that generates them. In synaptic signaling, the signal molecules (neurotransmitters) secreted by a cell (neuron) bind to the receptors on a target cell at a specialized cell junction, called *synapse*.

The cellular receptors are very specific protein molecules on the plasma membrane, in the cytoplasm, or in the nucleus, that are capable of recognizing and binding the extracellular signaling molecules, also called *ligands*. As a consequence of ligand–receptor interaction, the cell may generate a cascade of intracellular signals that alter the pattern of gene expression and the behavior of the cell. One of the final steps in the signal transduction pathway is the phosphorylation of an effector protein by a protein kinase. Through cascades of highly regulated protein phosphorylation, elaborate sets of interacting proteins relay most signals from the cell surface to the nucleus, thereby altering the cell's pattern of gene expression and, as a consequence, its behavior.

Small hydrophobic signal molecules, including the thyroid and steroid hormones, diffuse into the cell and activate receptor proteins that regulate gene expression. Some dissolved gases, such as nitric oxide and carbon monoxide, activate an intracellular enzyme (guanyl cyclase), which produces cyclic GMP in the target cell. Most of the extracellular signal molecules are hydrophilic and activate transmembrane receptor proteins on the surface of the cell membrane. The ligands that bind with membrane receptors include hormones, neurotransmitters, lipoproteins, antigens, infectious agents, drugs, and metabolites.

Generally, receptors are classified on the basis of their location and function. Three main families of cell surface receptors (Table 7.4) have been identified. Following the binding of a specific signal, ion-channel-linked receptors open or close briefly to allow transport of molecules into the cell. G-protein-linked receptors activate or inactivate plasma membrane-bound enzymes or ion channels via trimeric GTP-binding proteins (G proteins). Some G-protein-linked receptors activate or inactivate adenyl cyclase and alter the intracellular concentration of cyclic AMP, while some others generate inositol triphosphate (IP_3), which increases intracellular Ca^{2+} levels. A rise in cyclic AMP or Ca^{2+} levels stimulates a number of kinases and phosphorylates target proteins on serine or threonine residues. Enzyme-linked receptors, such as protein kinases phosphorylate specific proteins in the target cell. There are five

Table 7.4 Cell surface receptors

Receptor family	Enzyme	Second messenger	Signaling molecule
A. Ion-channel-linked			
G-protein-linked	Activate adenyl cyclase	Increase cyclic AMP	TSH, ACTH, LH, Adrenaline, glucagon, and vasopressin
	Inhibit adenyl cyclase	Decrease cyclic AMP	Cholera toxin, pertussis toxin
	Activate phosphoinositide-specific phospholipase C	Inositol triphosphate (IP3) increases Ca^{2+}	Vasopressin, acetylcholine, and thrombin
	Activate or inactivate ion channels		Acetylcholine (nicotinic Ach receptors)
B. Enzyme-linked			
Receptor guanylyl cyclases	Activate guanylyl cyclase	Increase Cyclic GMP	Atrial natriuretic peptides (ANPs)
Receptor tyrosine kinases	Activate tyrosine kinase	Phosphorylate-specific tyrosine residues	Growth factors (PDGF, FGF, VEGF, M-CSF), and insulin
Tyrosine-kinase-associated receptors	Receptor dimerization	same as above	Cytokines, interleukin-2, growth hormone, prolactin
Receptor tyrosine phosphatases	Activate tyrosine phosphatase	Remove phosphate groups from tyrosine residues	Extracellular antibodies
Receptor serine/threonine kinases		Phosphorylate serine and threonine residues	

known classes of enzyme-linked receptors (Table 7.4). Among these, receptor tyrosine kinases and tyrosine-kinase-associated receptors are by far the most common. Most of the mutant genes (*Ras*, *Src*, *Raf*, *Fos*, and *Jun*) that encode the proteins in the intracellular signaling cascades that are activated by tyrosine kinases were identified as *oncogenes* in cancer cells, as their inappropriate activation causes a cell to proliferate excessively. By contrast, the normal genes are, therefore, referred to as *protooncogenes*.

7.7   Transport Through the Cell Membrane

About 56% of the adult human body is fluid. One third of the fluid is outside the cells and is called *ECF* while the remainder is called *ICF*. The ECF (the internal environment) is in constant motion throughout the body and contains the ions (sodium, chloride, and bicarbonate) and nutrients (oxygen, glucose, fatty acids, and amino acids) needed by cells for the maintenance of life. Cells secrete various intracellular signal molecules and expel metabolites and waste products into the ECF. The cellular intake or output of different molecules occurs by different transport mechanisms of the plasma membrane, depending on the chemical and biochemical characteristics of the solute molecules.

The cell membrane consists of a lipid bilayer that is not miscible with either the ECF or the ICF and provides a barrier for the transport of water molecules and water-soluble substances across the cell membrane. Water and small molecules diffuse through the membrane via gaps or transitory spaces in the hydrophobic environment created by the random movement of fatty acyl chains of lipids.

The transport proteins within the lipid bilayer, however, provide different mechanisms for the transport of molecules across the membrane. Membranes of most cells contain pores or specific *channels* that permit the rapid movement of solute molecules across the plasma membrane. Examples of pores are plasma membrane gap junctions and nuclear membrane pores. Channels are selective for specific inorganic ions, whereas pores are not selective. Voltage-gated channels, such as the sodium channel, control the opening or closing of some channels by changes in the

transmembrane potential. Chemically regulated channels, such as the nicotinic–acetylcholine channel, open or close on the basis of the binding of a chemical to the channel.

Plasma membranes contain transport systems (transporters) that involve intrinsic membrane proteins and actually translocate the molecule or ion across the membrane by binding and physically moving the substance. Transporters have an important role in the uptake of nutrients, maintenance of ion concentrations, and control of metabolism. Some carrier proteins transport a single solute or molecule across a membrane, and these are called *uniporters*. With some other carrier proteins (coupled transporters), transfer of one solute depends on the simultaneous or sequential transfer of a second solute, either in the same direction (*symport*) or in the opposite direction (*antiport*). Transporters are classified on the basis of their mechanism of translocation of a substance and the energetics of the system. Transporters have specificity for the substance to be transported, have defined reaction kinetics, and can be inhibited by both, competitive and noncompetitive inhibitors. Membranes of all cells contain highly specific transporters for the movement of inorganic anions and cations (Na^+, K^+, Ca^{2+}, Cl^-, HCO_3^-), and uncharged and charged organic compounds (amino acids, sugars).

Transport through the lipid bilayer or through the transport proteins involves simple diffusion, passive transport (facilitated diffusion), or active transport mechanisms. Certain macromolecules may also be transported by vesicle formation involving either endocytosis or exocytosis mechanisms. The major transport systems in mammalian cells are summarized in Table 7.5.

Table 7.5 Transport mechanisms across plasma cell membrane

Mechanism	Transport process	Example
A. Nonspecific processes		
Simple diffusion	Direct through the membrane and is dependent on concentration gradient	Oxygen movement into cells
Osmosis	Direct diffusion of water molecules across a semipermeable membrane	Movement of water into cells, when placed in hypotonic solution
Endocytosis		
Phagocytosis	Particles are engulfed by membrane through vesicle formation	Ingestion of bacteria or particles by leukocytes
Pinocytosis	Fluid is engulfed by membrane through vesicle formation	Transport of nutrients by human egg cells
Exocytosis	Extrusion of material from a cell involves membrane vesicles	Secretion of proteins by cells via small membrane vesicles
B. Specific processes		
Facilitated diffusion	Transport of molecules into the cells involve protein channels or transporters and is dependent on concentration gradient	Movement of glucose into most cells
Primary active transport	Transport of molecules against concentration gradient involves carrier protein and requires energy derived by hydrolysis of ATP	Na^+, K^+, Ca^{2+}, H^+ and Cl^- ions
Secondary active transport	As a consequence of primary active transport, sodium ions can pull other solutes into the cell (cotransport)	Glucose and amino acids
Receptor-mediated endocytosis	Endocytosis is triggered by the binding of a molecule to a specific receptor on the cell surface followed by internalization of vesicles	Cholesterol (LDL) and transferrin uptake by cells

7.7.1   Diffusion

Body fluids are composed of two types of solutes: electrolytes, which ionize in solution and exhibit polarity (cations and anions), and non-electrolytes, such as glucose, creatinine, and urea, that do not ionize in solution. The continuous movement of solute molecules among one another in liquids or in gases is called *diffusion*. The solute molecules in the ECF or in the cytoplasm can spontaneously diffuse across the plasma membrane. However, the direction of movement of solutes by diffusion is always from a higher to a lower concentration and Fick's first law of diffusion describes the rate. The overall effect of diffusion is the passive movement of molecules down a concentration until the concentration on each side is at chemical equilibrium. Diffusion through the cell membrane is divided into two separate subtypes called simple diffusion and facilitated diffusion (Fig. 7.3).

7.7.1.1 Simple Diffusion

Simple diffusion can occur through the cell membrane either through the intermolecular interstices of the lipid bilayer or through transport proteins (watery channels). The diffusion rate of a solute depends on its size (diffusion coefficient) and its lipid solubility. In addition, the diffusion rate is influenced by the differences in electrical potential across the membrane. Diffusion of small uncharged molecules (water, urea, glyc-
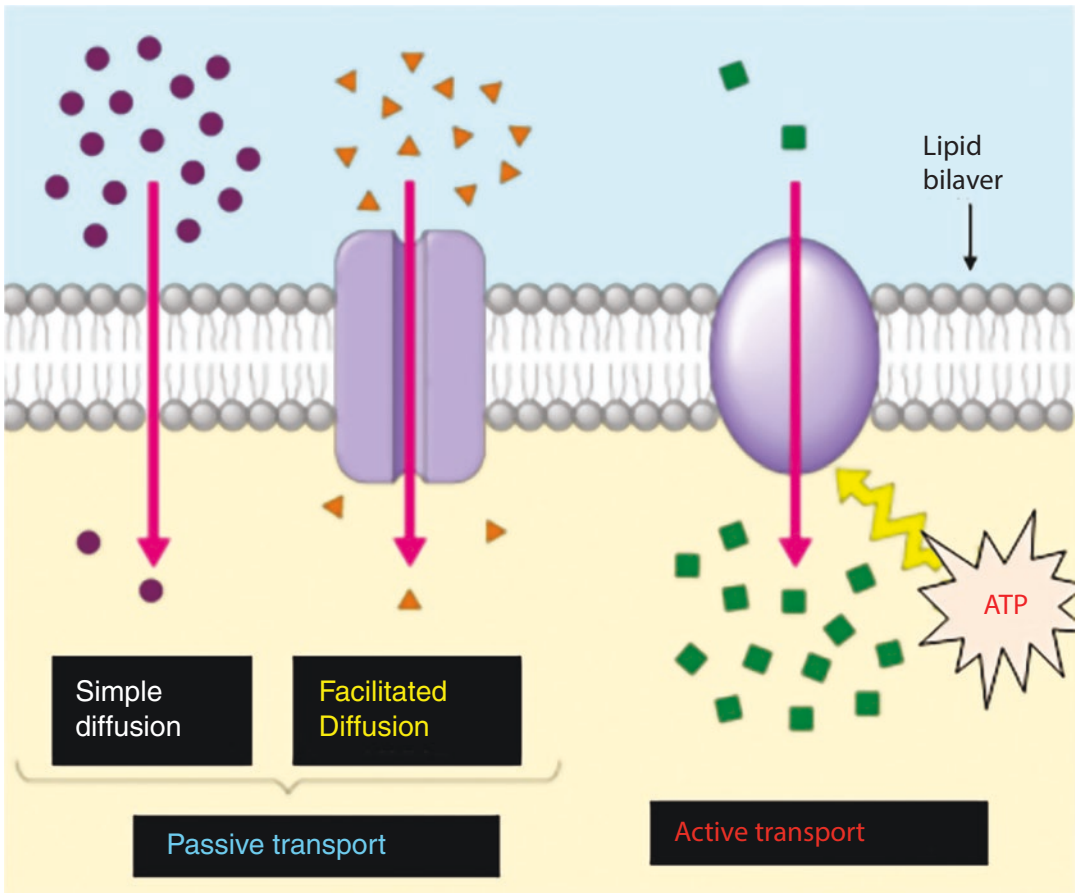
Fig. 7.3 Membrane transport mechanisms of small molecules; simple diffusion is simply dependent on the concentration gradient while facilitated diffusion involves specific membrane transporters, such as channel proteins or carrier proteins. Active transport requires expenditure of energy

erol) and hydrophobic molecules, such as gases (O_2, N_2, CO_2, NO), occurs rapidly and depends entirely on the concentration gradient. Uncharged lipophilic molecules (fatty acids, steroids) diffuse relatively rapidly but, hydrophilic substances (glucose, inorganic ions) diffuse very slowly. *Osmosis* is a special case of diffusion in which free passage of water molecules (but not that of solute molecules) across a cell membrane is permitted.

7.7.1.2 Facilitated Diffusion

Passive transport or facilitated diffusion (also known as carrier-mediated diffusion) involves the translocation of a solute through a cell membrane down its concentration gradient, as in simple diffusion, without expenditure of metabolic energy. However, facilitated diffusion requires the interaction of a carrier protein (transporter) with the solute molecules. Upon entering the protein channel, the solute chemically binds to the transporter and induces a conformational change in the carrier protein, so that the channel is open on the intracellular side and releases the molecule (Fig. 7.3). The rate of diffusion is dependent on the concentration gradient and approaches a maximum, called V_{max}, as the concentration of solute increases. It is very important to recognize that in facilitated diffusion, the transporters are very specific for a solute and exhibit saturation kinetics. Transport of D-glucose is facilitated and a family of transporters (glucose permeases or GLUT 1–6) has been identified. Similarly, an anion transporter ($Cl^- $–$HCO_3^-$ exchanger) in erythrocytes involves antiport (two molecules in opposite directions) movement of Cl and HCO_3^- ions.

7.7.2 Active Transport

Active transport systems or pumps move the solute molecules through a cell membrane against their concentration gradient and require the expenditure of some form of energy (Fig. 7.3). As a result, the concentration of solute molecules on either side of plasma membrane is not equal. For example, the concentration of Na^+ ions in the ECF is 10 times more than the concentration of Na^+ ions in the cytoplasm, while the converse is true with K^+ ions. In active transport, the transporters are very specific for a solute and exhibit saturation kinetics. In addition, the carrier protein imparts energy to the solute to move against electrochemical or concentration gradient. If the energy source is removed or inhibited, the active transport mechanism is abolished. Most of the ions, amino acids, and certain sugars are actively transported across the plasma membrane.

In primary active transport, the energy is derived directly from the hydrolysis of ATP to ADP. The best-known active transport system is the $Na^+ + K^+$-dependent ATPase pump (Fig. 7.3) found in virtually all mammalian cells. The transporter protein is an enzyme, ATPase. When three sodium ions bind on the inside and two potassium ions bind on the outside, the ATPase function of the transporter is activated. Following hydrolysis of one molecule of ATP, the liberated energy causes conformational change in the carrier protein, releasing sodium ions to the outside and potassium ions to the inside. The process leads to an electrical potential, with the inside of the cell being more negative than the outside. The excitable tissues (muscle and nerve), kidneys, and salivary glands have a high concentration of the $Na^+ + K^+$-dependent ATPase pump. The other important primary active transport pumps are for the transport of Ca^{2+} and H^+ ions.

The secondary active transport represents a phenomenon called cotransport in which molecules are transported through the plasma membrane using the energy obtained not directly from the hydrolysis of ATP, but from the electrochemical gradient across the membrane. When sodium ions are transported out of the cells, an electrical potential develops which provides energy for the sodium ions to diffuse into the interior. This diffusion energy of sodium ions can pull other molecules into the cell. Glucose and many amino acids are transported into most cells via sodium cotransport system. Following the binding of sodium and glucose molecules to specific sites on the sodium–

glucose transport protein, a conformational change is induced, and both the molecules are transported into the cell.

7.7.3 Transport by Vesicle Formation

Transport of macromolecules, such as large proteins, polysaccharides, nucleotides, and even other cells across the plasma membrane, is accomplished by a unique process called *endocytosis* that involves special membrane-bound vesicles. The material to be ingested is progressively enclosed by a small portion of the plasma membrane, which first invaginates and then pinches off to form an intracellular vesicle. Many of the endocytosed vesicles end up in lysosomes, where they are degraded. Endocytosis is subcategorized into two types: *pinocytosis* involves ingestion of fluid and solutes via small vesicles, while *phagocytosis* involves ingestion of large particles such as microorganisms via large vesicles called phagosomes.

Specialized cells that are professional phagocytes, such as macrophages and neutrophils, mainly carry out phagocytosis. For example, more than 10^{11} senescent red blood cells are phagocytosed by macrophages every day in a human body. In order to be phagocytosed, particles must bind to specialized receptors on the plasma membrane. Phagocytosis is a triggered process that requires the activated receptors to transmit signals to the interior of the cell to initiate the response. The Fc receptors on macrophages recognize and bind the Fc portion of antibodies that recognize and bind microorganisms.

Most cells continually ingest bits of their plasma membrane in the form of small pinocytic (endocytic) vesicles that are subsequently returned to the cell surface. The plasma membrane has highly specialized regions, called clathrin-coated pits, that provide an efficient pathway for taking up macromolecules via a process called receptor-mediated endocytosis. Following binding of macromolecules to specific cell surface receptors in these clathrin-coated pits, the macromolecule-receptor complex is internalized. Most receptors are recycled via transport vesicles back to the cell surface for reuse. More than 25 different receptors are known to participate in receptor-mediated endocytosis of different types of molecules. The low-density lipoprotein (LDL) and transferrin are the most common macromolecules that are transported into the cell via receptor-mediated endocytosis.

The reverse of endocytosis is *exocytosis* that involves transport of macromolecules within vesicles from the interior of a cell to the cell surface or into the ECF. Proteins and certain neurotransmitters can be secreted from the cells by exocytosis in either a constitutive or a regulated process. For example, insulin molecules stored in intracellular vesicles are secreted into the ECF following fusion of these vesicles with the plasma membrane. By contrast, neurotransmitter molecules stored in synaptic vesicles of a presynaptic neuron are released into a synapse only in response to an extracellular signal.

7.7.4 Transmission of Electrical Impulses

Nerve and muscle cells are "excitable," which implies that they are capable of self-generation of electrochemical impulses at their cell membranes. These impulses can be employed to transmit signals, such as nerve signals, from the central nervous system to many tissues and organs throughout the body. There is a difference in the ionic composition of ECF and ICF. Whenever ion channels open or close, there is a change in the movement of ions across a cell membrane. Movement of electrical charges is called a *current*. The flow of the current reflects the charge separation across the membrane, i.e., its voltage or *membrane potential*, and is a measure of the electrical driving force that causes ions to move. When cells are excited, there is a change in current or voltage and information passes along the nerves as electrical currents and associated voltage changes (impulses).

All body cells are electrically polarized, with the inside of the cell being more negatively

charged than the outside. The difference in electrical charge or voltage is known as the *resting membrane potential* and is about −70 to −85 mV. The resting membrane potential is the result of the concentration gradient of ions and differences in the relative permeability of the membrane for different ions. The concentration of K^+ is higher inside the cell than outside, whereas the concentration of Na^+ is low inside cells and high outside. This difference in concentration is maintained by the Na^+–K^+-ATPase pump. In addition, the cell membrane is more permeable to K^+ than to other ions, such as Na^+ and Cl^-, and K^+ can diffuse easily from ICF to ECF. Within the cell, there is an excess of anions because of negatively charged proteins that are impermeable.

When a cell, such as a neuron, is stimulated through voltage-regulated channels in sensory receptors or at synapses, ion channels for sodium open and, as a result, there is a net movement of Na^+ into the cell, and the membrane potential decreases making the cell more positively charged. The decrease in resting membrane potential is known as *depolarization*. The point, at which the rapid change in the resting membrane potential reverses the polarity of the cell is referred to as an *action potential* or simply a *nerve impulse*. Immediately following an action potential, the membrane potential returns to the resting membrane potential. The increase in membrane potential is known as *repolarization* that results in the negative polarity of the cell as the voltage-gated sodium channels close and potassium channels open. The Na^+–K^+-ATPase pump moves K^+ back into the cell and Na^+ out of the cell. The absolute refractory period is the period of time during which it is impossible to generate another action potential, while the relative refractory period is the period of time in which a second action potential can be initiated by stronger-than-normal stimulus.

Depolarization, i.e., the opening of sodium ion channels, generates a nerve impulse and is propagated along the nerve, because the opening of sodium ion channels facilitates the opening of other adjacent channels, causing a wave of depolarization to travel down the membrane of nerve

cell. When a nerve impulse reaches the far end of a nerve cell, the axon tip, the wave of depolarization causes the release of a neurotransmitter. At a neuromuscular junction, the release of acetylcholine depolarizes the muscle membrane and opens the calcium ion channels, permitting the entry of calcium ions into the cell, which triggers muscle contraction. In an excitatory neural synapse, the neurotransmitter (acetylcholine) binds to the receptor in the postsynaptic nerve fiber and opens sodium ion channels that lead to the depolarization and propagation of an impulse. By contrast, in an inhibitory synapse the neurotransmitter (γ-aminobutyric acid or GABA, glycine) binds to the receptor in the postsynaptic nerve fiber and opens the potassium ion channels or chloride ion channels, resulting in the repolarization and inhibition of the impulse.

7.8   Cellular Metabolism

7.8.1   Role of ATP

All of the chemical reactions involved in maintaining essential cellular functions are referred to as cellular metabolism. The life processes are driven by energy; anabolism requires energy, while catabolism releases energy. Atoms can store potential energy by means of electrons at higher energy levels. Energy is stored in chemical bonds when atoms combine to form molecules. Cells extract the chemical energy from nutrients and transfer it to a molecule known as adenosine triphosphate (ATP). Each molecule of ATP has two high-energy phosphate bonds and each of the phosphate bonds contains about 12,000 cal of energy per mole of ATP under physiological conditions. Oxidative cellular metabolism and oxidative phosphorylation reactions result in the formation of ATP that is used throughout the cell to energize all the intracellular metabolic reactions. The function of ATP is not only to store energy but also to transfer it from one molecule to another. The phosphate bond in ATP molecule is very labile and is broken down to form adenosine diphosphate (ADP) and a phosphoric acid radical with the release of

energy. ATP is used to promote three major categories of cellular function: membrane transport of ions such as Na^+, K^+, Ca^{2+}, Mg^{2+}, and Cl^-, synthesis of biochemicals, such as proteins, enzymes, and nucleotides, and mechanical work, such as muscle contraction.

7.8.1.1 Production of ATP

The catabolism of nutrients can be divided into three different phases. Phase 1 represents the process of digestion that happens outside the cells where proteins, polysaccharides, and fats are broken down into their corresponding smaller subunits: amino acids, glucose, and fatty acid. In phase 2, the small molecules are transported into the cell where the major catabolic processes take place with the formation of acetyl-CoA and limited amounts of ATP and NADH. Finally, in phase 3, the acetyl-CoA molecules are degraded in mitochondria to CO_2 and H_2O with the generation of ATP.

Cellular oxidation–reduction reactions play a key role in energy flow within a cell and electrons transfer the energy from one atom to another, either by oxidation (loss of electrons) or by reduction (gain of electrons). In a biological system, oxidation refers to the removal of a hydrogen atom (proton plus electron) from a molecule, while reduction involves the gain of a hydrogen atom by another molecule. In many of these enzyme-catalyzed oxidation–reduction reactions, involving the formation of ATP, cells employ coenzymes (cofactors) that shuttle energy as hydrogen atoms are transferred from one reaction to another. One of the most important coenzymes is nicotinamide adenine dinucleotide (NAD+) that can accept an electron and a hydrogen atom, and gets reduced to form NADH.

7.8.1.2 Glycolysis

The most important process in phase 2 of the catabolism is the degradation of glucose in a sequence of ten biochemical reactions, known as glycolysis or oxidative cellular metabolism. Glycolysis can produce ATP in the absence of oxygen. Each glucose molecule is converted into two pyruvate molecules with a net generation of six ATP molecules. If oxygen is absent, or significantly reduced within the cell, the pyruvate is converted to lactic acid, which then diffuses into ECF. In many of the normal cells, ATP generation by glycolysis accounts for less than 5% of the overall ATP generation within the cell.

7.8.1.3 Oxidative Phosphorylation

Phase 3 begins in the mitochondria with a series of reactions called citric acid cycle (also called the tricarboxylic acid cycle or the Krebs cycle), and ends with oxidative phosphorylation. Following glycolysis, in the presence of oxygen, pyruvate molecules enter the mitochondria and are converted to acetyl groups of acetyl coenzyme A (Acetyl-CoA). The amino acid and fatty acid molecules are also converted to Acetyl-CoA.

The citric acid cycle begins with the interaction of acetyl-CoA and oxaloacetate to form the tricarboxylic acid molecule called citric acid which, subsequently, is oxidized to generate two molecules of CO_2 and oxaloacetate. The energy liberated from the oxidation reactions is utilized to produce three molecules of NADH and one molecule of reduced flavin adenine nucleotide ($FADH_2$). Oxidative phosphorylation is the last step in the catabolism, in which NADH and $FADH_2$ transfer the electrons to a series of carrier molecules, such as cytochromes (the electron-transport chain), on the inner surfaces of the mitochondria with the release of hydrogen ions. Subsequently, the molecular oxygen picks up electrons from the electron-transport chain to form water, releasing a great deal of chemical energy that is used to make the major portion of the cellular ATP. The energy released in the electron-transfer steps causes the protons to be pumped outward. The resulting electrochemical proton gradient across the inner mitochondrial membrane induces the formation of ATP from ADP and phosphoric acid radical. The aerobic oxidation of glucose results in a maximal net production of 36 ATP molecules, all but four of them produced by oxidative phosphorylation.

7.9   DNA and Gene Expression

7.9.1   DNA: The Genetic Material

The ability of cells to maintain a high degree of order depends on the hereditary or genetic information that is stored in the genetic material, the DNA. Within the nucleus of all mammalian cells, a full complement of genetic information is stored and the entire DNA is packaged into 23 pairs of chromosomes. A chromosome is formed from a single enormously long DNA molecule that consists of many small subsets called genes each of which represents a specific combination of DNA sequence designed for a specific cellular function. The three most important events in the existence of a DNA molecule are replication, repair, and expression.

The chromosomes can undergo self-replication that permits DNA to make copies of itself, as the cell divides and transfers the DNA (23 pairs of chromosomes) to daughter cells, which can, thus, inherit every property and characteristic of the original cell. There are approximately 30,000 genes per human genome which control every aspect of cellular function, primarily through protein synthesis. The sequence of amino acids in a particular protein or enzyme is encoded in a specific gene. Most of the chromosomal DNA, however, does not code for proteins or RNAs. The central dogma of molecular biology is that the overall process of information transfer in the cell involves transcription of the DNA into RNA molecules, which subsequently generate specific proteins on ribosomes by a process known as translation.

A major characteristic of DNA is its ability to encode an enormous quantity of biological information. Only a few picograms (10^{-12} g) of DNA are sufficient to direct the synthesis of as many as 100,000 distinct proteins within a cell. This supreme coding effectiveness of DNA is because of its unique chemical structure.

7.9.1.1 DNA Structure
As described previously, DNA was first discovered in 1869 by the chemist, Friedrich Miescher who extracted a white substance from the cell nuclei of

human pus and called it "nuclein." Because nuclein is slightly acidic, it is known as nucleic acid. In the 1920s, the biochemist, Levine identified two types of nucleic acids: DNA and RNA. Levine also concluded that the DNA molecule is a polynucleotide formed by the polymerization of nucleotides. Each nucleotide subunit of a DNA molecule is composed of three basic elements: a phosphate group, a five-carbon sugar (deoxyribose), and one of the four types of nitrogen-containing organic bases. Two of the bases, thymine and cytosine, are called pyrimidines, while the other two bases, adenine and guanine, are called purines. Their first letters commonly represent the four bases: T, C, and A, G.

The presence of the 5′-phosphate and the 3′-hydroxyl groups in the deoxyribose molecule allows the DNA to form a long chain of polynucleotides by joining nucleotides through phosphodiester bonds. Any linear strand of DNA will always have a free 5′-phosphate group at one end and a free 3′-hydroxyl group at the other; therefore, the DNA molecule has an intrinsic directionality (5′ → 3′ direction). Although some forms of cellular DNA exist as single-stranded structures, the most widespread DNA structure discovered by Watson and Crick, in 1953, represents the DNA as a double helix containing two polynucleotide strands that are complementary mirror images of each other (Fig. 7.4). The "backbone" of DNA molecule is composed of deoxyribose sugars joined by phosphodiester bonds to phosphate groups, while the bases are linked in the middle of the molecule through hydrogen bonds. The relationship between bases in the double helix is described as complementary, because adenine always bonds with thymine and guanine always bonds with cytosine. As a consequence, the double-stranded DNA contains equal amounts of purines and pyrimidines. An important structural characteristic of the double-stranded DNA is that its strands are antiparallel meaning that the two strands are aligned in opposite directions.

7.9.1.2 DNA Replication
In order to serve as the basic genetic material, all the chromosomes in the nucleus duplicate their
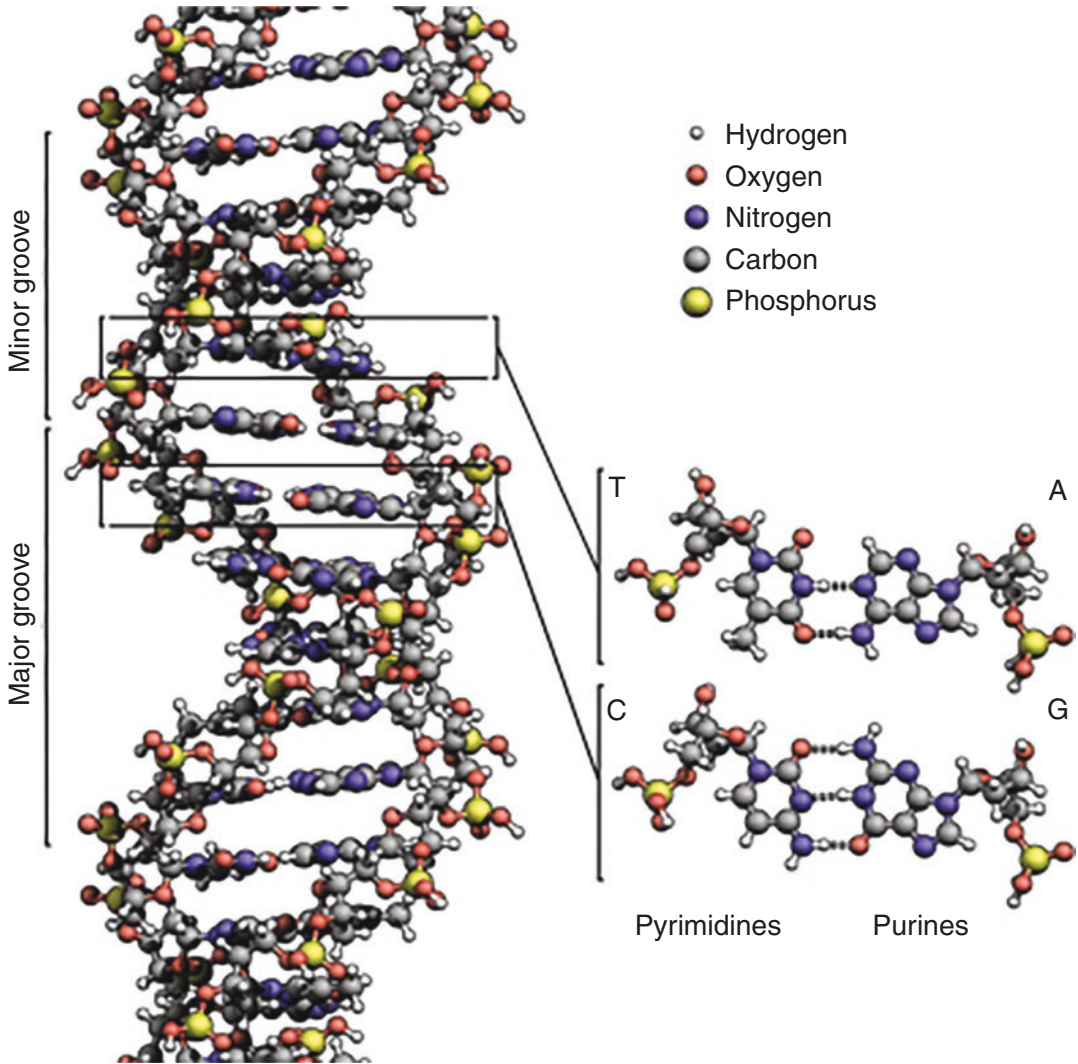
Fig. 7.4 DNA double helix (DNA—Wikipedia)

DNA before every cell division. When a DNA molecule replicates, the double-stranded DNA separates or unzips at one end, forming a replication fork (Fig. 7.5). The principle of complementary base pairing dictates that the process of replication proceeds by a mechanism in which a new DNA strand that matches each of the original strands that serve as a template, is synthesized. If the sequence of the template is ATTGCAT, the sequence of the new strand in the duplicate must be TAACGTA. Replication is semiconservative in the sense that at the end of each round of replication, one of the parental strands is maintained intact, and combines with one newly synthesized complementary strand.

DNA replication requires the cooperation of many proteins and enzymes. While DNA helicases and single-strand binding proteins help unzip the double helix and hold the strands apart, a self-correcting DNA polymerase moves along in a 5′ → 3′ direction on a single strand (leading strand) and catalyzes nucleotide polymerization or base pairing. Because the two strands are antiparallel, this 5′ → 3′ DNA synthesis can take place continuously on the leading strand only, while the base pairing on the lagging strand is
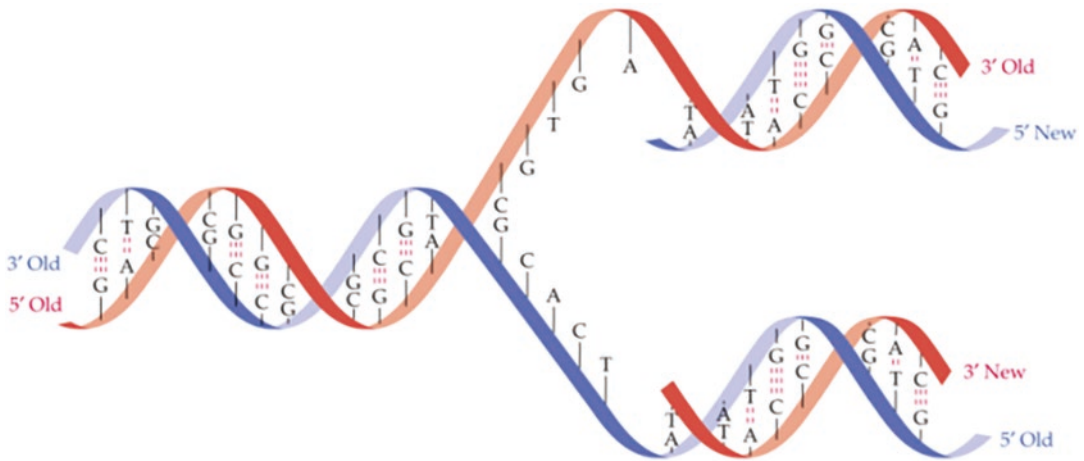
Fig. 7.5 DNA replication

discontinuous and involves synthesis of a series of short DNA molecules that are subsequently sealed together by the enzyme DNA ligase. In mammals, DNA replication occurs at a polymerization rate of about 50 nucleotides per second. At the end of the replication, a repair process known as DNA proofreading is catalyzed by DNA ligase and DNA polymerase enzymes, which cut out the inappropriate or mismatched nucleotides from the new strand and replace these with the appropriate complementary nucleotides. The replication process occurs with few mistakes being made; thus, the DNA sequences are maintained with very high fidelity. For example, a mammalian germline cell with a genome of 3×10^9 base pairs is subjected on average to only about 10–20 base pair changes per year. However, genetic change has great implications for evolution and human health and is the product of mutation, and recombination.

7.9.1.3 Gene Mutation
A mutation is any inherited change in the genetic material involving irreversible alterations in the sequence of DNA nucleotides. These mutations may be phenotypically silent (hidden) or expressed (visible). Mutations may be classified into two categories: base substitutions and frameshift mutations. Point mutations are base substitutions involving one or a few nucleotides in the coding sequence and may include replacement of

a purine–pyrimidine base pair by another base pair (transitions) or a pyrimidine–purine base pair (transversions). Point mutations cause changes in the hereditary message of an organism and may result from physical or chemical damage to the DNA or from spontaneous errors made during replication. Frameshift mutation involves spontaneous mispairing and may result from the insertion or deletion of a base pair. Mutational damage to the DNA is generally caused by three sources: (a) ionizing radiation causes breaks in the DNA double strand as a result of the action of free radicals on phosphodiester bonds, (b) ultraviolet radiation creates DNA cross-links because of the absorption of UV energy by pyrimidines, and (c) chemical mutagens modify the DNA bases and alter the base pairing behavior. Mutations in germline tissue are of enormous biological significance, while somatic mutations may cause cancer.

7.9.1.4 DNA Recombination
DNA can undergo important and elegant exchange events through recombination. These change events refer to a number of distinct processes of rearranging the genetic material. Recombination is defined as the creation of new gene combinations and may include the exchange of an entire chromosome or rearrangement of the position of a gene or a segment of a gene on a chromosome. Homologous or general recombi-

nation produces an exchange between a pair of distinct DNA molecules, usually located on two copies of the same chromosome. Sections of DNA may be moved back and forth between chromosomes but, the arrangement of genes on a chromosome is not altered. An important example is the exchange of sections of homologous chromosomes in the course of meiosis that is characteristic of gametes. As a result, homologous recombination generates new combinations of genes that can lead to genetic diversity. In a site-specific recombination, DNA homology is not required; it involves the alteration of the relative positions of short and specific nucleotide sequences in either one or both of the two participating DNA molecules. Transpositional recombination involves the insertion of viruses, plasmids, and transposable elements or transposons into the chromosomal DNA. Gene transfer in general represents a unidirectional transfer of genes from one chromosome to another. The acquisition of an AIDS-bearing virus by a human chromosome is an example of a gene transfer.

7.9.2 Gene Expression and Protein Synthesis

7.9.2.1 DNA Transcription

Proteins are the tools of heredity. The essence of heredity is the ability of the cell to use the information in its DNA to control and direct the synthesis of all proteins in the body. The production of RNA is called transcription and it is the first stage of gene expression (Fig. 7.6). The result is the formation of messenger RNA (mRNA) from the base sequence specified by the DNA template. All types of RNA molecules are transcribed from the DNA. An enzyme called RNA polymerase first binds to a promoter site (beginning of a gene), unwinds the two strands of the DNA double helix, moves along the DNA strand, and synthesizes the RNA molecule by binding complementary RNA nucleotides with the DNA strand. Upon reaching the termination sequence, the enzyme breaks away from the DNA strand

and at the same time a RNA molecule is released into the nucleoplasm. It is important to note that only one strand (the sense strand) of the DNA helix contains the appropriate sequence of bases to be copied into an RNA sense strand. This is accomplished by maintaining the $5' \rightarrow 3'$ direction in producing the RNA molecule. As a result, the RNA chain is complementary to the DNA strand and is called the primary RNA transcript of the gene. This primary RNA transcript consists of long stretches of noncoding nucleotide sequences called introns that intervene between the protein coding nucleotide sequences called exons. In order to generate mRNA molecules, all the introns are cut out and the exons are spliced together. Further modifications to stabilize the transcript include 5-methylguanine capping at the $5'$ end and polyadenylation at the $3'$ end. The spliced, stabilized mRNA molecules are finally transported to the endoplasmic reticulum in the cytoplasm where proteins are synthesized.

7.9.2.2 RNA Structure

Both transcription and translation are mediated by a RNA molecule, which is an unbranched linear polymer of ribonucleoside $5'$-monophosphates. RNA is chemically similar to DNA. The main difference between RNA and DNA is that the RNA molecule contains ribose sugar and another pyrimidine, uracil, in place of thymine. RNAs are classified according to the different roles they play in the course of the protein synthesis. The length of the molecules varies from approximately 65 to 200,000 nucleotides depending on the role they play. There are many types of RNA molecules within a cell and some RNAs contain modified nucleotides which provide greater metabolic stability. mRNA molecules carry the genetic code to the ribosomes where they serve as templates for the synthesis of proteins. A transfer RNA (tRNA) molecule, also generated in the nucleus, transfers specific amino acids from the soluble amino acid pool to the ribosomes and ensures the alignment of these amino acids in a proper sequence. Ribosomal RNA (rRNA) forms the structural framework of

Fig. 7.6 Transcription and translation. http://fajerpc.magnet.fsu.edu/Education/2010/Lectures/26_DNA_Transcription_files/image006.jpg
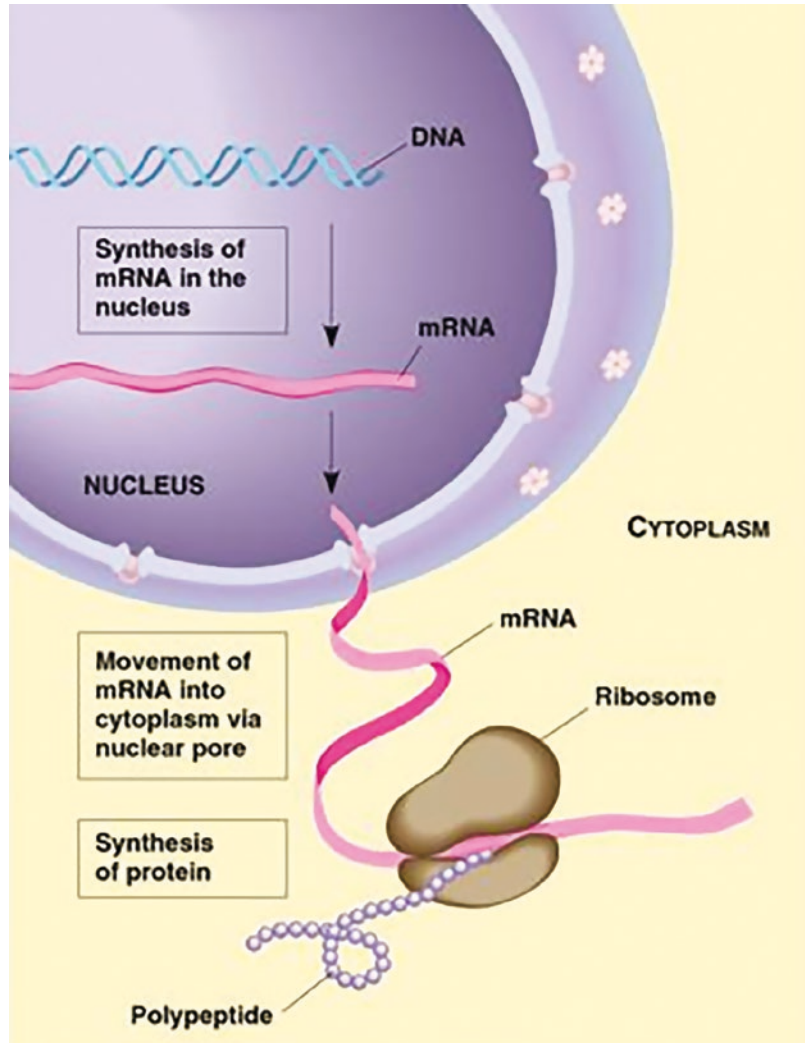
ribosomes where most proteins are synthesized. All RNA molecules are synthesized in the nucleus. While the enzyme, RNA polymerize II, is mainly responsible for the synthesis of mRNA, RNA polymerase I and III mediate the synthesis of rRNA and tRNA.

7.9.2.3 Genetic Code

The genetic code in a DNA sense strand consists of a specific nucleotide sequence that is coded in successive "triplets" that will eventually control the sequence of amino acids in a protein molecule. A complementary code of triplets in mRNA molecules, called codons, is synthesized during the transcription. For example, the successive triplets in a DNA sense strand are represented by bases, GGC, AGA, and CTT. The corresponding complementary mRNA codons, CCG, UCU, and GAA, represent the three amino acids proline, serine, and glutamic acid, respectively. Each amino acid is represented by a specific mRNA codon. The various mRNA codons for the 20 amino acids and the codons for starting and stopping of protein synthesis are summarized in Table 7.6. The genetic code is regarded as degenerate, because most of the amino acids are represented by more than one codon. An important feature of the genetic code is that it is universal; all living organisms use precisely the same DNA code to specify the sequence of amino acids in proteins.

Table 7.6 Amino acids and the genetic code

Amino acid	Abbreviation	Lettercode			RNA	codons		
Neutral amino acids								
Glycine	gly	G	GGU	GGC	GGA	GGG		
Alanine	ala	A	GCU	GCC	GCA	GCG		
Valine	val	V	GAU	GUC	GUA	GUG		
Leucine	leu	L	CUU	CUC	CUA	CUG	UUA	UUG
Isoleucine	ile	I	AUU	AUC	AUA			
Praline	pro	P	CCU	CCC	CCA	CCG		
Phenylalanine	phe	F	UUU	UUC				
Tyrosine	tyr	Y	UAU	UAC				
Tryptophan	try	W	UGG					
Serine Threonine	ser thr	S T	UCU ACU	UCC ACC	UCA ACA	UCG ACG	AGC	AGU
Cysteine	cys	C	UGU	UGC				
Methionine	met	M	AUG					
Asparagine	asn	D	AAU	AAC				
Glutamine	gln	Q	CAA	CAG				
Acidic amino acids								
Aspartic acid	asp	N	GAU	GAC				
Glutamic acid	glu	E	GAA	GAG				
Basic amino acids								
Lysine	lys	K	AAA	AAG				
Arginine	arg	R	CGC	CGA	CGG	AGA	AGG	
Histidine	his	H	CAU	CAC				

7.9.2.4 DNA Translation: Protein Synthesis

More than half of the total dry mass of a cell is made up of proteins. The second stage of gene expression is the synthesis of proteins, which requires complex catalytic machinery. The process of mRNA-directed protein synthesis by ribosomes is called translation and is dependent on two other RNA molecules, rRNA and tRNA. Ribosomes are the physical structures in which proteins are actually synthesized and are composed of two subunits: a small subunit with one rRNA molecule and 33 proteins, and a large subunit with four rRNAs and 40 proteins. Proteins that are transported out of the cell are synthesized on ribosomes that are attached to the ER, while most of the intracellular proteins are made on free ribosomes in the cytoplasm. A tRNA molecule contains about 80 nucleotides and has a site for attachment of an amino acid. Because tRNA needs to bind to mRNA to deliver a specific amino acid, tRNA molecules consists of a complementary triplet of nucleotide bases, called anticodon. Each tRNA acts as a carrier to transport a specific amino acid to the ribosomes and for each of the 20 amino acids, there are 20 different tRNA molecules.

Protein biosynthesis is a complex process and involves bringing together mRNA, ribosomal subunits, and the tRNAs. Such an ordered process requires a complex group of proteins, known as initiation factors, that help initiate the synthesis of the protein. The first step in the translation is the recognition of mRNA by ribosomes and its binding to mRNA molecule at the 5′ end. Immediately, the appropriate tRNA that carries a particular amino acid (methionine) to the 3′ end of mRNA is attached to the ribosome and binds mRNA at the start codon (AUG). The process of translation then begins by bringing in tRNAs that are specified by the codon–anticodon interaction. The ribosome exposes the codon, immediately adjacent to the AUG, on the mRNA to allow a specific anticodon to bind to the codon. At the same time, the amino acids (methionine and the incoming amino acid) are linked together by a peptide bond and the tRNA carrying methionine is released. Next, the ribosome moves along the mRNA molecule to the next codon, when the next tRNA binds to the complementary codon, placing the amino acid adjacent to the growing polypeptide chain. The process is continued until the ribosome reaches a chain-terminating nonsense stop codon (UAA, UAG, UGA). In other words, the process stops when a release factor binds to the nonsense codon, stops the synthesis of protein, and releases the protein from the ribosome. Some proteins emerging from the ribosome are ready to function, while others undergo a variety of posttranslational modifications to convert the proteins to functional forms, or to facilitate the transport to intracellular or extracellular targets.

7.10   Disease and Pathophysiology

7.10.1 Homeostasis

The term *homeostasis* is used by physiologists to describe the maintenance of static, or constant conditions in the internal environment by means of positive and negative feedback of information. About 56% of the adult human body is fluid. Most of the fluid is ICF and about one-third is ECF that is in constant motion throughout the body and contains the ions (sodium, chloride, and bicarbonate) and nutrients (oxygen, glucose, fatty acids, and amino acids) needed by the cells for the maintenance of life. Claude Bernard (1813–1878) defined ECF as the internal environment of the body and hypothesized that the same biological processes that make life possible are also involved in disease (Wagner 1995b). The laws of disease are the same as the laws of life. All the organs and tissues of the body perform functions that help maintain homeostasis. As long as the organs and tissues of the body perform functions that help maintain homeostasis, the cells of the body continue to live and function properly.

7.10.2 Disease Definition

At the present time, precisely defining what disease is, is as complex as defining what exactly life is. It may be relatively easier to define disease at a cellar and molecular level than at the level of an individual. Throughout the history of medicine, two main concepts of disease have been dominant. The *ontological* concept views a disease as an entity that is independent, self-sufficient, and running a regular course with a natural history of its own. The physiological concept defines disease as a deviation from the normal physiology or biochemistry; the disease is a statistically defined deviation of one or more functions in a patient from those of healthy people of the same age and sex under very similar circumstances.

At birth, molecular blueprints collectively make up a person's genome or genotype that will be translated into cellular structures and functions. A single gene defect can lead to biochemical abnormalities that produce many different clinical manifestations of disease, or phenotypes, a process called *pleiotropism*. Many different gene abnormalities can result in the same clinical manifestations of disease; this process is called genetic heterogeneity. Thus, diseases can be defined as abnormal processes as well as abnormalities in the molecular concentrations of different biological markers, signaling molecules, and receptors.

7.10.3 Pathophysiology

In 1839, Theodor Schwann discovered that all the living organisms are made up of discrete cells. In 1858, Rudolph Virchow observed that a disease could not be understood unless it is realized that the ultimate abnormality must lie in the cell. He correlated disease with cellular abnormalities as revealed by chemical stains, thereby founding the field of cellular pathology. Consequently, he defined pathology as physiology with obstacles.

Most diseases begin with a cell injury that occurs if the cell is unable to maintain homeosta-

sis. Since the time of Virchow, gross pathology and histopathology have been a foundation of the diagnostic process and the classification of disease. Traditionally, the four aspects of a disease process that form the core of pathology are etiology, pathogenesis, morphologic changes, and clinical significance. The altered cellular and tissue biology, and all forms of loss of function of tissues, and organs are, ultimately, the result of cell injury and cell death. Therefore, knowledge of the structural and functional reactions of cells and tissues to injurious agents, including genetic defects, is the key for understanding the disease process.

Currently diseases are defined and interpreted in molecular terms and not just with general descriptions of altered structures. Pathology is evolving into a bridging discipline that involves both basic science and clinical practice and is devoted to the study of the structural and, functional changes in cells, tissues, and organs that underlie disease. The molecular, genetic, microbiologic, immunologic, and morphologic techniques help to understand both, the ontological and the physiological causes of disease.

7.10.3.1 Altered Cellular and Tissue Biology

The normal cell is able to handle normal physiologic and functional demands, so-called normal homeostasis. However, physiologic and morphologic cellular adaptations normally occur in response to excessive physiologic conditions or some adverse, or pathologic stimuli. The cells adapt in order to escape and protect themselves from injury. An adapted cell is neither normal nor injured but has an altered steady state and preserves the viability of the cell. If a cell cannot adapt to severe stress or pathologic stimuli, the consequence may be *cellular injury* that disrupts cell structures or deprives the cell of oxygen and nutrients. Cell injury is reversible up to a certain point, but irreversible (lethal) cell injury ultimately leads to cell death, generally known as *necrosis*. By contrast, an internally controlled suicide program, resulting in cell death, is called *apoptosis*.

Cellular Adaptations

Some of the most significant physiologic and pathologic adaptations of cells involve changes in cellular size, growth, or differentiation. These include (a) *atrophy*, a decrease in size and function of the cell, (b) *hypertrophy*, an increase in cell size, (c) *hyperplasia*, an increase in cell number, and (d) *metaplasia*, an alteration of cell differentiation. The adaptive response may also include the intracellular accumulation of normal and abnormal endogenous substances (lipids, protein, glycogen, bilirubin, and pigments), or abnormal exogenous products. Cellular adaptations are a common and central part of many disease states. The molecular mechanisms leading to cellular adaptations may involve a wide variety of stimuli and various steps in the cellular metabolism. Increased production of cell signaling molecules, alterations in the expression of cell surface receptors, and overexpression of intracellular proteins are typical examples.

7.10.3.2   Cellular Injury

Cellular injury occurs if the cell is unable to maintain homeostasis. The causes of cellular injury may be *hypoxia* (oxygen deprivation), infection, or exposure to toxic chemicals. In addition, immunologic reactions, genetic derangements, and nutritional imbalances may also cause cellular injury. In hypoxia (oxygen deprivation), glycolytic energy production may continue but, *ischemia* (loss of blood supply) compromises the availability of metabolic substrates and may injure tissues faster than hypoxia. Various types of cellular injuries and their responses are summarized in Table 7.7.

Biochemical Mechanisms

Regardless of the nature of the injurious agents, there are a number of common biochemical themes or mechanisms responsible for cell injury.

1. ATP depletion: It is one of the most common consequences of ischemic and toxic injury. ATP depletion induces cell swelling, decreases protein synthesis, decreases membrane transport, and increases membrane permeability.

Table 7.7 Progressive types of cell injury and responses

Type	Responses
Adaptation	Atrophy, hypertrophy, hyperplasia, and metaplasia
Active cell injury	Immediate response of "entire cell"
Reversible	Loss of ATP, cellular swelling, detachment of ribosomes, and autophagy of lysosomes
Irreversible	"Point of no return" structurally when vacuolization occurs of the mitochondria and calcium moves into the cell.
Necrosis	Common type of cell death with severe cell swelling and breakdown of organelles
Apoptosis	Cellular self-destruction for elimination of unwanted cell population
Chronic cell injury (subcellular alterations)	Persistent stimuli response may involve only specific organelles or cytoskeleton, e.g., phagocytosis of bacteria
Accumulations or Infiltrations	Water, pigments, lipids, glycogen, and proteins
Pathologic calcification	Dystrophic and metastatic calcification

The above table modified from reference (McCance and Huether 1998)

2. Oxygen and oxygen-derived free radicals: Ischemia causes cell injury by reducing blood supply and cellular oxygen. Radiation, chemicals, and inflammation generate oxygen free radicals that cause the destruction of the cell membrane and cell structure.
3. Intracellular Ca^{2+} and loss of calcium homeostasis: Most of the intracellular calcium is in the mitochondria and endoplasmic reticulum. Ischemia and certain toxins increase the concentration of Ca^{2+} in the cytoplasm resulting in the activation of a number of enzymes, which causes intracellular damage, and increases the membrane permeability.
4. Mitochondrial dysfunction: A variety of stimuli (free Ca^{2+} levels in cytosol, oxidative stress) cause mitochondrial permeability transition (MPT) in the inner mitochondrial membrane, resulting in the leakage of cytochrome c into the cytoplasm.

5. Defects in membrane permeability: All forms of cell injury, as well as many bacterial toxins and viral proteins, damage the plasma membrane. As a result, there is an early loss of selective membrane permeability.

Intracellular Accumulations

Normal cells generally accumulate certain substances such as electrolytes, lipids, glycogen, proteins, calcium, uric acid, and bilirubin that are involved in normal metabolic processes. As a manifestation of injury and metabolic derangements in cells, abnormal amounts of various substances, either normal cellular constituents or exogenous substances, may accumulate in the cytoplasm or nucleus, either transiently or permanently. One of the major consequences of the failure of the transport mechanisms is cell swelling due to excess intracellular water. Abnormal accumulations of organic substances, such as triglycerides, cholesterol and cholesterol esters, glycogen, proteins, pigments, and melanin, may be caused by disorders in which the cellular capacity exceeds the synthesis or catabolism of these substances. Dystrophic calcification occurs mainly in the injured or dead cells, while metastatic calcification may occur in the normal tissues. Hypercalcemia may be a consequence of increased parathyroid hormone, destruction of bone tissue, renal failure, and vitamin D-related disorders. All of these accumulations harm cells by "crowding" the organelles and by causing excessive, and harmful metabolites that may be retained within the cell or expelled into the ECF and circulation.

7.10.3.3 Necrosis

Cellular death resulting from the progressive degradative action of enzymes on the lethally injured cells, ultimately leading to the processes of cellular swelling, dissolution, and rupture, is called necrosis. The morphologic appearance of necrosis is the result of denaturation of proteins and enzymatic digestion (autolysis or heterolysis) of the cell. Different types of necrosis occur in different organs or tissues. The most common type, *coagulative necrosis*, resulting from hypoxia and ischemia, is characterized by the denaturation of cytoplasmic proteins, breakdown of organelles, and cell swelling. It occurs primarily in the kidneys, heart, and adrenal glands. *Liquefactive necrosis* may result from ischemia or bacterial infections. The cells are digested by *hydrolases* and the tissue becomes soft and liquefies. As a result of ischemia, the brain tissue liquefies and forms cysts. In an infected tissue, hydrolases are released from the lysosomes of neutrophils; they kill bacterial cells and the surrounding tissue cells resulting in the accumulation of pus. *Caseous necrosis* (in which the dead tissue maintains a cheese-like appearance) present in the foci of tuberculous infections is a combination of coagulative and liquefactive necrosis. In *fat necrosis*, the *lipase* enzymes break down triglycerides and form opaque chalky necrotic tissue as a result of saponification of free fatty acids with alkali metal ions. In a patient, the necrotic tissue and the debris usually disappear by a combined process of enzymatic digestion, and fragmentation or become calcified.

7.10.3.4 Apoptosis

Apoptosis, a type of cell death implicated in both normal and pathologic tissue, is designed to eliminate unwanted host cells in an active process of cellular self-destruction effected by a dedicated set of gene products. Apoptosis occurs during normal embryonic development and is a homeostatic mechanism to maintain cell populations in tissues. It also occurs as a defense mechanism in immune reactions and during cell damage by disease or noxious agents. Various kinds of stimuli may activate apoptosis. These include injurious agents (radiation, toxins, free radicals), specific death signals (TNF and *Fas* ligands), and withdrawal of growth factors, and hormones. Within the cytoplasm, a number of protein regulators (Bcl-2 family of proteins) either promote or inhibit cell death. In the final phase, the execution *caspases* activate the proteolytic cascade that eventually leads to the intracellular degradation, fragmentation of nuclear chromatin, and breakdown of the cytoskeleton. The most important morphologic characteristics are cell shrinkage, chromatin condensation, and formation of cytoplasmic blebs, and apoptotic bodies that are, sub-

sequently, phagocytosed by adjacent healthy cells, and macrophages. Unlike necrosis, apoptosis involves nuclear and cytoplasmic shrinkage, and affects scattered single cells.

Further Reading

Alberts B, Bray D, Lewis J, et al. Molecular biology of the cell. 3rd ed. New York, NY: Garland; 1994.

Cotran RS, Kumar V, Collins T. Robbins pathologic basis of disease. 6th ed. Philadelphia, PA: Saunders; 1999.

Devin TM. Textbook of biochemistry with clinical correlates. 4th ed. New York, NY: Wiley; 1997.

Guyton AC, Hall JE. Human physiology and mechanisms of disease. 6th ed. Philadelphia, PA: Saunders; 1997.

McCance KL, Huether SE. Pathophysiology. The Biologic basis for disease in adults and children. 3rd ed. St. Louis, MO: Mosby; 1998.

Raven PH, Johnson GB. Biology. 3rd ed. St. Louis, MO: Mosby; 1992.

Virchow R. Disease, life and man. Stanford, CA: Stanford University Press; 1958. (translated by Rather LJ).

Wagner HN Jr. Nuclear medicine: what it is and what it does. In: Wagner Jr HN, Szabo Z, Buchanan JW, editors. Principles of nuclear medicine. Oxford: Saunders; 1995a. p. 1–8.

Wagner HN Jr. The diagnostic process. In: Wagner Jr HN, Szabo Z, Buchanan JW, editors. Principles of nuclear medicine. Philadelphia, PA: Saunders; 1995b.

Scientific achievement is rooted in the past, is cultivated to full stature by many contemporaries, and… No individual alone is responsible for a single steppingstone along the path of progress. (Ernest O. Lawrence)

8.1 Natural Radioactivity

The phenomenon of spontaneous, continuous, and uncontrollable disintegration of an unstable atomic nucleus accompanied by the emission of radiations (such as α, β⁻, and γ) is called natural radioactivity. This spontaneous disintegration of an unstable nucleus of one naturally occurring radioisotope of one element (parent) into an isotope of another element (daughter) continues until a stable nucleus is formed. Isotopes of chemical elements can exist in nature either as stable nuclides, or as radionuclides. Primordial radionuclides (such as ^{238}U, ^{235}U, and ^{232}Th) created before the earth was formed exist in the present time because their half-lives are so long (>100 million years) and that they have not yet completely decayed. Secondary radionuclides (such as ^{226}Ra, ^{227}Ac, ^{227}Th, ^{223}Ra) with shorter half-lives than primordial radionuclides are radiogenic isotopes derived from the decay of primordial radionuclides. These secondary radionuclides are generated in the decay chains of ^{238}U, ^{235}U, and ^{232}Th whereas cosmogenic radionuclides (such as ^{14}C) are present because they are continually being formed in the atmosphere due to cosmic rays. In nature, 34 primordial radionuclides and 61 nonprimordial radionuclides exist as naturally occurring radioisotopes of many elements. All elements heavier than lead (with $Z > 82$) and elements technetium ($Z = 43$) and promethium ($Z = 61$) are all unstable, and exist only as radionuclides.

8.1.1 Decay Chain

The decay chain or radioactive cascade refers to a series of radioactive decays of different radioactive decay products as a sequential series of nuclear transformations until eventually a stable isotope of lead or thallium is reached. Three decay chains of primordial nuclides of uranium and thorium have been observed in nature (Fig. 8.1a–d). The 3 decay chains have a long-lived parent at the top (^{232}Th, ^{238}U, and ^{235}U) and slowly decay by α and β⁻ emission and ultimately reach a stable isotope of lead. In 1940s, based on the large-scale artificial production of a new radionuclide ^{237}Np, investigators have identified the hitherto extinct fourth decay chain.

In the thorium (4n) series, the radionuclides of interest are ^{224}Ra, ^{212}Pb, and ^{212}Bi. In the neptunium series (4n + 1), the radionuclides of interest are ^{229}Th, ^{225}Ra, ^{225}Ac, and ^{213}Bi. Based on uranium series (4n + 2), the Curies discovered the radioisotopes of two new elements (^{226}Ra, and ^{210}Po). In
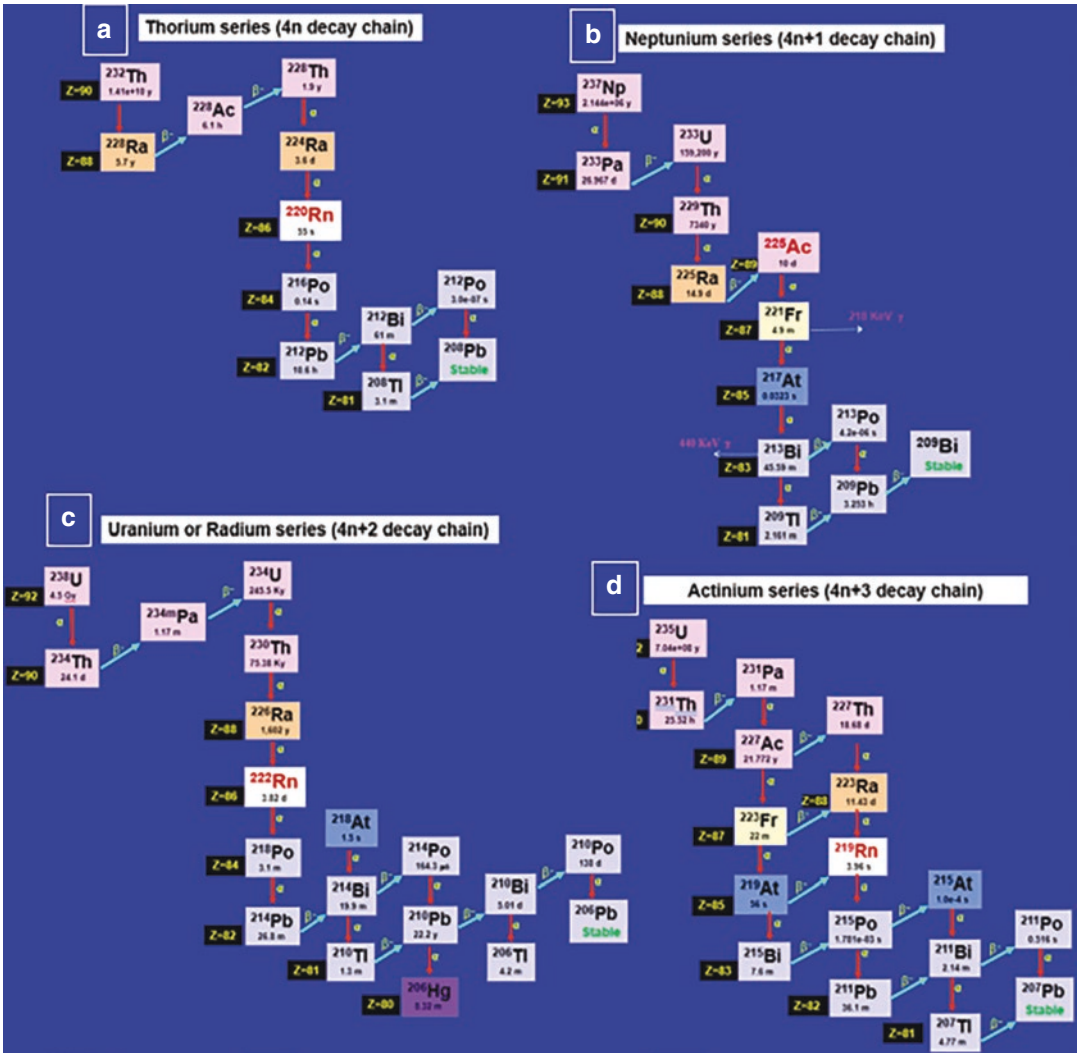
Fig. 8.1 The decay chains of primordial radionuclides ^{232}Th (**a**), ^{238}U (**c**), ^{235}U (**d**), and artificially produced ^{237}Np (**b**). All these four radionuclides ultimately become stable isotopes of lead

the actinium series (4n + 3), ^{227}Th, and ^{223}Ra are of medical interest. While the radionuclides observed in the decay chains are of medical interest, the commercial supply of the α emitting radionuclides for radionuclide therapy is primarily based on the artificial production of radionuclides.

8.2   Nuclear Transformation

The discovery of radioactivity in the late nineteenth century showed that some nuclei spontaneously transform into nuclei with a different

number of protons, thereby producing a different element. When scientists realized that these naturally occurring radioactive isotopes decayed by emitting subatomic particles, they realized that—in principle—it should be possible to carry out the reverse reaction, converting a stable nucleus to another more massive nucleus by bombarding it with subatomic particles in a nuclear transmutation reaction. In the last 100 years, more than 3000 radionuclides have been artificially produced in reactors, particle accelerators, cyclotrons, and radionuclide generators.

When two nuclei come close together, a *nuclear reaction* can occur that results in a *nuclear transformation*, which is the conversion of one nuclide to another nuclide. Whereas *nuclear transmutation* is the conversion of one chemical element or an isotope into another chemical element. A transmutation can be achieved either by nuclear reactions (in which an outside particle reacts with a nucleus) or by radioactive decay, where no outside cause is needed. The term *transmutation* dates back to alchemy, when the alchemists in the Middle Ages pursued the philosopher's stone, which was believed to be capable of transforming the base metals (such as lead and bismuth) into gold.

As discussed earlier, radioactive decay by α or β process will result in natural transmutation of radioactive isotopes of one chemical element to a stable or radioactive isotope of another chemical element. The first nuclear transmutation was accomplished by Patrick Blackett and Rutherford following bombardment of natural nitrogen (^{14}N) atoms with α particles (He nuclei) from a radium–carbon source [1]. More specifically, they observed that a nitrogen nucleus was converted into an isotope of oxygen, ^{17}O with the emission of a proton. The process that Rutherford discovered was the disintegration of the stable nucleus and the formation of a stable oxygen isotope. In 1925, using the cloud chamber, Blackett confirmed Rutherford's observation.

$$^{14}_{7}\text{N} + {}^{4}_{2}\text{He} \rightarrow {}^{17}_{8}\text{O} + {}^{1}_{1}\text{H} \qquad (8.1)$$
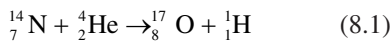
In 1932, when Chadwick bombarded a stable beryllium atom with α particles, the element beryllium was converted into a stable carbon isotope with the emission of a neutron [1].

$$^{9}_{4}\text{Be} + {}^{4}_{2}\text{He} \rightarrow {}^{12}_{6}\text{C} + {}^{1}_{0}n \qquad (8.2)$$
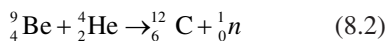
In the two nuclear reactions described above, the nuclear transformation involved conversion of a stable isotope of one element into a stable isotope of another element.

8.2.1 Artificial Production of Radioactivity

In 1934, Irene Curie and her husband Frederic Joliot were the first to produce an unstable radioisotope that decayed by positron emission and the first to discover the artificial production of radioisotopes [2].

$$^{27}_{13}\text{Al} + {}^{4}_{2}\text{He} \rightarrow {}^{30}_{15}\text{P} \rightarrow {}^{1}_{0}n \qquad (8.3)$$

$$^{30}_{15}\text{P} \rightarrow {}^{30}_{14}\text{Si} + \beta^{+} \qquad (8.4)$$
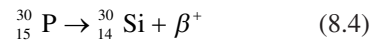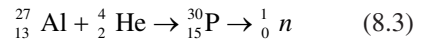
As shown above, the stable Al atom absorbs the helium nucleus and is converted into an unstable ^{30}P radionuclide ($T_{1/2}$ = 3 min), which in turn is converted into a stable ^{30}Si atom following positron emission. Soon after the discovery of artificial radioactivity, physicists realized that charged protons with higher energies would be better projectiles for nuclear transformation reactions. During 1930s, charged-particle *accelerators* were developed to generate very high-energy subatomic particles, such as protons, deuterons, and α particles.

For almost two decades following Rutherford's pioneering work, α particles from natural radioisotopes such as ^{238}U and ^{234}Th were used as projectiles to induce nuclear reactions. Following the discovery of neutrons by Chadwick in 1932, Fermi realized that a neutron beam could be used as a projectile to induce a nuclear reaction, because neutrons are neutral and not repelled by the stable target nucleus. He also realized that neutron-rich atoms decay by beta emission and that the daughter nuclide with an extra proton is normally an element with an atomic number, $Z + 1$. In 1934, Fermi bombarded ^{238}U with neutrons and reported the discovery of element 93 (transuranic element not found in nature) [1]; however, this turned out to be a false claim. In 1937, a colleague of Fermi, Emilio Segre bombarded the stable ^{98}Mo with neutrons (a reaction known as *neutron activation*) and pro-

duced the element 43, which he called technetium (meaning artificial).

$$\underset{42}{^{98}}\text{Mo} + \underset{0}{^{1}}n \rightarrow \underset{42}{^{99}}\text{Mo} \xrightarrow{\beta^-} \underset{43}{^{99m}} \text{Tc} \xrightarrow{IT} \underset{43}{^{99}} \text{Tc} \quad (8.5)$$
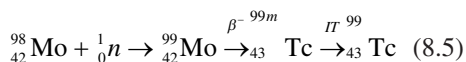
8.2.2   Nuclear Fission

In Germany, Otto Han and Lise Meitner continued the experimental strategy to produce transuramics by bombarding uranium with neutrons. Hahn and Strassmann at the Kaiser Wilhelm institute for chemistry in Berlin bombarded uranium with slow neutrons and discovered that the element barium had been produced. They reported their findings by mail to Meitner in Sweden. Hahn and Strassmann, however, submitted their findings to *Naturwissenschaften* on December 22, 1938, without waiting for Meitner's reply. Meitner

and her nephew Frisch theorized, and then proved, that the uranium nucleus had been split with the production of two new nuclides, free neutrons, and liberation of 200 MeV energy. By analogy with the division of biological cells, Frisch named the process "fission" (Fig. 8.2).

Hahn discovered that the nucleus of uranium undergoes fission (later identified as ^{235}U), when struck by a neutron [1]. More specifically, the ^{235}U nucleus absorbs the neutron to form a very highly unstable ^{236}U nucleus, which at once explodes to form two fission fragments (radionuclides) that are neutron rich and decay by beta emission. Meitner and Frisch had correctly interpreted Hahn's results to mean that the nucleus of uranium had split roughly in half. Subsequently in 1939, Niels Bohr had an insight that the fission with low-energy neutrons was due to the U-235 isotope, while at high energies it was mainly due to the far more abundant U-238 isotope.
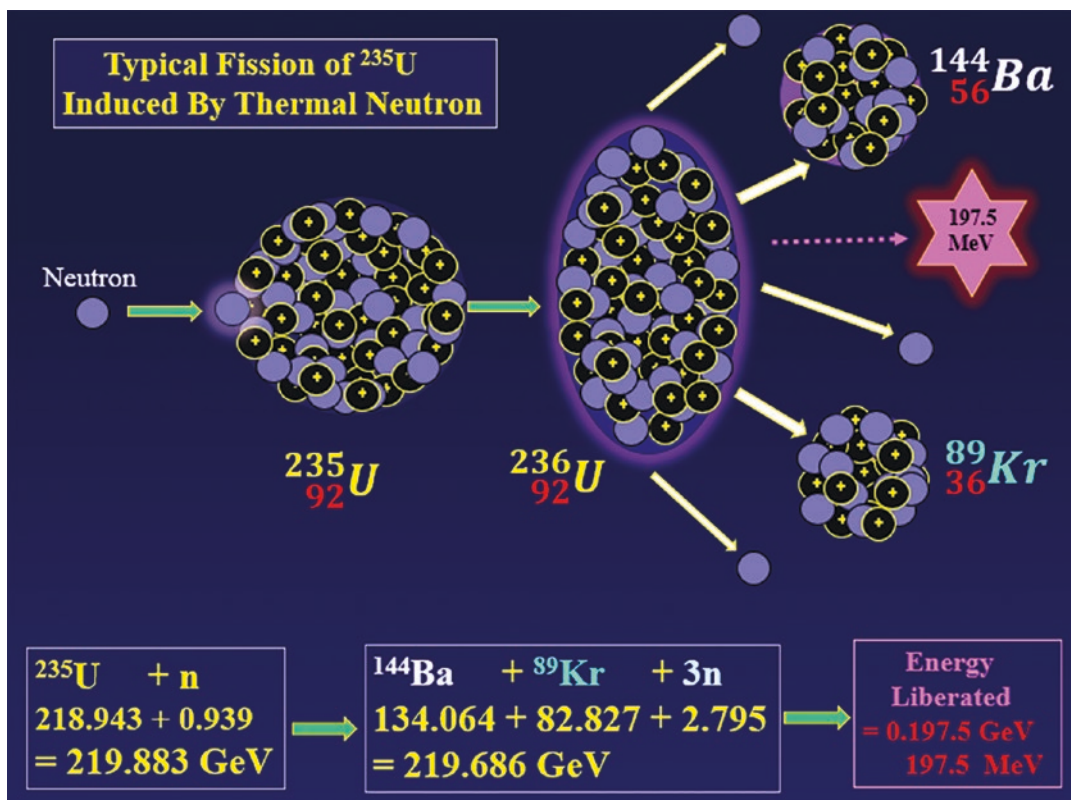
Fig. 8.2 Nuclear Fission of ^{235}U results in the formation of two low atomic number elements (^{144}Ba and ^{89}Kr) with the release of 3 neutrons and a very large amount of energy (MeV)

At the Radiation Laboratory in Berkely, California, physicists finally succeeded in the artificial production of transuramic elements, neptunium ($Z = 93$) and plutonium ($Z = 94$) by bombarding uranium with neutrons. In addition, with the availability of neutrons and high-energy charged particles, hundreds of nuclear reactions have been developed over the years to produce artificial radioisotopes that are either neutron rich or neutron deficient (proton rich). As discussed in the previous chapter, neutron-rich radionuclides decay by β^- or β^-, γ emission, while neutron-deficient radionuclides decay by β^+ or EC. Both these decay modes may also involve emission of gamma photons. In addition, positron annihilation will also lead to the emission of high-energy annihilation photons. Some of the early applications of radioisotopes in medicine involved naturally occurring radionuclides. It is the production of artificial radioisotopes, however, that eventually facilitated the development of nuclear medicine with molecular imaging technologies and targeted radionuclide therapies.

8.2.3   Nuclear Reactions

In a nuclear reaction, when the atoms of a stable element (target) are bombarded by a subatomic particle (called projectiles) such as neutron, proton, deuteron, or an α particle, the nucleus of the stable atom absorbs the subatomic particle. The resultant *compound nucleus* is very unstable and excited. The compound nuclei have lifetimes on the order of approximately 10^{-16} s. The compound nucleus may decay in one or more ways, depending on its neutron/proton ratio and excitation energy. It may quickly decompose by emitting some radiation (subatomic particle and/or gamma radiation) to form an unstable product radionuclide.

The general equation for a nuclear reaction can be written as follows:

$$T(P,R)Y \qquad (8.6)$$

where T represents the target nuclide, P is the projectile, the incident or bombarding particle, R

represents the radiation (subatomic particle or γ photons) emitted by the compound nucleus, and Y represents the unstable product radionuclide. The P and R in parenthesis, written as (P, R), represent the nuclear reaction. Reactions such as (p, n), (p, α), (d, α), (n, p), and (n, γ) are some of the common nuclear reactions used to produce artificial radioisotopes. In the case of neutron bombardment (e.g., in a reactor), there is no Coulomb repulsion from the positively charged nucleus, and neutrons easily penetrate the nucleus. In the production of radionuclides in a cyclotron, however, the accelerated charged particle must have an energy greater than the electrostatic repulsion between the positive charge of projectile and the positive charge of target nucleus.

8.2.3.1 Excitation Energy and Q Value
The total amount of *excitation energy* (U) of the compound nucleus is given by the following equation [3]:

$$U = \frac{M_T}{M_T + M_P}T_P + S_P \qquad (8.7)$$

where, M_T = mass of the target nucleus; M_P = mass of the incident particle or the projectile; T_P = kinetic energy of the incident particle; S_P = binding energy of the incident particle in the compound nucleus.

In any nuclear reaction, the total kinetic energy of the products (radiation R and product nucleus Y) may be either greater or less than the total kinetic energy of the reactants (target T and projectile P). The Q *value* is the difference between the energy levels of the reactants and products. Q value can be calculated based on the relationship, $E = mc^2$ and by knowing the rest energies of all the particles involved.

$$Q = (M_T + M_P - M_R - M_Y)(c^2) \qquad (8.8)$$

If Q is a positive quantity, energy is given off in a nuclear reaction (*exoergic*). If Q is a negative quantity (*endoergic*), kinetic energy (KE) must be supplied to the reacting particles so that the KE + $Q \geq 0$.

8.2.3.2 Activation Cross Section

For any specific nuclear reaction, the probability that a bombarding particle will interact with, or activate the target nucleus employs the idea of *cross section* (σ), which is expressed as an effective area [4]. It is assumed that each target nucleus presents a certain area, called its cross section, to the incident particle. Therefore, the greater the cross section, the greater the likelihood of reaction. However, the activation cross section depends on the energy of the bombarding particle and the nature of the specific nuclear reaction. It is the effective "target area" presented by the target nucleus; the SI unit for nuclear cross section is m^2. The customary unit, however, is *barn*, where

$$1\,\text{barn} = 1b = 10^{-24}\,cm^2 \text{ or } 10^{-28}\,m^2 = 100\,fm^2 \quad (8.9)$$

$$1\,\text{millibarn}\,(mb) = 10^{-3}\,b \text{ or } 10^{-27}\,cm^2 \text{ or } 10^{-31}\,m^2 \quad (8.10)$$

The cross sections for most nuclear reactions depend on the energy of the incident particle. The nuclear cross sections for thermal neutrons (0.025 eV) with no charge are higher than those for charged particles. The positively charged bombarding particle must have kinetic energy sufficient to overcome the coulomb barrier and the negative Q value (kinetic energy of the products is less than that of the reactants). The higher the atomic number (Z) of the target atom, the higher the kinetic energy (E) of the charged particle needed for a higher nuclear cross section [5]. For many low Z materials, it is possible to use a low-energy accelerator, but for high Z materials, it is necessary to increase the particle energy. A graphical relationship between σ and E for a specific nuclear reaction is known as *excitation function*. The excitation function for ^{18}F production is shown in Fig. 5.3 [6], as an example.

8.2.3.3 Activity

The amount of radioactivity (dps) produced by irradiation of a target material with a charged-particle beam can be described by the following equation [3]:

$$A\,(dps) = Inx\sigma\left(1 - e^{-\lambda t}\right) \quad (8.11)$$

In the above equation, I is the beam current or the number of bombarding particles per $cm^{-2}\,s^{-1}$; n is the number of target nuclei in cm^{-3}; x is the thickness of a target in cm; σ is the nuclear cross section, expressed in cm^2 per nucleus; λ is the decay constant of the product radionuclide; and t is the time of irradiation in seconds.

Saturation Yield

The amount of radioactivity (mCi) produced in a nuclear reaction is generally decay corrected to the end of bombardment (EOB). The saturation yield (mCi/μA) is the theoretical maximum rate of production of a radioisotope for given beam energy conditions and can be calculated using the following equation:

$$\text{Saturation yield}\,(mCi\,/\,\mu A) = \frac{A_0}{I\left(1 - e^{\lambda t}\right)} \quad (8.12)$$

where A_0 is the activity (mCi) at EOB, I is the beam current, and $1 - e^{-\lambda t}$ is the saturation factor for the radioisotope (Fig. 8.3).

Equation (8.11) is valid only for thin targets where the target beam is not attenuated. With thick targets (in which the energy of bombarding particle is completely absorbed), the particle beam is attenuated, and the target nuclei are bombarded with particles of varying energies. Yields with thick targets, therefore, depend on the energy and stopping power (or specific energy loss) in MeV cm^2 g^{-1} of the bombarding particle.

Specific Activity (SA)

SA is generally, defined as the amount of radioactivity per unit mass of an element, molecule, or compound, which implies that the mass represents the combined mass of radioactive species and the nonradioactive (stable or cold) counterpart. The unit of SA can be expressed as mCi/mg^{-1}, Ci/mmol^{-1}, or GBq μmol^{-1}. When dealing with chemical or molecular reactions, the stan-

Fig. 8.3 Excitation function of the $^{18}O(p,n)^{18}F$ reaction. Results from several investigators were plotted with the *solid line* representing the data from the Julich group [6]
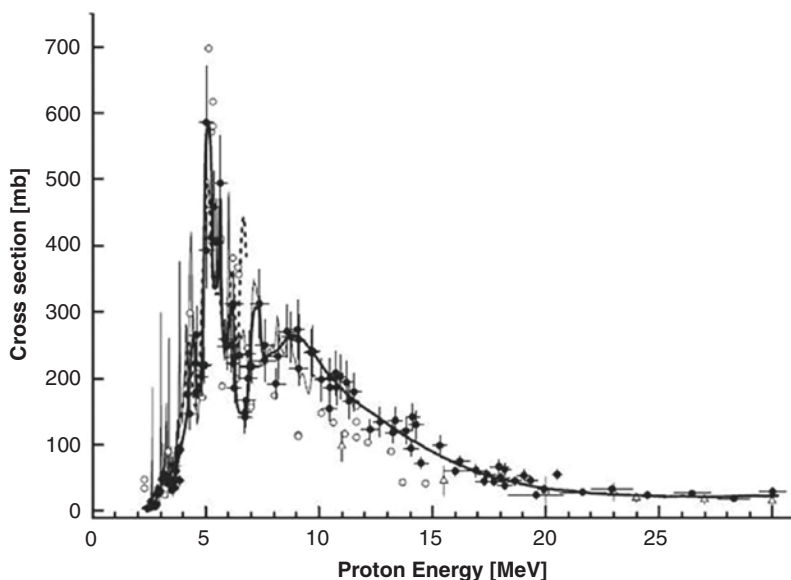
dard way to express SA is mCi µmol^{-1}. Because 1 mole represents 6.02×10^{23} atoms or molecules (Avogadro's number), one µmol consists of 6.02×10^{17} atoms or molecules.

For example, when ^{11}C radionuclide is produced in a cyclotron as [^{11}C]CO_2 gas, ^{11}C carbon atoms are always contaminated with natural carbon (^{12}C) and it is very difficult to obtain pure [^{11}C]CO_2 only. Therefore, if the SA of [^{11}C]CO_2 produced in a cyclotron target is 1.0 Ci µmol^{-1}, it implies that 1.0 Ci of radioactivity is present in a total mass of 1 µmole of carbon dioxide gas or a total of 6.02×10^{17} molecules (3.4×10^{14} molecules are present as [^{11}C]CO_2). That means, for every molecule of [^{11}C]CO_2 there are about 1700 molecules of cold, nonradioactive CO_2. The theoretical maximum SA (9220 Ci/µmole) is never really achieved in routine production of positron-emitting radionuclides. However, the SA concept is very important in dealing with PET radiopharmaceuticals, especially in the preparation of radiolabeled receptor-binding radiopharmaceuticals.

Carrier-Free

Carrier-free means that the radioactive species is not contaminated with nonradioactive counterpart, known as *carrier*. In the production of radionuclides in a cyclotron, the target element is converted into a different element (with a higher atomic number). As a result, cyclotron-produced radionuclides are supposed to be *carrier-free* (CF). Practically, however, it is very difficult to eliminate the contamination of natural carbon, fluorine, or trace metals during the synthesis procedure. A more appropriate concept is *no carrier added* (NCA) because the carrier, a stable, nonradioactive species, is not intentionally added. To facilitate chemical and biochemical reactions, a carrier may be added intentionally during radioisotope production. Such preparations should specifically be reported as *carrier added* (CA).

8.3   Production of Radionuclides by Accelerators

A particle accelerator is a machine that accelerates elementary particles, such as protons and electrons, to very high energies and to contain them in well-defined beams. A particle source provides the charged particles that are to be accelerated and then electric fields are used to speed up and increase the energy of a beam of particles. The beam of particles travels inside a vacuum in the metal beam pipe. The vacuum is crucial to maintaining an air and dust-free envi-

ronment for the beam of particles to travel unob-structed. Electro-magnets steer and focus the beam of particles while it travels through the vacuum tube.

There are two basic classes of accelerators: electrostatic and electrodynamic (or electromag-netic) accelerators. Electrostatic accelerators use static electric fields to accelerate particles. The most common types are the Cockcroft-Walton generator and Van de Graaff generator. *Electrodynamic* accelerators, on the other hand, use changing electromagnetic fields (nonreso-nant magnetic induction, or resonant circuits or cavities excited by oscillating radiofrequency (RF) fields) to accelerate particles. In addition, there are two basic types of particle accelerators: linear accelerators (LINAC) and circular accel-erators (cyclotrons). Linear accelerators propel particles along a linear, or straight, beam line. Circular accelerators propel particles around a circular track.

In 1932, two physicists, John Douglas, and Ernest Thomas Walton, working at the Cavendish laboratory in Cambridge performed the first arti-ficial nuclear disintegration in history using an electrostatic particle accelerator (Cockcroft–Walton generator) that generates a high DC volt-age and accelerates a proton by passing it through a single DC potential difference between two electrodes. They won the Nobel Prize in 1951 for "Transmutation of atomic nuclei by artificially accelerated atomic particles." The disintegration of lithium into α particles by protons was achieved using a proton beam with <0.77 MeV of energy [1]. Following absorption of the proton, the element lithium atom was converted into beryllium nucleus, which quickly split into two helium nuclei [7].

$$_3^7\text{Li} + _1^1\text{H} \rightarrow _4^8\text{Be} \rightarrow 2_2^4\text{He} \qquad (8.13)$$
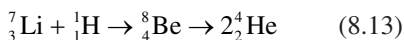
It soon became apparent that protons with higher energies were needed to penetrate the repulsive coulomb forces of the nucleus to produce nuclear transformations involving higher Z elements. More specifically, based on the principle of linear acceleration, very high voltage (millions of volts) is necessary to increase the kinetic energy of charged particles.

8.3.1   Linear Particle Accelerator (LINAC)

LINAC accelerates charged subatomic particles or ions to a high speed by subjecting them to a series of oscillating electric potentials along a linear beam line. They were originally invented in 1920s. The design of a LINAC, however, depends on the type of particle that is being accelerated: protons, electrons, or ions.

The radiofrequency (RF) LINAC produces repeated acceleration of ions through relatively small potential differences. Charged particle or ion is injected into an accelerating tube contain-ing number of electrodes. A high-frequency alter-nating voltage from an oscillator is applied between groups of electrodes. An ion traveling down the tube will be accelerated in the gap between the electrodes if the voltage is in the proper phase. The distance between electrodes increases along the length of the tube so that the particle stays in phase with the voltage.

LINAC (Fig. 8.4) consists of a series of tubes connected to a high-voltage power supply, which can provide alternating polarities to the tubes. At first, the odd-numbered tubes in (1, 3, 5, …) are negatively charged and the even-numbered tubes are positively charged to attract the protons from the H^+ ion source. As the protons enter and pass through tube-1, the polarities of the tubes are reversed. As tube-1 is now positive and tube-2 is negative, protons are attracted to tube-2. This process continues through many tubes, until the velocity and energy of the protons increase.

8.3.1.1 Proton Accelerator

American Physicist Luis Alvarez developed the designs for proton LINAC in 1946. The two largest proton linear accelerators are the LANSCE linac at Los Alamos (800 MeV) and the Spallation Neutron Source Linac at ORNL
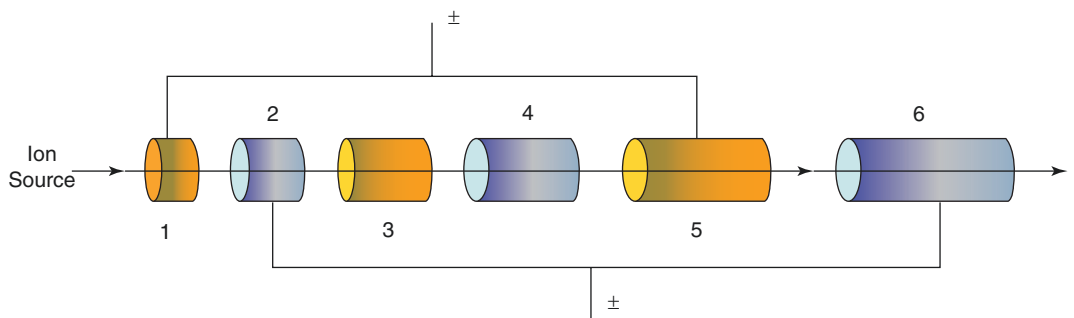
Fig. 8.4 A linear accelerator (LINAC) based on a voltage multiplying circuit designed to accelerate protons along a linear path to achieve higher energies

(1000 MeV). In the United States, the two accelerator installations with significant radionuclide production programs are the Brookhaven Linac Isotope Producer (BLIP) facility at Brookhaven National Laboratory and the Los Alamos National Laboratory Isotope Production facility (LANL-IPF) at the Los Alamos National Laboratory. The BLIP facility consists of a 30 m beam line and can generate 200 MeV protons with 170 μA beam current. The LANF-IPF facility produces radioisotopes at beam currents up to 275 μA using the 100 MeV proton beam generated at the front end of the Los Alamos Neutron Science Center (LANSCE) accelerator. The radioisotopes commonly produced at these two facilities include ^{68}Ge, ^{82}Sr, ^{225}Ac, and ^{67}Cu.

A compact proton-LINAC based radioisotope production, already commercially available, since 2005, is the PULSAR®7 system, by AccSys Technology Inc. It produces a 7 MeV proton beam with 9 mA current for [^{18}F]FDG production [8]. Such low energy has been chosen to reduce the footprint, weight, and cost of the accelerator, allowing, the installation of the accelerator in medical trailers, the only truly mobile PET lab available.

8.3.1.2   Electron Accelerator

The electron linear accelerator (e-LINAC) is an instrument for the acceleration of electrons to high energies by means of guided electromagnetic waves. It may serve as a source of both energetic electrons and X-rays. Although very high energies have been achieved with LINAC to serve the purposes of investigations in nuclear physics, moderate energies (3–30 MeV) are sufficient for external beam radiation therapy. E-LINACs in the 5–10-MeV range are used for irradiation sterilization of medical disposables such as syringes and surgical kits.

The LINAC uses microwave technology to accelerate electrons and then allows these electrons to collide with a heavy metal target (such as tungsten) to produce high-energy bremsstrahlung radiation (X-rays).

When a high-speed projectile electron comes close to the nucleus of the tungsten atom in the target, the positively charged nucleus causes the electron to decelerate and change direction. This deceleration results in a loss of kinetic energy, which is converted into X-rays. Bremsstrahlung X-rays have a spectrum of energies with an average energy proportional to the peak kilovolts used. However, the quantity of bremsstrahlung X-rays is related more to mAs (tube current) than peak kilovolts.

Even though the basic technology has been around for decades, only recently have e-LINACs capable of producing photons with sufficient energy and flux for radioisotope production become available [9, 10]. Photonuclear production of radionuclides using (γ, p) and (γ, n) nuclear reactions provide significant advantages compared to conventional cyclotron-produced methods. Housed in Argonne National Low

Energy Accelerator Facility (LEAF) at the Argonne National Laboratory is a newly upgraded 55 MeV/25-kW e-LINAC, capable of producing a wide range of radioisotopes (^{99}M0, ^{67}Cu, and ^{47}Sc).

8.3.2   Cyclotron

In 1929, Ernest O. Lawrence, an American physicist and inventor at the University of California, Berkeley, conceived the idea of a cyclic accelerator or *cyclotron*. In the presence of a static magnetic field, an ion of specific charge, when introduced at the center of a cyclotron, will accelerate in an expanding spiral path by use of an alternating radiofrequency electric field [11]. In 1939 Lawrence was awarded the Nobel Prize in Physics. The first cyclotron built by Lawrence had a diameter of a few inches and the glass vacuum chamber in which ions were supposed to circulate, could be held in one hand (Fig. 8.5). In 1939, Lawrence's 60-inch cyclotron, with 16 MeV protons was the most powerful accelerator in the world at the time. Glenn T. Seaborg and Edwin M. McMillan used it to discover plutonium, neptunium, and many other transuranic elements and isotopes, for which they received the 1951 Nobel Prize in chemistry.

8.3.2.1   Negative Ion Cyclotron

Traditionally, cyclotrons were designed to accelerate positive ions (H$^+$, ^{2}H$^+$, and α^{2+}). The first cyclotron designed to accelerate negative ions of hydrogen, or deuterium atoms with two electrons in the *K*-shell (H$^-$ and ^{2}H$^-$) was built in 1966. Since the 1980s, all the medical and commercial cyclotrons are basically negative ion cyclotrons. One of the most important advantages of the negative ion cyclotron is the elimination of a complex *beam extraction system* needed to extract fixed energy positively charged particles. As a result, negative ion cyclotrons provide the opportunity to extract beams with different energies thereby allowing for the simultaneous bombardment of two different targets [12, 13].

The cyclotron (Fig. 8.6) consists of three major components: an electromagnet with a field strength

Fig. 8.5 The first working model of a 4.5 in. cyclotron, which accelerated protons to 80 KeV energy [11]

of 1.5–2.0 tesla, a pair of semicircular hollow copper electrodes, called *dees* located between the poles of the magnet, and an ion source (Penning ion gauge) capable of generating high-intensity negative ions. The entire structure of the cyclotron is kept under high vacuum (up to 10^{-7} torr). Following ionization of the hydrogen gas in an ion source, the ions (protons or deuterons) are injected into the center of the gap between the dees. When a 20–30 MHz radiofrequency alternating potential of 30–100 kV, generated with an oscillator, is applied to the dees, the negative ions will accelerate towards a dee that is at a positive potential. Because the magnetic field is perpendicular to the plane of the dees and particle motion, the negative ions will trace a circular path. Further, because the electrical potential on the dees is alternatively positive and negative, the ions will gain energy at each crossing of the gap between the dees, as they move outward in a spiral path from the center. Lawrence [11] described the basic operational equations as follows:
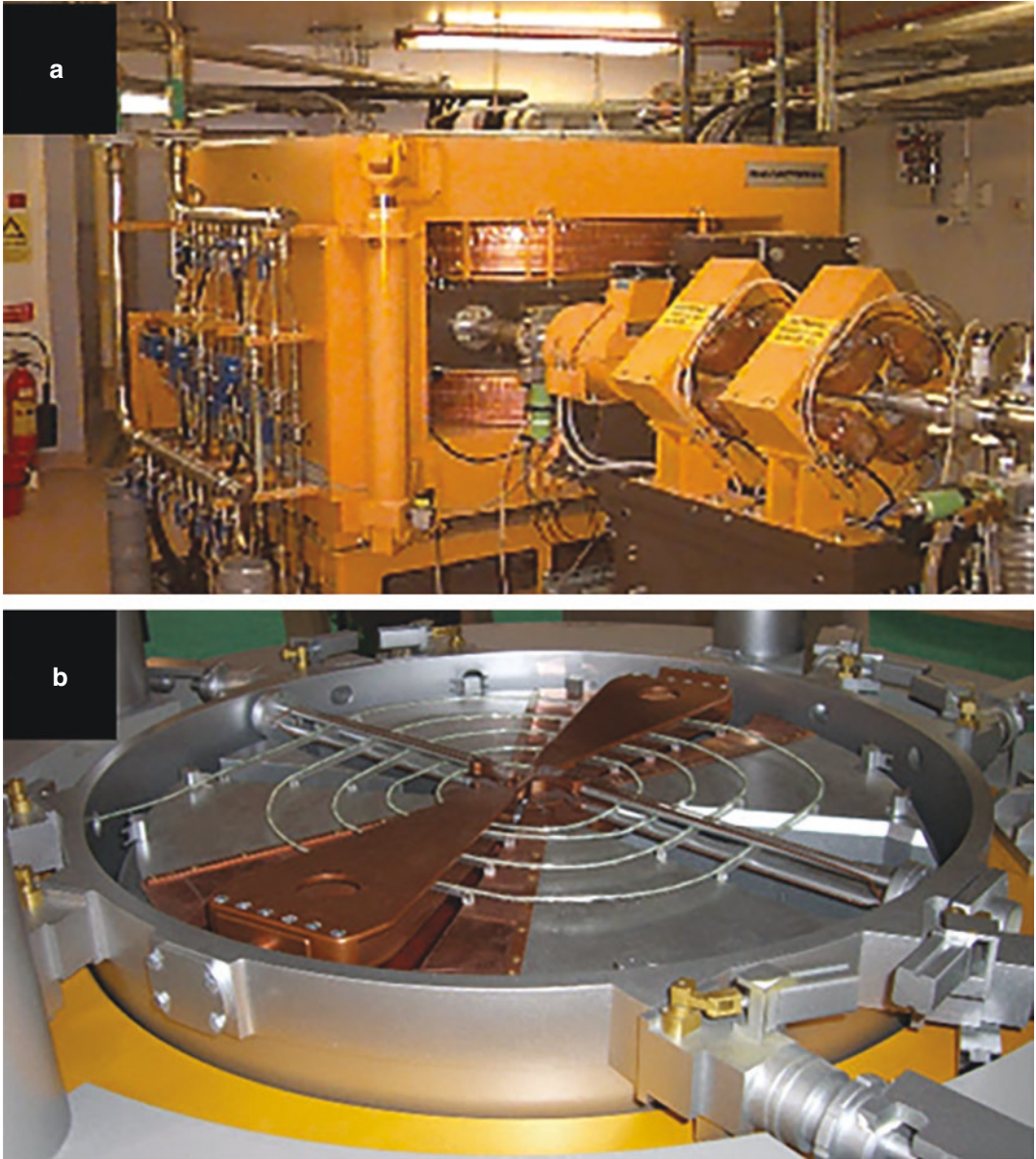
Fig. 8.6 A negative ion cyclotron (EBCO-TR19) with an external beam line (**a**). A model of the vacuum chamber (CTI systems) showing the copper electrodes (dees) in which a negatively charged proton beam making circular orbits (**b**)

Particle Energy

The magnetic force operating on the ion is a centripetal force (Bev), which is exactly balanced by the centrifugal effect (mv^2/r).

$$\text{Bev} = \frac{mv^2}{r} \text{ and } r = \frac{mv}{Be} \qquad (8.14)$$

In the above equations, B is the magnetic field strength while m, e, and v represent the mass, charge, and velocity of the ion, respectively. Finally, r represents the radius of the ion's orbit. For a given cyclotron, the maximum kinetic energy that an ion can attain can be estimated if B and r are kept constant.

$$E = \frac{B^2 r^2}{2} \left(\frac{e^2}{m} \right) \qquad (8.15)$$

The final energy of the particles is, therefore, dependent on the strength of the magnetic field and the diameter of the accelerating chamber, the dees. Cyclotrons can only accelerate particles to speeds much slower than the speed of light, non-relativistic speeds.

A *synchrocyclotron* is a cyclotron in which the frequency of the driving RF electric field is varied to compensate for relativistic effects as the particles' velocity begins to approach the speed of light. This is in contrast to the classical cyclotron, where the frequency was held constant. An alternative to the synchrocyclotron is the *isochronous cyclotron*, which has a magnetic field that increases with radius, rather than with time. Isochronous cyclotrons (also known as Azimuthally-Varying-Field or AVF Cyclotron) are capable of producing much greater beam current than synchrocyclotrons.

Beam Extraction

Once the desired kinetic energy of the accelerating particles is achieved, the positively charges ions (H^+ and $2H^+$) are extracted from the cyclotron by passing the negative ion beam through an ultra-thin foil of carbon (graphite), which strips the electrons. The positively charged beam will rotate in an opposite direction, which can then be directed to bombard an appropriate target to produce a positron-emitting radioisotope. The typical intensities (beam currents) and the energies of proton and deuteron beams generated in commercial cyclotrons are shown in Table 8.1. The beam current is generally expressed in units of microampere (μA). For example, a 1 μA proton beam current is equal to 6.25×10^{12} protons or deuterons/s.

Types of Cyclotrons

Almost all current available commercial cyclotrons are negative ion machines. Close to 1500 cyclotrons are used in nuclear medicine worldwide, for the production of radionuclides. A wide range of cyclotrons for isotope production have been developed by companies and research centers and may be categorized into 3 types of cyclotrons: (a) Low-energy cyclotrons for PET radioisotope production (<15 MeV, 10–150 μA current). These small-sized medical cyclotrons (SMC) are also referred to as PET cyclotrons. (b) Medium-energy cyclotrons (15–30 MeV, 100–1000 μA) for novel PET nuclides, and SPECT radionuclides. (c) Higher energy cyclotrons (>35 MeV, 500–1000 μA) for the production of therapeutic nuclides and also the parent nuclides for the radionuclide generators. The technical features of several medical cyclotrons are summarized in Table 8.1.

8.3.3 PET Radionuclides

The greatest advantage of PET is the potential to image and study biochemical processes in vivo, without altering or affecting the homeostasis in any way. Low atomic number elements such as carbon, nitrogen, oxygen, and phosphorous are naturally stable. The development of cyclotrons in the 1930s created an opportunity to produce positron-emitting radioisotopes of carbon (^{11}C), nitrogen (^{13}N), and oxygen (^{15}O) and fluorine (^{18}F). Since the 1950s, these four PET radionuclides played a significant role in the development of biochemistry and pharmacology.

The most important nuclear reactions used in the production of positron-emitting radionuclides for imaging and therapy are summarized in Tables 5.2, 5.3, and 5.4. Many reviews have been

Table 8.1   Medical cyclotrons for the production of positron-emitting radionuclides

Company	Cyclotron Model	Particle beam			Number of targets
		Type	Energy MeV	Current μA	
GE	GENtrace™	H⁻	7.8		3
GE	MINItrace™ Quilin	H⁻	9.6	>50	5
GE	PETtrace™ 800 series	H⁻/D⁻	16.5 /8.6	60–160	6
Siemens/CTIᵃ	Eclipse HP/RDS-111	H⁻	11	>120	4 or 8
Siemens	Eclipse RD	H⁻	11	>80	2 × 8ᵇ
IBA	Cyclone 3	D⁺	3.6	50	2
IBA	Cyclone 10/5	H⁻/D⁻	10/5	60/35	8
IBA	Cyclone 11	H⁻/	11	120	8
IBA	Cyclone 18/9 Cyclone® KIUBE	H⁻/D⁻ H⁻	18/9 13–18	80/35 100–300	8 8
IBA	Cyclone-30	H⁻/D⁻	30/15	400–1200	8
IBA	Cyclone-70	H⁻/α²⁻	70/?	<1500	8
ACSI	TR-14	H⁻	14	>100	2 × 4ᶜ
ACSI	TR-19	H⁻/D⁻	19/8	300/100	2 × 4ᶜ
ACSI	TR-24	H⁻	24	300	2 × 4ᶜ
ACSI	TR-30	H⁻/D⁻	30/15	1500/400	2 × 4ᶜ
ABT MII	BG-75	H⁺	7.5	5	3*
Alcen-PMB	iMiTrace superconducting	H⁻	12	50	4
Ionetix	Ion-12sc s-c	H-	12	10	
CIEMAT/Cern	AMIT s-c	H⁻	12.5	>25	
PMB-ALCEN	LOTUS s-c	H⁻	12	50	4
BEST CSI	Best 15P	H⁻	15	400	4
BEST CSI	Best 25P	H⁻	15–25	400	4
BEST CSI	Best 35P	H⁻	15–35	<1000	4–6
Best CSI	Best 70P	H⁻	35–70	<1000	6
Sumitomo	HM12	H⁻/D⁻	12/6	>120	8
Sumitomo	HM18	H⁻/D⁻	18/10	>180	8
CIAE	CYCIAE-14	H⁻	14	400	8
CIAE	CYCIAE-70	H⁻/D⁻	70/33	700	8

ᵃSelf shielding for cyclotrons is standard
ᵇTwo beam ports, each with an eight-target carousel
ᶜTwo beam ports, each with a four-target carousel

published on the cyclotron production of positron-emitting radionuclides. The International Atomic Energy Agency (IAEA) published a technical report [14] in 2009 on the physical characteristics and production methods of cyclotron-produced radionuclides.

The target designed for the production of a positron-emitter consists of a target body suitable for the bombardment of a specific target material (gas, liquid, or solid) that undergoes nuclear transformation. Typical gas targets are made up of aluminum, while the liquid targets are made up of aluminum, silver, titanium, and niobium. A generic cyclotron target (Fig. 8.7) consists of a sealed metal tube with a window of thin metal foil at one end to allow the particle beam to pass through and irradiate the target material. In order to dissipate the excess heat generated during irradiation, the target body is generally surrounded by a cooling water jacket, while helium gas is circulated through the foils separating the target material and the vacuum isolation foil through which the beam enters the target (Table 8.2).

8.3.3.1 Oxygen-15

^{15}O decays ($T_{1/2} = 2.04$ months) to nitrogen-15, emitting a positron. ^{15}O was one of the first artificial radioisotopes produced by low-energy deu-
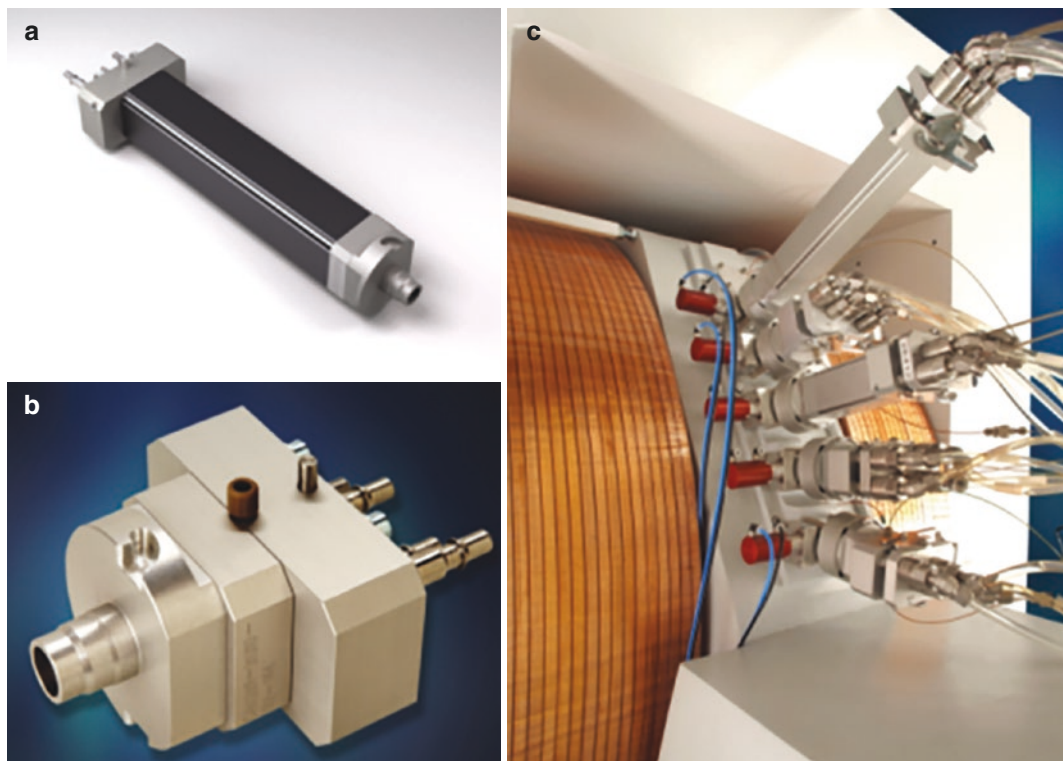
Fig. 8.7 ^{14}N gas target chamber (**a**) for the production of ^{11}C as carbon dioxide and an [18]O water target chamber (**b**) for the production of ^{18}F as fluoride. Placement of these targets in the PETtrace (GE) cyclotron (**c**)

terons using a cyclotron [15]. [15]O can be produced by different nuclear reactions, including [14]N(d,n)[15]O, [16]O(p,pn)[15]O, and [15]N(p,n)[15]O. For the [15]N(p,n)[15]O reaction, low-energy protons (<11 MeV) MeV) or the medium-energy protons (>16.6 MeV) can be used. To use low-energy protons, however, the target must be highly enriched ^{15}N gas [5, 16]. The most common nuclear reaction and most economic method used for the production of [15]O is deuteron bombardment of ^{14}N atoms using natural nitrogen containing 0.2–0.5% oxygen as the target gas and the target body is generally made of aluminum. The oxygen-15 ion combines with an oxygen atom to form the stable oxygen gas [^{15}O]O_2. To produce [15]O as [^{15}O]CO_2 gas, the target nitrogen gas is mixed with 2–2.5% carbon dioxide.

To produce [^{15}O]water outside the target, a stream of nitrogen gas continuously flows through the target to a hot cell containing a water synthesis module, in which [15]O combines with H_2 gas in the presence of palladium–aluminum catalyst at high temperatures (300–400 °C) to produce water vapor, which then bubbles into a saline solution and is drawn into a syringe where it can be applied to the subject. [^{15}O]water is used for measuring and quantifying blood flow using PET in the heart, brain, and tumors.

8.3.3.2 Nitrogen-13 and [^{13}N]Ammonia

The first production of ^{13}N was based on bombarding boron atoms with α particles [2]. The most common nuclear reaction for the production of ^{13}N is [16]O(p, α)[13]N. The natural stable oxygen atoms are bombarded with proton (10–15 MeV) using oxygen gas target or liquid (water) target [5, 17, 18]. When ^{13}N is produced in the target, it reacts with water forming nitrate and nitrite ions. The addition of a reducing agent, such as titanium chloride, to the target water will generate [^{13}N]NH_3. With a pressurized target, aqueous ethanol can be used in the

Table 8.2 Cyclotron-produced radionuclides for PET

Radionuclide	$T_{1/2}$	Decay Mode	%	Energy β^+_{max} (MeV)	γ (MeV)	Production Method Nuclear reaction	Target Material
^{15}O	2.0 min	β^+ EC	99.9 0.1	1.732		^{14}N(d, n)^{15}O	N_2 gas
^{13}N	10.0 min	β^+ EC	99.8 0.2	1.199		^{16}O(p, α)^{13}N	H_2O
^{11}C	20.4 min	β^+ EC	99.8 0.2	0.960		^{14}N(p, α)^{11}C	N_2 + <1% O_2
^{18}F	110 min	β^+ EC	96.9 3.1	0.634		^{18}O(p, n)^{18}F ^{20}Ne(d, α)^{18}F	[^{18}O]H_2O Ne + 0.2% F_2
^{68}Ga	67.8 min	β^+ EC	88.9 11.1	1.899	1.077 (3%)	^{68}Zn(p, n)^{68}Ga	Solid/liquid
^{44}Sc	3.97 h	β^+ EC	94 6	1.474	1.157 (100%)	^{44}Ca(p, n)^{44}Sc ^{45}Sc(p,2n)^{44}Ti$\rightarrow$^{44}Sc	Solid/liquid
^{64}Cu	12.7 h	β^+ β^- EC	17.86 39.00 43.08	0.653	1.346 (0.48%)	^{64}Ni(p, n)^{64}Cu	Solid/liquid
^{66}Ga	9.5 h	β^+ EC	56.5 43.5	4.153	1.037 (37%)	^{66}Zn(p, n)^{66}Ga	Solid
^{86}Y	14.7 h	β^+ EC	31.9 68.1	1.221	1.077	^{86}Sr(p, n)^{86}Y	Solid
^{89}Zr	3.267 days	β^+ EC	22.7 76.2	0.902	0.909 (99%)	^{89}Y(p, n)^{89}Zr	Solid/liquid
^{124}I	4.176 days	β^+ EC	22.7 77.3	2.138	0.602 (63%)	^{124}Te(p, n)^{124}I ^{124}Te(d, 2n)^{124}I	Solid

National Nuclear Data Center (NNDC): NuDat 3.0 @NuDat 3 (bnl.gov)

target since ethanol acts as a hydroxyl free radical scavenger to improve the production of [^{11}N]NH$_3$.

Because the half-life of ^{13}N is very short (9.97 min), it is very difficult to synthesize ^{13}N-labeled radiotracers for routine clinical PET studies. In the 1970s, [^{13}N] ammonia (NH$_3$ or NH$_4^+$ ion) has been shown to be clinically useful as a myocardial perfusion imaging agent. The production of ^{13}N involves the generation of [^{13}N] NH$_3$ gas directly in the target itself.

8.3.3.3 Carbon-11

^{11}C decays 100% by positron decay with a maximum b+ energy of 968 keV. The most common nuclear reaction used to produce ^{11}C is ^{14}N(p, α)^{11}C. Natural nitrogen gas is bombarded with protons [5, 19, 20]. Because nitrogen gas is relatively inert, it does not interfere with the carbon chemistry and can be easily eliminated. By mixing trace amounts (<1%) of oxygen or hydrogen

with the target nitrogen gas, the chemical forms of ^{11}C produced in the target can be either [^{11}C] CO$_2$ or [^{11}C]CH$_4$ (methane). The gas target body is basically made up of an aluminum cylinder (or cone shape) that should be able to handle gas (10–100 cc) at pressures of 300–800 psi. Beam currents of 20–40 µA are typically used. It is very important to prepare or polish the inside of the aluminum target to significantly reduce the contamination of natural carbon. As the natural nitrogen gas is also contaminated with CO$_2$ gas, it is essential to use extremely high purity (99.99999%) target gases.

Specific activity of ^{11}C is very important to prepare receptor specific C-11 radiotracers. [^{11}C]CO$_2$ can be produced in most cyclotron targets with a SA of 5–20 Ci/µmol at EOB. Even higher SA can be achieved by producing [^{11}C] CH$_4$ directly in the target. The theoretical SA is 9600 Ci/µmol. If possible, all sources of carrier carbon need to be assessed and eliminated.

8.3.3.4 Fluorine-18

Among halogens, ^{18}F ($T_{1/2}$ = 109.8 months) is the most important radionuclide for PET. Because the atomic radius of fluorine is similar to that of hydrogen, in most molecules, fluorine can be used as pseudo-hydrogen.

There are several nuclear reactions are available to produce F-18. Since fluorine can be introduced into molecules using its nucleophilic and electronegative property, the two common nuclear reactions are ^{18}O(p, n)^{18}F and 20Ne(d, α)^{18}F. Basically, there are two kinds of targets used in a cyclotron to produce two different chemical forms of F-18 radionuclide. A liquid target for the production of ^{18}F as nucleophilic fluoride ion (^{18}F$^-$) and a gas target for the production of ^{18}F as electrophilic fluorine as [^{18}F]F$_2$ gas [21, 22].

The most common nuclear reaction used to produce ^{18}F as fluoride ion is on the basis of proton bombardment of ^{18}O atoms using highly enriched [^{18}O] water as the target material [5, 22]. The coproduction of ^{13}N via the ^{16}O(p, α)^{13}N reaction should be taken into account when using ^{18}O of lower enrichment (<90%). A typical target body is made of titanium and niobium to hold 0.3–3.0 mL of target water. Several curies of ^{18}F can easily be made in 1–2 h using 10–19 MeV protons with 20–35 μA beam current. While the theoretical SA of ^{18}F is 1700 Ci/μmol^{-1}, the NCA ^{18}F is generally produced with a SA of <10 Ci/μmol^{-1}.

The most common nuclear reaction to produce [^{18}F] fluorine gas is on the basis of deuteron bombardment of ^{20}Ne atoms using natural neon gas [5]. A passivated nickel target (NiF) is loaded with neon gas containing 0.1% of natural fluorine gas. Following bombardment for 1–2 h with 8–9 MeV deuterons, <1.0 Ci of [^{18}F]F$_2$ is generated with a very low SA of (10–20 mCi/μmol^{-1}). A "double shoot" method was developed to produce [^{18}F]fluorine gas on the basis of proton bombardment of ^{18}O atoms using [^{18}O]oxygen gas loaded into a gas target [23]. After irradiation, ^{18}F species stick to the walls of the target. The ^{18}O target gas is removed from the target, which is then loaded with argon gas mixed with 1% of cold fluorine gas. A second short irradiation for

<10 min will generate [^{18}F]F$_2$ gas. This method is very useful to make electrophilic ^{18}F, using cyclotrons generating proton beams only. Since [^{18}F]F$_2$ is always diluted with carrier (cold) fluorine gas, the SA of electrophilic [^{18}F] fluorine is very low and not optimal for synthesizing high SA ^{18}F labeled radiopharmaceuticals.

8.3.3.5 Bromine-75 and Br-76

Both these radionuclides are generally made by proton (17 MeV) bombardment of ^{76}Se atoms using enriched ^{76}Se (96%) Cu$_2$Se as the target material [5]. Subsequently, ^{76}Br is separated from the solid target by thermal diffusion. The longer half-life (16.2 h) of ^{76}Br is favorable for the synthesis of radiopharmaceuticals and commercialization. However, ^{76}Br has a complex decay scheme and high-energy positrons which may provide an unfavorable radiation dose to the patient.

^{75}Br with a shorter half-life (97 min) may be more optimal for developing PET radiopharmaceuticals. One of the common nuclear reactions is ^{76}Se(p,2n)^{75}Br, but the energy of proton needed for this reaction is between 18–28 MeV. ^{75}Br is separated from a solid target by dry distillation method and trapped using platinum wool.

These two bromine radioisotopes generally are not used in the development of PET radiopharmaceuticals for imaging studies.

8.3.3.6 Iodine-124

^{124}I ($T_{1/2}$ = 4.2 days) has often been considered as an impurity in the preparations of ^{123}I. The half-life of ^{123}I is long enough to image the distribution of monoclonal antibodies using PET. However, it also has many gamma emissions (such as 0.602 and 1.691 MeV) and some low-energy beta emissions contributing to the dosimetry.

The best nuclear reaction for the production of ^{124}I is the ^{124}Te(p, n)^{124}I reaction on enriched ^{124}Te target [24, 25]. The solid target material consists of a solid solution matrix containing aluminum oxide and enriched ^{124}Te oxide. The separation of iodine from tellurium can be accomplished by distillation of ^{124}I from the tellurium oxide matrix at 750 °C. The iodine is carried away from the target with a sweep of either oxygen or helium

and trapped on a thin pyrex glass tube that is coated with a small amount of sodium hydroxide.

Since the radioiodination of proteins and peptides is relatively easy, [124]I has significant potential for the development of radiopharmaceuticals for PET. However, the longer half-life and complicated decay schemes with high-energy positrons may make this radionuclide suboptimal for diagnostic studies, as the radiation dose to the patient can be relatively high.

8.3.3.7 Gallium-66 and Gallium-68

[66]Ga ($T_{1/2}$ = 9.4 h) and [68]Ga ($T_{1/2}$ = 67.71 months) are the two gallium PET radionuclides of interest. The short half-life ^{68}Ga emits positrons (β^+, 89%; E_{max} = 1.899 MeV) and has the favorable positron energy for PET imaging studies. While [66]Ga has relatively longer half-life, but very high-energy positrons (β^+, 54.7%; E_{max} = 4.1 MeV) and several high-energy gamma photons (0.291–4.806 MeV), it is not ideal for imaging studies.

[66]Ga can be produced using proton bombardment based on any of these nuclear reactions; [66]Zn(p,n)[66]Ga, [67]Zn(p,2n)[66]Ga, and [66]Zn(p,3n)[66]Ga. Among these [66]Zn(p,n)[66]Ga reaction is the most common method using 7–15 MeV protons (at high beam currents) and enriched [66]Zn metal target, electrodeposited on a copper backing plate [5]. Subsequently, [66]Ga can be easily separated from zinc by cation-exchange or solvent extraction techniques.

[68]Ga production method is based on [68]Zn(p,n)[68]Ga nuclear reaction. It is generally necessary to bombard isotopically enriched [68]Zn(>98%) since several radioisotopes of gallium with longer half-lives than ^{68}Ga are also coproduced when irradiating natural Zn. However, despite use of isotopically enriched [68]Zn, small amounts of [66]Ga and ^{67}Ga will occur via [68]Zn(p,3n)[66]Ga and [68]Zn(p,2n)[67]Ga reactions. As shown in Fig. 8.8, the composition of the isotopically enriched [68]Zn and the proton energy (~11 MeV) must be selected wisely to balance yield and achieve a purity suitable for human use [26]. For solid targets, ^{68}Ga may be a) electroplated on copper or silver supports, b) used as metal foils, on aluminum support. The irradiation of a [68]Zn solution

(as zinc nitrate, 1–2 M) in a liquid target (a solution target) also provides a practical and inexpensive alternative to produce clinical quantities of [68]Ga.

Purification of ^{68}Ga from the zinc target is generally performed based on solid phase using either cation-exchange resin or hydroxamate resin. For additional purification, anion-exchange resins AG-1X8, TK200 (Trioctylphosphine oxide), UTEVA® (diamyl, amylphosphonate), DGA (tetra-n-octyldiglycolamide) can be used. Finally, ^{68}Ga is supplied as high specific activity, no-carrier-added gallium chloride solution in <0.1 M hydrochloric acid.

8.3.3.8 Copper-64

Copper has several positron-emitting radioisotopes, such as [61]Cu, [62]Cu, and [64]Cu. Because of its longer half-life of 12.7 h and low-energy positrons, ^{64}Cu is more appropriate for developing commercial PET radiopharmaceuticals. It can be produced via the [64]Ni(p,n)[64]Cu nuclear reaction using enriched nickel solid target foils [5]. Subsequently, ^{64}Cu is separated by dissolving the target in an acidic solution, followed by ion-exchange chromatography. Using similar techniques, [61]Cu can also be produced via the [61]Ni(p,n)[61]Cu nuclear reaction, using enriched nickel solid target foils.

8.3.3.9 Yttrium-86

[86]Y ($T_{1/2}$ = 14.7 h) is a medium half-life radionuclide emitting very high-energy (3.15 MeV) positrons not ideal for high-resolution quantitative PET studies. In addition, it has several high-energy γ emissions. As a trivalent metal, it binds strongly to DOTA-conjugated peptides and antibodies.

It can be produced via the [86]Sr(p,n)[86]Y nuclear reaction using isotopically enriched [86]Sr foil or strontium carbonate pellet. The proton reaction can be carried out at relatively low energies (10–15 MeV). Subsequently, [86]Y can be separated by dissolving the target in an acidic solution, followed by precipitation and purification by ion-exchange chromatography. The specific activity of the final purified [86]Y chloride preparations is 15–30 mCi/mg.
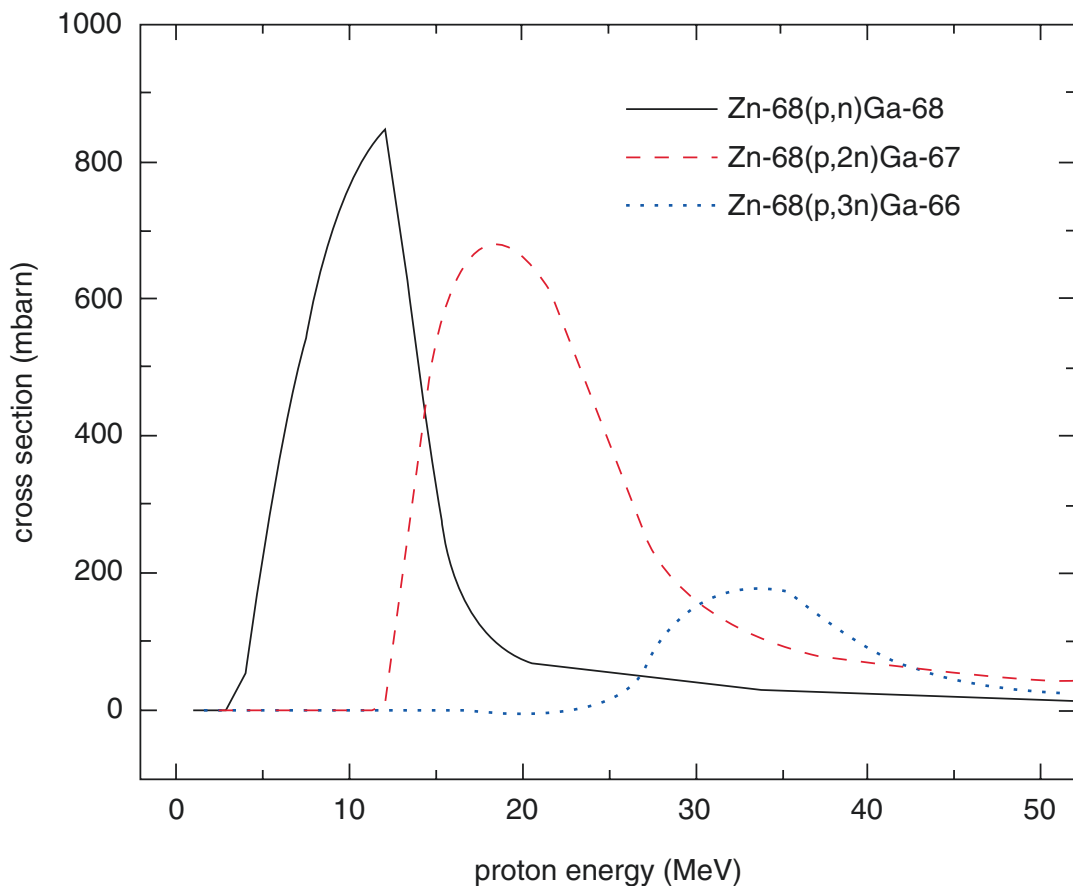
Fig. 8.8 Excitation function for the ^{68}Zn(p,n)^{68}Ga, ^{68}Zn(p,2n)^{67}Ga and ^{68}Zn(p,3n)^{66}Ga reactions. Data from (From [26])

8.3.3.10 Zirconium-89

Zr-89 ($T_{1/2}$ = 3.3 days) is a transition metal and has ideal physical characteristics for immuno-PET imaging studies. The most commonly used nuclear reaction is the ^{89}Y(p,n)^{89}Zr reaction, because a higher yield of ^{89}Zr can be produced from ^{89}Y, which is 100% naturally abundant in the earth's crust [27]. Typically, a proton beam (14–15 MeV) is used to bombard an yttrium foil solid target for 2–3 h with a 65–80 µA beam current. No other radionuclides are produced as impurities. ^{89}Zr can also be produced using ^{89}Y(d,2n)^{89}Zr reaction using 15–20 MeV deuteron energy. In this reaction, an yttrium pellet is used and irradiated with a 16-MeV deuteron beam. ^{89}Zr can be easily purified and separated

from the target by ion-exchange chromatography (using hydroxamate resin column) and supplied as ^{89}Zr oxalate.

8.3.3.11 Scandium-44

^{44}Sc is a transition metal with similar chemical properties as gallium. ^{44}Sc with a half-life of 3.97 h is an attractive alternative to ^{68}Ga with only 68 min half-life. It can be produced via the ^{44}Ca(p, n)^{44}Sc nuclear reaction with a proton beam (11–18 MeV at 30-50 µA beam current) using an enriched ^{44}Ca target as $CaCO_3$ or CaO [28, 29]. ^{44}Sc can be easily separated from the target material using DGA extraction resin and concentrated using SCX cation-exchange resin.

8.3.4 SPECT Radionuclides

8.3.4.1 Gallium-67

^{67}Ga ($T_{1/2}$ = 3.26 days) decays to stable zinc by electron capture with several γ photons of 93.3 keV (37.0%), 184.6 keV (20.4%), and 300.2 keV (16.6%). As a trivalent metal gallium behaves in the body in a similar way to ferric iron. It is a diagnostic imaging agent in the detection and localization of certain neoplasms and inflammatory lesions.

^{67}Ga can be produced by several nuclear reactions using high-energy protons (20–25 MeV). The most common reactions are ^{68}Zn(p,2n)^{67}Ga and ^{66}Zn(d,n)^{67}Ga. The enriched ^{68}Zn may be pressed or electroplated onto a copper plate. Following irradiation, the zinc target is dissolved in concentrated hydrochloric acid (7 N) and ^{67}Ga is extracted into an organic phase using isopropyl ether. Following evaporation of the organic phase, ^{67}Ga is formulated as chloride using dilute HCl (0.1 N). The typical SA of ^{67}Ga is around 1000 mCi/mg (67 mCi/μmol) and radionuclidic purity is about 99.4%. The ion-exchange method involves dissolving the zinc target in concentrated HCL and separating the ^{68}Ga using Dowex 50 W-X8 resin (Table 8.3).

8.3.4.2 Indium-111

^{111}In ($T_{1/2}$ = 2.83 days) decays to stable cadmium by electron capture with two γ photons of 171.3 keV (90.2%), and 245.4 keV (94%). ^{111}In is a very important radionuclide for imaging studies in nuclear medicine and several radiopharmaceuticals were developed in the last 4 decades.

^{111}In can be produced by proton bombardment of natural ^{111}Cd or enriched ^{112}Cd using either ^{111}Cd(p,n)^{111}In reaction or ^{112}Cd(p, 2n)^{111}In reaction. Following irradiation, the cadmium target is dissolved in mineral acid and the acidity is kept at 1 N using HCl.

^{111}In is separated from the target using anion-exchange resin and HCl (1 N). The high SA, no-carrier-added ^{111}In has a radionuclidic purity of ≥99.9%.

8.3.4.3 Thallium-201

^{201}Tl ($T_{1/2}$ = 73.06 h) decays to stable mercury atom by electron capture with several γ photons of low abundance; 135 keV (2.65%), and 167 keV (10%). The low-energy X-rays (70–80 KeV) from the mercury atom are used for SPECT studies to assess myocardial blood flow.

The most common nuclear reaction used to produce ^{201}Tl is the ^{203}Tl(p, 3n)^{201}Pb→^{201}Tl reaction using high-energy protons (25–35 MeV) on enriched ^{203}Tl target. After irradiation, ^{201}Pb is separated from the target ^{203}Tl. Subsequently, ^{201}Pb is allowed to decay for several days to generate the daughter ^{201}Tl, which then is separated and purified from lead.

8.3.4.4 Iodine-123

^{123}I can be produced directly in a cyclotron using ^{124}Te(p,2n) reaction. The most common methods,

Table 8.3 Cyclotron-produced Radionuclides for SPECT

Radio nuclide	$T_{1/2}$	Decay		Energy		Production method	
		Mode	%	γ (KeV)	%	Nuclear reaction	Target
^{123}I	13.22 h	EC	100	159	83.6	^{123}Te(d, 2n)^{123}I ^{124}Xe(p,2n)^{123}Cs→ ^{123}Xe→$_{β-}$^{123}I	Solid/Gas
^{67}Ga	3.262 days	EC	100	93 185 300	38.6 28.4 16.6	^{68}Zn (p,2n) ^{67}Ga ^{66}Zn (d,n) ^{67}Ga	Solid
^{111}In	2.805 days	EC	86	171 245	90.7 94.1	^{112}Cd (p, 2n) ^{111}In ^{111}Cd (p, n) ^{111}In	Solid
^{201}Tl	3.042 days	EC	100	69–82 (X-ray) 167	75 10	^{203}Tl(p, 3n)^{201}Pb→$_{β-}$ ^{201}Tl	Solid

National Nuclear Data Center (NNDC): NuDat 3.0 @NuDat 3 (bnl.gov)

however, use indirect methods based on the following nuclear reactions:

$$^{127}\text{I}\left(p,5n\right)^{123}\text{Xe} \rightarrow {}^{123}\text{I} \qquad (8.16)$$

$$^{124}\text{Xe}\left(p,2n\right)^{123}\text{Cs} \rightarrow {}^{123}\text{Xe} \rightarrow {}^{123}\text{I} \quad (8.17)$$

$$^{124}\text{Xe}\left(p,pn\right)^{123}\text{Xe} \rightarrow {}^{123}\text{I} \qquad (8.18)$$
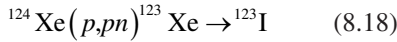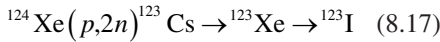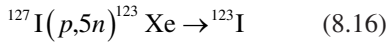
The high SA, NCA ^{123}I is supplied as sodium iodide in a 0.1 N NaOH solution with a radionuclidic purity >99.8%.

8.3.5   Therapy Radionuclides

8.3.5.1 Astatine-211

Astatine (Greek *astatos*, meaning "unstable") is the rarest naturally occurring element in the earth's crust, and continuously produced, as a result of the decay of radioactive thorium and uranium ores. Astatine element belongs to the halogen family and was first discovered in 1940 at the University of California, Berkeley, where it was produced by α particle bombardment of natural bismuth, ^{209}Bi [30]. All of astatine's isotopes are short-lived; the most stable is ^{210}At, with a half-life of 8.1 h. Since it decays to ^{210}Po (an α-particle emitter with a half-life of 138 days), it is not suitable for medical purposes. ^{211}At decays with a half-life of 7.2 h and emits two α particles through a split decay pathway with energies of 5.87 and 7.45 MeV (Fig. 8.9). One path is to ^{207}Bi by α particle emission followed by electron capture to ^{207}Pb, and the other is by electron capture to ^{211}Po followed by emission to ^{207}Pb. An advantage of this decay path is that ^{211}Po emits 77–92 keV characteristic X-rays which can be used for imaging.

A more practical and direct method of producing ^{211}At is by cyclotrons utilizing the nuclear reaction ^{209}Bi(α,2n)^{211}At. The excitation function for the ^{209}Bi(α, 2n)^{211}At reaction indicates that the maximum production yield can be obtained using an α-beam of 31–35 MeV. However, the typical energy of 28 MeV is used to avoid or minimize
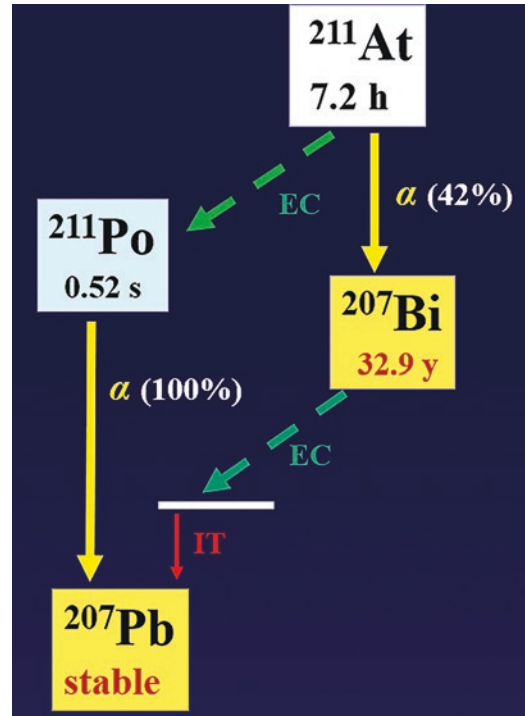
Fig. 8.9   Decay scheme of astatine-211 (^{211}At)

the production of unwanted ^{210}At contaminants. The efficiency of cyclotron production of ^{211}At is related to the helium ion source, the a-beam energy, the current of the beam, and the cooling of the target. These parameters need to be optimized, taking into account the described physical properties of bismuth and astatine. Currently, ^{211}At is routinely produced in the United States (Seattle, Bethesda, and Durham) and Denmark (Copenhagen).

Alternative methods for producing ^{211}At involve accelerator production of ^{211}Rn ($T_{1/2}$ = 14.6 h), which can be obtained by proton spallation of uranium or thorium targets or by irradiation of natural bismuth with lithium-7 atoms [30]. ^{211}Rn/^{211}At generators may facilitate easier distribution due to the relatively longer half-life of ^{211}Rn. However, only 27.4% of ^{211}Rn decays to ^{211}At while 72.6 decays to ^{211}Po (Table 8.4).

8.3.5.2 Actinium-225

^{225}Ac ($T_{1/2}$ = 10 days) is a pure α emitter, and is an isotope of radioactive actinium element, ^{227}Ac

Table 8.4 Cyclotron-produced radionuclides for therapy

Radio nuclide	$T_{\frac{1}{2}}$	Decay Mode	%	Energy MeV	γ (KeV)	Production method Nuclear reaction	Target
^{67}Cu	2.576 days	β^-	100	$E_{max} = 0.562$	184.6 (48.7%)	^{70}Zn (p, α) ^{67}Cu ^{68}Zn (p, 2p) ^{67}Cu ^{68}Zn (γ, p) ^{67}Cu	Solid
^{211}At	7.2 h	α	41.8	5.867 α	77–92 X-rays	^{209}Bi (α, 2n) ^{211}At	Solid
^{225}Ac	10 days	α	100	5.830 α		^{226}Ra(p,2n)^{225}Ac	Solid

National Nuclear Data Center (NNDC): NuDat 3.0 @NuDat 3 (bnl.gov)
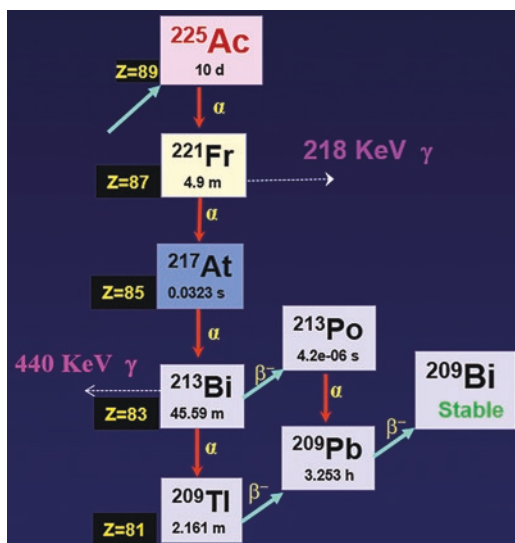
Fig. 8.10 Decay scheme of actinium-225 (^{225}Ac). Before Ac-225 reaches stable bismuth isotope, several radionuclides are generated as decay product, which decay either by alpha or beta emission

($T_{\frac{1}{2}}$ = 21.7 years), originally was discovered in 1989, in the pitchblende ore by a French chemist Andre-Louis Debierne. The name actinium originates from the ancient Greek *aktis, or aktinos* meaning beam or ray. Ac-225 does not exist in nature but was discovered in 1947 as part of the radioactive neptunium decay series (Fig. 8.1b) by the American and Canadian physicists. At present, Ac-225 is available for clinical use from the radioactive decay of ^{229}T and ^{225}Ra (refer to Thorium "cow" generator). The decay of ^{225}Ac generates 5 α particles and 3 β^- particles (Fig. 8.10).

^{225}Ac can be produced using accelerators and reactors based on several nuclear reactions as shown in Fig. 8.11. The potential of using low-energy cyclotrons (<20 MeV) based on ^{226}Ra(p, 2n)^{225}Ac nuclear reaction was first reported in 2005 [31]. This reaction has a high (710 mb) cross section peak at 16.8 MeV. Another advantage of this approach is that it would not coproduce long-lived ^{227}Ac contaminants. However, some ^{226}Ac ($T_{\frac{1}{2}}$ = 29.4 h) and ^{224}Ac ($T_{\frac{1}{2}}$ = 2.9 h) may be coproduced as impurities. It was estimated that a 20 MeV proton beam (with 500 μA current) incident on a ^{226}Ra target (~1 g) could produce a theoretical maximum of TBq (108 Ci) of ^{225}A per month [32]. Another estimate reported that a 24 h proton irradiation (16 MeV at 100 μA) of a 50 mg ^{226}Ra target may produce approximately, 5 GBq of ^{225}Ac. A major challenge, however, with this cyclotron method is related to the preparation and handling of targets containing milligram amounts of ^{226}Ra ($T_{\frac{1}{2}}$ = 1600 years), and management of its gaseous decay product ^{222}Rn ($T_{\frac{1}{2}}$ = 3.8 days).

Large-scale production of ^{225}Ac has been investigated based on the spallation of ^{232}Th targets with highly energetic protons (>70 MeV) [33–35]. The nuclear reaction ^{232}Th(p, x)^{225}Ac was studied at different proton energies and beam currents (Table 8.11). The feasibility of this spallation method based on ^{232}Th target has been demonstrated at the Institute for Nuclear Research, Russian Academy of Sciences, in Troitsk, Russia, and at Los Alamos National Laboratory in the United States [36]. In recent years, the routine production of ^{225}Ac has been successfully established within the United States, Department of Energy Tri-Lab (ORNL, BNL, LANL) effort. The spallation of thorium produces number of isotopes other than ^{225}Ac (such as radium isotopes). The separation and

Fig. 8.11 Different nuclear reactions used to produce Ac-225 based on accelerator, cyclotron, and reactor facility

Table 8.5 Accelerator production of ^{225}Ac: The effect of beam energy and current

Accelerator facility	Proton beam		Monthly production	
	MeV	μA	GBq	Ci
iThemba LABS, South Africa	66	250	127.7	3.450
Los Alamos National Laboratory, USA	100	250	444.0	12.0
INR	160	120	1002	27.08
Arrownax	70	2x370	462.1	12.49
Brookhaven National Laboratory, USA	200	173	2675.84	72.32
TRIUMF, Canada	500	120	11,266.5	304.05

Maximum Ac-225 produced at ORNL based on Th-229 generator is about 1.0 Ci/year
Table modified from [32]
National Nuclear Data Center (NNDC): NuDat 3.0 @NuDat 3 (bnl.gov)

purification of ^{225}Ac are a very complicated process. However, large quantities of ^{225}Ac (2–11 TBq/month) can be produced compared to the current method of Ac-225 production using Th-229 generator. The main limitation of the process, however, is the coproduction of long-lived ^{227}Ac ($T_{1/2}$ = 21.8 years) at levels of 0.1–0.2% activity (at EOB) (Table 8.5).

8.4 Production of Radionuclides in a Nuclear Reactor

8.4.1 Nuclear Fission

Nuclear fission is a nuclear reaction or a nuclear transmutation process in which the nucleus of an

atom splits into two or more smaller lighter nuclei or isotopes of several elements. In addition, a large amount of energy is released. In high mass number isotopes, spontaneous fission may occur. A slow-moving neutron is absorbed by a ^{235}U nucleus, turning it briefly into an excited ^{236}U, which, in turn, splits into fast-moving lighter elements (fission products) and releases 2 or 3 free neutrons and high-energy prompt γ rays (Fig. 8.2). For heavy nuclides, fission is an exothermic radiation which can release large amounts of energy both as electromagnetic radiation and as kinetic energy of the fragments. The isotopes of heavy elements that can sustain a fission chain reaction are called nuclear fuels and are said to be *fissile*. The most common nuclear fuels are ^{235}U, ^{233}U, and ^{239}Pu. These fuels break apart into a bimodal range of chemical elements (fission products) with atomic numbers (A) centering near 95 ± 15 and 135 ± 15. (Fig. 8.12).
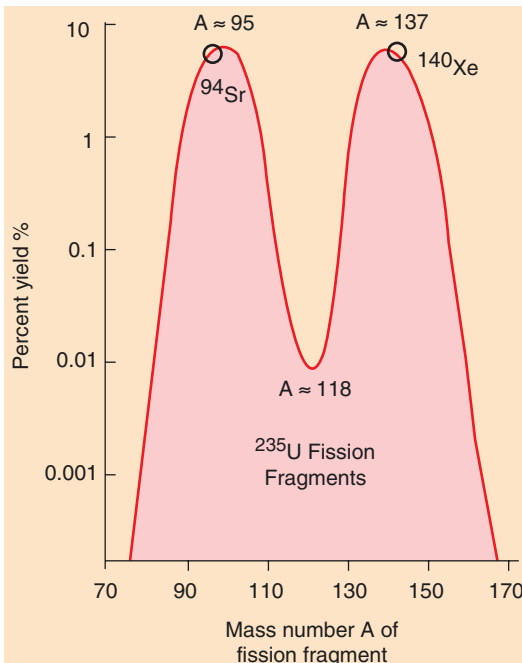
Fig. 8.12 Fissionable nuclides (such as ^{235}U and ^{238}Pu) break apart into a bimodal range of chemical elements (fission products) with atomic numbers (A) centering near 95 ± 15 and 135 ± 15. The most common fission products produced in a reactor are ^{131}I and ^{99}Mo

Shortly after the discovery of nuclear fission, scientists realized that, because fission leads to the release of additional neutrons, in a given mass of uranium fuel, known as the critical mass, a self-sustaining sequence of additional fissions can lead to a *chain reaction*, induced by at least one fission neutron. Such a reaction, in which the *multiplication factor* (MF) is ≥1, is called a *critical* reaction. However, if too few neutrons cause fissions, the reaction is *sub-critical* (MF <1) and will stop. If the frequency of fissions increases at a faster rate (MF >1), the "run-away" reaction can be *supercritical* and may lead to a nuclear explosion. In 1942, Fermi was able to demonstrate that by carefully controlling the availability of neutrons, a sustained chain reaction (MF = 1) can be maintained. The *nuclear reactor* operates based on the principle of *controlled chain reaction*.

Compared to ^{238}U, the cross section for induced fission reaction with slow or *thermal neutrons* (0.25 eV) is much higher for ^{235}U. Because the natural uranium contains only 0.7% of ^{235}U isotope, *enriched uranium* containing >3% of ^{235}U, is typically used as the fuel in a reactor core. In a nuclear reactor (Fig. 8.13), the fuel cells containing enriched uranium (as UF_6 or UO_2) pellets are surrounded by a *moderator*, graphite, or heavy water, to slow down the energetic fission neutrons. *Control rods* (cadmium and boron) capable of absorbing neutrons, but not undergoing any nuclear reaction, are used to sustain the chain reaction. Following the absorption of a neutron, the natural ^{238}U decays by emitting a beta particle to become ^{239}Np, which in turn emits a beta particle to become ^{239}Pu. These reactions are the basis of a *breeder reactor*, in which uranium produces more fuel in the form of ^{239}Pu.

8.4.2 Radionuclides Produced by Fission

The research reactors used for radioisotope production could be either a) swimming pool type
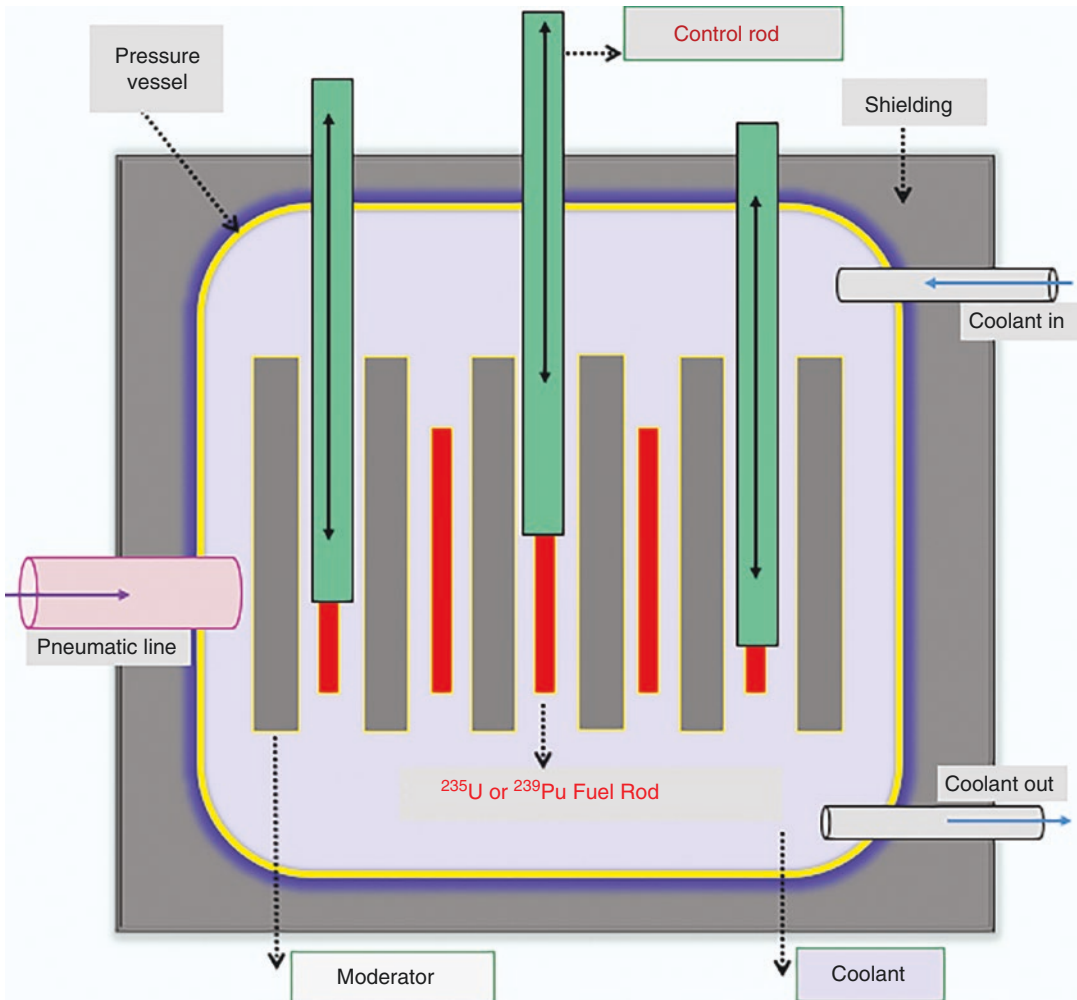
Fig. 8.13 Nuclear reactor facility animation showing reactor core with ^{235}U or ^{239}Pu radionuclides and the control rods containing boron or cadmium capable of absorbing fission neutrons

reactors with enriched uranium and light water as the moderator or b) cooled tank type reactors with natural uranium and heavy water as the moderator. When the reactor is in operation, the nuclear reaction (n, f) produces many neutron-rich fission fragments (Z = 28–65), which decay by β^- emission. Radionuclides, such as ^{99}Mo, ^{131}I, ^{90}Sr, ^{89}Sr, and ^{137}Cs, accumulate in the fuel rods to produce enormous activity (thousands of GBq). All the fission fragments can be chemically separated and purified to yield no-carrier-added, high SA radionuclides.

8.4.3 Radionuclides Produced by Neutron Activation

A nuclear reaction in which a neutron is captured or absorbed by the nucleus of a stable atom, leading to a nuclear transformation, is called *neutron activation*. The most common nuclear reactions are (n, γ) (n, p), (n, 2 n), and (n, α), in which the atomic mass or atomic number of the target nucleus may change.

The neutrons released during the fission reaction have a wide range of energies, from a few

KeV to 10 MeV. The average energy is approximately 2 MeV, which decreases substantially as a result of collisions with other atoms in the core and the moderator. The average energy of thermal neutrons at room temperature is about 0.038 eV. Neutrons between 0.01 and 0.1 MeV are known as slow or resonance neutrons, while neutrons with >0.1 MeV are known as fast neutrons. In general, the cross section (σ) for thermal neutrons in neutron activation reactions is very high, compared to that of higher energy neutrons.

In a (n,γ) reaction, the target nucleus with a mass number A captures a neutron to become an unstable, excited radioisotope of the target nucleus, with a mass number $A + 1$. The excited nucleus immediately emits a γ-photon, and the product radionuclide will eventually decay by beta emission to reach a ground state. Because the product nuclide is an isotope of the target element, the product cannot be separated and purified to avoid the contamination of the carrier. As a result, radioisotopes produced using (n, γ) reaction are generally very low in SA. However, it is possible to produce carrier-free, high SA

nuclides in a reactor using (n, p) reactions. Important therapeutic radionuclides produced by fission and by neutron activation are summarized in Table 8.6.

8.4.4   Beta Emitting Radionuclides for Therapy

8.4.4.1   Phosphorous-32

Georg de Hevesy (Nobel Laureate and the inventor of the tracer principle) in 1935 was the first investigator to use ^{32}P in biological research. ^{32}P ($T_{\frac{1}{2}}$ = 14.268 days) decays into ^{32}S by β^- (E_{max} = 1.709 MeV) particle emission. ^{32}P has been available for the treatment of myeloproliferative neoplasms for over 80 years. It was first used in 1938 by John H. Lawrence to treat polycythemia and chronic leukemia. ^{32}P can be produced in a reactor by neutron activation using either $^{31}P(n, \gamma)^{32}P$ or $^{32}S(n, p)^{32}P$ nuclear reaction and supplied as orthophosphoric acid in water with a specific activity of 8–9 Ci (314–337 TBq)/ mMole. In a (n, p) reaction, the target and the product are two different elements. As a result, it

Table 8.6 Reactor produced radionuclides for therapy

Radio nuclide	$T_{\frac{1}{2}}$ Days	Decay Mode	%	$\beta^- E_{max}$ MeV	γ- Energy KeV	%	Production method Nuclear reaction
^{89}Sr	50.53	β^-	100	1.501	910	1	^{88}Sr (n, γ) ^{89}Sr ^{89}Y (n, p) ^{89}Sr
^{32}P	14.268	β^-	100	1.710	–	–	^{31}P (n, γ) ^{32}P ^{32}S (n, p) ^{32}P
^{169}Er	9.392	β^-	100	0.351	–	–	^{168}Er(n, γ) ^{169}Er
^{131}I	8.025	β^-, γ	100	0.606	364.5	81.5	^{235}U n, fission)^{131}I ^{130}Te(n, γ)^{131}Te$\rightarrow_{\beta-}$ ^{131}I
^{177}Lu	6.6443	β^-, γ	100	0.497	113 208.4	6.6 10.4	^{176}Lu(n, γ)^{177}Lu ^{176}Yb ((n, γ)^{177}Yb$\rightarrow_{\beta-}$ ^{177}Lu
^{186}Re	3.7186	β^-, EC	92.5	1.070	137.2	9.5	^{185}Re(n, γ)^{186}Re
^{198}Au	2.694	β^-, γ	100	0.961	411.8	95.6	^{197}Au(n, γ)^{198}Au
^{98}Y	2.67	β^-	100	2.28	–	–	^{235}U(n, fission)^{90}Sr$\rightarrow_{\beta-}$ ^{90}Y
^{67}Cu	2.576	β^-, γ	100	0.561	184.6	48.7	^{67}Zn (n, p) ^{67}Cu
^{153}Sm	1.9375	β^-, γ	100	0.807	103.2	29	^{152}Sm(n, γ)^{153}Sm
^{166}Ho	1.120	β^-, γ	100	1.854	80.6	6.56	^{165}Ho (n, γ) ^{166}Ho
^{188}Re	0.708	β^-, γ	100	2.120	155	15.5	^{187}W(n, γ)^{188}W$\rightarrow_{\beta-}$ ^{188}Re
^{117m}Sn	13.76	IT	100	0.152 (CE)	159		^{116}Sn(n, γ)^{117m}Sn

National Nuclear Data Center (NNDC): NuDat 3.0 @NuDat 3 (bnl.gov)

is very easy to separate the product from the target, chemically.

8.4.4.2 Iodine-131

[131]I is an important radioisotope of iodine discovered by Glenn Seaborg and John Livingood in 1938 at the University of California, Berkeley. ^{131}I decays with a half-life of 8.02 days with β^- (E_{max} = 606 KeV) and γ (364 KeV) emissions. ^{131}I is a major fission product of ^{235}U and ^{239}Pu comprising nearly 2.8336% of the total products of fission (by weight). In comparison, the long-lived ^{129}I fission product is only 0.9%. However, extracting the iodine from spent nuclear fuel would require expensive and time-consuming reprocessing in a sophisticated facility. Also, extracting only approximately 3% of the fuel would produce a large amount of nuclear waste. Radionuclidic purity of fission produced ^{131}I is not less than 99.9% of the total radioactivity. The specific activity is approximately 130 Ci/mg or 4.81TBq/mg.

As described earlier, ^{131}I can be produced by the fission of enriched ^{235}U based on (n, f) nuclear reaction. However, a more practical method of ^{131}I production is based on (n, γ) reaction in a research reactor using ^{130}Te target. Natural tellurium is easily available and is a mixture of several stable isotopes. ^{130}Te is approximately 30% of natural Te element. Certain (n, γ) reactions produce a short-lived radioisotope of the target element, which decays by beta emission to another unstable radioactive nuclide with longer half-life compared to that of the intermediate. As shown below, both the ground state ^{131}Te and metastable ^{131m}Te decay to^{131}I.
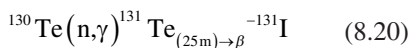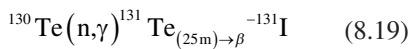
$$^{130}\text{Te}(\text{n},\gamma)^{131}\text{Te}_{(25m)\to\beta}^{-131}\text{I} \qquad (8.19)$$

$$^{130}\text{Te}(\text{n},\gamma)^{131}\text{Te}_{(25m)\to\beta}^{-131}\text{I} \qquad (8.20)$$

Following neutron irradiation, ^{131}I is extracted from the natural tellurium target generally by the dry distillation method. The process involves heating the irradiated sample to release the ^{131}I and ^{131}I in a sodium hydroxide solution (pH 8–10). The specific activity (~TBq/mg) is generally less than that of fission produced ^{131}I (4–5 TBq/mg).

8.4.4.3 Yttrium-90

^{90}Y ($T_{1/2}$ = 64.1 h) is one of the important radionuclides for TRT. It is a pure β^- emitter with very high-energy (E_{max} = 2.28 MeV) and no γ emissions. Selective internal radiation therapy (SIRT) with ^{90}Y-labeled microspheres has become a widely employed brachytherapy for the treatment of primary and metastatic hepatic malignancies.

It can be produced in a reactor by neutron irradiation of stable yttrium-89 via ^{89}Y(n, γ)^{90}Y reaction. Exposing a 1 cm cube (approximately 5 g), natural yttrium target to 10^{14} n/cm^2/s flux would create Y-90 at a rate of 1.1 Ci/hr. To make high specific activity ^{90}Y, e-LINAC is used to generate a neutron beam (12.1 MeV) and directing the neutron beam onto the zirconium target (^{90}Zr) to isotopically convert some of the atoms to ^{90}Y via ^{90}Zr(n, p)^{90}Y. However, the most common method of producing high specific activity ^{90}Y is the nuclear decay of parent isotope ^{90}Sr ($T_{1/2}$ = 29 years), which is a fission product of uranium. The theoretical specific activity is 20 GBq(540 mCi)/μg of Yttrium-90.

8.4.4.4 Lutetium-177

Lutetium is a transition metal and the last member of lanthanide series. ^{177}Lu ($T_{1/2}$ = 6.734 days) is a low-energy β^- emitter (E_{max} = 0.498 MeV) with suitable γ photons (113 and 208 KeV) suitable for SPECT imaging studies. ^{177}Lu-DOTATATE (Lutathera®) is the first therapeutic ^{177}Lu peptide radiopharmaceutical approved by FDA for TRT of patients with neuroendocrine tumors (NETs). Several ^{177}Lu labeled peptides and antibodies are in Phase II-III clinical trials for TRT.

In a nuclear reactor, ^{177}Lu can be produced by direct neutron activation using enriched ^{176}Lu or through the indirect route by activation of ^{176}Yb followed by β^- decay to ^{177}Lu (Fig. 8.14). For both methods, the amount of ^{177}Lu produced, however, depends on the neutron energy, neutron flux, and the irradiation time [37, 38]. The direct production route also results in formation of a small amount of long-lived metastable ^{177m}Lu in activity (<0.02%). The specific activity depends on the ^{176}Lu enrichment and one can obtain 20–40 Ci/mg with >80% enriched ^{176}Lu targets.

Fig. 8.14 Nuclear Reactions commonly used to produce Lu-177
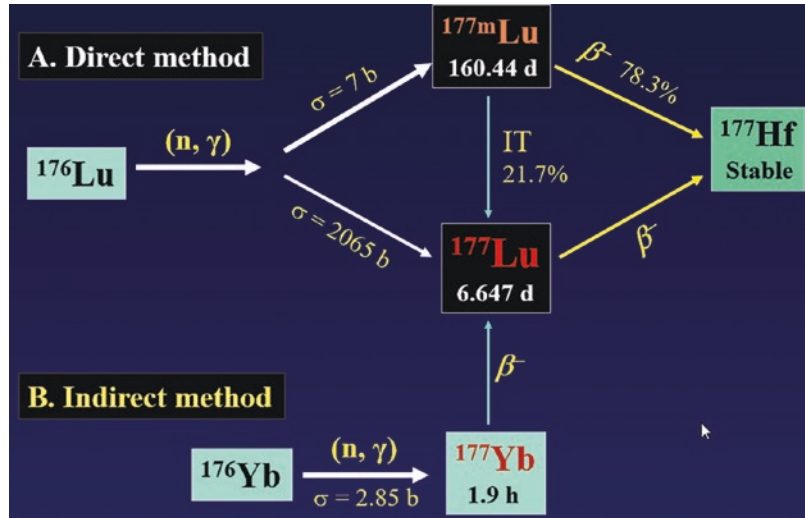
The major advantage of the indirect method with ^{176}Yb target followed by the decay of ^{177}Yb provides no-carrier-added (NCA) ^{177}Lu which is then separated by suitable radiochemical processes. In addition, the indirect method does not produce any ^{177m}Lu radionuclide impurity. With enriched ^{176}Yb targets, it is possible to achieve very high specific activity approaching the theoretical specific activity of 110 Ci (4.07 TBq)/mg [37] (Fig. 8.14).

8.4.4.5 Copper-67

^{67}Cu, a transition metal ($T_{1/2}$ = 2.58 days), decays by β^- emission (E_{max} = 0.562 MeV) and provides several γ photons (91, 93, 184 KeV) for SPECT. Despite the potential for both imaging and therapy, the use of ^{67}Cu for therapy has been hampered for decades by its limited supply and low specific activity. The production of ^{67}Cu has been tested both in reactors and in cyclotrons on a variety of nuclear reactions such as ^{67}Zn(n,p)^{67}Cu, ^{68}Zn(p, 2p)^{67}Cu, and ^{70}Zn(p, α)^{67}Cu. The ^{68}Zn(p,2p)^{67}Cu route of production (using 70 MeV proton) appears to be the most attractive method. However, large quantities of ^{64}Cu($T_{1/2}$ = 12.7 h) and ^{67}Ga ($T_{1/2}$ = 78.3 h) are the major radionuclidic impurities. The specific activity is <20 Ci/mg [39].

A major breakthrough in the production of high specific activity ^{67}Cu is based on the photonuclear activation, using highly enriched (98.9%) ^{68}Zn targets. For the ^{68}Zn(γ,p)^{67}Cu reaction high-energy γ rays can be produced by bremsstrahlung conversion of electrons from e-LINAC [39, 40]. The specific activity of ^{67}Cu so produced has reached over 5.55 GBq/μg (150 mCi/μg). Due to this breakthrough in ^{67}Cu production, no-carrier-added ^{67}Cu has been made available in large scales at the US-DOE National Isotope Development Center.

8.4.4.6 Scandium-47

^{47}Sc with a half-life of 3.35 days and low-energy β^- particles (E_{max} = 441 keV) is ideal for therapy. In addition, the emission of 159 KeV γ photons is ideal for SPECT imaging studies. Also, ^{43}Sc ($T_{1/2}$ = 3.89 h, $E_{\beta + avg}$ = 476 keV, I = 88.1%) and ^{44}Sc($T_{1/2}$ = 3.97 h, $E_{\beta + avg}$ = 632 keV, I = 94.3%) have been proposed for PET imaging studies.

^{47}Sc can be produced by two different neutron induced reactions: ^{46}Ca(n, γ)^{47}Ca→^{47}Sc or ^{47}Ti(n, p). The (n, γ) reaction is induced by thermal neutrons, while the (n, p) reaction requires fast neutrons (>1 MeV). Enriched ^{46}Ca as CaCO$_3$ is generally used for thermal neutron activation reaction. The chemical separation of Sc from Ca was performed using DGA resin and SCX cation-exchange cartridges.

^{47}Sc can be produced with higher specific activities via the ^{48}Ti(γ, p)^{47}Sc using the photonuclear reaction by irradiation of a natural titanium target foil stack using bremsstrahlung

radiation generated by impinging 22 MeV electrons onto a 0.762-mm-thick tungsten radiator [41, 42]). Target foils dissolved in 2.0 M H_2SO_4. ^{47}Sc ions can be separated from natural titanium using AG-MP 50 cation-exchange resin. The recovered ^{47}Sc is purified using CHELEX 100 ion-exchange resin.

8.4.4.7 Strontium-89

^{89}Sr ($T_{1/2}$ = 50.53 days) is an alkaline earth metal and undergoes β^- decay (E_{max} = 1.495 MeV) into ^{89}Y with no gamma emissions. ^{89}Sr chloride (Metastron™) is used for bone pain palliation. ^{89}Sr is a anthropogenic radionuclide that is produced as a result of nuclear fission at thermal neutron fission yields of 4.69 ± 0.06% [43].

^{89}Sr can also be produced by neutron activation using ^{88}Sr(n, γ)^{89}Sr using SrCO$_3$ as the target with neutrons having a thermal neutron spectrum. A highly enriched target ^{88}Sr (>99%) is used to eliminate strontium-85 impurity. This is a convenient production method and takes place in a normal research reactor. ^{89}Sr can also be produced via ^{89}Y(n, p)^{89}Sr nuclear reaction using fast neutrons and yttrium oxide pellets.

8.4.4.8 Strontium-90

^{90}Sr ($T_{1/2}$ = 28.8 years) undergoes β^- decay (E_{max} = 0.546 MeV) into ^{90}Y. ^{90}Sr is produced as a result of nuclear fission at thermal neutron fission yields of 5.73 ± 0.13% [43]. The approximate specific activity of ^{90}Sr is about 140 mCi/mg. ^{90}Sr →^{90}Y generator provides significant amounts of ^{90}Y for radionuclide therapy studies.

8.4.4.9 Samarium-153

^{153}Sm($T_{1/2}$ = 1.93 days) is a transition metal and one of the elements in the lanthanide series. It decays by β^- emission (E_{max} = 0.810 MeV) to europium-153, with useful γ emissions (103 KeV). ^{153}Sm-EDTMP or Lexidronam (Quadramet®) is clinically used for bone pain palliation.

^{53}Sm is produced by neutron activation of both natural Sm$_2$O$_3$ and 98% enriched ^{152}Sm$_2$O$_3$ targets via ^{152}Sm(n, γ)^{153}Sm nuclear reaction [44]. Specific activity achieved at EOB is 14.8–16.8 GBq (400–450 mCi)/mg oxide. The specific activity of enriched ^{152}Sm targets can be up to 1200 mCi/mg.

8.4.4.10 Holmium-166

^{166}Ho($T_{1/2}$ = 26.763 h) is a transition metal and one of the elements in the lanthanide series. It decays by β^- emission (E_{max} = 1.854 MeV)) to erbium-166, with useful γ emissions (81 KeV) for SPECT. Several clinical applications for therapy are under investigation [45].

^{166}Ho is most frequently produced via the ^{165}Ho(n, γ)^{166}Ho nuclear reaction [44]. Because ^{165}H0 has a natural abundance of 100% and a cross section of 64 b, it can be produced with a high purity. However, ^{166m}Ho ($T_{1/2}$ = 1200 years), a beta emitter may be produced as a radionuclidic impurity. The specific activity is NLT 75 mCi/mg.

^{166}Ho can also be produced by an indirect method via the ^{164,165}Dy(2n, γ)^{166}Dy$_→$^{166}Ho nuclear reaction. The cross section of ^{164}Dy is extremely high (2650 b). The second neutron irradiation of the unstable ^{165}Dy is necessary to result in ^{166}Dy, which decays by beta emission to carrier-free ^{166}Ho. A ^{166}Dy$_→$^{166}Ho generator can provide on-site supply of high specific activity ^{166}Ho for targeted therapy.

8.4.4.11 Rhenium-186, Re-188

^{186}Re ($T_{1/2}$ = 3.718 days) is a transition metal and decays by β^- emission (E_{max} = 1.07 MeV) with useful γ photons (137 KeV) for SPECT. The primary production of ^{186}Re in a reactor is via ^{185}Re (n, γ) nuclear reaction using enriched ^{185}Re target (>94%). The typical specific activity is 1.84 Ci/mg [46].

High specific activity ^{186}Re can be produced through cyclotron irradiation of enriched tungsten-186 target via the ^{186}W(d, 2n)^{186}Re nuclear reaction [47]. The target thickness and beam currents are critical to achieve high specific activity. Specific activity of 80 Ci/mg was obtained using a graphite-encased ^{186}W target and 18.7 MeV deuteron bombardment for 2 h, at a beam current of 27 μA [48].

^{188}Re ($T_{1/2}$ = 16.9 h) also decays by β^- emission (E_{max} = 2.12 MeV) with useful γ photons (155 KeV) for SPECT. ^{188}Re as no-carrier-added

nuclide can be produced in high specific activity from the ^{188}W→^{188}Re generator system.

Rhenium and technetium elements exhibit similar chemical properties and preparation and targeting of $^{186/188}$Re radiopharmaceuticals for therapy is similar to imaging agents prepared with ^{99m}Tc, the most commonly used diagnostic radionuclide.

8.4.4.12 Tin-117 m

^{117m}Sn ($T_{1/2}$ = 13.6 days) is a post-transition metal that decays by isomeric transition and emits low and mono-energetic conversion electrons (0.127, 0.129, and 0.152 MeV). It also emits γ photons (159 KeV) suitable for SPECT. Bone marrow toxicity of this radionuclide is low because of its short range (~3 mm) electrons. It is a novel radionuclide with low-energy electrons for radionuclide therapy applications including rheumatoid arthritis and bone pain palliation,

^{117m}Sn can be produced in large quantities as a low specific activity (up to 21 mCi/mg) product in reactors via the ^{116}Sn(n, γ)^{117m}Sn or ^{117}Sn(n, n'γ)^{117m}Sn reactions. A carrier-free, high specific activity (up to 20 Ci/mg) isotope can be manufactured with >50 MeV cyclotrons employing either stable antimony target ^{nat}Sb(p, x)^{117m}Sn or ^{116}Cd(α, 3n) nuclear reactions [49, 50].

8.4.4.13 Molybdenum-99

Technetium-99 m ($T_{1/2}$ = 6 h), the most widely used radioisotope in nuclear medicine, is produced via the decay of its parent radionuclide, ^{99}Mo ($T_{1/2}$ = 65.94 h), which decays by β^- (E_{max} = 1.214 MeV) and γ (181, 740, and 778 KeV) emissions. Mo-99 is produced by the fission of ^{235}U in the highly enriched uranium (HEU)-bearing targets by irradiating them with thermal neutrons. ^{99}Mo is a major fission product of ^{235}U comprising nearly 6.1% of the total products of fission (by weight). The amount of ^{99}Mo produced in a target is a function of irradiation time, the thermal neutron fission cross section for ^{235}U, the thermal neutron flux on the target, the mass of U-235 in the target, and the half-life of Mo-99 (IAEA TR). For typical reactor thermal

neutron fluxes on the order of 10^{14} neutrons per square centimeter per second, irradiation times of about 5 to 7 days are required to achieve near maximum ^{99}Mo production in the targets No-carrier-added ^{99}Mo is supplied as molybdate in 0.2 N NaOH solution with a radionuclidic purity of NLT 95%. Several radionuclidic impurities (^{103}Ru, ^{131}I, and ^{132}Te) may be present in the final product.

^{99}Mo can also be produced in a reactor using neutron activation via ^{98}Mo(n, γ)^{99}Mo nuclear reaction. However, the specific activity of ^{99}Mo is very low since the target ^{98}Mo cannot be separated from ^{99}Mo by chemical separation methods since they both are isotopes of the same element.

There are alternative routes for generating ^{99}Mo that do not require a fissionable target, such as high or low enriched uranium (i.e., HEU or LEU) [51]. Cyclotron production of ^{99}Mo is based on proton bombardment of ^{100}Mo(p, 2n)^{99}Mo nuclear reaction, while photonuclear activation using e-LINAC is based on ^{100}Mo(γ, n)^{99}Mo reaction using enriched ^{100}Mo target. Photons for this reaction are provided from the electron deceleration radiation. This technology uses high-energy X-rays produced by a 30–35 meV, 100 kW electron beam to irradiate a ^{100}Mo target [52].

8.4.4.14 Tungsten-188

^{188}W ($T_{1/2}$ = 69.78 days) is a transition metal and decays 100% by β^- emission to ^{188}Re which also decays by β^- *emission to stable ^{188}Os.* ^{188}W is primarily used as a parent for the ^{188}W→^{188}Re generator system. ^{188}W is produced in a reactor by double neutron capture of enriched ^{186}W (>90%) targets by the double neutron capture pathway (IAEA.) via the nuclear reactions, ^{186}W(n, γ)^{187}W(n,γ)^{188}W. High neutron flux (>8–10 × 10^{14}/ cm^2/s) reactor is essential to produce high specific activities.

^{188}W is produced at the US-DOE High Flux Isotope Reactor at Oak Ridge National Laboratory and is offered as sodium tungstate in NaOH solution or loaded on a ^{188}W→^{188}Re generator.

### 8.4.5	Alpha Emitting Radionuclides for Therapy

#### 8.4.5.1	Radium-223

^{223}Ra ($T_{1/2}$ = 11.4 days), historically known as actinium-X, was discovered in 1905 by T. Godlewski, a Polish chemist. ^{223}Ra dichloride (RaC$_2$) is an alpha particle-emitting radiotherapy drug (known as Alpharadin or Xofigo®) that mimics calcium and forms complexes with hydroxyapatite at areas of increased bone turnover. In 2013, it was the first α- particle-emitting radiopharmaceutical approved by FDA for therapy as a treatment for metastatic bone cancer in patients with castration-resistant prostate cancer (CRPC).

Although ^{223}Ra is naturally formed in trace amounts by the decay of ^{235}U, it is generally made artificially in a reactor, by neutron activation of ^{226}Ra to produce ^{227}Ra, which decays to ^{227}Ac, which in turn decays via ^{227}Th to ^{223}Ra. This decay path makes it convenient to prepare ^{223}Ra by "milking" it from an ^{227}Ac→^{223}Ra generator. The six-stage decay of ^{223}Ra to stable ^{207}Pb occurs via short-lived daughters (Fig. 8.15) and is accompanied predominantly by the emission of 5 alpha particles (5–7.5 MeV). There are also beta and gamma emissions with different energies and emission probabilities.
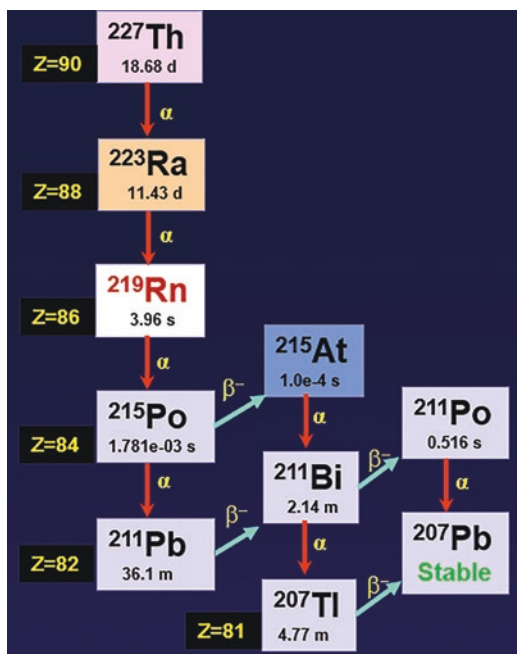
#### 8.4.5.2	Actinium-225

As ^{225}Ac does not occur in any appreciable quantities in nature, it must be synthesized in specialized nuclear reactors. The majority of ^{225}Ac results from the alpha decay of parent nuclide, ^{229}Th. It is also possible to breed ^{225}Ac by neutron activation from ^{226}Ra via the ^{226}Ra(p,2n)^{225}Ac nuclear reaction. The potential to populate ^{225}Ac using a ^{226}Ra target was first demonstrated in 2005, the production and handling of ^{226}Ra, however, are difficult because of the respective cost of extraction and hazards of decay products such as ^{222}Rn gas [32]. For the current methods of ^{225}Ac production, refer to Fig. 8.11.

## 8.5	Radionuclide Generators

Certain radionuclides may be generated by longer-lived parent radionuclide. The parent radionuclide can be made in a reactor or in a cyclotron. Both parent and daughter radionuclide pair may exist either in a transient or in a secular equilibrium when the parent is a longer-lived radionuclide than the daughter. If the parent and daughter nuclides are two different elements, they can be separated chemically, and the radioactivity of the daughter can be of high SA. Such a parent–daughter (mother–daughter) radionuclide pair is ideal to build a generator system to produce the daughter radionuclide, when needed [53, 54]. The *radionuclide generator* is a device used to separate the daughter radionuclide from the parent radionuclide. Various types of physicochemical separation methods, such as distillation or liquid/liquid extraction may be used. A chromatographic method based on an inorganic or resin adsorbent material, however, is the most practical method for routine clinical utility. Several important radionuclide generator systems (Table 8.7) are available commercially to produce radionuclides of clinical interest.

Fig. 8.15 ^{223}Ra (the daughter of ^{227}Th) decay scheme shows emission of several α and β$^-$ particles before it reaches stable ^{207}Pb

Table 8.7 Radionuclide generator systems for imaging and therapy

Parent				Daughter				
Nuclide	$T_{\frac{1}{2}}$	Decay	Parent produced by	Nuclide	$T_{\frac{1}{2}}$	Decay	E_{mean} MeV	Particles/decay
^{99}Mo	2.75 days	β^-	^{235}U-fission	^{99m}Tc	6.0 h	IT	0.140γ	–
^{82}Sr	25.34 days	EC	Accelerator	^{82}Rb	75 s	β^+	1.480	–
^{62}Zn	9.19 h	EC	Cyclotron	^{62}Cu	9.7 months	β^+	1.319	–
^{68}Ge	271 days	EC	Accelerator	^{68}Ga	67.7 months	β^+	0.829	–
^{90}Sr	28.8 years	β^-	Fission product	^{90}Y	2.67 days	β^-	0.932	–
^{188}W	69.8 days	β^-	Reactor	^{188}Re	17.0 h	β^-	0.763	–
^{228}Th	1.9125 years	α	Decay chain	^{212}Pb	10.64	β^-	0.101	$1\beta^-$
^{224}Ra	3.632 days	α	Decay chain	^{212}Bi	60.1 months	β^-,α	7.8	$1\alpha, 1\beta^-$
^{225}Ac	10.0 days	α	Decay chain/ accelerator	^{213}Bi	45.6 months	β^-,α	8.32	$2\alpha, 3\beta^-$
^{211}Rn	14.6 h	EC, α	Cyclotron	^{211}At	7.214 h	α	6.78	$2\alpha, 2EC$
^{227}Ac	21.772 years	β^-, α	Decay chain	^{223}Ra	11.43 days	α	6.59	$5\alpha, 4\beta^-$
^{229}Th	7932 years	α	Decay chain	^{225}Ac	10.0 days	α	6.87	$5\alpha, 3\beta^-$
^{227}Ac	21.772 years	β^-, α	Decay chain	^{227}Th	18.697 days	α	6.46	$7\alpha, 4\beta^-$

8.5.1   Generators for SPECT/PET Imaging

8.5.1.1 ^{99}Mo→ ^{99m}Tc Generator

The ^{99}Tc generator was first developed in 1960s at the Brookhaven National Laboratories in New York [55]. As discussed earlier, ^{99}Mo is one of the fission products of ^{235}U fission, known as "fission moly" and is produced in very high SA compared to ^{99}Mo which is produced by neutron activation. Most commercial generators are made with fission produced ^{99}Mo. The generator is made on the basis of a solid column method, in which 5–10 g of preheated alumina (Al$_2$O$_3$) is loaded in a plastic or glass column. The ^{99}Mo activity (2–32 Ci) in the form of molybdate ion is adsorbed on the column. The column is thoroughly washed to remove undesirable contaminants. The amount of ^{99}Mo activity on the column along with the date and time of calibration, for each generator, is provided. Commercial generators are sterilized and well shielded with lead or depleted uranium.

After the generator has been washed and calibrated, at time T_0, there is no ^{99m}Tc activity on the column. As ^{99}Mo($T_{1/2}$ = 66 h) decays, ^{99m}Tc activity ($T_{1/2}$ = 6 h) is produced and builds up in the column as a function of time, as shown in Fig. 8.16. Unlike molybdenum, technetium does not bind to alumina but, is immediately converted into ^{99m}Tc-pertechnetate ion (^{99m}TcO4$^-$), which is the most stable chemical form of technetium with an oxidation state of +7. Typically, >75% of ^{99m}Tc-activity can be eluted with 3–10 mL of physiological saline solution. The equations to estimate the amount of ^{99m}Tc activity in a generator have been previously shown (Eqs. (4.21) and (4.23)).

Small amounts of ^{99}Mo activity may occasionally *breakthrough* (leakage or partial elution) the column into the ^{99m}Tc-pertechnetate solution. The maximum ^{99}Mo contamination allowed is 0.15 µCi/mCi^{-1} or 0.15 KBq MBq^{-1} of ^{99m}Tc-pertechnetate solution at the time of elution. Each ^{99m}Tc dose to a patient, however, should not contain >5 µCi of ^{99}Mo activity. As a chemical impurity, Al ion concentration should be <10–20 µg mL^{-1} of eluant.

Both, ^{99}Mo (13%) and ^{99m}Tc decay producing the long-lived ^{99}Tc, which in turn decays slowly by beta emission, to the stable ^{99}Ru. Since ^{99m}Tc and ^{99}Tc are isomers and chemically the same

Fig. 8.16 In a radionuclide generator, the build-up of daughter activity is a function of time (half-life): Approximately 90% of the expected daughter activity will build up in the generator after 4 half-lives of daughter radionuclide. 50% of the expected activity will build up only after 1 half-life of the daughter
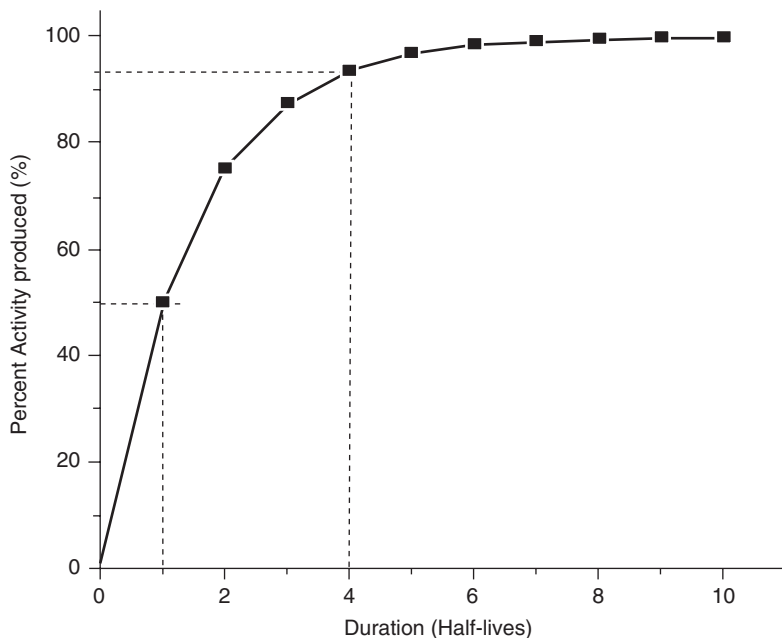
element, ^{99}Tc may act as a carrier in the preparation of ^{99m}Tc radiotracers. If the generator is eluted once a day (every 24 h), the number of ^{99m}Tc atoms is 27% of the total Tc atoms. If the generator is eluted after 4 days, for example, the number of ^{99m}Tc atoms is only 5% of the total Tc atoms.

8.5.1.2 ^{82}Sr→ ^{82}Rb Generator (Cardiogen®)

^{82}Rb chloride was the first PET radiopharmaceutical approved by the FDA in 1989 for assessment of regional myocardial perfusion. Cardiogen® was first manufactured and supplied by Bracco Diagnostics. Rb-82 generator (RUBY-FILL™, is supplied by Jubilant DraxImage Inc). The parent ^{82}Sr ($T_{1/2}$ = 25.6 days) is a neutron-deficient radionuclide that decays by electron capture and is produced using a high-energy cyclotron [56]. ^{82}Sr (90–150 mCi) is loaded on a stannic oxide column and the daughter ^{82}Rb ($T_{1/2}$ = 75 s) is eluted from the column with a sterile saline solution using an infusion pump calibrated to administer a specific unit dose to a patient.

8.5.1.3 ^{68}Ge→ ^{68}Ga Generator

In many PET facilities, ^{68}Ga is routinely used for transmission scans (for attenuation correction of PET data) using a ^{68}Ge rod source (5–10 mCi). The parent ^{68}Ge is a long-lived ($T_{1/2}$ = 271 days) neutron-deficient radionuclide, generally produced by a high-energy cyclotron based on spallation reaction [3]. The ^{68}Ga generator was developed, in 1960s for brain imaging studies [57] and, subsequently, improved [58].

Following several modifications in the chromatographic column technology, ^{68}Ga is currently produced using several ^{68}Ge/^{68}Ga generator systems in the clinical and research environments. For example, titanium dioxide-based IGG100 (Eckert & Ziegler), Galli EO (IRE Elit), Obninsk (Cyclotron Co.Ltd.), tin dioxide-based iThemba (iThemba Labs), and do-decyl gallate-modified silica-based ITG (ITG). These commercial generators are supplied with 10–100 mCi capacity, have very low ^{68}Ge-breakthrough, very low metal/chemical impurities, and are eluted with <0.1 M HCl.

8.5.1.4 ^{62}Zn→ ^{62}Cu Generator

Several ^{62}Cu radiotracers are under development and clinical evaluation for assessing perfusion and hypoxia. ^{62}Zn ($T_{1/2}$ = 9.13 h) is a neutron-deficient radionuclide produced by the proton irradiation of a copper disc or copper electroplated alloy on the basis of the nuclear reaction ^{63}Cu(p,2n)^{62}Zn using 26–21 MeV protons [3]. ^{62}Zn is separated from the target copper using an anion-exchange column. Subsequently, an acidic solution of ^{62}Zn can be loaded onto an anion-exchange column and the daughter ^{62}Cu ($T_{1/2}$ = 9.76 min) can be eluted from the generator for the preparation of radiotracers [59–61].

8.5.2 Generators for Radionuclide Therapy

8.5.2.1 ^{90}Sr→^{90}Y0 Generator

The ^{90}Sr parent radionuclide is very long-lived ($T_{1/2}$: 28.8 years) and the generators theoretically have a very long lifetime. However, ^{90}Sr may induce substantial radiation degradation of the column matrix. Several methods were developed to produce the generator system [62]. One of the designs (developed in Italy) consisted of two cation-exchange columns connected in series. The first column (cross-linked cation-exchange resin) contained the adsorbed ^{90}Sr, while the second served as a safety column to trap any possible leakage of ^{90}Sr from the first column, and the ^{90}Y is eluted with acetate buffer solution. The pH and molarity of the acetate solution are optimized to efficiently elute the ^{90}Y in low volumes and to avoid the breakthrough of ^{90}Sr. The maximum permissible levels are extremely low and set up to 74 kBq (2 μCi) to prevent excessive body burden. Several ^{90}Y labeled peptides and antibodies have been developed for therapy [46].

8.5.2.2 ^{188}W→^{188}Re Generator

Alumina-based chromatographic generator systems, similar to those available for ^{99m}Tc, are prepared for obtaining ^{188}Re as ReO_4^-. Active acidic aluminum oxide is used to prepare the columns. Tungsten-188 (185 GBq/g) as sodium tungstate 0.26 M sodium hydroxide solution is used to load

on the column after adjusting the pH to 2–3. The column is washed with 100 mL of 0.9% NaCl solution (normal saline) and, after allowing growth of the ^{188}Re, eluted with 10 mL of saline. However, ^{188}ReO$_4^-$ eluent from the generator is not suitable for the direct formulation of radiopharmaceuticals. Concentration of the generator eluent solution is essential to radioactive concentration sufficient for radiopharmaceutical formulation [63]. The generator system is commercially available from several manufacturers.

8.5.2.3 ^{227}Ac$_{\to}$ ^{227}Th$_{\to}$ ^{223}Ra Generator

^{223}Ra ($T_{1/2}$ = 11.4 days) belongs to the alkaline earth family and is generated naturally from the decay of ^{235}U. However, for practical reasons, ^{223}Ra is artificially produced through a generator from ^{227}Ac parent ($T_{1/2}$ = 21.8 years), which also is produced artificially in a reactor starting from ^{226}Ra. A natural source of ^{227}Ac, originating from the decay chain of ^{235}U, is also available in limited quantities. The decay scheme (Fig. 8.15) of ^{227}Th shows the daughter ^{223}Ra and all the decay products from Ra-223.

The generator method is based on using 2-mL cartridges of UTEVA and DGA resins. The source material containing the mixture of ^{227}Ac, ^{227}Th, and ^{223}Ra isotopes in 4 M nitric acid is loaded onto the cartridges. Thorium is retained by UTEVA resin, while actinium is retained by DGA resin. Radium is not retained by these two cartridges. Currently, the clinical and commercial production of ^{223}RaCl$_2$ (Bayer Health Care Pharmaceuticals) involves ^{227}Ac and ^{227}Th isolation from a ^{231}Pa source (3.28×10^4 years) [64].

8.5.2.4 ^{229}Th$_{\to}$^{225}Ac Generator (Thorium Cow)

Actinium-225 is a pure α emitter with a half-live of 10 days. ^{225}Ac is mainly produced by isolation from ^{229}Th ($T_{1/2}$ = 7340 years), which is a decay product of uranium-233 ($T_{1/2}$ = 165,000 years). ^{233}U is a fissile isotope of uranium and was artificially produced by neutron irradiation of natural thorium. Between 1995 and 2005, ^{229}Th generated by the decay of ^{233}U (Fig. 5.11) was extracted and stored at Oak Ridge National Laboratory (ORNL). This ^{229}Th now exists at ORNL ($\sim$5.55 GBq

(150 mCi), or $\sim$704 mg) and another (1.7 (46 mCi), or 215 mg) at the Institute for Transuranium Elements (ITU, Karlsruhe, Germany). A third ^{229}Th source (5.55 GBq (150 mCi), 704 mg) obtained from Russia ^{233}U stockpiles exists at the Leipunskii Institute for Physics and Power Engineering (IPPE, Obninsk, Russia). These three sources provide the ^{229}Th (parent) needed to make the ^{225}Ac generator and provide approximately 26.6 GBq (720 mCi) at ORNL and 13.1 GBq (350 mCi) at ITU) of ^{225}Ac annually.

ORNL is a major producer of ^{225}Ac based on Th-229 generator. The chemical separation process consists of anion-exchange separation using hydrochloric and nitric acids followed by cation-exchange separation for the final purification. Gamma spectroscopy is used for quality control analysis of the final product before shipping, and mass spectroscopy data are used to evaluate chemical purity.

8.5.2.5 ^{225}Ac$_{\to}$ ^{213}Bi Generator

The use of radioisotopes to trace flow of molecules through the body was first proposed by George Charles de Hevesy in 1913. He saw the practical use in 1927 when ^{214}Bi was used as a tracer to study the velocity of blood.

Bismuth-213 is a hybrid α/β$^-$ emitter with a half-life of 45.6 min. It is generated as a decay product of ^{225}Ac (Fig. 8.10). In addition, the decay of ^{213}Bi is accompanied by a 440 keV γ photon emission. The generator requires purified ^{225}Ac and uses an organic anion-exchange system (AG-MP 50 resin) capable of isolating ^{213}Bi from a HCl solution of ^{225}Ac. The anion resin is then washed and stripped of the Bi product using a sodium acetate buffer [65]. A commercial Ac-225/Bi-213 Generator is currently supplied by iTM, Germany.

8.5.2.6 ^{228}Th$_{\to}$^{224}Ra$_{\to}$ ^{212}Pb$_{\to}$ ^{212}Bi Generator

Bismuth-212 is a hybrid α/β$^-$ emitter with a half-life of 60.6 min and is generated from the decay of ^{228}Th, ^{224}Ra, and ^{212}Pb (Fig. 8.17). The major disadvantage of ^{212}Bi is the high-energy (2.6 MeV) γ emission of ^{208}Tl, one of the decay products of ^{212}Bi.
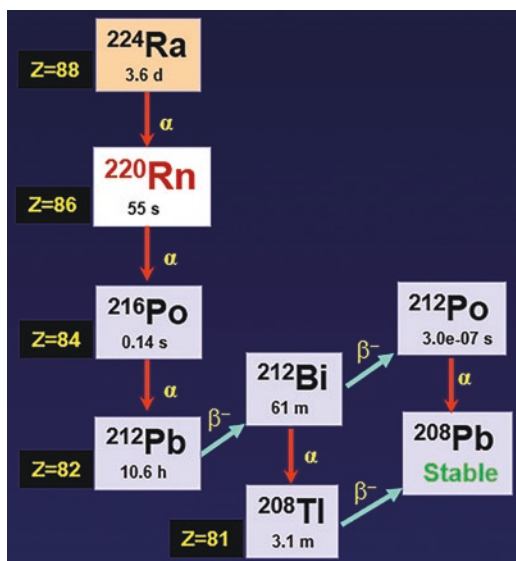
Fig. 8.17 Ra-224 decay scheme. [224]Ra (parent radionuclide) generator is used to produce [212]Pb and/or [212]Bi nuclides

The original [228]Th→[212]Bi generator used a Na_2TiO_3 column to bind both [228]Th and its immediate daughter radionuclide [224]Ra. The generator was operated by eluting [220]Rn with water into a reservoir, waiting a few minutes for the radon gas to decay to [212]Pb, followed by passing that solution through an organic cation-exchanger to absorb the [212]Pb. This generator based on [228]Th experienced problems with radiolytic damage in the resin with consequent diminished yield and was also a serious radiation safety problem.

To avoid problems originating from [228]Th-based generators, another generator based on [224]Ra ($T_{1/2}$ = 3.7 days) was designed [66, 67]. [224]Ra is separated from [228]Th by absorbing [228]Th as the nitrate complex onto an anion-exchanger, while [224]Ra elutes through the column. The [224]Ra is then absorbed on to the macroporous organic cation ion-exchange resin (AG-MP 50) which then serves as the source for either a [212]Bi or [212]Pb. [212]Bi can selectively be eluted from the generator with low acid concentrations of HI (0.05–0.2 M). At higher acid concentrations, a mixture of both [212]Pb and [212]Bi can be eluted. Alternatively, [212]Pb can be first eluted with 2 M HCl. The [212]Pb eluate is then diluted to 0.1 M HCl and loaded onto a small

AG-50 × 4 resin and the [212]Bi eluted from the resin with 0.2 M hydroiodic acid. [224]Ra→[212]Pb→[212]Bi generator is available for distribution from the NIDC of the US Department of Energy.

8.5.2.7 [227]Ac→[227]Th→[223]Ra Generator

[227]Th belongs to the actinium series and has a physical half-live of 18.72 days. The decay chain of [227]Th generates 6 α particles with an average energy of 6.02 MeV. [227]Th can be produced by natural decay of [227]Ac ($T_{1/2}$ = 21.8 years), which can be produced in a reactor by neutron irradiation based on nuclear reaction, [226]Ra (n, γ)[227]Ra. [227]Ra ($T_{1/2}$ = 42 min), which in turn decays by β^- disintegration to provide the desired [227]Th. The long half-life of [227]Th allows for transportation and preparation of the radiopharmaceuticals.

References

1. Segrè E. From x-rays to quarks. Modern physicists and their discoveries. New York: Freeman; 1980.
2. Joliot F, Curie I. Artificial production of a new kind of radioelement. Nature. 1934;133:201–2.
3. Finn RD, Schlyer DJ. Production of radionuclides for PET. In: Wahl RL, Buchanan JW, editors. Principles and practice of positron emission tomography. Philadelphia: Williams & Wilkins; 2002.
4. Beiser A. Concepts of modern physics. 5th ed. New York: McGraw-Hill; 1995.
5. Schlyer DJ. Production of radionuclides in accelerators. In: Welch MJ, Redvanley CS, editors. Handbook of radiopharmaceuticals, radiochemistry. And applications. New York: Wiley; 2003. p. 1–70.
6. Hess E, Takacs S, Scholten B, et al. Excitation function of the [18]O(p,n)[18]F nuclear reaction from threshold up to 30 MeV. Radiochim Acta. 2001;89:357–62.
7. Cockcroft JD, Walton ETS. Experiments with high velocity positive ions. II. The disintegration of elements by high velocity protons. Proceedings of the Royal Society A. 1932;137:229–42.
8. Oliver C. Compact and efficient accelerators for radioisotope production. In: Proceedings of IPAC2017, Copenhagen; 2017. ISBN 978-3-95450-182-34824.
9. Inagaki M, Sekimoto S, Tanaka W, et al. Production of [47]Sc, [67]Cu, ^{68}Ga, [105]Rh, ^{177}Lu, and [188]Re using electron linear accelerator. J Radioanal Nucl Chem. 2019;322:1703–9.
10. Onishchyuk EA, Kurachenko YA, Matusevich ES. High-power electron accelerator for the production of neutrons and radioisotopes. Nucl Energ

Technol. 2020;6(1):49–54. https://doi.org/10.3897/nucet.6.51781.

11. Lawrence EO, Livingston MS. The production of high-speed protons with the use of high voltages. Phys Rev. 1931;38:834.

12. Satyamurthy N, Phelps ME, Barrio JR. Electronic generators for the production of positron emitter labeled radiopharmaceuticals: where would PET be without them? Clin Positron Imag. 1999;2:233–53.

13. Schmor P. Review of cyclotrons for the production of radioactive isotopes for medical and industrial applications. Rev Accel Sci Technol. 2011;4(1):103–16.

14. IAEA TR-468. Cyclotron produced radionuclides: physical characteristics and production methods. Vienna, Austria: IAEA; 2009.

15. Livingston MS, McMillian E. The production of radioactive oxygen. Phys Rev. 1934;46:439–40.

16. Vera-Ruiz H, Wolf AP. Excitation function of ^{15}O production via the ^{14}N(d, n)^{15}O. Radiochim Acta. 1977;24:65–7.

17. Berridge MS, Landmeier BJ. In target production of [^{13}N] ammonia; target design, production, and operating parameters. Appl Radiat Isot. 1993;44:1433–41.

18. Tilbury RS, Dahl JR. ^{13}N species formed by the proton irradiation of water. Radiat Res. 1979;79:22–33.

19. Bida GT, Ruth TJ, Wolf AP. Experimentally determined thick target yields for the ^{14}N(p,α)^{11}C reaction. Radiochim Acta. 1980;27:181–5.

20. Casella VR, Christman DR, Ido T, et al. Excitation function for the ^{14}N(p,α)^{11}C reaction up to 15 MeV. Radiochim Acta. 1978;25:17–20.

21. Casella V, Ido T, Wolf AP, et al. Anhydrous F-18 labeled elemental fluorine for radiopharmaceutical preparation. J Nucl Med. 1980;21:750–7.

22. Ruth TJ, Wolf AP. Absolute cross section for the production of ^{18}F via the ^{18}O(p,n)^{18}F reaction. Radiochim Acta. 1979;26:21–4.

23. Nickels RJ, Hichwa RD, Daube ME, et al. An ^{18}O target for the high yield production of ^{18}F fluoride. Int J Appl Radiat Isot. 1983;34:625–9.

24. Scholten B, Kovacs Z, Tarkanyi F, et al. Excitation functions of ^{124}Te(p, xn)$^{124, 123}$I reactions for 6–31 MeV with special reference to the production of ^{124}I at a small cyclotron. Appl Radiat Isot. 1995;46:255–9.

25. Sheh Y, Koziorowski J, Balatoni J, et al. Low energy cyclotron production and chemical separation of no-carrier added iodine-124 from a reusable enriched tellurium-124 dioxide/aluminum oxide solid solution target. Radiochim Acta. 2000;88:169–73.

26. IAEA TECDOC-1863. Ga-68 cyclotron production IAEA, Vienna, Austria, 2019.

27. Kasbollah A, Eu P, Cowell S, Deb P. Review on production of ^{89}Zr in a medical cyclotron for PET radiopharmaceuticals. J Nucl Med Technol. 2013;41(1):35–41.

28. Müller C, Bunka M, Reber J, et al. Promises of cyclotron-produced ^{44}Sc as a diagnostic match for trivalent β− −emitters: in vitro and in vivo study of a ^{44}Sc-DOTA-folate conjugate. J Nucl Med. 2013;54:2168–74.

29. Van der Meulen NP, Hasler R, Talip Z, et al. Developments toward the implementation of ^{44}Sc production at a medical cyclotron. Molecules. 2020;25:4706–22.

30. Francisco DC, Liberal G, O'Sullivan JM. Targeted alpha therapy: current clinical applications. Cancer Biother Radiopharma. 2020;35(6):404–17.

31. Apostolidis C, Molinet R, McGinley J, et al. Cyclotron production of Ac-225 for targeted alpha therapy. Applied Radiation and Isotopes. 2005;62(3):383–7.

32. Robertson AKH, Ramogida CF, Schaffer P, Radchenko V. Development of ^{225}Ac radiopharmaceuticals: TRIUMF perspectives and experiences. Curr Radiopharm. 2018;11(3):156–72.

33. Ermolaev SV, Zhuikov BL, Kokhanyuk VM, et al. Production of actinium, thorium and radium isotopes from natural thorium irradiated with protons up to 141 MeV. Radiochim Acta. 2012;100:223–9.

34. John K. US DOE tri-lab research and production effort to provide accelerator produced ^{225}Ac for radiotherapy: 2019 update. Eur J Nucl Med Mol Imaging. 2019;46:S722.

35. Weidner JW, Mashnik SG, John KD, et al. Proton-induced cross sections relevant to production of ^{225}Ac and ^{223}Ra in natural thorium targets below 200MeV. Appl Radiat Isotop. 2012;70:2602–7.

36. Zhuikov BL, Kalmykov SN, Ermolaev SV, et al. Production of ^{225}Ac and ^{223}Ra by irradiation of Th with accelerated protons. Radiochemistry. 2011;53:73–80.

37. Banerjee S, Pillai MRA, Knapp FF. Lutetium-177 Therapeutic Radiopharmaceuticals: Linking Chemistry, Radiochemistry, and Practical Applications. Chem Rev. 2015;15:(8):2934–74.

38. Dash A, Pillai MRA, Knapp FF. Production of ^{177}Lu for targeted radionuclide therapy: available options. Nucl Med Mol Imaging. 2015;49:85–107.

39. Medvedev DG, et al. Development of a large-scale production of Cu-67 from Zn-68 at the high energy proton accelerator: closing the Zn-68 cycle. Appl Radiat Isot. 2012;70:423–9.

40. Ehst DA, Smith NA, Bowers DL, Makarashvili V. Copper-67 production on electron linacs—photonuclear technology development. AIP Conf Proc. 2012;1509:157–61.

41. Mamtimin M, Harmon F, Starovoitova VN. Sc-47 production from titanium targets using electron linacs. Appl Radiat Isotop. 2015;102:1–4.

42. Rotsch DA, Brown MA, Nolen AN, et al. Electron linear accelerator production and purification of scandium-47 from titanium dioxide targets. Appl Radiat Isotop. 2018;131:77–82.

43. Nicholas AL, Aldama DL, Verpelli M. Handbook of nuclear data for safeguards. International Atomic Energy Agency. IAEA-INDC (NDS)-0534. 2008.

44. IAEA TECDOC-1340. Manual for reactor produced isotopes. Vienna, Austria: IAEA; 2003.

45. Klaassen NJM, Arntz MJ, Arranja AG, et al. The various therapeutic applications of the medical isotope holmium-166: a narrative review. EJNMMI Radiopharm Chem. 2019;2019(4):19–45.

46. IAEA RR-S5. Yttrium-90 and Rhenium-188 radio-pharmaceuticals for radionuclide therapy. In: Radioisotopes and radiopharmaceuticals series, No.5. Vienna, Austria: IAEA; 2015.

47. Khandaker MU, Nagatsu K, Minegishi K, et al. Cyclotron production of no carrier added Re radionu-clide for theranostic applications. Appl radiat Isotop. 2020;166:109428.

48. Balkin ER, Cutler CS. Scale-up of high specific activity ^{186g}Re production using graphite-encased thick ^{186}W targets and demonstration of an effi-cient target recycling process. Radiochim Acta. 2017;105:1071–81.

49. Stevenson NR, George GS, Simon J, et al. Methods of producing high specific activity Sn-117m with com-mercial cyclotrons. J Radioanalytical Nucl Chem. 2015;305:99–108.

50. Duchemin C, Essayan M, Guertin A, et al. How to produce the highest tin-117m specific activity? CTR-PHE, S35; 2016.

51. Ruth TJ. The medical isotope crisis: how we got here and where we are going. J Nucl Med Technol. 2014;42:245–8.

52. Hasan S, Prelas MA. Molybdenum-99 production path-ways and the sorbents for ^{99}Mo/^{99m}Tc generator systems using (n, γ) ^{99}Mo: a review. SN Appl Sci. 2020;2:1782.

53. Qaim SM. Cyclotron production of generator radio-nuclides. Radiochim Acta. 1987;41:111–7.

54. Welch MJ, McCarthy TJ. The potential role of generator-produced radiopharmaceuticals in clinical PET. J Nucl Med. 2000;41:315–7.

55. Richards P. The Tc-99m generator. Report No BNL-9061. Upton, New York: Brookhaven National Laboratory; 1965.

56. Thomas KE. Strontium-82 production at Los Alamos National Laboratory. Appl Radiat Isot. 1987;38:175–80.

57. Yano Y, Anger HO. A gallium-68 positron cow for medical use. J Nucl Med. 1964;5:485.

58. Schuhmacher J, Maier-Borst W. A new $_{68}$Ge/$_{68}$Ga radioisotope generator system for production of ^{68}Ga in dilute HCl. Int J Appl Radiat Isot. 1981;32:31–6.

59. Fukumura T, Okada K, Suzuki H, et al. An improved ^{62}Zn/^{62}Cu generator based on a cation exchanger and its fully remote-controlled preparation for clinical use. Nucl Med Biol. 2006;33:821–7.

60. Haynes NG, Lacy JL, Nayak N, et al. Performance of a ^{62}Zn/^{62}Cu generator in clinical trials of PET perfu-sion agent ^{62}Cu-PTSM. J Nucl Med. 2000;41:309–14.

61. Robinson GD Jr, Zielinski FW, Lee AW. The ^{62}Zn/^{62}Cu generator: a convenient source of 62Cu for radiophar-maceuticals. Int J Appl Radiat Isot. 1980;31:111–6.

62. IAEA-TRS-470. Therapeutic radionuclide generators ^{90}Sr/^{90}Y and ^{188}W/^{188}Re generators. Vienna, Austria: IAEA; 2009.

63. Boschi A, Uccelli L, Pasquali M, et al. ^{188}W/^{188}Re generator system and its therapeutic applica-tions. J Chem. 2014;2014:529406. https://doi.org/10.1155/2014/52940.

64. Larsen G, Henriksen O, Bruland. Preparation and Use of Radium-223 to Target Calcified Tissues for Pain Palliation, Bone Cancer Therapy, and Bone Surface Conditioning. Google Patents. 2003.

65. Bray LA, Tingey JM, DesChane JR, et al. Development of a unique bismuth (Bi-213) automated generator for use in cancer therapy. Ind Eng Chem Res. 2000;39(9):3189–94.

66. Yong K, Brechbiel MW. Towards translation of ^{212}Pb as a clinical therapeutic; getting the lead in! Dalton Trans. 2011;40(23):6068–76.

67. Pruszyński M, Walczak R, Rodak M, et al. Radiochemical separation of 224Ra from 232U and 228Th sources for 224Ra/212Pb/212Bi generator. Appl Radiat Isot. 2021;172:109655.

An experiment is a question which science poses to Nature, and a measurement is the recording of Nature's answer. (Max Planck)

9.1 Radiotracer Vs. Radiopharmaceutical

In the 1920s, George de Hevesy, coined the term *radioindicator* or *radiotracer* and introduced the *tracer principle* in biomedical sciences. Initially, β^--emitting radioisotopes were used as therapeutic agents. For example, ^{32}P was used for the treatment of *polycythemia vera* and *leukemia*, and ^{131}I was used for the treatment of thyroid disease (toxic and nontoxic goiter) and thyroid cancer.

Following the discovery of the scintillation scanner by Benedict Casen, ^{131}I was introduced as a radiotracer for diagnostic imaging purpose. In 1956, Merrill Bender introduced ^{131}I-labeled serum albumin as a radiotracer to image brain tumors. The introduction of the Anger camera and the ^{99m}Tc generator, in the 1960s, stimulated the development of a number of radiolabeled compounds as radiotracers for diagnostic studies in nuclear medicine.

A radiotracer can be defined as a specific radiolabeled molecule (or probe) that resembles or traces the in vivo behavior of a natural molecule and can be used to provide information about a specific biological process. The degree of similarity between the radiotracer and the natural substance, however, may vary depending on the particular radiotracer. For example, $[^{11}C]$ glucose and $[^{14}C]$glucose are true tracers of glucose because they are chemically identical to natural glucose, while $[^{18}F]$fluorodeoxyglucose (FDG), an analog of glucose, also traces glucose, but does not behave identically to glucose since it is chemically different.

One of the most important characteristics of a true radiotracer is the ability to study the components of a homeostatic system without disturbing their function. Occasionally, the term *radioligand* is also used in the context of imaging studies. A radioligand can be defined as any radiolabeled molecule that can bind with another molecule or substance (binder) in a predictable way under controlled conditions. For example, ^{68}Ga-Dotatate (Netspot) is a radioligand that binds, specifically, to somatostatin type 2 receptors (SSTR-2) in patients with neuroendocrine tumors (NETs), while $[^{18}F]$Fluorodeoxyglucose (FDG) is a radiotracer used to image glucose metabolism in tumor tissue, heart, and brain.

9.1.1 Radiopharmaceutical Vs. Radiochemical

All radiolabeled compounds or substances used for the purpose of diagnosis or therapy have been defined as *radioactive drugs* or *radiopharmaceuticals* by the U.S. Food and Drug Administration

(FDA). Diagnostic radiopharmaceuticals are administered in trace amounts (<100 μg) and, typically, do not induce any physiological response or pharmacological effect in patients. The term radioindicator, however, may be more appropriate to describe radiolabeled compounds or substances used for the purpose of diagnosis.

In 1954, the U.S. Atomic Energy Commission (AEC) and, subsequently, the U.S. Nuclear Regulatory Commission (NRC) were given the responsibility for directing the medical use of reactor-produced byproducts. Since the 1960s, the stated mission of the FDA has been to "assure safety and efficacy in marketed medicinal agents and medicinal devices." In 1972, the FDA took over the responsibility to regulate the medical usage of reactor-produced radiolabeled compounds from the NCR. Subsequently, in 1975, the FDA decided to also assume the responsibility for the cyclotron-produced radiolabeled compounds. In addition, the FDA adopted the same regulations for radiolabeled compounds (or nuclear medicine imaging probes) as those in existence for traditional drugs (pharmaceuticals). As a result, the term "radiopharmaceutical" has become the official FDA categorization for all radioindicators and radiotracers used for diagnosis and therapy. Although the field of nuclear medicine evolved into a more sophisticated molecular imaging technology, the FDA continues to extend the usage of the term "radiopharmaceuticals" to include the novel radiolabeled molecular imaging probes or radiotracers.

The term *radiochemical* is sometimes used for any radiolabeled compound or radiotracer. From the standpoint of chemistry and radiochemical purity, there is no difference between the terms radiochemical and radiopharmaceutical. From a regulatory point of view, however, a radiopharmaceutical must also be sterile, pyrogen free, safe for human use, and efficacious for a specific indication. In contrast, a radiochemical may not be sterile and pyrogen-free and is not an FDA-approved agent for routine human use.

9.2 Radiopharmaceuticals for Molecular Imaging (RP-MI)

The terms, radiotracer, radioligand, and radiolabeled molecular imaging probe (RMIP), have specific meaning depending on their specific use and application. However, from a regulatory point of view, the term radiopharmaceutical represents any radiolabeled molecule intended for human use.

The members of the molecular imaging center of excellence (MICoE) standard definitions task force recently developed the following standard definitions and terms [1]:

- Molecular imaging is the visualization, characterization, and measurement of biological processes at the molecular and cellular levels in humans and other living systems.
- Molecular imaging agents are "probes used to visualize, characterize, and measure biological processes in living systems". Both, endogenous molecules and exogenous probes can be molecular imaging agents.

Because the emphasis of this textbook is on molecular imaging and targeted radionuclide therapy, it is important to understand the subtle difference between the conventional nuclear imaging technology and the molecular imaging technology. Some of the radiopharmaceuticals used in nuclear medicine are *nonspecific*, while all the RP-MI, by definition, are highly *specific* for the measurement of a specific biological process and, therefore, can be regarded as targeted radiopharmaceuticals for imaging.

The current FDA-approved radiopharmaceuticals for SPECT and PET can be divided into "specific" and nonspecific agents (Table 9.1). Several examples would clearly illustrate the difference between specific and nonspecific agents. Radioiodide (^{123}I, ^{124}I, or ^{131}I) is a very good example of a molecular imaging probe; just like

Table 9.1 FDA-approved radiopharmaceuticals for planar imaging, SPECT, and PET

Radiopharmaceuticals	Trade Name	Indications
Non-specific radiopharmaceuticals		
^{99m}Tc pertechnetate		Salivary and lacrimal gland imaging, vesicoureteral imaging
^{99m}Tc-macroaggregated albumin (MAA)		Evaluation of pulmonary perfusion Evaluation of peritoneo-venous shunt patency
^{99m}Tc-sulfur colloid		Image area of functioning RES in liver, spleen and bone marrow, localization of lymph nodes draining a primary tumor
^{99m}Tc-tilmanocept	Lymphoseek®	Lymphatic mapping and to locate lymph nodes draining a primary tumor site
^{99m}Tc-pyrophosphate		Bone imaging and blood pool imaging to detect GI bleeds
^{99m}Tc-mebrofenin	Choletec®	Hepatobiliary imaging agent
^{99m}Tc-bicisate	Neurolite®	To assess rCBF and to localize stroke
^{99m}Tc-exametazine	Ceretec™	To assess rCBF and to localize stroke
^{99m}Tc-medronate (MDP)		Bone imaging to delineate areas of altered osteogenesis
^{99m}Tc-oxidronate (HDP)		Bone imaging to delineate areas of altered osteogenesis
^{99m}Tc-Pentetate (DTPA)		Renal imaging and function
^{99m}Tc-mertiatide	MAG3™	Renal imaging and function
^{99m}Tc-succimer (DMSA)		Evaluation of renal parenchymal disorders
^{99m}Tc-sestamibi	Cardiolite®	Myocardial perfusion and evaluation of breast lesions
^{99m}Tc-tetrofosmin	Myoview™	Myocardial perfusion
^{201}Tl chloride		Myocardial perfusion
^{67}Ga-citrate		Detection of certain tumors and acute infection
^{111}In pentetate		Radionuclide cisternography
^{111}In oxyquinoline		Label leukocytes and to localize areas of acute infection
Specific (targeted radiopharmaceuticals or radiolabeled molecular imaging probes (RMIP))		
^{123}I sodium iodide (Liquid or capsules)		Thyroid uptake by active transport via NaI transporter evaluation of thyroid function and morphology
^{131} sodium iodide (Liquid or capsules)		Evaluation of thyroid function and detection of metastases associated with thyroid malignancies
^{111}In pentetreotide	Octreoscan™	Localization of primary and metastatic NETs bearing SSTRs
[^{123}I]Iobenguane	Adreview™	Detection of primary or metastatic pheochromocytoma or neuroblastoma via norepinephrine transporter
[^{123}I]Ioflupane	DaTscan™	Imaging striatal dopamine transporters in patients with parkinsonian syndrome
^{82}Rb chloride	Cardiogen-82®, Rubi-fill®	As a K⁺ analog, to evaluate regional myocardial perfusion
[^{13}N]Ammonia		To evaluate regional myocardial perfusion
[^{18}F]Fludeoxyglucose (FDG)		To assess abnormal glucose metabolism in oncology To assess myocardial hibernation To identify foci of epileptic seizures
[^{18}F]Sodium Fluoride		To delineate areas of altered osteogenesis
[^{18}F]Florbetapir	Amvid™	To estimate β-amyloid neuritic plaque density in patients with cognitive impairment
[^{18}F]Florbetaben	Neuraceq™	To estimate β-amyloid neuritic plaque density in patients with cognitive impairment
[^{18}F]Flutemetamol	Vizamyl™	To estimate β-amyloid neuritic plaque density in patients with cognitive impairment
[^{18}F]Flortaucipir	Tauvid™	To estimate the density and distribution of aggregated tau neurofibrillary tangles (NFTs)
[^{18}F]Piflufolastat	Pylarify®	To detect PSMA-positive lesions in prostate cancer

Table 9.1   (continued)

Radiopharmaceuticals	Trade Name	Indications
[11C]Choline		To help identify potential sites of prostate cancer recurrence
[18F]Fluoroestradiol	Cerianna™	For the detection of estrogen receptor-positive lesions in patients with breast cancer
[18F]Fluciclovine	Auxumin™	Prostate cancer recurrence
[18F]Fluorodopa		To visualize dopaminergic nerve terminals in the striatum in patients with suspected Parkinsonian syndromes (PS)
68Ga-DOTATATE	NETspot	For localization of SSTR-positive NETs
64Cu-DOTATATE	Detectnet	For localization of SSTR-positive NETs
68Ga-DOTATOC		For localization of SSTR-positive NETs
68Ga-PSMA-HBED-CC		PSMA-positive lesions in prostate cancer

the natural iodide (I^-), it is actively transported into the thyroid gland via sodium iodide symporter (NIS) and incorporated into the thyroid hormones. In contrast, ^{99m}Tc pertechnetate (TcO_4^-), while useful for thyroid imaging, is not a specific radiotracer to assess thyroid function. ^{67}Ga citrate is a nonspecific diagnostic imaging agent to identify both tumor tissue and abscess (or infection), while ^{111}In-labeled leukocytes are highly specific to detect the sites of acute infection but, not tumor tissue.

The metabolic and molecular information provided by [18F]FDG-PET can be considered as the first validated "clinically useful" molecular imaging technique. FDG is a substrate for the enzyme *hexokinase* and highly specific in assessing the glucose metabolism of any tissue. FDG, however, is a non-specific molecular imaging probe to image malignant tissue, since it is also taken up by inflammatory tissue, macrophages, and many other normal cells that have augmented glucose utilization. In contrast, ^{111}In-DTPA-octreotide (OctreoScan) or ^{68}Ga-Dotatate (NetSpot) are highly specific agents to image neuroendocrine tumors (NETs) expressing somatostatin type 2 (SSTR 2) receptors. Therefore, ^{111}In-DTPA-octreotide and ^{68}Ga-Dotatate are truly targeted radiopharmaceuticals (or RMIPs) designed for molecular imaging studies based on SPECT and PET, respectively [2].

9.2.1   Molecular Medicine and Theranostics

As previously discussed, the term *homeostasis* is used by physiologists to describe maintenance of static, or constant, conditions in the internal environment by means of positive and negative feedback of information. Diseases can be defined as abnormal processes as well as abnormalities in molecular concentrations of different biological markers, signaling molecules and receptors. In the last two decades, there has been a revolution in our basic understanding of the biology and biochemistry of disease. With the elucidation of the human genome and the description of the genetic abnormalities, responsible for numerous diseases, we now have a better understanding of the basic molecular pathways, proteins, and signal transduction processes that are present in the normal cell.

The basis of molecular medicine is that chemical disturbances will precede anatomical abnormalities in disease. The new generation of molecular therapeutics is based on the rational drug design to reverse or control chemical imbalances by targeting key specific receptors, enzymes, membrane transporters, and antigens. The ultimate goal of molecular medicine is to treat the disease in its early stages with an appropriate patient-specific "targeted molecular

therapy." In order to achieve this goal, it is essential to develop highly specific RP-MI. In the design and development of an ideal radiotracer, it is important to identify first a specific biological target, and then design a radiopharmaceutical, which may be a biochemical or a synthetic molecule (targeting vehicle or vector), specific for the biological target (receptor, enzyme, protein, antigen) or a biological process (such as metabolism, angiogenesis, and apoptosis) in an organ, or tissue of interest. Subsequently, an appropriate radionuclide (such as ^{18}F, ^{123}I, ^{68}Ga, ^{64}Cu) can be used to synthesize a radiopharmaceutical suitable for imaging based on either PET or SPECT techniques. A schematic of a targeted radiopharmaceutical for molecular imaging studies is shown in Fig. 9.1.

The development of RP-MI will greatly benefit from the science of molecular medicine and from the chemical insights of molecular therapeutics. The human brain uses glucose as the primary source of energy for its physiological functions. Alteration of blood glucose levels leads to hypo/

hyperglycemic conditions. Consequently, the brain undergoes dysregulation of glucose metabolism which is further associated with various pathological disorders causing cognitive impairment and loss of critical brain functions. Glucose metabolism is connected with multiple other metabolic pathways in order to generate adequate energy for neuronal cells to carry out their functions. Therefore, glucose homeostasis plays a prominent role in the maintenance of healthy brain physiology. The Warburg effect, first proposed in 1920s, describes a phenomenon in which cancer cells take up glucose more and preferentially metabolize glucose by glycolysis, producing lactate as an end product, even in the presence of oxygen. 2-deoxy-2-[^{18}F]fluoro-D-glucose (FDG), a glucose analog was developed in 1970s, by substituting ^{18}F for the normal hydroxyl group at the C-2 position in the glucose molecule (Fig. 9.2). FDG-PET was used for 20 years to image glucose metabolism of brain and heart before it was discovered that FDG is useful as a diagnostic radiopharmaceutical for the detection of various tumors
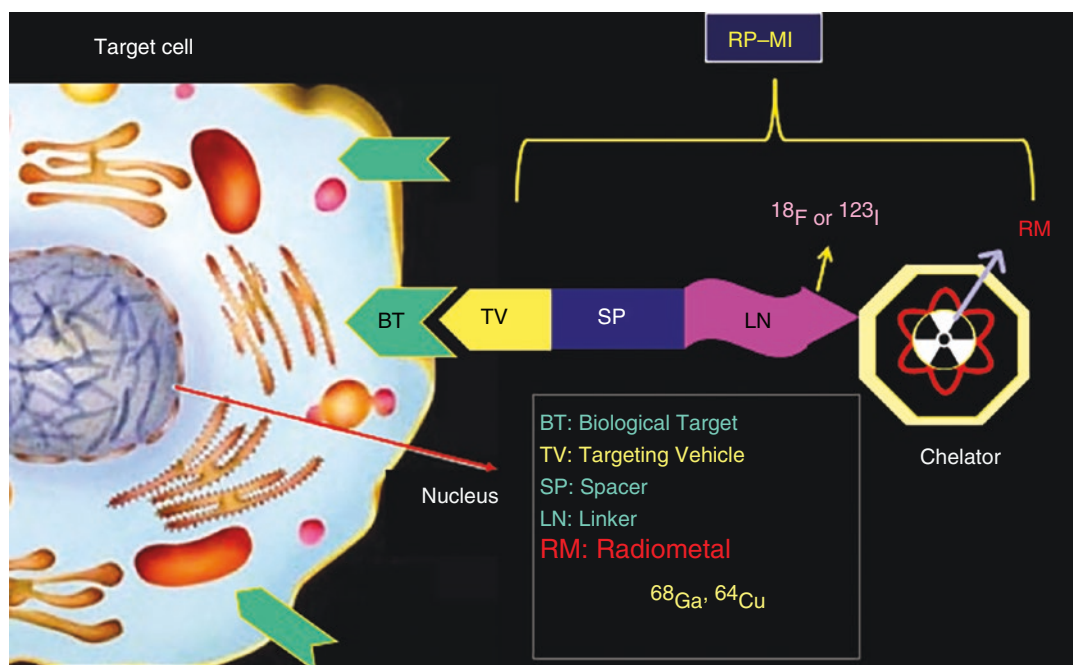
Fig. 9.1 Schematic of a targeted radiopharmaceutical for molecular imaging based on PET or SPECT. The targeting vehicle (vector) specific for a biological target can be labeled with ^{18}F or ^{123}I. However, labeling (or complexation) with radiometals such as ^{68}Ga or ^{64}Cu requires conjugation of a chelator to the targeting vehicle via spacer/linker
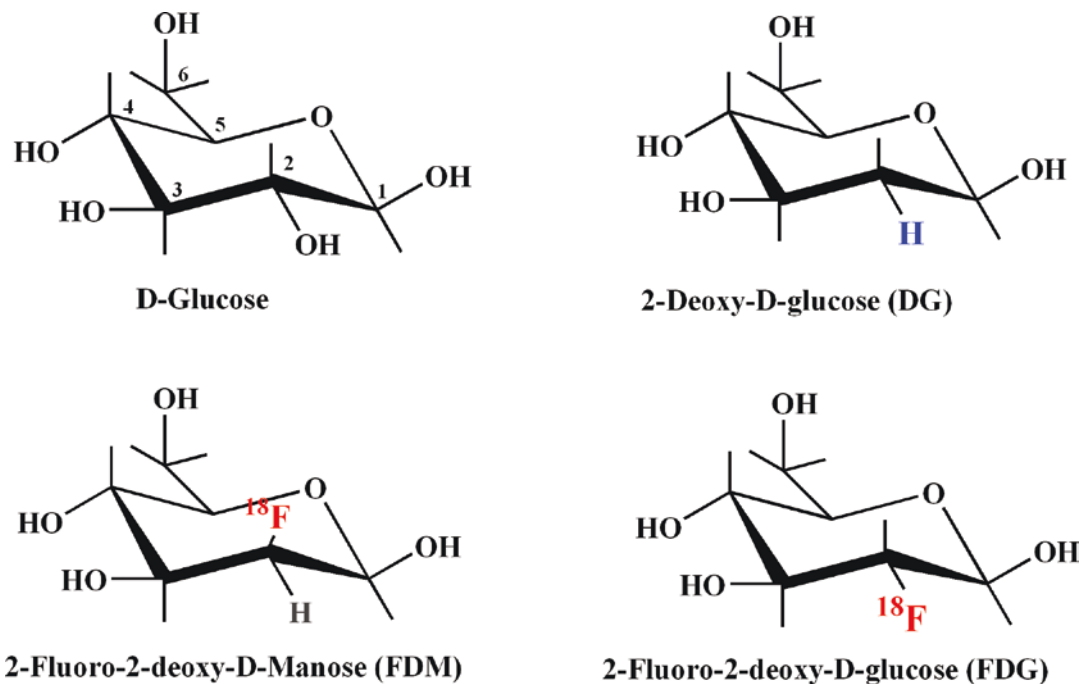
Fig. 9.2 Analogs of D-glucose: Substitution of hydrogen or fluorine atom for the hydroxyl group on C-2 position of glucose would produce DG and FDG, which can be transported into the cell by glucose transporters similar to that of D-glucose

and also to assess tumor response to chemotherapy. FDG revolutionized nuclear medicine and accelerated the development of molecular imaging technology. The glucose molecule, however, is not suitable for radiolabeling with beta emitters such as ^{131}I, ^{90}Y, and [177]Lu.

Molecular imaging agents and drugs (therapeutics) share common concepts of structural design and mechanisms of localization and/or action because they target the same enzyme, receptor, or antigen. Drugs block or inhibit their targets and restore the chemical imbalance associated with a disease, while RPMIs, at tracer levels, can provide noninvasive quantitative assessment of the functional status of the molecular target in a specific disease. For example, the discovery of SSTRs in patients with NETs led to the development of chemotherapy based on octreotide (Sandostatin®), which binds specifically to SST type 2 receptors. Radiolabeled analogs of octreotide such as ^{111}In-DOTA-octreotide, ^{68}Ga-Dotatate, and ^{68}Ga-dotatoc provided imaging agents to detect SSTR-2 positive lesions in patients with NETs. The same molecule used for imaging is labeled with β^- emitting radionuclide (^{177}Lu) to synthesize a therapeutic agent (^{177}Lu-dotatate or Lutathera™) for TRT of patients with NETs. Receptor specific chemotherapeutic drug lead to the development of MIPs, and MIPs in turn lead to the development of drugs for TRT. Thus, a diagnostic imaging agent and a therapeutic drug may have similar structural requirements, being the same molecule or structural analogs of each other [3].

The concept of theranostics integrates two distinct approaches that both encompass all steps of patients' management. Theranostics in nuclear medicine is a personalized approach to treating cancer, using similar (or same) molecules for both imaging (diagnosis) and therapy. A target specific biomolecule is designed in such a manner that it can be labeled with a γ or β^+ emitting radionuclide for SPECT or PET imaging, and it can also be labeled with a therapeutic radionu-

Table 9.2   Theranostic radiopharmaceuticals

Disease/Indication	Target	Radiopharmaceutical for	
		Molecular imaging	Therapy
Therapy of neuroendocrine tumors (NETs)	SSTR-2 Agonist	^{68}Ga-Dotatate[a]	^{177}Lu-Dotatate[a]
		^{64}Cu-Dotatate[a]	^{177}Lu-EB-Tate
			^{177}Lu-Dotatoc
			^{90}Y-Dotatoc
			^{177}Lu-Satoreotide tetraxetan
	SSTR-2 antagonist	^{68}Ga-NODAGA-JR11 (OPS202)	^{177}Lu-DOTA-JR11 (OPS201)
	Glucagon-like peptide-1 (GLP-1R)	^{68}Ga-DOTA-Exendin-4	^{177}Lu-DOTA-Exendin-4
Melanoma, multiple myeloma, small-cell lung cancer, NETs	CXCR4	^{68}Ga-Pentixafor	^{177}Lu-Pentixafor
Metastatic castration resistant prostate cancer (mCRP)	Bone mineral (hydroxyapatite)	[^{18}F]sodium fluoride[a]	^{223}Ra dichloride[a] ^{153}Sm-EDTMP
	Prostate specific membrane a antigen (PSMA)	^{68}Ga-PSMA-11[a]	^{177}Lu-PSMA-617 ^{225}Ac-PSMA-617
		[^{18}F]PSMA-1007	^{177}Lu-PSMA-I&T ^{225}Ac-PSMA-617
		[^{18}F]rhPSMA-7.3	
	GRPR	^{68}Ga-RM2	^{177}Lu-RM2
		^{68}Ga-NeoBOMB-1	
Pancreatic adenocarcinomas	Neurotensin receptor (NTSR1)	^{111}In-3B-227	^{177}Lu-3B-227
Bone marrow ablation in leukemias	CD-45	^{131}I-IOMAB, Apamistamab	^{131}I-IOMAB, Apamistamab

[a]Radiopharmaceuticals approved by FDA for routine clinical studies

clide decaying by β^-, α, or *EC* (emitting Auger electrons) [4–8]. Several theranostic radiopharmaceuticals of clinical importance are listed in Table 9.2.

The success of theranostics in the clinic has already been well established with the introduction of somatostatin analogues for PET/SPECT imaging and TRT in patients with SSTR-positive NETs. The future of theranostics is very promising and several theranostic radiopharmaceuticals in phase II/III clinical studies for both imaging and therapy are summarized in Table 9.2.

9.2.2   RPMI: Categories and Types

A number of biological processes and biochemical targets (Table 9.3) have been identified in order to develop target specific molecular imaging radiopharmaceuticals for PET and SPECT. On the basis of these molecular targets, imaging probes can be divided into nine different categories:

1. Probes for the determination of perfusion and membrane transport
2. Probes based on specific substrates for metabolism
3. Probes based on enzyme-mediated transformation
4. Probes based on receptor-mediated interactions
5. Probes based on antigen-antibody interactions
6. Probes based on abnormal protein expression or protein deposits
7. Probes based on nucleic acids (DNA and RNA)
8. Probes based on nanoparticles
9. Probes based on cellular migration or trafficking

Table 9.3 Radiopharmaceuticals for molecular imaging: Biological target and biochemical process

Biochemical process	Specific target	Radiopharmaceutical
Thyroid function	Sodium iodide symporter (NIS)	[123, 124, 131]I sodium iodide
Glucose metabolism	*Glucose transporters and hexokinase*	[18F]FDG
Fatty acid metabolism	*Thiokinase*	[18F]FTHA
Membrane synthesis	*Choline kinase*	[18F]Fluorocholine
DNA synthesis	*Thymidine kinase*	[11C]thymidine, [18F]FLT
Amino acid transport	Sodium dependent and sodium independent carrier mediated process	[18F] FACBC or fluciclovine [18F]fluoro-m-tyrosine
Dopamine synthesis and metabolism	*Aromatic amino acid decarboxylase (AAADC*	[18F]FDOPA
Nigrostriatal neuronal degeneration	Dopamine transporter	[123I]Ioflupane (DatScan)
Dopamine receptor	Dopamine D2 receptor	[11C]Raclopride, 123I-IBZM
Dopamine reuptake	Dopamine presynaptic transporter	[18F]FP-CIT, 123I-β-CIT
Altered osteogenesis	Bone mineral (hydroxyapatite)	[18F]Sodium Fluoride
Neuroendocrine tumor	Norepinephrine transporter	[123I]iobenguane (MIBG) (Adreview™)
Receptor binding	Estrogen receptor	[18F]Fluoroestradiol
	Androgen receptor	[18F]Fluorodihydroxytestosterone (FDHT)
	Somatostatin receptor (SSTR-2)	111In-DTPA-Octreotide 68 Ga-Dotatate, 64Cu-Dotatate
Macrophage (microglia)	Peripheral benzodiazepine receptor	[11C]PK11195
Tumor antigen	Prostate-Specific Membrane Antigen (PSMA)	68Ga-PSMA-11, [18F]Piflufolastat, [18F] PSMA-1007, [18F]-rhPSMA-7.3 111In-DOTA-huJ591 mAb 89Zr-IABM2 minibody
Dementia, amyloid burden	*β-Amyloid*	[11C]PIB, [18F]Florbetapir, [18F]Florbetaben, [18F]Flutemetamol
Dementia, tau burden	Aggregated tau neurofibrillary tangles (NFTs)	[18F]Flortaucipir
Apoptosis	Phosphatidylserine	124I-Annexin V
Angiogenesis	Integrin receptors, $\alpha_V \beta_3$	18F-FB– E[c(RGDyK)]2
Hypoxia	Acidic pH in cells	[18F]FMISO

Imaging radiopharmaceuticals may also be classified based on their clinical utility and the nature of application for which they are designed as tools in the drug development program [9]. Four classes of RMIPs have been identified:

1. A *radiolabeled drug substance* in which the cold stable atom is replaced by a radioisotope of the same element, which can be used for assessing the pharmacokinetics and biodistribution of the parent drug.
2. A *radioligand* with good binding affinity for a biologic target, which can be used to evaluate the effect of other unlabeled compounds at that target.
3. A *pathway marker* interacting with one component of a set of related biologic molecules,

which may be used to probe the overall status of that system.

4. A *biomarker*, or surrogate marker, which provides a more general readout at the level of cell or organ for a specific biological process.

9.2.3   Choice of Radionuclide for SPECT and PET

A number of radionuclides that emit either γ photons or β+ are available (Table 9.4) for developing radiopharmaceuticals for imaging studies. These radionuclides, basically, belong to three groups of chemical elements: elements of organic radionuclides (C, N, and O), halogens (F and I), and metals (Cu, Ga, Y, Sc, In, Zr, and Tc). Certain

Table 9.4 Radionuclides useful for developing radiopharmaceuticals for PET and SPECT

Elements	For PET			For SPECT		
	Radionuclide	$T_{1/2}$	β^+ (MeV)	Radionuclide	$T_{1/2}$	γ (MeV)
Organic elements	^{11}C	20.4 min	0.959			
	^{13}N	9.96 min	1.197			
	^{15}O	2.03 min	1.738			
Halogens	^{18}F	109.8 min	0.635			
	^{75}Br	98 min	1.74			
	^{76}Br	16.1 hours	3.98			
	^{124}I	4.2 days	2.13	^{123}I	13.2 h	0.159
				^{131}I	8.04 d	0.364
Metals	^{66}Ga	9.45 hours	4.153	^{67}Ga	78.2 h	0.093, 0.184, 0.296
	^{68}Ga	68.3 min	1.898			
				^{111}In	67.2 h	0.173, 0.247
	^{44}Sc	3.92 hours	1.470			
	^{61}Cu	3.32 hours	1.220	^{67}Cu	2.6 d	0.185, 0.92
	^{62}Cu	9.76 min	2.910			
	^{64}Cu	12.8 hours	0.656			
	^{86}Y	14.74 hours	3.150			
	^{89}Zr	78.4 hours	0.900			
	^{94m}Tc	52 min	2.440	^{99m}Tc	6.0 h	0.140
	^{52}Mn	5.6 days				

elements (I, Cu, Ga, and Tc) are useful for the development of radiotracers for both PET and SPECT using a radioisotope of the same chemical element.

The organic radionuclides that decay by positron emission are ^{11}C, ^{13}N, and ^{15}O. These three radionuclides are isotopes of natural elements that are part of the majority of biochemicals and drugs. Interestingly, for these three elements there are no corresponding radioisotopes that decay by γ emission. Radiopharmaceuticals developed with the organic positron emitters are true molecular imaging radiotracers since these probes, biochemically, are indistinguishable from their natural counterparts. For example, [^{11}C]thymidine, [^{11}C]choline, [^{13}N]NH$_3$, or [^{15}O] water is chemically and biochemically the same as the corresponding unlabeled molecule.

The group of elements known as halogens (F, Cl, Br, and I) are very unique in nature. While chloride and iodide ions are quite common in the human body, fluorine, and bromine atoms, generally, are not part of the natural molecules. Among all the halogens, however, the fluorine atom is the only one that closely mimics the hydrogen atom

in size (Table 9.5) [10]. The van der Wall's radii of fluorine and hydrogen are very similar, 1.35 and 1.2 Å, respectively. As a result, one can expect that, in any given organic molecule, the C-F bond closely mimics the biological behavior of the C-H bond. In addition, the fluorine atom is also the most electronegative of all halogens. As a result, the fluorine atom introduces a polarity more akin to a hydroxyl substituent in a molecule. The other halogens are bigger in size and are less electronegative compared to fluorine. Consequently, labeling a biochemical with bromine or iodine radioisotopes would alter the biological behavior of the molecule. However, halogen atoms in drug molecules are quite common and, sometimes, the halogen-containing drug molecules may have even greater affinity for a receptor or an enzyme, in vivo, than the nonhalogenated molecules [10]. In the last two decades, several radiopharmaceuticals were developed based on ^{123}I for SPECT imaging studies. Compared to the positron emitter, ^{124}I, the theoretical specific activity (Table 9.6) of ^{123}I is even higher (because of shorter half-life). Organic molecules containing aromatic rings can be eas-

Table 9.5 Comparison of physico-chemical parameters of halogens with hydrogen and hydroxyl group

	Hydrogen	Fluorine	Oxygen (OH)	Iodine
Electronegativity	2.2	3.98	3.44	2.66
[a]Bond length, Å	1.09	1.39	1.43	2.14
Van Der Wal's radius, Å	1.20	1.35	1.40	2.15
Bond energy, KCal/mol^{-1}	99	116	85	51

[a]Bond length for $-CH_2X$ reported here where X = H, F, or OH. Table modified from Park et al. [10]

Table 9.6 Specific activity (SA) of radionuclides

	Maximum SA		Practical SA
Nuclide	mCi/μg	Ci/μmole	Ci/μmole
[11]C	838,000	9220	<100
[18]F	95,000	1170	10–20 as F$^-$ < 0.03 as F$_2$
[68]Ga	40,600	2766	
[67]Ga	597	47	<3.35
[111]In	423	40	<5.55
[123]I	1926	237	
[124]I	250	31	

ily labeled with radionuclides. Therefore, ^{123}I and [124]I play a major role in the development of radiotracers for molecular imaging studies.

Among the metals (Table 9.4), Ga, In, and Y are trivalent and have similar chemistries. The transition metals such as copper, scandium, and zirconium have complex coordination chemistries. The radionuclides of all these metals can be used to label peptides and proteins using bifunctional chelating agents. [111]In, ^{64}Cu, and ^{68}Ga-labeled octreotide analogs (^{111}In-DTPA-octreotide, ^{64}Cu-dotatate, and ^{68}Ga-dotatate) have already been approved by FDA as molecular imaging probes for SPECT and PET imaging studies to detect SSTR-2 positive NETs. Among the transition metals, radioisotopes of copper have useful physical characteristics to develop RMIPs. Several other positron-emitting metals, such as [44]Sc, [89]Zr, and [94m]Tc (Table 9.4), may also be useful for developing imaging agents.

9.2.4 General Criteria for the Design of RP-MI

For any radiopharmaceutical to be successful as an imaging agent for PET or SPECT, the radio-pharmaceutical must have the following ideal characteristics:

- Rapid plasma clearance to reduce blood pool background in the target tissue
- Rapid washout or clearance from nonspecific areas
- Low nonspecific binding
- Preferably must be stable in vivo, and no metabolism
- High membrane permeability and intracellular trapping
- Target specificity and high affinity for molecular targets
- Specific activity must be high to prevent saturation of specific binding sites
- Tissue distribution, localization, and target binding should be favorable for developing simple kinetic modeling to estimate quantitative data
- Radiation dosimetry must be favorable for multiple diagnostic imaging studies (if necessary)
- Synthesis of radiopharmaceutical under GMP conditions must be rapid and suitable for automation using automated synthesis modules

Developing a specific molecular imaging radiotracer involves careful design of the structural requirements in a molecule in order to optimize target specificity and at the same time optimize the pharmacokinetic and pharmacodynamic behavior of the probe to meet the demand of the imaging technique. The physicochemical properties of the radiopharmaceutical, such as size, charge, solubility, lipophilicity, and SA are very important criteria, and must be addressed in designing the structural features of the molecule. Factors, such as rapid metabolism and plasma

protein binding (PPB), and nonspecific binding in nontarget tissues are not desirable for optimal in vivo behavior. It is important to identify the most appropriate structural analog that meets most of the criteria for an ideal imaging agent. Some of these criteria will be discussed in greater detail with specific examples, later, in order to emphasize the importance of a careful design of structural features in order to develop a clinically useful MIP.

9.2.4.1 The Size of MIP

The molecular size or molecular mass of the MIP is one of the major properties of a molecule that determines the rate of clearance from circulation. Small organic molecules, natural or synthetic, clear from circulation rapidly and provide much higher target/background ratios. With small

organic molecules, however, it may not be possible to put more than one radiolabel per molecule. Also, with small molecules, it may be difficult to optimize high SA and high target affinity, and to achieve appropriate pharmacokinetic and metabolic behavior. Therefore, with large proteins, such as antibody molecules (150,000 Da), it may be possible to label with more than one radiolabel per molecule. Liposomes and nanoparticles, because of their size, shape, structural flexibility, multivalency/multifunctionality characteristics, may offer greater potential for developing high specific activity imaging agents. Among the radiopharmaceuticals approved for routine clinical studies (Table 9.1), all of them are small molecules (<1500 Da) as shown in Fig. 9.3.

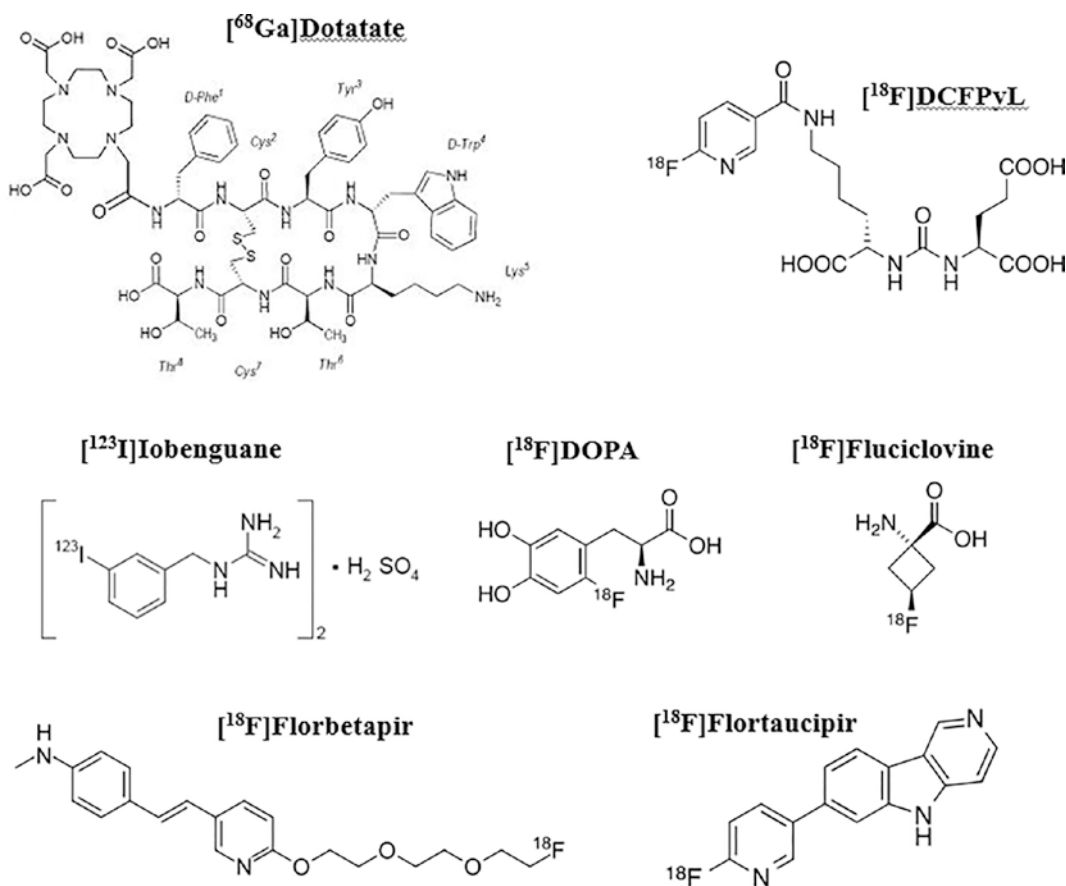Since small molecules clear from circulation rapidly, radiolabeling with radionuclides with

Fig. 9.3 Examples of small molecule radiopharmaceuticals for PET. Among the agents shown in the table, ^{68}Ga-Dotatate is relatively large (1500 Da) compared to Fluciclovine (132 Da)

short-half life (such as ^{18}F, ^{68}Ga, and [44]Sc) also facilitates developing radiopharmaceuticals that deliver less radiation dose to the critical organs. Therefore, radioimmunoimaging based on monoclonal antibodies labeled with longer-lived nuclides (such as [124]I and [89]Zr) are becoming relatively less popular for routine diagnostic imaging studies. However, radioimmunoimaging with mAbs is very important in the research and development of radioimmunoconjugates for RIT.

9.2.4.2 The Position of Radiolabel in the Radiotracer

The position of the radiolabel in the molecular imaging probe must be carefully selected so that the presence of a radionuclide at that position preserves the overall chemical and pharmacological properties of the parent unlabeled molecule. In addition, the position of the radiolabel must also preserve the metabolic stability of the radiopharmaceutical during the time course of the imaging study. The importance of the position of the radiolabel in the imaging probe is illustrated using FDG and FLT molecules.

Design of FDG Molecule

2-[18F]Fluoro-2-deoxy-d-glucose (FDG) is regarded as the most important, clinically useful, and successful radiopharmaceutical in nuclear medicine. The design of FDG [11, 12] is a perfect example to illustrate the significance of the position of the ^{18}F atom in the FDG molecule (Fig. 9.2).

In the 1940s, 6-deoxy-6-[19F]fluoro-6-deoxy-D-glucose ([6-19F]FDG) was first reported [12]. In 1954, it was suggested that the hydroxyl group on carbon 2 was not essential for (1) the carrier-mtediated membrane transport into the cell, and (2) the substrate specificity of D-glucose for *hexokinase*-mediated phosphorylation reaction [13]. It also became apparent that the hydroxyl group on C-2 was essential for further metabolism of the glucose-6-phosphate. Subsequently, 2-fluoro-[19F]2-deoxy glucose ([2-19F] FDG) was developed as an anticancer agent [12]. However, due to the very high toxicity of FDG, further clinical studies with FDG were abandoned. Later, 2-[14C]-2-deoxy glucose (CDG) was developed

as a tracer to measure cerebral glucose metabolism in animals based on autoradiography [14].

On the basis of Sokoloff's work, [11C]CDG would be an appropriate tracer for PET imaging studies [15]. However, the attachment of the ^{18}F atom to the carbon 2 atom in the D-glucose molecule is justified since FDG is a good substrate for *hexokinase*. The kinetic constant (K_m) of the reaction with hexokinase for FDG (0.19 ± 0.03) is very similar to that of D-glucose (0.17). Attaching the ^{18}F atom to carbon 3 or 4 alters the substrate specificity significantly ($K_m > 70$) [3]. Also, the ^{18}F atom in the C-2 position prevents further metabolism of the molecule. As a result, FDG-6-phosphate accumulates in the cell.

Another interesting difference between FDG and CDG concerns the renal excretion of the molecule. The hydroxyl group on C-2 is essential for the active transport across the renal tubules for reabsorption of D-glucose. In contrast to CDG, FDG is not reabsorbed, but excreted. As a result, the body background of the ^{18}F activity is less and the radiation dosimetry with FDG is much more favorable.

Design of FLT Molecule

The DNA synthesis is a measure of cell proliferation. The four nucleotides required for DNA synthesis are cytosine, guanine, adenine, and thymidine. Thymidine is the only one incorporated exclusively into the DNA and not into the RNA [16]. Intracellularly, thymidine is first phosphorylated in the cytoplasm by the enzyme *thymidine kinase-1* (*TK-1*) to thymidine monophosphate (TMP), prior to incorporation into the DNA. [3H] Thymidine was introduced to measure thymidine incorporation into DNA (thymidine labeling index) in tumor tissue [17, 18]. The nonradioactive 3-[19F]fluoro-3-deoxythymidine (FLT) (Fig. 9.4) was first developed in 1969 as an anticancer agent [19]. Subsequently, [11C]thymidine was introduced as a PET tracer [20]. Almost two decades later, 3-[18F]fluoro-3-deoxythymidine (FLT), the metabolically stable thymidine analog, was introduced for PET imaging studies [21].

FLT is transported into the cell similar to thymidine and then phosphorylated to [18F]FLT-5′-monophosphate by the enzyme, *TK-1*. FLT-MP is
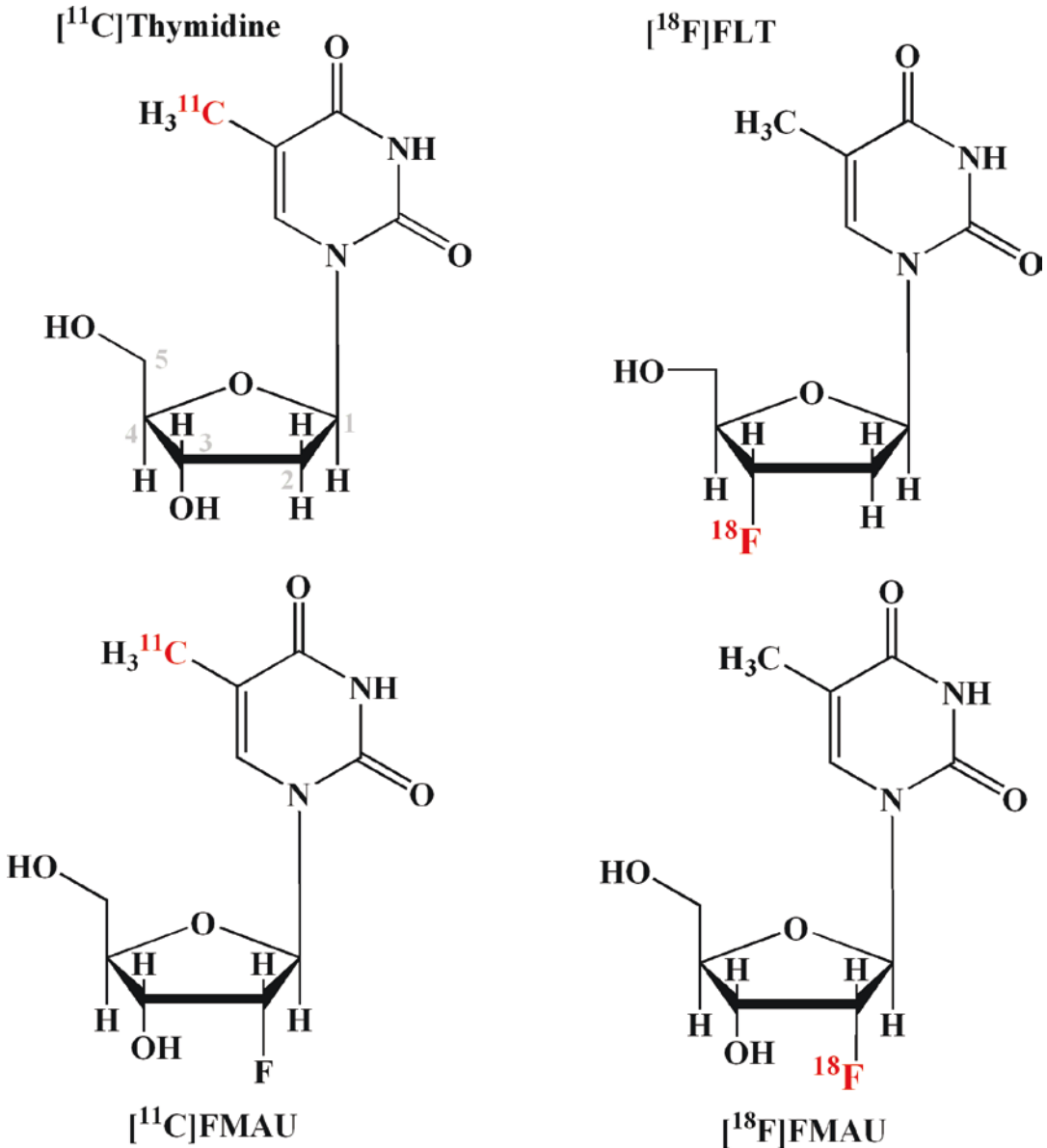
Fig. 9.4 Radiolabeled analogs of thymidine for imaging DNA synthesis: The hydroxyl group on C-3 in the sugar is essential for incorporation into DNA synthesis

further phosphorylated to FLT-TP by the enzyme *thymidylate kinase* [22]. FLT phosphates, however, are (1) impermeable to the cell membrane, (2) resistant to degradation, and (3) metabolically trapped inside the cells. The incorporation of FLT into the DNA, however, is relatively insignificant (<1%).

The pyrimidine analogs, 2′-fluoro-5-[11C] methyl-1-β-ᴅ-arabinofuranosyluracil (FMAU) and 2′-[18F]fluoro-5-methyl-1-β-ᴅ-arabinofuranosyluracil (FMAU) have been shown to be useful for imaging tumor cell proliferation [23, 24]. FMAU can be taken up by cells and phosphorylated by TK-1 and TK-2 and sub-

sequently incorporated into DNA, by *DNA polymerase*. FMAU employs the same DNA synthetic pathway as thymidine and, therefore, has the potential to image DNA synthesis. It is important to recognize that FMAU is incorporated into DNA synthesis, but not into FLT [22, 25]. This observation suggests that the hydroxyl group on the C-3 atom (Fig. 9.4) is essential for the incorporation of thymidine analogs into DNA, but not for substrate specificity of the enzyme TK-1. Despite the fact that FLT lacks the hydroxyl group on C-3, necessary for its incorporation into DNA, it appears to outperform both FMAU and FIAU in terms of uptake and retention based on in vitro studies [26].

Design of MIBG

In the 1980s, Dr. Wieland and his colleagues at the University of Michigan developed an analog of norepinephrine (NE), known as [131]I-*meta*-iodobenzylguanidine (MIBG), a diagnostic tracer to allow imaging of the adrenal medulla [27, 28]. MIBG was developed by linking the benzyl portion of bretylium with the guanidine group of guanethidine (Fig. 9.5). Among the three isomers of iodobenzylguanidines, the meta isomer (MIBG) has less in vivo deiodination and liver uptake than the other two isomers. In 1994, [^{131}I]MIBG, also known as iobenguane sulfate I-131 intravenous (*low SA (LSA) formulation*), received FDA approval as an imaging agent for the localization of specific sites of pheochromocytomas and neuroblastomas. In 2008, [^{123}I] MIBG or iobenguane I-123 injection was also approved by FDA as a tumor imaging agent (AdreviewTM; GE Healthcare). To develop derivatives of MIBG for PET studies, iodine atom was replaced with fluorine directly to obtain ^{18}F-meta-fuorobenzylguanidine, ([^{18}F]MFBG ([^{18}F]PFBG) [29].

9.2.4.3 Stereospecificity

As discussed in Chap. 6, *stereoisomers* have the same bonds, but exhibit different spatial arrangements of their atoms. One type, known as optical isomerism, is exhibited by molecules with asymmetric carbon atoms (chiral centers) that have non-superimposable mirror images. The optical isomers, called *enantiomers,* rotate plane-polarized
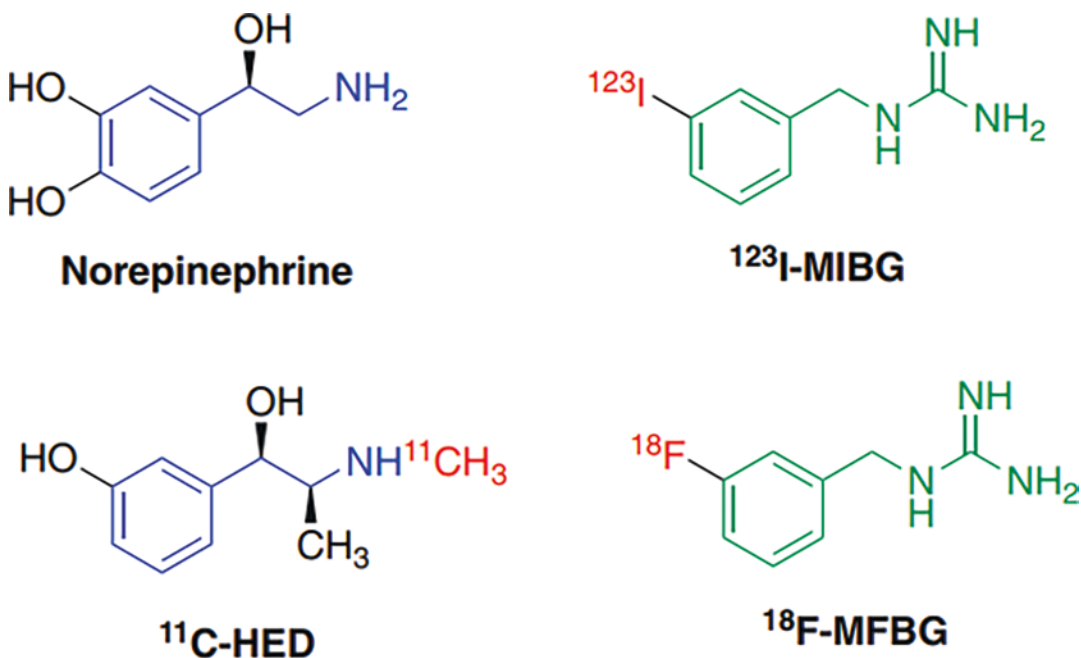
Fig. 9.5 Norepinephrine analogs specific for norepinephrine transporter. It is the meta position of iodine or fluorine atom in the aromatic ring that has better tumor uptake and retention

light in opposite *directions: dextrorotatory* (D or (+)) and *levorotatory* (L or (−)). These designations only refer to the experimental values of rotation, while the letters D and L relate asymmetric centers to glyceraldehydes (as in sugars), for which an absolute stereochemistry has been defined. On the basis of this designation, in the case of amino acids, L-amino acids are often dextrorotatory. Only L-amino acids are found in nature.

A molecule is said to be *chiral* if it exists as an *enantiomer*. Molecular targets such as receptors and enzymes often exhibit stereoselectivity or binding selectivity for one enantiomer over the other. The stereochemical requirements of biological activity have consequence for the radiolabeled amino acids and sugars [11]. For example, only the radiolabeled L-amino acid and D-glucose analogs are biologically active. Further, it is important to recognize that radiolabeled drug molecules also exhibit stereoselective binding to neuroreceptors. For example, only the [^{11}C]-(+) McN-5652 binds to the serotonin transporter [30] and [^{11}C]dexetimide binds to the muscarinic cholinergic receptor [31].

Development of [^{18}F]-rhPSMA-7.3

The importance of stereospecificity on the in vivo behavior and target specificity of a radiotracer is best illustrated based on the design and development of PSMA agent. To develop an ideal theranostic small molecule PSMA inhibitor, [^{18}F]

rhPSMA-7 was developed as a radio hybrid (rh) PSMA inhibitor since the molecule can be labeled with ^{18}F as well as a radiometal (^{68}Ga, ^{177}Lu, or ^{225}Ac) [32, 33]. Subsequently, based on preclinical evaluation [^{18}F]rhPSMA-7.3 was selected as the lead compound since it is a single diastereoisomer form of ^{18}F-rhPSMA-7, which has been shown to have good diagnostic efficacy in patients with primary and recurrent prostate cancer [33].

[^{18}F,^{nat}Ga]rhPSMA-7 represents a mixture of four stereoisomers (Fig. 9.6), differing in the stereoconfiguration of the diaminopropionic acid branching unit (*D*-Dap or *L*-Dap) and the glutamic acid pendant arm at the DOTAGA-chelator (*R*-DOTA-GA or *S*-DOTA-GA). Four rhPSMA-7 isomers are as follows:

[^{18}F,^{nat}Ga]rhPSMA-7.1 (D-Dap–R-DOTA-GA)
[^{18}F,^{nat}Ga]rhPSMA-7.2 (L-Dap–R-DOTA-GA)
[^{18}F,^{nat}Ga]rhPSMA-7.3 (D-Dap–S-DOTA-GA)
[^{18}F,^{nat}Ga]rhPSMA-7.4 (L-Dap–S-DOTA-GA)

Based on HPLC analysis, the investigators discovered that [^{18}F,^{nat}Ga]rhPSMA-7.3 was the predominant species. Biodistribution studies in tumor bearing mice indicated that [^{18}F,^{nat}Ga] rhPSMA-7.3 has high tumor accumulation and low uptake in blood, liver, and kidneys. Therefore, it was selected as the preferred isomer and transferred into clinical studies [34].
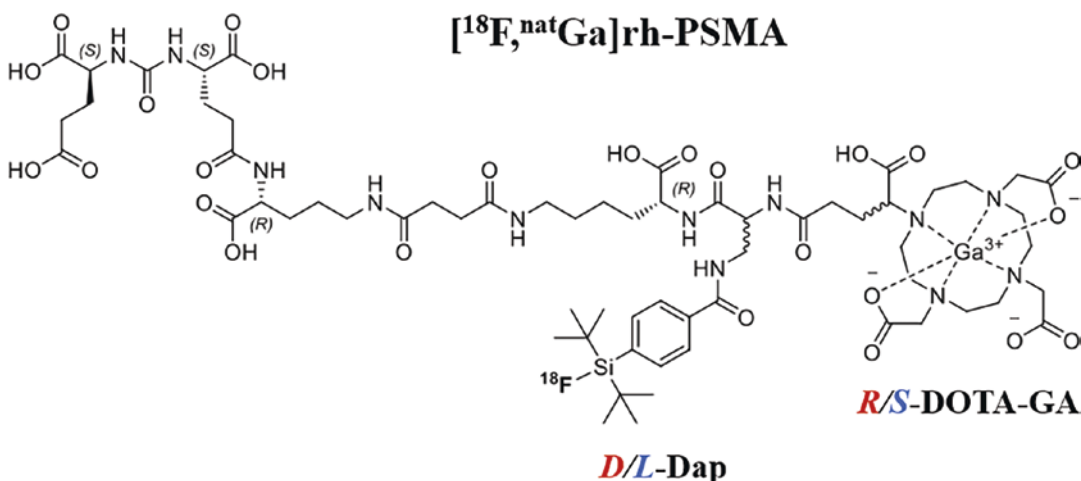
Fig. 9.6 [^{18}F,^{nat}Ga]rhPSMA-7 small molecule PSMA inhibitor: It is a mixture of four stereoisomers

9.2.4.4 Lipophilicity

Lipophilicity is the affinity of a molecule or moiety for a lipophilic environment. Molecular size, mass (weight), and hydrogen-bonding capacity also contribute to the overall lipophilicity of the molecule [35]. Lipophilicity is a fundamental physicochemical property of a compound and plays a pivotal role in the absorption, distribution, metabolism, and elimination of drug molecules. The most common experimental lipophilicity measurement involves partitioning of a compound between an octanol and a buffer, where the log of the ratios of the compound concentration in the octanol layer is divided by that in the buffer layer, often called the Log P. Lipophilicity is also expressed in several different ways, including terms such as Log P, clog P, delta Log P, and Log D, depending on the method of estimation [36].

Very polar compounds, normally, exhibit high water solubility, fast clearance through the kidneys, and often contain ionizable functional groups that limit blood-brain barrier (BBB) penetration. In general, only the neutral, lipophilic molecules can pass through the BBB and enter into the brain tissue. The brain penetration, and specific to nonspecific binding ratios, exhibited in vivo by radiotracers, involves a complex interplay between many critical factors, including lipophilicity, receptor affinity, metabolism, molecular size, and shape, etc. Based on an extensive literature search, Waterhouse recently noted that for most neutral radiotracers, the relationship between lipophilicity and molecular weight shows the expected parabolic relationship [36] (Fig. 9.7). The general criteria for adequate brain penetration and optimum target to nontarget ratios of high SA radiotracers are as follows:

Fig. 9.7 Lipophilicity (log P) vs. brain uptake for simple low- mass radiolabeled compounds, such as [^{11}C]ethanol and [^{11}C] butanol. The results indicate that the brain uptake of these radiotracers does indeed correlate with lipophilicity and that the relationship is parabolic in nature. Also, the uptake is dependent on the blood flow [36]
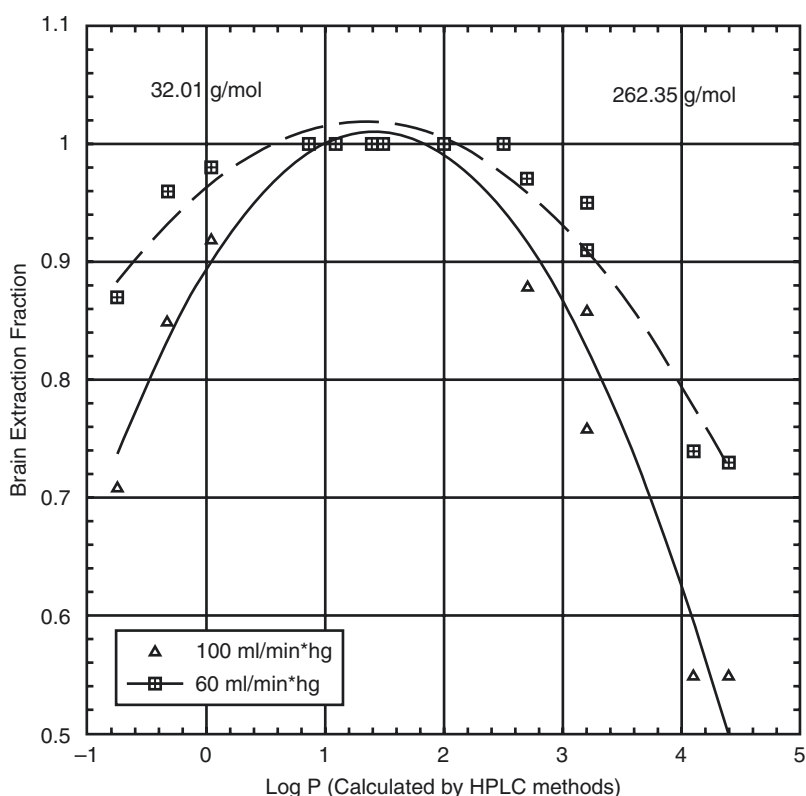
- Log P or Log D < 3.5
- Molecular weight <450 g mol^{-1}
- An absence of functional groups that will strongly ionize at physiological pH
- No appreciable affinity for efflux pumps (such as PGP)
- No appreciable affinity for specific binding sites for high-capacity peripheral sites, including albumin or other plasma proteins
- Not a substrate for enzymes at the BBB

9.2.4.5 Plasma Protein Binding

It is well documented that both, specific and non-specific binding (NSB) of drugs can occur with plasma proteins, cell membranes, and other components present in the blood [37]. NSB may be saturable when drugs are administered at high-enough mass and bioavailability may not be an issue. The NSB of radiotracers, however, may significantly reduce the bioavailability [37]. NSB to albumin and other plasma proteins is known to correlate positively and linearly with increasing lipophilicity [38]. Some radiotracers exhibit high NSB (>90%) and may enter the brain nearly as well as those that exhibit much lower plasma protein binding [35]. In addition, increasing lipophilicity has been correlated with increased lung deposition, liver and spleen uptake, and higher affinity to many metabolic enzymes such as cytochrome P450. Such processes serve to decrease the percentage of the administered dose that may enter the brain and other target organs, and tissues.

9.2.4.6 Metabolism

In the design of a radiotracer for molecular imaging, it is especially important that the label (radionuclide) is ideally in a metabolically stable position. When a radiotracer is injected into a human subject, the signal from the radionuclide is detected, regardless of whether it is coming from the intact radiotracer or from a radiolabeled metabolic fragment. The fate of the radionuclide, as a result of metabolism, must be considered in selecting the position of the label in a molecule. Peripheral metabolism, especially in the blood, may dramatically decrease the delivery of the probe to the target site. Also, metabolism of the

radiopharmaceutical at or near the target site may decrease the specific binding to the molecular target. In addition, the quantitative estimation of molecular target concentration based on kinetic modeling may get complicated if the metabolic products are also trapped at the target site. Whatever the case may be, it is essential that all the metabolic products and their relative concentrations are known so that a meaningful interpretation of the imaging data can be made. Several examples will be discussed to emphasize the importance of metabolism in molecular imaging studies.

[^{18}F]FDOPA Metabolism

In the presynaptic dopaminergic neuron, the amino acid tyrosine is converted to dihydroxy-phenylalanine (L-DOPA). Subsequently, *DOPA decarboxylase* or *aromatic amino acid decarboxylase* (*AAAD*) converts L-DOPA to dopamine. The position of the ^{11}C or ^{18}F label in the L-DOPA molecule clearly illustrates the importance of metabolism and its role in drug design (Fig. 9.8). A ^{11}C label can be introduced in the carboxyl group (COOH) as in the case of [^{11}C-carboxyl]L-DOPA. Since AAAD eliminates the carboxyl group, the ^{11}C label is quickly lost. However, if the β-carbon atom is labeled with ^{11}C, as in the case of [β-^{11}C]l-DOPA, the ^{11}C activity is still retained with the dopamine molecule [39].

[^{18}F]6-Fluoro-l-DOPA (FDOPA) was also developed as a tracer to examine the transport of dopamine precursor from plasma and its decarboxylation by AAAD to fluorodopamine [40]. FDOPA, however, undergoes extensive metabolism in vivo [41] as shown in Fig. 9.9. FDOPA is decarboxylated by *aromatic L-amino acid decarboxylase* (AAAD) to produce [^{18}F] Fluorodopamine (FDA). FDOPA can be *O*-methylated by catechol-*O*- methyltransferase (COMT) to 3-*O*-methyl-6-[^{18}F] fluoro-L-dopa (3-OMFDOPA), which is uniformly distributed throughout the brain. Fluorodopamine (FDA) can be oxidized by *monoamine oxidase (MAO)* to L-3,4-dihydroxy-6-[^{18}F]fluorophenyl-acetic acid ([^{18}F]FDOPAC), which is subsequently *O*-methylated by COMT to 6-[^{18}F] fluorohomovanillic acid ([^{18}F]FHVA). AAAD and *COMT* are also present in peripheral tissues, such as liver, kid-

L-DOPA

6-[18F]Fluoro-L-DOPA (FDOPA)

[11C-carboxyl]L-DOPA

[β-11C]L-DOPA
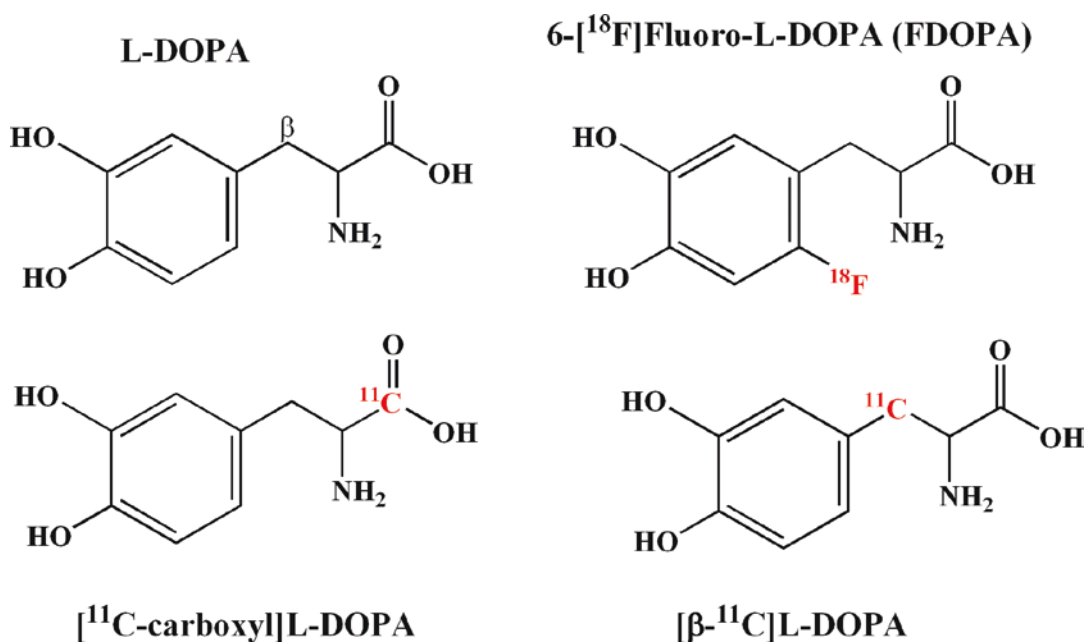
Fig. 9.8 Radiolabeled analogs of L-DOPA: The position of 11C or 18F label is very important to prevent metabolic degradation and elimination in vivo

6-[18F]Fluoro-L-DOPA (FDOPA)

6-[18F]Fluorodopamine (FDA)

AAAD

COMT

MAO

[18F]3-OMFDOPA

COMT

6-[18F]FDOPAC

6-[18F]FHVA
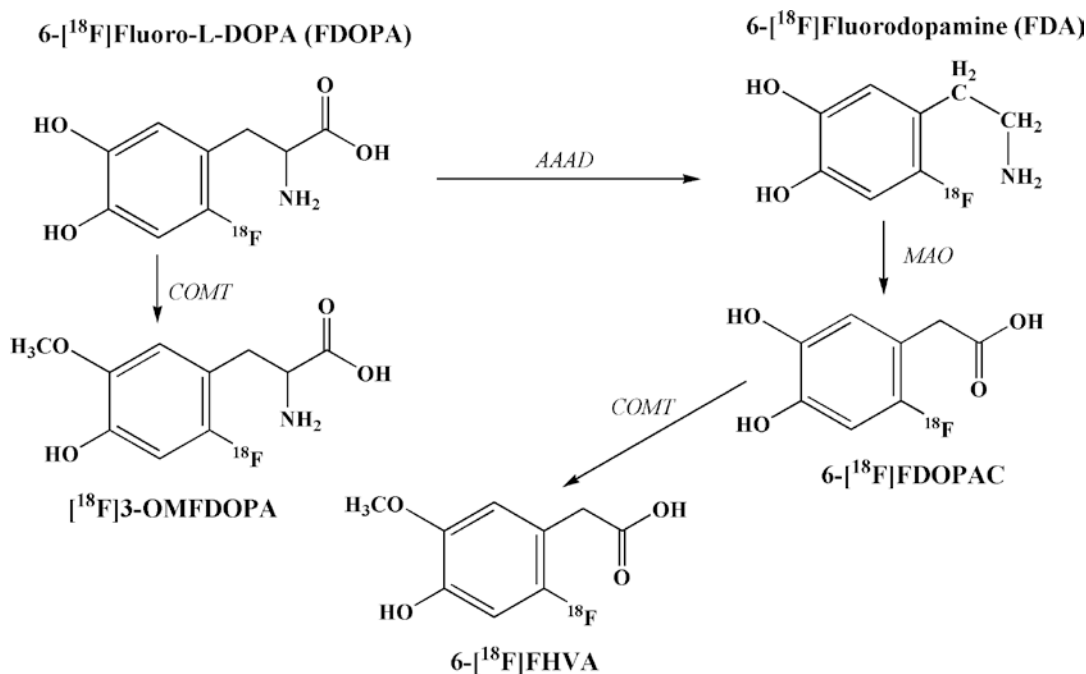
Fig. 9.9 In vivo metabolism of FDOPA

neys, and lung. Both, the decarboxylation of the compound and the release of radiometabolites into the blood, however, can be reduced with carbidopa, a decarboxylase inhibitor.

While FDOPA has already demonstrated its value as a diagnostic probe in Parkinson's disease and in neuroendocrine tumors, the metabolic profile of this probe, however, complicates the estimation of quantitative parameters by kinetic modeling.

Thymidine Metabolism

[11C]Thymidine was developed as a PET tracer to image tumors and measure proliferation rate. Analysis of thymidine PET images, however, is complicated by the fact that the tracer is rapidly metabolized (Fig. 9.10). As a result, much of the 11C activity imaged in thymidine studies is in the form of labeled metabolites, which are no longer available to be incorporated into the DNA.

The large pools of *thymidine phosphorylase* (*TP*) present in the blood, liver and spleen rapidly degrade thymidine in vivo. Thymidine can be degraded by *TP* to thymine and then be reduced to dihydrothymine (DHT), β-ureidoisobutyric acid (BUIB), and β-amino isobutyric acid (BAIB). For thymidine, labeled at the C-2 position, degradation products beyond BUIB do not contain the label, which leaves the pathway as [11C]CO_2. Degradation takes place rapidly in the liver and blood, and labeled metabolites appear in significant quantities in the blood within minutes after injection [42].

Thymidine can be labeled with 11C in the methyl (11CH_3) or in the C-2 (11CO) position of
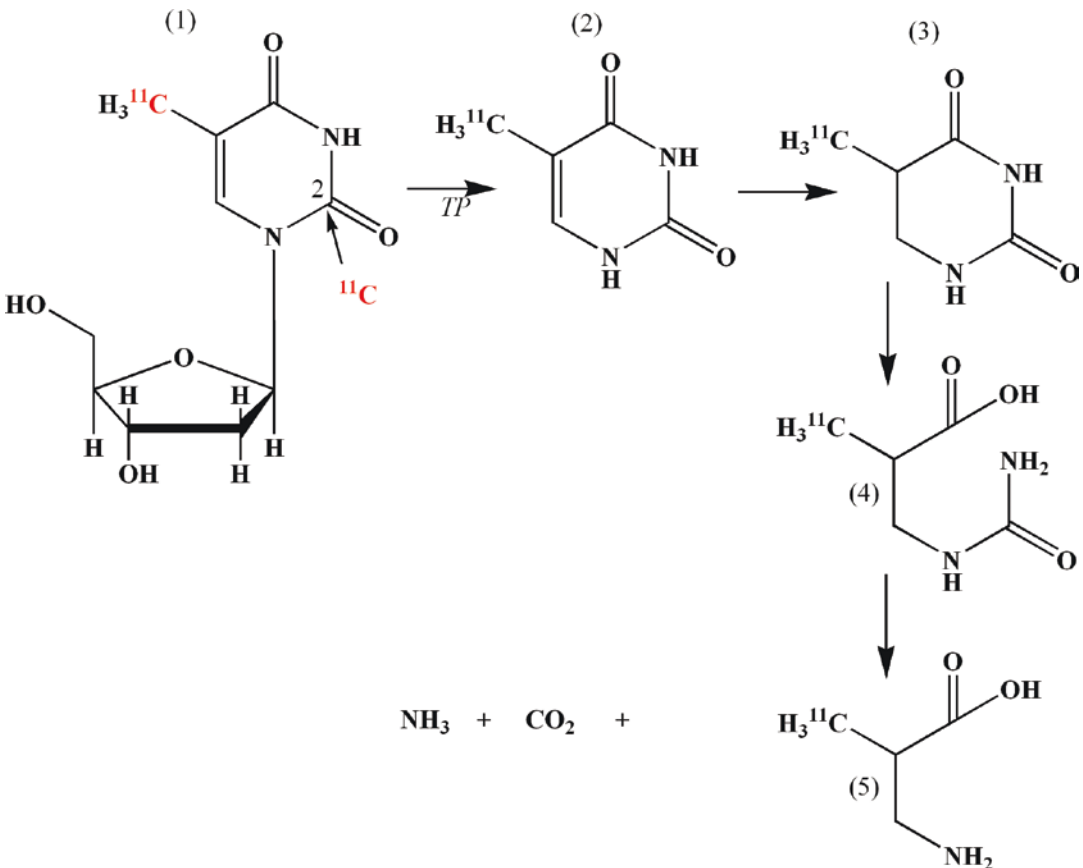
Fig. 9.10 In vivo metabolism of [11C]thymidine: Labeling C-2 in the carbonyl group will result in the elimination of 11C activity as CO_2. Labeling the methyl group with 11C provides relatively more stable tracer for imaging DNA synthesis

the pyrimidine ring. The former gives rise to acidic metabolites, which can accumulate in cells in a number of pathways and limit the ability to develop a comprehensive, validated kinetic model to measure the DNA synthesis using methyl-labeled thymidine. On other hand, the C-2 label is lost as $[^{11}C]CO_2$, which rapidly enters the large bicarbonate pool in the body.

To overcome the practical limitations of $[^{11}C]$ thymidine imaging, metabolically stable ^{18}F-labeled thymidine analogs, FLT and FMAU (Fig. 9.4) have been developed [21, 43]. FLT does not generate significant metabolites during the imaging procedure as does $[^{11}C]$thymidine. FLT is not a substrate for *TP*, the enzyme that breaks the bond between the pyrimidine and deoxyribose. However, FLT is glucuronidated in the liver and then delivered to the blood. FLT-glucuronide is restricted to the vascular space and is cleared by the kidneys.

Metabolism of WAY-100,635

WAY-100,635 is a $5HT_{1A}$ receptor antagonist (Fig. 9.11). Initially, the ^{11}C label was introduced in the methoxy group (OCH_3). Subsequently, ^{11}C was introduced in the carbonyl (CO) position to reduce the contribution of labeled metabolites [44]. The molecule was finally modified resulting in a ^{18}F-labeled analog with improved metabolic stability and greater potential for commercial distribution.

A key step in the development of a new molecular imaging agent is to characterize its binding specificity in vivo by imaging studies. It is important to compare the biodistribution and pharmacokinetics of radiotracer with and without a pharmacological dose of the radiolabeled compound to assess the specificity and saturation ability. In order to address the significance of the metabolism on a specific binding at the target site, radiotracer should be labeled at different positions in the molecule and then the in vivo distribution and kinetics of these analogs should be compared.

9.2.4.7 Specific Activity

As previously discussed, SA ($Ci/\mu mole^{-1}$) of the RMIP is very important for molecular imaging studies based on PET and SPECT since it is a measure of the number of probe molecules that can give a radioactive signal in a given mass of RMIP. The SA needed for a given radiotracer depends on the concentration of the target molecules (receptors, enzymes of antigens) present in a given cell or tissue (Table 9.7). Typically, the concentration of high-affinity molecular targets is between $10^{-12}–10^{-9}$ moles L^{-1}. For neuroreceptor and gene imaging studies very high SA ($2–10$ Ci $\mu mole^{-1}$) is absolutely necessary. For enzyme-mediated molecular imaging studies, $100–1000$ times lower SA may be adequate. For animal (rodent) studies, based on MicroPET and MicroSPECT, it is important to recognize that the SA requirements may be even higher than what is needed for clinical studies [45]. The relative size of the brain in different species (humans, rats, and mice) and dopamine receptor levels in striatum are compared in Table 9.7. With the typical dose of $[^{11}C]$raclopride (SA = 1.0 Ci μmol^{-1}) injected for imaging studies, the receptor occupancy in mice is almost 70% compared to relatively insignificant levels of occupancy in humans (Table 9.8). These results suggest that for MicroPET imaging studies, the SA of radiotracers must be at least ten times more than what is needed for human studies.

9.2.4.8 Radiopharmaceutical: Mechanism of Localization

Radiotracers can be generally classified based on their ability to image a specific biochemical process or based on their unique mechanism of localization in a specific organ/tissue of interest (Table 9.2). The localization of RMIP in a specific target organ or tissue of interest depends on three important phenomena:

- Rapid blood clearance and transport of radiotracer to the target organ or tissue of interest.
- Transport of radiotracer from capillaries into the extracellular fluid and subsequent transport into the cells through the cell membrane. Transport processes such as simple diffusion, facilitated diffusion, active transport, and receptor-mediated endocytosis (Chap. 7, Sect.
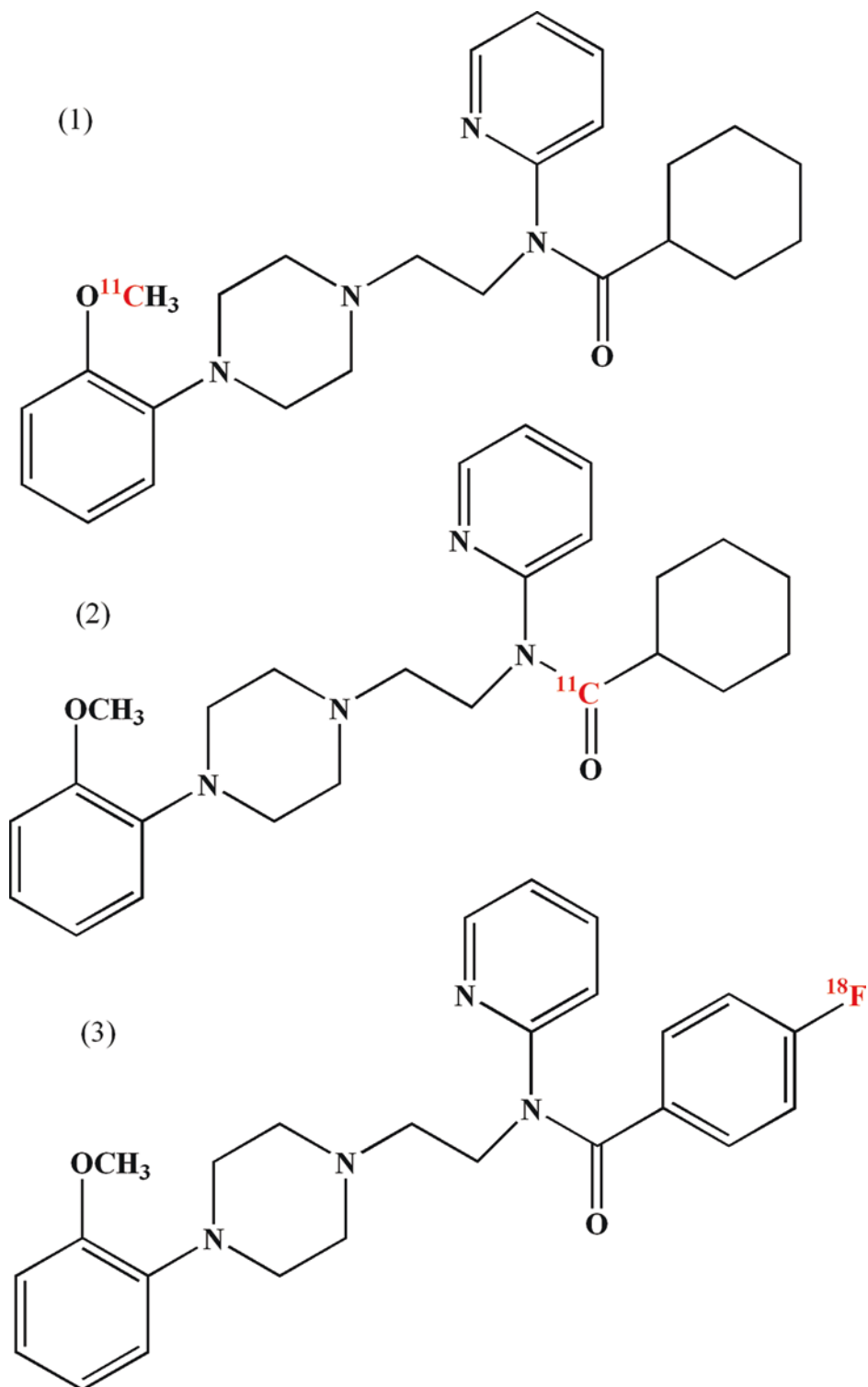
Fig. 9.11 Radiolabeled WAY-100,635, a 5HT$_{1A}$ receptor antagonist: ^{11}C in the carbonyl position (2) provides a more stable radiotracer when compared to ^{11}C labeling in the methoxy group (1). The ^{18}F-labeled analog provides even greater in vivo stability and is the preferred radiotracer (3)

7.7) play a very important role in the localization of the radiotracer at the target site.

- Localization at the target site and intracellular trapping may be due to any one of these following biochemical processes:

  - Specific binding to receptors on the cell membrane or within the cell
  - Internalization of radiotracer-receptor complex
  - Specific binding to the extracellular or intracellular antigens
  - Specific enzyme-mediated intracellular metabolism, followed by trapping of metabolites
  - Incorporation into the biochemical synthesis of intracellular proteins or DNA

9.2.5 General Methods of Radiolabeling

Depending on the type of radioisotope chosen and the method used to radiolabel, three different strategies can be employed to synthesize radiopharmaceuticals as shown below:

Table 9.7 Specific activity requirements for molecular imaging probes

Imaging study based on	SA (Ci μmole^{-1}) of radiotracer for	
	PET	SPECT
Enzyme-mediated cellular trapping	0.01–0.1	0.1–0.5
Antigen-antibody binding	0.1–1.0	1–5
Neuroreceptor binding	2–10	2–10
Gene expression	2–10	>10

1. *Isotope exchange*: Radiopharmaceutical can be prepared by direct exchange (isotopic substitution) of one or more stable atoms of an element in a molecule with one or more nuclides of a radioisotope of the same element. The radiolabeled molecule and the unlabeled molecule are chemically identical and behave in vivo in a similar manner. This method of radiolabeling is generally used to prepare radioiodinated radiopharmaceuticals in which the stable ^{127}I atom is replaced with a ^{123}I or ^{124}I atom (Chap. 10). Also, in the preparation of ^{11}C compounds, the stable ^{12}C atom is replaced with a ^{11}C radionuclide but, the preparation of ^{11}C compounds may involve multistep alkylation reactions (Chap. 11).

2. *Introduction of a foreign element*: Radiotracers can be prepared by the introduction of a foreign element or radionuclide in a parent MIP. Most of the radiopharmaceuticals are prepared based on this method. The radiolabeled compound and the unlabeled molecule are not chemically identical and may have different in vivo behavior. For example, preparation of [^{18}F]FDG (Fig. 9.1) involves the introduction of an ^{18}F atom in the deoxyglucose (DG) molecule. Also, in the preparation of radioiodinated peptides and hormones, ^{123}I or ^{124}I is added to the parent molecule that does not contain a natural stable iodine atom.

3. *Metal chelation*: This method also introduces a foreign element, (radiometal such as ^{99m}Tc, ^{64}Cu, ^{68}Ga, and ^{111}In) into an organic compound, known as bifunctional chelating agent (BFC). One or more atoms (such as O, N, and S) in the BFC donate a pair of electrons to the foreign metal atom to form coordinate cova-

Table 9.8 Brain dopamine D_2 receptor occupancy of [^{11}C]Raclopride in different species[a]

Species	Body wt. (g)	Brain wt. (g)	Stratum wt. (g)	D_2/D_3 receptor mol kg^{-1}	Dose(mCi)	[^{11}C]Raclopride (mCi μmol^{-1})	Occupancy(%)
Humans	70,000	1500	40	13.6	10–15	1000	<1.0
Rats	250	1.5	0.05	19.8	1.0	1000	19.0
Mice	25	0.4	0.03	20.0	1.0	1000	70.0

[a]The above table was modified from reference [45]

lent bonds (Chap. 11). As a result, the chemical and biological properties of the radiometalchelate complex are different than that of the chelating agent. Two important radiopharmaceuticals prepared based on metal chelation are ^{68}Ga-PSMA-11 and ^{68}Ga-PSMA-617 using either acyclic chelator DTPA-HBED-CC or cyclic chelator DOTA. The chemical structures of ^{68}Ga-PSMA-HBED-CC (also known as PSMA-11), and ^{68}Ga-PSMA-617 are shown in the Fig. 9.12. Both the labeled and unlabeled molecules have affinity to prostate specific membrane antigen (PSMA).

4. Certain peptides and macromolecules such as monoclonal antibodies can be labeled with radiometals based on the metal chelation method, as described above. This technique, however, requires conjugation of a bifunctional chelate (BFC) to the peptide or protein first and then subsequent chelation of the radiometal by the BFC molecule. The radiometal is not directly incorporated into the peptide or protein molecule.

9.2.5.1 Important Factors of Radiolabeling

In developing an appropriate radiolabeling technique, suitable for a specific RMIP, several important factors need to be considered in order to optimize the synthesis procedure.

Efficiency of Radiolabeling   During the synthesis of RMIP, the percent of radioactivity incorporated in the desired chemical form of RMIP compared to the total radioactivity in the reaction mixture is given by the labeling yield or labeling efficiency (LE), which may be expressed as a percent at the end of the synthesis (%LE @EOS) or at the end of bombardment (% LE @EOB), as in the case of cyclotron-produced PET radiopharmaceuticals. It is always desirable to have very

Fig. 9.12 Synthesis ^{68}Ga-PSMA-11 is based on acyclic chelator HBED-CC, while synthesis of ^{68}Ga-PSMA-617 is based on cyclic chelator DOTA
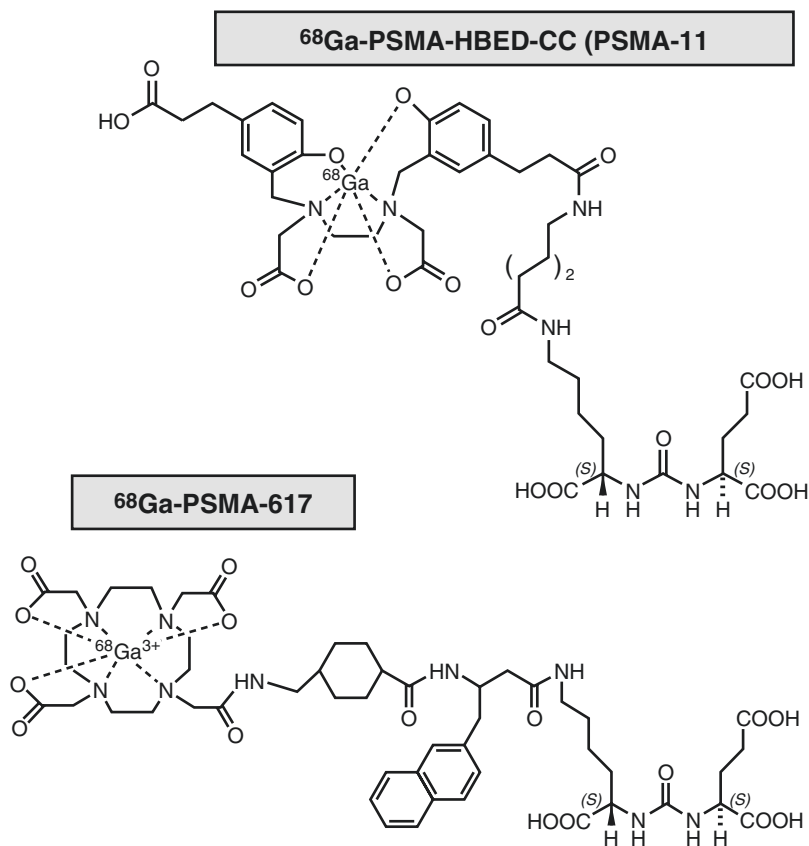
high labeling LE, but sometimes 2–5% LE is acceptable, provided the radiolabeled product is pure and acceptable for human studies.

Purification of the Final Product Most radiopharmaceutical preparations require a purification step to separate or isolate the desired RMIP from the unlabeled radiochemical contaminants and/or undesirable chemical species present in the reaction mixture. High-pressure liquid chromatography (HPLC) is one of the most common techniques used to obtain the purified RMIP. A number of solid-phase purification techniques, using mini cartridges based on alumina and ion exchange resins, are becoming increasingly popular. The *radiochemical purity* (RCP) of the final RMIP must be very high (>95%) for human studies, while the contamination of the final RMIP formulation with the undesirable radiochemical impurities must be very low (<5–10%). For every radiopharmaceutical, an acceptable quality control criterion, especially regarding the purity of the final radiolabeled drug product, must be carefully established.

Radiolysis Radiolabeled compounds may be degraded or decomposed by the high-energy radiations involving both γ photons and electrons (both β⁻ and β⁺). When radiations from a radionuclide in a radiotracer molecule break the chemical bonds, within the same molecule, then such a process is known as *autoradiolysis*. The high-energy radiation may generate free radicals in water, such as hydrogen peroxide and perhydroxyl free radicals, which in turn may damage the radiotracer molecules. Radiolysis is very much dependent on the concentration of the final radiolabeled drug product formulation (activity/mL); the higher the concentration, the greater the radiolysis effect. Peptides and protein molecules may be more susceptible for radiation damage than small organic molecules.

Stability of the Radiopharmaceutical The in vitro chemical stability of radiotracer is very important for optimal shelf life. In addition, the in vivo stability is critical for optimal targeting of the imaging probe. Radiopharmaceuticals prepared, based on metal chelation, may be unstable in vivo because of the presence of competing metallic ions and binding agents.

9.2.6 Automated Synthesis Modules

Computer-controlled automation of the synthesis of PET radiopharmaceuticals is desirable for routine commercial production and to reduce the radiation exposure to the personnel involved in the production of these PET drugs. A number of automated synthesis modules (ASM) for routine production of radiolabeled precursors (such as ¹¹CH₃I) or FDA-approved PET radiopharmaceuticals ready for clinical studies are commercially available (Fig. 9.13). The main purpose of the ASMs is to:

- Reduce exposure to high levels of harmful radiation
- Reduce the need for manual steps to accelerate the overall radiolabeling synthesis procedure
- Use the time of personnel efficiently and minimize operator errors due to the operator
- Obtain better reproducibility of RMIP synthesis from batch-to-batch
- Facilitate compliance with FDA regulations regarding GMP

ASMs are based on the principle of unit operations, in which a complex synthetic procedure is reduced to a series of simple operations (or reactions), such as evaporation, fluorination, chromatography, hydrolysis, purification, and sterilization. These operations are controlled by PCs with software programs that are user friendly and flexible enough to change various reactions conditions. For the development of ¹¹C PET radiopharmaceuticals, ASMs capable of generating [¹¹C]Methyl iodide or triflate are critical for the reliable synthesis of radiotracers.

Some of these ASMs, such as the TracerLab FX are based on the use of sterile disposable kits

Fig. 9.13 Automated synthesis modules for the production of PET radiopharmaceuticals. FASTlab HPLC+ for efficient HPLC purification and reformulation in one system with increased flexibility and efficiency of R&D tracer production for ^{18}F and ^{68}Ga radiopharmaceuticals, Neptis® perform an innovative synthesizer for the automated production of the largest range of [^{18}F] fluoride-based radiotracers via nucleophilic synthesis. Neptis® xSeed™ is a multi-run synthesizer designed specifically for research and development. Synthera®+, the most compact radiosynthesis module. Trasis-All-in-One PET tracer synthesizer, the cutting-edge solution for tracer production and development for ^{18}F, ^{11}C, and radio-metals. ITM-iQS-Theranostics Synthesizer for various radiometals for PET and therapy

with ready-to-use reagent vials for each batch production. At this time, several commercial ASMs are used routinely for the synthesis of ^{18}F-labeled radio-chemically pure, sterile, and pyrogen-free FDA-approved radiopharmaceuticals used in clinical studies. Several ASMs for the manufacture of radiolabeled metal complexes are also in routine use in many commercial manufacturing facilities.

References

1. Mankoff DA. A definition of molecular imaging. J Nucl Med. 2007;48:18N and 21N.
2. O'Dorisio TM, Harris AG, O'Dorisio MS. Evolution of neuroendocrine tumor therapy. Surg Oncol Clin N Am. 2020;29:145–63.
3. Barrio JR. The molecular basis of disease. In: Phelps ME, editor. PET: molecular imaging and its biological applications. New York: Springer; 2004.
4. Duan H, Iagaru A, Aparici CM. Precision medicine in nuclear medicine and molecular imaging. Nanotheranostics. 2022;6(1):103–17.
5. Herrmann K, Larson SM, Weber WA. Theranostic concepts: more than just a fashion trend—introduction and overview. J Nucl Med. 2017;58:1S–2S.
6. Herrmann K, Schwaiger M, Lewis JS, et al. Radiotheranostics: a roadmap for future development. Lancet Oncol. 2020;21:e146–56.
7. Hoffman JM, Gambhir SS. Molecular imaging: the vision and opportunity for radiology in the future. Radiology. 2007;244:39–47.
8. Weber WA, Czernin J, Anderson CJ, et al. The future of nuclear medicine, molecular imaging, and theranostics. J Nucl Med. 2020;61(12):263S–72S.
9. Maclean D, Northrop JP, Padgett HC, et al. Drugs and probes: the symbiotic relationship between pharmaceutical discovery and imaging science. Mol Imaging Biol. 2003;5:304–11.
10. Park KB, Kitteringham NR, O'Neill PM. Metabolism of fluorine-containing drugs. Annu Rev Pharmacol Toxicol. 2001;41:443–70.
11. Fowler JS, Ido T. Design and synthesis of 2-deoxy-2-[^{18}F]fluoro-D-glucose (^{18}FDG). In: Welch MJ,

Redvanley CS, editors. Handbook of radiopharmaceuticals. New York: Wiley; 2003.

12. Pacák J, Černý M. History of the first synthesis of 2-deoxy-2-fluoro-D-glucose the unlabeled forerunner of 2-deoxy-2-[18F]fluoro-D-glucose. Mol Imaging Biol. 2002;4:352–4.

13. Sols A, Crane RA. Substrate specificity of brain *hexokinase*. J Biol Chem. 1954;210:581–95.

14. Sokoloff L. Mapping of local cerebral functional activity by measurement of local cerebral glucose utilization with [14C]deoxyglucose. Brain. 1979;102:653–68.

15. MacGregor RR, Fowler JS, Wolf AP, et al. A synthesis of 11C-2-deoxy-D-glucose for regional metabolic studies. J Nucl Med. 1981;22:800–3.

16. Cleaver JE. Thymidine metabolism and cell kinetics. Front Biol. 1967;6:43–100.

17. Cronkite EP, Fliedner TM, Bond VP, et al. Dynamics of hemopoietic proliferation in man and mice studied by 3H-thymidine incorporation into DNA. Ann N Y Acad Sci. 1959;77:803.

18. Livingston RB, Ambus U, George SL, et al. In vitro determination of thymidine-[H-3] labeling index in human solid tumors. Cancer Res. 1974;34:1376–80.

19. Langen P, Etzold Z, Hintsche R, et al. 3′deoxy-3′fluoro-thymidine, a new selective inhibitor of DNA synthesis. Acta Biol Med Ger. 1969;23:759–66.

20. Christman D, Crawford EJ, Friedkin M, et al. Detection of DNA synthesis in intact organisms with positron-emitting methyl-[C-11]-thymidine. Proc Natl Acad Sci U S A. 1972;69:988–92.

21. Shields AF, Grierson JR, Kozawa SM, et al. Development of labeled thymidine analogs for imaging tumor proliferation. Nucl Med Biol. 1996;23:17–22.

22. Seitz U, Wagner M, Neumaier B, et al. Evaluation of pyrimidine metabolising enzymes and in vitro uptake of 3′-[18F] fluoro-3′-deoxythymidine ([18F]FLT) in pancreatic cancer cell lines. Eur J Nucl Med Mol Imaging. 2002;29:1174–81.

23. Conti PS, Alauddin MM, Fissekis JR, et al. Synthesis of 2′fluoro-5-[11C]-methyl-1-beta-D-arabinofuranosyluracil ([11C]-FMAU): a potential nucleoside analog for in vivo study of cellular proliferation with PET. Nucl Med Biol. 1995;22:783–9.

24. Sun H, Sloan A, Mangner TJ, et al. Imaging DNA synthesis with [18F]FMAU and positron emission tomography in patients with cancer. Eur J Nucl Med Mol Imaging. 2005;32:15–22.

25. Shields AF. PET imaging with 18F-FLT and thymidine analogs: promise and pitfalls. J Nucl Med. 2003;44:1432–4.

26. Grierson JR, Schwartz JL, Muzi M, et al. Metabolism of 3′-deoxy-3′-[18F]fluorothymidine in proliferating A549 cells: validations for positron emission tomography. Nucl Med Biol. 2004;31:829–37.

27. Wieland DM, Wu J, Brown LE, et al. Radiolabeled adrenergic neuron blocking agents: adrenomedullary imaging with [131I]iodobenzylguanidine. J Nucl Med. 1980;21:349–53.

28. Wieland DM, Brown LE, Tobes MC, et al. Imaging the primate adrenal medulla with [123I] and [131I] meta-iodobenzylguanidine: concise communication. J Nucl Med. 1981;22:358–64.

29. Garg PK, Garg S, Zalutsky MR. Synthesis and preliminary evaluation of para- and meta-[18F]fluorobenzylguanidine. Nucl Med Biol. 1994;21(1):97–103.

30. Szabo Z, Kao PF, Scheffel U, et al. Positron emission tomography imaging of serotonin transporters in the human brain using [11C](+)McN5652. Synapse. 1995;20:37–43.

31. Dannals RF, Langstrom B, Ravert HT, et al. Synthesis of radiotracers for studying muscarinic cholinergic receptors in the living human brain using positron emission tomography [11C]dexetemide and [11C]levetimide. Int J Radiat Appl Instrum A. 1988;39:291–5.

32. Wurzer A, Di Carlo D, Schmidt A, et al. Radio hybrid ligands: a novel tracer concept exemplified by (18)F- or (68)Ga-labeled rhPSMA inhibitors. J Nucl Med. 2020a;61(5):735–42.

33. Wurzer A, Parzinger M, Konrad M, et al. Preclinical comparison of four [18F,natGa]rhPSMA-7 isomers: influence of the stereoconfiguration on pharmacokinetics. EJNMMI Res. 2020b;10:149.

34. Langbein T, Wang H, Rauscher I, et al. Utility of 18F-rhPSMA-7.3 positron emission tomography for imaging of primary prostate cancer and pre-operative efficacy in N-staging of unfavorable intermediate to very high-risk patients validated by histopathology. J Nucl Med. 2022;63(9):1334–42. https://doi.org/10.2967/jnumed.121.263440.

35. Riant JP, Tillement JP. Drug transfer across the blood-brain barrier and improvement of brain delivery. Fundam Clin Pharmacol. 1999;13:16–26.

36. Waterhouse RN. Determination of lipophilicity and its use as a predictor of blood–brain barrier penetration of molecular imaging agents. Mol Imaging Biol. 2003;5:376–89.

37. Kosa T, Maruyama T, Otagiri M. Species differences of serum albumins: I. Drug binding sites. Pharm Res. 1997;14:1607–12.

38. Kratochwil NA, Huber W, Muller F, et al. Predicting plasma protein binding of drugs: a new approach. Biochem Pharmacol. 2002;64:1355–74.

39. Bergstrom MJ, Eriksson B, Oberg K, et al. In vivo demonstration of enzyme activity in endocrine pancreatic tumors. Decarboxylation of C-11 DOPA to Carbon-11 dopamine. J Nucl Med. 1996;37:32–7.

40. Firnau G, Sood S, Chirakal R, et al. Cerebral metabolism of 6-[18F]fluoro-L-3,4-dihydroxy-phenylalanine in the primate. J Neurochem. 1987;48:1077–82.

41. Luxen A, Guillaume M, Melega WP, et al. Production of 6-[18F]fluoro-L-dopa and its metabolism in vivo- a critical review. Int J Rad Appl Instrum B. 1992;19:149–58.

42. Mankoff DA, Shields AF, Krohn KA. PET imaging of cellular proliferation. Radiol Clin N Am. 2005;43:153–67.

43. Grierson JR, Shields A. Radiosynthesis of 3′-Deoxy-3′-[^{18}F]fluorothymidine:[^{18}F]FLT for imaging of cellular proliferation in vivo. Nucl Med Biol. 2000;27:143–56.

44. Pike VW, McCarron JA, Lammertsma AA, et al. Exquisite delineation of 5HT1A receptors in human brain with PET and [carbonyl-^{11}C]WAY-100,635. Eur J Pharmacol. 1996;301:R5–7.

45. Kung M-P, Kung H-F. Mass effect of injected dose in small rodent imaging by SPECT and PET. Nucl Med Biol. 2008;32:673–8.

Radiohalogens for Molecular Imaging (Fluorine and Iodine)

10

If your experiment needs statistics, you ought to have done a better experiment.

Ernest Rutherford

10.1 Fluorine-18 Radiopharmaceuticals for Molecular Imaging

F-18 as a radionuclide for medical imaging was first reported in 1962 to image skeletal metastases using ^{18}F as sodium fluoride ($[^{18}$F]NaF) [1]. In the early 1970s, the anti-cancer drug 5-fluorouracil was labeled with ^{18}F to study the biodistribution and pharmacokinetics [2]. The first synthesis of $[^{18}$F]fluoro-2-deoxy-D-glucose (FDG) was developed at the Brookhaven National Laboratories (BNL) in Long Island, New York, by Dr. Alfred Wolf, and his colleagues to study the cerebral glucose metabolism based on positron emission tomography (PET) [3]. The first $[^{18}$F]FDG scans were obtained at the University of Pennsylvania in 1979 with $[^{18}$F]FDG that was synthesized at BNL [4]. The 1986 landmark paper by Dr. Hamacher and colleagues (at the Institut fur Nuklearchemie, Julich GmbH, FRG) published in the Journal of Nuclear Medicine, represents a major milestone in the present use of $[^{18}$F]FDG in clinical nuclear medicine worldwide [5]. More specifically, they developed an efficient stereospecific synthesis of No-Carrier-Added FDG using aminopolyether-supported nucleophilic substitution.

In 1994, FDG-PET was approved by the Food and Drug Administration (FDA) for the measurement of regional glucose metabolism in the human brain to assist in the diagnosis of seizures. The fact that cancer cells exhibit an increased rate of glycolysis has been known since the 1920s, and FDG-PET is able to assess a fundamental alteration in the cellular metabolism of glucose that is common to all neoplasms. Increased cellular glucose uptake is one of the key alterations associated with the high glycolytic rate of cancer cells. In March 2000, the FDA approved the use of $[^{18}$F] FDG to assist in the evaluation of malignancy in patients with known or suspected abnormalities found by other testing methods or in patients with an existing diagnosis of cancer.

FDG-PET revolutionized the clinical management of patients in oncology and promoted the advancement of molecular imaging based on radiopharmaceuticals labeled with a number of positron-emitting radionuclides. Around the world, >1200 cyclotron facilities routinely manufacture ^{18}F-labeled radiotracers. In the last four decades, ^{18}F radionuclide has been the most popular radionuclide for developing PET radiopharmaceuticals. As of January 2022, there are 17 FDA-approved PET radiopharmaceuticals out of which 10 are based on ^{18}F radionuclide (Table 10.1). In addition, hundreds of ^{18}F-labeled radiotracers are under preclinical or clinical investigation. Several recent publications have

Table 10.1 ^{18}F-labeled PET radiopharmaceuticals approved by FDA

Radiopharmaceutical	Trade name	Target	Indication	FDA approval
[^{18}F]fluorodeoxyglucose		*Hexokinase*	Oncology, cardiology, and neurology	2000
[^{18}F]fluoride		Hydroxyapatite		2000
[^{18}F]florbetapir	Amvid™	β-amyloid	Alzheimer's disease (AD) and other causes of cognitive decline	2012
[^{18}F]flutemetamol	Vizamyl™			2013
[^{18}F]florbetaben	Neuroceq™			2014
[^{18}F]fluciclovine	AuxuminTM	Amino acid transporters		2016
[^{18}F]fluorodopa		*Aromatic amino acid decarboxylase*	Parkinsonian syndromes (PS)	2019
[^{18}F]fluoroestradiol	Cerianna™	Estrogen receptors	Recurrent or metastatic breast cancer	2020
[^{18}F]flortaucipir	Tauvid™	Aggregated tau neurofibrillary tangles (NFTs)	Cognitive impairment, evaluated for AD	2020
[^{18}F]piflufolastat	Pylarify®	Prostate specific membrane antigen (PSMA)	Prostate cancer recurrence and metastases	2021

Table 10.2 Physical properties of hydrogen and halogens

	Element			
Physical property	H	F	Br	I
Atomic number	1	9	35	53
Atomic radius (pm)	31	71	120	139
Ionic radius (pm)	154	136	196	216
Electron structure	$1s^1$	[He] $2s^2$ $2p^5$	[Ar] $3d^{10}$ $4s^2$ $4p^5$	[Kr] $4d^{10}$ $5s^2$ $5p^5$
Electronegativity	2.20	3.98	2.96	2.66
Oxidation state	−1, +1	−1	−1, +1, +3, +5	−1, +1, +5, +7
First ionization potential (ev)	13.12	17.42	11.84	10.44

extensively discussed ^{18}F production, radiochemistry, labeling challenges, and potential clinical applications [6–9].

10.1.1 Halogens

The family of Group 7A elements in the periodic table fluorine, chlorine, bromine, iodine, and astatine, known as *halogens*, are nonmetals, and generally not found in nature as free elements. Instead, they are found as halide ions (X⁻) in various minerals and seawater. Radioisotopes of chlorine and astatine are not useful for imaging and are not discussed further in this chapter. Some of the important physical properties of

fluorine, bromine, and iodine are compared to those of hydrogen in Table 10.2. Stable isotopes of halogens and the corresponding radionuclides of halogens useful for developing molecular imaging agents are listed in Table 10.3.

All halogens are characterized by the presence of 5 *p* electrons and 2 *s* electrons in the outermost valence shell (np^5, ns^2). The electronegativity values reveal that among halogens, fluorine has the greatest attraction for electrons and iodine has the least. This means that a F⁻ ion is more stable than an I⁻ ion. Since fluorine is the most electronegative element, it has only one oxidation state (−1). In contrast, bromine and iodine may attain positive oxidation states when interacting with the more electronegative element—oxygen. The

Table 10.3 Stable isotopes and radioisotopes of halogens

Halogen	Stable isotopes		Radioactive isotopes				Energy of β⁺ particle (MeV)	
	Nuclide	%	Nuclide	$T_{1/2}$	Decay	%	E_{max} (MeV)	E_{mean} (MeV)
Fluorine	¹⁹F	100	¹⁸F	109.77 min	β⁺	96.73	0.6335	0.2498
					EC	3		
Bromine	⁷⁹Br	50.69	⁷⁵Br	96.73 min	β⁺	75	2.040	0.732
	⁸¹Br	49.31			EC	24		
			⁷⁶Br	16.2 hours	β⁺	55	3.941	1.180
					EC	43		
Iodine	¹²⁷I	100	¹²³I	13.2 hours	EC	100		
					γ	84	0.159 γ	
			¹²⁴I	4.176 days	β+	25	2.137	0.820
					EC, γ	75	0.602, 0.722, 1.69 γ	
			¹³¹I	8.025 days	β⁻, γ	87	0.6 MeV β⁻	0.189
						82	0.364 γ	

higher ionization potentials of halogens suggest that it is difficult to remove an electron from halogen atoms. Also, among halogens, fluorine is the most powerful oxidizing agent, while iodine is the most powerful reducing agent.

The chemistry of bromine and iodine, however, is, in many aspects more similar compared to the chemistry of fluorine. In general, halogens can react as *electrophiles*, electron-deficient positively charged species; or *nucleophiles*, electron-rich negatively charged species. Electrophiles (X⁺) seek electron-rich reactants, such as carbon atoms with high local electron densities, while nucleophiles (X⁻) seek electron-deficient reactants. Since the radioisotopes of bromine are not used clinically, only the radiochemistry of fluorine and iodine will be discussed in this chapter.

10.2 Chemistry of ¹⁸F-Labeled Radiopharmaceuticals

10.2.1 Production of Fluorine-18

The production of ¹⁸F radionuclide was first reported in 1937 based on the nuclear reaction ²⁰Ne(d,α)¹⁸F, developed at the Radiation Laboratory of the University of California [10]. Several nuclear reactions are reported for the production of ¹⁸F radionuclide using the cyclotron. ¹⁸F is produced with a cyclotron primarily based on the nuclear reaction

¹⁸O(p,n)¹⁸F by proton (¹H) irradiation of ¹⁸O, a stable naturally occurring isotope of oxygen. When the target is liquid H₂¹⁸O, an aqueous solution of ¹⁸F-fluoride ion (used for nucleophilic reactions) is obtained; when the target is ¹⁸O₂ gas, [¹⁸F]F₂ gas (used for electrophilic reactions) is obtained. [¹⁸F]F₂ is also prepared from deuteron-irradiation of neon gas based on nuclear reaction, ²⁰Ne(d,α)¹⁸F. The production method used is dependent on the desired subsequent chemical reactions [8, 11].

The most common method for the production of ¹⁸F as no carrier added (*nca*) nucleophilic fluoride ion (¹⁸F⁻) is based on the use of water target. Several curies (~370 GBq) of ¹⁸F can easily be made in 1–2 h using 10–19 MeV protons using 20–35 μA. Recently, cyclotron targets have been developed to produce >10 Ci of ¹⁸F as fluoride. While the theoretical SA of ¹⁸F is 1700 Ci/μmol, the NCA) ¹⁸F produced is generally <10 Ci/μmol (~100 GB/ μmol).

The most common nuclear reaction to produce ¹⁸F as electrophilic fluorine gas ([¹⁸F]F₂) is based on the reaction ²⁰Ne(d,α)¹⁸F. Following bombardment for 1–2 h, with 8–9 MeV deuterons, <1.0 Ci (37 GBq) of [¹⁸F]F₂ is generated with very low SA (10–20 mCi/μmole⁻¹). A "double shoot" method was developed to produce [¹⁸F] fluorine gas based on the reaction ¹⁸O(p,n)¹⁸F using [¹⁸O]O₂ gas. Electrophilic [¹⁸F]F₂ has much lower specific activity (100–600 MBq/μmol) because fluorine-19 gas (0.1–0.3%) must be

added as a carrier to extract the $[^{18}F]F_2$ from the target. The SA becomes crucial when preparing radiotracers for low-capacity systems such as ligand-receptor binding. The addition of a carrier, stable fluorine gas ($[^{19}F]F_2$) leads to increased mass of the final radiotracer, which may result in receptor saturation and reduction of PET signal from specific binding. High mass may also cause pharmacological effects. The high yield from cyclotron production along with higher SA that is crucial for PET imaging of receptor-ligand interaction dictates that most of the fluorine-18 reactions in nuclear medicine use nucleophilic ^{18}F-fluoride. However, it is important to understand that fluorination chemistry with $[^{18}F]F_2$ gas is less cumbersomes compared to the nucleophilic reaction with $[^{18}F]$fluoride ions.

10.2.1.1 [^{18}F]Fluoride Production Using [^{18}O]H$_2$O Target

Several important considerations are as follows:

- The cross section for the $^{18}O(p,n)^{18}F$ nuclear reaction is 2.3–18.0 MeV and peaks at 6 MeV protons. The broad cross section for this reaction permits the production of large quantities of ^{18}F using medium-energy cyclotron (16–20 MeV protons). A major advantage of this route of production is that there are no competing nuclear reactions yielding radionuclide impurities while using higher-energy protons.
- Isotopically enriched (~98%) water $[^{18}O]H_2O$ is used as recommended target material to produce $[^{18}F]$fluoride. ^{13}N will be produced based on $^{16}O(p,\alpha)^{13}N$ nuclear reaction.
- Higher beam currents increase production yields. Typical beam currents are 20–40 μA but, commercial cyclotrons up to 300 μA beam current are available in the market for routine production of ^{18}F. For example, IBA Kiube or Advanced cyclotron with 18 or 20 MeV proton at 300 μAs beam current can produce 1110 GBq (30 Ci) of $[^{18}F]$fluoride [8].
- Metallic target body (0.5–4.0 mL volume) used should be inert, withstand high temperatures, and must have high thermal conductivity to enable heat transfer during proton

bombardment. The target metal should not react with the $[^{18}F]$fluoride ions and not reduce the chemical reactivity of the fluoride ion. While silver, aluminum, nickel, titanium, niobium, and tantalum metals are used for target body, niobium and tantalum targets are finding increasing usage by cyclotron manufacturers.

- The most commonly used materials to make target foils are havar, aluminum, niobium, and titanium. Havar is a cobalt-based alloy containing several metals (such as Co, Cr, Ni, Mn, and Fe), which can produce long-lived radioisotopes (such as ^{56}Co, ^{57}Co, ^{58}Co, ^{51}Cr, and ^{54}Mn). The amount of these impurities produced depends on the material used for target foil and the proton dose (μAh). Higher beam currents may produce higher levels of impurities [12].
- The materials used for $[^{18}F]$fluoride transfer lines (Tefzel, PEEK, and PP) must be resistant to high pressure up to 3000 psi (210 bar), flexible robust, and should not decrease the specific activity of $[^{18}F]$fluoride ion.

10.2.1.2 ^{18}F-Labeled Precursors

In addition, to the two primary ^{18}F precursors ($[^{18}F]$fluoride and $[^{18}F]F_2$ gas), several secondary precursors have been developed to radiolabel a number of organic molecules. Figure 10.1 shows examples of secondary precursors. Fluoride ion has to be activated (discussed below) prior to fluorination reactions. Metal fluorides (such as $K^{18}F$, $Cs^{18}F$) and tetra-n-butyl ammonium fluoride ($nBu_4N^{18}F$) are the most widely used ^{18}F pre-
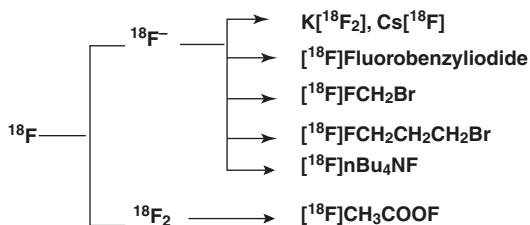
Fig. 10.1 ^{18}F primary and secondary precursors used in nucleophilic and electrophilic fluorination reactions

Table 10.4 Physicochemical properties of carbon-fluorine bond

Element	Electro negativity	Bond length CH$_2$X, Å	Van der Walls radius (Å)	Bond energy (kcal mol^{-1})
H	2.1	1.09	1.20	98
F	4.0	1.39	1.35	112
O (OH)	3.5	1.43	1.40	85

cursors in nucleophilic fluorination reactions [13], while [^{18}F]CH$_3$COOF (acetyl hypofluorite) is the most common precursor in the electrophilic reactions.

10.2.2 F-18 Radiochemistry

For the development of PET radiopharmaceuticals, ^{18}F appears to be an ideal radionuclide due to the several reasons summarized below: Some of these are related to the inherent nature of the element fluorine (Table 10.4), some are related to the radionuclide ^{18}F (Table 10.3) and its versatile chemistry, and others are related to the imaging instrumentation.

- F-18 decays predominantly by positron emission (97%) and the rest by electron capture (3%), making it one of the best PET radionuclides with high abundance (196%) of 511 keV photons.
- Can be produced in high specific activity (20–50 Ci/μmol).
- Can be produced in large amounts (>10 Ci) in a cyclotron.
- Low positron energy (Emax = 0.635 MeV) with a short range in tissue (R$_{Max}$ = 2.4 mm) and provides high resolution images.
- Fluorine is a favorable element for drug development due to its physical properties such as high electronegativity, small van der Waals radius (1.37 Å), and ability to form a strong bond with carbon; Fluorine is the most electronegative of all elements and can react with many organic and inorganic chemicals.
- The C-F energy bond is 112 kcal/mol compared to C-H bond energy of 98 kcal/mol. It is more thermally stable and oxidation resistant and, hence, yields highly stable products. This property is especially useful because the

radiopharmaceuticals produced with 18F are highly stable despite the deposition of a significant amount of radiation energy due to the decaying 18F; it can react as an electrophile or a nucleophile chemical species.

- Relatively high labeling yields (20–70%) in the synthesis of ^{18}F-PET tracers.
- Acceptable radiation dosimetry for multiple studies in a patient.
- The physical $T_{\frac{1}{2}}$ (110 min) allows for the transport from the production site to the PET centers.

The fluorine atom is only slightly smaller than a hydrogen atom (Table 10.2). The replacement of a hydrogen atom or hydroxyl group by a fluorine atom is a strategy, widely used in drug development, to alter the biological function. The introduction of a fluorine atom as a substitute to a hydrogen atom or a hydroxyl group (F for H or OH) in a drug or metabolic substrate, however, does not cause any steric changes (Table 10.3) but, may induce changes in the in vivo behavior of the fluorinated molecule [14]. For example, as a substituent, fluorine can alter the metabolic properties of the parent molecule and prolong drug action by preventing hydroxylation. Also, the higher electronegativity of the fluorine atom may alter the lipophilicity of the compound. A large number of pharmaceuticals contain fluorine atom and in the last few decades, hundreds of ^{18}F-labeled radiotracers have been developed.

The design and synthesis of ^{18}F-labeled radiopharmaceuticals of clinical interest (have been extensively reviewed previously in several publications [15–19]. Many different approaches have been used to produce ^{18}F-labeled radiopharmaceuticals and new developments on fluorination chemistry are constantly published. This chapter describes general considerations with respect to the synthesis of FDA-approved radiopharmaceuticals.

10.2.3   Fluorination Reactions

Three important strategies are used for the attachment of ^{18}F atom to the molecule of interest.

- Creation of a C-F bond through nucleophilic fluorination reactions using $[^{18}F]$fluoride ion.
- Creation of a C-F bond through electrophilic fluorination reactions using $[^{18}F]F_2$ gas. Reaction of $[^{18}F]F+$ electrophilic fluorination.
- Creation of a C-C bond starting from a $[^{18}F]$ Fluorinated synthon.

10.2.3.1   Nucleophilic Fluorination Reactions

Although fluoride ion is a strong nucleophile, in aqueous solution it forms hydrogen bonds with the surrounding water molecules and becomes unreactive for nucleophilic substitution. The $[^{18}F]$ fluoride ion is first extracted from target water and then activated.

Metal target impurities need to be removed as well as water, often by SPE purification, followed by azeotropic evaporation (acetonitrile/water) in the presence of cationic counterion. The first step is to trap the $[^{18}F]$fluoride ion in target water using an anionic exchange cartridge such as quaternary ammonium chloride polymer (QMA). The target water with metal impurities is collected separately and the $[^{18}F]$fluoride ion is recovered from the QMA with K_{222}/tetrabutyl ammonium (TBA) carbonate solution. The solubility and nucleophilicity of fluoride ion in organic solvents is enhanced by the addition of a phase transfer catalyst (PTC) (such that the cryptand Kryptofix$_{222}$ complexes potassium) or by the addition of bulky tetrabutylammonium cation. Radiofluorinations are typically conducted in the presence of poorly nucleophilic bases (typically carbonate or bicarbonate ions). The fluoride ion is dried by the removal of water, assisted by azeotropic distillation of water using acetonitrile.

Sometimes, the $[^{18}F]$fluoride ion is first converted to another reactive species, such as alkyl halides (Fig. 10.1) ($[^{18}F]$fluorobromoethane, $[^{18}F]$fluorobromopropane) and benzylic halides [13].

The most successful approach to preparing high SA ^{18}F radiotracers is based on nucleophilic fluorination reactions. Synthesis of ^{18}F radiopharmaceuticals using fluoride ion utilizes two general categories or types of chemical reactions [13]; (1) aliphatic nucleophilic substitution, also known as substitution nucleophilic bimolecular (S_N2) and (2) aromatic nucleophilic substitution (S_NAr).

Nucleophilic Aliphatic Substitution

Aliphatic nucleophilic fluorination involves the SN_2 substitution of $[^{18}F]$fluoride into precursors that contain a leaving group (LG). The fluoride ion attacks and binds to the carbon atom of the substrate at 180° opposite to a leaving group (Fig. 10.2) which is a weak base such as iodide, bromide, triflate, tosylate, nosylate, mesylate, etc. Choosing the best leaving group is a critical step of the radiosynthetic design and should take into consideration the reactivity of the leaving group and the stability of the precursor to basic conditions of the fluorination reaction. Also, competing sites of nucleophilic attack (such as acid, alcohol, or amine groups) in the molecule of interest need to be protected when precursors are developed, as shown in Fig. 10.3. Typically, these reactions are performed in polar aprotic solvents, often in acetonitrile, DMF, or DMSO. Overall, aliphatic nucleophilic substitution with $[^{18}F]$fluoride remains a method of choice and well established for the majority of routine ^{18}F radiotracer productions (such as $[^{18}F]$ FDG, $[^{18}F]$FCH, $[^{18}F]$Florbetaben, and $[^{18}F]$FLT) and is employed in most commercially available synthesis platforms.

Nucleophilic Aromatic Substitution

S_NAr nucleophilic reactions were designed to incorporate ^{18}F atom directly into the aromatic ring as well as into prosthetic groups containing the aromatic ring of a molecule. In these reactions, the leaving group is activated by the electron-withdrawing groups *ortho* and or *para* to the leaving group (Fig. 10.2), such as halide, NO_2, and R_3N^+. A wide range of precursors (Fig. 10.3), leaving groups, and reaction conditions can be utilized for ^{18}F-fluoride nucleophilic substitution (Fig. 10.2). Dipolar aprotic

1. Aliphatic Nucleophilic Substitution (S_N2)
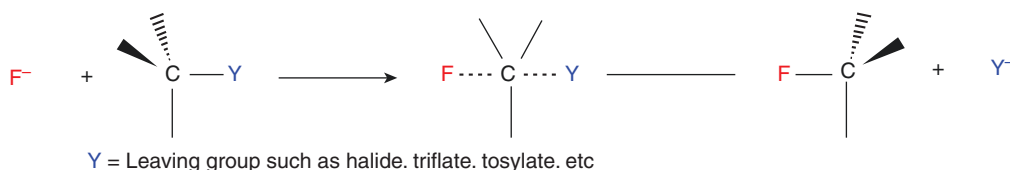
Y = Leaving group such as halide. triflate. tosylate. etc

2. Aromatic Nucleophilic Substitution (S_NAr)

Y = Leaving group such as halide. NO_2, R_3N

A = Electron withdrawing group such as CHO, COR, COOR, CN, NO_2

3. Electrophilic fluorination

Y = Leaving group such as H, SnR_3, HgR, SiR_3

A = Electrondonating group such as OH, OCH_3, NH_2, SR
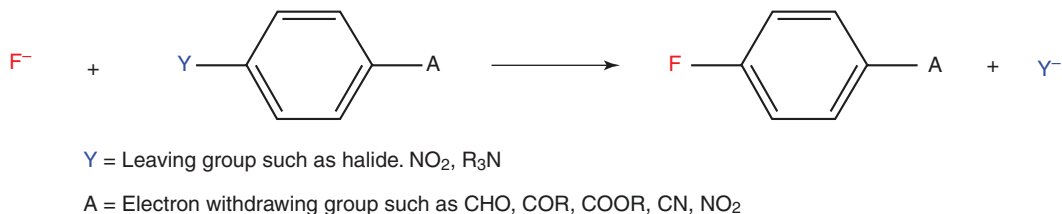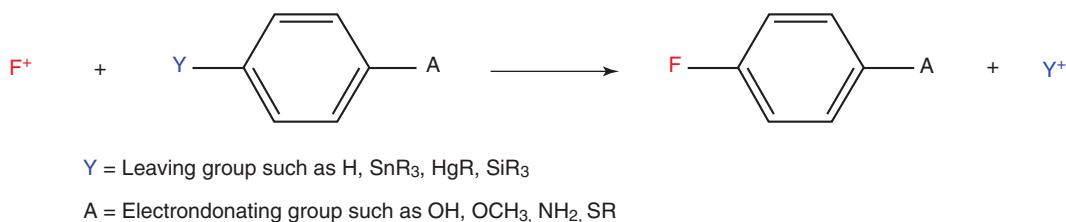
Fig. 10.2 Nucleophilic and electrophilic fluorination reactions

solvents such as dimethyl sulfoxide (DMSO), N, N-dimethylformamide (DMF), dimethylacetamide, and CH_3CN are preferred solvents. It is important to optimize the fluorination reaction for a particular tracer by selecting the right solvent, temperature, counterion, and concentration. For S_NAr reactions, it is necessary that the aromatic ring must be electron deficient in order to achieve fluorination. Heteroarenes containing a nitrogen atom are more electron deficient than the corresponding aromatic hydrocarbon and, thus, are amenable to direct substitution for [18F]-fluoride without an additional activating group [11]. [18F]Flutemetamol (Fig. 10.11), [18F]Flumazenil, and [18F]PSMA-1007 are some of the important radiopharma-

ceuticals synthesized based on S_NAr nucleophilic fluorination reaction.

To introduce an [18F] into arenes that are not bearing electron-withdrawing substituents, several methods have been developed and include Balz-Schiemann reaction, Wallach reaction, and reactions using diaryliodonium salts, and triazenes as precursors [8].

10.2.3.2 Electrophilic Fluorination Reactions

The $[^{18}F]F_2$ precursor has only one of the atoms as [18F], while the other atom is stable [19F] atom. Therefore, the labeling yields are always <50%. Since fluorine is a nonselective electrophile and acts as an oxidizing agent, it is frequently con-
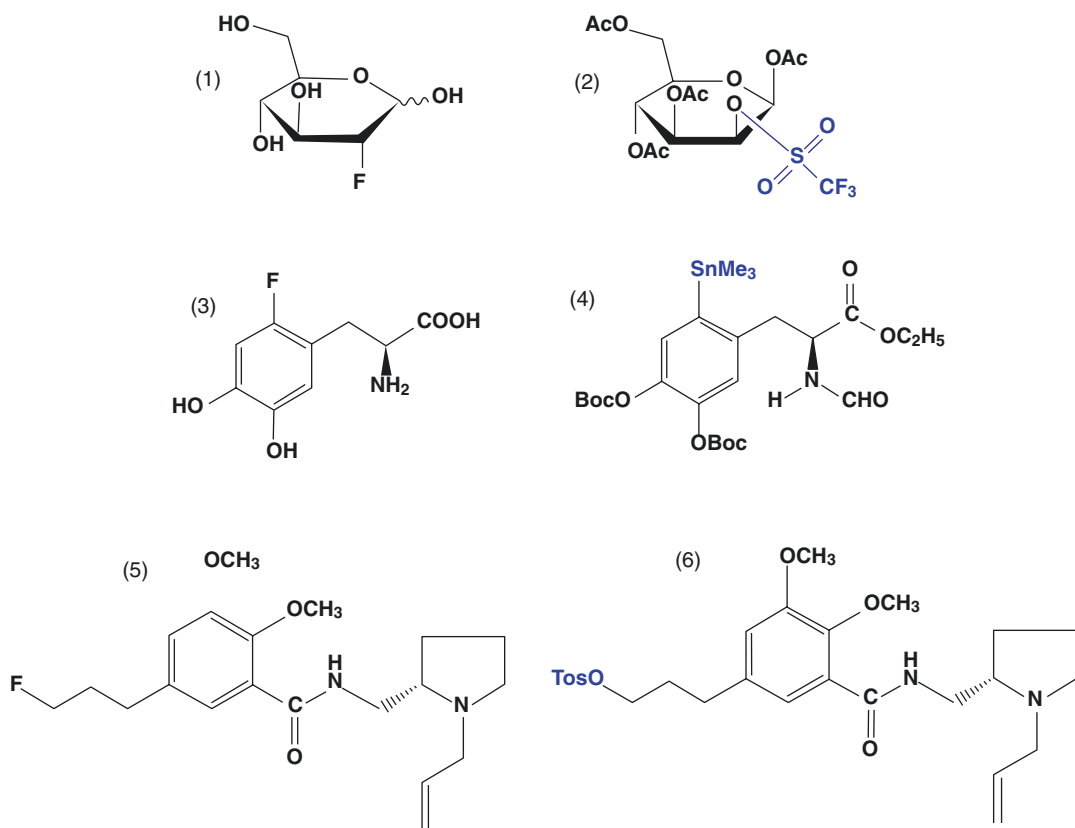
Fig. 10.3 Organic precursors for the synthesis of ^{18}F-labeled radiopharmaceuticals: For FDG synthesis, glucose (1) is converted to mannose triflate (2). For FDOPA synthesis, L-DOPA (3) is converted to trimethyl-stannyl L-DOPA (4). For these two precursors, the functional groups (OH, COOH, and NH$_2$) are protected to prevent fluorination. For the synthesis of fallypride (5), the precursor is simply a tosyl-fallypride analog (6)

verted to [^{18}F]acetyl hypofluorite, a milder fluorinating agent, much less reactive and with greater solubility than the elemental fluorine. With these precursors, direct electrophilic fluorinations are not necessarily regioselective and the ^{18}F atom can attack any of the C–C double bonds in the molecule. Therefore, these precursors are used only in rare situations where nucleophilic reactions are not appropriate. However, regioselective electrophilic fluorodemetallation reactions were developed to take advantage of the reactive electrophiles in the preparation of ^{18}F PET tracers. Electrophilic fluorination reactions (Fig. 10.2) are facilitated by the presence of electron-donating groups (such as OH, OCH$_3$, NH$_2$, etc.) and appropriate

leaving groups (such as H, SnR$_3$, SiR$_3$, and HgR) in the precursor molecule.

In order to synthesize relatively high SA ^{18}F radiotracers based on electrophilic reactions, a multistep method was also developed to generate high SA [^{18}F]F$_2$ by using [^{18}F]fluoride ion [20]. The reactive ^{18}F$^-$ is first converted to [^{18}F]methyl fluoride and purified by gas chromatography. Subsequently, when methyl fluoride is passed through a discharge chamber (operating at 20–30 kV and 280 μA), small amounts of high SA [^{18}F]F$_2$ can be generated and collected using very small amounts of carrier (<0.2 μmole) fluorine gas. Several mild electrophilic fluorination reagents such as ^{18}F-N-fluorobenzenesulfonimide (^{18}F-NFSi) and ^{18}F-Selectfluor can be used.

However, these methods have not been utilized for clinically useful ^{18}F tracers [11].

10.2.3.3   Organic Precursors for ^{18}F Labeling

The synthesis of ^{18}F-labeled PET tracer is a multistep process, and it is ideal to introduce ^{18}F in the last step to reduce synthesis time. In the design and development of a PET tracer, the most important step is the synthesis of an appropriate precursor of the desired radiotracer, which will facilitate ^{18}F labeling. As discussed above, the ^{18}F reactions require an appropriate leaving group (halide, triflate, triflate, tosylate, H, SnR$_3$, etc.) in the precursor molecule.

In addition, the molecules to be labeled may have a number of functional groups (such as OH, COOH, NH$_2$), which may react and interfere with the labeling of radioisotope in a specific position in a molecule. Therefore, in order to facilitate the regioselective labeling of substrates, organic precursors have to be synthesized first with protective groups attached to functional groups. It is very important that the protective groups are very stable during the labeling procedure and can be removed (functional groups deprotected) rapidly and easily under conditions favorable to maintain the stability of the radiolabeled molecule. A number of precursors for ^{18}F labeling have been developed over the years and are now commercially available.

Several examples of precursors with appropriate leaving and protective groups, developed for the synthesis of [^{18}F]FDG, [^{18}F]Fallypride, and [^{18}F]FDOPA are shown in Fig. 10.3. In the case of FDG, the precursor mannose triflate was developed, in which the four hydroxyl groups of deoxyglucose are protected by adding acetate (Ac) groups. Also, in order to facilitate ^{18}F labeling, a leaving group, trifluoromethane sulfonate (TFMS) is added to the carbon in the second position. S$_N$Ar nucleophilic reactions were designed to incorporate the ^{18}F atom directly into the aromatic ring as well as into the prosthetic groups containing the aromatic ring of a molecule. In these reactions, the leaving group is activated by the electron-withdrawing groups ortho and or para to the leaving group. The precursors for the synthesis of ^{18}F-altanserin [21] and [^{18}F]MPPF [22] have been designed to have a leaving nitro group (NO$_2$) situated para to a carbonyl group, which activates the leaving group to be substituted by the reactive [^{18}F]fluoride ion.

In the preparation of certain radiotracers, the ^{18}F-labeled alkyl halides are prepared first using aliphatic nucleophilic reaction and the [^{18}F]alkyl halide (also known as "synthon") is subsequently used to prepare the radiotracer of interest [23]. For example, [^{18}F]fluorobromomethane is reacted with *N,N*-dimethylamino-ethanol (precursor) to synthesize [^{18}F]fluoromethylcholine (FCH) [24, 25]. Similarly, 1-[^{18}] fluoro-3-bromopropane is used to synthesize [^{18}F]β-CFT-FP [26].

10.2.4 Radiotracers Based on Nucleophilic Reactions

A number of radiotracers of clinical interest (Tables 10.1 and 10.5), such as 2-deoxy-2-[^{18}F]fluoro-D-glucose (FDG), [^{18}F]3′-deoxy-3′-fluorothymidne (FLT), 9-(4-[^{18}F]fluoro-3-hydroxymethylbutyl)-guanine (FHBG), 1-amino-3-[^{18}F] fluorocyclo-butane-1-carboxylic acid (FCBCA), [^{18}F] Fallypride, and 16α-[^{18}F]Fluoroestradiol, can all be prepared using commercially available precursors [8, 11, 19, 27–30].

10.2.4.1   [^{18}F]FDG

The original synthesis developed by the Brookhaven group, in 1976, was based on electrophilic reaction [3]. Most of the current synthesis procedures use a modification of a nucleophilic procedure developed in 1986 [31]. The synthesis of FDG is the most established procedure to date, and PET centers all over the world use automated synthesis modules for the production, and distribution of FDG. The synthesis of FDG (Fig. 10.4) involves the following basic steps:

Table 10.5 ^{18}F-labeled PET radiopharmaceuticals of clinical interest

Biochemical process	Radiotracer	Mechanism of uptake or localization
Glucose metabolism	[18F]FDG	Substrate for *hexokinase* in glucose metabolism
Bone metabolism	18F-fluoride	Incorporation in the hydroxyapatite crystals in bone
Membrane synthesis	[18F]Fluoromethylcholine [18F]Fluoroethylcholine	Substrates for *choline kinase* in choline metabolism
Lipid synthesis	[18F]Fluoroacetate	Substrate for *acetyl-CoA synthetase*
Amino acid transport	[18F]FACBC [18F]FDOPA [18F]FET	Uptake facilitated by the amino acid transporters
Brain amyloid burden	[18F]Florbetapir	Bind to β-amyloid plaques
	[18F]Florbetaben	
	[18F]Flutemetamol	
Brain tau neurofibrillary tangles	[18F]Av-1451 [18F]MK-6240	Bind to neurofibrillary tangles in Alzheimer disease
Precursor for dopamine synthesis	[18F]FDOPA	Substrate for aromatic amino acid decarboxylase
Antigen binding	[18F]DCFPyL [18F]PSMA-1007 [18F]rhPSMA-7.3	Binds specifically to the zinc-binding site of prostate-specific membrane antigen (PSMA)
Fibroblasts in the tumor microenvironment	18F-labeled FAP inhibitors	Specific binding to fibroblast activating protein
DNA synthesis	[18F]Fluorothymidine (FLT)	Substrates for *thymidine kinase* in DNA synthesis
	[18F]FMAU	
Hypoxia	[18F]FMISO, [18F]FAZA	Intracellular reduction and binding
	[18F]FAZA	
Neuroinflammation	[18F]DPA-714 [18F]JNJ-64413739	Specific binding to TSPO on activated microglia
Estrogen/progesterone receptors	16α-[18F]fluoro-17β-estradiol ([18F]FES) [18F]fluoro-furanyl-norprogesterone ([18F]FFNP)	Specific binding to estrogen and progesterone receptors in breast cancer
Androgen receptor	[18F]Fluorodihydroxytestosterone FDHT	Specific binding to androgen receptor in prostate cancer
Somatostatin receptors	Al[18F]-NOTA-octreotide Gluc-Lys-[18F]FP-TOCA [18F]FET-βAG-TOCA	Specific binding to somatostatin receptor (SSTR-II) in neuroendocrine tumors
Dopamine receptors	[18F]Fallypride	Specific binding to D2/D3 receptors
Dopamine transporters	[18F]FP-CIT	Binding to presynaptic dopamine transporters
Benzodiazepine receptors	[18F]flumazenil	Specific binding to central benzodiazepine receptors to assess neuronal integrity
Amino acid transport and protein synthesis	[18F]FDOPA	Precursor for the synthesis of dopamine
Apoptosis	18F-Annexin V,	Specific binding to phosphatidylserine (PS)
Angiogenesis	18F-FB-E[c(RGDyK)]2	Integrin receptors ($\alpha_v\beta_3$) on endothelial cells
Myocardial perfusion	[18F]Flurpiridaz	Specific binding to mitochondrial complex
Gene expression	[18F]oligonucleotide	In vivo hybridization with mRNA
	[18F]FHBG	Substrate to herpes virus *thymidine kinase*
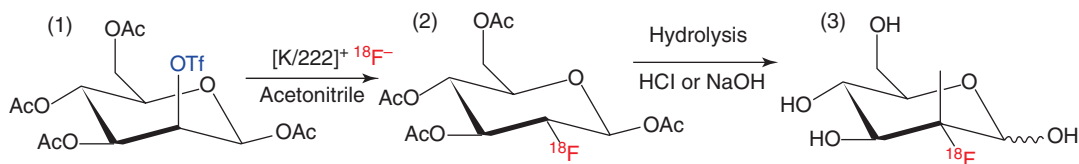
Fig. 10.4 Synthesis of [18F]fluoro-2-deoxy-D-glucose or FDG (3). Following evaporation and drying, the K[18F] and kryptofix complex are incubated at 80 °C with the precursor mannose triflate (1) in acetonitrile. Subsequently, FDG (3) is obtained following acid or base hydrolysis of the fluorinated intermediate (2)

- Following production of 18F in the cyclotron, the target water ([18O]H2O), containing several curies of [18F]fluoride ion, is trapped on a small column of anion exchange resin (Waters Accel plus QMA cartridge) and then collected in a vial for future use.
- The [18F]fluoride ion is eluted into a reaction vial using a solution of aqueous base, potassium carbonate (K2CO3), and Kryptofix 222 in acetonitrile. Some procedures substitute Kryptofix with either tetramethyl ammonium carbonate or tetrabutyl ammonium bi-carbonate or hydroxide.
- The residual water is removed by repeated azeotropic distillations using anhydrous acetonitrile and a stream of nitrogen.
- The organic precursor, mannose triflate (10–25 mg) in acetonitrile, is added to the dried fluoride ion and the mixture is heated at 80–90 °C for 5 min.
- In order to generate FDG from [18F]acetyl-protected FDG (intermediate complex), hydrolysis of acetyl groups (deprotection) is performed using an acidic (HCl) solution by heating the mixture at 130 °C for 10–15 min. With automated synthesis modules, the acetylated FDG intermediate is loaded on a solid support (C18 Sep-Pak® cartridge) and hydrolysis is performed under basic conditions at room temperature using KOH or NaOH solution.
- The purification procedures involve passing the intermediate mixtures or the final FDG solution through the C18 Sep-Pak and alumina cartridges and washing them with water to eliminate Kryptofix and organic solvent contamination.
- The purified FDG is finally obtained from the cartridge by eluting it with physiological saline, sterilizing it by passing it through a 0.2 μ membrane filter, and collecting it in a sterile vial.
- Almost all of the automated FDG synthesis modules provide FDG with a radiochemical yield of 40–70% and a radiochemical purity of >90% in 30–45 min of total synthesis time.

10.2.4.2   [18F]Flt

The synthesis of FLT was first reported in 1991, but the low radiochemical yield prevented routine clinical use of the compound. Subsequent improvements in synthesis and radiochemical yields helped start clinical evaluations of FLT [32]. Since then, a number of precursors and different labeling protocols have been evaluated to improve labeling yields and radiochemical purity [33–36]. The most reliable radiosynthesis of [18F] FLT involves a simple three-step procedure based on a protected nosylate precursor known as 3-*N*-Boc-5′-*O*-dimethoxytrityl-3′-*O*-nosyl-thymidine (Fig. 10.5). Fluorination reactions involve displacement of a 3-*O*-nosyl group with [18F]fluoride and yield an 18F-labeled protected intermediate, which generates [18F]FLT following hydrolysis. The final radiochemical yields of FLT vary (10–40%) and depend on the amount of mass, precursor, and kryptofix used. Increased amounts of precursor may result in higher labeling yields but may also increase the chemical impurities in the final product. It has also been shown that the kryptofix plays a very important role and that by carefully adjusting the precursor/ kryptofix molar ratio, higher labeling yields with minimal chemical impurities can be obtained [36]. HPLC purification is essential to reduce chemical impurities (Fig. 10.6). A fully auto-
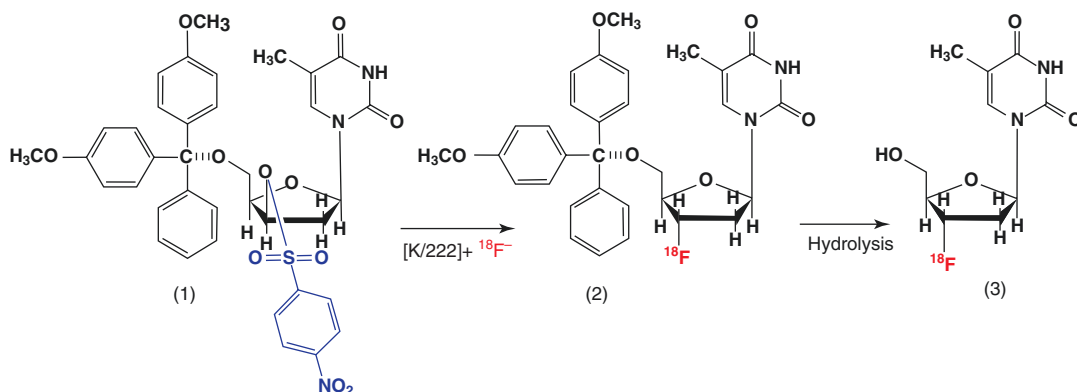
Fig. 10.5 Synthesis of 3′-deoxy-[^{18}F]fluorothymidine or FLT (3). The protected nosylate precursor, 3-*N*-Boc-5′-*O*-dimethoxytrityl-3′-*O*-nosyl-thymidine (1). The fluori-nated intermediate (2) upon hydrolysis will produce FLT, which subsequently is purified using HPLC
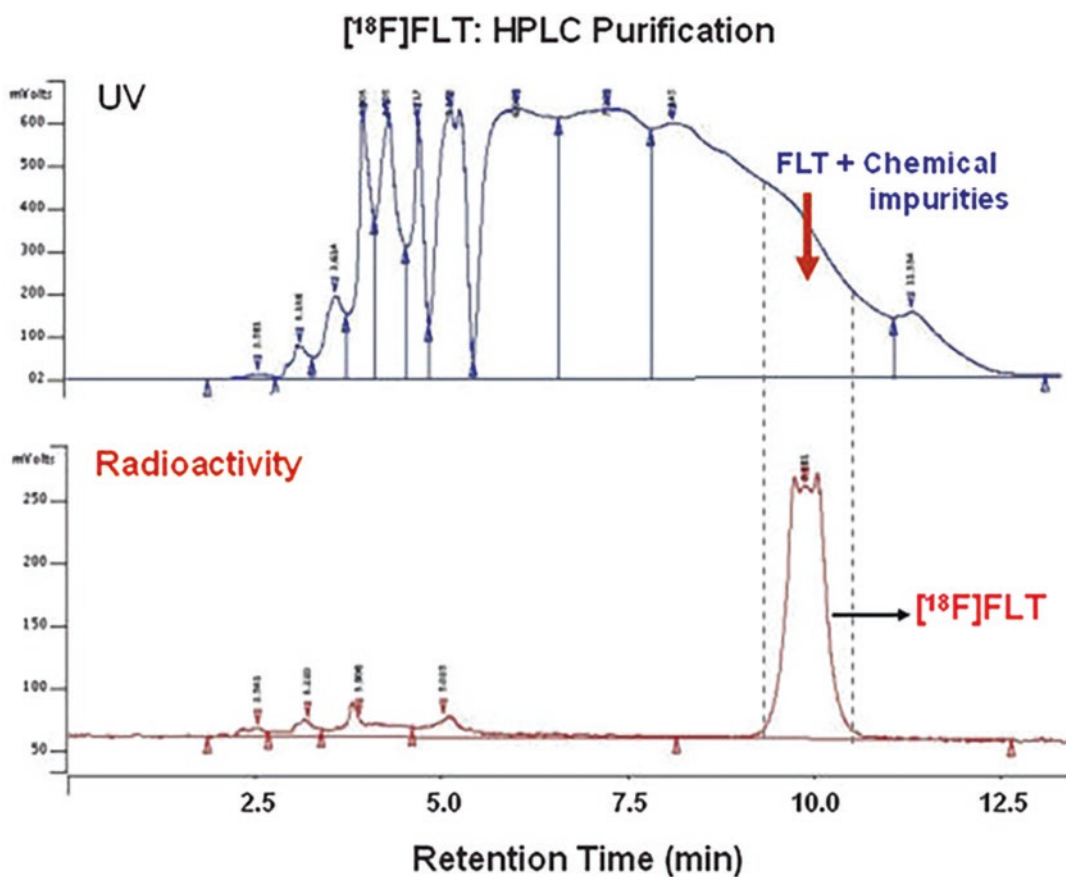
Fig. 10.6 Purification of FLT using HPLC: Following fluorination and hydrolysis, several radiochemical and chemical impurities are generated as seen by UV absor-bance (*top*). The fraction of eluent representing FLT radioactive peak (*bottom*) is collected

mated method for the synthesis of FLT with a 50% radiochemical yield, by modifying a commercial FDG synthesizer and its disposable fluid pathway has also been reported [35].

10.2.4.3   [18F]FMISO Synthesis

The first synthesis of fluoronitroimidazoles was reported in 1986 [37]. Subsequently, a two-step synthesis of FMISO was developed with a high yield (40% at EOB) and purity with a SA of 37 TBq mmol^{-1} [38]. The first step involves the synthesis of fluoroalkylating agent [18F]epifluorohydrin, which subsequently reacts with 2-nitroimidazole to yield FMISO. HPLC purification is needed to obtain high radiochemical purity. Further modifications have been reported with increasing labeling yields [39, 40]. The most practical method is based on the nucleophilic substitution of the tosylate leaving group by [18F]fluoride on the tetrahydropyranyl-protected precursor 1-(2′-nitro-1′-imidazolyl)-2-O-tetrahydropyranyl-3-O-toluenesulfonylpropanediol (NITTP), followed by the hydrolysis of the protecting group (Fig. 10.7). An automated synthesis of [18F] FMISO by this method, using either HPLC or Sep-Pak for the purification of the radiotracer, was also reported [41]. The radiochemical yield obtained when using NITTP was found to be ≤40% and reproducible, with a radiochemical purity ≥97% and a SA of about 34 TBq mmol^{-1}. Further, the whole synthesis time was <50 min.

10.2.4.4   [18F]Fluoroestradiol (FES)

FES, a PET radiotracer for the estrogen receptor (ER) in breast cancer, was the first receptor-targeted PET radiotracer for oncology and is continuing to prove its value in clinical research, antiestrogen development, and breast cancer care. The story of its conception, design, evaluation, and use in clinical studies parallels the evolution of the whole field of receptor-targeted radiotracers, [42]. The first synthesis of FES [43] was based on the nucleophilic displacement of the aliphatic triflate of 3,16β-bis (trifluoromethane-sulfonyloxy)-estrone using tetrabutylammonium [18F]fluoride, followed by hydrolysis and ketone reduction. HPLC purification provided a 30% radiochemical yield of FES in about 90 min. Subsequently, a new procedure was developed in which the nucleophilic substitution of [19F]fluoride led directly to [19F]FES using-3-O-Methoxymethyl-16, 17-O-sulfuryl-16-epiestriol (MMSE) as a precursor [44]. This procedure worked well with non-radioactive fluoride, with carrier-added [18F] fluoride. The first successful preparation with [18F]fluoride with further modifications, however, was published subsequently [45]. A one-pot synthesis of FES (Fig. 10.8) based on the MMSE precursor was also developed to provide radiochemical yields of 30–45% with a SA of about 37 GBq μmol^{-1} (1.0 Ci μmol^{-1}) in 60–120 min.
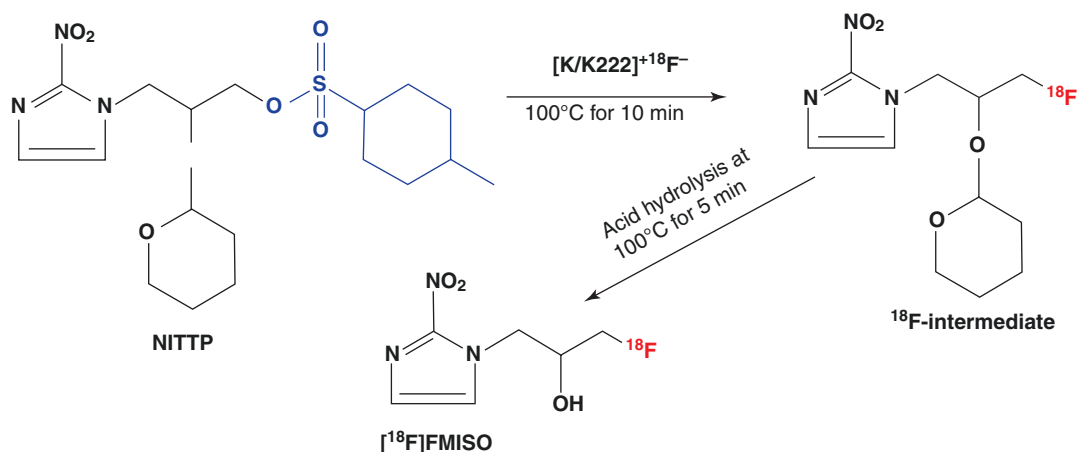
Fig. 10.7 Synthesis of [18F]Fluoromisonidazole (FMISO) (3): Following fluorination reaction with the precursor, NITTP (1), the intermediate (2) is hydrolyzed to yield the final drug product
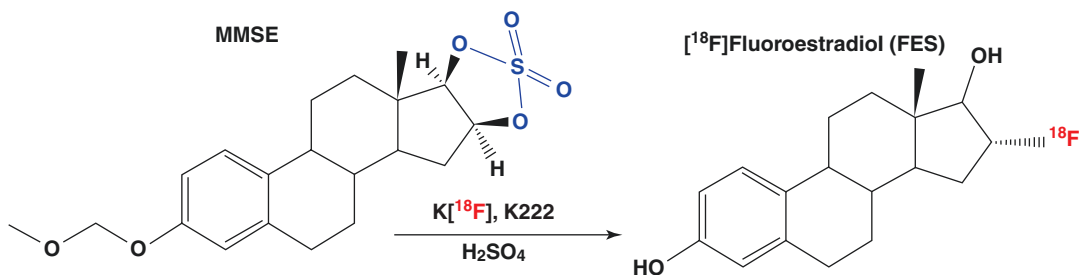
Fig. 10.8 Synthesis of 16α-[¹⁸F]Fluoroestradiol (FES) (3): The precursor is 3-*O*-Methoxymethyl-16, 17-*O*-sulfuryl-16-epiestriol (MMSE) (1). The fluorinated intermediate (2) after hydrolysis will produce FES
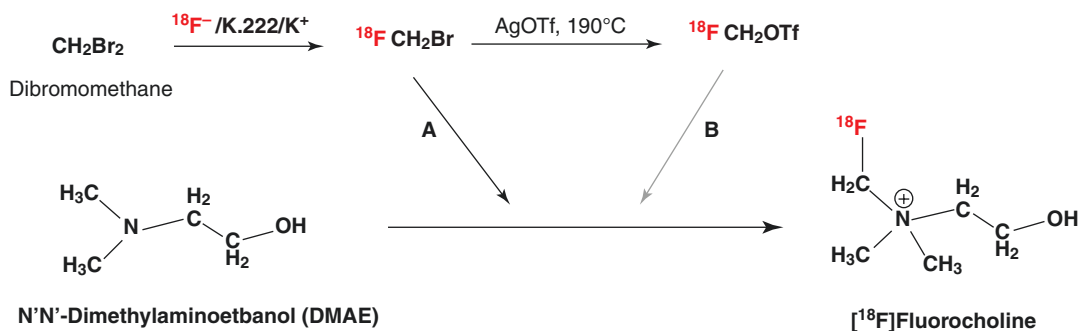
Fig. 10.9 Synthesis of [¹⁸F]fluorocholine (FCH): Dibromomethane is first fluorinated to generate fluorobromomethane (FBR) which reacts with the precursor, dimethylethanolamine to produce FCH. In a second method, FBR can also be converted to fluoromethyltriflate which would react more efficiently with the precursor to produce FCH

Subsequently, an automated module for the synthesis of FES was developed using the same method to give about 50% radiochemical yields in 50 min [46].

10.2.4.5   FCH Synthesis

In the1990s, Hara and his colleagues developed the synthesis of both [¹¹C] choline (CH) and the ¹⁸F-labeled choline analog, 2-[¹⁸F]fluoroethylcholine (FEC) [47]. Subsequently, on the basis of structural similarity, it was speculated that [¹⁸F]fluoromethylated choline (FCH) would mimic choline transport and metabolism more closely than FEC [24] and the first synthesis of FCH based on nucleophilic fluorination method was reported. The ¹⁸F precursor, [¹⁸F]fluorobromomethane (FBM) was first prepared using [¹⁸F]fluoride and dibromomethane (DBM). Subsequently, FBM was reacted with dimethylethanolamine to yield FCH with

radiochemical purity greater than 98% and an uncorrected radiochemical yield of 20–40%. This method was modified to automate the synthesis using a commercial FDG synthesis module [48]. An automated method of FCH synthesis was also achieved by the reaction of [¹⁸F]fluoromethyl triflate (FMT) with dimethylethanolamine on a Sep-Pak column [25]. The total time required for obtaining the finished chemical was 30 min, while the radiochemical yield (decay corrected) was 80% with a radiochemical and chemical purity of >98%. The synthesis procedure using both FBM and FMT is shown in Fig. 10.9.

10.2.4.6   [¹⁸F]FACBC (Fluciclovine F18, Axumin)

Fluciclovine F18 or [¹⁸F]FACBC (1-amino-3-fluomcyclobutane-1-carboxylic acid), an unnatural amino acid, is transported across cell

membranes by amino acid transporters (LAT1 and ASCT2), which are upregulated in prostate cancer cells. In 2016, the FDA approved AXUMIN for PET imaging in men with suspected prostate cancer recurrence. The investigators at Emory University, Atlanta, Georgia developed the first synthesis of [18F]FACBC [49]. The no-carrier-added nucleophilic radiofluorination with K-18F and subsequent hydrolysis procedures are similar to those used for the production of [18F]FDG (Fig. 10.10). A solution of 8 mg l-terr-butyl carbamate-3-trifluromethanesulfonoxy-l-cyclobutane l-carboxylic acid methyl ester (precursor) in dry acetonitrile was added to the reaction vial, and the fluorination (no carrier added [INCA]) reaction was performed at 85 °C for 5 m. Following sepPak purification and hydrolysis, the final drug product was obtained.

10.2.4.7   Florbetapir and Flutemetamol

The presence of β-amyloid plaques (Aβ plaque) in the brain is a defining pathologic feature for Alzheimer disease. Fluoropegylated stilbene derivatives were successfully developed for detecting Aβ plaques in the living human brain. 18F-AV-45 (Florbetapir) and 18F-AV-1 (BAY94–9172, Florbetaben) are structurally related agents [50, 51]. FDA approved both these agents in 2012 and 2013 for PET imaging of amyloid burden in the brain.

The synthesis of 18F-AV45 is based on a nucleophilic substitution reaction similar to that of [18F]FDG synthesis, followed by an acid hydrolysis (Fig. 10.11a) [50]. Briefly, *nca* [18F] fluoride was extracted using Accel Plus QMA cartridge, and then eluted a 1 mL mixture of

Fig. 10.10 Synthesis of [18F]FACBC

a

Precursor (2)   [18F]Florbetapir

b

Precursor (1)
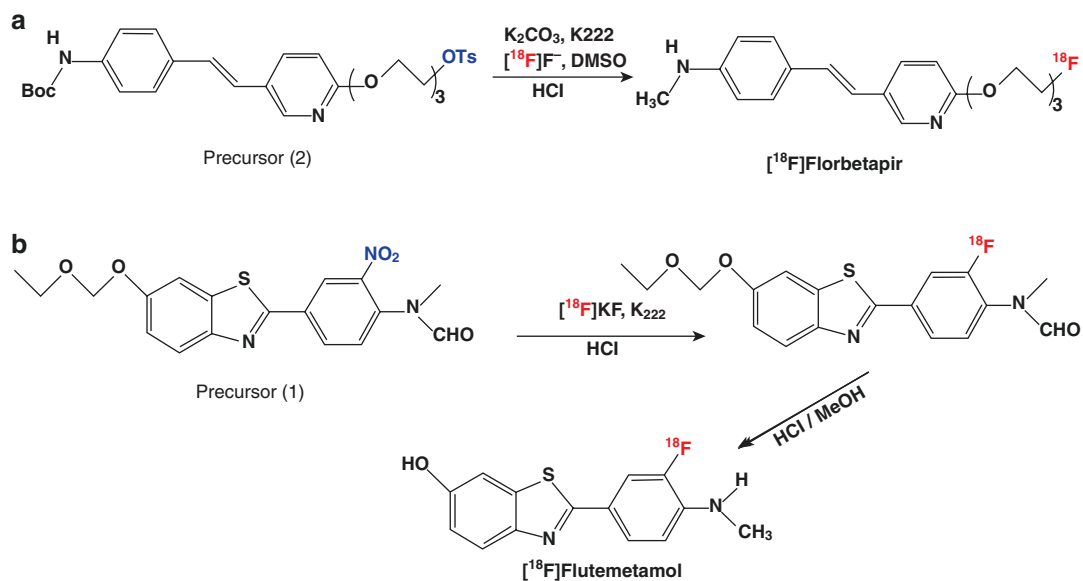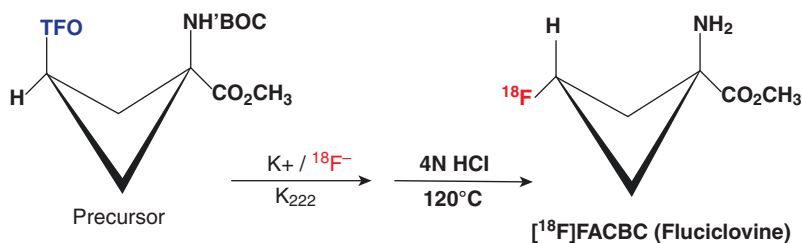
[18F]Flutemetamol

Fig. 10.11 Synthesis of [18F]Florbetapir (**a**) and [18F]Flutemetamol (**b**) involves nucleophilic substitution reactions
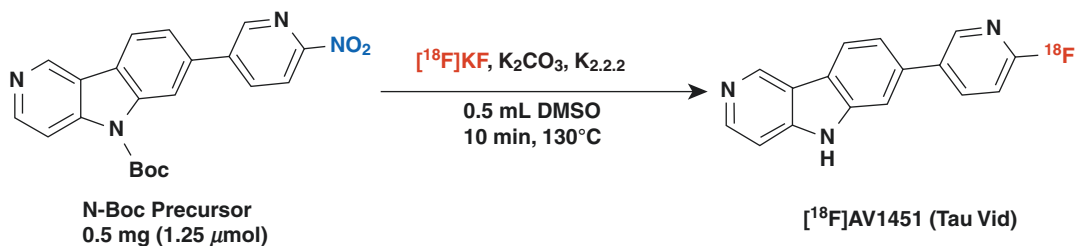
Fig. 10.12 Synthesis of [^{18}F]AV1451

K$_2$CO$_3$ (3.6 mg)/K222 (7.1 mg) in a solution of acetonitrile/water. Following azeotropic drying, the dry [^{18}F]fluoride was reacted with the 1 mg of precursor (AV-105) in DMSO and heated for 10 min at 130 °C. Following alkaline hydrolysis, sepPak, and HPLC purification the final drug product 18F-AV-45 was prepared in saline containing sodium ascorbate.

The ^{11}C-labeled Pittsburgh compound B (^{11}C) PiB), a neutral derivative of thioflavin-T (termed benzothiazole-aniline or BTA derivative), is the most commonly used PET tracer for the detection of Aβ plaques in many research investigations. But the short half-life of ^{11}C restricts the use of this tracer for commercial distribution. ^{18}F-labeled PiB derivative, 3'-F-PiB, is also known as GE-067 and Flutemetamol [52]. The general synthetic route involves nucleophilic substitution of a nitro group in the precursor (AH111907) by [^{18}F]fluoride followed by deprotection (Fig. 10.11b) [53]. However, the physicochemical similarity of the product to its deprotected precursor requires the use of HPLC to obtain the required purification. Sodium methoxide reacts selectively with the nitro-containing precursor to give species which are much more polar than flutemetamol. Flutemetamol was separated from these polar species using 2 reverse phase and 1 normal phase SPE cartridges [54].

10.2.4.8   AV-1451 (Flortaucipir, TauvidTM)

In May 2020, the FDA approved flortaucipir, also called [^{18}F]AV-1451 or [^{18}F]T807], as the first PET drug to image the presence of tau tangles, one of the hallmarks of Alzheimer's disease [55].

The synthesis of [^{18}F]AV1451 (Fig. 10.12) is based on AV1451 N-Boc nitro-precursor and nucleophilic fluorination (Fig. 10.12) [56]. The precursor in DMSO (0.5 mg in 500 μL) was added to the dried [^{18}F]fluoride and was heated to 130 °C with stirring for 10 min. Subsequently, the reaction mixture was cooled, diluted with HPLC mobile phase, and purified by semi-preparative HPLC. The product peak (tR = 21–22 min) was collected into the dilution flask and diluted with 50 mL of sterile water. The resulting solution was passed through an Oasis HLB cartridge, which was then washed with 10 mL of sterile water. [^{18}F]AV1451 was eluted with 0.5 mL of EtOH and collected in the Tracerlab FXFN product vial, containing 3 mL of saline. The sepPak was washed with 6.5 mL of saline to bring the final formulation volume to 10 mL. The final sterile drug product was obtained following 0.22 μm membrane filtration.

10.2.4.9   DCFPyL (Pylarify)

In May 2021, the FDA approved the ^{18}F-labeled prostate-specific membrane antigen (PSMA)–targeted positron emission tomography (PET) imaging agent ^{18}F-DCFPyL (Pylarify), a small molecule PSMA inhibitor for use in prostate cancer [57]. The development of PSMA inhibitors has been mainly based on the Lys-urea-Glu (KuE) core as binding motif (Chap. 22). The investigators at John Hopkins reported the first synthesis of this tracer [58]. [^{18}F]DCFPyL was synthesized in two steps from the p-methoxybenzyl (PMB) protected lys-C(O)-glu urea precursor using 6-[^{18}F]fluoro-nicotinic acid tetrafluorophenyl ester ([^{18}F]F-Py-TFP) for the fluorination reaction. Subsequently, a revised procedure was developed using a pros-
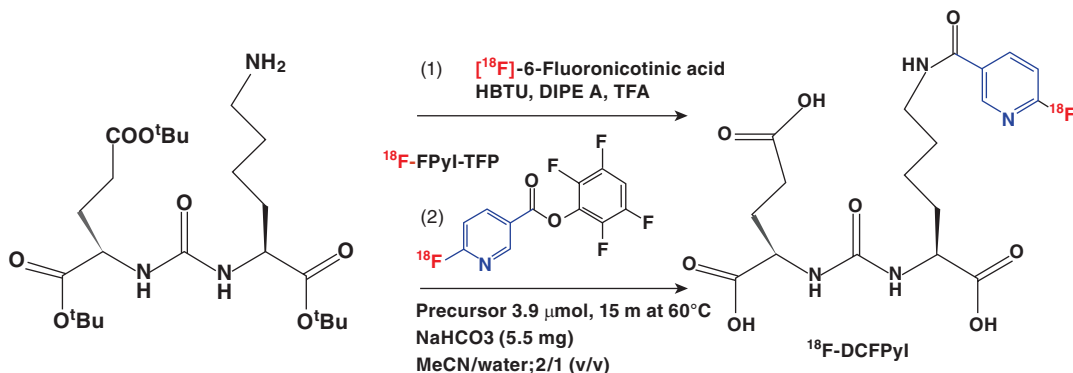
Fig. 10.13 Synthesis of [18F]DCFPyl

thetic group [18F]FPYL-TFP as the fluorinating agent [59, 60]; et al. 2017). The [18F]F-labeled prosthetic group, 2,3,5,6-tetrafluorophenyl-6-[18F]fluoronicotinate (18F-FPyL-TEP) [61] was synthesized and purified by solid-phase extraction, followed by coupling to (S)-di-tert-butyl 2-(3-((S)-6-amino-1-(tertbutoxy)-1-oxohexan-2-yL)ureido)pentanedioate formate salt and acid hydrolysis to afford [18F]DCFPyL The synthesis of 18F-DCFPyL based on these two methods is shown in Fig. 10.13.

10.2.5   Radiotracers Based on Electrophilic Reaction

10.2.5.1   Synthesis of 6-[18F]Fluoro-L-DOPA (FDOPA)

The first 18F-labeled analog of L-DOPA was 5-[18F] Fluoro-DOPA [62]. The metabolism of this tracer, however, was accelerated because the fluorine atom was close to the hydroxyl groups of FDOPA. Consequently, 6-[18F]Fluoro-L-DOPA was developed, and the first FDOPA-PET brain imaging was performed to visualize the dopaminergic neurons in the basal ganglia [63]. A number of methods have been developed to synthesize FDOPA [64–67]. The organic precursor is an aryl-substituted trialkyl tin derivative in which the trimethylstannyl group (Sn(CH3)3) is replaced by the 18F atom. The electrophilic radiofluorination by destannylation of FDOPA precursor has emerged as the preparation method of choice and has been used by many groups, employing a custom-built apparatus or a commercial PC-controlled auto-

mated synthesis module. Fluorination of the precursor (Fig. 10.14a) in freon solvent can be performed using [18F]F2 gas directly or acetylhypofluorite reagent, [18F]CH3COOF. Finally, following acidic removal (deprotection) of the protective groups using HBr or HCl, [18F]FDOPA can be generated. HPLC purification is required to achieve high chemical and radiochemical purity. The final-decay corrected yields are typically 20–30% and the SA is about 37 GBq μmol^{-1} (1.0 Ci μmol^{-1}) at the EOS. Nucleophilic methods using the [18F]fluoride ion have been developed and may have the potential to provide a higher yield and a higher SA.

Similarly, the synthesis of [18F]fluoro-meta-tyrosine (FMT) [68] and [18F]β-CFT [69] have been developed using fluorodemetallation reactions. In general, electrophilic fluorination reactions produce low SA (<30 mCi μmole^{-1}) PET radiopharmaceuticals.

Given that radioactive fluoride ([18F]F$^-$) can be produced in multi-curie amounts, nucleophilic radiosynthesis of [18F]FDOPA using [18F]F$^-$ is desired to reach large amount of radioactivity with high molar activity. For conventional nucleophilic aromatic substitution (SNAr) synthesis of [18F] FDOPA requires the existence of strong electron-withdrawing groups in the ortho- or para-positions of the aromatic structure and an appropriate leaving group [70, 71]. Nucleophilic synthesis using (S)-3-(5-formyl-4-methoxymethoxy-2-nitro-phenyl)-2-(trityl-amino)-propionic acid tert-butyl ester (precursor) can be performed as shown in Fig. 10.14b.

a Electrophilic Synthesis

[¹⁸F]FDOPA

b Nucleophilic synthesis
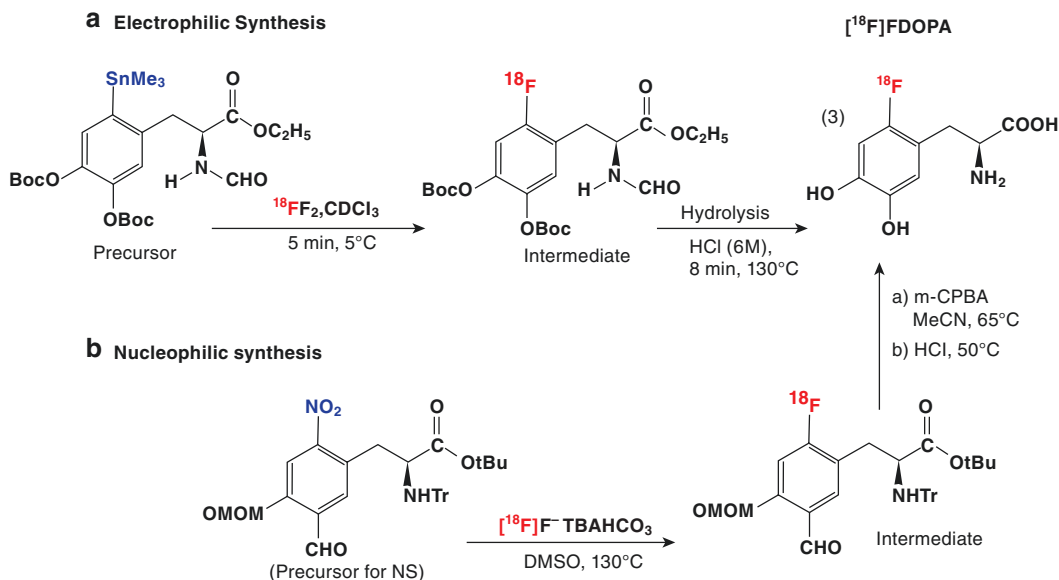
Fig. 10.14 (**a**) Electrophilic Synthesis of 6-[¹⁸F]fluoro-L-FDOPA (FDOPA). The precursor is an aryl-substituted trialkyl tin derivative, known as Triboc-L-Dopa ethyl ester. The fluorinated intermediate upon hydrolysis will produce [¹⁸F]FDOPA. (**b**) Nucleophilic synthesis using [¹⁸F]Fluoride.

The precursor is (S)-3-(5-formyl-4-methoxymethoxy-2-nitro-phenyl)-2-(trityl-amino)-propionic acid tert-butyl ester (Precursor for NS). Following reaction with fluoride and upon hydrolysis of the intermediate with meta-chloroperoxybenzoic acid (mCPBA), [¹⁸F]FDOPA can be obtained

10.2.6 F-18 Labeling of Peptides and Biomolecules

¹⁸F has the ideal half-life and a unique and diverse chemistry for labeling of peptides and biomolecules. Fluorination of peptides may be conducted by direct methods or indirect methods. Direct methods are those in which the ¹⁸F-fluoride is reacted directly with the peptide, which may have been previously modified to facilitate radiolabeling, and only subsequent purification is required to obtain the final product. Indirect methods require the prior radiosynthesis of a prosthetic group (PG) and subsequent bioconjugation to peptide that has been modified for site-specific reaction [6, 11, 18, 72].

Several successful attempts to introduce ¹⁸F directly into small peptides have been reported in the literature [73]. Direct substitution methods, however, usually require some non-physiological conditions of pH or temperature and most peptides do not tolerate such conditions and may undergo hydrolysis. The use of PGs for

the direct ¹⁸F-labelling of peptides was first reported based on trimethylammonium-substituted modified peptides. This methodology has demonstrated usefulness toward direct ¹⁸F-fluorination of peptides containing histidine, tryptophan, lysine, and arginine residues without the need of protecting groups [6]. Several new strategies for direct ¹⁸F labeling have also been developed, recently. An elegant site-selective C–H ¹⁸F-fluorination of leucine residue within peptide using [¹⁸F]-N-fluorobenzenesulfonimide ([¹⁸F]NFSI) showed that a combination of photoactivated sodium decatungstate and ([¹⁸F]NFSI effects site-selective ¹⁸F-fluorination at the branched position, in leucine residues, in unprotected and unaltered native peptides [74]. A method to introduce a 4-[¹⁸F]fluorophenylalanine residue into peptide sequences by chemo selective radiodeoxyfluorination of a tyrosine residue can label small peptides by formally replacing a single hydrogen, the para-hydrogen atom in Phenylalanine residue with [¹⁸F]fluoride [75].

In the indirect labeling methods, the peptides are attached to the PGs mostly through amine- or thiol-reactive groups via acylation, alkylation, amidation, imidation, oxime, hydrazone formation, or using click chemistry [11]. Selected examples of prosthetic groups (Fig. 10.15) include N-(hydroxysuccinimidyl)-[^{18}F]fluorobenzoate [^{18}F]SFB, [^{18}F]fluoroben-

zoic acid [^{18}F]FBA, [^{18}F]FBAM, and [^{18}F] FBEM. The choice of prosthetic group, however, is critical for radiotracer development, as it may adversely alter the physical and physiological characteristics of the labeled molecule. Several examples of radiofluorination techniques based on substitution or addition reactions are shown in Fig. 10.16.
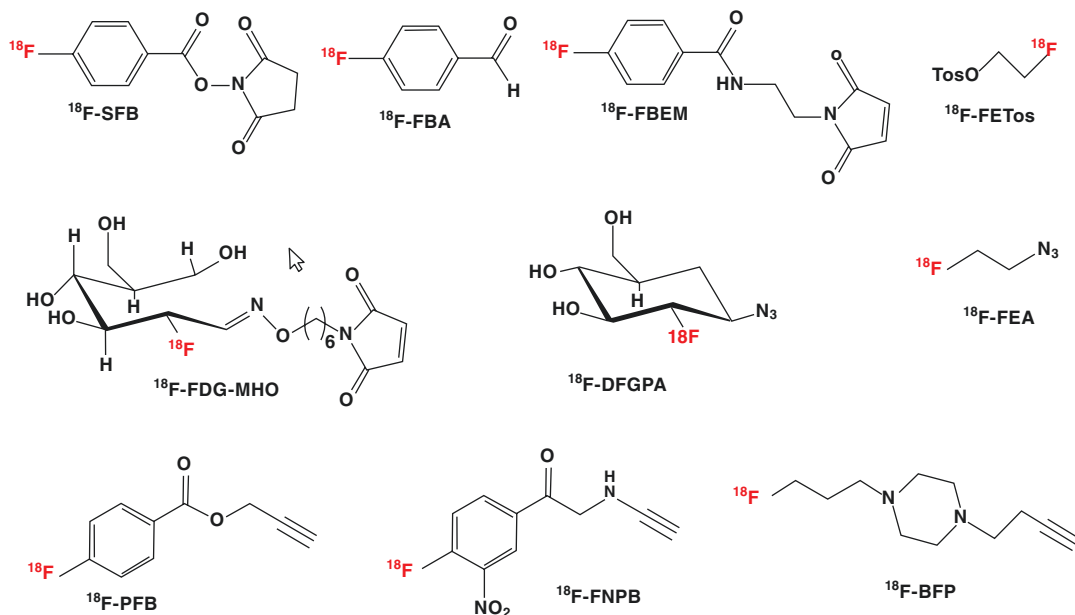
Fig. 10.15 ^{18}F-labeled prosthetic groups (PG) commonly used for the preparation of ^{18}F-labeled radiopharmaceuticals

Fig. 10.16 Examples of radiofluorination techniques based on substitution or addition reactions commonly used in the synthesis of ^{18}F-labeled peptides. Isotope exchange (**a**), click chemistry (**b**), and Fluorinate prosthetic group (**c**)
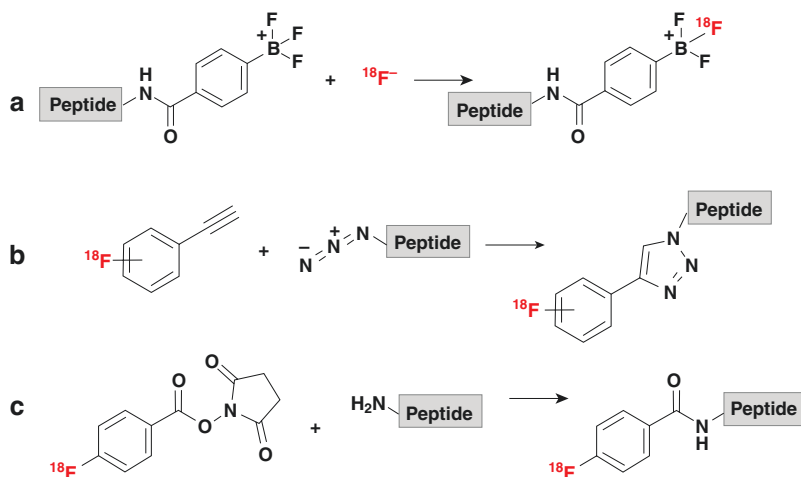
10.2.6.1   Click Chemistry for ¹⁸F Labeling

Click chemistry was introduced in 2001 to describe Cu(I)-catalyzed formation of 1,2,3-triazole by Huisgen's [2 + 3] cycloaddition of terminal alkynes and azides [76]. These reactions include certain characteristics such as high yields and broad substrate scope, and tolerance of air, and moisture [77, 78]. In 2006, ¹⁸F-labeled peptides were prepared based on copper-catalyzed azide-alkyne cycloaddition (CuAAC) [79]. 2-[¹⁸F]fluoroethylazide ([¹⁸F]FEA (Fig. 10.15) despite the difficult handling of volatile [1⁸F]FEA, is convenient for labeling using automated synthesis modules. Hence, FEA is the most popular ¹⁸F-prosthetic group used in click chemistry for the preparation of various radiotracers and biomolecules [77]. Since copper is known to be toxic, copper-free click (CFC) reaction was developed, which was referred to as strain-promoted azide-alkyne cycloaddition (SPAAC) [80]. As an alternative to SPAAC reaction, another click ligation method, known as the inverse electron demand [4 + 2] Diels-Alder (IEDDA) cycloaddition between a 1,2,4,5-tetrazine and strained alkene dienophile, was also developed [81]. Several PGs used in click chemistry are shown in Fig. 10.15. Radiosynthesis of ¹⁸F-galacto-RGD peptide using the click reaction is shown in Fig. 10.17.

10.2.6.2   ¹⁸F Labeling Based on [¹⁸F] AlF²⁺ Cation

Since fluorine was known to bind and form stable complexes with many metals, a successful method was developed to form a stable NOTA Al − ¹⁸F complex of a peptide conjugated with macrocyclic chelators (such as NOTA) [82]. This labeling methodology has been used by several groups for the labeling of small molecules, peptides, and proteins using several acyclic and macrocyclic chelators (Fig. 10.18) [9, 11, 84]. The Al-[¹⁸F]fluoride ([¹⁸F]AlF) radiolabeling method combines the favorable decay characteristics of ¹⁸F with the convenience and familiarity of metal-based radiochemistry. This method has been used to parallel ⁶⁸Ga radiopharmaceutical developments. As such, the [¹⁸F]AlF method is popular and widely implemented in the development of radiopharmaceuticals for the clinic [83].

In the last ten years, the heteroatom-based ¹⁸F methodologies, click chemistry, and the Al-based ¹⁸F radiochemistry have grown substantially. The [¹⁸F]AlF method has benefited from the application of new macrocyclic chelating moieties. The use of these methods to label peptide probes is becoming more common, with many performing well in clinical trials. The simplicity and practicality of these methods represent a major advantage over the
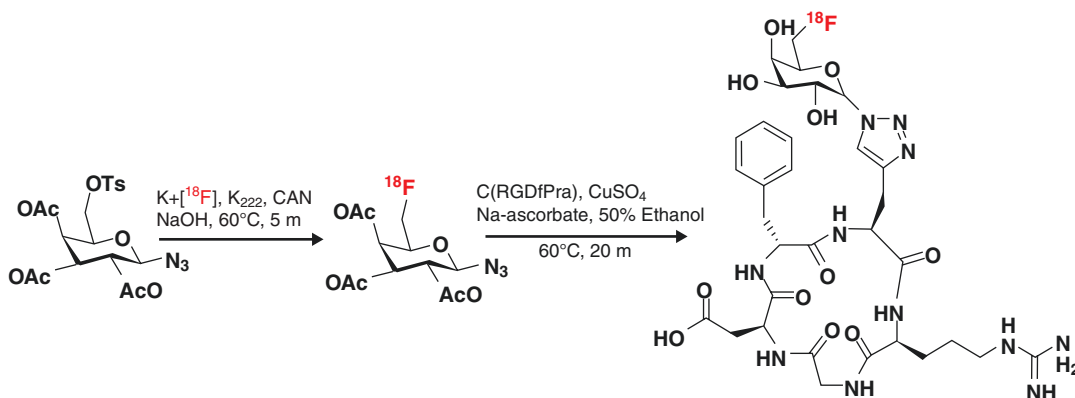
Fig. 10.17   Synthesis of ¹⁸F-galacto-RGD peptide using the click reaction
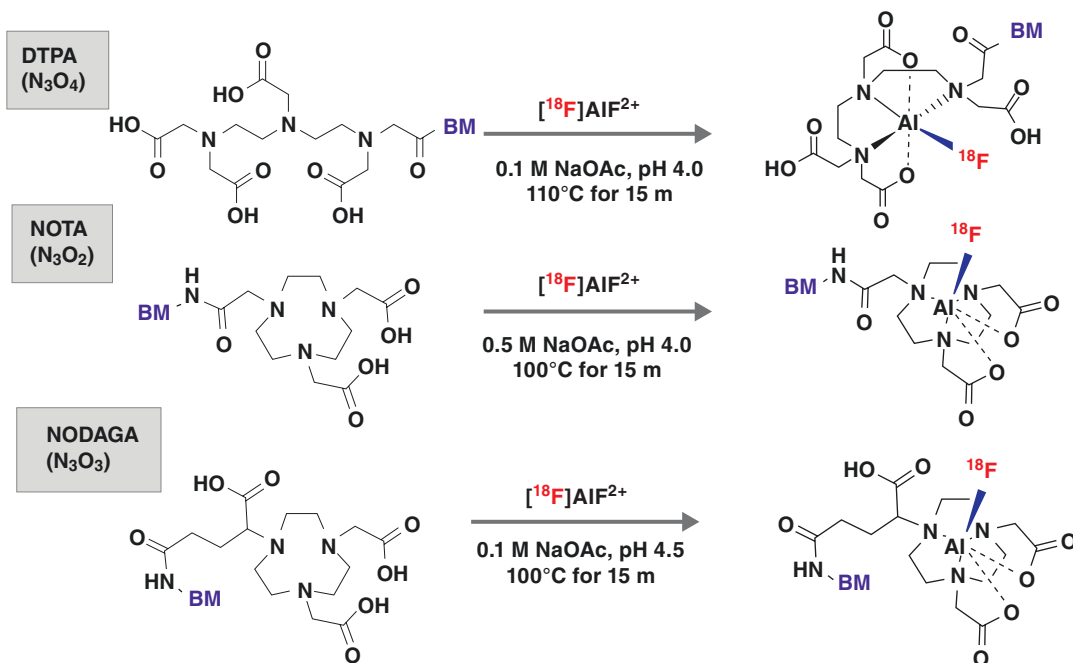
Fig. 10.18 ^{18}F labeling of peptides or biomolecules (BM) using aluminum-fluoride method [18F]AlF. (Figure modified from [83])

classical carbon-fluorine bond formation reactions, and they may soon be used to create compounds to replace some standard clinical tracers used for PET imaging [8].

10.3 Radioiodinated Radiopharmaceuticals

Among the radioisotopes of iodine, ^{123}I, [124]I, and ^{131}I have physical characteristics suitable for developing molecular imaging radiopharmaceuticals for both PET and SPECT (Table 10.2). Since ^{131}I decays by β^- emission, it is predominantly useful for radionuclide therapy. However, the abundant 364 KeV γ emissions and relatively longer half-life (8.025 days) of ^{131}I do offer certain advantages in developing certain radiotracers with relatively longer biological clearance, such as monoclonal antibodies. However, the β^+ emitter [124]I with a moderate half-life (4.2 days) may be more appropriate for developing radioiodin-

ated antibodies as imaging probes based on PET. Several important and clinically useful radioiodinated molecular imaging agents are summarized in Table 10.6.

10.3.1 Production of ^{123}I and [124]I

Depending on the target material and the proton energy used in the cyclotron, several nuclear reactions can be utilized to produce ^{123}I, as shown below.

Currently, the best source of ^{123}I, having the least contamination with other radioiodides, is the proton bombardment of highly enriched [124]Xe. Based on this method, high purity, no-carrier-added (nca) [123]I can be produced with high SA (8695 GBq mmol^{-1}), suitable for preparing receptor-binding radiopharmaceuticals [85]. The reaction, (*p*,5 *n*) using natural iodine target also produces high SA ^{123}I but requires 69–70 MeV protons.

Table 10.6 ^{123}I-labeled PET radiopharmaceuticals of clinical interest

Radioiodinated compound	Biological process	
[131I]MIBG sulfate (*low specific activity*)	Imaging of adrenal tumors	1994[a]
[123I]MIBG (Adreview)	For the detection of primary or metastatic pheochromocytoma or neuroblastoma	2008[a]
[131I]MIBG (Iobenguane, Azedra) (*high specific activity*)	Pheochromocytoma, Paraganglioma. NETs	2018[a]
[123I]Ioflupane (FP-CIT, DaTSCAN)	For brain DaT visualization in patients with suspected Parkinsonian syndromes (PS)	2011[a]
123I-IBZM	Dopamine D_2 receptors	
123I-Iomezenil	Central benzodiazepine receptors	
123I-β-CIT	Brain dopamine transporters (DaT)	
123I-BMIPP	Myocardial free fatty acid metabolism	
123I-Iodo-α-methyltyrosine	Brain amino acid transport	

[a]FDA-approved radiopharmaceuticals

$$^{124}Te\left(p,2n\right)^{123}\text{I}$$

$$^{124}Xe\left(p,2p\right)^{123}\text{I}$$

$$^{124}Xe\left(p,pn\right)^{123}Xe_{\left(T\frac{1}{2}=2.08\text{h}\right)} \rightarrow^{123}\text{I}$$

$$^{124}Xe\left(p,pn\right)^{123}Cs_{\left(T\frac{1}{2}=5.9\min\right)} \rightarrow^{123}Xe_{\left(T\frac{1}{2}=2.08\text{h}\right)} \rightarrow^{123}\text{I}$$

$$^{127}\text{I}\left(p,5n\right)^{123}Xe_{\left(T\frac{1}{2}=2.08\text{h}\right)} \rightarrow^{123}\text{I}$$
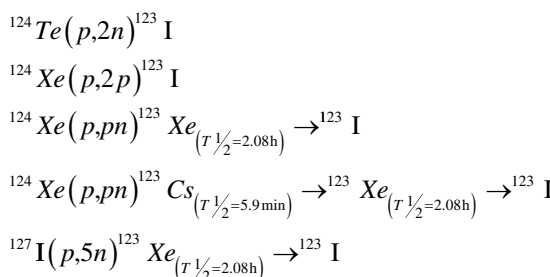
The most common method used for ^{124}I production is based on the reaction ^{124}Te$(p,n)^{124}$I using enriched ^{124}Te and low energy <15 MeV protons. [86]. The solid target material consists of a solid solution matrix containing aluminum oxide and enriched ^{124}Te oxide. [^{124}I]iodide is recovered from the target using dry distillation. The volatile radioiodine is trapped on a thin pyrex glass tube coated with a small amount of sodium hydroxide. The SA of ^{124}I is typically around 150 mCi/μg^{-1}.

10.3.2 Chemistry of Iodine and Radioiodination

Iodine (I_2) sublimes at atmospheric pressure and temperature, resulting in a blue-violet gas with an irritating odor. Iodine occurs in nature mostly in the form of salts or iodides of sodium and potassium. Iodine exists as a diatomic molecule, I_2, in its elemental state, and unlike fluorine, can also

exist in several oxidation states. Several iodine oxides (such as I_2O_4, I_4O_9, I_2O_7, I_2O_5) do exist in nature but, readily decompose to iodine and oxygen at high temperatures. Iodine dissolves readily in nonpolar solvents, such as chloroform and carbon tetrachloride but, is only slightly soluble in water. Elemental iodine (I_2) is where two iodine atoms share a pair of electrons to achieve a stable octet for themselves. The iodide anion (I^-), is the strongest reducing agent among the stable halogens, being the most easily oxidized back to diatomic I_2.

The free molecular iodine (I_2) has the structure of I^+–I^- in aqueous solution. However, the electrophilic species (I^+) does not exist as a free species but, forms complexes with nucleophilic entities such as water or pyridine. The reactions with water can be written as follows:

$$I_2 + H_2O \rightarrow H_2OI^+ + I^- \quad (10.1)$$

$$I_2 + OH^- \rightarrow HOI + I^- \quad (10.2)$$

$$3I_2 + 6OH^- \rightarrow 5I^- + OI_3^- + 3H_2O \quad (10.3)$$

The hydrated iodonium ion, H_2OI^+, and the hypoiodous acid, HOI, are believed to be highly reactive electrophilic species. In an iodination reaction (Fig. 10.19), radioiodination occurs by (a) electrophilic substitution of a hydrogen ion in a molecule of interest by a radio-iodonium ion or (b) nucleophilic substitution (isotope exchange), where a stable iodine atom that is already present

Fig. 10.19 Electrophilic and nucleophilic radioiodination reactions

Electrophilic Radioiodination
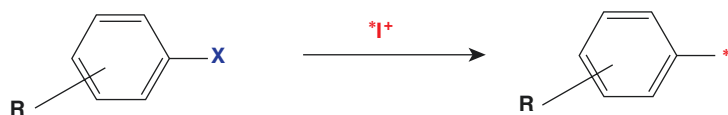
where X = H, HgCl, T1(OCOCF$_3$)$_2$, Sn(CH$_3$)$_3$, Si(CH$_3$)$_3$

Nucleophilic Radioiodination
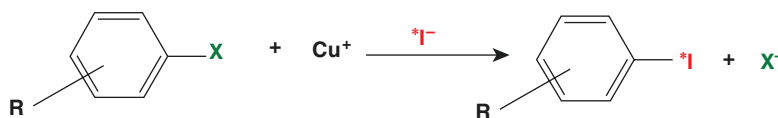
where X = I, Br

in the molecule is exchanged with a radioactive iodine atom.

The advantages and disadvantages of different radioiodination techniques have been reviewed extensively [85, 87–89]. In the preparation of radioiodinated compounds, the radioiodine is preferentially attached to a carbon atom, in a vinylic or aromatic moiety, in which the C-I bond strength is relatively high compared to aliphatic C-I bond. Since radioiodine isotopes (^{123}I, [124]I, and ^{131}I) are produced in iodide form, early methods have involved nucleophilic substitution reactions, such as the use of high temperature and solid-state halogen exchange reactions. Alternatively, radioactive iodide can be oxidized to iodine or iodine monochloride and used in electrophilic substitution reactions, such as the iododestannylation of aryltin compounds.

10.3.2.1 Electrophilic Substitution Reaction

The electrophilic species (HO*I, H$_2$O*I) generated from the radioiodide and the oxidant react directly with the aromatic moiety of the compound to be labeled. The aromatic amino acids tyrosine and histidine are the sites of iodination in protein molecules [90, 91]. With tyrosine substitution of a hydrogen ion with the reactive iodonium ion occurs *ortho-* to the phenolic hydroxyl group. With histidine, substitution occurs at the second position of the imidazole ring. Electrophilic substitutions can often be performed quickly on a nonderivatized substrate under mild reaction conditions.

The most frequently used oxidizing agents (Fig. 10.20) are peracetic acid and the *N*-chloro compounds, such as chloramine-T, iodogen, and succinimides. The *N*-chloro compounds are the most popular oxidants; however, their relatively strong oxidizing properties often induce by-products. To limit these oxidative side reactions, chloramine-T is immobilized on spherical polystyrene particles (iodobeads), while iodogen, which contains four functional chlorine atoms, is coated as a thin layer on the walls of a reaction vessel. Of the two immobilized oxidants, which are mostly used for protein labeling, iodogen is the best to prevent loss of immunoreactivity [92]. For the labeling of small organic molecules, peracetic acid is also often preferred due to its mild oxidizing properties.

The enzyme lactoperoxidase from bovine milk is also an effective oxidant for iodide oxidation and the radioiodination of proteins. In the presence of minute quantities of hydrogen peroxide (H$_2$O$_2$), lactoperoxidase oxidizes and binds radioiodide to proteins in the reaction mixture. The pH optimum of iodide oxidation by lactoperoxidase is 4–8.5, with an optimum at pH 5. The reaction is extremely rapid under very mild conditions and the denaturation of proteins is low. The separation of lactoperoxidase from the labeled protein may be avoided by using the immobilized enzyme [93]. This technique applies

Fig. 10.20 Oxidizing agents commonly used in radioiodination reactions
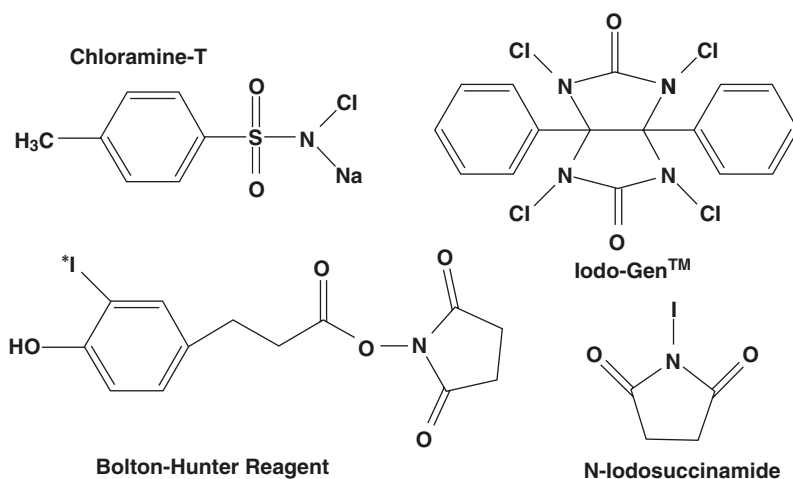
immobilized lactoperoxidase together with glucose oxidase, which produces H_2O_2 in the presence of glucose.

Proteins lacking tyrosine amino acid residues or proteins sensitive against the denaturing influence of oxidizing agents are indirectly radioiodinated via amide bond formation at lysine residues using Bolton and Hunter reagent [90]. A prosthetic group for radioiodination contains an aromatic moiety, like tyrosine, which can be iodinated and covalently attached to the lysine moiety in the protein under milder conditions than those found in direct radioiodinations.

The addition of one radioiodine atom to large molecules such as antibodies does not usually affect their immunoreactivity. The labeling process using oxidation agents as well as the addition of reducing agents to stop the labeling reaction may have destructive effects on sensitive sites of the biomolecules. Depending on the labeling conditions, denaturation can occur due to oligomerization, conformational changes due to the changes of functional groups, or the cleavage of disulfide bonds. Consequently, labeling reactions must be adapted and optimized to the individual proteins or peptides, including proof of functional integrity.

10.3.2.2 Nucleophilic Substitution Reaction

Direct replacement of stable iodine isotopes on organic molecules by a radioiodine, also called isotopic exchange, is a well-known radioiodination method. The reaction is usually performed with the radioiodide ion at very high temperature and most often in the presence of sulfate salts and oxidants, such as oxygen from the air. The method of choice in nucleophilic radioiodination is the well-established Cu(I)-catalyzed halogen–halogen exchange reaction in an acidic, aqueous medium (Fig. 10.19). The exchange reaction can be either isotopic (*I/I) or non-isotopic (*I/Br), which specifically enables the synthesis of a high SA radiopharmaceuticals [94]. A nucleophilic exchange can be successfully applied on activated (presence of electron-deficient substituents, e.g., carbonyl group) or nonactivated (e.g., alkyl group) aromatic compounds. However, in organic media, electron-donating substituents are also well tolerated. The purity, labeling yield, and SA can be controlled by carefully optimizing the concentration of copper and the precursor.

10.3.3 $^{123/131}$I-Labeled Radiopharmaceuticals

In the last four decades, several $^{123/131}$I-labeled small molecules, peptides, and mAbs were developed as radiopharmaceuticals for imaging and TRT ([95, 96]. However, [^{123}I]Iobenguane (Adreview) and [^{123}I]Ioflupane (DaTSCAN) are the only two radiopharmaceuticals that received FDA approval for planar/SPECT imaging studies.

[^{131}I]Iobenguane (MIBG sulfate) was approved also as an imaging agent in 1994. More recently, [^{131}I]Iobenguane I-131 injection (AZEDRA®), with a higher specific activity, was approved as an imaging and therapeutic agent.

10.3.3.1 Synthesis of [^{131}I]MIBG (Iobenguane)

The drug substance iobenguane I-131 is a substituted benzylguanidine with I-131 in the meta position of the benzene ring. Iobenguane I-131 is also described as [^{131}I]meta-iodobenzylguanidine (MIBG). specific activity of ~2500 mCi/mg (92,500 MBq/mg).

The synthesis of [^{131}I]MIBG (Fig. 10.21a) was first developed based on the radioiodide exchange reaction [97, 98]. The SA of ^{131}I-MIBG based on this method is typically <400 MBq/µmole^{-1}). Subsequently, several radioiodination methods were developed to increase the specific activity [99]. High SA [^{131}I]MIBG for therapy was produced using the Ultratrace solid-phase electrophilic substitution reaction method [100]. The Ultratrace process uses a solid polystyrene resin containing the covalently bound stannylbenzylguanidine precursor, which undergoes a 1:1 displacement reaction with radioiodine (Fig. 10.21b). Briefly, the solid-phase precursor
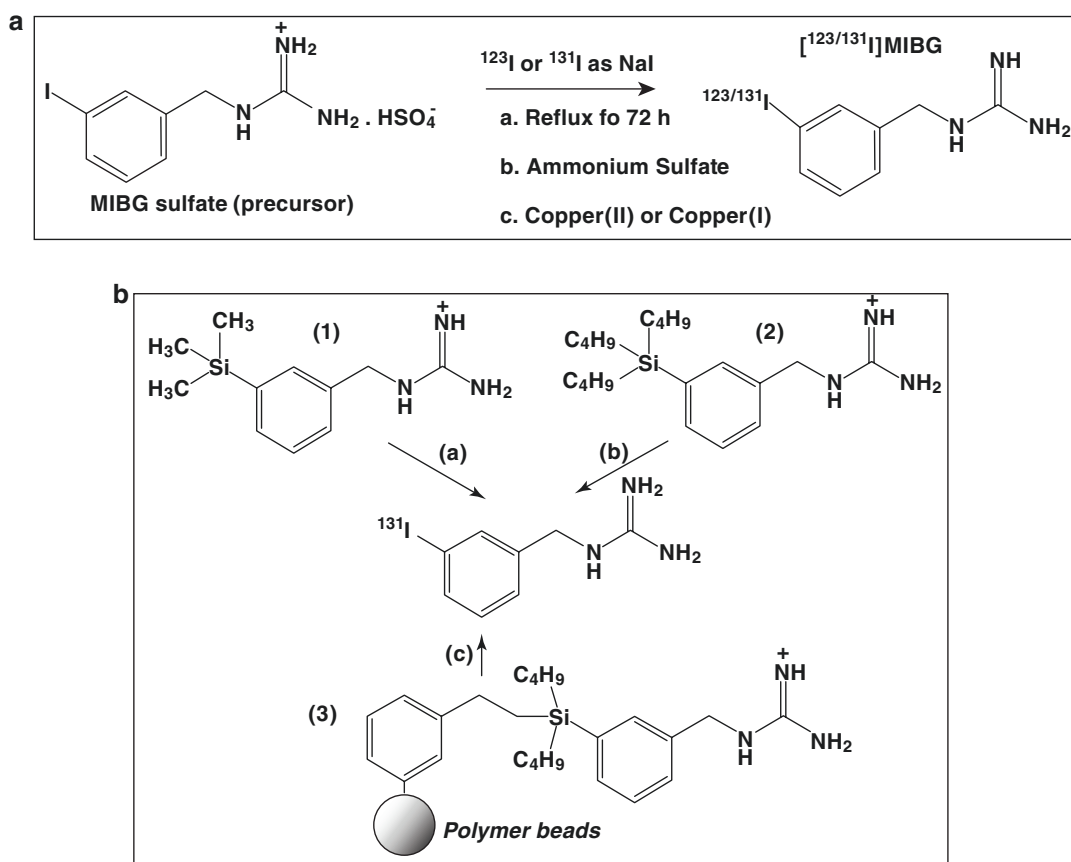
Fig. 10.21 Synthesis of [^{131}I]MIBG: Nucleophilic radioiodination or radioiodide exchange reaction (**a**) using catalysts such as ammonium sulfate or copper ions results in low-specific activity MIBG. Electrophilic radioiodination in the presence of an oxidizing agent to synthesize high-specific activity MIBG (**b**) was based on a trimethylsilicontin BG precursor (1), tri-butylsilicontin BG precursor (2) or di-butylsilicontin BG precursor (3) attached to a polymer
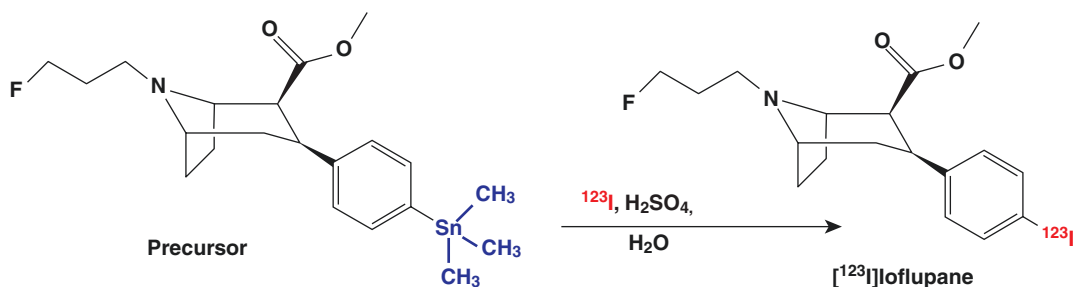
Fig. 10.22 Synthesis of [^{123}I]Ioflupane (FP-CIT) iodo-destannylation of the trimethyl-stannyl precursor

is suspended in a dilute mixture of radioactive ^{131}I-sodium iodide, H_2O_2/HOAc at 25 °C for 60 min. The oxidized ^{131}I-iodine reacts to disrupt the covalent bond between the tin and benzylguanidine (BG) precursor with radioiodine insertion at the *meta* position of the phenyl ring to form [^{131}I]MIBG, which simultaneously cleaves from the resin and dissolves into the liquid phase. The labeled [^{131}I]MIBG is then purified by using cation exchange cartridge. The formulated final product solution is membrane filtered and aseptically filled into 30-mL glass vials, which are then aseptically capped, sealed, and frozen. The RCP of the drug product is >97% and the minimum SA is about 1650 mCi/mg or 460 mCi/μmol.

10.3.3.2   Synthesis of [^{123}I]Ioflupane

The dopamine transporter (DaT) imaging provides an objective tool for the assessment of dopaminergic function of presynaptic terminals which is valuable for the differential diagnosis of Parkinsonian disorders related to a striatal dopaminergic deficiency from movement disorders not related to a striatal dopaminergic deficiency. DAT imaging with [^{123}I]Ioflupane SPECT can be used to confirm or exclude a diagnosis of dopamine-deficient parkinsonism in cases where the diagnosis is unclear. The synthesis [^{123}I] β-CIT-FP (Ioflupane) was prepared as previously described for the synthesis of [^{123}I]β-CIT by iodo-destannylation of the trimethyl-stannyl precursor with ^{123}I sodium iodide in the presence of peracetic acid at pH 3–4 and purified by HPLC (Fig. 10.22) [101].

10.3.3.3   Synthesis of Radioiodinated Peptides

The overexpression of peptide receptors in certain tumors as compared to endogenous expression levels represents the molecular basis for the design of peptide-based tools for targeted nuclear imaging and therapy. Recent developments and synthetic methods have been reviewed [102]. ^{125}I-labeled peptides are routinely used in preclinical studies and autoradiography studies to determine receptor expression and density. ^{124}I and ^{131}I nuclides are a perfect theranostic pair for the development of radiopharmaceuticals. Targeting somatostatin (SST) receptor, the vasoactive intestinal peptide receptor (VPAC-1), and the αvβ3 integrin receptor are some of the major areas of iodinated tracer development. However, none of them has been approved as a radiopharmaceutical, thus far but, radioiodinated biomolecules have a significant potential as targeted radiopharmaceuticals.

References

1. Blau M, Nagler W, Bender MA. Fluorine-18: a new isotope for bone scanning. J Nucl Med. 1962;3:332.
2. Fowler JS, Finn RD, Lambrecht RM, Wolf AP. The synthesis of ^{18}F-5-fluorouracil. J Nucl Med. 1973;14:63–4.
3. Ido T, Wan CN, Casella VR, Fowler JS, et al. Labeled 2-deoxy-D-glucose analogs: ^{18}F labeled 2-deoxy-2-fluoro-D-glucose, 2-deoxy-2-fluoro-D--mannose and ^{14}C-2-deoxy-2-fluoro-D-glucose. J Label Compd Radiopharmacol. 1978;14:175–83.
4. Petroni D, Menichettii L, Poli M. Historical and radiopharmaceutical relevance of [^{18}F]FDG. J Radioanal Nucl Chem. 2020;323:1017–31.

5. Fowler JS. ^{18}F-FDG radiosynthesis: a landmark in the history of PET. J Nucl Med. 2020;61(12):105s–109s.

6. Ajenjo J, Destro G, Cornelissen B, Gouverneur V. Closing the gap between ^{19}F and ^{18}F chemistry. EJNMMI Radiopharm Chem. 2021;6:33.

7. Halder R, Ritter T. ^{18}F-fluorination: challenge and opportunity for organic chemists. J Org Chem. 2021;86(20):13873–13884.

8. IAEA. TECDOC-1968 production and quality control of Fluorine-18 labelled radiopharmaceuticals. Vienna: International Atomic Energy Agency; 2021. p. 2021.

9. Kumar K, Ghosh A. ^{18}F-AlF labeled peptide and protein conjugates as positron emission tomography imaging pharmaceuticals. Bioconjug Chem. 2018;29(4): 953–975.

10. Snell AH. A new radioactive isotope of fluorine, Minutes of the Pasadena Meeting. Phys Rev. 1937.

11. Jacobson O, Kiesewetter DO, Chen X. Fluorine-18 radiochemistry, labeling strategies and synthetic routes. Bioconjug Chem. 2015;26(1):1–18.

12. Kambali I, Parwanto, Suryanto H, et al. Dependence of 18F production yield and radioactive impurities on proton irradiation dose. Phys Res Int V. 2017;2017:2124383.

13. Kilbourn MR (1990) Fluorine-I8 labeling of radiopharmaceuticals. National Academy of Sciences, National Academy Press, Nuclear Science Series no. NAS-NS-3203.

14. Park BK, Kitteringham NR, O'Neill PM. Metabolism of fluorine-containing drugs. Annu Rev Pharmacol Toxicol. 2001;41:443–70.

15. Coenen HH, Elsinga P, Iwata R, et al. Fluorine-18 radiopharmaceuticals beyond [F-18]FDG for use in oncology and neurosciences. Nucl Med Biol. 2010;37(7):727–40.

16. Cole EL, Stewart MN, Littich R, et al. Radiosynthesis using fluorine-18: the art and science of late stage fluorination. Curr Top Med Chem. 2014;14(7):875–900.

17. Huang Y-Y. An overview of PET radiopharmaceuticals in clinical use: regulatory, quality and pharmacopeia monographs of the United States and Europe; 2018. https://doi.org/10.5772/intechopen.79227.

18. Richter S, Wuest F. ^{18}F-labeled peptides: the future is bright. Molecules. 2014;19:20536–20556.

19. Vallabhajosula S. ^{18}F-labeled PET radiopharmaceuticals in oncology: an overview of radiochemistry and mechanisms of tumor localization. Semin Nucl Med. 2007;37:400–419.

20. Nickels RJ, Daube ME, Ruth TJ. An oxygen target for the production of [^{18}F]F$_2$. Appl Radiat Isot. 1984;35:117.

21. Tan PZ, Baldwin RM, Tao FU, et al. Rapid synthesis of F-18 and H-2 dual-labeled altanserin. A metabolically resistant PET ligand for 5-HT1A receptors. J Label Compd Radiopharm. 1999;42:457–67.

22. Le Bars D, et al. High-yield radiosynthesis and preliminary in vivo evaluation of p-[^{18}F]MPPF, a fluoro analog of WAY-100635. J Nucl Med Biol. 1998;25(4):343–50.

23. Block D, Coenen HH, Stocklin G, et al. The NCA nucleophilic ^{18}F-fluorination of I,N-disubstituted alkanes as fluoroalkylation agents. J Label Compd Radiopharm. 1987;24:1029–42.

24. DeGrado TR, Baldwin SW, Wang S, et al. Synthesis and evaluation of ^{18}F-labeled choline analogs as oncologic PET tracers. J Nucl Med. 2001;42:1805–14.

25. Iwata R, Pascali C, Bogni A, et al. [^{18}F]Fluoromethyl triflate, a novel and reactive [^{18}F]fluoromethylating agent: preparation and application to the on-column preparation of [^{18}F]fluorocholine. Appl Radiat Isot. 2002;57:347–52.

26. Kamarainen EL, Kyllonen T, Airaksinen A, et al. Preparation of [^{18}F]CFT-FP and [^{11}C]CFT-FP, selective radioligands for visualization of the dopamine transporter using positron emission tomography (PET). J Label Compd Radiopharm. 2000;43:1235–44.

27. Couturier O, Luxen A, Chatal J-F, et al. Fluorinated tracers for imaging cancer with positron emission tomography. Eur J Nucl Med Mol Imaging. 2004;31:1182–206.

28. Shiue CY, Welch MJ. Update on PET radiopharmaceuticals: life beyond fluorodeoxyglucose. Radiol Clin N Am. 2004;42:1033–53.

29. Stocklin GL. Is there a future for clinical fluorine-18 radiopharmaceuticals (excluding FDG)? Eur J Nucl Med. 1998;25:1612–6.

30. Varagnolo L, Stokkel MPM, Mazzi U, et al. ^{18}F-labeled radiopharmaceuticals for PET in oncology, excluding FDG. Nucl Med Biol. 2000;27:103–112.

31. Hamacher K, et al. Efficient stereospecific synthesis of no-carrier added 2-[^{18}F]fluoro-2-deoxy-D-glucose using amino-polyether supported nucleophilic substitution. J Nucl Med. 1986;27:235–8.

32. Grierson JR, Shields AF. Radiosynthesis of 3′-Deoxy-3′-[^{18}F]fluoro thymidine: [^{18}F]FLT for imaging of cellular proliferation in vivo. Nucl Med Biol. 2000;27:143–56.

33. Martin SJ, Eisenbarth U, Wagner-Utermann U, et al. A new precursor for the radiosynthesis of [^{18}F] FLT. Nucl Med Biol. 2002;29:263–73.

34. Oh SJ, et al. High radiochemical yield synthesis of 3′-deoxy-3′-[^{18}F]Fluorothymidine using (5′-O-dimethoxytirtyl-2′-deoxy-3′-Onosyl-β-D-threo-pentofuranosyl)thymine and its 3-N-BOCprotected analogue as a labeling precursor. Nucl Med Biol. 2003;30:151–7.

35. Oh SJ, Mosdzianowski C, Chi DY, et al. Fully automated synthesis system of 3′-deoxy-3′-[^{18}F]fluorothymidine. Nucl Med Biol. 2004;31:803–9.

36. Suehiro M, Vallabhajosula S, Goldsmith SJ, et al. Investigation of the role of the base in the synthesis of [^{18}F] FLT. Appl Radiat Isot. 2007;65:1350–8.

37. Jerabeck PA, Patrick TB, Kilbourn MR, et al. Synthesis and biodistribution of [18F] labeled fluoronitroimidazoles: potential in vivo markers of hypoxic tissue. Int J Rad Appl Instrum A. 1986;37:599–605.

38. Grierson JR, Link JM, Mathis CA, et al. A radiosynthesis of fluorine-18 fluoromisonidazole. J Nucl Med. 1989;30:343–50.

39. Kamarainen EL, Kyllonen T, Nihtila O, et al. Preparation of fluorine-18-labeled fluoromisonidazole using different synthesis methods. J Label Compd Radiopharm. 2004;47:37–45.

40. Patt M, Kuntzsch M, Machulla HJ. Preparation of [18F] fluoromisonidazole by nucleophilic substitution on THP-protected precursor: yield dependence on reaction parameters. J Radioanal Nucl Chem. 1999;240:925–7.

41. Tang G, Wang M, Tang X, et al. Fully automated one-pot synthesis of [18F]fluoromisonidazole. Nucl Med Biol. 2005;32:553–8.

42. Katzenellenbogen JA. The quest for improving the management of breast cancer by functional imaging: the discovery and development of 16α-[18F]fluoroestradiol (FES), a PET radiotracer for the estrogen receptor, a historical review. Nucl Med Biol. 2021;92:24–37.

43. Kiesewetter DO, Kilbourn MR, Landvatter SW, et al. Preparation of four fluorine-18 labeled estrogens and their selective uptakes in target tissues of immature rats. J Nucl Med. 1984;25:1212–21.

44. Tewson TJ. Synthesis of 16α-fluoroestradiol using fluoride ion as a source of fluorine. J Nucl Med. 1983;24:P52.

45. Lim JL, Zheng L, Berridge MS, et al. The use of 3-methoxymethyl-16β, 17β-Epiestriol-O-cyclic sulfone as the precursor in the synthesis of F-l 8–16α-Fluoroestradiol. Nucl Med Biol. 1996;23:911–5.

46. Romer J, Fuchtner F, Steinbach J, et al. Automated production of 16α-[18F]fluoroestradiol for breast cancer imaging. Nucl Med Biol. 1999;26:473–9.

47. Hara T, Kosaka N, Kishi H. Development of [18F]-Fluoroethylcholine for cancer imaging with PET: synthesis, biochemistry, and prostate cancer imaging. J Nucl Med. 2002;43:187–99.

48. Tadino V, Kothari PJ, Vallabhajosula S, et al. [18F]-Fluoroalkylation using the "loop" system. J Nucl Med. 2004;45:P445.

49. Shoup TM, Olson J, Hoffman JM, et al. Synthesis and evaluation of [18F]1-Amino-3-fluorocyclobutane 1-carboxylic acid to image brain tumors. J Nucl Med. 1999;40(2):331–8.

50. Choi SR, Golding G, Zhuang Z, et al. Preclinical properties of [18F]-AV-45: a PET agent for a beta plaques in the brain. J Nucl Med. 2009;50:1887–94.

51. Stephenson KA, Chandra R, Zhuang ZP, et al. Fluoro-pegylated (FPEG): imaging agents targeting Ab aggregates. Bioconjug Chem. 2007;18:238–46.

52. Mathis CA, Mason S, Lopresti BJ, Klunk WE. Development of positron emission tomography β-amyloid plaque imaging agents. Semin Nucl Med. 2012;42(6):423–32.

53. Jackson A, Smith GE, Brown SL, et al. Radiosynthesis, biodistribution and metabolic fate of three PET agents for amyloid-β in rats: [18F] Flutemetamol, Florbetapir F18 ([18F-AV-45]) and Florbetaben (BAY 94-9172). Eur J Nucl Med Mol Imaging. 2011;38(Suppl. 2):S231–2.

54. Fairway S, Mantzilas D, Horn E, Powell N. Development of a solid phase extraction (SPE) based purification method for production of the amyloid imaging agent [18F]Flutemetamol. J Nucl Med. 2010;51(s2):140.

55. Zhang W, Xu S, Yu H, et al. Radioactive synthesis of tau PET imaging agent [18F]-AV-1451 and its role in monitoring the progression of Alzheimer's disease and supporting differential diagnosis. Ann Nucl Med. 2021;35:139–47.

56. Mossine AV, Brooks AF, Henderson BD, et al. An updated radiosynthesis of [18F]AV1451 for tau PET imaging. EJNMMI Radiopharm Chem. 2017;2:7.

57. Rowe SP, Buck A, Bundschuh RA. [18F] DCFPyL PET/CT for imaging of prostate cancer. Nuklearmedizin. 2022;61:240. https://doi.org/10.1055/a-1659-0010.

58. Chen Y, Pullambhatla M, Byun Y, et al. 2-(3-{1-Carboxy-5-[(6-[18F]fluoro-pyridine-3-carbonyl)-amino]-pentyl}-ureido)-pentanedioic acid, [18F]DCFPyL, a PSMA-based PET imaging agent for prostate cancer. Clin Cancer Res. 2011;17:7645.

59. Szabo Z, et al. Initial evaluation of [18F]DCFPyL for prostate-specific membrane antigen (PSMA)-targeted PET imaging of prostate cancer. Mol Imaging Biol. 2015;17(4):565–74.

60. Bouvet V, Wuest M, Jans H-S, et al. Automated synthesis of [18F]DCFPyL via direct radiofluorination and validation in preclinical prostate cancer models. EJNMMI Res. 2016;6:40.

61. Olberg DE, Arukwe JM, Grace D, et al. One step radiosynthesis of 6-[(18F)]fluoronicotinic acid 2,3,5,6-tetrafluorophenyl ester ([(18F)]F-Py-TFP): a new prosthetic group for efficient labeling of biomolecules with fluorine-18. J Med Chem. 2010;53:1732–40.

62. Firnau G, Nahmias C, Garnett ES. The preparation of [18F]5-fluoro-DOPA with reactor produced fluorine-18. Int J Appl Radiat Isot. 1973;24:182–4.

63. Firnau G, Chiakal R, Garnett ES. Aromatic radiofluorination with [18F] fluorine gas: 6-[18F]fluoro-L-dopa. J Nucl Med. 1984;25:1228–33.

64. Adam MJ, Ruth TJ, Grierson JR, et al. Routine synthesis of L-[18F]6-fluorodopa with fluorine-18 acetyl hypofluorite. J Nucl Med. 1986;27:1462–6.

65. Dolle F, Demphel S, Hinnen F, et al. 6-[18F]Fluoro-L-DOPA by radiofluoro-destannylation: a short and simple synthesis of a new labeling precursor. J Label Compd Radiopharm. 1998;41:105–14.

66. Luxen A, Perlmutter M, Bida GT, et al. Remote, semiautomated production of 6-[18F]fluoro-L-dopa for human studies with PET. Int J Rad Appl Instrum A. 1990;41:275–81.

67. Namavari M, Bishop A, Satyamurthy N, et al. Regioselective radiofluorodestannylation with [^{18}F]F$_2$ and [^{18}F]CH$_3$COOF. A high yield synthesis of 6-[^{18}F]Fluoro-LDOPA. Int J Rad Appl Instrum A. 1992;43:989–96.

68. VanBrocklin HF, Blagoev M, et al. A new precursor for the preparation of 6-[^{18}F]Fluoro-L-m-tyrosine (FMT): efficient synthesis and comparison of radiolabeling. Appl Radiat Isot. 2004;61(6):1289–94.

69. Happaranta M, Bergman J, Laakso A, et al. [^{18}F]CFT ([^{18}F]WIN,35428), a new radioligand to study the dopamine transporter with PET. Biodistribution in rats. Synapse. 1996;23:321–7.

70. Andersen VL, Soerensen MA, Dam JH, et al. GMP production of 6-[^{18}F]Fluoro-L-DOPA for PET/CT imaging by different synthetic routes: a three-center experience. EJNMMI Radiopharm Chem. 2021;6:21.

71. Jiang H, Jain MK, Cai H. HPLC-free and cassette-based nucleophilic production of [^{18}F]FDOPA for clinical use. Am J Nucl Med Mol Imaging. 2021;11(4):290–9.

72. Fani M, Maeske HR, Okavi SM. Radiolabeled peptides: valuable tools for the detection and treatment of cancer. Theranostics. 2012;2(5):481–501.

73. Krishnan HS, Ma L, Vasdev N, Liang SH. ^{18}F-labeling of sensitive biomolecules for positron emission tomography. Chemistry. 2017;23(62):15553–15577.

74. Yuan Z, Nodwell MB, Yang H, et al. Site-selective, late-stage C−H ^{18}F-fluorination on unprotected peptides for positron emission tomography imaging. Angew Chem Int Ed Engl. 2018;57:12733–6.

75. Maschauer S, Haubner R, Kuwert T, Prante O. ^{18}F-Glyco-RGD peptides for PET imaging of integrin expression: efficient radiosynthesis by click chemistry and modulation of biodistribution by glycosylation. Mol Pharm. 2014;11:505–15.

76. Rickmeier J, Ritter T. Site-specific deoxyfluorination of small peptides with [^{18}F]fluoride. Angew Chem Int Ed. 2018;57:14207–11.

77. Choi JY, Lee BC. Click reaction: an applicable radiolabeling method for molecular imaging. Nucl Med Mol Imaging. 2015;49:258–67.

78. Kolb HC, Finn MG, Sharpless KB. Click chemistry: diverse chemical function from a few good reactions. Angew Chem Int Ed. 2001;40:2004–21.

79. Marik J, Sutcliffe JL. Click for PET: rapid preparation of [^{18}F]fluoropeptides using CuI catalyzed 1,3-dipolar cycloaddition. Tetrahedron Lett. 2006;47:6681–4.

80. Codelli JA, Baskin JM, Agard NJ, Bertozzi CR. Second-generation difluorinated cyclooctynes for copper-free click chemistry. J Am Chem Soc. 2008;130(34):11486–93.

81. Blackman ML, Royzen M, Fox JM. Tetrazine ligation: fast bioconjugation based on inverse-electron-demand Diels-Alder reactivity. J Am Chem Soc. 2008;130:13518–135189.

82. McBride WJ, Sharkey RM, Karacay H, et al. A novel method of ^{18}F radiolabeling for PET. J Nucl Med. 2009;50:991–8.

83. Archibald SJ, Allott L. The aluminum-[^{18}F]fluoride revolution: simple radiochemistry with a big impact for radiolabelled biomolecules. EJNMMI Radiopharm Chem. 2021;6:30.

84. Fersing C, Bouhlel A, Cantelli C, et al. A comprehensive review of non-covalent radiofluorination approaches using aluminum [^{18}F]fluoride: will [^{18}F]AlF replace ^{68}Ga for metal chelate labeling? Molecules. 2019;24(16):2866.

85. Eersels JLH, Travis MJ, Herscheid JDM. Manufacturing I-123-labeled radiopharmaceuticals: pitfalls and solutions. J Label Compd Radiopharm. 2005;48:241–57.

86. Sheh Y, Koziorowski J, Balatoni J, et al. Low energy cyclotron production and chemical separation of no-carrier added iodine-124 from a reusable enriched tellurium-124 dioxide/aluminum oxide solid solution target. Radiochim Acta. 2000;88:169–73.

87. Dubost E, McErlain H, Babin V. Recent advances in synthetic methods for radioiodination. J Org Chem. 2020;85:8300–10.

88. Kabalka GW, Mereddy AR. A facile no-carrier-added radioiodination procedure suitable for radiolabeling kits. Nucl Med Biol. 2004;31:935–8.

89. Mushtaq S, Jeon J, Shaheen A, et al. Critical analysis of radioiodination techniques for micro and macro organic molecules. J Radioanal Nucl Chem. 2016;309:859–89.

90. Bolton AE, Hunter WM. The labeling of proteins to high specific radioactivities by conjugation to a ^{125}I containing acylating agent. Biochem J. 1973;133:529–38.

91. Greenwood FC, Hunter WM, Glover JS. The preparation of ^{131}I-labeled human growth hormone of high specific radioactivity. Biochem J. 1963;89:114–23.

92. Richardson AP, Mountford PJ, Baird AC, et al. An improved iodogen method of labeling antibodies with ^{123}I. Nucl Med Commun. 1986;7:355–62.

93. David GS, Reisfeld RA. Protein iodination with solid state lactoperoxidase. Biochemistry. 1974;13(5):1014–1021.

94. Mertens J, Gysemans M. Cu(1$^+$) assisted nucleophilic exchange, application and mechanistic approach. In: Emram AM, editor. New trends in radiopharmaceutical synthesis, quality assurance, and regulatory control. New York: Plenum; 1991.

95. Bourguignon MH, Pauwels EK, Loc'h C, Mazière B. Iodine-123 labelled radiopharmaceuticals and single-photon emission tomography: a natural liaison. Eur J Nucl Med. 1997;24(3):331–44.

96. Kung HK, Kung M-P, Choi SR. Radiopharmaceuticals for single-photon emission computed tomography brain imaging. Semin Nucl Med. 2003;33(1):2–13.

97. Wieland DM, Wu J, Brown LE, Mangner TJ, et al. Radiolabeled adrenergic neuron-blocking agents: adre-

nomedullary imaging with 131I-iodobenzylguanidine. J Nucl Med. 1980;21:349–53.

98. Wieland DM, Mangner TJ, Inbasekaran MN, et al. Adrenal medulla imaging agents: a structure-distribution relationship study of radiolabeled aralkylguanidines. J Med Chem. 1984;27:149–55.

99. Vallabhajosula S, Nikolopoulou A. Radioiodinated Metaiodobenzylguanidine (MIBG): Radiochemistry, Biology, and Pharmacology. Seminars in Nuclear Medicine. 2011;41(5):324–333.

100. Barrett JA, Coleman RE, Goldsmith SJ, Vallabhajosula S, et al. First-in-man evaluation of 2 high-affinity PSMA-avid small molecules for imaging prostate cancer. J Nucl Med. 2013;54(3):380–7.

101. Neumeyer JL, Campbell A, Wang S, et al. N-.omega.-fluoroalkyl analogs of (1R)-2.beta.-carbomethoxy-3.beta.-(4-iodophenyl)tropane (.beta.-CIT): radiotracers for positron emission tomography and single photon emission computed tomography imaging of dopamine transporters. J Med Chem. 1994;37(11):1558–61.

102. Oliveira MC, Correia DG. Biomedical applications of radioiodinated peptides. Eur J Med Chem. 2019;179:56–77.

Organic Radionuclides for Molecular Imaging (C, N, and O)

11

Science is built up of facts, as a house is built of stones; but an accumulation of facts is no more a science than a heap of stones is a house. (Henri Poincaré)

11.1 Advantages of Organic Radionuclides

All natural organic molecules or biochemicals in the human body and many drug molecules are made up of carbon, hydrogen, nitrogen, and oxygen. The organic radionuclides useful for developing radiotracers for PET are ^{11}C, ^{13}N, and ^{15}O (Table 11.1). These three elements, however, do not have any radionuclides suitable for developing radiotracers for SPECT.

Among the three organic radionuclides, ^{11}C offers the greatest potential to develop radiotracers for routine clinical applications because ^{11}C, as a label, can be easily substituted for a stable carbon in an organic compound without changing the biochemical and pharmacological properties of the molecule. Furthermore, the short half-life of ^{11}C provides favorable radiation dosimetry to perform multiple studies in the same subject under different conditions. The short half-life of ^{11}C may be disadvantageous for commercial production of radiotracers but, has significant potential for developing:

Table 11.1 Organic chemical elements: stable and radioactive isotopes

Element	Radionuclide	Decay mode	%	Half-life	β⁺ Energy (MeV) β⁺ E_{mean} (MeV) Max	Mean	Range (mm) Max	Mean
Carbon	^{10}C	β⁺ and γ		19.3 s	3.65			
	^{11}C	β⁺, EC	99.8	20.3 months	0.960	0.382	4.2	1.2
	^{12}C	Stable	98.9					
	^{13}C	Stable	1.1					
	^{14}C	β⁻	100	5715 years	0.156 (β⁻)			
Nitrogen	^{13}N	β⁺ decay	99.8	9.97 months	1.1999	0.492	5.5	1.8
	^{14}N	Stable	99.634					
	^{15}N	Stable	0.366					
Oxygen	^{14}O	β⁺ and γ		70.6 s	5.143			
	^{15}O	β⁺ decay	99.9	122.2 s	1.732	0.735	8.4	3.0
	^{16}O	Stable	99.762					
	^{17}O	Stable	0.038					
	^{18}O	Stable	0.20					

- Radiotracers with high specific activity (SA) to study drug interactions associated with exceedingly small concentrations of neuroreceptors.
- Radiolabeled drugs for monitoring the response to treatment.
- The relatively short physical half-life of ^{11}C (20 min) allows for multiple imaging studies to be obtained in the same subject within a brief period of time (3–4 h) with the same tracer (at base line followed by experimental intervention) or with multiple tracers to assess the specificity of the receptor interaction.

Compared to ^{11}C, the potential clinical utility of ^{13}N and ^{15}O radiotracers is extremely limited. In the last four decades, [^{13}N]ammonia and [^{15}O] water are the only tracers that have shown clinical utility in the assessment of regional blood flow, and perfusion. The radiochemistry of ^{13}N and ^{15}O is described briefly at the end of this chapter.

11.2 ^{11}C-Labeled Radiopharmaceuticals

^{11}C was first produced in 1934 [1] and the first biological application was based on the use of [^{11}C] CO_2 to investigate the photosynthesis in plants [2]. [^{11}C]CO was the first radiotracer used in human subjects to investigate the fixation of CO by red blood cells [3]. Several reviews have extensively discussed the chemistry and potential application of ^{11}C-labeled radiotracers [4–9]. In the last three decades, a spectrum of carbon-11 PET radiotracers has been developed to image many of the upregulated and emerging targets for the diagnosis, prognosis, prediction, and therapy in the fields of oncology, cardiology, and neurology.

11.2.1 Production of ^{11}C

The most commonly used method of ^{11}C production is based on the nuclear reaction, ^{14}N$(p,\alpha)^{11}$C, in which the natural nitrogen gas is used as the target. One of the competing nuclear reactions is ^{14}N$(p,pn)^{13}$N or via ^{16}O$(p,\alpha)^{13}$N but, the relative amount of ^{13}N activity produced is dose-dependent and short irradiation times may lead to relatively enormous amounts of ^{13}N [5, 10]. With trace amounts of oxygen in the target (<1%), [^{11}C]CO_2 and [^{11}C]CO are formed [11]. With relatively higher proton energies (>13 MeV), longer irradiation times (>30 min) and higher beam currents (>30 μA), the most predominant ^{11}C precursor generated is [^{11}C]CO_2 gas. In the presence of hydrogen (5%) in the target, [^{11}C]methane (CH_4) and [^{11}C]hydrogen cyanide (HCN) can be produced by a recoil synthesis; however, due to radiolysis, [^{11}C]CH_4 is the main precursor available for processing [12, 13].

^{11}C radioactivity from the cyclotron target can be recovered in the form of two major precursors: [^{11}C]carbon dioxide or [^{11}C]methane. Subsequently, these gases can be converted into several secondary precursors, such as methyl iodide, methyl triflate, HCN, nitromethane, and phosgene.

11.2.1.1   Specific Activity (SA) of ^{11}C

The theoretical SA of ^{11}C is 9220 Ci μmol^{-1} or 9.22 Ci nmol^{-1} (Table 11.2). Since the contamination of the target and the gas lines with stable ^{12}C is unavoidable, ^{11}C is always contaminated with ^{12}C atoms. Also, both CO_2 and CH_4 gases are present in the atmosphere and provide a ubiquitous source of carrier as a contaminant that decreases the SA. As a consequence, the practical SA of ^{11}C precursors achieved from the typical production in a cyclotron target varies from 0.01 to 0.1 Ci nmol^{-1} depending on a number of

Table 11.2 Specific activity (SA) of ^{11}C and ^{18}F

Radionuclide	Half-life	Theoretical SA		Practical SA	
	min	Ci nmol^{-1}	nmol Ci^{-1}	Ci nmol^{-1}	nmol Ci^{-1}
^{11}C	20.4	9.22	0.108	0.01–0.1	10–100
^{18}F	110	1.71	0.585	0.001–0.02	50–1000

factors. In other words, every ^{11}C atom is contaminated with 100 or 1000 atoms of stable carbon atoms, which implies that the majority of the mass is mostly due to stable ^{12}C and extraordinarily little of the carbon is from the ^{11}C activity. There is a significant potential and also a need to improve the SA of ^{11}C production with the current cyclotron targets, and generate ^{11}C precursors with ultrahigh SA.

11.2.2 ^{11}C Precursors

The carbon-11 precursors (Fig. 11.1) are classified into primary and secondary based on their utility, and wide range of applications in the radiolabeling of various compounds like aliphatic, aromatic, and heterocyclic compounds after the production of carbon-11 radionuclide. The carbon-11 precursors in the chemical form of $[^{11}C]CO_2$ and $[^{11}C]CH_4$ are considered as the primary precursors, which can be produced during in-target production. These are converted into secondary precursors by rapid and efficient online or one-pot synthetic procedures to produce building blockers for generating carbon-11 radiotracers. Most of the ^{11}C tracers are synthesized using the secondary precursors. Several useful transformations for the generation of secondary precursors are summarized in Fig. 11.1. From the secondary precursors such as

[^{11}C]methyl iodide, other secondary precursors can be synthesized, as shown in Fig. 11.2.

[^{11}C]Methyl iodide is the precursor of choice for introducing ^{11}C into organic molecules. However, a number of other precursors (Fig. 11.1) have been developed in the last few decades in order to meet the demands of synthetic strategies used for the development of ^{11}C-labeled radiotracers. [^{11}C]Methyl iodide can also be used to prepare a number of secondary ^{11}C precursors, such as methyl triflate ($CH_3OSO_2CF_3$), methyl lithium, nitromethane, and methyl magnesium iodide or bromide. Starting with [^{11}C]methane, precursors, such as hydrogen cyanide, cupric cyanide, carbon tetrachloride, and phosgene can be prepared [14, 15].

Methyl triflate, introduced in 1991 as an alkylating agent, is more advantageous than methyl iodide for alkylation reactions under mild conditions [16]. More specifically, it can be easily prepared by passing [^{11}C]methyl iodide through a small soda-glass column containing sliver triflate-impregnated graphitized carbon and the conversion to [^{11}C]methyl triflate is very efficient, and fast. The other precursor for methylations under mild conditions is methyl lithium [^{11}C] CH_3Li, which can be prepared by an equilibrium reaction between *n*-butyl lithium (*n*-BuLi) and [^{11}C] methyl iodide [17].

The Grignard reagent, methyl magnesium iodide, [^{11}C]CH_3MgI, is useful to add a methyl
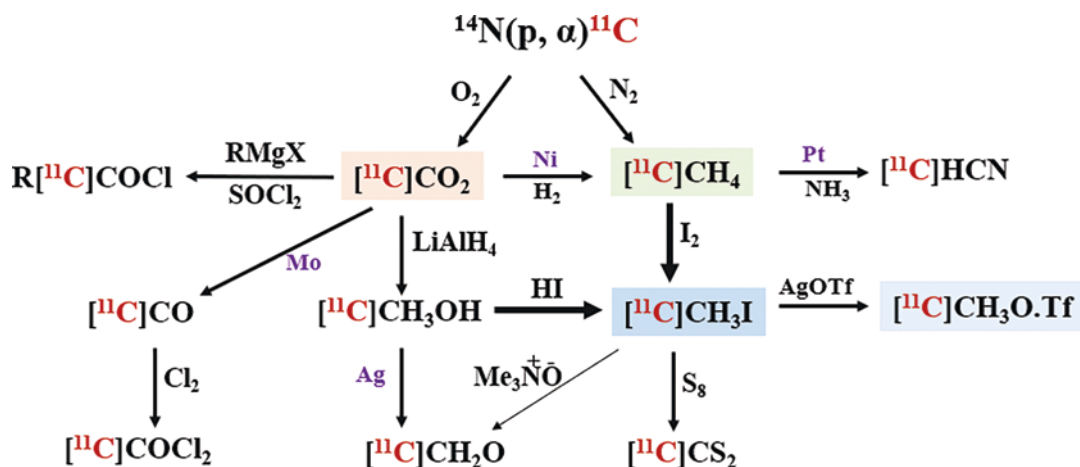
Fig. 11.1 ^{11}C-labeled precursors prepared from [^{11}C]carbon dioxide and [^{11}C] methane

Fig. 11.2 Methods for the synthesis of ¹¹C-labeled precursors

[¹¹C]CH₃I $\xrightarrow[\text{150°C}]{\text{AgOSO}_2\text{CF}_3}$ [¹¹C]CH₃OSO₂CF₃

[¹¹C]CH₃I + n-BuLi $\xrightarrow{\hspace{3cm}}$ [¹¹C]CH₃Li + BuI

[¹¹C]CH₃I + Mg $\xrightarrow[\text{Iodobenzene}]{\text{Diethyl ether, Iodine}}$ [¹¹C]CH₃MgI

[¹¹C]CH₃I $\xrightarrow[\text{80°C}]{\text{AgNO}_2}$ [¹¹C]CH₃NO₂

[¹¹C]CH₄ + NH₃ $\xrightarrow[\text{100°C}]{\text{Pt}}$ H[¹¹C]CN $\xrightarrow[\text{Na}_2\text{S}_2\text{O}_3]{\text{CuSO}_4}$ Cu[¹¹C]CN

[¹¹C]CH₄ + Cl₂ $\xrightarrow[\text{390°C}]{}$ [¹¹C]CCl₄ $\xrightarrow[\text{300°C}]{\text{Fe/O}_2}$ [¹¹C]COCl₂

[¹¹C]CO₂ $\xrightarrow[\text{450°C}]{\text{Zn asbestos}}$ [¹¹C]CO $\xrightarrow[\text{280°C}]{\text{PtCl}_4}$ [¹¹C]COCl₂
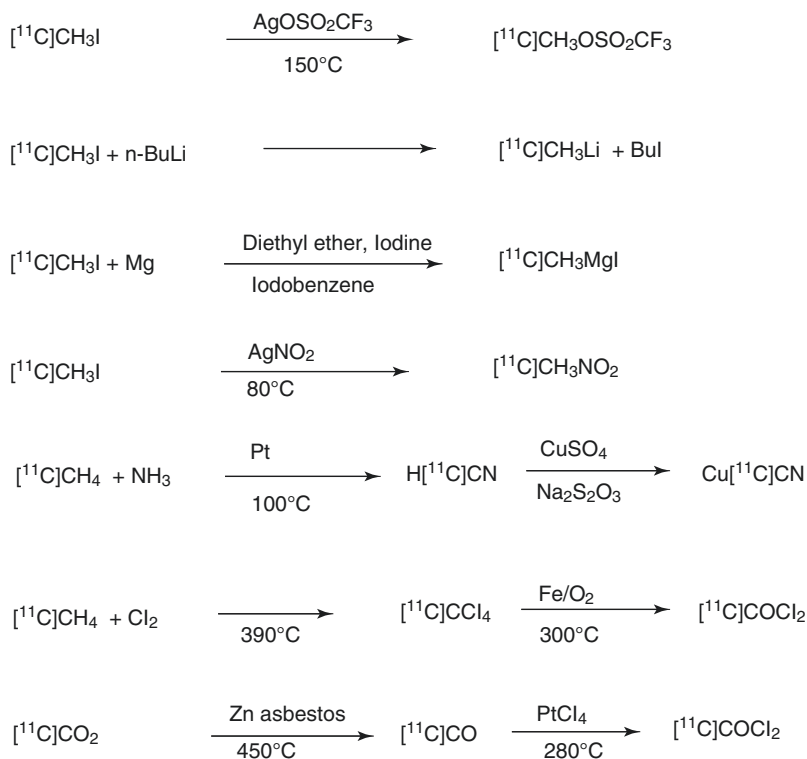
group to a carbonyl (CO) group in a molecule. This precursor can be prepared by the interaction of [¹¹C]methyl iodide with magnesium turnings mixed with iodobenzene in ether [18].

Nitroalkanes, such as nitromethane [¹¹C] CH₃NO₂, can easily be converted into carbon nucleophile in the presence of a base. Also, an aldehyde group in a molecule can easily be substituted with a nitromethane. Subsequently, the nitrogroup can be reduced to an amine [19]. [¹¹C] CH₃NO₂ can also be easily prepared by the reaction of methyl iodide with silver nitrate at 80 °C [20]. Other nitroalkanes, such as nitroethane and nitropropane, can also be prepared similarly.

Cyanide (HCN) can be an extremely useful precursor for replacing halogen atoms, through nucleophilic substitution, with the cyano group. [¹¹C]HCN can be used to label amines, amino acids, aldehydes, and acids, and can be easily prepared by the reaction of [¹¹C]methane with ammonia over a platinum catalyst, at a very high temperature [12]. Since copper salts mediate certain aromatic nucleophilic substitutions, [¹¹C] HCN can easily be converted to Cu[¹¹C]CN [21].

Phosgene, [¹¹C]COCl₂) is a useful precursor that can be prepared easily by the catalytic chlorination of [¹¹C] CO, which typically is produced through the reduction of [¹¹C]CO₂ over hot zinc [22]. Phosgene can also be prepared by converting [¹¹C]methane to carbon tetrachloride, [¹¹C] CCl₄ through reaction with hot Cl₂ gas. Carbon tetrachloride is then mixed in a stream of oxygen gas and passed through a second furnace at 300 °C containing iron granules [23]. [¹¹C] Phosgene has been used to prepare [¹¹C] urea, a precursor for the synthesis of 2-[¹¹C]thymidine.

11.2.2.1   [¹¹C]Methylation Reaction

The most common method in ¹¹C chemistry is heteroatom methylation using [¹¹C]methyl iodide or iodomethane (CH₃I) and [¹¹C]methyl triflate (CH₃Tf), the most common precursors used to make ¹¹C radiotracers. CH₃I was first prepared in 1976 to synthesize [¹¹C]methionine [24]. Two methods are used for the synthesis of [¹¹C] CH₃I (Fig. 11.3). In a "liquid-phase" synthesis, [¹¹C] CO₂ is first reduced to methanol [¹¹C]CH₃OH, using lithium aluminum hydroxide (LiAlH₄)

Fig. 11.3 Synthesis of [^{11}C]methyl iodide: Liquid phase method (**a**) and gas phase method (**b**)

a Liquid Phase

$$[^{11}C]CO_2 \xrightarrow{\text{LiAlH}_4} [^{11}C]CH_3O^- \xrightarrow{\text{HI}} [^{11}C]CH_3I$$

b Gas Phase

$$[^{11}C]CO_2 \xrightarrow[\substack{\text{Shimmalite Ni} \\ \text{H}_2, 350^\circ\text{C}}]{\text{Molecular sieve}} [^{11}C]CH_4 \xrightarrow[350^\circ\text{C}]{\text{I2 vapors}} [^{11}C]CH_3I$$

GE TRACERlab^{TM} FX2 MeI

TRACElab^{TM} FX2 C

Fig. 11.4 TRACERlab FX2 MeI provides a patented gas phase [^{11}C] methyl iodide production method via direct reaction of Iodine with [^{11}C] methane. [^{11}C] methane can either be supplied from a [11C] methane target, or in case a [^{11}C]CO$_2$ target is used, the integrated conversion step of [^{11}C]CO$_2$ to [^{11}C] methane can be utilized. TRACERlab FX2 C provides [^{11}C]methyl iodide or [^{11}C]methyl triflate production and methylation of PET tracers in one module. For labeling processes starting directly with [^{11}C]CO$_2$ the methylation step can be bypassed

which then reacts with hydroiodic acid (HI) to generate methyl iodide. In a "gas-phase" synthesis, [^{11}CH$_4$] gas (either from the target directly or produced from [^{11}CO$_2$]) reacts with iodine vapors generating methyl iodide [25, 26]. Commercial automated synthesis modules (Fig. 11.4) are available to synthesize [^{11}C]CH$_3$I and [^{11}C]CH$_3$. Tf. The [^{11}C]methylation reactions for making [^{11}C]-radiotracers are described according to the final bond between the carbon-11 and the other atom; the most common alkylations can be divided into N-alkylation, O-alkylation, and S-alkylation. The N-alkylation reaction uses [^{11}C]CH$_3$I or [^{11}C]CH$_3$OTf as an electrophile to react with a either a primary, secondary, or even tertiary amine group to give the corresponding [^{11}C]N-methyl radiotracer.

Generally, the radiochemical purity and SA of [^{11}C] CH$_3$I depend on the synthesis procedure and the automated module employed [27, 28]. The specific activity of [^{11}C]CH$_3$I (collected in DMF or acetone) can be determined by analytical HPLC using a Novapak C$_{18}$ column (Waters, 4.6×150 mm) and a mobile phase consisting of acetonitrile/water (40/60) containing 0.1 M ammonium formate at a flow rate of 2 mL min^{-1}. The retention time of [^{11}C]CH$_3$I is 2.7 min (Fig. 11.5). The gas-phase method generates higher SA of [^{11}C]CH$_3$I and may be appropriate for receptor binding radiotracers [29].

Fig. 11.5 Radiochemical purity of [¹¹C]methyl iodide (produced based on gas phase method) based on analytical HPLC
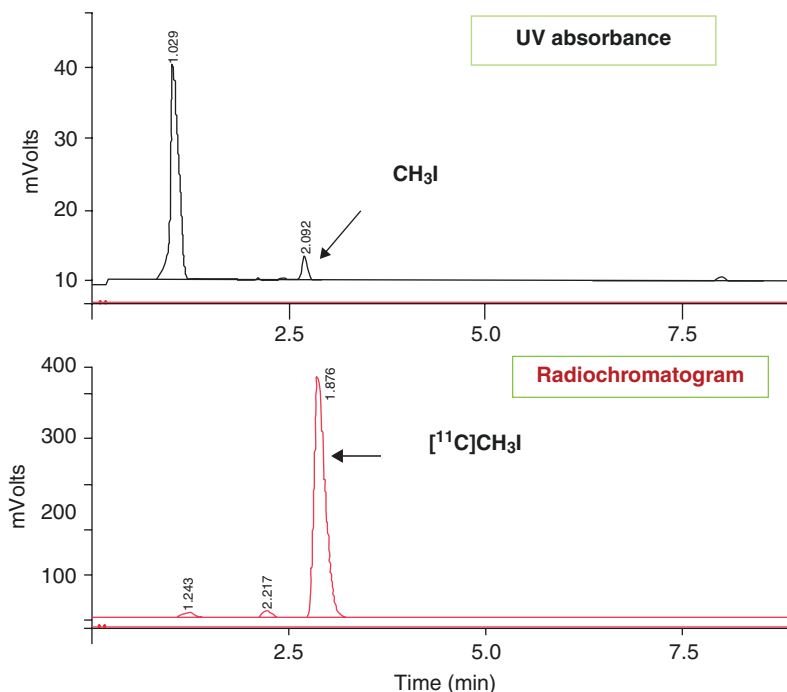
11.2.3   Synthesis of ¹¹C Labeled MIPs

A number of ¹¹C-labeled molecular imaging probes of significant clinical interest have been developed in the last few decades (Table 11.3). Historically, several different approaches have been used for the production of ¹¹C-labeled radiotracers, but the most practical approaches have been based on either (a) organic synthetic methods or (b) enzyme catalysis [4, 14].

The methods based on organic synthesis typically involve alkylations of C, N, O, and S nucleophiles with [¹¹C]methyl iodide or [¹¹C]methyl triflate. The alkylation reactions require an organic precursor, also known as *nor* compound (a molecule of interest without a methyl group on a specific C, N, O, or S atom). If a molecule of interest has several reactive groups, the organic precursors must have protective groups that can be easily deprotected by hydro-

lysis following methylation to generate the final drug product. This is the most common synthetic approach used in the routine production of ¹¹C-labeled radiopharmaceuticals and several examples are discussed below. ¹¹C labeling based on methyl-iodide or triflate method may not be possible in certain compounds and ¹¹C labeling through C-C bond formation may be the correct approach. Therefore, several different methods have been developed in recent years to synthesize ¹¹C-labeled radiotracers [5, 7]. The first novel method is the direct formation of ¹¹C-labeled carbonyl groups, where organic bases are utilized as "[¹¹C]CO_2 fixation agents." The second method is a low pressure [¹¹C]carbonylation technique that utilizes solvable xenon gas. These new methods have been reviewed recently in greater detail [7]. In summary, the following methods are utilized for the synthesis of ¹¹C-labeled tracers through C-C bond formation [7]:

Table 11.3 Examples of C-11-labeled PET radiotracers developed for applications in oncology, cardiology, neurology, and psychiatry

Biological process	Radiotracer	Target mechanism of uptake	Clinical application
Phosphatidylcholine (PC) Membrane synthesis	[¹¹C]Choline (CHO)	*Choline kinase*	Prostate cancer, brain tumors
DNA synthesis	[¹¹C]Thymidine, [¹¹C]4-DST	*Thymidine kinase (TK)*	Tumor aggressiveness (Ki67)
Amino acid transport and protein synthesis	[¹¹C]L-methionine [¹¹C]phenylalanine [¹¹C]ACBC [¹¹C]5–5-HTP) [¹¹C]AMT	Amino acid transporters (LAT 1–4)	Many tumors, including brain tumors, prostate cancer, and neuroendocrine tumors (NETs)
Cardiac oxygen metabolism	[¹¹C]Acetate	Utilized in TCA cycle and oxidative phosphorylation	Myocardial blood flow and oxygen consumption
Fatty acid metabolism	[¹¹C]Palmitate	β-Oxidation in mitochondria	Myocardial metabolism and infarct quantitation
Cardiac neuroreceptors	[¹¹C]CGP-12388	β-Receptor antagonists	Heart failure
Myocardial neuronal imaging	[¹¹C] Hydroxyephedrine (HED)	Norepinephrine reuptake transporter (NET)	Heart failure and NETs
Dopamine transporters (DATs)	[¹¹C]-L-DOPA	Analog of L-DOPA, substrate for AAAD	Parkinson's disease (PD)
	[¹¹C]Cocaine	Bind selectively to DAT	Cocaine addiction
	[¹¹C]β-CIT	DAT	Parkinson's disease (PD)
	[¹¹C]PE2i	DAT	Parkinson's disease (PD)
Vesicular monoamine transporter type 2 (VMAT2)	[¹¹C]DTBZ	DAT	Parkinson's disease (PD)
Dopamine D₁ receptors	[¹¹C]NNC-112 [¹¹C]SCH-23390	D₁ receptor antagonist	Schizophrenia, PD, cognitive disorders
Dopamine D₂/₃ receptors	[¹¹C]Raclopride [¹¹C]FLB-457	Non-selective antagonists for D₂/₃ receptors	Schizophrenia, PD, drug addiction, anxiety, Huntington's disease (HD)
	(+)-[¹¹C]PHNO	Specific for D₃ receptors	PD
Monoamine oxidase (MAO) expression	[¹¹C]clorgyline [¹¹C]-L-deprenyl	Suicide MAO inhibitors	PD
Adenosine receptors	[¹¹C]KF18446 [¹¹C]MPDX	A₂A receptor	HD, chronic diffuse axonal injuries
Glutamatergic receptors (GluR)	[¹¹C]ABP-688	Selective metabotropic GluR antagonist	HD, Alzheimer disease (AD)
	[¹¹C]MeNBI	GluN1/GluN2 containing NMDA receptors	Various neurological disorders
Opiate receptors	[¹¹C]Carfentanil	High-affinity μ opiate receptor agonist	Cocaine addiction
	[¹¹C]Diprenorphine	Nonselective partial opiate receptor (μ, δ, κ) agonist	HD
GABA receptors	[¹¹C]Flumazenil (FMZ)	GABA_A receptor antagonist	Amyotrophic lateral sclerosis (ALS), epilepsy
	[¹¹C]PK11195 [¹¹C]DPA-713	Peripheral benzodiazepine (PBR) receptor	Activate microglia in neuroinflammation
Serotonergic system	[¹¹C]HTP [¹¹C]AMT	Serotonin synthesis	Serotonin metabolism NETs

Table 11.3 (continued)

Biological process	Radiotracer	Target mechanism of uptake	Clinical application
Serotonin receptors	[11C]WAY100635	5HT$_{1A}$ receptor antagonist	ALS, AD-dementia, temporal lobe epilepsy
	[11C]Desmethyl WAY100635		
	[11C]MDL-100907	5HT$_{2A}$ receptor antagonist	
	[11C]NMSP		
Serotonin transporter (SERT)	(+)-[11C]McN-5652	Binds to SERT	Depression, AD-dementia
	[11C]DSAB		
	[11C]DASB		
	[11C]Citalopram		
Cholinergic system	[11C]Nicotine	nAchR subtype α4β2	Leaning, memory, and AD
	[11C]epibatidine		
	[11C]MP4P	Acetylcholinesterase enzyme inhibitor	AD
	[11C]MP4A		
Amyloid plaques	[11C]6-OH-BTA-1(PiB)	Binds β-amyloid plaque	AD, mild cognitive impairment (MCI)
	[11C]AZD2184		
	[11C]SB-13		
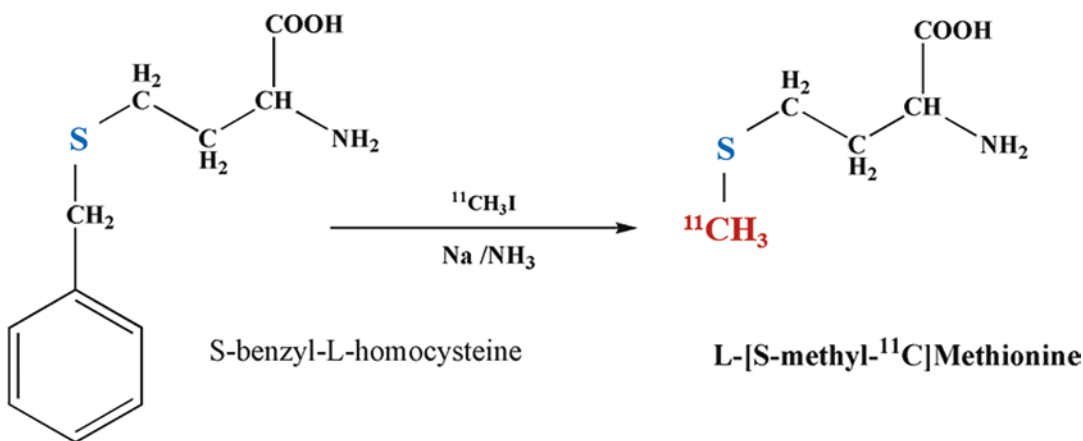
Fig. 11.6   Synthesis of L-[S-methyl-11C]methionine

- The alkylation of carbanions (nucleophiles) with 11C-labeled alkyl halides, nitroalkanes, and cyanide.
- The carboxylation of organometallic reagents, copper, and other metal-mediated catalysts.
- Transition-metal-mediated (Pd, Rh) chemical reactions with [11C]CH$_3$I and [11C]CO.
- Well-known reactions mechanisms like Stille reaction, Negishi coupling reaction, Suzuki cross-coupling reaction, and Heck reaction.

11.2.3.1   L-[S-Methyl-11C]Methionine

The amino acid L-Methionine, labeled with 11C in the methyl position, has been used for imaging of brain tumors. The routine production involves an alkylation on a sulfur nucleophile by the reaction of [11C] methyl iodide with S-benzyl-L-homocysteine in the presence of liquid ammonia and sodium, as shown in Fig. 11.6 [24, 30]. Following reverse phase HPLC of the reaction mixture, the final drug

product, L-[S-methyl-¹¹C]methionine, is eluted using a phosphate buffer.

11.2.3.2 Synthesis of [O-Methyl-¹¹C] Raclopride

Raclopride is a dopamine D_2 receptor antagonist and is one of the most extensively used neuroreceptor imaging probes. Raclopride is labeled with ¹¹C by O-methylation using [¹¹C]methyl iodide, as shown in Fig. 11.7. The enantiomerically pure S-precursor (O-desmethylraclopride) in DMSO is reacted with [¹¹C] CH₃I in the presence of sodium hydroxide. The purified drug product, [¹¹C]raclopride, is obtained following reverse phase HPLC of the reaction mixture using a C-18 column, a 10 mM phosphoric acid,

and acetonitrile (70:30 v/v) as an eluent. The fraction containing [¹¹C]raclopride is, subsequently, evaporated to remove acetonitrile, reformulated in physiological saline, and sterilized by membrane filtration.

11.2.3.3 Synthesis of R-[N-Methyl-¹¹C] PK11195

PK11195, a peripheral benzodiazepine receptor ligand, labeled with ¹¹C, was originally developed as a tracer to image activated microglia in the brain [31, 32]. PK11195 can be labeled with ¹¹C by N-methylation using [¹¹C]methyl iodide, as shown in Fig. 11.8. The precursor, R-desmethyl PK11195 (1.0 mg), is mixed with KOH (20 mg) in DMSO (0.4 mL) for 5 min. Subsequently, the
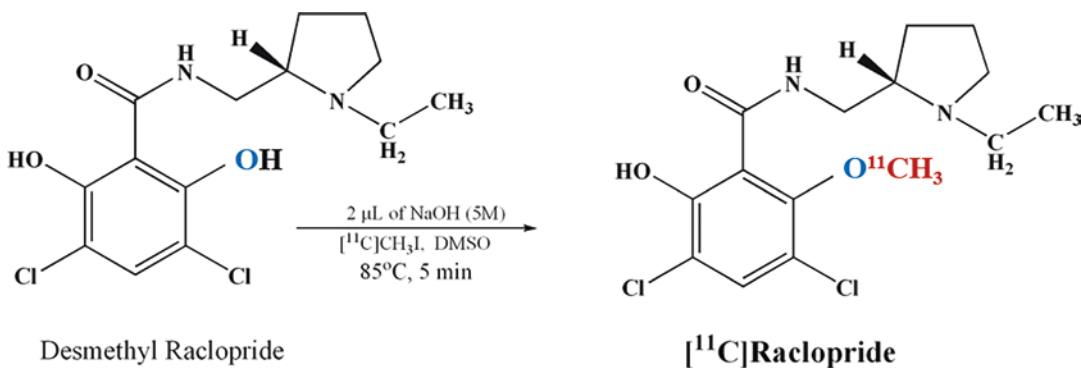
Fig. 11.7 Synthesis of [¹¹C]Raclopride
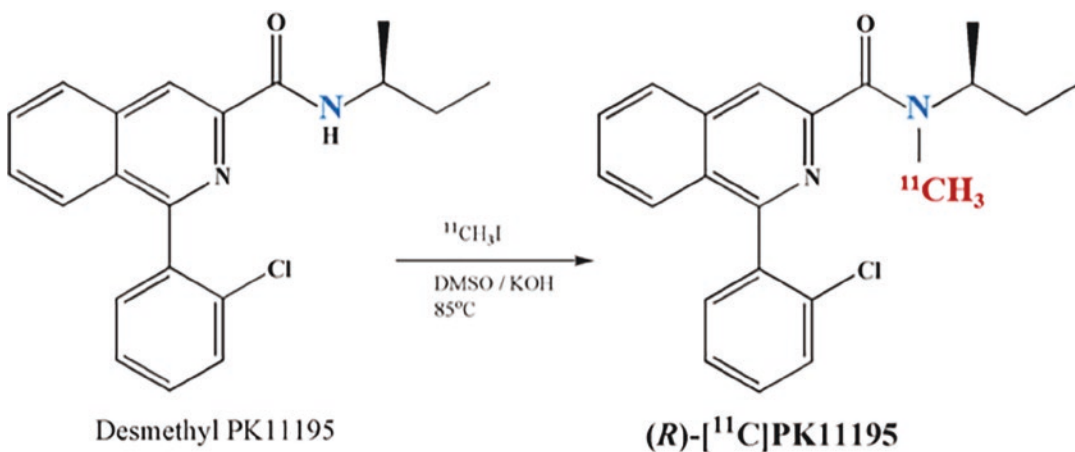
Fig. 11.8 Synthesis of [¹¹C]PK11195

mixture is reacted with [¹¹C]CH₃I for 3 min at 80 °C. The mixture is diluted with 2–3 mL of mobile phase (70% methanol and 30% water) and purified using reverse phase HPLC column. The eluent fraction containing the drug product is passed through a C18 sep-pack cartridge to remove methanol. The final drug product is reformulated in 10% ethanol and physiological saline, and sterilized by membrane filtration.

11.2.3.4 [¹¹C]PIB

Based on an amyloid dye thioflavin-T, a ¹¹C tracer, *N*-Methyl-¹¹C-2-(4′-methylaminophenyl)-

6-hydroxy-benzothiazole (¹¹C-6-OH-BTA-1, also known as "Pittsburgh Compound-B" or [¹¹C]-PIB), was developed to image brain amyloid plaques in patients with Alzheimer's disease [33, 34]. PIB can be labeled with ¹¹C by *N*-methylation using [¹¹C] methyl iodide, as shown in Fig. 11.9. The precursor, desmethyl PIB with a protective group known as MOMO-BTA-0 (1.5 mg) is mixed with KOH (10 mg) in DMSO (0.4 mL) for 5 min. Subsequently, the mixture is reacted with [¹¹C]CH₃I for 5 min at 125 °C. At the end, the protective group is removed by hydrolysis at 80 °C for 5 min using 0.5 mL of
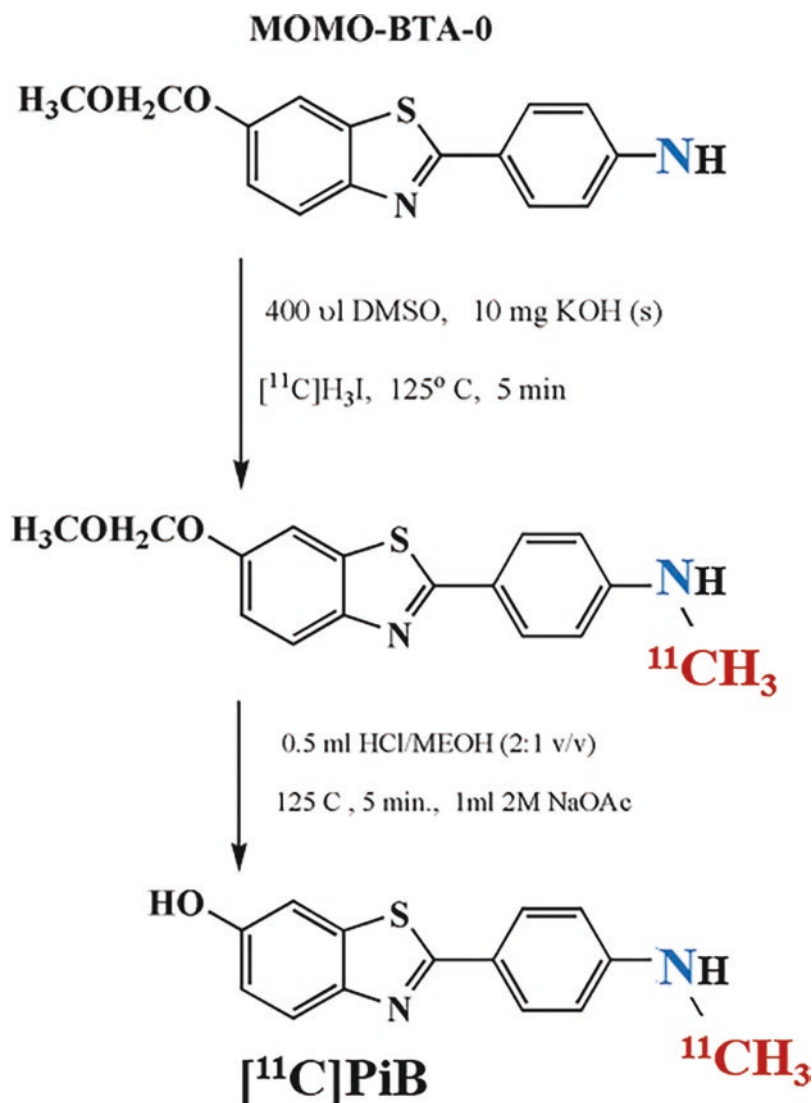
Fig. 11.9 Synthesis of [¹¹C]PIB

methanolic HCl (2:1). The mixture is diluted with mobile phase (35%) acetonitrile and 65% triethyl ammonium phosphate, pH 7.2), and purified using reverse phase HPLC. The eluent fraction containing [¹¹C]PIB is passed through the C18 sep-pak cartridge to remove the organic solvent. The final drug product can be reformulated in physiological saline with 10% ethanol and sterilized by membrane filtration.

The preparation of PiB based on the secondary precursors [¹¹C]CH₃I or [¹¹C]CH₃OTf is always time and activity consuming. As discussed before, any approach capable of eliminating the steps of synthesis of the ¹¹C-methylating agents would be advantageous for a better overall performance in terms of the RCY and the available activity for PET scans. [¹¹C]CO₂ is an attractive starting material for synthesizing ¹¹C-labeled tracers. The use of [¹¹C]CO₂ via the so-called fixation to synthesize ¹¹C-ureas, ¹¹C-carbamates, ¹¹C-oxazolidinones, ¹¹C-carboxilic acids, and ¹¹C-amides is well-documented in the literature [5, 7]. Therefore, several investigators developed methods to synthesize [¹¹C]PiB using [¹¹C]CO₂ directly from the cyclotron [35].

11.2.3.5   Synthesis of [¹¹C]5-Hydroxy-ʟ-Tryptophan (HTP)

Preparation of certain ¹¹C radiopharmaceuticals can be very complicated and may involve many steps in the synthesis followed by purification procedures. ¹¹C-labeled amino acids can be prepared using enzyme catalyzed reactions (specially to prepare the desired enantiomer with biological activity rather than a racemic mixture). For example, in the synthesis of [¹¹C]5-HTP [36], [¹¹C]-ʟ-alanine is synthesized first, by reacting [¹¹C]CH₃I with *N*-(Diphenyl methylene)glycine tertiary butyl ester. Subsequently, [¹¹C]-ʟ-alanine is converted to pyruvic acid using enzymes GPT, DAO and GPT. The interaction of labeled alanine with 5-hydroxyindole, in the presence of *tryptophanase*, will finally produce [¹¹C]5-HTP (Fig. 11.10). The final drug product is purified by HPLC and sterilized by membrane filtration.

11.2.3.6   Synthesis of [¹¹C]Choline (CHO)

The biological basis of [¹¹C]choline as a cancer imaging PET tracer is its role as a precursor in the biosynthesis of phosphatidylcholine and the biosynthesis of phospholipid-rich mem-
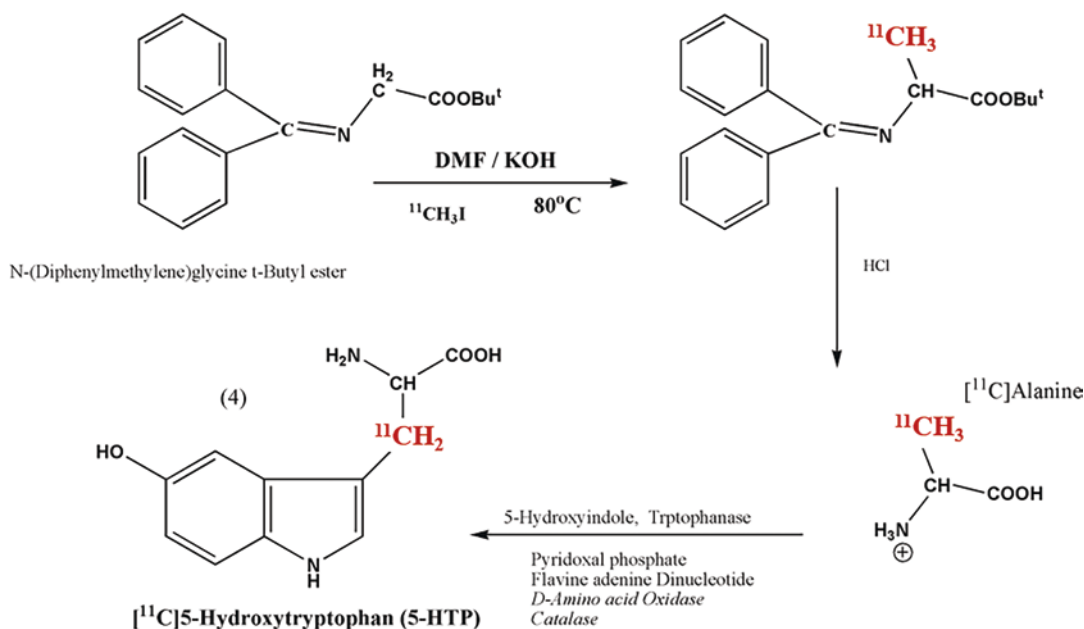
Fig. 11.10   Synthesis of [¹¹C]5-Hydroxytryptophan (5HTP)
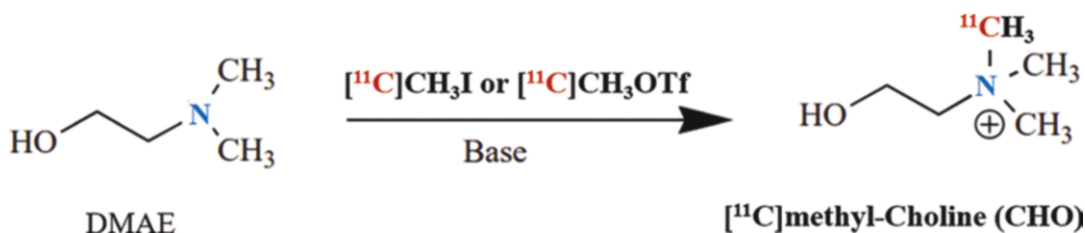
Fig. 11.11 Synthesis of [11C]Choline based on [11C]CH₃I (methyl iodide) and 2-amino-(N,N-dimethyl)-ethanol (DMAE) precursor

branes. CHO-PET is used to image tumors, prostate cancer, and breast cancer in patients. The original synthesis of [11C] choline trapped the [11C]CH₃I in a reaction flask, then reacted with 2-amino-(N,N-dimethyl)-ethanol (DMAE) in acetone with KHCO₃ as base (Fig. 11.11). After stirring the reaction mixture at room temperature for 20 min, the final HPLC product has high specific activity (37 GBq/μmol), high radiochemical purity as well as chemical purity (98%), in about 30% radiolabeling yield [37, 38]. Subsequently, investigators have been optimizing the procedure and modifying automated systems to make the production of CHO more efficient with greater activities per single batch run [9]. [11C]choline has been produced via N-[11C]methylation of the precursor DMAE with either [11C]methyl iodide/bromide or [11C]methyl triflate, followed by purification using solid phase extraction (SPE) method [39].

[11C]Choline is the first and the only PET radiopharmaceutical approved by FDA for routine clinical studies. In spite of the extraordinary clinical investigations with hundreds of 11C-labeled PET radiotracers in neurology, oncology, and cardiology, the clinical utility of these tracers is still not well established.

11.3   13N-Labeled Radiopharmaceuticals

13N was first produced by the bombardment of boron with α particles using the $^{10}B(\alpha,n)^{13}N$ reaction [40]. The first 13N radiotracer of biological

interest was [13N]ammonia (NH₃). A number of nuclear reactions were used over the years to produce 13N [41]. However, the most popular method of producing 13N is based on the proton (8–15 MeV) bombardment of natural oxygen gas, using the $^{16}O(p,\alpha)^{13}N$ reaction [42]. 13N can also be produced by the proton (4–9 MeV) bombardment of isotopically enriched 13C using the $^{13}C(p,n)^{13}N$ reaction [43].

11.3.1 [13N]Ammonia (NH₃)

The most predominant chemical species of 13N produced in the water target is [13N]nitrate $\left(NO_3^-\right)$, while the other two species, [13N]nitrite (NO₂) and [13N] ammonia, may represent only a small fraction of the total 13N radioactivity (Table 11.4). [13N]ammonia is formed as the primary product by the abstraction of hydrogen atoms from the water, as shown in the Fig. 11.12. As the irradiation dose to target is increased, radiolytic oxidation occurs producing oxoanions of nitrogen, consisting of mainly nitrates and nitrites [44]. The most common method of increasing the radiochemical yield of [13N] ammonia is by the addition of free radical scavengers, such as ethanol and acetic acid, to the target water [45]. Subsequently, the $\left[^{13}N\right]NH_4^+$ ion can be trapped on a small cation exchange cartridge from which it can be eluted using physiological saline.

[13N]Ammonia can be used to prepare a number of 13N-labeled amino acids for the determination of protein synthesis rates in tumors. [13N]

Table 11.4 Methods for the production of ^{13}N and ^{15}O radiotracers

Target material	Nuclear reaction	In-target product(s)	Post irradiation treatment	Final product
H_2O	$^{16}O(p,\alpha)^{13}N$	NO_3^-, BO_2^-, NH_2^+	Reduction of anions using DeVarda's alloy and NaOH	$[^{13}N]NH_3$
H_2O/Ethanol (1 mM)	$^{16}O(p,\alpha)^{13}N$	NH_4^+	Radiochemical purification using cation exchange cartridge	$[^{13}N]NH_3$
N_2/O_2 (0.1–4.0%)	$^{14}N(d,n)^{15}O$	$[^{15}O]O_2$	Remove traces of NO_2 and O_3	$[^{15}O]O_2$
	$^{15}N(d,n)$ ^{15}O			
N_2/CO_2 (0.1–2.0%)	$^{14}N(d,n)^{15}O$	$[^{15}O]CO_2$	Remove traces of $[^{15}O]O_2$	$[^{15}O]CO_2$ with trace ^{13}N levels
N_2/H_2 (5.0%)	$^{14}N(d,n)^{15}O$	$[^{15}O]CO_2$	Remove traces of $[^{15}O]O_2$	$[^{15}O]CO_2$ with trace ^{13}N levels

Fig. 11.12 Reactions of ^{13}N with water in the cyclotron target

$$^{13}N + HOH \longrightarrow ^{13}NH_3$$

$$^{13}NH_3 + HOH \longrightarrow ^{13}NH_4^+ + OH^-$$

$$^{13}NH_4^+ \dashrightarrow ^{13}NO_3^- + ^{13}NO_2^-$$
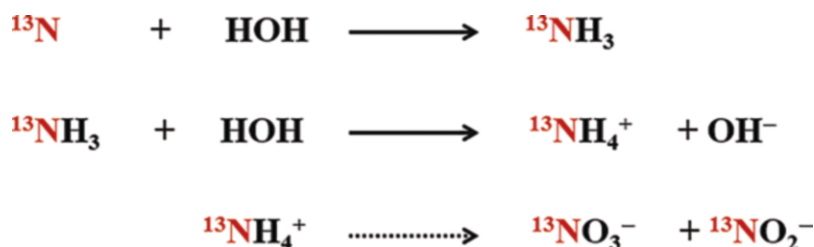
Ammonia has also been used to prepare ^{13}N-labeled anticancer drugs, such as CCNU, BCNU, and cisplatin [44].

11.3.2 Synthesis of [¹³N]Gemcitabine

Gemcitabine (Gemzar®, Eli Lilly) is a chemotherapy drug most commonly used to treat non-small cell lung, pancreatic, bladder, and breast cancer. [¹³N]Gemcitabine (GT) can be prepared using [¹³N]ammonia, as shown in Fig. 11.13. Following production of [¹³N]ammonia based on $^{16}O(p,\alpha)^{13}N$ reaction, the target water is passed through an ion exchange CM cartridge to trap [¹³N] ammonia. Subsequently, it is eluted into a vial containing a DeTet, (a gemcitabine precursor containing a tetrazol group) using 0.6 mL of sodium acetate buffer (1 M, pH 8.5). The mixture is then heated at 150–160 °C for 5 min. Finally, at the end of the reaction, the mixture is filtered and the filtrate is purified by HPLC to isolate the pure [¹³N]GT, which is then sterilized using membrane filtration [46].

11.4 ¹⁵O-Labeled Radiotracers

The potential utility of [¹⁵O]oxygen to study regional tracer biology was first demonstrated in murine experimental neoplasms at the Washington University in St Louis [47]. Since that time, different chemical forms of ^{15}O, such as carbon dioxide (CO_2), carbon monoxide (CO), water (H_2O), and n-butanol ($CH_3(CH_2)_3OH$) have been used to study oxygen metabolism, blood volume, and blood flow in humans with PET.

^{15}O can be produced in a cyclotron using a variety of nuclear reactions [44] but, the most commonly used reactions are $^{14}N(d,n)^{15}O$ and $^{15}N(p,n)^{15}O$. The chemical forms of ^{15}O generated in the target vessel depend on the nuclear reaction, energy of the bombarding particle, and the mixture of target gases (such as N_2/O_2, N_2/CO_2, and N_2/H_2) (Table 11.4).

11.4.1 ¹⁵O-Labeled Gases

When N_2 gas is bombarded with deuterons, the presence of oxygen (0.1–4.0%) leads to the gen-
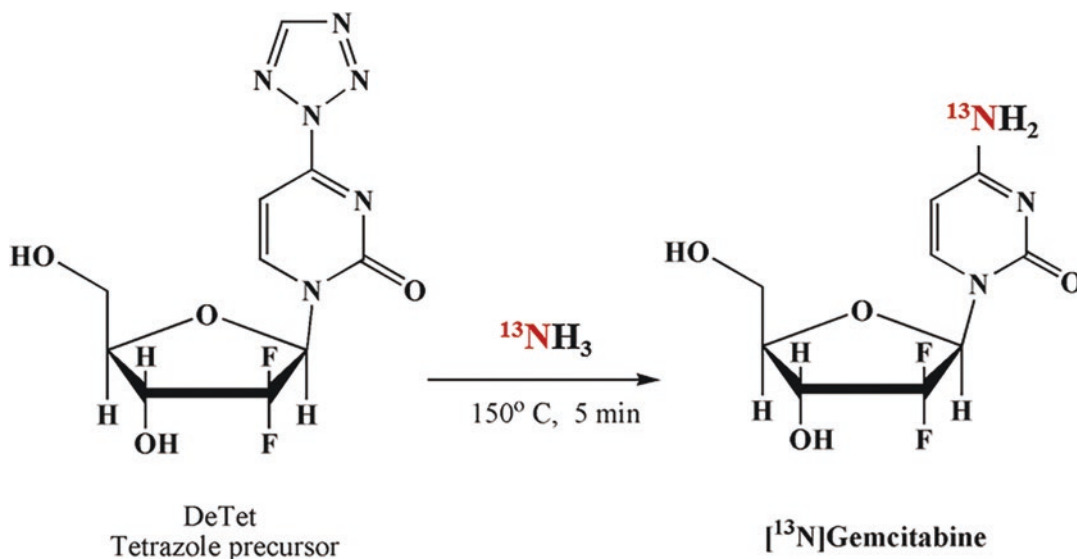
Fig. 11.13 Synthesis of [¹³N]Gemcitabine

eration of [^{15}O]O$_2$ with higher radiochemical purity. Subsequently, [^{15}]O$_2$ can be used to synthesize labeled CO and CO$_2$ gases.

[^{15}O]CO can be synthesized, when [^{15}]O$_2$ is reacted with carbon (activated charcoal) at 900–950 °C. However, when [^{15}]O$_2$ reacts with carbon at 400–450 °C, the predominant species formed is [^{15}O]CO$_2$. Methods for the in-target production of ^{15}O-labeled CO and CO$_2$ gases have also been developed. When the target N$_2$ gas is mixed with minimal O$_2$ levels (0.25%), [^{15}O]CO is produced. Also, the presence of a source of hot carbon within the target volume has been shown to be optimal for the in-target production of [^{15}O]CO [48, 49]. When N$_2$/CO$_2$ gas mixture is used as the target gas, the product ^{15}O$_2$ is converted to [^{15}O] CO$_2$ in the target. Due to secondary nuclear reaction, ^{12}C(d,n)^{13}N, the major radionuclidic impurity in [^{15}O]CO$_2$ preparations is [^{13}N]N$_2$ gas.

11.4.2 Synthesis of [¹⁵O]Water

When a N$_2$/H$_2$ mixture is bombarded with deuterons, the predominant ^{15}O-labeled product in the target vessel is [^{15}O]H$_2$O [50]. Also, [^{15}O]H$_2$O is readily synthesized outside the target by the palladium-catalyzed reaction of [^{15}O]O$_2$ with H$_2$ gas [51]. A flow of purified [^{15}O]O$_2$ in nitrogen is mixed with hydrogen and passed over a few pellets of palladium-alumina catalyst, and the resulting [^{15}O]H$_2$O vapor is trapped by bubbling the nitrogen carrier through a sterile saline solution. Based on this principle, an advanced automated system for the administration of [^{15}O]water at the bedside was developed by the investigators at the Hammersmith Hospital in London.

References

1. Crane HR, Lauritsen CC. Further experiments with artificially produced radioactive substances. Phys Rev. 1934;45:497.
2. Ruben S, Hassid WZ, Kamen MD. Reactive carbon in the study of photosynthesis. J Am Chem Soc. 1939;61:661.
3. Tobias CA, Lawrence JH, Roughton FJW. The elimination of carbon monoxide from human body with reference to possible conversion of CO to CO$_2$. Am J Phys. 1945;145:253.
4. Antoni G, Kihlberg T, Langstrom B. Aspects on the synthesis of ^{11}C-labeled compounds. In: Welch MJ, Redvanley CS, editors. Handbook of radiopharmaceuticals. West Sussex: Wiley; 2003.
5. Dahl K, Halldin C, Schou M. New methodologies for the preparation of carbon-11 labeled radiopharmaceuticals. Clin Transl Imaging. 2017;5:275–89.
6. Fowler JS, Ding Y-S. Chemistry. In: Wahl RL, Buchanan JW, editors. Principles and practice of positron emission tomography. Philadelphia, PA: Lippincott Williams and Wilkins; 2002.

7. Goud NS, Bhattacharya A, Joshi RK, et al. Carbon-11: radiochemistry and target-based PET molecular imaging applications in oncology, cardiology, and neurology. J Med Chem. 2021;64:1223–59.

8. Långström B, Kihlberg T, et al. Compounds labeled with short-lived β+ emitting radionuclides and some applications in life sciences. The importance of time as a parameter. Acta Chem Scand. 1999;53:651–69.

9. Tu Z, Mach RH. C-11 radiochemistry in cancer imaging applications. Curr Top Med Chem. 2010;10:1060–95.

10. Qaim SM, Clark JC, Crouzel C, et al. PET radionuclide production. In: Stöcklin P, editor. Radiopharmaceuticals for positron emission tomography. Dordrecht: Kluwer Academic; 1993.

11. Bida GT, Ruth TJ, Wolf AP. Experimentally determined thick target yields for the 14N (p,α) reaction. Radiochim Acta. 1978;27:181–5.

12. Christman DR, Finn RD, Kalstrom KI, et al. The production of ultra high specific activity ^{11}C labeled hydrogen cyanide, carbon dioxide, carbon monoxide, and methane via the 14N(p, α)11C reaction. Int J Appl Radiat Isot. 1975;26:435–41.

13. Lamb JF, James RW, Winchell HS. Recoil synthesis of high specific activity ^{11}C-cyanide. Int J Appl Radiat Isot. 1971;22:475–9.

14. Antoni G, Långström B. Progress in ^{11}C radiochemistry. In: Bailey DL, Townsend DW, Valk PE, Maisey MN, editors. Positron emission tomography- basic sciences. London: Springer; 2005. p. 223–36.

15. Ferrieri RA. Production and application of synthetic precursors labeled with carbon-11 and fluorine-18. In: Welch MJ, Redvanley CS, editors. Handbook of radiopharmaceuticals. West Sussex: Wiley; 2003.

16. Jewett DM. A simple synthesis of [^{11}C]methyl triflate. Appl Radiat Isot. 1991;43:1383–5.

17. Reiffers S, Vallburg W, Wiegman T, et al. Carbon-11 labeled methyl lithium as a methyl donating agent: the addition to 17-keto steroids. Int J Appl Radiat Isot. 1980;31:535–9.

18. Elsinga PH, Keller E, De Groot TJ, et al. Synthesis of [^{11}C]methyl magnesium iodide and its application to the introduction of [^{11}C]-N-ter-butyl groups and [^{11}C]-sec-alcohols. Appl Radiat Isot. 1995;46:227–31.

19. Schoeps K-O, Halldin C, Nagren K, et al. Preparation of [1-^{11}C]dopamine, [1-^{11}C]p-tyramine, and [1-^{11}C]m-tyramine. Nucl Med Biol. 1993;20:669–78.

20. Schoeps K-O, Stone-Elander S, Halldin C. On-line synthesis of [^{11}C]nitroalkanes. Appl Radiat Isot. 1989;40:261–2.

21. Ponchant M, Hinnen F, Demphel S, et al. [^{11}C] copper(I) cyanide: a new radioactive precursor for ^{11}C-cyanation and functionalization of haloarenes. Appl Radiat Isot. 1997;48:755–62.

22. Roeda D, Crouzel C, Zanten V. Synthesis of ^{11}C-urea for medical use. Radiochem Radioanal. 1978;33:175–6.

23. Steel CJ, Brady F, Luthra, et al. An automated radiosynthesis of 2-[^{11}C]thymidine using anhydrous [^{11}C]urea derived from [^{11}]phosgene. Appl Radiat Isot. 1999;51:377–88.

24. Långström B, Lundqvist H. The preparation of [^{11}C] methyl iodide and its use in the synthesis of [methyl-^{11}C]-L-methionine. Int J Appl Radiat Isot. 1976;27:357–63.

25. Larsen P, Ulin J, Dahlstrom K, et al. Synthesis of [^{11}C] iodomethane by iodination of [^{11}C]methane. Appl Radiat Isot. 1997;48:153–7.

26. Link JM, Krohn KA, Clark JC. Production of [^{11}C] CH$_3$I by single pass reaction of [^{11}C]CH$_4$ with I$_2$. Nucl Med Biol. 1997;24:93–7.

27. Kothari PJ, Suehiro S, Vallabhajosula S. Evaluation of commercial automated [^{11}C]methyl iodide (MeI-plus) synthesis module. J Label Compd Radiopharm. 2005;48:S226.

28. Makiko S, Kothari PJ, Vallabhajosula S. Quality control studies of [^{11}C]methyl iodide produced in liquid and gas phase synthesis modules. J Label Compd Radiopharm. 2005;48:S213.

29. Kothari PJ, Vallabhajosula S, Lampiri E, Goldsmith SJ. An improved gas phase module (GE TracerLab FXc) for the production of [^{11}C]methyl iodide. J Nucl Med. 2007;48:181p.

30. Schmitz F, Plenevaux A, Del-Fiore G, et al. Fast routine production of L-[^{11}C-methyl]-methionine with Al$_2$O$_3$/KF. Appl Radiat Isot. 1995;46:893–7.

31. Banati RB, Goerres GW, Myers R, et al. [^{11}C](R)-PK11195 positron emission tomography imaging of activated microglia in vivo in Rasmussen's encephalitis. Neurology. 1999;53:2199–203.

32. Hashimoto KI, Inoue O, Suzuki K, et al. Synthesis and evaluation of ^{11}C-PK11195 for in vivo study of peripheral-type benzodiazepine receptors using positron emission tomography. Ann Nucl Med. 1989;3:63–71.

33. Mathis CA, Bacskai BJ, Kajdasz ST, et al. A lipophilic thioflavin-T derivative for positron emission tomography (PET) imaging of amyloid in brain. Bioorg Med Chem Lett. 2002;12:295–8.

34. Mathis CA, Wang Y, Holt DP, et al. Synthesis and evaluation of ^{11}C-labeled 6-substituted 2-aryl benzothiazoles as amyloid imaging agents. J Med Chem. 2003;46:2740–54.

35. Buccino P, Savio E, Porcal W. Fully automated radiosynthesis of the amyloid tracer [^{11}C]PiB via direct [^{11}C]CO$_2$ fixation-reduction EJNMMI. Radiopharm Chem. 2019;4:14.

36. Bjurling P, Watanabe Y, Tokushige M, et al. Synthesis of β-^{11}C-labeled L-tryptophan and 5-hydroxy-L-tryptophan using a multi-enzymatic reaction route. J Chem Soc Perkin Trans. 1989;1:1331–4.

37. Hara T, Kosaka N, Shinoura N, Kondo T. PET imaging of brain tumor with [methyl-^{11}C]choline. J Nucl Med. 1997;38(6):842–7.

38. Hara T, Kosaka N, Kishi H. PET imaging of prostate cancer using carbon-11-choline. J Nucl Med. 1998;39(6):990–5.

39. Pascali C, Bogni A, Iwata R, et al. [^{11}C]Methylation on a C18 Sep-Pak cartridge: a convenient way to pro-

duce [N-methyl-^{11}C] choline. J Labelelled Compd Rad. 2000;43(2):195–203.

40. Joliot F, Curie I. Artificial production of a new kind of radioelement. Nature. 1934;133:201–2.

41. Schlyer DJ. Production of radionuclides in accelerators. In: Welch MJ, REdvanley CS, editors. Handbook of radiopharmaceuticals, radiochemistry and applications. New York: Wiley; 2003.

42. Tilbury RS, Dahl JR, Marano SJ. N-13 species formed by proton irradiation of water. J Label Compd Radiopharm. 1977;13:208.

43. Ferrieri RA, Schlyer DJ, Wieland BW, et al. On-line production of [N-13]-nitrogen from solid enriched [C-13] targets and its application to [N-13]ammonia using microwave radiation. Int J Appl Radiat Isot. 1983;34:897–900.

44. Clark JC, Aigbirhio FI. Chemistry of nitrogen-13 and oxygen-15. In: Welch MJ, Redvanley CS, editors. Handbook of radiopharmaceuticals. West Sussex: Wiley; 2003.

45. Wieland BW, Bida G, Padgett H, et al. In-target production of ^{13}N-ammonia via proton irradiation of dilute aqueous ethanol and acetic acid mixtures. Appl Radiat Isot. 1991;42:1095–8.

46. Vallabhajosula S, Zatorski A, Kothari PJ, et al. [^{13}N] gemcitabine: a new PET tracer to assess gemcitabine (GT) tumor uptake. J Nucl Med. 2008;49(s1):98.

47. Ter-Pogossian MM, Powers WE. The use of radioactive oxygen-15 in the determination of oxygen content in malignant neoplasms. In: Exterman RC, editor. Radioisotopes in scientific research, III. Oxford: Pergamon Press; 1958.

48. Berridge MS, Terris AH, Cassidy EH. Low carrier production of water and carbon monoxide. Appl Radiat Isot. 1990;41:1173–5.

49. Votaw JR, Satter MR, Sunderland JJ, et al. The Edison lamp: [^{15}O]carbon monoxide production in the target. J Label Compd Radiopharm. 1986;23:1211–3.

50. Vera Ruiz H, Wolf AP. Direct synthesis of ^{15}O-labeled water at high specific activities. J Label Compd Radiopharm. 1978;15:185–9.

51. Clark JC, Crouzel V, Meyer CJ. Current methodology for oxygen-15 production for clinical use. Appl Radiat Isot. 1987;38:597–600.

Metal Radionuclides for Molecular Imaging

12

> *The doubter is a true man of science; he doubts only himself and his interpretations, but he believes in science.*
>
> *Claude Bernard*

12.1 Introduction

Several prominent investigators have recently stated that the future of nuclear medicine is molecular imaging and theranostics [1, 2]. Nuclear medicine now provides diagnostic, prognostic, predictive, and intermediate endpoint biomarkers in oncology, cardiology, neurology, and infectious and inflammatory disorders. Whole-body target expression can be quantified and used for predicting therapy response. Treatment-induced metabolic changes serve as early prognosticators of therapy effectiveness. At the same time, technologic advances such as total-

body hybrid PET/CT PET/MR imaging are revolutionizing the diagnostic capabilities of PET systems. In the last 20 years, ^{18}F-labeled PET tracers dominated the field of molecular imaging. As of January 2022, there are 16 FDA-approved PET tracers, out of which 10 are based on ^{18}F and only 4 or based on radiometals (Table 12.1) [3]. With the FDA approval of ^{68}Ga-Dotatate, ^{68}Ga-Dotatoc, ^{68}Ga-PSMA−11, and ^{64}Cu-dotatate, the future of molecular imaging in the coming decade may be based on PET radiopharmaceuticals with radiometals.

Extensive knowledge, experience, and understanding of the metal chemistry at the tracer level

Table 12.1 Approved metal-based radiopharmaceuticals in clinical use for PET and SPECT

Radiopharmaceutical	Trade name	Decay	Target	Indication	FDA approval
^{111}In-DTPA-octreotide	OctreoScan	*EC*	Somatostatin type II receptor (SSTR-II)	Neuroendocrine tumors	1994
[99m]Tc-Apcitide (^{99m}Tc-P280)	AcuTect	*IT*	GP II$_b$/III$_a$ receptor	Deep vein thrombosis (DVT)	1997
^{68}Ga-DOTA-TOC (^{68}Ga-endotreotide)	Somakit	β^+	Somatostatin type II receptor (SSTR-II)	Neuroendocrine tumors	2016, 2019
[99m]Tc-Hynic-octreotide	Tektreotyd	*IT*			2018
^{68}Ga-DOTATATE	NetSpot®	β^+			2018
[64]Cu-Dotatate	DetectNet	β^+, β^-, *EC*			2020
^{68}Ga-PSMA-11		β^+	Prostate specific membrane antigen (PSMA)	Prostate cancer	2020

would enable us to develop a number of new molecular imaging radiotracers based on β^+-emitting radiometals. ^{99m}Tc and ^{111}In labeled SPECT radiopharmaceuticals will continue to play a prominent role in the development of SPECT radiopharmaceuticals. Since targeted radionuclide therapy (TRT) is primarily based on metal radionuclides (such as ^{90}Y, ^{177}Lu, ^{225}Ac, and ^{227}Th), the theranostics and personalized medicine dictate that the development of radiopharmaceuticals for imaging and therapy must be based on theranostic pair of radiometals. The advantages of metal-labeled molecular imaging radiotracers can be summarized as follows:

- Easy availability: ^{68}Ga generators are available for easy in-house preparation based on kit production.
- Cyclotron production of metallic nuclides (^{68}Ga, ^{89}Zr, and ^{44}Sc) has been optimized using medical cyclotrons using primarily (*p,n*) nuclear reactions.

- Fifty-year experience with the development of bifunctional chelating agents (BFCs) and metal-labeled radiopharmaceuticals.
- Ability to label target specific biomolecules (peptides and proteins).
- Availability of theranostic radionuclide pairs for imaging and therapy.
- High SA of radiometal.
- High SA of metal-labeled peptide and/or protein.
- High in vivo stability of metal-labeled tracers.
- Favorable radiation dosimetry, especially with ^{68}Ga and ^{44}Sc.

12.2   Radiometals for PET and SPECT

Radioisotopes of various metals useful for PET and SPECT imaging studies are listed in Tables 12.2 and 12.3. The selection of a radiometal for

Table 12.2 Important radioisotopes of metals useful for PET and SPECT

Metal		Stable isotopes		Radioactive isotopes				
Z	Name	Nuclide	%	Nuclide	$T_{1/2}$ (h)	Decay	% β^+ emission	SA (Ci µmole^{-1})
21	Scandium	^{45}Sc	100	^{44}Sc	3.927	EC, β^+	β^+ (94.27)	
22	Titanium	^{46}Sc	8.25	^{45}Ti	3.10	EC, β^+	β^+ (84.82)	
		^{47}Sc	7.44					
		^{48}Sc	73.72					
		^{49}Sc	5.41					
		^{50}Sc	5.18					
27	Cobalt	^{59}Co	100	^{55}Co	17.53	EC, β^+	β^+ (77)	
29	Copper	^{63}Cu	69.17	^{60}Cu	0.39	EC, β^+	β^+ (93)	
		^{65}Cu	30.83	^{61}Cu	3.32	EC, β^+	β^+ (62)	
				^{62}Cu	0.163	EC β^+	β^+ (98)	19,310
				^{64}Cu	12.80	EC, β^+, β^-	β^+ (19)	245
31	Gallium	^{69}Ga	60.10	^{66}Ga	9.45	EC, β^+	β^+ (62)	331
		^{71}Ga	30.90	^{67}Ga	78.24	EC, γ		40
				^{68}Ga	1.14	EC, β^+	β^+ (90)	2766
37	Rubidium	^{85}Rb	72.16	^{82}Rb	75 s	EC, β^+	β^+ (96)	
		^{87}Rb	27.84					
39	Yttrium	^{89}Y	100	^{86}Y	14.74	EC, β^+	β^+ (34)	213
40	Zirconium	^{90}Zr	51.45	^{89}Zr	78.48	EC, β^+	β^+ (23)	39.9
		^{91}Zr	11.22					
		^{92}Zr	17.15					
		^{94}Zr	17.38					
		^{96}Zr	2.80					
49	Indium	^{113}In	4.3	^{110}In	1.1	EC, β^+, γ	β^+ (71)	
		^{115}In	95.7	^{111}In	67.2	EC, γ		47
	Technetium	No stable isotope		^{94m}Tc	0.88	EC, β^+	β^+ (72)	
				^{99m}Tc	6.01	IT		522

Table 12.3 The most common nuclear reactions for the production of positron-emitting radiometals

Radiometal	Nuclear reaction	Target abundance (%)	Proton energy range (MeV)
^{44}Sc	^{44}Ca (p,n) ^{44}Sc	2.086	~11
^{45}Ti	^{45}Sc (p,n) ^{45}Ti	100	~11
^{61}Cu	^{61}Ni (p,n) ^{61}Cu	1.25	9–12
^{64}Cu	^{64}Ni (p,n) ^{64}Cu	0.91	8–15
^{66}Ga	^{66}Zn (p,n) ^{66}Ga	27.8	8–15
^{67}Ga	^{68}Zn $(p,2n)$ ^{67}Ga	19.0	12–22
^{68}Ga	^{68}Zn (p,n) ^{68}Ga	>97%	11–12
^{86}Y	^{86}Sr (p,n) ^{86}Y	9.86	10–15
^{89}Zr	^{89}Y (p,n) ^{89}Zr	100	~14
^{94m}Tc	^{94}Mo (p,n) ^{94m}Tc	9.12	10–15
^{110}In	^{110}Cd (p,n) ^{110}In	12.5	10–20
^{111}In	^{112}Cd $(p,2n)$ ^{111}In	24.0	12–22

labeling a specific peptide or protein is dependent on several factors, such as physical half-life, SA, type(s) of decay and emission(s), energy of the emission(s), and cost and availability. In addition, pharmacokinetics, drug delivery of the radio-metal-complex to the target site and clearance of the radiometal complex from both the target and nontarget tissues are all important factors that determine the selection of an appropriate radiometal in tracer development.

Among the β^+-emitting metallic nuclides, ^{64}Cu ($T = 12.6$ h), ^{66}Ga ($T_{1/2} = 9.45$ h), ^{86}Y ($T_{1/2} = 14.74$ h), and ^{89}Zr ($T_{1/2} = 3.27$ days) are more appropriate for development of commercial PET radiopharmaceuticals since they can be transported across the country. For most of these metallic radionuclides, cyclotron production methods have been optimized, using medical cyclotrons using primarily (p,n) nuclear reactions (Table 12.3). The two nuclides with short half-lives, ^{68}Ga ($T_{1/2} = 68.3$ min) and ^{62}Cu ($T_{1/2} = 9.76$ min) can be produced on demand from commercial generator systems without the need for an on-site cyclotron. However, cyclotron production methods for ^{68}Ga have been well optimized both for liquid targets (3–5 GBq) and solid targets (50–100 GBq). Also, the ^{82}Sr($T_{1/2} = 25$ days) $\rightarrow$ ^{82}Rb ($T_{1/2} = 75$ seconds) generator (cardioGen-82®) has been FDA approved for myocardial perfusion studies. The positron-emitting metals such as ^{44}Sc, ^{45}Ti, and radiometals ^{55}Co have optimal half-lives and positron kinetic energies and are actively investigated by several groups for labeling small molecules, and peptides for molecular imaging studies.

12.2.1 Specific Activity of Radiometals

The SA of the radiometal is an indicator of potency; the higher the SA of the radiometal, the higher is the SA of the radiometal-labeled biomolecule. The theoretical SA of carrier-free radiometals, useful for developing PET and SPECT radiotracers, is shown in Table 12.2. The practical SA that can be achieved by cyclotron production or by generator, however, depends on many other factors. In general, SA of all β^+-emitting radiometals is much higher than the corresponding SPECT nuclides, except for ^{89}Zr. Also, the SA of ^{68}Ga (2.766 Ci nmol^{-1}) is even much higher than that of ^{18}F (1.71 Ci nmol^{-1}).

The maximum theoretical SA of ^{64}Cu is ~4000 mCi μg^{-1} but, the cyclotron production of ^{64}Cu achieves a maximum SA of ~200 mCi μg^{-1} at EOB [4]. In practice, purity control difficulties in solid target production often cause much lower SA to be delivered due to cold Cu contamination. In comparison, the SA of generator-produced ^{62}Cu is >70,000 mCi μg^{-1} and levels approaching this maximum can be routinely achieved.

12.2.2 Decay Characteristics of Radiometals

The intensity of β^+ emission from a radionuclide or branching ratio directly affects the rate of true coincidences because lower β^+ decay fraction results in fewer annihilation events per MBq [5].

Also, the β^+ must slow down and rest before it can annihilate with an electron. Thus, annihilation takes place in a spherical volume whose radius depends on the energy. Consequently, with PET, positrons with lower energy will have shorter range in tissue and higher expected spatial resolution [6]. In addition, the ability to visualize a lesion depends on the amount of activity in the lesion compared to the background. The short half-life metals such as ^{68}Ga are ideal for radiotracers, such as peptides and small molecules, which clear from circulation rapidly.

Another important consideration is the emission of γ photons associated with certain positron emitters. The number of photons, amount of energy, and the abundance (%) for several radiometals useful for PET are shown in Table 12.4. Except for ^{62}Cu, ^{64}Cu, and ^{68}Ga, all other radiometals have significant gamma emissions. Radionuclides, such as ^{66}Ga, ^{86}Y, ^{89}Zr, and ^{124}I, have a very high proportion of γ emission compared to the intensity of β^+ emission. Detection of gamma photons or scattered photons, along with annihilation photons, may reduce the coincidence count rate performance (true counts) in several different ways [7, 8]. Also, the associated gamma emission will have a significant impact on the radiation dose to the patient, radiation exposure, and burden to the technical staff [5].

For the development of PET tracers, it is important to recognize that each radionuclide has unique imaging characteristics with respect to image quality, biological vector compatibility, cost, availability, and dosimetry. In principle, PET performance, in terms of spatial resolution and the range in tissue (Table 12.5), will change with positron-emitting radionuclide due to the kinetic energy of the positron [6, 9, 10]. Therefore, it is vital to understand and characterize the variables that will impact image quality. Among the radiometals listed in Tables 12.4 and 12.5, the positron from ^{64}Cu has lowest energy compared to that from ^{86}Y and ^{66}Ga. In contrast, the positron from ^{89}Zr has energy comparable to that of ^{18}F. As a result, ^{89}Zr has become more popular for the molecular imaging studies, especially with monoclonal antibodies.

Table 12.5 Range of positrons in water[a]

Radionuclide	T½	β + Emean (KeV)	CDSA range[b] (mm)
^{72}As	26 h	1170	5.16
^{68}Ga	68 m	830	3.37
^{86}Y	14.7 h	660	2.50
^{89}Zr	78.4 h	396	1.23
^{18}F	110 m	250	0.62
^{52}Mn	5.59 d	242	0.59

[a]Data from [6]
[b]Continuous slowing down approximation (CSDA) for the average energy of positron

Table 12.4 Positron-emitting radionuclides and decay characteristics

Nuclide	T½	β^+ decay (%)	β^+ Energy (MeV) E_{max}	E_{mean}	Major γ energy (KeV) and abundance (%) 1	2	3
^{44}Sc	3.927	94.27	1.473	0.632	1157 (100)		
^{45}Ti	3.10	84.82	1.027	0.439			
^{55}Co	17.53	76.0	1.498	0.573	931 (75)	1408 (16.9)	
^{62}Cu	0.163	97.83	2.937	1.319			
^{64}Cu	12.80	17.6	0.653	0.2782	1346 (0.47)		
^{66}Ga	9.49	57.0	4.153	1.75	1039 (37)	2751 (23)	4.295 (4)
^{68}Ga	1.14	88.9	1.899	0.830	1077 (3)		
^{82}Rb	75 s	95.4	3.382	1.481	777 (13.4		
^{86}Y	14.74	31.9	3.141	0.662	443 (17)	627 (33)	1.076 (83)
^{89}Zr	78.48	22.74	0.902	0.396	908 (100)		
^{94m}Tc	0.88	72.0	2.47	1.0942	871 (94.2)	1522 (4.5)	1869 (5.7)

12.3 Chemistry of Radiometals

Some of the important physical properties and the electron configuration of various metals useful in developing molecular imaging probes are summarized in Table 12.6. Among these metals, gallium and indium are post-transition metals (group 13 or IIIB in the periodic table). All other metals, useful for developing radiopharmaceuticals for molecular imaging, are transition metals with complex coordination chemistries. The therapeutic radionuclides ^{177}Lu (lanthanide), ^{225}Ac, and ^{227}Th (actinides) are included here to compare the chemistry with PET/SPECT nuclides. All the metals in Table 12.6 requite a bifunctional chelating agent (BFC) to complex the radiometal and to form a covalent bond with the targeting vehicle (or vector), such as small molecule, peptide, or protein (monoclonal intact antibodies (mAb) or different size fragments derived from antibodies). Figure 12.1 shows a schematic of metal-based molecular imaging radiopharmaceutical composed of four different components: targeting vehicle, spacer, linker, and chelating agent.

12.3.1 Chelators for Metal Complexation

Coordination chemistry is the study of compounds that have a central metal atom (coordination center) surrounded by molecules or anions, known as ligands. The ligands are attached to the central metal atom by coordinate bonds (also known as dipolar or dative bonds), in which both electrons in the bond are supplied by the same atom on the ligand. The atom within a ligand that is bonded to the central metal atom or ion is called the donor atom. The number of donor atoms attached to the central atom, or ion, is called the coordination number. In coordination compounds, the metal ions have two types of valences; *primary valence* (also known as oxidation state) refers to the ability of metal ion to form ionic bonds with oppositely charged ions, while *secondary valence* (also known as coordination number) refers to the ability of a metal ion to bind to Lewis bases (ligands) to form complex ions. Therefore, the coordination number is the number of bonds formed by the

Table 12.6 Physical and chemical characteristics of radiometals

	Transition metals					Post-transition metals		Lanthanides	Actinides	
Property	Sc	Cu	Y	Zr	Tc	Ga	In	Lu	Ac	Th
Atomic number	21	29	39	40	43	31	49	71	89	90
Group	3	11	3	4	7	13	13	3	n/a	n/a
Block	d	d	d	D	d	p	p	D	f?	f
Atomic radius (pm)	162	128	181	160	136	122	163	174	126	108–135
Ionic radius (pm)	75–87	80	90–108	109	56	47–62	62–92	86–103	112	105
Electron structure	[Ar] $3d^1$ $4s^2$	[Ar] $3d^{10}\,4s^1$	[Kr] $4d^1$ $5s^2$	[Kr] $4d^2$ $5s^2$	[Kr] $4d^5$ $5s^2$	[Ar] $3d^{10}\,4s^2$ $4p^1$	[Kr] $4d^{10}\,5s^2$ $5p^1$	[Xe] $4f^{14}$ $5d^1\,6s^2$	[Rn] $6d^1\,7s^2$	[Rn] $6d^2$ $7s^2$
Electronegativity	1.36	1.90	1.22	1.33	1.90	1.81	1.78	1.27	1.1	1.3
Oxidation state	+3	+1, +2	+3	+4	−1 to +7	+3	+3	**+3**	+3	+4
Coordination number	6–8	4	6–9	6–8	2–8	6	4–8	6–9	9–10	>8

Data for effective ionic radii were derived from http://abulafia.mt.ic.ac.uk/shannon/ptable.php
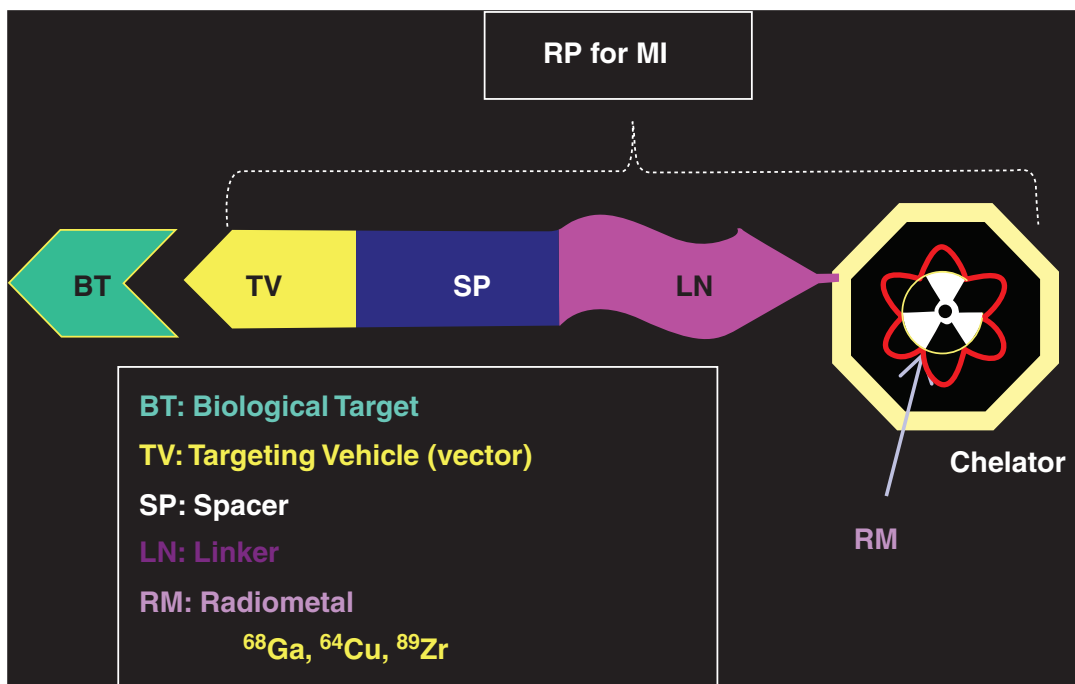
Fig. 12.1 Schematic of a metal-based molecular imaging radiopharmaceutical for PET and SPECT

metal ion with the atoms (that can donate a pair of electrons) in a chelating agent. This number varies from 2 to 8 (Table 12.6), depending on the size, charge, and electron configuration of the metal ion. The ligand geometric arrangements of coordination compounds can be linear, square planar, tetrahedral, or octahedral, depending on the coordination number.

Monodentate ligands (such as F^-, Cl^- ions) donate one pair of electrons to the central metal atoms. Polydentate ligands, also called chelates or chelating agents, donate more than one pair of electrons to the metal atom forming a stronger bond and a more stable complex. The metal complex can be neutral or charged. When the metal complex is charged, it is stabilized by neighboring counter-ions. These metal complexes are called chelate complexes and the formation of such complexes is called chelation or complexation and coordination. Alfred Werner, a Swiss chemist, won the Nobel Prize in chemistry in 1913 for his work on transition metal complexes.

As shown in Fig. 18.1, the radiometals used for imaging and targeted therapy form strong coordinate covalent bonds with chelating agents. The main goal in the synthesis of metal-based radiopharmaceuticals is to form a robust coordination complex that is stable and does not release the free metal in vivo. BFCs serve the dual purpose of radiometal complexation and bioconjugation to the targeting vehicle (or the vector). Two classes of chelators known as acyclic and macrocyclic have been developed in the last four decades for the development of metal-based radiopharmaceuticals.

12.3.1.1 Chelating Agents

Some of the important acyclic and macrocyclic chelators used in the synthesis of metal-based therapeutic radiopharmaceuticals are shown in the Figs. 12.2 and 12.3 and summarized in Table 12.7. Each of these chelating agents differ in size and offer different donor groups such as carboxylic acids, alcohols, amines, thiols, and phosphonic acids. Since the chelating agent must form complexes with the metal ion with high thermodynamic stability and kinetic inertness at pH 5–7.5, chelating agents must meet specific
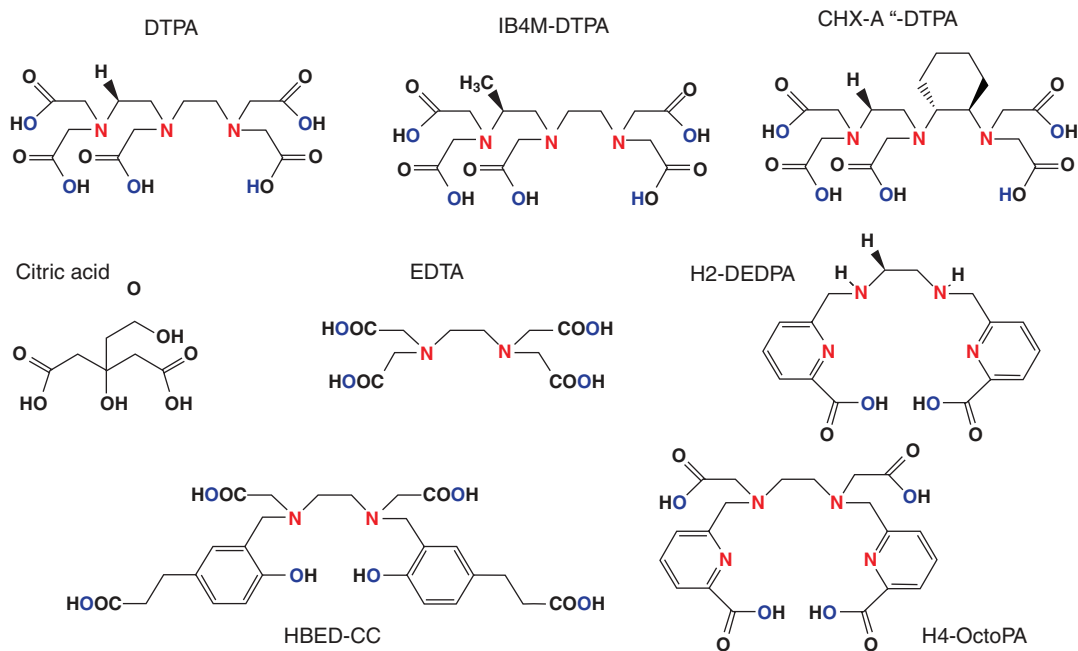
Fig. 12.2 Acyclic chelators used to prepare radiometal therapeutic radiopharmaceuticals. The nitrogen and oxygen donor atoms for metal coordination shown in color

Fig. 12.3 Macrocyclic chelators used to prepare radiometal therapeutic radiopharmaceuticals. The nitrogen and oxygen donor atoms for metal coordination shown in color

Table 12.7 Acyclic and macrocyclic chelators used to prepare radiometal therapeutic radiopharmaceuticals

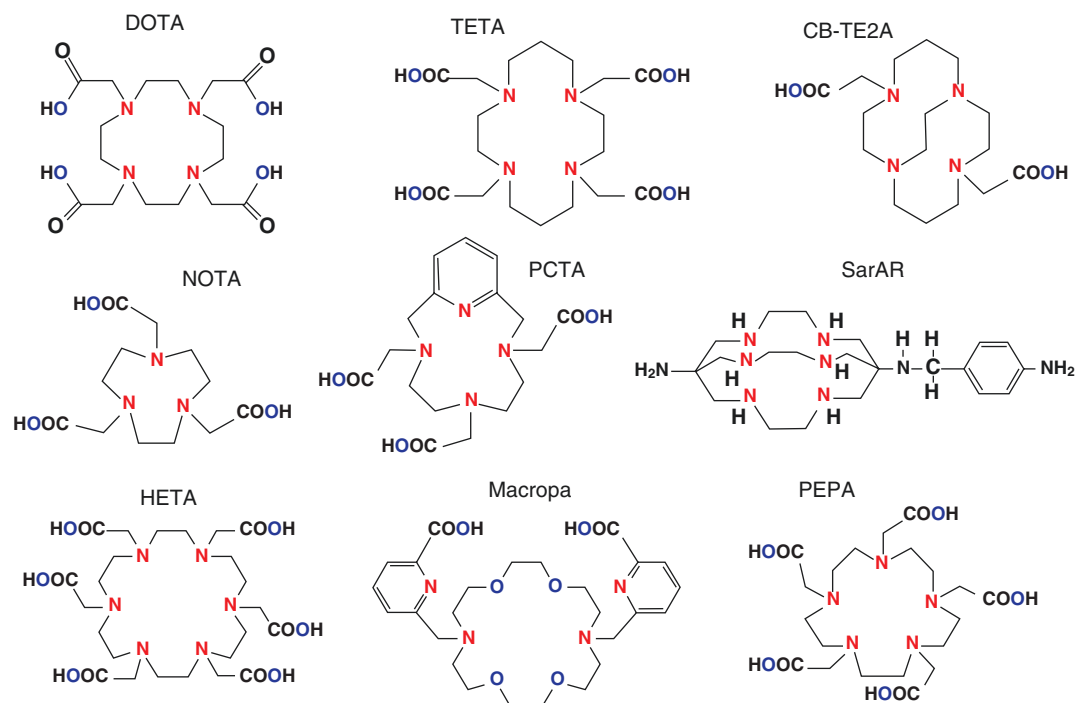| Chelator	Chemical name	Donor atoms	CN	Metal
DTPA	Diethylenetriaminepentaacetic acid	N_3O_5	8	Ga, In
CHX-A''-DTPA	Trans-(S,S)-cyclohexane-1,2-diamine-pentaacetic acid	N_3O_5	8	Y
EDTA	Ethylenediaminetetraacetic acid	N_2O_4	6	Ga, In
H$_2$dedpa	1,2-[[6-(carboxy)-pyridin-2-yl]-Methylamino] ethane	N_4O_2		
H$_4$octapa	N,N′-bis(6-carboxy-2-pyridylmethyl)-Ethylenediamine-N,N′-diacetic acid	N_4O_4	8	
HBED-CC	3-[3-[4-[5-(2-carboxyethyl)-2-hydroxyphenyl]-1,4-bis (carboxymethylamino)butyl]-4-hydroxyphenyl]propanoic acid	N_2O_6	8	Ga
Desferrioxamine B (DFO)	1-Amino-6,17-dihydroxy-7,10,18,21-tetraoxo-27-(N-acetyl hydroxylamino)-6,11,17,22-tetraazaheptaeicosane	O_6	6	Zr
NOTA	1,4,7-triazacyclononane-1,4,7-tri-acetic acid	N_4O_3	6	Ga, Sc
DOTA	1,4,7,10-tetraazacyclododecane-1,4,7,10-tetraacetic acid	N_4O_4	8	In, Sc, Ga, Y, Bi, Lu, Ac, Th
TETA	1,4,8,11-tetraazacyclotetradecane-1,4,8,11-tetraacetic acid	N_4O_4	8	Cu
CB-TE2A	4,11-bis-(carboxymethyl)-1,4,8,11-tetraazabicyclo[6.6.2]-hexadecane	N_4O_2	6	Cu
SarAr	1-N-(4-aminobenzyl)-3,6,10,13,16,19-hexaazabicyclo[6.6.6]eicosane-1,8-diamine (SarAr)	N_6	6	Cu
PCTA	3,6,9,15-Tetraazabicyclo[9.3.1]pentadeca-1(15),11,13-triene-3,6,9-triacetic acid	N_4O_3	7	Ga, Cu

requirements. The fundamental metal ion characteristics (Table 12.6), such as atomic number, charge, and radius, which vary from metal ion to metal ion, and result in distinct preferences for geometry, coordination number, and ionic/covalent bond contribution. For optimal stability, the coordinating functional groups of the chelator should adopt the favored geometry of the metal ion while, simultaneously, satisfying metal coordination requirements to prevent competition from extraneous ligands, especially in biological systems [11–13]. The metal-ligand compatibility is dependent on the hard-soft acid-base (HSAB) character of the involved atoms.

Most of the radiometals are hard acids with 2+ and 3+ as their major oxidation states in aqueous solution. Hard metal ions have high charge density, have nonpolarizable electron shells, and tend to form predominantly ionic bonds, in which electrostatic attraction is the primary driving force of bond formation. A useful metric for hard-soft character is the Drago-Wayland parameter, I_A,

$(I_A = E_A/C_A)$ which conveys the electrostatic (EA) and covalent (CA) contributions to the formation constants of Lewis acid-base complexes (includes metal complexes) in aqueous solution [13]. A higher value of I_A indicates greater hardness of the metal (Table 12.8). Therefore, hard metal ions prefer hard donating groups (e.g., carboxylic acids), which possess dense anionic character (e.g., carboxylic acids). Conversely, soft metals have low charge density and polarizable electron shells, and form covalent bonds with softer, more electron-disperse donor groups.

Acyclic Chelating Agents

Diethylenetriaminepentaacetic acid (DTPA) was one of the first acyclic chelators (Fig. 12.2) used in the 1980s to label peptides and antibodies with ^{111}In and [90]Y. DTPA has been successfully used to develop FDA approved peptide, ^{111}In-DTPA-Octreotide (Octreoscan®), a SPECT imaging agent for the detection of neuroendocrine tumors. Subsequently, several DTPA analogs such as

Table 12.8 Metal-chelate complexes and stability parameters[a]

Metal			DOTA			DTPA		
	Hardness	I_A	CN	Log K_{ML}	pM	CN	Log K_{ML}	pM
Sc^{3+}	Hard	10.49	N_4O_4	27.0–30.8	23.9–26.5	N_3O_5	26.3–27.4	
Cu^{2+}	Borderline soft		N_4O_2	22.7	17.6			
Ga^{3+}	Hard	7.07	N_4O_2	21.3–26.1	15.2	N_3O_4	24.3	20.2
Y^{3+}	Hard	10.64	N_4O_4	24.3–24.9	19.3–19.8	N_3O_5	21.9–22.5	17.6–18.3
In^{3+}	Borderline hard	6.3	N_4O_4	23.9	18.8	N_3O_5	29.0–29.5	24.4–25.7

[a]The table is revised from reference Kostelnik and Orvig 2018

1B4M-DTPA (Tiuxetan) and CHX-A"-DTPA were developed to improve the in vivo stability of radiolabeled complexes. To increase the stability, preorganizing groups have been attached to the carbon backbone which can stabilize the conformation of the free chelator to form a more kinetically stable complex. Tiuxetan was used to develop the FDA-approved ^{111}In or ^{90}Y-labeled anti-B1 mAb (Zevalin®) for the targeted therapy of patients with non-Hodgkin's lymphoma (NHL).

EDTA analogs such as HBED-CC, H4-Octopa were also developed to improve stability of metal-labeled complexes in vivo. HBED-CC chelator was used to prepare FDA approved ^{68}Ga-PSMA-11 for imaging PSMA-positive prostate cancer. Acyclic chelators are of special interest when antibodies or short-lived radiometals are used because radiolabeling can be performed within minutes at room temperature.

Macrocyclic Chelating Agents

Macrocyclic ligands are not only multi-dentate, but because they are covalently constrained to their cyclic form, they allow less conformational freedom. The ligand is said to be pre-organized for binding and there is little entropy penalty for wrapping it around the metal ion. To increase the kinetic stability of metal complexes, the structure of acyclic polyamino-polycarboxylate ligands was modified to cyclic chelates such as DOTA, NOTA, TETA, PEPA, and HEHA (Fig. 12.3).

The first synthesis of DOTA was reported in 1976 by Stetter and Frank. DOTA (also known as H4DOTA) is derived from the macrocycle, cyclen. Subsequently, macrocyclic BFCs based on DOTA were developed by strategically incorporating functionalized side chain to facilitate binding to antibodies [14]. In the last three decades, DOTA chelator and its derivatives have become the most important chelating agents in the development of both diagnostic and therapeutic radiopharmaceuticals.

DOTA-based chelators tend to exhibit high in vivo stability for most trivalent radiometals but, require somewhat elevated temperatures and/or longer complexation reaction times. For antibodies, higher temperature is not appropriate but, if peptides are used as vector molecules, the slow kinetic of formation can be overcome by heating (close to 100 °C) or the use of microwave technology, which usually does not destroy the biomolecule. Once the metal is inside the macrocyclic tetraaza core, the metal will remain there under physiological conditions [15].

12.3.1.2   Stability of Metal-Chelate Complex

The electronegativity and oxidation state play a major role in the formation of metal-ligand complexes. Evaluation of a chelator's metal affinity requires knowledge of its acid-base properties (protonation constants) and the thermodynamic stability of its metal complexes. The metal ions dissolved in water are complexed to form aqua ions. However, in the presence of a chelating agent or the ligand (L) with greater affinity for the metal than the affinity of OH^- ion for the metal, the formation of metal-chelate complex is preferred, as shown below.

$$M + L \rightleftharpoons ML \qquad (12.1)$$

$$K_s = \frac{[ML]}{[M][L]} \qquad (12.2)$$

In the above equation, [ML] represents the concentration of the metal-ligand complex, while

[M] and [L] represent the concentrations of the free metal and the free ligand, respectively. The stability of the metal-ligand complex is defined by the stability constant ($K_{S \text{ or }} K_{ML}$) when the system reaches an equilibrium between interacting chemical species [16]. The higher the value of K_{ML}, the greater the thermodynamic stability of the metal-ligand complex (Table 12.8). The values of K_{ML} (such as 10^4 or 10^{30}) are normally represented as log K_{ML} values (such as 4 and 30). A more useful thermodynamic parameter is the *pM value* ($-\log[M]_{Free}$), and the pM values are linearly correlated with K_{ML} values and express the extent to which a metal ion complex is formed in solution under physiologically relevant conditions [13]. The K_{ML} values are usually determined for metal-chelate reactions under ideal conditions of buffer, pH and temperature, and do not necessarily reflect the stability of metal-ligand complex in vivo. For a specific metal, a chelating agent with a higher *pM* value is desirable but, does not predict kinetic stability.

It is important to appreciate that the stability constant can only reveal the direction of the reaction (formation or dissociation) but, not the rate of the reaction. For example, when a purified metal-ligand complex is injected into the circulation, the rate of dissociation of the complex may be significantly increased due to extreme dilution of the complex. Therefore, the *kinetic stability* of the metal-ligand complex is very important under in vivo conditions where competing ions (such as Fe^{3+}, Ca^{2+}, Cu^{2+}, Zn^{2+}) and ligands (serum proteins, enzymes) may augment the transchelation of the radiometal [16]. A quantity known as *conditional stability constant* can be measured or estimated as a function of pH and in the presence of different amounts of other competing ligands. The in vivo stability or the kinetic inertness of a radiotracer is evaluated more appropriately based on biodistribution studies in animal models using a radiometal-labeled chelate conjugated target vehicle (vector) with high radiochemical purity (RCP) and optimal specific activity (SA).

12.3.1.3 Bifunctional Chelating Agents

When a chelating agent has two different functional groups (such as alcohol, carboxylic acid, or amide), it is called a bifunctional chelating agent (BFC or BFCA). The BFC consists of a chelating moiety to complex the radiometal and a functional group for the covalent attachment of the biomolecule (such as peptide and mAb). The BFCs contain a side chain (not participating in the chelation of metal) for conjugation to a peptide or protein. The side chain can be attached to the carbon backbone of the chelate (C-functionalized chelate) or by substitution to one of the nitrogen atoms in the molecule. C-functionalized chelating agents are preferable and provide greater stability to the metal-chelate complex, since all the donor atoms (nitrogen and oxygen) will be available for coordination with the metal ion. Once an appropriate chelating agent is selected for a specific metal, BFC is synthesized by adding the functional group to the chelating agent. Some of the most common commercially available BFCs used in the synthesis of radiometal complexes for therapeutic applications are shown in Fig. 12.4. In the last three decades, an array of reactive functional groups for conjugation of BFCs to proteins have been reported in the literature [13, 17–19].

As shown in Fig. 12.1, in the design of target-specific metal-labeled radiopharmaceuticals, a pharmacokinetic modifying (PKM) linker is attached between the targeting vehicle and the BFC-radiometal complex. The RKM Linkers and spacers are often employed to separate the BFC and the bioconjugate for two reasons. The first is to avoid detrimental interactions of the biomolecule with the coordination complex formation of the chelator with the radiometal. The second more important reason is to modify the excretion kinetics and optimize the biodistribution and pharmacokinetics of the radiolabeled complex to enhance the target/background (T/B) ratios. These linkers can be neutral or charged (cationic or anionic), or metabolically cleavable and biodegradable. A simple hydrocarbon chain will increase lipophilicity while a peptide sequence
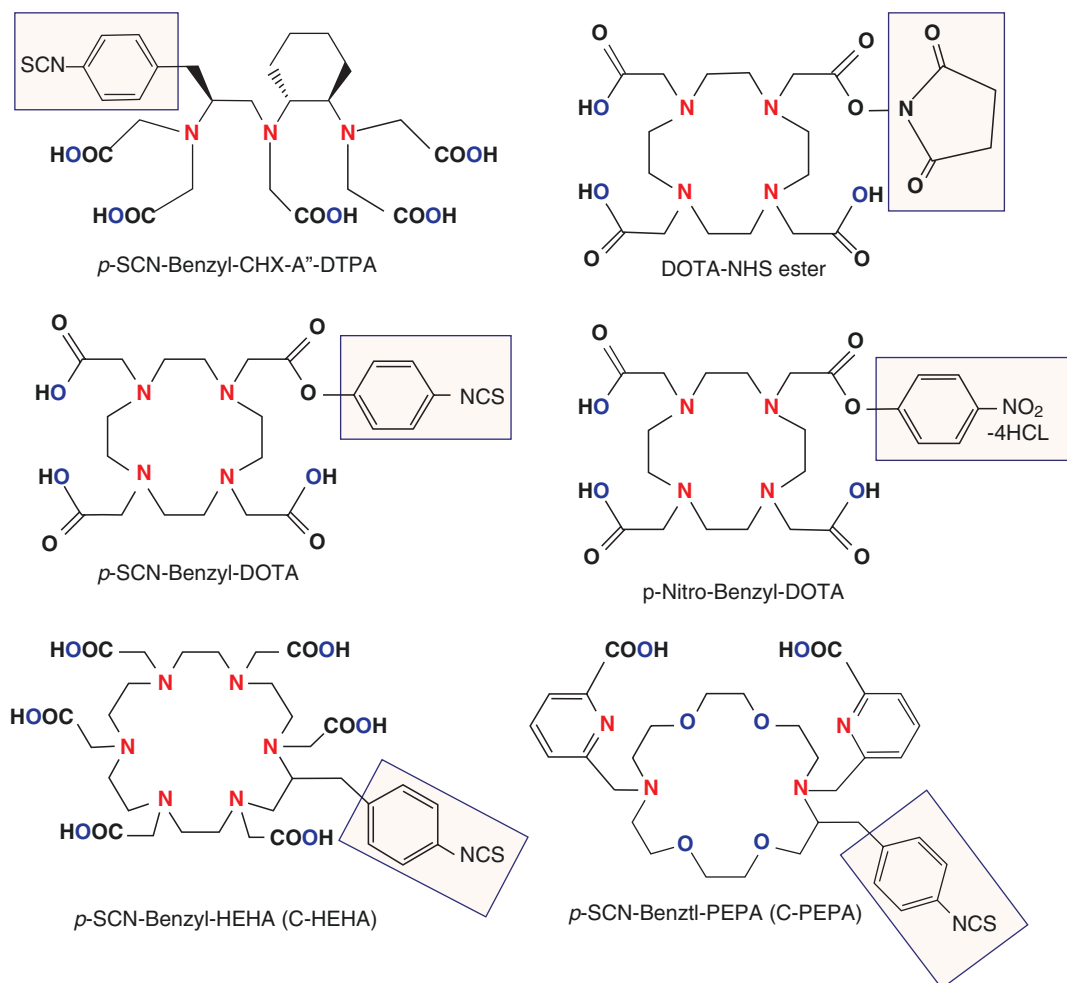
Fig. 12.4 Bifunctional chelating agents (BFCA) commonly used to conjugate a biomolecule and complex a radiometal. The nitrogen and oxygen donor atoms for metal coordination shown in color

will increase hydrophilicity and renal clearance. Polyethylene glycol (PEG) linker can alter the excretion kinetics and improve tumor targeting.

Coupling of BFC to Biomolecule

To combine a biomolecule with a BFC, two different strategies are generally used. In the pre-conjugation strategy, the BFC is first radiolabeled with the metal and the purified radiometal-BFC complex is then conjugated to the biomolecule. Since the conjugation step is not quantitative and requires additional purification steps, pre-conjugation strategy may not be practical for routine use. In the post-conjugation radiolabeling

approach, the BFC is first conjugated to the bio-molecule and the purified BFC-biomolecule complex (precursor) can be stored under appropriate conditions for several months or years before the labeling with the radiometal is performed. To achieve high labeling yields and radiochemical purity (RCP), the precursor mass (molar ratio) should be significantly more than the radiometal mass. This strategy is more practical and suitable for routine manufacture of therapeutic radiopharmaceuticals.

Coupling of the biomolecule or the targeting vector to the BFC often relies on nucleophilic attack from the bioconjugate. Electrophiles, such

as anhydrides, bromo- or iodoacetamides, iso-thiocyanates, N-hydroxysuccinimide (NHS) esters, carboxylic acid active esters, and maleimides are typical groups for conjugation that have been developed to modify biomolecules with the appropriate BFCAs. Primary amines are reactive towards isothiocyanates and active esters, while maleimide is reactive towards thiols [19]. The use of copper mediated "click-chemistry" and Diels-Alder coupling has also been utilized in the preparation of radiometal complexes of biomolecules. Some of the most important and routinely used strategies for conjugating BFC to a biomolecule are summarized in Fig. 12.5.

The activation of a carboxylate group of the BFC via an active ester, which reacts with a primary amine of the biomolecule (sidechain of a lysine residue or N-terminal amine of a peptide) leads to a peptide bond that is highly stable under physiological conditions. An example of the activation of the carboxylate is the formation of N-hydroxysuccinimide (NHS) ester. Isothiocyanates are reactive to amines, as well. They may be formed from nitro groups and

react in aqueous solutions at pH 9–9.5 with primary amines to form thiourea bonds. This reaction restricts this method to biomolecules that are not sensitive to alkaline conditions. Maleimides react selectively with the thiol groups (from cysteine) in the biomolecules and form a thioether bond with the BFC. The pH for this reaction is close to 7 so that this reaction is ideal for biomolecules. Anhydrides of the BFC react with primary amines of the biomolecules. The dianhydride of DTPA might react with the biomolecule to form a DTPA-monoamide as well as a DTPA-bisamide and cross-linkage of two biomolecules may occur. To avoid cross-linkage, asymmetric anhydrides of DTPA and DOTA have been developed and used.

12.3.2 Chemistry of Post-transition Metals

Both gallium and indium have a filled d shell and three electrons in the outermost shell (Table 12.6). For these two metals, the most important oxidation state is +3. Their coordination chemistry is some-
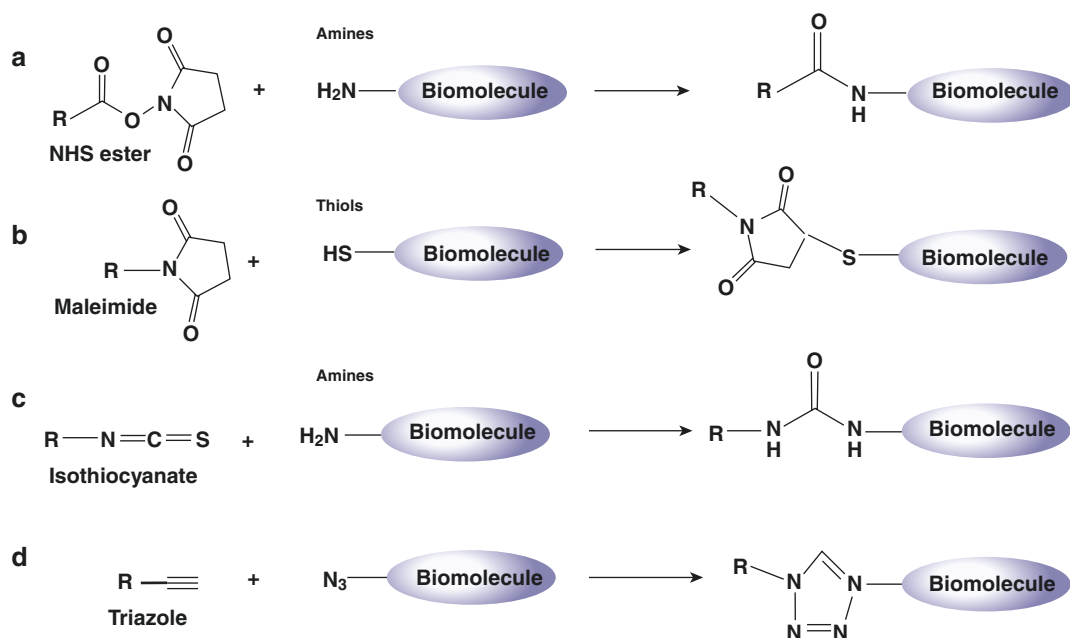

Fig. 12.5 Conjugation reactions commonly used for the covalent attachment of BFCA (R) to a targeting biomolecule with the formation of an amide (**a**), thioether (**b**), thiourea (**c**), and triazole bond (**d**)

what similar; however, due to small differences in their ionic radii and electronegativities, minor but, significant differences do exist in their chemistries. The trivalent metals share chemical characteristics with ferric ion (Fe^{3+}). This similarity with ferric ion is important in the development of radiopharmaceuticals since iron is an essential element in the human body and a number of iron binding proteins, such as transferrin (in blood), exist to transport, and store iron in vivo. As a result, the atoms of iron always compete with these radiometals for specific binding with proteins, such as transferrin, lactoferrin, and ferritin, in vivo [20].

The aqueous chemistry of Ga and In is dominated by their ability to form strong complexes (both soluble and insoluble) with the hydroxyl ion. The fully hydrated (hexaaquo) M^{3+} ions are only stable under acidic conditions. As the pH is raised above 3, these three metals form insoluble hydroxides ($M(OH)_3$). A variety of OH intermediates are formed as a function of pH and the mass of the metal. Gallium is more amphoteric than indium and yttrium. As a result, at physiological pH, gallium exists predominantly as a soluble species, $[Ga(OH)_4]^-$ (gallate) [21]. With indium, soluble $[In(OH)_4]^-$ starts forming only at pH values higher than 7.0. The total solubility of these metals at the physiological pH is very limited; very high SAs of radiometals are needed to keep them soluble in water. However, it is a common practice to add weak chelating agents (such as citrate, acetate, or tartrate ion) to complex the metal and prevent precipitation at the neutral pH. For example, ^{67}Ga is used in the clinic as ^{67}Ga-citrate. Following intravenous administration, ^{67}Ga binds to transferrin in plasma and is transported to tumors and infectious foci as "Ga-transferrin complex" [22].

The coordination chemistry of the metallic radionuclide will determine the geometry and stability of the "metal-chelate complex." Both, Ga and In are classified as hard acids and prefer hard bases [20]. It has been shown that in +3 oxidation state, both Ga and In form thermodynamically stable complexes with either 4, 5, or 6 coordinate ligands, with 6-coordiante being the most stable. The advantage of using the acyclic chelators (DTPA and EDTA) is their extremely fast and high radiolabeling efficiency under mild conditions, and greater thermodynamic stability; however, their kinetic lability often results in the dissociation of the radiometal. The macrocyclic chelates (NOTA, DOTA, and TETA), however, provide greater thermodynamic stability as well as kinetic stability. While Ga and In form greater thermodynamically stable complexes with NOTA, DTPA and EDTA, Y prefers DOTA. The labeling kinetics of DOTA-based BFCs is usually slow and much more dependent on the radiolabeling conditions, including the DOTA-conjugate concentration, pH, reaction temperature, heating time, buffer agent and concentration, and presence of other metallic impurities such as Fe^{3+} and Zn^{2+} [23].

12.3.2.1 ^{68}Ga-Labeled Radiopharmaceuticals

The recent FDA and European agencies approval of ^{68}Ga-labeled molecular imaging agents (^{68}Ga-Dotatate, ^{68}Ga-Dotatoc, and ^{68}Ga-PSMA-11) and the development of ^{68}Ga-PET is a true landmark in molecular imaging that will allow for the use of diverse molecules, and receptor analogues in clinical practice. With the introduction of ^{111}In-DTPA-octreotide (OctreoScan), in the 1990s, metal-based molecular imaging agents introduced a paradigm shift in the development of radiopharmaceuticals. But the inherent superiority of PET imaging is a clear advantage compared to planar and/or SPECT (Fig. 12.6). The ability to use ^{68}Ge/^{68}Ga generator up to a year is cost-effective negating the need for an on-site cyclotron [25–28]. Recent developments in the cyclotron production (5–100 GBq) of ^{68}Ga based on liquid [29] and solid targets [30] will also revolutionize the commercial distribution of ^{68}Ga-labeled radiopharmaceuticals [31].

^{68}Ga Generator

The ^{68}Ga generator was first developed in the 1960s for brain imaging studies [32]. Subsequent generators utilized ^{68}Ge germanate adsorbed on tin dioxide and ^{68}Ga was eluted with HCl [33, 34]. The use of a relatively high concentrations of HCl (1.0 N) presents a problem due to the volatility of $GeCl_4$ and the subsequent spread of airborne, long-lived ^{68}Ge contamination. In addi-

^{111}In-DTPA-Octreotide

^{68}Ga-DOTATATE-PET

^{111}In-Octreoscan
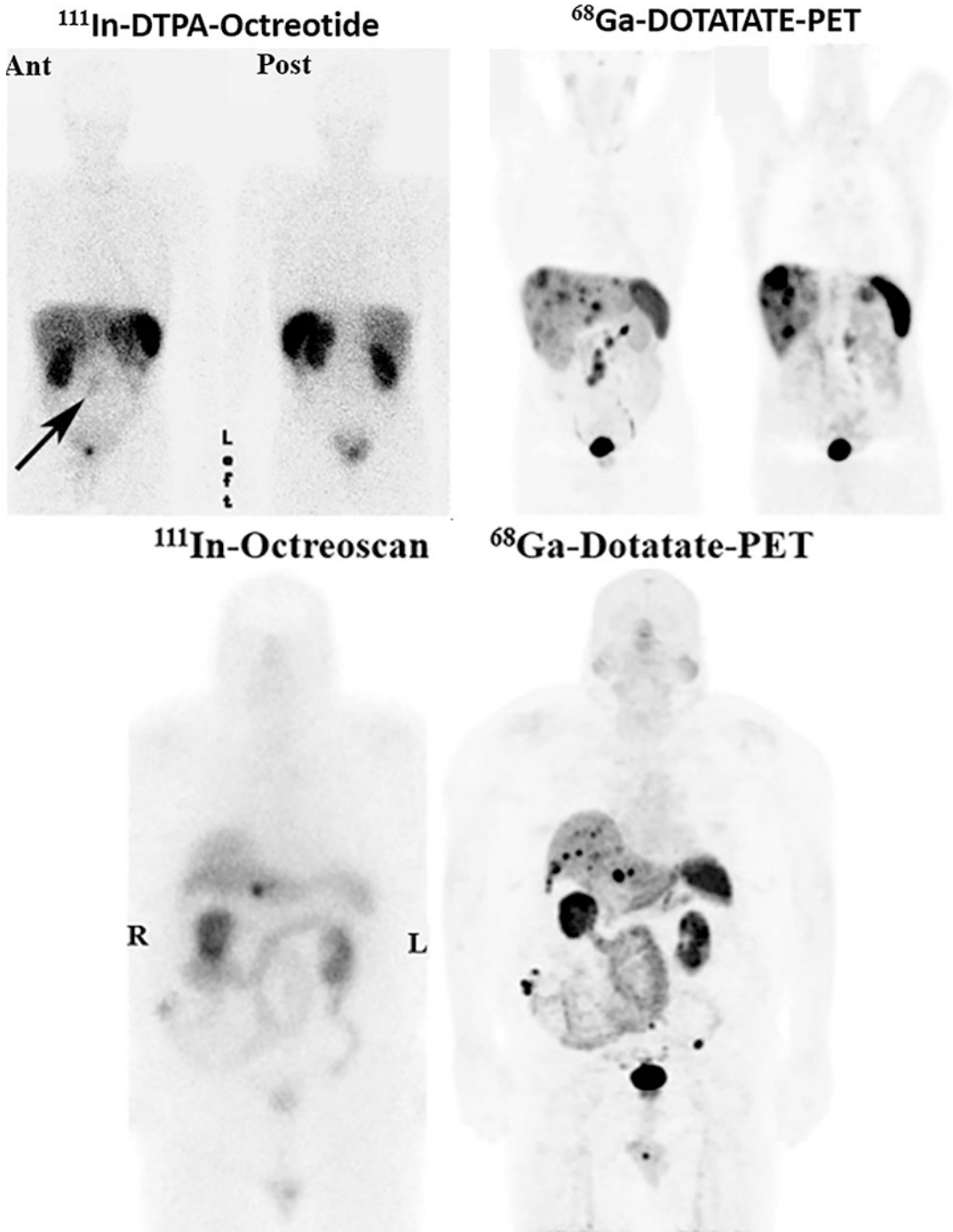
^{68}Ga-Dotatate-PET

Fig. 12.6 Comparison of ^{68}Ga-Dotatate-PET with ^{111}In-DTPA-octreotide in a patient with low-grade metastatic midgut neuroendocrine tumor (NET). Anterior and posterior whole-body planar ^{111}In-DTPA-octreotide scintigraphy shows low-grade mesenteric metastases but, no liver metastases. ^{68}Ga-DOTATATE PET shows multiple metastases in liver and mesentery [24]

tion, ^{68}Ga is eluted in a large volume of acid (>5 mL), containing metal impurities that are known to bind with high affinity to DOTA. Commercial ^{68}Ga generators (Fig. 12.7) are available based on the use of TiO_2 as an inorganic matrix to immobilize ^{68}Ge in the oxidation state IV$^+$ [35, 36]. Consequently, ^{68}Ga (III) can be easily separated by eluting it with dilute HCl. It has also been reported that the SA of the generator eluted ^{68}Ga can be as high as 27 Ci µmol^{-1} [37]. Some of these generators, however, are not necessarily optimized for the synthesis of ^{68}Ga-labeled radiopharmaceuticals. The eluates have rather large volumes with a pH of 1, breakthrough of ^{68}Ge (the parent radionuclide) increas-

ing with time or frequency of use, and impurities such as stable Zn(II), Ti(IV), Fe(III). In order to avoid these impurities, additional concentration and purification can be performed using a miniaturized column with organic cation-exchanger resin and hydrochloric acid/acetone eluent [38]. The processed ^{68}Ga fraction can be directly transferred to solutions containing labeling precursors such as DOTATOC. Labeling yields of >95% and specific activities of (50–500 MBq nmol^{-1}) can be obtained under optimized conditions. Further, fully automated synthesis modules (Fig. 12.8) have been developed to prepare ^{68}Ga radiopharmaceuticals for clinical use [39–41].

Fig. 12.7 ^{68}Ge → ^{68}Ga generators from different manufacturers

ITM IQS Theranostics Synthesizer   **Trasis All-in One Mini**

Fig. 12.8 Examples of automated synthesis modules for the labeling of metal radiopharmaceuticals

68Ga-DOTA-TOC

In the late 1990s, several octreotide analogs conjugated with DOTA chelator were introduced in order to develop 90Y-labeled SST analog for PRRT. Among these SST analogs, DOTATOC was shown to be suitable for labeling with either 90Y or 67Ga [42, 43]. DOTATOC exhibits high affinity (IC_{50}) for human SSTR-2 (14 ± 2.6 nM) with much lower binding affinity for all other human SSTRs. A marked improvement of SSTR-2 affinity was found for Ga-DOTATOC (2.5 nM) compared with the Y-DOTATOC (11 nM) and OctreoScan (22 nM) [44]. In 2001, it was reported that 68Ga-DOTATOC-PET results in high tumor to non-tumor contrast and low kidney accumulation and yields higher detection rates (>30% more lesions) as compared with OctreoScan scintigraphy [45–47]. Since its introduction, 68Ga-DOTATOC has been extensively used in Europe over the last two decades. A systematic review and meta-analysis concluded that 68Ga-DOTATOC is useful for evaluating the presence and extent in disease for staging and restaging, and for assisting in the treatment decision making for patients with NETs [48].

68Ga-DOTA-TOC was approved in several European countries in 2016 (IASOtoc®) and in 2018 (TOCscan®). Also, in Europe a kit preparation for 68Ga-labeling of DOTA-TOC (SomaKit TOC®) was approved by the European Medicines Agency (EMA) in September of 2016. Use of this kit along with an authorized 68Ge/68Ga-generator enables on-site preparation of 68Ga-DOTATOC. In the United States, the FDA approved the ready-to-use 68Ga-DOTATOC in August of 2019. The holder of the NDA (New Drug Application) or marketing authorization is the UIHC–PET Imaging Center (University of Iowa Health Care (UIHC)), in Iowa, USA [49].

68Ga-DOTATATATE

DOTATATE is an SST analog and an SSTR agonist that closely simulates DOTATOC, in which the C-terminal threoninol (an amino alcohol) is replaced by threonine (Fig. 12.9). This chemical modification resulted in a nine-fold higher affinity (1.5 nM) for the SSTR-2 as compared with DOTATOC (14 nM). Also, the affinity of Ga-DOTATATE (0.2 nM) for SSTR-2 is 12 times higher compared to that of Ga-DOTATOC (2.5 nM) [44]. Preclinical studies in animal models demonstrated that DOTATATE may be a better SST analog for the development of radiotracers for imaging and targeted therapy compared to DOTATOC [50, 51]. No human data, however, was available at that time to support the preclinical observations.

Based on direct comparison of PET/CT studies with 68Ga-DOTATOC and 68Ga-DOTATATE it was concluded that both these radiotracers pos-

Fig. 12.9 The structure of radiometal- (68Ga, 64Cu, or 177Lu) labeled DOTA-TATE (DOTA-Tyr3-octreotide) complex
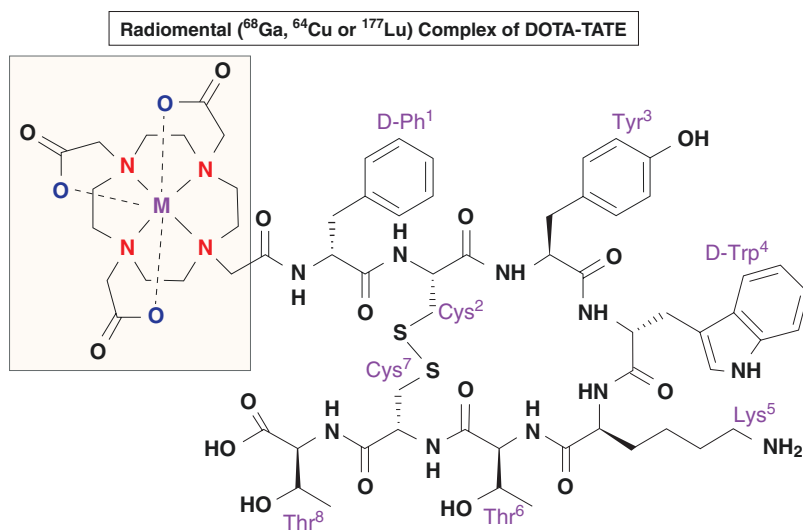
sess a comparable diagnostic accuracy for the detection of NET lesions, with ^{68}GaDOTATOC having a potential advantage. The approximately tenfold higher affinity for the SSTR-2 of ^{68}Ga-DOTATATE does not prove to be clinically relevant. Also, the study found that the SUV_{max} of ^{68}Ga-DOTATOC scans tended to be higher than their ^{68}Ga-DOTATATE counterparts [52].

In June of 2016, the FDA approved ^{68}Ga-DOTATATE (NETSPOT™) for the localization of SSTR positive NETs in adult and pediatric patients. NETSPOT™ is the new market name for Somakit-TATE (a kit for the preparation of ^{68}Ga-dotatate injection using ^{68}Ga chloride from the GalliaPharm ^{68}Ga/^{68}Ga generator from Eckert & Ziegler). ^{68}Ga-dotatate received Orphan Drug Designation from both the FDA and the European Medicines Agency (EMA) in March of 2014.

^{68}Ga-PSMA-HBED-CC (or ^{68}Ga-PSMA-11)

Prostate specific membrane antigen (PSMA) was discovered as a novel antigenic marker in prostate cancer cells. PSMA, is also known as glutamate carboxypeptidase II (GCPII), N-acetyl-L-aspartyl-L-glutamate peptidase I (*NAALADase I*) or N-acetyl-aspartyl-glutamate (*NAAG) peptidase*. PSMA is an enzyme that is encoded by the *folate hydrolase* (FOLH1) gene in humans [53]. In the last 15 years, several radiometal-labeled PSMA inhibitors have been developed for molecular imaging and targeted therapy (Chap. 22). In 2012, the development of PSMA-HBED-CC (also known as PSMA-11 or DKFZ-PSMA-11) at the German Cancer Research Centre (GCRC) and the University Hospital at Heidelberg by Drs. Eder, Haberkorn and Afshar-Oromieh should be regarded as a major milestone in the development of radiolabeled PSMA inhibitors for molecular imaging, and targeted therapy.

PSMA-11 consists of a Glu-urea-Lys motif conjugated with the highly efficient and Ga-specific acyclic chelator HBED-CC (Fig. 12.2) via an aminohexanoic acid (Ahx) spacer [54]. The advantage of HBED-CC chelator is that it can form efficient ^{68}Ga complex at room temperature with extremely high thermodynamic stability. In the first human studies, direct comparison to [^{18}F]FCH, ^{68}Ga-PSMA-targeted PET imaging was able to detect lesions much earlier in patients with low

PSA values and showed a reduced background activity in healthy tissue [55]. Subsequently, several clinical studies documented the clinical utility of ^{68}Ga-PSMA-11 (Fig. 22.23) for molecular imaging of prostate cancer [56]. The FDA approved ^{68}Ga-PSMA-11 in 2020 for PET imaging of PSMA positive prostate cancer.

12.3.3 Chemistry of Transition Metals

As shown in Table 12.6, several positron-emitting radioisotopes of transition metals such as such ^{44}Sc, ^{45}Ti, ^{52}Fe, ^{55}Co, ^{64}Cu, ^{86}Y, ^{89}Zr, and ^{94m}Tc have also been found to have suitable radioactive decay, and emission characteristics for PET imaging studies.

The definition of a transition metal according to IUPAC is "an element whose atom has a partially filled *d* sub-shell, or which can give rise to cations with an incomplete *d* sub-shell." Based on this definition, Sc and Y are not transition metals. However, it is also generally accepted that "transition metal" as any element in the d-block of the periodic table, which includes groups 3 to 12 or any element that can participate in the formation of chemical bonds with the valence electrons in two shells instead of only one. For the current discussion, the PET radiometals, ^{44}Sc and ^{86}Y, will be regarded as transition metals. The other important transition metals are ^{64}Cu, ^{89}Zr, and ^{99m}Tc.

12.3.3.1   Scandium-44

Scandium is the smallest of the rare-earth metals, with an ionic radius of 75–87 pm. Scandium readily loses 3 electrons in the outer shells (d^1s^2) and is found almost exclusively as a trivalent cation (Sc^{3+}) with the high coordination preference (CN = 6–8), and ionic bonding tendency ($I_A = 10.49$). It begins to hydrolyze at pH 2.5 and precipitation of $Sc(OH)_3$ occurs at pH 7–11 (Kostelnik and Orvig 2018). Sc^{3+} has a high preference for hard donating groups and favors a coordination number of eight, even in its hydrated form. DOTA is widely used for scandium-based radiopharmaceuticals. The high stability (log K_{ML} = 27.0–30.8) and pM value (23.9–26.5) support the use of DOTA analogs for the majority of Sc^{3+} based radiopharmaceuticals (IAEA-

TECDOC1945, 2021). [44]Sc-labeled molecular imaging probes are in pre-clinical and proof-of-concept phase clinical evaluations [57–59]. [44]Sc holds great promise for future applications as a novel PET nuclide for diagnostic imaging and for monitoring therapy in clinics. The relatively longer half-life (4 h) compared to ^{68}Ga provides great advantage for commercialization and distribution of doses similar to that with ^{18}F labeled radiopharmaceuticals.

12.3.3.2 Yttrium-86

Yttrium, like Sc, also loses the outer 3 electrons and is predominantly found as a trivalent cation (Y^{3+}). But the ionic radius of yttrium cation (90–108 pm) closely resembles that of lanthanides and prefers coordination number of 8 or 9 [13]. Most of Y radiotracers were developed using either DOTA or CHX-A''-DTPA for chelation. These chelates quantitatively radiolabel yttrium radionuclides at low concentrations and show kinetic stability under physiological conditions [60]. With the acyclic DTPA analogs, the stereochemistry of CHX-DTPA was shown to be of major importance, with markedly higher kinetic stability observed with CHX-A''-DTPA, compared to CHX-B″-DTPA. H_4octapa, an octa-dentate analogue of H_2dedpa based around a picolinic acid scaffold, also demonstrated high radiolabeling yields and serum stability [18].

While the potential utility of [86]Y-labeled peptides for PET imaging studies in patients has been documented [61], the physical half-life of [86]Y is suboptimal (not long enough) to follow the in vivo kinetics of labeled mAbs. It is more appropriate to use long-lived positron emitter, [89]Zr for developing immuno-PET to allow optimal target/background ratios with radiolabeled mAbs.

12.3.3.3 Copper-64

The relatively longer half-life and low positron energy (T½ = 12.7 h; 0.653 β^+) of ^{64}Cu is appropriate for PET imaging. Copper exhibits a rich coordination chemistry with complexes known in oxidation states ranging from 0 to +4, although the +2 (cupric) and the +1 (cuprous) oxidation states are by far the most common [62, 63]. Cu^{2+} and Cu^+ oxidation states favor dissimilar ligand donors and coordination geometry. The electron configuration and chemical hardness of Cu^{2+} (d^9) dictates a preference for borderline hard Lewis base donors, such as aliphatic and aromatic amines, as well as carboxylate donors; however, Cu^{2+} can also accommodate softer donors, such as thiolate and carbazone [11]. Cu^{2+} can accommodate a variety of coordination numbers and geometries, including square planar, square pyramidal, trigonal bipyramidal, and octahedral. In vivo, under hypoxic conditions, Cu^{2+}, however, can be reduced to Cu^+ oxidation state causing instability of Cu^{2+} coordination complexes. In contrast, Cu^+ (d^{10}) exhibits a preference for soft donors (thiol, thio-ether, and imidazole) and a tetrahedral geometry.

The two well well-known [62]Cu-based PET imaging agents are both small metal complexes of acyclic chelator, thiosemicarbazone; [62]Cu-diacetyl-bis(N4-thiosemi-carbazone or [62]Cu-PTSM and Cu-diacetyl-bis(N4-methylthiosemicarbazone or Cu-ATSM [64]. In both cases, a Cu^{2+} center is coordinated in a square planar geometry by the two nitrogen atoms and two sulfur atoms of the thiosemicarbazone [63]. Under reducing, oxygen-deficient conditions, the reduced Cu^+ species dissociates from the chelator and binds to intracellular proteins. This approach may provide a simple method to develop copper-based small molecule radiopharmaceuticals.

For the development of kinetically inert copper complexes, the chelators must provide a rigid coordination environment that disfavors fluxional changes of the coordination environment, and the Cu^{2+} radiolabeled complex must be resistant to reduction under physiological conditions. For several decades, most of the chelator development for Cu nuclides has focused on polyaza macrocyclic BFCs, such as DOTA, NOTA, TETA, and TE2A complexes. While DOTA complexes have shown clinical utility, the Copper complexes of TETA and TE2A exhibit greater thermodynamic stability and kinetic inertness [11]. Recently in 2020, the FDA approved ^{64}Cu-DOTATATE for PET imaging studies in patients with SSTR positive NETs. The superior quality of ^{64}Cu-Dotatate images suggest that for PET imaging studies with ^{64}Cu-labeled peptides acquired in 1–3 h after tracer administration, the DOTA chelator is able to provide adequate in vivo stability. However, to improve greater structural rigidity, cross-bridged chelators, such as

CB-TE2A, were developed. While these chelators have kinetic stability, they still require higher temperatures for quantitative labeling. The sarcophagine family of chelators (Fig. 12.4), based on hexaazamacrobicyclic cage, were also investigated to develop copper-labeled radiopharmaceuticals [65]. The Sar, DiamSar, and SarAr chelators coordinate copper extremely quickly over a pH range of 4.0–9.0 and have shown superior performance, including quantitative radiolabeling at room temperature, and excellent in vitro, and in vivo stability [66]. NOTA and NOTA type derivatives also showed fast complexation at room temperature and high kinetic inertness in vivo [67]. ^{64}Cu and ^{67}Cu (a beta emitter) is a theranostic pair which has a significant potential for the development of tracers for imaging and targeted therapy. Several ^{64}Cu-labeled PET radiopharmaceuticals are under clinical evaluation [68, 69].

^{64}Cu-DOTATATE (DetectNet)

The initial studies with ^{64}Cu-TETA-octreotide in patients with NETs showed high rate of lesion detection, sensitivity, and favorable dosimetry and pharmacokinetics [62]. Since ^{64}Cu forms more stable complex with DOTA chelator, ^{64}Cu-DOTATATE has been studied as a potential PET radiotracer for SSTR-based imaging. The first human study clearly supports the clinical use of ^{64}Cu-DOTATATE for PET studies with excellent imaging quality, reduced radiation burden, and increased lesion detection rate when compared with OctreoScan [70, 71].

In a head-to-head comparison with ^{68}Ga-DOTATOC-PET in patients with NETs, ^{64}Cu-DOTATATE-PET scans detected more lesions although patient-based sensitivity was the same for both agents [72]. Recently in a prospective trial in patients with Known or Suspected SSTR positive NETs PET/CT scan with ^{64}Cu-DOTATATE was considered a safe imaging technique that provides high-quality and accurate images at a dose of 148 MBq (4.0 mCi) for the detection of SSTR expressing NETs [73]. The lower positron energy of ^{64}Cu compared to that of ^{68}Ga (0.65 vs. 1.90 MeV), which translates to lower positron range (0.56 vs. 3.5 mm), is thought to explain the anticipated improved spatial resolution and diagnostic performance of ^{64}Cu-DOTATATE (Fig. 12.10).

Fig. 12.10 Comparison of ^{64}Cu-DOTATE-PET and ^{111}In-DTPA-Octreotide (OctreoScan) in the same patient with NETs with multiple bone and soft tissue metastases ([71])
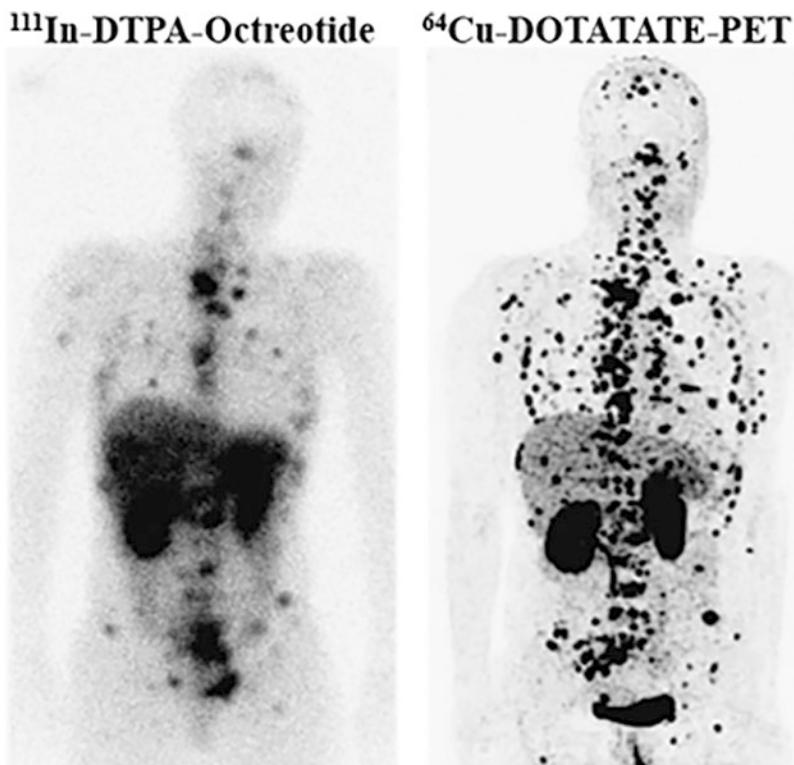
^{111}In-DTPA-Octreotide

^{64}Cu-DOTATATE-PET

Additionally, the longer physical half-life of ^{64}Cu (12.7 h) may increase the shelf-life of ^{64}Cu-DOTATATE and provide a more flexible scanning window, making it attractive for routine clinical imaging.

In September 2020, the *FDA approved ^{64}Cu-DOTATATE injection (DetectNet) for the localization of SSTR-positive NETs.*

12.3.3.4 Zirconium-89

^{89}Zr, a transition metal, has an ideal physical half-life (78.4 h) and appropriate β^+ energy ($E_{mean} = 0.39$ MeV) for PET imaging studies [74, 75]. The most preferred method of production is based on the reaction $^{89}Y(p,n)^{89}Zr$ using ^{89}Y (natural abundance 100%) foil as the target material [76]. Subsequently, ^{89}Zr is purified by anion-exchange chromatography. Zr complexes with hydroxamates in acidic solutions (>1 N HCl), compared to other metallic impurities (Fe, Al, Y), that do not interact. The most common and convenient chemical form is ^{89}Zr in oxalic acid (0.5 M) with a purity >99.99% [77, 78]. The availability of carrier-free ^{89}Zr as either zirco-

nium-89 oxalate ($[^{89}Zr(C_2O_4)_4]^{4-}$) or ^{89}Zr chloride ($[^{89}Zr]ZrCl_4$) is essential to the development of effective immuno-PET agents. ^{89}Zr is typically obtained with high radiochemical yields (~90%) and effective molar (specific) activities of around 60 GBq/μmol [79].

Zr, a second-row transition metal can exist in several oxidation states including Zr(II), Zr(III) and Zr(IV), which is its preferred oxidation state. ^{89}Zr is typically present in solution as Zr^{4+} and is a hard Lewis acid with strong affinity for hard Lewis bases such as oxygen.

When ^{89}Zr was first investigated for PET imaging, common universal metal chelators such as EDTA, DTPA, and desferrioxamine (DFO), were used to investigate the coordination requirements for ^{89}Zr complexation [80–82]. Based on these studies it was concluded that the hard oxophilic ^{89}Zr ion prefers an octadentate coordination sphere. In the ^{89}Zr–DFO complex, the three hydroxamates occupy only six of the preferred eight coordination sites of the Zr^{4+} ion (Fig. 12.11), leaving a gap in the ligand sphere where other ions and molecules can interact,
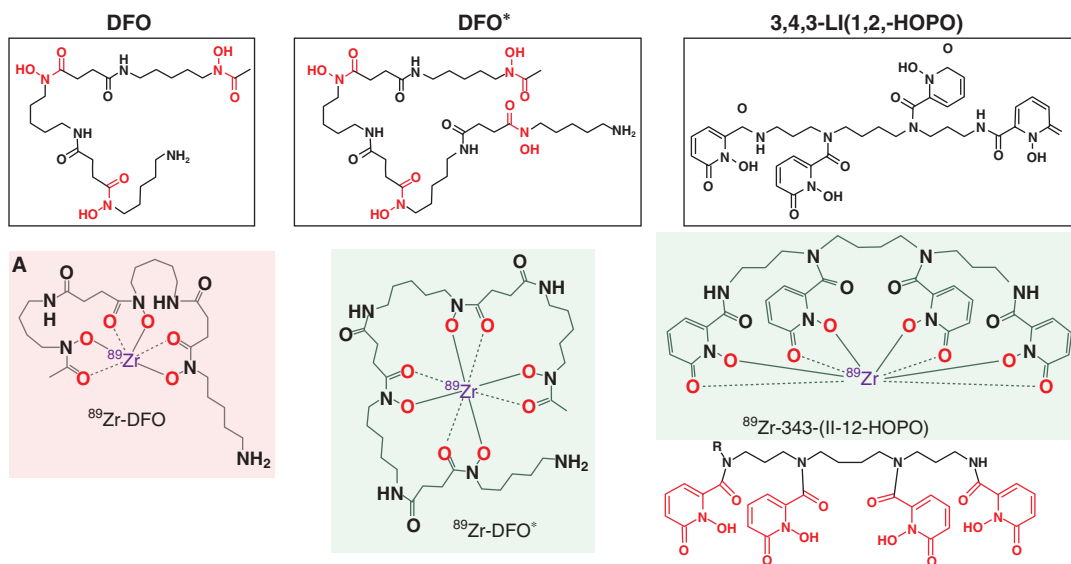

Fig. 12.11 ^{89}Zr chelating agents and the coordination complexes. DFO chelator provides six oxygen donor atoms to form hexadentate ^{89}Zr-DFO complex. In contrast, both DFO* and HOPO chelators form more stable octadentate coordination complexes

destabilize, or break the complex [83]. This has led to suboptimal stability with DFO in preclinical in vivo models and uptake of free ^{89}Zr in bones. Multiple research groups have developed octadentate chelators for ^{89}Zr to solve this issue while keeping synthesis, coupling, and radiolabeling conditions facile, and mild. A modified DFO chelator with additional hydroxamate functionalities (known as DFO*) provided the eight coordination donors for ^{89}Zr. Hydroxypyridinones (HOPOs) represent another family of compounds with good chelating properties. Recent investigations indicate that ^{89}Zr complexes of DFO* and the 3,4,3-(LI-1,2-HOPO) (Fig. 12.11) demonstrated a high inertness, qualifying them for further comparative in vivo investigation to determine the most appropriate alternative to DFO for clinical application [83–85]. In the last ten years, the potential clinical value of ^{89}Zr-based PET studies with proteins (antibodies), however, was based on the DFO chelator.

12.4   Immuno-PET and SPECT

In the early 1980s, clinical nuclear imaging studies provided the proof of principle that tumor lesions could be imaged using radiolabeled mAbs. FDA approved four radiolabeled (with ^{111}In or ^{99m}Tc) mAbs for diagnostic imaging studies. However, the diagnostic accuracy of these antibody-based scans was limited due to poor resolution of the Anger gamma cameras at that time. In addition, with the introduction of FDG-PET and PET/CT, antibody-based imaging for staging and restaging of cancer patients became obsolete. With the availability of relatively long half-life positron emitters (^{124}I, $T_{1/2}$ = 4.2 d and ^{89}Zr, $T_{1/2}$ = 3.266 d), a revival of imaging with radiolabeled antibodies based on PET imaging has taken place [86]. By combining the sensitivity of PET imaging and the specificity of antibodies, immuno-PET imaging has become a promising tool for monitoring the heterogeneity of specific gene expression, and predicting the efficacy of RIT. ^{111}In labeled mAbs are still useful for the initial development work based on SPECT imaging, however, the lack of absolute quantitation with SPECT does not support clinical utility for dosimetry studies and to monitor response to RIT.

^{89}Zr half-life is quite appropriate to study antibody biodistribution, and in the same range as the therapeutic radiometals such as ^{90}Y and ^{177}Lu. Several radiometals have been investigated for long-duration PET studies, including ^{64}Cu, ^{86}Y, and ^{66}Ga, although ^{89}Zr best fulfills many of the desired properties with its 3.27 day half-life and 23% positron emission. In addition, other favorable physical properties include minimal contamination from the 909-keV prompt γ-photons within the 511-keV PET energy window, as well as superior spatial resolution compared with many other positron-emitting isotopes as a result of the relatively low excess decay energy (E_{mean} = 396 keV).

In 2003, ^{89}Zr-labeled antibodies were introduced as chemical and biological surrogates for immunoPET studies to assess the biodistribution of ^{90}Y and ^{177}Lu-labeled antibodies [77, 78]. The first human study was published in 2006 with ^{89}Zr-labeled chimeric mAb U36 in patients with squamous head and neck cancers [87]. ^{89}Zr-PET imaging localized cervical lymph node metastasis with a high accuracy (93%). It has been shown that radiation doses of RIT with ^{90}Y-ibritumomab tiuxetan (Zevalin) can be predicted by immuno-PET with ^{89}Zr-ibritumomab tiuxetan and other ^{90}Y- and ^{177}Lu-labeled mAbs [88]. In the last 15 years, a number of studies have been conducted to investigate the feasibility of ^{89}Zr immuno-PET for predicting the efficacy of RIT and antibody therapies, imaging target expression or density, detecting target-expressing tumors, and monitoring of anti-cancer chemotherapies. Many FDA approved mAbs for immunotherapy (such as trastuzumab, bevacizumab, cetuximab, and rituximab) have been labeled with ^{89}Zr (Table 19.7) and were evaluated as radiopharmaceuticals for immunoPET [89, 90]. PET/CT scans with ^{89}Zr-trastuzumab are shown in
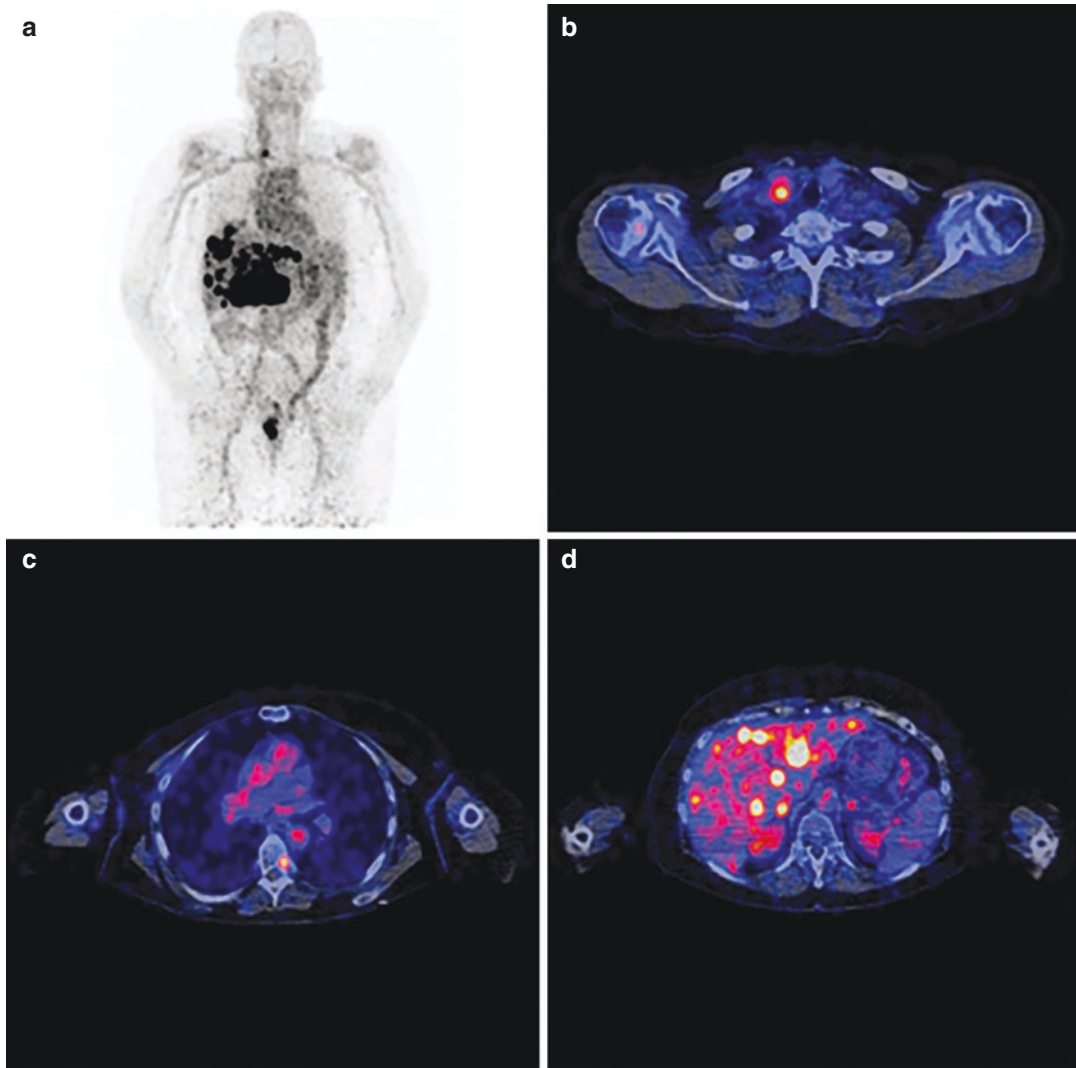
Fig. 12.12 ^{89}Zr-trastuzumab (anti-HER2 mAb)) PET/CT scan in a patient with HER2–positive metastatic breast cancer 4 days after the injection (37 MBq in 50 mg antibody). (**a**) The scan showing ^{89}Zr activity in circulation, uptake in intrahepatic metastases, and intestinal excretion. (**b**) Transverse plane of fused PET/CT of chest showing tracer uptake in cervical lymph node. (**c**) Transverse plane showing tracer uptake in metastasis (left side) in T7. (**d**) Transverse plane showing tracer uptake in liver metastases ([91])

Fig. 12.12. ^{111}In and ^{177}Lu-DOTA-huJ591 (anti-PSMA) mAb imaging studies showed excellent targeting of PSMA expression in mCRPC. However, the ^{89}Zr-IAB2M minibody (derived from J591 mAb) detected more lesions than the standatd bone scan, and FDG-PET (Fig. 12.13). Immuno-PET using ^{89}Zr has the advantages of having high resolution and high specificity but, compared to ^{18}F-labeled radiotracers, patients generally receive higher radiation dose from ^{89}Zr-mAb PET (~20–40 mSv for 37–74 MBq) [90].

12.4.1 ImmunoPET: Applications

The concept of immunoPET originally meant to describe PET imaging of radiolabeled intact full-
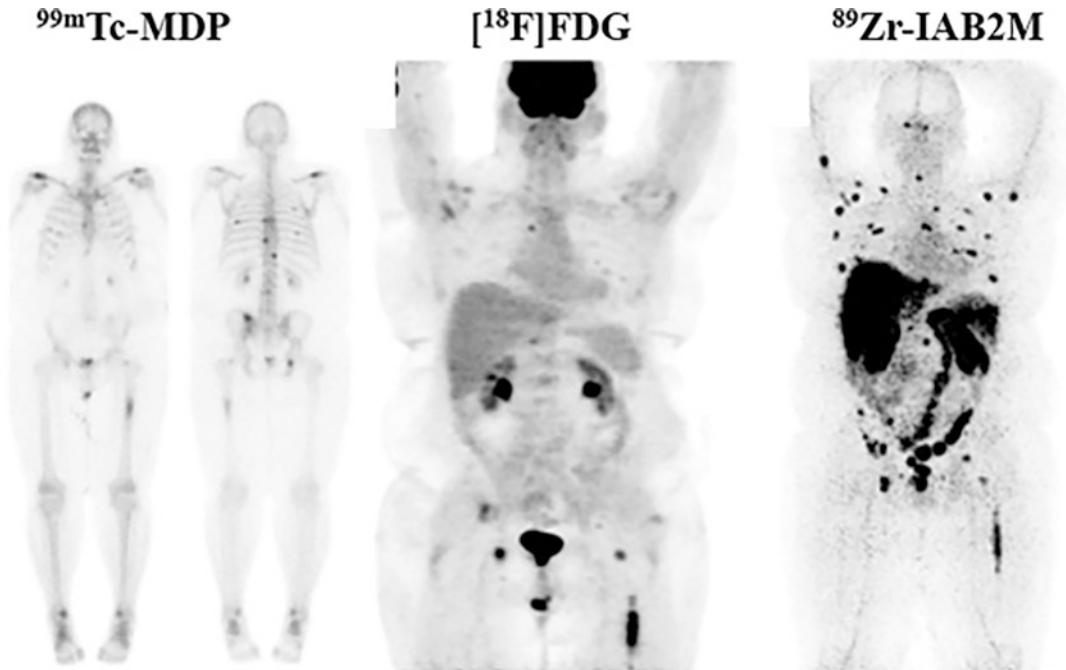
Fig. 12.13 ^{89}Zr-IAB2M-PET imaging in mCRPC. Targeting with IAB2M (minibody fragment from J591 mAb). Comparison with Bone scan and FDG-PET. ^{89}Zr-IAB2M scan shows more lesions than bone scan or FDG-PET ([92])

length mAbs. However, immunoPET now includes radiolabeled antibody fragments or mimetics as targeting vectors. A variety of radionuclides and mAbs have been used to develop molecular imaging probes for immunoPET (Table 12.9). The clinical application of immunoPET imaging has increased our understanding of tumor heterogeneity and refined clinical disease management, and includes the following applications [89]:

- To facilitate better management of cancer patients since it has the potential to provide excellent specificity and sensitivity in detecting primary tumors.
- To detect lymph node and distant metastases.
- Following immunoPET imaging, patients with positive findings can be selected for subsequent therapies (e.g., antibody therapy and antibody-based RIT), whereas patients with

negative or heterogeneous findings may need multidisciplinary treatments.
- As a theranostic companion immunoPET can provide radiation dosimetry prior to administering the therapeutic radiopharmaceuticals.
- immunoPET imaging is useful for improved triage during early disease stages and to facilitate image-guided surgery.
- The information provided by immunoPET will significantly enhance the existing diagnostic methods for better tumor characterization. One can envision that, in the future, tumors may be classified not only according to their origins and mutation status but also, according to the expression of specific tumor antigens.
- Molecular imaging for cancer immunotherapy with radiolabeled probes (^{111}In and ^{89}Zr-labeled mAbs) targeting PD-1 and PD-L1 can provide in vivo, real-time, and non-invasive imaging of tumor biomarker expression, and immune responses to novel therapies.

Table 12.9 Radiolabeled mAbs and fragments as molecular imaging probes for Immuno-PET[a]

Radiolabeled antibody	Target	Targeting vector	Cancer types
[89]Zr-Df-cetuximab	EGFR	mAb	Solid tumors
[89]Zr-Panitumumab	EGFR	mAb	Colorectal cancer
[89]Zr-Df-trastuzumab	HER2	mAb	Breast cancer, esophagogastric adenocarcinoma (EGA)
[64]Cu-DOTA-trastuzumab	HER2	mAb	BC
[89]Zr-Df-Pertuzumab	HER2	mAb	BC
[124]I-trastuzumab	HER2	mAb	Gastric cancer, gastroesophageal cancer
[64]Cu-DOTA-Patritumab	HER3	mAb	Solid tumors
[89]Zr-GSK2849330	HER3	mAb	Solid tumors
[89]Zr-lumertuzumab	HER3	mAb	Solid tumors
[89]Zr-Df-bevacizumab	VEGF	mAb	Solid tumors
[89]Zr-cmAb U36	CD44v6	mAb	Squamous cell carcinoma of the head and neck (HNSCC)
[89]Zr-RG7356	CD44	mAb	Solid tumors
[89]Zr-rituximab	CD20	mAb	Lymphoma
[89]Zr-DFO-5B1	CA19.9	mAb	Pancreatic cancer
[89]Zr-huJ591	PSMA	mAb	Prostate cancer
[89]Zr-girentuximab	CAIX	mAb	Renal cell carcinoma
[89]Zr-DFO-MSTP2109A	STEAP1	mAb	Prostate cancer
[89]Zr-fresolimumab	TGF-β	mAb	Glioma
^{68}Ga-ABY-025	HER2	Affibody	Breast cancer
^{68}Ga-HER2-nanobody	HER2	Nanobody	Breast cancer
[89]Zr-IAB2M	PSMA	minibody	Prostate cancer
^{68}Ga-IMP288	CEA	BsAb	Medullary thyroid cancer
[89]Zr-AMG 211	CEA/CD3	BiTE	Gastrointestinal adenocarcinoma
[89]Zr-Df-IAB22M2C	CD8	Minibody	Solid tumors
[89]Zr-atezolizumab ^{111}In-atezolizumab	PD-L1	mAb	Non-small cell lung cancer (NSCLC), bladder cancer, triple negative breast cancer (TNBC)
[89]Zr-Nivolumab	PD1	mAb	Lung cancer

[a]Table modified from [89]

The clinical studies with radiolabeled antibodies and antibody fragments are very limited but, they have, clearly, demonstrated that immuno-PET provides high resolution images needed for diagnosis and treatment assessment. More research and extensive imaging clinical trials are needed to refine immuno-PET for the diagnosis of cancers and assessment of response to therapy. ImmunoPET studies will be essential for the assessment of target antigen expression and identification of patient right patient for a specific RIT clinical trial.
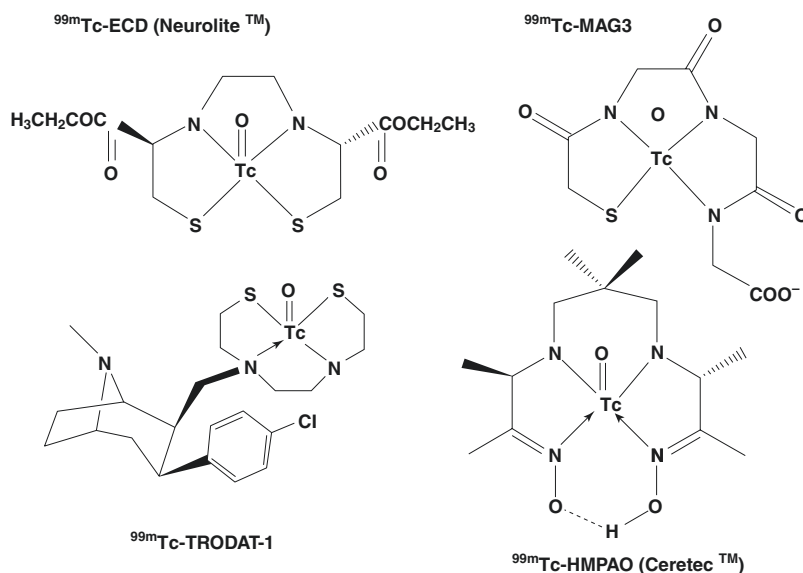
12.5 Tecnetium-99m Chemistry

Technetium (Tc) was first discovered in 1937 by Emilio Segre and Carlo Perrier. Because it was artificially produced by bombarding molybdenum with deuterons, the name technetium for this new element was derived from the Greek word *technetos*, meaning artificial. Trace amounts of ^{99}Tc, however, were isolated from a uranium-rich ore in 1961 and more than 20 isotopes of technetium are known, all of which are radioactive. The most useful isotope, the metastable ^{99m}Tc ($T_{1/2}$ = 6.01 h), decays by isomeric transition to the relatively long-lived ^{99}Tc ($T_{1/2}$ = 2.1 × 10^5 year) following emission of a 140 KeV gamma photon. As previously noted, in 1958 scientists at the Brookhaven National Laboratory (BNL) reported the development of the first ^{99m}Tc generator based on the parent radioisotope ^{99}Mo. Since the 1970s, ^{99m}Tc radiopharmaceuticals have played a major role in the advancement of nuclear medicine as a diagnostic specialty. Also, since the SA ^{99m}Tc can be very high (599 Ci µmol^{-1}), it is an excellent nuclide for developing molecular imaging radiopharmaceuticals for SPECT. ^{94m}Tc, a positron-emitting radionuclide ($T_{1/2}$ = 53 min) with even higher theoretical SA, may also have significant potential for developing radiopharmaceuticals for use with PET.

Tc is a second row group VII transition metal that is capable of multiple oxidation sates (−1 to +7). In aqueous solution, the pertechnetate anion, $^{99m}TcO_4^?$, is the most stable chemical species with a + 7 oxidation state. Because of the similar size and charge as that of iodide (I$^-$), the in vivo distribution of pertechnetate is similar to that of an iodide ion [93]. However, because pertechnetate is chemically stable and inert, it cannot bind directly to any organic molecule or chelate. Following reduction by appropriate reducing agents, pertechnetate can be transformed into lower oxidation states that are chemically more reactive. Several reducing agents have been investigated with stannous chloride (SnCl$_2$) being the most widely used agent for preparing complexes of Tc(V) and Tc(I), while boron-hydrides are used to prepare organometallic Tc(I) complexes. During reduction by the stannous ion (Sn^{2+}), in an appropriate buffer and pH, the presence of a ligand stabilizes Tc in its lower oxidation state. In a specific Tc-complex, the oxidation state of Tc, however, depends on the chelate and pH [93]. As a transition metal, Tc can adopt a large number of coordination geometries, depending on the donor atoms and the type of the chelating agent. Several donor atoms, such as N, S, O, and P, geometrically arranged in a chelating molecule, can form coordination complexes with technetium. A number of ligands, such as DTPA, Dimercaptosuccinic acid (DMSA), iminodiacetic acid (IDA) derivatives (such as HIDA, DISIDA, BrIDA), phosphates, and phosphonates (such as PYP, MDP, EHDP) have been labeled with ^{99m}Tc and routinely used for diagnostic imaging studies in nuclear medicine.

The radiopharmaceutical chemistry of Tc(V) is dominated by the [TcO]$^{3+}$ core, which is stabilized by a wide range of donor atoms (N, S, O), but prefers thiolate, amido, and alkoxide ligands. Several tetra-ligand chelates designed to bind to Tc(V), typically form complexes (such as N$_2$S$_2$, N$_3$S, N$_3$O, and N$_4$) having square pyramidal geometries (Fig. 12.14. The ^{99m}Tc complex of mercaptoacetyltriglycine (MAG3) forms a square pyramidal complex with Tc(V) with the basal plane consisting of three nitrogen atoms and one sulfur donor atom. A variety of BFCs, such as N$_2$S$_2$ diamidedithios, N$_3$S triamide thiols, N$_4$ tetraamines or hydrazinonicotinic acid (HYNIC), have been evaluated upon conjugation to peptides to achieve labeling with ^{99m}Tc.

^{99m}Tc-ECD (Neurolite ^{TM})

^{99m}Tc-MAG3

^{99m}Tc-TRODAT-1

^{99m}Tc-HMPAO (Ceretec ^{TM})

The direct method of ^{99m}Tc labeling to peptides uses a reducing agent to break a disulfide bridge of a peptide for binding of ^{99m}Tc to thiol groups in the peptide molecules. This method often suffers from lack of specificity and poor in vivo stability. In the indirect method, ^{99m}Tc is bound to the peptide through a BFC, which can be conjugated to the peptide either before (post-labeling approach) or after labeling with ^{99m}Tc. In the 1990s several approaches have been developed to label peptides and proteins with ^{99m}Tc. New directions in developing chelators for developing ^{99m}Tc-chelate-biomolecule complex have been reviewed [11, 94]. Three important labeling methods have been developed based on three commonly used Tc-coordination environments (cores) as shown in Fig. 12.15:

• The MAG$_3$-based bifunctional chelates (Tc(V) oxo core).
• The N-oxysuccinimidylhydrazino-nicotinamide system and (Tc(V) HYNIC core).
• The recently described single amino acid chelates for the Tc(I)-fac-tricabonyl core.

Mixed aminothiol-based chelators such as N$_2$S$_2$ ligand bisaminoethanethiol (BAT) and N3S ligand mercaptoacetyltriglycine (MAG$_3$) were

developed to label biomolecules based on Tc(V) O core. ^{99m}Tc-MAG3 (Mertiatide) was developed in 1986 as an anionic kidney functional imaging agent. The parent ligand is readily derivatized as the S-acetyl MAG$_3$-ethyl ester, containing a p-isothiocyanatobenzyl substituent, or as the S-acetyl MAG3-hydroxysuccinimidyl ester for conjugation to biomolecules. In the 1990s, MAG3 ligand was used to develop ^{99m}Tc-P829 peptide (Depreotide) for somatostatin receptor imaging. The original octreotide peptide was modified to eliminate the disulfide bridge to prevent reduction during the synthesis of ^{99m}Tc-P829 complex (Fig. 12.15). Tc-MAG3 core is robust and provides chemical versatility for the development of bifunctional tracers. There are drawbacks, such as the use of stannous chloride as a reducing agent and the need for elevated pH condition, that may lead to aggregation of proteins, as well as nonquantitative radiolabeling yields [11].

An alternative pendant approach to ^{99m}Tc radiolabeling of biomolecules was provided by the introduction of hydrazinenicotinic acid (HYNIC) as a bifunctional chelator [95, 96]. HYNIC with co-ligands like tricine and ethylenediamine diacetic acid (EDDA), in the presence of SnCl$_2$ performs fast and efficient labeling. Based on this Tc(V)HYNIC core, many small molecules, pep-

Fig. 12.15 The three important Tc-coordination cores commonly used to develop radiomet-labeled peptides. Tc-P829 was developed based on Tc(V)oxo core. Tc-HYNIC-octreotide was developed based on Tc(V) HYNIC core. Tc-MIP-1404 was developed based on (Tc(I)-fac-tricaconyl core)

tides, and proteins were labeled as imaging agents [97]. For example, Tyr[3]-octreotide (TOC) was successfully labeled based on Tc-HYNIC core (Fig. 20.15). Since the HYNIC occupies only one or two coordination positions for ^{99m}Tc, co-ligands (such as tricine and EDDA) are needed to complete Tc's coordination positions. Changes in co-ligand number and type will have effect on the in vivo behavior of ^{99m}Tc radiopharmaceutical. It has been understood that [HYNIC-[99m]Tc(tricine)$_2$] complexes usually are not very stable in solutions and could appear in different isomeric forms based on pH, temperature, and time [98].

12.5.1 Tc-Tricarbonyl Core, [Tc(CO)₃]⁺

A major advancement in Tc chemistry has been the discovery that a highly adaptable tricabonyl Tc core makes it possible to prepare organometallic complexes in aqueous solution [99]. In an effort to develop new organometallic precursors, for the preparation of ^{99m}Tc-complexes, investigators have shown that, by treating pertechnetate $\left(TcO_4^\circ\right)$ with sodium borohydride (NaBH$_4$) in the presence of carbon monoxide (CO) gas, one can produce the reactive Tc(I) species, Tc(CO)$_3$(OH$_2$)$_3$]⁺ [99, 100]. In this complex, the three facially oriented water molecules are sufficiently labile so that they can be readily displaced by a variety of mono-, bi- and tridentate ligands. Since it is difficult to work with CO gas, the technology is based on the use of a solid reagent, potassium boranocarbonate (K$_2$H$_3$BCO$_2$), which acts as both a reducing agent and a source of CO gas. The kit is available from Mallinckrodt (Tyco) Medical under the trade name Isolink. Further, it has been shown that both, bidentate and tridentate chelates bind rapidly to the [Tc(CO)$_3$]⁺ core on a macroscopic scale and at the tracer level. ^{99m}Tc-tricarbonyl core is the favorite strategy for labeling of peptides because: a) a high labeling yield is achieved, b) purification is not needed after labeling protocol, and c) attachment of ^{99m}Tc-tricarbonyl to the peptide is easy and convenient [98]. Preclinical studies with several biomolecules labeled with Tc-tricarbonyl core revealed that these labeled compounds are biologically, kinetically, and thermodynamically stable for imaging studies.

Based on the chemistry of the organometallic fragment $[^{99m}Tc][Tc(CO)_3(H_2O)_3]+$, two radiopharmaceuticals, ^{99m}Tc-MIP-1404 and ^{99m}Tc-MIP-1405 were developed by Molecular Insight Pharmaceuticals (MIP). The preparation of these complexes was accomplished using a standard methodology and commercially available IsoLink kits (Covidien, Dublin, Ireland) and the imidazole chelator, which contains three nitrogen atoms suitable for binding to the $^{99m}Tc(I)$- tricarbonyl-core (Fig. 12.15). The lead compound ^{99m}Tc-MIP-1404 (Trofolastat) completed phase III clinical trials as an imaging agent for the detection of prostate specific membrane antigen (PSMA) positive prostate cancer [101, 102].

References

1. Duclos V, Iep A, Gomez L, et al. PET molecular imaging: a holistic review of current practice and emerging perspectives for diagnosis, therapeutic evaluation and prognosis in clinical oncology. Int J Mol Sci. 2021;22:4159.
2. Weber WA, Czernin J, Anderson CJ, et al. The future of nuclear medicine, molecular imaging, and theranostics. J Nucl Med. 2020;61(12):263s–72s.
3. Halder R, Ritter T. ^{18}F-fluorination: challenge and opportunity for organic chemists. J Org Chem. 2021;86(20):13873–13884.
4. McCarthy DW, Shefer RE, Klinkowstein RE, et al. Efficient production of high specific activity ^{64}Cu using a biomedical cyclotron. Nucl Med Biol. 1997;24:35–43.
5. Williams HA, Robinson S, Julyan P, et al. A comparison of PET imaging characteristics of various copper radioisotopes. Eur J Nucl Med Mol Imaging. 2005;32:1473–80.
6. Carter LM, Kesner AL, Pratt EC. The impact of positron range on PET resolution, evaluated with phantoms and PHITS Monte Carlo simulations for conventional and non-conventional radionuclides. Mol Imaging Biol. 2020;22(1):73–84.
7. Haddad F, Ferrer L, Guertin A, et al. ARRONAX, a high-energy and high-intensity cyclotron for nuclear medicine. Eur J Nucl Med Mol Imaging. 2008;35:1377–87.
8. Robinson S, Julyan PJ, Hastings DL, et al. Performance of a block detector PET scanner in imaging non-pure positron emitters–modeling and experimental validation with 124I. Phys Med Biol. 2004;49:5505.
9. Dalen J, Visser E, Laverman P, et al. Effect of the positron range on the spatial resolution of a new generation pre-clinical PET scanner using F-18, Ga-68, Zr-89 and I-124. J Nucl Med. 2008;49:404.
10. Jødal L, Loirec CL, Champion C. Positron range in PET imaging: an alternative approach for assessing and correcting the blurring. Phys Med Biol. 2012;57:3931.
11. Boros E, Packard AB. Radioactive transition metals for imaging and therapy. Chem Rev. 2019;119(2):870–901.
12. Boros E, Holland JP. Chemical aspects of metal ion chelation in the synthesis and application antibody-based radiotracers. J Labelled Comp Radiopharm. 2018;61(9):652–71.
13. Kostelnik TI, Orvig C. Radioactive main group and rare earth metals for imaging and therapy. Chem Rev Chem Rev. 2019;119(2):902–56.
14. Meares CF, Goodwin DA. Linking radiometals to proteins with bifunctional chelating agents. J Protein Chem. 1984;3:215–28.
15. Baranyai Z, Tircsó G, Rösch F. The use of the macrocyclic chelator DOTA in radiochemical separations. Eur J Inorg Chem. 2020;2020:36–56.
16. Brunner UK, Renn O, Ki M, et al. Radiometals and their chelates. In: Wagner Jr HN, Szabo Z, Buchanan JW, editors. Principles of nuclear medicine. Philadelphia: WB Saunders; 1995.
17. Brechbiel MW. Bifunctional chelates for metal nuclides. Q J Nucl Med Mol Imaging. 2008;52(2):166–73.
18. Price EW, Orvig C. Matching chelators to radiometals for radiopharmaceuticals. Chem Soc Rev. 2014;43:260.
19. Sarko D, Eisenhut M, Haberkorn U, Mier W. Bifunctional chelators in the design and application of radiopharmaceuticals for oncological diseases. Curr Med Chem. 2012;19:2667–88.
20. Weiner RE, Thakur ML. Chemistry of gallium and indium radiopharmaceuticals. In: Welch MJ, Redvanly CS, editors. Handbook of radiopharmaceuticals. West Sussex: Wiley; 2003.
21. Green MS, Welch MJ. Gallium radiopharmaceutical chemistry. Int J Rad Appl Instrum B. 1989;16:435–48.
22. Vallabhajosula S, Harwig JF, Siemsen JK, et al. Radiogallium localization in tumors: blood binding and transport and the role of transferrin. J Nucl Med. 1980;21:650–6.
23. Kukis DL, DeNardo SJ, DeNardo GL, et al. Optimized conditions for chelation of yttrium-90-DOTA immunoconjugates. J Nucl Med. 1998;39:2105–10.
24. Srirajaskanthan R, Kayani I, Quigley AM, et al. The role of ^{68}Ga-DOTATATE PET in patients with neuroendocrine tumors and negative or equivocal findings on ^{111}In-DTPA-octreotide scintigraphy. J Nucl Med. 2010;51:875–82.
25. Al-Nahhas A, Win Z, Szyszko T, et al. What can gallium-68 PET add to receptor and molecular imaging? Eur J Nucl Med Mol Imaging. 2007;34:1897–901.

26. Dijkgraaf I, Boerman OC, Oyen WJ, et al. Development and application of peptide-based radiopharmaceuticals. Anti Cancer Agents Med Chem. 2007;7:543–51.

27. Maecke HR, Andre JP. ^{68}Ga-PET radiopharmacy: a generator-based alternative to [18]Fradiopharmacy. Ernst Schering Res Found Workshop. 2007;62:215–242.

28. Velikyan I. Prospective of ^{68}Ga-radiopharmaceutical development. Theranostics. 2014;4(1):47–80.

29. Pandey MK, Byrne JF, Schlasner KN, et al. Cyclotron production of ^{68}Ga in a liquid target: effects of solution composition and irradiation parameters. Nucl Med Biol. 2019;74-75:49–55.

30. Nelson BJB, Wilson J, Richter S, et al. Taking cyclotron ^{68}Ga production to the next level: expeditious solid target production of ^{68}Ga for preparation of radiotracers. Nucl Med Biol. 2020;80-81:24–31.

31. Kumar K. The current status of the production and supply of Gallium-68. Cancer Biother Radiopharm. 2019;35(3):3301163.

32. Yano J, Anger OH. A gallium-68 positron cow for medical use. J Nucl Med. 1964;5:484–7.

33. Loc'h C, Mazièré B, Comar D. A new generator for ionic gallium-68. J Nucl Med. 1980;21:171–3.

34. Schuhmacher J, Maier-Borst W. A new [68]Ge/^{68}Ga radioisotope generator system for production of ^{68}Ga in dilute HCl. Int J Appl Radiat Isot. 1981;32:31–6.

35. Rosch F. Past, present and future of [68]Ge/^{68}Ga generators. Appl Radiat Isot. 2013;13:24–30.

36. Kumar K. The Current Status of the production and supply of gallium-68. Cancer Biother Radiopharm 2020;35(3):163–6.

37. Breeman WAP, Verbruggen AM. The [68]Ge/^{68}Ga generator has high potential, but when can we use ^{68}Ga-labelled tracers in clinical routine? Eur J Nucl Med Mol Imaging. 2007;34:978–81.

38. Zhernosekov KP, Filosofov DV, Baum RP, et al. Processing of generator-produced ^{68}Ga for medical application. J Nucl Med. 2007;48:1741–8.

39. Azhdarinia A, Yang DJ, Chao C, et al. Infrared-based module for the synthesis of 68Ga-labeled radiotracers. Nucl Med Biol. 2007;34(1):121–7.

40. Decristoforo C, Knopp R, von Guggenberg E, et al. A fully automated synthesis for the preparation of ^{68}Ga-labelled peptides. Nucl Med Commun. 2007;28:870–5.

41. Velikyan I, Maecke H, Langstrom B. Convenient preparation of ^{68}Ga-based PET radiopharmaceuticals at room temperature. Bioconjug Chem. 2008;19(2):569–73.

42. De Jong M, Bakker WH, Krenning EP, et al. Yttrium-90 and indium-111 labelling, receptor binding and biodistribution of [DOTA[0],D-Phe[1],Tyr[3]]octreotide, a promising somatostatin analogue for radionuclide therapy. Eur J Nucl Med. 1997;24:368–71.

43. Otte A, Jermann E, Behe M, et al. DOTATOC: a powerful new tool for receptor-mediated radionuclide therapy. Eur J Nucl Med. 1997;24:792–5.

44. Reubi JC, Schär J-C, Waser B, et al. Affinity profiles for human somatostatin receptor subtypes SST1–SST5 of somatostatin radiotracers selected for scintigraphic and radiotherapeutic use. Eur J Nucl Med. 2000;27:273–82.

45. Hofmann M, Maecke H, Borner A, et al. Biokinetics and imaging with the somatostatin receptor PET radioligand ^{68}Ga-DOTATOC: preliminary data. Eur J Nucl Med. 2001;28:1751–7.

46. Koukouraki S, Strauss LG, Georgoulias V, et al. Evaluation of the pharmacokinetics of ^{68}Ga-DOTATOC in patients with metastatic neuroendocrine tumors scheduled for ^{90}Y-DOTATOC therapy. Eur J Nucl Med Mol Imaging. 2006;33:460–6.

47. Kowalski J, Henze M, Schuhmacher J, et al. Evaluation of positron emission tomography imaging using [^{68}Ga]-DOTA-DPhe1-Tyr[3]-octreotide in comparison to [^{111}In]-DTPAOC SPECT. First results in patients with neuroendocrine tumors. Mol Imaging Biol. 2003;5:42–8.

48. Graham MM, Gu X, Ginader T, et al. ^{68}Ga-DOTATOC imaging of neuroendocrine tumors: a systematic review and metaanalysis. J Nucl Med. 2017;58:1452–1458.

49. Hennrich U, Benešová M. [^{68}Ga]Ga-DOTA-TOC: the first FDA-approved ^{68}Ga-radiopharmaceutical for PET imaging. Pharmaceuticals. 2020;13:38. https://doi.org/10.3390/ph13030038.

50. De Jong M, Breeman WAP, Bakker WH, et al. Comparison of ^{111}In-labeled somatostatin analogues for tumor scintigraphy and radionuclide therapy. Cancer Res. 1998;58:437–41.

51. Kwekkeboom DJ, Bakker WH, Kooji PPM, et al. [^{177}Lu-DOTA[0],Tyr[3]]octreotate: comparison with [^{111}In-DTPA°]octreotide in patients. Eur J Nucl Med. 2001;28:1319–25.

52. Poeppel TD, Binse I, Petersenn S, et al. ^{68}Ga-DOTATOC versus ^{68}Ga-DOTATATE PET/CT in functional imaging of neuroendocrine tumors. J Nucl Med. 2011;52:1864–1870.

53. O'Keefe DS, Su SL, Bacich DJ, et al. Mapping, genomic organization and promoter analysis of the human prostate-specific membrane antigen gene. Biochim Biophys Acta. 1998;1443:113–27.

54. Eder M, Schäfer M, Bauder-Wust U, et al. ^{68}Ga-complex lipophilicity and the targeting property of a urea-based PSMA inhibitor for PET imaging. Bioconjug Chem. 2012;23:688–697.

55. Afshar-Oromieh A, Haberkorn U, Eder M, et al. [^{68}Ga]Gallium labelled PSMA ligand as superior PET tracer for the diagnosis of prostate cancer: comparison with ^{18}F-FECH. Eur J Nucl Med Mol Imaging. 2012;39:1085–6.

56. Bois F, Noirot C, Dietemann S, et al. [^{68}Ga]Ga-PSMA-11 in prostate cancer: a comprehensive review. Am J Nucl Med Mol Imaging. 2020;10(6):349–74.

57. Chaple IF, Lapi SE. Production and use of the first-row transition metal PET radionuclides [43,44]Sc, [52]Mn, and [45]Ti. J Nucl Med. 2018;59:1655–9.

58. Müller M, Domnanich KA, Umbricht CA, van der Meulen NP. Scandium and terbium radionuclides for radiotheranostics: current state of development towards clinical application. Br J Radiol. 2018;91(1091):20180074.

59. Sinnes J-P, Bauder-Wüst U, Schäfer M, et al. [68]Ga, [44]Sc and ^{177}Lu-labeled AAZTA5 -PSMA-617: synthesis, radiolabeling, stability and cell binding compared to DOTA-PSMA-617 analogues. EJNMMI Radiopharm Chem. 2020;5:28.

60. Chakravarty R, Chakraborty S, Dash A. A systematic comparative evaluation of 90Y-labeled bifunctional chelators for their use in targeted therapy. J Labelled Comp Radiopharm 2014;57(2):65–74.

61. Lövqvist A, Humm JL, Sheikh A, et al. PET imaging of [86]Y-labeled anti-Lewis Y monoclonal antibodies in a nude mouse model: comparison between [86]Y and ^{111}In radiolabels. J Nucl Med. 2001;42:1281–7.

62. Anderson CJ, Dehdashti F, Cutler PD, et al. Copper-64-TETA-octreotide as a PET imaging agent for patients with neuroendocrine tumors. J Nucl Med. 2001;42:213–21.

63. Anderson CJ, Wadas TJ, Wong EH, et al. Cross-bridged macrocyclic chelators for stable complexation of copper radionuclides for PET imaging. Q J Nucl Med Mol Imaging. 2008;52:185–92.

64. Cowley AR, Dilworth JR, Donnelly PS, et al. Bifunctional chelators for copper radiopharmaceuticals: the synthesis of [Cu(ATSM)-amino acid] and [Cu(ATSM)-octreotide] conjugates. Dalton Trans. 2007;(2):209–17.

65. Di Bartolo NM, Sargeson AM, Donlevy TM, Smith SV. Synthesis of a new cage ligand, SarAr, and its complexation with selected transition metal ions for potential use in radio-imaging. J Chem Soc Dalton Trans. 2001;15:2303–9.

66. Dearling JLJ, Voss SD, Dunning P, et al. Imaging cancer using PET — the effect of the bifunctional chelator on the biodistribution of a ^{64}Cu-labeled antibody. Nucl Med Biol. 2011;38(1):29–38.

67. De Silva RA, Jain S, Lears KA et al. Copper-64 radiolabeling and biological evaluation of bifunctional chelators for radiopharmaceutical development. Nucl Med Biol. 2012;39(8):1099–104.

68. Gutfilen B, Souza SA, Valentini G. Copper-64: a real theranostic agent. Drug Des Devel Ther. 2018;12:3235–45.

69. Zhou Y, Li J, Xu X, et al. ^{64}Cu-based radiopharmaceuticals in molecular imaging. Technol Cancer Res Treat. 2019;18:1–10.

70. Carlsen EA, Johnbeck CB, Binderup T, et al. ^{64}Cu-DOTATATE PET/CT and prediction of overall and progression-free survival in patients with neuroendocrine neoplasms. J Nucl Med. 2020;61:1491–1497.

71. Pfeifer A, Knigge U, Mortensen J, et al. Clinical PET of neuroendocrine tumors using ^{64}Cu-DOTATATE: first-in-humans study. J Nucl Med. 2012;53:1207–15.

72. Johnbeck CB, Knigge U, Loft A, et al. Head-to-head comparison of ^{64}Cu-DOTATATE and

73. Delpassand ES, Ranganathan D, Wagh N, et al. ^{64}Cu-DOTATATE PET/CT for imaging patients with known or suspected somatostatin receptor–positive neuroendocrine tumors: results of the first U.S. prospective, reader-masked clinical trial. J Nucl Med. 2020;61:890–896.

74. Dejesus OT, Nickles RJ. Production and purification of [89]Zr, a potential PET antibody label. Appl Radiat Isot. 1990;41(8):789–90.

75. Kasbollah A, Eu P, Cowell S, Deb P. Review on production of 89Zr in a medical cyclotron for PET radiopharmaceuticals. J Nucl Med Technol. 2013;41(1):35–41.

76. Link JM, Krohn KA, Eary JF, et al. Zr-89 for antibody labeling and positron emission tomography. J Label Compd Radiopharm. 1986;23:1297–8.

77. Verel I, Visser GWM, Boellaard R, et al. Quantitative [89]Zr immuno-PET for in vivo scouting of ^{90}Y-labeled monoclonal antibodies in xenograft-bearing nude mice. J Nucl Med. 2003b;44:1663–70.

78. Verel I, Visser GWM, Boellaard R, et al. [89]Zr Immuno-PET: comprehensive procedures for the production of [89]Zr-labeled monoclonal antibodies. J Nucl Med. 2003;44:1271–1281.

79. Holland JP, Sheh Y, Lewis JS. Standardized methods for the production of high specific-activity zirconium-89. Nucl Med Biol. 2009;36(7):729–39.

80. Meijs WE, Herscheid JDM, Haisma HJ, Pinedo HM. Evaluation of desferal as a bifunctional chelating agent for labeling antibodies with Zr-89. Int J Rad Appl Instrum A. 1992;43(12):1443–7.

81. Severin GW, Engle JW, Nickles RJ, Barnhart TE. [89]Zr radiochemistry for PET. Med Chem. 2011;7(5):389–394.

82. Zeglis BM, Lewis JS. The bioconjugation and radiosynthesis of [89]Zr-DFO-labeled antibodies. J Vis Exp. 2015;2015:e52521.

83. Damerow H, Hübner R, Judmann B, et al. Side-by-side comparison of five chelators for [89]Zr-labeling of biomolecules: investigation of chemical/radiochemical properties and complex stability. Cancers (Basel). 2021;13(24):6349.

84. Bhatt NB, Pandya DN, Wadas TJ. Recent advances in zirconium-89 chelator development. Molecules. 2018;23:638.

85. Feiner IVJ, Brandt M, Cowell J, et al. The race for hydroxamate-based zirconium-89 chelators. Cancers (Basel). 2021;13:4466.

86. Chomet M, van Dongen GAMS, Vugts DJ. State of the art in radiolabeling of antibodies with common and uncommon radiometals for preclinical and clinical Immuno-PET. Bioconjug Chem. 2021;32:1315–30.

87. Börjesson PKE, Jauw YWS, Boellaard R, et al. Performance of immuno-positron emission tomography with zirconium-89-labeled chimeric monoclonal antibody U36 in the detection of lymph node

metastases in head and neck cancer patients. Clin Cancer Res. 2006;12:2133–40.

88. Perk LR, Visser GW, Vosjan MJ, et al. (89)Zr as a PET surrogate radioisotope for scouting biodistribution of the therapeutic radiometals (90)Y and (177) Lu in tumor-bearing nude mice after coupling to the internalizing antibody cetuximab. J Nucl Med. 2005;46:1898–906.

89. Wei W, Rosenkrans CT, Liu J. ImmunoPET: concept, design, and applications. Chem Rev. 2020;120(8):3787–851.

90. Yoon J-K, Park B-N, Ryu E-K, et al. Current perspectives on [89]Zr-PET imaging. Int J Mol Sci. 2020;21(12):4309.

91. Moek KL, Giesen D, Kok IC. Theranostics using antibodies and antibody-related therapeutics. J Nucl Med. 2017;58:83S–90S.

92. Pandit-Taskar N, O'Donoghue JA, Ruan S, et al. First-in-human imaging with [89]Zr-Df-IAB2M anti-PSMA minibody in patients with metastatic prostate cancer: pharmacokinetics, biodistribution, dosimetry, and lesion uptake. J Nucl Med. 2016;57(12):1858–64.

93. Deutsch E, Libson K, Jurisson S, et al. Technetium chemistry and technetium radiopharmaceuticals. Prog Inorg Chem. 1983;30:75–139.

94. Boschi A, Uccelli L, Martini P. A picture of modern Tc-99m radiopharmaceuticals: production, chemistry, and applications in molecular imaging. Appl Sci. 2019;9:2526. https://doi.org/10.3390/app9122526.

95. Babich JW, Fischman AJ. Effect of "co-ligand" on the biodistribution of ^{99m}Tc-labeled hydrazino nicotinic acid derivatized chemotactic peptides. Nucl Med Biol. 1995;22:25–30.

96. Banerjee SR, Maresca KP, Francesconi L, et al. New directions in the coordination chemistry of [99m]Tc: a reflection on technetium core structures and a strategy for new chelate design. Nucl Med Biol. 2005;32:1–20.

97. Mikulová MB, Mikuš P. Advances in development of Radiometal labeled amino acid-based compounds for cancer imaging and diagnostics. Pharmaceuticals. 2021;14(2):167.

98. Piramoon M, Hosseinimehr SJ. The past, current studies and future of organometallic [99m]Tc(CO)$_3$

99. Alberto R, Schlibi R, Schubiger AP. First application of fac-$[^{99m}Tc(OH_2)_3(CO)_3]^+$ in bioorganometallic chemistry: design, structure, and in vitro affinity of a 5-HT1A receptor ligand labeled with [99m]Tc. J Am Chem Soc. 1999;121:6076–7.

100. Waibei R, Alberto R, Willude J, et al. Stable one-step technetium-99m labeling of His-tagged recombinant proteins with a novel Tc(I)-carbonyl complex. Nat Biotechnol. 1999;17:897–901.

101. Schmidkonz C, Götz TI, Atzinger A, et al. ^{99m}Tc-MIP-1404 SPECT/CT for assessment of whole-body tumor burden and treatment response in patients with biochemical recurrence of prostate cancer. Clin Nucl Med. 2020;45(8):e349-e357.

102. Vallabhajosula S, Nikolopoulou A, Babich JW. ^{99m}Tc-labeled small-molecule inhibitors of prostate-specific membrane antigen: pharmacokinetics and biodistribution studies in healthy subjects and patients with metastatic prostate cancer. J Nucl Med. 2014;55(11):1791–1798.

103. Bartolo ND, Sargeson AM, Smith SV. New ^{64}Cu PET imaging agents for personalized medicine and drug development using the hexa-aza cage, SarAr. Org Biomol Chem. 2006;4:3350–7.

104. Brandt M, Cardinale J, Aulsebrook ML, et al. An overview of PET radiochemistry, part 2: radiometals. J Nucl Med. 2018;59:1500–6.

105. Chakrabarti A, Zhang K, Aruva MR, et al. KRAS mRNA expression in human pancreatic cancer xenografts imaged externally with [^{64}Cu]DO3A-peptide nucleic acid-peptide chimeras. Cancer Biol Ther. 2007;6:948–56.

106. Otte A, Mueller-Brand J, Dellas S, et al. Yttrium-90-labelled somatostatin-analogue for cancer treatment. Lancet. 1998;351:417–8.

107. Sarduy E, Ellison PA, Barnhart TE, et al. PET radiometals for antibody labeling. J Labelled Comp Radiopharm. 2018;61(9):636–51.

108. Verel I, Visser GWM, Van Dongen GAMS. The promise of immuno-PET in radioimmunotherapy. J Nucl Med. 2005;46:164S–71S.

Everything that can be counted does not necessarily count; everything that counts cannot necessarily be counted. (Albert Einstein)

13.1 Quantitation

Molecular imaging of radiotracer distribution by PET or SPECT following intravenous injection shows the pattern of relative uptake of radioactivity in different organs and also in different regions within any particular organ of interest. These imaging studies permit measurement of the time course of uptake and clearance of specific tracers. Quantitative measurement of the local radiotracer activity is essential to assess the local physiological function quantitatively. Semi-quantitative methods have been developed for the interpretation of routine clinical diagnostic studies. However, absolute measurement of physiologic parameters generally requires accurate measurement of radioactivity concentrations in the arterial blood and in a specific region of interest (ROI) or volume of interest (VOI) in a tissue, in order to extract quantitative information based on tracer kinetic or compartmental modeling techniques.

In PET, the count rate per voxel in the reconstructed tomographic image, in principle, is proportional to the activity concentration in a given ROI. Since the attenuation and scatter corrections are not reliable in SPECT, the count rate per voxel in a SPECT image does not necessarily reflect the true activity concentration. As a result, true quantitation with SPECT technique is not practically feasible at this time. Some of the basic principles and concepts involved in quantitative methods will be described briefly here with specific examples.

13.1.1 Standardized Uptake Value

To make the PET images quantitative, the PET camera is first calibrated using a cylindrical phantom with known radioactivity concentration (Bq mL^{-1}). The count rate per voxel (cps or cpm) is then divided by the measured system calibration factor, CF [(Bq cc^{-1})/(cps voxel^{-1})], to convert cps in a given ROI to the corresponding activity concentration units, C_t (Bq cc^{-1}).

Following administration of a PET radiotracer, the image acquisition represents a sum of coincidence counts due to true, scatter, and random events. At the end of the image acquisition, the following corrections are required to make the PET data truly quantitative:

- Attenuation correction (performed using the CT scan data).
- Scatter and random correction.

- Energy correction.
- Linearity distortion correction.
- Normalization and dead time correction.
- Dose calibrator cross calibration with PET scanner.

It is common practice in animal studies to express the biodistribution of radiotracers using the parameter, the percent injected dose per gram of tissue (%ID/g of tissue), which is calculated using the following equation.

$$\%ID/g = \frac{\text{Activity in a gram of tissue}(C_t)}{\text{Injected dose}} ? 100 \qquad (13.1)$$

The %ID/g parameter, however, does not take into consideration the total body mass (weight) of a patient. The standardized uptake value (SUV) measured with a PET scanner is a semi-quantitative unit developed in order to include the total body weight of a patient [1–5].

$$SUV = \frac{C_t \text{ in a } ROI(\text{MBq}/\text{cc})}{\text{Injected dose } (\text{MBq})} ? \text{Body wt}(g) ? 100 \qquad (13.2)$$

$$SUV_{ROI} = A_{ROI}(T_S)/\text{Conc}_S(T_S)$$

where, Conc = Dose/wt, and T_s = the time of the scan.

The SUV value, therefore, is a unitless number that normalizes the lesion uptake to the injected dose per unit of body weight. It has also been proposed that normalization of SUV based on body surface area (BSA) may improve the accuracy of SUV but, a method of normalization has not been routinely employed by most PET users. It is important to recognize that many factors (dose infiltration, serum glucose levels, total body fat, and the lesion volume) other than the metabolic status of the lesion can significantly affect the reliability of the SUV measurement in routine clinical practice. In addition, a number of factors, including regional blood flow, enzyme activity, active transport mechanisms, and binding site concentrations, may also contribute to the amount of radioactivity present in a given ROI at any given time. The SUV determination is regarded as semiquantitative since it does not consider many of these biochemical processes and all the possible contributions to overall tissue activity levels.

The quantification of [^{18}F]FDG uptake by using the maximum standardized uptake value (SUV$_{max}$) is the traditional PET-derived parameter used as a biomarker of glucose metabolism of several biological processes for both diagnostic and follow-up purposes. Several other parameters have also been developed such as SUV$_{mean}$, SUV$_{peak}$, SUV$_{max}$, or SUV$_{peak}$ corrected for lean body mass (SUL$_{max}$ and SUL$_{peak}$). Sometimes, a simple traditional parameter such as Target/Background (T/B) ratio may be utilized. It is important to optimize quantitative techniques since disease progression and response to therapy are determined based on the PET SUV values [2].

13.2 Physiological Modeling

PET and SPECT permit sequential measurements of the radioactivity distribution in vivo following intravenous administration of a radiopharmaceutical at tracer levels. The mea-

sured time-activity distribution, however, is influenced by various factors, such as blood flow, clearance from plasma, the number of specific and nonspecific binding sites, and their affinity. For a tracer to have any value in clinical practice, the uptake and distribution of the tracer must quantitatively and accurately reflect the concentration of available binding sites or the rate of some biochemical processes. The extraction of quantitative values from dynamic PET imaging data requires the fitting of the data to a mathematical model that describes the uptake and retention of the tracer in tissue. Tracer kinetic physiologic modeling provides the link between activity levels measured in a specific ROI in the functional scan and the physiologic parameters associated with the particular function being studied. The kinetic models can be classified as noncompartmental, compartmental, or distributive. With most molecular imaging radiopharmaceuticals, compartmental models have become the model of choice. These models describe mathematically using a set of differential equations, the transfer and behavior of the radiotracer between compartments, each of which represents distinct anatomic, physiologic, or biochemical space (such as capillaries, extracellular, intracellular, and

receptor-bound). It is important to realize that the segmentation of the physiologic processes into these compartments is only a simple approximation to derive quantitative parameters and may not necessarily reflect real in vivo biological processes.

13.2.1 Radiotracer Binding

The radiotracers or the radioligands used in molecular imaging studies are generally assumed to bind selectively to the target site receptor (R) or an enzyme (E). The simplest model is the bimolecular reaction [6], describing the kinetics of the radioligand (L) binding with a specific receptor (R) or an enzyme (E) to form a complex, LR or LE. According to the law of mass action (Eq. 13.3), the rate of the reaction will proceed in proportion to the product of concentration of the reactants. Several equations pertinent to ligand-receptor interactions and their relationships are summarized in Fig. 13.1.

$$[\mathbf{L}]+[\mathbf{R}]\underset{\mathbf{k_{on}}}{\overset{\mathbf{k_{off}}}{?}}[\mathbf{RL}] \quad\quad (13.3)$$

$$\textit{At}\text{ equilibrium,}\quad \mathbf{k_{on}}[\mathbf{L}][\mathbf{R}]?\mathbf{K_{off}}[\mathbf{RL}] \quad\quad (13.4)$$

$$\text{The equilibrium constant,}\quad \mathbf{K_D}=\mathbf{K_{off}}/\mathbf{K_{on}} \quad\quad (13.5)$$

$$\text{The total number of receptors,}\quad \mathbf{B_{max}}=[\mathbf{R}]+[\mathbf{RL}] \quad\quad (13.6)$$

$$\text{The concentration of bound receptors}\quad [\mathbf{RL}]=\frac{\mathbf{B_{max}}[\mathbf{L}]}{[\mathbf{L}]+\mathbf{K_D}} \quad\quad (13.7)$$

$$\text{The Binding Potential }(BP)\quad \mathbf{BP}=\frac{\mathbf{B_{max}}}{\mathbf{K_D}}=\frac{[\mathbf{RL}]}{[\mathbf{L}]}=\frac{\mathbf{B}}{\mathbf{F}} \quad\quad (13.8)$$

Fig. 13.1 Basic equations of ligand (L) and receptor (R) binding or interaction
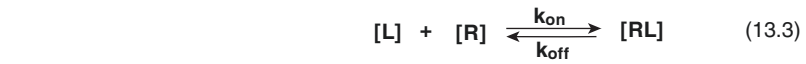
$$[L] + [R] \underset{k_{off}}{\overset{k_{on}}{\rightleftharpoons}} [RL] \qquad (13.3)$$

At equilibrium,

$$k_{on}[L][R] \longrightarrow K_{off}[RL] \qquad (13.4)$$

The equilibrium constant,

$$K_D = K_{off}/K_{on} \qquad (13.5)$$

The total number of receptors,

$$B_{max} = [R] + [RL] \qquad (13.6)$$

The concentration of bound receptors

$$[RL] = \frac{B_{max}[L]}{[L] + K_D} \qquad (13.7)$$

The Binding Potential (BP)

$$BP = \frac{B_{max}}{K_D} = \frac{[RL]}{[L]} = \frac{B}{F} \qquad (13.8)$$

13.2.1.1 Binding Potential

In PET and SPECT studies with high SA radiotracers (L^*), the concentration of the bound receptors [RL^*] is very small (<5%), and the receptor concentration [R] is approximately equal to B_{max}. Under these conditions, the binding potential (BP) is defined as B_{max}/K_d and is equal to the ratio of the bound radioligand concentration to the free radioligand concentration (B/F) at equilibrium (Eq. 13.8). BP is proportional to B_{max} if K_d can be regarded as a constant [7, 8, 9].

13.2.1.2 Affinity

The affinity of a ligand for a receptor refers to the binding strength and can be expressed as a K_D or K_i value, which can be calculated from the measured IC_{50} value as shown in Fig. 13.2.

In a typical "saturation" radioligand binding assay experiment in vitro, increasing amounts of a radioligand are added to a fixed concentration of receptors, and the amount of radiotracer bound B or [RL] is measured as a function of [L]. Nonlinear regression analysis can be used to fit the data to the Eq. 13.7 in order to estimate both B_{max} and K_D (Fig. 13.3).

The IC_{50} value is also determined in vitro by measuring the competitive effect of different concentrations of the ligand of interest (10^{-12}–10^{-4} M) on the binding of a reference radioligand with known affinity and concentration to a preparation of cells or cell membranes known to
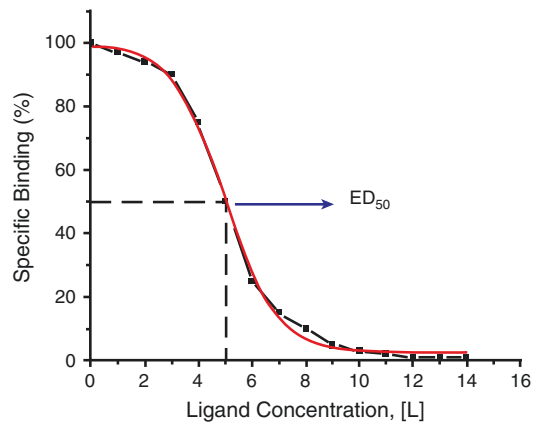

Fig. 13.2 Saturation of specific binding sites by carrier-added ligand concentration, [L]. ED_{50} can be defined as the [L], which reduces the specific binding signal by 50%. The specific binding can be determined ex vivo studies, or in vivo using MicroPET or MicroSPECT imaging

express specific receptors for the ligand under investigation.

In order to obtain high contrast images, the radiotracer must have high affinity (low K_D) for its receptor. The required affinity, however, depends on the receptor concentration, B_{max}, in a given ROI. Typically, for radio labeled antagonists, high affinity in the nanomolar range is needed to obtain high contrast images.

In order to image the distribution of one specific receptor subtype, the radioligand should preferably bind only to that specific receptor with

high affinity. Certain radioligands, may have affinity for many receptor subtypes or even different receptors. Therefore, in addition to high affinity, radioligands should also have *selectivity*, which is defined as the ratio of affinity of a ligand for the receptor of interest to the affinity for each of the other receptor types.

13.2.2 Tracer Kinetics

Following intravenous administration, the radiotracer is cleared from circulation rapidly and enters a tissue compartment in which the tracer may bind to an enzyme, a specific receptor, or even undergo metabolism and subsequent intracellular trapping. For most of the radiotracers, the kinetics can be described using a maximum of three different compartments (Fig. 13.4). The

first compartment is the arterial blood, in which the radiotracer may be present either as "free" species or exhibit plasma protein binding (PPB). From the arterial blood, the radiotracer passes through a second compartment (extracellular or intracellular fluid), also known as a free compartment. The third compartment is the region where the tracer is bound to either an enzyme or a specific receptor, or metabolically trapped.

In tracer kinetic modeling, certain fundamental or physiologically reasonable assumptions are usually made to minimize the number of kinetic parameters needed to improve the fit to the measured data (from imaging studies) to the physiological model or to simplify the imaging and analysis protocols. These simplifications, however, must be physically meaningful and must be validated against the complete model [8, 9].

Although most physiological and biological processes are nonlinear, the behavior (transport and or chemical reactions) of radiotracers in vivo is assumed to be linear or approximately linear due to the fact that the mass of the tracer is very small. First-order kinetics can describe the exchange of a radioligand between compartments.

- In general, the system under study is effective in a *steady state* and the administration of the radioligand does not perturb the steady state.
- Since arterial blood delivers radioligand to all tissues, the input function is always the blood time-activity concentration (TAC). Also, the radioligand can pass back and forth freely from the arterial plasma to the free compartment.
- For most radioligands, the nonspecific-binding (NSB) compartment is assumed to be in rapid
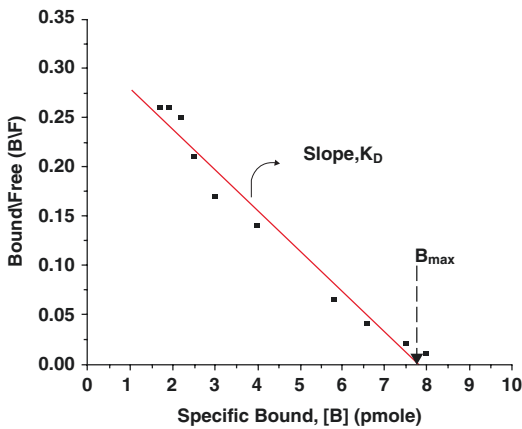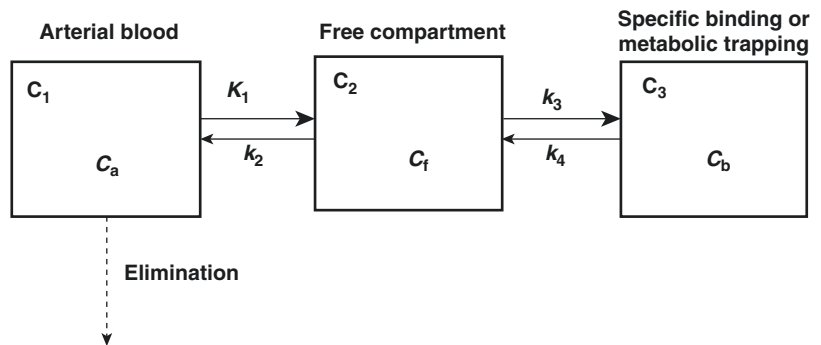

Fig. 13.3 A Scatchard plot of the ligand (L)-receptor (R) binding data in order to estimate receptor concentration (B_{max}) and affinity (K_D)

Fig. 13.4 Two and three compartment models used to describe radiotracer kinetics in vivo. Different terms used to describe the movement of radiotracer in different compartments are listed in Table 13.1

equilibrium with the free compartment and the two compartments are treated as a single compartment.

A number of parameters used in the modeling equations below and the terms used in the description of 3-compartmental model are defined in Table 13.1.

13.2.2.1 Two-Compartment Model

This model, generally, represents the movement of the radiotracer between the blood pool (C_1) into the tissue pool (C_2), as shown in Fig. 13.4. The change of tissue concentration of the radiotracer (C_t) over time is described by the following differential equation.

$$\frac{dC_t}{dt} = K_1 C_a \, ? \, k_2 C_t \qquad (13.9)$$

In the above equation, K_1 describes the speed of transfer of the ligand from the blood to the tissue and depends on the concentration of the tracer in the plasma $C_a(t)$ and on the properties of the transport process (e.g., the activity of carrier enzyme). Because the tracer dose does not saturate the transport process, the transfer from the blood to the tissue is simply given by the product of $K_1 C_a(t)$. Similarly, the transport from the tissue to the blood is given by the product of $k_2 C_t(t)$.

This two-compartment (or one tissue compartment) model is generally utilized with some minor modifications in the measurement of radiotracer transport across the BBB.

The measurement rCBF is one of the major clinical applications of PET using freely diffusible radiotracers, such as [^{15}O]water. With diffusible radiotracers, the initial tracer activity in the brain is directly related to the blood flow (F) [10, 11]. Free diffusion of the tracer also leads to equilibration of C_t with that of C_v (concentration in out flowing venous blood). Thus, C_t is the same as $C_v \lambda$, where λ is the tissue/blood partition coefficient (synonymous with distribution volume) of the radiotracer. As a result, Eq. 13.9 is modified to replace K_1 with F and k_2 with F/λ, as shown below.

$$\frac{dC_t}{dt} = FC_a \, ? \, \frac{F}{?} C_t \qquad (13.10)$$

Table 13.1 Important parameters used in physiological modeling

Parameter	Description	Units
C_a	Tracer concentration in arterial blood or plasma	Bq mL^{-1}
C_f	Free tracer concentration in tissue	Bq mL^{-1}
C_t	Concentration of free tracer in tissue	Bq mL^{-1}
C_b	Concentration of tracer specifically bound to receptors, enzyme, or metabolically trapped	Bq mL^{-1}
K_1	Kinetic constant for transfer of tracer from blood to tissue ($C_a \rightarrow C_f$)	mL min^{-1} g^{-1}
k_2	Kinetic constant for transfer of tracer from tissue to blood ($C_f \rightarrow C_a$)	L min^{-1}
k_3	Kinetic constant for conversion of free tracer in tissue to specific binding or metabolic trapping ($C_f \rightarrow C_b$)	L min^{-1}
k_4	Kinetic constant for the dissociation of specifically bound or metabolically trapped tracer to free tracer in tissue ($C_b \rightarrow C_f$)	L min^{-1}
DV	Distribution volume	mL g^{-1} of tissue
B_{max}	Maximum receptor binding capacity	Mol g^{-1}
K_D	Equilibrium dissociation constant	
BP	Binding potential	mL g^{-1}
K_M	Michaelis-Menten constant (substrate concentration at half-maximum velocity)	
λ	Tissue/blood partition coefficient	
E	Tracer extraction fraction from blood (capillaries) into tissue	Unit less parameter
P	Capillary permeability for the tracer	cm min^{-1}
S	Capillary surface area	cm^2 g^{-1}

For radiotracers that are not entirely freely diffusible, the first pass extraction from the blood to the tissue is important. The transfer from the blood to the brain (K_1) is determined by the product of the blood flow (F) and tracer extraction fraction (E). The relationship between E, S, P, and F is given by the Renkin-Crone equation [12].

$$E = 1 ? e^{? \frac{PS}{F}} \qquad (13.11)$$

When the tracer arrives in the capillaries, some fraction of it is extracted into the tissue across the capillary walls. This unidirectional extraction fraction (E) is a unitless parameter and depends on the capillary permeability (P) for the tracer, total available capillary surface area (S), and the blood flow (F). The extraction fraction, E, will increase if S or P increases, but E will decrease if blood flow, F, increases.

13.2.2.2 Three-Compartment Model

Many radiotracers undergo metabolism (FDG, FDOPA, FLT) or are bound to specific receptors in the brain or some other tissues (Raclopride, Flumazenil, FET, Ga-DOTATOC). For most of the molecular imaging radiotracers, metabolism and specific intracellular binding are the physiological processes of interest. The dynamic behavior of many of these radiotracers in vivo is assumed to follow a standard three-compartment kinetic model (Fig. 13.4) with a single arterial input function and two tissue compartments.

Compartment C_1 represents the arterial concentration of the free, unmetabolized tracer. The passage into the tissue is considered to appear either through passive diffusion in the presence of a concentration gradient or through an active transport mechanism. Compartment C_2 is the first tissue compartment and represents an extra vascular pool of the tracer in the tissue; this tracer is available for binding or further reaction. Compartment C_3 is the concentration of the tracer that is specifically bound to the target molecule (C_b) or has undergone some chemical reaction or metabolism (C_m). The transfer of the radiotracer in these three compartments is described by the following two differential equations.

$$\frac{dC_2}{dt} = K_1 C_a ? (k_2 + k_3) C_2 + k_4 C_3 \quad (13.12)$$

$$\frac{dC_3}{dt} = k_3 C_2 ? k_4 C_3 \qquad (13.13)$$

For radiotracers with irreversible metabolism or metabolic trapping (such as FDG and FLT), k_4 is negligibly small, and the total tissue tracer activity, $C_f(t)$, can be split into two components, the reversible free tracer, $C_f(t)$, and the trapped metabolized tracer, $C_m(t)$.

FDG Metabolism: Measurement of MRglc

The technique of measuring MRglc using FDG metabolic intracellular trapping is based on the autoradiographic DG technique [13, 14]. It is important to understand that the transport of FDG and the enzyme mediated reactions are distinct from those for glucose. In order to estimate MRglc, however, the competitive kinetics between FDG and glucose must be taken into account.

In a 3-compartmental model (Fig. 13.4), C_1 represents FDG in plasma, C_2 represents free FDG in tissue, and C_3 represents FDG-6-phosphate. The basis for using FDG as a tracer to measure FDGglc is because FDG-6-phosphate is not a substrate for further metabolism, unlike glucose-6-phosphate. As a result, with FDG, only the transport and phosphorylation steps are incorporated into this model and not the remaining steps as in glycolysis. To calculate MRglc, however, measurement of the plasma glucose concentration (C_a^o) is needed to estimate intracellular glucose levels. A *lumped constant* (LC) was introduced to correct the differences in the in vivo behavior of FDG and glucose. The actual value of LC may vary (0.4–0.8) depending on the tissue (brain, myocardium, tumor) or plasma glucose levels. Based on the measured rate constants for FDG, LC, and (C_a^o), the MRglc can be calculated, at steady state, using the following equations:

$$\text{MRglc} = \left(\frac{K_1 \, k_3}{k_2 + k_3} \right) \frac{C_a^0}{LC} \qquad (13.14)$$

$$\text{MRglc} = K^? \frac{C_a^0}{LC} \qquad (13.15)$$

Since arterial blood sampling is not practical in routine clinical applications, several different approaches have been developed to measure MRglc [1, 8, 15]. The Patlak plot is one approach that is based on a graphical method, which estimates the influx rate constant, K_1^* using only the time-activity data of dynamic FDG-PET images [16].

Receptor Binding

The dynamics of receptor binding studied by PET and SPECT imaging techniques can be analyzed using the 3-compartmental model (Fig. 13.4). In this model, C_a represents the unmetabolized free radioligand in the blood, C_f (or C_2) represents both the free, and the nonspecifically bound radioligand, and finally C_b represents only the receptor bound radioligand. The transfer of receptor binding radioligand in a 3-compartment model can be described using the differential equations, shown above (13.13 and 13.14), in which C_2 represents the free (nonspecifically bound) radioligand, while C_3 represents C_b, the receptor bound radioligand. The rate constant K_1, k_2, k_3 and k_4 are defined as delivery, washout, forward receptor-ligand reaction, and reverse receptor–ligand reaction, respectively. Many of the neuroreceptor ligands are lipophilic and may have nonspecific protein binding in blood or in tissue. Therefore, the fraction of the free ligand in the plasma (f_1) and the fraction of the free ligand in the tissue (f_2) that is available for specific receptor binding are important in the calculations.

Unlike the radiotracers that undergo metabolism, with the receptor binding radioligands, SA of the radioligand is very important. Since an unlabeled ("cold") ligand is present in the preparations of many radioligands, the cold ligand competes for the specific receptor binding sites with the labeled radioligand. Therefore, k_3 is very much dependent on the SA of the radioligand, as shown below:

$$k_3\left(t\right) = k_{on}f_2\left(B_{max} ? \frac{C_b}{SA}\right) \qquad (13.16)$$

In the above equation, if the SA is high, then C_b/SA (occupancy of receptors by the labeled compound) is negligibly small, and $k_3 \approx k_{on}.f_2.B_{max}$. If the receptor occupancy by the radioligand cannot be disregarded, k_3 is not constant, and the individual variables and constants must be determined separately by compartmental analysis, complicated curve-fitting, and analytic procedures. The clinical imaging studies would then require multiple radioligand injections with different SAs in order to determine the receptor density, $B_{max,}$ or affinity, K_D [17].

In routine clinical PET or SPECT neuroreceptor imaging studies, with a single radioligand, one can only determine the BP, which is B_{max} relative to K_D. (BP = B_{max}/K_D). Also, to prevent saturation effects, the intravenously administered radioligand should preferably bind to only a small fraction (<5%) of all the available receptor sites. Therefore, it is essential that the radioligand must be prepared in high SA (>1.0 Ci μmol^{-1}) so that the total mass of the ligand administered (labeled + cold ligand) is minimal. Very high SA is especially desirable when the receptor concentration is low, or when the radio labeled agonists are used to image high affinity receptor states. Under these conditions, the BP is related to the kinetic constants and can be estimated based on the following equation:

$$BP = \left(\frac{k_1\ k_3}{k_2\ k_4\ f_1}\right) \qquad (13.17)$$

Under equilibrium conditions,

$$\left(\frac{k_1\ k_3}{k_2\ k_4\ f_1}\right) = \frac{C_b}{f_1 C_p} \qquad (13.18)$$

The equilibrium *distribution volume* (DV or *V*) of compartment C_i is defined as the ratio of the tracer concentration in this compartment to the free arterial concentration ($f_1 C_f$) at equilibrium. With neuroreceptor imaging studies, we have

$$V_2 = \frac{C_t}{f_1 C_p}; \quad V_3 = \frac{C_b}{f_1 C_p}; \quad V_T = V_2 + V_3 \quad (13.19)$$

V_3, in the above equation, is the closest PET and SPECT equivalent of BP (BP = B/F), discussed under classical in vitro conditions, as shown in Eq. 13.8. While C_3 represents the receptor bound activity (B), the product $f_1 C_p$ represents the free ligand activity in plasma (L) [8, 9]. BP was originally defined as a ratio of B_{max}/K_D (based on in vitro receptor binding studies) or k_3/k_4 (based on kinetic parameters) [18].

The determination of BP based on the equation for V_3, described above, does require an arterial input function based on blood samples to determine (a) the free concentration of the radioligand (C_p) in plasma and (b) the free fraction in plasma (f_1). At equilibrium, the free radioligand concentration in plasma ($f_1 C_p$) can be assumed to be equal to the free radioligand concentration in the tissue ($f_2 C_t$). Since a reliable f_1 measurement is difficult to obtain for many tracers, the term f_1 is often neglected and assumed to be a constant across subjects. This leads to a more practical definition of BP and V_3 denoted here BP and V'_3 [9]:

$$BP = V_3 = \frac{C_b}{f_1 C_p} = BP^? = V_3^? = \frac{C_b}{C_p} \quad (13.20)$$

In order to avoid blood samples, one can also assume that a reference tissue compartment ($C_{t, ref}$) represents both free radioligand and nonspecifically bound radioligand. Now, at equilibrium, the BP can be expressed relative to the free and nonspecific binding in a reference tissue region such as the cerebellum ($C_3/C_{t, ref}$) [8, 9], as shown below:

$$BP^? = V_3^? = \frac{C_b}{C_p} = BP^? = V_3^? = \frac{V_3}{V_2} = \frac{C_b}{C_{t,ref}} \quad (13.21)$$

13.2.2.3   Graphical Analysis Methods

Graphical analysis (GA) techniques are simple methods for the analysis of data from radiotracer PET and SPECT imaging studies. In the initial evaluation of new radiotracers, they provide a visual way to distinguish between reversible and irreversible types of binding. They also provide considerable ease of computation compared to the optimization of individual model parameters in the solution of the differential equations generally used to describe the binding of radiotracers. GA methods are based on reformulating the model equations so that a linear relationship exists between the data and some quantitative parameter describing the nature of radio tracer binding or metabolism. These methods, however, do require an arterial input function although in some instances a reference region devoid of specific binding sites can be used in place of the plasma input function.

Patlak Plot

The theoretical foundation of GA for irreversible tracers was first developed and applied initially for the estimation of MRglc from dynamic FDG-PET data [16, 19]. The method is based on performing linear regression on the total tissue concentration ($C_p^?$) divided by the plasma concentration at time ($C_T^?$), as a function of the integral of the plasma concentration divided by the plasma concentration at time t (Table 13.1). The Patlak equation predicts that if one plots:

$$\frac{C_T^?(t)}{C_P^?(t)}(y?\,axis) \quad vs. \quad \frac{\int_0^t C_P^?(t)\,dt}{C_P^?(t)} \ (x?\,axis) \quad (13.22)$$

Table 13.2 Plasma and brain tissue time-activity data[a] following administration of [^{18}F]FDG

Time	Plasma	Time	Tissue	$\dfrac{C_{\mathrm{T}}^{?}(t)}{C_{\mathrm{P}}^{?}(t)}$	$\dfrac{?_0^t C_{\mathrm{P}}^{?}(t)\mathrm{d}t}{C_{\mathrm{P}}^{?}(t)}$
min	nCi/mL	min	nCi/mL		
0.28	0.02	0.23	0.0	0	0
0.73	201	1.23	33	0.5	0.03
0.98	1150	2.23	96	2.3	0.13
1.48	1454	3.48	125	6.3	0.33
1.95	832	5.48	145	13	0.64
2.97	478	8.98	155	34	1.47
3.47	379	17.48	158	103	3.9
4.97	249	27.48	163	210	7.64
7.97	120	37.48	168	336	12.15
11.95	62	47.48	172	462	16.64
19.95	31	57.48	175	641	23.03
29.95	18	67.48	177	819	29.36
39.95	12	77.48	179	1028	36.82
59.97	7	87.48	180	1368	48.92
89.95	3.4	97.48	181	1694	60.55
119.95	1.8	112.48	182	2329	83.13

[a]The above simulated data is reproduced from [20]
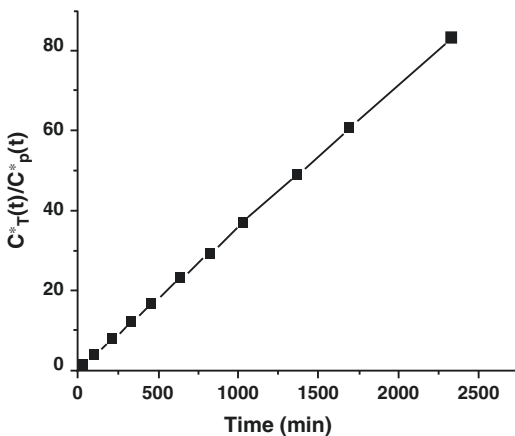

Fig. 13.5 The Patlak equation predicts that after some time $t > t^*$, a plot of total tissue concentration ($C_{\mathrm{p}}^{?}$) divided by the plasma concentration at time ($C_{\mathrm{T}}^{?}$) as a function of the integral of the plasma concentration divided by the plasma concentration at time t becomes linear. The plot based on data from Table 13.2 shows that the slope K^* is 0.036 [20]

The plot (Fig. 13.5) becomes linear over time with a slope of K^* (the influx constant) describing the transfer of the tracer from the plasma compartment to the irreversible compartment. It is important to note that K^* is dependent both on the binding or trapping rate and on the transport rate constants, K_1 and k_2. The Patlak plot is applicable for radiotracers that are metabolically trapped (FDG, FLT, FDOPA) but, not for receptor binding radioligands.

Logan Plot

Based on the original work of Patlak, the GA for reversible receptor binding radiotracers was initially developed by Logan [21, 22] and further refinements were proposed by Ichise [23, 24]. In the Logan plot, the integral of the ROI activity over the current ROI activity in the receptor binding tissue is plotted versus the integral of the plasma activity over the current ROI in the receptor binding tissue.

$$\frac{?_0^t C_{\mathrm{t}}(?)\mathrm{d}?}{C_{\mathrm{t}}(t)}\left(y\,?\,\mathrm{axis}\right) \quad vs. \quad \frac{?_0^t C_{\mathrm{p}}(?)\mathrm{d}?}{C_{\mathrm{t}}(t)}\left(x\,?\,\mathrm{axis}\right) \tag{13.23}$$
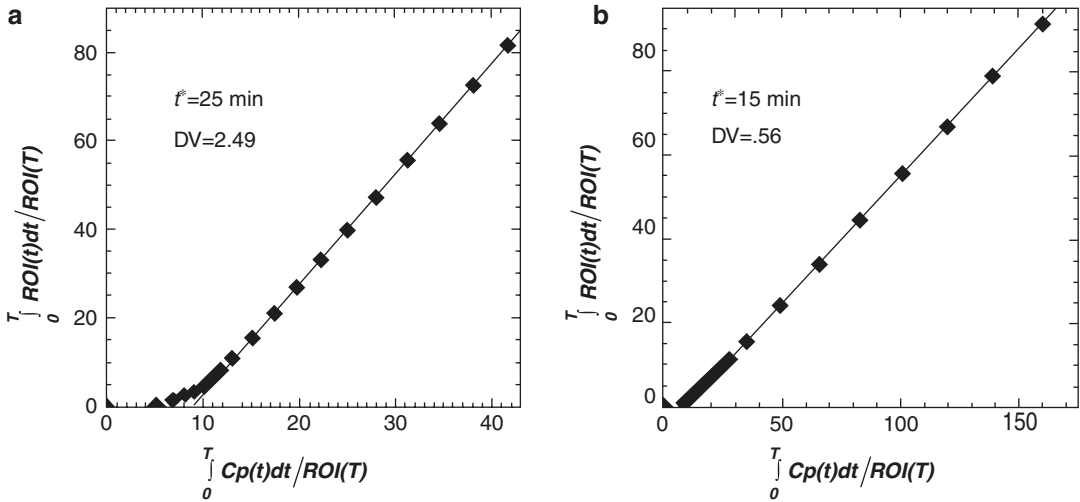
Fig. 13.6 Logan plots of graphical analysis: Time constant for start of the linear analysis for the basal ganglia is 25 min (**a**) and for the cerebellum it is 15 min (**b**). The shorter time for the cerebellum is due to its more rapid kinetics

The plot (Fig. 13.6) eventually becomes linear with a slope equal to the total radioligand volume of the distribution (V_T). The time to reach linearity (equilibrium), however, depends on the number of compartments and the nature of the radioligand.

The GA can be extended to obtain a distribution volume ratio (DVR) directly without blood sampling by using a tissue reference region (T_{ref}) instead of the plasma integral. This can be done by rearranging the GA equation for the T_{ref} to solve for the plasma integral in terms of the T_{ref} radioactivity. Based on the Logan plots, DV_{rec} and DV_{ref} tissue regions can also be determined separately in order to calculate the distribution volume ratio (DVR). Then the BP is given by

$$BP^? \left(\frac{VD_{rec}}{VD_{ref}} \right)?1 = DVR?1 \qquad (13.24)$$

References

1. Acton PD, Zhuang H, Alavi A. Quantification in PET. Radiol Clin North Am. 2004;42:1055–62.
2. Hofheinz F, Apostolova I, Oehme L. Test–retest variability in lesion SUV and lesion SUR in ^{18}F-FDG PET: an analysis of data from two prospective multi-center trials. J Nucl Med. 2017;58(11):1770–5.
3. Huang S. Anatomy of SUV: standardized uptake value. Nucl Med Biol. 2000;27:643–6.
4. Kinahan PE, Fletcher JW. PET/CT standardized uptake values (SUVs) in clinical practice and assessing response to therapy. Semin Ultrasound CT MR. 2010;31(6):496–505.
5. Zasadny KR, Wahl RL. Standardized uptake values of normal tissues at PET with 2-[fluorine-18]-fluoro-2-deoxy-D-glucose: variations with body weight and a method for correction. Radiology. 1993;189:847–50.
6. Michaelis L, Menten ML. Die Kinetik der Invertinwirkung. Biochem Z. 1913;49:1333.
7. Farde L, Eriksson L, Blomquist G, et al. Kinetic analysis of central [11C]raclopride binding to D2-dopamine receptors studied by PET: a comparison to the equilibrium analysis. J Cereb Blood Flow Metab. 1989;9:696–708.
8. Ichise M, Meyer JH, Yonekura Y. An introduction to PET and SPECT neuroreceptor quantification models. J Nucl Med. 2001;42(5):755–63.
9. Laruelle M, Slifstein M, Huang Y. Relationships between radiotracer properties and image quality in molecular imaging of the brain with positron emission tomography. Mol Imaging Biol. 2003;5:363–75.
10. Lassen NA, Ingvar DH, Skinhoj G. Brain function and blood flow. Sci Am. 1978;239:62–71.
11. Raichle ME, Martin WR, et al. Brain blood flow measured with intravenous [15O]H2O. II. Implementation and validation. J Nucl Med. 1983;24:790–8.
12. Crone C. Permeability of capillaries in various organs as determined by the indicator diffusion method. Acta Physiol Scand. 1964;58:292–305.

13. Phelps ME, Huang SC, Hoffman EJ, et al. Tomographic measurement of local cerebral glucose metabolic rate in human with [^{18}F]2-fluoro-2-deoxyglucose. Validation of method. Ann Neurol. 1979;6:371–88.

14. Sokoloff L, Reivich M, Kennedy C, et al. The [^{14}C] de-oxyglucose method for the measurement of local cerebral glucose utilization: theory, procedure, and normal values in the conscious and anesthetized albino rat. J Neurochem. 1977;28:897–916.

15. Mankoff DA, Muzi M, Krohn KA. Quantitative positron emission tomography imaging to measure tumor response to therapy: what is the best method? Mol Imaging Biol. 2003;5:281–5.

16. Patlak CS, Blasberg RG, Fenstermacher JD. Graphical evaluation of blood-to-brain transfer constants from multiple-time uptake data. J Cereb Blood Flow Metab. 1983;3(1):1–7.

17. Heiss W-D, Herholz K. Brain receptor imaging. J Nucl Med. 2006;47:302–12.

18. Mintun MA, Raichle ME, Kilbourn MR, et al. A quantitative model for the in vivo assessment of drug binding sites with positron emission tomography. Ann Neurol. 1984;15:217–27.

19. Patlak CS, Blasberg RG. Graphical evaluation of blood-to-brain transfer constants from multiple-time uptake data. Generalizations. J Cereb Blood Flow Metab. 1985;5(4):584–90.

20. Gambhir SS. Quantitative assay development for PET. In: Phelps ME, editor. PET molecular imaging and its biological applications. New York: Springer; 2004.

21. Logan J. Graphical analysis of PET data applied to reversible and irreversible tracers. Nucl Med Biol. 2000;27(7):661–70.

22. Logan J. A review of graphical methods for tracer studies and strategies to reduce bias. Nucl Med Biol. 2003;30:833–44.

23. Ichise M, Fujita M, Seibyl J, et al. Graphical analysis and simplified quantification of striatal and extrastriatal dopamine D2 receptor binding with [^{123}I]epidepride SPECT. J Nucl Med. 1999;40:1902.

24. Logan J, Fowler J, Volkow N, et al. Graphical analysis of reversible radioligand binding from time-activity measurements applied to [N-^{11}C-methyl]-(−)-cocaine PET studies in human subjects. J Cereb Blood Flow Metab. 1990;10:740–7.

I believe there is no philosophical high-road in science, with epistemological signposts. No, we are in a jungle and find our way by trial and error, building our road behind us as we proceed. (Max Born)

14.1 Cancer and Molecular Imaging

Cancer does not refer to a single disease. Rather, it consists of more than 100 different diseases. The American Cancer Society defines cancer as "a group of diseases" characterized by uncontrollable growth and spread of abnormal cells. If the spread is not controlled, it can result in death. A long-standing goal of cancer research has been to identify the molecular mechanisms by which cancers develop, then design the diagnostic techniques (both imaging and non-imaging) to detect those molecular markers of cancers early, and finally to develop targeted specific therapeutic strategies for the treatment of cancer. One of the goals of the precision medicine era is to better tailor treatments to the individual's particular cancer.

A cancer biomarker refers to a substance or process that is indicative of the presence of cancer in the body. Molecular imaging (an imaging biomarker) is a type of medical imaging that provides detailed pictures of what is happening inside the body at the molecular and cellular level which allows physicians to see how the body is functioning and to measure its chemical and biological processes. The molecular imaging paradigm has evolved in recent years and considers new ways of applying molecular imaging to predict and assess response to twenty-first century cancer therapeutics, including the unique ability of molecular imaging to capture targeted therapy delivery to tumor sites [1]. Personalized medicine in nuclear medicine is theranostics based on molecular imaging and targeted radionuclide therapy (TRT). The main purpose of imaging in oncology is early detection to enable interception, if not prevention, of full-blown disease, such as the appearance of metastases. Because biochemical changes occur before changes in anatomy, molecular imaging, particularly when combined with liquid biopsy for screening purposes, promises especially early localization of disease for optimum management [2]. Molecular imaging biomarker with PET/CT and SPECT/CT may play different roles (diagnostic, predictive, therapeutic, or pharmacodynamic biomarker) in the clinical decision pathway as shown in Table 14.1.

Traditional noninvasive imaging techniques, such as CT and MRI, are used primarily for imaging anatomical and morphological changes associated with an underlying pathology. These techniques, however, often lack the necessary sensitivity and specificity for early diagnoses of many cancers and for the detection of sub-centimeter neoplasms, and preneoplastic dis-

Table 14.1 Role of several types of biomarkers in cancer

Biomarker	Role in the clinical decision and management pathway
Prognostic	To determine if it is likely to develop a particular cancer
Diagnostic	To identify/detect a particular cancer
Predictive	Can a specific drug be optimal for therapy of a specific drug
Therapeutic	Does the drug reach a specific target
Pharmacodynamic	To determine the optimal dose of a therapeutic drug for a specific patient
Recurrence	To predict the recurrence of cancer

ease. In order to develop effective treatment modalities, especially, patient-specific treatments, more sensitive and specific detection of early malignancies is essential.

Radioisotope-based molecular imaging techniques such as PET and SPECT have the potential to capture functional or phenotypic changes associated with abnormal molecular mechanisms by which cancers develop. It is an emerging field that aims to integrate patient-specific and disease-specific molecular information with traditional anatomical or structural imaging readouts. Also, the hybrid or fusion-imaging of PET/CT and SPECT/CT improves the sensitivity and specificity of clinical imaging technique.

Highly "tumor-specific" and "tumor cell signal-specific" radiopharmaceuticals are essential to meet the growing demand of radioisotope-based molecular imaging technology for various applications to manage the overly complex patient-specific tumor biology. Molecular imaging has made rapid strides that go beyond the clinical applications of FDG-PET, to probe multiple aspects of tumor biology. The real power of molecular imaging, however, goes beyond diagnosis by identifying different biologic processes in a tumor using tracers that characterize both genotypic and phenotypic signatures. Future clinical trials, with appropriate study design and regulatory guidance, will need to examine, prospectively,

the use of imaging to help select cancer treatment. This is an important paradigm shift for PET, moving beyond detection in the direction of treatment selection [1, 2, 3].

14.1.1 Radiopharmaceuticals for Molecular Imaging

With the discovery of [18F]fluorodeoxyglucose (FDG) in the 1970s, molecular imaging based on PET started with the studies on brain glucose metabolism [4]. In 1994, the FDA approved the use of FDG-PET for one medical center to measure the regional glucose metabolism in the human brain to assist in the diagnosis of seizures. There have been reports about the use of FDG for oncology imaging since the 1980s, however, no formal phase I, II, and III clinical studies were performed by any commercial sponsor. Based on published literature, the FDA determined the safety and efficacy of FDG, and in 2000 approved the clinical use of FDG-PET in oncology.

The investigators at the Erasmus University Medical Center (EUMC), Rotterdam in the Netherlands developed [123I-Tyr3]octreotide as an imaging agent to localize neuroendocrine tumors (NETs). Due to biliary excretion, and intestinal accumulation of I-123 activity, [123I-Tyr3]octreotide was not ideal for the detection of lesions in the abdomen. Therefore, the investigators at EUMC developed [111In-DTPA-D-Phe1]octreotide (also known as 111In-pentetreotide, OctreoScan). Dr. Krenning's team at EUMC performed planar and SPECT imaging studies in more than 1000 patients with NETs [5]. In 1994, the FDA approved 111In-pentetreotide (OctreoScan, Mallinckrodt) as an agent for the scintigraphic localization of primary and metastatic neuroendocrine tumors bearing somatostatin receptors.

In the last three decades, numerous radiopharmaceuticals have been developed for molecular imaging studies in oncology. As of March 2022, twelve radiopharmaceuticals have been approved by the FDA and European agencies for imaging studies in oncology based on PET and SPECT (Table 14.2). Many new radiopharmaceuticals

Table 14.2 FDA-approved PET and SPECT radiopharmaceuticals for MI studies

	Chemical name	Trade name	Indications	FDA approval
1	^{111}In-pentetreotide	Octreoscan™	For localization of SSTR-positive NETs.	1994
2	[18F]Fludeoxyglucose (FDG)		To assess abnormal glucose metabolism in oncology	2000
3	[18F]Sodium fluoride		To delineate areas of altered osteogenesis	2000
4	[123I]Iobenguane	AdreView™	For the detection of primary or metastatic pheochromocytoma or neuroblastoma	2008
5	[11C]Choline		To help identify potential sites of prostate cancer recurrence	2012
6	68Ga-DOTATATE	NETspot	For localization of SSTR-positive NETs	2016
7	[18F]Fluciclovine	Auxumin™	Prostate cancer recurrence	2016
8	68Ga-DOTATOC		For localization of SSTR-positive NETs	2019
9	[18F]Fluoroestradiol	Cerianna™	For the detection of estrogen receptor-positive lesions in patients with breast cancer	2020
10	64Cu-DOTATATE	Detectnet	For localization of SSTR-positive NETs	2020
11	68Ga-PSMA-HBED-CC		PSMA-positive lesions in prostate cancer	2020
12	[18F]Piflufolastat	Pylarify®	To detect PSMA-positive lesions in prostate cancer	2021

Table 14.3 PET radiopharmaceuticals: mechanisms of uptake and localization

Biochemical process	Radiotracer	Mechanism of uptake or localization
Blood flow/ perfusion	[14O]Water	Freely diffusible across membranes
Membrane synthesis	[18F]Fluorocholine	Substrates for *choline kinase* in choline metabolism
Lipid synthesis	[18F]Fluoroacetate	Acetate is activated to acetyl-CoA in both the cytosol and mitochondria by *acetyl-CoA synthetase*
DNA synthesis	[11C]Thymidine, [18F] Fluoro-thymidine	Substrates for *thymidine kinase (TK-1)* in DNA synthesis and reflects tumor cell proliferation rate
Hypoxia	[18F]FMISO	Intracellular reduction and binding
Protein synthesis	[11C]L-methionine, [18F] FMT, [18F]FET	Transport into the cells involves amino acid carrier protein. Intracellular trapping involves protein synthesis or transmethylation
Tumor antigens	124I-, 64Cu-, 86Y-labeled mAbs	Specific binding to tumor-associated antigenic-binding sites (such as CEA, PSMA, CD20, and CD22)
Apoptosis	124I-Annexin V, 64Cu-Annexin V	Specific binding to Phosphatidylserine (PS) on cell membrane
Angiogenesis	RGD peptide, 18F-FB-E[c(RGDyK)]2	Integrin receptors ($\alpha_v\beta_3$) on endothelial cells of neovasculature
Gene expression	[18F]Oligonucleotide	In vivo hybridization with mRNA
	[18F]FHBG	Substrate to herpes virus *thymidine kinase*

are under active clinical investigation (Table 14.3) and, hopefully, some of these investigational tracers receive FDA approval in the near future. In this chapter the basic aspects of tumor biology and the design, and development strategies of the approved, and several promising new radiopharmaceuticals are presented.

14.2 Tumor Pathology and Biology

14.2.1 Histopathology

Social control genes regulate cell division, proliferation, and differentiation under normal conditions. An uncontrolled growth of an abnormal cell will

give rise to a tumor or neoplasm that can either be *benign* or *malignant*. A tumor is regarded as cancer only if it is malignant. In the past, the general concept was that tumors of certain phenotypes arise from their normal cell counterpart. However, there is evidence which indicates that most tumors arise from immature cells that can transform and acquire phenotypic features similar to those of one or more normal cell types [6]. *Transformation* is the process by which a normal cell becomes a cancer cell. Cancer cells are characterized by *anaplasia* or loss of *differentiation* and become more like embryonic undifferentiated cells.

The classification and typing of tumors are based on histopathological diagnosis [7]. In general, a benign tumor is composed of well-differentiated cells that resemble their normal counterpart, remain localized, and cannot spread to other sites. Malignant tumors are neoplasms that extend into surrounding tissue, are capable of invading lymphatics and blood vessels, and can be transported to distant sites. Certain tumors may exhibit intermediate behavior and are designated as "borderline or undermined," which represents low-grade malignant tumors. Currently, the malignant category is restricted to tumors that have metastatic properties. *Metastases* are tumor implants discontinuous with the primary tumor. All tumors have two components: proliferating *neoplastic cells* and supportive *stroma*, which is host-derived and made up of connective tissue and blood vessels. While the neoplastic cells determine the nature of the tumors, tumor growth and evolution depend on the stroma [6].

Cancer cells differ according to the cell type from which they derive. The common characteristics of cancerous tissue include local increase in cell population, loss of normal arrangement of cells, variation of cell shape and size, increase in nuclear size and density of staining, increase in mitotic activity, and abnormal mitoses and chromosomes. Progressive infiltration, invasion, and the destruction of the surrounding tissue accompany the growth of cancer. A number of cell surface changes occur in cancer cells resulting in a decreased communication or signaling between cells and an altered membrane transport or permeability. Cells become anchorage-independent and are allowed to metastasize.

14.2.1.1   Grading and Staging

Tumor grade is a qualitative assessment of the differentiation of the tumor compared to normal tissue at a specific site; the grading scheme provides a measure of the degree of malignancy. In general, a three-grade system as defined based on the subjective judgment of the pathologist is as follows:

Grade I: Well-differentiated
Grade II: Moderately differentiated
Grade III: Poorly differentiated

The rate of tumor growth depends on the tumor type and grade. In general, most benign tumors grow slowly while most malignant neoplasms grow much faster. Also, rapidly growing malignant tumors are generally well differentiated (grade 1) and contain central areas of necrosis due to poor blood (oxygen) supply.

Staging of cancer depends on the size of the primary neoplasm, its extent to regional lymph nodes, and the presence or absence of metastasis. The TNM system is an expression of the anatomical extent of disease and is based on the assessment of three components:

T: The extent of the primary tumor
N: Absence or presence and the extent of regional lymph node metastasis
M: Absence or presence of distant metastasis

The above TNM classification assumes that cancers of similar histological type or site of origin share similar patterns of growth and extension. The tumor staging will help plan the treatment strategy, indicate prognosis, and assist in the evaluation of therapy.

14.3   Molecular Basis of Cancer

14.3.1   Hallmarks of Cancer

Cancer is a group of diseases involving abnormal cell growth with the potential to invade or spread to other parts of the body. Benign tumors do not spread but, metastasis is the spread of cancer to other locations in the body. Most cancer deaths

are due to cancer that has metastasized. The hallmarks of cancer, an idea coined by Douglas Hanahan and Robert Weinberg in 2000 to identify different biological capabilities acquired during the multistep development of human tumors [8, 9]. Subsequently, a more organized and updated picture of cancer hallmarks was also proposed [10] and summarized as follows:

- Selective growth and proliferative advantage (self-sufficiency of growth signals turned on by activated oncogenes, while insensitivity to anti-growth signals by the inactivation of tumor-suppressor genes)
- Altered stress responses favoring overall survival and propagation (such as increased DNA repair mechanisms, upregulate autophagy, evading programmed cell death or apoptosis, and avoid senescence)
- Sustained angiogenesis and vascularization (by VEGF overexpression)
- Invasion and metastasis
- Metabolic rewiring (deregulated metabolism)
- Immune modulation (evading the immune system)
- An abetting microenvironment

The acquired capabilities described above refer mainly to the cellular and tissular hallmarks of cancer. Cancer is not just a lump of cells that divide, invade, and spread randomly but, rather, a multi-layered precisely tuned process that requires the participation of the whole organism. Geographically separated cancer tissues communicate between themselves, forming a system that interacts with the rest of the organism through cancer-induced systemic pathogenic networks. Based on this approach, Doru Paul recently introduced six systemic hallmarks of cancer that emerge because of these interactions [11]. The first systemic hallmark is the cancer system itself established through the connections between the primary tumor, the bone marrow, and the distal metastasis. The five other systemic hallmarks are the global inflammation, the immunity inhibition, the metabolic changes leading to cachexia, the propensity to thrombosis, and the neuroendocrine changes.

Tumor development and survival is a chaotically governed process involving the interplay between cancer cells, normal stromal cells, and host defense mechanisms. Generally, CD8+cytotoxic T cells (CTL) and CD4+helper T (Th)1 cells curb cancer development via mechanisms commonly involving their production of interferon (IFN)-γ and cytotoxins [9]. The immune system interacts intimately with tumors over the entire process of disease development and progression to metastasis. This complex cross-talk between immunity and cancer cells can both inhibit and enhance tumor growth and is now classified as a hallmark of cancer. The immune system plays a critical role in maintaining an equilibrium between immune recognition and tumor development with a dual capacity to both promote and suppress tumor growth. Despite immune surveillance, tumors continue to develop with intact immune systems.

14.3.2 Genetic Changes

Carcinogenesis is a multistep process at both, the phenotypic and genetic levels [8]. The genetic hypothesis of cancer implies that cancer results from the clonal expansion of a single progenitor cell. In the first step (initiation), the cell has incurred genetic damage in the DNA caused by a point mutation, gene deletion, or gene rearrangement. In the second step (promotion), the initiated cells become cancerous. In the third step (progression), the cancerous cell becomes biologically defective or undifferentiated. Because of this multistep process, most human tumors, however, do show genetic heterogeneity even if they originate from a single cell.

A wide variety of chromosomal alterations are found in cancers, such as change in number, translocations, rearrangements, amplifications, and deletions. Many of these changes are associated with genes that are solely responsible for causing cancer. The principal targets of genetic damage are three classes of normal regulatory genes; *oncogenes*, *antioncogenes*, and genes that regulate apoptosis [6]. Damage to DNA repair genes may also be involved in carcinogenesis. A

number of biochemical features associated with the genetic changes that clearly distinguish malignant proliferation from normal growth patterns are as follows:

- Tumor cells usually have an unlimited potential for tumor growth and are, thus, immortalized.
- Tumor cells exhibit a variety of metabolic differences when compared to their normal untransformed counterparts.
- Malignant cells have the ability to escape the human immune surveillance pathways.

14.3.2.1   Oncogenes

Genes that promote autonomous cell growth are called oncogenes or cancer-causing genes. These are derived from proto-oncogenes, which are normally present in the human genome and are essential for normal cell growth. The mutant *alleles* of proto-oncogenes are called oncogenes. Many oncogene products and oncoproteins are part of the cell's signal transduction pathway (Table 14.4). Some oncogenes code for proteins that are either growth factors or growth factor receptors. Some oncoproteins are transmembrane signal molecules, such as *tyrosine kinases*. The activation of a mutated oncogene could greatly affect a cell's growth potential by increasing the production of growth factors, increasing the growth factor receptor expression on the cell surface, or by encoding a protein that binds to DNA and stimulates cell division. The protein molecules involved in the signaling pathways are called *signal-transducing proteins* and are responsible for the communication between growth factor receptors and their nuclear targets.

14.3.2.2   Antioncogenes

In a normal cell, the physiological function of *antioncogenes* or cancer suppressor genes is to regulate cell growth and to prevent tumor formation. The loss of these genes, however, is a key event in many human tumors. Tumor suppressor genes encode proteins that act as negative transducers of growth factor stimulation. The loss of tumor suppressor genes, such as *Rb* and *p53*, is associated with a wide variety of human malignancies. The *p53* gene encodes a 53 kDa protein that binds in the nucleus and at high levels causes the cell to undergo apoptosis [12]. A mutated *p53* allele in a cancer cell may encode a mutant form of p53 protein without the ability to induce apoptosis. Mutations of the *p53* gene is the common DNA abnormality in more than 50% of cancers. Some cancers in which the loss of function of the tumor suppressor genes may be involved are summarized in Table 14.4.

Table 14.4   Oncogenes and antioncogenes

Gene	Gene product	Biologic function	Cancer
Oncogenes: cancer-causing genes			
Sis	PDGF-β chain	Heparin-binding GF	Astrocytoma, osteosarcoma
int-2	Fibroblast GF	Platelet-derived GF	Breast cancer, melanoma
Erb-B2	EGF receptor	GF receptor	Breast, ovarian, and lung cancer
Fms	CSF-1 receptor	GF receptor	Leukemia
Abl	Tyrosine kinase	Intracellular signaling	Chronic myeloid leukemia
Ras	GTP-binding protein	Intracellular signaling	Many cancers
c-myc	Transcriptional factor	Binds DNA	Burkitt's lymphoma
L-myc	Transcriptional factor	Binds DNA	Small cell carcinoma of lung
Antioncogenes: tumor-suppressor genes			
Rb	Transcription factor	Regulation of cell cycle	Retinoblastoma, osteosarcoma
p53	Transcription factor	Regulation of cell cycle and apoptosis	Most human cancers
NF-1	GTPase activating protein	Inhibition of ras signal transduction	Schwannomas, neurofibroma
WT-1	Nuclear transcription factor	Binds DNA	Wilm's tumor

14.3.2.3   Tumor Antigens

Most tumor cells synthesize many proteins or *glycoproteins* that are antigenic in nature. These antigens may be intracellular, expressed on the cell surface, or shed or secreted from the cell into the extracellular fluid or circulation. These tumor-associated antigens (TAA) may also be expressed in small amounts in normal cells but, typically, tumor cells produce them in large amounts. Based on the source and origin of antigen, TAAs can be categorized into five distinct groups [6].

(a) Oncofetal antigens: These antigens are derived from *epitopes* that were expressed in fetal life and appear on tumor cells as a result of undifferentiated growth process associated with malignant process. These antigens are not expressed in completely differentiated cells. Some of these antigens, such as *Carcinoembryonic antigen* (CEA) and *Alpha-fetoprotein* (AFP), are expressed on the cell surface, and are also present in the circulation.

(b) Epithelial surface antigens: These antigens are derived from cell surface structural components that are exposed due to an architectural disruption of malignant tissue. Antigens, such as *epithelial membrane antigen* (EMA) and *human milk fat globule* (HMFG), are excluded from the blood by biological barriers, and are present in the tumor tissue only.

(c) Tumor-derived antigens: These epitopes are expressed mainly by tumor tissues and in some tumors, there may even be an increase in the expression of these epitopes. The antigen, *tumor-associated glycoprotein-72* (TAG-72), is expressed on the tumor cell surface in a variety of adenocarcinomas, such as colon, breast, and ovarian. *Prostate-specific antigen* (PSA) and *prostatic acid phosphatase* (PAP) are secreted by prostate carcinoma cells and are present in the tumor tissue, and in circulation. *Prostate-specific membrane antigen* (PSMA) is an integral transmembrane glycoprotein with intra and extracellular epitopes.

(d) Receptor antigens: Tumor cells express regulator receptors that promote interaction with a number of growth factors. The increased expression of receptor proteins on tumor tissues may be regarded as receptor antigens. The human *epidermal growth factor receptor* (EGF-r) is a transmembrane glycoprotein that contains extracellular and cytoplasmic epitopes for EGF binding. EGF-r overexpression has been found in a variety of malignant epithelial tumors arising in the breast, colon, lungs, and bladder.

(e) Viral antigens: These epitopes are present in certain tumor cell membranes where the induction of malignancy is associated with the presence of transforming genes carried by the DNA viruses. Congenital or acquired immunodeficiency developed Epstein–Barr virus (EBV)-positive malignancies (such as Burkitt's lymphoma) are examples of receptor antigens.

14.3.3   Tumor Angiogenesis

Blood supply is one of the key factors that could modify the rate of tumor growth. Perfusion supplies nutrients, oxygen, as well as growth factors. Beyond 1–2 mm in diameter, the tumor fails to proliferate because hypoxia induces apoptosis. Angiogenesis or *neovascularization* is a necessary biologic correlate of malignancy [6]. Tumor vascularization occurs through several distinct biological processes, which not only vary between tumor type and anatomic location but, also occur simultaneously within the same cancer tissue. These processes are orchestrated by a range of secreted factors and signaling pathways, and can involve participation of non-endothelial cells, such as progenitors or cancer stem cells [13]. Tumor-associated angiogenic factors, such as *vascular endothelial growth factor* (VEGF) and *basic fibroblast growth factor* (bFGF), may be produced by tumor cells or derived from inflammatory cells (e.g., macrophages). Hypoxia promotes angiogenesis by the release of *hypoxia-inducible factor-1* (HIF-1), which controls the transcription of VEGF.

A number of anti-angiogenesis molecules may be produced by tumor cells themselves (such as *thrombospondin-1*) or may induce the production of these factors (*angiostatin*, *endostatin*, and

vasculostatin) by other cells. The balance between the angiogenic and antiangiogenic factors controls tumor growth.

14.3.4 Tumor Microenvironment

14.3.4.1 Apoptosis

Apoptosis is executed by a family of intracellular proteases called, *caspases* and occurs as an end result of signaling through the death receptor CD95 (Fas) and by DNA damage [6]. Defects in the processes that control normal apoptosis extend the life of the cell and also promote cancer growth. Several genes that regulate apoptosis have been identified. Apoptosis may be inhibited by *cytochrome c* from mitochondria, which forms a complex with APAF-1, ATP, and procaspase 9. The release of cytochrome is important in apoptosis and is regulated by the genes of the *BCL2* family, which inhibit apoptosis by inhibiting the release of cytochrome *c* [14].

14.4 PET and SPECT Radiopharmaceuticals in Oncology

14.4.1 Objectives

A variety of both genetic and tumor microenvironmental factors determine the behavior of cancer. The alterations in genotype, phenotypic functional changes (Table 14.5), such as altered metabolism, proliferation, protein synthesis, and angiogenesis that occur in cancer tissue, ultimately lead to the development of discrete mass lesions. The challenge of an imaging technique is to demonstrate the morphology (structure and tissue characterization) and functional status of tumor tissue. Tumors are classified on the basis of the tissue of origin, cell type, whether benign or malignant, degree of differentiation, anatomic site, and function. Because of this diversity, no single imaging technique is capable of detecting all tumors. While the radiological techniques (X-ray, CT, MRI, Ultrasound) can provide information, regarding location and size of the tumor with better resolution than nuclear imaging tech-

niques, these lack the specificity and sometimes cannot even distinguish residual, viable disease from fibrosis. PET and SPECT techniques, on the other hand, have the potential to provide functional status of the tumor tissue (metabolism, receptor expression) and offer higher specificity with limited resolution. The application of molecular imaging procedures in oncology can best be classified based on the various objectives of the imaging, as described below:

(a) Diagnosis of malignancy: Differentiating malignant from benign disease
(b) Identifying the site(s) of disease: In order to plan biopsy or surgery especially when cancer is suspected based on clinical biomarkers
(c) Detecting the primary tumor: In patients with metastatic disease with an unknown or small primary tumor
(d) Grading malignancy: Based on quantifying the amount of radiotracer uptake
(e) Staging disease: Whole body scans would provide the relative uptake of tracer throughout the body
(f) Residual disease: Identification of residual viable cell mass following treatment
(g) Detection of recurrences: Confirming the sites of recurrent (new) disease
(h) Measuring the response to therapy: Objective assessment of the efficacy of specific treatment modalities
(i) Guide radiation therapy: Identify regions of tumor tissue with differences in radiosensitivity for effective radiation treatment

In the last 10 years, several new radiotracers have been proposed and were evaluated in preclinical and clinical studies in order to characterize the tumor biology more appropriately. Several publications have extensively reviewed the potential advantages and limitations of many PET radiopharmaceuticals [16–22] (Shiue and Welch 2004). ^{18}F-labeled radiotracers appear to be the most attractive option, mainly due to the wide availability of ^{18}F and the possibility of automated routine synthesis of these agents. In addition to ^{18}F-labeled tracers, ^{68}Ga, ^{64}Cu, and ^{89}Zr-labeled PET radiopharmaceuticals have also

Table 14.5 Molecular and functional alterations in cancer[a]

Function	Increased	Decreased
Glucose metabolism	X	
Amino acid transport	X	
Protein synthesis	X	
DNA synthesis	X	
Membrane or lipid synthesis	X	
Receptor expression	X	
Angiogenesis, vascular density	X	
Vascular permeability	X	
Oncogene products	X	
Signal transduction	X	
Hypoxia	X	
Oxygen tension		X
Blood flow	X	X
Apoptosis	X	X
Many other genetic markers	X	X

[a] Modified from Wahl [15]

been approved by the FDA for imaging studies in neuroendocrine tumors and prostate cancer (Table 10.2). The advantages of many of these tracers are based on their ability to image a specific biochemical process or based on their unique mechanism of localization in a specific organ/tissue of interest.

14.4.2 Radiopharmaceuticals: Biochemical Basis of Localization

14.4.2.1 Glycolysis
The most important molecule to provide energy for various biochemical reactions in the body is adenosine triphosphate (ATP), which is generated in the mitochondria following the metabolism of glucose in the mitochondria. Accelerated glucose metabolism is one of the phenotypic or functional changes observed in cancer tissue, first observed by Warburg, more than 80 years ago [23, 24]. The transport of glucose into cells is mainly through *facilitated diffusion*, also called *carrier-mediated diffusion*, since the carrier facilitates the transport of glucose into the cell. This mechanism, however, also allows the glucose molecule to diffuse out of the cell. Insulin can increase the rate of facilitated diffusion 10- to

20-fold. Six isoforms of glucose transporters (GLUT) have been identified, which differ in kinetic properties and tissue location. It has been shown that the overexpression of GLUT-1, GLUT-3, and GLUT-5 plays a key role in the increased transport of glucose by tumor cells [15]. Glucose may also be transported into the cell by active transport, which mostly occurs in the renal tubules and gastrointestinal membrane.

The phosphorylation of glucose (Fig. 14.1), an initial and important step in cellular metabolism, is catalyzed by the enzyme *glucokinase* in the liver and *hexokinase (HK)* in most other cells. Four distinct types of hexokinases are known; Type-1 is predominant in the brain, Type-2 in insulin-sensitive tissue, Type-3 is present in any other tissue, and Type-4 is known as glucokinase in the liver. In the cytosol, glucose is phosphorylated by the enzyme *hexokinase* to glucose 6-phosphate, which subsequently is metabolized to carbon dioxide and water. This phosphorylation step is almost completely irreversible except in the liver, kidney, and GI epithelium. The enzyme *glucose-6-phosphatase*, responsible for the breakdown of phosphorylated glucose is absent in most cancer cells [25]. As a result, once glucose enters the cells, it goes through the glycolysis pathway.

Tumor pH
In glucose metabolism, the initial reaction sequence known as "glycolysis" takes place in the cytoplasm where glucose is converted to two molecules of pyruvate. Under anaerobic conditions (hypoxia), this mechanism is unavailable; pyruvate is converted to lactic acid by lactate dehydrogenase (LDH) and accumulates. Consequently, the pH of the tumor tissue is slightly acidic compared to that of normal tissue pH of 7.4 [23]. The acidic pH of the tumor tissue possibly may play a significant role in the localization of several radiotracers in tumors.

2-[18F]Fluoro-2-Deoxy-D-Glucose (FDG)
In the 1950s it was shown that the hydroxyl group on carbon-2 of the glucose molecule (Fig. 14.2) is not necessary for phosphorylation by *hexokinase*. The deoxyglucose (DG) enters the cell

Fig. 14.1 Intracellular metabolism of glucose and [^{18}F] FDG. Unlike glucose, FDG-6-phosphate does not undergo further metabolism, and is trapped in the cell
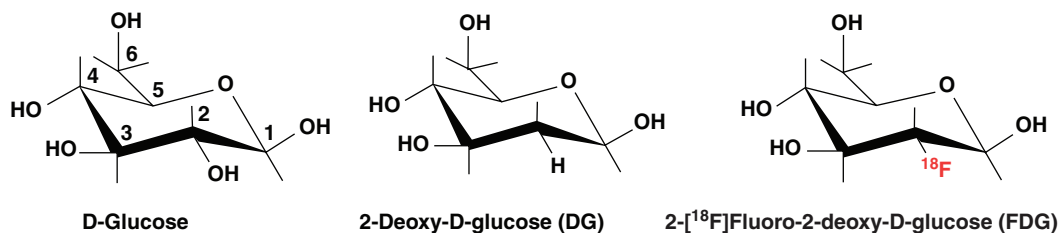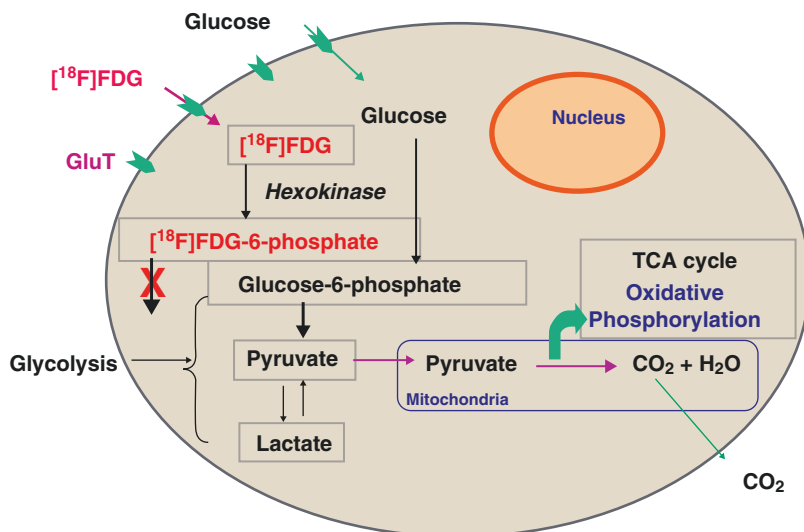

Fig. 14.2 *D*-Glucose analogs deoxyglucose (DG) and 2-deoxy-[^{18}F]fluoro-deoxyglucose (FDG)

similar to glucose and is converted to deoxyglucose 6-phosphate which, however, does not undergo further metabolism and is trapped in the cell [26]. Therefore, the design of the FDG molecule is based on labeling a carbon-2 atom in DG with ^{18}F [27]. Incidentally, the C–F bond, which is more stable than the C–H bond, is chemically unrecognizable by *hexokinase*. As a glucose analog, FDG enters the cell membrane using the same transporters as glucose. It is then phosphorylated into [^{18}F]FDG-6-phosphate. This metabolite is not a substrate for further enzymes and, thus, is trapped and accumulates inside the cell (Fig. 14.1) in proportion to the metabolism of glucose. Experimental studies in vitro and in vivo have clearly documented that the magnitude of the FDG uptake in tumors, in general, relates quite directly to the number of viable cells [15]. FDG is a model PET radiopharmaceutical and is regarded as the "molecule of the century" in nuclear medicine. The simplified mechanism of uptake of FDG by tumor cells is now well understood. FDG-PET can therefore be considered as the imaging of the rate-limiting step of glucose metabolism, namely the hexokinase activity. The imaging signal detected with PET tomography is achieved based on the trapped phosphorylated metabolite.

The glycolytic activity of a given tumor is generally assumed to be characteristic of its state of differentiation. The extent of FDG uptake in tumors, especially untreated tumors, appears to relate directly to the number of viable cells. However, it has also been shown that inflammatory cells (macrophages) in tumors also accumulate FDG. It has also been well documented that FDG-PET is clinically useful for the staging and restaging of malignancy, metabolic characterization of malignancy, and monitoring of response to therapy (Fig. 14.3) [15, 28–30].
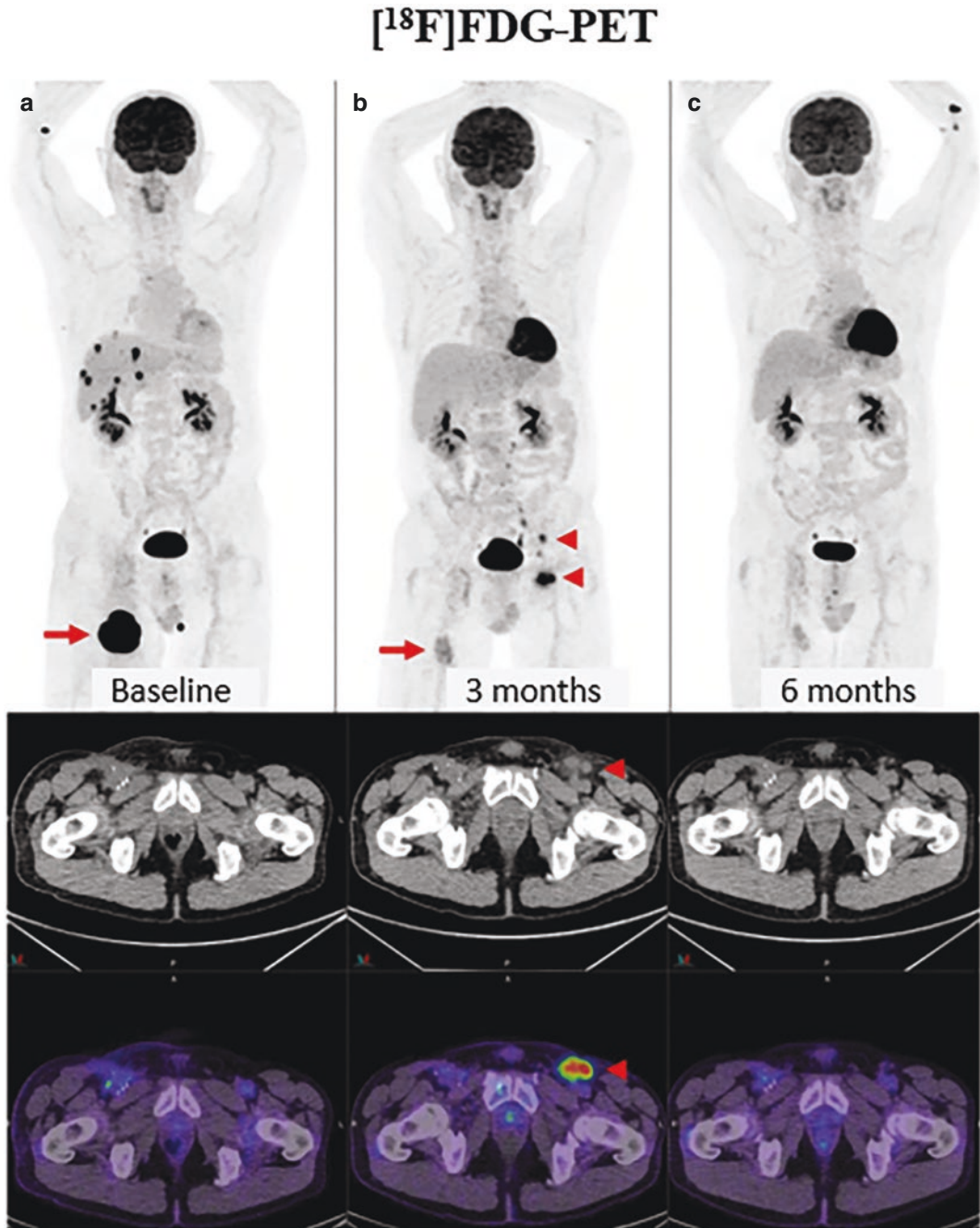
[^{18}F]FDG-PET

Fig. 14.3 [^{18}F]FDG-PET/CT: New lymph nodes in draining basin of regressing metastasis. (**a**, **b**) Metastatic melanoma (**a**, arrow) after 4 cycles of combination ipilimumab and nivolumab demonstrated marked regression of right thigh lesion and complete metabolic response of multiple liver and adrenal metastases (**b**, arrow); however, new FDG-avid lymph nodes were noted in left inguinal and iliac regions (**b**, arrowheads). (**c**) Biopsy of these lymph nodes showed reactive T cells that resolved on subsequent scan [31]

Table 14.6 Some of the factors affecting FDG uptake in tumors[a]

Factor	Increased	Decreased
Viable cancer cell number	X	
Tumor perfusion	X	
Hypoxia	X	
Glucose transporter expression	X	
Hexokinase activity	X	
Inflammation or infection	X	
Receptor agonists	X	
Chemotherapy acute	X	
Radiation therapy acute	X	
Receptor blockade		X
Chemotherapy effective		X
Radiation therapy chronic		X
Hyperglycemia		X
Insulin		X
Necrosis		X

[a] Modified from Wahl [15]

Limitations of FDG-PET: Although FDG-PET/CT imaging provides high specificity and sensitivity in several types of cancer, with many applications in the clinical management of an oncologic patient, it is important to recognize that FDG is not a "specific" radiotracer for imaging malignant disease. A number of factors (Table 14.6) can affect the FDG uptake in tumors and may explain the causes of false-positive and false-negative imaging data [15]. Various tissues and processes in the body use glucose to generate ATP to meet the increased energy demands. For example, the normal brain depends exclusively on glucose metabolism. Further, inflammatory cells and macrophages have higher glucose metabolic rates and accumulate higher amounts of FDG than tumor cells. Since FDG competes with glucose, the net uptake of FDG by tumor tissue depends on the plasma glucose levels. In any given patient the absolute tumor uptake of FDG depends on many factors and may not necessarily reflect tumor aggressiveness, or the rate of tumor proliferation [15].

14.4.2.2 Bone Metabolism

Bone is a rigid connective tissue and is made up of two types of tissues: compact or cortical and cancellous and trabecular, or spongy bone. While the cortical bone forms the outer layer (cortex), the spongy bone in the medulla contains the bone marrow. Three types of cells are seen in the bone: (a) osteoblasts that produce the organic bone matrix, (b) osteocytes that produce the inorganic matrix, and (c) osteoclasts, which are active in bone resorption. At the molecular level, the bone matrix is composed of approximately 35% organic (such as collagen, proteoglycans, albumin,) and 65% inorganic matrix, which includes cations (Na^+, K^+, Ca^{2+}, Mg^{2+}, Sr^{2+}), anions (F^-, OH^-, PO_4^-, and Cl^-) and the hydroxyapatite crystals, $Ca_{10}(PO_4)_6(OH)_2$ [32].

The normal bone undergoes constant remodeling, maintaining a balance between osteogenesis (osteoblastic) and bone resorption (osteoclastic) activity. Various primary tumors originate from the bone. In addition, in metastatic bone disease, bone involvement by cancer occurs most commonly when the tumor cells from other cancers (such as prostate and breast cancer) are transported into the marrow. Most of the bone metastases are found in the red active marrow present mainly in the axial skeleton. As the lesion grows in the marrow, the surrounding bone undergoes osteoclastic and osteoblastic reactive changes [33, 34]. The osteoblastic component of the metastasis represents the reaction of normal bone to the metastatic process and most sites of malignant bone involvement show increased reactive osteoblastic activity. In general, the radiographic appearance of a bone metastasis may be lytic, sclerotic (blastic), or mixed. Rapidly growing aggressive metastases tend to be lytic, whereas sclerosis is considered to indicate a slower tumor growth rate. Sclerosis may also be a sign of repair after treatment [34]. The incidence of lytic, blastic, and mixed types of bone metastases is different in various tumor types. In general, the purpose of bone imaging is to identify early bone involvement and to determine the full extent of the skeletal disease, to assess the presence of accompanying complications, such as fractures and cord compression, and to monitor response to therapy [33]. Detection of bone involvement by various imaging modalities is based on either direct visualization of the tumor infiltration or detection of the reaction of bone to the malignant process.

[¹⁸F]Sodium fluoride (NaF)

In 1940, the absorption of fluorides by enamel, dentin, bone, and hydroxyapatite was first reported [35]. [¹⁸F]-Fluoride was first introduced as a bone-imaging agent in 1962 [36]. The FDA approved the NDA for bone imaging to define areas of altered osteogenic activity in 1972. In plasma, [¹⁸F]fluoride ions do not bind to plasma proteins and clear from circulation faster than ⁹⁹ᵐTc-phosphonates. Fluoride ions diffuse through capillaries into the bone's extracellular fluid and are chemisorbed onto the bone surface by exchanging with the hydroxyl (OH) groups in hydroxyapatite crystal of bone to form fluoroapatite [37]. The fluoride bone uptake mechanism is similar to that of ⁹⁹ᵐTc-MDP. The uptake of both tracers in malignant bone lesions reflects the increased regional blood flow and bone turnover. However, due to faster blood clearance and higher capillary permeability, fluoride uptake in bone metastases is significantly higher than that in normal bone [37]. While increased fluoride uptake has been reported in both sclerotic and lytic metastases [38, 39], the uptake of ⁹⁹ᵐTc-MDP in lytic lesions is, relatively, nonsignificant. Since both these tracers may also be seen in benign bone pathologies and nonmalignant orthopedic problems, bone agents are not considered as tumor-specific tracers. Although the ¹⁸F-fluoride uptake mechanism corresponds to the osteoblastic activity, it is also sensitive for detection of lytic and early marrow-based metastases, by identifying their accompanying reactive osteoblastic changes, even when minimal. Also, the instant fusion of increased fluoride uptake with morphological data of CT using hybrid PET/CT systems improves the specificity of ¹⁸F-fluoride-PET in cancer patients by accurately differentiating between benign and malignant sites of uptake [39]. A comparison of ⁹⁹ᵐTc-MDP planar and SPECT images with [¹⁸F]fluoride-PET images is shown in Fig. 14.4. It must also be noted that FDG-PET is also useful to detect bone metastases. Unlike fluoride and phosphonates, the uptake of FDG, however, is directly into tumor cells and not into the reactive bone.

14.4.2.3   DNA Synthesis

Increased cellular proliferation is a hallmark of the cancer phenotype [8]. Increased mitotic rate, cell proliferation, and lack of differentiation are regarded as the main factors responsible for the accelerated growth of malignant tissue. Most benign tumors grow slowly over a period of years, while most malignant tumors grow rapidly, sometimes at an erratic pace. Cellular proliferation is specific to tumors, whereas increased glucose metabolism is not only a feature of tumors but, is also associated with a variety of other processes, including inflammation. Certain anticancer drugs were designed to stop cell division but, may not necessarily lead to the cell death. As a result, tumor cellular proliferation drops without any significant change in the tumor energy metabolism. Therefore, molecular imaging probes, designed specifically to measure proliferation, are tumor-specific and may provide an impetus for PET imaging to be indicated as an appropriate technique, especially for measuring early response to treatment.

The DNA synthesis is a measure of proliferation. Since the number of cells in the *S*-phase of cell cycle is higher in tumor tissue than in normal cells, there is also an increased requirement of substrates (nucleotides) for DNA synthesis in the tumor [40]. The four nucleotides required for DNA synthesis are cytosine, guanine, adenine, and thymidine. Thymidine is the only one incorporated exclusively into the DNA but, not into RNA. Intracellularly, thymidine is first phosphorylated in the cytoplasm by the enzyme *thymidine kinase-1* (*TK-1*) to thymidine monophosphate (TMP), prior to incorporation into the DNA. The level of *TK-1* in a cell increases several-fold as it goes from a resting state to the proliferative phase and is destroyed at the end of the *S*-phase [40]. TMP is then further phosphorylated to thymidine diphosphate (TDP) and then to thymidine triphosphate, (TTP) prior to incorporation into the DNA (Fig. 14.5). Therefore, several radiolabeled thymidine analogs (Fig. 14.6) have been developed that have the potential to provide a measure of DNA synthesis and tumor cell proliferation. In
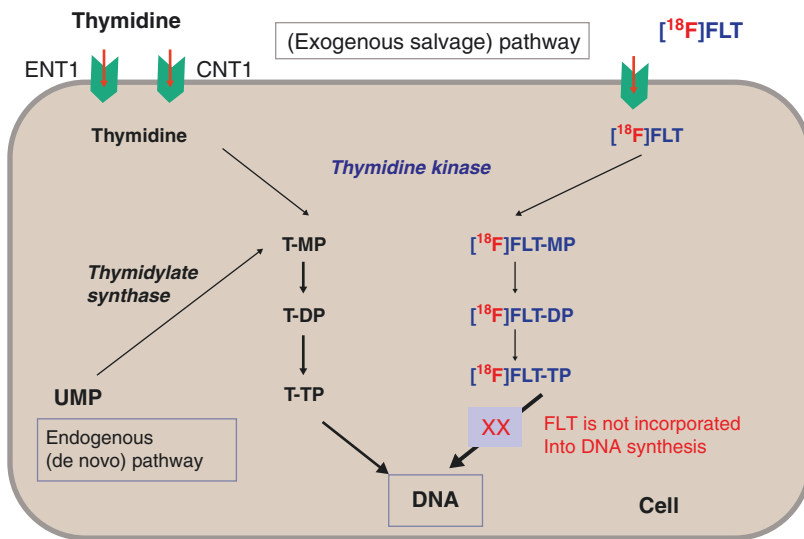
Fig. 14.5 Intracellular metabolism of thymidine and [^{18}F]FLT: in an exogenous salvage pathway, FLT is transported into the cell and phosphorylated by *thymidine kinase* similar to thymidine
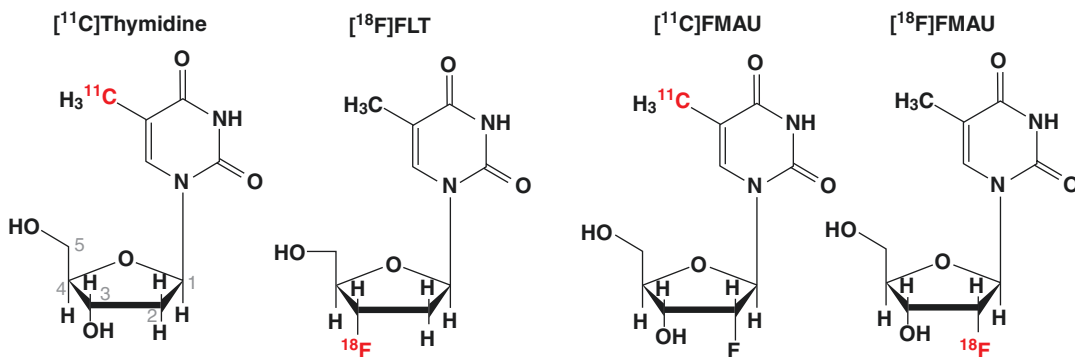
Fig. 14.6 Radiolabeled thymidine and uridine analogs to assess tumor cell proliferation
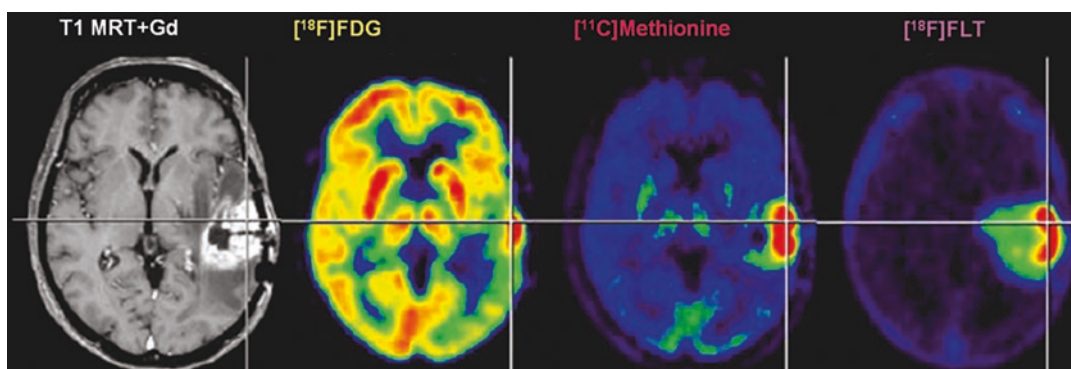

Fig. 14.7 [^{18}F]FLT-PET and [^{11}C]Methionine-PET to assess increased cell proliferation in a patient with brain tumor. Comparison with FDG-PET. Gd-MRI shows alteration of BBB and the extent of peritumoral edema

contrast, TK-2 is a mitochondrial enzyme and is not regulated by the cell cycle.

3′-deoxy-3′-[^{18}F]fluorothymidine ([^{18}F]FLT)

In the 1950s, [^{3}H]Thymidine was introduced to measure thymidine incorporation into the DNA (thymidine labeling index) in tumor tissues [40, 41]. Subsequently in 1972, [^{11}C]thymidine was developed as a PET tracer to measure the proliferation rate [42]. However, due to the rapid in vivo metabolism of this tracer, [^{11}C]thymidine is not optimal for routine PET imaging studies. In 1996, metabolically stable thymidine analogs, which are also substrates for the enzyme *TK-1,* were developed [43, 44].

[^{18}F]FLT or FLT is the most extensively investigated PET biomarker to image cell proliferation. FLT is transported into the cell similar to thymidine and then phosphorylated to [^{18}F]FLT-5′-monophosphate by the enzyme, *TK-1*. In vitro studies with tumor cell lines have demonstrated

that FLT-MP is further phosphorylated to FLT-TP by the enzyme *thymidylate kinase* [45, 46]. FLT phosphates, however, are impermeable to the cell membrane, resistant to degradation, and are metabolically trapped inside the cells. The incorporation of FLT into DNA, however, is relatively insignificant (<1%).

FLT uptake and PET quantitative measures (SUV and FLT flux) have been shown to correlate with pathology-based proliferation measurements, including the Ki-67 score in a variety of human cancers [47]. FLT-PET may, therefore, be a useful tool for assessing tumor aggressiveness, predicting outcome, planning therapy, or monitoring response to treatment. FLT-PET has shown greater specificity for cancer than FDG-PET, which can show false-positive uptake in areas of infection or inflammation (Fig. 14.7). FLT-PET should be considered a powerful addition to FDG-PET, providing additional diagnostic specificity and important

biological information that could be useful in predicting the prognosis, planning the treatment, and monitoring the response [48–51].

The pyrimidine analog, 2′-fluoro-5-methyl-1-β-D-arabino-furanosyluracil (FMAU) labeled with ^{11}C or ^{18}F has been shown to be useful for imaging tumor cell proliferation [52–55]. FMAU can be taken up by cells and phosphorylated by TK-1 and TK-2 followed by DNA incorporation through *DNA polymerase* [56]. FMAU employs the same DNA synthetic pathway as thymidine and, therefore, has the potential to image DNA synthesis in tumors and normal proliferating tissues.

14.4.2.4   Membrane Lipid Synthesis

All cells utilize choline (CH), a quaternary ammonium base, as a precursor for the biosynthesis of phospholipids, which are essential components of all membranes [57]. In 1998, choline received the status of vitamin (group B) from the US Food and Nutrition Board of the Institute of Medicine. Choline enters most cells using specific low affinity, sodium-independent transporters. Within the cell, choline can be phosphorylated, acetylated, or oxidized (Fig. 14.8). The phosphorylation of choline is catalyzed by the enzyme *choline kinase* [58].

Phosphorylcholine is an intracellular storage pool of choline and is further incorporated into phosphatidylcholine (lecithin), a major phospholipid of all membranes [57]. Choline is also a precursor for the synthesis of the neurotransmitter, acetylcholine. In addition, the metabolic pathway of choline also involves oxidation to betaine aldehyde and then to betaine in the blood, liver, and kidneys, the major sites for choline oxidation [59, 60].

It has been suggested that the malignant transformation of cells is associated with the induction of *choline kinase* activity resulting in increased levels of phosphorylcholine. Furthermore, it is also known that rapidly proliferating tumors contain large amounts of phospholipids, particularly lecithin [61]. The formation and accumulation of membrane phospholipids are coordinated with the cell cycle and occur during the *S* phase [62, 63]. The cells depleted with choline cannot synthesize lecithin, resulting in the arrest in the *G*1 phase. Thus, it is assumed that the uptake of radiolabeled choline reflects the proliferative activity by estimating membrane lipid synthesis. Tumor cells with a high proliferation rate will have high uptake of choline in order to keep up with the increased demands for the synthesis of phospholipids.
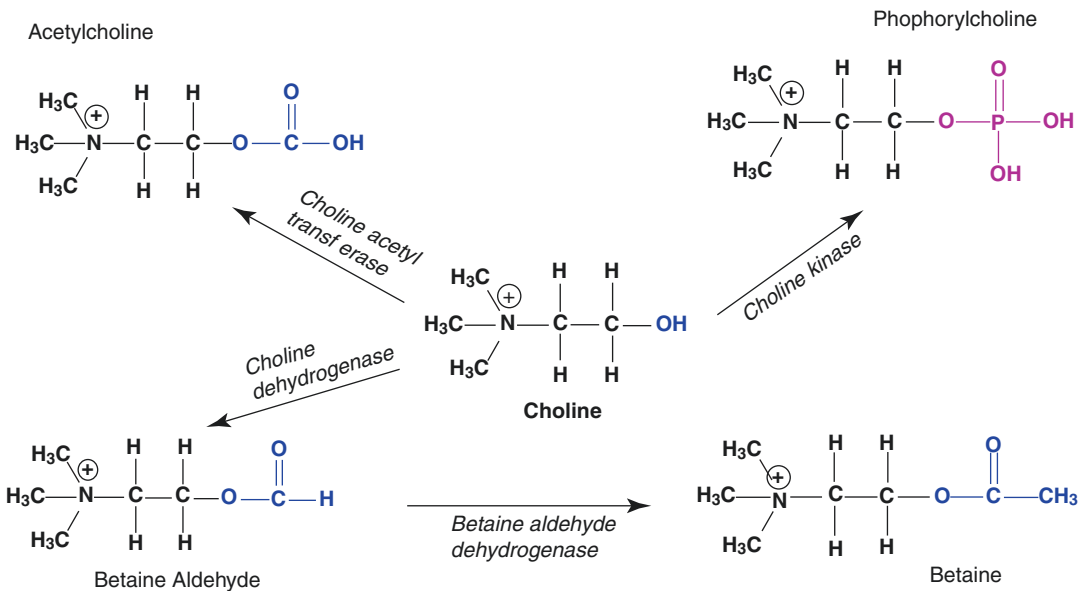

Fig. 14.8 Metabolism of choline. Following phosphorylation by the enzyme *choline kinase*, phosphorylcholine is converted to lecithin and gets incorporated in the membrane synthesis

[¹¹C]Choline (CH)

[¹¹C]Choline was introduced in 1997 as a potential PET tracer to image brain and prostate cancer [64]. Based on meta-analysis of publications that critically evaluated the role of choline PET in restaging patients with PCa recurrence, it was concluded that Choline-PET/CT represent high sensitivity and specificity techniques for the detection of locoregional and distant metastases in PCa patients with recurrence of disease (Fig. 14.9) [66, 67]. In 2012, the FDA approved the clinical use of [¹¹C]Choline for PET

[¹¹C]Choline-PET/CT
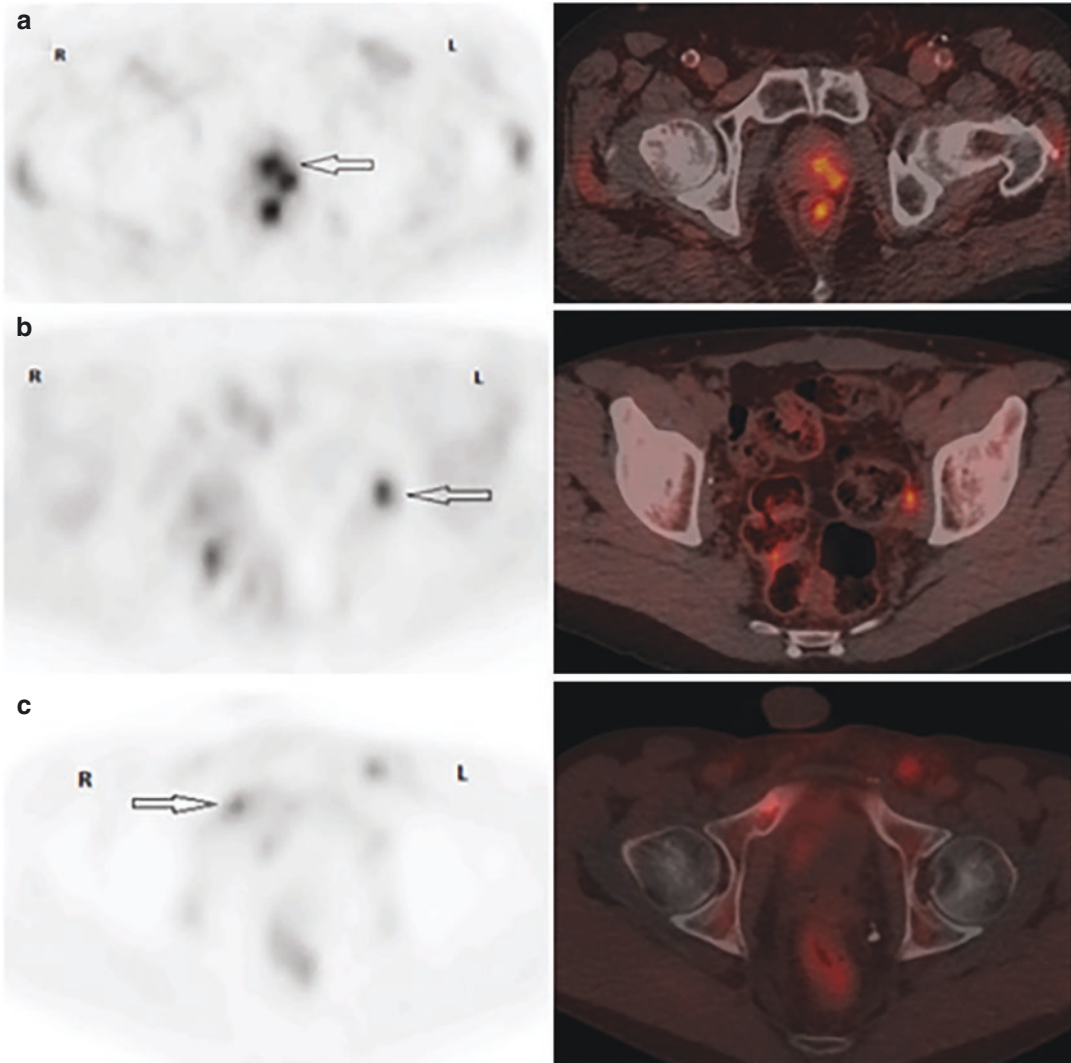
Fig. 14.9 Patient examples of pelvic axial [¹¹C]Choline PET and PET/CT. (**a**) PCa 4.3 y after intensity-modulated radiotherapy (Gleason 7 [4+3]; PSA, 2.28 ng/mL). PET/CT shows suspected left posterior prostatic uptake (SUV$_{max}$, 3.3), scored 2 (arrow). Local biopsy was positive for PCa. (**b**) PCa 6.4 y after RP plus pelvic lymph node dissection (Gleason 8 [4+4]; PSA, 0.48 ng/mL). PET/CT shows suspected focal uptake (SUV$_{max}$, 4.5) in nonenlarged left obturator lymph node, scored 2 (arrow). Histology was positive for PCa. (**c**) PCa 10 mo after RP plus pelvic lymph node dissection (Gleason 8 [4+4]; PSA, 0.46 ng/mL;). PET/CT shows 2 suspected bone foci, one in right pubic ramus (SUV$_{max}$, 3) with sclerotic lesion on CT (arrow) and the other in posterior eighth rib (not shown). Biopsy of right pubic ramus was positive for PCa. (Figure from [65])

imaging in recurrent prostate cancer at the Mayo Clinic (Rochester, MN). The prescribing information clearly indicated CH-PET imaging of patients with suspected prostate cancer recurrence and noninformative bone scintigraphy, CT, or MR imaging. In these patients, [11C]choline PET imaging may help identify potential sites of prostate cancer recurrence for subsequent histologic confirmation. However, CH-PET suffers from unsatisfactory sensitivity, particularly at PSA levels below 2 ng/mL [67]. False-positive PET scans were observed in 15–47% of patients in these studies. Several publications also showed that CH-PET is useful in the diagnosis of brain tumors and in lung, esophageal, colorectal, and bladder cancers.

[18F]Fluorocholine (FCH)

Since [11C]choline is rapidly oxidized in vivo, 18F-labeled choline analogs (Fig. 14.10), [18F] Fluoromethylcholine or fluorocholine (FCH), and [18F] fluoroethylcholine (FECH) were developed [68, 69]. In vitro studies have clearly documented that these fluorinated choline analogs are good substrates for the enzyme *choline kinase* but, not for the enzymes involved in the oxidation of choline. As a result, no fluorinated derivatives of betaine have been observed [68]. The biodis-

that of choline, except for their very rapid urinary excretion. The majority of clinical studies have focused on the use of the FCH-PET in prostate cancer for detecting primary and metastatic cancer. Experience with other tumor types, such as brain and liver tumors, has been reported. In most organs, high tumor-to-background contrast is achieved with FCH within minutes of injection due to very rapid blood clearance. Excellent discrimination can be achieved in the brain, where there is very little physiological uptake of FCH. In other organs, such as the liver, malignant discrimination is still possible despite a moderate degree of physiological uptake. Although the renal excretion of FCH is not ideal for evaluations of the urinary tract, it has not proven intractable in actual practice. While the clinical utility of FCH-PET was well documented, direct comparison with 68Ga-PSMA-PET studies demonstrated an overall superior performance of [68Ga] Ga-PSMA compared to [18F]FCH for PET/CT imaging in prostate cancer patients referred for staging and restaging. Such superiority was mostly notable in patients with low PSA levels, small sub-centimetric bone lesions, small pelvic lymph nodes, and hepatic involvement. However, [18F]FCH PET/CT was more useful in particular clinical conditions. [18F]FCH detected additional

Fig. 14.10 Radiolabeled analogs of choline: [11C] Choline (CH) and [18F] Fluorocholine (FCH) have been investigated extensively in patients

[methyl-11C]Choline

Deshydroxy [18F]Fluorocholine

[18F]Fluoroethylcholine

[18F]Fluorocholine
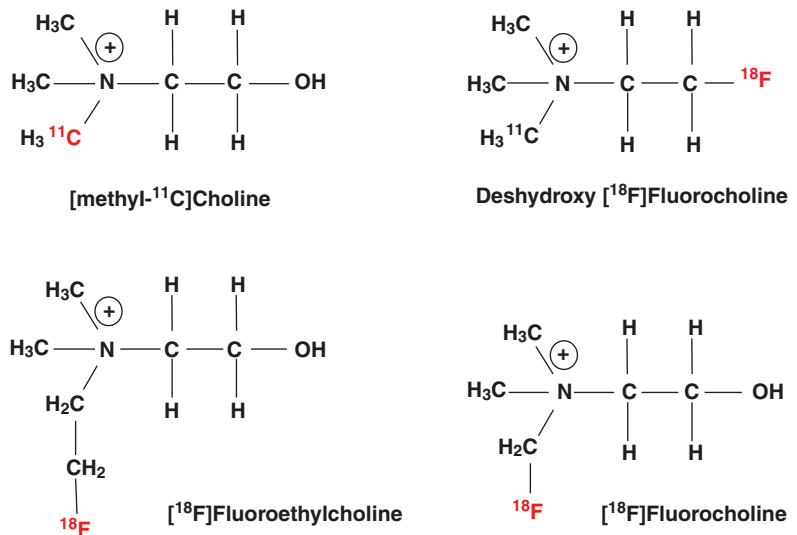
tribution of both, FCH and FECH, is similar to

bony lesions not seen with [68Ga]Ga-PSMA, par-

ticularly in high-risk hormone-resistant PC patients, suggesting poorly differentiated metastases [70].

14.4.2.5   Amino Acid Transport and Protein Synthesis

The tumor growth and development are characterized by an increase in the rate of protein synthesis. Since amino acids (AA) are the building blocks for protein synthesis, carrier-mediated transport of AAs into cells is one of the most important and essential steps in protein synthesis. Subsequently, AAs are converted to the aminoacyl-t-RNA, which forms the polypeptide chain in the ribosome. AAs also undergo metabolism, such as transamination and decarboxylation. They also are precursors for many other biomolecules, such as hormones or neurotransmitters, and enter several metabolic cycles as, for example, methyl group donors.

Although AAs may simply diffuse into the cells, their transport principally depends on more than 20 ubiquitous membrane transport systems. According to the need for sodium ions, AA transport system can be divided into the following two categories [19, 71–73]:

1. Na+-dependent AA transport systems, including system ASC (alanine-serine-cysteine preferred), system A (alanine preferred), system N (glutamine, aspartic acid, and histidine preferred), X-AG (transport L-glutamic acid, D-/L-aspartic acid) and B^{0+} (transport neutral and basic amino acids)
2. Na+-independent AA transport systems, including system L (leucine preferred), y^+ (CAT) (selectively transport basic amino acids), y^+L (transport neutral and basic amino acids), B^{0+} (transport neutral and basic amino acids), and X-C (transport cystine and glutamic acid). System **A**, system **L,** and system **ASC** are the most common amino acid transport systems. These amino acids are retained in the tumor cells because of their higher metabolic activities than most normal cells. Malignant transformation increases the use of amino acids for energy, protein synthesis, and

cell division. Since tumor cells often overexpress transporter systems, an overall increase in the AA transport and/or an increase in the protein synthesis rate by tumor cells may reflect proliferation [74]

[^{11}C]Methionine

[carboxyl-^{11}C]-L-leucine, [^{11}C]-L-methionine, and [^{11}C]-L-tyrosine participate in the synthesis of proteins and these ^{11}C-labeled AAs were introduced almost 40 years ago as tumor imaging agents. Since they undergo metabolism in vivo, the exact position where ^{11}C is incorporated in the molecule is crucial for the measurement of protein synthesis.

The ^{11}C-labeled amino acid with significant clinical potential for tumor imaging is [^{11}C] methionine (Fig. 14.10), which is accumulated to a higher extent in malignant tumors compared with most normal tissues [75]. For imaging of brain tumors, in particular, this tracer has been shown to be superior to FDG [49, 76]. A comparison of [^{11}C]-L-methionine-PET with FDG and FLT in a patient with brain tumor is shown in Fig. 14.7. [^{11}C]methionine PET is one of the most commonly used PET tracers for evaluating brain tumors. However, pitfalls due to physiological uptake, anatomical variations, vascular disorders, and non-tumorous lesions, such as inflammation and benign brain tumors, can potentially affect the image interpretation and cause false positives, and negatives [77]. Also, [^{11}C]methionine-PET does not show clear predictive value through semi-quantitative or visual analyses, because of a significant degree of overlap among tumors of several grades.

[^{18}F]FMT and [^{18}F]FET

Several ^{18}F-labeled tracers have been developed based on tyrosine and phenylalanine (Fig. 14.11). The tumor uptake of ^{18}F-labeled AAs is mainly related to the carrier-mediated active transport and not to the protein synthesis. Several important ^{18}F-labeled amino acids are under extensive clinical investigation [78]. Among them, L-3-[^{18}F]
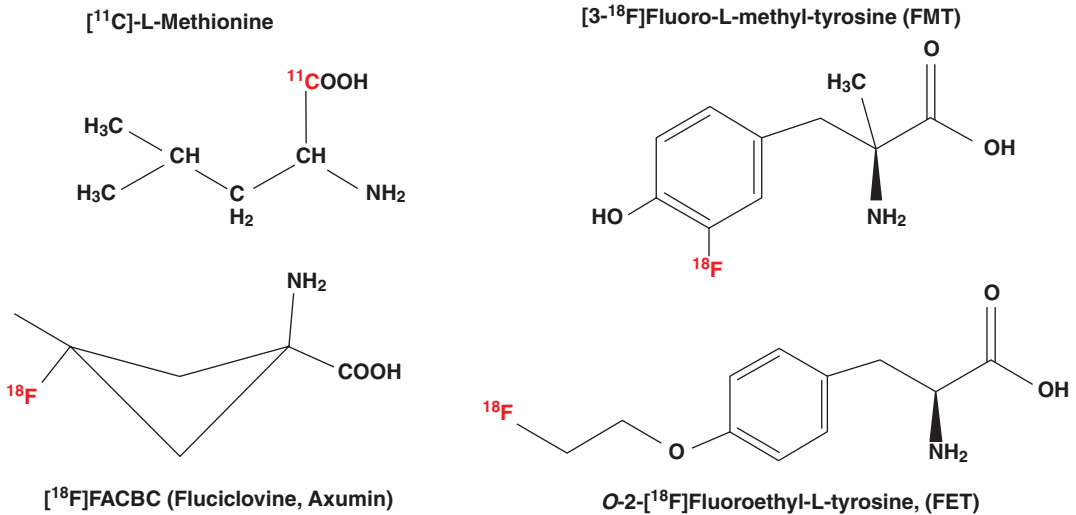
Fig. 14.11 Radiolabeled amino acid (AA) analogs with potential clinical utility to assess cell proliferation based on increased AA membrane transport

fluoro-α-methyl-tyrosine (FMT) and O-(2-[¹⁸F] fluoroethyl)-ʟ-tyrosine (FET) have shown significant diagnostic potential to image brain tumors (Fig. 14.12) [73, 80–82]. Also, a radioiodinated tracer, 3-[¹²³I]iodo-α-methyl-ʟ-tyrosine (IMT) is frequently used for SPECT. A comparison of FET-PET and IMT-SPECT is shown in Fig. 14.15.

[¹⁸F]Fluciclovine (Axumin, FACBC)

The potential clinical utility of a synthetic, nonmetabolizable amino acid analog of leucine, known as anti-1-amino-3-[¹⁸F]fluorocyclo-butane-1-carboxylic acid (FACBC) (Fig. 14.10) was first demonstrated in preclinical studies [84]. With FACBC, the cellular uptake is through, both, the ʟ-type transporter and the energy-dependent A-type transporters. As a result, it can be accumulated intracellularly and retained in high concentrations. Several clinical studies have also demonstrated its potential clinical utility in the detection of both, primary and metastatic prostate carcinoma (Fig. 14.13) and also primary brain tumors [85, 86].

As a diagnostic agent, Axumin-PET is indicated for imaging in men with suspected prostate cancer recurrence based on elevated PSA levels [65, 87, 88]. Several studies have shown that Axumin PET findings played a key role in treatment modification

by finding otherwise undetected lesions [89, 90]. Axumin uptake in areas of benign prostate pathology, however, may be indistinguishable from uptake in areas of prostate cancer. Fluciclovine-PET could be considered an alternative tracer superior to [¹¹C] choline in the setting of patients with biochemical recurrence after radical prostatectomy [91]. Several reports indicate that FACBC-PET may be used for breast cancer imaging studies. [¹⁸F]fluciclovine PET/CT visualizes malignant tumors including invasive lobular breast cancer (ILC) and invasive ductal breast cancer (IDC). In primary and metastatic breast cancers the uptake was significantly higher than in benign breast lesions and normal breast tissue [73, 92].

[¹¹C]5-HTP and [¹⁸F]FDOPA

Neuroendocrine tumors (NETs) are a heterogeneous group of neoplasms characterized by their endocrine metabolism and histological pattern. The endocrine cells from which NETs derive are capable of producing biogenic amines and polypeptide hormones. Carcinoids, together with the endocrine pancreatic tumors (EPTs) such as, gastrinomas, insulinomas, and glucagonomas, belong to the so-called NETs and, therefore, have been regarded as APUD-omas characterized by their capacity for
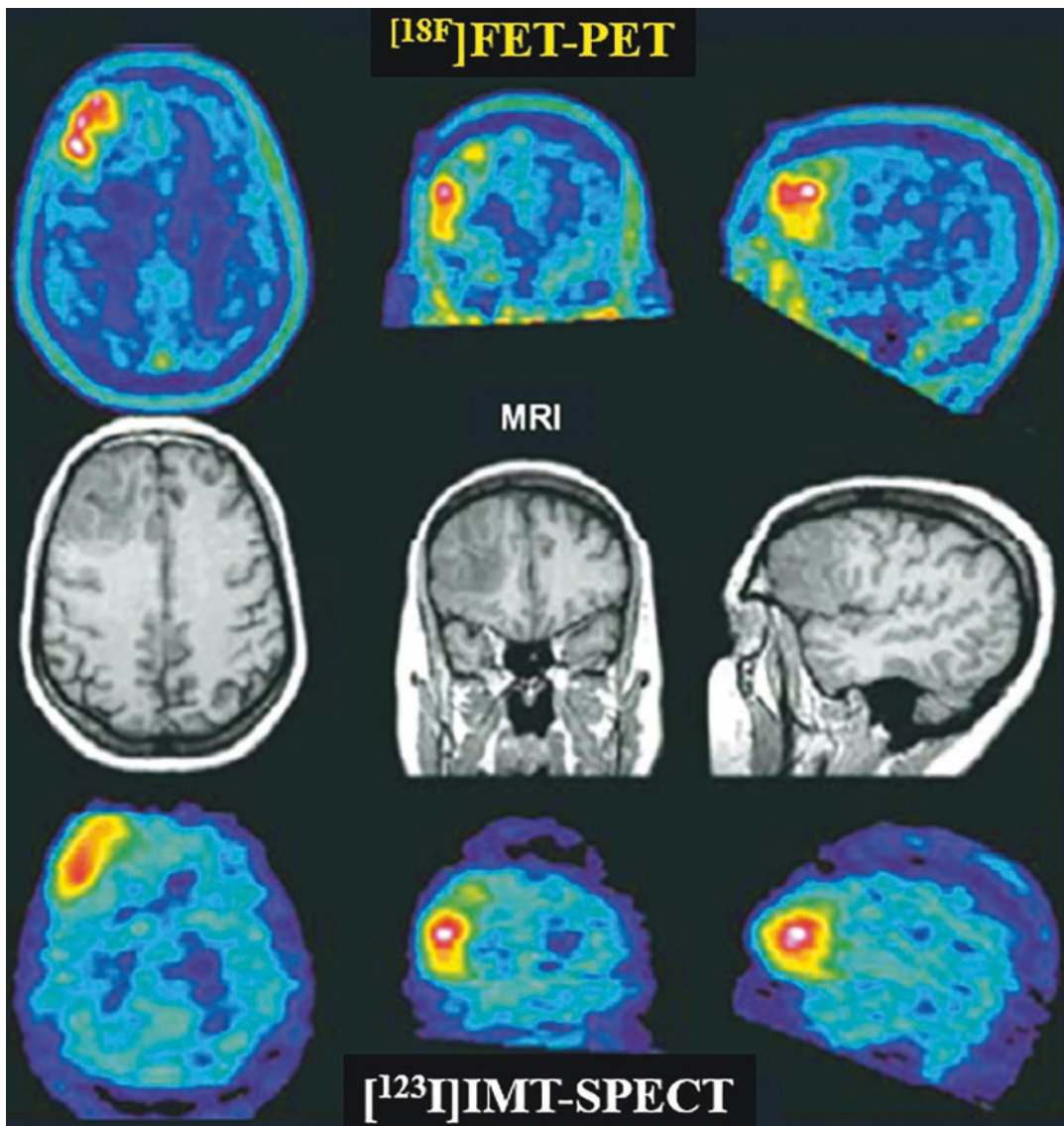
Fig. 14.12 Comparison of [¹⁸F]FET-PET and ¹²³I-IMT-SPECT to image tumor cell proliferation in a patient with brain tumor [79]

amine precursor uptake and decarboxylation [93]. NETs are often highly differentiated and slow growing and tend to express hormonal activity corresponding to that of the normal cell type.

Amine precursors such as 5-hydroxy-L-tryptophan (5-HTP) and L-dihydroxy-phenylalanine (L-dopa), thus, are taken up by the tumor cells. Subsequently, through the action of *aromatic amino acid decarboxylase* (AADC),

these precursors become decarboxylated and converted to the corresponding amines serotonin, and dopamine. The resulting amines are then stored within the cell and, in response to stimuli, are released into the circulation through exocytosis. Based on the biochemical mechanism described above, ¹¹C-labeled amine precursors L-DOPA and 5-HTP (Fig. 14.14) were developed for PET imaging of NETs [94, 95]. ¹⁸F-labeled

[¹⁸F]Fluciclovine-PET/CT
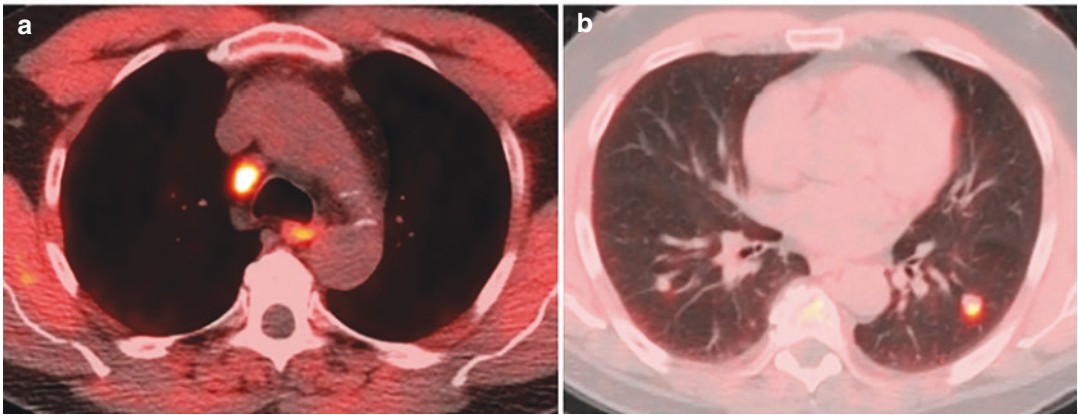
Fig. 14.13 [¹⁸F]Fluciclovine-PET in a patient with biochemical recurrence of prostate cancer after prostatectomy (PSA level, 16.4 ng/mL; doubling time, 6.4 months). Metastatic mediastinal (**a**) and pulmonary nodules (**b**) were detected on transaxial PET/CT. Patient was started on hormonal therapy with subsequent resolution of lymphadenopathy and pulmonary nodules and undetectable PSA (Figure from [89])
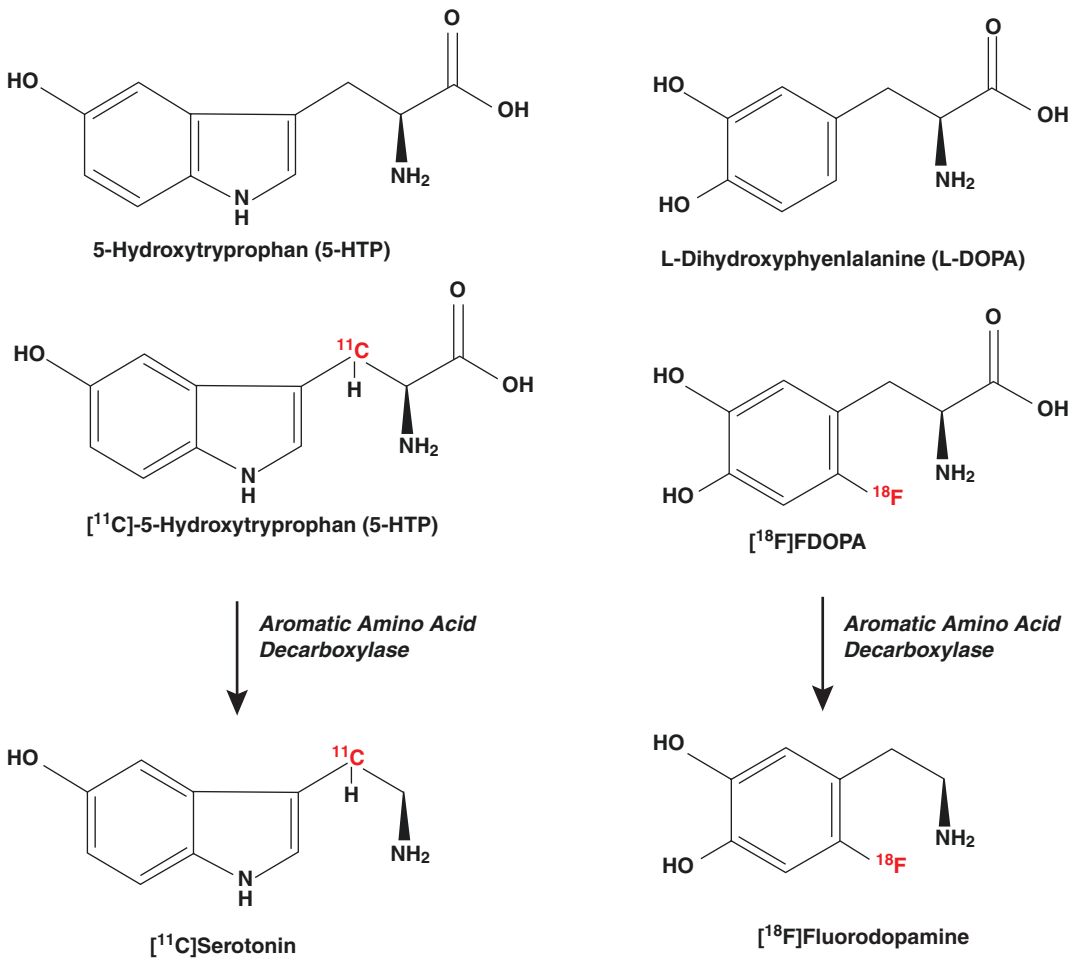

Fig. 14.14 Serotonin and dopamine are neurotransmitters in the brain. Based on the amino acid precursors, several radiolabeled analogs of 5-HTP and ʟ-DOPA were developed for imaging neuroendocrine tumors

L-DOPA (FDOPA), developed initially for imaging the dopamine metabolism in the brain, is also being evaluated for imaging NETs [96].

Following in vivo metabolism, [^{11}C]5-HTP is rapidly decarboxylated to [^{11}C]5-Hydroxytryptamine (serotonin). Subsequently, [^{11}C]serotonin is further metabolized to [^{11}C]5-hydroxy indole acetic acid (HIAA) by the enzyme *monoamine oxidase* (MAO). Finally, both of these C-11 metabolites are excreted into the urine.

[^{18}F]FDOPA is converted to [^{18}F]Fluorodopamine (FDA), which can be oxidized by the enzyme MAO to L-3,4-dihydroxy-6-[^{18}F]fluorophenyl-acetic acid ([^{18}F] FDOPAC), which subsequently is O-methylated by catechol O-methyl transferase (COMT) to 6-[^{18}F]fluoro-homovanillic acid ([^{18}F]FHVA). Both *AAAD* and *COMT* are present in peripheral tissues such as liver, kidneys, and lungs. Further, both the decarboxylation of the radiolabeled amino acid precursors and the release of radiometabolites into the blood can be reduced with carbidopa, a *decarboxylase* inhibitor. Carbidopa pretreatment improves overall image quality, image interpretation, and may help detection of more lesions [97].

Based on a number of clinical studies, it has been documented that [^{11}C]5-HTP-PET is clinically useful for the detection of NETs [98, 99]. 5-HTP-PET can also be helpful for evaluating the metabolic effects of treatment, which are not obtained with other imaging modalities. This functional approach to imaging, however, may yield false-negative results in detecting undifferentiated carcinoids.

[^{18}F]FDOPA was proposed initially as a biomarker for melanomas. The ability of NETs to accumulate and decarboxylate L-DOPA is well known and increased activity of l-*DOPA decarboxylase* was found to be a hallmark of NETs [100]. FDOPA uptake was reported in infrequent tumors such as medullary thyroid carcinomas (MTC), phaeochromocytomas (PGL), and paragangliomas [101–104]. A recent review indicates that [^{18}F]FDOPA PET and related hybrid modalities(CT/MRI) yield good diagnostic performance in patients with intestinal NETs, PGL, and neuroblastoma (NB) and can be a suitable alternative to other PET methods in these settings. Also, FDOPA-PET is the best radiopharmaceutical in detecting rMTC even if the detection rate is suboptimal [105]. While somatostatin receptor (SSTR)-PET is clearly superior to FDOPA-PET for certain NENs, FDOPA-PET/CT can perform better than SSTR-PET in small intestine NETs (Fig. 14.15) [83].

As an amino acid analog, FDOPA is taken up at the BBB in the normal brain. In patients with brain tumors, the diagnostic accuracy of FDOPA has been compared with FDG [49, 86, 106, 107] and F-DOPA demonstrated excellent visualization of high- and low-grade tumors, and was able to detect low-grade, and recurrent tumors with greater sensitivity than FDG.

In 2019, [^{18}F]FDOPA was approved by the FDA for detection of dopaminergic nerve terminals in the striatum of adult patients with suspected Parkinsonian Syndromes. Hopefully, FDOPA-PET will also be approved for PET imaging of neuroendocrine neoplasms in the near future.

14.4.2.6 Tumor Hypoxia

Tumor hypoxia, a hallmark of malignancy, is a common and important feature of the tumor microenvironment. It is the consequence of an oxygen delivery versus consumption mismatch that occurs when cell proliferation outstrips neo-angiogenesis during tumor growth. This results in extremely low oxygen levels (<5 mmHg) in tumors versus 40–60 mmHg in healthy tissues [108]. In malignant tumors, hypoxia is an indicator of poor prognosis, regardless of the treatment modality used [109]. With increasing tumor size, there is a reduced ability of the local vasculature to supply sufficient oxygen to the rapidly dividing tumor cells [110]. The resulting hypoxia may inhibit new cell division or even lead to cell death but, it may also lead to adaptive responses that will help cells to survive and progress. The presence of hypoxia in tumors has long been established as a key factor in tumor progression and in the resistance of tumors to therapy [111]. Well-oxygenated cells are more sensitive to the cytotoxic effects of ionizing radiation compared to poorly oxygenated cells. Therefore, hypoxia in tumor tissue seems to be an important prognostic
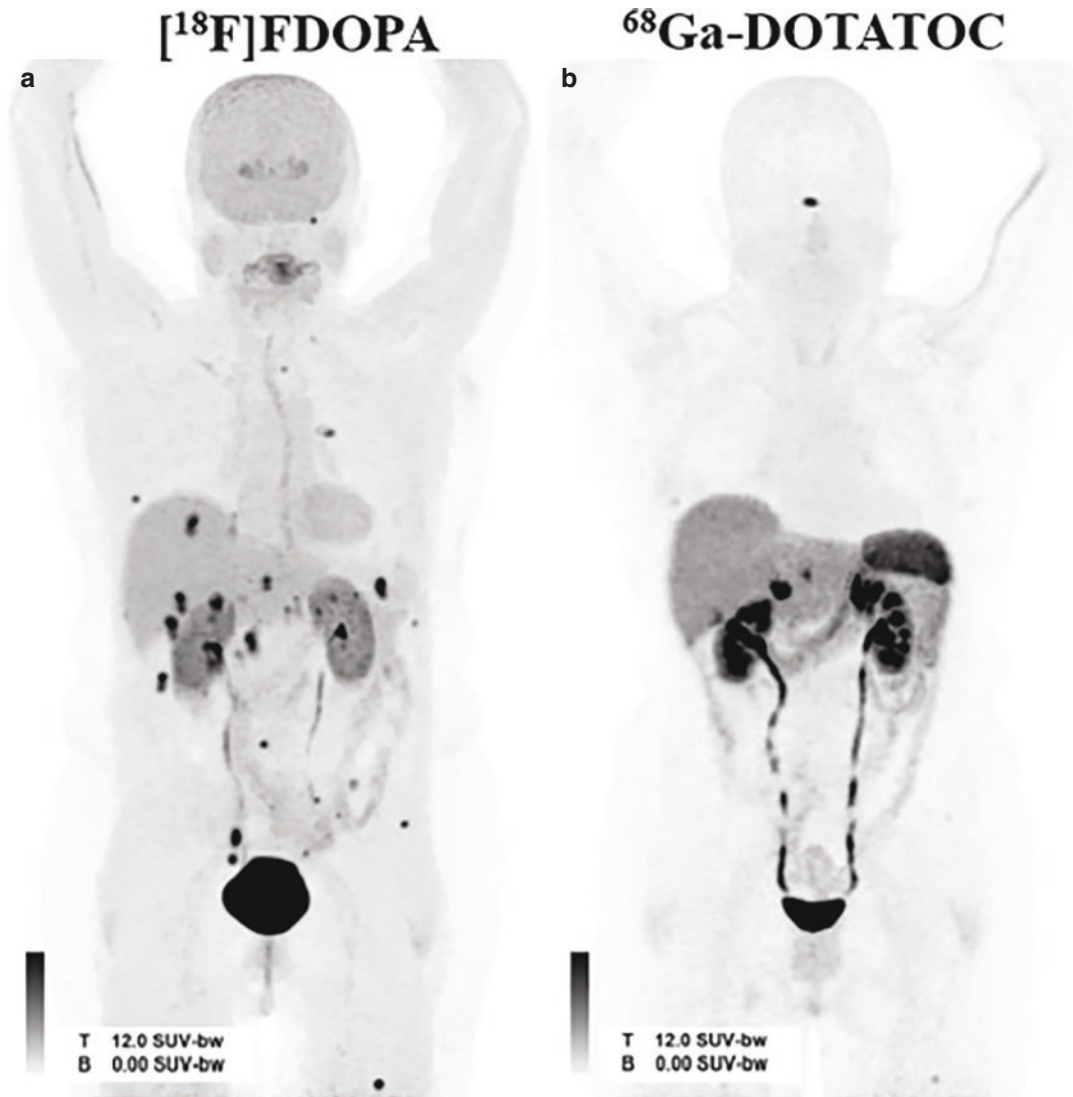
[¹⁸F]FDOPA

⁶⁸Ga-DOTATOC

Fig. 14.15 [¹⁸F]FDOPA-PET (**a**) showing the superiority over ⁶⁸Ga-DOTATOC (**b**) in a patient with small intestine neuroendocrine tumor (NET). (Figure from [83])

indicator of response to either chemotherapy or radiation therapy.

2-Nitroimidazole (azomycin) was developed in the 1950s as an antibiotic targeted against anaerobic germs. In 1979, nitroimidazoles were first introduced as bioreducible markers of hypoxia and as sensitizing factors for radiation therapy of hypoxic tumors [112]. It has been observed that nitroimidazoles enter the cells by passive diffusion and undergo a single electron reduction to form a potentially reactive species

[113]. When oxygen is abundant, the molecule is immediately reoxidized. However, under hypoxic conditions, further reduction of the nitroimidazole molecule that forms covalent bonds to intracellular macromolecules, in a process of metabolic trapping within the hypoxic cell, occurs (Fig. 14.16).

For correct visualization of the hypoxic areas of the tumor, it is important that, regardless of the cell type, retention occurs in the hypoxic cells and not in oxygenated or necrotic cells. To

Fig. 14.16 The mechanism of intracellular trapping of nitroimidazoles. Under hypoxic conditions, the nitro group undergoes electron reduction to form reactive radicals which after further reduction form covalent bonds with intracellular macromolecules
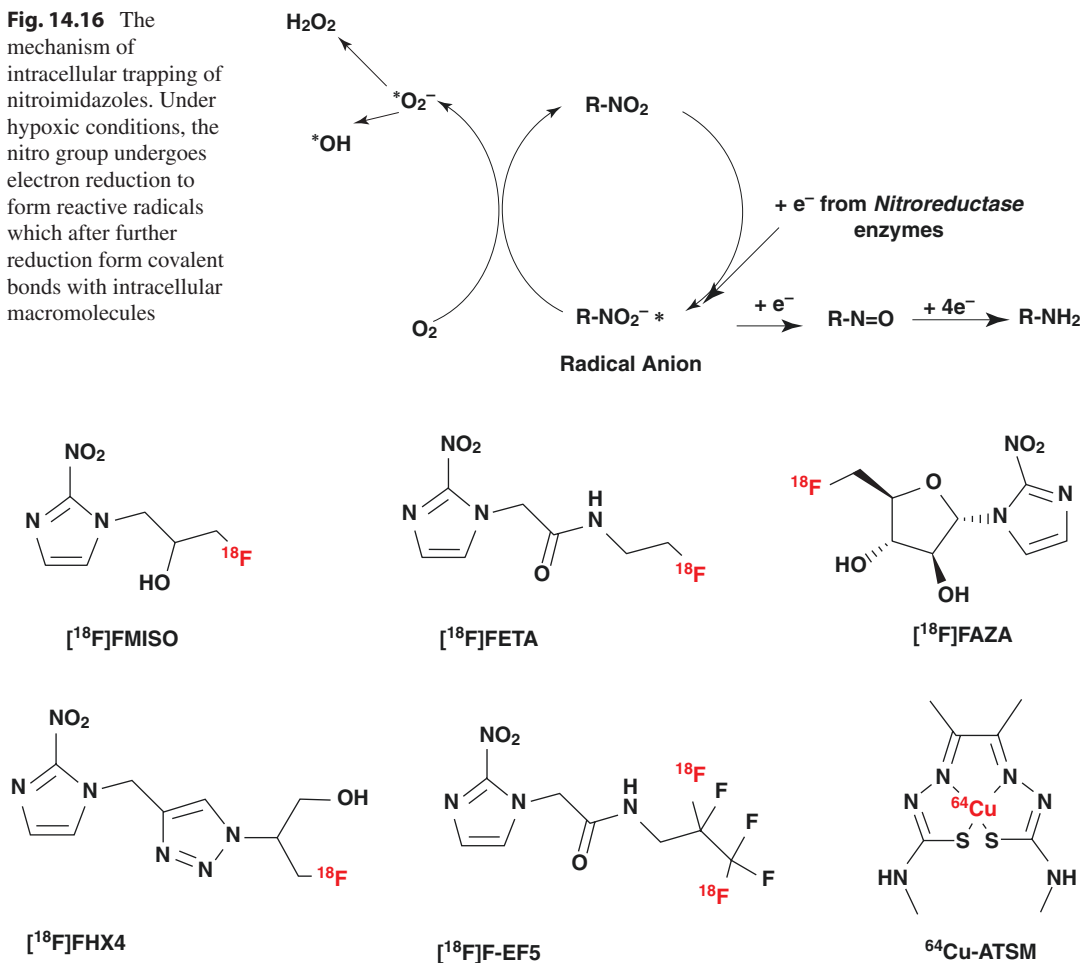

Fig. 14.17 ^{18}F-labeled nitroimidazole analogs to image hypoxia

achieve this goal, the radiopharmaceutical should be sufficiently lipophilic to have high cellular uptake and rapid equilibrium, or it should be hydrophilic and have faster clearance kinetics, resulting in better contrast between hypoxia and normoxia [114]. Two main tracer classes have been developed to specifically study regional tumor hypoxia with PET: [18F]labeled nitroimidazoles and Cu-labeled diacetyl-bis(N4-methylthiosemicarbazone) analogs [115]. The clinical significance of hypoxia PET imaging is to identify individuals with poor prognosis and those likely to benefit from hypoxia-targeted therapy. Several studies have shown that hypoxia PET imaging predicts outcome. Application of this imaging technique for radiotherapy planning

using specific radiotracers allows precise definition of the hypoxic areas and, consequently, a more individualized treatment [114].

[18F]Fluoromisonidazole (FMISO)

FMISO (Fig. 14.17) was first introduced as a tracer for determining tumor hypoxia [116]. It binds selectively to hypoxic cells both in vitro and in vivo. FMISO-PET has been used to quantitatively assess tumor hypoxia in the lung, brain, and head-and-neck cancer patients and in patients with myocardial ischemia. FMISO is relatively hydrophobic and diffuses across cell membranes, showing a passive distribution in normal tissues. Because of high lipophilicity, slow clearance kinetics, reaction mechanisms, low uptake in

hypoxic cells, and the absence of active transport of this radiotracer, the identification and quantification of hypoxic tumor areas necessitate imaging for longer periods of time post injection. FMISO is the most extensively studied hypoxic PET radiopharmaceutical ([114, 117–119]). The diagnostic performance FMISO-PET in glioblastomas is shown in Fig. 14.18.

Several other analogs (Fig. 14.17), such as [18F] fluoroerythronitroimidazole (FETNIM), [18F] Fluoroetanidazole (FETA), 1-(5-[18F]Fluoro-5-deoxy-α-D-arabino-furanosyl)-2-nitroimidazole (FAZA), [18F]2-(2-nitro-1H-imidazol-1-yl)-N-(2,2,3,3,3-Pentafluoropropyl)-acetamide (EF5), and [18F]3-fluoro-2-(4-((2-nitro-1H-imidazol-1- yl) Methyl)-1H-1,2,3-triazol-1-yl)propan-1-ol (HX4) have been developed with more favorable pharmacokinetics [118, 120–123]. FETNIM is more hydrophilic than FMISO and shows promise for hypoxia imaging in humans. FETA demonstrates oxygen-dependent binding and retention in tumors that are very similar to that for FMISO but metabolizes less rapidly. Recently, it has also been reported that FAZA displays a hypoxia-specific uptake mechanism and provides tumor-to-background ratios (T/B ratios) superior to that of the standard hypoxia tracer FMISO [122]. In patients with head and neck and non-small cell lung cancer, FMISO-PET has been used to document the extent of hypoxic tissue and/or as a prognostic indicator of treatment response. Overall decrease in tumor uptake of both FMISO and FDG may predict treatment response and overall survival [124].

Cu(II)-diacetyl-*bis*(N4-methylthiosemicarbazone) (Cu-ATSM) has efficient uptake and washout kinetics due to its high

Fig. 14.18 Comparison of hypoxia imaging ([18F]FMISO-PET) to glucose metabolism ([18F]FDG-PET) hypoxia imaging with glucose metabolism in a patient with glioblastoma. The FDG uptake in the tumor was comparable to that of contralateral cerebral cortex (**c**). In contrast, the FMISO uptake (**d**) was higher in the tumor than in the surrounding brain tissue. The FLAIR image showed a high-signal tumor in the left hemisphere (**a**). The tumor was enhanced by gadolinium contrast material (**b**) (Figure from [117])
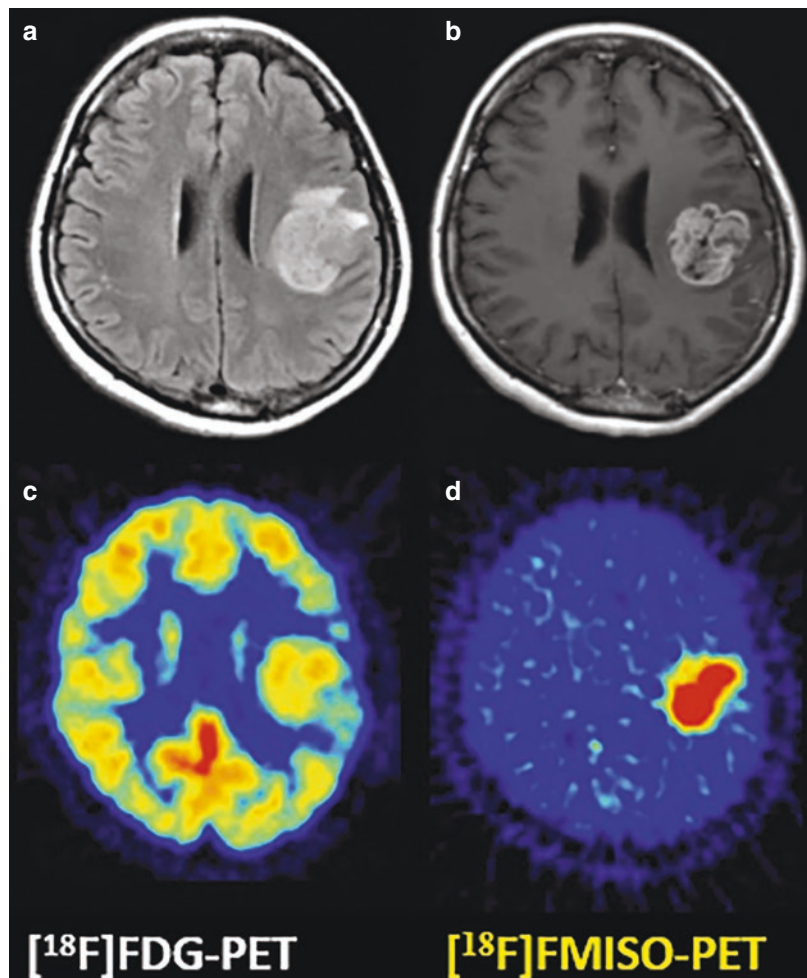
membrane permeability and fast tumor uptake [125, 126]. Preliminary clinical studies with [60]Cu-ATSM and [62]Cu-ATSM have shown it to be a selective marker for hypoxia in human cancers and predicted response to therapy. ^{64}Cu-ATSM is useful for tumors of the head and neck, lungs, kidneys, colon, rectum, bladder, and uterus [125, 127].

All the PET radiopharmaceuticals developed for imaging hypoxia have limitations, as none exhibits entirely ideal properties and all are still under investigation. While [^{18}F]FMISO is the most studied radiopharmaceutical, ^{18}F-EF5 and ^{18}F-FAZA are promising candidates but need further clinical studies.

14.4.2.7   Angiogenesis

Angiogenesis, the formation of new blood vessels, is an important aspect of the tumor phenotype. It is essential to deliver nutrients for tumor growth, invasion, and metastatic spread. Tumors switch to angiogenesis under a variety of stress signals, which results in tumor growth and metastases. As a general rule, tumors do not grow beyond 1 to 2 mm without producing new blood vessels [128]. Many solid tumors develop areas of hypoxia during their evolution. This is primarily caused by the unregulated cellular growth, which results in a greater demand for oxygen for energy metabolism. Hypoxia in tumor cells leads to amplification and overexpression of various signaling factors, such as HIF-1α or HIF-2α, which promote tumor growth, invasion, metastasis, and resistance to apoptosis. Tumor hypoxia and angiogenesis are intimately related and HIF-1α is probably the single most important factor promoting the expression of proangiogenic proteins [129]. Although angiogenesis is a frequent consequence of hypoxia, some tumors develop extensive angiogenesis without the presence of hypoxia and, vice versa. The emergence of angiogenesis, as an important target for cancer therapy, has prompted a great deal of new research in an attempt to understand this molecular process and to develop molecular imaging probes to image accelerated angiogenesis or monitor the response to antiangiogenic therapies.

Cell adhesion receptors of the integrin family are responsible for a wide range of cell–extracel-lular matrix and cell–cell interactions and have been well studied in many tumor types. One of the most prominent members of this receptor class is $\alpha_V\beta_3$ integrin, which is highly expressed on activated endothelial cells, which undergo angiogenesis and vascular remodeling, and solid tumor cells, particularly in pathways stimulated by vascular endothelial growth factor [130]. It is not expressed on mature vessels or on nonneoplastic epithelium. The expression of integrin $\alpha_V\beta_3$ on sprouting capillary cells and its interaction with specific matrix ligands has been shown to play a key role in angiogenesis and metastasis [6]. The data from preclinical tumor models and from phase I/II clinical trials suggest that antibody, peptide, and peptidomimetic antagonists of $\alpha_v\beta_3$ integrin inhibit tumor angiogenesis and metastasis [131].

As angiogenesis is a multi-factorial process, there are a multitude of potential targets for molecular imaging. These targets can be subdivided into direct targets (specific receptors on or near the cell that are related to angiogenesis) and indirect targets (glucose metabolism, hypoxia—which are only indirectly correlated with angiogenesis) [132]. The indirect targeting is based on [^{18}F]FDG and hypoxia tracers, [^{18}F]FMISO, [^{18}F]FAZA, and [^{18}F]-HX4. The direct contacting PET radiotracers are mostly based on the αv integrins, which are overexpressed on the surface of endothelial cells during angiogenesis [132, 133]. Several types of integrins can also imply different metastatic progresses: exosomal integrin $\alpha v\beta 5$ was associated with liver metastasis, whereas exosomal integrins $\alpha 6\beta 4$ and $\alpha 6\beta 1$ correlate with lung metastasis. $\alpha v\beta 3$ integrin is one of the most studied integrins as it represents a highly specific biomarker to distinguish new from mature capillaries, allowing vascular mapping of angiogenesis in tumors. Vascular endothelial growth factor (VEGF) interacting with its receptor tyrosine kinase (VEGFR) is an important mediator of the angiogenesis pathway and consequently a potential imaging target.

RGD-Motif

Arginylglycylaspartic acid (RGD) is the most common peptide motif responsible for cell adhe-

sion to the extracellular matrix. Several radiolabeled ligands of the $\alpha_V\beta_3$ receptor have been developed based on the integrin's recognition of the RGD sequence of adhesive proteins first reported using ^{125}I-labeled RGD [134]. A dimeric RGD peptide, E-[c(RGDfK)]$_2$, was labeled with several radionuclides (^{111}In, ^{99m}Tc, ^{64}Cu, ^{68}Ga and ^{18}F). Dimeric and multimeric RGD peptides were also developed because polyvalency may improve receptor binding, and are better than that of monomeric RGD peptides based on polyvalency. The cyclic RGD peptide, E[c(RGDyK)]$_2$ has been labeled with ^{18}F by conjugation coupling with *N*-succinimidyl-4-^{18}F-fluorobenzoate (^{18}F-SFB) and product, ^{18}F-FB– E[c(RGDyK)]$_2$ or ^{18}F-FRGD2 has shown high integrin specificity and in vivo targeting in tumor-bearing mice [135]. A RGD peptide tetramer was also developed with repeating c(RGDfK) units connected through glutamate linkers and, subsequently, conjugated with DOTA. The ^{64}Cu-DOTAE{E[c(RGDfK)]$_2$}$_2$ has shown favorable biokinetics [136].

[18]F-galacto-RGD (FG-RGD) peptide was developed for specific imaging of $\alpha_V\beta_3$ receptor expression and a significant correlation has been demonstrated in tumor xenografts between FG-RGD uptake and $\alpha_V\beta_3$ receptor expression [137]. In cancer patients, FG-RGD has shown accumulation in some of the tumor lesions, however, in a comparative study, no correlation between FDG and FG-RGD RGD tracer uptake in the tumors was found, indicating that the sensitivity of FG-RGD for tumor detection is clearly inferior to that of FDG [138]. Several radiotracers based on RGD-motif, such as ^{18}F-Galacto-RGD, ^{18}F-RGD-K5, and ^{68}Ga-NODAGA-RGD, are under active clinical investigation [133, 139, 140]. No single tracer has shown optimal imaging characteristics to detect angiogenesis although, the RGD tracer family seems to show the highest potential for the development of a molecular imaging radiopharmaceutical [132].

14.4.2.8   Apoptosis

Apoptosis, also known as programmed cell death, is central to homoeostasis and the normal development, and physiology in all multicellular organisms, including humans [141]. Evading apoptosis or resisting cell death has been proposed as a hallmark of cancer [8, 9]. The formation of cancer, as a result of dysregulation of apoptosis, and the successful treatment of cancer (iatrogenic modification, cell removal) both represent opposite sides of the apoptosis coin [142, 143]. Tumor cells tend to evade apoptosis for promoting tumor progression and drug resistance. Therefore, it was believed that testing and monitoring apoptosis levels in these patients can not only provide useful information on the disease diagnosis and staging but, also conduce to the efficacy assessment of their treatments [144].

Apoptosis is an active, highly conserved, and genetically controlled process. The basic biochemical and morphological changes of apoptosis have been reviewed extensively [142, 143]. The histological changes of apoptosis are preceded by an initiation stage called the "lag or trigger phase." Multiple triggers of apoptosis are known, such as withdrawal of growth factors, DNA damage, immune reactions, ionizing radiation, chemotherapy, and ischemic injury. Most apoptotic pathways, however, converge on a common cascade of cysteine aspartate–specific proteases, collectively known as the *caspases*, which upon activation cross-link and cleave specific intracellular proteins involved with apoptosis. A milestone in apoptosis research is the discovery of the apoptosis receptor APO-1 (CD95, Fas) [145]. The biochemical events associated with the interaction of death receptors and caspases leading to apoptosis are shown in Fig. 14.19.

Even at the early stages of apoptosis, the cell membrane displays functional alterations. The hallmark of the start of the execution phase is the redistribution and exposure of phosphatidylserine (PS) on the cell surface. PS is normally restricted to the inner surface (inner leaflet) of the lipid bilayer by an ATP-dependent enzyme called *translocase* [146]. Translocase, in concert with a second ATP-dependent enzyme, *floppase*, which pumps cationic phospholipids, such as phosphatidylcholine (PC) and sphingomyelin to the cell surface, maintains an asymmetric distribution of different phospholipids between the inner and
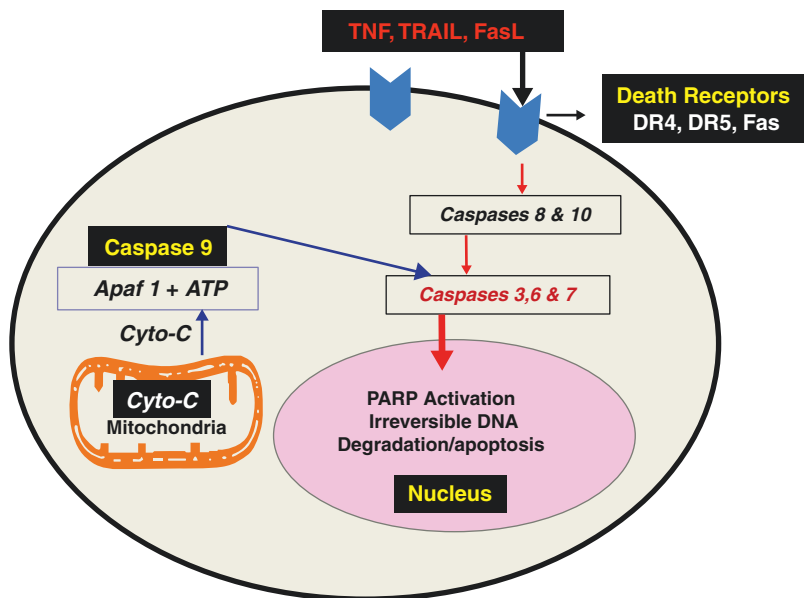
Fig. 14.19 Biochemical events in apoptosis. Extrinsic pathway of apoptosis is initiated by the binding of specific ligands to the death receptors. These ligands include tumor necrosis factor (TNF), a TNF-related, apoptosis-inducing ligand (TRAIL), and Fas ligand (FasL). The intrinsic pathway is initiated by cytochrome c from the mitochondria into the cytosol. The final enzyme activated within the cascade is caspase-3, following which the morphologic events of apoptosis quickly follow, resulting in the orderly breakdown of cellular proteins, including the cytoskeleton and nuclear matrix

outer leaflets of the plasma membrane. The rapid redistribution of PS and PC across the cell membrane (measured in minutes), at the beginning of the execution phase of apoptosis is facilitated by a calcium ion-dependent deactivation of translocase and floppase, and activation of a third enzyme, called *scram-blase* [142]. PS can also be expressed at low levels in a reversible fashion under conditions of cell stress by the presence of physiological stressors, such as nitric oxide, p53 activation, allergic mediators, and growth factor deprivation. Therefore, PS expression can be used to define tissues at risk for cell death that may recover or be amenable to prompt therapeutic intervention.

Radiotracers for Imaging Apoptosis
An ideal apoptosis radiotracer for clinical practice should be specific for apoptotic cells, with rapid clearance, nontoxicity, and high stability. Based on the characteristic biochemical changes associated with apoptosis, a great number of radiotracers for SPECT and PET (such as ^{99m}Tc-HYNIC-Annexin V, ^{18}F-ML-10, ^{18}F-CP18, and ^{18}F-ICMT-11), have been developed to target the extruded phospholipid (i.e., PS and PE), activated caspase 3, and altered membrane permeability [144, 147–149]. Out of these imaging agents, ^{99m}Tc-Annexin V was by far the only one that has been extensively investigated in clinical studies.

Annexin V ($\approx$36,000 kDa) is an endogenous human protein that is widely distributed intracellularly in the placenta, endothelial cells, kidneys, myocardium, skeletal muscle, skin, red cells, platelets, and monocytes [150]. Annexin V binds to the externalized PS with extremely high affinity (K_d = 7 nmol/l), as well as specificity.

^{99m}Tc-labeled recombinant human (rh)–annexin V was introduced in the 1990s as a tracer for imaging apoptotic tissue [151]. In the first clinical study with cancer patients (SCLC and NDCLC, lymphoma, and metastatic breast cancer), ^{99m}Tc-Annexin V-SPECT was performed prior to therapy and immediately after the first course of treatment [152]. In the majority of

patients, the relative change in ^{99m}Tc-annexin uptake corresponded to the treatment response, compared to the baseline. Subsequently, more stable agents such as ^{99m}Tc-BTAP-Annexin V, and ^{99m}Tc-HYNIC-annexin V were also developed. Since PS is also exposed on necrotic cells, radiotracers based on annexin V may not be capable to distinguish between necrosis and apoptosis [144].

A group of small amphipathic molecules (Aposense family) has been designed to identify the altered membrane permeability in apoptotic cells and then distinguish them from viable ones. [^{18}F]-labeled 2-(5-fluoropentyl)-2-methyl malonic acid ([^{18}F]ML-10) (Fig. 14.20), a low-molecular-mass PET apoptotic tracer derived from the Aposense family, is the first clinically available apoptosis probe for in vivo imaging. Being investigated in multicenter preclinical and clinical trials, [^{18}F] ML-10 shows high stability, safety, specificity, and rapid biodistribution [153, 154]. Additionally, [^{18}F]ML-10 could be transported through the cytoplasmic membrane in apoptotic cells, whereas there is no [^{18}F]ML-10 membrane transportation in necrotic cells.

Therefore, unlike Annexin V, [^{18}F]ML-10 can distinguish apoptosis from necrosis [154]. In a clinical study with [^{18}F]ML-10, the performance of early-response after CyberKnife (CK) stereotactic treatment on patients with intracranial tumors was investigated. Heterogeneous changes of apoptosis in tumors before and after CK treatment were observed on voxel-based analysis of PET images. A positive correlation was observed between the change in radioactivity (X) and subsequent tumor volume as shown in Fig. 14.20 [154].

Caspase-3 is the main executor of apoptosis which may act as an ideal tool for apoptosis imaging. In vivo imaging of apoptosis through targeting activated caspases was possible via two different approaches: use of caspase inhibitors or substrates [149]. To date, multiple types of radiolabeled caspase-3 ligands (such as ^{18}F-ICMT-11 and ^{18}F-CP-18) have been synthesized and some of them are under clinical investigation [144]. However, ^{18}F-ICMT-11, caspase inhibitor appears to be limited by binding site saturation and ^{18}F-CP18, a substrate-based apoptosis targeting peptide, has a low radioactivity in target tissues.

Fig. 14.20 ^{18}F-ML-10 chemical structure of (**a**). [^{18}F]FML-10 PET imaging of apoptosis before (**b**) and 48 h after cyberknife stereotactic treatment (**c**) of a female patient, diagnosed with lung cancer brain metastases, showing an obvious and uniform increase of radiotracer uptake following treatment (image modified from [56])
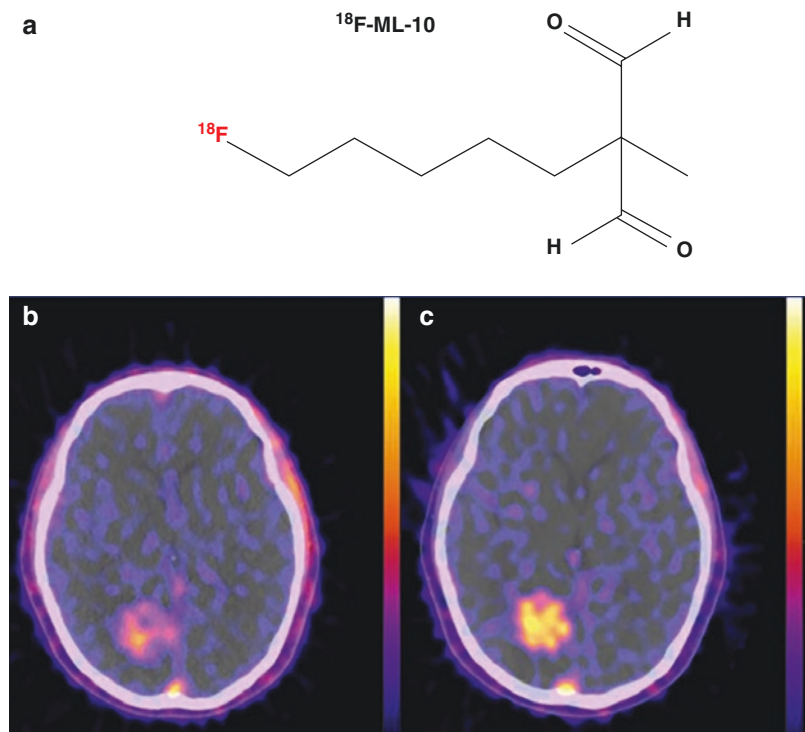
14.4.2.9 Norepinephrine Transporters (NET)

The norepinephrine transporter (NET), also known as noradrenaline transporter (NAT) is a monoamine transporter and is responsible for the sodium-chloride (Na^+/Cl^-)-dependent reuptake of extracellular norepinephrine (NE) (also known as noradrenaline) [155]. Tumors arising from the neural crest share the characteristic of amine precursor uptake and decarboxylation (APUD), and contain large amounts of adrenaline, dopamine and serotonin within the secretory granules in the cytoplasm. Tumors of the adrenergic system include neuroblastoma, pheochromocytoma (arise in adrenal medulla), and paragangliomas (extra-adrenal tissue). These cancers of sympathetic neuronal precursors express the norepinephrine transporter (NET), a 12 domain, transmembrane protein which functions to shuttle norepinephrine across the cell membrane. NET has very high affinity and specificity for norepinephrine and its analogs. NET actively transports norepinephrine primarily into adrenal chromaffin cells, and presynaptic terminals by an ATP-dependent, and specific process known as Uptake-1 [155, 156]. Uptake-1 transportation, however, is saturable and dependent upon serum sodium and chloride, temperature, pH, oxygen, and vascularity. Norepinephrine is also brought into cells by passive, nonspecific diffusion (a process known as Uptake-2) that is energy independent, unsaturable, and results in low-level norepinephrine accumulation in most tissues. Cells store norepinephrine within numerous neurosecretory vesicles via the vesicular monoamine transporter (VMAT) [156]. The expression NET in neuroendocrine neoplasms (NENPs), specifically neuroblastoma provide the basis and rationale for the use of radiolabeled norepinephrine analogs for targeted imaging, and treatment of neuroblastoma [157].

[123/131I]MIBG (Iobenguane, Adreview, Azedra)
In the 1980s, Dr. Wieland and his colleagues at the University of Michigan developed an analog of NE, known as [131]I-*meta*-iodobenzylguanidine (MIBG), a diagnostic tracer to allow imaging of the adrenal medulla [158, 159]. MIBG (Fig. 14.21) was developed by linking the benzyl portion of bretylium with the guanidine group of guanethidine. Among the three isomers of iodobenzylguanidines, the meta isomer (MIBG) has less in vivo deiodination and liver uptake than the other two isomers. MIBG accumulates both in normal sympathetically innervated tissues, such as the heart and salivary glands, but also in tumors that express NET, specifically those of neural crest, and neuroendocrine origin. With MIBG the primary uptake in cancer cells is by active transport (Uptake-1), which is approximately 50 times more efficient than passive transport [156, 160]. NE analogs can inhibit Uptake-1 and any decrease in the activity of the Na/K-ATPase leads to reduced uptake, and increased outward transport of NR, and its analogs [156].

The potential use of MIBG to image pheochromocytoma and neuroblastoma was also reported in the early 1980s [161, 162]. In 1984, the first therapy with MIBG was described in patients with pheochromocytoma [163]. In the same period, the first reports appeared on the use of MIBG in patients with neuroblastoma [164] and neuroendocrine carcinomas [165]. In the last four decades several studies in many countries demonstrated the clinical utility of [123/131I]-MIBG imaging and targeted therapy in patients with neuroblastoma, pheochromocytoma and neuroendocrine tumors [156, 157].

In 1994, [131I]MIBG also known as iobenguane sulfate I-131 intravenous (*low specific activity formulation*), received FDA approval as an imaging agent for the localization of specific sites of pheochromocytomas and neuroblastomas. In 2008, [123I]MIBG or iobenguane I-123 injection (Adreview®) was also approved by the FDA as a tumor imaging agent (Adreview®). Recently in 2018, [131I]Iobenguane (Azedra®) (high specific activity formulation) was also FDA approved for the treatment of adult and pediatric patients 12 years and older with iobenguane scan positive, unresectable, locally advanced, or metastatic pheochromocytoma or paraganglioma who require systemic anticancer therapy.

[18F]MFBG and [18F]FIBG
To develop derivatives of MIBG for PET studies, two methods have been used to introduce the [18]F
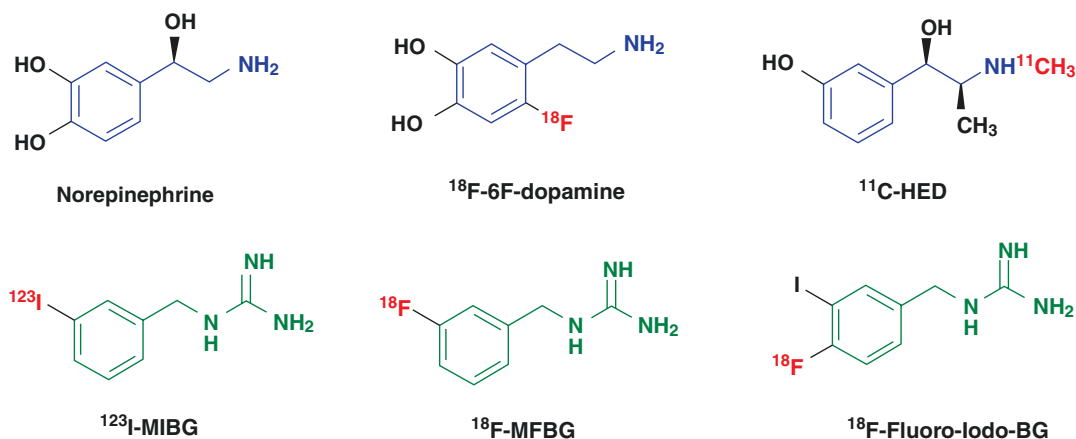
Fig. 14.21 Radiolabeled analogs of norepinephrine and dopamine for imaging studies in oncology

atom directly onto the benzylguanidine core structure: first, replace the iodine with fluorine directly to obtain ^{18}F-meta- and para-fluorobenzylguanidine ([^{18}F]MFBG and [^{18}F] PFBG) (Fig. 14.21) [166]; or add an additional fluorine to the MIBG structure to get [18]F-(4-fuoro-3-iodobenzyl)guanidine ([^{18}F]FIBG) [167]. Preclinical PET studies demonstrated higher [^{18}F]MFBG tumor uptake, and tumor/normal ratios compared to [^{123}I]MIBG [168]. The first clinical study with [^{18}F]MFBG showed excellent in vivo stability and safety as well as a favorable biodistribution with good targeting of lesions in patients with NETs (Fig. 14.22). MFBG-PET/CT demonstrated high promise for imaging in patients, especially for children with neuroblastoma [169].

Preclinical studies with [^{18}F]FIBG demonstrated excellent tumor detectability and uptake comparable to MIBG. Moreover, [^{131}I]FIBG showed a greater therapeutic effect in malignant PCC than did [^{131}I]-MIBG [170]. These results support the potential usefulness of FIBG as a theranostic agent since both ^{18}F and ^{131}I can be labeled to the same targeting molecule FIBG.

[^{11}C]Hydroxyephedrine (HED)
HED is a norepinephrine analog (Fig. 14.21) that binds to the NET) [171]. HED-PET has shown high diagnostic potential in patients with PCC/PGL and neuroblastoma [172–174]. HED-PET can be used as an accurate tool for the diagnosis/

ruling out of PCC and PGL in complex clinical scenarios, in contrast to CT/MRI characterization. In a major study, HED PET/CT was performed in a cohort of 102 patients, where 19 patients were correctly identified as having PCC, 6 with PGL, and 75 successfully excluded from having either. [175]. Sensitivity, specificity, positive and negative predictive values of HED-PET/CT for PCC/PGL diagnosis was 96%, 99%, 96%, and 99%, respectively.

6-[^{18}F]Fluorodopamine (FDA)
FDA, a sympathoneural imaging agent developed at the National Institute of Health (NIH), is an analog of dopamine and a metabolite of FDOPA. In catecholamine-synthesizing cells, FDA is transported actively and avidly by, both, the plasma membrane NET and the intracellular vesicular monoamine transporter. It has also been shown that FDA is a better substrate for the cell membrane NET system when compared with most amines including NE and MIBG [176]. In 2001, the first clinical results using FDA-PET scanning for the diagnostic localization of PCC were reported [177]. In patients with known disease, FDA-PET scanning localized PCC with high sensitivity. In patients in whom the diagnosis of PCC is considered but excluded because of negative plasma metanephrine results, FDA-PET scans were consistently negative. Also, FDA-PET was found to show more promising results when compared with [[123/131]I]MIBG scintigraphy
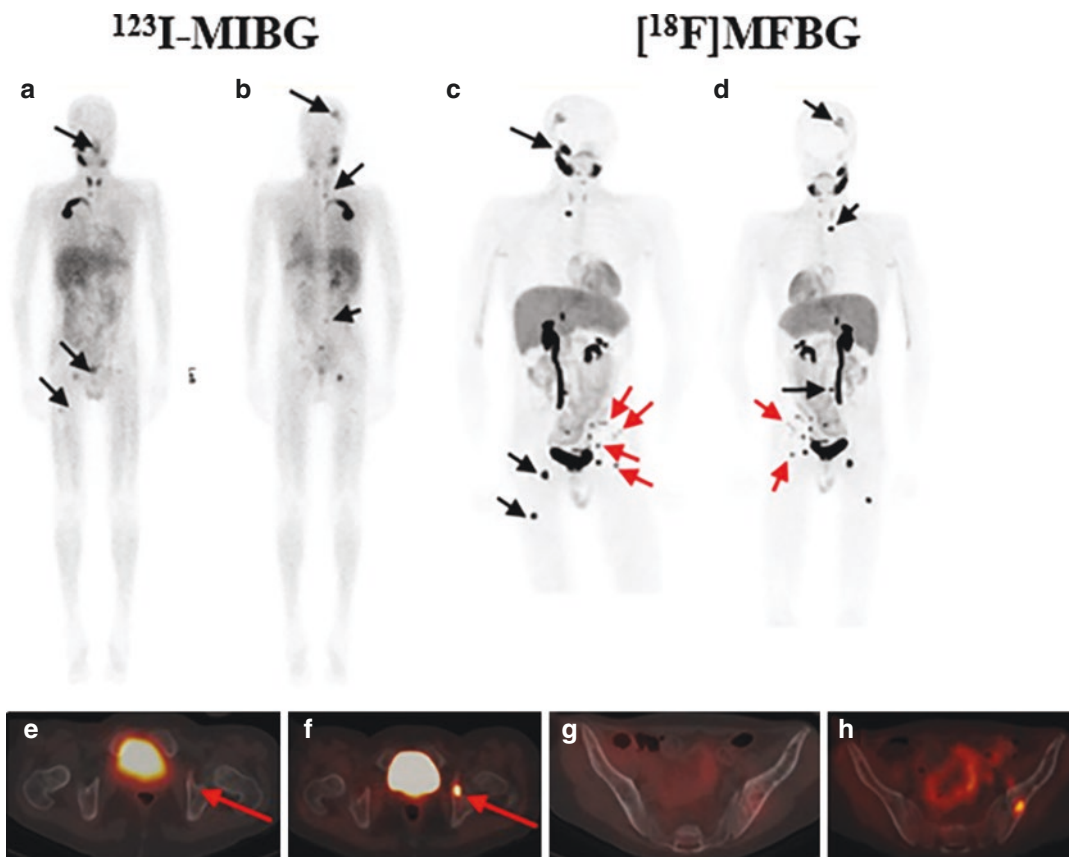
Fig. 14.22 ^{123}I-MIBG scan (**a**, **b**) vs. [^{18}F]MFBG-PET (**c**, **d**) in a patient with neuroblastoma. ^{123}I-MIBG images show foci of suspicious activity in skull, lumbar vertebra, right and left acetabula, and right femur (black arrows). [^{18}F]FMBG-PET (one week later) shows all lesions seen on ^{123}I-MIBG scan but with greater contrast and clarity (black arrows). Additional lesions (red arrows) are seen on MFBG-PET (F and H) that were not seen on MIBG-SPECT (**e**, **g**) (image modified from [169])

in the diagnostic localization of VHL-related adrenal PCC, with a 100% rate of localization [176]. In a head-to-head comparison between FDA and FDG, FDOPA, and MIBG scintigraphy, nonmetastatic paragangliomas (PGLs) were equally well localized by these techniques. For the detection of metastases seen on CT, however, FDA was superior to both FDOPA and MIBG scanning [178].

14.4.2.10 Estrogen Receptors

Breast cancer remains one of the most important health problems worldwide. In the family of steroid receptors (SRs), estrogen receptor (ER), progesterone (PR) and, androgen (AR) play a crucial role in the pathogenesis of the disease. They function predominantly as nuclear receptors to regulate gene expression, however, their full spectrum of action reaches far beyond this basic mechanism [179]. In breast cancer, the stimulatory effect of estrogen and progesterone are mediated through nuclear ER and PR. Estrogen produces many physiological effects primarily by regulating gene expression by binding to specific ERs. Therefore, ER expression is an important determinant of breast cancer behavior and is critical for response to endocrine therapies. Breast cancer endocrine therapy is based on targeting ER. The major drugs in use are tamoxifen (selective estrogen receptor modulator—SERM), acting mostly as an ER antagonist, and aromatase inhibitors (AIs) which repress the synthesis of

Fig. 14.23 Chemical structures of estradiol and 16α-[18F]Fluoro-17β-Estradiol (FES), a PET radiotracer to image estrogen receptors in patients with breast cancer
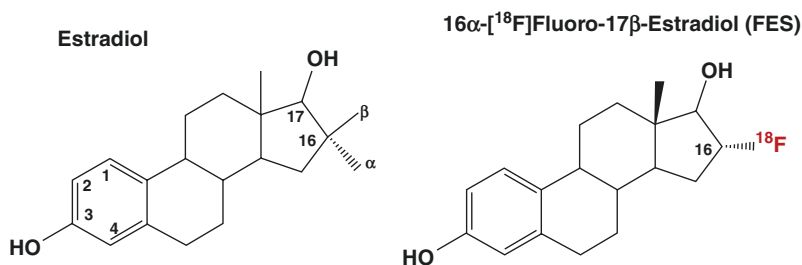
ER ligands by blocking the conversion of androgens to estrogens [179, 180].

Estrogen is predominantly a sex hormone produced in the ovaries of females and in testes of males. Estradiol (Fig. 14.23), the most potent form of estrogen in the body binds to ERs found in the cell nucleus of the female reproductive tract, breast, pituitary, hypothalamus, bone, liver, and other tissues, as well as in various tissues in men [181]. For decades, it was assumed there was only one type of ER known as αER. However, a second ER form, βER, found to bind estradiol with a comparable K_d to αER, was also described. Like αER, βER is a nuclear receptor that looks nearly identical to alpha in its so-called DNA-binding domain, the segment of the receptor that acts as a genetic switch, flicking some genes on and some genes off. While the αER predominates in the uterus and mammary gland, the βER is mostly in the ovaries, the testes, and also in osteoblasts.

The growth of breast epithelial cells is an estrogen-mediated process that depends on estrogen acting through an ER and results in the induction of a PR. The ER status is an important prognostic factor in breast cancer because ER+ tumors have a slower rate of growth and are likely to respond to hormonal therapy [181]. The main mechanism of action of antiestrogen tamoxifen is believed to be the blockade of the division of estrogen-dependent tumor cells with arrest in the G_0 or G_1 phase of the cycle. However, 30–40% of all breast cancers do not express estrogen receptors (EŘ), and of the tumors with ER+, up to 50% will not respond to endocrine treatment [182].

More than 70% of primary breast cancers are hormone-receptor positive and determination of ER status in a primary breast lesion is an integral part of the initial patient workup. Breast tissue is relatively easy and safe to biopsy, and immunohistochemical (IHC) analysis is consequently standardized. Despite a favorable prognosis and effective therapies available for ER-positive breast cancer, metastatic breast cancer (MBC) from an ER-positive primary tumor is responsible for the majority of breast cancer–related deaths [183]. Hormone receptor-directed therapy can only be effective if there is ER expression in metastatic lesions. Because there are many classes of treatment options for patients with breast cancer metastases, a noninvasive method which would accurately evaluate and quantify the presence of ER on the tumor and its metastases could help in the selection of patients for treatment and in predicting the therapeutic response [184].

16α-[18F]Fluoro-17β-Estradiol (FES, Cerianna™)

In the last 40 years, a number of steroidal and nonsteroidal estrogens have been labeled with positron-emitting halogens. Retention of radiolabeled estradiol in estrogen target tissues through specific binding on the αER target was first reported in 1967 [185]. Estradiol and its derivatives are lipophilic and transported in the bloodstream bound either to a sex hormone-binding protein (SBP) or to albumin. SBP binding protects steroids against liver metabolism and ensures their transport to the target tissues. Moreover, their affinity for SBP also contributes to their cell uptake, through membrane receptors for SBP [181]. SBP receptors are present in a higher percentage of ER+ tumors (75%) than in ER-tumors (37%). Thus, membrane sequestration of estradiol is likely to occur preferentially in hormone-responsive tumors.

The most promising radiolabeled estrogen analog, identified to date is 16α-[^{18}F]fluoro-17β-estradiol (FES) (Fig. 14.23), which has good ER-binding affinity and can be prepared effectively with a higher SA [186, 187]. A number of clinical trials have documented the potential utility of FES-PET to identify ER+ breast tumors. FES-PET, however, is not necessarily an optimal tracer due to its rapid conversion to circulating radiometabolites, which prevent optimal localization of the tracer at ER-binding sites [187]. FES-PET assesses ER functioning in a manner analogous to in vitro ligand-binding assays and several reports clearly showed the FES-PET method to be an excellent noninvasive method for determining ER status in multiple lesions throughout the body (with the exception of the liver, whence it is cleared) [183]. ER positivity by [^{18}F]FES

PET has been shown to predict beyond the standard clinical and pathological predictors, longer progression-free survival (PFS) on endocrine monotherapy, potentially impacting therapy choices in patients with a clinical dilemma. Positive status percent agreement between the [^{18}F]FES PET-CT results and ER status by immunohistochemical assay was 76·6% and the negative status percent agreement was 100.0% [188]. Comparison of FES-PET and FDG-PET in a patient with breast cancer metastases is shown in Fig. 14.24.

The ^{18}F-FES PET scan—approved by the FDA in 2020—was shown to solve 87% of dilemmas, providing physicians with information for personalized treatment decision-making. [^{18}F]FES is indicated for the detection of ER-positive lesions as an adjunct to biopsy in patients with recurrent or metastatic breast cancer.
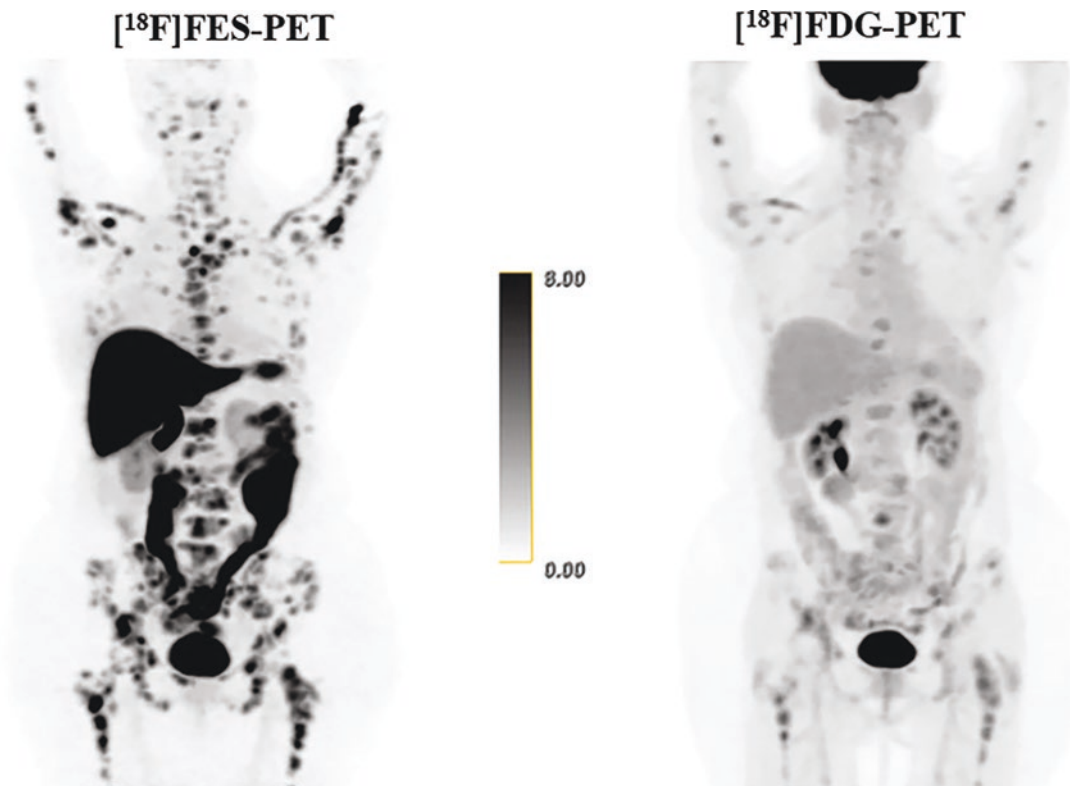

Fig. 14.24 Comparison of estrogen receptor (ER) imaging with glucose metabolism in a patient with breast cancer metastases. [^{18}F]FES-PET shows significantly more metastatic lesions and tumor burden compared to [^{18}F]FDG-PET (Figure from [189])

14.4.2.11   Somatostatin Receptors

The most characteristic feature of neuroendocrine neoplasms (NENs) is the homogeneous overexpression of specific G-protein coupled peptide hormone receptors (PHRs) on the tumor cell surface [190]. The PHRs control hormone secretion and cell proliferation in NENs and represent molecular targets for the development of diagnostic and therapeutic radiopharmaceuticals. Somatostatin receptors (SSTRs) are the best-known and well-studied PHRs in neuroendocrine tumors (NETs). Most of the NETs are characterized by the expression of SSTRs on the cell membrane, and five different, G-protein-coupled SSTR subtypes (SSTR 1–5) have been identified [191]. However, SSTR-2 is the most common receptor subtype expressed in around 90% of GEP-NENs. The expression of SSTRs is less frequent and in lower density in poorly differentiated compared to well-differentiated subtypes. Lung NENs also express SST with the subtypes 2, 3 and 5 being the most common.

Lower expression of SSTRs has been shown in pheochromocytoma, medullary thyroid cancer (MTC) and benign insulinomas.

The natural ligand somatostatin (SST), a neuropeptide, also known as somatotropin release-inhibiting factor (SRIF), was originally discovered in 1973 as a hypothalamic neuropeptide based on its ability to inhibit growth hormone (GH) release from the anterior pituitary [192]. The clinical utility of native human SST-14 was limited by its short half-life (<3 min). The investigators at Sandoz (Novartis) synthesized the first agonist analog octreotide (SMS 201-995, Sandostatin), a longer-acting fragment of the eight amino acid ring of the native SST [193]. The amino acid sequence of SST and its analogs is shown in Fig. 14.25. The amino acid, lysine, within the ringed portion is considered to be the primary peptide-binding site of SST, octreotide, and lanreotide to the SSTR-2A, the most prevalent receptor of the five SSTR subtypes on neuroendocrine cells and their NETs. The synthetic
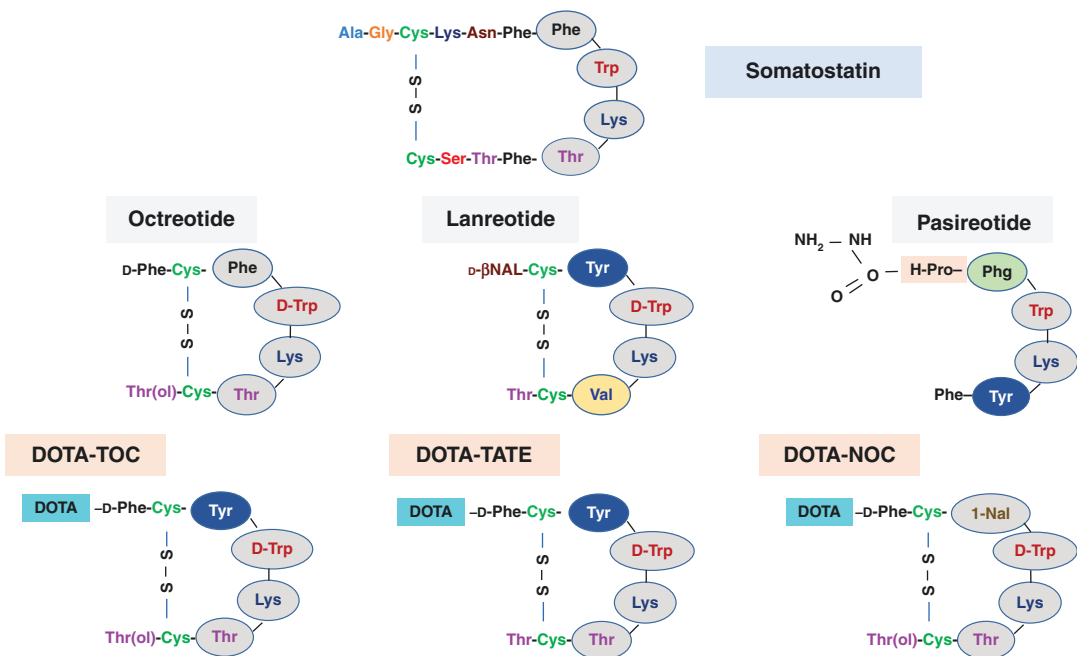

Fig. 14.25 The amino acid sequence of somatostatin (SST) and synthetic analogs of somatostatin. Octreotide, lanreotide, and pasireotide are used for therapy in patients with neuroendocrine tumors (NETs). DOTA-TOC, DOTA-TATE, and DOTA-NOC can be labeled with ^{68}Ga and ^{64}Cu for PET imaging studies and ^{90}Y, ^{177}Lu, and ^{225}Ac for targeted radionuclide therapy

Table 14.7 Somatostatin analogs: affinity profiles IC_{50}^{a} for the somatostatin receptor (SSTR) subtypes

Peptide	SSTR1	SSTR2	SSTR3	SSTR4	SSTR5
Somatostatin	5.2	2.7	7.7	5.6	4.0
Octreotide	>1000	0.4	4.4	>1000	5.6
DTPA-octreotide	>10,000	12	376	>1000	299
DOTA-TOC	>10,000	14	880	>1000	393
DOTA-TATE	>10,000	1.5	>1000	433	>1000
DOTA-NOC	>10,000	1.9	40	260	7.2
In-DTPA-octreotide	>10,000	22	182	>1000	237
Ga-DOTA-TOC	>10,000	2.5	613	>1000	60
Ga-DOTA-TATE	>10,000	0.2	<1000	300	377
Ga-DOTA-NOC	>1000	1.9	40	260	7.2
In-DOTA-JR11	>1000	3.8	>1000	>1000	>1000
Ga-DOTA-JR11 (Ga-OPS201)	>1000	29	>1000	>1000	>1000
Ga-NODAGA-JR11 (Ga-OPS202)	>1000	1.2	>1000	>1000	>1000

[a] IC_{50} values expressed in nanomoles [191, 194]

octapeptide SST analogs (SSAs) have a similar STTR-binding profile, with high SSTR2 and moderate SSTR5 affinity (Table 14.7). Both, octreotide and lanreotide, are very effective FDA-approved drugs for hormonal syndrome control in functioning tumors and exert an antiproliferative effect by inducing cell cycle arrest and apoptosis, and through immunomodulatory effects, and angiogenesis inhibition [195]. Octreotide and other SST synthetic analogs are potent agonists, and selectively bind to SSTR-2 and 5 receptor subtypes. The binding of agonists leads to receptor-mediated internalization and intracellular trapping of the radionuclide providing adequate time for imaging studies. In contrast, the SSTR antagonist is not internalized but, may offer the possibility to bind to more receptor sites and with a longer retention time [196]. The following SSTR agonist peptide radiopharmaceuticals are in clinical use. The high-level expression of SSTRs 2 and 5 on the tumor cell surface in most neuroendocrine tumors (NETs) provides the basis not only for sensitive functional imaging but, also for a tumor-targeted therapy with commonly "cold", as well as radioisotope-labeled "hot" somatostatin analogs.

Following the discovery of octreotide in 1982 at the Sandoz Research Institute in Basel, Switzerland, Jean Claude Reubi and colleagues demonstrated, for the first time, based on autoradiography, the presence of SSTR receptors on the surface of intestinal NET) cells using ^{125}I-octreotide [197]. Subsequently, the investigators at the Erasmus University Medical Center (EUMC) in Rotterdam developed [^{123}I-Tyr[3]] octreotide as an imaging agent to localize NETs. Due to biliary excretion and intestinal accumulation of I-123 activity, [^{123}I-Tyr[3]]octreotide, however, was not ideal for the detection of lesions in the abdomen.

^{111}In-DTPA-Octreotide (OctreoScan™)

Since ^{111}In is an ideal radiometal for SPECT imaging studies, the investigators at EUMC developed the DTPA conjugated derivative of octreotide (SDZ 215-811), as a precursor for ^{111}In labeling. Dr. Krenning's team at EUMC performed planar and SPECT imaging studies with [^{111}In-DTPA-D-Phe[1]]octreotide (also known as ^{111}In-pentetreotide) in more than 1000 patients with NETs [5].

OctreoScan was studied in nine unblinded clinical studies in a total of 365 patients. The most common tumors were carcinoids (132 of 309 evaluable patients). Scintigraphic results were compared to results of conventional localization procedures (CT, ultrasound, MRI, angiography, surgery and/or biopsy). OctreoScan results were consistent with the final diagnosis (success) in 86.4% of evaluable patients (OctreoScan, package insert, 12/2018). In 1994, the FDA approved ^{111}In-pentetreotide as an agent for the scintigraphic localization of primary and

metastatic NETs-bearing SSTRs. OctreoScan was the first peptide-based radiopharmaceutical ever approved for peptide receptor scintigraphy (PRS) for localization of primary and metastatic NETs-bearing SSTRs.

^{68}Ga-DOTATOC

In the late 1990s several octreotide analogs conjugated with DOTA chelator were introduced in order to develop ^{90}Y-labeled SST analog for PRRT. Among these SST analogs, DOTATOC was shown to be suitable for labeling with either ^{90}Y or ^{67}Ga [198]. DOTATOC exhibits high affinity (IC_{50}) for human SSTR-2 (14 ± 2.6 nM) with much lower binding affinity for all other human SSTRs (Table 14.7). A marked improvement of SSTR-2 affinity was found for Ga-DOTATOC (2.5 nM) compared with OctreoScan (22 nM) [199]. In 2001, it was reported that ^{68}Ga-DOTATOC-PET results in high tumor to nontumor contrast and low kidney accumulation and yields higher detection rates (>30% more lesions) as compared with OctreoScan scintigraphy [200]. Since its introduction, ^{68}Ga-DOTATOC has been extensively used in Europe in the last two decades. A systematic review and meta-analysis concluded that ^{68}Ga-DOTATOC is useful for evaluating the presence and extent of disease for staging and restaging, and for assisting in the treatment decision-making for patients with NETs [201].

^{68}Ga-DOTATOC was approved in several European countries in 2016 (IASOtoc®) and in 2018 (TOCscan®). Also, in Europe, a kit preparation for ^{68}Ga-labeling of DOTATOC (SomaKit TOC®) was approved by the European Medicines Agency (EMA) in 2016. Use of this kit along with an authorized ^{68}Ge/^{68}Ga-generator enables on-site preparation of ^{68}Ga-DOTATOC. In the United States, the FDA approved the ready-to-use ^{68}Ga-DOTATOC in August of 2019. Holder of the NDA (New Drug Application) or marketing authorization is the UIHC–PET Imaging Center (University of Iowa Health Care (UIHC)), in Iowa, USA [202]. It is indicated for use with PET for the localization of SSTR-positive NETs in adult and pediatric patients. The safety and efficacy of ^{68}Ga-DOTATOC Injection were established in two single-center, open-label studies in which 282 patients with known or suspected SSTR-positive NETs received a single dose. A total of 238 of the 282 patients (84%) had a history of neoplasm at the time of Ga-68 DOTATOC imaging.

^{68}Ga-DOTATATATE (NetSpot)

DOTATATE is an SST analog and an SSTR agonist that closely simulates DOTATOC, in which the C-terminal threoninol (an amino alcohol) is replaced by threonine (Fig. 14.26). This chemical modification resulted in a ninefold higher affinity (1.5 nM) for the SSTR-2 as compared with DOTATOC (14 nM). Also, the affinity of Ga-DOTATATE (0.2 nM) for SSTR-2 is 12 times higher compared to that of Ga-DOTATOC (2.5 nM) [199]. Direct comparison of PET/CT studies with ^{68}Ga-DOTATOC and ^{68}Ga-DOTATATE suggests that both these radiotracers possess a comparable diagnostic accuracy for the detection of NET lesions, with ^{68}Ga-DOTATOC having a potential advantage.

In June 2016, the FDA approved ^{68}Ga-DOTATATE (NETSPOT™) (Fig. 14.27) for the localization of SSTR-positive NETs in adult and pediatric patients [203, 204]. NETSPOT™ is the new market name for Somakit-TATE (a kit for the preparation of ^{68}Ga-dotatate injection using ^{68}Ga chloride from the GalliaPharm ^{68}Ga/^{68}Ga generator from Eckert & Ziegler). ^{68}Ga-dotatate received Orphan Drug Designation from both the FDA and the European Medicines Agency (EMA) in March 2014. The efficacy of NETSPOT was established in three open-label single-center studies in patients with known or suspected NETs. ^{68}Ga-Dotatate is indicated for use with PET for the localization of SSTR-positive NETs in adult and pediatric patients. ^{68}Ga-Dotatate PET scans detect more SSTR-positive metastatic lesions compared to ^{111}In-OctreoScan. (Fig. 14.28). In patients with poorly differentiated NETs, ^{68}Ga-Dotatate scans may be SSTR-negative but, FDG-PET scans clearly identify the aggressive NET tumors (Fig. 14.29) [206].

^{68}Ga-DOTA-NOC

[DOTA^0,1-Nal^3]-octreotide (DOTANOC) is a peptide that has the potential to target a broader

SSTR Agonists

Octreotide: d-Phe^1-Cys^2-Phe^3-D-Trp^4-Lys^5-Thr^6-Cys^{7}Thr(ol)^8

DOTA-TOC: d-Phe^1-Cys^2-Tyr^3-D-Trp^4-Lys^5-Thr^6-Cys^{7}Thr(ol)^8

DOTA-TATE: d-Phe^1-Cys^2-Tyr^3-D-Trp^4-Lys^5-Thr^6-Cys^{7}Thr^8

SSTR Antagonists

SSTR-2-ANT (BASS): p-NO$_2$-Phe^1-D-Cys^2-Tyr^3-D-Trp^4-Lys^5-Thr^6-Cys^7-d-Tyr^8-NH$_2$

LM3 p-Cl-Phe^1-D-Cys^2-Tyr^3-D-Aph^4(Cbm)-Lys^5-Thr^6-Cys^7-d-Tyr^8-NH$_2$

JR10 p-NO$_2$-Phe^1-D-Cys^2-Tyr^3-D-Aph^4(Cbm)-Lys^5-Thr^6-Cys^7-d-Tyr^8-NH$_2$

JR11 (Satoreotide) p-Cl-Phe^1-D-Cys^2-Aph^3(Hor)-D-Aph^4(Cbm)-Lys^5-Thr^6-Cys^7-d-Tyr^8-NH$_2$

Fig. 14.26 The amino acid sequences of somatostatin receptor (SSTR) agonists and antagonists

Fig. 14.27 The chemical structure of radiometal (^{68}Ga, ^{64}Cu, or ^{177}Lu)-labeled DOTA-TATE (DOTA-Tyr^3-octreotide) complex
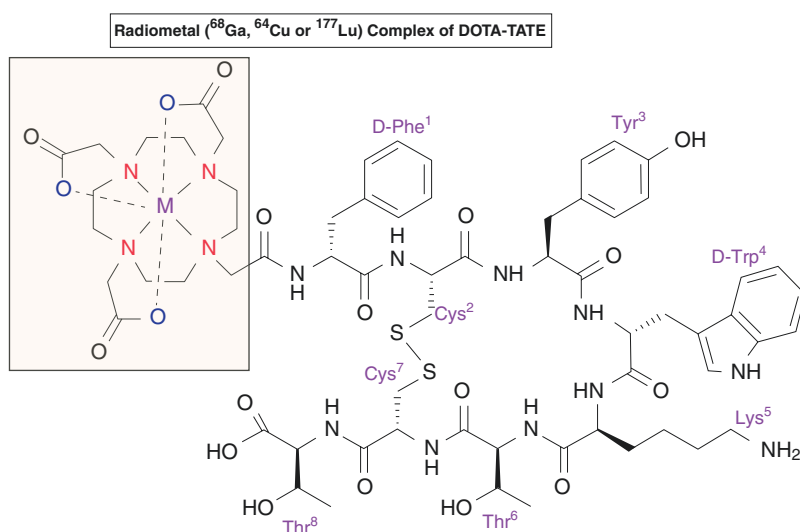
range of SSTR subtypes, including SSTR-2,3, and 5 [207]. The affinity for SSTR-2,3, and 5 are 1.9, 40, and 7.2 nM respectively (Table 14.7). Direct comparison with ^{68}Ga-DOTATOC and ^{68}Ga-DOTATATE PET studies in patients with NETs indicated that ^{68}Ga-DOTANOC detects more metastases than do SSTR-2-specific tracers [208, 209]. Based on a retrospective study of patients with NETs (n = 445) who underwent ^{68}Ga-DOTANOC PET/CT, it was concluded that ^{68}Ga-DOTANOC PET/CT is a highly sensitive and specific study for the diagnosis and follow-up of patients with NETs [210]. The sensitivity, specificity, negative-predictive value, and
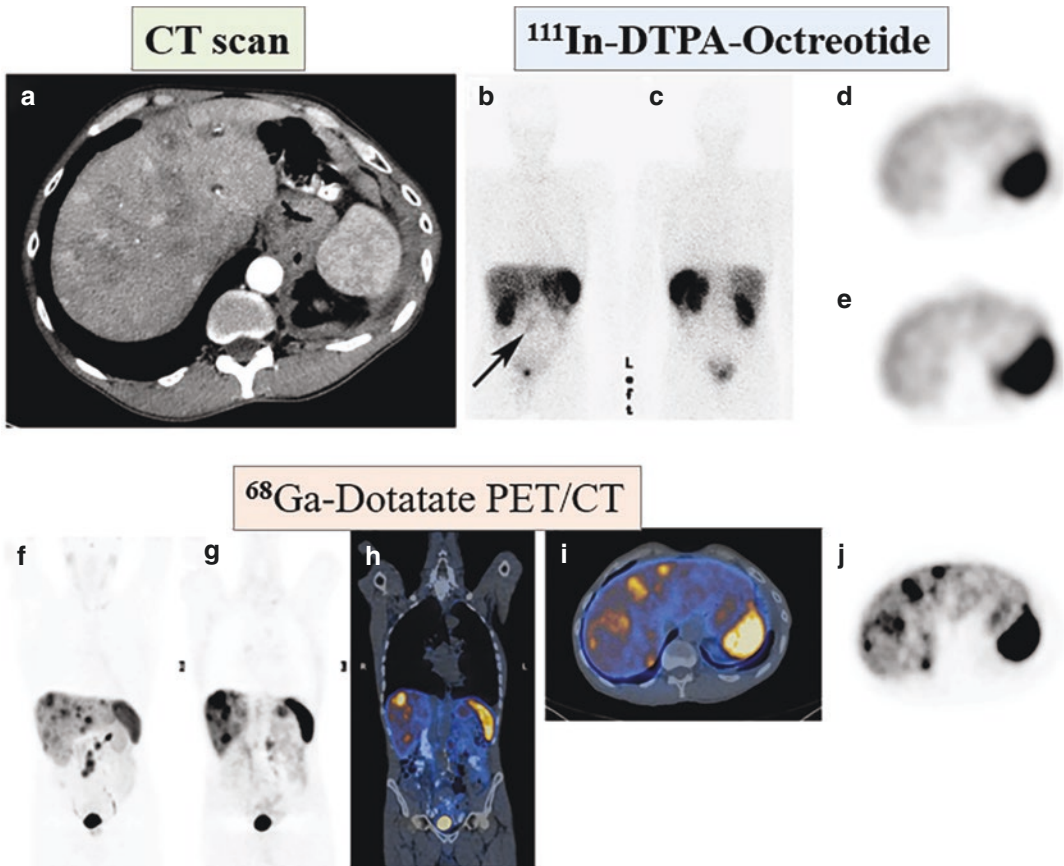
Fig. 14.28 Comparison of ^{68}Ga-Dotatate-PET with ^{111}In-DTPA-octreotide in a patient with low-grade metastatic midgut neuroendocrine tumor (NET)). (**a**) Arterial-phase CT shows multiple arterially enhancing and low-attenuation liver metastases. (**b**, **c**) Anterior and posterior whole-body planar ^{111}In-DTPA-octreotide scintigraphy shows low-grade mesenteric metastases but, no liver metastases. (**d**, **e**) Axial SPECT at level of spleen shows heterogeneous liver uptake with no discernable liver deposits. (**f–h**) ^{68}Ga-DOTATATE PET shows multiple deposits in liver and mesentery. (**g**) Coronal PET anterior to kidney shows multiple liver metastases. (**h**) ^{68}Ga-DOTATATE PET/CT of **g**. (**i**) Axial PET/CT at level of spleen shows multiple liver metastases. (**j**) Axial PET at level of spleen shows multiple liver metastases [205]

positive-predictive value of were 87, 98, 80, and 99%, respectively.

[64]Cu-DOTATATE (DetectNet)

The relatively longer half-life and low positron energy ($T\frac{1}{2} = 12.7$ h; $0.653\ \beta^+$) of ^{64}Cu is appropriate for PET imaging. The initial studies with ^{64}Cu-TETA-octreotide showed high rate of lesion detection, sensitivity, and favorable dosimetry and pharmacokinetics [211]. Since ^{64}Cu forms more stable complex with DOTA chelator, ^{64}Cu-DOTATATE has been studied as a potential PET radiotracer for SSTR-based imaging. The first human study clearly supports the clinical use of ^{64}Cu-DOTATATE for PET studies with excellent imaging quality, reduced radiation burden, and increased lesion detection rate when compared with OctreoScan [212, 213].

In a head-to-head comparison with ^{68}Ga-DOTATOC-PET in patients with NETs, ^{64}Cu-DOTATATE-PET scans detected more lesions although patient-based sensitivity was the same for both agents. [214]. Recently in a prospective trial in patients with Known or Suspected SSTR-positive NETs PET/CT scan with ^{64}Cu-DOTATATE was considered a safe imaging
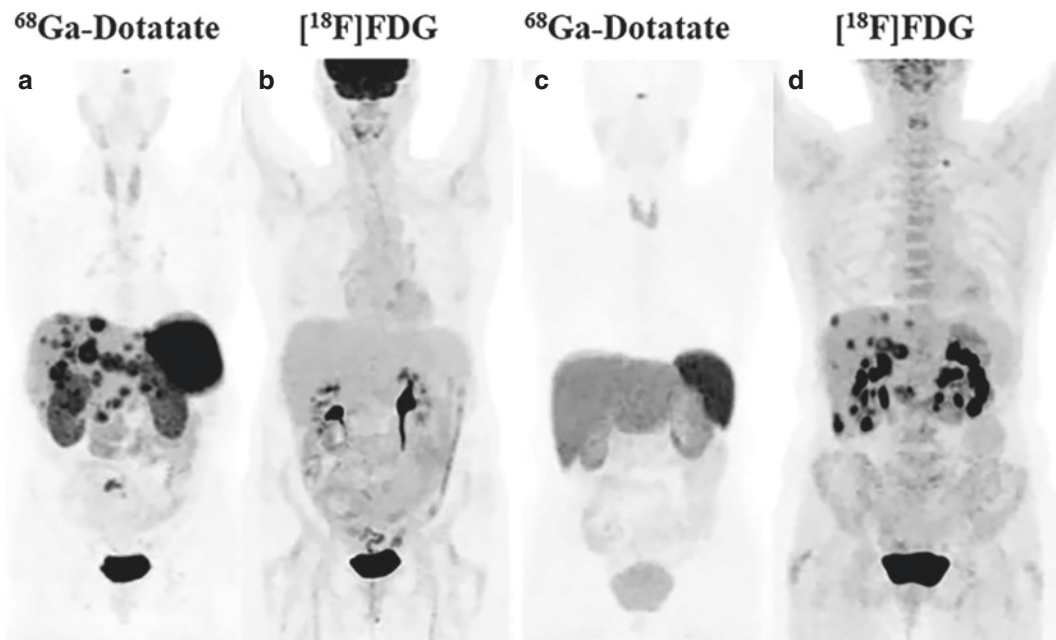
Fig. 14.29 Patterns of ^{68}Ga-Dotatate-PET and [^{18}]FDG-PET in NETs. In the first patient (**a**, **b**) with grade 1 (Ki-67 <1%) well-differentiated NET), the scans demonstrate SSTR-positive and FDG-negative phenotype, while in the second patient (**c**, **d**) with a poorly differentiated grade 3 NET) (Ki-67, 70%), the scans demonstrate SSTR-negative and FDG-positive phenotype (From [206])

technique that provides high-quality and accurate images at a dose of 148 MBq (4.0 mCi) for the detection of SSTR expressing NETs [215]. The lower positron energy of ^{64}Cu compared to that of ^{68}Ga (0.65 vs. 1.90 MeV), which translates to lower positron range (0.56 vs. 3.5 mm), is thought to explain the anticipated improved spatial resolution and diagnostic performance of ^{64}Cu-DOTATATE (Fig. 14.30) Additionally, the longer physical half-life of ^{64}Cu (12.7 h) may increase the shelf-life of ^{64}Cu-DOTATATE, and provide a more flexible scanning window, making it attractive for routine clinical imaging.

In September 2020, the FDA has approved ^{64}Cu-DOTATATE injection (DetectNet) for the localization of SSTR-positive NETs. Two single-center, open-label studies confirmed the efficacy of the diagnostic agent. The results of the study-1 ($n = 63$) showed that the percent reader agreement for positive detection was 91% and negative detection was 80–95%. Study-2 was a retrospective analysis in which investigators examined published findings collected from 112 patients and the results demonstrated similar performance as in study-1 (Detectnet, package insert 2020).

SSTR Antagonists
While the agonists activate SSTRs and internalize into tumor cells, the antagonists interact with SSTRs, and block or reduce the physiological effect of an agonist [216]. It has been shown that potent SSTR antagonists, known to poorly internalize into tumor cells, may be as good as, or even superior to, agonists for developing radiopharmaceuticals for imaging and therapy, and some antagonist analogs show rapid blood clearance, poor kidney retention, and better accumulation in the tumor tissue [194, 196].

The second generation of antagonists include LM3, JR10, and JR11. The amino acid sequence of these antagonists is shown in Fig. 14.26. Among the radiolabeled SSTR-2 antagonists investigated, the analog JR11 performed the best in preclinical settings. PET/CT with ^{68}Ga-NODAGA-JR11 (or ^{68}Ga-OPS202) detected significantly more metastases with higher tumor-
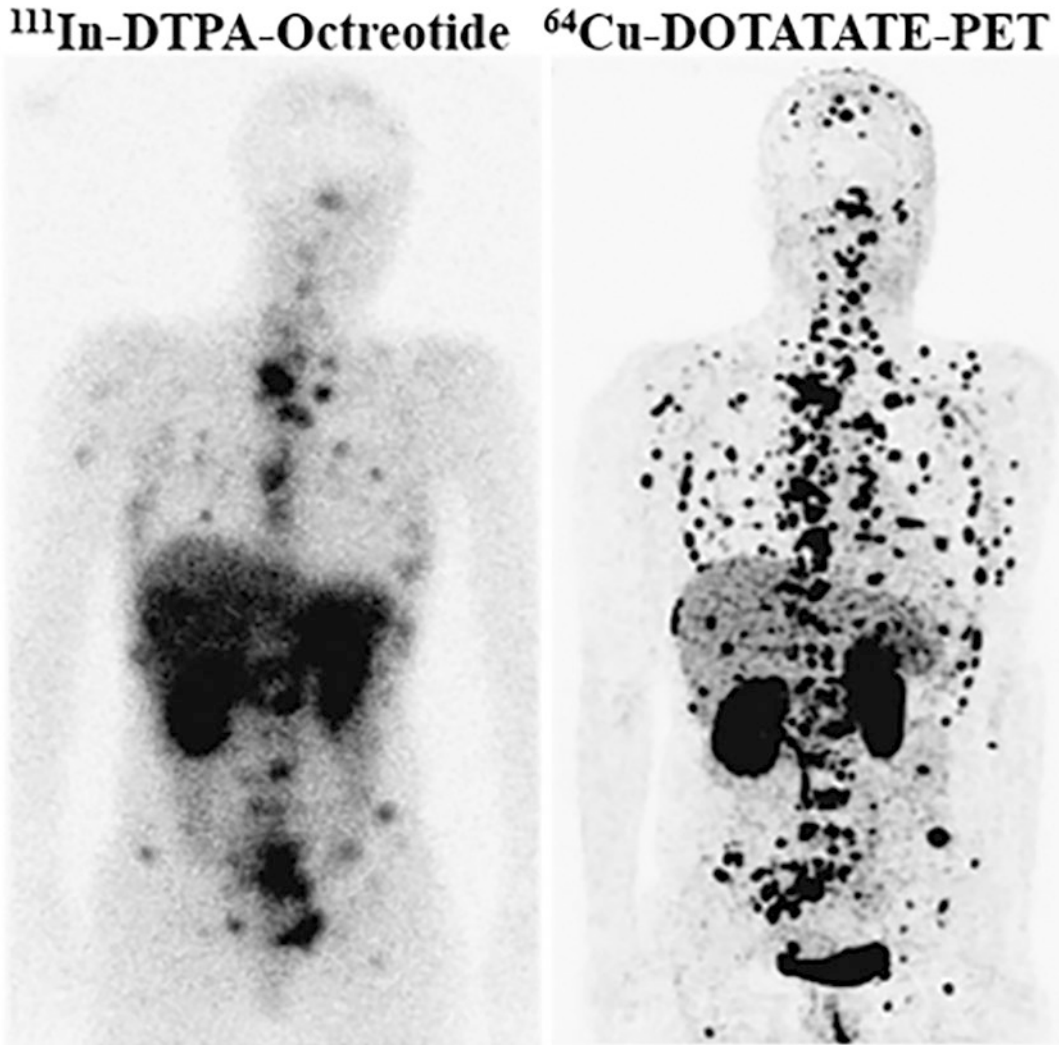
^{111}In-DTPA-Octreotide ^{64}Cu-DOTATATE-PET

Fig. 14.30 Comparison of ^{64}Cu-DOTATEPET and ^{111}In-DTPA-Octreotide (OctreoScan) in the same patient with NETs with multiple bone and soft tissue metastases (from [212])

to-background ratios than the SSTR agonist ^{68}Ga-DOTATOC [217] (Fig. 14.31).

Since the SSTR-2 affinity of ^{68}Ga-NODAGA-LM3 was tenfold higher than that of ^{68}Ga-DOTA-LM3, a phase 1 study compared the biodistribution of these two agents [218]. Both tracers showed favorable biodistribution, high tumor uptake, and good tumor retention, resulting in high image contrast, and good tumor uptake and retention.

14.4.2.12   Glucagon-Like Peptide 1 Receptor (GLP-IR)

GLP-1 is a neuropeptide hormone composed of 36 AAs and stimulates insulin secretion from beta cells after nutrient intake through the GLP-1 receptor [219]. The corresponding receptor (GLP-1R) is a member of the G protein-coupled receptor family and was found to be overexpressed in insulinoma, an unusually benign insulin-secreting NET of the pancreas.
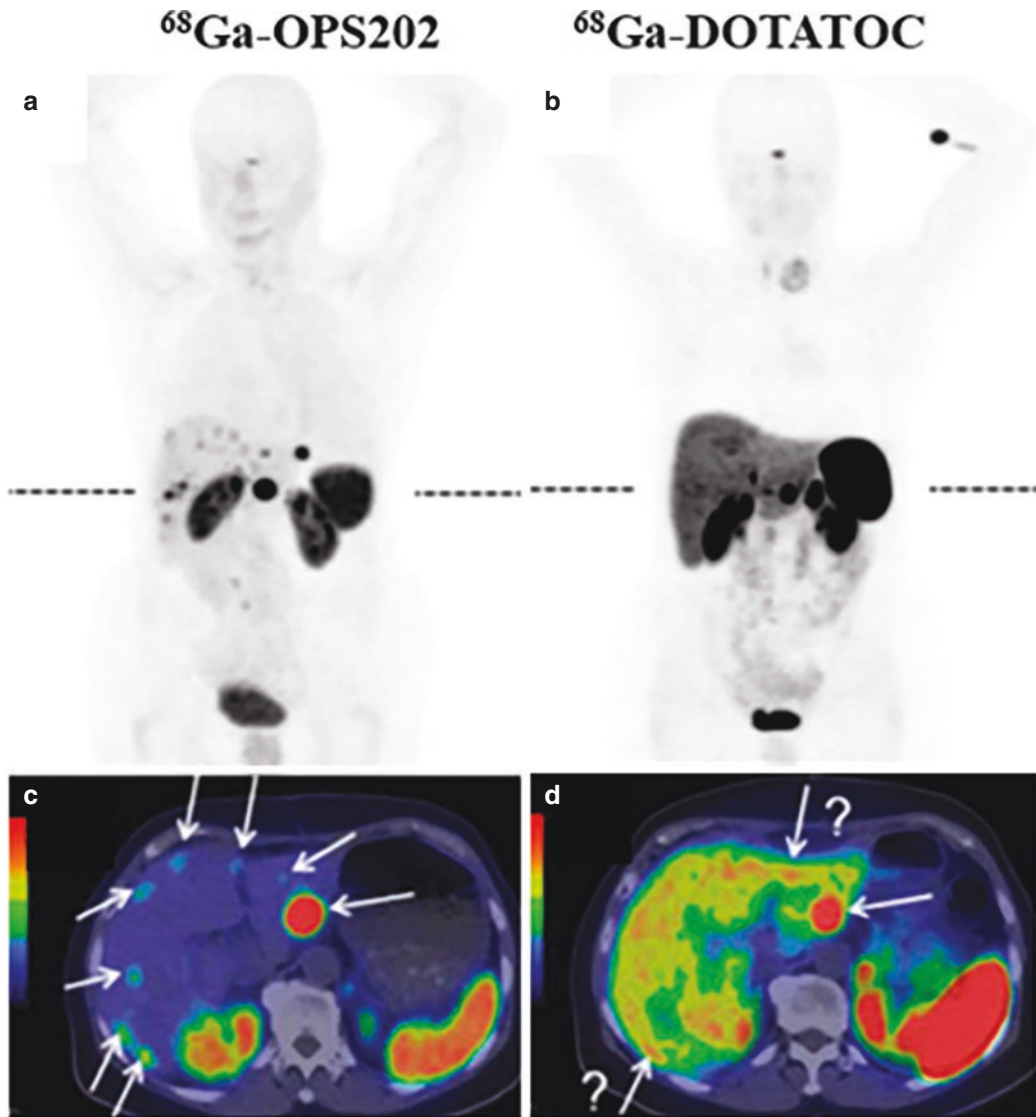
Fig. 14.31 [^{68}Ga]Ga-OPS202 PET/CT (**a**, **b**) and [^{68}Ga]Ga-DOTATOC PET/C.T (**c**, **d**) images of a patient with ileal neuroendocrine tumors, showing bilobar liver metastases (dashed lines indicate level of transaxial slices). Studies were performed on the same scanner within 2 months. With the antagonist, OPS-202, the background activity was lower in liver, intestine, and thyroid than with agonist DOTATOC allowing better identification of the lesions in the liver which are confirmed by subsequent MRI. (Figure modified from [217])

Gastrinomas, pheochromocytoma, PGL and MT carcinomas also express GLP-1Rs but, with lower density and/or incidence. The native ligand GLP-1 has a short half-life ($\leq$2 min) in humans owing to rapid degradation by dipeptidyl-peptidase-4 (DPP4). However, GLP-1 stable analogs (containing 39 AAs) have been synthesized for the GLP-1R targeting, from which exendin-4 (agonist) and exendin-3 (antagonist) have been widely studied [220]. Exendin-4 has been radiolabeled with several radionuclides (^{99m}Tc, ^{111}In, and ^{68}Ga) to develop radiopharmaceuticals for imaging insulinoma [221, 222]. The first exendin-4–based imaging tracer that was developed is the [Lys^{40}(Ahx-DTPA-[^{111}In]In)NH$_2$]-exendin-4 [223].

In a proof-of-principle study ^{68}Ga-DOTA-exendin-4 PET/CT showed better performance compared with ^{111}In-DOTA-exendin-4 SPECT/CT [224]. The diagnostic accuracy of ^{68}Ga-DOTA-exendin-4 PET/CT was evaluated in a prospective crossover imaging study in patients (*n* = with occult insulinomas [225]. In this prospective study, the accuracy of ^{68}Ga-DOTA-exendin-4 PET/CT was 93.9% which was significantly higher than for ^{111}In-DOTA-exendin SPECT/CT (67.5%) and MRI (67.6%). Another study with ^{68}Ga-NOTA-exendin-4 PET/CT reported an excellent sensitivity of more than 97% [226].

14.4.2.13   Chemokine Receptor-4 (CXCR-4)

Chemokines and their receptors were originally identified as mediators of inflammatory diseases and are being increasingly recognized as serving a critical communication bridge between tumor cells and stromal cells to create a favorable microenvironment for tumor growth, and metastasis [227]. Chemokine receptors with seven transmembrane domains are found on the surface of certain cells that interact with a type of cytokine, called a chemokine. There have been 20 distinct chemokine receptors discovered in humans and they were divided into 4 different families (C, CC, CXC, CX3C) [228]. Chemokine receptor 4 (CXCR4) is a member of G-protein coupled receptors which are involved in several physiological functions, such as cell migration, alteration of gene expression, and cell skeleton rearrangement via interaction with its ligand, CXCL12, also known as stromal cell-derived factor-1α (SDF-1α). The interactions between CXCL12 and CXCR4 comprise a biological axis that affects the growth, angiogenesis and metastasis of cancer [229]. Overexpression of CXCR4 has been reported in a variety of malignancies. Therefore, CXCR4 is an ideal target for tumor imaging and therapy.

In the last decade, several radiolabeled peptides for targeting CXCR4 receptor have been developed. Among several antagonists evaluated, the cyclic pentapeptide analog $cyclo(D\text{-}Tyr^1\text{-}D\text{-}[NMe]Orn^2(AMBS\text{-}[^{68}Ga]DOTA)\text{-}Arg^3\text{-}Nal^4\text{-}Gly^5)$ (^{68}Ga-PentixaFor)

showed high affinity and selectivity for human CXCR4, and rapid renal excretion [230]. In patients with small cell lung cancer (SCLC), ^{68}Ga-PentixaFor was positive in 8/10 patients and revealed more lesions with significantly higher tumor-to-background ratios than SSTR-PET [231]. In a study involving 12 patients with GEP NENs, SSTR-PET was clearly superior compared to FDG-PET and ^{68}Ga-Pentixafor, respectively. While CXCR4 was negative in all grade-1 patients, 50% of grade 2 patients, and 80% of grade 3 patients showed ^{68}Ga-Pentixafor-positive lesions [232]. In poorly differentiated neuroendocrine carcinomas, ^{68}Ga-PentixaFor PET/CT was inferior to FDG-PET/CT [233] (Fig. 14.32). ^{68}Ga-pentixafor-PET is positive in a patient with SCLC compared to SSTR-PET with ^{68}Ga-DOTATOC (Fig. 14.32 and 21.22) [231].

14.4.2.14   Prostate-Specific Membrane Antigen (PSMA)

PSMA was discovered in 1987 as a novel antigenic marker in prostate cancer cells and in the serum of prostate cancer patients. PSMA is also known as glutamate carboxypeptidase II (GCPII), N-acetyl-L-aspartyl-L-glutamate peptidase I (*NAALADase I*), or N-acetyl-aspartyl-glutamate (NAAG) peptidase, which is an enzyme that is encoded by the *folate hydrolase* (FOLH1) gene in humans [234]. PSMA/GCPII plays separate roles and functions in different tissues, such as the prostate, kidney, small intestine, central and peripheral nervous system, and thus is recognized by different names. In the last two decades, PSMA has emerged as the preeminent prostate cancer target for developing both diagnostic and therapeutic agents in prostate cancer [235].

PSMA is a class II transmembrane glycoprotein with an approximate molecular weight of 84 kDa [235]. PSMA has a unique 3-part structure: a short N-terminal cytoplasmic tail, a single membrane-spanning helix, and an extracellular part. The bulk of PSMA protein is the extracellular part. In PCa, the expression of PSMA/GCPII is negatively regulated by androgens [236]. PSMA expression on the cell surface increases with androgen receptor AR inhibition [235] and is favored by other growth factors, such
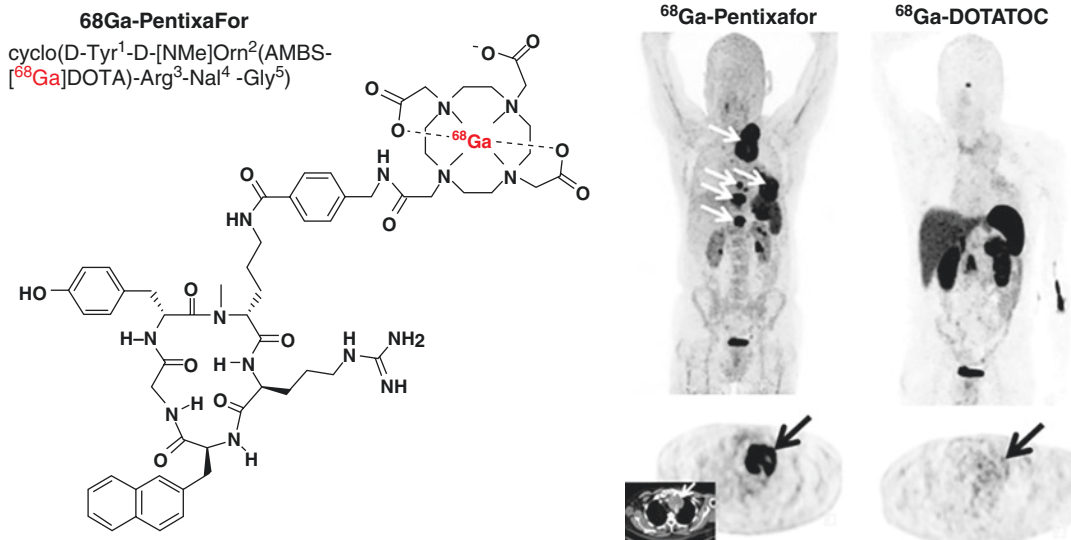
68Ga-PentixaFor

cyclo(D-Tyr^1-D-[NMe]Orn^2(AMBS-[^{68}Ga]DOTA)-Arg^3-Nal^4-Gly^5)

Fig. 14.32 ^{68}Ga-Pentixafor is an antagonist for molecular imaging of chemokine receptor (CXCR4). ^{68}Ga-Pentixafor-PET scan is positive for CXCR4 receptors in a patient with recurrent small cell lung cancer (SCLC) compared to SSTR imaging. Pentixafor-PET demonstrates intense tracer retention in mediastinal lymph nodes, bone, and pleural lesions [231]

as basic fibroblast growth factor, TGF, and EGF. Also, the degree of PSMA/GCPII expression is positively correlated with the Gleason score and disease progression. PSMA is considered to be the most well-established target antigen in prostate cancer, since it is highly and specifically expressed at all tumor stages on the surface of prostate tumor cells [237, 238]. PSMA switches from a cytosolically located protein in the normal prostate to a membrane-bound protein in prostatic carcinoma. The majority of PSMA expression appears to be restricted to the prostate and the level of PSMA expression is increased with increased tumor dedifferentiation, and in metastatic and hormone-refractory cancers [239, [240] . In addition to expression by prostate cells, it can be expressed also by non-prostate tissues, such as small intestine, proximal renal tubules, and salivary glands, albeit at levels 100- to 1000-fold less than in prostate tissue. PSMA expression was also found on the vascular endothelium of solid tumors and sarcomas but, not of normal tissues [235]. The rapid internalization and recycling of PSMA means that high concentrations of a targeted drug can be accumulated in PSMA/GCPII-positive cells.

^{177}Lu- and ^{225}Ac-labeled huJ591 (anti-PSMA mAb) is under active clinical investigation for the development of targeted radionuclide therapy of metastatic castration-resistant prostate cancer (mCRPC) (Chap. 22). While ^{111}In-, ^{177}Lu-, and ^{89}Zr-labeled huJ591 mAbs demonstrated the diagnostic potential of antibody targeting of PSMA, the development of ^{68}Ga- and ^{18}F-labeled small molecule PSMA inhibitors have revolutionized the role of molecular imaging radiopharmaceuticals in the diagnosis and clinical management of patients with prostate cancer. The development of PSMA inhibitors for imaging and therapy was reviewed recently in several publications [241, 242].

Small Molecule PSMA Inhibitors
The two distinct enzyme activities of PSMA include *folate hydrolase* and *NAALADase 1*. The role of these two enzymes is to release the terminal glutamate residue from the substrate molecule. PSMA binds with folate(poly)gamma glutamate in the intestine and releases the glutamate and folic acid. In the brain, PSMA hydrolyzes the N-acetyl-L-aspartyl-L-glutamate (NAAG) substrate to yield aspartate and gluta-

mate. The *NAALADase* enzyme activity of PSMA has been explored for the development of radiopharmaceuticals for molecular imaging and TRT. Studies of the *NAALADase* enzyme structure have revealed an active binding site with two zinc cations (Zn^{++}) participating in the NAAG binding, called the "*NAAG binding pocket*", which is also the site for the binding of PSMA inhibitors [243].

The clinical success of radiolabeled PSMA inhibitors is based on a small motif binding to the catalytic NAAG hydrolyzing site in the PSMA molecule. The 2-[3-(1,3-dicarboxypropyl)-ureido]pentanedioic acid (DUPA) motif contains a urea bond (−NH-CO-NH-) formed by the conjugation of two amino acids (Glu and Asp). In 2002, Dr. Pomper's group at the John Hopkins School of Medicine (JHSM) reported the synthesis of the first radiolabeled PSMA inhibitor, [^{11}C]DCMC) with nanomolar affinity. Extensive structure-activity studies suggested that the L-glutamic acid must remain intact without structural modification to maintain the desired biological function. Hence, a variety of PSMA inhibitors have been synthesized based on DUPA motif with modification at the aspartate end by replacing aspartic acid with other amino acids, such as lysine, glutamic

acid, or their derivatives [244]. The chemical structures of important radiolabeled PSMA inhibitors useful for molecular imaging of prostate cancer are shown in Fig. 14.33.

^{68}Ga-PSMA-HBED-CC (or ^{68}Ga-PSMA-11)

In 2012, the development of PSMA-HBED-CC (also known as PSMA-11 or DKFZ-PSMA-11), at the German Cancer Research Centre (GCRC) and the University Hospital at Heidelberg by Drs. Eder, Haberkorn, and Afshar-Oromieh, should be regarded as a major milestone in the development of radiolabeled PSMA inhibitors for molecular imaging and targeted therapy.

PSMA-11 consists of a Glu-urea-Lys motif conjugated with the highly efficient and Ga-specific acyclic chelator HBED-CC via an aminohexanoic acid (Ahx) spacer [245]. In the first human studies, direct comparison to [^{18}F] FCH, ^{68}Ga-PSMA-targeted PET imaging was able to detect lesions much earlier in patients with low PSA values and shows a reduced background activity in healthy tissue [246]. Subsequently, several clinical studies documented the clinical utility of ^{68}Ga-PSMA-11 for molecular imaging of prostate cancer [247]. Compared to the standard bone scan to identify the meta-
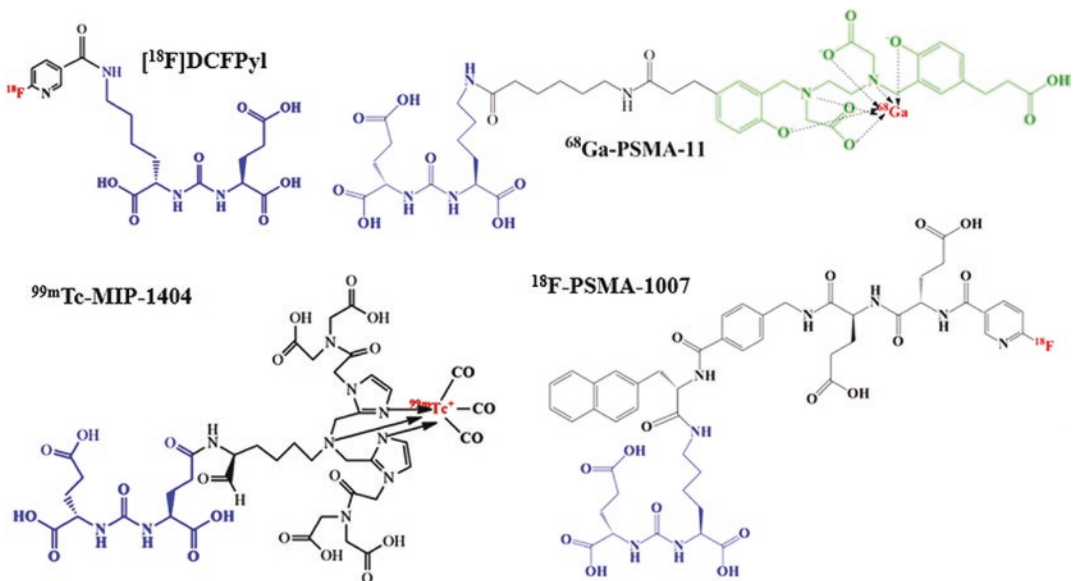

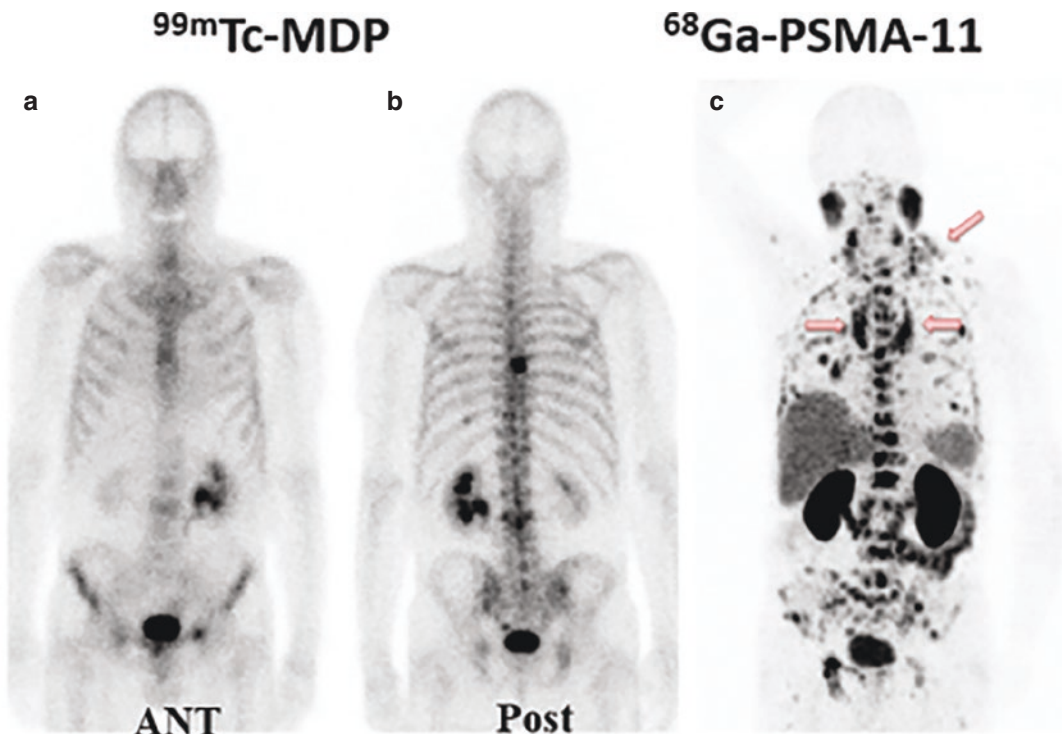**Fig. 14.33** PSMA inhibitors for molecular imaging of prostate cancer

^{99m}Tc-MDP

^{68}Ga-PSMA-11

Fig. 14.34 ^{99m}Tc-MDP bone scan vs. ^{68}Ga-PSMA-PET: a 72-year-old patient with hormone and chemorefractory prostate cancer who underwent bone scintigraphy was referred for ^{223}Ra therapy. PSMA PET/CT (**c**) showed diffuse bone and bone marrow metastases, most not detectable by bone scan (**a**) and (**b**). Apart from bone metastases, there were many lymph node metastases, for example, mediastinal and left clavicular (pink arrows). PSA level at the time of PET imaging was 630 ng/mL, ALP in reference range. Based on PSMA scan, patient was not a candidate for ^{223}Ra therapy, but underwent radioligand therapy with ^{177}Lu-PSMA-617 [248]

static lesions, PSMA-PET scan may provide added value of detecting more lesions in patients with newly diagnosed prostate cancer (Fig. 14.34) [249].

The FDA approved ^{68}Ga-PSMA-11 [250] based on the evidence from two clinical trials in patients with prostate cancer. Some patients were recently diagnosed with prostate cancer. Other patients were treated before, but there was suspicion that the cancer was spreading because of rising PSA level. Both trials were conducted at 2 sites in the USA (FDA package insert). Trial-1 enrolled patients who were recently diagnosed with prostate cancer and were awaiting surgery for the removal of the prostate and the nearby lymph nodes. Trial-2 enrolled patients who were already treated for prostate cancer but, had rising PSA levels, suspicious for cancer spreading. In patients scheduled for radical prostatectomy, the positive predictive value was 61% and negative predictive value was 84%. The sensitivity was 47% and specificity was 90%. In patients with biochemical recurrence, the likelihood of identifying a ^{68}Ga-PSMA-11 PET positive lesion generally increased with higher serum PSA level (36% at <0.5 ng/mL to 91% at >2.0 ng/mL).

^{18}F]DCFPyl (Pylarify™)

[^{18}F]DCFBC was the first ^{18}F-labeled PSMA inhibitor, developed in 2008 at JHSM, based on Cys-Urea-Glu pharmacophore and was successfully evaluated in several clinical studies. The major drawbacks of this tracer are slow blood clearance and high background activity. As a result, early imaging studies did not provide optimal sensitivity.

The next generation compound from JHSM is [18F]DCFPyl (Fig. 14.33), developed also based on Lys-Urea-Glu motif, was hydrophilic and shows faster renal excretion [76]. In patients with biochemical recurrence, direct comparison of [18F]DCFPyl with 68Ga-PSMA-11 indicated that [18F]DCFPyL is noninferior to 68Ga-PSMA-11, and that imaging with [18F]DCFPyL]-PET may even exhibit improved sensitivity in localizing relapsed tumors after prostatectomy for moderately increased PSA levels [251]. A pilot study comparing [18F]DCFPyl to [18F]PSMA-1007 observed that excellent image quality was achieved with both agents, resulting in identical clinical findings. Nonurinary excretion of 18F-PSMA-1007, however, might present some advantage with regard to delineation of local recurrence or pelvic lymph node metastasis in selected patients; the lower hepatic background might favor [18F]DCFPyL in late stages, when

rare cases of liver metastases can occur (Fig. 14.35) [252].

The FDA approval was based on data from two studies, the OSPREY and CONDOR trials, which investigated the safety and diagnostic performance of 18F-DCFPyL in prostate cancer [253]. In the phase 2/3 OSPREY trial, improvements in the specificity (96–99%) and positive predictive value (78–91%) of the agent were observed when compared with conventional imaging for metastatic prostate cancer. Eligible patients in the OSPREY trial were divided into two cohorts, with cohort A including patients with high-risk, locally advanced prostate cancer, and cohort B including patients with metastatic or recurrent disease. In the phase 3 CONDOR study, a median PSA level of 0.8 ng/mL was observed among the 208 evaluable patients, with 68.8% having a PSA level of less than 2.0 ng/mL. The primary end point of correct localization
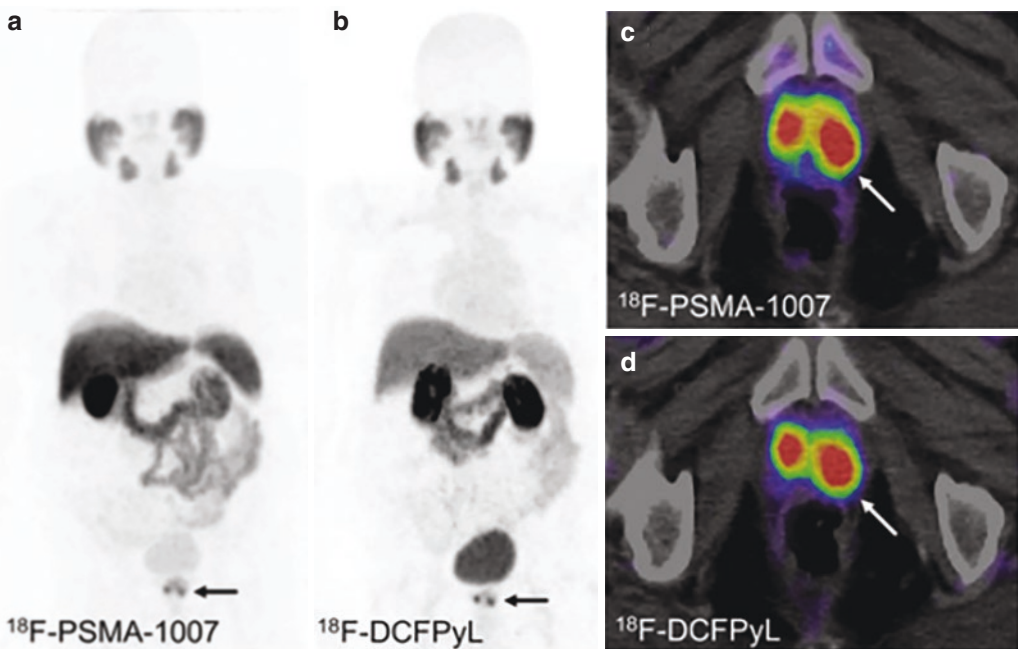
Fig. 14.35 PET/CT images of 65-year-old patient referred because of a Gleason score of 7a (3 1 4) and a PSA serum level of 55.2 ng/mL. Patient was examined with 18F-PSMA-1007 (**a**, **c**) and 18F-DCFPyL (**b**, **d**). Images showed bifocal prostate cancer (arrows).

Delineation of tumor growth in both lobes of prostate was possible with both tracers. SUV_{max} was 17.68 and 19.65 in right lobe and 14.21 and 16.60 in left lobe for 18F-DCFPyL and 18F-PSMA-1007, respectively [252]

rates (CLRs), identified by PyL–PET/CT and evaluated by three blinded independent central readers were observed at 85.6% (95% CI, 78.8–92.3%), 87.0% (95% CI, 80.4–93.6%), and 84.8% (95% CI, 77.8–91.9%) [254].

[18F]rhPSMA-7.3

A unique and novel class of theranostic agents named radiohybrid (rh) PSMA inhibitors based on Glu-Urea-Lys pharmacophore were developed by Drs. Wester and colleagues at the Technical University of Munich, Garching, Germany (TUMG). Radiohybrid concept represents a molecular species that offers two binding sites for radionuclides, a silicon-fluoride acceptor (SiFA) for 18F and a chelator (such as DOTA) for radiometallation. One of these binding sites is radiolabeled, the other one is labeled with a stable nuclide, thus is silent. The lead compound [18F]Ga-rhPSMA-7 with natGa-DOTAGA complex was evaluated in patients with biochemical recurrence [255]. The biodistribution was found to be similar to that of established PSMA ligands, and [18F,natGa]rhPSMA-7 PET/CT demonstrated high detection rates in early biochemical recurrence after radical prostatectomy, especially among patients with low PSA values. [18F]

Ga-rhPSMA-7, however, represents a mixture of four stereoisomers (Fig. 14.36) [256, 257] [Based on preclinical studies, [18F,natGa] rhPSMA-7.3 was identified as the preferred isomer since it showed high tumor accumulation and low uptake by liver and kidney with low blood levels. [18F]-rhPSMA-7.3 completed recruitment of patients in phase III trials (sponsored by BlueEarth Diagnostics) for prostate cancer (PCa) imaging. In order to assess the role in primary staging, [18F]-rhPSMA-7.3 PET/CT studies in patients (*n* = 279) with primary prostate cancer were evaluated [258]. [18F]-rhPSMA-7.3 offers superior diagnostic performance to morphological imaging for primary N-staging of newly diagnosed PCa, shows lower inter-reader variation, and offers good distinction between primary tumor, and bladder background activity.

99mTc-MIP-1404 (Trofolostat™)

In 2012, the investigators at Molecular Insight Pharmaceuticals in Boston reported the development of two high affinity 99mTc-labeled PSMA inhibitors, 99mTc-MIP-1404 (Fig. 14.33) and 99mTc-MIP-1405 based on Glu-Urea-Glu and Glu-Urea-Lys pharmacophores and 99mTc
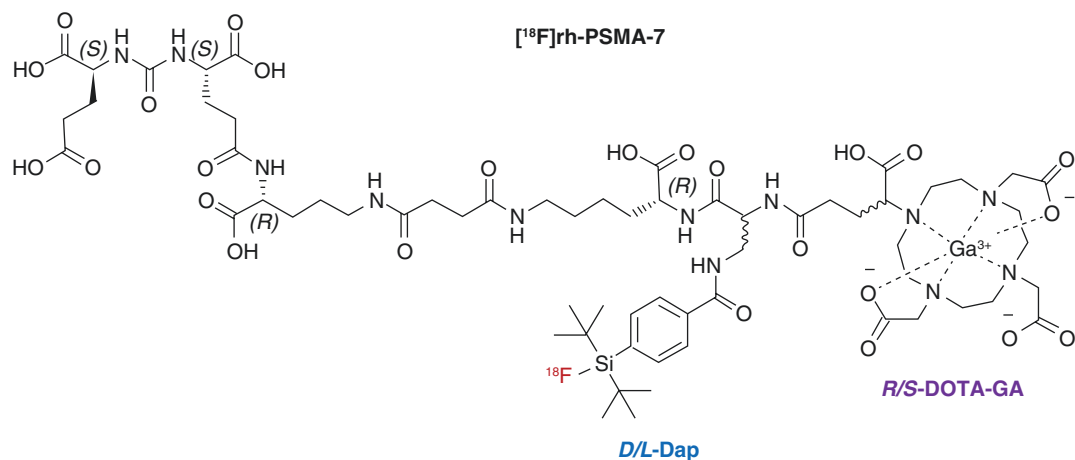

Fig. 14.36 Diastereomeric mixture [18F,natGa]rhPSMA-7 is composed of the four isomers [18F, natGa]rhPSMA-7.1 to 7.4, differing in the stereoconfiguration of diaminopropi-onic acid (D-/L-Dap) and DOTA-GA (R-/S-DOTAGA). The predominant species is [18F,natGa]rhPSMA-7.3 [24]
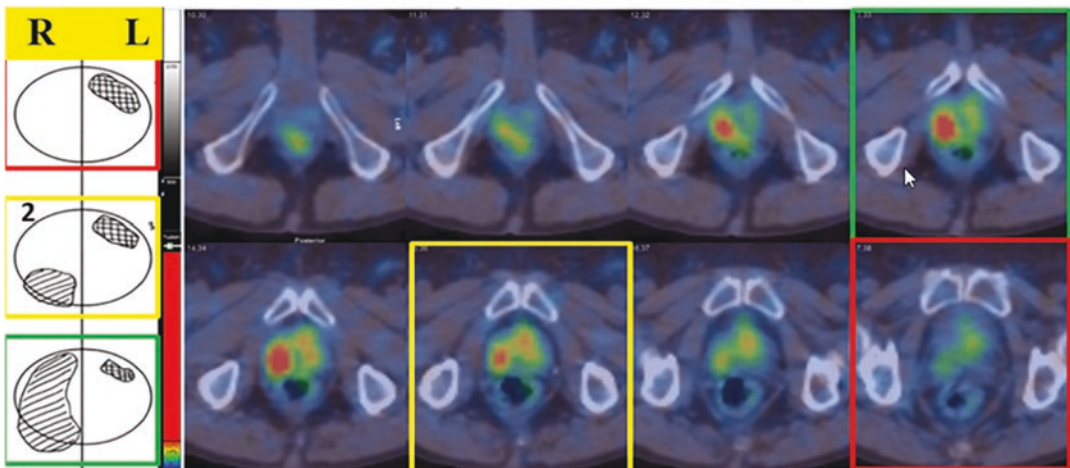
Fig. 14.37 ^{99m}Tc-MIP-1404 images in a high-risk prostate cancer patient scheduled for prostatectomy and extended pelvic node lymph node dissection. ^{99m}Tc-MIP-1404 SPECT clearly identified the prostate cancer foci (Gleason score >7) in the prostate gland, confirmed by histopathology (Vallabhajosula et al. from Weill Cornell Medicine, NY)

tricarbonyl core chemistry. The first human studies in patients with mCRPC showed both ^{99m}Tc tracers localized to lesions in bone and soft tissue that correlated with radiologic evidence of metastatic disease identified by the bone scan [259]. Based on these results a preliminary phase I study and a multicenter phase II study were conducted in high-risk prostate cancer patients scheduled for prostatectomy and extended pelvic node lymph node dissection. In all subjects with Gleason score >7, ^{99m}Tc-MIP-1404 SPECT clearly identified the PCa foci in the prostate gland, confirmed by histopathology (Fig. 14.37), and PSMA staining [260]. Because ^{99m}Tc-MIP-1404 (Trofolostat™) showed minimal urinary excretion, it had a distinct advantage for detecting prostate cancer in the gland and pelvis at the initial stages of the disease and was selected for phase II/III studies to determine sensitivity and specificity to detect prostate cancer in high-risk patients. Subsequently, Trofolastat™, has been investigated (by Progenics Pharmaceuticals) in several clinical trials. ^{99m}Tc-MIP-1404 was the first ^{99m}Tc-PSMA imaging agent to finalize phase 3 clinical trials. It is therefore expected that ^{99m}Tc-MIP-1404

may be available as a "technetium instant kit" in the near future.

14.4.2.15 Fibroblast Activating Protein (FAP)

Malignant tumors consist of cancer cells but, also, of a variety of nonmalignant cells that create and shape the tumor microenvironment (TME), also called tumor stroma. The TME consists of tumor cells and nontumor cells such as bone marrow-derived stem cells (BMDSC), B and T lymphocytes, natural killer (NK) cells, normal epithelial cells, activated fibroblasts (CAFs), macrophages (T1 and T2), and ECM 5 extracellular matrix. The development of CAFs in the tumor stroma is accompanied by morphologic and molecular changes leading to a spindle-shaped form, and the expression of particular surface markers, such as the a-smooth muscle actin, the platelet-derived growth factor b, and the fibroblast activation protein (FAP) [261]. In solid cancers, activated fibroblasts acquire the capacity to provide fertile soil for tumor progression. Specifically, cancer-associated fibroblasts (CAFs) establish a strong relationship with cancer cells. Cancer cells and CAFs are partners in crime and their interaction

is supported by inflammation [262, 263; Linder et al 2019].

FAP, also known as seprase or prolyl-endopeptidase-FAP, is a type II membrane-bound glycoprotein enzyme with peptidase activity. FAP is highly expressed on the cell surface of CAFs but, not quiescent fibroblasts. Since the volume of stroma can be larger than cancer cell volume, stroma-CAFs targeted PET and SPECT imaging may be more sensitive than glucose metabolic PET imaging for detecting small lesions, and lesions with low or heterogeneous glucose metabolism or those located in close vicinity to highly glycolytic normal tissues [264–266]. FAP is expressed in more than 90% of human epithelial cancers, is absent from normal tissues in adult humans, and has a large extracellular domain, with the catalytic site also located extracellularly. It is important to recognize that, like glucose metabolism, FAP expression is not cancer-specific due to its expression in many tissue-remodeling processes. As a result, FAP-targeted PET imaging may be useful for many non-oncologic imaging applications, such as myocar-dial infarction and chronic inflammatory diseases.

Radiolabeled Small Molecule Inhibitors for FAP

The first account of clinical FAP-targeting was reported in 1994 with ^{131}I-F19 mAb, which was able to detect lesions of diameter as small as 1 cm at 3–5 days after injection [267]. In the last 5 years, a variety of quinoline-based FAP inhibitors (FAPI) were coupled to chelators (such as DOTA and NOTA) and showed specific binding of radiolabeled FAP inhibitors to human and murine FAP, with rapid and almost complete internalization [264]. The highly selective and potent inhibitors based on a (4-quinoinolyl) glycinyl-2-cyanopyrrolidine scaffold was originally developed in 2013 [268]. Some of the FAPI-precursors designed on the basis of this motif are shown in Fig. 14.38.

The proof-of concept and the potential of radiolabeled small molecule PSMI for molecular imaging studies were reported in 2018 by the investigators at German Cancer Research Center
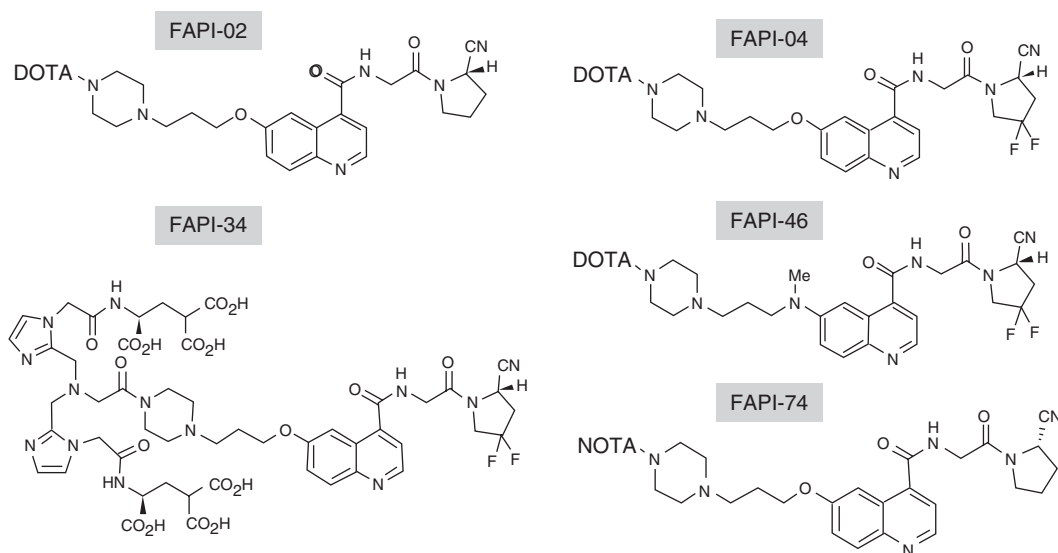

Fig. 14.38 Fibroblast activating protein inhibitor (FAPI) precursors to label radiometals (^{68}Ga or ^{177}Lu) and to perform molecular imaging and targeted radionuclide therapy

(DKFZ), Heidelberg, Germany. ^{68}Ga-FAPI-02 PET/CT studies were performed in three patients with cancer. ^{68}Ga-FAPI-02 shows significantly higher uptake in tumor lesions compared to FDG (Fig. 14.39) 14.44). Based on these studies, the investigators concluded that radiolabeled FAPIs allow fast imaging with very high contrast in tumors having a high stromal content and may therefore serve as pantumor agents. Coupling of these molecules to DOTA or other chelators allows labeling not only with ^{68}Ga but also with therapeutic isotopes such as ^{177}Lu or ^{90}Y.

The pantumor (multiple cancers) imaging characteristic of radiolabeled PSMI inhibitors is shown in (Fig. 14.40). In 80 patients who had 28 different tumor entities, with 54 primary tumors and 229 metastases, ^{68}Ga-FAPI-02 and ^{68}Ga-FAPI-04 uptake discriminated three different groups: the highest average SUV_{max} (>12) was found in sarcoma, esophageal cancer, breast cancer, cholangiocarcinoma, and lung cancer; an intermediate SUV_{max} (6–12) was seen in hepatocellular, colorectal, head and neck, ovarian, pancreatic, and prostate cancer; and the lowest uptake SUV_{max} (6) was observed in pheochromocytoma, renal cell cancer, differentiated thyroid cancer, adenoid cystic cancer, and gastric cancer. Nevertheless, high variations in uptake were observed across and within all tumor entities [264, 272].

FAPI-PET emerges as a novel and highly promising technique for molecular imaging studies in various malignant and nonmalignant diseases. Current studies indicate that FAPI is equal or even superior to the current standard oncological tracer FDG in several oncological diseases. FAPI-PET seems to present lower background activity, stronger uptake in tumor lesions, and thus sharper contrasts. The significant tumor uptake of FAP inhibitors will encourage the development of therapeutic radiopharmaceuticals that can be used for a wide variety of cancers, unlike SSTR or PSMA-based therapeutic radiopharmaceuticals.

14.4.3 Antigen-Antibody Binding

14.4.3.1   Antibody Structure and Function

A century ago, Paul Ehrlich postulated the notion that a *magic bullet* could be developed to selectively target disease and he envisioned that antibody could act as such [274]. The introduction of hybridoma technology for the mAb development turned this magic bullet concept into a reality [275]. The first generations of mAbs were of murine origin and had limited clinical use; however, developments in recombinant DNA technology have resulted in the production of chimeric, humanized, and complete human mAbs (Fig. 14.41).

Antibodies (Abs) are large glycoproteins that belong to the immunoglobulin (Ig) superfamily. The basic structure of Abs is composed of two heavy and two light chains in the shape of a Y (Fig. 14.41). At each tip of the Y lies the fragment antigen-binding (Fab) portion of the antibody which is responsible for recognition of the specific antigen. The fragment crystallizable (Fc) region located at the base of the Y structure is recognized by Fc receptors (FcRs) found on a wide range of immune cells. Most of the FDA-approved mAbs belong to the IgG_1 subclass, which has a long half-life and triggers potent immune-effector functions, such as complement-dependent cytotoxicity (CDC), complement-dependent cell-mediated cytotoxicity (CDCC), and antibody-dependent cellular cytotoxicity (ADCC).

Antibodies are heavy proteins of about 10 nm in size with a molecular mass of ~150 kDa, arranged in three globular regions that roughly form a Y shape. Also, each IgG molecule consists of four polypeptide chains; two identical *heavy chains* and two identical *light chains* connected by disulfide bonds. Each chain is made up of 1–4 domains; light chains consist of one variable domain V_L and one constant domain C_L, while heavy chains contain one variable domain V_H and
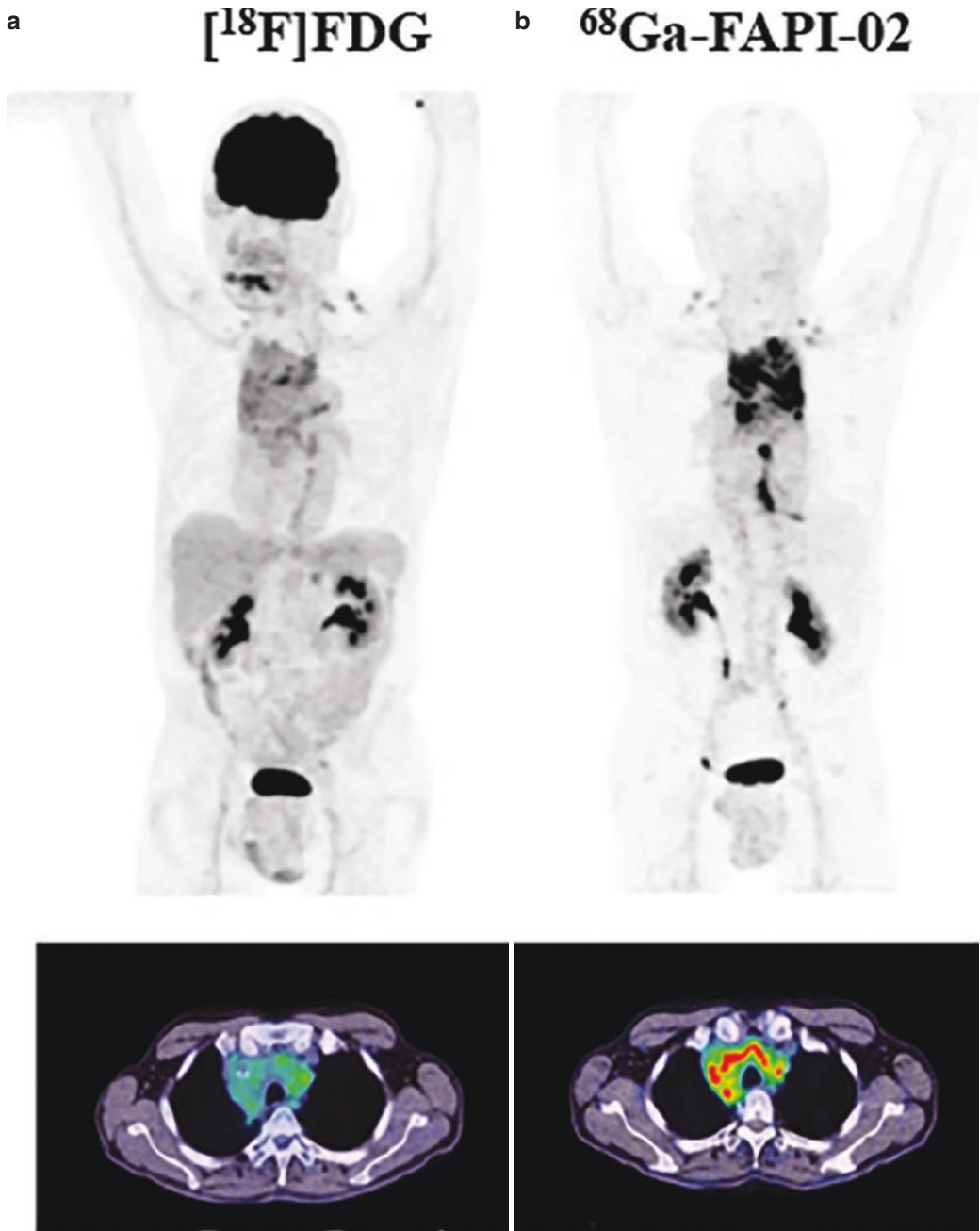
a $[^{18}F]FDG$ **b** $^{68}Ga-FAPI-02$

Fig. 14.39 Comparison of ^{68}Ga-FAPI-02-PET/CT with $[^{18}F]FDG$-PET/CT in a patient with locally advanced lung adenocarcinoma. ^{68}Ga-FAPI-02 (**b**) is seen to selectively accumulate in FAP-expressing tissue and to be signifi-cantly higher than $[^{18}F]FDG$ (**a**) in malignant lesions. Unlike FDG, ^{68}Ga-FAPI-02 shows no uptake in the brain, spleen, or liver. (Figure from [273])
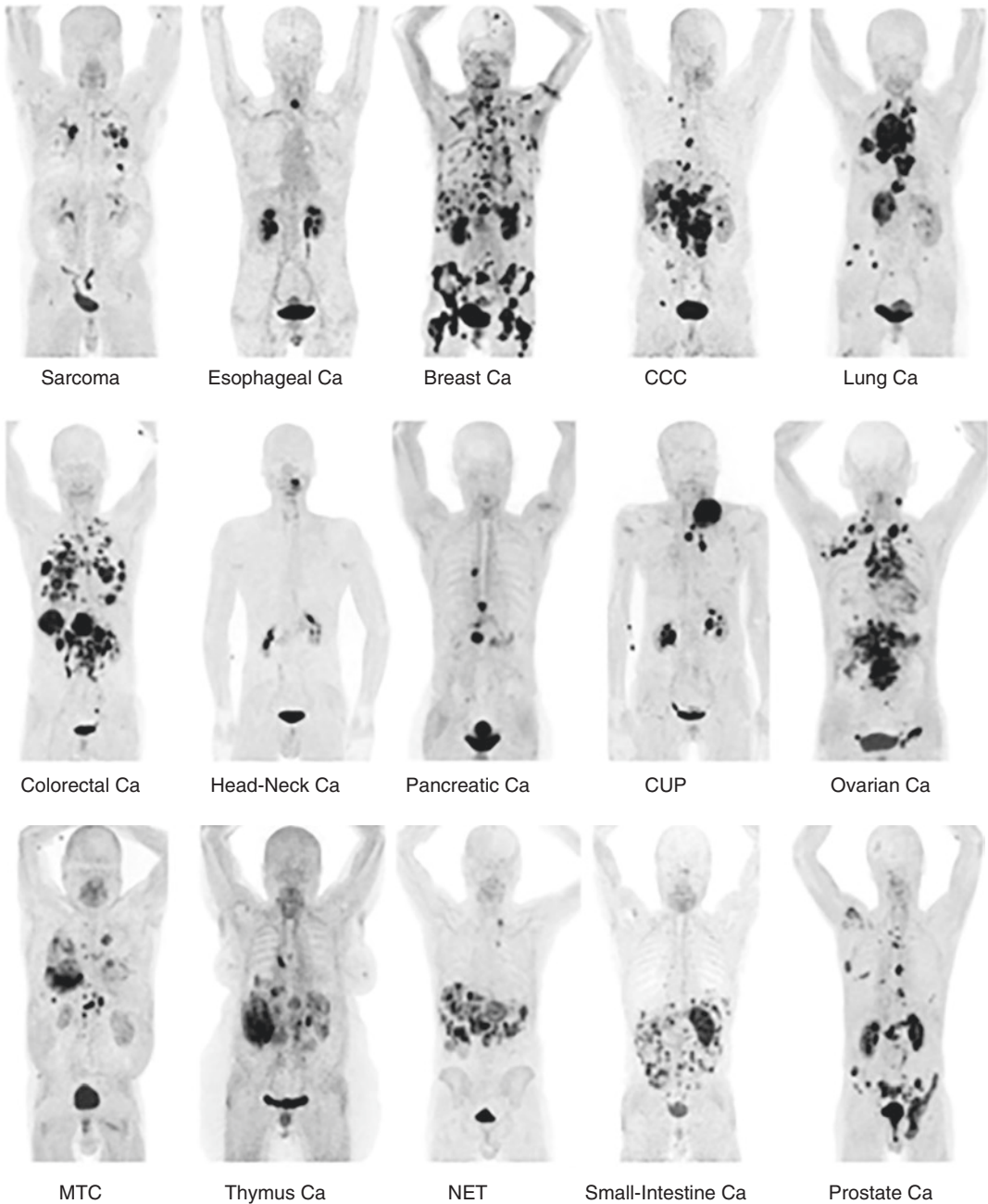
Fig. 14.40 PET imaging with ^{68}Ga-labeled FAPI tracers. By targeting the cancer-associated fibroblasts, FAPI-PET provides a very low uptake in the nontarget organs, and a fast background clearance. FAPI tracers allowed the detection of different tumor entities with high specificity. (Figure from [272])
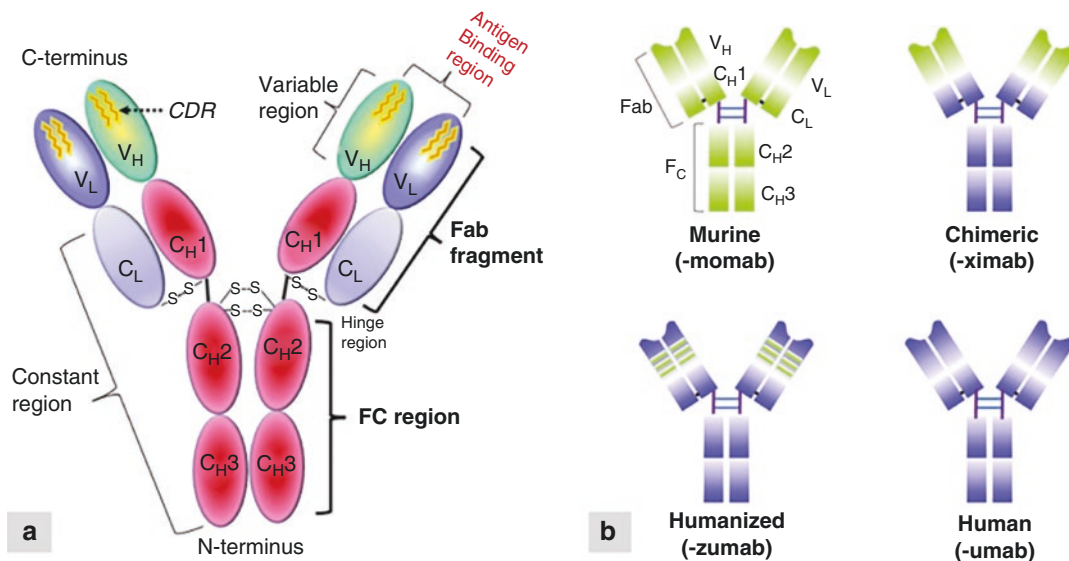
Fig. 14.41 (**a**) The fundamental structure of an intact, single immunoglobulin G (IgG) molecule has a pair of light chains and a pair of heavy chains. Light chains are composed of two separate regions (one variable region (V_L) and one constant region (C_L)), whereas heavy chains are composed of four regions (V_H, C_{H1}, C_{H2}, and C_{H3}). The complementarity-determining regions (CDRs) are found in the variable fragment (Fv) portion of the antigen-binding fragment (Fab). (**b**) Schematic overview of mAb humanization from murine antibodies (green domains) to fully human antibodies (blue domains) and associated suffixes. In the chimeric mAb, the variable regions are of murine origin and the rest of the chains are of human origin. Humanized mAb only includes the hypervariable segments of murine origin. *CH* domains of the constant region of the heavy chain, *CL* constant domain of the light chain, *Fab* and *Fc* fragments resulting from proteolysis, *VH* variable domain of the heavy chain, *VL* variable domain of the light chain (The figure on right (**b**) was modified from [133])

three to four constant domains C_{H1}-C_{H4}. Each IgG has two Fabs, each containing one V_L, V_H, C_L, and C_{H1} domains, as well as the Fc fragment. The subregion of each Fab fragment containing the variable regions (V_L and V_H) that binds to the antigen is referred to as F_V region and the existence of two identical antibody-binding sites (divalent) allows antibody molecules to bind strongly to multivalent antigen molecules.

The mouse hybridoma technology was initially used to produce murine monoclonal antibodies (Fig. 14.41b). These mouse-derived mAbs (*momab*) elicit an immune response resulting in the production of human-anti-mouse-antibodies (HAMAs) which interfere with therapeutic applications [276]. The antibody engineering technology identified regions that could be 'humanized' without compromising the functionality of IgG molecule, resulting in chimeric antibodies (*ximab*) and 'humanized' antibodies (*zumab*) and, finally, fully human antibody (*umab*) [277]. Chimeric mAbs are constructed with variable regions (V_L and V_H) derived from a murine source and constant regions derived from a human source. Humanized therapeutic mAbs are predominantly derived from a human source except for the complementarity-determining regions (CDRs), which are murine.

Antibodies are physically stable and experience a prolonged serum half-life resulting in an average half-life of several weeks and accumulate in the liver and kidney. Antibody engineering enabled the production of a wide variety of IgG derivatives (Fig. 14.42) with significant differences in size (25–100 kDa) to improve pharmacokinetics, tumor localization, and antigen binding [278–280].
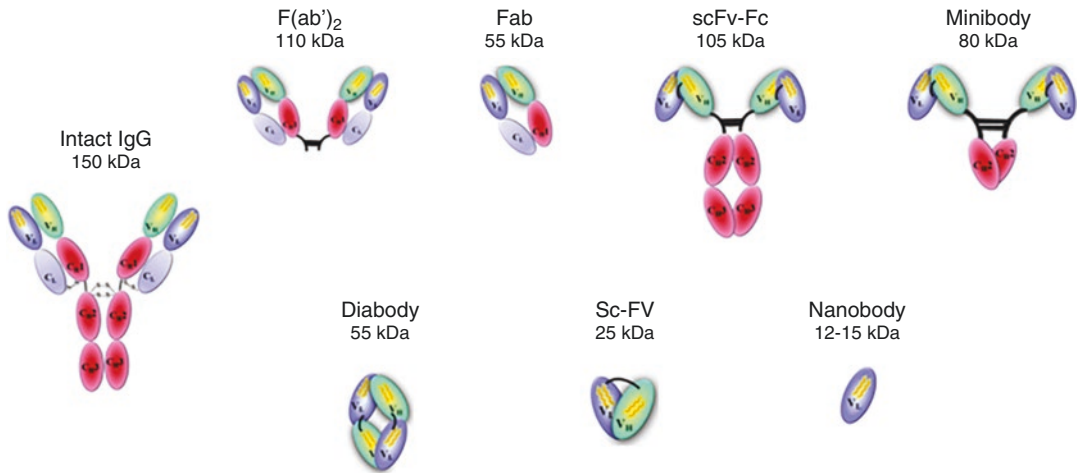
Fig. 14.42 Antibody fragments and derivatives of varied sizes, and molecular weights

Pharmacokinetics of Antibodies and Fragments

Intact mAbs have a long residence time in humans, ranging from a few days to weeks, which results in optimal tumor-to-nontumor ratios at 2–4 days post injection. In contrast, mAb fragments have a much faster blood clearance and as a result, optimal tumor-to-nontumor ratios can be obtained at earlier time points; however, the absolute tumor uptake may be much lower compared to intact mAbs. In general, intact mAbs are preferable for therapy, while the optimal format for diagnosis is still under discussion.

Size is one factor that impacts the circulation time of Abs [281, 282]. A full IgG mAb is a large 150-kDa protein that can remain in circulation for 3–4 weeks while being metabolized slowly by the reticuloendothelial system. In contrast, a 25-kDa monovalent fragment (scFv) has a blood clearance time of <10 h with primarily renal excretion in 2–4 h. The Fv fragment, consisting only of the V_H and V_L domains, is the smallest immunoglobulin fragment available that carries the whole antigen-binding site. However, scFvs have never fared well in the clinic, despite their small size (25 kDa), because of their poor tumor retention. Molecules with molecular weights above >70 kDa (the glomerular filtration threshold) remain in circulation much longer than smaller more rapidly eliminated molecules.

The development of smaller, antigen-binding antibody fragments, derived from conventional antibodies or produced recombinantly, has been growing at a fast pace. Antibody fragments can be used on their own or linked to other molecules to generate numerous possibilities for bispecific, multi-specific, multimeric, or multifunctional molecules, and to achieve a variety of biological effects. They offer several advantages over full-length monoclonal antibodies, particularly a lower cost, and because of their small size they can penetrate tissues, access challenging epitopes, and have potentially reduced immunogenicity [283].

14.4.3.2   Immuno-PET and SPECT

In the early 1980s clinical nuclear imaging studies provided the proof of principle that tumor lesions could be imaged using radiolabeled mAbs. FDA approved four radiolabeled (with ^{111}In or ^{99m}Tc) mAbs for diagnostic imaging studies. However, the diagnostic accuracy of these antibody-based scans was limited due to poor resolution of the Anger gamma cameras at that time. In addition, with the introduction of FDG-PET and PET/CT, antibody-based imaging for staging and restaging of cancer patients became obsolete [284]. With the availability of relatively long half-life positron emitters ([124]I, $T_{1/2} = 4.2$ d, and [89]Zr, $T_{1/2} = 3.266$ d), a revival of imaging with radiolabeled antibodies based on PET imaging has taken place. By combining the sensitivity of PET imaging and the specificity of antibodies, immuno-PET imaging has become a

promising tool for monitoring the heterogeneity of specific gene expression and predicting the efficacy of RIT. ^{111}In-labeled mAbs are still useful for the initial development work based on SPECT imaging but, the lack of absolute quantitation with SPECT does not support clinical utility for dosimetry studies and to monitor response to RIT.

[89]Zr for ImmunoPET

The cyclotron production of [89]Zr was first reported in 1990 [285]. [89]Zr half-life is quite appropriate to study antibody biodistribution and in the same range as the therapeutic radiometals such as ^{90}Y and [177]Lu. Several radiometals have been investigated for long-duration PET studies, including ^{64}Cu, [86]Y, and [66]Ga, although [89]Zr best fulfills many of the desired properties with its 3.27-d half-life and 23% positron emission. In addition, other favorable physical properties include minimal contamination from the 909-keV prompt γ-photons within the 511-keV PET energy window, as well as superior spatial resolution compared with many other positron-emitting isotopes as a result of the relatively low excess decay energy (E_{mean} = 396 keV).

In 2003, [89]Zr-labeled antibodies were introduced as chemical and biological surrogates for immunoPET studies to assess the biodistribution of [90]Y- and ^{177}Lu-labeled antibodies [286, 287]. The first human study was published in 2006 with [89]Zr-labeled chimeric mAb U36 in patients with squamous head and neck cancers [288]. [89]Zr-PET imaging localized cervical lymph node metastasis with a high accuracy (93%). It has been shown that radiation doses of RIT with ^{90}Y-ibritumomab tiuxetan (Zevalin) can be predicted by immuno-PET with [89]Zr-ibritumomab tiuxetan [289, 290] and other [90]Y- and ^{177}Lu-labeled mAbs [291]. In the last 15 years, a number of studies have been conducted to investigate the feasibility of [89]Zr immuno-PET imaging for predicting the efficacy of RIT and antibody therapies, imaging target expression, detecting target-expressing tumors, and the monitoring of anti-cancer chemotherapies. Many FDA-approved mAbs for immunotherapy (such as trastuzumab, bevacizumab, cetuximab, and rituximab) have been labeled with [89]Zr (Table 19.7) and were evaluated as radiopharmaceuticals for immunoPET [292, 293]. PET/CT scan of [89]Zr-trastuzumab is shown in Fig. 14.43. [111]In-
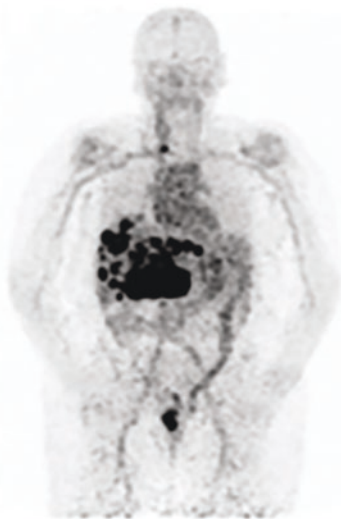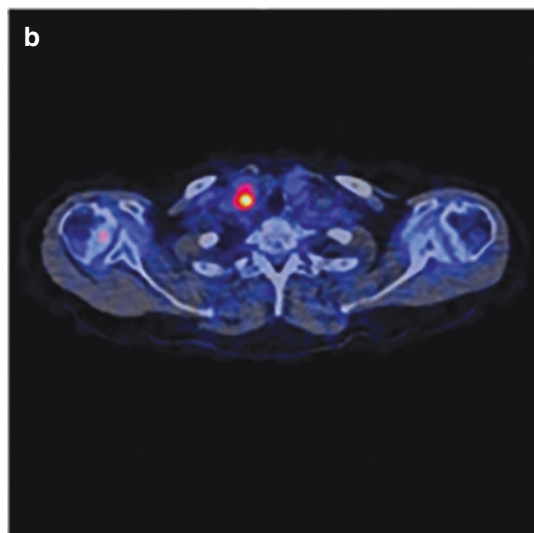
Fig. 14.43 [89]Zr-trastuzumab PET/CT scan in a patient with human epidermal growth factor receptor 2–positive metastatic breast cancer 4 days after injection of [89]Zr-trastuzumab (37 MBq in 50 mg antibody). (**a**) The scan showing 89Zr activity in circulation, uptake in intrahepatic metastases, and intestinal excretion. (**b**) Transverse plane of fused PET/CT of chest showing tracer uptake in cervical lymph node. (**c**) Transverse plane showing tracer uptake in metastasis (left side) in T7. (**d**) Transverse plane showing tracer uptake in liver metastases (Figure from [269])
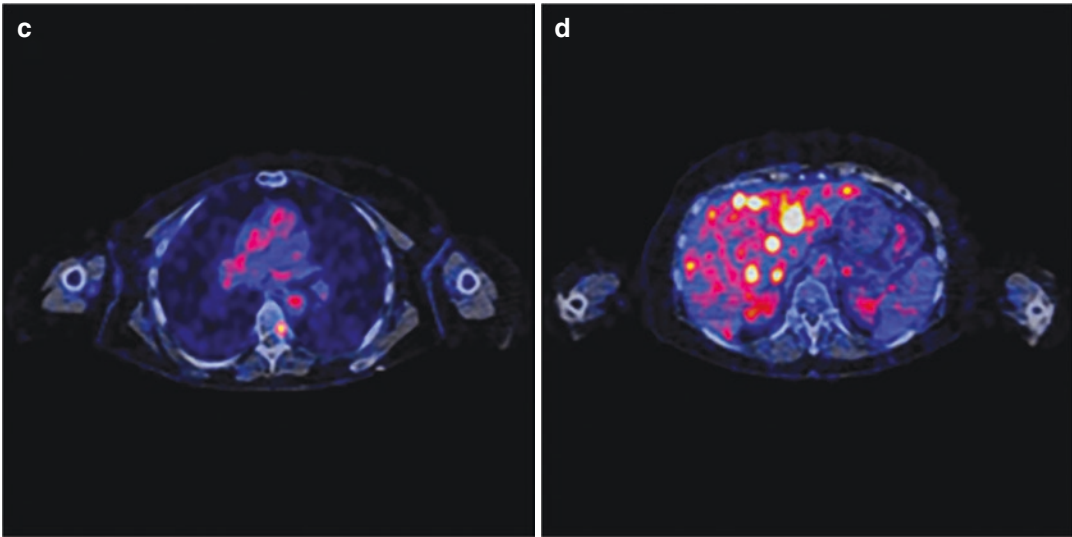
Fig. 14.43 (continued)
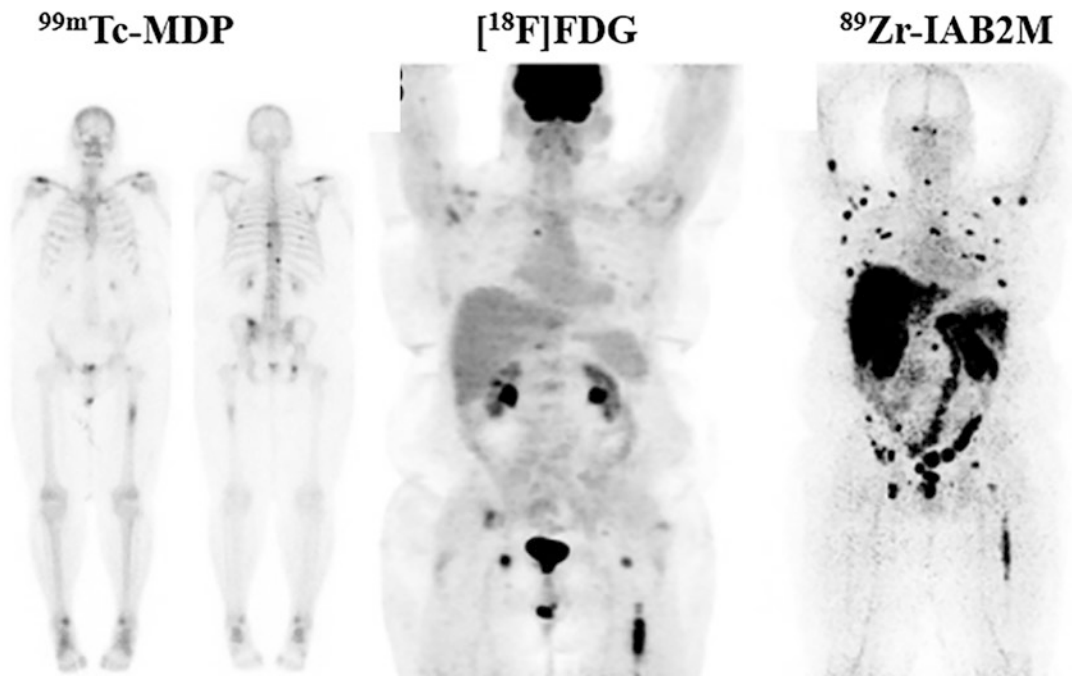
Fig. 14.44 [89]Zr-IAB2M-PET imaging in mCRPC. Targeting with IAB2M (minibody fragment from J591 mAb). Comparison with Bone scan and FDG-PET. [89]Zr-IAB2M scan shows more lesions than bone scan or FDG-PET (From [270])

and ^{177}Lu-labeled huJ591 (anti-PSMA) mAb imaging studies showed excellent targeting of PSMA expression in mCRPC [294, 295]. However, the [89]Zr-IAB2M minibody (derived from J591 mAb) detected more lesions than bone scan and FDG-PET (Fig. 14.44). Immuno-PET using [89]Zr has the advantage of a high resolution and high specificity but, compared to ^{18}F-labeled

radiotracers, patients generally receive higher radiation dose from [89]Zr-mAb PET (~20–40 mSv for 37–74 MBq) [293].

[124]I for ImmunoPET
Based on the long half-life and physical properties of the positron-emitting isotope of iodine, [124]I may be used for both imaging (positron) as well as for ^{131}I dosimetry. The relatively low percentage of high-energy positrons (22.7%) and a high percentage of cascade gamma photons in the background compared to the conventional PET isotopes make imaging with [124]I technically challenging. However, optimizing image acquisition parameters and appropriate corrections within the image reconstruction process improve the image quality [296].

I-124 is an attractive radionuclide for the development of mAbs for immunoPET. In 2007, [124]I-gerentuximab (anticarbonic anhydrase IX chimeric G250 mAb) PET clearly detected clear cell renal cancer [297]. This study indicated that immuno-PET/CT might be helpful in clinical decision-making and may aid in the surgical management of small renal masses scheduled for partial nephrectomy. These promising results formed the basis for a multicenter phase III registration trial in 226 patients [298]. [124]I-huA33 mAb-PET images in a patient with colorectal cancer also showed excellent localization of lesions in the liver, two days post administration of the radiolabeled antibody (360 MBq/10 mg mAb) [299]. These early studies documented that immunoPET with [124]I can provide the tissue concentration and pharmacokinetics of radiolabeled antibodies. [124]I-labeled Trastuzumab, huA33, and cG250 have shown promise in human clinical trials but, there is no FDA-approved [124]I-labeled mAb. The major disadvantage of [124]I PET scans are poor resolution of images due to the high energy of positrons, and in vivo dehalogenation of [124]I-labeled proteins [296].

ImmunoPET: Applications
The concept of immunoPET was originally meant to describe PET imaging of radiolabeled intact full-length mAbs. However, immunoPET now includes radiolabeled antibody fragments or mimetics as targeting vectors. A variety of radionuclides and mAbs have been used to develop molecular imaging probes for immunoPET (Table 14.8). The clinical application of immunoPET imaging has increased our understanding of tumor heterogeneity and refined clinical disease management, and includes the following applications [292]:

- To facilitate better management of cancer patients since it has the potential to provide excellent specificity and sensitivity in detecting primary tumors.
- To detect lymph node and distant metastases.
- Following immunoPET imaging, patients with positive findings can be selected for subsequent therapies (e.g., antibody therapy and antibody-based RIT), whereas patients with negative or heterogeneous findings may need multidisciplinary treatments.
- As a theranostic companion, immunoPET can provide radiation dosimetry prior to administering the therapeutic radiopharmaceuticals.
- immunoPET imaging is useful for improved triage during early disease stages and to facilitate image-guided surgery.
- The information provided by immunoPET will significantly enhance the existing diagnostic methods for better tumor characterization. One can envision that tumors may be classified not only according to their origins and mutation status but also according to the expression of specific tumor antigens in the future.

14.4.3.3 Molecular Imaging for Cancer Immunotherapy
The recent success of cancer immunotherapy especially with the checkpoint inhibitors has renewed interest in the development of molecular imaging of immune system and tumor microenvironment. A variety of biomarkers that predict tumor response to immunotherapy have been evaluated, including the expression levels of the programmed cell death protein 1 (PD-1) or its ligand (PD-L1). The expression of these two immune markers is dynamic and depends on prior therapies [300].

The immune system maintains a delicate balance between eradicating infection/cancers and

Table 14.8 Radiolabeled mAbs and fragments as molecular imaging probes for Immuno-PET

Radiolabeled antibody[a]	Target	Targeting vector	Cancer types
^{89}Zr-Df-cetuximab	EGFR	mAb	Solid tumors
^{89}Zr-Panitumumab	EGFR	mAb	Colorectal cancer
^{89}Zr-Df-trastuzumab	HER2	mAb	Breast cancer, esophagogastric adenocarcinoma (EGA)
^{64}Cu-DOTA-trastuzumab	HER2	mAb	BC
^{89}Zr-Df-pertuzumab	HER2	mAb	BC
^{124}I-trastuzumab	HER2	mAb	Gastric cancer, gastro-esophageal cancer
^{64}Cu-DOTA-patritumab	HER3	mAb	Solid tumors
^{89}Zr-GSK2849330	HER3	mAb	Solid tumors
^{89}Zr-lumertuzumab	HER3	mAb	Solid tumors
^{89}Zr-Df-bevacizumab	VEGF	mAb	Solid tumors
^{124}I-huA33	A33	mAb	Colorectal cancer
^{89}Zr-cmAb U36	CD44v6	mAb	Squamous cell carcinoma of the head and neck (HNSCC)
^{89}Zr-RG7356	CD44	mAb	Solid tumors
^{89}Zr-rituximab	CD20	mAb	Lymphoma
^{89}Zr-DFO-5B1	CA19.9	mAb	Pancreatic cancer
^{89}Zr-huJ591	PSMA	mAb	Prostate cancer
^{89}Zr-girentuximab	CAIX	mAb	Renal cell carcinoma
^{124}I-cG250	CAIX	mAb	Renal cell carcinoma
^{89}Zr-DFO-MSTP2109A	STEAP1	mAb	Prostate cancer
^{89}Zr-fresolimumab	TGF-β	mAb	Glioma
^{68}Ga-ABY-025	HER2	Affibody	Breast cancer
^{68}Ga-HER2-nanobody	HER2	Nanobody	Breast cancer
^{89}Zr-IAB2M	PSMA	minibody	Prostate cancer
^{68}Ga-IMP288	CEA	BsAb	Medullary thyroid cancer
^{89}Zr-AMG 211	CEA/CD3	BiTE	Gastrointestinal adenocarcinoma
^{89}Zr-Df-IAB22M2C	CD8	Minibody	Solid tumors
^{89}Zr-atezolizumab ^{111}In-atezolizumab	PD-L1	mAb	Non-small cell lung cancer (NSCLC), Bladder cancer, Triple negative breast cancer (TNBC)
^{18}F-BMS-986192	PD1	Adnectin (monobody	Lung cancer
^{89}Zr-Nivolumab	PD1	mAb	Lung cancer

[a] Table modified from Wei et al. [292]

maintaining self-tolerance, in part by the expression of immune checkpoints that control immune response. One major checkpoint inhibitor pathway is the PD-1 pathway. PD-1 is a negative costimulatory receptor expressed on the surface of activated T and B cells. PD-L1 is a surface glycoprotein ligand for PD-1 that facilitates immunosuppression on both, antigen-presenting cells and human cancers. PD-L1 downregulates T-cell activation and cytokine secretion by binding to PD-1. Tumors exploit these checkpoint pathways

by expressing coinhibitory proteins to evade antitumor immune responses. Elevated PD-L1 expression is correlated with poor prognosis in some cancers, which suggests that PD-L1 upregulation is a mechanism for tumor immune evasion. PET and SPECT imaging with radiolabeled probes targeting PD-1 and PD-L1 can provide in vivo, real-time, and noninvasive imaging of tumor biomarker expression and immune responses to novel therapies, and in addition, may also help to overcome some of the chal-

lenges of tumor biopsies. The FDA has approved several mAbs blocking the PD-1/PD-L1 interaction. These agents include PD-1 inhibitors nivolumab, pembrolizumab, and cemiplimab, and PD-L1 inhibitors atezolizumab, avelumab, and durvalumab. Given the clinical success of PD-1 and PD-L1 inhibition for the treatment of advanced cancers, many radioligand imaging studies have targeted this receptor/ligand pair by radiolabeling PD-1 or PD-L1 antibodies.

^{89}Zr-atezolizumab

In patients with locally advanced or metastatic bladder cancer, NSCLC, or triple-negative breast cancer, PET/CT imaging was performed with ^{89}Zr-atezolizumab prior to treatment with atezolizumab [301]. Uptake of the radiotracer was noted in the bone marrow, spleen, and tumors. Importantly, heterogeneity in uptake was observed intratumorally in large tumors as well as in different metastatic lesions in the same patient, supporting the notion of tumor biomarker

heterogeneity and demonstrating the power of PET molecular imaging to visualize real-time biomarker expression. Furthermore, on a per-lesion level, the baseline uptake on PD-L1 PET imaging was correlated with lesions demonstrating the best response to anti-PD-L1 immunotherapy. Compared with biopsy samples for PD-L1 IHC and RNA sequencing, ^{89}Zr-atezolizumab uptake was more strongly related to response, progression-free survival, and overall survival. These preliminary studies demonstrate the power of molecular immunoPET imaging to potentially personalize a patient's therapeutic regimen based on targeted biomarker expression [300, 301].

^{18}F-BMS-986192 and ^{89}Zr-Nivolumab

In patients with advanced NSCLC, PET/CT imaging was performed with ^{18}F-BMS-986192 (adnectin, ~10 kDa and specific for PD L-1) and ^{89}Zr-Nivolumab (anti-PD-1 mAb), prior to treatment with nivolumab (Fig. 14.45). Tracer uptake was heterogeneous both between patients, as well
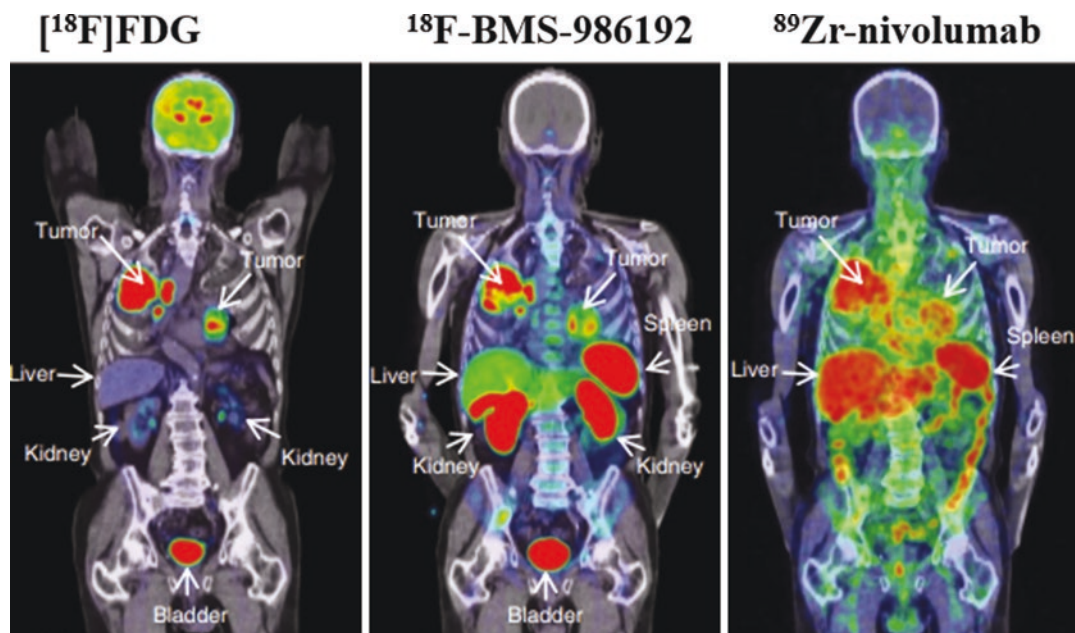
Fig. 14.45 FDG PET (225 MBq) scan demonstrates high glucose metabolism of tumors in both lungs and mediastinal lymph nodes. ^{18}F-BMS-986192 PET (146 MBq) scan at 1 h and ^{89}Zr-labeled Nivolumab PET (37.1 MBq) at 162 h post injection. Both immunoPET scans demonstrate het-

erogeneous tracer uptake within and between tumors. BMS-986192 is an adnectin, ~10 kDa, and specific for PD L-1 and nivolumab is an anti-PD-1 mAb). (Figure modified from [271])

as within patients between different tumor lesions. ^{18}F-BMS-986192 identified more lesions and uptake in tumor lesions (SUV$_{peak}$), correlated with tumor PD-L1 expression, measured by IHC. [89]Zr-nivolumab uptake correlated with PD-1 positive tumor-infiltrating immune cells. They also demonstrated a correlation between tumor tracer uptake and response to nivolumab treatment for both tracers. These first in human studies suggest that ^{18}F-BMS-986192 and [89]Zr-nivolumab PET-CT may be useful imaging biomarkers to noninvasively evaluate PD-1 and PD-L1 expression [271, 302]

The clinical studies with radiolabeled antibodies and antibody fragments are extremely limited but clearly demonstrated that immuno-PET provides high-resolution images needed for diagnosis and treatment assessment. More research and extensive imaging clinical trials are needed to refine immuno-PET for the diagnosis of cancers and assessment of response to therapy. ImmunoPET studies will be essential for the assessment of target antigen expression and identification of right patient for a specific RIT clinical trial.

References

1. Sellmyer MA, Lee IK, Mankoff DA. Building the bridge: molecular imaging biomarkers for 21st century cancer therapies. J Nucl Med. 2021;62(12):1672–6.
2. Rowe SP, Pomper MG. Molecular imaging in oncology: current impact and future directions. CA Cancer J Clin. 2021;72(4):333–52. https://doi.org/10.3322/caac.21713.
3. Rajendran JG. Mankoff DA: Beyond Detection: Novel applications for PET Imaging to guide cancer therapy. J Nucl Med. 2007;48:855–856
4. Petroni D, Menichettii L, Poli M. Historical and radiopharmaceutical relevance of [^{18}F]FD. J Radioanal Nucl Chem. 2020;23:1031.
5. Krenning EP, Kwekkeboom DJ, Bakker WH, et al. Somatostatin receptor scintigraphy with [^{111}In-DTPA-D-Phe[1]]- and [^{123}I-Tyr[3]]-octreotide: the Rotterdam experience with more than 1000 patients. Eur J Nucl Med. 1993;20:716–31.
6. Kumar V, Cotran RS, Robbins SL. Basic pathology. 6th ed. Philadelphia: Saunders; 2003.
7. Ibrahim EM, Al-Maghrabi JA. Basis of tumor imaging 1: principles of tumor pathology and biology. In: Elgazzar A, editor. The pathologic basis of nuclear medicine. 2nd ed. Berlin: Springer; 2006.
8. Hanahan D, Weinberg RA. The hallmarks of cancer. Cell. 2000;100:57–70.
9. Hanahan D, Weinberg RA. Hallmarks of cancer: the next generation. Cell. 2011;144:646–74.
10. Fouad YA, Aanei C. Revisiting the hallmarks of cancer. Am J Cancer Res. 2017;7(5):1016–36.
11. Paul D. The systemic hallmarks of cancer. J Cancer Metastasis Treat. 2020;6:29.
12. Kirsch DG, Kastan MB. Tumor suppressor p53: implications for tumor development and prognosis. J Clin Oncol. 1998;16:3148–68.
13. Lugano R, Ramachandran M, Dimberg A. Tumor angiogenesis: causes, consequences, challenges, and opportunities. Cell Mol Life Sci. 2020;77:1745–70.
14. Adams JM, Cory S. Life-or-death decisions by the Bcl-2 protein family. Trends Biochem Sci. 2001;26:61–6.
15. Wahl RL. Principles of cancer imaging with fluorodeoxyglucose. In: Wahl RL, Buchanan JW, editors. Principles and practice of positron emission tomography. Philadelphia: Williams & Wilkins; 2002.
16. Stocklin GL. Is there a future for clinical fluorine-18 radiopharmaceuticals (excluding FDG)? Eur J Nucl Med. 1998;25:1612–6.
17. Varagnolo L, Stokkel MPM, Mazzi U, et al. 18F-labeled radiopharmaceuticals for PET in oncology, excluding FDG. Nucl Med Biol. 2000;27:103–12.
18. Coenen HH, Elsinga PH, Iwata B, et al. Fluorine-18 radiopharmaceuticals beyond [^{18}F]FDG for use in oncology and neurosciences. Nucl Med Biol. 2010;37:727–40.
19. Couturier O, Luxen A, Chatal JF, et al. Fluorinated tracers for imaging cancer with positron emission tomography. Eur J Nucl Med Mol Imaging. 2004;31:1182–206.
20. IAEA. TECDOC-1968 production and quality control of fluorine-18 labelled radiopharmaceuticals. Vienna: International Atomic Energy Agency; 2021.
21. Vallabhajosula S. 18F-Labeled PET radiopharmaceuticals in oncology: an overview of radiochemistry and mechanisms of tumor localization. Semin Nucl Med. 2007;37:400–19.
22. Shiue CY, Welch MJ. Update on PET radiopharmaceuticals: life beyond fluorodeoxyglucose. Radiol Clin N Am. 2004;42:1033–53
23. Warburg O. On the origin of cancer cells. Science. 1956;123:309–14.
24. Warburg O, Posener K, Negelein E. The metabolism of cancer cells. Biochem Z. 1924;142:129–69.
25. Jana S, Abdel Dayem HM. Basis of tumor imaging 2: principles of tumor pathology and biology. In: Elgazzar A, editor. The pathologic basis of nuclear medicine. 2nd ed. Berlin: Springer; 2006.
26. Sols A, Crane RA. Substrate specificity of brain hexokinase. J Biol Chem. 1954;210:581–95.
27. Ido T, Wan CN, Casella JS, et al. Labeled 2-deoxy-D-glucose analogs: [18]F labeled 2-deoxy-2-fluoro-D-glucose, 2-deoxy-2-fluoro-D-mannose and

^{14}C-2-deoxy-2-fluoro-D-glucose. J Label Compd Radiopharm. 1978;14:175–83.

28. Gambhir SS, Czernin J, Schwimmer J, et al. A tabulated summary of the FDG PET literature. J Nucl Med. 2001;42(suppl 5):1S–93S.

29. Hofman MS, Hicks RJ. How we read oncologic FDG PET/CT. Cancer Imaging. 2015;16:35. https://doi.org/10.1186/s40644-016-0091-3.

30. Margolis DJA, Hoffman JM, Herfkens RJ, et al. Molecular imaging techniques in body imaging. Radiology. 2007;245:333–56.

31. Iravani A and Hicks RJ. Imaging the Cancer Immune Environment and Its Response to Pharmacologic Intervention, Part 2: The Role of Novel PET Agents. J Nucl Med. 2020;61(11):1553–9.

32. Elgazzar AH, Shehab D. Musculoskeletal system. In: Elgazzar A, editor. The pathologic basis of nuclear medicine. 2nd ed. Berlin: Springer; 2006.

33. Even-Sapir E, Metser U, Flusser G, et al. Assessment of malignant skeletal disease with ^{18}F-fluoride PET/CT. J Nucl Med. 2004;45:272–8.

34. Hamaoka T, Madewell JE, Podoloff DA, et al. Bone imaging in metastatic breast cancer. J Clin Oncol. 2004;22:2942–53.

35. Volker JF, et al. The absorption of fluorides by enamel, dentin, bone, and hydroxyapatite as shown by the radioactive isotope. J Biol Chem. 1940;134:543–8.

36. Blau M, Nagler W, Bender MA. A new isotope for bone scanning. J Nucl Med. 1962;3:332–4.

37. Blake GM, Park-Holohan SJ, Cook GJ, et al. Quantitative studies of bone with the use of ^{18}F-fluoride and ^{99m}Tc-meth-ylene diphosphonate. Semin Nucl Med. 2001;31:28–49.

38. Schiepers C, Nuytes J, Bormans G, et al. Fluoride kinetics of the axial skeleton measured in vivo with fluorine-18-fluo-ride PET. J Nucl Med. 1997;38:1970–6.

39. Even-Sapir E, Mishani E, Flusser G, et al. 18F-fluoride positron emission tomography and positron emission tomography/computed tomography. Semin Nucl Med. 2007;37:462–9.

40. Cleaver JE. Thymidine metabolism and cell kinetics. Front Biol. 1967;6:43–100.

41. Livingston RB, Ambus U, George SL, et al. In vitro determination of thymidine-[H-3] labeling index in human solid tumors. Cancer Res. 1974;34:1376–80.

42. Christman D, Crawford EJ, Friedkin M, et al. Detection of DNA synthesis in intact organisms with positron-emitting methyl-[C-11]-thymidine. Proc Natl Acad Sci U S A. 1972;69:988–92.

43. Shields AF, Grierson JR, Kozawa SM, et al. Development of labeled thymidine analogs for imaging tumor proliferation. Nucl Med Biol. 1996;23:17–22.

44. Shields AF, Grierson JR, Dohmen BM, et al. Imaging proliferation in vivo with [F-18]FLT and positron emission tomography. Nat Med. 1998;4:1334–6.

45. Grierson JR, Schwartz JL, Muzi M, et al. Metabolism of 3′-deoxy-3′-[F-18]fluorothymidine in proliferating A549 cells: validations for positron emission tomography. Nucl Med Biol. 2004;31:829–37.

46. Seitz U, Wagner M, Neumaier B, et al. Evaluation of pyrimidine metabolizing enzymes and in vitro uptake of 3′-[^{18}F]fluoro-3′-deoxythymidine ([^{18}F]FLT) in pancreatic cancer cell lines. Eur J Nucl Med Mol Imaging. 2002;29:1174–81.

47. Salskov A, Tammisetti VS, Grierson J, et al. FLT: measuring tumor cell proliferation in vivo with positron emission tomography and 3′-Deoxy-3′-[^{18}F] fluorothymidine. Semin Nucl Med. 2007;37:429–39.

48. Bollineni VR, Kramer GM, Jansma EP, et al. A systematic review on [^{18}F]FLT-PET uptake as a measure of treatment response in cancer patients. Eur J Cancer. 2016;55:81–97.

49. Chen W, Delaloye S, Silverman DHS, et al. Predicting treatment response of malignant gliomas to bevacizumab and irinotecan by imaging proliferation with [18F] fluorothymidine positron emission tomography: a pilot study. J Clin Oncol. 2007;25:4714–21.

50. Mankoff DA, Shields AF, Krohn KA. PET imaging of cellular proliferation. Radiol Clin N Am. 2005;43:143–67.

51. Minamimoto R, Fayad L, Vose J, et al. 18F-Fluorothymidine PET is an early and superior predictor of progression-free survival following chemoimmunotherapy of diffuse large B cell lymphoma: a multicenter study. Eur J Nucl Med Mol Imaging. 2021;48:2883–93.

52. Alauddin MM. Journey of 2′-deoxy-2′-fluoro-5-methyl-1-β-D-arabinofuranosyluracil (FMAU): from antiviral drug to PET imaging agent. Curr Med Chem. 2018;25(16):1867–78.

53. Conti P, Alauddin M, Fissekis J, et al. Synthesis of 2′-flu-oro-5-[11C]-methyl-1-beta-D-arabinofuranosyluracil ([^{11}C]-FMAU): a potential nucleoside analog for in vivo study of cellular proliferation with PET. Nucl Med Biol. 1995;22(6):783–9.

54. Conti PS, Bading JR, Mouton P, et al. In vivo measurement of cell proliferation in canine brain tumor using C-11 labeled FMAU and PET. Nucl Med Biol. 2008;35:131–41.

55. Shields AF. PET imaging with ^{18}F-FLT and thymidine analogs: promise and pitfalls. J Nucl Med. 2003;44:1432–4.

56. Sun H, Sloan A, Mangner T, et al. Imaging DNA synthesis in vivo with [F-18]FMAU and positron emission tomography in patients with cancer. Eur J Nucl Med Mol Imaging. 2005;32:14–22.

57. Zeisel SH. Dietary choline: biochemistry, physiology, and pharmacology. Annu Rev Nutr. 1981;1:95–121.

58. Clary GL, Tsai C-F, Guynn RW, et al. Substrate specificity of choline kinase. Arch Biochem Biophys. 1987;254:214–21.

59. Roivainen A, Forsback S, Grönroos T, et al. Blood metabolism of [methyl-^{11}C]choline; implications for in vivo imaging with positron emission tomography. Eur J Nucl Med. 2000;27:25–32.

60. Wettstein M, Weik C, Holneicher C, et al. Betaine as an osmolyte in rat liver: metabolism and cell-to-cell interactions. Hepatology. 1998;27:787–93.

61. Jackowski S. Coordination of membrane phospholipid synthesis with the cell cycle. J Biol Chem. 1994;269:3858–67.

62. Cornell R, Grove GL, Rothblat GH, et al. Lipid requirement for cell cycling: the effect of selective inhibition of lipid synthesis. Exp Cell Res. 1997;109:299–307.

63. Tedeschi G, Lundbom N, Raman R, et al. Increased choline signal coinciding with malignant degeneration of cerebral gliomas: a serial proton magnetic resonance spectroscopy imaging study. J Neurosurg. 1997;87:516–24.

64. Hara T, Kosaka N, Shinoura N, et al. PET imaging of brain tumor with [methyl-^{11}C] choline. J Nucl Med. 1997;38:842–7.

65. Michaud L, Touijer KA, Mauguen A. 11C-Choline PET/CT in recurrent prostate cancer: retrospective analysis in a large U.S. patient series. J Nucl Med. 2020;61:827–33.

66. Evangelista L, Zattoni F, Guttilla A, et al. Choline PET or PET/CT and biochemical relapse of prostate cancer: a systematic review and meta-analysis. Clin Nucl Med. 2013;38(5):305–14.

67. Fanti S, Minozzi S, Castellucci P, et al. PET/CT with ^{11}C-choline for evaluation of prostate cancer patients with biochemical recurrence: meta-analysis and critical review of available data. Eur J Nucl Med Mol Imaging. 2015;43(1):55–69.

68. DeGrado TR, Coleman RE, Wang S, et al. Synthesis and evaluation of ^{18}F labeled choline as an oncologic tracer for positron emission tomography: initial findings in prostate cancer. Cancer Res. 2001;61:110–7.

69. Hara T, Kosaka N, Kishi H. Development of [^{18}F]-fluoroethylcholine for cancer imaging with PET: synthesis, biochemistry, and prostate cancer imaging. J Nucl Med. 2002;43:187–99.

70. Paymani Z, Rohringer T, Vali R, et al. Diagnostic performance of [^{18}F]Fluorocholine and ^{68}Ga-PSMA PET/CT in prostate cancer: a comparative study. Clin Med. 2020;9(7):2308.

71. Jager PL, Vaalburg W, Pruim J, et al. Radiolabeled amino acids: basic aspects and clinical applications in oncology. J Nucl Med. 2001;42:432–45.

72. Langen KJ, Jarosch M, Muhlensiepen H, et al. Comparison of fluorotyrosines and methionine uptake in F98 rat gliomas. Nucl Med Biol. 2003;30:501–8.

73. Qi Y, Liu X, Li J, et al. Fluorine-18 labeled amino acids for tumor PET/CT imaging. Oncotarget. 2017;8(36):60581–8.

74. Zhang L, Sui C, Yang W, Qiuhua L. Amino acid transporters: emerging roles in drug delivery for tumor-targeting therapy. Asian J Pharm Sci. 2020;15(2):192–206.

75. Becherer A, Karanikas G, Szabo M, et al. Brain tumour imaging with PET: a comparison between [^{18}F]fluorodopa and [^{11}C]methionine. Eur J Nucl Med Mol Imaging. 2003;30:1461–7.

76. Chen Y, Pullambhatla M, Foss CA, et al. 2-(3-{1-carboxy-5-[(6-^{18}F]fluoro-pyridine3-carbonyl)-amino]-pentyl}-ureido)-pen tanedioic acid, [^{18}F]DCFPyL, a PSMA based PET imaging agent for prostate cancer. Clin Cancer Res. 2011;17:7645–53.

77. Ito K, Matsuda H, Kubota K. Imaging spectrum and pitfalls of 11C-methionine positron emission tomography in a series of patients with intracranial lesions. Korean J Radiol. 2016;17(3):424–34.

78. Pruis IJ, van Dongen GAMS, van Zanten SEMV, et al. The added value of diagnostic and theranostic PET imaging for the treatment of CNS tumors. Int J Mol Sci. 2020;21:1029.

79. Pauleit D, Floeth F, Tellmann L, et al. Comparison of O-(2-^{18}F-fluoroethyl)-L-tyrosine PET and 3-^{123}I-Iodo-α-methyl-L-tyrosine SPECT in brain tumors. J Nucl Med. 2004;45:374–81.

80. Inoue TJ, Tomiyoshi K, Higuchi T, et al. Biodistribution studies on L-3-[^{18}F]fluoro-α-methyl tyrosine: a potential tumor-detecting agent. J Nucl Med. 1998;39:663–7.

81. Langen KJ, Hamacher K, Weckesser M, et al. O-(2-[^{18}F] fluoroethyl)-L-tyrosine: uptake mechanisms and clinical applications. Nucl Med Biol. 2006;33:287–94.

82. Sun A, Liu X, Tang G. Carbon-11 and fluorine-18 labeled amino acid tracers for positron emission tomography imaging of tumors. Front Chem. 2017;5:124.

83. Imperiale A, Meuter L, Pacak K, Taïeb D. Imaging of small intestine neuroendocrine neoplasms: is SSTR PET the holy grail? J Nucl Med. 2021;62:1347–8.

84. Shoup TM, Olson JMH, Votaw J, et al. Synthesis and evaluation of [^{18}F] 1-amino-3-fluorocyclobutane-l-carboxylic acid to image brain tumors. J Nucl Med. 1999;40:331–8.

85. Schuster DM, John R, Votaw JR, Nieh PT, et al. Initial experience with the radiotracer anti-1-amino-3–[18]F-fluorocy-clobutane-1-carboxylic acid with PET/CT in prostate carcinoma. J Nucl Med. 2007;48:56–63.

86. Chen W. Clinical applications of PET in brain tumors. J Nucl Med. 2007;48:1468–81.

87. Michaud L, Beattie BJ, Akhurst T, et al. 18F-Fluciclovine (^{18}F-FACBC) PET imaging of recurrent brain tumors. EJNMMI. 2020;47:1353–67.

88. Rais-Bahrami S, Efstathiou JA, Turnbull CM, et al. 18F-Fluciclovine PET/CT performance in biochemical recurrence of prostate cancer: a systematic review. Diagnostics. 2021;11(2):304.

89. Parent EE, Schuster DM. Update on ^{18}F-fluciclovine PET for prostate cancer imaging. J Nucl Med. 2018;9:733–9.

90. Songmen S, Nepal P, Olsavsky T, Sapire J. Axumin positron emission tomography: novel agent for prostate cancer biochemical recurrence. J Clin Imaging Sci. 2019;9:49.

91. Bluemel C, Krebs M, Polat B, et al. 68Ga-PSMA-PET/CT in patients with biochemical prostate cancer recurrence and negative ^{18}F-choline-PET/CT. Clin Nucl Med. 2016;41:515–21.

92. Tade FA, Cohen MA, Styblo TM, et al. Anti-3-18F-FACBC (18F-fluciclovine) PET/CT of breast cancer: an exploratory study. J Nucl Med. 2016;57:1357–63.

93. Pearse AG. The APUD concept and hormone production. Clin Endocrinol Metab. 1980;9:211–22.

94. Bjurling P, Antoni G, Watanabe Y, et al. Enzymatic synthesis of carboxy-11C-labelled l-tyrosine, l-DOPA, l-tryptophan and 5-hydroxy-l-tryptophan. Acta Chem Scand. 1990;44:178–82.

95. Sundin A, Eriksson B, Bergstrom M, et al. Demonstration of (11C) 5-hydroxy-l-tryptophan uptake and decarboxylation in carcinoid tumors by specific positioning labeling in positron emission tomography. Nucl Med Biol. 2000;1:33–41.

96. Hoegerle S, Altehoefer C, Ghanem N, et al. Whole-body ^{18}F-DOPA PET for detection of gastrointestinal carcinoid tumors. Radiology. 2001;220:373–80.

97. Orlefors H, Sundin A, Lu L, et al. Carbidopa pretreatment improves image interpretation and visualization of carcinoid tumours with ^{11}C-5-hydroxytryptophan positron emission tomography. Eur J Nucl Med Mol Imaging. 2006;33:60–5.

98. Oberg K. Diagnosis and treatment of carcinoid tumors. Expert Rev Anticancer Ther. 2003;3:863–77.

99. Orlefors H (2003) Positron emission tomography in the management of neuroendocrine tumors. PhD Thesis, Uppsala University, Sweden

100. Gazdar AF, Helman LJ, Israel MA, et al. Expression of neuroendocrine cell markers L-dopa decarboxylase, chromogranin A, and dense core granules in human tumors of endocrine and nonendocrine origin. Cancer Res. 1988;48:4078–82.

101. Becherer A, Szabo M, Karanikas G, et al. Imaging of advanced neuroendocrine tumors with [^{18}F-FDOPA PET. J Nucl Med. 2004;45:1161–7.

102. Hoegerle S, Altehoefer C, Ghanem N, et al. 18F-DOPA positron emission tomography for tumor detection in patients with medullary thyroid carcinoma and elevated calcitonin levels. Eur J Nucl Med. 2002;28:64–71.

103. Hoegerle S, Nitzsche E, Altehoefer C, et al. Pheochromocytomas: detection with ^{18}F DOPA whole body PET–initial results. Radiology. 2002;222:507–12.

104. Jager PL, Chirakal R, Marriott CJ, et al. 6-L-18F-fluorodihydroxyphenyl-alanine PET in neuroendocrine tumors: basic aspects and emerging clinical applications. J Nucl Med. 2008;49:573–86.

105. Treglia G, Sadeghi R, Giovinazzo F, et al. PET with different radiopharmaceuticals in neuroendocrine neoplasms: an umbrella review of published meta-analyses. Cancer. 2021;13:5172.

106. Chen W, Silverman DHS, Delaloye S, et al. 18F-FDOPA PET imaging of brain tumors: comparison study with ^{18}F-FDG PET and evaluation of diagnostic accuracy. J Nucl Med. 2006;47:904–11.

107. Seibyl JP, Chen W, Silverman DHS. 3,4-Dihydroxy-6-[^{18}F]-fluoro-L-phenylalanine positron emission tomography in patients with central motor disorders and in evaluation of brain and other tumors. Semin Nucl Med. 2007;37:440–50.

108. Brown JM, Wilson WR. Exploiting tumour hypoxia in cancer treatment. Nat Rev Cancer. 2004;4(6):437–47.

109. Schöder H, Ong SC. Fundamentals of molecular imaging: rationale and applications with relevance for radiation oncology. Semin Nucl Med. 2008;38:119–28.

110. Vaupel P, Schlenger K, Hoeckel M. Blood flow and tissue oxygenation of human tumors: an update. Adv Exp Med Biol. 1992;317:139–41.

111. Foo SS, Abbott DF, Lawrentschuk N, et al. Functional imaging of intra-tumoral hypoxia. Mol Imaging Biol. 2004;6:291–305.

112. Chapman JD, Franko AJ, Sharplin J. A marker for hypoxic cells in tumours with potential clinical applicability. Br J Cancer. 1981;43:546–50.

113. Whitmore GF, Varghese AJ. The biological properties of reduced nitroheterocyclics and possible underlying biochemical mechanisms. Biochem Pharmacol. 1986;35:97–103.

114. Lopes S, Ferreira S, Caetano M. PET/CT in the evaluation of hypoxia for radiotherapy planning in head and neck tumors: systematic literature review. J Nucl Med Technol. 2021;49:10–1.

115. Lopci E, Grassi I, Chiti A. PET radiopharmaceuticals for imaging of tumor hypoxia: a review of the evidence. Am J Nucl Med. 2014;4(4):365–84.

116. Rasey JS, Grunbaum Z, Magee S, et al. Characterization of radiolabeled fluoromisonidazole as a probe for hypoxic cells. Radiat Res. 1987;111:292–304.

117. Hirata K, Kobayashi K, Tamaki N. Hypoxia imaging with ^{18}F-FMISO PET for brain tumors. In: Kuge Y, et al., editors. Perspectives on nuclear medicine for molecular diagnosis and integrated therapy. Berlin: Springer; 2016. p. 229–50.

118. Challapalli A, Carroll L, Aboagye EO. Molecular mechanisms of hypoxia in cancer. Clin Transl Imaging. 2017;5(3):225–53.

119. Huang Y, Fan J, Li Y, et al. Imaging of tumor hypoxia with radionuclide-labeled tracers for PET. Front Oncol. 2021. https://doi.org/10.3389/fonc.2021.731503.

120. Beck R, Roper B, Carlsen JM, et al. Pretreatment ^{18}F-FAZA PET predicts success of hypoxia-directed radiochemotherapy using tirapazamine. J Nucl Med. 2007;48:973–80.

121. Gronroos T, Eskola O, Lehtio K, et al. Pharmacokinetics of [^{18}F]FETNIM: a potential marker for PET. J Nucl Med. 2001;42:1397–404.

122. Piert M, Machulla HJ, Picchio M, et al. Hypoxia-specific tumor imaging with ^{18}F-fluoroazomycin arabinoside. J Nucl Med. 2005;46:106–13.

123. Rasey JS, Hofstrand PD, Chin LK, et al. Characterization of [^{18}F]fluoroetanidazole, a new

radiopharmaceutical for detecting tumor hypoxia. J Nucl Med. 1999;40:1072–9.

124. Lee ST, Scott AM. Hypoxia positron emission tomography imaging with ^{18}F-fluoromisonidazole. Semin Nucl Med. 2007;37:451–61.

125. Lapi SE, Lewis JS, Dehdashti F. Evaluation of hypoxia with copper-labeled diacetyl-bis(N-methyl-thiosemicarbazone). Semin Nucl Med. 2015;45:177–85.

126. Lewis JS, Welch MJ. PET imaging of hypoxia. Q J Nucl Med. 2001;45:183–8.

127. Fleming IN, Manavaki R, Blower PJ, et al. Imaging tumour hypoxia with positron emission tomography. Br J Cancer. 2015;112:238–50.

128. Folkman J. Tumor angiogenesis: therapeutic implications. N Engl J Med. 1971;285:1182–6.

129. Pugh CW, Ratcliffe PJ. Regulation of angiogenesis by hypoxia: role of the HIF system. Nat Med. 2003;9:677–84.

130. Friedlander M, Brooks PC, Shaffer RW, et al. Definition of two angiogenic pathways by distinct α_V integrins. Science. 1995;270:1400–2.

131. Jin H, Varner J. Integrins: roles in cancer development and as treatment targets. Br J Cancer. 2004;90:561–5.

132. Florea A, Mottaghy FM, Bauwens M. Molecular imaging of angiogenesis in oncology: current preclinical and clinical status. Int J Mol Sci. 2021;22(11):5544.

133. Liu J, Yuan S, Wang L, et al. Diagnostic and predictive value of using RGD PET/CT in patients with cancer: a systematic review and meta-analysis. Biomed Res Int. 2019;2019:8534761.

134. Haubner R, Wester H-J, Reuning U, et al. Radiolabeled $\alpha_V\beta_3$ integrin antagonists: a new class of tracers for tumor targeting. J Nucl Med. 1999;40:1061–71.

135. Zhang X, Xiong Z, Wu Y, et al. Quantitative PET imaging of tumor integrin $\alpha_V\beta_3$ expression with ^{18}F-FRGD2. J Nucl Med. 2006;47:113–21.

136. Wu Y, Zhang X, Xiong Z, et al. microPET imaging of glioma $\alpha_V\beta_3$ integrin expression using ^{64}Cu-labeled tetrameric RGD peptide. J Nucl Med. 2005;46:1707–18.

137. Haubner R, Wester HJ, Weber WA, et al. Noninvasive imaging of alpha$_v$ beta$_3$ integrin expression using ^{18}F-labeled RGD-containing glycopeptide and positron emission tomography. Cancer Res. 2001;61:1781–5.

138. Beer A, Lorenzen S, Metz S, et al. Comparison of integrin a$_v$b$_3$ expression and glucose metabolism in primary and metastatic lesions in cancer patients: a PET study using ^{18}F-Galacto-RGD and ^{18}F-FDG. J Nucl Med. 2008;49:22–9.

139. Durante S, Dunet V, Gorostidi F, et al. Head and neck tumors angiogenesis imaging with ^{68}Ga-NODAGA-RGD in comparison to ^{18}F-FDG PET/CT: a pilot study. EJNMMI Res. 2020;10:47.

140. Li L, Zhao W, Sun X. 18F-RGD PET/CT imaging reveals characteristics of angiogenesis in non-small cell lung cancer. Transl Lung Cancer Res. 2020;9(4):1324–32.

141. Kerr JF, Wyllie AH, Currie AR. Apoptosis: a basic biological phenomenon with wide-ranging implications in tissue kinetics. Br J Cancer. 1972;26(4):239–57.

142. Blankenberg FG. In vivo detection of apoptosis. J Nucl Med. 2008;49:81S–95S.

143. Letai A. Apoptosis and cancer. Annu Rev Cancer Biol. 2017;1:275–94.

144. Qin X, Jiang H, Liu Y, et al. Radionuclide imaging of apoptosis for clinical application. EJNMMI. 2021. https://doi.org/10.1007/s00259-021-05641-4.

145. Krammer PH. CD95's deadly mission in the immune system. Nature. 2000;407:789–95.

146. Zwaal RFA, Comfurius P, Bevers EM. Surface exposure of phosphatidylserine in pathological cells. Cell Mol Life Sci. 2005;62:971–98.

147. Wang X, Feng H, Zhao S, et al. SPECT and PET radiopharmaceuticals for molecular imaging of apoptosis: from bench to clinic. Oncotarget. 2017;8(12):20476–95.

148. Mosayebnia M, Hajiramezanali M, Shahhosseini S. Radiolabeled peptides for molecular imaging of apoptosis. Curr Med Chem. 2020;27:41).

149. Beroske L, den Wyngaert TV, Stroobants S, et al. Molecular imaging of apoptosis: the case of caspase-3 radiotracers. Mol Sci. 2021;22:3948.

150. Boersma HH, Kietselaer BL, Stolk LM, et al. Past, present, and future of annexin A5: from protein discovery to clinical applications. J Nucl Med. 2005;46:2035–50.

151. Tait JF, Cerqueira MD, Dewhurst TA. Evaluation of annexin V as a platelet-directed thrombus targeting agent. Thromb Res. 1994;75:491–501.

152. Belhocine T, Steinmetz N, Li C, Green A, et al. The imaging of apoptosis with the radiolabeled annexin V: optimal timing for clinical feasibility. Technol Cancer Res Treat. 2004;3:23–32.

153. Höglund J, Shirvan A, Antoni G, et al. 18F-ML-10, a PET tracer for apoptosis: first human study. J Nucl Med. 2011;52(5):720–5.

154. Sun L, Zhou K, Wang W, et al. [18F] ML-10 imaging for assessment of apoptosis response of intracranial tumor early after radiosurgery by PET/CT. Contrast Media Mol Imaging. 2018;2018:9365174.

155. Bonisch H, Bruss M. The norepinephrine transporter in physiology and disease. Handb Exp Pharmacol. 2006;175:485–524.

156. Streby KA, Shah N, Ranalli MA, Kunkler A, Cripe TP. Nothing but NET: a review of nor-epinephrine transporter expression and efficacy of ^{131}I-mIBG therapy. Pediatr Blood Cancer. 2015;62:5–11.

157. Pandit-Taskar P, Modak S. Norepinephrine transporter as a target for imaging and therapy. J Nucl Med. 2017;2017(58):39S–53S.

158. Wieland DM, Wu JL, Brown LE, et al. Radiolabeled adrenergic neuron blocking agents: adrenomedullary imaging with ^{131}I-iodobenzylguanidine. J Nucl Med. 1980;21:349–53.

159. Wieland DM, Brown LE, Tobes MC, et al. Imaging the primate adrenal medulla with [123I] and [131I] meta-iodobenzylguanidine: concise communication. J Nucl Med. 1981;22:358–64.

160. Vallabhajosula S, Nikolopoulou A. Radioiodinated metaiodobenzylguanidine (MIBG): radiochemistry, biology, and pharmacology. Semin Nucl Med. 2011;41(5):324–33.

161. Hattner RS, Huberty JP, Engelstad BL, et al. Localization of m-iodo(131I)benzylguanidine in neuroblastoma. AJR Am J Roentgenol. 1984;143(2):373–4.

162. Sisson JC, Frager MS, Valk TW, et al. Scintigraphic localization of pheochromocytoma. N Engl J Med. 1981;305(1):12–7.

163. Sisson JC, Shapiro B, Beierwaltes WH, et al. Radiopharmaceutical treatment of malignant pheochromocytoma. J Nucl Med. 1984;25:197–206.

164. Treuner J, Feine U, Niethammer D, et al. Scintigraphic imaging of neuroblastoma with [131I] iodobenzylguanidine. Lancet. 1984;1:333–4.

165. Hoefnagel CA, Voûte PA, de Kraker J, Marcuse HR. Radionuclide diagnosis and therapy of neural crest tumors using I-131-meta-iodobenzylguanidine. J Nucl Med. 1987;28:308–14.

166. Garg PK, Garg S, Zalutsky MR. Synthesis and preliminary evaluation of para- and meta-[18F]fluorobenzylguanidine. Nucl Med Biol. 1994;21(1):97–103.

167. Vaidyanathan G, Afeck DJ, Zalutsky MR. Validation of 4-[18F] fuoro-3-iodobenzylguanidine as a positron-emitting analog of MIBG. J Nucl Med. 1995;36:644–50.

168. Zhang H, Huang R, Cheung N-KV, et al. Imaging the norepinephrine transporter in neuroblastoma: a comparison of [18F]-MFBG and 123I-MIBG. Clin Cancer Res. 2014;20(8):2182.

169. Pandit-Taskar N, Zanzonico P, Staton KD, et al. Biodistribution and dosimetry of 18F-meta-fuorobenzylguanidine: a first-in human PET/CT imaging study of patients with neuroendocrine malignancies. J Nucl Med. 2018;59(1):147–53.

170. Yamaguchi A, Hanaoka H, Higuchi T, Tsushima Y. Radiolabeled (4-fuoro-3-iodobenzyl)guanidine improves imaging and targeted radionuclide therapy of norepinephrine transporter expressing tumors. J Nucl Med. 2018;59(5):815–21.

171. Chen X, Kudo T, Lapa C, et al. Recent advances in radiotracers targeting norepinephrine transporter: structural development and radiolabeling improvements. J Neural Transm. 2020;127:851–73.

172. Shulkin BL, Wieland DM, Schwaiger M, et al. PET scanning with hydroxyephedrine: an approach to the localization of pheochromocytoma. J Nucl Med. 1992;33:1125–31.

173. Shulkin BL, Wieland DM, Baro ME, et al. PET hydroxyephedrine imaging of neuroblastoma. J Nucl Med. 1996;37:16–21.

174. Yamamoto S, Hellman P, Wassberg C, et al. 11C-hydroxyephedrine positron emission tomography imaging of pheochromocytoma: a single center experience over 11 years. J Clin Endocrinol Metab. 2012;97:2423–32.

175. Vyakaranam AR, Crona J, Norlén O, et al. 11C-hydroxy-ephedrine-PET/CT in the diagnosis of pheochromocytoma and paraganglioma. Cancer. 2019;11(6):E847.

176. Kaji P, Carrasquillo JA, Linehan WM, et al. The role of 6-[18F]fluorodopamine positron emission tomography in the localization of adrenal pheochromocytoma associated with von Hippel-Lindau syndrome. Eur J Endocrinol. 2007;156:483–7.

177. Pacak K, Eisenhofer G, Carrasquillo JA, et al. 6-[18F] Fluorodopamine positron emission tomographic (PET) scanning for diagnostic localization of pheochromocytoma. Hypertension. 2001;38:6–8.

178. Timmers HJLM, Chen CC, Carrasquillo JA. Comparison of 18F-fluoro-L-DOPA, 18F-fluorodeoxyglucose, and 18F-fluorodopamine PET and 123I-MIBG scintigraphy in the localization of pheochromocytoma and paraganglioma. J Clin Endocrinol Metab. 2009;94:4757–67.

179. Kowalczyk W, Waliszczak G, Jach R, Dulinska-Litewka J. Steroid receptors in breast cancer: understanding of molecular function as a basis for effective therapy development. Cancer. 2021;13:4779.

180. Sundararajan L, Linden HM, Link JM, et al. 18F-fluoroestradiol. Semin Nucl Med. 2007;37:470–6.

181. Van de Wiele C, De Vos F, Slegers G, et al. Radiolabeled estradiol derivatives to predict response to hormonal treatment in breast cancer: a review. Eur J Nucl Med. 2000;27:1421–33.

182. Vollenweider-Zerargui L, Barrelet L, Wong Y, et al. The predictive value of estrogen and progesterone receptors' concentrations on the clinical behavior of breast cancer in women: clinical correlation on 547 patients. Cancer. 1986;57:1171–80.

183. Kurland BF, Wiggins JR, Coche A. Whole-body characterization of estrogen receptor status in metastatic breast cancer with 16α-18F-fluoro-17β-estradiol positron emission tomography: meta-analysis and recommendations for integration into clinical applications. Oncologist. 2020;25(10):835–44.

184. Grabher BJ. Breast cancer: evaluating tumor estrogen receptor status with molecular imaging to increase response to therapy and improve patient outcomes. J Nucl Med Technol. 2020;48:191–201.

185. Jensen EV, DeSombre ER, Jungblut PW. Estrogen receptors in hormone-responsive tissue and tumors. In Wissler RW, Dao TL, Wood S Jr (eds): Endogenous factors influencing host tumor balance. Chicago, University of Chicago Press. 1967.

186. Kiesewetter DO, Kilbourn MR, Landvatter SW, et al. Preparation of four fluorine-18-labeled estrogens and their selective uptakes in target tissues of immature rats. J Nucl Med. 1984;25:1212–21.

187. Mankoff DA, Tewson TJ, Eary JF. Analysis of blood clearance and labeled metabolites for the estrogen receptor tracer [F-18]-16 alpha-fluoroestradiol (FES). Nucl Med Biol. 1997;24:341–8.

188. Chae SY, Ahn SH, Kim S-B, et al. Diagnostic accuracy and safety of 16α-[18F]fluoro-17β-oestradiol PET-CT for the assessment of estrogen receptor status in recurrent or metastatic lesions in patients with breast cancer: a prospective cohort study. Lancet Oncol. 2019;20(4):546–55.

189. Ulaner GA, Jhaveri K, Chandarlapaty S, et al. Head-to-head evaluation of 18F-FES and 18F-FDG PET/CT in metastatic invasive lobular breast cancer. J Nucl Med. 2021;62:326–31.

190. Fani M, Maecke HR, Okarvi SM. Radiolabeled peptides: valuable tools for the detection and treatment of cancer. Theranostics. 2012;2(5):481–501.

191. Günther T, Tulipano G, Dournaud P, et al. International Union of Basic and Clinical Pharmacology. CV. Somatostatin receptors: structure, function, ligands, and new nomenclature. Pharmacol Rev. 2018;70:763–835.

192. Brazeau P, Vale W, Burgus R, et al. Hypothalamic polypeptide that inhibits the secretion of immunoreactive pituitary growth hormone. Science. 1973;179:77–9.

193. Bauer W, Briner U, Doepfner W, et al. SMS 201-995: a very potent and selective octapeptide analogue of somatostatin with prolonged action. Life Sci. 1982;31(11):1133–40.

194. Fani M, Nicolas GP, Wild D. Somatostatin receptor antagonists for imaging and therapy. J Nucl Med. 2017;58:61S–6S.

195. La Salvia A, Espinosa-Olarte P, Riesco-Martinez MDC, et al. Targeted cancer therapy: what's new in the field of neuroendocrine neoplasms? Cancer. 2021;13:1701.

196. Ginj M, Zhang H, Waser B, et al. Radiolabeled somatostatin receptor antagonists are preferable to agonists for in vivo peptide receptor targeting of tumors. Proc Natl Acad Sci U S A. 2006;103:16436–41.

197. Reubi JC, Hacki WH, Lamberts SW. Hormone-producing gastrointestinal tumors contain a high density of somatostatin receptors. J Clin Endocrinol Metab. 1987;65:1127–34.

198. De Jong M, Bakker WH, Krenning EP, et al. Yttrium-90 and indium-111 labelling, receptor binding and biodistribution of [DOTA0,D-Phe1,Tyr3]octreotide, a promising somatostatin analogue for radionuclide therapy. Eur J Nucl Med. 1997;24:368–71.

199. Reubi JC, Schär J-C, Waser B, et al. Affinity profiles for human somatostatin receptor subtypes SST1–SST5 of somatostatin radiotracers selected for scintigraphic and radiotherapeutic use. Eur J Nucl Med. 2000;27:273–82.

200. Hofmann M, Maecke H, Börner AR, et al. Biokinetics and imaging with the somatostatin receptor PET radioligand Ga-68 DOTATOC preliminary data. Eur J Nucl Med. 2001;28:1751–7.

201. Graham MM, Gu X, Ginader T, et al. 68Ga-DOTATOC imaging of neuroendocrine tumors: a systematic review and metaanalysis. J Nucl Med. 2017;58:1452–8.

202. Hennrich U, Benešová M. [68Ga]Ga-DOTA-TOC: the first FDA-approved 68Ga-radiopharmaceutical for PET imaging. Pharmaceuticals. 2020;13:38. https://doi.org/10.3390/ph13030038.

203. Durmo R, Filice A, Fioroni F, et al. Predictive and prognostic role of pre-therapy and interim 68Ga-DOTATOC PET/CT parameters in metastatic advanced neuroendocrine tumor patients treated with PRRT. Cancer. 2022;14(3):592.

204. Hofman MS, Lau WFE, Hicks RJ. Somatostatin receptor imaging with 68Ga DOTATATE PET/CT: clinical utility, normal patterns, pearls, and pitfalls in interpretation. Radiographics. 2015;35(2):500–16.

205. Srirajaskanthan R, Kayani I, Quigley AM, et al. The role of 68Ga-DOTATATE PET in patients with neuroendocrine tumors and negative or equivocal findings on 111In-DTPA-octreotide scintigraphy. J Nucl Med. 2010;51:875–82.

206. Pattison DA and Hofman MS. Role of Fluorodeoxyglucose PET/Computed Tomography in Targeted Radionuclide Therapy for Endocrine Malignancies. PET Clin. 2015;10:461–47

207. Wild D, Schmitt JS, Ginj M, et al. DOTA-NOC, a high-affinity ligand of somatostatin receptor subtypes 2, 3 and 5 for labelling with various radiometals. Eur J Nucl Med Mol Imaging. 2003;30:1338–47.

208. Kabasakal L, Demirci E, Ocak M, et al. Comparison of 68Ga-DOTATATE and 68Ga-DOTANOC PET/CT imaging in the same patient group with neuroendocrine tumours. Eur J Nucl Med Mol Imaging. 2012;39:1271–7.

209. Wild D, Fani M, Behe M, et al. First clinical evidence that imaging with somatostatin receptor antagonists is feasible. J Nucl Med. 2012;52:1412–7.

210. Mohamad H, Ali S, Emmanuel P, et al. The role of 68Ga-DOTA-NOC PET/CT in evaluating neuroendocrine tumors. Nucl Med Commun. 2017;38(2):170–7.

211. Anderson CJ, Dehdashti F, Cutler PD, et al. 64Cu-TETA-octreotide as a PET imaging agent for patients with neuroendocrine tumors. J Nucl Med. 2001;42:213–21.

212. Pfeifer A, Knigge U, Mortensen J, et al. Clinical PET of neuroendocrine tumors using 64Cu-DOTATATE: first-in-humans study. J Nucl Med. 2012;53:1207–15.

213. Carlsen EA, Johnbeck CB, Binderup T, et al. 64Cu-DOTATATE PET/CT and Prediction of overall and progression-free survival in patients with neuroendocrine Neoplasms. J Nucl Med. 2020;61:1491–7.

214. Johnbeck CB, Knigge U, Loft A, et al. Head-to-head comparison of 64Cu-DOTATATE and 68Ga-DOTATOC PET/CT: a prospective study of 59 patients with neuroendocrine tumors. J Nucl Med. 2017;58:451–7.

215. Delpassand ES, Ranganathan D, Wagh N, et al. 64Cu-DOTATATE PET/CT for imaging patients with known or suspected somatostatin receptor–positive neuroendocrine tumors: results of the first U.S. prospective, reader-masked clinical trial. J Nucl Med. 2020;61:890–6.

216. Eychenne R, Bouvry C, Bourgeois M, et al. Overview of radiolabeled somatostatin analogs for cancer imaging and therapy. Molecules. 2020;25:4012. https://doi.org/10.3390/molecules25174012.

217. Nicolas GP, Schreier N, Kaul F, et al. Sensitivity comparison of (68)Ga-OPS202 and (68)Ga DOTATOC PET/CT in patients with gastroenteropancreatic neuroendocrine tumors: a prospective phase II imaging study. J Nucl Med. 2018;59:915–21.

218. Huo L, Zhu W, Cheng Y. A prospective randomized, double-blind study to evaluate the safety, biodistribution, and dosimetry of 68Ga-NODAGA-LM3 and 68Ga-DOTA-LM3 in patients with well-differentiated neuroendocrine tumors. J Nucl Med. 2021;62(10):1398–405.

219. Mohtavinejad N, Shafiee Ardestani M, Khalaj A, et al. Application of radiolabeled peptides in tumor imaging and therapy. Life Sci. 2020;258:118206.

220. Mikulova MB, Mikus P. Advances in development of radiometal labeled amino acid-based compounds for cancer imaging and diagnostics. Pharmaceuticals. 2021;14:167–206.

221. Christ E, Antwi K, Fani M, Wild D. Innovative imaging of insulinoma: the end of sampling? A review. Endocr Relat Cancer. 2020;27:R79–92.

222. Jansen T, Van Lith S, Boss M, et al. Exendin-4 analogs in insulinoma theranostics. J Label Compd Radiopharm. 2019;62:656–72.

223. Wild D, Macke H, Christ E, Gloor B, Reubi JC. Glucagon-like peptide 1-receptor scans to localize occult insulinomas. N Engl J Med. 2008;359(7):766–8.

224. Antwi K, Fani M, Nicolas G, et al. Localization of hidden insulinomas with 68Ga-DOTA-exendin-4 PET/CT: a pilot study. J Nucl Med. 2015;56:1075–8.

225. Antwi K, Fani M, Heye T, et al. Comparison of glucagon-like peptide-1 receptor (GLP-1R) PET/CT, SPECT/CT and 3T MRI for the localization of occult insulinomas: evaluation of diagnostic accuracy in a prospective crossover imaging study. EJNMMI. 2018;45:2318–27.

226. Luo Y, Pan Q, Yao S, et al. Glucagon-like peptide-1 receptor PET/CT with 68Ga-NOTA-exendin-4 for detecting localized insulinoma: a prospective cohort study. J Nucl Med. 2016;57:715–20.

227. Kircher M, Herhaus P, Schottelius M, et al. CXCR4-directed theranostics in oncology and inflammation. Ann Nucl Med. 2018;32:503–11.

228. Kakinuma T, Hwang ST. Chemokines, chemokine receptors, and cancer metastasis. J Leukoc Biol. 2006;79:639–51.

229. Guo F, Wang Y, Liu J. CXCL12/CXCR4: a symbiotic bridge linking cancer cells and their stromal neighbors in oncogenic communication networks. Oncogene. 2016;35:816–26.

230. Demmer O, Gourni E, Schumacher U, et al. PET imaging of CXCR4 receptors in cancer by a new optimized ligand. ChemMedChem. 2011;6(10):1789–91.

231. Lapa C, Lückerath K, Rudelius M, et al. [68Ga] Pentixafor-PET/CT for imaging of chemokine receptor 4 expression in small cell lung cancer - initial experience. Oncotarget. 2016. https://doi.org/10.18632/oncotarget.7063

232. Werner RA, Weich A, Higuchi T, et al. Imaging of chemokine receptor 4 expression in neuroendocrine tumors - a triple tracer comparative approach. Theranostics. 2017;7:1489–98.

233. Weich A, Werner RA, Buck AK, et al. CXCR4-directed PET/CT in patients with newly diagnosed neuroendocrine carcinomas. Diagnostics. 2021;11(4):605. https://doi.org/10.3390/diagnostics11040605.

234. O'Keefe DS, Su SL, Bacich DJ, et al. Mapping, genomic organization and promoter analysis of the human prostate-specific membrane antigen gene. Biochim Biophys Acta Gene Struct Expr. 1998;1443:113–27.

235. Evans JC, Malhotra M, Cryan JF, O'Driscoll CM. The therapeutic and diagnostic potential of the prostate specific membrane antigen/glutamate carboxypeptidase II(PSMA/GCPII) in cancer and neurological disease. Br J Pharmacol. 2016;173:3041–307.

236. Israeli RS, Powell CT, Fair WR, Heston WD. Molecular cloning of a complementary DNA encoding a prostate specific membrane antigen. Cancer Res. 1993;53:227–30.

237. Horoszewicz JS, Kawinski E, Murphy GP. Monoclonal antibodies to a new antigenic marker in epithelial prostatic cells and serum of prostatic cancer patients. Anticancer Res. 1987;7:927–35.

238. Israeli RS, Powell CT, Corr JG, Fair WR, Heston WD. Expression of the prostate-specific membrane antigen. Cancer Res. 1994;54:1807–11.

239. Wright GL Jr, Haley C, Beckett ML, Schellhammer PF. Expression of prostate-specific membrane antigen (PSMA) in normal, benign and malignant prostate tissues. Urol Oncol. 1995;1:18–28.

240. Wright Jr GL, Grob BM, Grossman CH, et al. Upregulation of prostate-specific membrane antigen after androgendeprivation therapy. Urology 1996;48(2):326–34.

241. Abou D, Benabdallah N, Jiang W, et al. Prostate cancer theranostics – an overview. Front Oncol. 2020;10:884.

242. Ahmadzadehfar H, Rahbar K, Essler, Biersack HJ. PSMA-based theranostics: a step-by-step practical approach to diagnosis and therapy for mCRPC patients. Semin Nucl Med. 2020;50:98–109.

243. Bařinka C, Rojas C, Slusher B, Pomper M. Glutamate carboxypeptidase II in diagnosis and treatment of neurologic disorders and prostate cancer. Curr Med Chem. 2012;19:856.

244. Pastorino S, Riondato M, Uccelli L, et al. Toward the discovery and development of PSMA targeted inhibitors for nuclear medicine applications. Curr Radiopharm. 2020;13:63–79.

245. Eder M, Scheafer M, Bauder-Wust U, et al. 68Ga-complex lipophilicity and the targeting prop-

erty of a urea-based PSMA inhibitor for PET imaging. Bioconjug Chem. 2012;23:688–97.

246. Afshar-Oromieh A, Haberkorn U, Eder M, et al. [68Ga]Gallium labelled PSMA ligand as superior PET tracer for the diagnosis of prostate cancer: comparison with ^{18}F-FECH. Eur J Nucl Med Mol Imaging. 2012;39:1085–6.

247. Bois F, Noirot C, Dietemann S, et al. [68Ga] Ga-PSMA-11 in prostate cancer: a comprehensive review. Am J Nucl Med Mol Imaging. 2020;10(6):349–74.

248. Ahmadzadehfar H, Azgomi K, Hauser S, et al. 68Ga-PSMA-11 PET as a gatekeeper for the treatment of metastatic prostate cancer with [223]Ra: proof of concept. J Nucl Med. 2017;58:438–44.

249. Zacho HD, Ravn S, Afshar-Oromieh A, et al. Added value of 68Ga-PSMA PET/CT for the detection of bone metastases in patients with newly diagnosed prostate cancer and a previous 99mTc bone scintigraphy. EJNMMI Res. 2020;10:31.

250. Carlucci G, Ippisch R, Slavik R, et al. 68Ga-PSMA-11 NDA approval: a novel and successful academic partnership. J Nucl Med. 2021;62:149–55.

251. Dietlein F, Kobe C, Neubauer S, et al. PSA-stratified performance of [18]F- and ^{68}Ga-PSMA PET in patients with biochemical recurrence of prostate cancer. J Nucl Med. 2017;58:947–52.

252. Giesel FL, Will L, Lawal T, et al. Intraindividual comparison of ^{18}F-PSMA-1007 and [18]FDCFPyL PET/CT in the prospective evaluation of patients with newly diagnosed prostate carcinoma: a pilot study. J Nucl Med. 2018;59:1076–80.

253. Rowe SP, Buck A, Bundschuh RA, et al. [18F] DCFPyL PET/CT for imaging of prostate cancer. Nuklearmedizin. 2022;61(3):240–6.

254. Morris MJ, Rowe SP, Gorin MA, et al. Diagnostic performance of ^{18}F-DCFPyL-PET/CT in men with biochemically recurrent prostate cancer: results from the CONDOR phase III, multicenter study. Clin Cancer Res. 2021;27(13):3674–82.

255. Eiber M, Kroenke M, Wurzer A, Ulbrich L, Jooß L, Maurer T, et al. (18)F-rhPSMA-7 PET for the detection of biochemical recurrence of prostate cancer after radical prostatectomy. J Nucl Med. 2020;61(5):696–701.

256. Wurzer A, Di Carlo D, Schmidt A, et al. Radiohybrid ligands: a novel tracer concept exemplified by [18]F- or ^{68}Ga-Labeled rhPSMA inhibitors. J Nucl Med. 2020;61:735–42.

257. Wurzer A, Parzinger M, Konrad M. Preclinical comparison of four [(18)F, (nat)Ga]rhPSMA-7 isomers: influence of the stereo configuration on pharmacokinetics. EJNMMI Res. 2020;10(1):149.

258. Langbein T, Wang H, Rauscher I, et al. Utility of ^{18}F-rhPSMA-7.3 positron emission tomography for imaging of primary prostate cancer and pre-operative efficacy in N-staging of unfavorable intermediate to very high-risk patients validated by histopathology. J Nucl Med. 2022;63(9):1334–42.

259. Vallabhajosula S, Nikolopoulou A, Babich, et al. 99mTc-labeled small-molecule inhibitors of prostate-specific membrane antigen: pharmacokinetics and biodistribution studies in healthy subjects

and patients with metastatic prostate cancer. J Nucl Med. 2014;55(11):1791–8.

260. Vallabhajosula S, Polack BD, Babich JW. Molecular imaging of prostate cancer: radiopharmaceuticals for positron emission tomography (PET) and single-photon emission computed tomography (SPECT). In: Precision molecular pathology of prostate cancer. Berlin: Springer; 2018. p. 475–501.

261. Bu L, Baba H, Yoshida N, et al. Biological heterogeneity and versatility of cancer-associated fibroblasts in the tumor microenvironment. Oncogene. 2019;38:4887–901.

262. Kuzet S-E, Gaggioli C. Fibroblast activation in cancer: when seed fertilizes soil. Cell Tissue Res. 2016;365:607–19.

263. Jansen K, Heirbaut L, Cheng JD, et al. Selective inhibitors of fibroblast activation protein (FAP) with a (4-quinolinoyl)-glycyl-2-cyanopyrrolidine scaffold. ACS Med Chem Lett. 2013;4:491–6.

264. Altmann A, Haberkorn U, Siveke J. The latest developments in imaging of fibroblast activation protein. J Nucl Med. 2021;62(2):160–7.

265. Calais J. FAP: The next billion dollar nuclear theranostics target. J Nucl Med. 2020;61(2):163–5.

266. Dendl K, Schlittenhardt J, Staudinger F, et al. The role of fibroblast activation protein ligands in oncologic PET imaging. PET Clin. 2021;16(3):341–51.

267. Welt S, Divgi CR, Scott AM, et al. Antibody targeting in metastatic colon cancer: a phase I study of monoclonal antibody F19 against a cell-surface protein of reactive tumor stromal fibroblasts. J Clin Oncol. 1994;12:1193–203.

268. Jansen K, Heirbaut L, Verkerk R, et al. Extended structure-activity relationship and pharmacokinetic investigation of (4-quinolinoyl)glycyl-2-cyanopyrrolidine inhibitors of fibroblast activation protein (FAP). J Med Chem. 2014;57:3053–74.

269. Moek KL, Giesen D, Kok IC. Theranostics using antibodies and antibody-related therapeutics. J Nucl Med. 2017;58:83S–90S.

270. Pandit-Taskar N, O'Donoghue JA, Ruan S, et al. First-in-human imaging with [89]Zr-Df-IAB2M anti-PSMA minibody in patients with metastatic prostate cancer: pharmacokinetics, biodistribution, dosimetry, and lesion uptake. J Nucl Med. 2016;57:1858–64.

271. Niemeijer AN, Leung D, Huisman MC, et al. Whole body PD-1 and PD-L1 positron emission tomography in patients with non-small-cell lung cancer. Nat Commun. 2018;9:4664.

272. Kratochwil C, Flechsig P, Lindner T, Abderrahim L, Altmann A, Mier W, Adeberg S, Rathke H, Röhrich M, Winter H, et al. 68Ga-FAPI PET/CT: tracer uptake in 28 different kinds of cancer. J Nucl Med. 2019;60:801–5.

273. Loktev A, Lindner T, Mier W, et al. A tumor-imaging method targeting cancer-associated fibroblasts. J Nucl Med. 2018;59:1423–9.

274. Himmelweit B, editor. The collected papers of Paul Ehrlich. Elmsford: Pergamon; 1957.

275. Köhler G, Milstein C. Continuous cultures of fused cells secreting antibody of predefined specificity. Nature. 1975;256:495–7.

276. Hwang WYK, Foote J. Immunogenicity of engineered antibodies. Methods. 2005;36:3–10.

277. Harding FA, Stickler MM, Razo J, DuBridge RB. The immunogenicity of humanized and fully human antibodies: residual immunogenicity resides in the CDR regions. MAbs. 2010;2(3):256–65.

278. Dammes N, Peer D. Monoclonal antibody-based molecular imaging strategies and theranostic opportunities. Theranostics. 2020;10(2):938–55. https://doi.org/10.7150/thno.37443.

279. Holliger P, Hudson PJ. Engineered antibody fragments and the rise of single domains. Nat Biotechnol. 2005;23:1126–36.

280. Sharkey RM, Goldenberg DM. Perspectives on cancer therapy with radiolabeled monoclonal antibodies. J Nucl Med. 2005;46:114S–27S.

281. Boswell CA, Brechbiel MW. Development of radioimmunotherapeutic and diagnostic antibodies: an inside-out view. Nucl Med Biol. 2007;34:757–78.

282. Nelson AL. Antibody fragments-hope and hype. MAbs. 2010;2(1):77–83.

283. Bates A, Power CA. David vs. goliath: the structure, function, and clinical prospects of antibody fragments. Antibodies. 2019;8:28. https://doi.org/10.3390/antib802002.

284. Boerman OC, Oyen WJG. Immuno-PET of cancer: a revival of antibody imaging. J Nucl Med. 2011;52(8):1171–2.

285. DeJesus O and Nickels R. Production and purification of 89Zr, a potential PET antibody label. International Journal of Radiation Applications and Instrumentation. 1990;41:78–90

286. Verel I, Visser GWM, Boellaard R, et al. 89Zr immuno-PET: comprehensive procedures for the production of ^{89}Zr-labeled monoclonal antibodies. J Nucl Med. 2003;44:1271–81.

287. Verel I, Visser GWM, Boellaard R, et al. Quantitative ^{89}Zr immuno-PET for in vivo scouting of ^{90}Y-labeled monoclonal antibodies in xenograft-bearing nude mice. J Nucl Med. 2003;44:1663–70.

288. Borjesson PKE, Jauw YWS, Boellaard R, et al. Performance of immuno positron emission tomography with zirconium-89-labeled chimeric monoclonal antibody U36 in the detection of lymph node metastases in head and neck cancer patients. Clin Cancer Res. 2006;12:2133–40.

289. Muylle K, Flamen P, Vugts DJ. Tumour targeting and radiation dose of radioimmunotherapy with ^{90}Y-rituximab in CD20+ B-cell lymphoma as predicted by ^{89}Zr-rituximab immuno-PET: impact of preloading with unlabelled rituximab. Eur J Nucl Med Mol Imaging. 2015;42:1304–14.

290. Perk LR, Visser OJ, Stigter-van Walsum M, et al. Preparation and evaluation of ^{89}Zr-Zevalin for monitoring of ^{90}Y-Zevalin biodistribution with positron emission tomography. Eur J Nucl Med Mol Imaging. 2006;33:1337–45.

291. Perk LR, Visser GWM, Vosjan MJWD, et al. 89Zr as a PET surrogate radioisotope for scouting biodistribution of the therapeutic radiometals ^{90}Y and ^{177}Lu in tumor-bearing nude mice after coupling to the internalizing antibody cetuximab. J Nucl Med. 2005;46:1898–06.

292. Wei W, Rosenkrans CT, Liu J. ImmunoPET: concept, design, and applications. Chem Rev. 2020;120(8):3787–851.

293. Yoon J-K, Park B-N, Ryu E-K, et al. Current perspectives on ^{89}Zr-PET imaging. Int J Mol Sci. 2020;21(12):4309.

294. Bander NH, Trabulsi EJ, Kostakoglu L, Yao D, Vallabhajosula S, et al. Targeting metastatic prostate cancer with radiolabeled monoclonal antibody J591 to the extracellular domain of prostate specific membrane antigen. J Urol. 2003;170:171.

295. Bander NH, Milowsky MI, Nanus DM, Kostakoglu L, Vallabhajosula S, Goldsmith SJ. Phase I trial of ^{177}lutetium labeled J591, a monoclonal antibody to prostate-specific membrane antigen, in patients with androgen-independent prostate cancer. J Clin Oncol. 2005;23:4591–601.

296. Kumar K, Ghosh A. Radiochemistry, production processes, labeling methods, and ImmunoPET imaging pharmaceuticals of iodine-124. Molecules. 2021;26:414.

297. Divgi CR, Pandit-Taskar N, Jungbluth AA, et al. Preoperative characterisation of clear-cell renal carcinoma using iodine-124-labelled antibody chimeric G250 (^{124}I-cG250) and PET in patients with renal masses: a phase I trial. Lancet Oncol. 2007;8:304–10.

298. Divgi CR, Uzzo RG, Gatsonis C, et al. Positron emission tomography/computed tomography identification of clear cell renal cell carcinoma: results from the REDECT trial. J Clin Oncol. 2013;31:187–94.

299. Carrasquilo JA, Pandit-Taskar N, O'Donoghuye JA, et al. 124I-huA33 antibody PET of colorectal cancer. J Nucl Med. 2011;52:1173–80.

300. Lim EA, Drake CG, Mintz A. Molecular imaging for cancer immunotherapy. Immuno Oncol Technol. 2020;5(3):10–21.

301. Bensch F, van der Veen EL, Lub-de Hooge MN, et al. (89)Zr-atezolizumab imaging as a non-invasive approach to assess clinical response to PD-L1 blockade in cancer. Nat Med. 2018;24:1852–8.

302. Donnelly DJ, Smith RA, Morin P, et al. Synthesis and biologic evaluation of a novel (18)F-labeled adnectin as a PET radioligand for imaging PD-L1 expression. J Nucl Med. 2018;59:529–35.

*The brain is the last and grandest biological fron-
tier, the most complex thing we have yet discovered
in our universe. It contains hundreds of billions of
cells interlinked through trillions of connections.
The brain boggles the mind.* (James D. Watson)

15.1 Neuroscience

15.1.1 The Nervous System

The nervous system is traditionally divided into
central and peripheral components. The *central
nervous system* (CNS) comprises the brain (cere-
brum, cerebellum, and brain stem) and spinal
cord. The *peripheral nervous system* (PNS)
includes sensory neurons and motor neurons,
which connect CNS to sensory receptors and
muscles, and glands, respectively. In the PNS, the
somatic division innervates the skeletal muscles,
while the autonomic (sympathetic and parasym-
pathetic) division innervates smooth muscles,
cardiac muscle, and glands. In the PNS, *ganglia*
are accumulations of nerve cell bodies and their
supporting cells, while *nerves* are bundles of
nerve cell axons and their supporting cells.

15.1.2 Nerve Cells

The cells of the nervous system can be divided
into two broad categories: nerve cells or *neu-*

rons, and a variety of supporting cells, which
consist mostly of *neuroglial cells—referred to
simply as glial cells or glia (*from the Greek
word meaning glue).

The structure of neurons (Fig. 15.1) in many
respects resembles that of most other cells in the
body. The neuron has a cell body (containing a
nucleus, mitochondria, etc.) and specialized
extensions (for intercellular communication and
signaling), known as dendrites and axon.
Dendritic branches or processes are specialized
for receiving information from other cells, while
the axon is designed for signal conduction. Since
the fundamental purpose of neurons is to inte-
grate information from other neurons, the num-
ber of inputs received by each neuron in the
human nervous system ranges from 1 to approxi-
mately 100,000. Some neurons transmit locally,
while others may carry signals several feet away
from the cell body.

The glial cells are quite different from neurons;
they do not participate directly in electrical sig-
naling. Also, there may be three times more glial
cells than neurons, and these cells are usually
smaller and lack dendrites and axons. The main
role played by glia includes maintaining the ionic
milieu of nerve cells, modulating the rate of nerve
signal propagation/synaptic action, and aiding in
the recovery from neural injury. The three types of
glia are *astrocytes*, *oligodendrocytes*, and *microg-
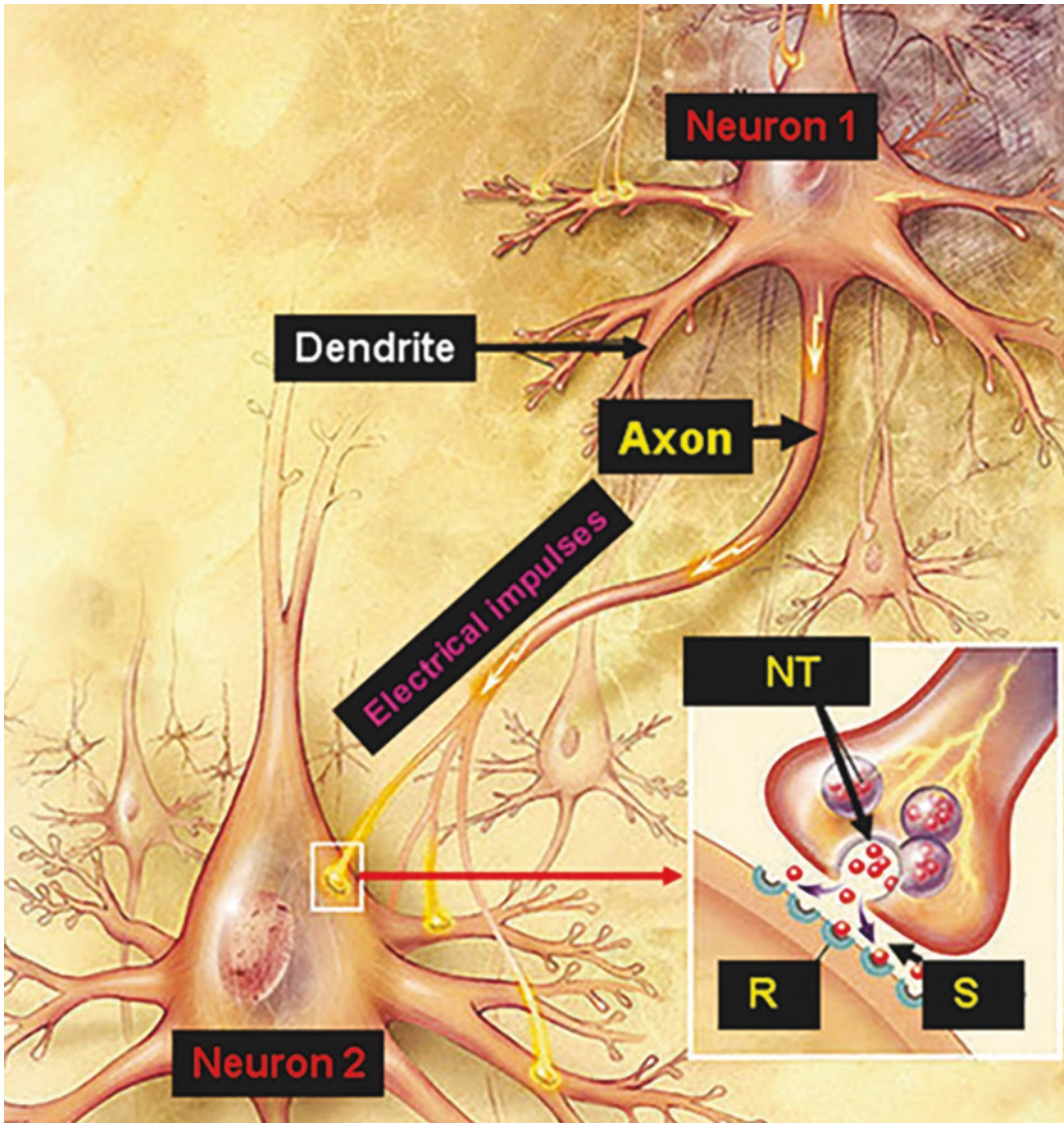lia*. Astrocytes maintain the appropriate chemical

Fig. 15.1 The structure of a neuron with a cell body, dendrites, and the axon. The nerve signals transmitted along the axon trigger the release of neurotransmitter molecules into the synapse, the point of contact between two neurons or between a neuron and a target cell. (Modified from image at WordPress.com weblog)

environment for neuronal signaling. Oligodendrocytes provide a wrapping (*myelin*) around some axons to increase the speed of signal conduction. Microglia, derived from hematopoietic stem cells, are similar in some ways to macrophages and help repair neural damage.

Neurons are organized into ensembles called circuits that process specific kinds of information. Neurons that carry information towards the CNS are called *afferent neurons*, while the neurons that carry information away from the CNS, are called *efferent neurons*. Neurons that participate only in the local circuits are called interneurons. Sensory circuits provide information about the internal and external environment, while motor circuits respond to sensory inputs by generating movement.

15.1.3 The Human Brain

The CNS includes the brain and the spinal cord. The human brain (Fig. 15.2) consists of approximately 10,000 different types of neurons and a total of 100 billion neurons, and the adult brain weighs nearly 1400 g. The brain is subdivided into three main regions: the *forebrain*, *midbrain,* and *hind brain*. Collectively, the midbrain and hind brain are called the *brain stem*. The hindbrain has three principal subdivisions: the medulla oblongata, the cerebellum, and the pons. The hindbrain tends to pass information to and receive controlling signals from the midbrain, which is itself controlled by the forebrain. The midbrain receives and processes sensory information and distributes it to different parts of the forebrain for further processing. The forebrain integrates sensory information of various kinds and formulates motor commands that are executed by other parts of the CNS.

The forebrain is subdivided into the diencephalon (thalamus and hypothalamus) and telencephalon (the cerebrum and basal ganglia). The thalamus is a sensory relay station that distributes sensory information to appropriate regions in the cerebral cortex, while the hypothalamus maintains homeostasis. The cerebral cortex is the outer layer of the cerebrum (the two cerebral hemispheres), which contains most of the neurons and occupies a large, convoluted surface area. The ridges are known as *gyri* and the valleys are called *sulci* or *fissures*. The cerebral cortex is involved in the complex processing of sensory information to form perceptions, in the planning and initiation of movements, and in associative learning and higher cognition.

Each cerebral hemisphere is conventionally divided into four lobes: the frontal, parietal, temporal, and occipital lobes. In addition to their role in primary and sensory processing, each lobe has characteristic cognitive functions (Fig. 15.3). The frontal lobe is critical in planning behavior, the parietal lobe in attending to important stimuli, the temporal lobe in recognizing objects and faces, and the occipital lobe in a variety of visual analyses. The hippocampus, a highly specialized cortical structure that is folded into the medial temporal lobe, plays a major role in memory.

When the brain is dissected, sectioned, or observed with noninvasive imaging techniques (CT, MRI, PET, SPECT), many deeper structures
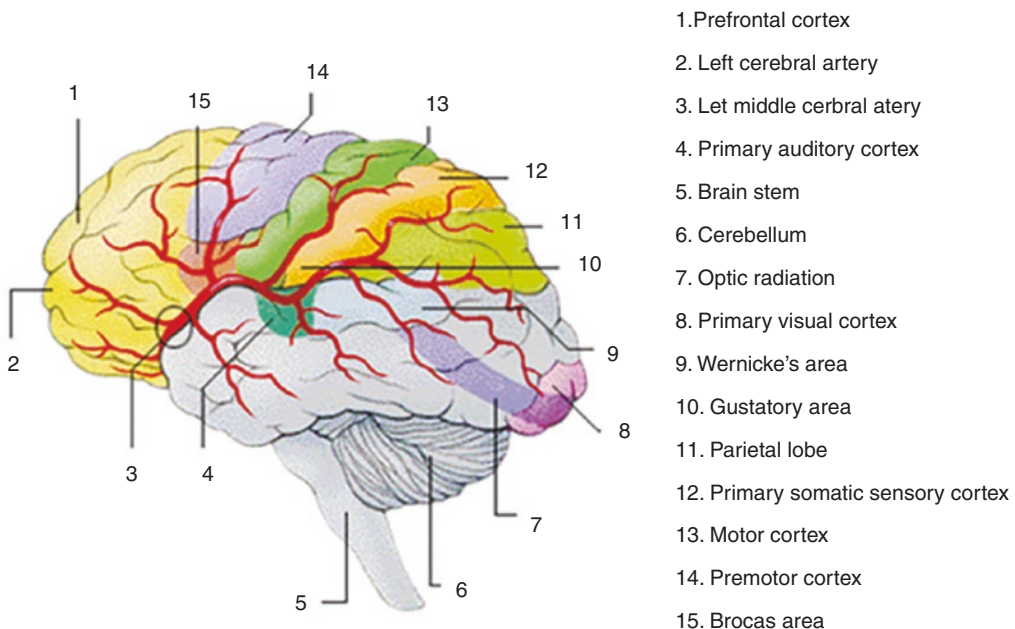
1. Prefrontal cortex
2. Left cerebral artery
3. Let middle cerbral atery
4. Primary auditory cortex
5. Brain stem
6. Cerebellum
7. Optic radiation
8. Primary visual cortex
9. Wernicke's area
10. Gustatory area
11. Parietal lobe
12. Primary somatic sensory cortex
13. Motor cortex
14. Premotor cortex
15. Brocas area

Fig. 15.2 The human brain showing the main lobes and major blood vessels
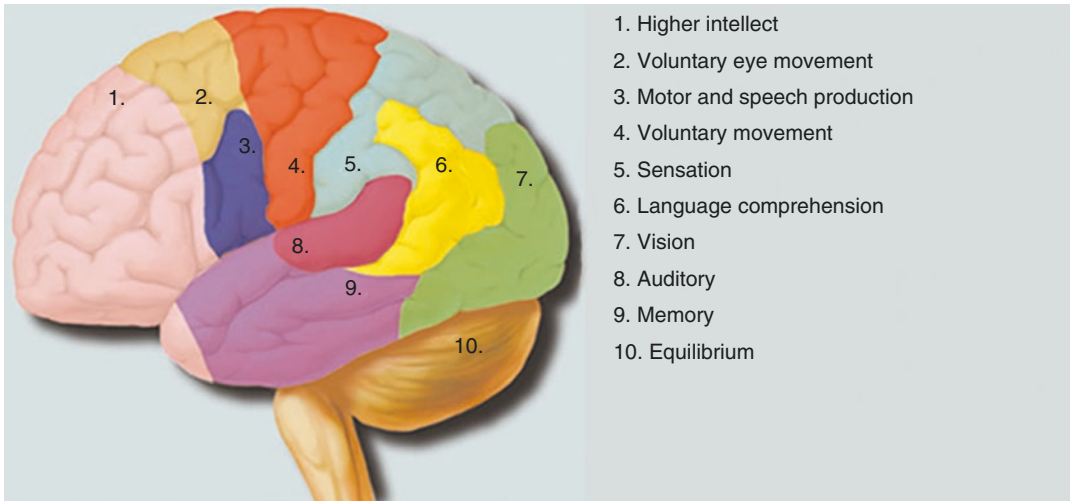
Fig. 15.3 The human brain showing the specific cortical areas associated with major functions

1. Higher intellect
2. Voluntary eye movement
3. Motor and speech production
4. Voluntary movement
5. Sensation
6. Language comprehension
7. Vision
8. Auditory
9. Memory
10. Equilibrium

are apparent. Most of the cerebral cortex is made up of six layers and is referred to as neocortex. The *gray matter* refers to the cortex, whether cerebral, cerebellar, or hippocampal, and is mainly made up of neuronal cell bodies, their dendrites, the axon terminals, and glia. The *white matter* makes up a large part of the subcortical tissue consisting mostly of axons entering or leaving the cortex. Among the internal structures, the *basal ganglia* play a major role in the organization and guidance of complex motor functions. The basal ganglia include the *striatum* (the *caudate* and the *putamen*) and the *globus pallidus*. Another important nucleus (collection of neurons) is the *amygdala*, which plays an important role in the emotional behavior.

The different parts of the cerebral hemispheres are interconnected by three large bundles of axons: the *corpus callosum*, *anterior commissure*, and *fornix*. The ventricular system in the CNS is a series of interconnected, fluid-filled spaces in the core of the forebrain and brain stem. The *cerebrospinal fluid* (CSF), produced by the choroid plexus, a network of specialized secretory tissue in the lateral, third, and fourth ventricles, percolates through the ventricular system into the *subarachnoid space*, which helps cushion the brain within the cranial cavity.

15.1.3.1   The Blood-Brain Barrier

The brain receives blood from two sources: the internal carotid arteries (ICA) and the vertebral arteries (VA). Many branches arising from ICA and VA supply blood to the brain and all the internal structures.

The blood supply of the brain is particularly significant because neurons are very sensitive to oxygen deprivation. The brain, more than any other organ, must be carefully shielded from toxic molecules and ionic species that would adversely affect the neuronal function. The interface between the walls of capillaries and the surrounding tissue is very important for the transport of various molecules and nutrients from the blood into the cells. In the brain, this interface has been given the special name, blood-brain barrier (BBB), since it protects and maintains homeostasis. Unlike in many other tissues, the adjacent capillary endothelial cells in the brain have very tight junctions, permitting the transport of molecules and ions, which can only move through the walls of the endothelial cell membranes. In addition to the tight junctions, the terminal regions of the astrocytic processes surround the outside of the capillary endothelial cells. As a result, only the neutral molecules that are lipid soluble (lipophilic) and molecules needed for cellular metabo-

lism (such as glucose) that can be transported by facilitated diffusion are permitted to enter the brain tissue. Therefore, BBB presents a significant challenge in the development of molecular imaging probes to assess brain function (Chap. 9).

15.1.4 Neural Signaling

Neurons have evolved as a sophisticated means of generating electrical signals to convey information over long distances and transmit the signal to other cells. Ion pumps and ion channels on the cell membrane create substantial transmembrane gradients for most ions and are responsible for ionic movements across the cell membrane. In general, there are many more K^+ inside the neuron than outside, and many more Na^+ outside the neuron than inside. As a result, generally, neurons generate a negative potential called the *resting membrane potential* (RMP), which is typically a fraction of a volt, -40 to -90 mV. An increase in the external K^+ concentration makes the RMP more positive. *Action potentials* represent transient changes in the RMP of neurons. An action potential (AP) is generated when a transient rise in Na^+ permeability allows a net flow of Na^+ across the membrane. As a result, the Na^+ is much more inside the neuron than outside. This influx of Na^+ represents passing an electrical current across the membrane. *Depolarization* occurs when the membrane potential is more positive than the RMP. The brief period of depolarization is quickly followed by an increase in K^+ permeability that repolarizes the membrane and produces a brief undershoot of the AP. The membrane potential soon returns to the RMP. It is important to recognize that the membrane is depolarized in an all-or-none fashion. APs are propagated along the length of the axons and are the fundamental electrical signals of neurons.

15.1.5 Synaptic Transmission

The point at which a signal or activity is transmitted from one nerve cell to another, or from a motor neuron to a muscle cell, is called a *synapse*. Synapses are classified into two general groups: electrical synapses and chemical synapses. In both types, the input cell, called the *presynaptic cell,* comes into contact with the output cell, called the *postsynaptic cell*.

In an electrical synapse, the membranes of the two communicating neurons are usually close together and are linked by a special kind of intercellular contact called a gap junction, which contains precisely aligned paired channels in the membrane of each neuron. The pores of the channels connect to one another allowing the exchange of ions and small molecules (such as ATP and second messengers). The gap junction permits the current to flow passively from the presynaptic neuron and initiates or inhibits the generation of a postsynaptic membrane potential. Hormone-secreting neurons within the hypothalamus communicate through gap junctions.

15.1.5.1 Chemical Synapses
A generalized structure of a chemical synapse is shown in Fig. 15.1. The separation between the presynaptic and postsynaptic neurons is called the synaptic cleft. Transmission between the two neurons is on the basis of special molecules called neurotransmitters. The sequence of events involved in the chemical neurotransmission at a synapse is as follows:

- In the presynaptic neuron, the neurotransmitter molecules are synthesized and stored in the vesicles.
- An action potential reaching the presynaptic neuron terminal causes the opening of voltage gated Ca^{2+} channels.
- The influx of Ca^{2+} causes vesicles to fuse with presynaptic membrane.
- The neurotransmitter molecules are released into the synaptic cleft via exocytosis.
- The transmitter binds to specific receptors on the membrane of a postsynaptic neuron leading to (a) change in ionic permeability of postsynaptic neuron or (b) an intracellular release or production of a second messenger, which in

turn interacts directly or indirectly with an ion channel, causing it to open or close.

- The postsynaptic current generated by the change in permeability of ions changes the membrane potential.
- The potential changes that increase the probability of firing an action potential are called excitatory, whereas those that decrease the probability of firing an action potential are called inhibitory.

15.1.6 Neurotransmitters and Receptors

Neurotransmitters are chemical signaling molecules released into the synaptic cleft from the presynaptic nerve terminal. The three major criteria that define a substance as a neurotransmitter are:

1. The transmitter must be present within the presynaptic neuron.
2. The substance must be released in response to presynaptic depolarization, which must occur in a Ca^{2+}-dependent manner.

3. Specific receptors for the substance must be present on the postsynaptic cell.

In contrast to neurotransmitters, certain hormones typically influence target cells far removed from the hormone-secreting cells. This "action at a distance" is achieved by the release of hormones into the blood stream. Certain molecules such as vasopressin, oxytocin, and some other peptides may act as neurotransmitters in the brain but, as hormones in a different part of the body.

In general, neurotransmitters can be classified into two broad categories: small molecule neurotransmitters and neuropeptides. The small molecule neurotransmitters (Fig. 15.4) can be subdivided into acetylcholine, the amino acids (glutamate, aspartate, GABA, glycine), and the biogenic amines (dopamine, norepinephrine, epinephrine, serotonin, histamine). Neuropeptides are relatively large molecules composed of 3–36 amino acids. The peptide neurotransmitters may contain any different combinations of polar, hydrophobic, acidic, or basic amino acids.

The small molecule neurotransmitters are synthesized in the presynaptic nerve terminals. The
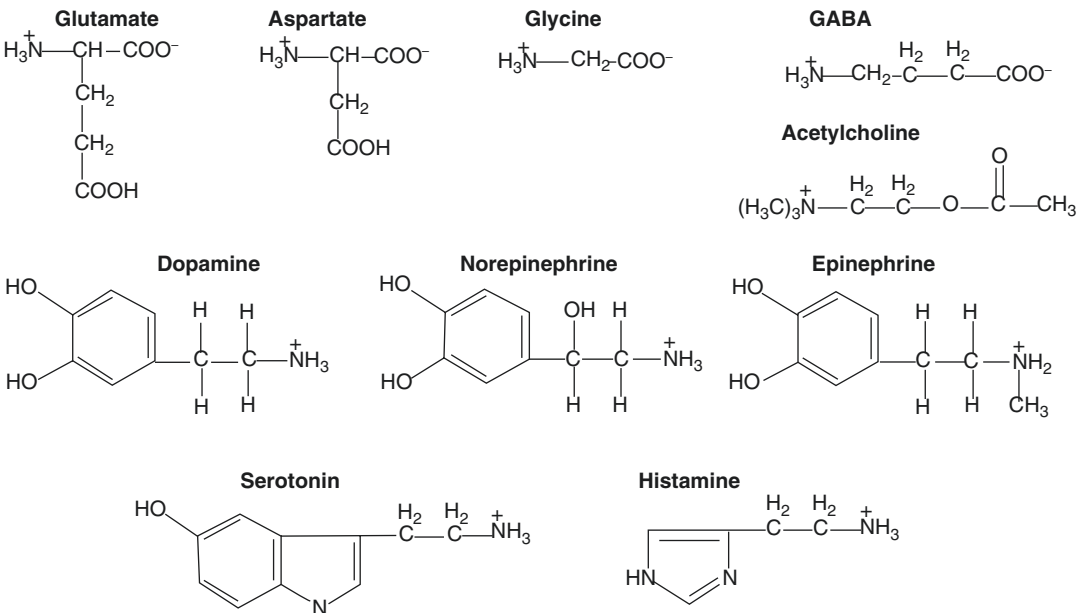

Fig. 15.4 The neurotransmitters can be chemically classified into three groups: amino acids, acetylcholine, and biogenic amines
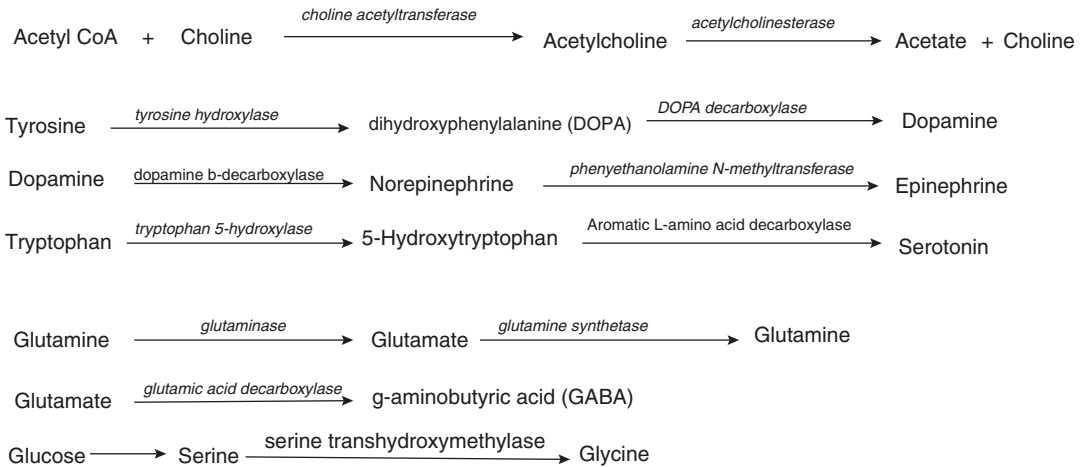
Fig. 15.5   The enzyme mediated synthesis of neurotransmitters in vivo

precursor molecules are taken up by the nerve terminals by specific transporters. Following enzyme mediated synthesis (Fig. 15.5), the free neurotransmitter molecules are loaded into synaptic vesicles by specific vesicular membrane transport proteins. Following release of neurotransmitters into the synaptic cleft, they may bind to specific neuroreceptors on the membrane of the postsynaptic neuron. The transmitters may also be enzymatically degraded quickly or transported back (reuptake) into the presynaptic neuron by specific reuptake transporters.

Neuroreceptors are protein molecules embedded in the plasma membrane of the postsynaptic neuron. These receptors act as on and off switches for the receptor function. Each receptor has a distinctly shaped part that selectively recognizes a particular chemical messenger. A neurotransmitter fits into this region in much the same way as a key fits into a lock. When the transmitter is in place, this alters the neuron's outer membrane potential (excitability) by opening or closing the ion channels and triggers a change, such as the contraction of a muscle or increased activity of an enzyme in the cell.

Two broadly different families of receptors are involved in neurotransmitter-receptor interaction. (a) The ligand-gated ion channels combine the receptor site and ion channel into one molecular entity and, therefore, give rise to rapid postsynaptic changes in the membrane potential. (b)

Metabotropic receptors, on the other hand, regulate the activity of ion channels indirectly via G-proteins and induce a slower, longer-lasting electrical response. These receptors may activate intracellular effector enzymes that modulate the phosphorylation of target proteins and/or gene transcription.

For each neurotransmitter, there may be more than one structurally and pharmacologically distinct receptor subtype (Table 15.1) that can be expressed on the membrane of a postsynaptic neuron depending on its exact location in the specific area of the brain. For example, dopamine has five receptor subtypes, while serotonin has 14 5-HT receptor subtypes [1]. Following binding of a neurotransmitter to a specific receptor or receptor subtype, the postsynaptic response, at a given synapse, is, therefore, dictated by the combination of receptor subtypes, G-protein subtypes, and ion channels that are expressed in a particular postsynaptic neuron. The second messengers are molecules that trigger the biochemical communication within cells, after the action of neurotransmitters at their specific receptors, and these intracellular effects may be responsible for long-term changes in the nervous system. These messengers convey the chemical message of a neurotransmitter (the first messenger) from the cell membrane to the cell's internal biochemical machinery. The effects of the second messenger may last for a few milliseconds to many minutes.

Table 15.1 Properties of some of the major neurotransmitters

Neurotransmitter	Receptors and subtypes	Postsynaptic effect	Specific role or functions
Acetylcholine (Ach)	Nicotinic, Muscarinic	Excitatory	Involved in muscle contraction, heartbeat, memory, sleep, and normal attention
Glutamate	NMDA	Excitatory	Learning and memory
Aspartate	NMDA	Excitatory	
GABA	GABA	Inhibitory	Mood, Coordinate movement
Dopamine	D_1–D_5	Excitatory	Regulate movement and endocrine function. Specific role in cognition and emotion
Norepinephrine or Noradrenaline	$\alpha_1, \alpha_2, \beta_{1-3}$	Excitatory	Regulate heart rate and blood pressure, learning and memory
Serotonin or 5-HT	$5\text{-HT}_{1A}, 5\text{-HT}_{2A}$	Excitatory	Sleep, mood, depression, anxiety
Enkephalin, Endorphin	δ and μ opioid receptors	Inhibitory	Minimize pain, induce sleep, enhance adaptive behavior

Knowledge of the role neurotransmitters play in the brain and the effect of drugs on receptor molecules are two of the most frequently studied areas in neuroscience. Armed with this information, scientists hope to understand the circuits responsible for disorders, such as Alzheimer's disease (AD), Parkinson's disease (PD), depression, and drug addiction. Sorting out the various chemical circuits involved in neuropsychiatric diseases is vital to understanding how the brain functions under normal physiological conditions and altered pathophysiological states. Radioisotope-based molecular imaging probes provide the highest specificity and sensitivity needed to study and noninvasively image the neuroreceptor interaction within the human brain.

15.2   Neurodegenerative Diseases

Neurodegenerative disorders (NDs) result from the gradual and progressive loss of neural cells, leading to nervous system dysfunction [2]. Many NDs including Alzheimer's disease (AD), Parkinson's disease (PD), multiple sclerosis (MS), amyotrophic lateral sclerosis (ALS), and Huntington's disease (HD) occur because of neurodegenerative processes. While the term "neurodegenerative" implies that it is the loss of neurons that causes the disease, it is possible that the neuronal demise is merely the final stage of a preceding period of neuron dysfunction. NDs clinical syndromes are often categorized by whether they

initially affect cognition, movement, strength, coordination, sensation, or autonomic control. However, NDs are defined as disorders showing distinct anatomical distribution and, as a result, different clinical phenotypes. For example, AD is characterized by the loss of neurons and synapses in the cerebral cortex and certain subcortical regions resulting in gross atrophy of the affected regions; PD results from the death of dopamine-generating cells in the substantia nigra, a region of the midbrain. In HD, loss of medium spiny neurons occurs mainly in the striatum (basal ganglia), but also in the frontal and temporal cortices. Although progressive neuronal loss is a hallmark of NDs, some neurological impairment may reflect neuron dysfunction rather than loss of neurons [3]. A spectrum of immunohistochemically detectable proteins deposited in the central nervous system (CNS) serve as a basis for protein-based disease classification [4], summarized in Table 15.2. Furthermore, it has become evident that there is considerable overlap between deposited proteins and pathologies. Accordingly, diagnostic criteria and disease staging have been updated [5].

Known risk factors for NDs include certain genetic polymorphisms and increasing age. Other possible causes may include gender, poor education, endocrine conditions, oxidative stress, inflammation, stroke, hypertension, diabetes, smoking, head trauma, depression, infection, tumors, vitamin deficiencies, immune and metabolic conditions,

Table 15.2 Common neurodegenerative diseases characterized by the deposition of aggregated proteins

Neurodegenerative disease	Aggregated protein	Location	Microscopic lesion
AD	Aβ	Extracellular	Amyloid plaque
AD	Tau	Intracytoplasmic (neurons)	Neurofibrillary tangle
Pick's disease			Pick bodies
CBD/PSP		Intracytoplasmic (neurons, oligodendroglia, and astrocytes)	Tau-positive inclusions
PD	α-Synuclein	Intracytoplasmic (neurons)	Lewy bodies
DLB			
AD			Lewy bodies (seen in Lewy body variant)
MSA		Intracytoplasmic (oligodendroglia)	Glial cytoplasmic inclusions
TSEs, also known as prion diseases, including CJD, GSS	PrP	Extracellular	Prion plaques
ALS	SOD1	Intracytoplasmic (neurons)	Hyaline inclusions
Huntington disease (HD)	Huntington (containing polyglutamine repeat expansion)	Intranuclear (neurons)	Neuronal inclusions
Spinocerebellar ataxia	Ataxin (containing polyglutamine repeat expansion)	Intranuclear (neurons)	Neuronal inclusions

Aβ amyloid-β, *AD* Alzheimer's disease, *ALS* amyotrophic lateral sclerosis, *CBD* corticobasal degeneration, *CJD* Creutzfeldt-Jakob disease, *DLB* dementia with Lewy bodies, *GSS* Gerstmann-Sträussler-Scheinker disease, *MSA* multiple system atrophy, *PD* Parkinson's disease, *PrP* protease-resistant prion protein, *PSP* progressive supranuclear palsy, *SOD1* superoxide dismutase-1, *TSEs* transmissible spongiform encephalopathies

and chemical exposure. NDs are associated with several insults, such as misfolded proteins, reactive oxygen and nitrogen species, mitochondrial-complex inhibition, calcium entry, excitotoxicity, trophic-factor withdrawal, death-receptor activation, and finally, they trigger programmed cell death (PCD) also known as apoptosis). Temporal studies of neurodegenerative models suggest, however, that PCD may be a relatively late event in the neurodegenerative process, and that death is preceded by early functional alterations (e.g., electrophysiological deficits and cellular stress pathway activation) and microanatomical deficits, such as neurite retraction and synapse loss [6]. These functional alterations may be associated with regional and focal abnormalities in blood flow/perfusion, glucose metabolism, and neuroreceptor expression. As mentioned earlier, most of the NDs are associated with abnormal accumulations of soluble and insoluble proteins (Table 15.2).

15.2.1 Dementia

Dementia is a serious loss of cognitive ability in a previously unimpaired person beyond what might be expected from normal aging. Dementia is a nonspecific illness syndrome in which affected areas of cognition might be memory, attention, language, and problem solving. It is normally required to be present for at least 6 months to be diagnosed. Dementia that begins gradually and worsens progressively over several years is usually caused by neurodegenerative disease, that is, by conditions affecting only or primarily the neurons of the brain and causing a gradual but irreversible loss of function of these cells.

Alzheimer's disease (AD) is the most common form of dementia in persons older than 65 years old. Many causes of dementia, as well as other syndromes of cognitive impairment, can mimic the clinical state of dementia [7]. Some of the major other causes of cognitive decline

include dementia with Lewy bodies (DLB), vascular disease (VaD), frontotemporal lobar degeneration (FTLD), and Parkinson's dementia (PD) [7]. Although it is recognized that AD and other causes of dementia are distinct diseases, in the early stages, it is difficult to differentiate between the onset of AD and other types of age-related cognitive decline.

15.2.1.1   Alzheimer's Disease (AD)

The most common cause of decline that eventually leads to dementia and the most studied is AD, a disease that is present in approximately two thirds of cases of dementia. This incurable, degenerative, and terminal disease was first described by the German psychiatrist and neuropathologist Alois Alzheimer in 1906 and was named after him [8]. On the basis of histopathologic examination of brain tissue, Dr. Alzheimer described two of the hallmarks of AD, numerous globs of sticky proteins; β-amyloid (Aβ) plaques in the spaces between neurons and a tangled

bundle of fibrils within neurons known as neurofibrillary tangles (NFTs). Mild cognitive impairment (MCI), also known as incipient dementia or isolated memory impairment, is a diagnosis given to individuals who have cognitive impairments beyond those expected for their age and education but, that do not interfere significantly with their daily activities [9]. It is considered the boundary or transitional stage between normal aging and dementia. The most-studied type of MCI involves a memory problem and is called amnestic MCI. that is frequently seen as a risk factor for AD [10]. A hypothetical timeline for the onset and progression of AD neurodegeneration and cognitive impairments progressing from normal control to MCI and on to AD is shown in Fig. 15.6. A series of events might occur in the brain during many years. This gradual process, which results from the combination of biological, genetic, environmental, and lifestyle factors, eventually sets some people on a course to MCI and possibly AD [11].
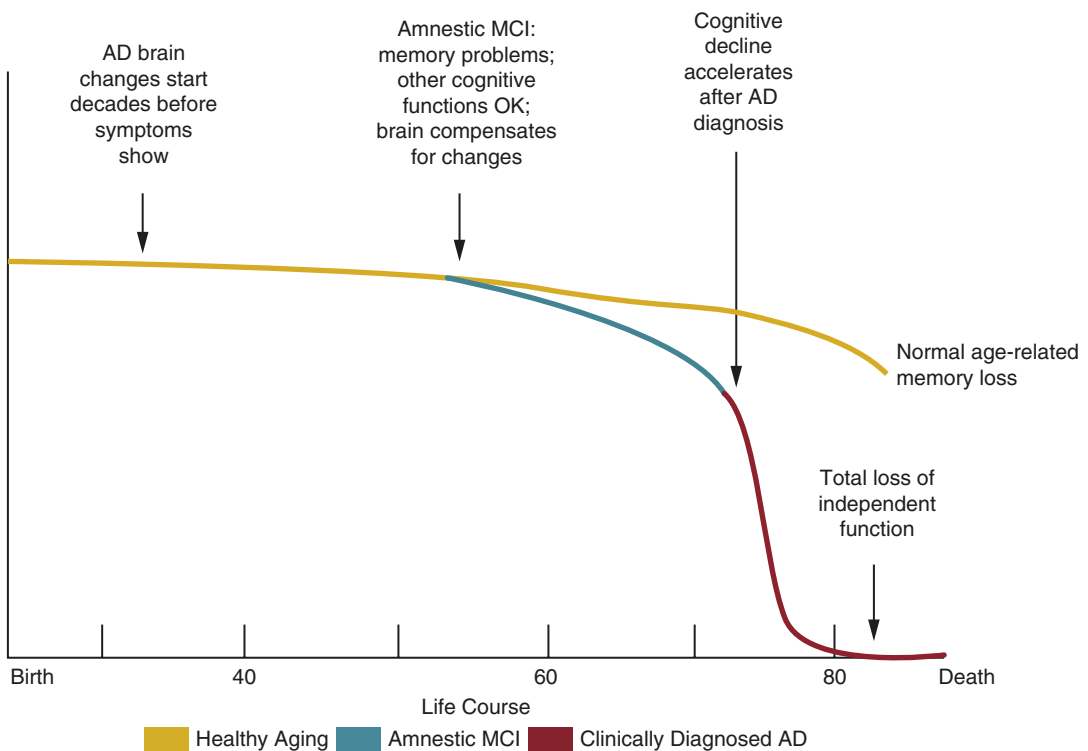

Fig. 15.6   Charting the course from healthy aging to AD (NIH publication number 08-3782)

β-Amyloid

AD is clinically, neuropathologically, and genetically heterogeneous. Depending on the stage of disease, the brain might appear unremarkable to the naked eye or might be grossly atrophic, which is usually symmetrical. AD affects mainly the frontal, temporal, and parietal lobes with relative sparing of the sensorimotor cortices and occipital lobe, although all cortical areas might be affected in the most severe cases [12]. AD is defined histologically by the presence of extracellular Aβ plaques and intraneuronal NFTs in the cerebral cortex. The senile or neuritic plaque, or Aβ is one of the signature lesions of the AD brain. These complex extracellular structures range in size from 50 to 200 μm and are readily visualized by silver impregnation methods. Immunohistochemistry, however, generally reveals much more extensive pathology than that seen by traditional silver and other staining methods. The classic senile plaque consists of an amyloid core with a ring or crown, as seen in the cross section with the light microscope, and of argyrophilic axonal and dendritic processes, amyloid fibrils, astrocytic processes, and microglial cells [12]. The neuritic processes of the senile plaque are often dystrophic and contain abnormal paired helical filaments made up largely of hyperphosphorylated tau protein. In AD, however, the Aβ component far outweighs the other amyloid-related protein components, such as NFTs, on a total mass basis in most brain regions [13, 14].

According to the amyloid hypothesis, the accumulation of Aβ in the brain is the primary influence driving AD pathogenesis. The rest of the disease process, including formation of NFT-containing tau protein, is proposed to result from an imbalance between Aβ production and Aβ clearance [15].

PHF-tau Protein Fibril Deposits

The second histologic signature lesion of AD is the NFT composed mainly of hyperphosphorylated forms of the microtubule-associated protein tau [16]. The NFT, however, is not specific to AD and also occurs in aging and other neurodegenerative diseases, such as Down syndrome, dementia pugilistica, and postencephalitic parkinsonism [12]. NFTs and Lewy bodies (composed mainly of α-synuclein protein) are not amyloids; instead, they are defined as "close relatives" of amyloids because of their predominantly intracellular or intraneuronal locations.

Tau protein belongs to a group of proteins referred to as microtubule-associated proteins (MAPs). NDDs characterized by pathological tau accumulation are termed "tauopathies." AD and related tauopathies are histopathologically characterized by slow and progressive neurodegeneration, which is associated mostly with intracellular accumulation of tau protein leading to the so-called neurofibrillary tangles (NFTs) and other inclusions containing modified tau [17].

The physiological function of tau is to bind to tubulin to stabilize microtubules, which is critical for the axonal support of neurons. Based on the number of tubulin-binding repeats within the protein, six tau isoforms have been identified. These isoforms of tau protein differ according to the contents of 3–4 tubulin-binding domains and vary in size from 352 to 441 amino acid residues. The phosphorylation of tau regulates its activity to bind to microtubules. A normal level of phosphorylation is required for the optimal function of tau; hyperphosphorylation leads to a loss of biological activity. Although the underlying mechanisms leading to tau hyperphosphorylation, misfolding, and aggregation remain unclear, tau aggregation and deposition follow a stereotyped spatiotemporal pathway at the intraneuronal level as well as in its topographical and neuroanatomical distribution in the brain [18, 19]. The hyperphosphorylated tau accumulates as paired helical filaments (PHF) that in turn aggregate into masses inside nerve cell bodies known as NFTs and as systrophic neurites associated with amyloid plaques. PHF are composed of disulfide-linked antiparallel hyperphosphorylated tau proteins [16]. Human post-mortem studies indicate that the density of NFTs, which are aggregates of PHF-tau, but not Aβ plaque deposition, correlates with neurodegeneration and cognitive impairment [20].

Neurodegeneration and neuronal dysfunction are caused by the binding of extracellular Aβ oligomers to the neuronal surface, leading to functional disruption of a number of receptors, finally culminating in dysfunction and neurode-

generation [21]. The accumulation of hyperphos-phorylated tau protein in neurons self-aggregates and forms paired helical filaments (PHF), which leads to the formation of intracellular NFTs, which ultimately block the neuronal transport system [21].

15.2.2 Parkinson's Disease

PD is the prototypic movement disorder described almost 200 years ago by James Parkinson and is characterized by a constellation of motor (slow-ness of movement, muscular rigidity, tremor, and postural instability) and non-motor symptoms (cognitive dysfunction and psychiatric features) that inexorably progress over time [22]. Idiopathic PD is the most common movement disorder among a spectrum of diseases with common fea-tures but with different causes, prognosis, and clinical course. Under normal circumstances, nerve cells in the substantia nigra communicate with other cells in the nearby striatum (the cau-date nucleus and putamen) by releasing dopa-mine at nerve terminals in that region. Many neurons in the substantia nigra are destroyed in individuals with PD causing slowed movements, rigidity, and tremors. The demonstration of intra-cytoplasmic Lewy bodies is the pathological hall-mark of PD and is necessary for a definitive diagnosis of PD [23, 24].

The discovery in the late 1950s that the level of dopamine (Fig. 15.4) was decreased in the brains of Parkinson's patients was followed in the 1960s by the successful treatment of this disorder by the administration of the drug L-DOPA (levodopa), which is converted to dopamine in the brain. Levodopa is now combined with another drug, carbidopa, that reduces the periph-eral breakdown of levodopa, thus allowing greater levels to reach the brain and reducing side effects. The discovery in the late 1970s that the neurotoxin, 1-methyl-4-phenyl-1,2,3,6-tetrahydropyridine (MPTP), can cause parkin-sonism in drug addicts has stimulated intensive research on the causes of the disorder [25]. MPTP was found to be converted in the brain to a sub-stance that destroys dopamine neurons, thus, the disturbance of dopamine synthesis is the hall-mark of PD.

The diagnosis of PD is primarily made on the basis of clinical assessment and becomes difficult by the variability of the disease presentation, rate of progression, and response to medications. Morphological imaging techniques, such as CT and MRI, may help to exclude other diseases that may lead to Parkinsonism. In fact, PD and the secondary or atypical Parkinsonian syndromes (APS) of multiple system atrophy (MSA), pro-gressive supranuclear palsy (PSP), and cortico-basal syndrome (CBS), dementia with Lewy bodies (DLB) are proteinopathies which are characterized by aggregation of misfolded proteins like alpha synuclein seen in PD and MSA or Tau seen in PSP and CBS.

Essential tremor (ET), drug-induced Parkinsonism (DIP), and other forms of non-dopamine deficiency etiologies (non-DDA) may present clinical features such as bradykinesia, atypical tremor, rigidity, postural instability/gait impairment resembling PS or PD without evi-dence of dopaminergic deficit [26, 27]. Therefore, clinically uncertain Parkinsonian syndrome (CUPS) presents an important challenge to clini-cians because an accurate diagnosis is required in order to provide patients with the appropriate therapies and prognosis.

15.3 Radiopharmaceuticals for Brain Imaging in Neurology

The radiopharmaceuticals for molecular imaging studies are based on positron-emitting radionu-clides (^{11}C and ^{18}F) for PET and gamma photon-emitting radionuclides (^{123}I and ^{99m}Tc) for SPECT. Since the physical half-life of positron-emitting radionuclides is relatively short (^{18}F, 109.8 min; ^{11}C, 20.4 min), the manufacture and distribution of PET radiopharmaceuticals is accomplished by several hundred PET radiophar-macies. In contrast, the distribution of SPECT radiopharmaceuticals (^{99m}Tc, 6 h; ^{123}I, 13 h) has been well established in the last five decades. The unique value of ^{11}C is not only that carbon is

present in virtually all biomolecules and drugs, which allows for isotopic labeling of their chemical structures but, also, that a given molecule can be radiolabeled at different functions or sites, thereby permitting in-vivo explorations of metabolic pathways.

Among all the halogens, the fluorine atom is the only one that closely mimics the hydrogen atom in size; the van der Waals radii of fluorine and hydrogen are very similar, 1.35 and 1.2 Å, respectively. As a result, one can expect that in any given organic molecule, a C-F bond closely mimics the biological behaviour of a C-H bond. In addition, the fluorine atom is also the most electronegative of all halogens and introduces a polarity more akin to a hydroxyl substituent in a molecule. Halogen atoms in drug molecules are quite common and, sometimes, the halogen-containing drug molecules may have even greater affinity for a receptor or an enzyme in vivo than the non-halogenated molecules [28]. In the last three decades, a number of radiopharmaceuticals have been developed based on ^{123}I for SPECT imaging studies as well. Since organic molecules containing an aromatic ring can easily be labeled with radionuclides of iodine, ^{123}I plays a major role in the development of SPECT radiopharmaceuticals.

The most common radiopharmaceuticals used for brain imaging studies are generally lipophilic and neutral compounds with limited protein binding. Initially, they should be able to penetrate freely through the intact blood-brain barrier (BBB) by simple diffusion and remain trapped in neuronal tissue for enough time to permit imaging by PET or SPECT. The main factors which regulate passage across the BBB are ionic selectivity and lipid solubility [29]. Osmotic pressure and specific and non-specific binding to plasma proteins, cell membranes, and other components present in the bloodstream may also affect the permeability of BBB and brain uptake of the administered radiopharmaceuticals. In the absence of radiotracer binding to these metabolic (biological) barriers, free diffusion of lipophilic, small, neutral compounds, occurs directly through the endothelial cells of the BBB [29].

The changes in electrical activity of neurons (excitation or inhibition) have been indirectly attributed to the alterations in the regional cerebral blood flow (rCBF) or local cerebral metabolic rate for glucose (LCMRglc). The functional coupling of rCBF and LCMRglc has been well established in the normal human brain and certain neurological diseases. However, brain function is directly related to neural signaling and transmission of electrical activity via chemical and electrical synapses. In order to optimize the individualized patient treatment on the basis of targeted molecular therapies and to select appropriate patients for specific drugs, noninvasive molecular imaging techniques are needed that can quantitatively assess the functional status and the underlying neurotransmitter and/or neuroreceptor abnormalities associated with a specific neuropsychiatric disease or disorder.

The FDA-approved and investigational radiopharmaceuticals specifically for brain imaging studies are listed in Table 15.3. These targeted molecular imaging probes were designed specifically, for both diagnosis and assessment of treatment response. The potential clinical utility and limitations of the current FDA-approved radiopharmaceuticals and the new investigational drugs will be described briefly in this chapter. Several reviews recently discussed the clinical application of radiopharmaceuticals in neurodegenerative diseases [30–35].

15.3.1 Cerebral Blood Flow and Perfusion

CBF has been traditionally measured quantitatively either as a *flow rate*, expressed as volume of blood flowing per unit of time (mL min^{-1}) or as a *rate of tissue perfusion*, expressed as volume of blood flowing through a given quantity of tissue per unit of time (mL min^{-1} 100 g^{-1}). However, with respect to physiologic function, perfusion directly relates to the supply of metabolic nutrient delivery to the tissue through the capillary beds. While there is a tight coupling between blood flow and metabolism in normal conditions, the coupling is disturbed in pathophysiologic

Table 15.3 FDA-approved and investigational radiopharmaceuticals for molecular imaging of neurodegenerative diseases by PET and SPECT

Brain function/mechanism	Radiopharmaceutical	Target	Neurodegenerative disease
FDA-approved radiopharmaceuticals			
Blood flow	[^{15}O]Water ^{99m}Tc-HMPAO (Ceretec®) ^{99m}Tc-ECD (Neurolite®) [^{123}I]Iofetamine (SPECTamine)		Dementia, PD
Glucose metabolism	2-[^{18}F]-fluoro-2-deoxy-D-glucose (FDG)	*Hexokinase*	AD, MCI, FTD, PD, MSA, DLB
Brain amyloid burden	[^{18}F]AV-45 (florbetapir) [^{18}F]AV-1 (florbetaben) [^{18}F]-3′-F-PiB (flutemetamol)	Amyloid-β (Aβ)	AD, MCI, FTD, DLB
Neurofibrillary tangles (NFTs) and aggregated tau (τ) proteins	[^{18}F]AV-1451 (T807, Flortaucipir)		AD
Dopaminergic system	^{123}I-FP-CIT (DaTSCAN)	Dopamine transporter (DaT)	Parkinsonian syndromes, essential tremor
	[^{18}F]FDOPA	*Aromatic l-amino acid decarboxylase (AAAD)*	PD, essential tremor, DLB
Investigational radiopharmaceuticals (INDs)			
Amyloid-β (Aβ)	[^{11}C]PiB [^{11}C]AZD2184 [^{18}F]NAV-4694 (AZD 4694)	Amyloid-β (Aβ)	AD, MCI, FTD, DLB
Neurofibrillary tangles (NFTs) and aggregated tau (τ) proteins	[^{18}F]FDDNP [^{18}F]THK-523 [^{18}F]THK-5105	Hyperphosphorylated tau as paired helical filaments (PHF)	AD, TBI
Neuroinflammation	[^{11}C]PK11195 [^{11}C]PBR28 [^{11}C]DPA713 [^{11}C]DAA1106 [^{11}C]SSR180575 [^{18}F]DPA714 [^{18}F]FEDAA1106	Peripheral benzodiazepine receptor (PBR), also known as the translocator protein (TSPO) in activated microglia	Dementia, MCI, PD
	[^{11}C]-L-Deuteriodeprenyl (DDP)	Activated astrocytes	MCI
	[^{11}C]Arachidonic acid	*Acyl-CoA-synthetase*	AD
Dopaminergic system	[^{18}F]FDOPA	*Aromatic l-amino acid decarboxylase (AAAD)*	PD, essential tremor, DLB
	[^{11}C]β-CFT [^{11}C]PE2i [^{18}F]FP-CIT ^{123}I-Altropane	Dopamine transporter (DAT)	PD, essential tremor, DLB
	[^{11}C]DTBZ [^{18}F]FP-DTBZ (AV-133)	Vesicular monoamine transporter (VMAT)	PD, essential tremor, DLB
	[^{11}C]Raclopride [^{11}C]FLB 457 [^{18}F]Fallypride ^{123}I-IBZM	Dopamine D2 receptor	MSA
Cholinergic system	[^{11}C]MP4A [^{11}C]AMP	*Acetylcholinesterase (AChE)*	AD
	[^{11}C]Nicotine [^{18}F]FA [^{18}F]AZAN [^{18}]Nifene	α$_4$β$_2$ Nicotinic acetylcholine receptor (nAChR)	AD

Table 15.3 (continued)

Brain function/mechanism	Radiopharmaceutical	Target	Neurodegenerative disease
Serotonergic system	[^{11}C](+)McN-5652 [^{11}C]DASB [^{11}C]MDAM ^{123}I-ADAM 123I-βCIT	Serotonin transporter (SERT)	
	[^{11}C]WAY 100635 or [^{11}C]WAY [^{11}C]DWAY [^{18}F]MPPF	Serotonin receptor, 5-HT$_{1A}$	
	[^{18}F]Altanserin [^{11}C]MDL100 907	Serotonin receptor, 5-HT$_{2B}$	
Glutamate receptors	[^{11}C]CNS 5161	Ionotropic NMDA receptor	TBI, PD, AD
	[^{11}C]ABP688 [^{18}F]SP203b [^{18}F]F-PEB	Metabotropic receptors	

conditions associated with several neuropsychiatric diseases.

A number of radiotracers have been used to assess CBF or perfusion. When the tracer reaches the capillaries, the process whereby a tracer leaves the blood pool and enters the tissue is critical for the quantitative measurement of perfusion. The fraction of the tracer which is extracted from the capillaries is referred to as the *extraction fraction* (*E*), a unitless parameter that can be estimated on the basis of the following Renkin-Crone equation:

$$E = 1 - e^{-PS/F} \qquad (15.1)$$

The magnitude of *E* depends on the total available capillary surface area (*S*), the capillary permeability (*P*) for the tracer, and the blood flow (*F*). *E* increases as *S* or *P* increases but, decreases with increased *F*, because the tracer spends less time in the capillaries of that region. In the above equation, *P* for a specific radiopharmaceutical depends on the physicochemical properties of the radiotracer.

An ideal flow radiotracer accumulates in a tissue or clears from it, in proportion linear to the blood flow. Such a linear relationship between blood flow and uptake or clearance of the tracer should be constant and independent of pathophysiological changes and metabolism of that tissue. [^{15}O]water most closely meets the criteria of an ideal tracer for measuring blood flow or tissue perfusion. It is freely diffusible and the first-pass extraction approaches unity and is independent of tissue blood flow and metabolic state. This tracer is, therefore, the most common radiotracer used for the measurement of rCBF [36, 37]. Besides [^{15}O]water, several other tracers such as [^{18}F]fluoromethane, [^{11}C]butanol, and ^{77}Kr have been used to image brain blood flow.

Since CBF is related primarily to the synaptic activity at the level of the neuron's cell body, the gray matter requires 3–4 times more blood flow compared to that of white matter. In the normal brain, the rCBF is dependent on vascular integrity, cerebral anatomy, and cerebral function. Over the years, the rCBF measurements, in normal human subjects, have provided quantitative estimation but, have yielded values that showed wide variation. Most published studies have reported values in the range of 40–80 mL min^{-1} 100 g^{-1} for gray matter structure, while a recent study has estimated the cortical global flow to be 62 ± 10 mL min^{-1} 100 g^{-1} [38].

Iofetamine (^{123}I) (Perfusamine, SPECTamine), or *N*-isopropyl-(^{123}I)-*p*-iodoamphetamine (IMP), is a lipid-soluble amine used in cerebral blood perfusion imaging with SPECT [30]. This was the first radiopharmaceutical approved by the United States Food and Drug Administration (FDA) for use as a diagnostic aid in localization and evaluation of non-lacunar stroke and complex partial seizures, as well for the early diagnosis of AD

[39]. An analogue of amphetamine, iofetamine, has been shown to inhibit the reuptake of serotonin and norepinephrine as well as inducing the release of these neurotransmitters and dopamine, with similar potencies to other amphetamines.

SPECT radiopharmaceuticals (Fig. 15.7) for measuring rCBF are lipophilic agents, known as chemical microspheres, which are transported into brain tissue by diffusion and subsequently trapped intracellularly in proportion to blood flow. Two of the agents used clinically are 99mTc-HMPAO (Ceretec®) and 99mTc-ECD (Neurolite®). 99mTc-HMPAO is converted to one or more polar species by an assumed interaction with glutathione [40], while 99mTc-ECD is retained in the brain tissue after being hydrolyzed to ionized non-diffusible metabolites by interaction with esterases in the brain cells [41]. While assessment of rCBF using SPECT tracers has provided diagnostic clinical information, the SPECT technique does not provide high-resolution images and the data is not optimal for quantitative estimation of rCBF, and perfusion. An advance in voxel-based statistical analysis, however, has markedly enhanced the value of brain perfusion SPECT in diagnosing early AD at the stage of mild cognitive impairment (MCI) [42]. Brain perfusion SPECT has well-recognized clinical applications mainly in dementia, cerebrovascular disease, epilepsy, and traumatic brain injury (TBI) [30, 43]. This technique generally adds valuable information to the clinical management of patients with brain disorders of a broad variety, helping in diagnosis, therapeutic management, and follow-up. The presence of hypometabolism or hypoperfusion in parietal association areas, in association with entorhinal atrophy on MRI at the MCI stage, has been reported to predict a rapid conversion to AD. Dementia with Lewy bodies (DLB) is the second most common form of degenerative dementia and neuroimaging findings indicated a relative preservation of medial temporal lobe structures and rCBF in DLB. Comparison of brain perfusion SPECT images for moderate AD and moderate DLB are shown in Fig. 15.8. DLB showed lower perfusion in the occipital cortex than AD. In contrast, AD showed lower perfusion in the medial temporal areas [42]. A recent review concludes that brain SPECT, as a biomarker of neurodegeneration in dementia, is still a valid option in the current era of molecular imaging based on PET radiotracers [44].

15.3.2 Cerebral Oxygen Metabolism

In addition to the measurement of rCBF, estimation of the cerebral blood volume (CBV) and cerebral metabolic rate of oxygen ($CMRO_2$) permit the discrimination of various compensatory mechanisms in occlusive vascular diseases. The ratio of CBF/CBV indicates a perfusion reserve, while the oxygen extraction fraction (OEF) is a marker of a metabolic reserve. The OEF reflects arteriovenous oxygen difference divided by the arterial oxygen content. Almost 40 years ago, the methods of quantitative measurement of rCBF, $CMRO_2$, and OEF were described in detail [45–47].

The continuous inhalation of either molecular oxygen, $[^{15}O]O_2$ or carbon dioxide, $[^{15}O]$
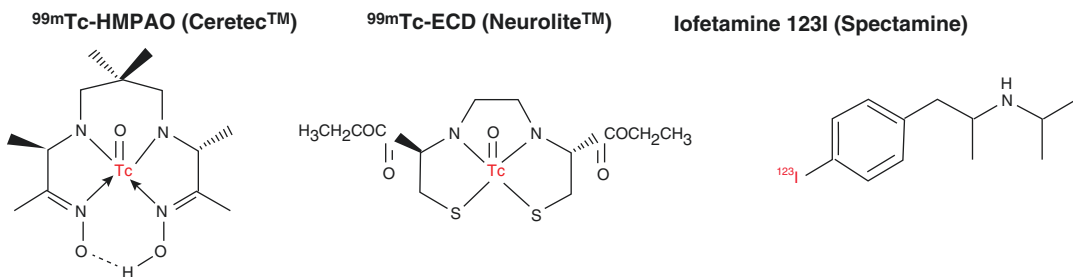

Fig. 15.7 SPECT radiopharmaceuticals for imaging regional brain blood flow/perfusion
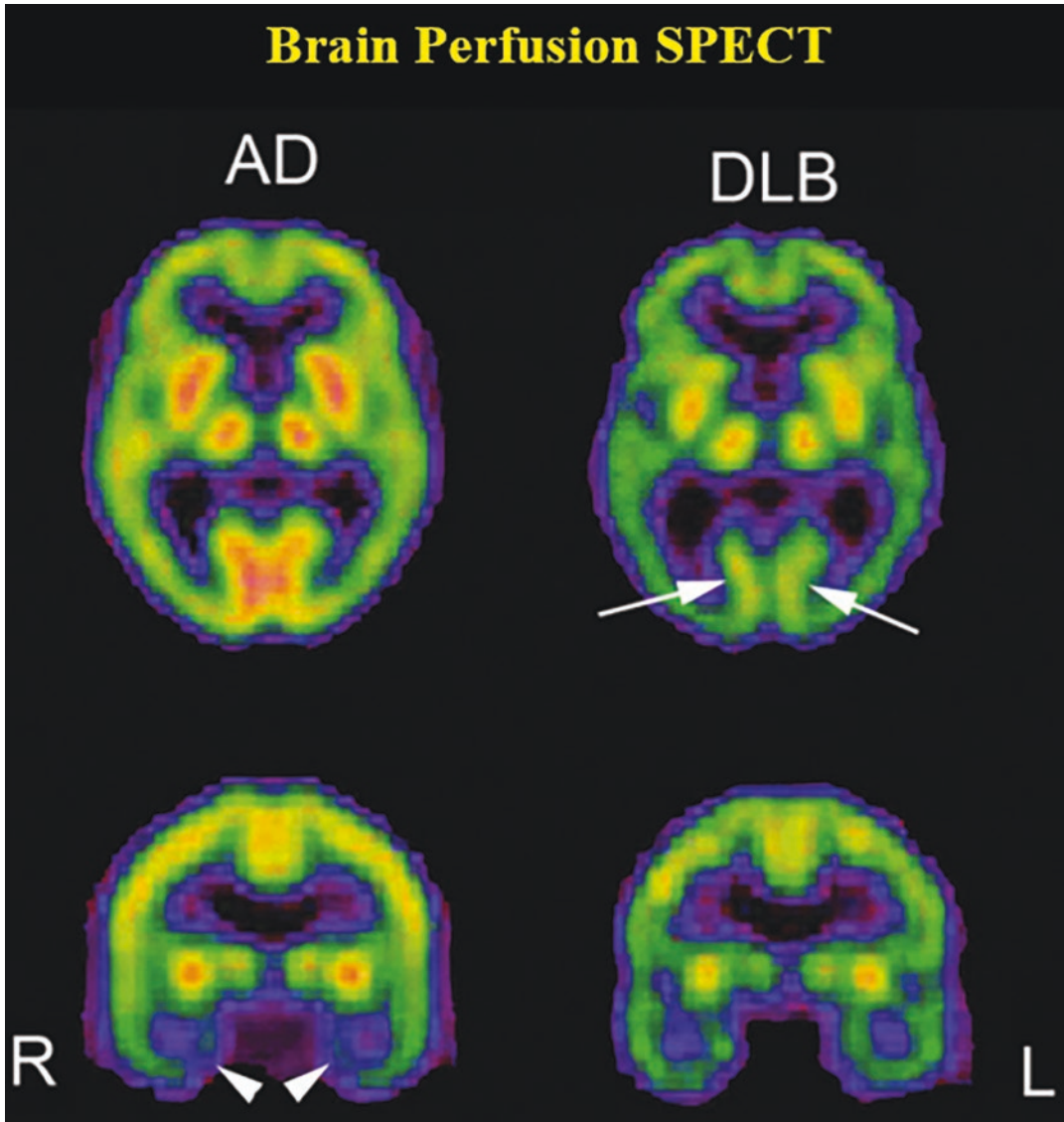
Fig. 15.8 Comparison of brain perfusion SPECT images for moderate AD and moderate Lewy body dementia (DLB). DLB showed lower perfusion in occipital cortex than AD (arrows). In contrast, AD showed lower perfusion in medial temporal areas (arrowheads). (Reproduced with permission from [42]). Role of neuroimaging in Alzheimer's disease, with emphasis on brain perfusion SPECT *J Nucl Med* **48**:1289–1300)

CO_2, will generate complementary images relating regional oxygen uptake and blood flow, while the assessment of CBV can be performed using carbon monoxide, $[^{15}O]CO$, a tracer that would label RBCs in vivo. The $CMRO_2$ can be estimated on the basis of the following relationship [45]:

$$CMRO_2 = CBF \times OEF \times \text{total blood oxygen count} \quad (15.2)$$

CBF, $CMRO_2$, and OEF have been determined in normal human subjects (Table 15.4) on the basis of steady-state inhalation methods [45]. Methods have also been developed to measure

Table 15.4 Normal Values of CBF, CMRO$_2$, and CMRglc in human adults

Brain region	CBF mL/min/100 g	CMRO$_2$ mL O$_2$/min/100 g	μmol/min/100 g	CMRglc mg/min/100 g	μmol/min/100 g
Gray matter, temporal lobe	65.3 ± 7.0	5.88 ± 0.57	255 ± 25	7.9 ± 2.1	44 ± 12
Thalamus	–	–	–	6.5 ± 1.2	36 ± 7
White matter	21.4 ± 1.9	1.81 ± 0.22	78 ± 9	4.1 ± 1.4	23 ± 8

Data from Mazziotta et al. [41]

these quantitative parameters on the basis of the autoradiographic technique, using intravenous administration of [^{15}O]H$_2$O [36].

15.3.3 Cerebral Glucose Metabolism

Energy metabolism in the adult human brain depends almost completely on the oxidation of glucose [49]. Since the brain does not store oxygen and glucose, it has been hypothesized that the regional rCBF is continuously regulated to supply these nutrients locally based on the demands of neural activity. The deoxyglucose autoradiographic technique [50] based on [^{14}C] deoxyglucose (DG) was the basis for imaging in-vivo glucose metabolism and measure the regional metabolic rate (rCMRglu).

2-[^{18}F]Fluoro-2-deoxy-D-glucose (FDG) (Fig. 15.9) was initially developed as a tracer to assess cerebral glucose metabolism. Based on the FDG-PET imaging technique [51–53] and arterial sampling of ^{18}F blood activity, the global and regional cerebral metabolic rates of glucose utilization (CMRglc) has been estimated and expressed as mg min^{-1} 100 g^{-1} or μmol min^{-1} 100 g^{-1} by several investigators [48, 52]. In 2005, FDA approved the use of FDG-PET in patients with AD and FTD.

Since FDG is a glucose analogue, with physiological aspects almost identical to glucose using it as a PET tracer allows the measurement of glucose consumption. FDG is transported from the blood to the brain by a carrier-mediated diffusion mechanism, also known as facilitated transport. FDG differs from glucose in that an ^{18}F atom replaces the hydroxyl group at the second carbon atom of the molecule. FDG and glucose are phosphorylated by *hexokinase* as the first step of the glycolytic process. Glucose is then phosphorylated to glucose 6-phosphate and continues along the glycolytic pathway for energy production. FDG is also phosphorylated to FDG 6-phosphate but, this is trapped in the cytoplasm since it is not a substrate for further metabolism. Further, since glucose is the only source of energy for the brain, it reflects the neuronal integrity of underlying brain pathology. In NDs, specific brain regions degenerate, and specific patterns of metabolic brain activity have been observed. The altered synaptic activity or density, in a specific brain region, is accompanied by proportional changes in capillary perfusion and local glucose consumption. The uptake of FDG also depends on the consumption of glucose by the astrocytes in interaction with neuronal function, on the transport mediated by the glucose transporter 1 across the blood-brain barrier, and possibly during pathological inflammatory conditions on microglial activation states [54].

FDG-PET imaging thus makes it possible to identify disease-specific cerebral metabolic brain patterns in several NDs at an early stage and can be used to assist in differential diagnosis (Fig. 15.10), because different dementia syndromes demonstrate different patterns of hypometabolism [56]. Classically, patients with AD have a pattern of bilateral parietotemporal hypometabolism (Fig. 15.8) that is not generally seen in patients with other forms of dementia or in age matched control subjects [57]. The decline of the FDG uptake in the posterior cingulate, hippocampus, parietotemporal, and prefrontal associa-
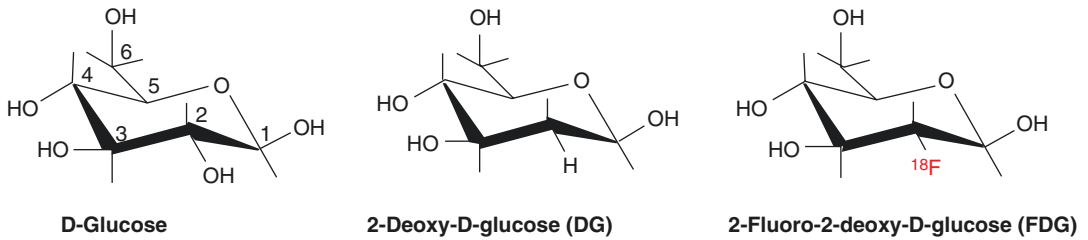
Fig. 15.9 The chemical structures of glucose, deoxyglucose, and FDG. [18]F radionuclide replaces hydroxyl group attached to C-2 atom of glucose molecule
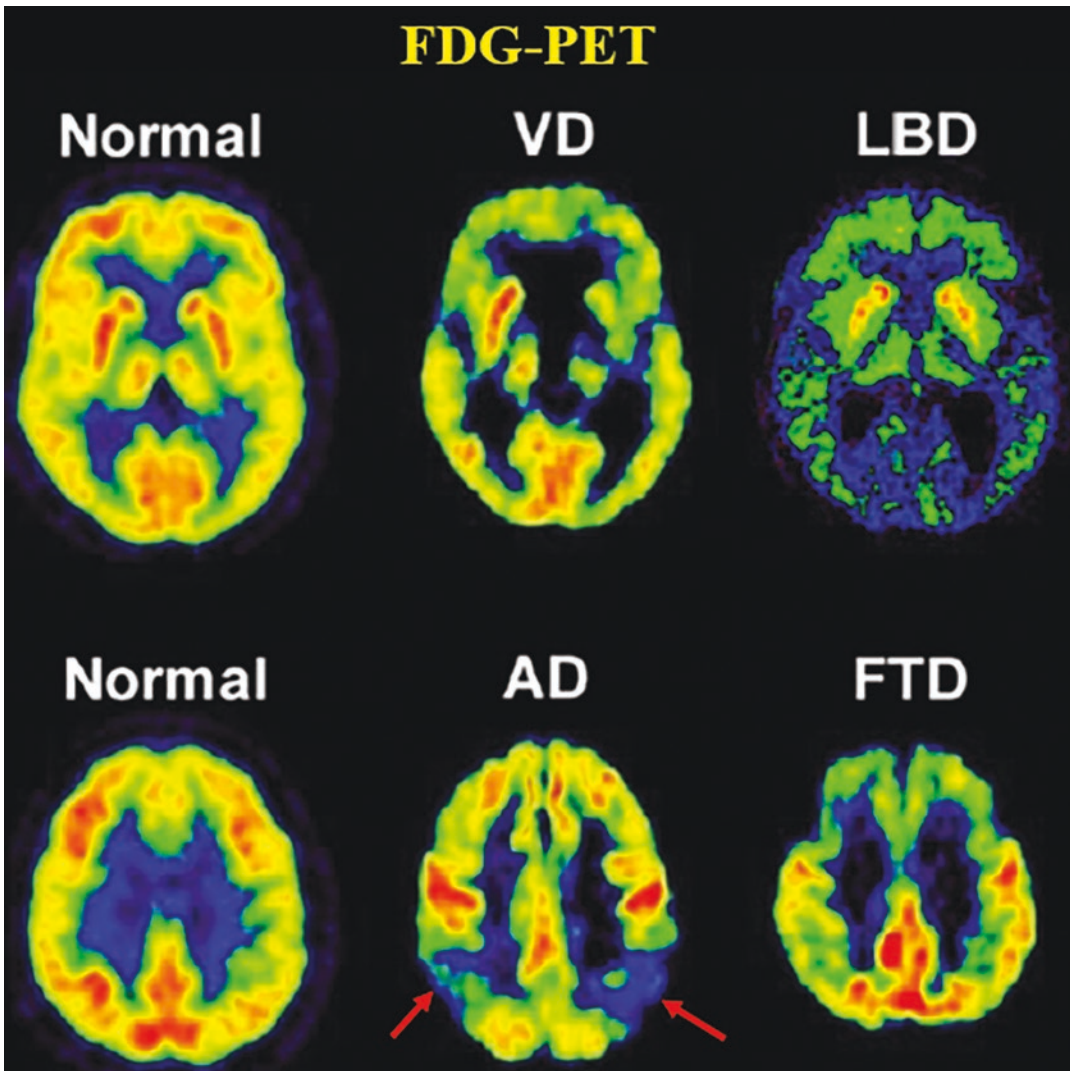

Fig. 15.10 FDG-PET in Alzheimer's disease (AD) and differential diagnosis of AD from other forms of dementia such as vascular dementia (VD), Lewy body dementia (LBD), and frontotemporal dementia (FTD). (From Jacobs et al. [55])
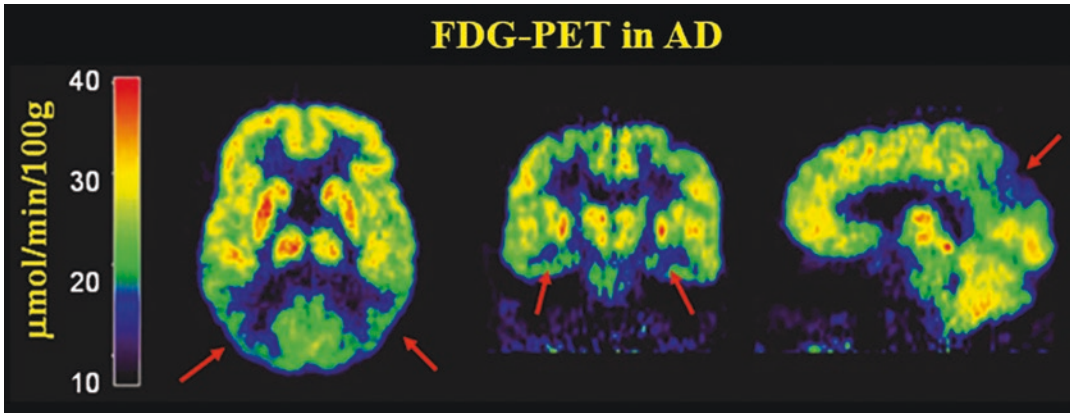
Fig. 15.11 FDG-PET in Alzheimer's disease showing typical areas of hypometabolism in posterior cingulate, parieto-temporal, and temporomesial cortices. (From Jacobs et al. [55])

tion cortices (Fig. 15.11) allows for the identification of mild to moderate AD with high sensitivity and specificity. Also, there is typically sparing of the basal ganglia, thalamus, cerebellum, and primary sensory cortex. Even early in the disease process, before the appearance of volume loss, FDG-PET has been helpful in diagnosing AD. Histopathologically confirmed sensitivity and specificity of PET for detecting the presence of AD are in the range of 92–94% and 71–73%, respectively [58].

In frontotemporal dementia (FTD), hypometabolism is seen predominantly in the frontal lobe but, parietal and temporal cortical uptake depends on the disease stage [59]. It has also been shown that the measurements of resting glucose metabolism can be helpful for separating typical from atypical Parkinsonian syndromes. In typical idiopathic PD, lentiform nucleus (striatum) glucose metabolism is preserved or raised, while it is reduced in most atypical cases, such as multiple system atrophy (MSA) (Fig. 15.12) [60].

Recent reviews conclude that a large body of literature has demonstrated that FDG-PET substantially improves diagnostic accuracy and differential diagnosis of several neurodegenerative diseases and enables earlier and better treatment planning. For epilepsy, FDG-PET can provide a key component of presurgical localization of the epileptogenic lesion or zone and can potentially help in the setting of diagnostic uncertainties [54, 61].

15.3.4 β-Amyloid Neuritic Plaque Density

Although a number of Aβ PET radiopharmaceuticals have been evaluated in clinical studies, currently, there are three FDA-approved radiopharmaceuticals to image amyloid burden in AD. In addition, several new agents are under active clinical investigation. Recent reviews have extensively discussed the advantages and limits of amyloid imaging in patients with AD [21, 30, 33, 35, 62, 63].

Neuropathologic evidence suggests that the characteristic neuropathologic hallmark in AD is the deposition of senile plaques (SPs) which contain Aβ aggregates and NFTs. The main constituents of Aβ-deposits in the AD brain are peptides of 40 and 42 amino acids, $A\beta_{40}$ and $A\beta_{42}$, respectively, generated from the cleavage of the amyloid precursor protein (Fig. 15.13) [64]. The subsequent arrangement of these peptide monomers into an amyloid fibril results in a characteristic β-plated sheet structure, which represents the target for tracers developed for noninvasive molecular imaging probes.

Compact plaques consist of a dense central core of amyloid fibrils, while noncompact plaques contain less fibrillar Aβ [65]. A shift of the brain Aβ from the soluble to the fibrillar form is closely associated with the onset of AD [66]. Previous neuropathologic studies have indicated that neuritic plaque densities are highest in the
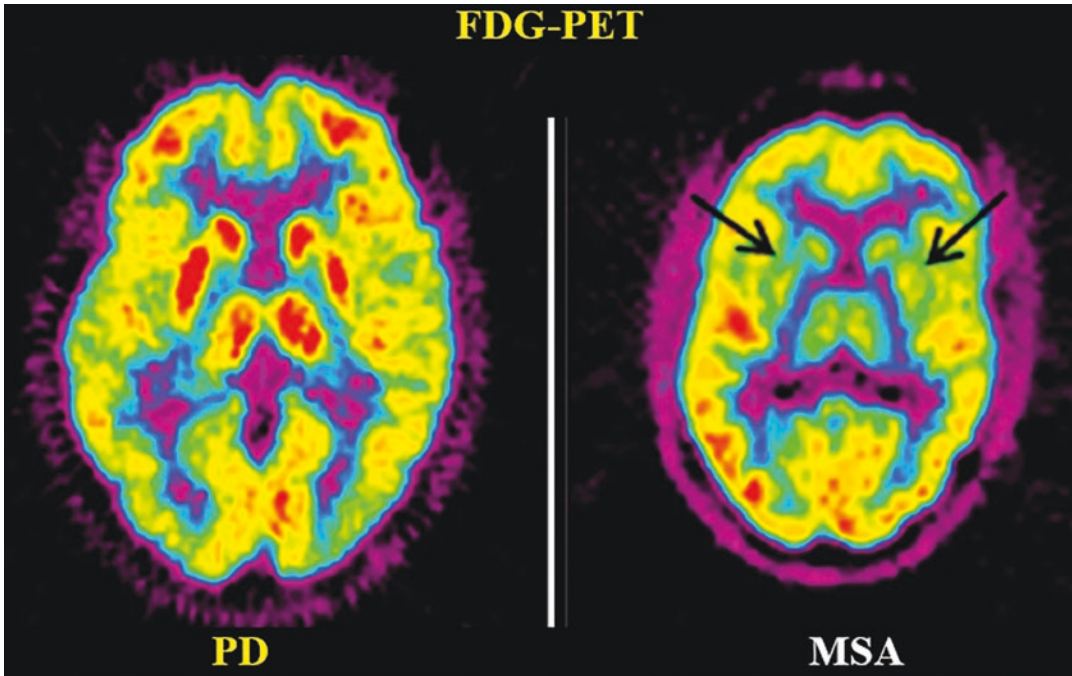
Fig. 15.12 FDG-PET images show significant striatal reduction of glucose metabolism (black arrows) in a patient with multiple system atrophy (MSA) compared to that in a patient with Parkinson's disease (PD). (From Brooks [60])
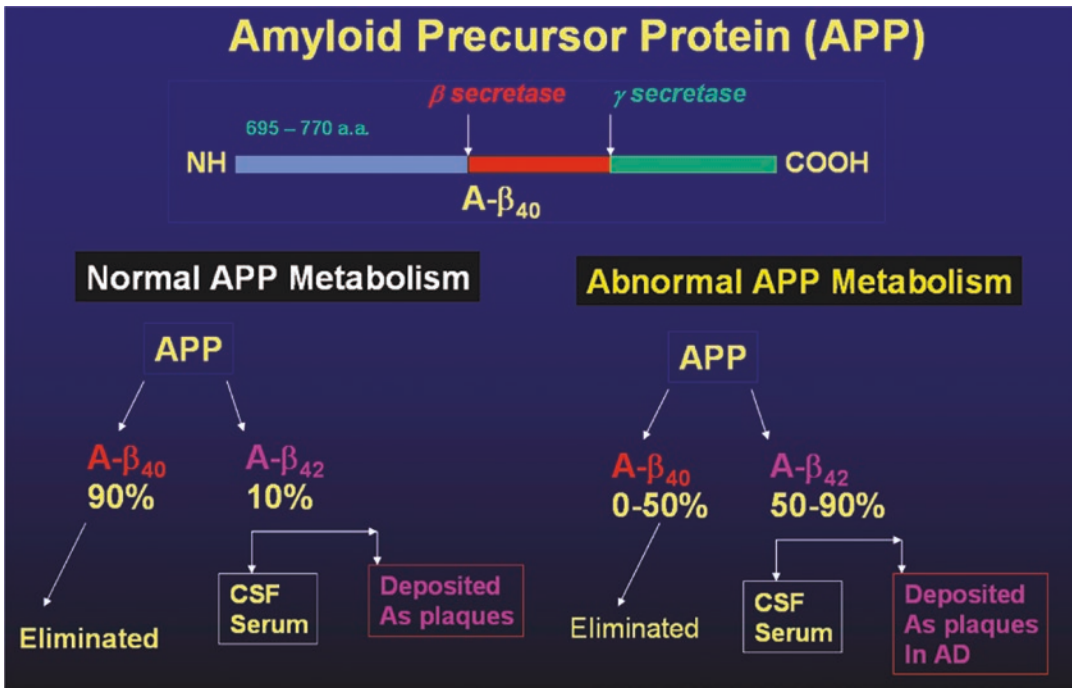

Fig. 15.13 Amyloid precursor protein (APP) metabolism, elimination, and deposition in the brain

neocortex, especially in the temporoparieto-occipital region, and lowest in the cerebellum.

The chemical backbones for developing amyloid radioligands were based on the histological dyes like Congo red, Thioflavin-T, and Chrysamine G, which bind to most amyloid deposits because of their β-sheet fibrillar nature, without specificity for any particular amyloid protein. The chemical structures and the relative binding affinities of ^{11}C- and ^{18}F-labeled Aβ binding radiopharmaceuticals are shown in Fig. 15.14 and Table 15.5.

The first radio tracer developed for imaging β-amyloid was [^{18}F]-FDDNP based on aminonaphthalene [67]. In vitro binding studies have shown that FDDNP was bound to the synthetic $Aβ_{1-40}$ with two binding sites, a high-affinity site (0.12 nM) and a low-affinity site (1.9 nM). In contrast, [^{18}F]-FDDP binding studies with postmortem AD homogenates have shown a B_{max} value of 144 nM with a K_D value of 0.75 nM [68] (Table 15.5).

15.3.4.1   [^{11}C]PiB and [^{18}F]-3′-F-PiB (Flutemetamol, Vizamyl)

Investigators from the University of Pittsburgh Medical Centre developed a series of ^{11}C-labeled arylbenzothiazole (BTA) neutral analogues of Thioflavin-T and reported the development of [^{11}C]6-OH-BTA-1 (also known as Pittsburgh compound B or PiB) which not only displays high affinity for aggregated Aβ but also provides

Table 15.5 Relative binding affinities of ^{11}C and ^{18}F-labeled PET radiopharmaceuticals for Aβ amyloid

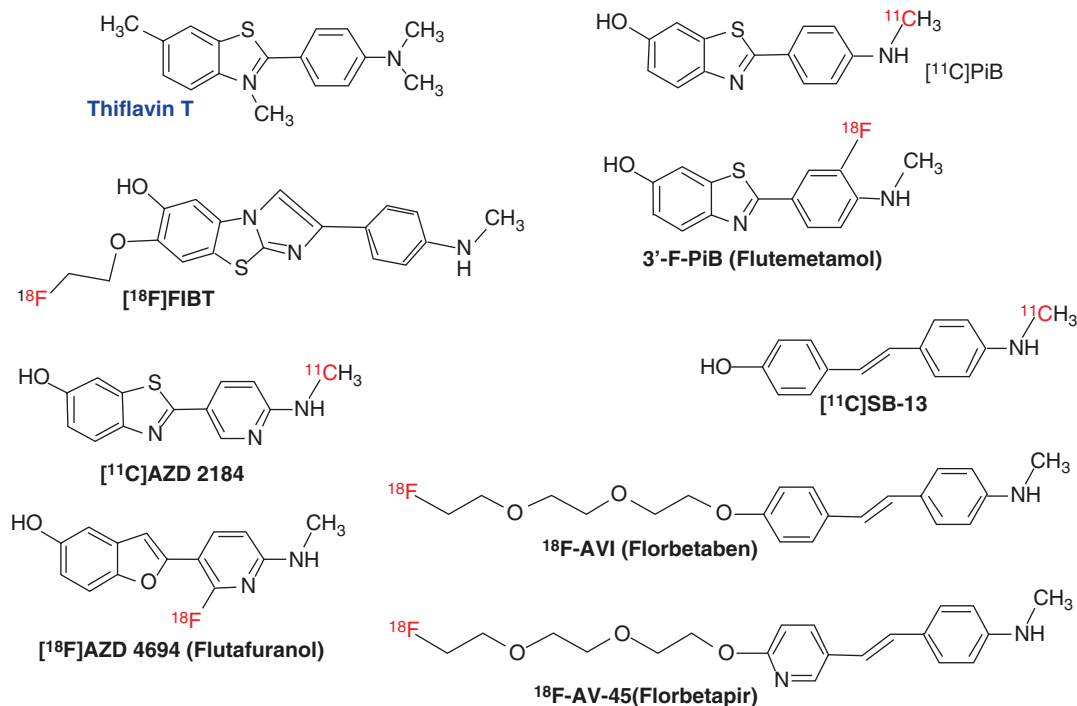| Amyloid binding ligand	K_i (nM)[a]	K_d (nM)
Thioflavin-T	>1000	
[^{11}C]PiB	0.87 ± 0.18	1.4 – 2.4
[^{18}F]Flutemetamol	0.74 ± 0.38	2.4
[^{18}F]Florbetaben	2.22 ± 0.54	
[^{18}F]Florbetapir	2.87 ± 0.17	3.72 ± 0.3
[^{18}F]Flutafuranol		2.30 ± 0.3
[^{18}F]FDDNP	172 ± 18	0.75
[18F]FIBT		0.72 ± 0.2

Fig. 15.14 The chemical structure of PET radiopharmaceuticals for imaging brain amyloid burden

the high brain uptake necessary for PET imaging studies [69, 70].

PiB was subsequently modified to introduce an ^{18}F atom in the aromatic ring to create 3′-F-PiB (GE067 or Flutemetamol F18) [71]. A direct comparison of the Aβ binding properties has demonstrated that the inhibition constant K_i of [^{3}H]3′-F-PiB (2.4 nM) is nearly identical to that of [^{3}H]PiB (1.9 nM). In addition, the amount of [^{3}H]3′-F-PiB bound to brain homogenates has been closely correlated with the Aβ content of these homogenates [72].

15.3.4.2 ^{18}F-AV-1 (Florbetaben, Neuraceq) and ^{18}F-AV-45 (Florbetapir, Amyvid)

Investigators at the University of Pennsylvania and Avid Pharmaceuticals initially reported the development of several iodinated derivatives based on the stilbene backbone that displayed good binding affinities for Aβ aggregates. A stilbene derivative with similar functional groups as PiB called [^{11}C]SB-13 (4-*N*-methylamino-4′-hydroxystilben) was found to display high specificity for amyloid plaques [73, 74]. Subsequently, a series of fluoropegylated stilbene derivatives were successfully prepared and tested [75–77]. The two structurally similar fluoropegylated agents developed commercially are [^{18}F]Florbetaben and [^{18}F]Florbetapir.

^{18}F-AV-1 and ^{18}F-AV-45 share common structural features to PiB. Both these tracers are small planar molecules with extended aromatic systems and alkylamino substitution. They compete pharmacologically for the same binding site on amyloid aggregates with similar affinity, and in human brain sections, they show the same pattern of labeling of Aβ plaques. ^{18}F-AV-1 has been shown to bind avidly to neuritic and diffuse Aβ plaques and to cerebral amyloid angiopathy in vitro; however, it does not show appreciable labeling of tangles, Pick bodies, Lewy bodies, or glial cytoplasmic inclusions. ^{18}F-AV-1 binds with high affinity to brain homogenates in patients with AD, and in AD tissue sections it selectively labeled Aβ plaques. At tracer concentrations, it did not show binding to the post-mortem cortex of patients with frontotemporal dementia or in

the post-mortem brain tissue of a variety of NDs, including tauopathies and α-synucleinopathies. Preclinical toxicity studies in several animal species showed a good safety profile with no observable effects at 100 times the expected human mass dose. In human subjects, the biodistribution of ^{18}F-AV-1 was compared to that of [^{11}C] PiB. Both tracers showed substantial clearance through the liver and excretion of radioactivity into the bowel. Both tracers also showed considerable renal excretion so that the data for the critical organs (i.e., gallbladder wall, liver, and urinary bladder wall) were the same [78]. In a proof-of-concept clinical study, ^{18}F-AV-1 PET scans showed potential utility in differential diagnosis of AD, frontotemporal lobe degeneration (FTLD), or healthy controls and may facilitate the integration of Aβ imaging into clinical practice [79].

In a direct binding assay on AD brain homogenates, ^{18}F-AV-45 displayed a high-binding affinity and specificity to Aβ plaques [75]. Further, an in-vitro binding assay was used to measure ^{18}F-AV-45 affinity to Aβ aggregates in the AD brain tissue homogenates [80]. The inhibition constants (K_i, nM) of various agents against the binding of ^{18}F-AV-45 to Aβ aggregates in post-mortem AD brain homogenates are presented in Table 11.3, and ^{18}F-AV-45 has shown excellent binding affinity (2.87 ± 0.17 nM).

15.3.4.3   [^{18}F]Flutafuranol (AZD4694, NAV4694)

Chemists at AstraZeneca in Sweden made a minor structural modification to PiB in order to develop a Aβ plaque-selective agent, [^{11}C] AZD2184, which has the positive attributes of PiB but with an apparent lower degree of non-specific binding [81]. In order to further reduce the non-specific binding, AZD2184 was structurally modified to develop a benzofuran-derived ^{11}C-labeled radioligand containing fluorine, known as 2-(2-fluoro-6-methylamino-pyridin-3-yl)-benzofuran-5-ol [^{11}C]AZD4694. In cortical sections from human AD brains, [^{3}H]AZD4694 selectively labeled β-amyloid deposits in grey matter, whereas there was a lower level of non-displaceable binding in plaque-devoid white mat-

ter [82]. ^{18}F-labeled [^{18}F]AZD4694 (NAV4694) has high affinity to Aβ fibrils in vitro and shows selective labeling of Aβ in cortical sections from post-mortem human AD brains. The clinical studies suggest that [^{18}F]AZD4694 has the potential for wide clinical application and satisfies the requirements for a promising Aβ radioligand, both for diagnostic use and for evaluation of disease-modifying therapies in AD [83, 84].

15.3.4.4   [^{18}F]FIBT

The best imidazobenzothiazole derivative [^{18}F] FIBT is regarded as the first high-contrast Aβ-imaging agent on par with florbetaben. It also displayed excellent pharmacokinetics, selectivity and high-binding affinity to Aβ fibrils in vitro and in vivo comparable to the gold standard PiB [85, 86]. It was also reported that FIBT has a better PK profile and specific binding affinity to Aβ than florbetaben in transgenic mice. FIBT has >300-fold selectivity for Aβ in comparison to the other amyloid protein aggregates; a $K_i \gg 1000$ nM to recombinant tau and $K_i \gg 1000$ nM to α-syn aggregates [21]. The pilot clinical studies in patients with dementia demonstrated excellent pharmacokinetics and brain amyloid uptake comparable to the gold standard PiB-PET [87].

15.3.4.5   Brain Amyloid-PET: Clinical Studies

As described earlier (Fig. 15.6), the pathologic process in dementia usually begins decades before symptoms are evident. Aβ-amyloid plaques are one of the hallmark brain lesions of AD. Three Aβ-amyloid-selective PET radiopharmaceuticals (Florbetapir, Florbetaben, and Flutemetamol) have been approved for clinical use in the USA, Europe, and Japan. The indication for these three agents is to estimate β-amyloid neuritic plaque density in adult patients with cognitive impairment who are being evaluated for AD and other causes of cognitive decline. A negative scan indicates sparse to no neuritic plaques and is inconsistent with a neuropathological diagnosis of AD at the time of image acquisition. A negative scan result, however, reduces the like-

lihood that a patient's cognitive impairment is due to AD. A positive scan indicates moderate to frequent amyloid neuritic plaques; neuropathological examination has shown this amount of amyloid neuritic plaque is present in patients with AD but, may also be present in patients with other types of neurologic conditions as well as older people with normal cognition. Amyloid-PET is an adjunct to other diagnostic evaluations. The clinical studies in the last 10 years have shown high correlation with Aβ amyloid neuropathologic findings and clinical utility [21, 33].

The clinical studies with all the current Aβ PET radiopharmaceuticals claim to have demonstrated an ability to discriminate between AD patients and healthy controls with high degrees of sensitivity and specificity (Fig. 15.15) [33, 88, 89]. In addition, several studies suggest that Aβ imaging can distinguish AD from non-AD dementia, such as FTD, VD (Fig. 15.16), and can help determine whether MCI is due to AD [90]. One of the major concerns is the high non-specific white matter binding of amyloid tracers (especially ^{18}F-labeled agents) and the potential spillover effects that can occur from this non-specific retention into neighboring gray matter.

Amyloid-PET imaging studies have shown that Aβ-amyloid accumulation is a slow and protracted process extending for more than two decades before the onset of the clinical phenotype. Although Aβ-amyloid burden on PET scan correlates with memory impairment and a higher risk for cognitive decline in the aging population and patients with MCI, it does not strongly correlate with cognitive impairment, synaptic activity, and neurodegeneration in AD, likely because Aβ-amyloid accumulation has already reached a plateau. Taking all this into account, it is clear that Aβ-amyloid deposition in the brain is not a benign process that is part of normal aging but, an early and necessary, although not sufficient, cause for cognitive decline in AD. This indicates the involvement of other downstream mechanisms, likely triggered by Ab-amyloid such as NFT formation, neuroinflammation, synaptic failure and eventual neuronal loss [33].
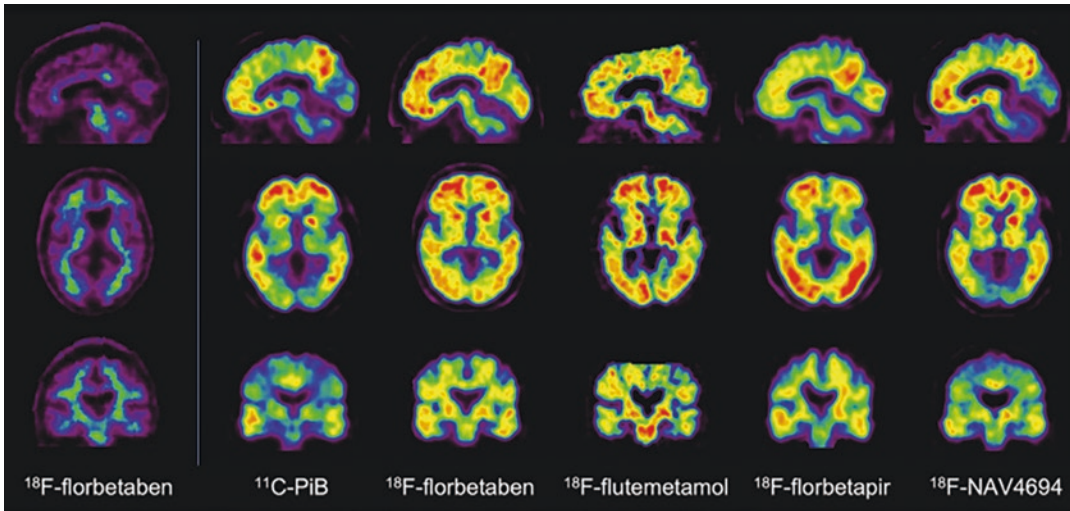
Fig. 15.15 Aβ-PET: Representative sagittal, transaxial, and coronal PET images in control patient without cognitive impairment (left column) and five different patients with Alzheimer disease (AD). [18F] florbetaben scan in control patient without cognitive impairment shows nonspecific tracer retention in white matter. All patients with AD have present high Ab burdens, reflected in marked radiotracer retention in cortical and subcortical gray matter areas. Tracer retention in AD is particularly higher in frontal, cingulate, precuneus, striatum, parietal, and lateral temporal cortices, whereas occipital, sensorimotor, and mesial temporal lobes are much less affected. All these tracers show a variable degree of nonspecific binding to white matter. (From Villemagne et al. [33])
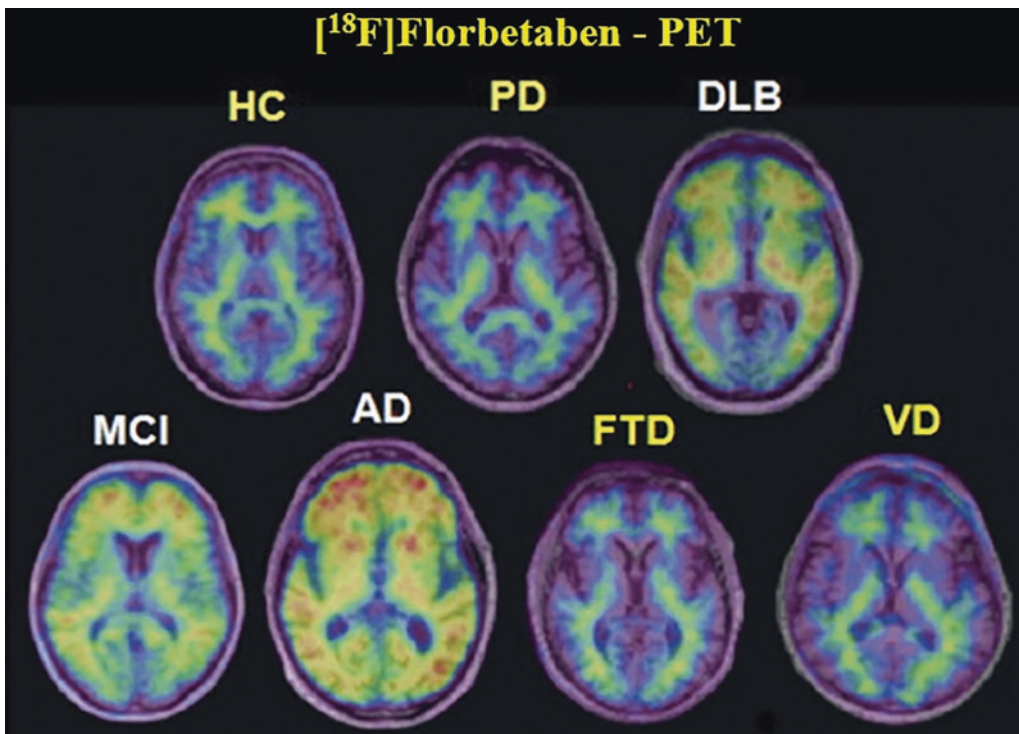
Fig. 15.16 ¹⁸F-Florbetaben PET in differential diagnosis of dementia in healthy control (HC), Parkinson disease (PD), dementia with Lewy bodies (DLB), Mild cognitive impairment (MCI), Alzheimer disease (AD), and pure vascular dementia (VD). (From Rowe et al. [79])

15.3.5 Tau Imaging in Dementia

Pathologic aggregates of tau protein are observed in several NDDs and are used to diagnose and stage disease postmortem. In spite of Aβ pathology temporarily preceding tau pathology, there is documented evidence to support the concept that the density and neocortical spread of NFTs correlate better with neurodegeneration and cognitive decline in AD patients [91]. Apart from AD, NFTs are also present in other dementias, like FTD, CBD, and PSP. A PET radiotracer that could quantify NFTs would help to understand the pathophysiology and clinical management not only of AD, but also these other NDD. The major clinical application of tau imaging will be tracking disease progression, disease staging, or as a surrogate marker of cognition.

The focus of tau PET ligand discovery and clinical research has largely centered on imaging NFTs observed in AD. Tau expressed in the human adult brain can have six isoforms that are frequently subdivided as 3-repeat (3R), or 4-repeat (4R) based on the number of repeat regions in the microtubule binding domain. In NDD, it is postulated that abnormal phosphorylation of tau results in dissociation of tau from the microtubule after which tau begins to self-aggregate forming insoluble aggregates of tau protein, and tau aggregates differ in the expression of 3R and 4R isoforms [92]. The structural differences between tau aggregates likely affect the accessibility of binding sites for PET radioligands, which has consequences for ligand specificity and sensitivity. In AD, the dissociated 3R and 4R tau form paired-helical filaments (PHF) which make up NFTs, a hallmark proteinopathy of AD [93]

Great progress has been made in the past 10 years, with the development of several selective tau tracers extensively used in clinical research studies (Fig. 15.17). There are several tracers for PET that have been developed and used for clinical assessment in patients with various tauopathies as "first-generation" tracers, such as ^{18}F-THK5317, ^{18}F-THK5351, ^{18}F-AV-1451, and [^{11}C]PBB3. Limitations of these tracers with regard to off-target binding and diagnostic range provided the motivation to develop a new generation of tau tracers, including ^{18}F-MK-6240, ^{18}F-PI-2620, ^{18}F-RO-948, ^{18}F-JNJ311/069, ^{18}F-GTP1, and ^{18}F-PM-PBB3 (Betthauser 2018) [21, 33, 94, 95].The most widely used early-generation selective tau tracer ^{18}F-flortaucipir (also known as
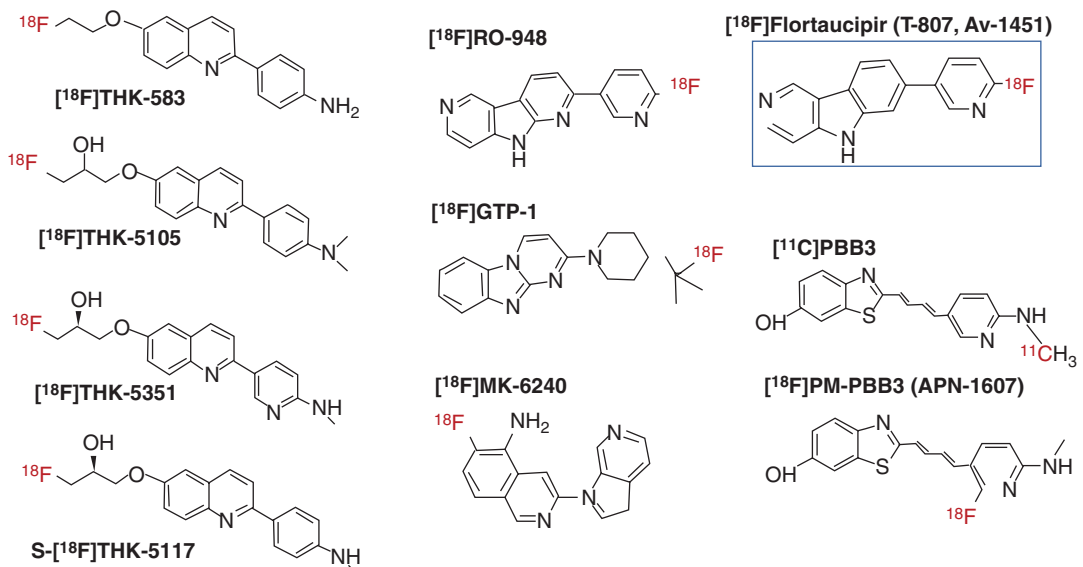

Fig. 15.17 Chemical structures of PET radiopharmaceuticals for imaging tau protein distribution in patients with dementia

AV1451, T807) has been recently approved for clinical use by the FDA under the name of Tauvid [94, 96].

15.3.5.1 Flortaucipir F18 Injection (AV-1451, T-807, Tauvid™)

Investigators at Siemens Medical Solution in the USA have designed and prepared a novel class of 5H-pyrido[4,3-b]indoles, and reported the preclinical characterization of two PET tracers [^{18}F] T807, and [^{18}F]T808 for imaging tau protein in AD [97, 98]. They both have sufficient affinity for tau (AD-PHF) 14.6 nM and 22 nM and with K_d(Aβ) /K_d(tau) 25 and 27, respectively, meaning a higher selectivity of tau aggregates over Aβ fibrils. Subsequently, [^{18}F]T807 (flortaucipir) was selected over [^{18}F]T808 for clinical development, because of the metabolic defluorination observed in some cases, and the significant accumulation of F-18 in the skull especially in late time points, that could confound PET images.

In 2013, Eli Lilly and Company (Avid Radiopharmaceuticals, a Lilly subsidiary) acquired the tau PET tracer, [^{18}F]T-807 program developed by Siemens Medical Solutions USA, Inc. The Initial flortaucipir-PET scans in controls and subjects with AD and MCI demonstrated an accumulation of the tracer with a distinct increasing neocortical distribution in tandem with the severity of dementia according to the known mode of spread of PHF in the brain in agreement with Braak's staging [99]. Off-target binding has been seen in flortaucipir PET studies in the meninges, striatum, choroid plexus, and midbrain. In the analysis of autopsy brain samples, it was found that flortaucipir also binds to vessels, iron-associated regions, substantia nigra, the leptomeningeal melanin, and also calcifications in the choroid plexus. Another important off-target binding of flortaucipir is to both isoforms of the MAO enzyme. Furthermore, there was difficulty in quantification due to the fact that it does not reach a steady-state during a typical imaging duration [21, 94, 96].

Tauvid™ is indicated for positron emission tomography (PET) imaging of the brain to estimate the density and distribution of aggregated tau neurofibrillary tangles (NFTs) in adult patients with cognitive impairment who are being evaluated for Alzheimer's disease (AD) (Fig. 15.18). In principle, tau PET imaging enables noninvasive detection of in vivo tau deposition patterns, facilitates differential diagnosis between neurodegenerative diseases, including different tauopathies, and predicts disease progression. Furthermore, tau PET imaging could potentially be applied to achieve the therapeutic effect evaluation of anti-tau treatment and develop a novel drug, thereby allowing preventive interventions [94].

15.3.5.2 [^{18}F]THK-5351

Since 2002, investigators at Tohoku University in Japan have been designing and screening benzoxazole, benzimidazole, quinolone, and other derivatives targeting β-sheet structures in brain sections. These investigators initially reported the first tau imaging agent, ^{18}F-THK523, which has a 20-fold higher binding potential (BP) for PHF-tau compared to Aβ$_{1-42}$ [101]. Subsequently, after careful structural modifications, [^{18}F]THK-5351 was identified as a tracer with better imaging characteristics, (Fig. 15.18) which displayed a quicker white matter washout (lower white matter retention) and higher specific binding to AD tau-associated regions of interest than [^{18}F]THK-5317 but, also, its retention correlated with extra-hippocampal sub-regional atrophy rather than hippocampal subfields, proffering hence different underlying mechanisms of atrophy in early AD. Another remarkable advantage it has over other tau tracers was the lack of significant retention in the choroid plexus or venous sinus, which could probably lead to a spill-in of tracer signals into the brain. Unfortunately, it has been reported to have high affinity to monoamine oxidase-B (MAO-B) in contrast with [^{18}F]THK-5117 and also showed a greater off-target binding in the midbrain, thalamus, and the basal ganglia [102, 103].

15.3.5.3 [^{18}F]MK-6240

The Investigators at Merk Developed [^{18}F] MK-6240, a Novel Ligand

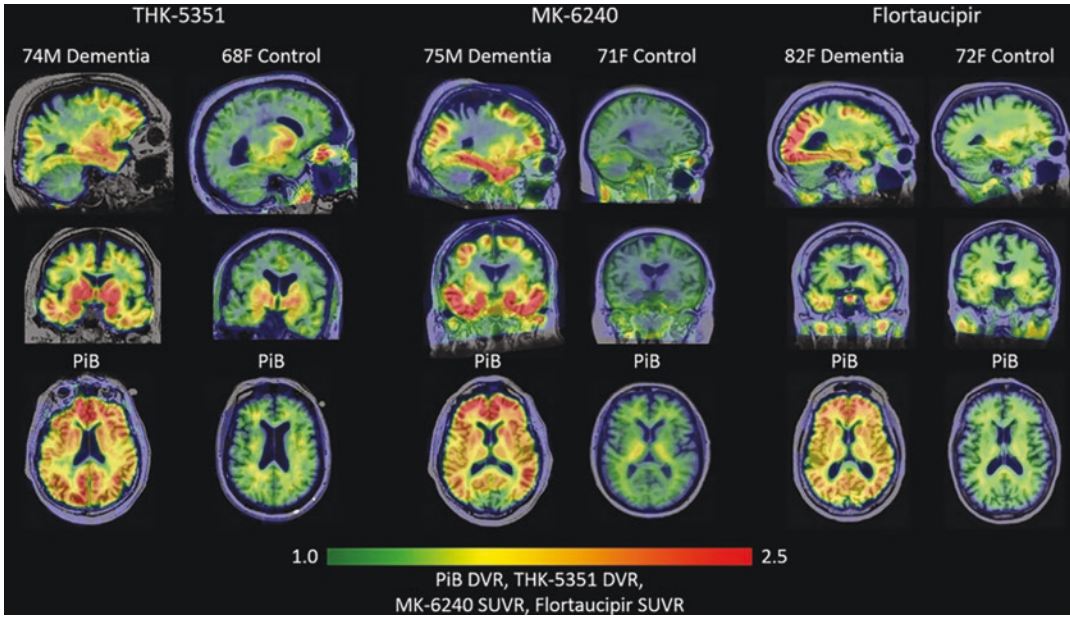The researchers from Merck & Co. reported the development of NFT PET tracer, ^{18}F-MK-6240, a

Fig. 15.18 Sample images for tau PET ligands. Parametric images comparing [18F]THK-5351, [18F]MK-6240, and [18F]Flortaucipir in amyloid negative con-trol and amyloid positive dementia cases. Each column of images represents an individual person. (From Betthauser et al. [100])

novel pyridine isoquinoline amine derivative, which displayed high affinity for NFTs and weak affinity for amyloid plaque. Additionally, MK-6240 showed favorably moderate lipophilic-ity [104]. It exhibited favorable pharmacokinet-ics, with a fast brain uptake and clearance. Uptake was higher in AD subjects and was considerably higher in brain regions expected to have NFT like in the hippocampus but very low uptake in the cerebellar gray matter suggests a potential use of the cerebellar gray matter as a reference region [21]. 18F-MK-6240 has also shown high affinity and selectivity for 3R/4R PHF-tau. Preclinical findings confirmed a lack of binding to MAO-A and MAO-B. Unlike flortaucipir and [18F]THK-5351 off-target binding was not seen in the cho-roid plexus and basal ganglia [204] but, like flortaucipir and various tau PET tracers, off-target binding to neuromelanin- and melanin-containing cells like the pigmented neurons in the substantia nigra, and meninges was observed [21, 92].

In vivo studies of 18F-MK-6240 (Fig. 15.19) show good reproducibility, an ability to differentiate cognitively normal subjects from MCI or AD patients, and sensitivity for detecting

tau in early disease stages (21). In a direct com-parison of PET studies in human subjects, both tau tracers 18F-MK-6240 and [18F]flortaucipir are capable of quantifying signal in a common set of brain regions that develop tau pathology in AD; these tracers perform equally well in visual inter-pretations. Each also shows distinct patterns of apparent off-target binding. 18F-MK-6240 showed a greater dynamic range in SUVR esti-mates, which may be an advantage in detecting early tau pathology or in performing longitudinal studies to detect small interval changes [105].

15.3.6 Dopaminergic System

Dopamine (3,4-dihydroxyphenethylamine) is a simple organic chemical that functions as a neu-rotransmitter in the brain. Dopaminergic system (Fig. 15.20) plays a major role in reward-motivated behavior, in motor control, and in con-trolling the release of several important hormones. As part of the reward pathway, dopamine is man-ufactured in nerve cell bodies located within the ventral tegmental area (VTA) and is released in
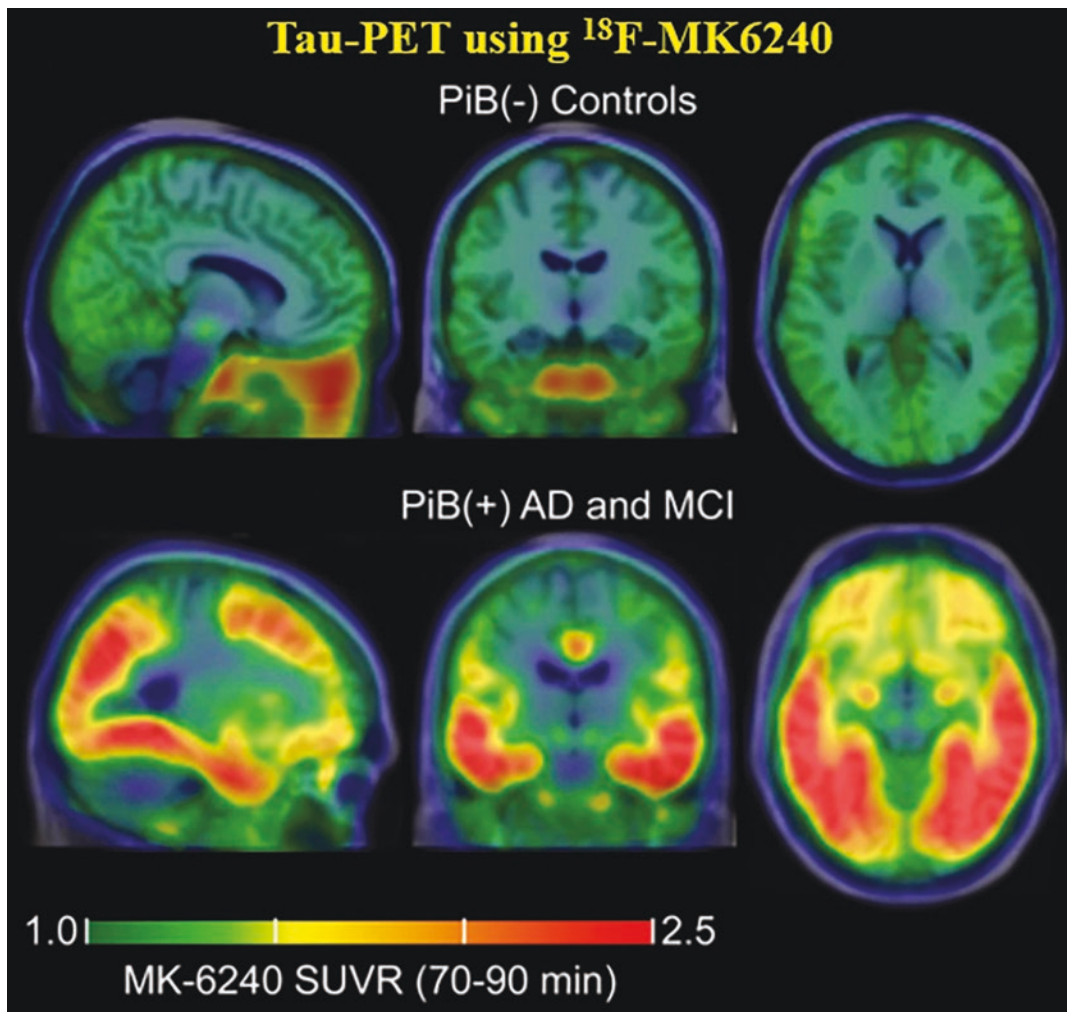
Fig. 15.19 Mean parametric ¹⁸F-MK-6240 SUVR(70–90 min) images taken across controls (top, *n* = 29) and PiB(+) AD and MCI individuals (bottom, *n* = 6) in MNI template space demonstrating common off-target and on-target binding. (From Betthauser et al. [100])

the nucleus accumbens and the prefrontal cortex. The motor functions of dopamine are linked to a separate pathway, with cell bodies in the substantia nigra that manufacture and release dopamine into the striatum. Dopamine is transported to the synaptic sites and packaged into vesicles for release, which occurs during synaptic transmission. Following the release of dopamine into the synapse, dopamine interacts with postsynaptic dopamine receptor sites. Free dopamine in the synapse is also reabsorbed into the presynaptic terminal via the dopamine transporter (DAT).

Since dopamine does not cross the BBB, it is synthesized in the dopaminergic neurons in the substantia nigra, the ventral tegmental area, and the retrorubral area of mesencephalon. It is synthesized in the neuron from the amino acid tyrosine and stored in the intracellular vesicles (Fig. 15.20). The amino acid tyrosine is first converted to L-DOPA by tyrosine hydroxylase (TH), a rate-limiting enzyme involved in the biosynthesis of dopamine. L-DOPA (precursor for dopamine) is then converted to dopamine by the enzyme *aromatic* l-*amino acid decarboxylase* (*AAAD*; also
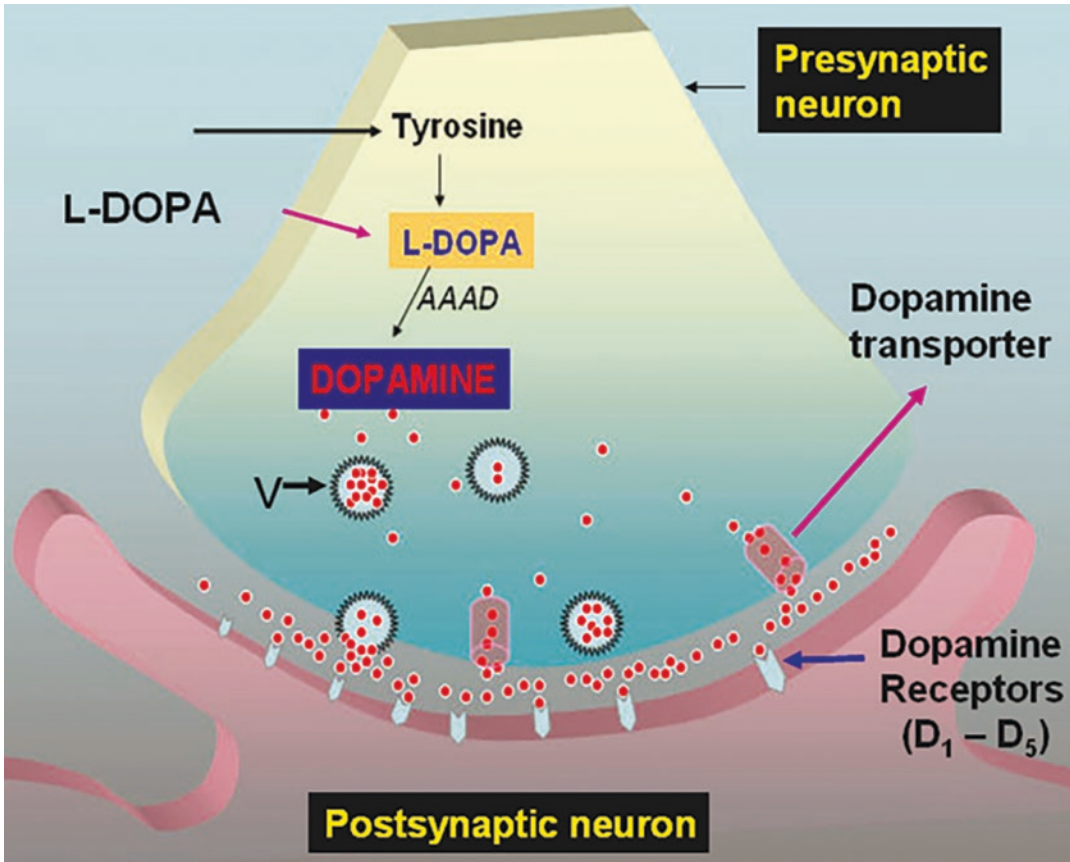
Fig. 15.20 The dopaminergic system: Dopamine, synthesized in the presynaptic neuron is stored in the vesicles (V) and released into the synapse. Dopamine binds to specific receptors on the postsynaptic membrane or is transported back into the presynaptic neuron via dopamine transporters

known as *DOPA decarboxylase* (*DDC*). Levodopa, a pure form of L-DOPA, is the most widely used treatment for PD. Based on this mechanism, [^{18}F]fluoro-L-DOPA (FDOPA) (Fig. 15.21) has been synthesized in order to image dopamine synthesis and metabolism in the presynaptic nerve terminals [106]. Following the transport into the neuron, FDOPA is converted to [^{18}F]fluorodopamine (FDA) by the enzyme *AAAD*. [^{18}F]FDOPA, however, is not an ideal radiotracer to study dopamine synthesis since quantitative analysis with FDOPA-PET in humans is flawed by the presence of radioactive metabolites, which cross the BBB and contribute significantly to the uptake of radioactivity in the brain [107].

Specific vesicular amine transporters (VMAT$_2$) transport dopamine and other mono-amines from the cytosol into the vesicles. The free dopamine in the cytosol is oxidized by the enzyme monoamine oxidase (MAO). Following release of the dopamine into the synapse, the dopamine interacts with the postsynaptic dopamine receptor sites. The five major subtypes of dopamine receptors can be classified into two major categories, depending on their ability to stimulate (D$_1$, D$_5$) or inhibit (D$_2$, D$_3$, D$_4$) adenylate cyclase, following binding to the receptor. The synaptic concentration of dopamine is regulated by the reuptake of dopamine into the presynaptic nerve terminal by specific dopamine transporters on the presynaptic plasma membrane. In the last four decades, the dopamine system has been a major focus in the development of PET and SPECT tracers.
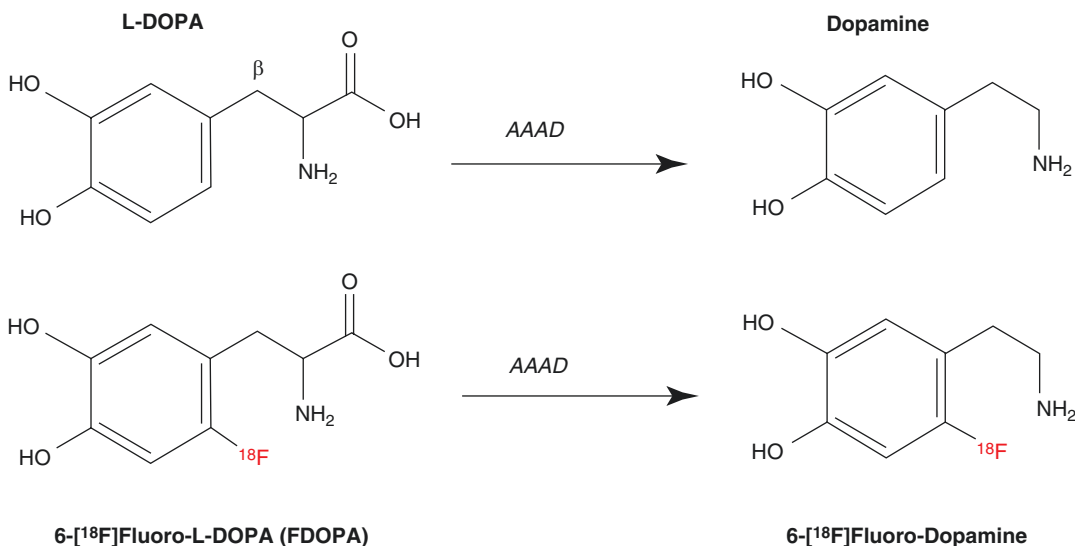
Fig. 15.21 Synthesis of dopamine from the precursor L-DOPA by the enzyme aromatic L-amino acid decarboxylase (AAAD). Similarly, [18F]FDOPA is converted to [18F]fluorodopamine

15.3.6.1 Dopamine transporter (DAT)

The dopamine transporter (also dopamine active transporter, DAT) is a membrane-spanning protein that pumps the dopamine out of the synaptic cleft back into the presynaptic neuron (Fig. 15.20). The driving force for DAT-mediated dopamine reuptake is the ion concentration gradient generated by the plasma membrane Na^+/K^+ ATPase.

Studies with [11C]cocaine initially showed that cocaine binds to DAT, blocks the reuptake of dopamine, and increases the intrasynaptic dopamine levels. Since cocaine is metabolized in the blood, several synthetic derivatives of a modified cocaine analogue (3-phenyltropane scaffold) have been developed and radiolabeled with PET and SPECT radionuclides to image the expression of DAT in the presynaptic neurons [108]. (−)-2-β-Carbomethoxy-3-β-(4-fluorophenyl)tropane (β-CFT, WIN 35 428) has been the gold standard for DAT studies in molecular biology and pharmacology. Some of the important PET and SPECT radiotracers useful for imaging DATs are shown in (Fig. 15.22). [11C]β-CFT, [11C]PE2i, [18F]FP-CIT, 123I-FP-CIT (or DaTSCAN), and 123I-altropane have all been well studied in human subjects. In addition, based on the N_2S_2 chelating agent known as bisaminoethanethiol (BAT), a

tropane analogue, 99mTc-TRODAT-1, was also developed for SPECT imaging studies [109].

15.3.6.2 Vesicular Monoamine Transporter (VMAT)

The type 2 VMAT is a relatively unspecific transporter, as it functions to move a wide variety of amines into the vesicle lumen, including dopamine, serotonin, norepinephrine, histamine, and a number of structurally related molecules [110]. The classical VMAT2 inhibitor, tetrabenazine, has long been used for the treatment of chorea associated with HD. In order to image the density of presynaptic dopaminergic terminals, α(+)-[11C]Dihydro-tetrabenazine ([11C]DTBZ), a stable, stereoselective tracer was developed [111, 112]. [11C]DTBZ (Fig. 15.23) binds selectively to VMAT2 and is less regulated by intrasynaptic dopamine than are other dopaminergic tracers [113]. Among the 18F-labeled analogues of DTBZ, it was reported that [18F]fluoropropyl-(+)-dihydrotetrabenazine ([18F]FP-(+)-DTBZ or AV-133) (Fig. 15.23) gave the highest specific signal in the assessment of presynaptic neuronal degeneration [113, 114]. These radiotracers are not specific for dopaminergic system. The PET images of VMAT2 provide a measurement
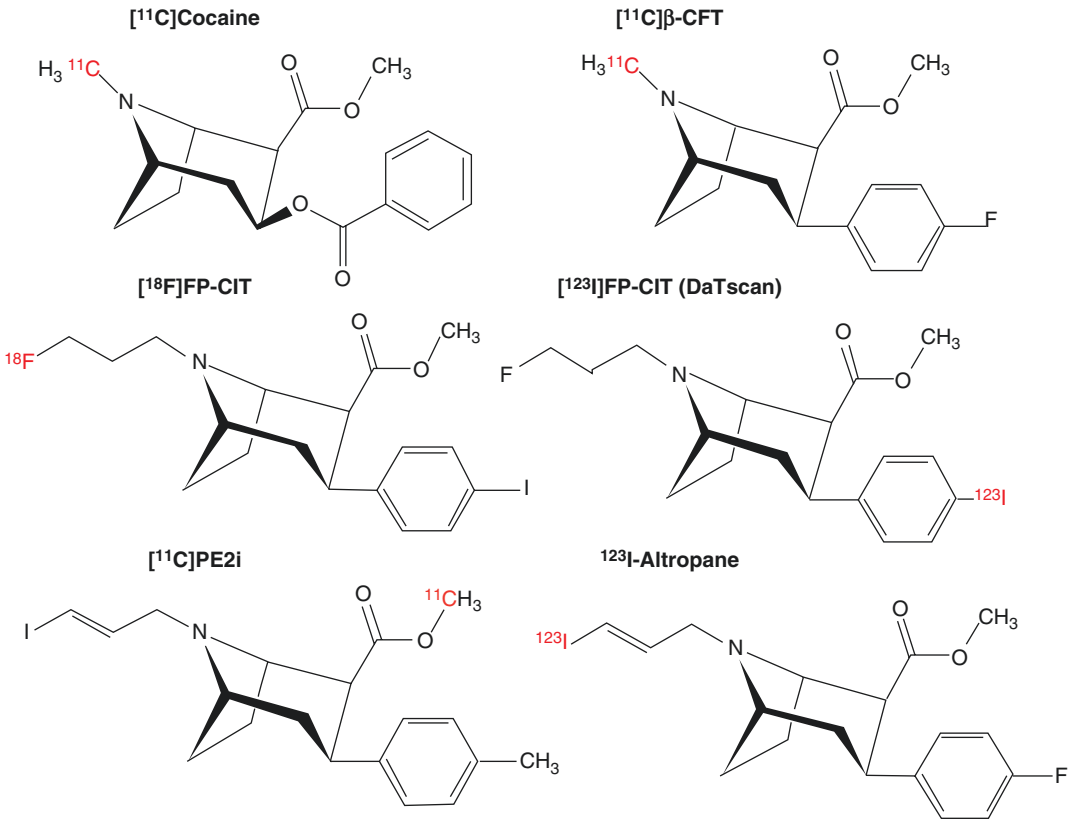
Fig. 15.22 Chemical structures of PET and SPECT radiopharmaceuticals (based on 3-phenyltropane scaffold) to image the expression of dopamine transporter (DAT) in the presynaptic dopaminergic neurons
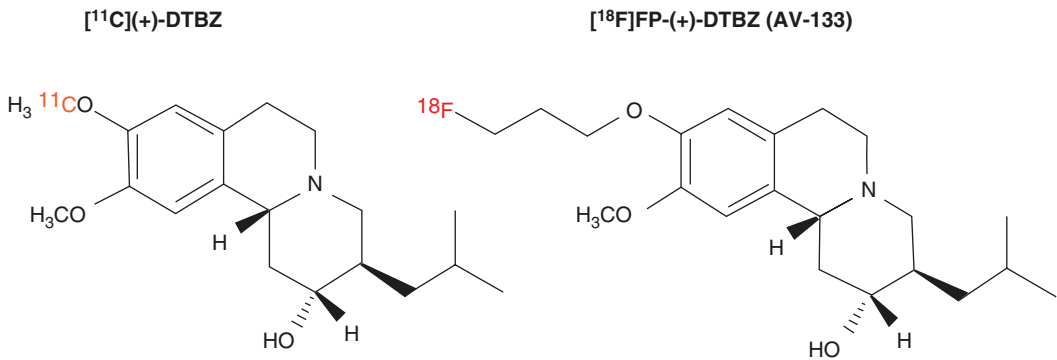

Fig. 15.23 Chemical structures of PET radiopharmaceuticals to image vesicular monoamine transporter (VMAT) density in the dopaminergic presynaptic neurons

reflecting the density and integrity of all three monoaminergic neurons [112].
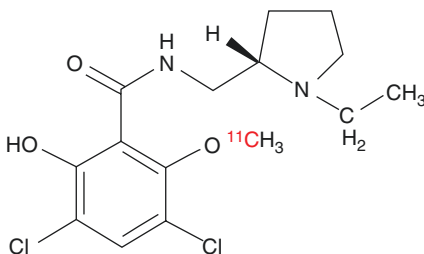
15.3.6.3 Dopamine Receptors

The five major subtypes of dopamine receptors can be grouped into two major categories, depending on their ability to stimulate (D_1, D_5) or inhibit (D_2, D_3, D_4) *adenylate cyclase*, following binding to the receptor. The D2-like receptor family is of great therapeutic interest because D_2 receptors have been identified as primary sites of action of most anti-Parkinson and antipsychotic drugs. The dopamine D_2 receptors are primarily expressed in the caudate putamen, nucleus accumbens, and olfactory tubercle, where they are involved in the modulation of locomotion, reward, reinforcement, memory, and learning. PET with high affinity and selective D_2 receptor radioligands could provide valuable knowledge about the impact of dopamine receptor density on the pathogenesis and devolvement of neuropsychiatric and neurological diseases. Initial studies were performed with [11]C- and ^{18}F-labeled *N*-methylspiperidol

(MSP), an irreversible antagonist not ideal for pharmacokinetic modeling and receptor quantitation studies. [11C]Raclopride (Fig. 15.24), a benzamide analogue with moderate affinity and reversible binding, is the most widely used PET tracer for imaging dopamine D_2 receptors in vivo [115, 116]. ^{123}I-iodobenzamide (IBZM), a radiotracer for SPECT, has also shown remarkable success in assessing dopamine D_2 receptor density in human subjects [114, 117]. Among the high-affinity reversibly binding radiotracers, [18F]fallypride [118] provides a longer scanning period while [11C]FLB-457 [119] has shown clinical utility to assess extrastriatal dopamine receptors.
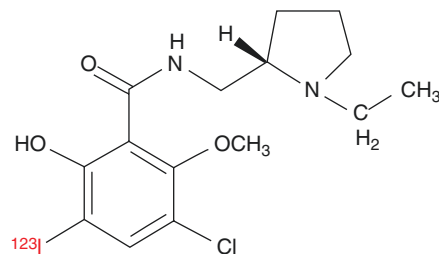
15.3.6.4 Parkinson Disease (PD and Differential Diagnosis)

Parkinsonism is defined as slowness of movement (bradykinesia) in association with rigidity and/or tremor and is related to basal ganglia dysfunction. Most often, a degeneration of dopaminergic nerve terminals is encountered, with PD being the commonest condition. PD is a progres-
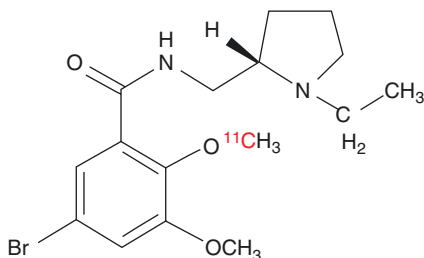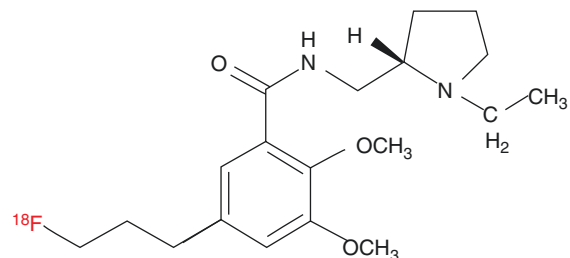

Fig. 15.24 Chemical structures of radiopharmaceuticals to image dopamine receptors. D_2/D_3 receptor ligands include raclopride, IBZM, fallypride, and FLB-457

sive neurodegenerative disease characterized primarily by the selective degeneration of dopaminergic neurons in the pars compacta of the substantia nigra (SN). Intraneuronal inclusions composed of aggregates of a-synuclein (α-syn), called Lewy bodies (LBs), are the other neuropathological hallmark [120]. In PD, a lower membrane DAT expression on presynaptic terminals may possibly reflect striatal dopamine terminal loss and is in direct proportion to the magnitude of the depletion of nigral cells. Atypical Parkinsonian syndromes include multiple system atrophy (MSA), progressive supranuclear palsy (PSP), corticobasal degeneration (CBD), and dementia with Lewy bodies (DLB).

Imaging may play a significant role in early PD, when the full triad of clinical symptoms and signs (rest tremor, bradykinesia, and rigidity) may not be apparent on examination. Differential diagnoses at this stage include benign essential or dystonic tremors and parkinsonism associated with exogenous agents, such as dopamine receptor-blocking drugs. These conditions are not associated with nigral degeneration or striatal dopamine deficiency [60] which may be assessed by imaging. Different imaging biomarkers may be beneficial in assessing dopaminergic integrity and assist clinicians to narrow the differential diagnosis in patients with motor symptoms [60, 121–127].

Molecular imaging studies can be performed using two different kinds of radiotracers to target the nerve terminals: (a) The enzymatic activity of AADC can be assessed using [^{18}F]FDOPA, which acts as a false substrate for AADC (being converted to F-dopamine) [128]. Therefore, the concentration of ^{18}F-FDOPA in dopaminergic neurons reflects the in situ synthesis of endogenous dopamine [129]. However, it must be noted that the extent of dopaminergic degeneration as detected by AADC ligands tends to be lower compared to other presynaptic targets, such as DAT ligands [123]. (b) Radiotracers specific for DAT (such as ^{18}F-FP-CIT or ^{123}I-FP-CIT and [^{11}C]PE2i) can be used. c) On the other hand, postsynaptic terminals integrity can be assessed using D2/D3 specific ligands such as [^{11}C] Raclopride and [^{18}F]Fallypride.

[^{18}F]FDOPA and ^{123}I-Ioflupane (FP-CIT, DaTscan)

DaTscan (Ioflupane I 123 Injection) was FDA approved in 2011 and is indicated for striatal dopamine transporter visualization using SPECT brain imaging to assist in the evaluation of adult patients with suspected PS. In these patients, DaTscan may be used to help differentiate essential tremor (with normal or negative SPECT scan) from tremor due to PS (positive or abnormal scan with decreased binding). The safety and efficacy of DaTscan were evaluated in two multicenter, single-arm studies that evaluated 284 adult patients with tremor.

Fluorodopa F 18 Injection (FDOPA) was FDA approved in 2019 and is indicated for use in PET to visualize dopaminergic nerve terminals in the striatum for the evaluation of adult patients with suspected PS. [^{18}F]FDOPA-PET was introduced in 1983 to image dopamine synthesis in vivo. In normal subjects, the images show higher tracer uptake in the striatum (caudate and putamen) and the midbrain, while uptake in the cerebral cortex and cerebellum is much lower (Fig. 15.25). In patients with PD, the tracer uptake and retention in the striatum are reduced, most markedly on the opposite side of the major motor signs [106]. Measurement of striatal uptake of [^{18}F]-DOPA is still regarded as one of the most reliable tools for the in vivo diagnosis of PD because it directly probes the nigro-striate synthesis of dopamine [121–123]. However, it undergoes metabolism and the two metabolites, [^{18}F] 6-fluoro-3,4-dihydroxyphenylacetic acid (^{18}FDOPAC) and [^{18}F]6-fluorohomovanillic acid (18FHVA) are responsible for enhanced background noise, and lower image contrast [123]. The safety and efficacy of FDOPA-PET (with prior administration of carbidopa) were evaluated in a prospective single-arm study conducted at a single center that enrolled 68 adult patients with possible PS.

[^{18}F]FDOPA-PET and DAT-PET or SPECT (using cocaine analogues) can discriminate PD patients from healthy controls [130]. As shown in Fig. 15.26, FP-CIT uptake is reduced in patients with PD compared to healthy controls. This would result in a greater reduction of striatal binding of FP-CIT (DaTscan) in the early phases
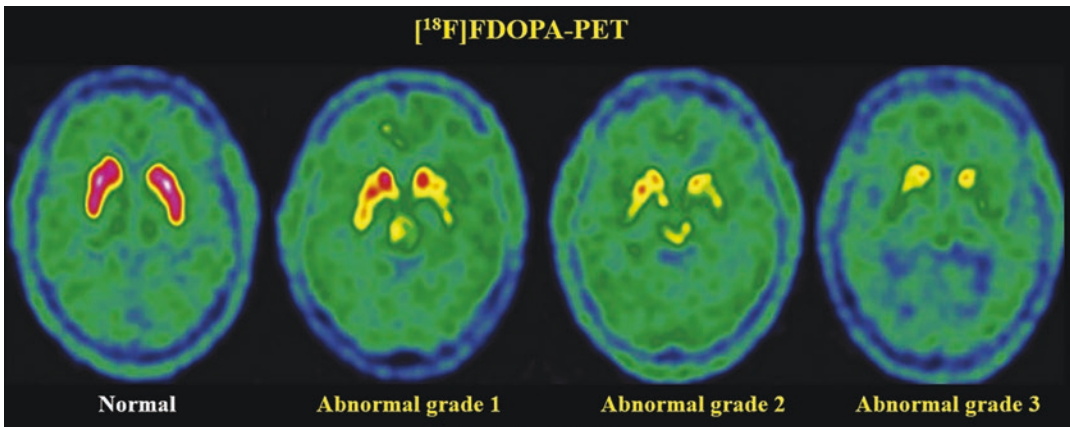
Fig. 15.25 [^{18}F]FDOPA-PET Representative example of Benamer grades, adapted to FDOPA uptake in patients with Parkinsonian syndromes. PET scans shown in the anterior commissure-posterior commissure plane and normalization of color scale on the basal ganglia. (From Emsen et al. [121])

of PD compared to FDOPA. It has also been suggested that, in the early stages of PD, *AADC* is upregulated, while DATs are downregulated as an early response to the reduction of the endogenous dopamine levels [131]. Therefore, FP-CIT might be more sensitive than FDOPA for detecting early striatal dopaminergic deficits [132]. When clinically probable PD and essential tremor patients have been compared, the striatal DAT imaging with DaTscan (Fig. 15.26) has been shown to differentiate these conditions with a sensitivity and specificity of over 90% [60]. Also, PD and MSA both show decreased presynaptic dopaminergic function by FDOPA or DaTscan. A recent review suggests that dual tracer PET with both FDG and FDOPA in patients with PS and cognitive disorders to optimize the management with an emphasis on the implementation of cognitive rehabilitation. Dopamine D_2 receptor imaging with [^{11}C]raclopride-PET or [^{123}I]IBZM-SPECT is abnormal (decreased uptake) in MSA but, not in PD. Based on DaT imaging with [^{11}C]-2β-carbomethoxy-3β-(4-fluorophenyl)-tropane ([^{11}C]CFT) and dopamine D2 receptor imaging with [^{11}C]raclopride, it was shown that the delayed (last) images clearly show that raclopride uptake is reduced in MSA but, not in PD (Fig. 15.27) [133].

VMAT imaging with [^{18}F]AV-133 allows for the assessment of nigrostriatal degeneration in Lewy body diseases. [^{18}F]AV-133 can robustly detect reductions of dopaminergic nigrostriatal afferents in patients with DLB and assist in the differential diagnosis from AD [134].

15.3.7 Neuroinflammation

Neuroinflammation is more closely associated with many neurological disorders such as stroke or trauma when acute, and with NDs when chronic [135–137]. A dominant response to all types of CNS injuries is the activation of microglia and astroglia, often referred to as gliosis, at the sites of damage. While it is becoming clear that activation of microglia and astroglia, and the attendant expression of proinflammatory cytokines and chemokines are often associated with disease, trauma, and toxicant-induced damage to the CNS, it is by no means clear that a cause-and-effect relationship exists between the presence of a neuroinflammatory process and neural damage. The inflammatory response in the brain is a double-edged sword. It is a self-defense reaction aimed at eliminating injurious stimuli and restoring tissue integrity. However, inflammation may become a harmful process when it becomes chronic. Chronic activation of the inflammatory response in NDs produces proinflammatory cytokines, prostaglandins, and reac-
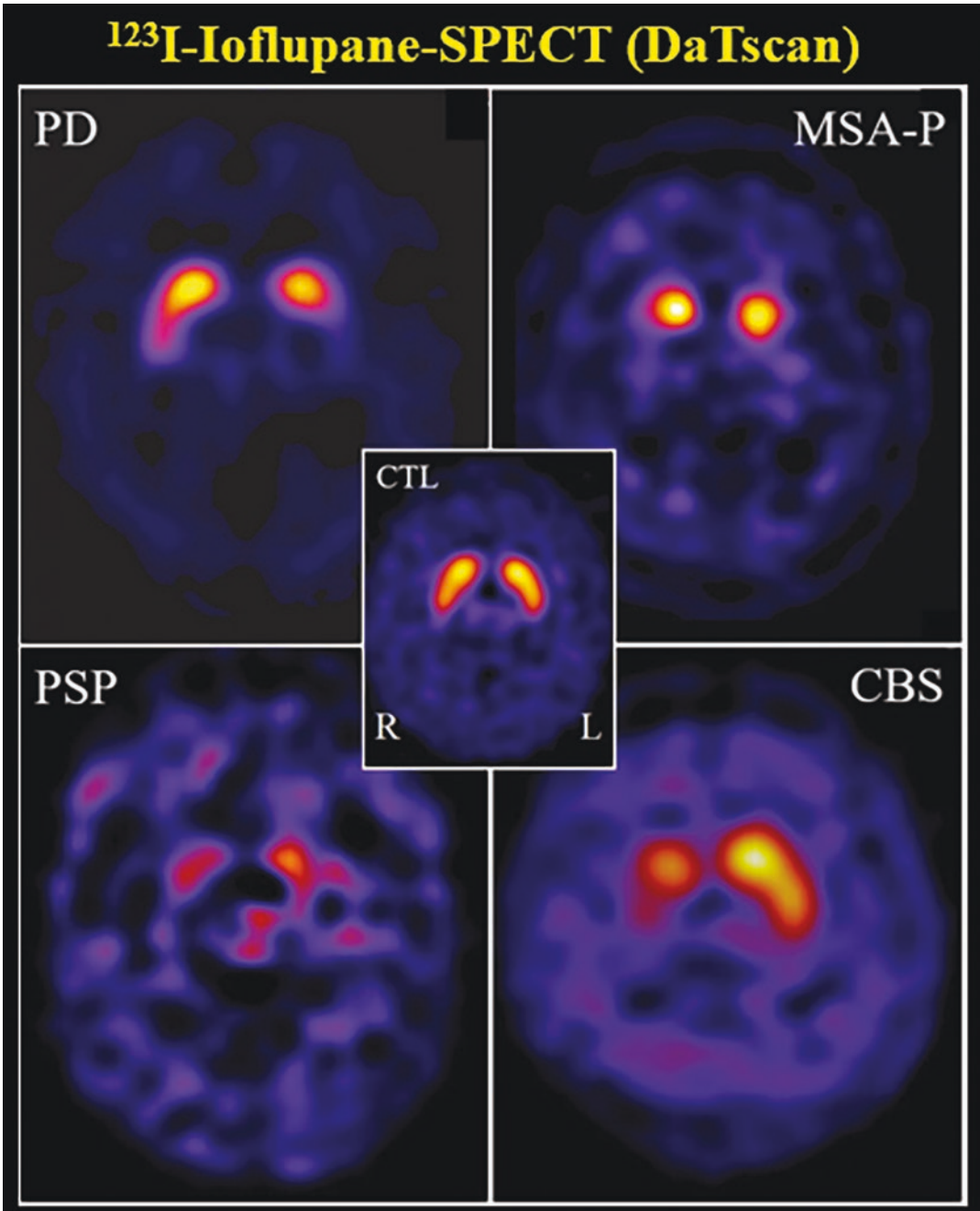
Fig. 15.26 Illustrative axial ^{123}I-FP-CIT (DaTscan) SPECT performed within 1 year of disease onset for neuropathologically-confirmed degenerative Parkinsonisms. A variable degree of presynaptic dopamine striatal uptake impairment is observed in PD, MSA-P, PSP, and CBS subjects in comparison to a control (CTL) subject (center image). In PD, we can observe a severe uptake reduction in the putamen (especially posterior part) and a relative asymmetry between left and right uptake, as this is the case for the CBS patient. Conversely, uptake impairment is more symmetrical for the MSA-P and PSP subjects and involves the whole striatum. (From Nicastro et al. [123])
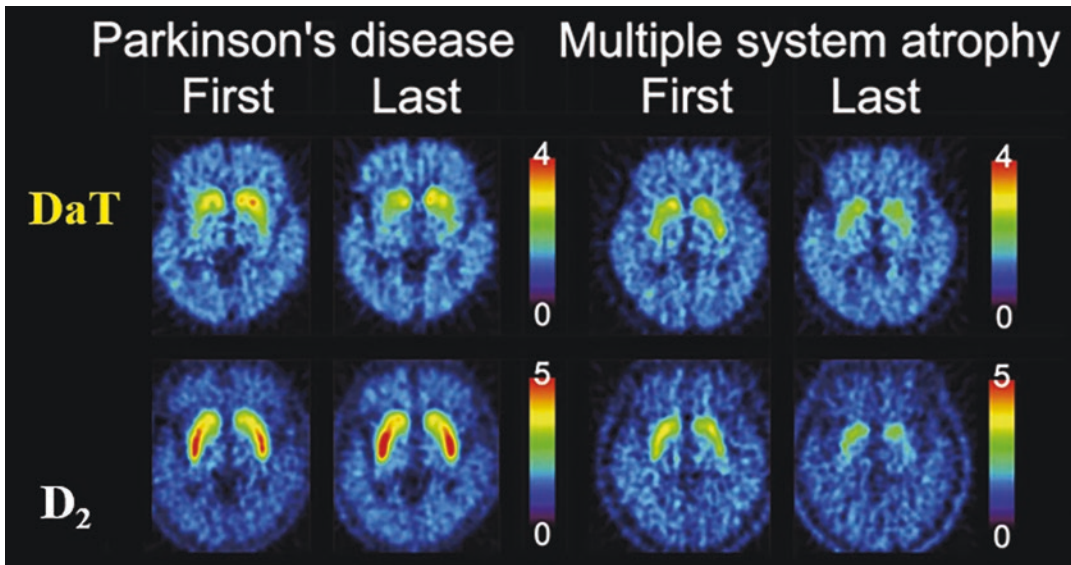
Fig. 15.27 DaT-PET with [^{11}C]CFT and dopamine D$_2$ receptor-PET with [^{11}C]raclopride. The rainbow scale represents the magnitude of uptake ratio index. The first and last images of DaT and D2 receptors in the patient with PD and MSA show that dopamine D2 receptor imaging can differentiate between PD and MSA. (From Ishibasi et al. [133])

tive oxygen species (ROS) that may induce neuronal dysfunction. Several studies have demonstrated a strong link between chronic inflammation and neurodegeneration. AD is characterized by the death of cells in the hippocampus and the frontal cortex secondary to chronic inflammation. In PD, chronic inflammation leads to loss of dopaminergic receptors in the substantia nigra. In amyotrophic lateral sclerosis (ALS) motor neurons are ultimately destroyed, while multiple sclerosis (MS) is an autoimmune disorder in which inflammatory cells attack the myelin sheath. Although activation of an acute inflammatory event is a necessary self-defense mechanism of the CNS against foreign antigens, prolonged activation of the inflammatory response can lead to chronic inflammation and cell death [138]. Despite widespread acceptance of the idea that inflammation contributes to NDs, it remains unclear at what stages of the disease inflammation is beneficial or detrimental.

The close inflammation–neurodegeneration relationship and the rising incidence of NDs have led to considerable interest in the detection and follow-up of neuroinflammation and in the monitoring of anti-inflammatory treatments. In addition, the generation of neuroinflammatory patterns of individual patients may help in stratifying patients for immunomodulatory therapies [137, 139]. To detect and monitor active neuroinflammation based on molecular imaging probes is a challenge. How well imaging can probe inflammation monitor response to anti-inflammatory response depends on the identification of an appropriate and specific molecular target as a biomarker for neuroinflammation.

15.3.7.1 Microglia and TSPO Binding Radiotracers

Microglia are the CNS-resident macrophages that are the critical convergence point for the many diverse triggers in orchestrating the activity of other immune cells in the brain. In the healthy adult brain, microglia appear as small, branched monocytic cells with little apparent activity and have long been considered quiescent. During neuroinflammation, in response to neuronal injury or even subtle perturbations of the CNS environment, microglia undergo drastic changes in their morphology, migrate towards the lesion

site, proliferate, and produce neurotoxic factors, such as proinflammatory cytokines and reactive oxygen species (ROS) [140].

A major hallmark of microglial activation is the expression of the translocator protein (TSPO), also known as the peripheral benzodiazepine receptor (PBR) [141]. TSPO expression is nearly absent in resting microglia but rapidly increases during inflammation. This increase in TSPO expression is correlated with the extent of microglial activation. This makes TSPO a biomarker and an attractive target for the imaging of cerebral inflammation. TSPO is an 18-kDa protein with five transmembrane domains. It is primarily situated at contact sites between inner and outer mitochondrial membranes and is part of the

mitochondrial permeability transition pore (MPTP). The best-characterized function of TSPO is the regulation of cholesterol translocation through mitochondrial membranes, which is the rate-determining step in steroid biosynthesis. Because TSPO is expressed on microglia and other immune cells, it also plays a role in immune regulation [142]. Some of the important PET radiotracers for imaging neuroinflammation are shown in Fig. 15.28.

Historically, (R)-[^{11}C]PK11195 is the first non-benzodiazepine and selective TSPO ligand with nanomolar binding affinity, and it is the prototypical reference for TSPO binding. Although PK11195-PET studies have provided numerous valuable insights on glial or macro-
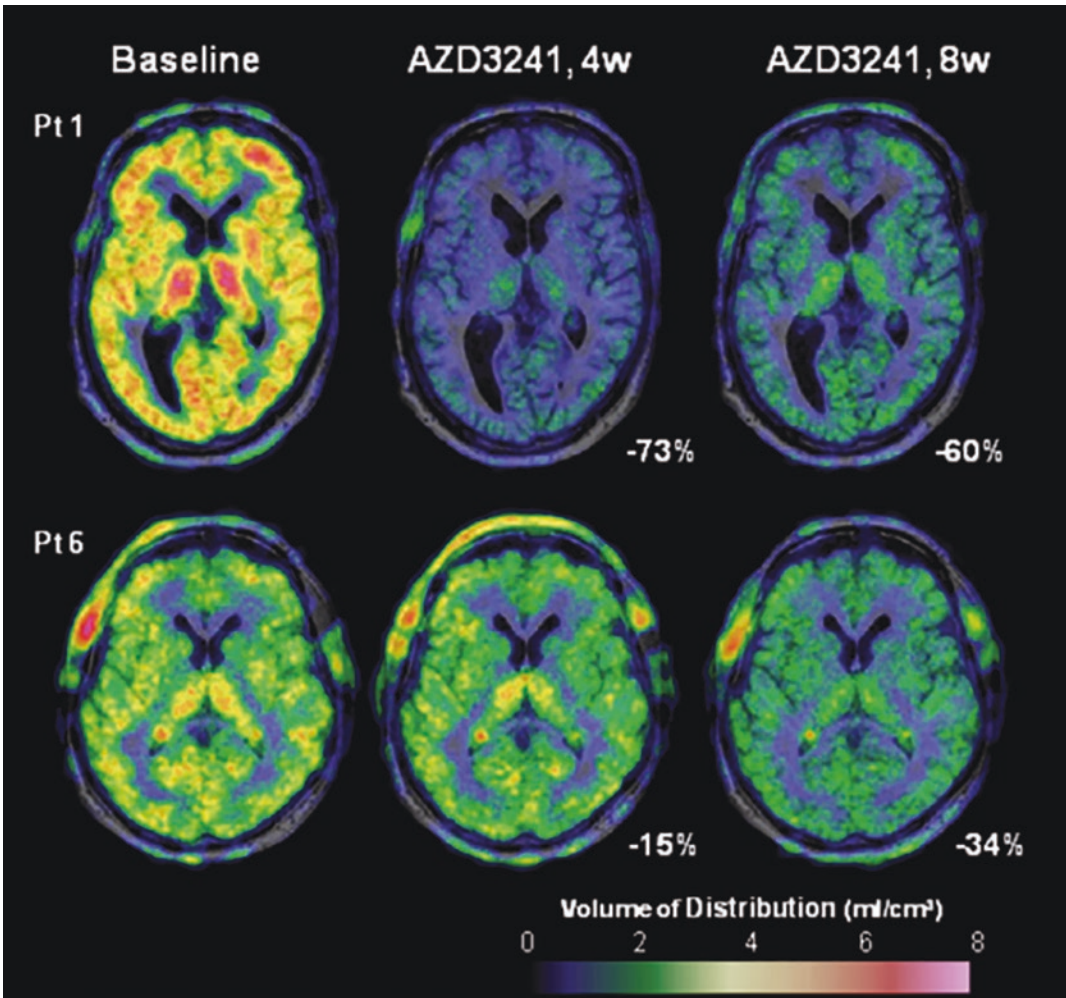

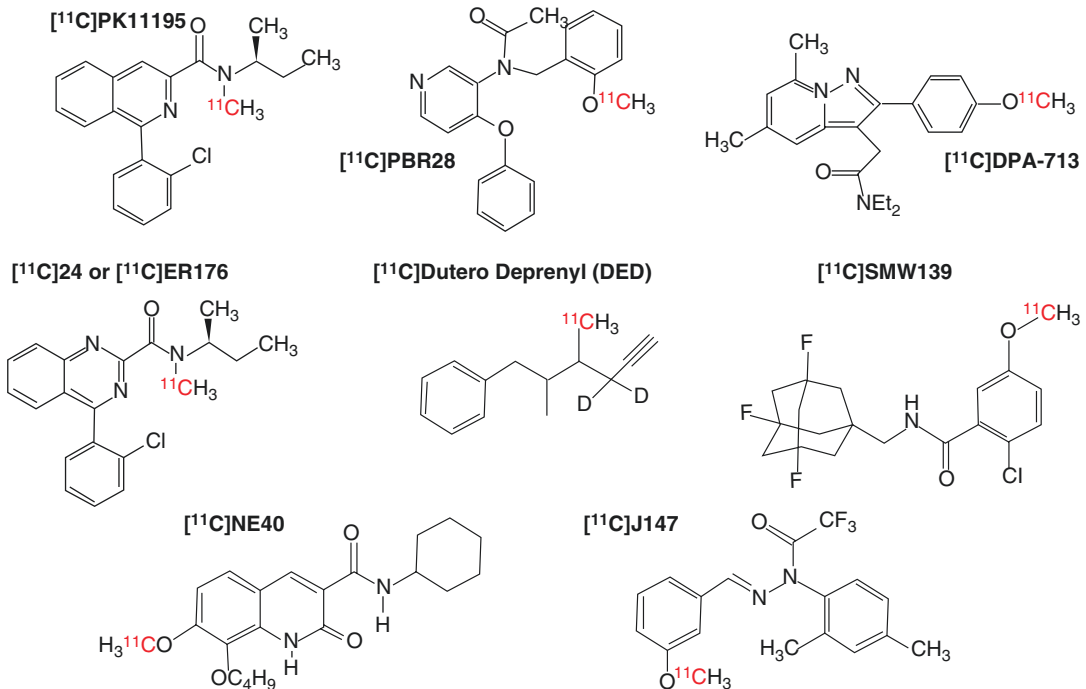**Fig. 15.28** Radiotracers for imaging neuroinflammation

Fig. 15.29 TSPO PET using [11C]PBR28-PET at baseline, at Weeks 4 and 8 after treatment with AZD3241. Changes in VT in percent are given for putamen; TSPO genotype: Patient 1 (Pt 1) = high affinity binder; Patient 2 (Pt 6) = mixed affinity binder. (From Jucaite et al. [145])

phage activation in different neurologic disorders, including dementia and stroke, its poor brain permeability and high plasma protein binding have limited its sensitivity, and overall clinical utility [137, 143, 144]. Among the second generation TSPO tracers, [11C]DPA-713 and [11C]PBR28 have been applied clinically in a range of neurologic disorders (Yoko Tura et al. 2017) [145]. [11C]PBR28-PET has been used to monitor immunomodulatory therapies in PD patients, wherein decreased binding of the radiotracer was found after treatment with myeloperoxidase inhibitor AZD3241 (Fig. 15.29) [145]. This provides proof-of-concept data that TSPO PET could be used for clinical therapy monitoring. An important limitation, however, regarding clinical application of second-generation tracers is their universal sensitivity to the rs6971 TSPO polymorphism, which results in high-, mixed-, and low-affinity binders [137]. Another important disadvantage of TSPO-PET studies is that TSPO is widely expressed throughout the brain and there is no

brain region with a complete lack of the protein, making the modeling of PET studies more complicated since there is no reference region [137].

Recent advances in TSPO PET, therefore, have focused on the development of third-generation tracers (Fig. 15.29) insensitive to the rs6971 polymorphism [146]. [11C]ER176, a quinazoline analog of PK11195, was identified as a promising candidate and is under clinical investigation. Some non-TPSO neuroinflammatory PET tracers, including [11C]NE40 targeting the cannabinoid type 2 receptor and [11C]-JNJ717 and [11C] SMW139 targeting the P2X7R receptor, are also presently under clinical investigation.

15.4 Epilepsy

Epilepsy is a disorder characterized by recurrent unprovoked seizures; it reflects underlying brain dysfunction that is variable and multifactorial [147]. MRI is the modality of choice for identification of morphologic and functional abnormali-

ties to complement the video EEG information. About 60–70% of patients experience focal or partial seizures and 30–40% generalized seizures [148]. Despite the wide range of treatments available for controlling seizures, approximately 20–30% of patients continue to have uncontrolled seizures. Functional imaging plays an important role in the care of patients with no structural lesions in the brain (nonlesional epilepsy), who make up 20–50% of patients with medically refractory epilepsy [147].

Epilepsy surgery is an effective technique for patients with intractable focal onset medically refractory epilepsy and has a reported success rate of 55–80% [147]. Postsurgical success depends on accurate presurgical localization of the epileptogenic focus. Accordingly, precise identification of the epileptogenic focus is vital for effective seizure control and minimization of morbidity associated with epilepsy surgery. The seizure-onset zone is the region in which the seizures actually originate, while the epileptogenic zone is a theoretical construct, which is defined in terms of different cortical zones [149].

In the 1980s, [18F]FDG-PET was used as a molecular imaging probe to image the epileptic focus (Fig. 15.30). It was soon recognized that focal *interictal* hypometabolism correlated with the localization of the epileptic focus, and the method was widely implemented in presurgical epilepsy evaluation [150]. In 1994, the FDA approved the first indication of FDG-PET for the identification of regions of abnormal glucose metabolism associated with foci of epileptic seizures. Subsequently, several PET and SPECT radiopharmaceuticals were evaluated to study the molecular mechanisms of epilepsy. Recent reviews discussed the advantages and limitations of different tracers used in molecular imaging of epilepsy [147, 151–154].

15.4.1 Blood Flow and Metabolism

Patients with complex partial seizures (epilepsy that leads to temporary impairment but, not loss of consciousness) may be referred for functional brain imaging studies to assess the ictal perfusion or interictal glucose metabolism. During the epileptic activity, a hyperperfusion of the seizure onset zone occurs because of an autoregulatory response to the local neuronal hyperactivity. When a SPECT blood flow tracer (^{99m}Tc-HMPAO or ^{99m}Tc-ECD) is injected intravenously immediately after the start of a seizure, the ictal SPECT images reflect the hyperperfusion changes in the early phase of the seizure. However, if the tracer is injected after the seizure is terminated, hypoperfusion in the seizure onset zone can be observed. Ictal-SPECT is the only imaging modality that can define the ictal onset zone in a reliable and consistent manner. Brain glucose metabolism, as a measure of neural activity, can be studied with FDG-PET, which identifies cerebral hypometabolism characterizing epileptogenic sites (Fig. 15.30). FDG-PET is useful for presurgical planning in most temporal lobe epilepsy (TLE) patients. However, different antiepileptic drugs have shown to affect the cerebral glucose metabolism to varying degrees, with phenobarbital being a greater depressant (up to 37%) than valproate, carbamazepine, or phenytoin [156].

The main limitation of interictal FDG-PET is that it cannot precisely define the surgical margin as the area of hypometabolism usually extends beyond the epileptogenic zone. Various neurotransmitters (GABA, glutamate, opiates, serotonin, dopamine, acetylcholine, and adenosine) and receptor subtypes are involved in epilepsy [157]. Since the late 1990s, the potential clinical utility of [11C]flumazenil PET in epilepsy has been investigated. This radioligand binds to the benzodiazepine site on the γ-aminobutyric acid (GABA$_A$) receptor complex and has shown promising results in the localization and lateralization of the epileptic focus [155, 158]. The area of abnormality on Flumazenil-PET is usually smaller and more circumscribed than the area of hypometabolism on FDG images (Fig. 15.30). Studies have demonstrated that ^{11}C-α-methyl-L-tryptophan PET, or [11C]AMT (to study synthesis of serotonin) can detect the epileptic focus within malformations of cortical development and helps in differentiating epileptogenic from non-epilep-
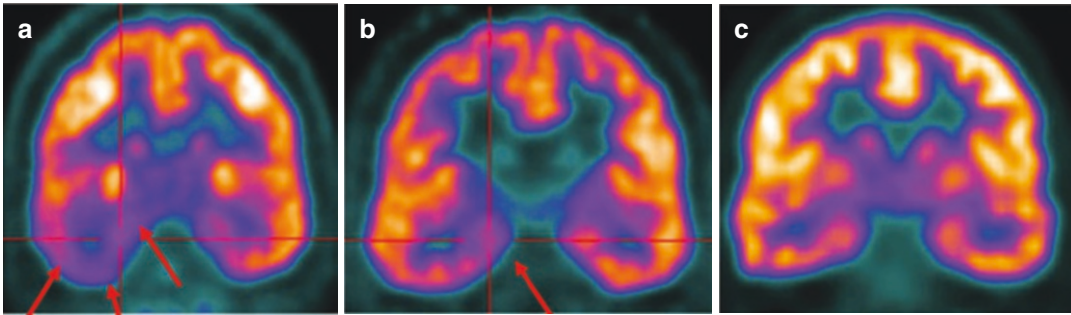
Fig. 15.30 Static [18F]FDG-PET and [18F]FMZ PET. Coronal images used for masked visual review. (**a**) FDG-PET image shows extensive hypometabolism throughout right temporal lobe (arrows). (**b**) 18F-FMZ (flumazenil) PET image shows more restricted localization to mesial temporal region in same patient (arrows). (**c**) Symmetric FMZ distribution in control subject. (From Vivash et al. [155])

togenic tubers in patients with tuberous sclerosis complex.

15.5 Neurooncology

Brain neoplasms include primary brain neoplasms which stem from the brain parenchyma and metastatic lesions originating from other primary malignancies outside of the brain (such as lung, breast, and skin). The most common types of primary brain tumors include glioma, which is the most lethal brain tumor, accounting for about 45% to 50% of total primary brain tumors, followed by meningiomas, the second commonest, and comprising nearly 15% of all the primary brain neoplasms. According to the WHO Classification of Tumors of the Central Nervous System (CNS) 2016, tumors are graded into four grades based on the histopathologic characteristics in which grade 1 represents benign features and grade 4 indicates the most malignant tumors [159]. Glioma is a tumor originating from glial cells of the brain. There are many types of glial cells and the tumors that arise from each type are named according to the cell type of origin (such as astrocytoma, oligodendroglioma and mixed glioma). Glioblastoma, on the other hand, is the most invasive primary brain tumor and the commonest primary brain tumor. Glioma may or may not be malignant while glioblastoma is malignant. Glioma has a better prognosis than glioblastoma. Treatment of glioblastoma is a challenge because tumor cells are resistant to routine treatments. Symptomatic treatment, surgery, radiotherapy, and chemotherapy may be administered with varying degrees of success. A meningioma is a tumor that grows from the meninges—the protective membranes that cover the brain and spinal cord. Most meningiomas are benign (not cancer) and slow growing; however, some can be malignant.

15.5.1 Imaging in Neuro-oncology

MRI with gadolinium contrast agent is used as the standard method of choice in the practice of brain tumors. Functional MR imaging (fMRI) using the Blood Oxygen Level Dependent (BOLD) technique provides functional map for each patient facilitates the surgical planning and averts the unsolicited collateral damage to vital brain regions during surgery and radiotherapy. In neuro-oncology, PET-imaging can be performed in several clinical indications [160]. In clinical neuro-oncology, [18F]-FDG is currently the most commonly used PET tracer and has been utilized mainly to differentiate the tumor recurrence from radiation-induced changes. Novel PET tracers can offer biologic information not imaged via [18F]-FDG PET. PET-imaging in brain tumors and in particular in gliomas can be indicated using several different radiopharmaceuticals (Table 15.6):

- At primary diagnosis: to differentiate grade III-IV gliomas from nonneoplastic lesions or grade I-II gliomas.
- To select the optimal biopsy site; to delineate tumor extent for surgery and radiotherapy; to aid in non-invasive grading of tumoral lesions.
- For diagnosis of tumor recurrence, differentiating it from treatment induced changes (such as pseudoprogression or radionecrosis).
- For disease and therapy monitoring, such as malignant transformation (of grade I–II gliomas), response assessment after chemotherapy and radiotherapy and to rule out pseudoresponse (especially when dealing with antiangiogenic drugs).

15.5.2   PET Radiotracers in Neuro-oncology

PET imaging is increasingly used to supplement MRI in the management of patient with brain tumors. Different PET radiotracers (Table 15.6) targeting different biological processes are used to accurately identify brain tumors and provide unique metabolic and biologic information. The main radiotracers implemented in clinical practice include [18F]FDG and radiolabeled amino acids ([11C]MET, [18F]FET, and [18F]FDOPA) targeting glucose metabolism and L-amino-acid transport

system. respectively. In addition, several radiotracers for cell proliferation ([18F]FLT), membrane synthesis ([11C]CH and [18F]FCH) have also been evaluated. Recent reviews described the advantages and limitations of different PET radiotracers evaluated in neuro-oncology [161–166].

[18F]FDG is a well-established and the most widely used tracer for PET imaging. An increased FDG uptake corresponds to increased glucose metabolism. [18F]FDG remains useful for intensely hypermetabolic brain lesions such as PCNSL, glioblastoma, and some metastases. However, the physiological high FDG uptake in the normal brain, limits the lesion-to-background contrast for brain tumors. Amino acid PET tracers have the advantage over FDG in that they do not accumulate too much in the normal brain. [11C]MET has been the first developed tracer in this field. Because of the short half-life of 11C (20 min) its availability is limited to centers with in-house cyclotron. [18F]FDOPA and [18F]FET are the most often used tracers and their uptake in brain tumors relies on the overexpression of large amino acid transporters of the L-type (LAT) [161].

[18F]FDOPA PET has a good accuracy for the diagnosis of primary brain tumors, with a sensitivity of 96% and a specificity of 86%. It is more specific than [18F]FDG [19] and performs as well as [11C]MET [163, 166]. It can also be used to

Table 15.6 PET radiopharmaceuticals in neurooncology

| Radiopharmaceuticals	Target/mechanism	
2-[18F]fluoro-2-deoxy-D-glucose ([18F]FDG)	*Glucose transporters and Hexokinase*	Glioma, primary CNS lymphoma, brain metastases
L-[methyl-11C]Methionine ([11C]MET)	Amino acid transporters L-type	Glioma Meningioma Brain metastases
O-(2-[18F]fluoroethyl)-L-tyrosine ([18F]FET)		
[18F]Fluciclovine (Axumin)		
3,4-dihydroxy-6-[18F]fluoro-L-phenylalanine ([18F]FDOPA)	*Aromatic amino acid decarboxylase (AAAD)*	
[11C]Choline ([11C]CH	Cell membrane synthesis	Glioma
[18F]Fluorocholine ([18F]FCH		
[18F]Fluorothymidine ([18F]FLT)	DNA synthesis	Glioma
[18F]Fluoromisonidazole ([18F]FMISO		
68Ga-DOTA-D-Phe-Tyr3-octreotate (DOTATATE)	Somatostatin receptor Type-2 (SSTR2)	Meningioma
68Ga-DOTA-Tyr3-octreotide (DOTATOC)		
68Ga-PSMA-11	Prostate specific membrane antigen	Residual or recurrent glioblastoma
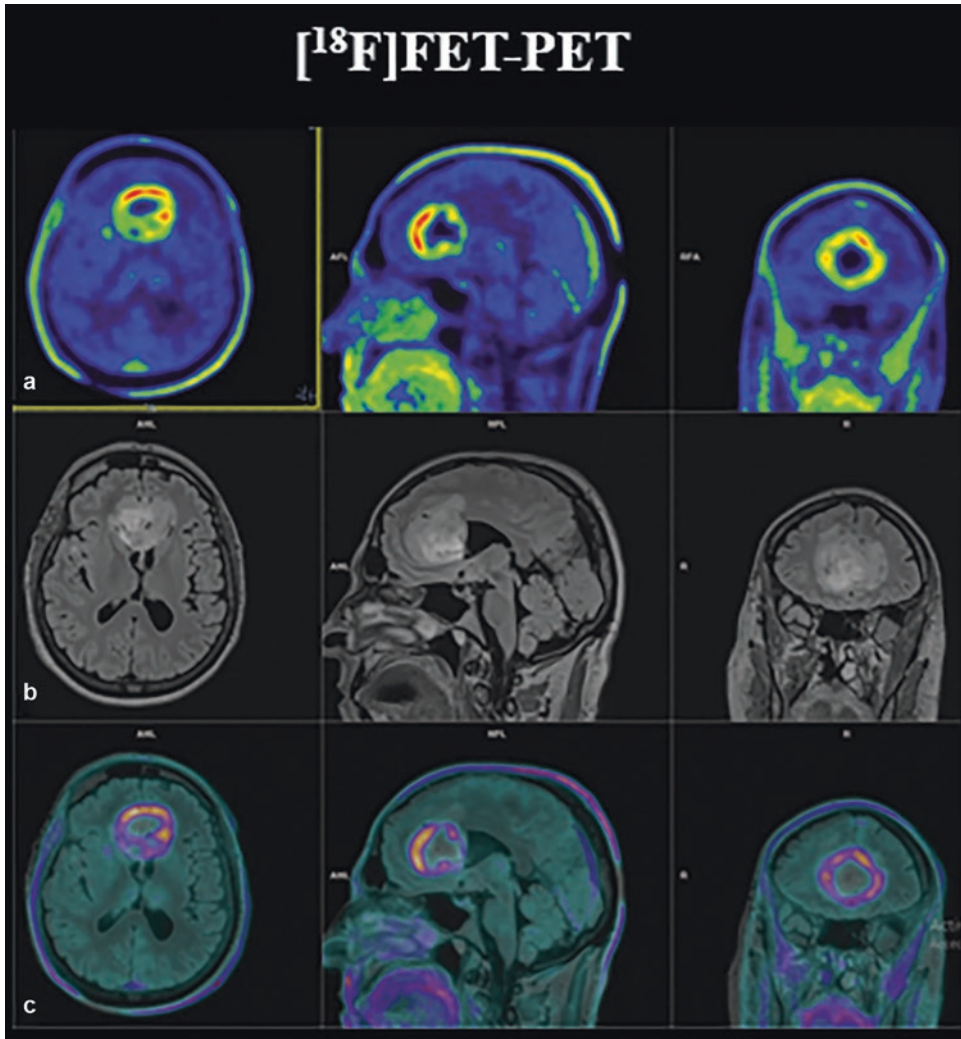
Fig. 15.31 Comparison of ^{18}F-FET PET and T2 (FLAIR) MRIs in a patient with high grade glioma. (**a**) ^{18}F-FET PET/CT shows metabolically active bifrontal tumor mass. (**b**) MRI shows T2 FLAIR-hyperintense tumor and perifocal edema. (**c**) MRI and ^{18}F-FET PET/CT image fusion reveal complementary information with inconsistent overlap of hypersignal in T2 and ^{18}F-FET uptake. (From Dissaux et al. [167])

differentiate high- and low-grade gliomas as the uptake is significantly higher in high-grade gliomas. A recent meta-analysis found a pooled sensitivity of 0.88 and a pooled specificity and 0.73 for glioma grading, making it a valuable clinical tool.

[^{18}F]FET-PET (Fig. 15.31) provides important diagnostic data concerning brain tumor delineation, therapy planning, treatment monitoring, and improved differentiation between treatment-related changes and tumor recurrence [164]. The accumulation of [^{18}F]FET in most benign lesions and healthy brain tissue has been shown to be low, thus providing a high contrast between tumor tissue and benign tissue alterations. Based on logistic advantages of F-18 labeling and convincing clinical results, [^{18}F]FET has widely replaced [^{11}C]MET.

A systematic review and metaanalysis including 39 studies based on several PET tracers for distinguishing tumor progression from treatment-related changes in high-grade glioma patients

concluded that PET can reliably differentiate tumor progression from treatment-related changes, with the highest diagnostic accuracy being reached among amino-acid tracers. Both [^{18}F]FET and [^{11}C]MET showed a comparably higher sensitivity than FDG [161].

Meningioma is the most common non-glial primary brain tumor, which represents approximately 35% of all brain tumors. A high SSTR type 2 density is found in all meningioma [166]. [^{68}Ga]Ga-SSTR PET tracers are an effective tool for imaging meningioma because there is no physiological uptake in the brain except for the pituitary gland. As a result, SSTR-PET provides a high tumor-to-background ratio. In a series of 21 meningioma patients, who underwent amino acid PET and PET with SSTR ligands, every tumor showed high SSTR ligand uptake while two meningiomas remained [^{18}F]FET-negative [165].

In the era of precision and personalized medicine, molecular imaging with PET can be of great value in the clinical management of primary and secondary brain tumors. The existing literature provides strong evidence that PET can efficiently supplement MRI in specific settings such as distinguishing recurrence from treatment related changes (TRC) in glioma and brain metastases. In addition to [^{18}F]FDG, [^{18}F]FDOPA, [^{18}F]FET, and ^{68}Ga-SSTR, ligands will continue to play a major role in the management of patients in neuro-oncology.

References

1. Barnes NM, Sharp T. A review of central 5-HT receptors and their function. Neuropharmacology. 1999;38:1083–152.
2. Kadir A, Nordberg A. Target-specific PET probes for neurodegenerative disorders related to dementia. J Nucl Med. 2010;51:1418–30.
3. Palop JJ, Chin J, Mucke L. A network dysfunction perspective on neurodegenerative diseases. Nature. 2006;443:768–73.
4. Skovronsky DM, Lee VMY, Trojanowski JQ, et al. Neurodegenerative diseases: new concepts of pathogenesis and their therapeutic implications. Annu Rev Pathol Mech Dis. 2006;1:151–70.
5. Kovacs GG, Budka H. Current concepts of neuropathological diagnostics in practice: neurodegenerative diseases. Clin Neuropathol. 2010;29(5):271–88.
6. Bredesen DE, Rao RV, Mehlen P. Cell death in the nervous system. Nature. 2006;443(7113):796–802.
7. Drzezga A. Basic pathologies of neurodegenerative dementias and their relevance for state-of-the-art molecular imaging studies. Eur J Nucl Med Mol Imaging. 2008;35:S4–S11.
8. Alzheimer A. Über eine eigenartige Erkrankung der Hirnrinde [About a peculiar disease of the cerebral cortex]. Allgemeine Zeitschrift fur Psychiatrie und Psychisch-Gerichtlich Medizin. 1907;64:146–8.
9. Petersen RC, Smith GE, Waring SC, et al. Mild cognitive impairment: clinical characterization and outcome. Arch Neurol. 1999;56:303–8.
10. Grundman M, Petersen RC, Ferris SH, et al. Mild cognitive impairment can be distinguished from Alzheimer disease and normal aging for clinical trials. Arch Neurol. 2004;61:59–66.
11. NIH PN 08-3792. National Institute on Aging (NIA) and National Institutes of Health (NIH): Alzheimer's disease: unraveling the mystery. NIH Publication Number 08-3792, September 2008. 2008.
12. Cairns RJ. Alzheimer's disease: neurodegeneration. In: Hof PR, Mobs CV, editors. Handbook of the neuroscience of aging. New York: Elsevier; 2009. p. 275–81.
13. Forman MS, Mufson EJ, Leurgans S, et al. Cortical biochemistry in MCI and Alzheimer disease: lack of correlation with clinical diagnosis. Neurology. 2007;68:757–63.
14. Mathis CA, Loprestia BJ, Klunk WE. Impact of amyloid imaging on drug development in Alzheimer's disease. Nucl Med Biol. 2007;34:809–22.
15. Hardy J, Selkoe DJ. The amyloid hypothesis of Alzheimer's disease: progress and problems on the road to therapeutics. Science. 2002;297:353–6.
16. Goedert M. Tau protein and the neurofibrillary pathology of Alzheimer's disease. Trends Neurosci. 1993;16:460–5.
17. Kolarova M, Garcia-Sierra F, Bartos A, et al. Structure and pathology of tau protein in Alzheimer disease. Int J Alzheimers Dis. 2012;2012:731526.
18. Braak H, Braak E. Evolution of neuronal changes in the course of Alzheimer's disease. J Neural Transm Suppl. 1998;53:127–40.
19. Villemagne VL, Furumoto S, Fodero-Tavoletti M, et al. The challenges of tau imaging. Fut Neurol. 2012;7(4):409–21.
20. Duyckaerts C, Brion JP, Hauw JJ, Flament-Durand J. Quantitative assessment of the density of neurofibrillary tangles and senile plaques in senile dementia of the Alzheimer type: comparison of immunocytochemistry with a specific antibody and Bodian's protargol method. Acta Neuropathol. 1987;73:167–70.
21. Uzuegbunam C, Librizzi D, Yousefi BH. PET radiopharmaceuticals for Alzheimer's disease and

Parkinson's disease diagnosis, the current and future landscape bright. Molecules. 2020;25:977. https://doi.org/10.3390/molecules25040977.

22. Seibyl JP. Single-photon emission computed tomography and positron emission tomography evaluations of patients with central motor disorders. Semin Nucl Med. 2008;38:274–86.

23. Fearnley JM, Lees AJ. Ageing and Parkinson's disease: substantia nigra regional selectivity. Brain. 1991;114:2283–301.

24. Hornykiewicz O. Basic research on dopamine in Parkinson's disease and the discovery of the nigrostriatal dopamine pathway: the view of an eyewitness. Neurodegener Dis. 2008;5:114–7.

25. Heiss WD, Herholz K. Brain receptor imaging. J Nucl Med. 2006;47:302–12.

26. Bega D, Kuo PH, Chalkidou A, et al. Clinical utility of DaTscan in patients with suspected Parkinsonian syndrome: a systematic review and meta-analysis. NPJ Parkinson's Dis. 2021;7:43. https://doi.org/10.1038/s41531-021-00185-8.

27. Benamer TS, et al. Accurate differentiation of parkinsonism and essential tremor using visual assessment of [123I]-FP-CIT SPECT imaging: the [123I]-FP-CIT study group. Mov Disord. 2000;15:503–10.

28. Park KB, Kitteringham NR, O'Neill PM. Metabolism of fluorine-containing drugs. Annu Rev Pharmacol Toxicol. 2001;41:443–70.

29. Waterhouse RN. Determination of lipophilicity and its use as a predictor of blood–brain barrier penetration of molecular imaging agents. Mol Imaging Biol. 2003;5:376–89.

30. Vallabhajosula S, Vallabhajosula B, Solnes L. Radiopharmaceuticals for molecular imaging of neurodegenerative diseases. In: Saba L, editor. Imaging in neurodegenerative disorders. Oxford: Oxford University Press; 2015. p. 151–7.

31. Cecchin D, Garibotto V, Law I, Goffin K. PET imaging in neurodegeneration and neuro-oncology: variants and pitfalls. Semin Nucl Med. 2021;51(5):408–18.

32. Dupont A-C, Largeau B, Guilloteau D, et al. The place of PET to assess new therapeutic effectiveness in neurodegenerative diseases. Contrast Media Mol Imaging. 2018;2018:7043578.

33. Villemagne VL, Barkhof F, Garibotto V, et al. Molecular imaging approaches in dementia. Radiology. 2021;298:517–30.

34. Zimmer L, Luxen A. PET radiotracers for molecular imaging in the brain: past, present and future. Neuroimage. 2012;61:363–70.

35. Vallabhajosula S. Positron emission tomography radiopharmaceuticals for imaging brain Beta-amyloid. Semin Nucl Med. 2011;41(4):283–99.

36. Herscovitch P, Markham J, Raichle ME. Brain blood flow measured with intravenous [15O] water, I: theory and error analysis. J Nucl Med. 1983;24:782–9.

37. Raichle ME, Martin WRW, Herscovitch P, et al. Brain blood flow measured with intravenous H₂¹⁵O. II. Implementation and validation. J Nucl Med. 1983;24:790–8.

38. Meltzer CC, Cantwell MN, Greer PJ, et al. Does cerebral blood flow decline in healthy aging? A PET study with partial volume correction. J Nucl Med. 2000;41:1842–8.

39. Druckenbrod RW, Williams CC, Gelfand MJ. Iofetamine hydrochloride I 123: a new radiopharmaceutical for cerebral perfusion imaging. DICP. 1989;23:19–24.

40. Jacquier-Sarlin MR, Polla BS, Slosman DO. Oxidoreductive state: the major determinant for cellular retention of ⁹⁹ᵐTc-HMPAO. J Nucl Med. 1996a;37:1413–6.

41. Jacquier-Sarlin MR, Polla BS, Slosman DO. Cellular basis of ECD brain retention. J Nucl Med. 1996b;37:1694–7.

42. Matsuda H. Role of neuroimaging in Alzheimer's disease, with emphasis on brain perfusion SPECT. J Nucl Med. 2007;48:1289–300.

43. Catafau AM. Brain SPECT in clinical practice. Part I: perfusion. J Nucl. 2001;42:259–71.

44. Ferrando R, Damian A. Brain SPECT as a biomarker of neurodegeneration in dementia in the era of molecular imaging: still a valid option? Front Neurol. 2021;12:629442.

45. Frackowiak RS, Lenzi GL, Jones T, et al. Quantitative measurement of regional cerebral blood flow and oxygen metabolism in man ¹⁵O and positron emission tomography: theory, procedure and normal values. J Comput Assist Tomogr. 1980;4:727–36.

46. Jones T, Chesler DA, Ter-Pogossian MM, et al. The continuous inhalation of oxygen-15 for assessing regional oxygen extraction in the brain of man. Br J Radiol. 1976;49:339–43.

47. Ter-Pogossian MM, Eichling JO, Davis DO, et al. The determination of regional cerebral blood flow by means of water labeled with radioactive oxygen-15. J Clin Invest. 1969;93:31–40.

48. Mazziotta JC, Phelps ME, Miller J. Tomographic mapping of human cerebral metabolism. Neurology. 1981;31:503–15.

49. Siesjo BK. Brain energy metabolism. New York: Wiley; 1978. p. 101–10.

50. Sokoloff L, Reivich M, Kennedy C, et al. The [14C] deoxyglucose method for the measurement of local cerebral glucose utilization: theory, procedure, and normal values in the conscious and anesthetized albino rat. J Neurochem. 1977;28:897–916.

51. Phelps ME, Huang SC, Hoffman EJ, et al. Tomographic measurement of local cerebral glucose metabolic rate in human with [18F]2-fluoro-2-deoxyglucose. Validation of method. Ann Neurol. 1979;6:371–88.

52. Huisman MC, van Golen LW, Hoetjes NJ. Cerebral blood flow and glucose metabolism in healthy volunteers measured using a high-resolution PET scanner. EJNMMI Res. 2012;2:63.

53. Schmidt KC, Lucignani G, Sokoloff L. Fluorine-18-fluorodeoxyglucose PET to determine regional cerebral glucose utilization: a re-examination. J Nucl Med. 1996;37:394–9.

54. Guedj E, Varrone A, Boellaard R, et al. EANM procedure guidelines for brain PET imaging using [18F] FDG, version 3. EJNMMI. 2022;49:632–51.

55. Jacobs AH, Winkler A, Castro MG, et al. Human gene therapy and imaging in neurological diseases. Eur J Nucl Med Mol Imaging. 2005;32:S358–83.

56. Bohnen NI, Djang DSW, Herholz K, et al. Effectiveness and safety of 18F-FDG PET in the evaluation of dementia: A review of the recent literature. J Nucl Med. 2012;53:59–71.

57. Silverman DHS. Brain 18F-FDG PET in the diagnosis of neurodegenerative dementias: comparison with perfusion SPECT and with clinical evaluations lacking nuclear imaging. J Nucl Med. 2004;45:594–607.

58. Silverman DHS, Mosconi L, Ercoli L, et al. Positron emission tomography scans obtained for the evaluation of cognitive dysfunction. Semin Nucl Med. 2008;38:251–61.

59. Mosconi L, Tsui WH, Herholz K, et al. Multicenter standardized 18F-FDG PET diagnosis of mild cognitive impairment, Alzheimer's disease, and other dementias. J Nucl Med. 2008;49:390.

60. Brooks DJ. Imaging approaches to Parkinson disease. J Nucl Med. 2010;51:596–609.

61. Lotan E, Friedman KP, Davidson T, Shepherd TM. Brain 18F-FDG-PET: utility in the diagnosis of dementia and epilepsy. IMAJ. 2020;22:178–84.

62. Filippi L, Chiaravalloti A, Bagni O, Schillaci O. 18F-labeled radiopharmaceuticals for the molecular neuroimaging of amyloid plaques in Alzheimer's disease. Am J Nucl Med Mol Imaging. 2018;8(4):268–81.

63. Kumar AP, Singh N, Nair D, Justin A. Neuronal PET tracers for Alzheimer's disease. Biochem Biophys Res Commun. 2022;587:58e62.

64. Price JL. Diagnostic criteria for Alzheimer's disease. Neurobiol Aging. 1997;18:S67–70.

65. Dickson DW. The pathogenesis of senile plaques. J Neuropathol Exp Neurol. 1997;56:321–39.

66. Wang J, Dickson DW, Trojanowski JQ, et al. The levels of soluble versus insoluble brain Aβ distinguish Alzheimer's disease from normal and pathologic aging. Exp Neurol. 1999;158:328–37.

67. Barrio JR, Huang S-C, Cole G, et al. PET imaging of tangles and plaques in Alzheimer's disease with a highly hydrophobic probe. J Label Compd Radiopharm. 1999;42:S194.

68. Agdeppa ED, Kepe V, Liu J, et al. Binding characteristics of radiofluorinated 6-dialkyl-amino-2-naphtylethylidene derivatives as positron emission tomography imaging probes for β-amyloid plaques in Alzheimer's disease. J Neurosci. 2001;21:1–5.

69. Klunk WE, Wang Y, Huang G-F, et al. Uncharged thioflavin-T derivatives bind to amyloid-beta protein with high affinity and readily enter the brain. Life Sci. 2001;69:1471–84.

70. Mathis CA, Bacskai BJ, Kajdasz ST, et al. A lipophilic thioflavin-T derivative for positron emission tomography (PET) imaging of amyloid in brain. Bioorg Med Chem Lett. 2002;12:295–8.

71. Klunk WE, Mathis CA. The future of amyloid-beta imaging: a tale of radionuclides and tracer proliferation. Curr Opin Neurol. 2008;21:683–7.

72. Mathis CA, Ikonomovicb MD, Debnath ML, et al. Comparison of the binding of 3′-F-PiB and PiB in human brain homogenates. Neuroimage. 2008;41(s2):T113–4.

73. Kung M-P, Hou C, Zhuang Z-P, et al. Binding of two potential imaging agents targeting amyloid plaques in postmortem brain tissues of patients with Alzheimer's disease. Brain Res. 2004;1025:98–105.

74. Verhoeff NP, Wilson AA, Takeshita S, et al. In-vivo imaging of Alzheimer disease beta-amyloid with [11C]SB-13 PET. Am J Geriatr Psychiatry. 2004;12:584–95.

75. Zhang W, Kung MP, Oya S, et al. 18F-labelled styrylpyridines as PET agents for amyloid plaque imaging. Nucl Med Biol. 2007;34:89–97.

76. Stephenson KA, Chandra R, Zhuang ZP, et al. Fluoro-pegylated (FPEG): imaging agents targeting Aβ aggregates. Bioconjug Chem. 2007;18:238–46.

77. Zhang W, Oya S, Kung MP, et al. F-18 stilbenes as PET imaging agents for detecting beta-amyloid plaques in the brain. J Med Chem. 2005;48:5980–8.

78. O'Keefe GJ, Saunder TH, Ng S, et al. Radiation Dosimetry of {beta}-Amyloid Tracers 11C-PiB and 18F-BAY94–9172. J Nucl Med. 2009;50:309–15.

79. Rowe CC, Ackerman U, Browne W, et al. Imaging of amyloid β in Alzheimer's disease with 18F-BAY94-9172, a novel PET tracer: proof of mechanism. Lancet Neurol. 2008;7:129–35.

80. Choi SR, Golding G, Zhuang Z, et al. Preclinical properties of 18F-AV-45: a PET agent for Aβ plaques in the brain. J Nucl Med. 2009;50:1887–94.

81. Johnson AE, Jeppsson F, Sandell J, et al. AZD2184: a radioligand for sensitive detection of betaamyloid deposits. J Neurochem. 2009;108:1177–86.

82. Juréus A, Swahn BM, Sandell J, et al. Characterization of AZD4694, a novel fluorinated A beta plaque neuroimaging PET radioligand. J Neurochem. 2010;114:784–94.

83. Cselényi Z, Jönhagen ME, Forsberg A, et al. Clinical validation of 18F-AZD4694, an amyloid-β-specific PET radioligand. J Nucl Med. 2012;53:415–24.

84. Therriault J, Benedet AL, Pascoal TA, et al. Determining Amyloid-β positivity using 18F-AZD4694 PET imaging. J Nucl Med. 2021;62:247–52.

85. Yousefi BH, Drzezga A, von Reutern B, et al. A novel (18)F-labeled Imidazo2,1-bbenzothiazole (IBT) for high-contrast PET imaging of β-Amyloid plaques. ACS Med Chem Lett. 2011;2:673–7.

86. Yousefi BH, Manook A, Grimmer T, et al. Characterization and first human investigation of FIBT, a novel fluorinated Aβ plaque neuro-

imaging PET radioligand. ACS Chem Nerosci. 2015;6:428–37.

87. Grimmer T, Shi K, Diehl-Schmid J, et al. 18F-FIBT may expand PET for β-amyloid imaging in neurodegenerative diseases. Mol Psychiatry. 2020;25:2608–19.

88. Clark CM, Pontecorvo MJ, Beach TG, et al. Cerebral PET with florbetapir compared with neuropathology at autopsy for detection of neuritic amyloid-beta plaques: a prospective cohort study. Lancet Neurol. 2012;11:669–78.

89. Rowe CC, Villemagne VL. Amyloid imaging with PET in early Alzheimer disease diagnosis. Med Clin N Am. 2013;97:377–98.

90. Laforce R Jr, Rabinovici GD. Amyloid imaging in the differential diagnosis of dementia: review and potential clinical applications. Alzheimers Res Therapy. 2011;3:31.

91. Maccioni RB, Farías G, Morales I, Navarrete L. The revitalized tau hypothesis on Alzheimer's disease. Arch Med Res. 2010;41:226–31.

92. Betthauser TJ. AD molecular: Imaging tau aggregates with positron emissions tomography. Prog Mol Biol Transl Sci. 2019;165:107–38.

93. Friedhoff P, von Bergen M, Mandelkow E-M, Mandelkow E. Structure of tau protein and assembly into paired helical filaments. Biochim Biophys Acta. 2000;1502(1):122–32.

94. Tian M, Civelek AC, Carrio I, et al. International consensus on the use of tau PET imaging agent 18F-fortaucipir in Alzheimer's disease. EJNMMI. 2022;49:895–904.

95. Wang YT, Edison P. Tau imaging in neurodegenerative diseases using positron emission tomography. Curr Neurol Neurosci Rep. 2019;19:45.

96. Hammes J, Bischof GN, Bohn KP, et al. One-Stop Shop: 18F-Flortaucipir PET differentiates amyloid-positive and -negative forms of neurodegenerative diseases. J Nucl Med. 2021;62:240–6.

97. Xia C-F, Arteaga J, Chen G. (18)FT807, a novel tau positron emission tomography imaging agent for Alzheimer's disease. Alzheimers Dement. 2013;9:666–76.

98. Zhang W, Arteaga J, Cashion DK, et al. A highly selective and specific PET tracer for imaging of tau pathologies. J Alzheimers Dis. 2012;31:601–12.

99. Mintun M, Schwarz A, Joshi A, et al. Exploratory analyses of regional human brain distribution of the PET tau tracer F18-labeled T807 (AV-1541) in subjects with normal cognitive function or cognitive impairment thought to be due to Alzheimer's disease. Alzheimers Dement. 2013;9:P842.

100. Betthauser TJ, Cody KA, Zammit MD, et al. In vivo characterization and quantification of neurofibrillary tau PET radioligand 18F-MK-6240 in humans from Alzheimer disease dementia to young controls. J Nucl Med. 2019;60:93–9.

101. Fodero-Tavoletti MT, Okamura N, Furumoto S, et al. 18F-THK523: a novel *in vivo* tau imaging ligand for Alzheimer's disease. Brain. 2011;134:1089–100.

102. Harada R, Okamura N, Furumoto S, et al. 18F-THK5351: a novel PET radiotracer for imaging neurofibrillary pathology in Alzheimer disease. J Nucl Med. 2016;57:208–14.

103. Harada R, Ishiki A, Kai H, et al. Correlations of 18F-THK5351 PET with postmortem burden of Tau and Astrogliosis in Alzheimer disease. J Nucl Med. 2018;59:671–4.

104. Hostetler ED, Walji AM, Zeng Z. Preclinical characterization of 18F-MK-6240, a promising PET tracer for in vivo quantification of human neurofibrillary tangles. J Nucl Med. 2016;57:1599–606.

105. Gogola A, Minhas DS, Villemagne VL, et al. Direct comparison of the Tau PET tracers 18F-Flortaucipir and 18F-MK-6240 in human subjects. J Nucl Med. 2022;63:108–16.

106. Garnett ES, Nahmias C, Firnau G. Central dopaminergic pathways in hemiparkinsonism examined by positron emission tomography. Can J Neurol Sci. 1984;11:174–9.

107. Firnau G, Sood S, Chirakal R, et al. Metabolites of 6-[18F] fluoro-L-dopa in human blood. J Nucl Med. 1988;29:363–9.

108. Riss PJ, Stockhofe K, Roesch F. Tropane-derived 11C-labelled and 18F-labelled DAT ligands. J Label Compd Radiopharm. 2013;56:149–58.

109. Kung MP, Stevenson DA, Plossl K, et al. [99mTc] TRODAT-1: a novel technetium-99 m complex as a dopamine transporter imaging agent. Eur J Nucl Med. 1997;24:372–80.

110. Wimalasena K. Vesicular monoamine transporters: structure-function, pharmacology, and medicinal chemistry. Med Res Rev. 2011;31(4):483–519.

111. Frey KA, Koeppe RA, Kilbourn MR, et al. Presynaptic monoaminergic vesicles in Parkinson's disease and normal aging. Ann Neurol. 1996;40:873–84.

112. Kilbourn MR. PET radioligands for the vesicular transporters for monoamines and acetylcholine. J Label Compd Radiopharm. 2013;56:167–71.

113. Koeppe RA, Gilman S, Junck L, Wernette K, Frey KA. Differentiating Alzheimer's disease from dementia with Lewy bodies and Parkinson's disease with (1)-[11C]dihydrotetra-benazine positron emission tomography. Alzheimers Dement. 2008;4(s1):S67–76.

114. Kung MP, Hou C, Goswami R, et al. Characterization of optically resolved 9-fluoropropyl-dihydrotetra-benazine as a potential PET imaging agent targeting vesicular monoamine transporters. Nucl Med Biol. 2007;34:239–46.

115. Farde L, Ehrin E, Eriksson L, et al. Substituted benzamides as ligands for visualization of dopamine receptor binding in the human brain by positron emission tomography. Proc Natl Acad Sci U S A. 1985;82:3863–7.

116. Volkow ND, Fowler JS, Gatley SJ, et al. PET evaluation of dopamine system of the human brain. J Nucl Med. 1996;37:1242–56.

117. Vallabhajosula S, Hirschowitz J, Machac J. Effect of haloperidol dose on I-IBZM brain SPECT imaging in schizophrenic patients. J Nucl Med. 1997;38:203–7.

118. Mukherjee J, Kang ZY, Brown T, et al. Preliminary assessment of extrastriatal dopamine D2 receptor binding in the rodent and nonhuman primate brains using the high affinity radioligand, ^{18}F-fallypride. Nucl Med Biol. 1999;26:519–27.

119. Halldin C, Farde L, Hogberg T, et al. Carbon-11-FLB 457: a radioligand for extra-striatal D_2 dopamine receptors. J Nucl Med. 1995;36:1275–81.

120. Dickson DW. (2018) Neuropathology of Parkinson disease. Parkinsonism Relat Disord. 2018;46:S30–3.

121. Emsen B, Villafane G, David J-P. Clinical impact of dual-tracer FDOPA and FDG PET/CT for the evaluation of patients with parkinsonian syndromes. Medicine. 2020;99(45):e23060.

122. Ibrahim N, Kusmirek J, Struck AF. The sensitivity and specificity of F-DOPA PET in a movement disorder clinic. Am J Nucl Med Mol Imaging. 2016;6(1):102–9.

123. Nicastro N, Nencha U, Burkhard PR, Garibotto V. Dopaminergic imaging in degenerative parkinsonisms, an established clinical diagnostic tool. J Neurochem. 2022.

124. Palermo G, Ceravolo R. Molecular imaging of the dopamine transporter cells. Cells. 2019;8:872.

125. Sioka C, Fotopoulos A, Kyritsis AP. Recent advances in PET imaging for evaluation of Parkinson's disease. Eur J Nucl Med Mol Imaging. 2010;37:1594–603.

126. Verger A, Grimaldi S, Ribeiro M-J, et al. Single photon emission computed tomography/positron emission tomography molecular imaging for parkinsonism: a fast-developing field. Ann Neurol. 2021a;90:711–9.

127. Verger A, Imbert L, Zaragori T. Dynamic amino-acid PET in neuro-oncology: a prognostic tool becomes essential. EJNMMI. 2021b;48:4129–32.

128. Brooks DJ, Pavese N. Imaging biomarkers in Parkinson's disease. Prog Neurobiol. 2011;95:614–28.

129. Garnett ES, Firnau G, Nahmias C. Dopamine visualized in the basal ganglia in living human brain. Nature. 1983;305:137–8.

130. Morbelli S, Esposito G, Arbizu J, et al. EANM practice guideline/SNMMI procedure standard for dopaminergic imaging in Parkinsonian syndromes 1.0. Eur J Nucl Med Mol Imaging. 2020;47(8):1885–912.

131. Lee CS, Samii A, Sossi V, et al. In vivo positron emission tomographic evidence for compensatory changes in presynaptic dopaminergic nerve terminals in Parkinson's disease. Ann Neurol. 2000;47:493–503.

132. Eshuis SA, Jager PL, Maguire RP, et al. Direct comparison of FP-CIT SPECT and F-DOPA PET in patients with Parkinson's disease and healthy controls. Eur J Nucl Med Mol Imaging. 2009;36:454–62.

133. Ishibashi K, Nishina H, Ishiwata K, Ishii K. Individual time course of pre- and postsynaptic PET imaging may improve differential diagnosis of Parkinson's disease and multiple system atrophy: a case report. BMC Res Notes. 2015;8:496.

134. Villemagne VL, Okamura N, Pejoska S, et al. In vivo assessment of vesicular monoamine transporter type 2 in dementia with Lewy bodies and Alzheimer disease. Arch Neurol. 2011;68:905–12.

135. Glass CK, Saijo K, Winner B, Marchetto MC, Gage FH. Mechanisms underlying inflammation in neurodegeneration. Cell. 2010;140:918–34.

136. Hoozemans JJM, Rozemuller AJM, van Haastert ES, et al. Neuroinflammation in Alzheimer's disease wanes with age. J Neuroinflammation. 2011;8:171.

137. Kreisl WC, Kim M-J, Coughlin J-M. PET imaging of neuroinflammation in neurological disorders. Lancet Neurol. 2020;19(11):940–50.

138. DeLegge MH, Smoke A. Neurodegeneration and Inflammation. Nutr Clin Pract. 2008;23:35–41.

139. Jain P, Chaney AM, Carlson ML, et al. Neuroinflammation PET imaging: current opinion and future directions. J Nucl Med. 2020;61:1107–12.

140. Kreutzberg GW. Microglia: a sensor for pathological events in the CNS. TINS. 1996;19:312–8.

141. Papadopoulos V, Baraldi M, Guilarte TR, et al. Translocator protein (18kDa): new nomenclature for the peripheral-type benzodiazepine receptor based on its structure and molecular function. Trends Pharmacol Sci. 2006;27(8):402–9.

142. Scarf AM, Kassiou M. The translocator protein. J Nucl Med. 2011;52:677–80.

143. Tronel C, Largeau B, Ribeiro MJS, et al. Molecular targets for PET imaging of activated microglia: the current situation and future expectations. Int J Mol Sci. 2017;18:802.

144. Werry EL, Bright FM, Piguet O, et al. Recent developments in TSPO PET imaging as a biomarker of neuroinflammation in neurodegenerative disorders. Int J Mol Sci. 2019;20:3161.

145. Jucaite A, Svenningsson P, Rinne JO, et al. Effect of the myeloperoxidase inhibitor AZD3241 on microglia: a PET study in Parkinson's disease. Brain. 2015;138:2687–700.

146. Zhang L, Huc K, Shaod T, et al. Recent developments on PET radiotracers for TSPO and their applications in neuroimaging. Acta Pharmaceut Sin B. 2021;11(2):373–93.

147. Ponisio MR, Zempel JM, Day BK, et al. The Role of SPECT and PET in epilepsy. AJR. 2021;216:759–68.

148. Newberg AB, Alavi A. PET in seizure disorders. Radiol Clin North Am. 2005;43:79–92.

149. Goffin K, Dedeurwaerdere S, Van Laere K, et al. Neuronuclear assessment of patients with epilepsy. Semin Nucl Med. 2008;38:227–39.

150. Kuhl DE, Engel J, Phelps ME, Selin C. Epileptic patterns of local cerebral metabolism and perfusion in humans determined by emission computed tomography of [18]FDG and [13]NH$_3$. Ann Neurol. 1980;8:348–60.

151. Galovic M, Koepp M. Advances of molecular imaging in epilepsy. Curr Neurol Neurosci Rep. 2016;16:58.

152. Kumar A, Chugani HT. The role of radionuclide imaging in epilepsy, part 2: epilepsy syndromes. J Nucl Med. 2013a;54:1924–30.
153. Kumar A, Chugani HT. The role of radionuclide imaging in epilepsy, part 1: sporadic temporal and extratemporal lobe epilepsy. J Nucl Med. 2013b;54:1775–81.
154. Yan R, Zhang H-Q, Wang J, et al. Application value of molecular imaging technology in epilepsy. Ibrain. 2021;7(3):200–10.
155. Vivash L, Gregoire M-C, Lau E-W, et al. 18F-Flumazenil: a g-Aminobutyric Acid A–specific PET radiotracer for the localization of drug-resistant temporal lobe epilepsy. J Nucl Med. 2013;54:1270–7.
156. Casse R, Rowe CC, Newton M, et al. Positron emission tomography and epilepsy. Mol Imag and Biol. 2002;4:338–51.
157. Sarikaya I. PET studies in epilepsy. Am J Nucl Med Mol Imaging. 2015;5(5):416–30.
158. Theodore WH. Presurgical focus localization in epilepsy: PET and SPECT. Semin Nucl Med. 2017;47:44–53.
159. Louis DN, Perry A, Reifenberger G, et al. The 2016 World Health Organization classification of tumors of the central nervous system: a summary. Acta Neuropathol. 2016;131:803–20.
160. Nandu H, Wen PY, Huang RY. Imaging in neuro-oncology. Ther Adv Neurol Disord. 2018:11. https://doi.org/10.1177/1756286418759865.

161. de Zwart PL, van Dijken BRJ, Holtman GA, et al. Diagnostic accuracy of PET tracers for the differentiation of tumor progression from treatment-related changes in high-grade glioma: a systematic review and metaanalysis. J Nucl Med. 2021;61: 498–504.
162. Shooli H, Dadgar H, Wáng Y-XJ, et al. An update on PET-based molecular imaging in neuro-oncology: challenges and implementation for a precision medicine approach in cancer care. Quant Imaging Med Surg. 2019;9(9):1597–610.
163. Somme F, Bender L, Namer IJ, et al. Usefulness of 18F-FDOPA PET for the management of primary brain tumors: a systematic review of the literature. Cancer Imaging. 2020;20:70.
164. Stegmayr C, Stoffels G, Filß C. Current trends in the use of O-(2-[18F]fluoroethyl)-L-tyrosine ([18F]FET) in neurooncology. Nucl Med Biol. 2021;92: 78–84.
165. Verger A, Kas A, Darcourt J, Guedj E. PET imaging in neuro-oncology: an update and overview of a rapidly growing area. Cancer. 2022;14:1103.
166. Zhang-Yin JT, Girard A, Bertaux M, et al. What does PET imaging bring to neuro-oncology in 2022? A review. Cancer. 2022;14:879.
167. Dissaux G, Basse V, Schick U, et al. Prognostic value of 18F-FET PET/CT in newly diagnosed WHO 2016 high-grade glioma. Medicine. 2020;99:e19017.

Almost all aspects of life are engineered at the molecular level, and without understanding molecules we can only have a very sketchy understanding of life itself. (Francis Harry Compton Crick)

16.1 Nuclear Cardiology

Coronary artery disease (CAD), stroke, and congestive heart failure (CHF) are responsible for the majority of all cardiovascular deaths. The current major diagnostic imaging procedures in nuclear cardiology to address the issues of CAD and heart failure are based on the assessment of myocardial blood flow (MBF) and substrate metabolism using FDA-approved SPECT and PET radiopharmaceuticals (Table 16.1). A number of review articles have extensively discussed various clinical issues and the relative significance of noninvasive imaging techniques in nuclear cardiology [1–4]. In the last 30 years, the application of qualitative perfusion imaging based on SPECT has been extended to allow for the combined evaluation of perfusion, perfusion reserve, and ventricular function. The coronary flow reserve (CFR) is a quantitative parameter defined by the ratio of maximal myocardial blood flow to the rest myocardial blood flow, which allows to give functional information on the whole coronary arterial tree, integrating both epicardial arteries and microcirculatory. The

CFR is a powerful tool to guide therapy and to assess prognosis [5]. With the improvements in SPECT instrumentation and with the availability of CZT-PECT and Dynamic PET scanners, the time has come for nuclear cardiology to provide the CFR measurements for clinical practice.

In cardiology, a paradigm shift is taking place with the emphasis from treatment to prevention of the disease. Current strategies involve the use of targeted markers of biological processes. With the recent advances in molecular biology, including genomics and proteomics, molecular imaging using biologically targeted radiopharmaceuticals will play a key role in this interdisciplinary approach to understanding the origins, pathogenesis, and progress of cardiac diseases, and in evaluating therapeutic interventions. Several molecular imaging radiopharmaceuticals with potential clinical utility are listed in Table 16.1. Today, molecular imaging of the heart is increasingly requested by cardiologists for infection, inflammation, infiltration, coronary atherosclerosis, vulnerable plaque, and heart failure. This trend is further fueled by the advent of an increasing spectrum of novel molecule-targeted drug interventions in cardiology, which require early identification of the most suitable patients and subsequent monitoring of success [4]. Several recent reviews discussed the potential clinical significance of different molecular imaging stud-

Table 16.1 Radiopharmaceuticals in nuclear cardiology

Assessment/mechanism	RP for SPECT	RP for PET
Myocardial perfusion/myocardial blood flow	^{201}Tl-chloride[a]	[^{15}O]-water
	^{99m}Tc-Sestamibi (Cardiolite™)[a]	^{82}Rb chloride[a]
	^{99m}Tc-Tetrofosmin (Myoview™)[a]	[^{13}N]Ammonia[a]
		[^{18}F]-Flurpiridaz
Blood pool/ejection fraction	^{99m}Tc-RBCs[a]	
Myocardial infarction	^{99m}Tc-PYP[a]	
Glucose metabolism (viability)		[^{18}F]Fluorodeoxyglucose (FDG)
Fatty acid metabolism	^{123}I-BMIPP	[^{11}C]Palmitate
		[^{18}F]FTHA
Oxidative metabolism		[^{11}C]Acetate
Myocardial sympathetic innervation	^{123}I-MIBG (Iobenguane)	[^{11}C]meta-hydroxyephedrine (HED)
β-adrenergic receptors		[^{11}C]CGP12177
Infection/inflammation	^{111}In or ^{99m}Tc labeled leukocytes	[^{18}F]FDG
Cardiac sarcoidosis	^{111}In-DTPA-Octreotide (Octreoscan)	[^{18}F]FDG
		[^{18}F]Fluorothymidine (FLT)
		^{68}Ga-Dotatate; ^{68}Ga-Dotatoc
Cardiac amyloidosis	^{99m}Tc-PYP	[^{11}C]PiB, [^{18}F]Flutemetamol
	^{99m}Tc-HMDP	[^{18}F]Florbetaben
	^{99m}Tc-DDP	[^{18}F]Florbetapir
	^{99m}Tc-Aprotinin	
Fibrosis: fibroblast activating protein (FAP)		68Ga-FAPI-04
Atherosclerosis		[^{18}F]FDG
		[^{18}F]Fluoride
Inflammatory pathway: chemokine receptor (CXCR4)	^{111}In-Pentixafor	^{68}Ga-Pentixafor

DPD = 3,3-diphosphono-1,2-propanodicarboxylic acid
[a]FDA approved agents

ies that are in clinical use and the new, and novel agents under investigation [4, 6–9].

16.2   The Clinical Problem

16.2.1 Coronary Artery Disease

The coronary arteries originate from the left and right coronary sinuses of the aorta (Fig. 16.1). The left main coronary artery divides into two major arteries: the left anterior descending artery (LAD) and the left circumflex artery (LCx). The right coronary artery (RCA) divides into a posterior descending artery (PDA) and a posterior left ventricular branch. The cardiac muscle has two
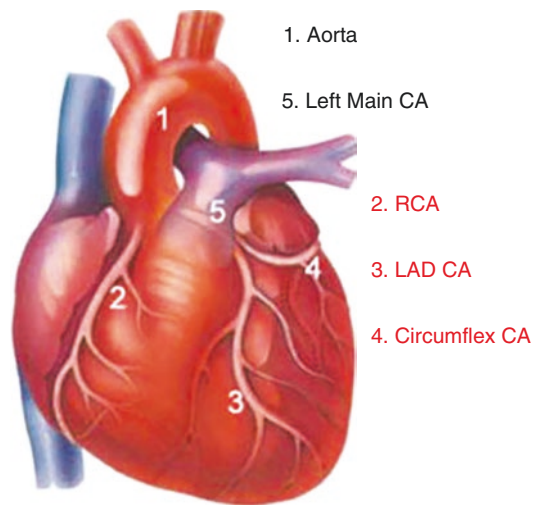

1. Aorta

5. Left Main CA

2. RCA

3. LAD CA

4. Circumflex CA

Fig. 16.1 Heart with coronary arteries

essential properties: electrical excitability and contractility. The ability of myocardial muscle cells to contract and generate the force necessary to maintain blood circulation is achieved through the unique contractile function of two proteins of the sarcomere (actin and myosin) of the syncytially arranged myocardial fibers. Also, the heart muscle has a rich supply of the high-energy phosphates needed for the contraction.

The majority of patients with acute coronary syndromes (ACS) present with unstable angina, acute myocardial infarction, and sudden coronary death. The disease may be asymptomatic until advanced in severity or complications. CAD is an immune inflammatory process, which, over decades, results in arterial narrowing [10, 11]. Atherosclerosis is a systemic disease with focal manifestations, and it is by far the most frequent underlying cause of CAD. It is also a complex
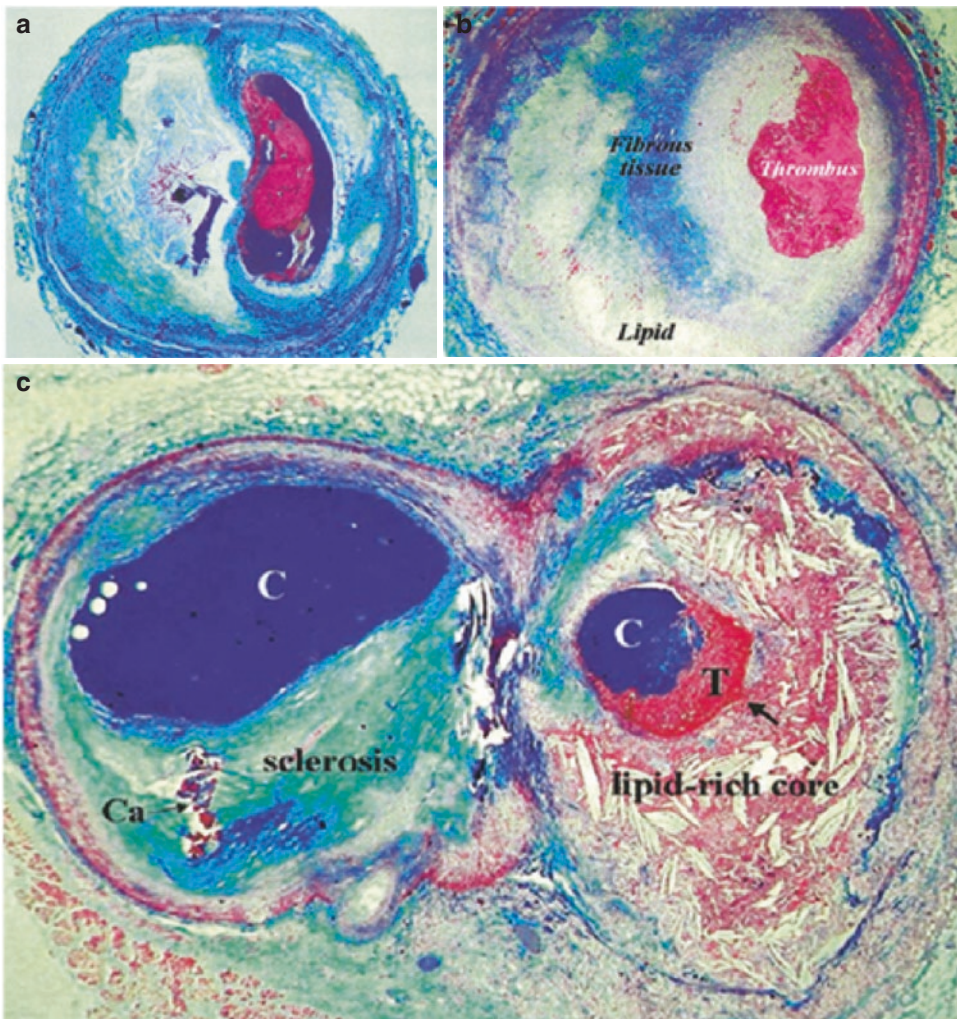

Fig. 16.2 Atherosclerosis and thrombosis in coronary arteries (CA): (**a**) cross-sectioned CA containing a ruptured plaque with a nonocclusive platelet-rich thrombus superimposed; (**b**) cross section of a CA containing a stenotic atherosclerotic plaque with an occlusive thrombosis superimposed (plaque erosion); (**c**) atherothrombosis: a variable mix of chronic atherosclerosis and acute thrombosis. Cross-sectioned arterial bifurcation illustrating a collagen-rich (*blue-stained*) plaque in the circumflex branch (*left*) and a lipid-rich and ruptured plaque with a nonocclusive thrombosis superimposed in the obtuse branch (*right*). *C* contrast in the lumen, *Ca* calcification, *T* thrombosis [12]

disease in which cholesterol deposition, inflammation, and thrombus formation play a major role. Atherosclerotic lesions (Fig. 16.2), according to the American Heart Association classification are divided into two groups: nonatherosclerotic intimal lesions and progressive atherosclerotic lesions [13]. A third group of lesions, healed atherosclerotic plaques, are the most prevalent lesions, particularly in the carotid arteries. A variety of factors contribute to the development and progression of atherosclerosis. Dysfunction of the endothelium, which maintains vascular homeostasis by regulating vascular tone, smooth muscle cell proliferation, and thrombogenicity, is thought to be the earliest step in the development of CAD. The endothelial dysfunction results in the imbalance of vascular regulatory mechanisms to cause damage to the arterial wall. Inflammation, macrophage infiltration, lipid deposition, calcification, extracellular matrix digestion, oxidative stress, cell apoptosis, and thrombosis are among other molecular mechanisms that contribute to plaque development and progression [10, 14, 15]. The practice of estimating the severity of atherosclerotic disease by using CT calcification was introduced in the 1980s and was standardized with the publication of a CT calcium score. The utility in early diagnosis is limited by the fact that the macrocalcifications visible on CT are a relatively late-

stage manifestation of atherosclerosis. By contrast, molecular imaging techniques can theoretically visualize the preliminary stages and microscopic manifestations of the disease process (such as inflammation, microcalcification) and, if validated, would constitute an ideal modality for early diagnosis and intervention [8].

Atherosclerosis, alone, is rarely fatal; it is thrombosis, superimposed on a ruptured or eroded atherosclerotic plaque, that precipitates life-threatening clinical events, such as acute coronary syndromes (ACS) and stroke [14]. Therefore, the term atherothrombotic disease is more appropriate since the atherosclerotic and the thrombotic processes are interdependent [12].

16.2.1.1   Vulnerable Plaque

Since the 1970s, scientists have sought to find the mechanisms responsible for converting chronic coronary atherosclerosis to acute coronary artery disease. Despite major advances in the treatment of coronary heart disease patients, a large number of victims of the disease, who are apparently healthy, die suddenly without prior symptoms. In the 1990s the term *vulnerable plaque* was introduced to describe the rupture prone plaques as being the underlying cause of most clinical coronary events [16]. Based on histopathological observations, a nonthrombosed lesion, that most resembles the acute plaque rupture, has been
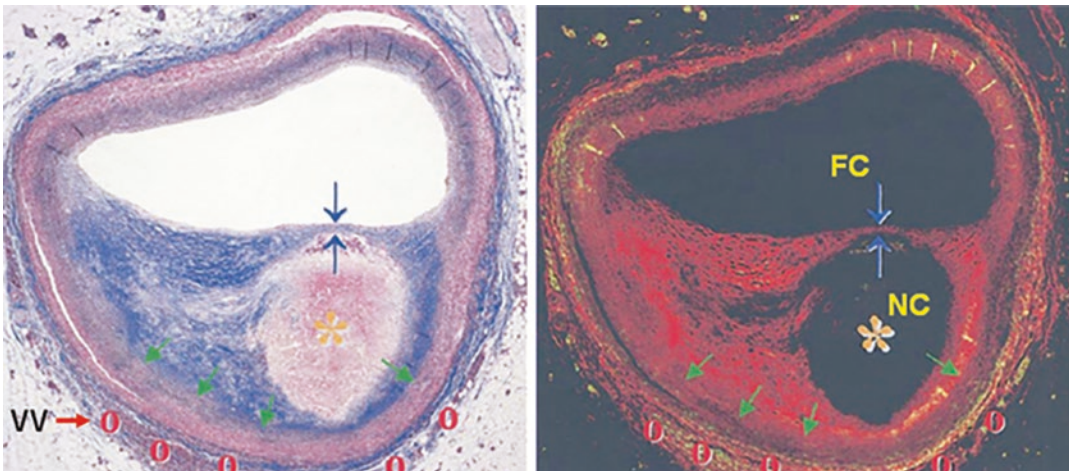

Fig. 16.3 Vulnerable plaque: cross section of a coronary artery containing plaque assumed to be rupture-prone containing a large lipid-rich necrotic core (NC), thin fibrous cap (FC), expansive remodeling (*green arrow*), and vasa vasorum and neovascularization (VV) [14]

identified as the thin cap fibroatheroma (TCFA), which is characterized by a necrotic core with an overlying fibrous cap measuring <65 μm, containing rare smooth muscle cells and numerous macrophages (Fig. 16.3) [14, 15]. An inflamed TCFA is suspected to be a high risk/vulnerable plaque [17, 18].

Stable plaques are characterized by intimal thickening associated with lipid deposition, a chronic inflammatory infiltrate but, without evidence of necrosis, whereas vulnerable and ruptured plaques are characterized by an "active" inflammation involved in the thinning of the fibrous cap, predisposing the plaque to rupture [13, 17]. Since rupture-prone plaques are not the only vulnerable plaques, it was proposed that all types of atherosclerotic plaques, with a high likelihood of thrombotic complications and rapid progression, should be considered as vulnerable plaques [19]. In addition, since the vulnerable blood (prone to thrombosis) and vulnerable myocardium (prone to fatal arrhythmia) play an important role in the clinical outcome, the term "vulnerable patient" has been regarded as being more appropriate [20, 21].

Molecular imaging of inflammation, atherosclerosis/atherothrombosis, and vulnerable plaque would play a major role in nuclear cardiology in the near future ([4, 6, 8, 19, 22, 23].

16.2.1.2 Myocardial Infarction

Myocardial infarction (MI) occurs in the setting of an acute coronary vessel occlusion, with a variable amount of spasm, and increased myocardial demand as contributing factors. Most of the ACS are thought to be the result of sudden luminal thrombosis which occurs from three different pathologies: plaque rupture, erosion, and calcified nodules [15]. Histopathological studies reveal a large peripheral zone infiltrate by neutrophils that surround the subendocardial central zone devoid of neutrophils. The peri-infarct zone is a complex collection of regions in different states of injury, depending on the amount of blood flow reduction, myocardial metabolic demand, and the rate of onset and duration of the blood flow reduction. Myocardial necrosis and severe acute ischemia lead to increased permeability, cell membrane disruption, and leakage. Different myocardial tissue states or zones, such as hibernating and stunned myocardium, may be present depending on the extent of damage, viability, and function [23]. The hibernating myocardium is the term applied to a dysfunctional myocardium with reduced perfusion (ischemia) at rest, but preserved cell viability.

16.2.2 Congestive Heart Failure

CHF stems from inadequate cardiac output, due to systolic or diastolic left ventricular function. The primary causes are ischemic heart disease and hypertension. Both, idiopathic cardiomyopathy (ICM) and ischemic cardiomyopathy (ISM) are widespread and are major underlying cardiac diseases responsible for heart failure. Besides the risk of sudden cardiac death, patients with CHF can have intraventricular dyssynchrony (or left bundle branch block), which causes the two ventricles to beat in an asynchronous fashion, reduces systolic function, and increases systolic volume. Autonomic dysfunction has been shown to increase the risk of death in patients with heart disease and may be applicable to all patients with cardiac disease, regardless of etiology [24]. The impaired cardiac presynaptic function has pathophysiological implications in the occurrence of lethal cardiac events in patients with heart failure.

The autonomic innervation of the heart is the primary extrinsic control mechanism regulating cardiac performance. The heart is innervated by the parasympathetic and sympathetic nerve fibers. The left ventricle of the heart is primarily supplied by sympathetic nerves that modify cardiovascular performance in adapting to the changing hemodynamic requirements. The parasympathetic nervous system primarily innervates the atria and the conduction system. The major neurotransmitters of the sympathetic and parasympathetic systems are norepinephrine and acetylcholine, which define the stimulatory and

inhibitory physiological effects of each system. There is a highly regulated balance in the sympathetic and parasympathetic input to optimize cardiac performance.

16.2.3 Cardiomyopathy

Cardiomyopathy is a diseased heart muscle that cannot function (contract) adequately and results in the failure of the heart muscle to meet the needs of the body for oxygen-rich blood and the removal of carbon dioxide, and other waste products. There are many causes of cardiomyopathy but, the end result is a heart that is weak and cannot maintain a normal ejection fraction or cardiac output. Primary cardiomyopathies are those that usually affect the heart alone. Secondary cardiomyopathies (such as sarcoidosis and amyloidosis) are those that are a result of an underlying condition affecting many areas of the body [25, 26].

16.2.3.1 Cardiac Sarcoidosis (CS)

Sarcoidosis is a systemic inflammatory disorder resulting from the combined effects of genetic susceptibility and environmental exposures. Sarcoidosis is a granulomatous disease that affects multiple organs and has no clearly defined etiology. Although much attention is focused on lymphocytes in directing inflammation in sarcoidosis, macrophages remain the dominant constituent of the sarcoidosis granuloma. The cardiovascular system is the third most common site of sarcoidosis and is involved in 25–50% of patients. Patients with heart failure have a particularly poor prognosis [25, 91]. The prevalence of sarcoidosis-related cardiomyopathy is increasing. Sarcoidosis impacts cardiac function through granulomatous infiltration of the heart, resulting in conduction disease, arrhythmia and/or heart failure. Diagnosis of CS can be challenging and requires clinician awareness as well as differentiation from overlapping diagnostic phenotypes such as other forms of myocarditis and arrhythmogenic cardiomyopathy [25]. Early diagnosis is the key to preventing the potentially devastating effects of cardiac sarcoidosis (CS).

Cardiac MRI offers high spatial resolution and enables evaluation of ventricular function, myocardial edema, and scarring. It provides high diagnostic value (sensitivity, 76–100%; specificity, 78–92%). However, contrast-enhanced cardiac MRI cannot be performed in patients with implantable devices and/or severe renal impairment [91]. Molecular imaging with PET radiotracers has the advantages of overcoming these disadvantages of cardiac MRI and provide definitive diagnosis of CS.

16.2.3.2 Cardiac Amyloidosis (CA)

CA is an infiltrative and restrictive cardiomyopathy that leads to heart failure, reduced quality of life, and death. CA is a disorder characterized by deposition of insoluble protein fibrils (i.e., amyloid) in the extracellular space. Fibrils from two protein precursors, amyloid immunoglobulin light chain (AL) and amyloid transthyretin (ATTR), are the main causes of cardiac amyloidosis [26]. Based on the protein fibrils, CA is categorized into two subtypes, transthyretin cardiac amyloidosis (ATTR-CA) and immunoglobulin light chain cardiac amyloidosis (AL-CA), characterized by the precursor protein that forms amyloid and infiltrates the myocardium. AL amyloidosis develops after deposition of misfolded proteins that originate from the AL fragments that are typically produced by bone marrow plasma cells. ATTR amyloidosis is caused by accumulation of transthyretin (TTR), a serum transport protein for thyroid hormone and retinol synthesized originally by the liver, and is classified into two subtypes: wild-type (ATTRwt-CA) and hereditary, previously called familial CA and now referred to as variant transthyretin CA (ATTRv-CA) [26]. CA is caused by cumulative myocardial deposition of insoluble amyloid that causes chamber stiffening, conduction disturbances, impaired diastolic function initially, and heart failure with preserved ejection fraction (HfpEF) that can progress to a reduced ejection fraction (EF). Transthyretin (alternatively, prealbumin) is a tetrameric protein mainly produced in the liver that transports thyroid hormone and retinol. With aging, or a destabilizing mutation, the tetramer dissociates into monomers

or oligomers that misfold and aggregate into amyloid fibrils.

Recent advances in therapeutic options render accurate and early diagnosis of CA critical. Previously, definitive diagnosis of ATTR-CA often required an endomyocardial biopsy staining positive with Congo Red, with confirmatory testing for ATTR via immunohistochemistry or serum/urine protein electrophoresis with immunofixation mass spectroscopy. Endomyocardial biopsy is highly sensitive and specific (nearly 100% for each) and is considered the gold standard for diagnosis [26]. However, given its invasive nature, biopsy was performed only when there was significant suspicion of CA. Radionuclide planar/SPECT imaging studies with ^{99m}Tc bone agents or β-amyloid binding PET radiotracers can provide non-invasive diagnostic information.

16.2.4 Fibrosis

Postinfarction remodeling involves infiltration of activated fibroblasts into affected myocardium to assist with repair and to maintain structural integrity of affected tissue. Myocardial fibrosis is a common endpoint of cardiovascular disease, characterized by resident cardiac fibroblast transdifferentiation and activation, which produce fibrillary collagen and reorganize extracellular matrix. Reparative or replacement fibrosis after ischemic injury culminates in scar formation and stabilization of the infarct [27]. The dynamic remodeling process is driven by a multitude of cells including cardiomyocytes, endothelial cells, immune cells, and cardiac fibroblasts. After MI, fibroblasts undergo dynamic phenotypic changes and differentiate into collagen-secreting protomyofibroblasts. These activated fibroblasts can further differentiate into mature myofibroblasts. After MI, activated fibroblasts migrate into the injured myocardium and contribute to tissue replacement, thereby helping to preserve the structural integrity of the infarcted heart. They secrete increased amounts of cytokines, growth factors, and pericellular proteases to maintain the extracellular matrix (ECM) and promote replace-

ment fibrosis—formation of a scar that stabilizes the ventricular wall and maintains the macroanatomy of the heart [28]. Excessive fibrosis, however, can lead to left ventricular stiffness, decreased contractility, and ultimately contributes to the progression to HF. Noninvasive imaging of activated fibroblasts could therefore provide unique opportunities to study cardiac remodeling over time and to monitor therapeutic interventions that aim to prevent a progressive decline of ventricular function [29, 30].

16.3   Radiopharmaceuticals in Nuclear Cardiology

SPECT and PET radiopharmaceuticals with specific clinical applications in cardiology are summarized in Table 16.1. The mechanisms of uptake and clinical utility of both approved and investigational radiopharmaceuticals will be described briefly in the following sections.

16.3.1 Myocardial Blood Flow/Perfusion

Myocardial perfusion Imaging (MPI) with SPECT has been the clinical workhorse for MPI, but over the past two decades, PET MPI is experiencing growth due to enhanced image quality that results in superior diagnostic accuracy over SPECT. Furthermore, dynamic PET imaging of the tracer distribution process from the time of tracer administration to tracer accumulation in the myocardium has enabled routine quantification of myocardial blood flow (MBF) and myocardial flow reserve (MFR) in absolute units [31].

MBF is regulated by anatomical, hydraulic, mechanical, and metabolic factors. Autoregulation of MBF is driven by changes in regional myocardial metabolism and oxygen consumption. Under resting conditions, MBF is one-fifth the maximum flow capacity, which occurs during reactive hyperemia and, or with maximum pharmacological vasodilation [32]. Near-maximal MBF can be produced by intense metabolic stress associated with exercise. The difference between the peak
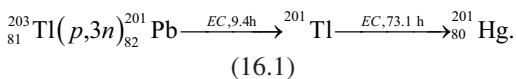
(under stress) and basal MBF represents the coronary flow reserve (CFR), which is reduced in the presence of severe CAD.

The resting MBF is not reduced until the stenosis exceeds 90% of the normal vessel diameter. The coronary flow reserve, however, is reduced with only a 50% diameter stenosis [33]. Therefore, myocardial perfusion imaging (MPI) is performed in conjunction with exercise or pharmacological vasodilatation (using adenosine, dipyridamole, or dobutamine) in order to identify subcritical coronary stenosis. MPI maps the relative distribution of coronary flow, which is normally almost uniform in the absence of prior infarction or fibrosis.

The ideal MPI radiopharmaceutical should have a linear relationship between myocardial uptake and blood flow, high first-pass extraction over a wide range of blood flow rates, low extracardiac uptake, minimal myocardial redistribution, and intrinsic chemical stability. The relationship between uptake and clearance of the radiotracer and MBF should be constant and independent of MBF, physiological and pathological changes of the myocardial tissue state, and the myocardial metabolism. Most radiotracers used for imaging the myocardial perfusion/blood flow, however, do not fully meet these requirements [2, 34].

16.3.1.1   SPECT Radiotracers for Perfusion

^{201}Tl as thallous chloride behaves like a K$^+$ analog and is highly extracted by the myocardial cell. It was first introduced in the 1970s as a radiopharmaceutical for myocardial perfusion imaging [35]. ^{201}Tl, with a physical half-life of 73.1 h, decays by electron capture to ^{201}Hg, which emits useful X-ray photons (69–80 KeV; 94.4% abundance) for gamma camera imaging studies. It is produced in a cyclotron and is indirectly based on the following nuclear reaction:

$$^{203}_{81}\text{Tl}\left(p,3n\right)^{201}_{82}\text{Pb}\xrightarrow{EC,9.4h}{}^{201}\text{Tl}\xrightarrow{EC,73.1\text{ h}}{}^{201}_{80}\text{Hg}.$$
(16.1)

Following intravenous administration, it is rapidly cleared from the circulation and normal myocardial tissue extracts about 85% of the amount present in the coronary arteries. At pH 4–7, ^{201}Tl predominantly exists as a monocation, and like K$^+$ ion, it relies on cell-membrane integrity and active metabolic transport using Na$^+$/K$^+$ pump for its uptake into the myocardial cells. Approximately 3–5% of the injected dose localizes in the normal myocardial tissue and after initial localization, there is rapid redistribution of ^{201}Tl activity in the myocardium. Early stress-induced defects, which later normalize in redistribution images, imply myocardial ischemia, while persistent defects indicate scarring.

Three important ^{99m}Tc labeled radiopharmaceuticals (Fig. 16.4) were introduced for myocardial perfusion imaging studies [36]; sestamibi (cardiolite®), tetrofosmin (Myoview™), and teboroxime (CardioTec), however, CardioTec is no longer commercially available. In the case of ^{99m}Tc-Sestamibi, six molecules of MIBI (2-methoxy isobutyl isonitrile) bind to the central ^{99m}Tc atom forming a coordination complex with a single positive charge. As a cationic complex, it is transported into the myocardium by passive diffusion (extraction efficiency < 60%), and the myocardial retention is due to mitochondrial binding. Tetrofosmin (^{99m}Tc-1,2-bis[bis(2-ethoxyethyl)phosphino]ethane) is also a monocation complex and is transported into the myocardial tissue similar to sestamibi.

16.3.1.2   PET Radiotracers for Perfusion

Several PET radiopharmaceuticals are available for evaluating the relative distribution of MBF and for measuring regional MBF in absolute quantitative units (mL/min/g) based on PET [2, 31].

As described previously, the first-pass unidirectional extraction fraction E is the fraction of the tracer that changes across the capillary membrane during a single transit of tracer bolus through the coronary circulation. For most diffusible radiotracers, such as [^{15}O]water, $E < 1$ declines with increasing MBF. The relationship between E and the permeability-surface product and blood flow is described by Renkin and Crone. It is also important to note that the E for radio-
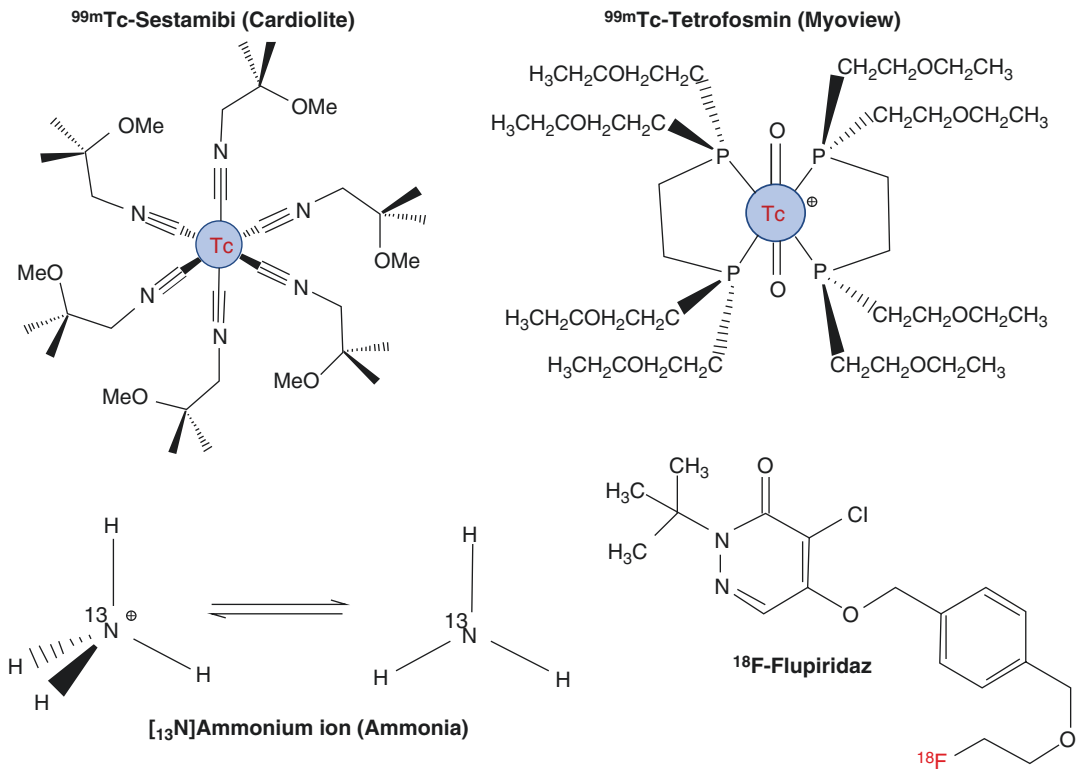
Fig. 16.4 SPECT and PET radiopharmaceuticals for myocardial perfusion imaging

tracers administered as bolus is generally higher than the steady state extraction fraction, also called the extraction ratio [34]. Also, the first-pass retention fraction R of the radiotracer may decrease at higher flow rates due to back diffusion of the radiotracer into the vascular space and blood. The plot of the myocardial net uptake ($E \times F$) for several radiotracers, as a function of MBF (Fig. 16.5), suggests that the net uptake would increase linearly with higher blood flows but, correlates nonlinearly with blood flow, except for [^{15}O]water.

[^{15}O]water meets the criteria for an ideal radiotracer for MBF measurement most closely. Based on a single tissue compartment model, MBF (mL min^{-1} g^{-1}) estimates in normal human subjects are 0.90 ± 0.22 at rest and 3.55 ± 1.15 with stress, based on intravenous dipyridamole [34].

[^{13}N]Ammonia (NH$_3$) in circulation exists predominantly as an ammonium ion NH$_4^+$ at normal pH. It may be actively transported into the myocardial cells via the Na$^+$/K$^+$ pump or by the pas-

sive diffusion of neutral lipid-soluble ammonia. Inside the cell, ammonia is quickly converted to ammonium ion which is rapidly converted and trapped as glutamine by the enzyme *glutamine synthase* [34]. Because of the large intracellular levels of glutamine, the washout of N-13 activity from the cell is minimal. Since the rate of their back-diffusion depends on MBF, the retained fraction R declines with higher flow.

Intrasubject comparison studies have demonstrated a close linear correlation between MBF estimates determined by [^{15}O]water and [^{13}N]ammonia techniques, over a range of flows from 0.5 to 5.0 mL min^{-1} g^{-1} [37]. Also, global and regional MBF estimates with [^{13}N]ammonia have shown a close correlation to MBF estimates which were determined based on the inert argon gas washout technique [38]. In patients with CAD and previous myocardial infarctions, MBF estimates with [^{13}N] ammonia and [^{15}O]water may markedly differ in regions of previously infracted myocardium [34]. MBF imaging with
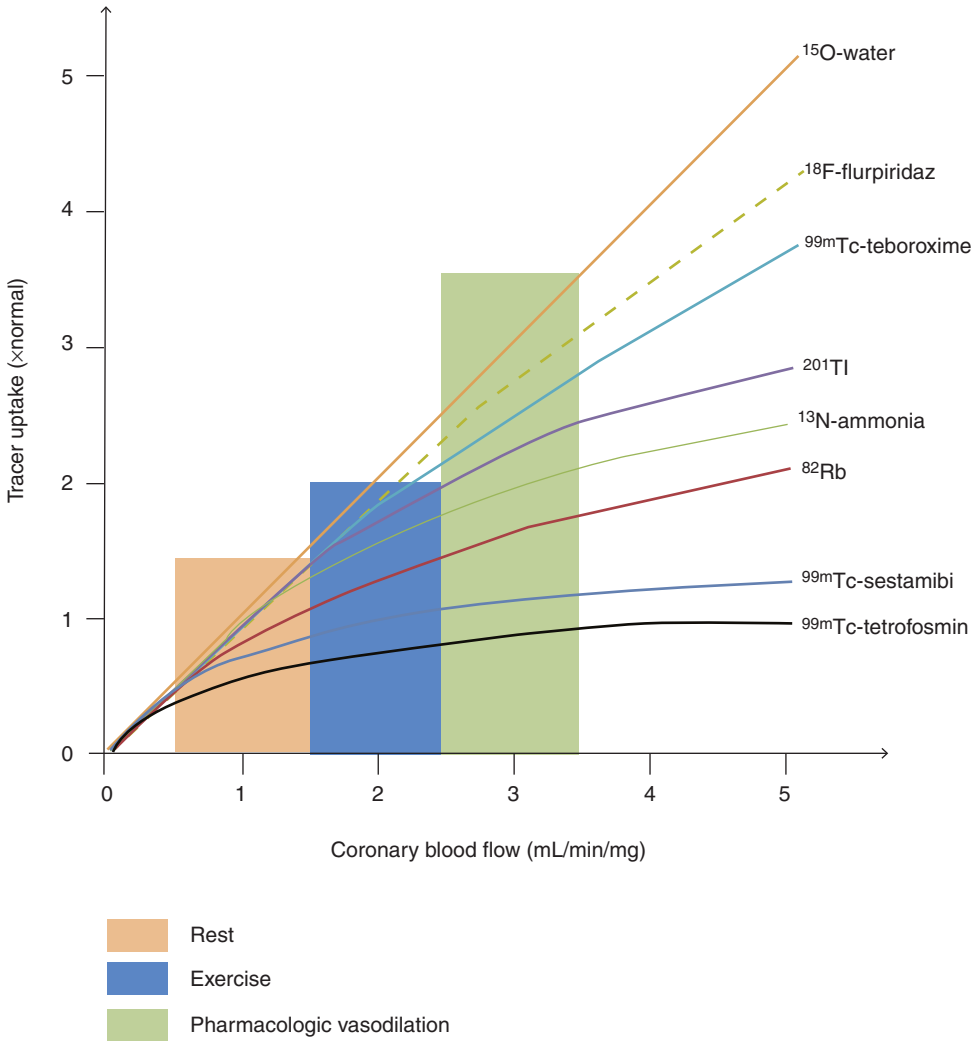
Fig. 16.5 Schematic representation of cardiac PET and SPECT radiotracers uptake in relation to myocardial perfusion. $[^{15}O]H_2O$ demonstrates close to linear uptake whereas the initial linear extraction of ^{99m}Tc labeled compounds plateau at approximately 2 mL/min/g. PET radiotracers $^{13}NH_4^+$ ion and $^{82}Rb^+$ fall between $^{201}Tl^+$ and the ^{99m}Tc-SPECT radiotracers, whereas ^{99m}Tc-teboroxime (discontinued) demonstrates superior extraction at high flow rates. $[^{18}F]$Flurpiridaz rivals $[^{15}O]H_2O$ with closer to linear extraction. (From [31])

$[^{13}N]$ammonia-PET, demonstrating anterior and lateral defects, is shown in Fig. 16.6.

$^{82}Rb^+$ as a K$^+$ analog, is actively transported into the myocardial cells via the Na$^+$/K$^+$ pump. The extraction fraction decreases at high flows and can be altered by drugs, severe acidosis, hypoxia, and ischemia. $^{82}Rb^+$ appears to leak from the irreversibly injured myocardium, but is retied or continues to accumulate in only reversibly injured myocardium [34]. In normal subjects, at baseline, and with dipyridamole stress, there is a close correlation between MBF estimates with $^{82}Rb^+$ and $[^{15}O]$water [40]. Comparison of ^{82}Rb-PET images with ^{99m}Tc-Tetrofosmin images obtained with SPECT-CZT scanner is shown in Fig. 16.7.

^{18}F-Flurpiridaz (BMS-747158-02, Lantheus Medical, Inc.) is a novel PET mitochondrial complex-1 inhibitor indicated for detection of CAD and risk stratification. Flurpiridaz is an analog of
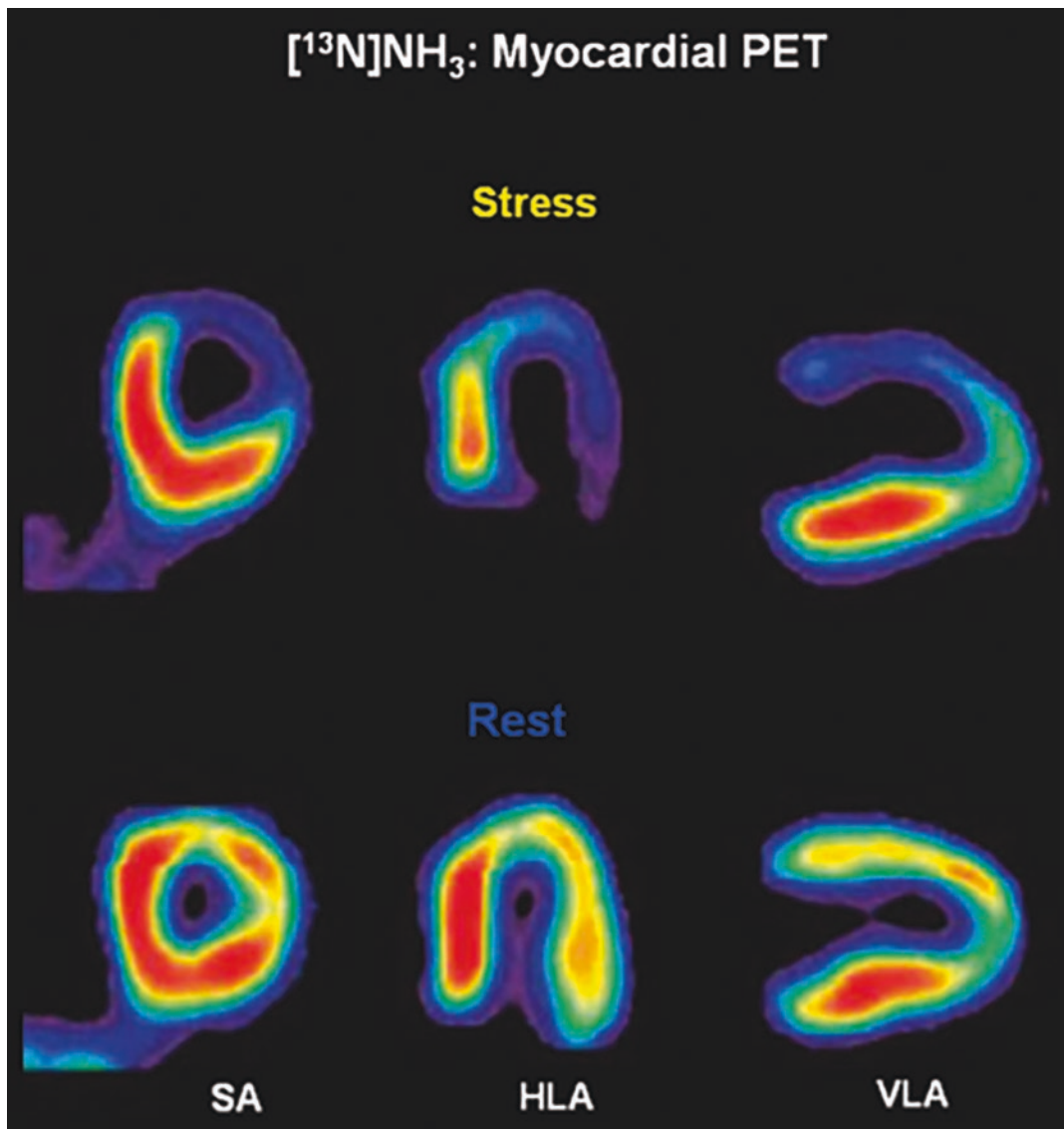
Fig. 16.6 Myocardial blood flow imaging with [^{13}N] ammonia-PET demonstrating anterior and lateral defects during pharmacological stress and significant improvement at rest, consistent with ischemia. *SA* short axis, *HLA* horizontal long axis, *VLA* vertical long axis [39]

mitochondrial complex-1 (MC1) inhibitor that specifically binds to the MC1 receptors on the inner mitochondrial membrane. Structurally it is an analog of the known MC-1 inhibitor, pyridaben. [^{18}F]Flurpiridaz can provide improved image quality due to the shorter positron range and longer half-life, enabling delayed imaging post injection. The longer half-life of ^{18}F also provides an opportunity for exercise stress protocols.

The superior pharmacokinetic profile of [^{18}F] Flurpiridaz, including its sustained myocardial extraction at high flow rates (Fig. 16.5), enables the possibility of enhanced assessment of absolute quantification of myocardial flow reserve to better identify multivessel disease, microvascular disease, and response to treatment of endothelial dysfunction [41]. [^{18}F]Flurpiridaz was evaluated in an initial Phase III trial with mixed results and
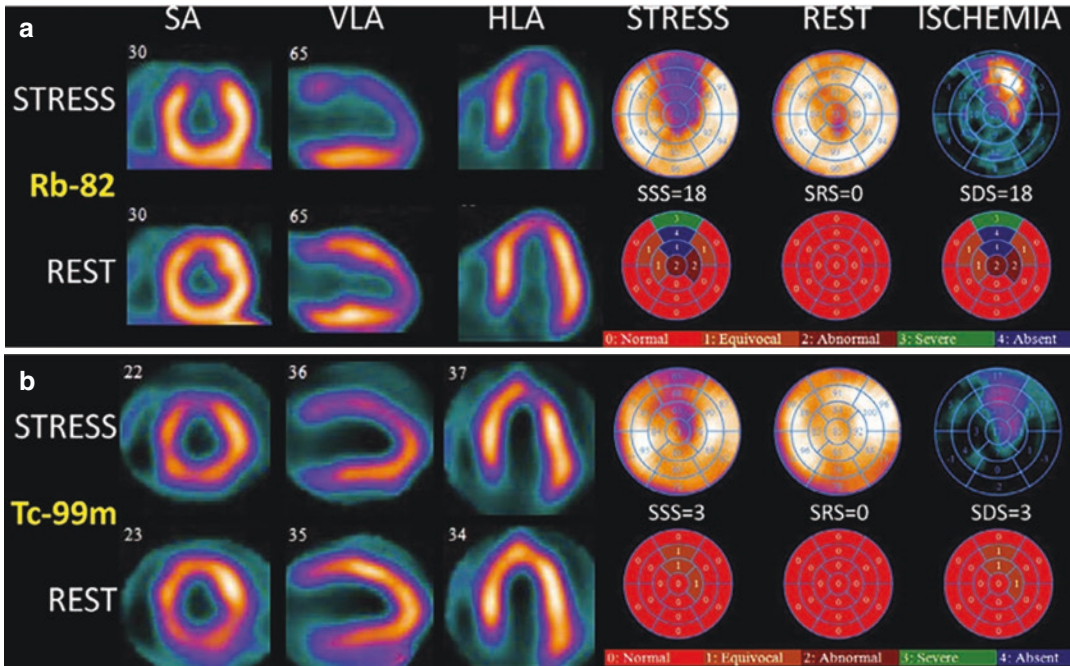
Fig. 16.7 [82]Rb-PET/CT (**a**) and ^{99m}Tc-Tetrofosmin SPECT-CZT (**b**) images in a 52-year-old man 3 months following PCI of the LAD coronary artery. Persantine [82]Rb-PET images demonstrate substantial residual ischemia in the LAD territory with sum stress and sum defect scores (SSS and SDS respectively) equal to 18 (26% of LV). Exercise ^{99m}Tc-SPECT images in the same patient showed milder ischemia with SSS = SDS = 3 (4% of LV) due to lower tracer retention and lower hyperemic stress compared to persantine 82Rb PET. (From [2])

is currently undergoing a second Phase III trial sponsored by GE Healthcare [2].

16.3.2 Myocardial Metabolism

Understanding the myocardial metabolism of substrates is very important for understanding the pathophysiology of various cardiac diseases and for designing therapeutic interventions. The heart requires a constant supply of energy to sustain contractile function. The energy is supplied by hydrolysis of ATP, which is primarily derived from the aerobic metabolism. The myocardium chooses between various substrates, such as free fatty acids (FFA), glucose, lactate, and ketone bodies (Fig. 16.8) [42]. The tricarboxylic acid (TCA) cycle is linked to the myocardial oxygen consumption via the electron transport chains, which supply most of the energy in the form of ATP. The amount of oxygen required, however, depends on the substrate. For example, one mol-ecule of glucose requires 12 oxygen atoms to produce 38 ATP molecules. In contrast, one mol-ecule of palmitate requires 46 oxygen atoms to produce 130 molecules of ATP. The selection of an appropriate substrate, however, depends on several conditions, such as plasma concentration of the substrate, hormonal control (insulin, gluca-gon, and catecholamines levels), stress, and physical activity.

In the normal myocardium, and also with moderate levels of exercise, FFAs are considered the preferred substrate for metabolism at rest. In the fasting state, FFA levels in circulation are high and insulin levels are low so that up to 80% of energy is derived from the FFA metabolism. A diet rich in carbohydrates increases the plasma glucose and insulin levels, and then glucose becomes the preferred substrate [43, 44]. With strenuous exercise, the release of lactate into the circulation from skeletal muscle increases and lactate will then become the major fuel for myo-cardial metabolism.
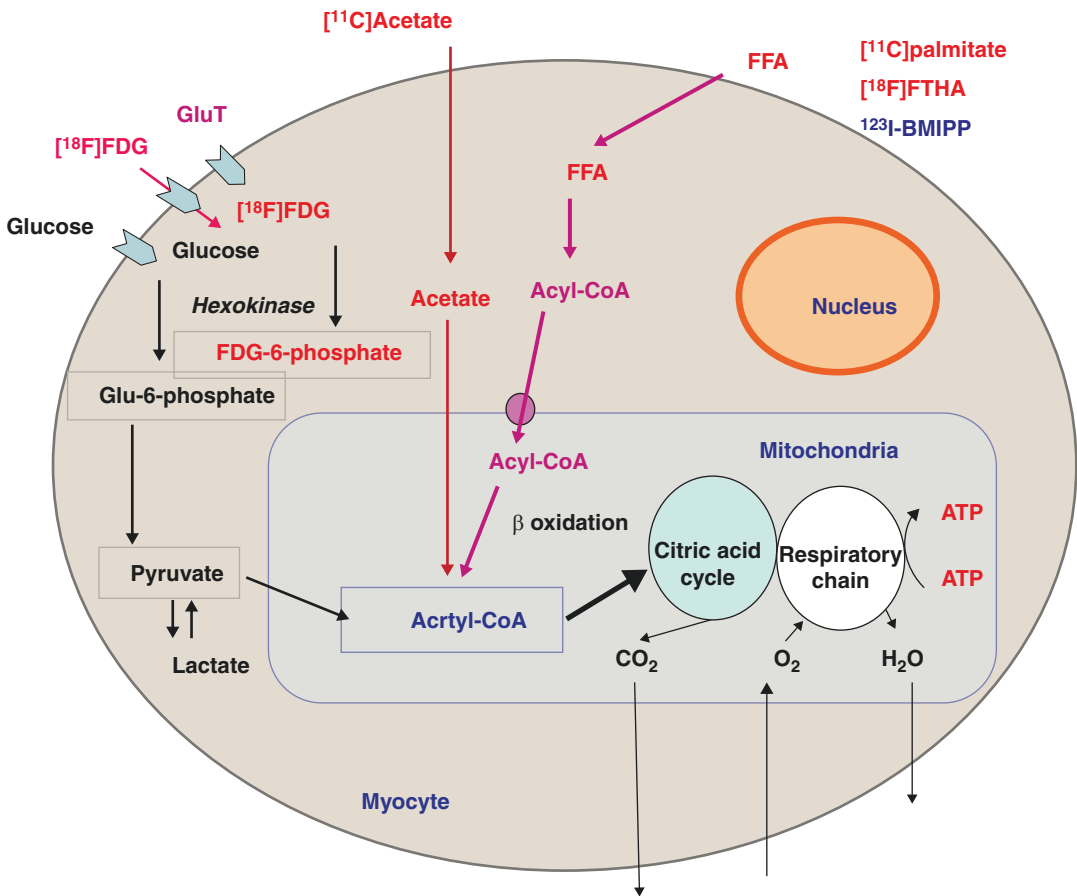
Fig. 16.8 PET and SPECT radiotracers to image myocardial substrate utilization and metabolism

In various pathological conditions, the myocardial metabolism can be changed significantly. In ischemic myocardium, the oxidative metabolism is reduced and as a result, there is a shift from an aerobic to an anaerobic metabolism. With the lack of a sufficient oxygen supply, glucose is now metabolized to lactate (glycolysis). With ischemia, glucose is the preferred substrate regardless of the availability of other fuels [44, 45]. For ischemic heart disease, the major player in the disease pathophysiology is the reduction in regional or focal perfusion. Changes in regional metabolism are a consequence of reduced blood flow to these areas.

Changes in myocardial metabolism may also play a key role in various other cardiac conditions, such as heart failure, cardiomyopathy, and diabetes, which involve the myocardium more globally, and involve the myocardium as a whole.

However, due to difficulties in evaluating metabolism in human subjects, the alterations in the myocardial metabolism under such conditions are poorly understood [46]. The substrate utilization may vary depending on the extent of CAD and prior drug therapy to improve LV function. For example, long-term treatment with a β-adrenergic receptor antagonist was reported to be associated with a switch in myocardial metabolism away from FFA oxidation towards glucose metabolism [47]. Studies in animal models of diabetes mellitus have demonstrated an upregulation of myocardial fatty acid utilization and a reduction of the insulin-mediated glucose transport. However, little is known about the effect of diabetes mellitus on the human heart.

In the era of traditional SPECT, MPI alone and exercise testing, with relatively long-lived tracers that are retained by the myocardium were

advantageous but, with the shift to more sensitive imaging devices (i.e., PET and cardiac-dedicated SPECT), MBF quantification and an emphasis on dose reduction, short-lived tracers offer more advantages.

16.3.2.1   Glucose Metabolism

Glucose is transported into the myocardial cell by facilitated diffusion of insulin-independent GLUT 1 and insulin-dependent GLUT 4 glucose transporters [48]. Intracellularly, glucose is rapidly phosphorylated to glucose 6-phosphate, which is further metabolized (glycolysis) to pyruvate. Under aerobic conditions, pyruvate is converted to acetyl-CoA, which enters the TCA cycle in the mitochondria for oxidative metabolism (Fig. 16.8). Under anaerobic conditions, pyruvate is further metabolized to lactic acid.

[18F]FDG that enters the myocardium is phosphorylated to FDG-6-phosphate but, then, does not enter further metabolic pathways; instead, it accumulates in the myocardium. Thus, the myocardial uptake of FDG reflects the uptake and metabolism of glucose [49, 50]. FDG-PET images reflect the relative distribution of FDG uptake in different regions of the myocardium. Also, the metabolic rate (MRglc) of glucose in absolute units can be measured with PET based on dynamic imaging studies, mathematical modeling, compartment model analysis, or graphical plot analysis. Since the rate of the glucose uptake and FDG uptake is not equal, a lumped constant (LC) was developed to convert the FDG uptake to glucose uptake. Usually, the value of LC is fixed, and is approximately 0.6–0.7 for the FDG-PET measurement of MRglc [51]. The LC, however, can vary over a wide range, depending on blood insulin levels and cardiac disease [52].
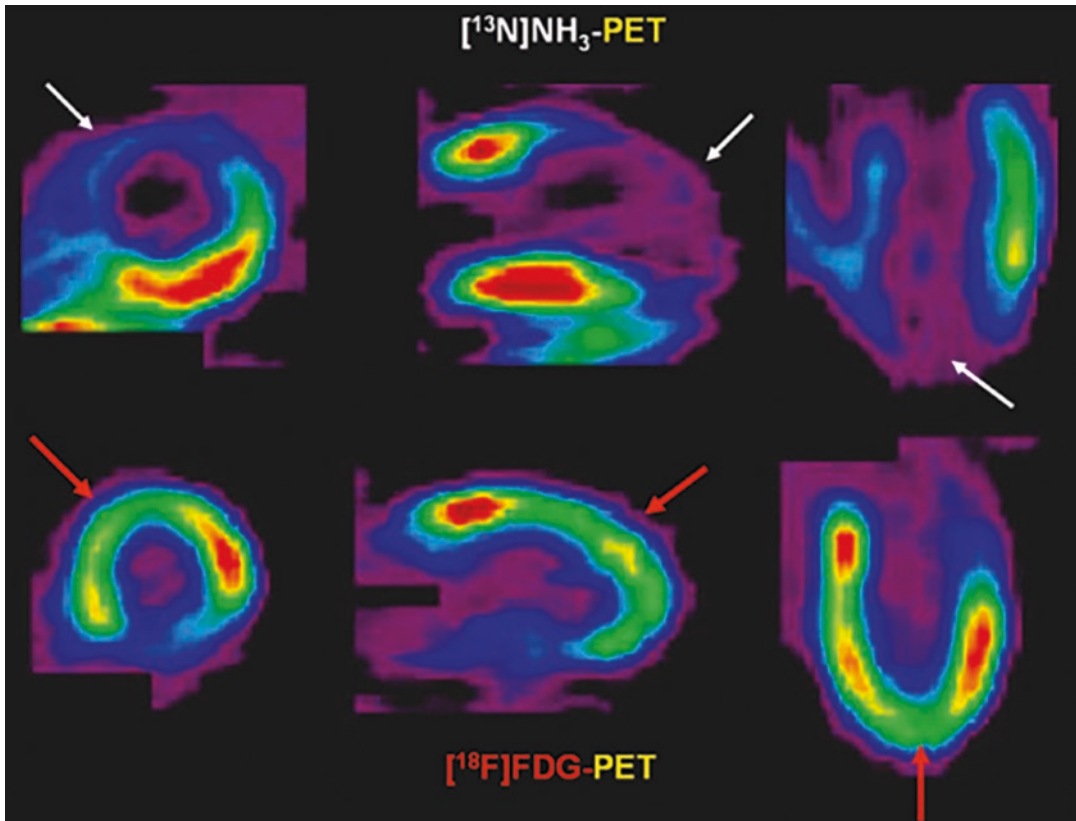

Fig. 16.9   FDG-PET to image myocardial viability. Classic mismatch showing FDG uptake in the areas of decreased myocardial perfusion identified by [13N]NH3

Detection of viability in ischemic heart disease is one of the most important aspects of the diagnostic and prognostic workup in patients with CAD. In some cases of hibernating myocardium, the resting flow based on PET or SPECT tracers cannot differentiate hibernating myocardium from irreversible myocardial scar formation. Relatively higher FDG uptake in an area of decreased myocardial blood flow in the dysfunctional myocardium, known as "flow metabolism mismatch," indicates viable myocardium [53]. As a result, FDG-PET is considered as one of the gold standards for the determination of myocardial viability (Fig. 16.9).

16.3.2.2   Fatty Acid Metabolism

Since the FFAs are hydrophobic, they are delivered to the heart by binding to plasma proteins, albumin, or lipoproteins. After dissociating from proteins, FFAs easily pass through the myocardial membrane by diffusion or a facilitated transport mechanism. Based on clinical and animal experiments, it has been shown that CD36 plays a cru-cial role in the fatty acid transport into the cells [54, 55]. Intracellularly, FFAs are activated as acylcoenzyme A (Acyl CoA) and then carried into the mitochondria through an acyl carnitine carrier system and catabolized by β-oxidation into two-carbon fragments, acetyl-CoAs, which enter the TCA cycle for further oxidative metabolism (Fig. 16.8). A part of FFAs is not oxidized but, is formed into triglycerides and myocardial structural lipids and stays in the myocardium for a long time. The straight-chain FFAs are generally metabolized through β-oxidation and released from the myocardium, while the development of modified FFAs is based on the concept of myocardial retention from metabolic trapping [56].

Radiolabeled Fatty Acids for PET

A physiological radiotracer 1-[^{11}C]palmitate (Fig. 16.10) was the first FFA introduced to image fatty acid metabolism of the heart [57]. Subsequently, 14(*RS*)-[^{18}F]fluoro-6-thia-heptadecanoic acid (FTHA) was developed as a metabolically trapped radiotracer [58].

Fig. 16.10 PET and SPECT radiotracers of free fatty acid analogs to assess myocardial metabolism
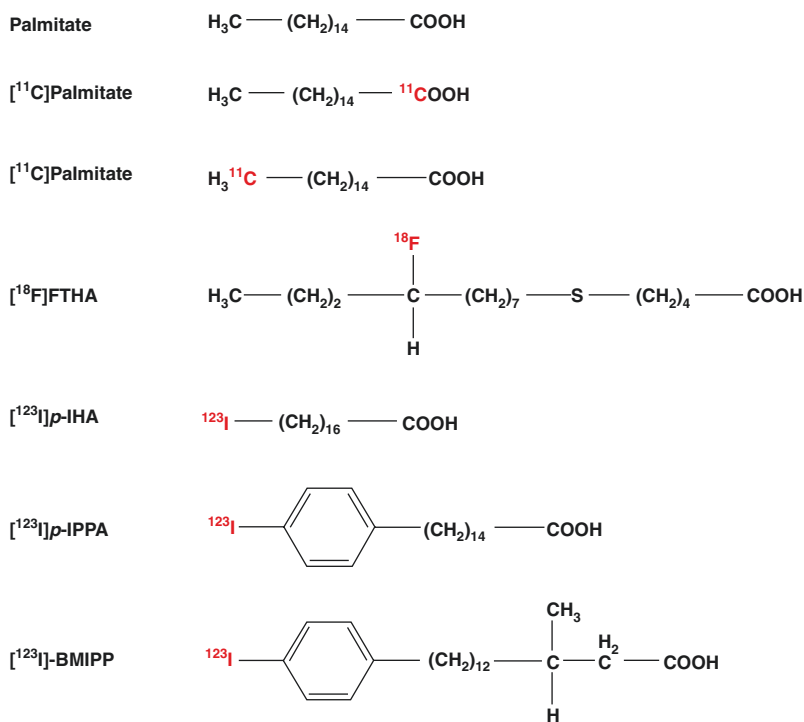
[^{11}C]Palmitate is biologically identical to non-radioactive circulating palmitate. The first-pass extraction fraction (0.67) is relatively high and the initial uptake, and regional distribution in the myocardium are largely determined by MBF [34]. It clears from the myocardium in a biexponential fashion. Once the tracer is taken up into the myocardium, β-oxidation breaks it down to generate acetyl-CoA. This [^{11}C] acetyl-CoA is oxidized via the citric acid cycle and finally released from the myocardium in the form of [^{11}C]CO$_2$. The rapid clearance fraction corresponds to β-oxidation, whereas the slow-washout fraction reflects the turnover rate of the intracellular lipid pool and is an index of FFA metabolism [56]. In severely ischemic myocardium, the regional uptake of [^{11}C]palmitate is reduced. The PET images provide a qualitative and semiquantitative evaluation of fatty acid metabolism. The quantitative value of myocardial fatty acid use and oxidation is difficult to estimate in absolute units (milliequivalents of free fatty acid per minute per gram of myocardium). Since the C-1 label of 1-[^{11}C]palmitate is removed in the initial step of β-oxidation, ω-[^{11}C]palmitate was proposed as a potential tracer to prolong the myocardial retention of trapped metabolites [59].

With FTHA, the rate of metabolic trapping is thought to be proportional to the rate of β-oxidation. In patients with CAD, estimates of myocardial FFA utilization (MFAU) in a normal myocardium were found to be approximately 5.8 ± 1.7 μmol 100 g^{-1} min^{-1}, while in patients with CHF, the MFAU was found to be elevated (19.3 ± 2.3 μmol 100 g^{-1} min^{-1}) [34, 60]. Further, because FTHA does not trace the FFA uptake under hypoxic conditions accurately, several ^{18}F analogs have been developed. It is still not clear which tracer is the most reliable or the most clinically useful PET tracer to image fatty acid metabolism in different cardiac diseases [46].

Radiolabeled Fatty Acids for SPECT

Since the 1970s several iodinated fatty acid tracers for SPECT have been developed (Fig. 16.10) by introducing radioiodine to the terminal position of fatty acids without significant alteration of the extraction efficiency, compared with the natural FFAs [55, 56, 61]. The two groups of iodinated fatty acid compounds include straight-chain FFAs and modified branched FFAs. In a clinical study, ^{123}I-16-iodoheptadecanoic acid (IHA), an analog of stearic acid demonstrated a high-quality image early after injection but, the image quality deteriorated rapidly because of the rapid reduction of myocardial counts and increase in background counts due to deiodinated radioiodine [62]. To prevent in vivo deiodination, the phenyl fatty acids were developed by attaching iodide to the para or ortho position of the phenyl ring (IPPA). For routine clinical use, however, the rate of metabolism and clearance of IPPA is still relatively too fast for SPECT imaging studies.

In order to develop a tracer with more prolonged cardiac retention and with improved image quality, a methyl branching was introduced at the β-carbon position to slow the myocardial clearance by inhibiting β-oxidation. Two iodinated branched fatty acid analogs, 15-(*p*-iodophenyl)-3-*R*,*S*-methylpentadecanoic acid (BMIPP) and 15-(*p*-iodophenyl)-3,3-methylpentadecanoic acid (DMIPP) were, therefore, developed [55, 56, 63, 64]. FTHA has shown to be metabolically retained in the myocardium and has very good imaging properties in normal human subjects, and in patients with CAD. The concept underlying BMIPP imaging is metabolic trapping of BMIPP-CoA, similar to FDG, but by inhibition of β-oxidation through the introduction of methyl branching, at the β-carbon position. Under the condition of ischemia, a reduction in BMIPP uptake is observed, reflecting the reduction in ATP production due to depressed oxidative fatty acid metabolism and substrate shift from fatty acids to glucose (Fig. 16.11). When compared with myocardial perfusion imaging, BMIPP imaging enables "ischemic memory imaging," with detection of previous myocardial ischemia (metabolically stunned myocardium) and viable but chronically dysfunctional myocardium (hibernating myocardium) [55]. Also, in cardiomyopathy, BMIPP imaging may be useful for the early detection of HCM, the differentiation of ischemic cardiomyopathy from idiopathic DCM, and also for the
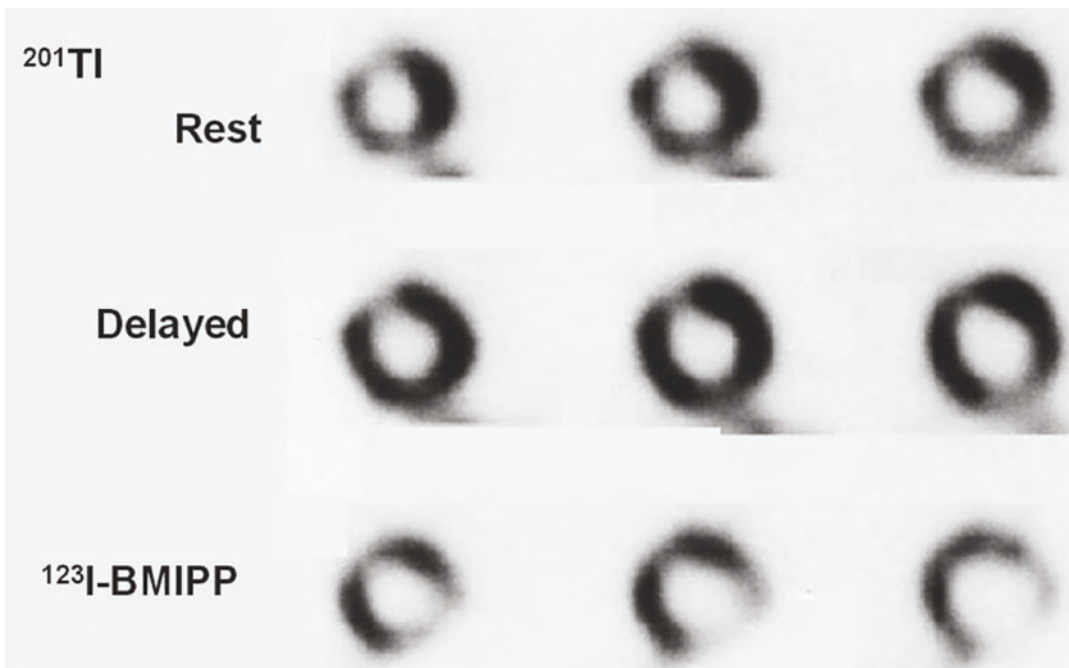
Fig. 16.11 Myocardial metabolic imaging using ^{123}I-BMIPP in patients with unstable angina: Although ^{201}Tl scans did not show definite perfusion abnormalities, decreased BMIPP uptake was noted in the lateral region, indicating decreased regional myocardial fatty acid metabolism [56]
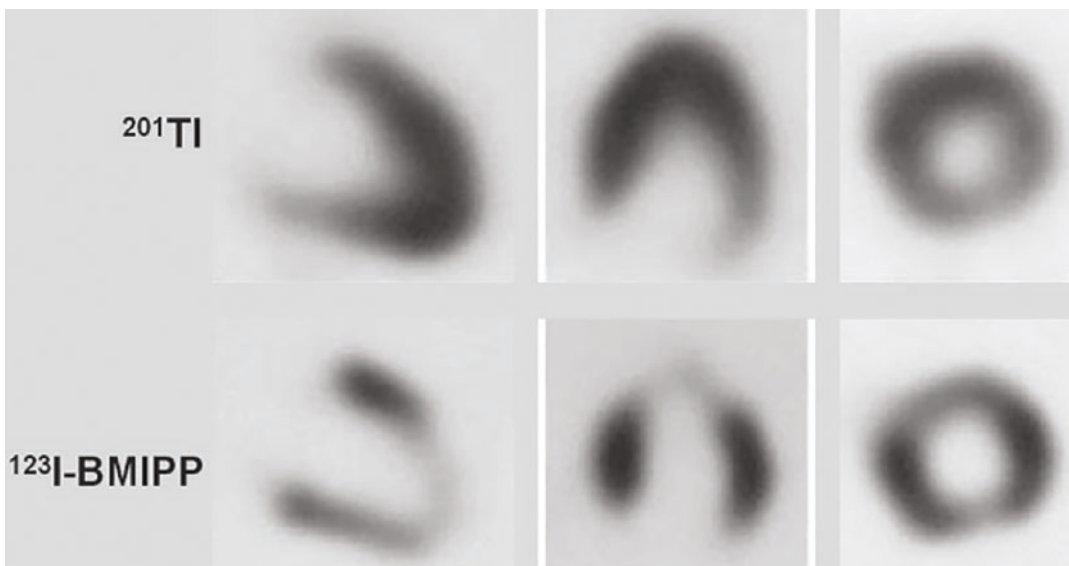
Fig. 16.12 Myocardial metabolic imaging using ^{123}I-BMIPP in patients with hypertrophic cardiomyopathy (HCM). There is increased ^{201}Tl uptake in the apex to the anteroseptal wall but, BMIPP uptake is reduced in that area. Discordant BMIPP uptake less than blood flow in the hypertrophic area is a rather early phenomenon of HCM [55]

prediction of prognosis (Fig. 16.12). ^{123}I-BMIPP has been the most commonly used commercially available SPECT tracer to assess fatty acid metabolism in patients, especially in some of the European countries and in Japan.

16.3.2.3   Oxidative Metabolism

The assessment of myocardial oxidative metabolism involves the estimation of myocardial ventricular oxygen consumption (MVO_2) in absolute units, mL $min^{-1}$ g^{-1}. Under steady-state conditions, MVO_2 provides an accurate measure of overall myocardial metabolism regardless of which substrate or fuel is used. Based on the determination of myocardial blood flow, using [15O] water, myocardial blood volume using [15O]CO, and oxygen inhalation studies using [15O]O_2, myocardial oxygen extraction can be determined. The MVO_2 is then estimated using the plasma oxygen content as the arterial input function. In normal subjects, an average MVO_2 is 0.097 ± 0.022 mL min^{-1} g^{-1} [65]. While this method provides an absolute quantitative estimation of regional MVO_2 in various cardiac diseases, the PET imaging studies involving 15O ($T_{1/2}$ = 2 min) are not practical for routine clinical use.

[11C]Acetate

Acetate is avidly extracted from the coronary circulation and rapidly distributed in the myocardium. In cytosol, it is activated to acetyl-CoA and, subsequently, enters the TCA cycle in the mitochondria for oxidation and metabolism to [11C]O_2 and water (Fig. 16.8). It is important to realize that the myocardial kinetics of [11C] acetate is independent of the metabolic milieu, such as the blood glucose level or FFA concentration in the blood [66]. Following intravenous bolus administration, the myocardial washout of activity demonstrates a biexponential clearance. The myocardial oxidative metabolism, however, can be estimated based on the rapid washout rate determined, using monoexponential curve fitting of the time–activity data [67]. Because of its high myocardial first-pass extraction fraction, the early phase (1–3 min) is flow-dependent and provides an estimation of regional myocardial perfusion [68]. With [11C]acetate, simultaneous determination of myocardial blood flow and oxygen consumption can be performed with a single data acquisition [46].

16.3.3   Myocardial Presynaptic Adrenergic Neuronal Imaging

The cardiac sympathetic nervous system remains of interest for molecular imaging, due to the direct relationship between sympathetic activity, cardiomyocyte β-adrenoceptor expression, and ventricle remodeling. In the failing heart, increased sympathetic drive leads to increased norepinephrine stimulation and downregulation of adrenoceptors, the pathophysiology underlying the common use of β-blocker therapy to normalize contractility [69].

The mammalian heart is characterized by dense adrenergic innervation with a norepinephrine (NE) concentration gradient from the atria to the base of the heart and from the base to the apex of the ventricles. In contrast, parasympathetic innervation is distributed throughout the atrial and ventricular walls, with a gradient from the former to the latter, with acetylcholine (ACh) being the main neurotransmitter. Both, the sympathetic and parasympathetic tones control the rate of the physiologic stimulation and conduction, while the contractile performance is primarily modulated by sympathetic neurotransmission. The major neurotransmitters of the sympathetic and parasympathetic systems, NE and ACh, define the stimulatory and inhibitory physiologic effects of each system.

The NE is produced from tyrosine within a neuron (Fig. 16.13). Tyrosine is converted to DOPA, which is converted to dopamine by *DOPA decarboxylase*. Dopamine is then transported by a vesicular monoamine transporter (VMAT2) into the vesicles, where it is converted to NE by dopamine β-hydroxylase. Adrenergic nerve stimulation leads to the release of NE into the synapse. The sympathetic neurotransmission in the heart is mediated by adrenoreceptors of type β_1 and β_2, which are located on the myocardial cells. Only a small amount of NE, released into the
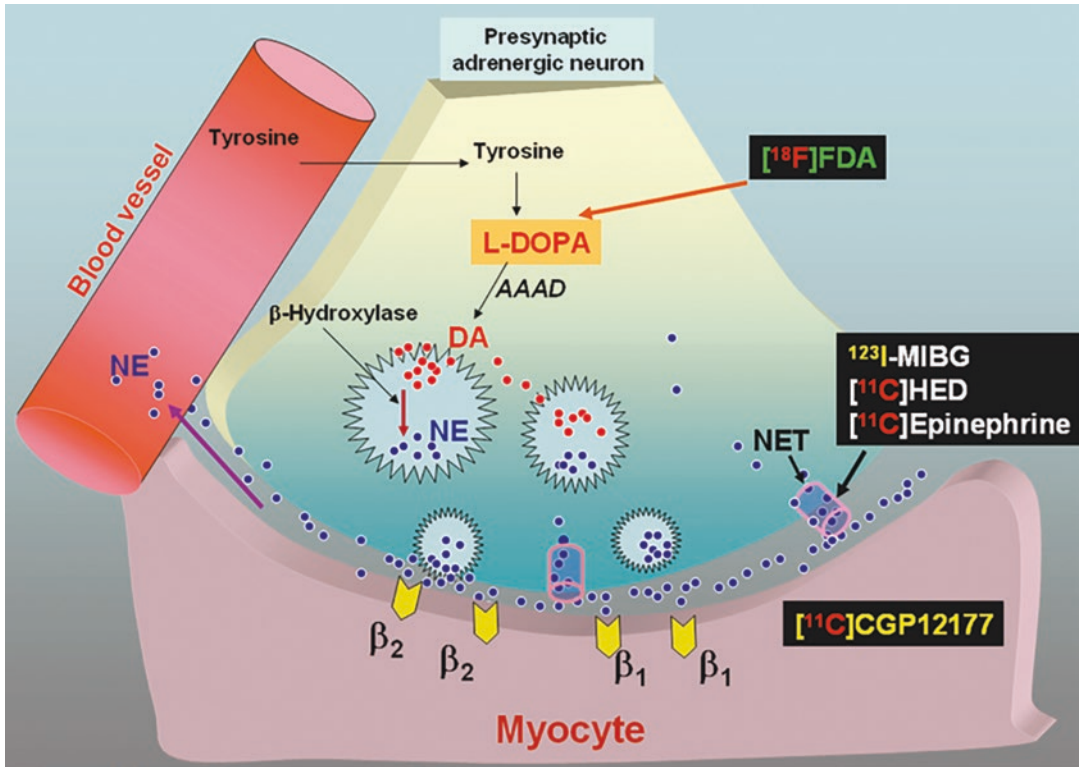
Fig. 16.13 Adrenergic neurotransmission in the heart. PET and SPECT tracers for imaging presynaptic adrenergic neurons and postsynaptic adrenoceptor density
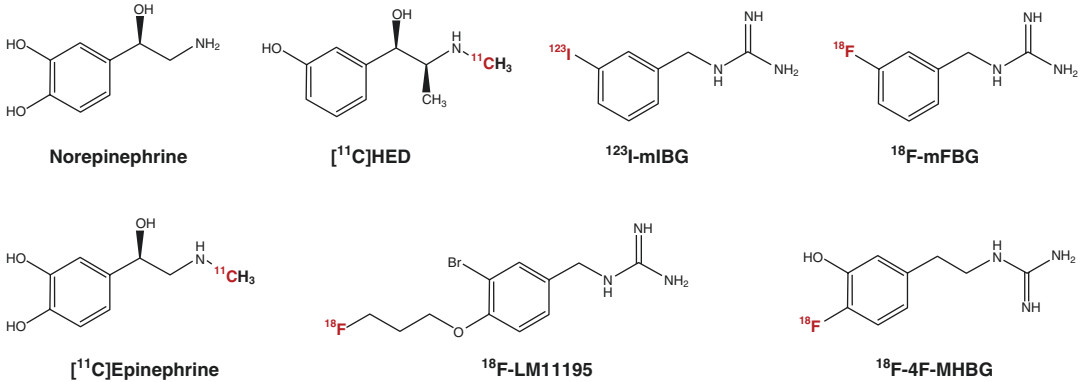

Fig. 16.14 Norepinephrine analogs labeled for PET and SPECT imaging studies to assess cardiac neurotransmission

synapse, binds to the adrenoreceptors while most of the NE in the synapse undergoes reuptake (uptake-1 mechanism) back into the presynaptic nerve terminal by a saturable and Na^+, temperature, and energy-dependent mechanism (uptake-1) via a neuronal norepinephrine transporter (NET) or by nonsaturable, and not Na^+, temperature, or energy dependent mechanism (uptake-2). The free cytosolic NE is degraded by MAO to dihydroxyphenylglycol (DHPG).

16.3.3.1　Radiotracers for Presynaptic Sympathetic Innervation

All of the radiotracers developed for imaging cardiac sympathetic innervation are analogs of NE (Fig. 16.14). As discussed earlier, NE within the synapse is transported back into the presynaptic neuron terminals via NETs, based on the uptake-1 mechanism. Structural analogs of NE are also transported into synaptic terminals by this uptake-1 mechanism [70].

[^{11}C]Hydroxyephedrine (HED)

PET radiotracers (Fig. 16.14) resemble the endogenous NE more closely than ^{123}I-MIBG. Two different groups of PET tracers are available for presynaptic sympathetic imaging of the heart; radiolabeled catecholamines and radiolabeled catecholamine analogs [71, 72].

[^{11}C]Hydroxyephedrine (HED) is the most widely used tracer for cardiac neuronal imaging. HED has a high affinity for the NETs and shows negligible non-specific binding. Following the transport into the presynaptic terminal, it is not metabolized by *MAO* or *COMT* enzymes [71, 73]. Since HED is not metabolized, it diffuses out of the nerve terminal and is transported back into the nerve terminal. Therefore, HED myocardial retention is actually dependent on both the continuous release and reuptake by NETs [72].

While HED is a false neurotransmitter, [^{11}C] epinephrine (EPI) is a more physiological tracer since it is primarily a circulating hormone produced together with NE by the adrenal medulla and other chromaffin tissues. Unlike HED, EPI is degraded by MAO but, its storage in the vesicles

is very efficient, preventing it from degradation and causing slow clearance of the tracer from the heart. Therefore, EPI reflects the whole cascade of uptake, metabolism, and storage of neurotransmission, while the primary target for HED and MIBG is the uptake-1 system. Both, HED and EPI can be synthesized with high chemical purity (>95%) and SA (33–74 GBq μmol^{-1}).

^{123}I-MIBG

Guanethidine is a potent neuron-blocking agent that acts selectively on sympathetic nerve endings. Based on this molecule, ^{131}I-*meta*-iodobenzylguanidine (MIBG) was initially developed as an agent for imaging tumors of adrenal medulla origin [74]. The avid heart uptake and retention of MIBG observed in animal biodistribution studies strongly suggested that MIBG might also be successfully used for imaging cardiac sympathetic neurons [75]. Consequently, ^{123}I-MIBG was developed for imaging the heart, in patient studies [76]. MIBG is transported into presynaptic terminals by the uptake-1 mechanism and is stored mainly in the NE storage vesicles. In other words, MIBG and NE have the same mechanisms for uptake, storage, and release. Unlike NE, MIBG does not bind to receptors on the myocardial cell membrane, and does not undergo any metabolism within the presynaptic terminals [71, 77]. As a result, MIBG is retained in sympathetic nerve endings, and provides clinically useful diagnostic information for different cardiac diseases.

For practical clinical application, the SA and radio-chemical purity of MIBG are critical factors. The unlabeled catecholamines (cold MIBG) may compete with the labeled tracer and may not only limit image quality but, also, cause pharmacologic action via adrenoceptor activation. The specific activity (SA) of commercial preparation of ^{123}I-MIBG (Adreview) is ~1.0 GBq/mg and is sub-optimal for imaging studies. Therefore, high SA ^{123}I-MIBG (>50 GBq) may be beneficial for clinical studies.

To overcome the limitations of [^{11}C]HED and ^{123}I-MIBG, several ^{18}F-labeled MIBG analogs

have been developed [78–81]. ^{18}F-*N*-[3-bromo-4-(3-fluoro-propoxy)-benzyl]-guanidine (^{18}F-LMI1195) showed specific uptake in the heart as assessed by in vivo PET imaging in rabbits. Stable retention under a desipramine chase indicates promising properties as a new class of PET tracer for visualizing the cardiac nervous system, mimicking physiologic norepinephrine turnover at nerve terminals [79]. In a phase I clinical study, [^{18}F]4F-MHPG and [^{18}F]3F-PHPG have demonstrated that both tracers provide high-quality cardiac PET images, with extremely low uptake in lungs and acceptable uptake levels in the liver. Comparing the two tracers, an advantage of [^{18}F]4F-MHPG is its more rapid clearance from the liver [78].

16.3.3.2   Radiotracers for Cardiac Neuroreceptors

The sympathetic adrenoreceptors β_1 and β_2, located on the myocardial cells, play a major role in the regulation of cardiac function. In the healthy myocardium, β_1-receptors are the most abundant, forming 80% of all β-receptors, while in heart failure the proportion of β_2-adrenoceptors may increase to 50% [72, 82]. Also, sympathetic activation results in the elevation of systemic catecholamine levels and subsequent downregulation of β-receptors. Many different pharmaceuticals, that act as cardiac receptor antagonists, such as β-blockers or β-receptor antagonists, are used in cardiological practice. The efficacy of these drugs depends on many different factors, especially the β-receptor density. Noninvasive imaging and quantitation of β-receptor density (B_{max}) before initiation of therapy with β-blockers might predict the outcome of therapy.

[^{11}C]CGP-12177 (4-(3-*t*-butylamino-2-hydroxypropoxy)-benzimidazol-1), a hydrophilic, nonselective antagonist, that binds to the β-receptors with high affinity (0.3 nmol L^{-1}), was one of the first ligands developed for cardiac PET adrenoreceptor imaging studies [83]. So far, [^{11}C]CGP-12167, is the only tracer, that has been used more extensively in patient populations, such as patients with dilated hypertrophic and arrhythmogenic right ventricular cardiomyopathy [71,

72]. Because of the difficulties involved in the synthesis of this tracer, the *N*-isopropyl derivative, [^{11}C]CGP-12388 was developed as an alternative for clinical use [84].

16.3.3.3   Clinical Applications

Sympathetic nerve endings are easily damaged by ischemia, in comparison to myocardial cells, and sympathetic function disorders are known to persist for a certain period even after alleviation of the ischemia. The utility of cardiac sympathetic imaging is most widely studied in patients who have heart failure with reduced ejection fraction (HFrEF) [6, 85, 86] (Fig. 16.15).

PET imaging of the cardiac autonomic nervous system has advanced in recent years and multiple pre- and postsynaptic tracers have been used to determine the involvement of the sympathetic dysinnervation at different stages of heart diseases, such as ischemia, heart failure, and arrhythmia. In general, [^{11}C]HED is the most widely used PET tracer for cardiac neuronal imaging. In a healthy heart, there is an even distribution of HED over the left ventricle, making it a valuable tracer for detecting specific regional defects of the presynaptic sympathetic system in disease [72]. In patients with dilated cardiomyopathy there is a loss of neurons or downregulation of uptake-1. In a patient with idiopathic dilated cardiomyopathy and severely reduced left ventricular ejection, the myocardial retention of HED was reduced significantly (Fig. 16.16). In heart failure patients, the extent of denervation denoted by HED retention predicts sudden cardiac arrest [87, 88]. The [^{11}C]HED is the most commonly used PET tracer for sympathetic nerve imaging. The superior sensitivity and quantitative capability of HED-PET allow for reliable assessment of regional neurohumoral abnormalities.

In patients with unstable angina, MIBG-SPECT makes it possible to identify the culprit coronary artery with a high probability and, thus, is of diagnostic value (Fig. 16.16). In patients with heart failure, the increased washout rate and the decreased heart/myocardium (H/M ratio) on the delayed MIBG image become marked with an increase in hypofunction in the left ventricle, regardless of the underlying diseases [89].
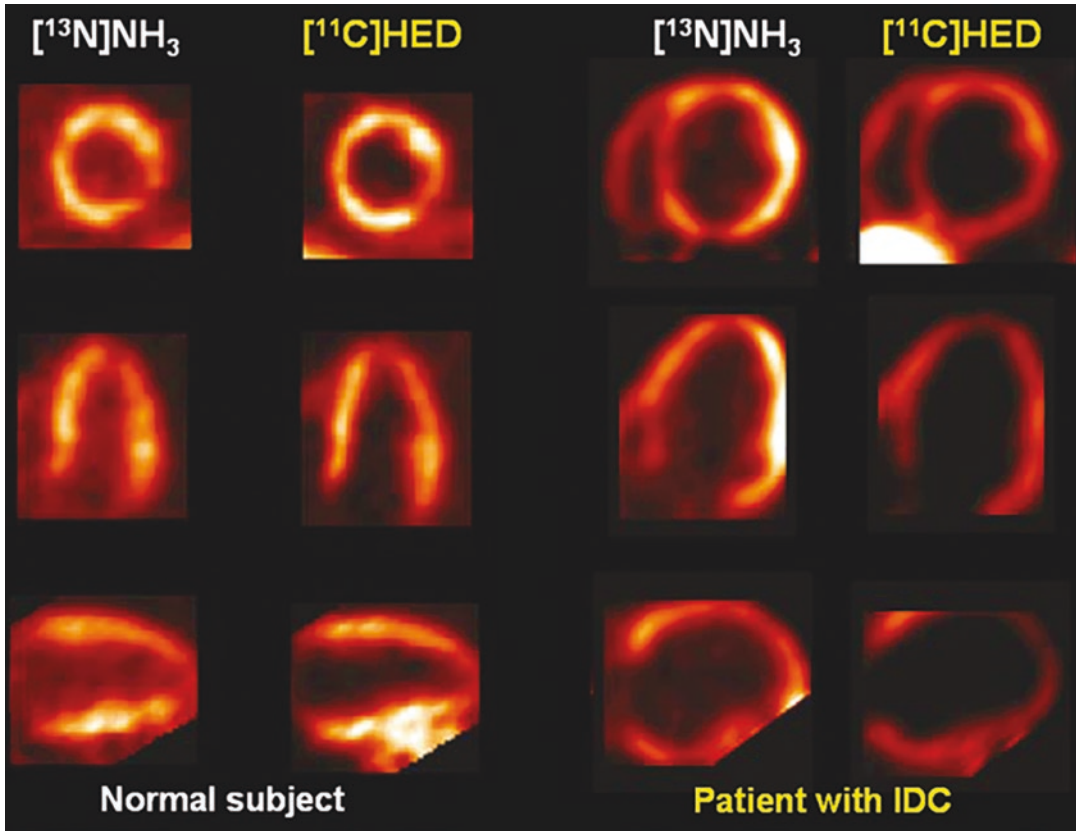
Fig. 16.15 [¹¹C]HED-PET for imaging presynaptic sympathetic innervation in the heart. In a normal subject, there is an even distribution of HED in the heart similar to the myocardial perfusion images of [¹³N] ammonia-PET. In a patient with idiopathic dilated cardiomyopathy (IDC) and severely reduced left ventricular ejection fraction (22%), there is a significantly reduced retention of HED compared with the myocardial perfusion [72]

Similar results have been reported from studies on dilated cardiomyopathy, hypertrophic cardiomyopathy (HCM), valvular heart disease, pulmonary hypertension, amyloidosis, and diabetes [77]. ¹²³I-MIBG planar/SPECT has been used in numerous studies to document regional denervation for arrhythmic event risk assessment [90].

16.3.4 Cardiac Sarcoidosis (CS)

As discussed earlier, CS occurs most commonly in patients who are 20–40 years old, with a predominance of female patients. The cardiovascular system is the third most common site of sarcoidosis and is involved in 25–50% of patients. Patients with heart failure have a particularly poor prognosis. Because corticosteroid therapy improves cardiac function and prognosis, accurate diagnosis, and timely intervention for improving outcomes is necessary [25, 91].

In the 1990s, it was documented that a combination of ²⁰¹Tl chloride and ⁶⁷Ga citrate scintigraphy may be useful not only in the diagnosis of cardiac sarcoidosis but, also, in the prediction of the effects of corticosteroids [92]. ⁶⁷Ga-SPECT/CT scanning was also shown to be a very useful diagnostic imaging technique because it improves the diagnostic specificity of ⁶⁷Ga-SPECT to allow the highly specific diagnosis of cardiac sarcoidosis [93].

It is well recognized that glucose metabolism is increased in inflammatory cells. Macrophages and CD4+ T cells present in sarcoid granulomas have a high energy demand requiring increased
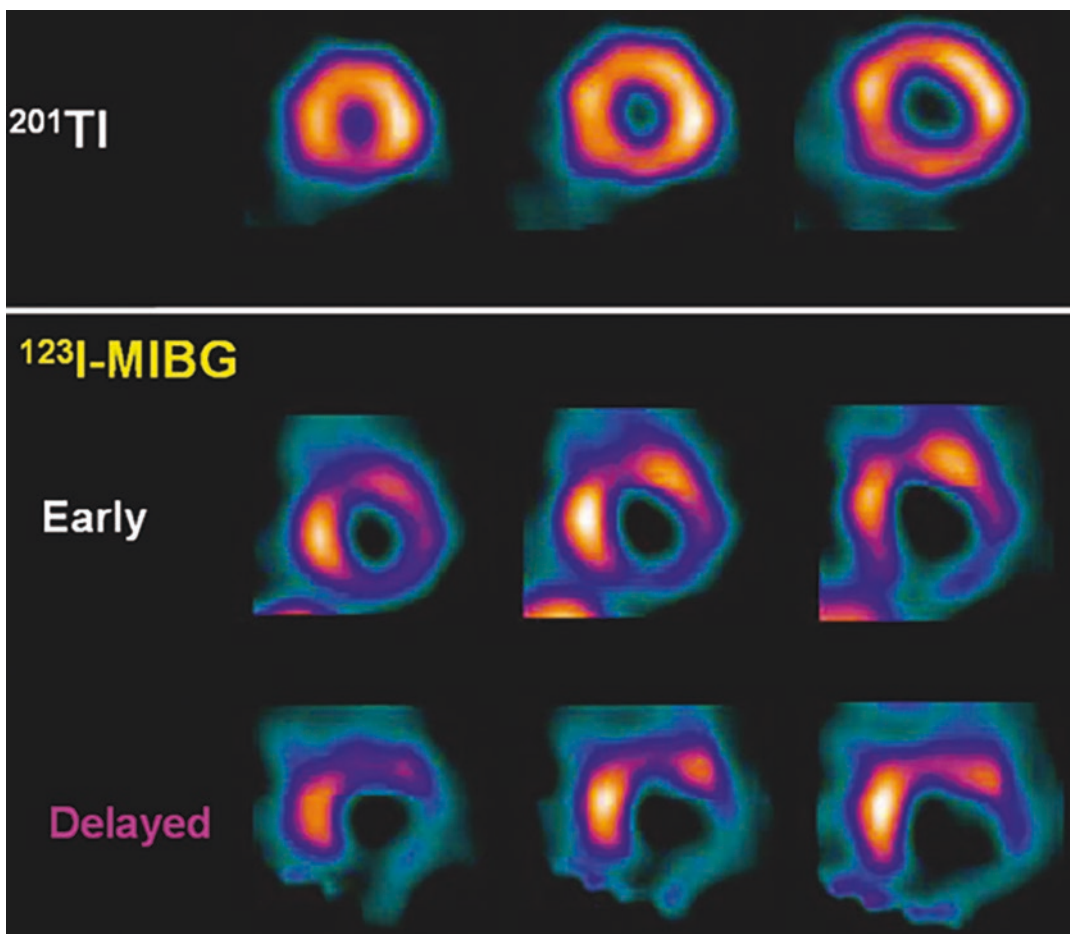
Fig. 16.16 ^{123}I-MIBG imaging in patient with ischemic heart disease. In a patient with unstable angina, myocardial perfusion with ^{201}Tl-SPECT at rest was relatively normal with no significant findings. In contrast, MIBG SPECT (early and delayed) showed decreased accumulation in the infero-posterior wall. Coronary angiography performed later, and advanced stenosis was recognized in the proximal part of the RCA [77]

glycolysis and, therefore, cellular inflammation can be detected by PET/CT using [^{18}F] FDG. Consequently, the clinical utility of FDG PET/CT for diagnosis and management in patients with known or suspected CS was investigated. Background cardiomyocyte uptake, however, represents a major limitation of FDG-PET scan, and may be suppressed by fasting, fatty meals, and heparin infusion, though nonspecific uptake may still be present in some patients [91].

FDG-PET is currently the best clinical tool for the assessment of myocardial inflammation in CS [25, 94]. Suppression of baseline myocardial FDG uptake via fasting and adoption of a very low carbohydrate diet allows for visualization of FDG uptake by inflammatory cells. The optimal PET protocol used to evaluate CS requires rest myocardial perfusion, cardiac and whole body FDG-PET imaging. FDG-PET imaging provides a good diagnostic accuracy for CS. However, accurate interpretation may be hampered by physiologic accumulation of FDG in the myocardium, which is seen in up to 20% of patients even after elaborate preparation [94]. Most patients with cardiac sarcoidosis have extracardiac involvement, and identification of the extracardiac lesions is essential in diagnostic evaluation of patients with suspected CS. The major advantage
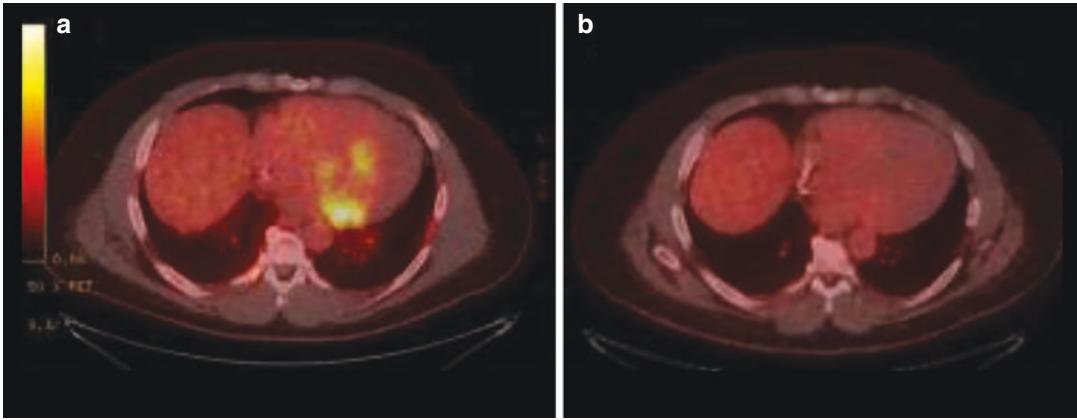
Fig. 16.17 Representative [¹⁸F]FDG-PET images from a patient with cardiac and pulmonary sarcoidosis. Baseline cardiac FDG-PET images (Panel **a**) demonstrate a moderate-sized area of abnormal FDG uptake extending to medial and basal segments of the inferior and inferoseptal wall. After treatment with prednisone and mycophenolate mofetil, there is resolution of cardiac FDG uptake (Panel **b**) [25]

of whole-body FDG PET/CT is that it enables evaluation of the systemic extent of sarcoidosis beyond the myocardium. Figure 16.17 shows the diagnostic value of FDG-PET in CS, and to monitor treatment response. The advantage of FDG-PET in the diagnosis of CS, the detection of the extracardiac sarcoidosis involvement, and the response to therapy is shown in Fig. 16.18.
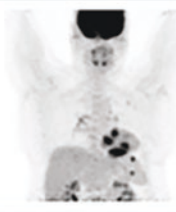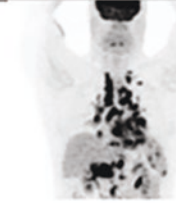
Radiotracers that do not have any uptake in the myocardium but, are taken up by inflammatory cells have also been evaluated for imaging CS. [¹⁸F]Fluorothymidine (FLT), a tracer to study cellular proliferation and DNA synthesis has been reported to be useful for the detection of CS [91, 96]. The main advantage is that FLT PET/CT can provide detectability as high as that for FDG PET/CT but, without fasting or change in the diet. In CS lesions containing granulomas with high-turnover traits, proliferation tracers accumulate predominantly in active lesions. A correlation between FLT uptake and myocardial scarring was observed indicating that FLT-PET/CT allows detection of areas that are developing into myocardial scars [97].

Somatostatin receptors (SSTRs), specifically subtype 2, are expressed not only in neuroendocrine tumors (NETs) but, also, on the surface of activated inflammatory cells such as macrophages, epithelioid cells, and multinucleated giant cells, which are the main constituents of sarcoid granuloma [98]. SSTR-agonists such as ¹¹¹In-DTPA-octreotide (Octreoscan) and ⁶⁸Ga labeled Dotatoc, dotatate, and Dotanoc have shown potential clinical utility for detecting CS [99–102]. SSTR imaging has the potential for differentiation of active CS lesions from those in the chronic phase because fibrotic tissue, which is seen in the chronic phase, lacks extensive SSTR expression [91].

16.3.5 Cardiac Amyloidosis (CA)

CA is more prevalent than previously expected, contributing to significant cases of heart failure with preserved ejection fraction [103]. Recent developments in treatment strategies have also shown the importance of early and accurate diag-

Fig. 16.18 FDG-PET to assess response to therapy in cardiac sarcoidosis (CS). Examples of using ^{18}F-FDG PET to assess response to therapy. (Top) Patient with no response to treatment. (Bottom) Patient with marked response of both extra CS and CS to treatment. (From [95])

nosis in CA. In patients with CA with amyloid fibril protein (AL-CA), novel antiplasma cell therapy has been proved effective, even in populations of patients with refractory disease. A lower mortality rate and improved overall survival can be achieved with earlier diagnosis of AL amyloidosis [42]. Introduction of therapy with the FDA-approved drug, tafamidis, which binds to transthyretin (TTR) and inhibits tetramer dissociation and amyloidogenesis, has improved outcomes in patients with ATTR-CA [26, 91]. The improved therapeutic options render accurate and early diagnosis critical.

Several ^{99m}Tc labeled bone-seeking SPECT radiopharmaceuticals (Fig. 16.19) have shown the clinical utility to detect and provide confirmatory diagnosis of CA. Additionally, PET techniques are emerging in amyloidosis [91, 104–108]. Although the role of the bone-seeking agent ^{18}F-sodium fluoride for the workup of ATTR-CA is still under debate because of low signal intensity, PET amyloid markers (Fig. 16.19) originally developed for neurology to identify β-amyloid in neurodegenerative disease have also been used to detect cardiac amyloidosis.

Fig. 16.19 Radiopharmaceuticals for imaging cardiac amyloidosis

Fig. 16.20 (Left) ^{99m}Tc-pyrophosphate planar scan showing avid myocardial tracer uptake (Perugini grade 3, myocardial uptake greater than rib). (Right) Cardiac SPECT showing diffuse myocardial tracer uptake in short-axis images (top row), vertical long-axis images (middle row), and horizontal long-axis (bottom row). This scan is diagnostic of ATTR cardiomyopathy if serum and urine studies for AL amyloidosis are negative. (From [106])

A resurgence of interest and an improved understanding of the performance characteristics of CA imaging with SPECT using [99mTc]-labeled bone-seeking tracers, such as PYP (pyrophosphate) DPD (3,3-diphosphono-1,2-propanodicarboxylic acid), and HEDP (hydroxymethylene diphosphonate), have been transformative for the field of CA and nuclear cardiology as well. The mechanism of uptake of bone agents is attributed to the binding to the microcalcifications in the amyloid fibrils, especially in the ATTR-CA but, not in the AL-CA. A meta-analysis of 5 studies found a sensitivity of 92.2% and specificity of 95.4% for detecting ATTR-CA, whereas its diagnostic performance for AL amyloidosis is poor (sensitivity and specificity <50%) [91]. ATTR-CA shows higher uptake of bone tracer (Fig. 16.20) because the density of microcalcifications is greater in ATTR amyloidosis than in AL amyloidosis [109]. Binding mechanisms and the effect of fibril type on tracer affinity need to be clarified. Thus, whereas scintigraphy with the [99mTc] bone-seeking tracers is a remarkably useful test for patients with suspected amyloidosis, vigilance is required to identify and further evaluate cases in which there is discordance between clinical and imaging findings [106].

[11C]PiB, a derivative of thioflavin-T, has been used with success in β-amyloid imaging in neurodegenerative diseases and has also been shown to accurately identify cardiac AL-amyloidosis [110]. Thus, it may prove to be useful to monitor response to therapeutic interventions or for prognostication in the realm of cardiac amyloidosis. Pilot studies reported that [18F]-labeled amyloid tracers, such as [18F]Florbetapir, have the potential to detect CA but, well clinical studies need to confirm the accuracy of the β-amyloid tracers for the diagnosis of CA [111].

Aprotinin (Trasylol), a small protein (6.511 kDa) bovine pancreatic trypsin inhibitor (BPTI) is an antifibrinolytic molecule that inhibits trypsin and related proteolytic enzymes. It was reported that [99mTc]-aprotinin binds to amyloid deposits which contain proteases. Pilot studies documented the potential of this tracer to detect

CA. However, more studies are needed to confirm the pilot data [112, 113].

16.3.6   Cardiac Fibrosis

Fibrosis is the excessive accumulation of extracellular matrix typically found in the remodeling left ventricle, resulting from activation of cardiac fibroblasts. The feasibility of imaging matrix metalloproteinases using radiopharmaceuticals such as [111In]-RP782 or [99mTc]-RP805, which accumulate in remodeling vasculature and myocardium has been reported. However, matrix remodeling is a relatively late pathogenetic process in ischemic heart failure progression, which may restrict the benefit for many patients [114]. Since fibroblasts comprise up to 50% of the cellular content of the heart, and fibrosis is the consequence of fibroblast activation, a promising target for molecular imaging is the fibroblast activation protein (FAP), which exhibits low expression by quiescent cardiac fibroblasts but, is rapidly upregulated in response to injury stimuli, and during fibroblast transdifferentiation [115, 116]. Also targeting activated myofibroblasts can depict the active disease at a very early stage where treatments would likely have the most benefit.

The feasibility of PET imaging of activated fibroblasts with [68Ga]-FAPI-04, a FAP inhibitor was first demonstrated in a preclinical model of myocardial infarction. [68Ga]-FAPI-04 uptake in the injured myocardium peaked on day 6 after coronary ligation. The tracer accumulated intensely in the MI territory, as identified by decreased [18F]FDG uptake and confirmed by PET/MR and H&E staining [28]. Autoradiography and H&E staining of cross-sections revealed that [68Ga]-FAPI-04 accumulated mainly at the border zone of the infarcted myocardium (Fig. 16.21). Subsequently, several clinical studies documented the potential of 68Ga labeled FAPI radiotracers to image the activated fibroblasts in the myocardium [117–120]. Figure 16.22 shows [68Ga]-FAPI-04 PET/CMR in a patient after myocardial infarction. Recently, another FAP-
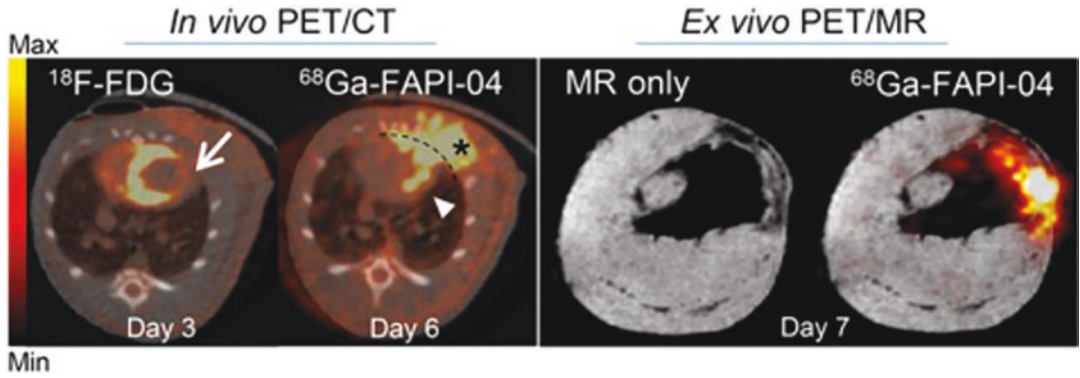
Fig. 16.21 Axial sections of in vivo PET/CT imaging with [^{18}F]FDG (day 3 after MI) and ^{68}Ga-FAPI-04 (day 6 after MI) and corresponding ex vivo PET/MRI with ^{68}Ga-FAPI-04 (day 7 after MI). [^{18}F]FDG image was used to identify areas of infarcted myocardium (arrow), where increased uptake of ^{68}Ga-FAPI-04 was apparent (arrowhead). ^{68}Ga-FAPI-04 exhibited elevated uptake in postsurgical scar (asterisk). The dashed line separates ^{68}Ga-FAPI-04 uptake in myocardium from surgical wound. High-resolution MR and PET/MR data confirmed infarcted area, where ^{68}Ga-FAPI-04 uptake was increased. (From [28])
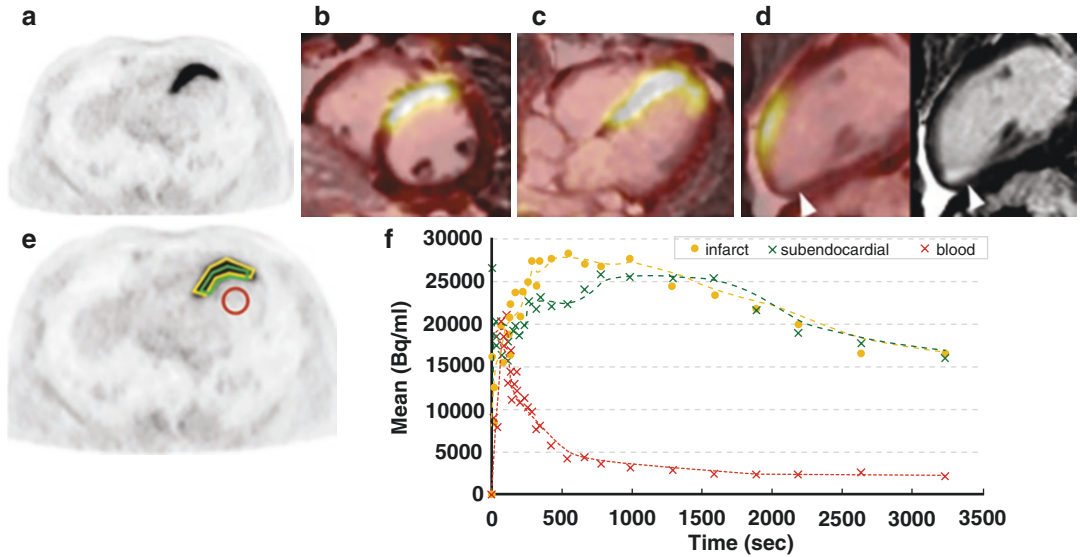
Fig. 16.22 ^{68}Ga-FAPI-04 PET/CMR in a patient after myocardial infarction. ^{68}Ga-FAPI-04 PET/CMR in a patient after acute STEMI in LAD territory and ^{68}Ga-FAPI-04 tracer kinetics. (**a**) Attenuation corrected axial PET. Fusion images of PET with 15 min late gadolinium enhancement sequences in (**b**) short axis, (**c**) horizontal long axis, and (**d**) vertical long axis and corresponding MR. Arrowhead indicates small mature scar. (**e**) Example placement of ROI for dynamic analysis. (**f**) ^{68}Ga-FAPI-04 tracer kinetics. Intense ^{68}Ga-FAPI-04 uptake was observed in anterior and anterior septum wall in LAD territory. No significant ^{68}Ga-FAPI-04 uptake is shown in the remote area similar to blood pool [119]

targeting PET radiotracer, ^{68}Ga-MHLL1, was evaluated for non-invasive tracking of dynamic fibrosis in an animal model. ^{68}Ga-MHLL1 displayed selective binding to FAP in the infarct and infarct border zone, as well as remote non-infarcted myocardium, post-MI [121].

Dedicated prospective clinical studies are necessary to determine the added value of FAP imaging of myocardial fibrosis for predicting functional outcomes in cardiac patients.

16.3.7 Inflammation and Atherosclerosis

Atherosclerosis is a well-known disease leading to cardiovascular events, including myocardial infarction and ischemic stroke. The biology of atherosclerosis (Fig. 16.23) provides a basis for the development of radiolabeled molecular imaging probes. Fundamentally, the process of inflammation regulates atherosclerosis. Specifically, the macrophage has emerged as the key cellular mediator of inflammation in atheroma, and participates in all phases of atherogenesis, including lesion initiation, progression, and complication [14, 19, 122].

The main structural change in the vascular wall in atherosclerosis is thickening, associated with the accumulation of lipid metabolism products in the intima, the development of fibrous transformation, necrosis and calcification, and the formation of atheroma. The growth of atherosclerotic plaque over time leads to increasing stenosis of the lumen of the vessel and impaired hemodynamics, which, within certain limits, can be partially or completely compensated both by the expansion of the vessel and by the elasticity of intact sections of the walls. Rupture of the plaque capsule, with subsequent thrombosis, can lead to both acute occlusion of the vessel itself

and embolism in its distal branches, which are direct causes of vascular events. Factors leading to a decrease in blood flow in the vessel can include either an increase in the size of the plaque itself, while maintaining its integrity, or a tear or complete rupture of the capsule with subsequent thrombosis on its surface or in the resulting crater. In addition, with the fragmentation of blood clots or the plaque itself, emboli may be formed that spread with the flow of arterial blood, occluding the lumen of blood vessels distal to the plaque. Atheroma that are prone to rupture are usually referred to as vulnerable. The concept of "vulnerable plaque" was first proposed by J. Muller et al. in 1989 to designate atherosclerotic plaques that do not affect hemodynamics but, at the same time, are dangerous from the point of view of thrombosis [16, 18, 123]. Fatal myocardial infarctions or sudden cardiac death have been presented as the first manifestation of coronary artery disease without preceding ischemic symptoms. Thus, vulnerable atherosclerotic plaque, also called 'active-forming' or 'rupture-prone' plaque, needs to be discriminated from stable plaques.

Thus, the biology of the atherosclerotic lesion itself provides the basis for the development of atherosclerosis-targeted molecular imaging probes (Table 16.1). A number of noninvasive
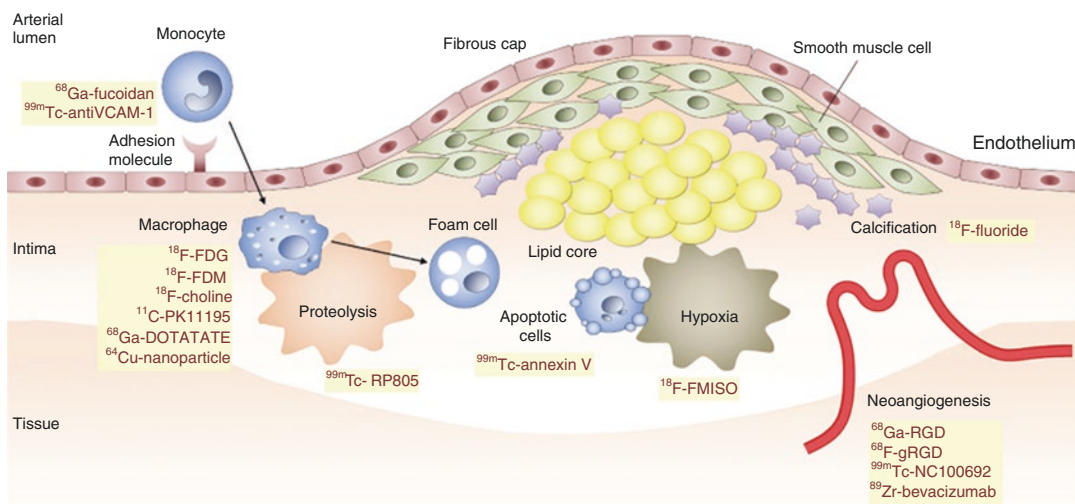
Fig. 16.23 Pathogenesis mechanism and molecular imaging targets in vulnerable plaque. (From Lee and Paeng [128])

and invasive diagnostic imaging techniques are being evaluated to accurately identify high-risk individuals, based on the presence of high-risk anatomical or structural features of atherosclerotic plaques in the coronary arteries. However, imaging coronary lesions is a challenge since they are contained within the wall of the vessel, and typically these lesions occupy a fraction of the vessel circumference and often extend from 1 to 2 cm. In addition, the residual activity of the radiotracer in blood, and the myocardial tissue uptake of the radiotracer make these lesions more difficult to detect. Molecular imaging technique based on specific β^+ emitting radiotracers, however, may provide the potential to detect coronary atherosclerotic lesions (Fig. 16.23).

16.3.7.1 Radiotracers for Vulnerable Plaque

In the 1970s it was first demonstrated that ^{125}I-labeled LDL localizes in the carotid atherosclerotic lesions in human subjects [124]. Since that time a number of radiolabeled LDL preparations, antibodies, and peptides have been extensively evaluated in animal models as potential radiotracers for imaging atherosclerotic lesions [19]. Molecular imaging based on PET and SPECT radiotracers is a rapidly evolving discipline that aims to develop imaging agents and technologies to visualize the specific molecular processes associated with vulnerable plaque. Several reviews discussed extensively the development and evaluation of PET and SPECT radiotracers for molecules imaging of atherosclerosis and vulnerable plaque [125–131].

In the 1990s, investigators at the Mount Sinai Medical Center in New York were the first to demonstrate that FDG-PET identifies macrophage-rich atherosclerotic lesions in hypercholesterolemic rabbits (Fig. 16.24). The histopathological data also suggested that the amount of FDG uptake in the lesion correlates with the macrophage density in the lesion [132, 133]. FDG accumulation in ruptured plaques has been first confirmed in the carotids of patients who presented transient ischemic attack where symptomatic carotid artery lesions exhibited higher FDG uptake than asymptomatic lesions [134]. Ex vivo incubation of excised carotid plaques with tritiated deoxyglucose confirmed
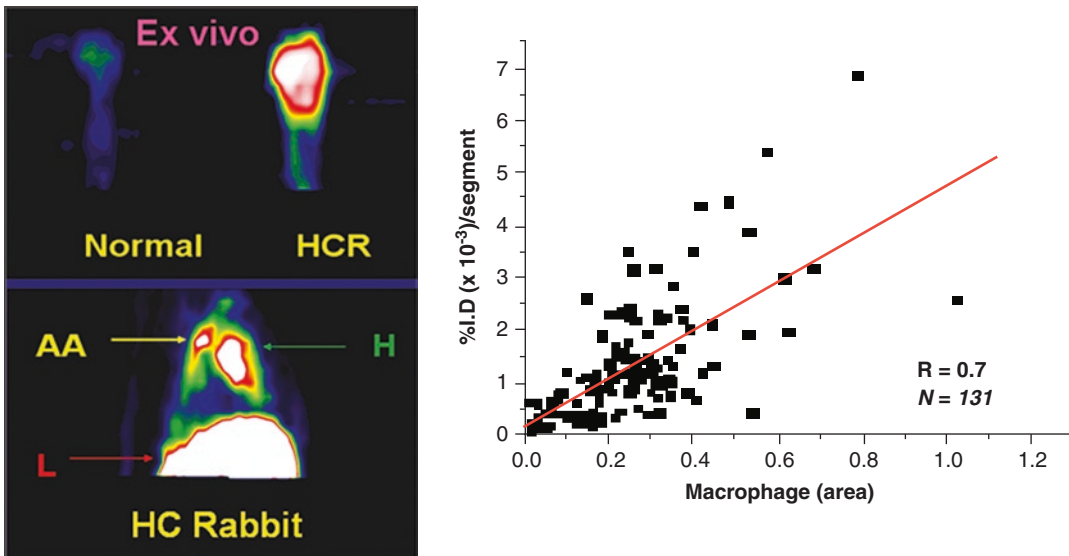
Fig. 16.24 [18F]FDG-PET to image atherosclerosis in hypercholesterolemic rabbits (HCR). The bottom in vivo image shows FDG uptake in the ascending aorta (AA) of HCR while the top ex vivo image shows comparison of HCR and normal aortas. The FDG uptake in the atherosclerotic lesions appears to depend on the macrophage density
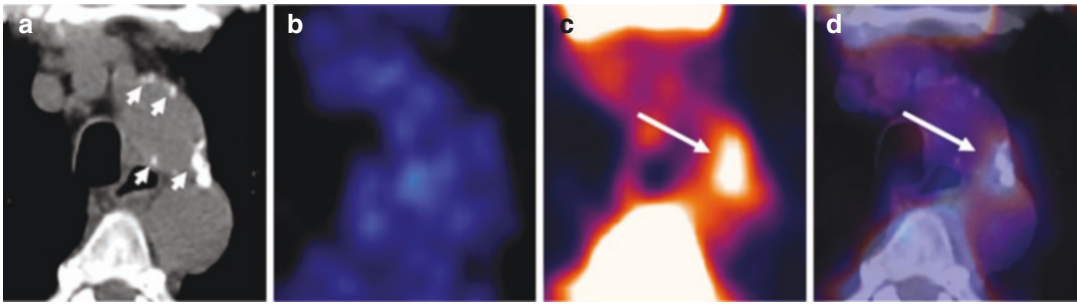
Fig. 16.25 Transaxial PET/CT images of atherosclerotic plaque in aortic arch: CT image (**a**), [18F]FDG PET image (**b**), 18F-fluoride PET image (**c**), and coregistered and fused [18F]FDG/18F-fluoride PET/CT image (**d**). Accumulation of 18F-fluoride is colocalized with large calcification but, not with [18F]FDG uptake. Short arrow five calcifications; long arrow five tracer uptake. (From [140])

that metabolic activities in plaques have a heterogeneous distribution and concentrate predominantly within macrophage-rich areas on autoradiographs [135]. Using carotid specimens from patients who had an endarterectomy after intravenous administration of [18F]FDG, microPET-MRI analysis confirmed that FDG accumulates mostly in regions of the plaque with high density of macrophages and foam cells but, also in regions with loose matrix containing activated smooth muscle cells, fibroblasts, and neovessels [136]. Subsequently, localization of FDG in human atheroma has been documented for the carotid arteries, aorta, and other major vessels [137, 138].

During the last two decades, FDG-PET imaging has emerged as a powerful tool to explore noninvasively inflammatory activities in atherosclerotic plaques providing new insights on the evolution of metabolic activities in the vascular wall over time. Vascular inflammation evaluated with FDG-PET appears to be an interesting marker of cardiovascular risk. Unlike circulating biomarkers, FDG-PET imaging provides a direct assessment of the intensity of inflammation in the vascular wall [127].

The most promising radiopharmaceutical that emerged in the past 10 years for plaque imaging is [18F]sodium fluoride [18F]NaF, a PET radiopharmaceutical for imaging metastatic bone lesions. [18F]NaF PET/CT (Fig. 16.25) showed the potential for the imaging of arterial calcification in major arteries [139, 140]. Fluoride-PET

has the potential to detect microcalcifications located in culprit lesions or high-risk plaques. In a prospective study of 40 patients with myocardial infarction and 40 with stable angina, [18F] NaF successfully identified vulnerable coronary lesions in 93% of the lesions implicated in causing the infarction [141]. Increased uptake was also observed in 45% of the patients with stable coronary artery disease being referred for invasive coronary angiography. In these patients and in 40 patients with stable angina, regions of 18F uptake correlated with intravascular ultrasound findings of microcalcification, a necrotic core, and positive remodeling. A major research study CAMONA (Cardiovascular Molecular Calcification Assessed by NaF PET/CT) was conducted to compare the performance of FDG- and NaF-PET for assessing atherosclerosis. Based on the data from this study, a recent review concludes that NaF as a PET tracer will play a critical role in detecting atherosclerosis in both normal aging as well as in patients with low or high risk for this potentially fatal disease [142]. Since [18F]Fluoride uptake is due to the presence of micro or macro calcifications, prospective clinical trials are needed to assess the prognostic value of [18F]Fluoride-PET as a novel biomarker for plaque vulnerability.

Several other potential atherosclerotic plaque imaging agents, many of which are still in preliminary preclinical and clinical studies, have been described. Some of these approaches include somatostatin receptor (SSTR) binding

ligands (^{68}Ga-Dotatoc, ^{64}Cu-Dotatate), the integrin $\alpha_v\beta_3$ binding RGD tripeptides analogs (^{18}F-Galacto-RGD, ^{18}F-Flotegatide, ^{18}F-Fluciclatide), and translocator protein (TSPO) specific inflammation markers ([^{11}C]PK11195; [^{18}F]PBR-714), chemokine receptor (CXCR4) specific ligands (^{68}Ga-Pentixafor). In addition, several potential molecular imaging targets and approaches which remain relatively unexplored in atherosclerosis. As imaging instruments (PET/CT and PET/MRI) become more advanced and artificial intelligence becomes more clinically useful, investigations will continue into the selection of appropriate molecular imaging probes for atherosclerosis and vulnerable plaque.

References

1. Berman DS, Shaw LJ, Hachamovitch R, et al. Comparative use of radionuclide stress testing, coronary artery calcium scanning, and noninvasive coronary angiography for diagnostic and prognostic cardiac assessment. Semin Nucl Med. 2007;37:2–16.

2. Klein R, Celiker-Guler E, Rotstein BH, deKemp RA. PET and SPECT tracers for myocardial perfusion imaging. Semin Nucl Med. 2020;50:208–18.

3. Schwaiger M, Bengel FM. From thallium scan to molecular imaging. Mol Imaging Biol. 2003;4:387–98.

4. Werner RA, Thackeray JT, Diekmann J, et al. The changing face of nuclear cardiology: guiding cardiovascular care toward molecular medicine. J Nucl Med. 2020;61:951–61.

5. Lairez O, Hyafil F, Manrique BA, et al. Assessment of coronary flow reserve in nuclear cardiology. Évaluation de la réserve coronaire en cardiologie Nucléaire. Médecine Nucléaire. 2020;44(3):172–80.

6. Farber G, Boczar KE, Wiefels CC, et al. The future of cardiac molecular imaging. Semin Nucl Med. 2020;50:367–85.

7. Glasenapp A, Hess A, Thackeray JT. Molecular imaging in nuclear cardiology: pathways to individual precision medicine. J Nucl Cardiol. 2020;27(6):2195–201.

8. Moghbel M, Al-Zaghal A, Werner TJ, et al. The role of PET in evaluating atherosclerosis: a critical review. Semin Nucl Med. 2018;48:488–97.

9. Yang M, Arsanjani R, Roarke MC. Advanced nuclear medicine and molecular imaging in the diagnosis of cardiomyopathy. AJR. 2020;215:1208–17.

10. Libby P. Inflammation in atherosclerosis. Nature. 2002;420:868–74.

11. Ross R. Atherosclerosis—an inflammatory disease. N Engl J Med. 1999;340:115–26.

12. Fuster V, Moreno PR, Fayad ZA, et al. Atherothrombosis and high-risk plaque part I: evolving concepts. J Am Coll Cardiol. 2005;46:937–54.

13. Spagnoli LG, Bonanno E, Sangiorgi G, et al. Role of inflammation in atherosclerosis. J Nucl Med. 2007;48:1800–15.

14. Falk E. Pathogenesis of atherosclerosis. J Am Coll Cardiol. 2006;47:C7–12.

15. Virmani R, Burke AP, Farb F, et al. Pathology of the vulnerable plaque. J Am Coll Cardiol. 2006;47:C13–8.

16. Muller JE, Abela GS, Nesto RW, et al. Triggers, acute risk factors and vulnerable plaques: the lexicon of a new frontier. J Am Coll Cardiol. 1994;23:809–13.

17. Moreno PR. Vulnerable plaque: definition, diagnosis, and treatment. Cardiol Clin. 2010;28(1):1–30.

18. Muller JE, Tawakol A, Kathiresan S, et al. New opportunities for identification and reduction of coronary risk: treatment of vulnerable patients, arteries, and Plaques. J Am Coll Cardiol. 2006;47:C2–6.

19. Vallabhajosula S, Fuster V. Atherosclerosis: imaging techniques and the evolving role of nuclear medicine. J Nucl Med. 1997;38:1688–96.

20. Naghavi M, Libby P, Falk E, et al. From vulnerable plaque to vulnerable patient. A call for new definitions and risk assessment strategies: part I. Circulation. 2003;108:1664–72.

21. Naghavi M, Falk E, Hecht HS, et al. From vulnerable plaque to vulnerable patient—part III: executive summary of the screening for heart attack prevention and education (SHAPE) task force report. Am J Cardiol. 2006;98(2A):2H–15H.

22. Strauss HW, Grewal RK, Pandit-Taskar N. Molecular imaging in nuclear cardiology. Semin Nucl Med. 2004;34:47–55.

23. Travin MI, Bergmann SR. Assessment of myocardial viability. Semin Nucl Med. 2005;35:2–16.

24. Barron HV, Lesh MD. Autonomic nervous system and sudden cardiac death. J Am Coll Cardiol. 1996;27:1053–60.

25. Gilotra NA, Griffin JM, Pavlovic N, et al. Sarcoidosis-related cardiomyopathy: current knowledge, challenges, and future perspectives state-of-the-art review. J Card Fail. 2022;28(1):113–32.

26. Rubin J, Maurer MS. Cardiac amyloidosis: overlooked, underappreciated, and treatable. Annu Rev Med. 2020;71:203–19.

27. Hara H, Takeda N, Komuro I. Pathophysiology and therapeutic potential of cardiac fibrosis. Inflamm Regen. 2017;37:13.

28. Varasteh Z, Mohanta S, Robu S, et al. Molecular imaging of fibroblast activity after myocardial infarction using a 68Ga-labeled fibroblast activation protein inhibitor, FAPI-04. J Nucl Med. 2019;60:1743–9.

29. de Haas HJ, van den Borne SW, Boersma HH, et al. Evolving role of molecular imaging for new under-

standing: targeting myofibroblasts to predict remodeling. Ann N Y Acad Sci. 2012;1254:33–4.

30. Park S, Nguyen NB, Pezhouman A, Ardehali R. Cardiac fibrosis: potential therapeutic targets. Transl Res. 2019;209:121–37.

31. Sogbein OO, Pelletier-Galarneau M, Schindler T. New SPECT and PET radiopharmaceuticals for imaging cardiovascular disease. BioMed Res Int. 2014;2014:942960.

32. Sinusas AJ, Zaret BL. Coronary artery disease. In: Wagner HN, Szabo Z, Buchanan JW, editors. Principles of nuclear medicine. 2nd ed. Philadelphia: Saunders; 1995.

33. Gould KL, Lipscomb K, Hamilton GW. Physiologic basis for assessing critical coronary stenosis: instantaneous flow response and regional distribution during coronary hyperemia as measures of coronary flow reserve. Am J Cardiol. 1974;33:87–94.

34. Schelbert HR. Positron emission tomography of the heart: methodology, findings in the normal and disease heart, and clinical applications. In: Phelps ME, editor. PET: molecular imaging and its clinical applications. New York: Springer; 2004.

35. Strauss HW, Harrison K, Langan JK, et al. Thallium-201 for myocardial imaging. Relation of thallium-201 to regional myocardial perfusion. Circulation. 1975;51:641–5.

36. Jain D. Technetium-99m labeled myocardial perfusion imaging agents. Semi Nucl Med. 1999;29(3):221–236.

37. Nitzsche EU, Choi Y, Czernin J, et al. Noninvasive quantification of myocardial blood flow in humans. A direct comparison of the [13N]ammonia and the [15O]water techniques. Circulation. 1996;93:2000–6.

38. Kotzerke J, Glatting G, van den Hoff J, et al. Validation of myocardial blood flow estimation with nitrogen-13 ammonia PET by the argon inert gas technique in humans. Eur J Nucl Med. 2001;28:340–5.

39. Machac J. Cardiac positron emission tomography imaging. Semin Nucl Med. 2005;35:17–36.

40. Lin JW, Sciacca RR, Chou RL, et al. Quantification of myocardial perfusion in human subjects using 82Rb and wavelet-based noise reduction. J Nucl Med. 2001;42:201–8.

41. Nekolla SG, Reder S, Saraste A, et al. Evaluation of the novel myocardial perfusion positron-emission tomography tracer 18F-BMS-747158-02: comparison to 13N-ammonia and validation with microspheres in a pig model. Circulation. 2009;119(17):2333–42.

42. Bing RJ. The metabolism of the heart. In: Harvey Society of NY, editor. Harvey lecture series. New York: Academic; 1954.

43. Heineman FW, Balaban RS. Effects of after load and heart rate on NAD(P)H redox state in the isolated rabbit heart. Am J Physiol Heart Circ Physiol. 1993;264:H433–40.

44. Opie LH, Owen P. Assessment of myocardial free NAD+/NADH ratios and oxaloacetate concentrations during increased mechanical work in isolated perfused rat heart during production or uptake of ketone bodies. Biochem J. 1975;148:403–15.

45. Liedtke AJ. Alterations of carbohydrate and lipid metabolism in the acutely ischemic heart. Prog Cardiovasc Dis. 1981;23:321–36.

46. Kudo T. Metabolic imaging using PET. Eur J Nucl Med Mol Imaging. 2007;34:S49–61.

47. Wallhaus TR, Taylor M, DeGrado TR, et al. Myocardial free fatty acid and glucose use after carvedilol treatment in patients with congestive heart failure. Circulation. 2001;103:2441–6.

48. Lopaschul GD, Stanley W. Glucose metabolism in the ischemic heart. Circulation. 1997;95:415–22.

49. Phelps ME, Huang SC, Hoffman EJ, et al. Tomographic measurement of local cerebral glucose metabolic rate in humans with (F-18)2-fluoro-2-deoxy-D-glucose: validation of method. Ann Neurol. 1979;6:371–88.

50. Sokoloff L, Reivich M, Kennedy C, et al. The [14C] deoxyglucose method for the measurement of local cerebral glucose utilization: theory, procedure, and normal values in the conscious and anesthetized albino rat. J Neurochem. 1977;28:897–916.

51. Krivokapich J, Huang SC, Selin CE, et al. Fluorodeoxyglucose rate constants, lumped constant, and glucose metabolic rate in rabbit heart. Am J Physiol. 1987;252:H777–87.

52. Botker HE, Bottcher M, Schmitz O, et al. Glucose uptake and lumped constant variability in normal human hearts determined with [18F]fluorodeoxyglucose. J Nucl Cardiol. 1997;4:125–32.

53. Tillisch J, Brunken R, Marshall R, et al. Reversibility of cardiac wall-motion abnormalities predicted by positron tomography. N Engl J Med. 1986;314:884–8.

54. Brinkmann JF, Abumrad NA, Ibrahimi A, et al. New insights into long-chain fatty acid uptake by heart muscle: a crucial role for fatty acid translocase/CD36. Biochem J. 2002;367:561–70.

55. Taki J, Matsunari I. Metabolic imaging using SPECT. Eur J Nucl Med Mol Imaging. 2007;34:S34–48.

56. Tamaki N, Morita K, Kuge Y, et al. The role of fatty acids in cardiac imaging. J Nucl Med. 2000;41:1525–34.

57. Schön HR, Schelbert HR, Robinson, et al. C-11 labeled palmitic acid for the noninvasive evaluation of regional myocardial fatty acid metabolism with positron-computed tomography. I. Kinetics of C-11 palmitic acid in normal myocardium. Am Heart J. 1982;103:532–47.

58. Stone CK, Pooley RA, DeGrado TR, et al. Myocardial uptake of the fatty acid analog 14-fluorine-18-fluoro-6-thia-heptadecanoic acid in comparison to beta-oxidation rates by tritiated palmitate. J Nucl Med. 1998;39:1690–6.

59. Buckman BO, Van Brocklin HF, Dence CS, et al. Synthesis and tissue distribution of [omega-^{11}C] palmitic acid. A novel PET imaging agent for cardiac fatty acid metabolism. J Med Chem. 1994;27:2481–5.

60. Taylor M, Wallhaus TR, Degrado TR, et al. An evaluation of myocardial fatty acid and glucose uptake using PET with [18F]fluoro-6-thia-heptadecatnoic acid and [18F]FDG in patients with congestive heart failure. J Nucl Med. 2001;42:55–62.

61. Poe ND, Robinson GD Jr, Zielinski FW. Myocardial imaging with 123I-hexadecenoic acid. Radiology. 1977;124:419–24.

62. Freundlieb C, Hock A, Vyska K. Myocardial imaging and metabolic studies with [16-123I]iodoheptadecanoic acid. J Nucl Med. 1980;21:1043–50.

63. Knapp FF Jr, Ambrose KR, Goodman MM. New radioiodinated methyl-branched fatty acids for cardiac studies. Eur J Nucl Med. 1986;12:S39–44.

64. Knapp FF Jr, Goodman MM, Callahan AP, et al. Radioiodinated 15-(p-iodophenyl)-3,3-dimethylpentadecanoic acid: a useful new agent to evaluate myocardial fatty acid uptake. J Nucl Med. 1986;27:521–31.

65. Yamamoto Y, de Silva R, Rhodes CG. Noninvasive quantification of regional myocardial metabolic rate of oxygen by 15O2 inhalation and positron emission tomography. Circulation. 1996;94:808–16.

66. Tamaki N, Magata Y, Takahashi N, et al. Myocardial oxidative metabolism in normal subjects in fasting, glucose loading and dobutamine infusion states. Ann Nucl Med. 1992;6:221–8.

67. Armbrecht JJ, Buxton DB, Brunken RC, et al. Regional myocardial oxygen consumption determined noninvasively in human with [11C]acetate and dynamic positron tomography. Circulation. 1989;80:863–72.

68. Sciacca RR, Akinboboye O, Chou RL, et al. Measurement of myocardial blood flow with PET using 1–11C-acetate. J Nucl Med. 2001;42:63–70.

69. Triposkiadis F, Karayannis G, Giamouzis G, et al. Nervous system in heart failure: physiology, pathophysiology, and clinical implications. J Am Coll Cardiol. 2009;2009(54):1747–62.

70. Raffel DM, Wieland DM. Assessment of cardiac sympathetic nerve integrity with positron emission tomography. Nucl Med Biol. 2001;28:541–59.

71. Carrio I. Cardiac neurotransmission imaging. J Nucl Med. 2001;42:1062–76.

72. Lautamäki R, Tipre D, Bengel FM, et al. Cardiac sympathetic neuronal imaging using PET. Eur J Nucl Med Mol Imaging. 2007;34:S74–85.

73. Rosenpire KC, Haka MS, Jewett DM, et al. Synthesis and preliminary evaluation of ^{11}C-meta-hydroxyephedrine: a false neurotransmitter agent for heart neuronal imaging. J Nucl Med. 1990;31:1328–34.

74. Wieland DM, Swanson DP, Brown LE, et al. Imaging the adrenal medulla with an I-131-labeled antiadrenergic agent. J Nucl Med. 1979;20:155–8.

75. Wieland DM, Brown LE, Rogers WL, et al. Myocardial imaging with a radioiodinated norepinephrine storage analog. J Nucl Med. 1981;22:22–31.

76. Kline RC, Swanson DP, Wieland DM, et al. Myocardial imaging with I-123-metaiodobenzylguanidine. J Nucl Med. 2001;22:129–32.

77. Yamashina S, Yamazaki J-I. Neuronal imaging using SPECT. Eur J Nucl Med Mol Imaging. 2007;34:S62–73.

78. Raffel DM, Jung Y-W, Koeppe RA, et al. First-in-human studies of [18F]fluorohydroxyphenethylguanidines: PET radiotracers for quantifying regional cardiac sympathetic nerve density. Circ Cardiovasc Imaging. 2018;11:e007965.

79. Werner RA, Rischpler C, Onthank D, et al. Retention kinetics of the 18F-labeled sympathetic nerve PET tracer LMI1195: comparison with 11C-hydroxyephedrine and 123I-MIBG. J Nucl Med. 2015;56:1429–33.

80. Zhang H, Huang R, Pillarsetty NK, et al. Synthesis and evaluation of [18F]fluorine-labeled benzyl-guanidine analogs for targeting the human norepinephrine transporter. Eur J Nucl Med Mol Imaging. 2014;41(2):322–32.

81. Pandit-Taskar N, Zanzonico P, Staton KD. Biodistribution and dosimetry of ^{18}F-meta-fluorobenzylguanidine: a first-in-human PET/CT imaging study of patients with neuroendocrine malignancies. J Nucl Med. 2018;59(1):147–53.

82. Schaèfers M, Riemann B, Levkau B, et al. Current status and future applications of cardiac receptor imaging with positron emission tomography. Nucl Med Commun. 2002;23:113–5.

83. Delforge J, Syrota A, Lancon JP, et al. Cardiac beta-adrenergic receptor density measured in vivo using PET, CGP12167, and a new graphical method. J Nucl Med. 1991;32:739–48.

84. Elsinga PH, van Waarde A, Vaalburg W. Receptor imaging in the thorax with PET. Eur J Pharmacol. 2004;499:1–13.

85. Werner RA, Chen X, Hirano M, et al. SPECT vs. PET in cardiac innervation imaging: clash of the titans. Clin Transl Imaging. 2018;6:293–303.

86. Zelt JGE, deKemp RA, Rotstein BH. Nuclear imaging of the cardiac sympathetic nervous system a disease-specific interpretation in heart failure. JACC Cardiovasc Imaging. 2020;13(4):1036–54.

87. Fallavollita JA, Heavey BM, Luisi AJ Jr, et al. Regional myocardial sympathetic denervation predicts the risk of sudden cardiac arrest in ischemic cardiomyopathy. J Am Coll Cardiol. 2014;63(2):141–9.

88. Fallavollita JA, Dare JD, Carter RL, et al. Denervated myocardium is preferentially associated with sudden cardiac arrest in ischemic cardiomyopathy: a pilot competing risks analysis of cause-specific mortality. Circ Cardiovasc Imaging. 2017;10(8):e006446.

89. Imamura Y, Ando H, Mitsuoka W, et al. Iodine-123 metaiodobenzylguanidine images reflect intense myocardial adrenergic nervous activity in congestive heart failure independent of underlying cause. J Am Coll Cardiol. 1995;26:1594–1599.

90. Dimitriu-Leen AC, Scholte AJHA, Jacobson AF. ^{123}I-MIBG SPECT for evaluation of patients with heart failure. J Nucl Med. 2015;56:25S–30S.

91. Hotta M, Minamimoto R, Awaya T, et al. Radionuclide imaging of cardiac amyloidosis and sarcoidosis: roles and characteristics of various tracers. RadioGraphics. 2020;40:2029–41.

92. Okayama K, Kurata C, Tawarahara K, et al. Diagnostic and prognostic value of myocardial scintigraphy with thallium-201 and gallium-67 in cardiac sarcoidosis. Chest. 1995;107(2):330–4.

93. Momose M, Kadoya M, Koshikawa M, et al. 67Ga SPECT and integrated low-dose CT scanning (SPECT/CT) in the diagnosis of cardiac sarcoidosis. Ann Nucl Med. 2007;21(10):545–51.

94. Chareonthaitawee P, Beanlands RS, Chen W, et al. Joint SNMMI–ASNC expert consensus document on the role of 18F-FDG PET/CT in cardiac sarcoid detection and therapy monitoring. J Nucl Med. 2017;58(8):1341–53.

95. Blankstein R, Waller AH. Evaluation of known or suspected cardiac sarcoidosis. Circ Cardiovasc Imaging. 2016;9(3):e000867. https://doi.org/10.1161/CIRCIMAGING.113.000867. PMID: 26926267.

96. Norikane T, Yamamoto Y, Maeda Y, et al. 18F-FLT PET imaging in a patient with sarcoidosis with cardiac involvement. Clin Nucl Med. 2015;40(5):433–34.

97. Martineau P, Pelletier-Galarneau M, Juneau D, et al. Imaging cardiac sarcoidosis with FLT-PET compared with FDG/perfusion-PET: a prospective pilot study. JACC Cardiovasc Imaging. 2019;12(11 Pt 1):2280–1.

98. ten Bokum AM, Hofland LJ, de Jong G, et al. Immunohistochemical localization of somatostatin receptor sst2A in sarcoid granulomas. Eur J Clin Invest. 1999;29(7):630–6.

99. Gormsen LC, Haraldsen A, Kramer S, et al. A dual tracer 68Ga-DOTA-NOC PET/CT and 18F-FDG PET/CT pilot study for detection of cardiac sarcoidosis. EJNMMI Res. 2016;6:52.

100. Kaushik P, Patel C, Gulati G, et al. Comparison of 68Ga-DOTANOC PET/CT with cardiac MRI in patients with clinical suspicion of cardiac sarcoidosis. Ann Nucl Med. 2021;35:1058–65.

101. Kwekkeboom DJ, Krenning EP, Kho GS, Breeman WA, Van Hagen PM. Somatostatin receptor imaging in patients with sarcoidosis. Eur J Nucl Med. 1998;25(9):1284–92.

102. Lapa C, Reiter T, Kircher M, et al. Somatostatin receptor based PET/CT in patients with the suspicion of cardiac sarcoidosis: an initial comparison to cardiac MRI. Oncotarget. 2016;7(47):77807–14.

103. Gilstrap LG, Dominici F, Wang Y, et al. Epidemiology of cardiac amyloidosis-associated heart failure hospitalizations among fee-for-service Medicare beneficiaries in the United States. Circ Heart Fail. 2019;12:e005407.

104. Dorbala S, Ando Y, Bokhari S, et al. ASNC/AHA/ASE/EANM/HFSA/ISA/SCMR/SNMMI expert consensus recommendations for multimodality imaging in cardiac amyloidosis: part 1 of 2-evidence base and standardized methods of imaging. J Card Fail. 2019;25:e1–39.

105. Garcia-Pavia P, Rapezzi C, Adler Y, et al. Diagnosis and treatment of cardiac amyloidosis: a position statement of the ESC Working Group on Myocardial and Pericardial Diseases. Eur Heart J. 2021;42:1554–68.

106. Masri A, Bukhari S, Eisele YS, Soman P. Molecular imaging of cardiac amyloidosis. J Nucl Med. 2020;61:965–70.

107. Paeng JC, Young J. Nuclear imaging for cardiac amyloidosis: bone scan, SPECT/CT, and amyloid-targeting PET Choi2. Nucl Med Mol Imaging. 2021;55:61–70.

108. Pelletier-Galarneau M, Abikhzer G, Giraldeau G, Harel F. Molecular imaging of cardiac amyloidosis. Curr Cardiol Rep. 2019;21:12.

109. Stats MA, Stone JR. Varying levels of small microcalcifications and macrophages in ATTR and AL cardiac amyloidosis: implications for utilizing nuclear medicine studies to subtype amyloidosis. Cardiovasc Pathol. 2016;25(5):413–7.

110. Lee S-P, Lee ES, Choi H, et al. 11C-Pittsburgh B PET imaging in cardiac amyloidosis. JACC Cardiovasc Imaging. 2015;8:50–9.

111. Sperry BW, Bock A, DiFilippo FP, et al. Pilot study of F18-florbetapir in the early evaluation of cardiac amyloidosis. Front Cardiovasc Med. 2019;8:693194.

112. Awaya T, Minamimoto R, Iwama K, et al. Performance of ^{99m}Tc-aprotinin scintigraphy for diagnosing light chain (AL) cardiac amyloidosis confirmed by endomyocardial biopsy. J Nucl Cardiol. 2020;27:1145–53.

113. Schaadt BK, Hendel HW, Gimsing P, et al. 99mTc-aprotinin scintigraphy in amyloidosis. J Nucl Med. 2003;44:177–83.

114. Thackeray JT. Molecular imaging using cardiac PET/CT: opportunities to harmonize diagnosis and therapy. Curr Cardiol Rep. 2021;23:96.

115. Tillmanns J, Hoffmann D, Habbaba Y, et al. Fibroblast activation protein alpha expression identifies activated fibroblasts after myocardial infarction. J Mol Cell Cardiol. 2015;87:194–203.

116. Varasteh Z, Weber WA, Rischpler C. Nuclear molecular imaging of cardiac remodeling after myocardial infarction. Pharmaceuticals. 2022;15:183.

117. Gu Y, Han K, Zhang Z, et al FAPI PET/CT for molecular assessment of fibroblast activation in right heart in pulmonary arterial hypertension: a single-center, pilot study. J Nucl Cardiol. 2022.

118. Heckmann MB, Reinhardt F, Finke D, et al. Relationship between cardiac fibroblast activation protein activity by positron emission tomography and cardiovascular disease. Circ Cardiovasc Imaging. 2020;13(9):e010628.

119. Notohamiprodjo S, Nekolla SG, Robu S, et al. Imaging of cardiac fibroblast activation in a patient after acute myocardial infarction using ^{68}Ga-FAPI-04. J Nucl Cardiol. 2022;29(5):2254–61.

120. Siebermair J, Kohler MI, Kupusovic J, et al. Cardiac fibroblast activation detected by Ga-68 FAPI PET imaging as a potential novel biomarker of cardiac injury/remodeling. J Nucl Cardiol. 2021;28(3):812–21.

121. Langer LB, Hess A, Korkmaz Z, et al. Molecular imaging of fibroblast activation protein after myocardial infarction using the novel radiotracer [^{68}Ga] MHLL. Theranostics. 2021;11:7755–66.

122. Jaffer FA, Libby P, Weissleder R. Molecular and cellular imaging of atherosclerosis. Emerging applications. J Am Coll Cardiol. 2006;47:1328–38.

123. Fuster V, Corti R, Fayad ZA, et al. Integration of vascular biology and magnetic resonance imaging in the understanding of atherothrombosis and acute coronary syndromes. J Thromb Haemost. 2003;1:1410–21.

124. Lees RS, Lees AM, Strauss HW. External imaging of human atherosclerosis. J Nucl Med. 1983;24:154–6.

125. Anzola LK, Rivera JN, Ramirez JC. Molecular imaging of vulnerable coronary plaque with radiolabeled somatostatin receptors (SSTR). Clin Med. 2021;10:5515.

126. Krishnan S, Otaki Y, Doris M, et al. Molecular imaging of vulnerable coronary plaque: a pathophysiologic perspective. J Nucl Med. 2017;58:359–64.

127. Lairez O, Hyafil F. A clinical role of PET in atherosclerosis and vulnerable plaques? Semin Nucl Med. 2020;50:311–8.

128. Lee SJ, Paeng JC. Nuclear molecular imaging for vulnerable atherosclerotic plaques. Korean J Radiol. 2015;16(5):955–66.

129. MacAskill MG, Newby DE, Tavares AAS. Frontiers in positron emission tomography imaging of the vulnerable atherosclerotic plaque. Cardiovasc Res. 2019;115(14):1952–62.

130. Nakahara T, Narula J, Strauss W. Molecular imaging of vulnerable plaque. Semi Nucl Med. 2018;48(3):291–8.

131. Migdalski A, Jawien A. New insight into biology, molecular diagnostics and treatment options of unstable carotid atherosclerotic plaque: a narrative review. Ann Transl Med. 2021;9(14):1207–18.

132. Vallabhajosula S, Machac J, Knesaurek K, et al. Imaging atherosclerotic lesions by PET using [^{18}F]fluorodeoxyglucose (FDG): preclinical studies in hypercholesterolemic rabbits. Circulation. 1995;92:313.

133. Vallabhajosula S, Machac J, Knesaurek K, et al. Imaging atherosclerotic macrophage density by positron emission tomography using [^{18}F]fluorodeoxyglucose (FDG). J Nucl Med. 1996;37:38p.

134. Rudd JH, Warburton EA, Fryer TD, et al. Imaging atherosclerotic plaque inflammation with [^{18}F]-fluorodeoxyglucose positron emission tomography. Circulation. 2002;105:2708–11.

135. Masteling MG, Zeebregts CJ, Tio RA, et al. High-resolution imaging of human atherosclerotic carotid plaques with micro ^{18}F-FDG PET scanning exploring plaque vulnerability. J Nucl Cardiol. 2011;18:1066–75.

136. Liu J, Kerwin WS, Caldwell JH, et al. High resolution FDG-microPET of carotid atherosclerosis: plaque components underlying enhanced FDG uptake. Int J Cardiovasc Imaging. 2016;32:145–52.

137. Ben-Haim S, Israel O. PET/CT for atherosclerotic imaging. Q J Nucl Med Mol Imaging. 2006;50:53–60.

138. Weissberg PL. Noninvasive imaging of atherosclerosis: the biology behind the pictures. J Nucl Med. 2004;45:1974–695.

139. Derlin T, Richter U, Bannas P, et al. Feasibility of ^{18}F-sodium fluoride PET/CT for imaging of atherosclerotic plaque. J Nucl Med. 2010;51:862–5.

140. Derlin T, Tóth Z, Papp L, et al. Correlation of inflammation assessed by ^{18}F-FDG PET, active mineral deposition assessed by 18F-fluoride PET, and vascular calcification in atherosclerotic plaque: a dualtracer PET/CT study. J Nucl Med. 2011;2011(52):1020–7.

141. Joshi NV, Vesey AT, Williams MC, et al. ^{18}F-fluoride positron emission tomography for identification of ruptured and high-risk coronary atherosclerotic plaques: a prospective clinical trial. Lancet. 2014;383:705–13.

142. Alavi A, Werner TJ, Raynor W, et al. Critical review of PET imaging for detection and characterization of the atherosclerotic plaques with emphasis on limitations of FDG-PET compared to NaF-PET in this setting. Am J Nucl Med Mol Imaging. 2021;11(5):337–51.

Hippocrates (ca. 460 BC–ca. 370 BC), a Greek physician (referred to as the Father of Medicine) described several kinds of cancer, referring to them by the term *karkinos (carcinos),* the Greek word for crab or crayfish, as well as carcinoma.

In the second century AD, the Greek physician Galen used *oncos* (Greek for swelling) to describe all tumours, reserving Hippocrates term *carcinos* for malignant tumours. Galen also used the suffix *-oma* to indicate cancerous lesions. It is from Galen's usage that we derive the modern word oncology. (WIKIPEDIA)

17.1 Introduction

Radiation therapy or radiotherapy is the medical use of ionizing radiation (high-energy electromagnetic waves or particles, such as X-rays, gamma rays, electron beams, or protons), generally as part of cancer treatments to control malignant cells. External beam radiation therapy (EBRT or XRT) or teletherapy, can be conducted using a γ beam from a radioactive cobalt-60 source, high-energy X-rays or electrons from linear accelerators (LINAC), and high-energy protons and neutrons from accelerators. In brachytherapy, a radioactive sealed source is put inside the body into or near the tumor. With some types of brachytherapy, Iridium-192 implants (wire or needles), or iodine-125 and palladium-103 seeds are used for treatment.

In systemic radiation therapy, also known as endoradiotherapy or radionuclide therapy (RNT), radioactive drugs (radiopharmaceuticals) given by mouth or injected directly into blood circulation (through a vein or an artery) are used to treat certain types of cancer. These radioactive drugs then travel throughout the body and deliver the radioactivity to both cancer cells and normal cells. Both teletherapy and brachytherapy play a key role in the treatment of cancer in a specific region in the body but, they are not useful for the treatment of widespread metastases.

Henri Becquerel received a skin burn from a vial of radium that he carried in his pocket. Pierre Curie performed experiments on his own skin to confirm this effect and suggested in 1903 that radium's ability to induce deep flesh burns might have potential in cancer therapy. Early attempts at radiation therapy utilized sources of radium salts to treat a variety of ailments including uterine cervical cancer, arthritis, skin lesions, lupus, and throat cancers [1]. In 1913, Frederick Proescher published the first study on the intravenous injection of radium for therapy of various diseases. Those early potential clinical uses have ended for health and safety concerns. However, the discovery of radium brought radioactivity to the attention of the general public and inspired many new uses of radioactivity.

In the 1920s, George de Hevesy, coined the term *radioindicator* or *radiotracer* and introduced the *tracer principle* in biomedical sciences. Also in 1920s, the first tracer study in rabbits was performed to investigate the absorp-

tion, circulation and excretion of labeled bismuth preparations containing Radium E (identified later as [210]Bi, a beta emitter with a half-life of 5 days) [2]. The study showed that bismuth hydroxide suspended in oil was most suitable for therapeutic application of syphilis [3]. Also, Chieivitz and Hevesy administered P-32 phosphate to rats and demonstrated the renewal of the mineral constituents of bone.

In 1936, John H. Lawrence, the brother of Ernest Lawrence, made the first clinical therapeutic application of an artificial radionuclide when he used phosphorus-32 to treat leukemia. In 1941, Saul Hertz gave a patient the first therapeutic dose of iodine-130 (a β^- emitter with a half-life of 12.36 h). However, the discovery of ^{131}I by Glenn Seaborg and John Livingood at the University of California, Berkeley, has been the success story in nuclear medicine. In 1946, the first patient received [^{131}I]iodide, the "atomic cocktail" for the treatment of thyroid cancer [4]. I-131 has the advantage of emitting both γ rays and β^- rays, the former enabling imaging for diagnosis and dosimetry and the latter being valuable for molecular radiotherapy of hyperthyroidism and thyroid cancer. [^{131}I]sodium iodide was the first radiopharmaceutical to receive regulatory approval for routine clinical use in patients with thyroid disease.

17.2   Radiopharmaceuticals

A radiotracer can be defined as a specific radiolabeled molecule that resembles or traces the in vivo behavior of a natural molecule and can be used to provide information about a specific biological process. A radioligand can be defined as any radiolabeled molecule that can bind with another molecule or substance (binder) in a predictable way under controlled conditions. All radiolabeled compounds or substances used for the purpose of diagnosis or therapy have been defined as radioactive drugs or radiopharmaceuticals by the U.S. Food and Drug Administration (FDA).

The term *unconjugated* radiopharmaceutical has been generally defined as referring to those

radionuclides that target specific disease sites by virtue of chemical, biologic, or physical affinity of radioisotope itself, rather than by virtue of carrier agents to which they are tagged. Because of the untagged nature of their use, *unconjugated* radiopharmaceuticals are also referred as *naked* radiopharmaceuticals. During the last couple of decades, there has been significant increase in the application of *conjugated* radiopharmaceuticals for targeted radionuclide therapy (TRT), mainly due to the development of a range of new carrier molecules (targeting vehicle), which can transport the radionuclide to a molecular target on the cancer cell (Fig. 17.1). The key factors that influence tumor localization of *conjugated* radiopharmaceuticals include the chemical and biochemical nature of the carrier molecule transporting the radionuclide of choice to the targeted area [5].

A century ago, Paul Ehrlich postulated the notion that a *magic bullet* could be developed to selectively target the disease and speculated that antibodies could function as magic bullets. The first demonstration of TRT was the use of ^{131}I-labeled polyclonal antibodies for the treatment of patients with melanoma. Several *unconjugated* or *conjugated* radiopharmaceuticals are now available commercially for the treatment of different benign diseases and malignancies (Table 17.1). In addition, some of the important new therapy radiopharmaceuticals under clinical investigation are summarized in Table 17.2. Several review articles and book chapters have extensively discussed the development of targeted radiopharmaceuticals for therapy [5–7].

17.2.1 Therapy Radiopharmaceuticals

Radiopharmaceutical therapy (RPT) or Targeted Radionuclide therapy (TRT) is defined by the delivery of radioactive atoms to tumor tissue or tumor-associated targets. Therapeutic radiopharmaceuticals may be structurally simple ions (^{131}I, [89]Sr^{2+}, and [223]Ra^{2+}), small molecules (^{131}I-MIBG and [153]Sm-EDTMP), complex molecules (^{131}I, ^{90}Y, or ^{177}Lu-labeled intact antibodies or antibody fragments), colloids (^{32}P chromic phosphate), or even particles (^{90}Y-labeled microspheres). The

Fig. 17.1 Schematic of a conjugated radiopharmaceutical for targeted radionuclide therapy (TRT)
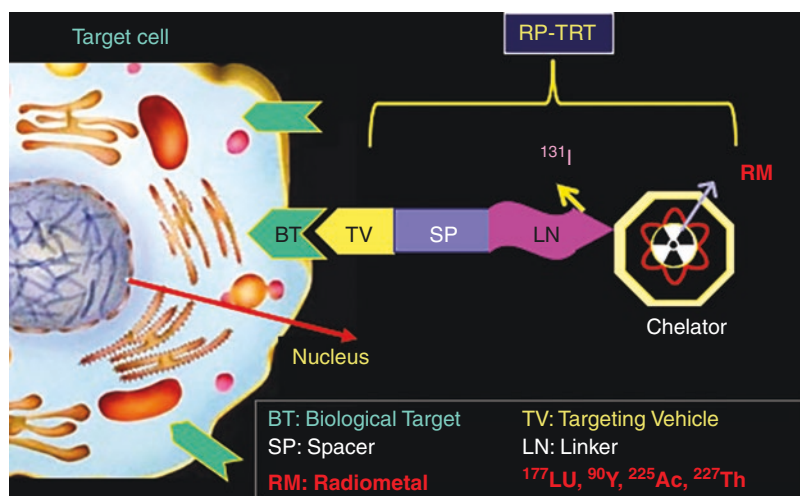
Table 17.1 FDA-approved radiopharmaceuticals for therapy

Radiopharmaceutical	Trade name	Decay	Target	Indication
[^{32}P]Sodium orthophosphate		β^-	Against primary cancers as well as distant metastases	Polycythemia vera
[^{131}I]Sodium iodide		β^-	Active transport via NaI symporter	Hyperthyroidism
				Thyroid cancer
[^{89}Sr]Strontium chloride	Metastron®	β^-	Bone hydroxyapatite	Palliative therapy of pain due to bone metastasis
[^{153}Sm]Lexidronam (EDTMP)	Quadramet®	β^-	Bone hydroxyapatite	Palliative therapy of pain due to bone metastasis
[^{223}Ra]Radium dichloride	Xofigo®	α	Bone hydroxyapatite	Metastatic prostate cancer
^{90}Y-labeled glass microspheres	Theraspheres®	β^-	Embolization of hepatic arterioles	Hepatic malignancy
^{90}Y-labeled resin microspheres	Sir Spheres®	β^-	Embolization of hepatic arterioles	Hepatic malignancy
^{131}I-Tositumomab	Bexxar®	β^-	CD-20 on B cells	Non-Hodgkin's follicular lymphoma
^{90}Y-Ibritumomab tiuxetan	Zevalin®	β^-	CD-20 on B cells	Non-Hodgkin's follicular lymphoma
[^{131}I]Iobenguane, MIBG	AZEDRA®	β^-	Norepinephrine transporter	Pheochromocytoma
				Paraganglioma. NETs
^{177}Lu-DOTATATE	LUTATHERA®	β^-	Somatostatin type II receptor (SSTR-II)	Neuroendocrine tumors
^{177}Lu-PSMA-617	Pluvicto	β^-	Prostate-specific membrane antigen (PSMA)	Metastatic castration-resistant prostate cancer (mCRPC)

tumor localization properties of a specific therapeutic radiopharmaceutical and the clinical application will depend on the route of administration, such as oral, intravenous, intra-arterial, intracavitary, and intra-articular approaches. The ideal physical and biological properties of a radiopharmaceutical intended for therapy should be such that a large, absorbed radiation dose is deposited in the tumor, or diseased tissue, with minimal radiation dose to the normal tissues. This requires the use of an appropriate radionuclide, administered in a suitable chemical form with optimal

Table 17.2 Therapy radiopharmaceutical under clinical investigation

Radiopharmaceutical		Decay	Target	Indication	Clinical trial
[131]I-Apamistamab (IOMAB-B)	Actinium Pharmaceuticals	β⁻	BC8 mAb targeting CD-45	Bone marrow ablation in AML	Phase III SIERRA trial
[225]Ac-Lintuzumab (Actimab-A)	Actinium Pharmaceuticals	α	M195 mAb	Bone marrow ablation in AML	Phase I and II
			Targeting CD-33		
[177]Lu-huJ591 mAb	Weill Cornell Medicine	β⁻	PSMA	CRMPC	Phase II
[225]Ac-huJ591 mAb	Weill Cornell Medicine	α	PSMA	CRMPC	Phase I, II
[177]Lu- DOTA-JR11	IPSEN	β⁻	SSTR mediated	NETs	Phase I, II
^{177}Lu-PSMA-R2	Novartis/AAA	β⁻	PSMA	Prostate cancer	Phase II
^{177}Lu-DOTA-N3-CTT1403	NCI	β⁻	PSMA	Prostate cancer	Phase I/II
[227]Th-MSLN-TTCa	Bayer	α	Mesothelin		Phase I
[227]Th-PSMA-TTCa	Bayer	α	PSMA	Prostate cancer	Phase I
[227]Th-CD22-TTC	Bayer	α	CD22 B-cell	Lymphoma	Phase I
[225]Ac- FPX-01a	J&J Fusion Pharma	α	Insulin growth factor 1	NSC lung cancer	Phase I
[225]Ac-PSMA-617	Endocyte/Novartis	A			

specific activity (mCi or MBq/mmol), and by an appropriate route of administration, which will allow selective uptake in the target tissue in sufficient concentration to elicit a therapeutic response. Different mechanisms, however, are involved in the delivery and accumulation of the therapeutic agent within the tumor cells. However, the remarkable potential of RPT directed against primary cancers as well as distant metastases, is now recognized as an effective and safe and treatment modality.

17.3   Radionuclides for Therapy

Although numerous radionuclides have potential applications in radionuclide therapy, only a very few radionuclides possess favorable nuclear, physical, chemical, and biological characteristics which would identify them as practical for clinical use. Some of the important radionuclides used in the development of therapeutic radiopharmaceuticals are listed in Table 17.3. The ideal radionuclides for therapy are those with an abundance of non-penetrating radiations, such as charged particles (α²⁺, β⁻, *and Auger electrons*) and lack of penetrating radiations (γ or X-rays).

While penetrating radiation is not essential for TRT, a small amount or abundance with an appropriate energy (100–400 KeV) may be useful for imaging studies to demonstrate tumor localization or altered biodistribution.

17.3.1   Radionuclides-Emitting Beta Particles

The physical characteristics of β⁻ emitting radionuclides are summarized in Table 17.4. In beta decay, fast energetic electron (β⁻) or positron (β⁺) is emitted from an atomic nucleus, transforming the original nuclide to an isobar of that nuclide. In neutron-rich nuclides, a neutron transforms it into a proton by the emission of an electron and an antineutrino. The fast energetic electrons are called beta (β⁻) particles. In neutron-deficient nuclides, a proton is converted into a neutron by the emission of a positron (β⁺) and a neutrino. Most of the radionuclides in routine clinical use are β⁻ emitters (^{131}I, ^{90}Y, ^{177}Lu, ^{89}Sr, and [153]Sm) with a wide range of half-lives ranging from 1.95 to 59.5 days Table 17.4. The kinetic energy spectrum of β⁻ particles consist of a continuum of energies ranging from almost zero to their maxi-

Table 17.3 Production methods of radionuclides used for therapy

Radionuclide	$T_{1/2}$ (days)	Decay	Production method (nuclear reaction)
^{32}P	14.268	β^-	^{31}P(n, γ)^{32}P
			^{32}S(n, p)^{32}P
^{89}Sr	50.53	β^-	^{88}Sr(n, γ)^{89}Sr, ^{89}Y(n, p)^{89}Sr
^{169}Er	9.4	β^-	^{168}Er(n, γ)^{169}Er
^{131}I	8.02	β^-, γ	^{235}U(n, fission)^{131}I
			^{130}Te(n, γ)^{131}Te $_{\to \beta}$^{131}I
^{161}Tb	6.90	β^-, γ	^{160}Gd(n, γ) ^{161}Gd $\to$ ^{161}Tb
^{177}Lu	6.73	β^-, γ	^{176}Lu(n, γ)^{177}Lu
			^{176}Yb(n, γ)^{177}Yb $_{\to \beta}$$^{-177}$Lu
^{186}Re	3.777	β^-	^{185}Re(n, γ)^{186}Re
^{198}Au	2.697	β^-	^{197}Au(n, γ)^{198}Au
^{90}Y	2.67	β^-	^{235}U(n, fission)^{90}Sr $_{\to \beta}$$^{-90}$Y
			^{90}Sr $_\to$ ^{90}Y0 Generator
^{67}Cu	2.58	β^-	^{67}Zn(n, p)^{67}Cu
^{153}Sm	1.9375	β^-	^{152}Sm(n, γ)^{153}Sm
^{77}As	1.60	β^-	^{nat}Ge(n, γ)77Ge $_{\to \beta}$$^{-77}$As
^{166}Ho	1.120	β^-	^{165}Ho(n, γ)^{166}Ho
^{188}Re	0.708	β^-	^{187}W(n, γ)^{188}W $_{\to \beta}$$^{-188}$Re
			^{188}W $\to$ ^{188}Re Generator
^{117m}Sn	0.566	IT, CE	^{116}Sn(n, γ)^{117m}Sn
			^{117}Sn (n, n′, γ) ^{117m}Sn
^{212}Pb $_\to$ ^{212}Bi[a]	0.442	β^-	^{228}Th $_\to$ ^{224}Ra $_\to$ ^{212}Pb $_\to$ ^{212}Bi *generator*
		α (from ^{212}Bi)	
^{213}Bi[a]	45.6 m	A	^{225}Ac $_\to$ ^{213}Bi generator
^{211}At	7.2 h	A	^{209}Bi(α, 2n)^{211} (accelerator produced)
^{149}Tr	4.12 h	α, and β^+	^{nat}Nd(^{12}C,xn)^{149}Dy $_\to$ ^{149}Tb (cyclotron produced)
^{225}Ac[a]	10.0	A	^{229}Th $_\to$ ^{225}Ac generator
			^{232}Th(p, x)^{225}Ac (accelerator produced)
^{223}Ra[a]	11.43	A	^{227}Ac $_\to$ ^{227}Th $_\to$ ^{223}Ra generator
^{227}Th[a]	18.7	α, and β^+	^{227}Ac $_\to$ ^{227}Th generator

[a] The alpha emitters are regarded as in vivo generators because following administration into a patient, they generate alpha-emitting daughters

mum energy (E_{max}), and the average energy (E_{avg}) of a β^- particle is about one-third of the maximum energy (Fig. 17.2a). The average range of electrons in tissue can be between 0.1 and 5.0 mm depending on the kinetic energy. As a result, beta particles can pass through several cells (10–1000), a useful property that has been termed "crossfire effect," which ensures sufficient dose delivery to each cell in a large tissue mass. The beta particle-emitting radionuclides can be arranged into three groups according to the mean range in tissue: short range (<1 mm), medium range (1–2 mm), and long range (>2 mm). It is important to match the range of the radionuclide

with the anticipated size of the tumor target. Small tumors were more effectively treated by a short-range b emitter, while a higher cure rate could be obtained in larger tumors with a long-range b emitter [8].

17.3.1.1 Phosphorous-32

^{32}P ($T_{1/2}$ = 14.268 days) decays into ^{32}S by the emission of β^- (E_{max} = 1.709 MeV) particles. ^{32}P has been available for the treatment of myeloproliferative neoplasms for over 80 years. ^{32}P can be produced in a reactor by neutron activation using ^{31}P(n, γ)^{32}P reaction. However, the specific activity of ^{32}P is very low since the product can't be

Table 17.4 Physical characteristics of beta-emitting radionuclides for targeted therapy

Radionuclide	$T\frac{1}{2}$ (days) Days	β⁻ particle energy (MeV) Max	Average	β⁻ particle range in soft tissue (mm) Max	Mean	Energy of γ photons KeV	%
^{199}Au	3.14	0.452	0.082		0.41	158	36.9
						494	97
^{169}Er	9.4	0.351	0.101		0.51	110	0.0014
^{177}Lu	6.73	0.497	0.133	1.8	0.67	113	6.6
						208	11
^{67}Cu	2.58	0.60	0.141		0.71	93.3	16
						184.6	47
^{161}Tb	6.9	0.593	0.154		0.77	74	9.8
						49	14.8
^{47}Sc	3.4	0.600	0.162		0.81	159	68
^{131}I	8.02	0.606	0.182		0.91	364	81
^{77}As	1.60	0.700	0.228		1.20	239	1.60
^{153}Sm	1.9375	0.808	0.229		1.20	70	5.25
						103	28.3
^{198}Au	2.697	0.960	0.315	3.6	1.60	411	95.6
^{186}Re	3.777	1.077	0.362	3.6	1.80	137	8.6
^{89}Sr	50.53	1.496	0.58	8.0	2.5	910	1
^{166}Ho	1.120	1.850	0.666	8.1	3.2	80.6	6.6
^{32}P	14.27	1.710	0.695	7.9	2.9	–	–
^{188}Re	0.708	2.12	0.764		3.5	188	15
^{90}Y	2.67	2.28	0.935	12	3.9	–	–
^{198}Au	2.697	0.96	99	3.6		411	95.6
^{90}Y	2.67	2.28	100	12.0	3.6		
^{117m}Sn	13.60	0.13	64.9	0.22		159	86.4
		0.15	26.2	0.29			

separated from the target by traditional methods. However, the ^{32}S(n, p)^{32}P nuclear reaction is ideal since the target and the product are two different elements. ^{32}P can be easily separated and purified from the target and is usually carried out following wet chemical extraction and dry distillation methods and supplied in high specific activity but, the contribution of the longer-lived ^{33}P ($T\frac{1}{2}$ 25.3 days) is of concern as a radionuclidic impurity. ^{32}P is supplied as orthophosphoric acid in water with a specific activity of 8–9 Ci (314–337 TBq)/mmol.

17.3.1.2   Iodine-131

^{131}I ($T_{\frac{1}{2}}$ 8.02 days) decays by the emission of β⁻ (E_{max} = 606 KeV) particles and γ (364 KeV) emissions to stable ^{131}Xe inert gas. ^{131}I sodium iodide solution has been used for the management of thyroid disorder for almost 80 years. As a halogen, it can be easily incorporated into organic molecules, peptides, and antibodies. [^{131}I] MIBG (*m*-iodobenzylguanidine) is widely used for the treatment of neuroendocrine tumors. ^{131}I-Tositumomab (anti CD20 antibody, Bexaar®) is used for the treatment of non-Hodgkin's lymphoma.

^{131}I is a major fission product of ^{235}U and ^{239}Pu. comprising nearly 2.8336% of the total products of fission (by weight). Radionuclidic purity of fission produced ^{131}I is ≥99.9% of the total radioactivity. The specific activity is approximately 130 Ci/mg or 4.81 TBq/mg. A more practical method of ^{131}I production is based on (n, γ) reaction in a research reactor using ^{130}Te target, which is approximately 30% of natural tellurium element. Certain (n, γ) reactions produce a short-lived radioisotope of the target element, which decays by beta emission to another unstable radioactive nuclide with longer half-life compared to that of the intermediate. As shown below,

Fig. 17.2 (**a**, **b**) Energy spectrum
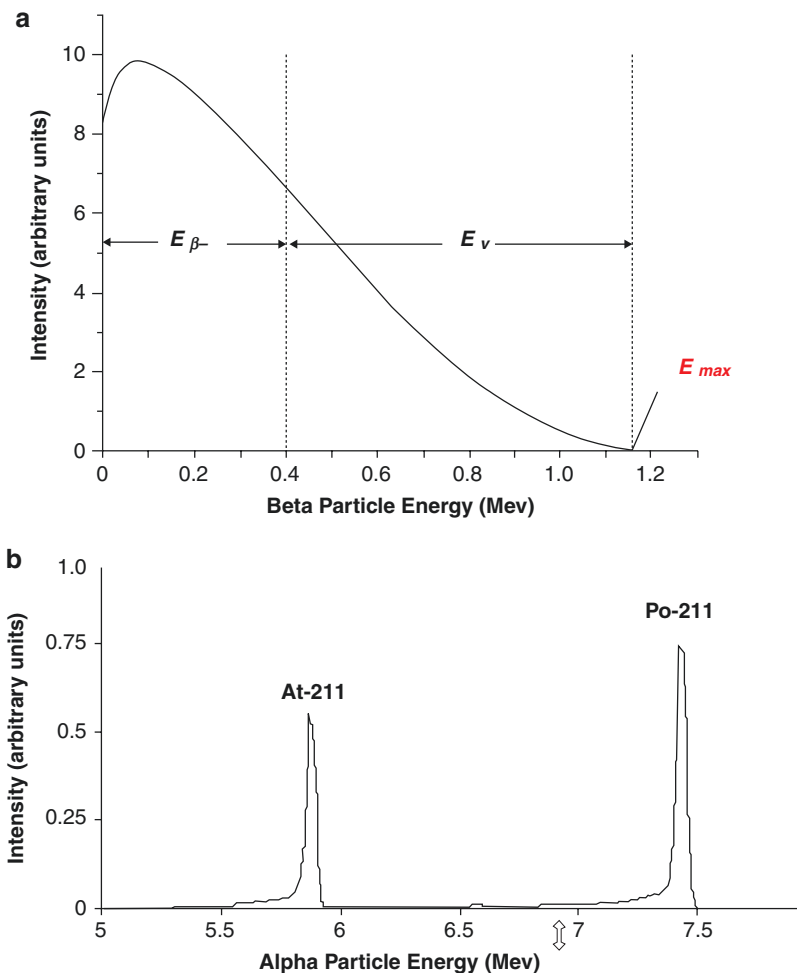
both the ground state ^{131}Te and metastable ^{131m}Te decay to ^{131}I.
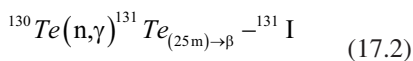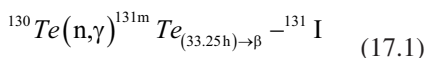
$$^{130}Te(n,\gamma)^{131m}Te_{(33.25\,h)\rightarrow\beta}\,-^{131}I \quad (17.1)$$

$$^{130}Te(n,\gamma)^{131}Te_{(25\,m)\rightarrow\beta}\,-^{131}I \quad (17.2)$$

Following neutron irradiation, ^{131}I is extracted from the natural tellurium target generally by the dry distillation method. The process involves heating the irradiated sample to release the ^{131}I and ^{131}I in a sodium hydroxide solution (pH 8–10). Use of natural tellurium target also results in the production of stable ^{127}I and long-lived ^{129}I as chemical and radionuclidic impurities. As a result, the specific activity is generally less than that of fission-produced ^{131}I (4–5 TBq/mg).

17.3.1.3 Yttrium-90

^{90}Y ($T_{1/2}$ 64.1 h) is a pure β^- emitter and decays to stable zinc-90 with very high energy (E_{max} =2.28 MeV) and no γ emissions. As a trivalent metal, yttrium exhibits relatively simple ion chemistry forming complexes with a variety of chelating agents. Selective internal radiation therapy (SIRT) with ^{90}Y-labeled microspheres has become a widely employed brachytherapy for the treatment of primary and metastatic hepatic malignancies. ^{90}Y-ibritumomab tiuxetan (Zevalin®) is used for the treatment of NHL.

^{90}Y can be produced in a reactor by neutron irradiation of stable yttrium-89 via ^{89}Y(n, γ)^{90}Y reaction [9]. Exposing a 1 cm cube (approximately 5 g), natural yttrium target to 10^{14} n/cm^2/s flux would create Y-90 at a rate of 1.1 Ci/h. To make

high specific activity ^{90}Y, e-LINAC is used to generate a neutron beam (12.1 MeV) and directing the neutron beam onto the zirconium target (^{90}Zr) to isotopically convert some of the atoms to ^{90}Y via ^{90}Zr(n, p)^{90}Y. However, the most common method of producing high specific activity ^{90}Y is by the decay of the parent isotope ^{90}Sr ($T\frac{1}{2}$ = 29 years), which is a fission product of uranium. ^{90}Sr → ^{90}Y generator has been in clinical use for the last 4 decades [10]. The theoretical specific activity is 20 GBq (540 mCi)/μg of Yttrium-90.

17.3.1.4   Lutetium-177

^{177}Lu ($T_{\frac{1}{2}}$ 6.734 days) is a low-energy β$^-$ emitter (E_{max} = 0.498 MeV) with suitable γ photons (113 and 208 KeV) suitable for SPECT imaging studies. ^{177}Lu-DOTATATE (Lutathera®) is the first ^{177}Lu peptide radiopharmaceutical approved by the FDA for TRT of patients with neuroendocrine tumors (NETs). Like other trivalent metals, ^{177}Lu forms strong complexes with bifunctional chelating agents. Several ^{177}Lu-labeled peptides and antibodies are in Phase II–III clinical trials for TRT.

^{177}Lu can be produced in a reactor by direct neutron activation via ^{176}Lu(n, γ)^{177}Lu reaction using enriched ^{176}Lu target. The direct production route also results in formation of a small amount of long-lived metastable ^{177m}Lu ($T_{\frac{1}{2}}$ 160 days) in activity (<0.02%). The specific activity depends on the ^{176}Lu enrichment and one can obtain 20–40 Ci/mg with >80% enriched ^{176}Lu targets. The amount of ^{177}Lu produced, however, depends on the neutron energy, neutron flux, and the irradiation time [11]. Using natural lutetium targets and high neutron flux reactors, it is possible to increase the yields and specific activity.

In the indirect route of neutron activation method, isotopically enriched ^{176}Yb target undergoes (n, γ) transmutation to produce ^{177}Yb which subsequently decays by β$^-$ emission ($T_{\frac{1}{2}}$ 1.9 h) to yield ^{177}Lu. The major advantage of the indirect method is the production of no carrier added (NCA) ^{177}Lu which is then separated by suitable radiochemical processes. In addition, the indirect method does not produce any ^{177m}Lu radionuclide impurity. With enriched ^{176}Yb targets, it is possible to achieve very high specific activity approaching the theoretical specific activity of 110 Ci (4.07 TBq)/mg [11].

17.3.1.5   Copper-67

^{67}Cu ($T_{\frac{1}{2}}$ 2.58 days) a transition metal, decays by the emission of low-energy β$^-$ particles (E_{max} = 0.562 MeV) and provides several γ photons (91, 93, 184 KeV) suitable for SPECT. The production of ^{67}Cu has been tested both in reactors and cyclotrons on a variety of nuclear reactions, such as ^{67}Zn(n,p)^{67}Cu, ^{68}Zn(p, 2p)^{67}Cu, and ^{70}Zn(p, α)^{67}Cu. The ^{68}Zn(p,2p)^{67}Cu route of production (using 70 MeV proton) appears to be the most attractive method. However, large quantities of ^{64}Cu ($T_{\frac{1}{2}}$ = 12.7 h) and ^{67}Ga ($T_{\frac{1}{2}}$ = 78.3 h) are the major radionuclidic impurities. The specific activity of ^{67}Cu is <20 mCi/μg [12].

A breakthrough in the production of high specific activity ^{67}Cu is based on the photonuclear activation, using highly enriched (98.9%) ^{68}Zn targets. For the ^{68}Zn(γ,p)^{67}Cu reaction, high-energy γ rays can be produced by bremsstrahlung conversion of electrons from e-LINAC [12, 13]. The specific activity of ^{67}Cu so produced has reached over 5.55 GBq/μg (150 mCi/μg). Due to this technical breakthrough in ^{67}Cu production, no-carrier-added ^{67}Cu has been made available in large scales at the US-DOE National Isotope Development Center.

17.3.1.6   Scandium-47

^{47}Sc ($T_{\frac{1}{2}}$ 3.35 days) with low-energy β$^-$ particles (E_{max} = 441 keV) is ideal for therapy. In addition, the emission of 159 KeV γ photons is appropriate for SPECT imaging studies. Also, the positron emitters ^{43}Sc ($T_{\frac{1}{2}}$ = 3.89 h, $E_{\beta+avg}$ = 476 keV, I = 88.1%) and ^{44}Sc ($T_{1/2}$ 3.97 h, $E_{\beta+avg}$ = 632 keV, I = 94.3%) have been proposed for PET imaging studies. Like lutetium and yttrium, scandium also is a trivalent metal and has favorable chemistry for chelation and attachment to various molecular targeting agents.

^{47}Sc can be produced by two different neutron-induced reactions: ^{46}Ca(n, γ)^{47}Ca → ^{47}Sc or ^{47}Ti(n, p)^{47}Sc. The (n, γ) reaction is induced by thermal neutrons, while the (n, p) reaction requires fast neutrons (>1 MeV). Enriched ^{46}Ca as $CaCO_3$ is generally used for thermal neutron activation reaction. The chemical separation of Sc from Ca is performed using DGA resin and SCX cation exchange cartridges.

47Sc can be produced with higher specific activities via the ^{48}Ti(γ, p)^{47}Sc photo nuclear reaction by irradiation of a natural titanium target [14–16]. Target foils dissolved in 2.0 M H_2SO_4. 47Sc ions can be separated from natural titanium using AG MP-50 cation exchange resin. The recovered 47Sc is purified using Chelex 100 ion exchange resin.

17.3.1.7   Terbium-161

161Tb ($T_{1/2}$ 6.9 days) emits low-energy β^- particles [E_{max} = 593 keV) and also γ photons (74 and 49 KeV), and is useful for imaging studies. In addition, 161Tb also emits a significant amount of conversion and Auger electrons. Greater therapeutic effect can therefore be expected in comparison to 177Lu [17]. It also emits low-energy photons that are useful for gamma camera imaging. The trivalent cation chemistry of terbium is similar to lutetium and is, therefore, compatible with existing radiolabeling techniques to develop 161Tb-labeled radiopharmaceuticals for TRT.

161Tb can be reactor-produced by double-neutron capture on natural terbium by the ^{159}Tb(2n, 2γ)^{161}Tb reaction. However, the specific activity is low and not optimal for TRT. The alternative reactor production route is via the ^{160}Gd(n, γ)^{161}Gd ($T_{1/2}$ 3.66 m), which quickly decays by β^- emission to 161Tb. To prevent the formation of several radionuclidic impurities it is important to use highly enriched 160Gd targets. The specific activities of ~100 mCi/mg can be obtained using this method [18].

17.3.1.8   Strontium-90

89Sr ($T_{1/2}$ = 50.53 days) is an alkaline earth metal and undergoes β^- decay (E_{max} = 1.495 MeV) into 89Y with no gamma emissions. 89Sr chloride (Metastron™) is used for bone pain palliation. 89Sr is anthropogenic radionuclide that is a fission product with yields of 4.69 ± 0.06% [19].

89Sr can also be produced by neutron activation using ^{88}Sr(n, γ)^{89}Sr using $SrCO_3$ as the target with thermal neutrons. A highly enriched target 88Sr (>99%) is used to eliminate strontium-85 impurity. This is a convenient production method and takes place in a normal research reactor. 89Sr can also be produced via ^{89}Y(n, p)^{89}Sr nuclear reaction using fast neutrons and yttrium oxide pellets.

17.3.1.9   Samarium-153

153Sm($T_{1/2}$ = 1.93 days) is a transition metal and one of the elements in the lanthanide series. It decays by β^- emission (E_{max} = 0.810 MeV) to europium-153, with useful γ emissions (103 KeV). 153Sm-EDTMP or Lexidronam (Quadramet®) is clinically used for bone pain palliation. 53Sm is produced by neutron activation of both natural Sm_2O_3 and 98% enriched $^{152}Sm_2O_3$ targets via ^{152}Sm(n, γ)^{153}Sm nuclear reaction (IAEA-TECDOC-1340). Specific activity achieved at EOB is 14.8–16.8 GBq (400–450 mCi)/mg oxide. The specific activity of enriched 152Sm targets can be up to 1200 mCi/mg.

17.3.1.10   Tin-117m

117mSn ($T_{1/2}$ 13.6 days) is a post-transition metal and decays by isomeric transition (*IT*) and emits low, and mono-energetic conversion electrons (0.127, 0.129, and 0.152 MeV). It also emits γ photons (159 KeV) suitable for SPECT. Bone marrow toxicity of this radionuclide is low because of its short-range (~3 mm) electrons. It is a novel radionuclide with low-energy electrons for radionuclide therapy applications, including rheumatoid arthritis and bone pain palliation, 117mSn can be produced in massive quantities as a low specific activity (up to 21 mCi/mg) product in reactors via the ^{116}Sn(n, γ)^{117m}Sn or ^{117}Sn(n,n$'\gamma$)^{117m}Sn reactions. A carrier-free, high specific activity (up to 20 Ci/mg) isotope can be manufactured with >50 MeV cyclotrons employing either stable antimony target ^{nat}Sb(p, x)^{117m}Sn or ^{116}Cd(α, 3n) nuclear reactions [20].

17.3.1.11   Re-186 and Re-188

186Re ($T_{1/2}$ = 3.718 days) is a transition metal and decays by β^- emission (E_{max} = 1.07 MeV) with useful γ photons (137 KeV) for SPECT. 188Re ($T_{1/2}$ = 16.9 h) also decays by β^- emission (E_{max} = 2.12 MeV) with useful γ photons (155 KeV) for SPECT. Since rhenium and technetium exhibit similar chemical properties, the preparation and targeting of 186/188Re radiophar-

maceuticals for therapy is similar to the preparation of ^{99m}Tc agents.

The primary production of ^{186}Re in a reactor is via ^{185}Re(n, γ)^{186}Re nuclear reaction using enriched ^{185}Re target (>94%). The typical specific activity is 1.84 Ci/mg [21]. High specific activity ^{186}Re can be produced using cyclotron irradiation of enriched tungsten-186 target via the ^{186}W(d, 2n)^{186}Re nuclear reaction. However, the target thickness and beam currents are critical to achieving high specific activity. Specific activity of 80 Ci/mg was obtained using a graphite-encased ^{186}W target and 18.7 MeV deuteron bombardment for 2 h, at a beam current of 27 μA [22].

^{188}Re as a no-carrier-added nuclide can be produced in high specific activity from the ^{188}W → ^{188}Re generator system. ^{188}W ($T_{1/2}$ 69.78 days) decay by β$^-$ emission to ^{188}Re. The parent ^{188}W is produced in a reactor by double neutron capture of enriched ^{186}W (>90%) targets via the nuclear reactions, ^{186}W(n, γ)^{187}W(n,γ)^{188}W. High neutron flux (>8–10 × 10^{14}/cm^2/s) reactor is essential to produce high specific activities.

17.3.1.12 Holmium-166

^{166}Ho ($T_{1/2}$ 26.763 h) decays by β$^-$ emission (E_{max} = 1.854 MeV)) to erbium-166, with useful γ emissions (81 KeV) for SPECT. Holmium is a transition metal and one of the elements in the lanthanide series and the chemistry is similar to that of lutetium. Several clinical applications for therapy are under investigation [23]. ^{166}Ho-DOTMP for multiple myeloma, and ^{166}Ho-EDTMP for bone pain palliation have been investigated.

^{166}Ho is most frequently produced via the ^{165}Ho(n, γ)^{166}Ho nuclear reaction (IAEA-TECDOC-1340). However, ^{166m}Ho ($T_{1/2}$ = 1200 years), a beta emitter may be produced as a radionuclidic impurity. The specific activity is NLT 75 mCi/mg. ^{166}Ho can also be produced by an indirect method via the ^{164,165}Dy(2n, γ)^{166}Dy → ^{166}Ho nuclear reaction. The cross-section of ^{164}Dy is extremely high (2650 b). The second neutron irradiation of the unstable ^{165}Dy is necessary to result in ^{166}Dy, which decays by beta emission to carrier-free ^{166}Ho. A ^{166}Dy → ^{166}Ho generator can provide on-site supply of high specific activity ^{166}Ho for targeted therapy.

17.3.1.13 Lead-212

^{212}Pb ($T_{1/2}$ = 10.6 h) is a β$^-$ emitter but its interest in TAT as an in vivo generator comes from the fact that its first daughter, ^{212}Bi, is an α emitter with a short half-life of 60.6 min. Lead is classified as a post-transition metal with a weak metallic character and the preferred oxidation state is +2. ^{212}Pb is produced following the ^{228}Th decay sequence and can be obtained using ^{228}Th or ^{224}Ra-based generators.

17.3.2 Radionuclides-Emitting Alpha Particles

Alpha (α) particles are naked ^{4}He nuclei with 2 positive charges, consisting of 2 protons and 2 neutrons that are 7300 times heavier than electrons. Alpha particles are mostly emitted by heavy radioactive elements, such as radium, actinium, thorium, and uranium, and their daughters (Table 17.5). Alpha particles are ejected from the nucleus with much higher kinetic energy (5–9 MeV) compared to that of beta particles. In addition, alpha particles are monoenergetic as shown in Fig. 17.2b The range (<100 μm) of α particles in tissue is equivalent to only a few cell diameters. The short range of a particles is ideally suited for the treatment of small-volume cancer tissue. However, the energy distribution between the α particle and the recoiling daughter atom is typically 98 to 2%. The energy imparted to the daughter recoil atom can reach 100 keV [24], which is far higher than the binding energy of the strongest chemical bonds. As a result, the daughter nuclide may be released from the targeting vehicle chelator and diffuse into surrounding normal tissue and induce toxic effects.

Compared to beta emitters, α-particle emitters for TRT offers several important advantages. Alpha particles have higher kinetic energy (5–9 MeV) and higher LET in biological tissue. For example, ^{211}At has a mean LET of 97 KeV/μm, compared to the LET (0.22 keV/μm) of high-energy (2.2 MeV) beta particle of ^{90}Y. As a result, the probability of creating cytotoxic double-stranded breaks (DSBs) of DNA is much higher, and the relative biological effectiveness (RBE) is also significantly higher compared to that of beta

Table 17.5 The physical characteristics of alpha-emitting radionuclides for targeted therapy

Radionuclide	$T_{\frac{1}{2}}$	Daughter(s)		α particle		β⁻ particle		γ-ray		X-ray	
	Days	Nuclide	$T_{\frac{1}{2}}$	MeV	%	MeV	%	MeV	%	KeV	%
²²⁷Th	18.7	²²³Ra	11.4 days	**6.0**	100			0.236	13	19	37
²²³Ra	11.435	²¹⁹Rn		**5.7**	100			0.690	14	83	25
		²¹⁹Rn	3.96 s	**6.8**	79.4			0.271	10	16	1
		²¹⁵Po	1.78 ms	**7.4**	99.9						
		²¹¹Pb	36.1 m			0.471	91	0.404	3.8		
		²¹¹Bi	2.14 m	**6.6**	83.5	0.172	0.3	0.351	13		
		²¹¹Po	0.516 s	**7.5**	98.9						
		²⁰⁷Tl	4.77 m			0.492	99.7				
		²⁰⁷Pb	Stable								
²²⁴Ra	3.63	²²⁰Rn		**5.7**	95.0			0.241	4.1		
		²²⁰Rn	55.6 s	**6.3**	99.9						
		²¹⁶Po	0.15 s	**6.8**	99.9						
		²¹²Pb	10.6 h	–	–	0.0935	83	0.238	43.7	77	17.5
		²¹²Bi	60.6 m	**6.1**	25	0.834	55	0.727	6.7	15	7.0
		²¹²Po	0.3 μs	**8.8**	100						
		²⁰⁸Tl	3.1 m			0.65	49	2.614	99.0		
		²⁰⁸Pb	Stable								
²²⁵Ac	10	²²¹Fr		**5.8**	50.7			0.1	1.0		
		²²¹Fr	4.8 m	**6.3**	83.3			0.218	11.4	17.5	2.0
		²¹⁷At	32.3 ms	**7.1**	99.9						
		²¹³Bi	45.6 m	**5.9**	1.9	0.492	66	0.440	26	79	1.8
		²¹³Po	3.72 μs	**8.4**	100						
		²⁰⁹Tl	2.161 m			0.178	0.4	1.567	99.7	75	9.7
		²⁰⁹Pb	3.253 h			0.198	100				
		²⁰⁹Bi	Stable								
²¹¹At	7.21 h	²⁰⁷Bi		**5.9**	42					79	
		²⁰⁷Bi	31.6 years			?		0.570			
		²¹¹Po	0.52 s	**7.5**	98.9						
		²⁰⁷Pb	Stable								
¹⁴⁹Tb	4.12 h	¹⁴⁵Eu		**4.0**	16.7	β⁺, 0.64	83.3	0.352	29.4	43	26
		¹⁴⁵Eu	5.9 days			β⁺, 0.74	1.7	0.894	66.0	40	40
		¹⁴⁵Sm	343.3 days					0.061	12.0	39	40
		¹⁴⁵Pr	17.7 years					0.072	2.0	37	71
		¹⁴⁵Nd	Stable								
		¹⁴⁹Gd	9.28 days					0.158	48.0	42	55
		¹⁴⁹Eu	93.1 days							40	40
		¹⁴⁹Sm	Stable								

Bold value indicates the alpha particle energy is very high

emitters. In addition, cytotoxicity of alpha particles is nearly independent of dose rate and oxygenation status of the cells. The oxygen enhancement ratio (OER), the ratio of dose required to kill a given fraction of cells in hypoxic vs. oxic conditions, decreases with increasing LET [25]. The OER reaches 1 with LET of 165 keV μm. Therefore, hypoxic and radioresistant tumors are more effectively killed by α radiation of LET >100 KeV/μm.

17.3.2.1 Astatine-211

²¹¹At ($T_{\frac{1}{2}}$ 7.2 h) is an artificially produced α emitter which decays via a branched pathway to stable ²⁰⁷Pb as shown in Fig. 17.3. ²¹¹At decays directly (41.7%) to ²⁰⁷Bi with the emission of an α particle (5.87 MeV), and ²⁰⁷Bi decays by beta emission to ²⁰⁷Pb. In the second branch ²¹¹At first decays by EC (58.3%) to ²¹¹Po which immediately decays by emission of an alpha particle (7.45 MeV) to ²⁰⁷Pb. The EC decay of ²¹¹At also leads to the generation

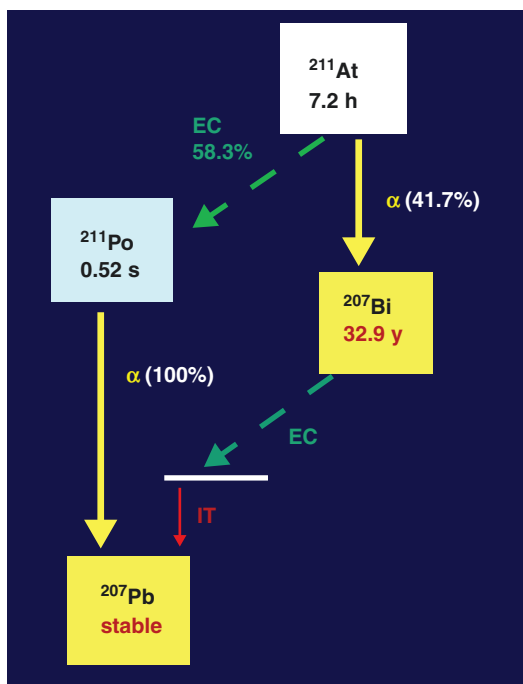**Fig. 17.3** At-211 decay results in the emission of 2 alpha particles with kinetic energies of 5.87 and 7.45 MeV

Fig. 17.4 Ac-225 decay results in the emission of 4 alpha particles (5.8–8.4 MeV) and 3 beta particles

of 77–92 KeV X-rays of polonium, which are suitable for SPECT imaging studies.

^{211}At is produced by cyclotron and α-particle bombardment via ^{209}Bi(α, 2n)^{211}At nuclear reaction using natural Bi-209 target. The thick target yield of ^{211}At is reported to be between 30 and 40 mCi/μA h at 28–29.5 MeV [21]. As the last member of the halogen family, astatine is the least electronegative in the halogen series and exhibits metallic properties. ^{211}At-labeled aromatic compounds are usually prepared by exchange halogenation or by electrophilic substitution on aromatic rings. ^{211}At has been extensively evaluated for alpha RT therapy in the last 3 decades [26].

17.3.2.2 Actinium-225

^{225}Ac is a pure α emitter with a half-life of 10 days, ^{225}Ac exhibits a complex decay scheme involving several radioactive isotopes (Fig. 17.4) before it reaches stable ^{209}Bi. ^{225}Ac and its daughters emit a total of four alpha particles. The two short-lived daughters, ^{221}Fr and ^{213}Bi emit useful γ photons (218 and 440 KeV). Quantitative

measurement of ^{225}Ac activity in a dose calibrator is possible, when these two daughters are in secular equilibrium with the parent. From a radiobiology point of view, there is concern that the release of these two relatively long-lived daughters may result in excessive toxicity to normal organs. It is especially important to design the chelator system to form stable complexes with actinium and the daughters so that the α particle recoil energy does not break chemical bonds and let the daughters diffuse into surrounding normal tissues.

^{225}Ac is mainly produced by isolation and purification from ^{229}Th ($T\frac{1}{2}$ = 7340 years), which is a decay product of uranium-233 ($T_{1/2}$ = 165,000 years). ORNL is a major producer of ^{225}Ac based on Th-229 generator (Thorium cow). The potential of using low-energy cyclotrons (<20 MeV) based on ^{226}Ra(p, 2n)^{225}Ac nuclear reaction was first reported in 2005 [27]. A major challenge, however, with this cyclotron method is related to the preparation and handling of targets containing milligram amounts of ^{226}Ra ($T_{1/2}$ = 1600 years), and management of its gaseous decay product ^{222}Rn ($T_{1/2}$ = 3.8 days).

Large-scale production of ^{225}Ac has been investigated based on the spallation of ^{232}Th targets with highly energetic protons (>70 MeV).

The nuclear reaction ^{232}Th(p, x)^{225}Ac was studied at different proton energies and beam currents. In recent years, the routine production of ^{225}Ac has been successfully established within the United States, Department of Energy Tri-Lab (ORNL, BNL, LANL) effort. The main limitation of the process, however, is the coproduction of long-lived ^{227}Ac ($T_{1/2}$ = 21.8 years) at levels of 0.1–0.2% activity (at EOB) [28].

17.3.2.3   Bismuth-213

^{213}Bi ($T_{1/2}$ 45.6 m) is a hybrid α/β$^-$ emitter, and finally becomes stable ^{209}Bi. It decays by β$^-$ (97.9%) to ^{213}Po which immediately decays by α emission to ^{209}Pb. In the second branch, it decays by α emission (2.1%) to ^{209}Tl. In addition, the decay of ^{213}Bi is also accompanied by a 440 keV γ photon emission. ^{213}Bi is generally produced as a decay product of ^{225}Ac (Fig. 17.4). The ^{225}Ac → ^{213}Bi generator requires purified ^{225}Ac and uses an organic anion-exchange system (AG-MP 50 resin) capable of isolating ^{213}Bi from a HCl solution of ^{225}Ac. The most established strategy is based on the direct generator method, in which the parent ^{225}Ac in acidic solution (e.g., 0.05 M HNO$_3$) is strongly retained by the sorbent. Elution is performed generally with a mixture of 0.1 M HCl/0.1 M NaI to obtain ^{213}Bi in the form of ^{213}BiI$_4^-$ and ^{213}BiI$_5^{2-}$ that can be directly used for radiochemistry purposes [29] A commercial ^{225}Ac → ^{213}Bi generator is currently supplied by iTM, Germany.

17.3.2.4   Thorium-227

^{227}Th ($T_{1/2}$ 18.7 days) decays to stable ^{207}Pb with 6 intermediate radionuclide progenies and a total of 6 α particles (Fig. 17.5). Massive quantities of ^{227}Th can be obtained by the beta decay of ^{227}Ac ($T_{1/2}$ 21.8 years), the long-lived isotope of actinium, identified in the ^{235}U decay products. The routine production of ^{227}Th is based on ^{227}Ac → ^{227}Th generator. ^{227}Th emits an α particle with 5.9 MeV energy and 236 KeV γ photons, suitable for imaging studies. ^{227}Th and all its daughters would deposit up to 34 MeV of energy at the target site.
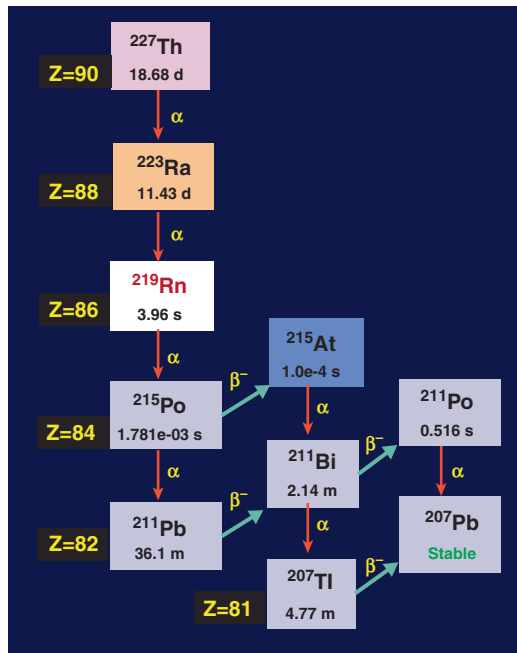
Fig. 17.5 Th-227 decay results in the emission of five alpha particles (5.7–7.5 MeV) and several beta particles. ^{223}Ra is the daughter nuclide obtained from ^{227}Th → ^{223}Ra generator

17.3.2.5   Radium-223

^{223}Ra ($T_{1/2}$ = 11.4 days) decays to stable ^{207}Pb with 5 intermediate radionuclide progenies and a total of 5 α particles (Fig. 17.5). ^{223}Ra is the first α emitter approved by the FDA in 2013 for the treatment of bone cancer in patients with prostate cancer. ^{223}Ra is a decay product of ^{227}Ac with a half-life of 21 years. Currently, the clinical and commercial production of ^{223}RaCl$_2$ (Bayer Health Care Pharmaceuticals) involves ^{227}Ac and ^{227}Th isolation from a ^{231}Pa source (3.28×10^4 years) [26].

17.3.2.6   Radium-224

^{224}Ra ($T_{1/2}$ = 3.63 days) decays to ^{208}Pb with 6 intermediate radionuclide progenies (Fig. 17.6). In Europe, short-lived ^{224}Ra was used for more than 40 years in the early 1900s in treating tuberculosis and ankylosing spondylitis [30]. A major problem of the use of ^{224}Ra clinically, however, is due to the presence of 2 daughters ^{212}Pb ($T_{1/2}$ 10.64 h) and ^{212}Bi ($T_{1/2}$ 60.6 min) which will

migrate from the target site and diffuses into the surrounding normal tissue and deliver toxic radiation dose. ^{212}Pb decays by β$^-$ emission to ^{212}Bi. Therefore, both these radionuclides, show potential for TAT, with ^{212}Pb being preferable to ^{212}Bi for clinical studies due to the longer half-life of ^{212}Pb, and because it can also generate ^{212}Bi in vivo, permitting more dose from ^{212}Bi progeny to be delivered to the target site.

17.3.2.7 Bismuth-212

^{212}Bi ($T\frac{1}{2}$ 60.6 min) is a hybrid α/β$^-$ emitter and has two decay modes (Fig. 17.6). It decays by α emission (36%) to ^{208}Tl, which in turn decays by β$^-$ emission to stable ^{208}Pb. In the second branch, it decays by beta emission (64%) to ^{212}Po, which immediately decays by alpha emission (100%) to stable ^{208}Pb. Both ^{212}Bi and ^{208}Tl also have extremely high-energy γ emissions not useful for imaging studies. ^{212}Bi is generally produced using either ^{224}Ra → ^{212}Bi generator or ^{212}Pb → ^{212}Bi generator. The parent ^{224}Ra first decays to ^{220}Rn gas, which is of great concern

from a radiation safety perspective. The decay product ^{208}Tl emits 2.6 MeV photons, which increases radiation exposure to personnel. Because of these practical concerns, ^{213}Bi may not be ideal for clinical studies.

17.3.2.8 Terbium-149

^{149}Tb ($T_{\frac{1}{2}}$ 4.1 h) decays by α emission as well as EC and positron emission. It ultimately decays to stable ^{145}Nd or ^{149}Sm. In the first branch, it decays to ^{145}Eu with the emission of α particles (4 MeV, 17.6%). In the second branch, ^{149}Tb decays to ^{149}Gd with the emission of positrons (E_{max} = 0.638 MeV, 83.3%). The decay scheme for ^{149}Tb is ideal to develop radiopharmaceuticals since it releases short-range α particles from only one radionuclide, with complementary positron emissions for PET imaging studies. Since there is only one α particle and no daughters with recoil energies, ^{149}Tb provides minimal toxicity [31]. ^{149}Tb can be produced in a cyclotron via ^{154}Gd(p, x)^{149}Tb spallation reaction using 70 MeV protons [32].

17.3.3 Radionuclides Emitting Low-Energy Electrons

Radionuclides that decay by electron capture (EC) or internal conversion (IC) emit electrons from the inner or outer shell electron orbits (Table 17.6). These electrons are called Auger electrons if they arise from higher shells and are called Coster-Kronig electrons if they originate from higher sub-shells. In contrast to β$^-$ particles, the average kinetic energy of these electrons is very low. As a result, low-energy Auger electrons traverse short distances (<μm) in biological tissue and deposit the energy in the immediate site of the decaying radionuclide. Therefore, to realize the full therapeutic potential of Auger electron emitters in TRT, it is necessary for the radionuclides to target the nuclear DNA within the cell [33]. When low-energy electron emitters are localized in cellular DNA, their RBE is similar to that observed with α-particle emitters [34].
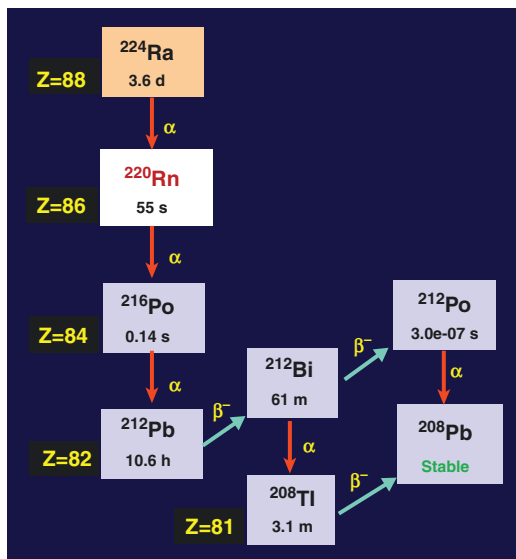

Fig. 17.6 Ra-224 decay scheme shows two radionuclides of interest. ^{212}Pb and ^{212}Bi. Both these two radionuclides are obtained using ^{224}Ra generator. While ^{212}Pb is not an alpha emitter, it is used as an in vivo generator for ^{212}Bi, which emits two alpha particles

Table 17.6 Radionuclides emitting low-energy Auger and internal conversion electrons

Radionuclide	$T_{\frac{1}{2}}$	Auger electrons			Internal conversion (IC) electrons		
		AEs/	E_{avg}/AE	E_{avg}/decay	IC-Es /	E_{avg}/IC-E	E_{avg}/decay
	Days	Decay	KeV	KeV	Decay	KeV	KeV
^{67}Ga	3.25	5	1.3	6.6	0.3	14.1	29.1
^{111}In	2.79	7.4	0.9	6.9	0.2	176.1	27.9
^{201}Tl	3.04	20.9	0.7	14.8	0.9	32.9	29.9
^{123}I	0.542	13.7	0.5	7.2	0.2	222.6	21
^{125}I	60.0	23	0.5	12.0	0.9	7.7	21
^{195m}Pt	4.0	36.6	0.6	23.1	2.8	58.1	161.5

Table modified from [33]

17.3.4 In Vivo Radionuclide Generators

Most of the radionuclides used in the development of diagnostic or therapeutic radiopharmaceuticals decay to a stable isotope of the same element or an isotope of another element. For example, the diagnostic nuclide F-18 decays by positron emission to stable oxygen-18. The therapy nuclide, I-131 decays by beta emission to stable Xe-131 inert gas. A radionuclide (parent) which decays to another radionuclide (daughter) or a series of radionuclides (decay chain) can be classified as in vivo radionuclide generators. ^{223}Ra dichloride (xofigo®) is a classic example of an in vivo generator since it generates four short-lived α-emitting daughters (^{219}Rn, ^{215}Po, ^{211}Bi, and ^{211}Po) at the target site following intravenous administration.

The term in vivo generator was first used to describe the use of targeted mAbs labeled with long-lived parent radionuclides that decay into short-lived daughter radionuclides. The concept is to combine the long half-life of the parent with the high decay energy of the daughter to achieve high-dose targeted radiotherapy [35–37]. Overall, the advantage of in vivo generators is to combine nuclear and chemical properties of the parent and daughter nuclides to better diagnose or treat physiological conditions. Some of the therapeutic radionuclide in vivo generator systems are listed in Table 17.7.

The most important consideration when employing an in vivo generator is the instability of the radiopharmaceutical that can result from the chemical transformation of one element to another. There are two opportunities for the daughter to separate from the parent, either because of the elemental differences between the parent and daughter or because of the physical and chemical disruption caused by the nuclear decay itself [35]. The recoil of the daughter nucleus could provide sufficient energy to dislodge the daughter from strong polydentate chelates. If the half-life of the daughter(s) is longer, they could diffuse into the surrounding normal tissue and deliver toxic radiation doses. For example, ^{227}Th, ^{223}Ra, and ^{225}Ac generate several daughters with half-lives long enough to diffuse into blood circulation and the normal tissues [38].

17.3.5 Mechanism and Biological Effects

The mechanism of action for radionuclide therapy is radiation-induced killing of cells. The ionizing radiation (especially the highly energetic particles such as electrons, protons, neutrons, and α particles) forms ions, the electrically charged particles, and deposits energy in the cells of the tissues it passes through. The energy dissipated per ionizing event is about 33 eV, which is more than enough to break a strong chemical bond, such as a C–C bond (4.9 eV). This deposited energy can kill cancer cells or cause genetic changes resulting in cancer cell death. Although radiation damages both normal cells as well as cancer cells, normal cells usually can repair themselves at a faster rate and retain its normal function status than the cancer cells. In addition,

Table 17.7 Radionuclide in vivo generator systems useful for targeted therapy

Parent				Daughter(s)				
Nuclide	$T_{1/2}$	Decay	E (MeV)	Nuclide	$T_{1/2}$	Decay	E (MeV)	Recoil E (KeV)
^{166}Dy	3.4 days	β^-	E_{max} 0.481	^{166}Ho	1.12 days	β^-	E_{max} 1.85	
^{212}Pb	10.64 h	β^-	E_{max} 0.574	^{212}Bi	1.01 h	α	6.1	
						β^-	E_{max} 2.254	
				^{212}Po	0.3 μs	α	8.8	
				^{208}Tl	3.1 min	β^-	E_{max} 1.803	
^{211}At	7.21 h	α	5.9	^{211}Po	0.52 s	α	7.5	
^{227}Th	18.67 days	α		^{223}Ra	11.435 days	α	5.7	108.4
^{223}Ra	11.435 days	α	5.7	^{219}Rn	3.96 s	α	6.8	104.5
				^{215}Po	1.78 ms	α	7.4	126.9
				^{211}Pb	36.1 min	β^-	E_{max} 1.361	
				^{211}Bi	2.14 min	α	6.6	140.1
				^{211}Po	0.516 s	α	7.5	
				^{207}Tl	4.77 min	β^-	E_{max} 1.423	
^{225}Ac	10.0 days	α	5.8	^{221}Fr	4.8 min	α	6.3	105.5
				^{217}At	32.3 ms	α	7.1	116.9
				^{213}Bi	45.6 min	α	5.90	132.8
						β^-	E_{max} 1.427	
				^{213}Po	3.72 μs	α	8.4	160.4
				^{209}Tl	2.161 min	β^-	E_{max} 3.97	
				^{209}Pb	3.253 h	β^-	E_{max} 0.644	

cancer cells in general are not as efficient as normal cells in repairing the damage caused by radiation treatment resulting in differential cancer cell killing [39].

17.3.5.1 Linear Energy Transfer (LET)

Radiation-induced ionization in the cells is the major cause of the biological effects of radiation. Specific ionization (SI) means the total number of ion pairs produced per unit length of the path of the incident radiation. For heavily charged particles, the SI increases with decreasing energy of the charged particles because of the increased probability of interaction at low energies. The quantity of linear energy transfer (LET) is the amount of energy deposited by the radiation per unit length of the path (KeV/μm). Low LET radiation (X-rays, γ-rays, electrons) deposits relatively a small quantity of energy while high LET radiation (protons, neutrons, and α particles) deposits higher energy in the targeted areas (Table 17.8).

The Bragg curve (Fig. 17.7) is a plot of the energy loss (or LET) of a charged particle

Table 17.8 Linear energy transfer (LET) and relative biological effectiveness (RBE) of radionuclide emissions

Radiation type	LET (KeV/μm)	RBE	Energy W_R
^{60}Co, γ-rays	0.2	0.8–0.9	1.0
LINAC X-rays (6–15 MeV)	0.3	~0.8	1.0
β particles (1 MeV)	0.3	0.9	1.0
X-rays, 250 kVp (standard)	2.0	1.0	1.0
Protons (150 MeV)	0.5	1.1	2.0
Neutrons	0.5–200	1–2	2.5–5.0
α-particles	50–200	5–10	20.0

Table modified from [40, 41]

during its travel through the matter. For protons and, α-rays, the peak (called Bragg peak) occurs immediately before the particles come to rest. In biological tissue, the complete energy of an α particle is dissipated in <100 μm (i.e., only a few cell diameters). The alpha particle LET, however, is inversely related to the energy and most of the alpha particle energy loss occurs at the end of the

Fig. 17.7 The Bragg curves for the four alpha particles emitted from the decay of ^{225}Ac and the daughter radionuclides. The higher the kinetic energy of the alpha particle, the lower the LET but, the longer the range of the particle in the tissue. (Figure modified from [42])
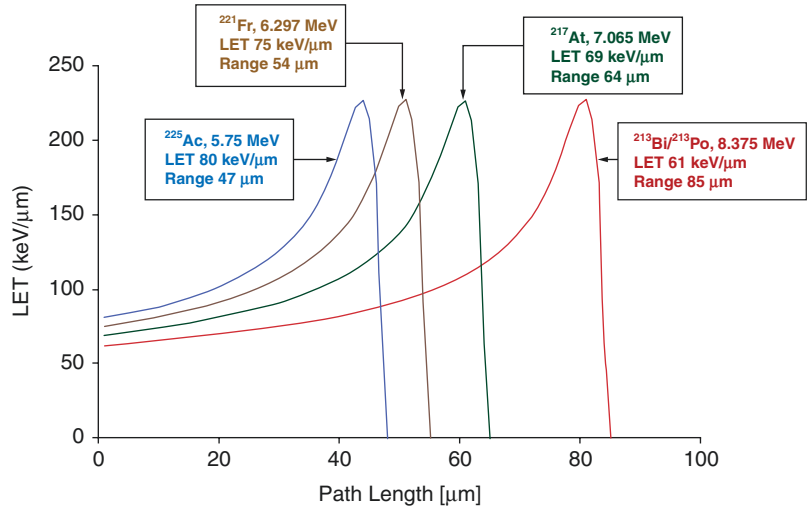
path, and at that moment the LET of the alpha particle increases to 200–250 keV/µm. The higher energy alpha particles lose less energy, or they have lower LET and vice versa.

17.3.5.2 Absorbed Dose vs. Equivalent Dose

The energy deposited by radiation in a target is called the "absorbed dose (D_T)", which is expressed as the total energy deposited in a unit volume of mass (m). The SI unit for D_T is the "***Gray***", which is equal to 1 J of energy absorbed in 1 kg of mass (any type of matter, living or non-living). When the mass of matter is biological tissue, the absorbed dose is given by another name, the "equivalent dose (H_T)", which is defined as the product of DT (Grays) and a radiation weighing factor, (W_R) for a specific radiation type. (W_R, formerly known as quality factor, Q). The SI unit for equivalent dose is the "***Sievert***", which has the same units as the Gray.

$$\text{Equivalent dose}\left(H_T\right) = \text{Absorbed dose}\left(D_T\right) \times \text{Radiation weighing factor}\left(W_R\right)$$

(17.3)

17.3.5.3 Relative Biological Effectiveness (RBE)

The absorbed dose (Gy) and equivalent dose (Sv) can be poor indicators of the biological effect of radiation, such as cell killing, since the biological effect can depend on the type of radiation, energy, and type of tissue. In radiobiology, RBE is an empirical value that varies depending on the type of ionizing radiation, the energies involved, the biological effects, and the oxygen effect. The RBE can help give a better measure of the biological effect of radiation. RBE is the ratio of biological effectiveness of one type of ionizing radiation relative to another, given the same amount of energy. The RBE for radiation of type R on a given tissue is defined as the ratio

$$RBE = D_X / D_R$$

(17.4)

where D_X is a reference absorbed dose of radiation of a standard type X, and D_R is the absorbed dose of radiation of type R that causes the same amount of biological damage. Distinct types of radiation have different biological effectiveness mainly because they transfer their energy to the tissue in different ways. As LET increases, relative biological effectiveness (RBE) increases and maximizes around 100 KeV/µm, and then RBE decreases with LET. Radiation weighing factors (W_R) used to convert absorbed dose to equivalent dose are not dependent on the type of tissue and, therefore, should not be used to estimate the RBE. As shown in Table 17.3 above, WR may be higher for particles.

17.3.6   Biological Effectiveness of Radionuclide Therapy

Radiation damage to the cell can be caused by the direct or indirect action of biological molecules [43]. In the direct action, the radiation hits the DNA molecule directly, causing single-stranded breaks (SSB) or double stranded breaks (DSB), disrupting the molecular structure (Fig. 17.8). Such structural change leads to cell damage or even cell death. This process becomes predominant with high-LET radiations, such as α-particles and neutrons, and high radiation doses. In the indirect action, the radiation hits the water molecules generating reactive oxygen species (ROS), such as hydrogen peroxide (H_2O_2) and free radicals (characterized by an unpaired electron), such as hydroxyl ($HO^{\bullet}$) group. In addition, indirect effects of radiation may also involve reactive nitrogen species (RNS). All the reactive molecules are toxic and can have many effects, including the oxidation of biological macromolecules and activation of intracellular signaling pathways. It has been found that the majority of radiation-induced damage results from the indirect action mechanism because water constitutes nearly 70% of the composition of the cell [44]. A widely accepted dogma in the field of radiation biology is that effects of ionizing radiation, such as cell death, chromosomal aberrations, DNA damage (both SSB and DSB), mutagenesis, and carcinogenesis, result from direct or indirect ionization of cell structures, particularly DNA. Overall, radiation-induced DNA damage is believed to activate a variety of signaling pathways leading to cell death, as well as accelerated senescence.

Recent investigations have challenged the classical DNA-centric view of radiation injury by demonstrating that proteins are also critical radiation targets that influence cell death mechanisms. In some cases, radiation-induced death by protein damage is proposed to be a consequence of reduced DNA repair fidelity, indirectly decreasing cell viability. In addition, recent studies also suggest that the detrimental effects of ionizing radiation are not restricted only to the irradiated cells but, also, to non-irradiated bystander or even distant cells manifesting various biological effects [45]

The molecular mechanisms of radiation-induced cellular injury, or biological effectiveness (cell killing) of radiation, however, depends on the LET of radiation, total dose, dose rate, and radio-sensitivity of the targeted cells or tissues. Low LET radiation (X-rays, γ-rays, electrons) deposits a relatively small quantity of energy while high LET radiation (protons, neutrons, and α particles) deposits higher energy in the targeted areas (Table 17.8). Radiation is generally more damaging in rapidly dividing cells and in undifferentiated cells. For example, untransformed epithelial cells of the gastrointestinal tract and progenitor cells of the hematopoietic system, which have rapid turnover rates, are generally more radiosensitive than the non-dividing neurons of the central nervous system. This differential proliferative capacity corresponds to the induction of Hematopoietic Syndrome at lower radiation exposures (0.7–10 Gy) compared to doses required for inducing Central Nervous System Syndrome (>50 Gy) [46].

17.3.6.1   Mechanisms of Cell Death

Radiation exposure to cells has been demonstrated to result in a variety of mechanisms of cell death, including necrosis, apoptosis, or autophagy. The basis for cellular selection for each mode, however, depends on a range of factors, including the specific cell type involved, the dose of radiation absorbed by the cell, and whether it is proliferating and/or transformed [46]. Many cancer cells, including lung, prostate, immortalized keratinocytes, and colon cancer cells, commit to apoptotic cell death when exposed to radiation ranging from 1 to 20 Gy. Low doses of radiation (0.1–2 Gy) have been demonstrated to induce apoptosis in human skin organotypic culture and murine epidermal cells.

The main goal of radiation therapy is to deprive cancer cells of their multiplication potential and eventually kill the cancer cells. Cancer cells whose DNA is damaged beyond repair stop dividing and die. Radiation therapy does not kill cancer cells right away. It takes hours, days, or weeks of treatment before cancer cells start to die after which cancer cells continue dying for weeks to months after radiation therapy ends. A deeper
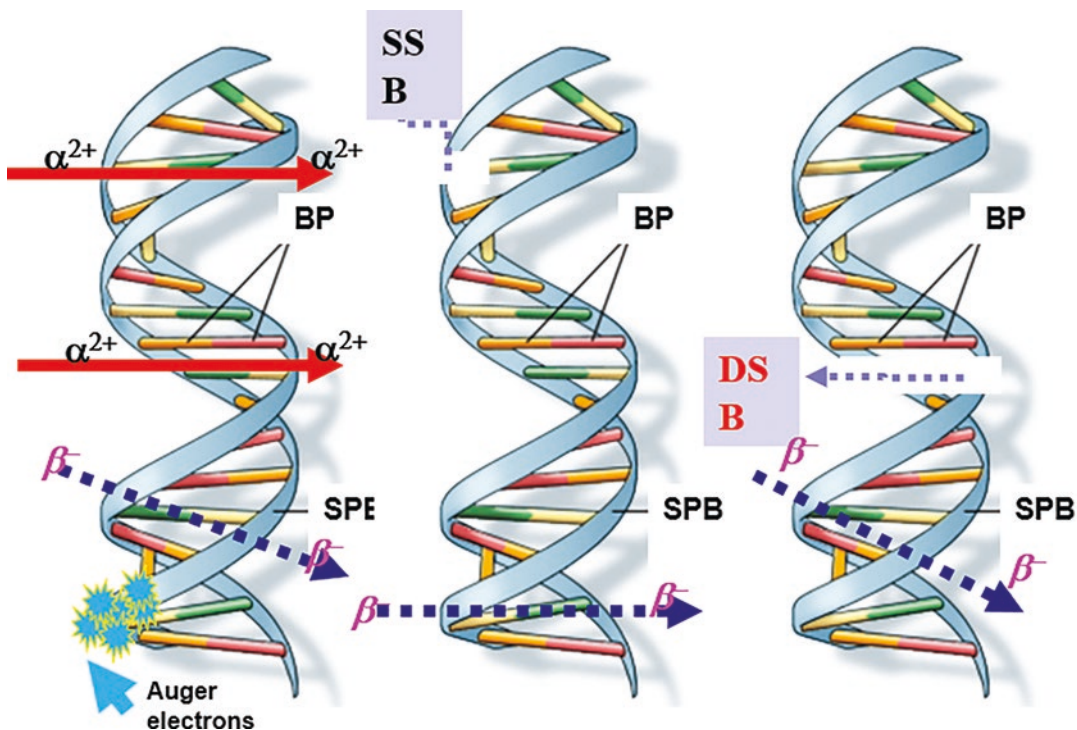
Fig. 17.8 Illustration of the interaction of radiation (β^-, α particles, and *Auger* electrons) with DNA. Alpha particles induce both single-strand and double-strand breaks in DNA but, beta particles pass through the double helix. Auger electrons will deposit all their energy very close to their origin

knowledge of the underpinning mechanisms and their interplay will reveal opportunities for enhancing the overall anti-tumor activity of RNT.

17.4 Design of Radiopharmaceuticals for TRT

17.4.1 Ideal Characteristics

TRT involves the use of a radiolabeled molecule to selectively deliver a cytotoxic level of radiation to a disease site. Advances in radionuclide production of alpha and beta emitters, tumor biology, recombinant antibody technology, and radiochemistry have led to a flurry of activity in the development and clinical application of target-specific therapeutic radiopharmaceuticals. In summary, an ideal radiopharmaceutical for

TRT, under ideal conditions, must have the following characteristics:

- High specificity and affinity for tumor cells
- In vivo stability in blood and within the tumor tissue with minimal metabolite formation
- Rapid blood clearance (to minimize bone marrow dose)
- Rapid targeting and significant retention of the therapeutic radionuclide (3–4 half-lives of the radionuclide) within the tumor
- Homogeneous radiation dose deposition within the tumor
- Rapid excretion from the body with minimal uptake and retention by normal tissues and cells
- Minimal hematologic toxicity in order to increase the maximum tolerated dose (MTD)
- to preserve dose-rate effect
- Acceptable toxicity to liver, spleen, and kidney
- No radiation-induced biologic effects such as mutation or transformations leading to secondary cancers.

To meet all the requirements described above, the design and development of a successful therapeutic radiopharmaceutical for TRT (Fig. 17.1) require the following steps:

1. Based on preclinical work, identifying the most appropriate and specific biological target (receptor or an antigen on the cancer cell membrane) for the therapy of a specific cancer.
2. Selection of a targeting vehicle (peptide, small organic molecule, monoclonal antibody, or a particle such as liposome or a nanoparticle) with high affinity and specificity for biological target.
3. Identifying an appropriate therapeutic radionuclide for a specific cancer tissue and appropriate to radiolabel the ideal targeting vehicle.
4. Careful design of the binding moiety (targeting vehicle-spacer-linker-chelate) with optimal biodistribution and pharmacokinetic parameters.
5. All the above steps require careful multistep matching of the (a) target and the ligand molecule, (b) the ligand and the radionuclide, (c) the tumor and radionuclide, and, finally, (d) the radionuclide and the chelator.

17.4.2 Selection of Therapeutic Radionuclide

Various radionuclides used for therapy are listed in Table 17.3. Although numerous radionuclides have potential applications in radionuclide therapy, only a very few radionuclides possess favorable physical, chemical, and biological characteristics which would identify them as practical for clinical use. Physical characteristics include physical half-life, type of emissions, energy of the emissions, daughter products, method of production, and radionuclidic purity. Biochemical characteristics include tissue targeting, retention of radioactivity in the tumor, in vivo stability, and toxicity.

The ideal radionuclides for therapy are those with an abundance of non-penetrating radiations,

such as charged particles (α^{2+}, β^-, *and Auger electrons*), and lack of penetrating radiations (γ or X-rays). While penetrating radiation is not essential for TRT, a small amount or abundance with an appropriate energy (100–400 KeV) may be useful for imaging studies to demonstrate tumor localization or altered biodistribution.

The energy of the charged particle determines the amount of energy deposited in each volume of the tissue. Therefore, the choice of a particular radionuclide is strongly dependent on the LET value and tissue range of emissions. Each type of particle emitted by the radionuclide has a different range and effective distance. The higher the LET of a specific radionuclide, the greater the relative biological effectiveness (RBE). The β^- particles, Auger electrons, and conversion electrons have the same mass but, different kinetic energy and different ranges (0.1–3.0 mm) in tissue. All electrons have low LET values (0.2 keV/μm) and their RBE is unity. In contrast, α particles are 8000 times heavier and have very high LET values (40–100 KeV/μm), and therefore the RBE values can be 5–10 depending on the tissue. When a therapy radiopharmaceutical has a non-uniform distribution within the tumor (>1 mm), radionuclides with high-energy β^- particles deposit energy in cells that do not take up the radioisotope, by the crossfire effect. Therefore, for large-volume tumor tissue, radionuclides with β^- emission are appropriate. In contrast, for the treatment of microscopic disease (<1.0 mm in diameter), α particles are ideal since they deposit their energy (5–9 Mev) over short distances. Radionuclides with Auger electrons or other low-energy electrons have a short range and, if the radionuclide is localized in the nucleus, most of the energy will be deposited locally and potentially damage cellular DNA.

The physical half-life ($T_{\frac{1}{2}p}$) of the therapeutic radionuclide is important since the time course of irradiation of a target is related to both the physical half-life and biological turnover or biological half-life ($T_{\frac{1}{2}b}$) of the radiopharmaceutical. One must select an appropriate radionuclide depending on the carrier molecule used to develop the therapeutic agent. For example, with an intact antibody molecule, radioisotopes with medium

half-life (3–10 days) are preferable, while with small molecules and peptides, the half-life of the radionuclide may not be a major factor to consider.

17.4.3 Theranostic Pair of Radionuclides

The concept of "theranostics" describes a clinical management system that allows the combined diagnosis, treatment, and follow-up of a disease in order to identify a sub-population of patients most likely to benefit from a targeted therapy in accordance with their "molecular profile". In personalized medicine, diagnostic molecular imaging (using SPECT or PET) is often employed for selecting appropriate and optimal therapies based on the context of a patient's genetic content or other molecular or cellular analysis to look at a patient on an individual basis that will allow for a more accurate diagnosis and specific treatment plan. In nuclear medicine, theranostics is a personalized approach to treating cancer, using the same or similar molecules for both imaging (diagnosis) and targeted therapy. After selecting a specific targeting vehicle, a diagnostic agent is prepared by attaching a radionuclide for PET or SPECT imaging study. The same targeting vehicle is also labeled with an appropriate therapeutic radionuclide-emitting beta, alpha or Auger electrons. It is important that the biodistribution, pharmacokinetics, and tumor uptake of both diagnostic and therapeutic agents are similar. The concept of theranostics was first introduced in the 1990s, however, ^{123}I or ^{131}I sodium iodide for diagnostic studies followed by treatment of thyroid disease with ^{131}I sodium iodide has been in clinical use for more than 70 years. Also, several laboratories developed ^{111}In-labeled octreotide as a chemical and biological surrogate of a therapeutic agent ^{90}Y-labeled octreotide since both radionuclides are trivalent metals.

Since ^{111}In imaging studies (planar and SPECT) did not provide quantitative data on radiation dosimetry in individual patients, researchers in Julich Germany came up with the idea of combining PET and radionuclide therapy by using a pair of radionuclides of the same element, one emitting positrons, and the other β⁻ particles (Table 17.9). [86]Y, a positron emitter was developed to perform patient specific dosimetry in patients receiving ^{90}Y-labeled therapeutic agent [47, 48].

17.4.4 Biological Target and Targeting Vehicle

Several biological targets expressing tumor-specific antigens or cell surface receptors are summarized in Tables 17.10 and 17.11. The targeting vehicles are small organic molecules (such as amino acids, MIBG, and steroid hormones), bioactive peptides, proteins or antibodies, and antibody fragments as shown in Tables 17.1 and 17.2. In the design of a target (binding site) specific radiopharmaceutical (Fig. 17.1), the choice of a biological target in the tumor tissue, however, depends on the following key factors:

- The accessibility of the target for the ligand is an important consideration. In this context, the microscopic environment of the target, including tumor vascularity, permeability, and oxygenation would all contribute to the net uptake of the radiopharmaceutical by the tumor.
- The number of binding sites (B_{max}) per tumor cell and the relative distribution and the expression of target molecules within the tumor tissue during each phase of the cell cycle. The concentrations of tumor-associated antigens and receptors among tumors from patients with a particular type of malignancy can vary from over 10^5 molecules per cell to undetectable levels. In addition, wide variations in antigen or receptor expression have been reported both, within the cells of a particular tumor, as well as between different tumors from the same patient.
- The expression of binding sites in the nontarget sites, such as blood and soft tissues (liver, kidney, spleen, and muscle).

Table 17.9 Theranostic radionuclides for imaging and therapy

Radionuclide for therapy						Radionuclide for PET					
Nuclide	T½	Decay	E_{max} MeV	γ-rays KeV	%	Nuclide	T½	Decay	E_{max} MeV	γ-rays KeV	%
^{131}I	8.02 days	β⁻ (100)	0.607	364.5	82	^{124}I	4.18 days	β⁺ (22)	2.14	603	61
										723	10
^{90}Y	2.70	β⁻ (100)	2.29	–	–	^{86}Y	14.7 h	β⁺ (33)	2.34	627.8	32.6
										1077	82.5
										1153	30.5
^{67}Cu	2.58 days	β⁻ (100)	0.577	184.6	48.6	^{64}Cu	12.7 h	β⁺ (17.8)	0.653	1346	0.53
								β⁻ (38.4)	0.571		
								EC(43.8)			
^{47}Sc	3.35 days	β⁻ (100)	0.610	159	68	^{44}Sc	3.9 h	β⁺ (94.3)	1.470	1157	99.9
^{89}Sr	55.5 days	β⁻ (100)	1.470	–	–	^{83}Sr	32.4 h	β⁺ (94.3)	1.274	381.3	19.6
^{161}Tb	6.9 days	β⁻ (100)	0.590	74.6	9.8	^{152}Tb	17.5 h	β⁺ (18.0)	2.500	344.3	57
^{149}Tb	4.1 h	α (16.7)	α 5.83	165	27.8	^{149}Tb	4.1 h	β⁺ (4.3)	0.600	165	28
		EC (79)		352	33			EC (79)		352	33
^{177}Lu	6.73 days	β⁻ (100)	0.498	113	6.4	^{68}Ga	67.6 min	β⁺ (90)	2.921	1077	3.0
				208	11	^{111}In	2.805 days	EC (100)	–	171.3	90
										245.4	94

Table 17.10 Tumor-specific biological targets (antigens and proteins) to develop therapeutic radiopharmaceuticals

Target	Patient population
CD20	Non-Hodgkin's lymphoma
Prostate-specific membrane antigen (PSMA)	Prostate cancer
Epidermal growth factor, EGFR (HER1)	Colorectal cancer
Human epidermal growth factor-1 (HER2)	Breast cancer
Human epidermal growth factor-3 (HER3)	Solid tumors
Carcinoembryonic antigen (CEA)	Colorectal cancer
CD-22	Non-Hodgkin lymphoma
CD-45	Acute myelogenous leukemia (AML)
CD-33	Acute myelogenous leukemia (AML)
Mesothelin (MSLN)	Ovarian or prostate cancer
Prostate stem cell antigen (PSCA)	Bladder, pancreatic, or prostate cancer
Placental growth factor (PLGF)	Glioblastoma multiforme
PD-1	Non-small-cell lung cancer (NSCLC), melanoma
PD-L1	Bladder cancer, NSCLC, triple-negative breast cancer (TNBC)
Transforming growth factor β (TGFβ)	Glioma
Vascular endothelial growth factor-A (VEGF-A)	Breast cancer, glioma, MM, NET, NSCLC, RCC

CD cell-surface differentiation antigen

Table 17.11 Peptide receptors as biological targets to develop therapeutic radiopharmaceuticals

Peptide	Receptor/ subtype	Tumor expression
Somatostatin	SSTR I–V	Neuroendocrine tumor, small cell lung, prostate cancer, breast cancer, colorectal carcinoma, gastric cancer, hepatocellular carcinoma
Bombesin	GRP-bombesin	Prostate, breast, small cell lung cancer (SCLC), gastric, ovarian, colon, and pancreatic cancers
	EGFR	Lung, breast, bladder, and ovarian cancers
Substance P	NK1	Glial tumors, astrocytomas, medullary thyroid cancer (MTC), and breast cancer
VIP	VPAC1	GI and other epithelial tumors
Integrins	$\alpha_V\beta_3$ integrin	Insulinomas, activated endothelial cells, glioblastomas, ovarian cancer.
CCK/gastrin	CCK2	MTC, insulinoma, SCLC, GISTs
Glucagon-like peptide 1 (GLP-1)	GLP-1-R	Insulinoma, gastrinoma
Neuropeptide-Y	NPY-R	Breast, ovarian, and adrenal tumors
Neurotensin	NT-R1	Exocrine pancreatic cancer, meningioma, Ewing sarcoma, and prostate cancer breast, colon, pancreatic, lung cancer

17.4.5 Radiolabeling Methods

Among the radionuclides listed in Table 17.3, ^{131}I, and [211]At belong to the halogen family (Group 17 in the periodic table). [211]At, however, is also regarded as a metalloid since it shares certain chemical properties with metals. All other radioisotopes listed are metals. The radionuclide production and the chemistry of halogens and radiometals are discussed in greater detail in Chaps. 8 and 18 of this book and in several review articles [49–52].

The labeling of peptides with radionuclides can be performed by direct labeling, with the addition of a prosthetic groups. Direct labeling is the method used to label peptides without using intermediates, such as BFCs. Direct labeling techniques are gen-

erally used mostly for radioiodination and in some cases labeling with Tc-99m. Prosthetic groups are small molecules which are able to bind with radionuclides in one site of the structure, and simultaneously with a peptide at a second site. Prosthetic groups are bifunctional agents that consist of a suitable site for radioiodination or fluorination and functional groups to allow covalent attachment of the peptide. Radiometals specifically require bifunctional chelating agents (BFC or BFCA) to obtain the best conjugation of radiometal with peptides. The bifunctional nature of the chelators means that they can coordinate (form a complex) a metal ion and can also be attached to the peptide. The most common chelating agents used for the development of radiolabeled small molecules, peptides, and proteins are analogs of DTPA and DOTA. The chemical structures of somatostatin analogs (octreotide and Tyr3-octreotide) conju-

gated with acyclic and macrocyclic BFCs are shown in Fig. 17.9. The design and development of radiolabeled peptides is discussed in greater detail in Chap. 20.

17.5 Therapy Radiopharmaceuticals Approved for Clinical Use

The therapy radiopharmaceutical may be a simple inorganic ion, metal complex, or particles. For TRT to be truly effective and specific, the carrier molecule or the targeting vehicle (ligand or vector), ideally, seeks the tumor cells and delivers the radionuclide to the tumor cells by specific binding to a target site, either on the cell surface or within the tumor cell. The selection of the targeting vehicle (such as antibodies and peptides)

and the preparation of target-specific therapeutic radiopharmaceutical (Fig. 17.1) involve complex design strategies.

17.5.1 Inorganic Ions

A classic example of TRT is the use of ^{131}I as sodium iodide (I$^-$) for the post-surgery treatment of thyroid cancer. The negatively charged radioiodide[^{131}I]I$^-$ ion selectively accumulates in thyroid cancer cells by active transport via an ion pump known as sodium iodide symporter (SIS). In this mechanism, the radionuclide as iodide ion is the active ingredient of the radiopharmaceutical and no specific ligand or carrier is required.

Similarly, with the calcium analogs, ^{89}Sr chloride and ^{223}Ra chloride, the positively charged (cationic) ^{89}Sr^{2+} ion and ^{223}Ra^{2+} ion follow the biochemical pathway of calcium within the bone and localize in the hydroxyapatite ($Ca_{10}(PO_4)_6(OH)_2$), the mineral content of bone. These ions are preferentially taken up into bone metastases with increased bone turnover and no specific carrier is required to bind to the osteoblastic bone formation at the metastatic sites.

17.5.1.1 Sodium Iodide I 131 Solution

Sodium Iodide I 131 (Na I-131) Solution Therapeutic [53] is supplied for oral administration as a stabilized aqueous solution. The solution is available in vials that contain from 185 to 5550 MBq (5–150 mCi) iodine-131 at the time of calibration. Sodium Iodide I 131 Solution Therapeutic is packaged in shielded screwcap 15 mL vials. The solution contains 0.1% sodium bisulfite and 0.2% edetate disodium as stabilizers, 0.5% sodium phosphate anhydrous as a buffer, and sodium iodide I-131 at concentrations of 185 or 925 MBq (5 or 25 mCi) per milliliter. The pH has been adjusted to between 7.5 and 9. The iodine-131 utilized in the preparation of the solution contains not less than 99% iodine-131 at the time of calibration.

Indications and Usage: Sodium Iodide I 131 Solution is indicated for the treatment of hyperthyroidism and thyroid carcinomas that can accumulate radioiodide. Palliative effects may be observed in patients with advanced thyroid malignancy if the metastatic lesions take up iodide.

Mechanism of Action: Taken orally, sodium iodide I-131 is rapidly absorbed and distributed within the extracellular fluid of the body. The iodide is concentrated in the thyroid via the sodium/iodide symporter and, subsequently, oxidized to iodine. The destruction of thyroidal tissue is achieved by the beta emission of sodium iodide I-131.

Pharmacodynamics: The therapeutic effects of sodium iodide I-131 are a result of the ionizing radiation absorbed by the thyroidal tissue. Tissue damage is the result of a direct insult to molecules by ionization and excitation and the consequent dissociation of those molecules. About 90% of local irradiation from sodium iodide I-131 is the result of beta radiation and 10% is the result of gamma radiation.

Pharmacokinetics: After oral administration, sodium iodide I-131 is absorbed rapidly from the upper gastrointestinal tract (90% in 60 min). The pharmacokinetics follow that of unlabeled iodide. After entering the bloodstream, the iodide is distributed into the extra-thyroidal compartment. From here it is predominantly taken up by the thyroid or excreted renally. In the thyroid, the trapped iodide is oxidized to iodine and organified. The sodium/iodide symporter (NIS) is responsible for the concentration of iodide in the thyroid. This active transport process is capable of concentrating iodide 20–40 times the plasma concentration under normal circumstances, and this may increase tenfold in the hyperthyroid state. NIS also mediates active iodide transport in other tissues, including salivary glands, nasolacrimal duct, lacrimal sac, gastric mucosa, lactating mammary gland, and the choroid plexus. The non-thyroidal iodide transporting tissues do not have the ability to organify accumulated iodide.

Drug Interactions: Many pharmacologic agents interact with sodium iodide I-131. These agents (anti-thyroid drugs, thyroid hormones, iodine-containing medications, X-ray contrast agents, topical iodide, and several drugs) may affect the iodide protein binding and alter the iodide pharmacokinetics and pharmacodynamics.

17.5.1.2   Metastron™ (Strontium-89 Chloride Injection)

Metastron is a sterile, non-pyrogenic, aqueous solution of Strontium-89 Chloride for intravenous administration. The solution contains no preservatives. Each milliliter contains 10.9–22.6 mg of strontium Chloride. The radioactive concentration is 37 MBq/mL (1 mCi/mL), and the specific activity is 2.96–6.17 MBq/mg (80–167 µCi/mg) at calibration. The pH of the solution is 4–7.5 [54].

Indications and Usage: Metastron (Strontium-89 Chloride Injection) is indicated for the relief of bone pain in patients with painful skeletal metastases.

Dosage and Administration: The recommended dose of Metastron is 148 MBq (4 mCi), administered by slow intravenous injection (1–2 min). Alternatively, a dose of 1.5–2.2 MBq/kg (40–60 µCi/kg) body weight may be used. Repeated administrations of Metastron should be based on an individual patient's response to therapy, current symptoms, and hematologic status, and are generally not recommended at intervals of less than 90 days.

Mechanism of action: Following intravenous injection, soluble strontium compounds behave like their calcium analogs, clearing rapidly from the blood and selectively localizing in bone mineral. Uptake of strontium by bone occurs preferentially in sites of active osteogenesis; thus, primary bone tumors and areas of metastatic involvement (blastic lesions) can accumulate significantly greater concentrations of strontium than surrounding normal bone.

Pharmacokinetics: Strontium-89 Chloride is retained in metastatic bone lesions much longer than in normal bone, where turnover is about 14 days. In patients with extensive skeletal metastases, well over half of the injected dose is retained in the bones. Excretion pathways are two-thirds urinary and one-third fecal in patients with bone metastases. Urinary excretion is higher in people without bone lesions. Urinary excretion is greatest in the first 2 days following injection.

17.5.1.3 ^{223}Ra Dichloride (Xofigo)

^{223}Ra dichloride, an alpha particle-emitting pharmaceutical is supplied as a clear, colorless, isotonic, and sterile solution to be administered intravenously with pH between 6 and 8. The drug product contains 1000 kBq or 27 µCi/mL of ^{223}Ra, corresponding to 0.53 ng Ra-223 at the reference date. Radium is present in the solution as a free divalent cation. Each vial contains 6 mL of solution (6000 kBq (162 µCi) radium-223 dichloride at the reference date). The inactive ingredients are 6.3 mg/mL sodium chloride USP (tonicity agent), 7.2 mg/mL sodium citrate USP (for pH adjustment), 0.2 mg/mL hydrochloric acid USP (for pH adjustment), and water for injection USP. The molecular weight of radium-223 dichloride, ^{223}RaCl$_2$, is 293.9 g/mol. The SA of radium-223 is 1.9 MBq or 51.4 µCi/ng.

^{223}Ra has a half-life of 11.4 days. The six-stage decay of radium-223 to stable lead-207 occurs via short-lived daughters and is accompanied predominantly by alpha emissions. There are also beta and gamma emissions with different energies and emission probabilities. The fraction of energy emitted from radium-223 and its daughters as alpha-particles is 95.3% (5–7.5 MeV). The fraction emitted as beta-particles is 3.6% (average energies are 0.445 and 0.492 MeV), and the fraction emitted as gamma-radiation is 1.1% (energy range of 0.01–1.27 MeV).

Indications and Dosage: Xofigo is indicated for the treatment of patients with castration-resistant prostate cancer, symptomatic bone metastases, and no known visceral metastatic disease. The dose regimen of Xofigo is 50 kBq or 1.35 µCi/kg body weight, given at 4-week intervals for 6 injections.

Mechanism of action: ^{223}Ra mimics calcium and forms complexes with the bone mineral hydroxyapatite at areas of increased bone turnover, such as bone metastases. The high LET of alpha particles (80 keV/µm) leads to a high frequency of double-strand DNA breaks in adjacent cells, resulting in an anti-tumor effect on bone metastases. The alpha particle range <0.1 mm (less than 10 cell diameters) limits damage to the surrounding normal tissue.

Pharmacokinetics: After intravenous injection, ^{223}Ra is rapidly cleared from the blood and is distributed primarily into bone or is excreted into

the intestines. At 4 h, about 4% of the injected radioactivity remains in blood, decreasing to less than 1% at 24 h after the injection. At 4 h post-injection, the percentage of the radioactive dose present in bone and intestine is, approximately, 61% and 49%, respectively.

The efficacy and safety of Xofigo were evaluated in a double-blind, randomized, placebo-controlled phase 3 clinical trial of patients with CRPC with symptomatic bone metastases. Patients receiving the treatment with ^{223}Ra exhibited a 3.6-month prolonged survival time (PST) over the placebo group and a 5.8-month improved timeframe before the occurrence of a systematic skeletal-related event with a reduction of occurrence of spinal compression [55, 56]

17.5.2 Inorganic Chelate Complex

With the success of ^{99m}Tc bone imaging agents (such as MDP, HDP, EHDP) for targeting bone mineral hydroxyapatite, several β^- particle-emitting radiometals that can form chelate complexes were investigated for the development of radiopharmaceuticals for bone pain palliation. ^{153}Sm ($T\frac{1}{2}$ = 46.7 h, E_{mean} = 233 KeV), a trivalent lanthanide has a short half-life and low-energy beta particles and is a suitable alternative to Sr-90 which has a long half-life and high-energy beta emission. In addition, ^{153}Sm also has suitable γ photons (103 KeV) which make it suitable for imaging studies. ^{153}Sm forms a stable coordination complex with bisphosphonate analog EDTMP and ^{153}Sm-EDTMP was approved in 1997 for bone pain palliation. In the last two decades, several metal complexes were investigated as potential therapeutic agents for bone pain palliation such as ^{166}Ho-EDTMP, ^{177}Lu-EDTMP, ^{90}Y-EDTMP, ^{170}Tm-EDTMP, ^{117m}Sn-DTPA, and recently ^{177}Lu-DOTAZOL.

17.5.2.1 ^{153}Sm-Lexidronam (Quadramet®)

^{153}Sm-EDTMP (Quadramet®) (Fig. 17.10) was designed so that a tetraphosphonate chelator, EDTMP, a polydentate ligand, chelates ^{153}Sm 1:1 by forming four O-Sm bonds and two N-Sm bonds. EDTMP is structurally similar to bisphosphonates, which target bone due to their great
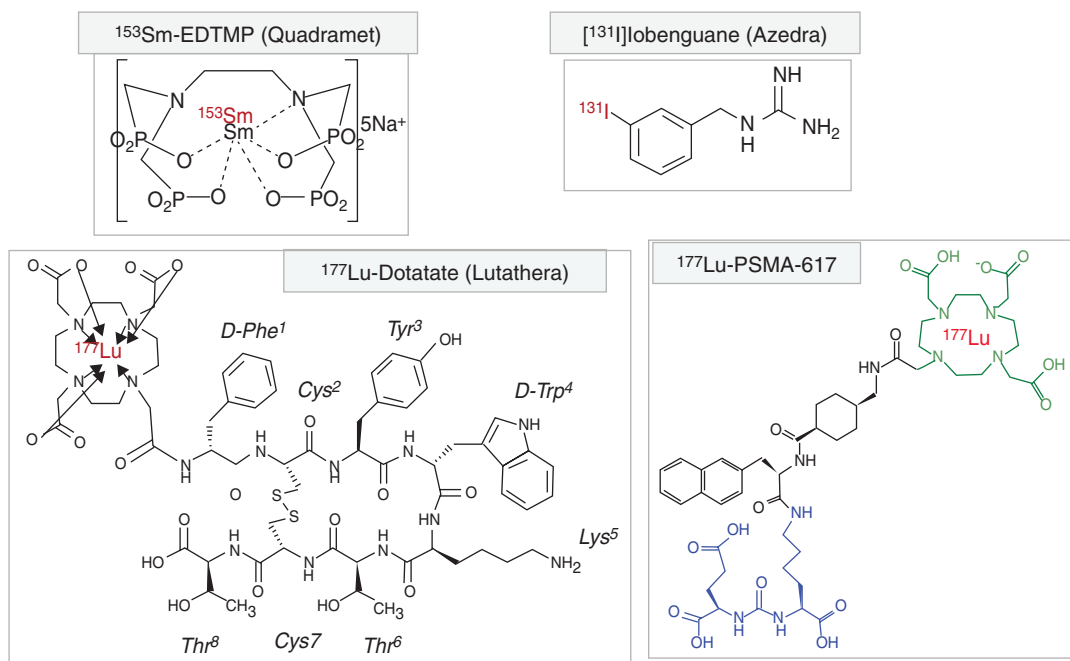

Fig. 17.10 Chemical structures of radiopharmaceuticals for TRT in clinical use

affinity for inorganic hydroxyapatite. The negatively charged ^{153}Sm-EDTMP readily chelates calcium cations and accumulates in the metastatic sites with increased metabolism and has higher calcium levels. QUADRAMET® is formulated as a sterile, non-pyrogenic, clear, colorless to light amber isotonic solution of samarium-153 lexidronam for intravenous administration [57].

Each milliliter contains 35 mg EDTMP·H$_2$O, 5.3 mg Ca[as Ca(OH)$_2$], 14.1 mg Na [as NaOH], equivalent to 44 mg Ca/Na EDTMP (anhydrous calc.), 5−46 μg samarium (specific activity of approximately 1.0−11.0 mCi/μg Sm), and 1850 ± 185 MBq (50 ± 5 mCi) of samarium-153 at calibration. The ionic formula is ^{153}Sm^{+3}[CH$_2$N (CH$_2$PO$_3$$^{2−}$)$_2$]$_2$ and the ionic formula weight is 581.1 Da (pentasodium form, 696). The pH of the solution is 7.0–8.5. QUADRAMET® is supplied frozen in single-dose glass vials containing 3 mL with 5550 MBq (150 mCi) of samarium-153 at calibration.

Indications: QUADRAMET® is indicated for relief of pain in patients with confirmed osteoblastic metastatic bone lesions that enhance on radionuclide bone scan.

Dosage and Administration: The recommended dose of QUADRAMET® is 1.0 mCi/kg, administered intravenously over a period of 1 min.

Clinical Pharmacology: QUADRAMET® has an affinity for bone and concentrates in areas of bone turnover in association with hydroxyapatite. It accumulates in osteoblastic lesions more than in normal bone with a lesion-to-normal bone ratio of approximately 5. The mechanism of action of QUADRAMET® in relieving the pain of bone metastases is not known. The greater the number of metastatic lesions, the more skeletal uptake of Sm-153 radioactivity. The total skeletal uptake of radioactivity is 65.5% ± 15.5% of the injected dose. Clearance of radioactivity from the blood demonstrated biexponential kinetics after intravenous injection in patients with a variety of primary cancers that were metastatic to bone. Over the first 30 min, the radioactivity in the blood decreased to 15 ± 8% of the injected dose. Less than 1% of the dose injected remained in the blood 5 h after injection. During the first 6 h, 34.5% (±15.5%) was excreted.

Drug Interactions: QUADRAMET® contains calcium and may be incompatible with solutions that contain molecules that can complex with and form calcium precipitates.

17.5.3　Particulate Carriers

Radiolabeled particles are generally used when the tumor is confined to a specific organ or an isolated body cavity. The goal is to obtain a uniformly distributed radiation dose within the cavity, while minimizing leakage into the rest of the body. In addition to stability, the most important characteristic of particulate carriers is their size because this dictates not only homogeneity of dose deposition but, also leakage from the treatment site. Two commercial preparations of ^{90}Y-labeled microspheres (20–60 μm), Theraspheres® and Sirspheres® are used for the treatment of hepatocellular carcinoma (HCC) and metastatic colorectal cancer [58]. Trans-arterial chemoembolization (TACE) involves administration of drugs intra-arterially for preferential localization in regions of tumor as majority of normal hepatic blood supply is via the portal vein and neo-angiogenic vessels are primarily connected to the hepatic artery. Following the release of the ^{90}Y-labeled microspheres in the hepatic artery via a microcatheter, the microspheres are permanently embedded in the terminal arterioles of the tumor. After the radio-embolization, the particles block the blood vessels and deliver the radiation dose locally. The ^{90}Y-labeled particles do not directly bind to cancer cells.

17.5.3.1　Theraspheres® Yttrium-90 Glass Microspheres

TheraSphere® consists of insoluble glass microspheres where yttrium-90 is an integral constituent of the glass. The mean sphere diameter ranges from 20 to 30 μm. Each milligram contains between 22,000 and 73,000 microspheres. TheraSphere® is supplied in 0.6 mL of sterile, pyrogen-free water contained in a 1.0 mL vial secured within a clear acrylic vial shield. TheraSphere® is available in 6 dose sizes: 3 GBq (81 mCi), 5 GBq (135 mCi), 7 GBq (189 mCi), 10 GBq (270 mCi), 15 GBq (405 mCi) and 20 GBq (540 mCi).

Indication: TheraSphere® is indicated for radiation treatment or as a neoadjuvant to surgery or transplantation in patients with unresectable hepatocellular carcinoma (HCC) who can have placement of appropriately positioned hepatic arterial catheters. The device is also indicated for HCC patients with partial or branch portal vein thrombosis/occlusion when clinical evaluation warrants the treatment. Theraspheres® has been used in the clinic for the last 8 years under a humanitarian device exemption (HDE) but, in March of 2021, Theraspheres® formally received FDA approval as a device.

Mechanism: Following embolization of the yttrium-90 glass microspheres in tumorous liver tissue, the beta radiation emitted provides a therapeutic effect [11, 27, 29, 59, 60]. The microspheres are delivered into the liver tumor through a catheter placed into the hepatic artery that supplies blood to the tumor. The microspheres, being unable to pass through the vasculature of the liver due to arteriolar capillary blockade, are trapped in the tumor and exert a local radiotherapeutic effect with some concurrent damage to surrounding normal liver tissue.

17.5.3.2 SirSpheres® Microspheres (Yttrium-90 Microspheres)

SIR-Spheres® microspheres consist of biocompatible microspheres containing yttrium-90 with a size between 20 and 60 μm in diameter. The average number of particles implanted is $30–60 × 10^6$. SIR-Spheres microspheres are provided in a vial with water for injection. Each vial contains 3 GBq of yttrium-90 ±10% (at the time of calibration) in a total of 5 cc water for injection. Each vial contains 40–80 million microspheres. SIR-Spheres® microspheres are a permanent implant.

Indications for Use: SIR-Spheres® microspheres are indicated for the treatment of unresectable metastatic liver tumors from primary colorectal cancer with adjuvant intra-hepatic artery chemotherapy (IHAC) of FUDR (Floxuridine).

17.5.4 Small Organic Molecules

MIBG was originally designed and developed in 1980 for imaging adrenal medulla [61]. MIBG, an analog of norepinephrine (Fig. 17.10) was synthesized by linking the benzyl portion of bretylium with the guanidine group of guanethidine. In 1994, [131I]MIBG also known as iobenguane sulfate I-131 intravenous (low specific activity *(LSA)* formulation), received FDA approval as an imaging agent for the localization of specific sites of pheochromocytomas and neuroblastomas (Pharmalucence 2008). In 2008, [123I]MIBG or iobenguane I-123 injection was also approved by the FDA as a tumor imaging agent (Adreview; GE Healthcare).

In 2018, the FDA approved high specific activity iobenguane I-131(Azedra™) for the treatment of paragangliomas and pheochromocytomas. It is also used for the treatment of pediatric patients with neuroblastoma [62]. The uptake of MIBG into the neuroendocrine cell is by two mechanisms—active and passive [63]. The active transport or the uptake-1 system is the dominant method of transport of MIBG into the cell. This is an active, sodium and energy-dependent amine uptake mechanism in the cell membrane of the sympathomedullary tissues. Within the cell, it is actively transported into the storage granules by an energy-dependent transport mechanism via vesicular monoamine transporters 1 and 2. This accumulation of MIBG in these neurosecretory granules forms the basis for imaging and therapy with $^{123}I/^{131}I$-labeled MIBG [62]. Small amount of MIBG is also present in the cytoplasm. The other mechanism is a passive diffusion of MIBG into the cells. The active uptake is more efficient and specific than the passive uptake.

17.5.4.1 AZEDRA® (Iobenguane I 131) Injection

The drug substance iobenguane I 131, also described as mIBG (Fig. 17.9), has a molecular weight of 279.1 Da. AZEDRA 555 MBq/mL (15 mCi/mL) injection is a sterile, clear, colorless to pale yellow solution. Each single-dose vial contains iobenguane (0.006 mg/mL), sodium ascorbate (58 mg/mL) and sodium gentisate (23 mg/mL) in water for Injection, USP. The pH range of the solution is 4.5–5.5, with a specific activity of ~2500 mCi/mg (92,500 MBq/mg) [64].

Indications and Usage: AZEDRA is indicated for the treatment of adult and pediatric patients

12 years and older with iobenguane scan positive, unresectable, locally advanced, or metastatic pheochromocytoma or paraganglioma who require systemic anticancer therapy.

Dosage and Administration: Recommended dosimetric dose: patients weighing more than 50 kg: 185–222 MBq (5–6 mCi); patients weighing 50 kg or less: 3.7 MBq/kg (0.1 mCi/kg); Recommended therapeutic dose: patients weighing >62.5 kg: 18.5 GBq (500 mCi) and patients weighing 62.5 kg or less: 0.296 GBq/kg (8 mCi/kg). Administer 2 therapeutic doses 90 days apart. As needed, adjust the therapeutic doses based on radiation dose estimate results from dosimetry study.

Mechanism of Action: Iobenguane is similar in structure to the neurotransmitter norepinephrine (NE) and is subject to the same uptake and accumulation pathways as NE. Iobenguane is taken up by the NE transporter in adrenergic nerve terminals and accumulates in adrenergically innervated tissues, such as the heart, lungs, adrenal medulla, salivary glands, liver, and spleen, as well as tumors of neural crest origin. Pheochromocytoma and paraganglioma (PPGL) are tumors of neural crest origin that express high levels of the NE transporter on their cell surfaces.

Pharmacodynamics: The effect of AZEDRA on the QTc interval was evaluated in 74 patients with unresectable pheochromocytoma or paraganglioma. At the recommended therapeutic dosage, no large mean increases from baseline in the QTc interval (i.e., >20 ms) were detected.

Pharmacokinetics: Iobenguane I 131 is primarily eliminated renally with cumulative excretion of $50 \pm 10\%$ within 24 h and $80 \pm 10\%$ within 120 h following AZEDRA administration. Unchanged I 131 accounted for an average of 94% and 93% radioactivity excreted in urine collected during 0–6 and 6–24-h post-dose, respectively. Minor metabolites detected in some patients included free I 131, quantifiable in 55% of 11 patients in Study IB11, as well as meta-iodohippuric acid (MIHA) and meta-iodobenzyl bisguanidine (MMIBG) quantifiable in one patient each.

Drug Interactions: Based on the mechanism of action of iobenguane, drugs that reduce catecholamine uptake or that deplete catecholamine stores may interfere with iobenguane uptake into cells and, therefore, interfere with dosimetry calculations or the efficacy of AZEDRA. Discontinue drugs that reduce catecholamine uptake or deplete catecholamine stores for at least five half-lives before administration of either the dosimetry or a therapeutic dose of AZEDRA. Do not administer these drugs until at least 7 days after each AZEDRA dose.

17.5.5 Regulatory Peptides Hormone Analogs

Peptides are formed when two or more amino acids are condensed together with the formation of a secondary amide bond, the so-called peptide bond or peptide unit. Most of the drawbacks of mAbs can be eliminated by using biomolecules like peptides [65]. Peptides are quickly cleared from the blood circulation by liver and kidney. In addition, the pharmacodynamic properties of peptides can be modulated by different synthetic modification and stabilization approaches. Peptides are generally considered safe since they feature low immunogenicity and produce non-toxic metabolites. Since peptides are small molecules, they can easily penetrate into the solid tumors unlike mAbs.

Various peptides, peptide receptors, and the corresponding eligible target-related tumors are summarized in Table 17.11. The overexpression of peptide receptors on tumor cells leads to the development of radiolabeled peptides for diagnosis and therapy [66, 67]. It has been demonstrated that only tumors expressing a high density of receptors can be selected for targeted therapy. A tumor-to-normal-cell expression ratio of 3:1 or higher is usually desired. Secondly, the amounts of overexpressed receptors must be sufficient to ensure drug delivery in appropriate amounts to obtain the desired therapeutic effect. Since peptide agonists are quickly metabolized (or inactivated) by amino peptidases, following binding to receptors, peptide radiopharmaceuticals are generally developed using chemically modified peptide analogs that may have greater affinity for the receptor but, block the receptor function.

17.5.5.1 Somatostatin Receptors

The most well-studied cell surface receptor is the somatostatin receptor (SSTR) family, which is comprised of five members (SSTR1-5). Their natural ligand is the disulfide-cyclized oligopeptide somatostatin (SST), which occurs in two isoforms SST-14 and SST-28. Human SST receptors (SSTR1-SSTR5) have been identified in most of the neuroendocrine tumors, small cell lung cancers, and medullary thyroid carcinoma, expressing high densities of SSTRs. The expression of SSTR subtypes in human tumor tissues, however, seems to vary among different tumor types. Although various SS receptor subtypes are expressed in tumors, SSTR2 is the predominant receptor subtype expressed in NETs. Since SST is degraded rapidly in vivo, octreotide (Sandostatin) was developed as a therapeutic agent. It is the presence of SSTR2 as well as its density which provides the molecular basis for several radiolabeled SS analogs (Fig. 17.9) that were developed for diagnosis and peptide receptor therapy (PRT). ^{111}In-DTPA-octreotide (Octreoscan) was the first peptide approved as an imaging agent in 1993.

The acronyms PRS (peptide receptor scintigraphy) and PRRT (peptide receptor radionuclide therapy) were originally coined in the 1980s by the investigators at the Erasmus University Medical Center, Rotterdam, in the Netherlands. Following the development of DOTA conjugated octreotide analogs (DOTATOC and DOTATATE) in the early 1990s, the first clinical results with ^{90}Y-DOTATOC demonstrated the potential therapeutic effectiveness of PRRT in patients with NETs [68]. Subsequently, the efficacy and safety of ^{177}Lu-DOTATOC and ^{177}Lu-DOTATATE were investigated extensively in several multicenter clinical trials. The FDA approval of ^{177}Lu-DOTATATE (Lutathera®) in 2017, a peptide radiopharmaceutical specific for SSTR, is clinically indicated for the treatment of neuroendocrine tumors started a new wave in the development of peptide-based radiopharmaceuticals for TRT.

17.5.5.2 Lutathera® (^{177}Lu-Dotatate) Injection

Lutathera® is a radiolabeled somatostatin analog [69]. The drug substance ^{177}Lu-dotatate is a cyclic peptide, Tyr[3]-octreotide linked with the covalently bound chelator DOTA (1,4,7,10-tetraazacyclododecane-1,4,7,10-tetraacetic acid) and labeled with ^{177}Lu radionuclide. The molecular weight is 1609.6 Da, and the structural formula is as shown in Fig. 17.10. Lutathera® 370 MBq/mL (10 mCi/mL) Injection is a sterile, clear, colorless to slightly yellow solution for intravenous use. Each single-dose vial contains acetic acid (0.48 mg/mL), sodium acetate (0.66 mg/mL), gentisic acid (0.63 mg/mL), sodium hydroxide (0.65 mg/mL), ascorbic acid (2.8 mg/mL), diethylene triamine pentaacetic acid (0.05 mg/mL), sodium chloride (6.85 mg/mL), and water for injection (ad 1 mL). The pH range of the solution is 4.5–6.

Indications and Usage: Lurathera® is indicated for the treatment of somatostatin receptor-positive gastroenteropancreatic neuroendocrine tumors (GEP-NETs), including foregut, midgut, and hindgut neuroendocrine tumors in adults.

Dosage and Administration: The recommended Lutathera dose is 7.4 GBq (200 mCi) every 8 weeks for a total of 4 doses. Premedication and Concomitant Medications: (a) Before initiating Lutathera® therapy, discontinue long-acting somatostatin analogs for at least 4 weeks. Administer short-acting octreotide, as needed, and discontinue at least 24 h prior to therapy dose. (b) Administer long-acting octreotide 30 mg intramuscularly between 4 and 24 h after each therapy dose. Do not administer long-acting octreotide within 4 weeks of each subsequent Lutathera® dose. (c) Initiate an intravenous amino acid solution (1.5–2.2 L) containing L-lysine (20–25 g) and L-arginine (20–25 g) 30 min before administering Lutathera and continued during, and for at least 3 h after Lutathera infusion.

Pharmacokinetics: Within 4 h after administration, Lu-177 dotatate distributes in kidneys, tumor lesions, liver, spleen, and, in some patients, pituitary gland and thyroid. The co-administration of amino acids reduced the median radiation dose to the kidneys by 47%. The effective blood elimi-

nation half-life is 3.5 ± 1.4 h and the mean terminal blood half-life is 71 ± 28 h. Lu-177 dotatate is primarily eliminated renally with cumulative excretion of 44% within 5 h, 58% within 24 h, and 65% within 48 h following Lutathera® administration.

Mechanism of Action: Lutathera® binds to somatostatin receptors with highest affinity for subtype 2 receptors (SSRT2). Upon binding to somatostatin receptor-expressing cells, including malignant somatostatin receptor-positive tumors, the compound is internalized. The β⁻ particles from Lu-177 induce cellular damage by formation of free radicals in somatostatin receptor-positive cells and in neighboring cells.

Drug Interactions: Somatostatin and its analogs competitively bind to somatostatin receptors and may interfere with the efficacy of Lutathera®. Discontinue long-acting somatostatin analogs at least 4 weeks and short-acting octreotide at least 24 h prior to each Lutathera® dose.

17.5.5.3 Other Peptide Receptors

Many other peptide receptors have been identified and are known to be overexpressed in several different cancers (Table 17.11). Radiolabeled peptides are being developed to target-specific receptors for Glucagon-like peptide 1 receptor (GLP-IR), Gastrin or cholecystokinin-2 receptor (CCK2R), Neurotensin receptor 1 (NTR1), Chemokine receptor-4 (CXCR), Vasoactive intestinal peptide (VIP), neurotensin (NT) receptor, substance-P, and neuropeptide-Y. Preclinical studies and phase I/II clinical studies demonstrated the potential of several radiolabeled peptides for both imaging studies, and for targeted radionuclide therapy.

17.5.6 Monoclonal Antibodies

An antibody (Ab), also known as an immunoglobulin (Ig) is a large protein used by the immune system to identify and neutralize foreign objects such as pathogenic bacteria and viruses. The antibody recognizes a unique molecule of the pathogen, called an antigen. The antibody molecule contains a paratope (antigen binding segment) that is specific for epitope (Ab binding segment) on an antigen. Antibody and antigen interact by spatial complementarity (like lock and key). The binding between antibody and antigen is reversible and, as a result, it is possible for an antibody to cross-react with different antigens of different relative affinities. Polyclonal antibodies (pAbs) are a heterogeneous mixture produced by different B cell clones in the body but, bind to many different epitopes of a single antigen. In contrast, mAbs are generated by identical B cells which are clones from a single parent cell. This means that the mAb binds to a single epitope and is monovalent. Georges Köhler and César Milstein invented the technology of producing mAbs [70] and started the modern era of antibody-based pharmaceuticals.

Antibodies are large glycoproteins and their basic structure is composed of two heavy and two light chains in the shape of a Y. At each tip of the Y lies the fragment antigen-binding (Fab) portion of the antibody which is responsible for recognition of the specific antigen. The fragment crystallizable (Fc) region located at the base of the Y structure mediates interactions between the antibody and other members of the immune system. Antibody Fc regions are recognized by Fc receptors (FcRs) found on a wide range of immune cells. IgG is the most often form used in antibody therapy due to the fact that IgGs interact with their associated type of Fc-receptor found on natural killer (NK) cells as well as neutrophils, monocytes, dendritic cells, and eosinophils to mediate specialized functions such as antibody-dependent cellular cytotoxicity (ADCC) and complement-dependent cytotoxicity (CDC). Intact mAbs have a long residence time in humans, ranging from a few days to weeks, which results in optimal tumor-to-non-tumor ratios at 2–4 days postinjection. In contrast, mAb fragments have a much faster blood clearance and, as a result, optimal tumor-to-nontumor ratios can be obtained at earlier time points. However, the absolute tumor uptake may be much lower compared to intact mAbs. Around the world, more than 600 therapeutic mAbs have been studied in clinical trials, and close to 80 therapeutic mAbs have been approved by the FDA for different diseases including cancer [71].

17.5.6.1 Radioimmunotherapy (RIT)

RIT exploits the ability of radiolabeled antibody conjugates (RACs) to target tumors in an antigen-specific manner for selective delivery of therapeutic radionuclide and localized release of cytotoxic ionizing but, non-penetrating radiations, such as α *particles and* β⁻ particles. The efficacy of RIT, however, depends on the type and size of cancer tissue and the choice of radionuclide, half-life, type of particle emission, kinetic energy, and range in tissue. The first use of radiolabeled antibody to treat cancer was performed in the 1950s by Dr. Beierwalters at the University of Michigan, USA, who used ^{131}I-tagged antibodies made in rabbits against patient's own neoplastic tissue [59].

After several decades of intense investigation with radiolabeled antibodies, only six radiolabeled antibodies have gained FDA approval for use in clinical oncology, including four immunodiagnostic agents and two targeted radioimmunotherapeutic agents (Table 17.2). As of December 2021, more than 30 mAbs have been approved for the treatment of cancer. RIT with antibodies, however, was not clinically successful except in hematological malignancies. Combining mAbs with therapeutic radionuclides was first studied in hematologic malignancies based on the rationale that these cancers are the most radiosensitive tumors compared to solid tumors [72, 73]. The FDA's approvals of 2 radiolabeled anti-CD20 mAbs, ^{90}Y-labeled Zevalin® (ibritumomab tiuxetan) in 2002 and ^{131}I-labeled Bexxar® in 2003 for the treatment of NHL were landmark events in the developmental history of TRT and RIT. Both these ^{90}Y- and ^{131}I-labeled anti-B1 mAbs produce overall response rates (ORR, 60–80%) and complete response rates (CRR, 15–40%) in relapsed NHL longer than the naked antibodies, such as rituximab [73].

17.5.6.2 ZEVALIN® (Ibritumomab Tiuxetan) Injection

Zevalin (ibritumomab tiuxetan) is the immunoconjugate resulting from a stable thiourea covalent bond between the mAb ibritumomab and the linker-chelator tiuxetan [*N*-[2-bis(carboxymethyl) amino]-3-(p-isothiocyanatophenyl)-propyl]-[*N*-[2-bis(carboxymethyl)amino]-2-(methyl)-ethyl] glycine. This linker-chelator provides a high affinity, conformationally restricted chelation site for ^{111}In or ^{90}Y. The approximate molecular weight of ibritumomab tiuxetan is 148,000 Da. The antibody moiety of Zevalin is ibritumomab, a murine IgG$_I$ kappa mAb directed against the CD20 antigen. Ibritumomab tiuxetan is a clear, colorless, sterile, pyrogen-free, preservative-free solution that may contain translucent particles. Each single-use vial includes 3.2 mg of ibritumomab tiuxetan in 2 mL of 0.9% sodium chloride.

Indications and Usage: Zevalin is indicated for the treatment of relapsed or refractory, low-grade, or follicular B-cell non-Hodgkin's lymphoma (NHL). Zevalin is also indicated for the treatment of previously untreated follicular NHL in patients who achieve a partial, or complete response to first-line chemotherapy.

Recommended Doses: Dose for biodistribution imaging study: 5 mCi of ^{111}In-Zevalin; Therapeutic dose: 0.4 mCi/kg (14.8 MBq/kg) for patients with normal platelet count; 0.3 mCi/kg (11.1 MBq/kg) in relapsed or refractory patients with platelet count of 10,000–149,000 cells/mm. Prior to the administration of the dosimetric or therapeutic dose, first administer rituximab 250 mg/m² intravenously at an initial rate of 50 mg/h. In the absence of infusion reactions, escalate the infusion rate in 50 mg/h increments every 30 min to a maximum of 400 mg/h. The dose of ^{90}Y-Zevalin should not exceed 32.0 mCi (1184 MBq). The specific activity of ^{90}Y-Zevalin is around 20 mCi/mg of antibody. ^{90}Y-Zevalin should not be injected into patients with altered biodistribution as determined by imaging with ^{111}In-Zevalin

Mechanism of Action: Ibritumomab tiuxetan binds specifically to the CD20 antigen (human B-lymphocyte-restricted differentiation antigen, Bp35). The apparent affinity (K_D) of ibritumomab tiuxetan for the CD20 antigen ranges between approximately 14 and 18 nM. The CD20 antigen is expressed on pre-B and mature B lymphocytes and on >90% of B-cell non-Hodgkin's lymphomas (NHL). The CD20 antigen is not shed from the cell surface and does not internalize upon antibody binding.

Pharmacodynamics: Administration of the Zevalin therapeutic regimen resulted in sustained depletion of circulating B cells. At 4 weeks, the median number of circulating B cells was zero. B-cell recovery began at approximately 12 weeks following treatment, and the median level of B cells was within the normal range by 9 months after treatment.

Pharmacokinetics: With ^{111}In-Zevalin imaging studies, only 18% of known sites of disease were imaged when ^{111}In-Zevalin was administered alone without unlabeled ibritumomab. However, when preceded by unlabeled ibritumomab (2.5 mg/kg), ^{111}In-Zevalin detected 92% of known disease sites. With ^{90}Y-Zevalin therapeutic dose administration, the mean effective half-life for Y-90 activity in blood was 30 h and the mean area under the fraction of injected activity (FIA) vs. time curve in blood was 39 h. Over 7 days, a median of 7.2% of the injected activity was excreted in urine.

17.5.6.3 BEXXAR® (Tositumomab and Iodine I 131 Tositumomab) Injection

The BEXXAR® therapeutic regimen is composed of the mAb tositumomab, and the radiolabeled mAb, ^{131}I-tositumomab. Tositumomab is a murine IgG$_{2a}$ lambda mAb directed against the CD20 antigen, produced in mammalian cells. The approximate molecular weight of tositumomab is 150 kDa. Tositumomab is supplied as a sterile, pyrogen-free, clear to opalescent, colorless to slightly yellow, preservative-free solution that must be diluted before intravenous administration. The formulation contains 100 mg/mL maltose, 8.5 mg/mL sodium chloride, 1 mg/mL phosphate, 1 mg/mL potassium hydroxide, and water for injection. The pH is approximately 7.2.

Tositumomab is covalently linked to ^{131}I and is supplied as a sterile, clear, preservative-free liquid. The drug product formulation contains 0.9–1.3 mg/mL ascorbic acid, 1–2 mg/mL maltose (dosimetric dose) or 9–15 552 mg/mL maltose (therapeutic dose), 4.4–6.6% (w/v) povidone, and 8.5–9.5 mg/mL sodium 553 chloride. The pH is approximately 7.0. I-131 tositumomab is supplied as a sterile, clear, preservative-free liquid.

The formulation for I-131 tositumomab contains 0.9–1.3 mg/mL ascorbic acid, 1–2 mg/mL maltose (dosimetric dose), or 9–15 mg/mL maltose (therapeutic dose), 4.4–6.6% (w/v) povidone, and 8.5–9.5 mg/mL sodium chloride. The pH is approximately 7.0.

For dosimetry studies, ^{131}I-tositumomab is supplied 12–18 mCi/vial (NLT 0.61 mCi/mL and 0.1 mg/mL). For therapy, ^{131}I-tositumomab is supplied 112–168 mCi/vial (NLT 5.6 mCi/mL and 1.1 mg/mL).

Dosage and Administration: The therapeutic regimen consists of two separate components (tositumomab and ^{131}I-tositumomab) administered in two separate steps (dosimetric dose and therapeutic dose) separated by 7–14 days. For dosimetry study, 450 mg of Tositumomab followed by 5 mCi of ^{131}I-Tositumomab (450 mg) and for therapy, 450 mg of Tositumomab followed by ^{131}I-Tositumomab therapy dose (the amount of ^{131}I activity to deliver 65–75 cGy depending on the platelet counts and total body residence time determined following dosimetric dose).

Mechanism of Action: Tositumomab binds specifically to an epitope within the extracellular domain of the CD20 molecule, expressed on normal B lymphocytes and on B-cell NHLs. non-Hodgkin's lymphomas. In addition to cell death mediated by the radioisotope, other possible mechanisms of action include ADCC, CDC, and CD20-mediated apoptosis.

Pharmacodynamics: The administration of the BEXXAR® therapeutic regimen resulted in sustained depletion of circulating CD20-positive cells (normal and malignant). At 7 weeks following treatment, the median number of circulating CD20-positive cells was zero with recovery beginning at approximately 12 weeks.

Pharmacokinetics: Prior administration of 475 mg of naked antibody decreased splenic targeting and increased the terminal half-life of the ^{131}I-tositumomab. Patient-specific dosing, based on total body clearance, provided a consistent radiation dose despite variable pharmacokinetics, by allowing each patient's administered activity to be adjusted for individual patient variables. The median total body effective half-life, in

patients with NHL was 67 h. Five days following the radiolabeled dose, the whole-body clearance was 67% of the injected dose. Due to in vivo dehalogenation, ^{131}I-tositumomab is not stable in vivo and the free I-131 activity is excreted in the urine.

17.6 Prostate Specific Membrane Antigen (PSMA)

In 1987, prostate-specific membrane antigen (PSMA) was discovered as a novel antigenic marker in prostate cancer cells and in the serum of prostate cancer patients. In the brain, PSMA is also known as *N*-acetyl-L-aspartyl-L-glutamate peptidase I (*NAALADase I*) or *N*-acetyl-aspartyl-glutamate (*NAAG) peptidase* [74]. PSMA is considered to be the most well-established target antigen in prostate cancer, since it is highly and specifically expressed at all tumor stages on the surface of prostate tumor cells compared with normal or hyperplastic prostates [75, 76]. PSMA is a class II transmembrane glycoprotein with a unique 3-part structure: a short N-terminal cytoplasmic tail, a single membrane-spanning helix, and an extracellular part. The bulk of PSMA protein is the extracellular part.

In 1997, Bander and his colleagues at Weill Cornell Medicine in New York reported the development J591 mAb to the extracellular domain of PSMA on viable tumor cells [77, 78]. J591 mAb targets the extracellular portion of PSMA and therefore, binds to the viable tumor cells [77]. In the last 20 years, several clinical studies documented the therapeutic potential of [90]Y-, [177]Lu-, and [225]Ac-labeled DOTA-huJ591 for RIT of mCRPC [79–81].

17.6.1 PSMA Inhibitors

The enzyme activity of PSMA includes *NAALADase 1*. In the brain, PSMA hydrolyzes the *N*-acetyl-L-aspartyl-L-glutamate (NAAG) substrate to yield aspartate and glutamate. Studies of the *NAALADase* enzyme structure

have revealed an active site containing two zinc cations (Zn^{++}) participating in the NAAG binding, called the "*NAAG binding pocket*", which is also the site for the binding of PSMA inhibitors [60]. The discovery of small molecule peptide PSMA inhibitors made it possible for the development of both diagnostic and therapeutic peptide radiopharmaceuticals. PSMA enzyme inhibitors mimic the structure of the substrate (NAAG), bind to PSMA, and reduce the ability of the enzyme to convert the substrate NAAG into aspartate and glutamate (Pastarino et al. 2020). The clinical success of radiolabeled PSMA inhibitors is based on a small motif binding to the catalytic NAAG hydrolyzing site in the PSMA molecule. This class of inhibitors contains a urea bond (−NH-CO-NH-) formed by the conjugation of two amino acids (Glu and Asp). Several groups have reported on the development of small-molecule inhibitors of PSMA comprising two amino acids joined through their NH_2 groups by a urea linkage (glutamate urea heterodimers) [81]. In the last 2 years, two radiolabeled PSMA inhibitors, ^{68}Ga-PSMA-11 and [^{18}F]DCFPyL have already been approved by the FDA for PET imaging studies of prostate cancer [83, 84].

17.6.1.1 ^{177}Lu-PSMA-617

To develop radiopharmaceuticals for TRT, two PSMA inhibitors, PSMA-617 and PSMA I&T were developed at the German Cancer Research Centre (GCRC) in Heidelberg, Germany based on Glu-Urea-Lys pharmacophore and DOTA or DOTAGA chelators respectively [85]. ^{177}Lu-PSMA-617 (Fig. 17.10) was quickly used as a therapeutic ligand because it has higher tumor uptake at later time points, lower spleen uptake, and highly efficient clearance from the kidneys [86]. Clinical studies have also evaluated the potential of ^{68}Ga-PSMA I&T for the detection of primary prostate cancer before prostatectomy [82].

The first clinical experience with ^{177}Lu-PSMA-617 targeted therapy in patients with advanced mCRPC demonstrated that ^{177}Lu-PSMA-617 is a promising new option for therapy of mCRPC [87]. Subsequently, two major clinical studies evaluated the safety and

efficacy of ^{177}Lu-PSMA-617 therapy in patients with mCRPC. A randomized, multi-center open-label phase 2 trial (TheraP trial) compared the efficacy of ^{177}Lu-PSMA-617 with cabazitaxel in patients with mCRPC [88]. The study results showed that ^{177}Lu-PSMA-617 treatment, compared to cabazitaxel, led to a higher PSA response and fewer grade 3 or 4 adverse events.

The VISION trial (Funded by Endocyte, a Novartis company) evaluated the advantages of ^{177}Lu-PSMA-617 over best supportive care in improving the overall survival (OS) and image-based progression-free survival (PFS) in patients with progressive mCRPC [89]. Five hundred and fifty-one patients were allotted to the ^{177}Lu-PSMA-617 group (who received 7.4 GBq of ^{177}Lu-PSMA-617 every 6 weeks in 4–6 cycles), while 280 patients were in the standard of care (SOC) group. The results of the study showed that the median PFS was significantly longer among patients in the ^{177}Lu-PSMA-617 arm at 8.7 months compared with 3.4 months in patients in the SOC-alone arm. There was a significant improvement in the OS in the patients who received ^{177}Lu-PSMA-617 compared to standard care alone (15.3 months vs. 11.3 months). Also, approximately 46% (vs. 7.1% in control group) of the patients had >50% reduction, and >33% (vs. 2% in control group) of the patients had >80% reduction in the PSA levels (SOC). The FDA granted priority review for the NDA for[177]Lu-PSMA-617 and approved in 2022 to treat patients with metastatic castration-resistant prostate cancer (mCRPC) who have previously received androgen-receptor pathway and taxane-based chemotherapy.

The successful completion of phase III clinical trial of ^{177}Lu-PSMA-617 (VISION Trial) and fast approval by FDA in the treatment of mCRPC may also help advance the development of several new peptide or protein based radiopharmaceuticals for TRT.

References

1. Troy DB, Beringer P, editors. Remington: the science and practice of pharmacy. 21st ed. Philadelphia: Lippincott Williams & Wilkins; 2006.

2. Christiansen JA, Hevesy GD, Lomholt S. Recherches, par une methode radiochimique, sur la circulationdu bismuth dans l'organisme. Compt Rend. 1924;178:1324.

3. Lomholt S. Notes on the pharmacology of bismuth, with reference to its employment in the therapy of syphilis. Br J Vener Dis. 1925;1(1):50–7.

4. Seidlin SM, Marinelli LD, Oshry E. Radioactive iodine therapy: effect on functioning metastases of adenocarcinoma of the thyroid. JAMA. 1946;32(14):838–47.

5. Vallabhajosula S. The chemistry of therapeutic radiopharmaceuticals. In: Aktolun C, Goldsmith SJ, editors. Nuclear medicine therapy: principles and clinical applications. New York: Springer Science+Business Media; 2013.

6. Chakravarty R, Chakraborty S. A review of advances in the last decade on targeted cancer therapy using [177]Lu: focusing on ^{177}Lu produced by the direct neutron activation route. Am J Nucl Med Mol Imaging. 2021;11(6):443–75.

7. Sgouros G, Bodei L, McDevitt MR, Nedrow JR. Radiopharmaceutical therapy in cancer: clinical advances and challenges. Nat Rev Drug Discov. 2020;19:589.

8. O'Donoghue JA, Bardiès M, Wheldon TE. Relationships between tumor size and curability for uniformly targeted therapy with beta-emitting radionuclides. J Nucl Med. 1995;36(10):1902–9.

9. IAEA-RRS-2. Production of long-lived parent radionuclides for generators: [68]Ge, [82]Sr, ^{90}Sr and [188]W. Vienna: International Atomic Energy Agency; 2010.

10. IAEA TRS-470. Therapeutic radionuclide generators: [90]Sr/^{90}Y AND [188]W/[188]Re generators. Vienna: International Atomic Energy Agency; 2009.

11. Banerjee S, Pillai MRA, Knapp FF. Lutetium-177 therapeutic radiopharmaceuticals: linking chemistry, radiochemistry, and practical applications. Chem Rev. 2015;115(8):2934–74.

12. Medvedev DG, Mausner LF, Meinken GE, et al. Development of a large-scale production of Cu-67 from Zn-68 at the high energy proton accelerator: closing the Zn-68 cycle. Appl Radiat Isot. 2012;70:423–9.

13. Ehst DA, Smith NA, Bowers DL, Makarashvili V. Copper-67 production on electron linacs—photonuclear technology development. AIP Conf Proc. 2012;1509:157–61.

14. Mamtimin M, Harmon F, Starovoitova VN. Sc-47 production from titanium targets using electron linacs. Appl Radiat Isot. 2015;102:1–4.

15. Mikolajczak R, Huclier-Markai S, Alliot C, et al. Production of scandium radionuclides for theranostic applications: towards standardization of quality requirements. EJNMMI Radiopharm Chem. 2021;6:19.

16. Rotsch DA, Brown MA, Nolen JA, et al. Electron linear accelerator production and purification of scandium-47 from titanium dioxide targets. Appl Radiat Isot. 2018;2018(131):77–82.

17. Lehenberger S, Barkhausen C, Susan Cohrs S, et al. The low-energy β⁻ and electron emitter [161]Tb as an alternative to ^{177}Lu for targeted radionuclide therapy. Nucl Med Biol. 2011;38(6):917–24.

18. Gracheva N, Müller C, Talip Z, et al. Production and characterization of no-carrier-added [161]Tb as an alternative to the clinically applied ^{177}Lu for radionuclide therapy EJNMMI. Radiopharm Chem. 2019;4:12.

19. Nicholas AL, Aldama DL, Verpelli M. Handbook of nuclear data for safeguards. International Atomic Energy Agency. 2008. IAEA-INDC (NDS)-0534.

20. Stevenson NR, St. George G, Simon J, Srivastava SC. Methods of producing high specific activity Sn-117m with commercial cyclotrons. J Radioanal Nucl Chem. 2015;305(1):99–108. https://doi.org/10.1007/s10967-015-4031-7.

21. IAEA-TRS-468. Cyclotron produced radionuclides: physical characteristics and production methods. Vienna: International Atomic Energy Agency; 2009.

22. Balkin ER, Cutler CS. Scale-up of high specific activity [186g]Re production using graphite-encased thick [186]W targets and demonstration of an efficient target recycling process. Radiochimica Acta. 2017;105:1071–81.

23. Klaassen NJM, Arntz MJ, Arranja AG, et al. The various therapeutic applications of the medical isotope holmium-166: a narrative review. EJNMMI Radiopharm Chem. 2019;4(1):19.

24. Kozempel J, Mokhodoeva O, Vlk M. Progress in targeted alpha-particle therapy. What we learned about recoils release from in vivo generators. Molecules. 2018;23:581.

25. Tinganelli W, Ma NY, Von Neubeck C, et al. Influence of acute hypoxia and radiation quality on cell survival. J Radiat Res. 2013;54(Suppl 1):23–30.

26. Eychenne R, Chérel M, Haddad F, et al. Overview of the most promising radionuclides for targeted alpha therapy: the "hopeful eight". Pharmaceutics. 2021;13:906.

27. Apostolidis C, Molinet R, McGinley J, et al. Cyclotron production of Ac-225 for targeted alpha therapy. Appl Radiat Isot. 2005;62:383–7.

28. IAEA Report. IAEA report on joint IAEA-JRC workshop "Supply of Actinium-225". Vienna: International Atomic Energy Agency; 2018.

29. Ahenkorah S, Cassells I, Deroose CM, et al. Bismuth-213 for targeted radionuclide therapy: from atom to bedside. Pharmaceutics. 2021;13:599.

30. Bertrand A, Legras B, Martin J. The use of radium-224 in the treatment of ankylosing spondylitis and rheumatoid synovitis. Health Phys. 1978;1:57–60.

31. Moiseeva AN, Aliev RA, Unezhev VN, et al. Cross section measurements of 151Eu(3He,5n) reaction: new opportunities for medical alpha emitter 149Tb production. Sci Rep. 2020;10:1–7.

32. Cavaier F, Haddad F, Sounalet T, et al. Terbium radionuclides for theranostics applications: a focus on MEDICIS-PROMEDR. Phys Procedia. 2017;90:157–63.

33. Ku A, Facca VJ, Cai Z, Reilly RM. Auger electrons for cancer therapy—a review. EJNMMI Radiopharm Chem. 2019;2019(4):27–63.

34. Howell RW, Rao DV, Hou D-Y, Narra VR, Sastry KSR. The question of relative biological effectiveness and quality factor for Auger emitters incorporated into proliferating mammalian cells. Radiat Res. 1991;128:282–92.

35. Edem PE, Fonslet J, Kjær A, et al. In vivo radionuclide generators for diagnostics and therapy bioinorganic chemistry and applications. Bioinorg Chem Appl. 2016;2016:6148357.

36. Mausner L, Straub R, Srivastava S. The in vivo generator for radioimmunotherapy. J Labell Comp Radiopharm. 1989;26(1–12):498–500.

37. McDevitt MR, Ma D, Lai L, et al. Tumor therapy with targeted atomic nanogenerators. Science. 2001;294:1537–40.

38. Kruijff RM, Wolterbeek HT, Denkova AG. A critical review of alpha radionuclide therapy—how to deal with recoiling daughters? Pharmaceuticals (Basel). 2015;8(2):321–36. https://doi.org/10.3390/ph8020321. Published online 2015 Jun 10.

39. Bhaskar R, Lee KA, Yeo R, Yeoh K-W. Cancer and radiation therapy: current advances and future directions. Int J Med Sci. 2012;9(3):193–9.

40. Murshed H. Radiation biology. In: Fundamentals of radiation oncology. 3rd ed. New York: Academic; 2019. p. 57–87.

41. Sinclair DW. Relative biological effectiveness (RBE), quality factor (Q) and radiation weighting factor (Wr). Ann ICRP. 2003;33(4):1–117.

42. Knapp FF, Dash A, editors. Radiopharmaceuticals for therapy. New Delhi: Springer-India; 2016.

43. Sia J, Szmyd R, Hau E, Gee HE. Molecular mechanisms of radiation-induced cancer cell death: a primer. Front Cell Dev Biol. 2020;8(41):1–8.

44. Desouky O, Ding N, Zhou G. Targeted and non-targeted effects of ionizing radiation. J Radiat Res Appl Sci. 2015;8:247–54.

45. Desouky O, Din N, Zhou G. Targeted and non-targeted effects of ionizing radiation. JRRAS March. 2015;1–8.

46. Panganiban R-AM, Snow AL, Day RM. Mechanisms of radiation toxicity in transformed and non-transformed cells. Int J Mol Sci. 2013;14:15931–58. https://doi.org/10.3390/ijms140815931.

47. Rösch F, Herzog H, Qaim SM. The beginning and development of the theranostic approach in nuclear medicine, as exemplified by the radionuclide pair [86]Y and [90]Y. Pharmaceuticals. 2017;10:56. https://doi.org/10.3390/ph10020056.

48. Qaim SM, Scholten B, Neumaier B. New developments in the production of theranostic pairs of radionuclides. J Radioanal Nucl Chem. 2018;318:1493–509.

49. Boros E, Packard AB. Radioactive transition metals for imaging and therapy. Chem Rev. 2019;119(2):870–901.

50. Kostelnik TI, Orvig C. Radioactive main group and rare earth metals for imaging and therapy. Chem Rev. 2019;119(2):902–56.

51. Nelson BJB, Andersson JD, Wuest F. Targeted alpha therapy: progress in radionuclide production, radiochemistry, and applications. Pharmaceutics. 2021;13:49. https://doi.org/10.3390/pharmaceutics13010049.

52. Price EW, Orvig C. Matching chelators to radiometals for radiopharmaceuticals. Chem Soc Rev. 2014;43(1):260–90.

53. PI-NaI-2012. Sodium iodide I 131 solution therapeutic for oral use. Package insert. Mallinckrodt, revised 01/2012.

54. PI-Metastron-2013. METASTRON™ (Strontium-89 chloride injection). Package insert. New York: GE Health Care; 2013.

55. Sartor O, Coleman R, Nilsson S, et al. Effect of radium-223 dichloride on symptomatic skeletal events in patients with castration-resistant prostate cancer and bone metastases: results from a phase 3, double-blind, randomized trial. Lancet Oncol. 2014;15(7):738–46.

56. Parker CC, Coleman RE, Sartor O, et al. Three-year Safety of Radium-223 Dichloride in Patients with Castrationresistant Prostate Cancer and Symptomatic Bone Metastases from Phase 3 Randomized Alpharadin in Symptomatic Prostate Cancer Trial. Eur Urol. 2018; 73:427.

57. PI-Quadramet-2018. Quadramet® (Samarium Sm 153 lexidronam injection). Package insert. North Billerica: Lantheus Medical Imaging Inc.; 2018.

58. Braat AJAT, Smits MLJ, Braat MNGJA, et al. ^{90}Y hepatic radioembolization: an update on current practice and recent developments. J Nucl Med. 2015;56:1079–108.

59. Beierwalters WH. Horizons in radionuclide therapy: 1985 update. J Nucl Med. 1981;26:421–6.

60. Bařinka C, Rojas C, Slusher B, Pomper M. Glutamate carboxypeptidase II in diagnosis and treatment of neurologic disorders and prostate cancer. Curr Med Chem. 2012;19:856.

61. Wieland DM, Wu J, Brown LE, Mangner TJ, et al. Radiolabeled adrenergic neuron blocking agents: adrenomedullary imaging with 131I-iodobenzylguanidine. J Nucl Med. 1980;21:349–53.

62. Agrawal A, Rangarajan V, Shah S, et al. MIBG (metaiodobenzylguanidine) theranostics in pediatric and adult malignancies. Br J Radiol. 2018;91:1091.

63. Vallabhajosula S, Nikolopoulou A. Radioiodinated metaiodobenzylguanidine (MIBG): radiochemistry, biology, and pharmacology. Semin Nucl Med. 2011;41:324–33.

64. PI-MIBG-2018. AZEDRA® (iobenguane I 131) injection, for intravenous use. Package Insert. New York, NY: Progenics Pharmaceuticals Inc, revised 07/2018.

65. Hoppenz P, Els-Heindl S, Beck-Sickinger AG. Peptide-drug conjugates and their targets in advanced cancer therapies. Front Chem. 2020;8:571.

66. Reubi J-C. Peptide receptors as molecular targets for cancer diagnosis and therapy. Endocr Rev. 2003;24:389–427. https://doi.org/10.1210/er.2002-0007.

67. Vrettos EI, Mezo G, Tzakos AG. On the design principles of peptide-drug conjugates for targeted drug delivery to the malignant tumor site. Beilstein J Org Chem. 2018;14:930–54. https://doi.org/10.3762/bjoc.14.80.

68. Otte A, Mueller-Brand J, Dellas S, et al. Yttrium-90-labelled somatostatin-analogue for cancer treatment. Lancet. 1998;351(9100):417–8.

69. PI-Lutathera-2018. LUTATHERA® (lutetium Lu 177 dotatate) injection. Package insert. Millburn: Advanced Accelerator Applications; 2018.

70. Köhler G, Milstein C. Continuous cultures of fused cells secreting antibody of predefined specificity. Nature. 1975;256:495–7.

71. Zahavi D, Weiner L. Monoclonal antibodies in cancer therapy. Antibodies. 2020;9(34). https://doi.org/10.3390/antib9030034.

72. Boswell CA, Brechbiel MW. Development of radio-immunotherapeutic and diagnostic antibodies: an inside-out view. Nucl Med Biol. 2007;34:757–78.

73. Larson SM, Carrasquillo JA, Cheung N-KV, Press OW. Radioimmunotherapy of human tumours. Nat Rev Cancer. 2015;15:347–60.

74. O'Keefe DS, Su SL, Bacich DJ, et al. Mapping, genomic organization and promoter analysis of the human prostate-specific membrane antigen gene. Biochim Biophys Acta. 1998;1443:113–27.

75. Horoszewicz JS, Kawinski E, Murphy GP. Monoclonal antibodies to a new antigenic marker in epithelial prostatic cells and serum of prostatic cancer patients. Anticancer Res. 1987;7:927–35.

76. Israeli RS, Powell CT, Corr JG, Fair WR, Heston WD. Expression of the prostate-specific membrane antigen. Cancer Res. 1994;54:1807–11.

77. Liu H, Moy P, Kim S, et al. Monoclonal antibodies to the extracellular domain of prostate-specific membrane antigen also react with tumor vascular endothelium. Cancer Res. 1997;57:3629–34.

78. Liu H, Rajasekaran AK, Moy P, et al. Constitutive and antibody-induced internalization of prostate-specific membrane antigen. Cancer Res. 1998;58:4055–60.

79. Tagawa ST, Akhtar NH, Nikolopoulou A, et al. Bone marrow recovery and subsequent chemotherapy following radiolabeled anti-prostate-specific membrane antigen monoclonal antibody J591 in men with mCRPC. Front Oncol. 2013;3:1–6.

80. Tagawa ST, Sun M, Sartor AO, et al. Phase I study of ^{225}Ac-J591 for men with metastatic castration-resistant prostate cancer (mCRPC). J Clin Oncol. 2021;39(Suppl 15):5015.

81. Vallabhajosula S, Nikolopoulou A, Jhanwar YS, et al. Radioimmunotherapy of metastatic prostate cancer with ^{177}Lu-DOTA-huJ591 anti prostate specific membrane antigen specific monoclonal antibody. Curr Radiopharm. 2016;9:44–53.

82. Pastorino S, Riondato M, Uccelli L, et al. Toward the discovery and development of PSMA targeted

inhibitors for nuclear medicine applications. Current Radiopharmaceuticals. 2020;13:63–79.

83. Carlucci G, Ippisch R, Slavik R, et al. ^{68}Ga-PSMA-11 NDA approval: a novel and successful academic partnership. J Nucl Med. 2021;62:149–55.

84. Morris MJ, Rowe SP, Gorin MA, et al. Diagnostic performance of ^{18}F-DCFPyL-PET/CT in men with biochemically recurrent prostate cancer: results from the CONDOR phase III, multicenter study. Clin Cancer Res. 2021;27(13):3674–82.

85. Weineisen M, Schottelius M, Simecek J, et al. [68]Ga- and ^{177}Lu-labeled PSMA I&T: optimization of a PSMA-targeted theranostic concept and first proof-of-concept human studies. J Nucl Med. 2015;56:1169–1176

86. Benešová M, Schäfer M, Bauder-Wüst U, et al. Preclinical evaluation of a tailor-made DOTA-conjugated PSMA inhibitor with optimized linker moiety for imaging and endoradiotherapy of prostate cancer. J Nucl Med. 2015;56(6):914–20.

87. Kratochwil C, Giesel FL, Stefanova M, et al. PSMA-targeted radionuclide therapy of metastatic castration-resistant prostate cancer with ^{177}Lu-labeled PSMA-617. J Nucl Med. 2016;57:1170–6.

88. Hofman MS, Emmett L, Sandhu S, et al. [^{177}Lu] Lu-PSMA-617 versus cabazitaxel in patients with metastatic castration-resistant prostate cancer (TheraP): a randomized, open-label, phase 2 trial. Lancet. 2021;397(10276):797–804.

89. Sartor O, de Bono J, Chi KN, Fizazi K, Herrmann K, Rahbar K, et al. Lutetium-177-PSMA-617 for metastatic castration-resistant prostate cancer. N Engl J Med. 2021;385:1091–103.

Chemistry of Therapeutic Radionuclides

18

> I am mindful that scientific achievement is rooted in the past, is cultivated to full stature by many contemporaries and flourishes only in favorable environment. No individual is alone responsible for a single steppingstone along the path of progress, and where the path is smooth progress is most rapid. In my own work this has been particularly true. (Ernest Lawrence)

18.1 Targeted Radionuclide Therapy

Radiopharmaceutical therapy (RPT) or Targeted Radionuclide therapy (TRT) is defined by the delivery of radioactive atoms to tumor tissue or tumor-associated targets. During the last 10 years, there has been significant increase in the application of *conjugated* radiopharmaceuticals for targeted radionuclide therapy (TRT), mainly due to the development of a range of new carrier molecules (targeting vehicle), which can transport the radionuclide to a molecular target on the cancer cell. In the design of target-specific radiopharmaceuticals, nonmetal radionuclides (such as ^{18}F, ^{11}C, and ^{123}I) or metallic radionuclides (such as ^{177}Lu, ^{225}Ac, and ^{227}Th) are incorporated into the drug molecule. The radiolabeling with nonmetal radionuclides involves mainly the covalent bond formation between the radionuclide and the ligand molecule, whereas metal-based radiopharmaceuti-

cals rely on the coordination chemistry of the radiometal. Most design strategies divide the radiopharmaceutical into four parts: targeting vehicle (or ligand), linker, chelate, and the radio-metal (Fig. 18.1). The ligand (bioconjugate) ensures the specific localization at the target site in the tumor tissue, while the radionuclide decay characteristics determine the diagnostic or therapeutic function of the radiopharmaceutical. Extensive knowledge, experience, and understanding of chemistry/radiochemistry of radionuclides at the tracer level, would enable us to develop therapy radiopharmaceuticals with appropriate in vivo behavior and tumor localization properties. Several reviews discussed, extensively, the chemistry of therapeutic radiopharmaceuticals [1–3].

18.1.1 Radionuclides for Therapy

Several important radionuclides used in the preparation of therapeutic radiopharmaceuticals are summarized in Table 18.1. The radionuclides that are used for therapy decay by emitting either β^- particles or α particles. The cytotoxic effects of therapy radionuclides are primarily due to irreversible DNA damage and cell death. Alpha particles with high LET deposit their high kinetic energy (5–8 MeV) over short distances (<100 μm) compared to low LET β^- particles (<15 mm). The
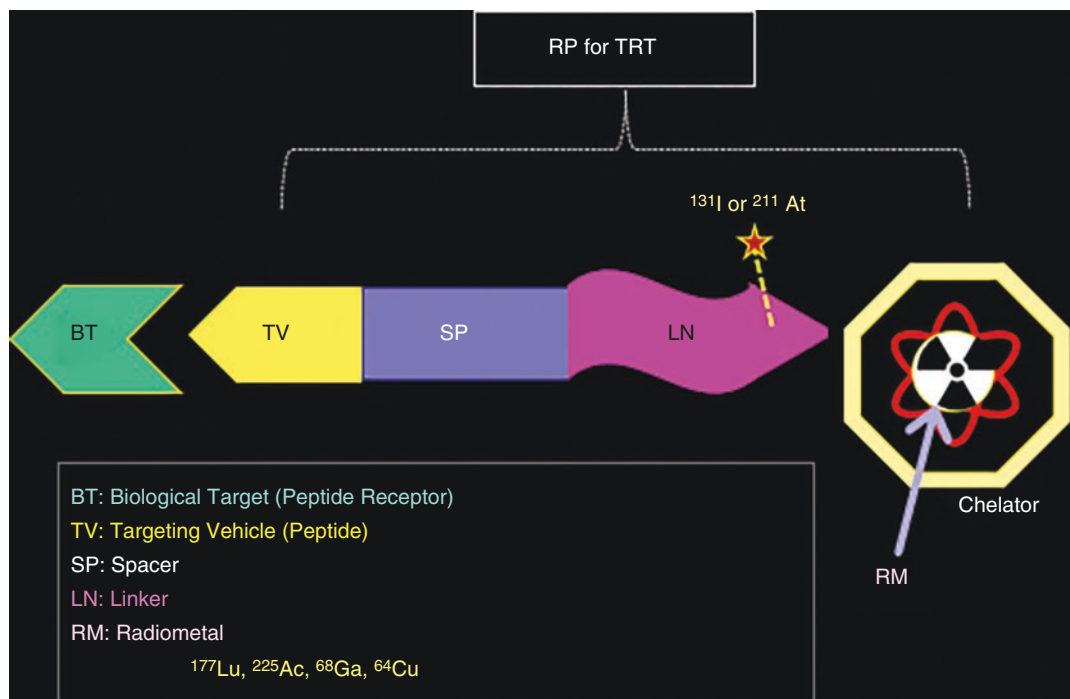
Fig. 18.1 Schematic of targeted radiopharmaceutical for molecular imaging and targeted therapy

decay mode and the kinetic energy of non-penetrating particle radiation will determine the particle range in the tissue, and the amount of energy absorbed (expressed in Grays) in the tissue.

Radionuclides useful for molecular imaging studies based on PET or SPECT decay either by positron (β^+) emission or by *EC* or isomeric transition. It is also important to recognize that several radionuclides are also available as theranostic-pair, ideal for both imaging and therapy (Table 18.2). Since isotopes of the same element (such as ^{123}I, ^{124}I, and ^{131}I) have similar chemistry, the in vivo behavior of both diagnostic and therapeutic radiopharmaceuticals will be identical. This contrasts with nonchemically identical matched pairs (such as ^{111}In/^{90}Y and ^{68}Ga/^{177}Lu), where diagnostic information is less representative of therapeutic dose distribution due to differences in radiotracer behavior. ^{111}In or ^{68}Ga labeled diagnostic radiopharmaceuticals can only be regarded as chemical/biological surrogates for ^{90}Y, ^{177}Lu, and other metal-labeled therapy radiopharmaceuticals.

Radionuclidic purity and specific activity (SA) of radionuclides are very important quality control indicators that provide quantitative information regarding the purity of the radionuclide and the mass of radionuclide for a given amount of activity (MBq or mCi per mg or μmole). Since the radionuclide purity and SA are very much dependent on the methods used to produce the radionuclides, the core concepts of radionuclide production are briefly summarized below.

18.1.2 Production of Radionuclides

In a nuclear reaction, when the atoms of a stable element (target) are bombarded by subatomic particles (such as neutron, proton, deuteron, or an α particle) or high energy γ radiation, the nucleus of the stable atom absorbs the subatomic particle or energy, gets very excited and quickly decomposes by emitting some radiation (such as subatomic particles or γ radiation) to form an unstable product radionuclide. The general equa-

Table 18.1 Radionuclides for developing radiopharmaceuticals for therapy

Radio-nuclide	$T_{1/2}$ Days	Decay	Radionuclide production by		
			Reactor	Cyclotron	Generator
^{89}Sr	50.53	β^-	^{88}Sr(n, γ)^{89}Sr		
			^{89}Y(n, p) ^{89}Sr		
^{117m}Sn	13.60	IT CE	^{116}Sn(n, γ)^{117m}Sn		
			^{117}Sn(n, n′, γ)^{117m}Sn		
^{32}P	14.268	β^-	^{31}P(n, γ)^{32}P		
			^{32}S(n, p)^{32}P		
			^{235}U(n, fission)^{131}I		
^{131}I	8.02	β^-, γ	^{130}Te(n, γ)^{131}Te → ^{131}I		
^{161}Tb	6.875	β^-	^{160}Gd(n, γ)^{161}Gd → ^{161}Tb		
^{177}Lu	6.73	β^-, γ	^{176}Lu(n, γ)^{177}Lu		
			^{176}Yb((n, γ)^{177}Yb → ^{177}Lu		
^{186}Re	3.777	β^-	^{185}Re (n, γ)^{186}Re		
^{47}Sc	3.35	β^-	^{46}Ca(n, γ)^{47}Ca → ^{47}Sc	^{48}Ti(γ, p)^{47}Sc	
			^{47}Ti(n, p)^{47}Sc		
^{90}Y	2.67	β^-	^{89}Y(n, γ)^{90}Y	^{90}Zr(n, p)^{90}Y	^{90}Sr → ^{90}Y
^{67}Cu	2.58	β^-	^{67}Zn(n, p)^{67}Cu	^{68}Zn(p, 2p)^{67}Cu	
				^{68}Zn(γ, p)^{67}Cu	
^{153}Sm	1.9375	β^-	^{152}Sm (n, γ)^{153}Sm		
^{166}Ho	1.120	β^-	^{165}Ho(n, γ)^{166}Ho		
^{188}Re	0.708	β^-	^{187}W(n, γ)^{188}W →$_{\beta^-}$ ^{188}Re		^{188}W → ^{188}Re
^{211}At	7.21 h	α		^{209}Bi(α, 2n)^{211}At	^{211}Rn→^{211}At
^{225}Ac	9.92	α		^{226}Ra(p, n)^{225}Ac	^{229}Th→^{225}Ac
				^{232}Th(p, x)^{225}Ac	
^{223}Ra	11.4	α			^{227}Ac→^{227}Th→^{223}Ra
^{212}Bi	60.6 months	α			^{224}Ra→^{212}Pb→^{212}Bi
^{213}Bi	45.6 months	α			^{225}Ac→^{213}Bi
^{227}Th	18.7	α			^{227}Ac→^{227}Th

tion for a nuclear reaction can be written as follows:

$$T(P,R)Y \tag{18.1}$$

where T represents the target nuclide, P is the projectile, R represents the radiation emitted by the compound nucleus, and Y represents the unstable product radionuclide. Nuclear reactions such as (p, n), (p, α), (d, α), (n, p), (n, γ) and (γ, p) are some of the common nuclear reactions used to produce artificial radioisotopes. Various production methods and nuclear reactions used to produce therapy radionuclides are summarized in Table 18.1. For a more detailed description of the methods used to produce radionuclides artificially, please refer to Chap. 8.

In the production of radionuclides using an accelerator (such as LINAC and cyclotron), the accelerated charged particle must have an energy

greater than the electrostatic repulsion between the positive charge of projectile and the positive charge of the target nucleus. Protons are generally accelerated to 10–70 MeV to produce therapeutic radionuclides. LINACS can also be used to generate high energy charged particles and photons to induce nuclear reactions. When isotopes of the stable elements are bombarded with positively charged particles, the product radionuclides are neutron deficient. The target nuclide and radionuclide produced are isotopes of different elements. As a result, high specific activity radionuclides can be produced. However, because of secondary nuclear reactions, radionuclidic impurities may be present in the final radionuclide preparation used to manufacture the radiopharmaceuticals.

Reactor production of radionuclides is based around the spontaneous fission of fissile materials (^{235}U or ^{238}Pu) that release neutrons capable of inducing fission

Table 18.2 Theranostic-pair of radionuclides for both targeted therapy and molecular imaging studies

Radionuclide for therapy						Radionuclide for PET					
Nuclide	T 1/2	Decay	E_{max} MeV	γ-Rays keV	%	Nuclide	T½	Decay	E_{max}	γ-Rays MeV	% keV
^{131}I	8.02 d	β⁻ (100)	0.607	364.5	82	^{124}I	4.18 days	β⁺ (22)	2.14	603 723	61 10
^{90}Y	2.70	β⁻ (100)	2.29	–	–	^{86}Y	14.7 h	β⁺ (33)	2.34	627.8 1077 1153	32.6 82.5 30.5
^{67}Cu	2.58 d	β⁻ (100)	0.577	184.6	48.6	^{64}Cu	12.7 h	β⁺ (17.8) β⁻ (38.4) EC (43.8)	0.653 0.571	1346	0.53
^{47}Sc	3.35 d	β⁻ (100)	0.610	159	68	^{44}Sc	3.9 h	β⁺ (94.3)	1.470	1157	99.9
^{89}Sr	55.5 d	β⁻ (100)	1.470	–	–	^{83}Sr	32.4 h	β⁺ (94.3)	1.274	381.3	19.6
^{161}Tb	6.9 d	β⁻ (100)	0.590	74.6	9.8	^{152}Tb	17.5 h	β⁺ (18.0)	2.500	344.3	57
^{149}Tb	4.1 h	α (16.7) EC (79)	α 5.83	165 352	27.8 33	^{149}Tb	4.1 h	β⁺ (4.3) EC (79)	0.600	165 352	28 33
^{177}Lu	6.73 d	β⁻ (100)	0.498	113 208	6.4 11	^{68}Ga	67.6 m	β⁺ (90)	2.921	1077	3.0
						^{111}In	2.805 days	EC (100)	–	171.3 245.4	90 94

or neutron activation of target material. In the case of neutron activation, there is no Coulomb repulsion from the positively charged nucleus. Therefore, thermal neutrons with low kinetic energy (0.025 eV) can easily penetrate the target nucleus. Since neutrons are absorbed by the target nuclei, the product radionuclide is neutron-rich and decays by β^- particle emission. Radionuclides produced by (n, γ) nuclear reaction are isotopes of the target element and, therefore, are very low in specific activity. For production of radionuclides via fission, however, neutron energies must be on the order of MeV. The fission product radionuclides generally have very high specific activity.

Radionuclide generators are an extremely desirable means of production of therapeutic radionuclides. The parent and daughter radionuclides are two different elements and can be chemically separated. The parent radionuclides are loaded onto a resin, or an inorganic adsorbent and the daughter radionuclide can be eluted or "milked," ideally resulting in isolation of activity with high radionuclidic purity and specific activity.

18.1.2.1   Radionuclidic Purity (RP) and Specific Activity (SA)

RP of a specific radionuclide is defined as the ratio, expressed as a percentage of desired radioactivity of the radionuclide from the total radioactivity, including the activity of the radionuclide contaminants. In addition, RP statement also provides the percentage of undesirable radionuclidic

impurities. Table 18.3 shows a comparison of specifications for ^{177}Lu chloride supplied by different suppliers. For example, ^{177}Lu may be 99.92% pure at EOB, and may have 0.05% ^{176m}Lu ($T_{1/2}$, 3.66 h) and 0.03 ^{177m}Lu ($T_{1/2}$, 160.4 days) as radionuclidic impurities. After 2 days, when all the ^{176m}Lu activity has decayed, the RP of ^{177}Lu may be slightly higher (99.97%), and the long-lived contaminant ^{177m}Lu will still be ~0.03%. However, as ^{177}Lu activity decays with time, the percentage of ^{177m}Lu contaminant will increase.

When ^{177}Lu is produced via ^{176}Lu(n, γ)^{177}Lu reaction using enriched ^{176}Lu target, the final product ^{177}Lu will also have ^{175}Lu and ^{176}Lu as non-radioactive stable isotope contaminants. The total mass of all non-radioactive and radioactive isotopes of lutetium (^{175}Lu + ^{176}Lu + ^{177}Lu + ^{176m}Lu + ^{177}Lu) represents the "total mass" of lutetium element, expressed in mg, μg, mmol, or μmol.

The non-radioactive isotopes of an element are known as the *"carrier."* When a radionuclide is considered *"carrier-free"* (CF or c.f.), it means that the radioactive isotope is not contaminated with the *carrier*. In the production of radionuclides in a cyclotron, the target element is converted into a different element (with a higher atomic number). As a result, cyclotron produced radionuclides are supposed to be CF. The term *"carrier-added"* (CA or c.a.) indicates a relatively high concentration of stable nuclides of the corresponding element, while *"no carrier-*

Table 18.3   Comparison of ^{177}Lu chloride supplied by two different suppliers

Specifications	Radionuclide		DOE
	^{177}Lu chloride, n.c.a. (*Endolucin beta*)[a]	^{177}Lu Lutetium chloride, c.a. (*LuMark*)[b]	
Specific activity	≥3000 GBq/mg at ART	≥500 GBq/mg at ART	
Radionuclidic purity	^{175}Yb≤0.01% All impurities ≤0.01%		
Radionuclidic impurities		^{177m}Lu: ≤0.024% Other impurities: ≤0.01%	
Radioactivity concentration	36–44 GBq/mL at ART	72–88 GBq/mL	
Chemical purity	Fe ≤ 0.25 μg/GBq, Cu ≤ 0.5 μg/GBq, Zn ≤ 0.5 μg/GBq, Pb ≤ 0.5 μg/GBq, ^{176}Yb ≤ 0.1 μg/GBq Sum of impurities ≤0.5 μg/GBq		
Radiochemical purity	≥99% as ^{177}LuCl$_3$	≥99% as ^{177}Lu^{3+}	

ART activity reference time
[a]ITG Isotope Technologies
[b]IDB Radiopharmacy

added" (NCA or n.c.a) suggests that the activity is essentially free from such contamination. A more appropriate concept is NCA than CF because the carrier is not intentionally added. To facilitate chemical and biochemical reactions during radioisotope production, a carrier may be added intentionally, and such preparations should specifically be reported as CA.

The quantity of desirable decays (amount of radioactivity, A) per unit mass of material is commonly described as molar activity or specific activity (Bq/mol or A/mol). SA is also expressed as GBQ or MBq/mg. A radionuclide supplied as n.c.a. material is more desirable to prepare radiopharmaceuticals than c.a. radionuclides, as it results in higher molar activity or SA. In general, accelerated produced radionuclides have higher SA than the neutron activation produced radionuclides. Generator produced radionuclides have specific activities closer to the theoretical specific activity values.

18.1.2.2   Chemical Purity (CP)

When the therapeutic radionuclides are used to prepare target specific radiopharmaceuticals, the CP of the radiometals is also very important. Since the mass of radionuclide is very low**,**

the metal ion impurities even at ppb levels act as pseudo-carriers, requiring higher concentrations of the targeting vectors to achieve high radiolabeling yields. Metal ion impurities (such as Al, Ca, Cu, Fe, Ni, Zn, and Pb) are likely to be present in the radionuclide solution and compete with the radionuclide to form thermodynamically and kinetically stable coordination complexes with the targeting vectors. Therefore, it is of utmost importance to determine the metal ion contamination and minimize their impact on the labeling yields of radiopharmaceuticals.

18.2   Chemical Groups Radionuclides

The periodic table of chemical elements (Fig. 18.2) shows the position and chemical group identity of the therapy radionuclides. ^{131}I is a reactive nonmetal and belongs to the halogen family (Group 17), while ^{211}At, a metalloid, also belongs to Group 17. All other therapy radionuclides are metals and belong to different groups as follows:

Fig. 18.2 Periodic table of elements

- Group 2 (alkaline earth metals): ^{89}Sr and $^{223/224}$Ra Group 2).
- Group 3 (lanthanides): ^{153}Sm, ^{161}Tb, ^{166}Ho, and ^{177}Lu.
- Group 3 (actinides): ^{225}Ac and ^{227}Th.
- Groups 3–12 (transition metals): ^{47}Sc, ^{67}Cu, ^{90}Y, and $^{186/188}$Re.
- Groups 14–15 (post-transition metals): ^{212}Pb and $^{212/213}$Bi.

The radionuclide production method determines if they are supplied for the manufacture of targeted radiopharmaceuticals, either in the form of c.a. or n.c.a. radio-chemicals. In either case, the radionuclide may be contaminated with trace levels of nonradioactive stable isotopes of the same element. Table 18.4 lists various radionuclides, decay properties, and the corresponding stable isotopes. When a radionuclide decays by beta, alpha, or positron emission, it becomes a different element as shown Table 18.4. It is important to recognize that the chemistry of the decay product nuclide will be totally different and that it is necessary to take this fact into consideration in the design of radiopharmaceutical.

Table 18.4 Radioisotopes of different elements useful for molecular imaging and targeted radionuclide therapy

	Element		Stable isotopes		Radioactive isotopes		Decay			Decay product
Z	Name	Group	Nuclide	%	Nuclide	$T_{1/2}$	Mode	%	Product	Group
21	Scandium	3 (TM)	^{45}Sc	100	^{44}Sc	4.04 h	β^+	94	^{44}Ca	2
					^{47}SC	3.35 days	β^-	100	^{47}Ti	4
29	Copper	11 (TM)	^{63}Cu	69.15	^{64}Cu	12.7 h	β^+	17.9	^{64}Ni	10
							EC	40	^{64}Ni	10
							β^-	39.0	^{64}Zn	12
			^{65}Cu	30.85	^{67}Cu	2.58 days	β^-	100	^{67}Zn	12
31	Gallium	13 (P-TM)	^{69}Ga	60.11	^{66}Ga	9.49 h	β^+	57	^{66}Zn	12
			^{71}Ga	39.89	^{67}Ga	3.258 days	EC	100	^{67}Zn	12
					^{68}Ga	1.13 h	β^+	89	^{68}Zn	12
38	Strontium	2 (AE)	^{84}Sr	0.56	^{89}Sr	50.563 days	β^-	100	^{89}Y	3
			^{86}Sr	9.86	^{90}Sr	28.9 years	β^-	100	^{90}Y	3
			^{87}Sr	7.0						
			^{88}Sr	82.58						
39	Yttrium	3 (TM)	^{89}Y	100	^{86}Y	14.7 h	β^+	32	^{86}Sr	2 Stable
					^{90}Y	2.666 days	β^-	100	^{90}Zr	4 Stable
49	Indium	13 (P-TM)	^{113}In	4.28	^{111}In	2.8 days	EC	100	^{111}Cd	12
			^{115}In	95.72						
53	Iodine	17 (Nonmetal)	^{127}I	100	^{123}I	13.2 h	EC	100	^{123}Te	16
					^{124}I	4.176 days	β^+	22	^{124}Te	16
							EC	78		
					^{131}I	8.02 days	β^-	100	^{131}Xe	18
62	Samarium	3 (LN)	^{144}Sm	3.08	^{153}Sm	46.284 h	β^-	100	^{153}Eu	3
			^{149}Sm	13.82						
			^{150}Sm	7.37						
			^{152}Sm	27.74						
			^{154}Sm	22.74						

Table 18.4 (continued)

Z	Element Name	Group	Stable isotopes Nuclide	%	Radioactive isotopes Nuclide	$T_{1/2}$	Decay Mode	%	Product	Decay product Group
65	Terbium	3 (LN)	^{159}Tb	100	^{149}Tb	4.12 h	α EC	17.7 82.3	^{145}Eu ^{149}Gd	3
					^{152}Tb	17.5 h	EC + β^+	100	^{152}Gd	
					^{155}Tb	5.32 days	EC	100	^{155}Gd	
					^{161}Tb	6.89 days	β^-	100	^{161}Dy	
67	Holmium	3 (LN)	^{165}Ho	100	^{166}Ho	26.824 h	β^-	100	^{166}Er	3
71	Lutetium	3 (LN)	^{175}Lu	97.401	^{177}Lu	6.647 days	β^-	100	^{177}Hf	4
			^{176}Lu	2.599						
75	Rhenium	7 (TM)	^{185}Re	37.4	^{186}Re	3.719 days	β^-	92.53	^{186}Os	8
			^{187}Re	62.6	^{188}Re	17.00 h	β^-	100.0	^{188}O	8
82	Lead	14 (P-TM)	^{204}Pb	1.4	^{212}Pb	10.64 h	β^-	100	^{212}Bi[a]	15
			^{206}Pb	22.1						
			^{207}Pb	24.1						
			^{208}Pb	52.4						
83	Bismuth	15(P-TM)	^{209}Bi	100	^{212}Bi	60.6 months	β^- α	64.06 35.94	^{212}Po[a] ^{208}Tl[a]	16 13
					^{213}Bi	45.61	β^- α	97.8 2.20	^{213}Po[a] ^{209}Tl[a]	16 13
85	Astatine	17 (metalloid)	No stable nuclide		^{211}At	7.21 h	α *EC*	42 58	^{207}Bi[a] ^{211}Po[a]	15 16
88	Radium	2 (AE)	No stable nuclide		^{223}Ra	11.43 days	α	100	^{219}Rn[a]	18
					^{224}Ra	3.632 days	α	100	^{220}Rn[a]	18
					^{226}Ra	1600 years	α	100	^{222}Rn[a]	18
89	Actinium	3 (AC)	No stable nuclide		^{225}Ac	9.92 days	α	100	^{221}Fr[a]	1
					^{227}Ac	21.772 years	α β^-	1.38 98.62	^{223}Fr[a] ^{227}Th[a]	1 3
90	Thorium	3 (AC)	^{230}Th	0.02	^{227}Th	18.68 days	α	100	^{223}Ra[a]	
			^{232}Th	99.98						

[a]Radionuclide decay product isotopes are also radioactive

18.3   Chemistry of Halogens

The halogen group consists of five elements (F, Cl, Br, I, and At) in the periodic table, organized under Group-17 (Fig. 18.2). The physical and chemical properties of halogens are compared to hydrogen in Table 18.5. These five elements are reactive nonmetals, although astatine is a metalloid. All halogens are characterized by the presence of two *s* electrons and five *p* electrons in the outer most valence shell. Among the halogens, fluorine has the highest electronegativity value (greatest attraction for electrons) and astatine the least. Iodine and astatine may attain positive oxidation states when interacting with more electronegative element oxygen. The higher ionization potentials of halogens suggest that it is difficult to remove an electron from halogen atoms. In general, halogens can react as *electrophiles*, electron-deficient positively charged species, or *nucleophiles*, electron-rich negatively charged species. *Electrophiles* seek electron-rich reactants, such as carbon atoms, with high local electron densities, while *nucleophiles* seek electron-deficient reactants. Astatine is the heaviest halogen with some of its chemical properties like those of iodine. However, in certain circumstances, astatine also has significant metallic

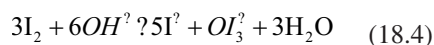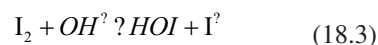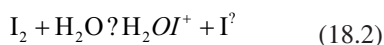**Table 18.5** Physical properties of halogens compared to hydrogen

Physical property	Element			
	H	F	I	At
Atomic number	1	9	53	85
Atomic radius (pm)	78	71	133	148
Ionic radius (pm)	154	133	216	62
Electron structure	$1s^1$	[He] $2s^2$, $2p^5$	[Kr] $4d^{10}$ $5s^2$, $5p^5$	[Xe] $4f^{14}$ $5d^{10}$ $6s^2$ $6p^5$
Electronegativity	2.20	3.98	2.66	2.20
Oxidation state		-1	$-1, +1, +5, +7$	$\mathbf{-1, +1}, +3, +5, +7$
First ionization potential (ev)	13.598	17.42	10.44	9.315

characteristics. An important consideration is that the carbon–halogen bond strength for astatine is lower than that for iodine.

18.3.1 Iodine and Radioiodination

Iodine (I_2) sublimes at atmospheric pressure and temperature resulting in a blue–violet gas with an irritating odor. Iodine occurs in nature mostly in the form of salts or iodides of sodium and potassium. Iodine exists as a diatomic molecule, I_2, in its elemental state, and unlike fluorine, can also exist in several oxidation states (Table 18.5). Several iodine oxides (such as I_2O_4, I_4O_9, I_2O_7, I_2O_5) do exist in nature but, readily decompose to iodine and oxygen at high temperatures. Iodine dissolves readily in nonpolar solvents, such as chloroform and carbon tetrachloride but, is only slightly soluble in water. Elemental iodine (I_2), where two iodine atoms share a pair of electrons to achieve a stable octet for themselves. The iodide anion (I^-) is the strongest reducing agent among the stable halogens, being the most easily oxidized back to diatomic I_2.

The free molecular iodine (I_2) has the structure of I^+–I^- in aqueous solution. However, the electrophilic species (I^+) does not exist as a free species but, forms complexes with nucleophilic entities, such as water or pyridine. The reactions with water can be written as follows:

$$I_2 + H_2O \rightleftharpoons H_2OI^+ + I^? \qquad (18.2)$$

$$I_2 + OH^? \rightleftharpoons HOI + I^? \qquad (18.3)$$

$$3I_2 + 6OH^? \rightleftharpoons 5I^? + OI_3^? + 3H_2O \qquad (18.4)$$

The hydrated iodonium ion, H_2OI^+, and the hypoiodous acid, HOI, are believed to be highly reactive electrophilic species. In an iodination reaction (Fig. 18.3), radioiodination occurs by (a) electrophilic substitution of a hydrogen ion in a molecule of interest by a radio-iodonium ion or (b) nucleophilic substitution (isotope exchange) where a stable iodine atom that is already present in the molecule is exchanged with a radioactive iodine atom.

The advantages and disadvantages of different radioiodination techniques have been reviewed extensively [4–7]. In the preparation of radioiodinated compounds, the radioiodine is preferentially attached to a carbon atom in a vinylic or aromatic moiety, in which the C-I bond strength is relatively high compared to aliphatic C-I bond. Since radioiodine isotopes (^{123}I, [124]I, and ^{131}I) are produced in iodide form, early methods have involved nucleophilic substitution reactions, such as the use of high temperature and solid-state halogen exchange reactions [8]. Alternatively, radioactive iodide can be oxidized to iodine or iodine monochloride and used in electrophilic substitution reactions, such as the iododestannylation of aryltin compounds [9].
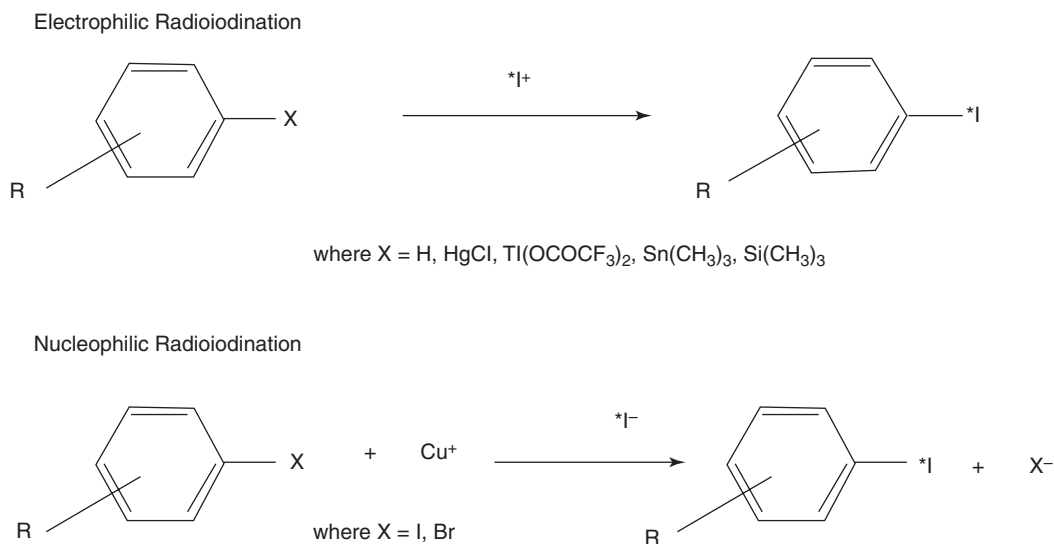
Electrophilic Radioiodination

where X = H, HgCl, Tl(OCOCF$_3$)$_2$, Sn(CH$_3$)$_3$, Si(CH$_3$)$_3$

Nucleophilic Radioiodination

where X = I, Br

Fig. 18.3 Electrophilic and nucleophilic radioiodination reactions

18.3.1.1 Electrophilic Substitution Reaction

The electrophilic species (HO*I, H$_2$O*I) generated from radioiodide and the oxidant react directly with the aromatic moiety of the compound to be labeled. The aromatic amino acids tyrosine and histidine are the sites of iodination in protein molecules [10, 11]. With tyrosine, substitution of a hydrogen ion with the reactive iodonium ion occurs *ortho-* to the phenolic hydroxyl group. With histidine, substitution occurs at the second position of the imidazole ring. Electrophilic substitutions can often be performed fast on a nonderivatized substrate under mild reaction conditions.

The most frequently used oxidizing agents (Fig. 18.4) are peracetic acid and the *N*-chloro compounds, such as chloramine-T, iodogen, and succinimides. The *N*-chloro compounds are the most popular oxidants; however, their relatively strong oxidizing properties often induce by-products. To limit these oxidative side reactions, chloramine-T is immobilized on spherical polystyrene particles (iodobeads) while iodogen, which contains four functional chlorine atoms, is coated as a thin layer on the walls of a reaction vessel. Of the two immobilized oxidants, which are mostly used for protein-labeling, iodogen is the best to prevent loss of immunoreactivity [12]. For the labeling of small organic molecules, peracetic acid is also often preferred due to its mild oxidizing properties.

The enzyme lactoperoxidase from bovine milk is also an effective oxidant for iodide oxidation and the radioiodination of proteins. In the presence of minute quantities of hydrogen peroxide (H$_2$O$_2$), lactoperoxidase oxidizes and binds radioiodide to proteins in the reaction mixture. The pH range for iodide oxidation by lactoperoxidase is 4–8.5 with an optimum at pH 5. The reaction is extremely rapid under very mild conditions and the denaturation of proteins is low. The separation of lactoperoxidase from the labeled protein may be avoided by using the immobilized enzyme [13]. This technique applies immobilized lactoperoxidase together with glucose oxidase, which produces H$_2$O$_2$ in the presence of glucose.
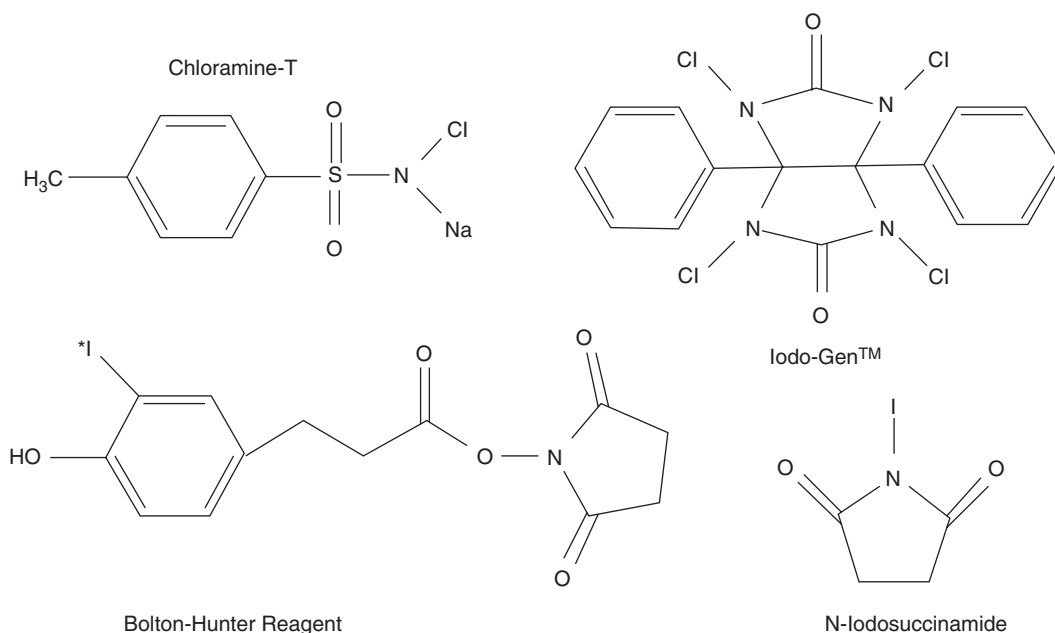
Fig. 18.4 Oxidizing agents commonly used in radioiodination reactions

Proteins lacking tyrosine amino acid residues or proteins sensitive against the denaturing influence of oxidizing agents are indirectly radioiodinated via amide bond formation at lysine residues using Bolton and Hunter reagent [11]. A prosthetic group for radioiodination contains an aromatic moiety, like tyrosine, which can be iodinated and covalently attached to the lysine moiety in the protein under milder conditions than those found in direct radioiodinations.

The addition of one radioiodine atom to large molecules, such as antibodies, does not usually affect their immunoreactivity. The labeling process using oxidation agents as well as the addition of reducing agents to stop the labeling reaction may have destructive effects on sensitive sites of the biomolecules. Depending on the labeling conditions, denaturation can occur due to oligomerization, conformational changes due to the changes of functional groups, or the cleavage of disulfide bonds. Consequently, labeling reactions must be adapted and optimized to the individual proteins or peptides, including proof of functional integrity.

18.3.1.2   Nucleophilic Substitution Reaction

Direct replacement of stable iodine isotopes in organic molecules by a radioiodine, also called isotopic exchange, is a well-known radioiodination method. The reaction is usually performed with the radioiodide ion at very high temperature, and most often in the presence of sulfate salts and oxidants, such as oxygen from the air. The method of choice in nucleophilic radioiodination is the well-established Cu(I)-catalyzed halogen–halogen exchange reaction in an acidic, aqueous medium (Fig. 18.3). The exchange reaction can be either isotopic (*I/I) or non-isotopic (*I/Br), which specifically enables the synthesis of a high SA radiopharmaceuticals [14]. A nucleophilic exchange can be successfully applied on activated (presence of electron-deficient substituents, e.g., carbonyl group) or non-activated (e.g., alkyl group) aromatic compounds. However, in organic media, electron-donating substituents are also well-tolerated. The purity, labeling yield and SA can be controlled by carefully optimizing the concentration of copper and the precursor.

18.3.1.3 ^{131}I-Labeled Therapeutic Radiopharmaceuticals

In the last four decades, several ^{131}I-labeled small molecules, peptides, and mAbs were developed as radiopharmaceuticals for TRT. However, ^{131}I-tositumomab (BEXXAR®) injection and Iobenguane I-131 injection (AZEDRA®) are the only two radiopharmaceuticals that have received FDA approval for targeted therapy.

^{131}I-Tositumomab (BEXXAR®)

The radioiodination of the mouse IgG_{2a} anti-B1 (anti-CD20) mAb was performed according to the iodogen method [15, 16]. Following purification through an ion exchange resin column, >90% of ^{131}I was protein bound with a maximum specific activity of 8.8 mCi/mg. The BEXXAR therapeutic regimen is supplied commercially as a sterile, clear, preservative-free liquid for intravenous administration. The dosimetric dosage form is supplied at nominal protein and activity concentrations of 0.1 mg/mL and 0.61 mCi/mL (at the time of calibration), respectively. The therapeutic dosage form is supplied at 1.1 mg/mL and 5.6 mCi/mL, respectively. Even though the SA of the therapeutic preparation is 5.1 mCi/mg, the SA is not a major issue for the therapeutic dose since 450 mg of cold antibody is administered 1 h prior to the radiolabeled preparation.

Iobenguane I-131 Injection (AZEDRA®)

The drug substance iobenguane I-131 is a substituted benzylguanidine with I-131 in the meta position of the benzene ring. Iobenguane I-131 is also described as $[^{131}I]$meta-iodobenzylguanidine (MIBG). The molecular weight is 279.1 Da. AZEDRA injection is supplied at a concentration of 555 MBq/mL (15 mCi/mL), and is a sterile, clear, colorless-to-pale-yellow solution. Each single-dose vial contains iobenguane (0.006 mg/mL), sodium ascorbate (58 mg/mL), and sodium gentisate (23 mg/mL) in water for injection. The pH range of the solution is 4.5–5.5, with specific activity of ~2500 mCi/mg (92,500 MBq/mg).

The synthesis of $[^{131}I]$MIBG (Fig 18.5a) was first developed based on the radioiodide exchange reaction (Weiland et al. 1986). The SA of ^{131}I-MIBG based on this method is typically <400 MBq/μmol). Subsequently, several radioiodination methods were developed to increase the specific activity [17]. High SA $[^{131}I]$MIBG for therapy was produced using the Ultratrace solid-phase electrophilic substitution reaction method [18]. The Ultratrace process uses a solid polystyrene resin containing the covalently bound stannylbenzylguanidine precursor, which undergoes a 1:1 displacement reaction with radioiodine (Fig 18.5b). Briefly, the solid-phase precursor is suspended in a dilute mixture of radioactive ^{131}I-sodium iodide, H_2O_2/HOAc at 25 °C for 60 min. The oxidized ^{131}I-iodine reacts to disrupt the covalent bond between the tin and benzylguanidine (BG) precursor with radioiodine insertion at the *meta* position of the phenyl ring to form $[^{131}I]$MIBG, which simultaneously cleaves from the resin and dissolves into the liquid phase. The labeled $[^{131}I]$MIBG is then purified by using cation exchange cartridge. The formulated final product solution is membrane filtered and aseptically filled into 30-mL glass vials, which are then aseptically capped, sealed, and frozen. The RCP of the drug product is >97% and the minimum SA is about 1650 mCi/mg or 460 mCi/μmol.

18.3.2 Chemistry of Astatine

Astatine is the rarest naturally occurring element present as the decay product of various heavier elements. Astatine was first discovered in the United States in 1940, where it was produced at the University of California, Berkeley through α particle bombardment of natural bismuth via $^{209}Bi(\alpha, 3n)^{210}At$ and $^{209}Bi(\alpha, 2n)^{211}At$ nuclear reactions [19]. All astatine isotopes are short lived and ^{210}At is the most stable isotope of astatine with a half-life of only 8.1 h. It decays by β^+ emission (99.8%) to ^{210}Po, an α emitter with a half-life of 138 days. Whereas ^{211}At ($T_{1/2}$ 7.21 h) decays by α emission (42%) to ^{207}Bi ($T_{1/2}$ 31.6 years), and by EC (58%) to ^{211}Po, which in turn quickly decays by α emission to stable ^{207}Pb. Since there are no stable or long-lived isotopes, many chemical and physical properties of astatine are still not known, but derived from its
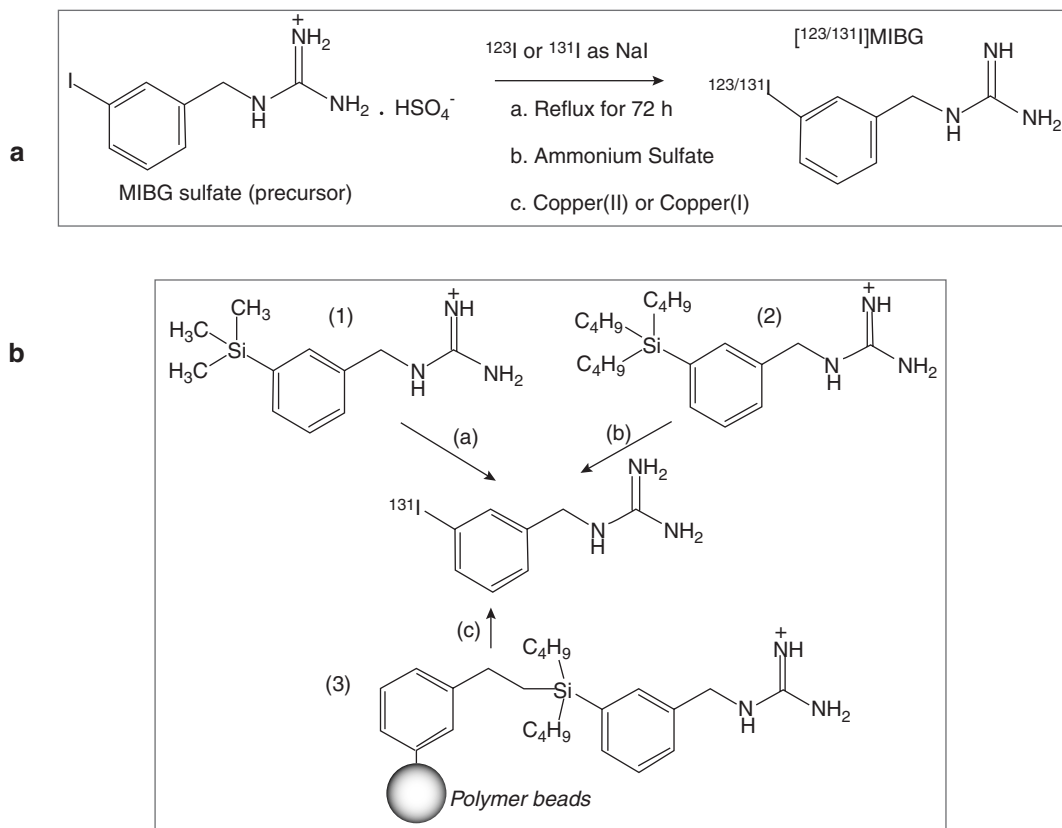
Fig. 18.5 Synthesis of [131I]MIBG: Nucleophilic radioiodination or radioiodide exchange reaction using catalysts, such as ammonium sulfate or copper ions, results in low specific activity MIBG (**a**). Electrophilic radioiodination (in the presence of an oxidizing agent) to synthesize high specific activity MIBG (**b**) based on a tri-methylsilicontin BG precursor (*1*), tri-butylsilicontin BG precursor (*2*), or di-butylsilicontin BG precursor (*3*) attached to a polymer

neighboring halogens [20]. A sample of the pure element has never been assembled because any macroscopic specimen would be immediately vaporized by the heat of its own radioactivity.

Some chemical properties of astatine, such as anion formation, align with other halogens. It also has some metallic characteristics as well, such as forming complexes with EDTA, and is capable of acting as a metal in antibody radiolabeling reactions. Most of the organic chemistry of astatine is, however, analogous to that of iodine [21]. Astatine has an electronegativity of 2.2, lower than that of iodine (2.66), and the same as hydrogen. It has been suggested that the cationic At(I) species is protonated hypoastatous acid (H_2OAt^+), showing analogy to iodine. In general, halogen properties can be used in astatine-labeling chemistry but, there are also some obvious differences between astatine and iodine [20]. For example, unlike iodine, astatine cannot be stably coupled to tyrosine residues of proteins. Instead of binding to tyrosine, 211At has been found to form weak bonds with the sulfhydryl groups of cysteine [21].

The development of radiopharmaceuticals with astatine has been directed to the formation of covalent bonds, such as the aryl–astatine bond. An overview of the different aromatic labeling strategies is shown in Fig. 18.6. The chemical reactions include halogen exchange, diazonium salt reactions, aryliodonium salt reactions, and electrophilic substitution of metal-functionalized aromatic compounds [20–22]. The most common reaction, however, appears to be electrophilic
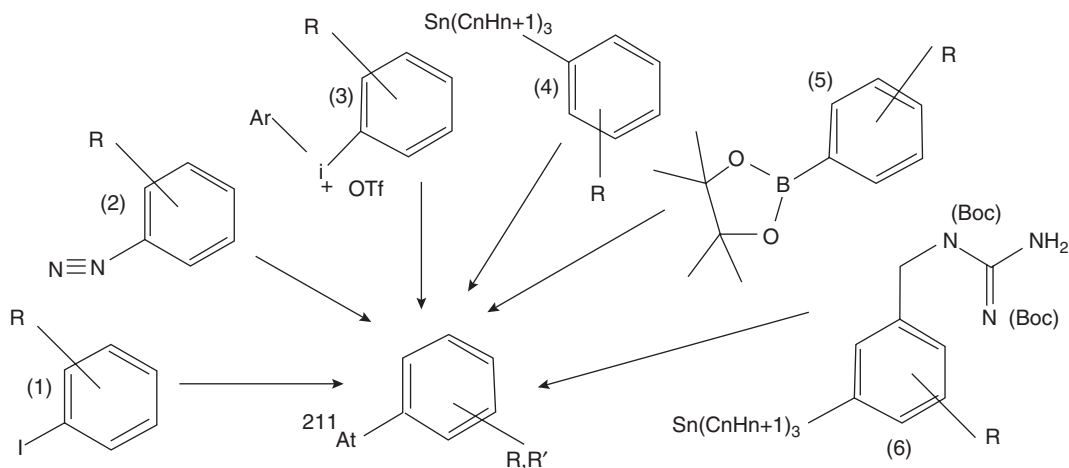
Fig. 18.6 Examples of different aryl functional groups for ^{211}At substitution reactions. (*1*). Iodine, isotope exchange, (*2*) diazonium salt, (*3*) aryliodonium salt, (*4*) aryl tin, (*5*) aryl boron pinacol ester, and (*6*). aryl tin with guanidine moiety. (Figure modified from [20])
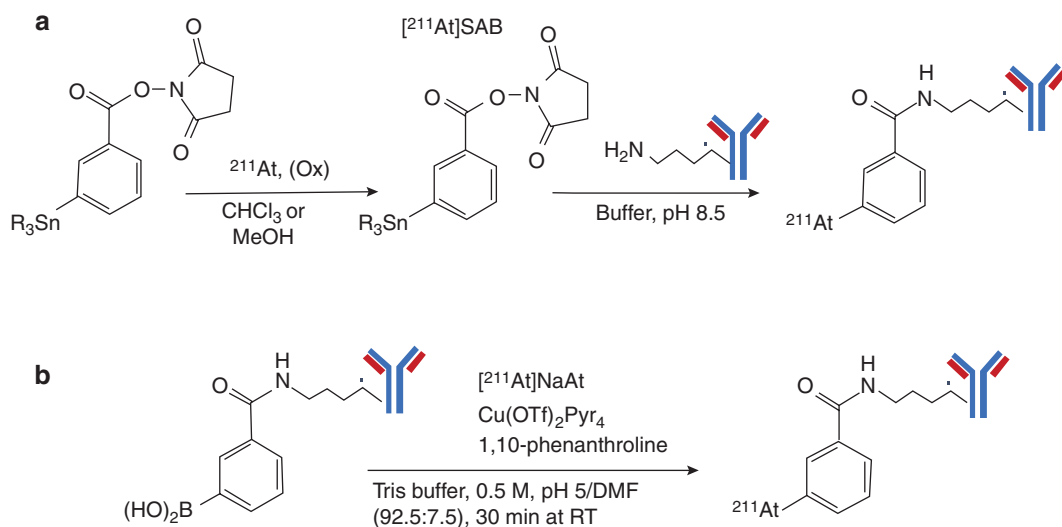

Fig. 18.7 Labeling of antibodies with ^{211}At. In a two-step procedure (**a**), the synthesis of stable astatoaryl prosthetic group ([^{211}At]SAB) is performed first followed by conju- gation to the amino groups of lysine residues in the pro- tein. In a highly efficient one-step procedure (**b**) a mAb preconjugated to an arylboronic acid moiety is used

substitution of At$^+$ on an organometallic precur- sor (demetallation reaction) since it exhibits many advantages over direct electrophilic aro- matic substitution because of the high reactivity of the carbon–metal bond leading to high yields and higher specific activities in mild conditions [23, 24]. The strategies developed after these ini- tial attempts consisted in two-step procedures, i.e., the synthesis of stable astatoaryl prosthetic groups followed by their conjugation to the pro- tein (Fig. 18.7a). The main approach uses N-succinimidyl-[^{211}At]astatobenzoate ([^{211}At] SAB) obtained by electrophilic astatodemetala- tion of the organotin precursor which is then con- jugated to the amino groups of lysine residues (Fig 18.7a) [25]. An efficient and fast procedure

was developed using one-step radiohalogenation of a mAb preconjugated to an arylboronic acid moiety, which outperforms the previously reported ones in terms of RCY, specific activity, and protocol duration (Fig. 18.7b). It is, furthermore, applicable to radioiodination, allowing the development of radiotheranostic pharmaceuticals based on ^{123}I or [124]I for imaging the lesions, and on ^{131}I or [211]At for therapy. In addition, because the preconjugated mAb can be stored for a longer period (>1 year) it opens the possibility to develop radiolabeling kits for easy development in a clinical setting [25]. This highly efficient copper-assisted halogenation (with ~90% labeling yields) can be performed in aqueous solution even at low precursor concentration, provided that a ligand such as 1,10 phenanthroline is added to keep the catalyst active.

Since higher bond energies between B-At have been reported compared with the C-At bond, several boron cage reagents, nido- and closo-carboranes were developed for radiohalogenation of biomolecules [26]. Proteins labeled with boron cage reagents were found to be more stable in vivo compared with the corresponding astatinated proteins labeled by aromatic reagents. [211]At radiopharmaceuticals that have been investigated for TRT include astatide, biotin conjugates, methylene blue, poly (ADP-ribose) polymerase (PARP) inhibitor, *meta*-astatobenzylguanidine (MABG), RGD peptide, monoclonal antibodies, and antibody fragments.

18.4   Chemistry of Radiometals

As discussed earlier in Sect. 17.3, except for ^{131}I and [211]At, all other radionuclides used in therapy are radiometals that decay either by emitting β^- particles or by emitting α particles. The physical and chemical characteristics of several radiometals are listed in Table 18.6. The s-block and p-block together are usually considered main-group elements, the d-block corresponds to the transition metals, and the f-block includes nearly all of the lanthanides and actinides. The alkaline earth metals Sr and Ra have two electrons in their valence shell and readily lose to form cations with charge +2, and an oxidation state of +2. All other metals can have +3 or +4 oxidation states and form complexes with bifunctional chelating (BFC) agents. The radionuclides of Gallium and Indium are not used for therapy, but [66]Ga, ^{68}Ga and ^{111}In are used for imaging studies, and, therefore, are included here for comparison with the therapy radionuclides.

18.4.1 Chelators for Metal Complexation

Coordination chemistry is the study of compounds that have a central metal atom (coordination center) surrounded by molecules or anions, known as ligands. The ligands are attached to the central metal atom by coordinate bonds (also known as dipolar or dative bonds), in which both electrons in the bond are supplied by the same atom on the ligand. The atom within a ligand that is bonded to the central metal atom or ion is called the donor atom. The number of donor atoms attached to the central atom or ion is called the coordination number. In coordination compounds, the metal ions have two types of valences; *primary valence* (also known as oxidation state) refers to the ability of metal ion to form ionic bonds with oppositely charged ions, while *secondary valence* (also known as coordination number) refers to the ability of a metal ion to bind to Lewis bases (ligands) to form complex ions. Therefore, the coordination number is the number of bonds formed by the metal ion with the atoms (that can donate a pair of electrons) in a chelating agent. This number varies from 2 to 8 (Table 18.6), depending on the size, charge, and electron configuration of the metal ion. The ligand geometric arrangements of coordination compounds can be linear, square planar, tetrahedral, or octahedral, depending on the coordination number.

Monodentate ligands (such as F^-, Cl^- ions) donate one pair of electrons to the central metal atoms. Polydentate ligands, also called chelates or chelating agents, donate more than one pair of electrons to the metal atom forming a stronger bond and a more stable complex. The metal com-

Table 18.6 Physical and chemical characteristics of radiometals

Property	Alkaline earth metals		Transition metals				Post-transition metals				Lanthanides				Actinides	
	Sr	Ra	Sc	Cu	Y	Re	Ga	In	Pb	Bi	Sm	Tb	Ho	Lu	Ac	Th
Atomic number	38	88	21	29	39	75	31	49	82	83	62	65	67	71	89	90
Group	2	2	3	11	3	7	13	13	14	15	n/a	n/a	n/a	3	n/a	n/a
Block	s	s	d	d	d	d	p	p	p	p	f	f	f	d	f?	f
Atomic radius (pm)	215		162	128	181	137	122	163	175	156	180	177	176	174	126	108–135
Ionic radius (pm)	118		75–87	80	90–108		47–62	62–92		96–117	103	92–110	103	86–103	112	105
Electron structure	$[Kr]$ $5s^2$	$[Rn]$ $7s^2$	$[Ar]3d^l$ $4s^2$	$[Ar]$ $3d^{10}$ $4s^1$	$[Kr]$ $4d^1$ $5s^2$	$[Xe]$ $4f^{14}$ $5d^5$ $6s^2$	$[Ar]$ $3d^{10}$ $4s^2$ $4p^1$	$[Kr]$ $4d^{10}$ $5s^2$ $5p^1$	$[Xe]$ $4f^{14}$ $5d^{10}$ $6s^2$ $6p^2$	$[Xe]$ $4f^{14}$ $5d^{10}$ $6s^2$ $6p^3$	$[Xe]$ $4f^6$ $6s^2$	$[Xe]$ $4f^9$ $6s^2$	$[Xe]$ $4f^{11}$ $6s^2$	$[Xe]$ $4f^{14}$ $5d^1$ $6s^2$	$[Rn]$ $6d^1$ $7s^2$	$[Rn]$ $6d^2$ $7s^2$
Electronegativity	0.95	0.9	1.36	1.90	1.22	1.9	1.81	1.78	1.87 2.33	2.02	1.17	1.2	1.23	1.27	1.1	
Oxidation state	+2	+2	+3	+1, +2	+3	−3 to +7	+3	+3	+2, +3	+3	0, +2, **+3**	0 +1 +2, **+3, +4**	0, +1, +2, **+3, +4**	0, +1, +2, **+3, +4**	+3	+4
Coordination number			6–8	4	6–9		6	4–8	8	8	6	6–9	6	6–9	9–10	>8

Data for effective ionic radii were derived from http://abulafia.mt.ic.ac.uk/shannon/ptable.php

plex can be neutral or charged. When the metal complex is charged, it is stabilized by neighboring counter-ions. These metal complexes are called chelate complex and the formation of such complexes is called chelation, complexation, and coordination. Alfred Werner, a Swiss chemist, won the Nobel Prize in chemistry in 1913 for his work on transition metal complexes.

As shown in Fig. 18.1, the radiometals used for imaging and targeted therapy form strong coordinate covalent bonds with chelating agents. The main goal in the synthesis of metal-based radiopharmaceuticals is to form a robust coordination complex that is stable and does not release the free metal in vivo. Bifunctional chelators (BFCs) serve the dual purpose of radiometal complexation and bioconjugation to the targeting vehicle (or the vector). Two classes of chelators known as acyclic and macrocyclic have been developed in the last four decades for the development of metal-based radiopharmaceuticals.

18.4.1.1 Chelating Agents

Some of the important acyclic and macrocyclic chelators used in the synthesis of metal-based therapeutic radiopharmaceuticals are shown in the Figs. 18.8 and 18.9 and summarized in Table 18.7. Each of these chelating agents differ in size and offer different donor groups, such as carboxylic acids, alcohols, amines, thiols, and phosphonic acids. Since the chelating agent must form complexes with the metal ion with high thermodynamic stability and kinetic inertness at pH 5–7.5, chelating agents must meet specific requirements. The fundamental metal ion characteristics (Table 18.6), such as atomic number, charge, and radius, vary from metal ion to metal ion and result in distinct preferences for geometry, coordination number, and ionic/covalent bond contribution. For optimal stability, the coordinating functional groups of the chelator should adopt the favored geometry of the metal ion while simultaneously satisfying metal coordination requirements to prevent competition from extraneous ligands, especially in biological systems [1]. The metal–ligand compatibility is dependent on the hard–soft acid-base (HSAB) character of the involved atoms.

Most of the therapeutic radiometals are hard acids with 2+ and 3+ as their major oxidation states in aqueous solution. Hard metal ions have
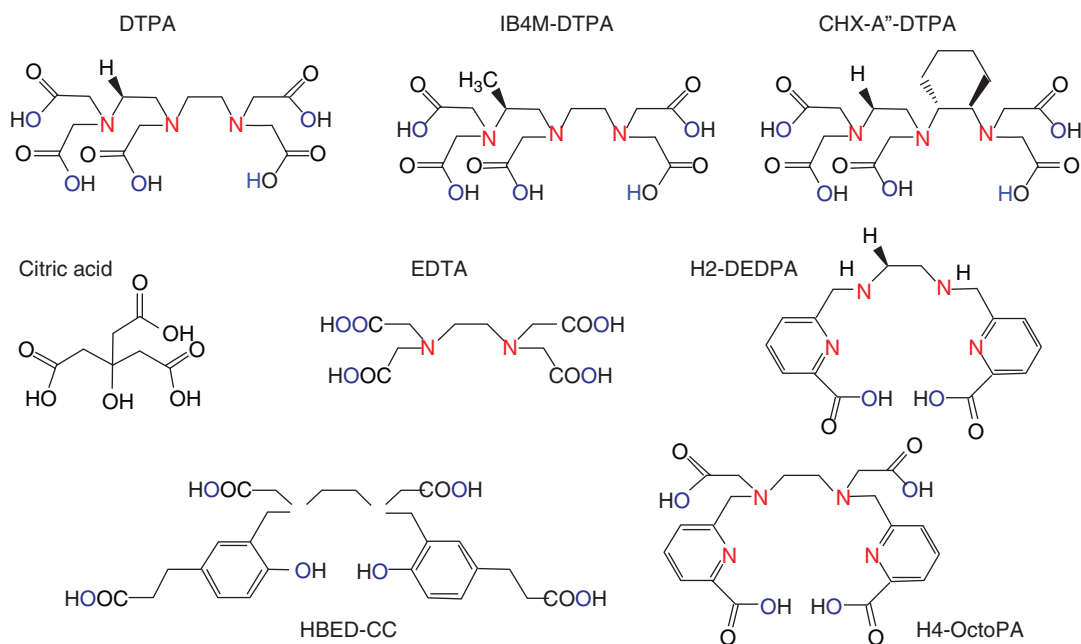

Fig. 18.8 Acyclic chelators used to prepare radiometal therapeutic radiopharmaceuticals
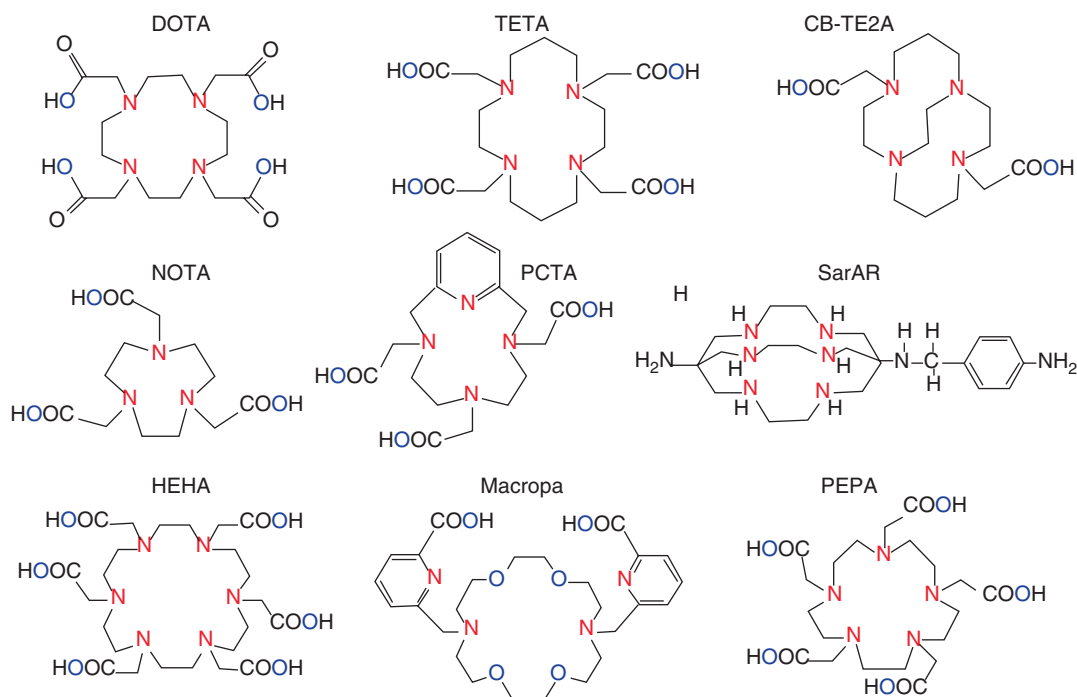
Fig. 18.9 Macrocyclic chelators used to prepare radiometal therapeutic radiopharmaceuticals

high charge density and nonpolarizable electron shells, and tend to form predominantly ionic bonds, in which electrostatic attraction is the primary driving force of bond formation. A useful metric for hard−soft character is the Drago−Wayland parameter, I_A, ($I_A = E_A/C_A$) which conveys the electrostatic (E_A) and covalent (C_A) contributions to the formation constants of Lewis acid−base complexes (includes metal complexes) in aqueous solution [1]. A higher value of I_A indicates greater hardness of the metal (Table 18.8). Therefore, hard metal ions prefer hard donating groups (e.g., carboxylic acids), which possess dense anionic character (e.g., carboxylic acids). Conversely, soft metals have low charge density and polarizable electron shells, and form covalent bonds with softer, more electron-disperse donor groups.

Acyclic Chelating Agents

Diethylenetriaminepentaacetic acid (DTPA) was one of the first acyclic chelators used in the 1980s to label peptides and antibodies with ^{111}In and

[90]Y. DTPA has been successfully used to develop FDA approved peptide, ^{111}In-DTPA-Octreotide (Octreoscan®), a SPECT imaging agent for the detection of neuroendocrine tumors. Subsequently several DTPA analogs such as 1B4M-DTPA (Tiuxetan), and CHX-A"-DTPA were developed to improve the in vivo stability of radiolabeled complexes. To increase the stability, preorganizing groups have been attached to the carbon backbone which can stabilize the conformation of the free chelator to form a more kinetically stable complex. Tiuxetan was used to develop the FDA-approved ^{90}Y labeled anti-B1 mAb (Zevalin®) for the targeted therapy of patients with non-Hodgkin lymphoma (NHL), while CHX-A"-DTPA chelator with cyclohexane backbone was used to develop [212/213]Bi labeled mAb conjugates.

EDTA analogs such as HBED-CC, H4-Octapa were also developed to improve stability of metal labeled complexes in vivo. Acyclic chelators are of special interest when antibodies or short-lived radiometals are used because radiolabeling can be performed within minutes at room temperature.

Table 18.7 Acyclic and macrocyclic chelators used to prepare radiometal therapeutic radiopharmaceuticals

Chelator	Chemical name	Donor atoms	CN	
DTPA	Diethylenetriaminepentaacetic acid	N_3O_5	8	Ga, in
IB4M-DTPA	6-methyl-diethylenetriamine-N,N,N',N'',N''-pentaacetic acid	N_3O_5	8	Y, Lu
CHX-A''-DTPA	Trans-(S,S)-cyclohexane-1,2-diamine-pentaacetic acid	N_3O_5	8	Y
EDTA	Ethylenediaminetetraacetic acid	N_2O_4	6	Ga, in
H_2dedpa	1,2-[[6-(carboxy)-pyridin-2-yl]-Methylamino]ethane	N_4O_2	8	
H_4octapa	N,N'-bis(6-carboxy-2-pyridylmethyl)-Ethylenediamine-N,N'-diacetic acid	N_4O_4	8	
HBED-CC	3-[3-[4-[5-(2-carboxyethyl)-2-hydroxyphenyl]-1,4-bis (carboxymethylamino) butyl]-4-hydroxyphenyl]propanoic acid	N_2O_6	8	Ga
NOTA	1,4,7-triazacyclononane-1,4,7-tri-acetic acid	N_4O_3	6	Ga, Sc
DOTA	1,4,7,10-tetraazacyclododecane-1,4,7,10-tetraacetic acid	N_4O_4	8	In, Sc, Ga, Y, bi, Lu, ac, Th
TCMC	1,4,7,10-tetrakis(carbamoylmethyl)-1,4,7,10-tetraazacyclododecane	N_4O^4	8	Pb
TETA	1,4,8,11-tetraazacyclotetradecane-1,4,8,11-tetraacetic acid	N_4O_4	8	Cu
CB-TE2A	4,11-bis-(carboxymethyl)-1,4,8,11-tetraazabicyclo[6.6.2]-hexadecane	N_4O_2	6	Cu
SarAr	1-N-(4-aminobenzyl)-3,6,10,13,16,19-hexaazabicyclo[6.6.6]eicosane-1,8-diamine (SarAr)	N_6	6	Cu
PCTA	3,6,9,15-Tetraazabicyclo[9.3.1]pentadeca-1(15),11,13-triene-3,6,9-triacetic acid	N_4O_3	7	Ga, cu
PEPA	1,4,7,10,13-pentaazacyclopentadecane-N,N',N'',N''',N''''-pentaacetic acid	N_5O_5	10	Ac
HEHA	1,4,7,10,13,16-hexaazacyclohexadecane-$N,N',N'',N''',N'''',N'''''$-hexaacetic acid	N_6O_6	12	Ac
Macropa-NH_2	4-amino-6-((16-((6-carboxypyridin-2-yl)methyl)-1,4,10,13-tetraoxa-7,16-diazacyclooctadecan-7-yl)methyl)picolinic acid			Ac

Table 18.8 Metal–chelate complexes and stability parameters[a]

Metal	Hardness	I_A	DOTA			DTPA		
			CN	Log K_{ML}	pM	CN	Log K_{ML}	pM
Sc^{3+}	Hard	10.49	N_4O_4	27.0–30.8	23.9–26.5	N_3O_5	26.3–27.4	
Cu^{2+}	Borderline soft		N_4O_2	22.7	17.6			
Ga^{3+}	Hard	7.07	N_4O_2	21.3–26.1	15.2	N_3O_4	24.3	20.2
Y^{3+}	Hard	10.64	N_4O_4	24.3–24.9	19.3–19.8	N_3O_5	21.9–22.5	17.6–18.3
In^{3+}	Borderline hard	6.3	N_4O_4	23.9	18.8	N_3O_5	29.0–29.5	24.4–25.7
Tb^{3+}	Hard	10.7	N_4O_4	23.6–27.0	–	N_4O_5	22.8	
Lu^{3+}	Hard	10.07	N_4O_4	21.6–29.2	17.1	N_4O_5	22.4–22.6	19.1
Bi^{3+}	Borderline hard	6.39	N_4O_4	30.3	27.0	N_4O_5	33.9–35.2	
La^{3+}	Hard	10.3	N_4O_4	20.7–22.9		N_4O_5	19.5	
AC^{3+}	Borderline hard	10.14						

[a]The table is revised from [1]

Macrocyclic Chelating Agents

Macrocyclic ligands are not only multi-dentate but, because they are covalently constrained to their cyclic form, they allow less conformational freedom. The ligand is said to be pre-organized for binding, and there is little entropy penalty for wrapping it around the metal ion. To increase the kinetic stability of metal complexes, the structure of acyclic polyamino-polycarboxylate ligands was modified to cyclic chelates such as DOTA, NOTA, TETA. PEPA, and HEHA (Fig. 18.9).

The first synthesis of DOTA was reported in 1976 [27]. DOTA (also known as H_4DOTA) is derived from the macrocycle, cyclen. Subsequently, macrocyclic BFCs based on DOTA were developed by strategically incorporating functionalized side chain to facilitate binding to antibodies [28]. In the last three decades, DOTA chelator and its derivatives have become the most important chelating agents in the development of both diagnostic and therapeutic radiopharmaceuticals.

DOTA-based chelators tend to exhibit high in vivo stability for most trivalent radiometals but, require somewhat elevated temperatures and/or longer complexation reaction times. For antibodies, higher temperature is not appropriate but, if peptides are used as vector molecules, the slow kinetic of formation can be overcome by heating (close to 100 °C) or with the use of microwave technology, which usually does not destroy the biomolecule. Once the metal is inside the macrocyclic tetraaza core, the metal will remain there under physiological conditions [29]. One way to overcome this problem of slower reaction kinetics of DOTA chelator is to increase the ring size of the macrocycle. Two larger chelators have been developed, one based on a pentaaza macrocycle (PEPA) and the other on a hexaaza macrocycle (HEHA). Both these chelators showed much faster labeling kinetics with some radiometals but, still have slower labeling kinetics than the acyclic chelator DTPA [30]. Also, pyridine-containing chelators, such as PCTA and DEPA, have also showed more facile radiolabeling while maintaining high kinetic inertness [1].

18.4.1.2   Stability of Metal–Chelate Complex

The electronegativity and oxidation state play a major role in the formation of metal–ligand complexes. Evaluation of a chelator's metal affinity requires knowledge of its acid−base properties (protonation constants) and the thermodynamic stability of its metal complexes. The metal ions dissolved in water are complexed to form aqua ions. However, in the presence of a chelating agent or the ligand (L) with greater affinity for the metal than the affinity of OH^- ion for the metal, the formation of metal–chelate complex is preferred, as shown below:

$$M + L \rightleftharpoons ML \tag{18.5}$$

$$K_s = \frac{[ML]}{[M][L]} \tag{18.6}$$

In the above equation, [ML] represents the concentration of the metal–ligand complex, while [M] and [L] represent the concentrations of the free metal and the free ligand, respectively. The stability of the metal–ligand complex is defined by the stability constant (K_S or K_{ML}) when the system reaches an equilibrium between interacting chemical species [31]. The higher the value of K_{ML}, the greater the thermodynamic stability of the metal–ligand complex (Table 18.6). The values of K_{ML} (such as 10^4 or 10^{30}) are normally represented as log K_{ML} values (such as 4 and 30). A more useful thermodynamic parameter is the *pM value* ($-\log[M]_{Free}$) since the *pM* values are linearly correlated with K_{ML} values and express the extent to which a metal ion complex is formed in solution under physiologically relevant conditions [1]. The K_{ML} values are usually determined for metal-chelate reactions under ideal conditions of buffer, pH, and temperature, and do not necessarily reflect the stability of metal–ligand complex in vivo. For a specific metal, a chelating agent with a higher *pM* value is desirable but, does not predict kinetic stability.

It is important to appreciate that the stability constant can only reveal the direction of the reaction (formation or dissociation) but, not the rate of the reaction. For example, when a purified metal–ligand complex is injected into the circulation, the rate of dissociation of the complex may be significantly increased due to extreme dilution of the complex. Therefore, the *kinetic stability* of the metal–ligand complex is very important under in vivo conditions, where competing ions (such as Fe^{3+}, Ca^{2+}, Cu^{2+}, Zn^{2+}) and ligands (serum proteins, enzymes) may augment the transchelation of the radiometal [31]. A quantity known as *conditional stability constant* can be measured or estimated as a function of pH and in the presence of different amounts of other competing ligands. The in vivo stability or the kinetic inertness of a radiotracer is evaluated more appropriately based on biodistribution studies in animal models using a radiometal--labeled chelate conjugated target vehicle (vector) with high radiochemical purity (RCP) and optimal specific activity (SA).

18.4.2 Bifunctional Chelating Agents

When a chelating agent has two different functional groups (such as alcohol, carboxylic acid, amide), it is called a bifunctional chelating agent (BFC or BFCA). The BFC consists of a chelating moiety to complex the radiometal and a functional group for the covalent attachment of the biomolecule (such as peptide and mAb). The BFCs contain a side chain (not participating in the chelation of metal) for conjugation to a peptide or protein. The side chain can be attached to the carbon backbone of the chelate (C-functionalized chelate), or by substitution to one of the nitrogen atoms in the molecule. C-functionalized chelating agents are preferable and provide greater stability to the metal–chelate complex, since all the donor atoms (nitrogen and oxygen) will be available for coordination with the metal ion. Once an appropriate chelating agent is selected for a specific metal, BFC is synthesized by adding the functional group to the chelating agent. Some of the most common commercially available BFCs used in the synthesis of radiometal complexes for therapeutic applications are shown in Fig. 18.10.

Based on acyclic chelators, BFCs were first developed in the 1970s [32]. Subsequently, BFCs of DTPA analogs were developed via mixed anhydride and cyclic anhydride [33, 34]. The first successful macrocyclic BFC was 2-*p*-nitrobenzyl-DOTA, which showed kinetic stability in serum under physiological conditions [35]. In the last three decades, an array of reactive functional groups for conjugation of BFCs to proteins have been reported in the literature [1, 36–38].

As shown in Fig. 18.1, in the design of target specific metal labeled radiopharmaceuticals, a pharmacokinetic modifying (PKM) linker is attached between the targeting vehicle and the BFC-radiometal complex. The PKM linkers and spacers are often employed to separate the BFC and the bioconjugate for two reasons. First, to avoid detrimental interactions of the biomolecule with the coordination complex formation of the chelator with the radiometal. The second more important reason is to modify the excretion kinetics and optimize the biodistribution and pharmacokinetics of the radiolabeled complex to enhance
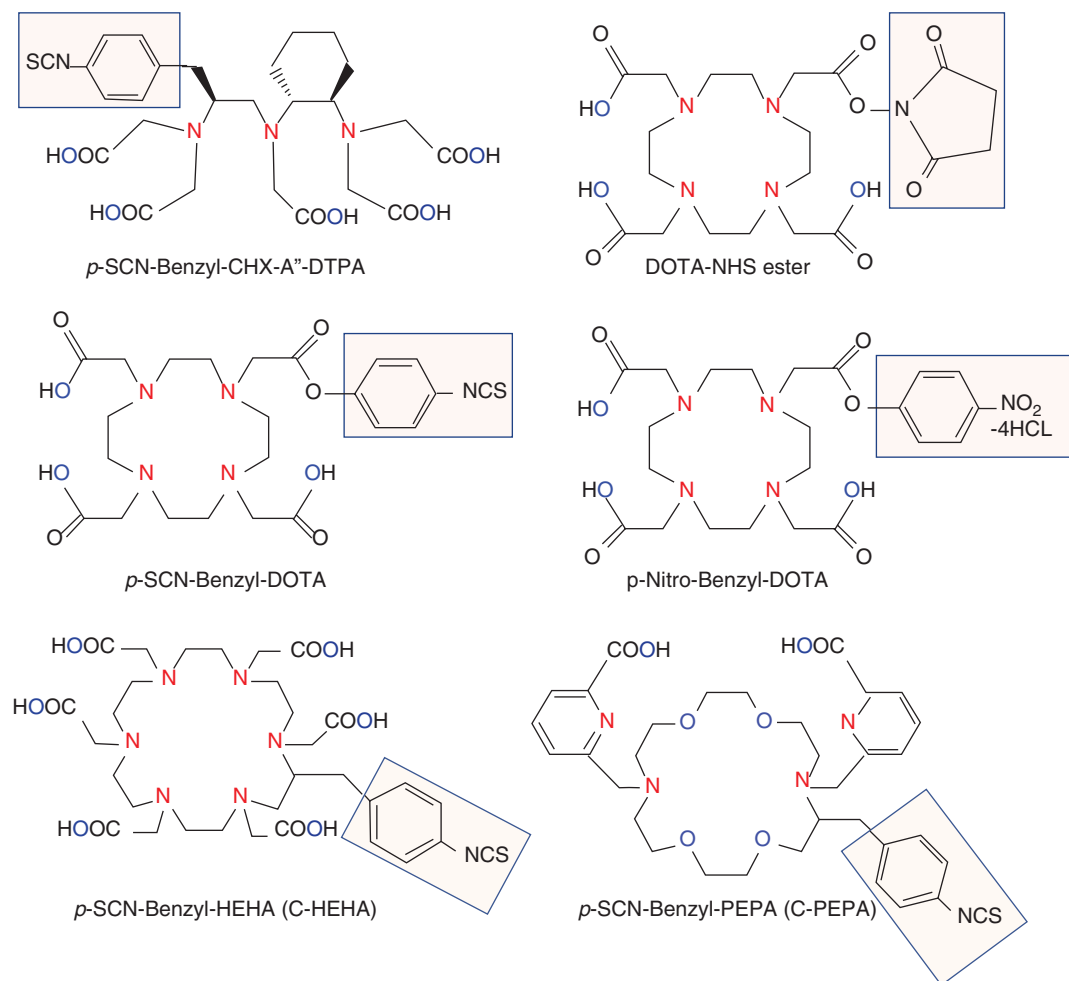
Fig. 18.10 Bifunctional chelating agents (BFCA) commonly used to conjugate a biomolecule and complex a radiometal

the target/background (T/B) ratios. These linkers can be neutral or charged (cationic or anionic) or metabolically cleavable and biodegradable. A simple hydrocarbon chain will increase lipophilicity, while a peptide sequence will increase hydrophilicity and renal clearance. Polyethylene glycol (PEG) linker can alter the excretion kinetics and improve tumor targeting.

18.4.2.1 Coupling of BFC to Biomolecule

To combine a biomolecule with a BFC, two different strategies are generally used. In the pre-conjugation strategy, the BFC is first radiolabeled with the metal and the purified radiometal-BFC complex is then conjugated to the biomolecule.

Since the conjugation step is not quantitative and requires additional purification steps, the pre-conjugation strategy may not be practical for routine use. In the post-conjugation radiolabeling approach, the BFC is first conjugated to the biomolecule and the purified BFC-biomolecule complex (precursor) can be stored under appropriate conditions for several months or years before the labeling with the radiometal is performed. To achieve high labeling yields and radiochemical purity (RCP), the precursor mass (molar ratio) can be significantly more than the radiometal mass. This strategy is more practical and suitable for routine manufacture of therapeutic radiopharmaceuticals.
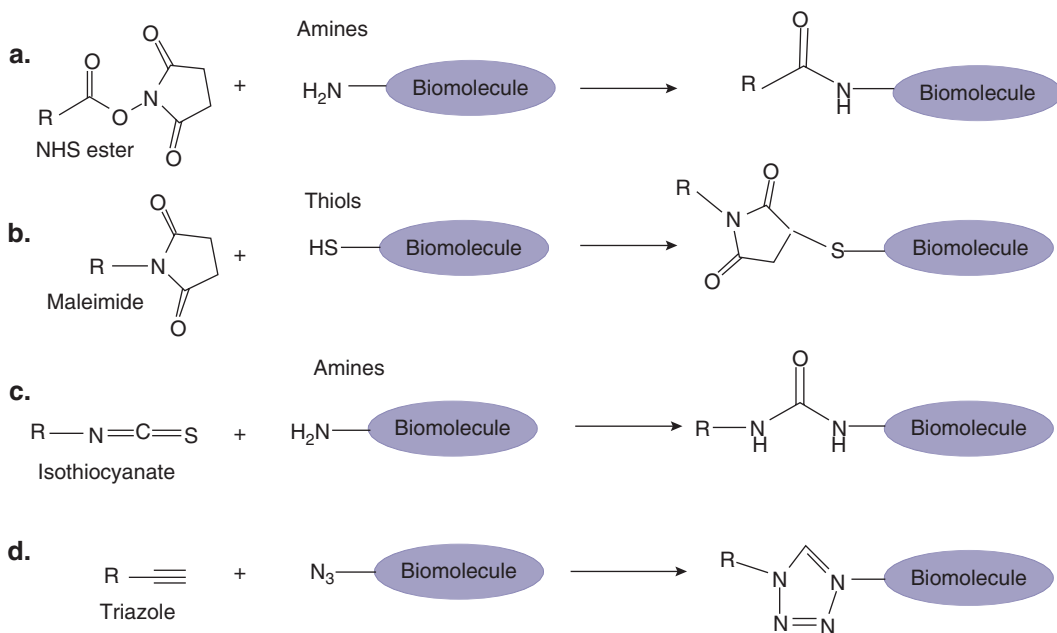
Fig. 18.11 Conjugation reactions commonly used for the covalent attachment of BFCA (R) to a targeting biomolecule with the formation of an amide (**a**), thioether (**b**), thiourea (**c**), and triazole bond (**d**)

Coupling of the biomolecule or the targeting vector to the BFC often relies on nucleophilic attack from the bioconjugate. Electrophiles, such as anhydrides, bromo- or iodoacetamides, isothiocyanates, N-hydroxysuccinimide (NHS) esters, carboxylic acid active esters, and maleimides, are typical groups for conjugation that have been developed to modify biomolecules with the appropriate BFCAs. Primary amines are reactive towards isothiocyanates and active esters, while maleimide is reactive towards thiols [37]. The use of copper mediated "click-chemistry" and Diels–Alder coupling have also been utilized in the preparation of radiometal complexes of biomolecules. Some of the most important and routinely used strategies for conjugating BFC to a biomolecule are summarized in Fig. 18.11.

The activation of a carboxylate group of the BFC via an active ester, which reacts with a primary amine of the biomolecule (sidechain of a lysine residue or N-terminal amine of a peptide) leads to a peptide bond that is highly stable under physiological conditions. An example of the activation of the carboxylate is the formation of N-hydroxysuccinimide (NHS) ester.

Isothiocyanates are reactive to amines as well. They may be formed from nitro groups and react in aqueous solutions at pH 9–9.5 with primary amines to form thiourea bonds. This reaction restricts this method to biomolecules that are not sensitive to alkaline conditions. Maleimides react selectively with the thiol groups (from cysteine) in the biomolecules and form a thioether bond with the BFC. The pH for this reaction is close to 7 so that this reaction is ideal for biomolecules. Anhydrides of the BFC react with primary amines of the biomolecules. The dianhydride of DTPA might react with the biomolecule to form a DTPA-monoamide as well as a DTPA-bisamide and cross-linkage of two biomolecules may occur. To avoid cross-linkage, asymmetric anhydrides of DTPA and DOTA have been developed and used.

18.4.3 Alkaline Earth Metals

The two important therapeutic radionuclides ^{89}Sr and ^{223}Ra belong to the family of alkaline earth metals (like calcium) and have similar properties.

They both have their outer s-orbital with its full complement of two electrons, which these two metals readily lose to form cations with charge $^{+2}$, and an oxidation state of $^{+2}$. These two metals readily react with halogens to form ionic halides, such as $SrCl_2$ and $RaCl_2$. They also react with oxygen to form oxides.

Metastron™ (Strontium-89 Chloride Injection) is indicated for the relief of bone pain in patients with painful skeletal metastases. It is a sterile, non-pyrogenic, aqueous solution of ^{89}Sr chloride (10.9–22.6 mg/mL) for intravenous administration. The radioactive concentration is 37 MBq/mL, and the SA is 2.96–6.17 MBq/mg at calibration. The pH of the solution is 4.0–7.5.

Xofigo® also known as Alpharadin is ^{223}Ra dichloride supplied as a clear, colorless, isotonic, and sterile solution to be administered intravenously with pH between 6 and 8. It is indicated for the treatment of patients with castration-resistant prostate cancer, symptomatic bone metastases, and no known visceral metastatic disease. Each mL of solution contains 1 MBq (27 microcurie), corresponding to 0.53 ng ^{223}Ra, at the reference date. ^{223}Ra is present in the solution as a free divalent cation. Each vial contains 6 mL of solution (6 MBq (162 µCi) ^{223}Ra dichloride at the reference date. SA is 1.9 MBq (51.4 µCi)/ng.

18.4.4 Transition Metals

The definition of a transition metal according to IUPAC is "an element whose atom has a partially filled d sub-shell, or which can give rise to cations with an incomplete d sub-shell." Based on this definition, Sc and Y are not transition metals. However, it is also generally accepted that "transition metal" is any element in the d-block of the periodic table, which includes groups 3–12 (Fig. 18.2), or any element that can participate in the formation of chemical bonds with the valence electrons in two shells instead of only one. For the current discussion, the therapeutic radiometals, ^{47}Sc, ^{90}Y, ^{67}Cu, and ^{186}Re, will be regarded as transition metals. These four metals form compounds in many oxidation states and can be bound to a variety of ligands,

and chelates, allowing for a wide variety of transition metal complexes.

Scandium is the smallest of the rare-earth metals, with an ionic radius of 75–87 pm. Scandium readily loses 3 electrons in the outer shells (d^1s^2) and is found almost exclusively as a trivalent cation (Sc^{3+}) with the high coordination preference (CN = 6–8) and ionic bonding tendency (I_A = 10.49). It begins to hydrolyze at pH 2.5 and precipitation of $Sc(OH)_3$ occurs at pH 7–11 [1]. Sc^{3+} has a high preference for hard donating groups and favors a coordination number of eight, even in its hydrated form. DOTA is widely used for scandium-based radiopharmaceuticals. The high stability (log K_{ML} = 27.0–30.8) and pM value (23.9–26.5) support the use of DOTA analogs for the majority of Sc^{3+} based radiopharmaceuticals [39].

Yttrium, like Sc, also loses the outer 3 electrons and is predominantly found as a trivalent cation (Y^{3+}). The ionic radius of yttrium cation (90–108 pm) closely resembles that of lanthanides and prefers coordination number of 8 or 9 [1]. Most of Y radiotracers were developed using either DOTA or CHX-A''-DTPA for chelation. These chelates quantitatively radiolabel yttrium radionuclides at low concentrations and show kinetic stability under physiological conditions [40]. With the acyclic DTPA analogs, the stereochemistry of CHX-DTPA was shown to be of major importance, with markedly higher kinetic stability observed with CHX-A''-DTPA, compared to CHX-B''-DTPA. H_4octapa, an octadentate analogue of H_2dedpa based around a picolinic acid scaffold, also demonstrated high radiolabeling yields and serum stability [41].

Copper exhibits a rich coordination chemistry with complexes known in oxidation states ranging from 0 to +4, although the +2 (cupric) and the +1 (cuprous) oxidation states are by far the most common. Cu^{2+} and Cu^+ oxidation states favor dissimilar ligand donors and coordination geometry. The electron configuration and chemical hardness of Cu^{2+} (d^9) dictates a preference for borderline hard Lewis base donors, such as aliphatic and aromatic amines, as well as carboxylate donors; however, Cu^{2+} can also accommodate softer donors such, as thiolate and carbazone [2].

Cu^{2+} can accommodate a variety of coordination numbers and geometries, including square planar, square pyramidal, trigonal bipyramidal, and octahedral. In vivo under hypoxic conditions, Cu^{2+}, however, can be reduced to Cu^+ oxidation state causing instability of Cu^{2+} coordination complexes. In contrast, Cu^+ (d^{10}) exhibits a preference for soft donors (thiol, thio-ether, and imidazole) and a tetrahedral geometry.

The two well well-known ^{62}Cu-based PET imaging agents are both small metal complexes of acyclic chelator, thiosemicarbazone; ^{62}Cu-diacetyl-bis(N4-thiosemi-carbazone or ^{62}Cu-PTSM and Cu-diacetyl-bis(N4-methylthiosemicarbazone) or Cu-ATSM. In both cases, a Cu^{2+} center is coordinated in a square planar geometry by the two nitrogen atoms and two sulfur atoms of the thiosemicarbazone. Under reducing, oxygen-deficient conditions, the reduced Cu^+ species dissociates from the chelator and binds to intracellular proteins [42]. This approach may provide a simple and direct method to develop copper-based small molecule radiopharmaceuticals.

For the development of kinetically inert copper complexes, the chelators must provide a rigid coordination environment that disfavors fluxional changes of the coordination environment, and the Cu^{2+} radiolabeled complex must be resistant to reduction under physiological conditions. For several decades, most of the chelator development has focused on polyaza macrocyclic BFCs such as DOTA, NOTA, TETA, TE2A complexes. While DOTA complex have shown clinical utility, the Copper complexes of TETA and TE2A exhibit greater thermodynamic stability and kinetic inertness [2, 43]. Recently, in 2020, the FDA approved ^{64}Cu-DOTATATE for PET imaging studies in patients with SSTR positive NETs. To improve greater structural rigidity, the cross-bridged chelators, such as CB-TE2A, were developed. While these chelators have kinetic stability, they still require higher temperatures for quantitative labeling [44]. The sarcophagine family of chelators based on hexaazamacrobicyclic cage were also investigated to develop copper-labeled radiopharmaceuticals [45, 46]. The Sar, DiamSar, and SarAr chelators coordinate copper extremely quickly over a pH range

of 4.0–9.0, and have shown superior performance, including quantitative radiolabeling at room temperature and excellent in vitro and in vivo stability [47, 48]. NOTA and NOTA type derivatives also showed fast complexation at room temperature, and high kinetic inertness in vivo [49].

Rhenium is the third-row congener of transition metal elements in Group-7, after manganese and technetium. Like Tc, Re with an outer electron configuration of d^5s^2 has a rich chemistry, with oxidation states ranging from -1 to $+7$ and coordination numbers up to nine. Rhenium can complex with a variety of ligands and BFCs [2, 50, 51]. The radiochemistry of $^{186/188}Re$ isotopes starts with the chemically stable perrhenate anion (ReO_4^-). Generally, the chemistry of Re is similar to that of Tc but, some important differences do exist between the two elements. Perrhenate has a considerably higher reduction potential than pertechnetate (-0.361 V versus -0.548 V, respectively). Generally, rhenium complexes are harder to reduce and easier to oxidize. Also, it is sometimes necessary to use different donor atoms to improve the redox stability of Re complexes in lower oxidation states.

The Re(V) mono-oxo-core $[ReO]^{3+}$ has been evaluated as a means of direct attachment to amino acid side chains of antibodies and peptides containing cysteine-thiol groups, often generated by reduction of disulfide bonds. Rhenium(V) complexes are primarily square-pyramidal with an oxo group at the apex and a mixture of amine, and sulfur donor atoms forming the base of the pyramid with the S donors included to improve the stability of the 5+ oxidation state [2]. One of the first Re(V) complexes evaluated for tumor imaging was the pentavalent $[^{186/188}Re$-O-$(DMSA)_2]^-$. The DMSA ligand exists in 2 isomers, racemic and meso forms, and the racemic isomer shows greater tumor uptake than the meso isomer [52]. ^{188}Re-O-DMSA-dianhydride, a BFC was also developed to enable coupling to antibodies and peptides. Since 6-hydrazinonicotinamide (HYNIC) BFC was not ideal to develop ^{188}Re labeled biomolecules, variants of HYNIC have been prepared by appending thioamide functional groups to HYNIC to form pyridylthiosemicarbazide ligand (SHYNIC) that

can form well-defined, very stable complexes with $[ReO]^{3+}$ core, while retaining the bioconjugation capability with biomolecules [53]. The Re(V) dioxo core $[ReO_2]^+$ within a tetraamine ligand set, provided by two ethylene diamine ligands or one linear or cyclic tetramine, has the potential to prepare bioconjugates with high stability. The 1,4,7,10-tetraazaundecane Re dioxo-complex can be used to conjugate biomolecules that are stable in physiological conditions [50].

Re(I), the $[Re(CO)3]^+$ core can be a versatile radiolabeling synthon for coupling to a range of chelators conjugated to targeting biomolecules, and also for direct labelling of proteins. The histidine, cysteine, or methionine residues in the biomolecule will help improve the binding of tricarbonyl core. A more targeted approach is to use synthetic, usually tridentate, BFCs to the tricarbonyl fragment to biomolecules. The most common is dipyridylamine (DPA) but, aliphatic amines and carboxylates can also be used [2]. $^{188}Re(CO)_3$-dipicolylamine-alendronate, a therapeutic agent for bone pain palliation, showed higher bone uptake than ^{188}Re-HEDP and higher stability with respect to oxidation compared to ^{188}Re perrhenate anion [54]. Based on DPA chelator, and the Re tricarbonyl core, the single amino-acid chelators" (SAACs) were developed, where the carboxylate moiety on the DPA ligand can serve as a linker to a wide range of biological vectors. DPA-SAAC was used for indirect labeling of ^{188}Re to IgG via an amide bond between the carboxylate moiety of the chelator and a free amine of the protein [55].

18.4.5 Post-Transition Metals

Among the post-transition metals shown in Table 18.6, the chemistry of gallium and indium are discussed in Chap. 12 since the radioisotopes of Ga and In are used only to develop radiopharmaceuticals for imaging. Radionuclides of lead (^{212}Pb) and bismuth (^{212}Bi and ^{213}Bi) are used for therapy. All the metals in this category are p-block elements since the p-orbital electrons participate in the formation of chemical bonds.

For radioisotopes of lead, the valence electron configuration is $6s^2, 6p^2$. For group-14 elements, the common oxidation date is +4 but, lead shows two oxidation states +4 and + 2, and the divalent state is more important [56]. There is a relatively large difference in the electronegativity of lead(II) at 1.87 and lead(IV) at 2.33. The two macrocyclic chelators DOTA and TCMC have been successfully used to form conjugates for labeling with ^{212}Pb. The TCMC chelate was specifically developed for chelating Pb(II) radionuclide, although DOTA is also known to form strong complexes with both lead and bismuth [57]. However, following the β^- decay of ^{212}Pb, a significant amount of the daughter ^{212}Bi is released from the macrocyclic cage resulting in distribution of free ^{212}Bi species to bone and other tissues. The structure of the Pb(II)-TCMC complex revealed that Pb(II) is fully encapsulated by the TCMC with the eight-coordinate sphere saturated by the four-ring nitrogen and four amide oxygen atoms, supporting this complex as more appropriate to develop therapeutic biomolecules with ^{212}Pb [58]. Recently pyridine-based DOTA derivative chelators also exhibited the ability to form stable complexes with $^{203/212}$Pb radionuclides [59].

Bismuth is a group 15 element with an outermost electron configuration of $6s^2 6p^3$. Due to the inert pair effect (the S^2 electrons remain unshared), Bi is most commonly found as a trivalent cation (Bi^{3+}) and + 3 is the most stable oxidation state. At low pH, Bi(III) readily undergoes hydrolysis to form Bi hydroxide, and weakly coordinating buffers, such as citrate or acetate, are used to prevent hydrolysis at typical labeling pH of 3–5 [1]. With an ionic radius of 96–117 *pm*, the most stable coordination complexes are octadentate. As a borderline metal ion, Bi has significant affinity for nitrogen and oxygen atoms, and complexation with amine donor groups is possible even at low pH [60].

Regarding the selection of BFCs for Bi^{3+}, the acyclic chelators, DTPA (Log K_{ML} = 33.9–35.2) and CHX-A''-DTPA (Log K_{ML} = 34.9–35.6) show very high thermodynamic stability. The $^{212/213}$Bi-DTPA complexes revealed inadequate kinetic inertness resulting in the kidney accumulation of free Bi

radioactivity during in vivo studies. In contrast, $^{212/213}$Bi-CHX-A"-DTPA complex has shown significantly improved kinetic inertness partially since the cyclohexyl moiety of CHX-A"-DTPA provides the chelator with additional rigidity and imposes a significant degree of preorganization on the metal ion binding site. Another potential acyclic chelator for Bi^{3+} cation is the inherently bifunctional picolinic acid-based scaffold, H4neunpa, which showed lower stability (log K_{ML} = 28.8) than that of DOTA, and DTPA but, the kinetic inertness is the same as DOTA (pM = 27) [61].

Among the macrocyclic chelators, both DOTA and Me-DO2PA showed high thermodynamic stability and kinetic inertness [60]. ^{213}Bi-DOTA complex (Log K_{ML} = 30.3; P_M = 27.0) and ^{213}Bi-Me-DO2PA complex (Log K_{ML} = 34.2; P_M = 28.6) have high kinetic stability. These complexes, however, may require labeling at higher temperatures and are not optimal for antibody labeling. NETA and DEPA chelators with macrocyclic backbone and a flexible acyclic tridentate iminodiacetic acid pendant arm are also good chelators for trivalent bismuth. ^{213}Bi-3p-C-NETA-trastuzumab and ^{213}Bi-3p-C-DEPA-trastuzumab complexes showed faster labeling kinetics and kinetic inertness compared to ^{213}Bi-DOTA complex [62, 63].

18.4.6 Lanthanides

The lanthanide series of chemical elements comprises 15 metals with atomic numbers lanthanum (Z = 57) to lutetium (Z = 71). All are f-block elements, except lutetium, which is regarded as a d-block element. Due to lanthanide contraction (due to poor shielding of 5 s and 5p electrons by the 4f electrons), the ionic radius decreases steadily from Ln^{3+} (103 pm) to Lu^{3+} (86.1 pm). All the lanthanide elements exhibit the oxidation state +3 due to the loss of two 6 s electrons and one 4f electron. The trivalent ions are hard acceptors and form more stable and stronger complexes (coordination numbers of 8–9) with oxygen-donor ligands than with nitrogen-donor ligands of chelating agents, such as DOTA. Among the lanthanides, the radionuclides

of samarium, terbium, holmium, and lutetium are important in the development of therapeutic radiopharmaceuticals. ^{153}Sm and ^{166}Ho form strong complexes with diphosphonates (such as EDTMP) and are used for bone pain palliation. The decay characteristics of these two metals are appropriate for developing therapeutic agents but, due to suboptimal specific activity, they have not been used for targeted therapy.

Terbium radioisotopes (^{149}Tb, ^{161}Tb ^{155}Tb, and ^{152}Tb) are of interest due to the existence of several clinically relevant radioisotopes with applications for both molecular imaging and targeted therapy. ^{149}Tb is an ideal theranostic nuclide since it decays by both α and positron decay modes. Terbium is most commonly found as a trivalent cation (Tb^{3+}), has an ionic radius of 0.92–1.10 Å, and favors a coordination number of 8 or 9. Tb^{3+} exhibits a preference for oxygen-based bonding, dominated by electrostatic interactions (IA = 10.07–10.30) [64]. The macrocyclic chelator DOTA forms thermodynamically stable complexes with Tb3$^+$ cations (log K_{ML} = 23.6–27.0) and can achieve quantitative radiolabeling at low concentrations but, does require elevated temperatures. Among the acyclic chelators, CHX-A"-DTPA is most favored due to radiolabeling capability (log K_{ML}, 22.8) at ambient temperatures needed for heat-sensitive targeting vectors [1].

Lutetium was independently discovered in 1907 by the French scientist Georges Urbain, an Austrian mineralogist, and an American chemist Charles James. ^{177}Lu ($T\frac{1}{2}$ = 6.7 days) is the ideal β^- radionuclide for theranostics, since it also emits γ-photons of 208 keV (11%) and 113 keV (6.4%), which are used for diagnostic evaluation and dosimetry. ^{177}Lu is generally seen as superior to both ^{131}I and ^{90}Y for targeted therapy [17, 65]. ^{177}Lu-Dotatate (Lutathera) was the first radiolabeled peptide to receive FDA approval for treatment of somatostatin receptor-positive neuroendocrine tumors.

Lutetium is most commonly found as a trivalent cation (Lu3+) and is the smallest of the lanthanide series with an ionic radius of 0.86–1.03 (CN = 6–9). Lutetium(III) prefers a coordination number between 8 and 9, with a slight preference for 8, as is common with the late lanthanides [64]. DOTA and DTPA are the most
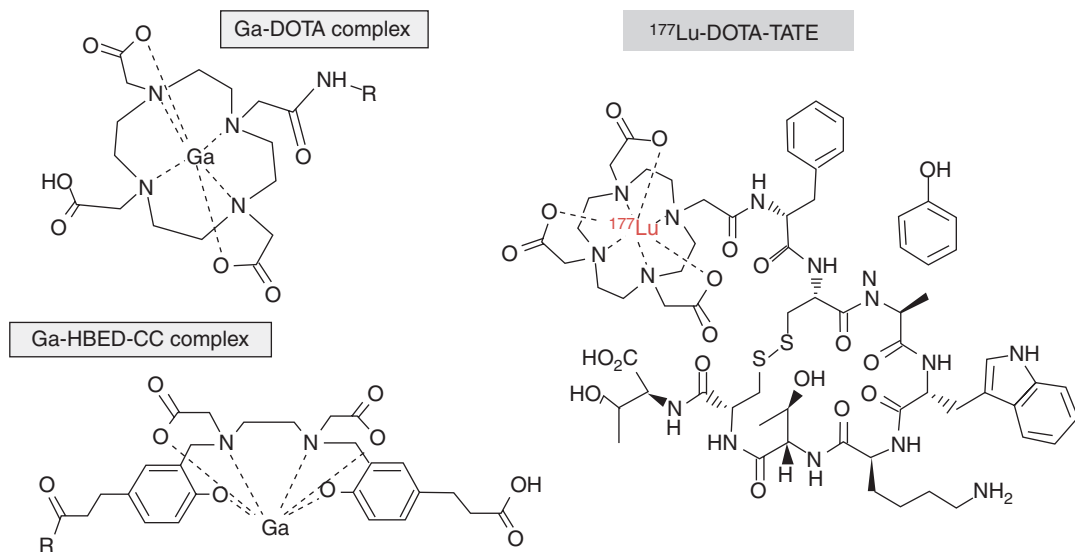
Fig. 18.12 The chemical structures of ^{177}Lu-dotatate and ^{68}Ga-DOTA complex are based on macrocyclic chelator DOTA. For ^{68}Ga, the acyclic chelator HBED-CC was used to synthesize ^{68}Ga-PSMA-11

commonly used chelators for ^{177}Lu radiotracers. The molecular structure of [Lu(DOTA)(H₂O)]⁻ demonstrates water-capped square antiprismatic geometry with high stability and inertness of ^{177}Lu-DOTA complex (Log K_{ML} = 21.6–29.2) [1]. With DOTA-conjugated peptides and small molecules, labeling at higher temperature (~90 °C) is critical to get high labeling yields. With heat-sensitive bioconjugates (such as antibodies), longer incubation times at 37 °C are required. Acyclic chelators such as DTPA analog (CHX-A"-DTPA) may provide rapid labeling at room temperature. Several chelators (such as NOTA, PCTA, H4octapa) were investigated as an alternative to DOTA but, DOTA-conjugated ^{177}Lu complexes have been studies extensively in patients. ^{177}Lu-Dotatate (Fig. 18.12) has been FDA approved, while ^{177}Lu-PSMA-617 finished phase III clinical trial and is under regulatory review.

18.4.7 Actinides

Actinium and thorium are the two important actinides for developing therapeutic radiopharmaceuticals. There is no stable actinium in nature. Actinium ([227]Ac, $T_{1/2}$ = 21.7 years) from the Greek

actinos meaning ray, was discovered by André-Louis Debierne (1899) in leftovers of uranium ore. It was also discovered independently in 1902 by a German Chemist Friedrich Oskar Giesel [66]. Among the isotopes of actinium, [225]Ac has become one of the most important alpha emitters for the development of therapeutic radiopharmaceuticals because it preferentially exists in the oxidation state +3 and forms relatively stable complexes with DOTA chelator, like the other trivalent metals such as ^{177}Lu and ^{90}Y and [68]Ga. Several [225]Ac-DOTA-labeled antibodies and peptides ([225]Ac-HuM195 mAb, [225]Ac-huJ591 mAb, and [225]Ac-PSMA-617) are in clinical trials. Large 18-membered macrocycles with 6 donor atoms (N or O) have been used to ease the steric constraints for large metal ions (such as [225]Ac) and to increase the coordination number [67]. Among these chelates, Macropa, HEHA, and Crown (Fig. 18.9) showed good labeling and high stability. Also, the labeling with these ligands is usually performed at room temperature within a few minutes [68–70]. Acyclic chelates (such as Py4pa) with picolinic acid moieties have demonstrated a high Ac labeling yield at low chelate concentrations and good in vivo stability [67]. The coordination number may vary between 8 and 9, depending on the chelate used and the number of donor atoms partici-

pating in the chelation. Detection of [225]Ac is challenging since it has ~1% γ-emission. The γ photons from the daughters [221]Fr ($T\frac{1}{2}$ = 4.8 min, 218 keV) and [213]Bi ($T\frac{1}{2}$ = 46 min, 440 keV) are commonly used when the parent and daughters reach secular equilibrium.

Thorium occurs in nature and was discovered in 1832 from the mineral rock thorite. Despite the fact that thorium preferentially exists in the oxidation state +4, it can possess different coordination numbers determined by the concrete chelating ligand [71]. [227]Th is the most promising for alpha therapy and the decay scheme is relatively similar to the one of [225]Ac; however, the half-life is almost doubled (18 days). [227]Th decays to [223]Ra, an alpha emitter with longer half-life (11.4 days). The dose-limiting side effect of [227]Th is mainly due to [223]Ra because free radium is taken up by the bone and [223]Ra and its daughters deposit energy in the vicinity of bone [71].

Thorium (4+) coordination chemistry is similar to that of zirconium (4+). At pH >7, thorium forms various water-insoluble oxides and, thus, precipitates out of a solution. Thorium is known as an oxophilic metal and prefers oxygen donors for metal coordination [70]. Thus, the use of DOTA as chelator is suboptimal. Despite the poor radiolabeling kinetics, the [227]Th-DOTA complex retains good stability in vivo (75), enabling its use for various TAT applications [72]. The Me-3,2-HOPO chelator with eight available oxygen donors for coordination provides extremely high stability constant with thorium. Labeling with this chelator is usually performed at room temperature within 1 h. Detailed analytic studies on Th^{4+} chelation with this ligand revealed that it possesses a large (~20 orders of magnitude) thermodynamic selectivity for +4 over +3 ions, and in vivo +3 ions such as Fe^{3+} cannot effectively displace the actinide. Me-3,2-HOPO chelate is regarded as the current gold standard for [227]Th chelation [67]. Since the chemistry of thorium mimics the chemistry of zirconium, [89]Zr a positron emitting radionuclide could be used as a theranostic analog for [227]Th labeled therapeutic radiopharmaceuticals.

References

1. Kostelnik TI and Orvig C. Radioactive Main Group and Rare Earth Metals for Imaging and Therapy. Chem Rev Chem Rev. 2019;119(2):902–56.

2. Boros E, Packard AB. Radioactive transition metals for imaging and therapy. Chem Rev. 2019;119(2):870–901.

3. Nelson BJB, Andersson JD, Wuest F. Targeted alpha therapy: Progress in radionuclide production, radiochemistry, and applications. Pharmaceutics. 2021;13:49. https://doi.org/10.3390/pharmaceutics13010049.

4. Kabalka GW, Mereddy AR. A facile no-carrier-added radioiodination procedure suitable for radiolabeling kits. Nucl Med Biol. 2004;31:935–38

5. Eersels JLH, Travis MJ, Herscheid JDM. Manufacturing I-123-labeled radiopharmaceuticals: Pitfalls and solutions. J Label Compd Radiopharm. 2005;48:241–57

6. Dubost E, McErlain H, Babin V. Recent Advances in Synthetic Methods for Radioiodination. J Org Chem. 2020;85:8300–10

7. Mushtaq S, Jeon J, Shaheen A, et al. Critical analysis of radioiodination techniques for micro and macro-organic molecules. J Radioanal Nucl Chem. 2016;309(2):859–89.

8. Mangner TJ, Jl W, Wieland DM. Solid-phase exchange radioiodination of aryl iodides. Facilitation by ammonium sulfate. J Org Chem. 1982;47(8):1484–8.

9. Baldwin RM, Zea-Ponce Y, Zoghbi SS, et al. Evaluation of the monoamine uptake site ligand [^{123}I] methyl 3β-(4-Iodophenyl)-Tropane-2β-carboxylate ([^{123}I]β-CIT) in non-human primates: pharmacokinetics, biodistribution and SPECT brain imaging coregistered with MRI. Nucl Med Biol. 1993;20(5):597–606.

10. Greenwood FC, Hunter WM, Glover JS. The preparation of 131I-labeled human growth hormone of high specific radioactivity. Biochem J. 1963;89:114–23

11. Bolton AE, Hunter WM. The labeling of proteins to high specific radioactivities by conjugation to a I-125 containing acylating agent. Biochem J. 1973;133:529–39.

12. Richardson AP, Mountford PJ, Baird AC, et al. An improved iodogen method of labeling antibodies with 123I. Nucl Med Commun. 1986;7:355–62

13. David GS, Reisfeld RA. Protein iodination with solid state lactoperoxidase. Biochemistry. 1974;13(5):1014–21.

14. Mertens J, Gysemans M. Cu(1+) assisted nucleophilic exchange, application and mechanistic approach. In: Emram AM (ed) New trends in radiopharmaceutical synthesis, quality assurance, and regulatory control. Plenum, New York. 1991.

15. Kaminski MS, Zasadny KR, Francis IR, et al. Radioimmunotherapy of B-cell lymphoma with [^{131}I]anti-B1 (anti-CD20) antibody. N Engl J Med. 1993;329(7):459–65.

16. Press OW, Eary JF, Appelbaum FR, et al. Radiolabeled-antibody therapy o B-cell lymphoma

with autologous bone marrow support. N Engl J Med. 1993;329:1219–24.

17. Vallabhajosula S, Nikolopoulou A. Radioiodinated metaiodobenzylguanidine (MIBG): radiochemistry, biology, and pharmacology. Semin Nucl Med. 2011;41:323–88.

18. Barrett JA, Joyal JL, Hillier SM, et al. Comparison of high-specific-activity Ultratrace[123/131]I-MIBG and carrier added [123/131]I-MIBG on efficacy, pharmacokinetics, and tissue distribution. Cancer Biother Radiopharm. 2010;25:299–308.

19. Corson DR, Mackenzie KR, Segre E. Astatine—the element of atomic number-85. Nature. 1947;159:24.

20. Lindegren S, Albertsson P, Back T, et al. Realizing clinical trials with astatine-211: the chemistry infrastructure. Cancer Biother Radiopharm. 2020;35(6):425–36.

21. Guérard F, Gestin J-F, Brechbiel MW. Production of [211At]-astatinated radiopharmaceuticals and applications in targeted α-particle therapy. Cancer Biother Radiopharm. 2013;28(1):1–20.

22. Dekempeneer Y, Back T, Aneheim E, et al. Labeling of anti-HER2 nanobodies with astatine-211: optimization and the effect of different coupling reagents on their in vivo behavior. Mol Pharm. 2019;16(8):3524–33.

23. Ogawa K, Takeda T, Mishiro K, et al. Radiotheranostics coupled between an at-211-labeled RGD peptide and the corresponding radioiodine-labeled RGD peptide. ACS Omega. 2019;4:4584–91.

24. Vaidyanathan G, Affleck DJ, Alston KL, et al. A kit method for the high level synthesis of [211At] MABG. Bioorg Med Chem. 2007;15(10):3430–6.

25. Guérard F, Maingueneau C, Liu L, et al. Advances in the chemistry of astatine and implications for the development of radiopharmaceuticals. Acc Chem Res. 2021;54(16):3264–75.

26. Wilbur DS, Chyan MK, Hamlin DK, et al. Reagents for astatination of biomolecules. 3. Comparison of closodecaborate(2-) and closo-dodecaborate(2-) moieties as reactive groups for labeling with astatine-211. Bioconjug Chem. 2009;20:591–602.

27. Stetter H, Wolfram F. Complex formation with tetraazacycloalkane-N,N',N'',N'''-tetraacetic acids as a function of ring size. Angew Chem Int Ed Engl. 1976;15(11):686. https://doi.org/10.1002/anie.197606861.

28. Meares CF. Goodwin DA. Linking radiometals to proteins with bifunctional chelating agents. J Protein Chem. 1984;3:215–28

29. Baranyai Z, Tircsó G, Rösch F. The use of the macrocyclic Chelator DOTA in radiochemical separations. Eur J Inorg Chem. 2020;2020:36–56.

30. Kodama M, Koike T, Mahatma AB, Kimura E. Thermodynamic and kinetic studies of lanthanide complexes of 1,4,7,10,13-pentaazacyclopentadecane-N,N',N'',N''',N''''-pentaacetic acid and 1,4,7,10,13,16-hexaazacyclooctadecane-N,N',N'',N''',N'''',N'''''-hexaacetic acid. Inorg Chem. 1991;30(6):1270–3.

31. Brunner UK, Renn O, Ki M, et al. Radiometals and their chelates. In: Wagner Jr HN, Szabo Z, Buchanan JW, editors. Principles of nuclear medicine. Philadelphia, PA: WB Saunders; 1995.

32. Sundberg MW, Meares CF, Goodwin DA, Diamanti CI. Selective binding of metal ions to macromolecules using bifunctional analogs of EDTA. J Med Chem. 1974;17:1304–7.

33. Hnatowich DJ, Layne WW, Childs RL, et al. Radioactive labeling of antibody: a simple and efficient method. Science. 1983;220:613–5.

34. Krejcarek GE, Tucker KL. Covalent attachment of chelating groups to macromolecules. Biochem Biophys Res Commun. 1976;77:581–5.

35. Moi MK, DeNardo SJ, Meares CF. Stable bifunctional chelates of metals used in radiotherapy. Cancer Res. 1990;50:789s–93s.

36. Brechbiel MW. Bifunctional chelates for metal nuclides. Q J Nucl Med Mol Imaging. 2008;52(2):166–73.

37. Sarko D, Eisenhut M, Haberkorn U, Mier W. Bifunctional chelators in the design and application of radiopharmaceuticals for oncological diseases. Curr Med Chem. 2012;19:2667–88.

38. Price EW. Orvig C. Matching chelators to radiometals for radiopharmaceuticals. Chem Soc Rev. 2014;43:260

39. IAEA-TECDOC-1945. Therapeutic radiopharmaceuticals labeled with cu-67, re-186 and Sc-47. Vienna: International Atomic Energy Agency; 2021.

40. Chakravarty R, Chakraborty S, Dash A. A systematic comparative evaluation of ^{90}Y-labeled bifunctional chelators for their use in targeted therapy. J Label Compd Radiopharm. 2014;57:65–74.

41. Price EW, Edwards KJ, Carnazza KE, et al. A comparative evaluation of the chelators H4Octapa and CHX-A-DTPA with the therapeutic radiometal [90]Y. Nucl Med Biol. 2016;43:566–76.

42. Ling X, Cutler CS, Anderson CJ. The radiopharmaceutical chemistry of the radioisotopes of copper. In: Lewis JS, et al., editors. Radiopharmaceutical chemistry. Cham: Springer Nature; 2019. p. 335–57.

43. Kukis DL, Li M, Meares CF. Selectivity of antibody-chelate conjugates for binding copper in the presence of competing metals. Inorg Chem. 1993;32:3981–2.

44. Sun X, Wuest M, Weisman GR, et al. Radiolabeling and in vivo behavior of copper-64-labeled cross-bridged cyclam ligands. J Med Chem. 2002;45:469–77.

45. Di Bartolo NM, Sargeson AM, Donlevy TM, Smith SV. Synthesis of a new cage ligand, SarAr, and its complexation with selected transition metal ions for potential use in radio-imaging. J Chem Soc Dalton Trans. 2001;15:2303–9.

46. Boschi A, Martini P, Janevik-Ivanovska E, Duatti A. The emerging role of copper-64 radiopharmaceuticals as cancer theranostics. Drug Discov Today. 2018;23(8):1489–501.

47. Dearling JL, Voss SD, Dunning P, et al. Imaging cancer using PET– the effect of the bifunctional chelator

on the biodistribution of a ^{64}Cu-labeled antibody. Nucl Med Biol. 2011;38:29–38.

48. Smith SV. Sarar technology for the application of copper-64 in biology and materials science. Q J Nucl Med Mol Imaging. 2007;51:1–10.

49. De Silva RA, Jain S, Lears KA, et al. Copper-64 radiolabeling and biological evaluation of bifunctional chelators for radiopharmaceutical development. Nucl Med Biol. 2012;39:1099–104.

50. Blower PJ. Rhenium-188 radiochemistry: challenges and prospects. Int J Nucl Med Res. 2017;2017:39–53.

51. Dilworth JR. Rhenium chemistry—then and now. Coord Chem Rev. 2021;436:213822.

52. Park J-Y, Lee T-S, Choi T-H, et al. A comparative study of [188]Re-(V)-meso-DMSA and [188]Re-(V)-rac-DMSA: preparation and in vivo evaluation in nude mice xenografted with a neuroendocrine tumor. Nucl Med Biol. 2007;34:1029–36.

53. North AJ, Karas JA, Ma MT, et al. Rhenium and technetium-oxo complexes with thioamide derivatives of pyridylhydrazine bifunctional chelators conjugated to the tumor targeting peptides octreotate and cyclic-RGDfK. Inorg Chem. 2017;56:9725–41.

54. Martin de Rosales RT, Finucane C, Foster J, et al. [188]Re(CO)3-dipicolylamine-alendronate: a new bisphosphonate conjugate for the radiotherapy of bone metastases. Bioconjug Chem. 2010;21:811–5.

55. Xia J, Long S, Yu J, et al. Pyridyl derivatives provide new pathways for labeling protein with fac-[[188]Re-(CO)3(H2O)3]+. J Radioanal Nucl Chem. 2009;281:493–500.

56. Baidoo KE, Milenic DE, Brechbiel MW. Methodology for labeling proteins and peptides with lead-212 ([212]Pb). Nucl Med Biol. 2013;40:592–9.

57. Chappell LL, Dadachova E, Milenic DE, et al. Synthesis, characterization, and evaluation of a novel bifunctional chelating agent for the lead isotope [203]Pb and [212]Pb. Nucl Med Biol. 2000;27:93–100.

58. Cuenot F, Meyer M, Espinosa E, et al. New insights into the complexation of lead(II) by 1,4,7,10-tetrakis(carbamoylmethyl)-1,4,7,10-tetraazacyclododecane (DOTAM): structural, thermodynamic, and kinetic studies. Eur J Inorg Chem. 2008;2008:267–83.

59. McNeil BL, Robertson AKH, Fu W, et al. Production, purification, and radiolabeling of the [203Pb/212]Pb theranostic pair. EJNMMI Radiopharm Chem. 2021;6(1):6.

60. Ahenkorah S Cassells I, Deroose CM, et al. Bismuth-213 for Targeted Radionuclide

Therapy: From Atom to Bedside. Pharmaceutics 2021;13(5):599.

61. Spreckelmeyer S, Ramogida CF, Rousseau J, et al. P-NO2-Bn-H4neunpa and H4neunpa-trastuzumab: bifunctional chelator for radiometal pharmaceuticals and ^{111}In immuno-single photon emission computed tomography imaging. Bioconjug Chem. 2017;28:2145–59.

62. Kang CS, Song HA, Milenic DE, et al. Preclinical evaluation of NETA-based bifunctional ligand for radioimmunotherapy applications using [212]Bi and [213]Bi: radiolabeling, serum stability, and biodistribution and tumor uptake studies. Nucl Med Biol. 2013;40:600–5.

63. Song HA, Kang CS, Baidoo KE, et al. Efficient bifunctional decadentate ligand 3p-C-DEPA for targeted α-radioimmunotherapy applications. Bioconjug Chem. 2011;22:1128–35.

64. Bunzli J-CG. Review: lanthanide coordination chemistry: from old concepts to coordination polymers. J Coord Chem. 2014;67:3706–33.

65. Vallabhajosula S, Harwig JF, Siemsen JK, et al. Radiogallium localization in tumors: blood binding and transport and the role of transferrin. J Nucl Med. 1980;21:650–6.

66. Kirby HW. The Discovery of Actinium. Isis 1971;62(3):290–308.

67. Yang H, Wilson JJ, Orvig C, et al. Harnessing a-emitting radionuclides for therapy: radiolabeling method review. J Nucl Med. 2022;63:5–13.

68. Deal KA, Davis IA, Mirzadeh S, et al. Improved in vivo stability of actinium-225 macrocyclic complexes. J Med Chem. 1999;42(15):2988–92.

69. Thiele NA, Brown V, Kelly JM, et al. An eighteen-membered macrocyclic ligand for actinium-225 targeted alpha therapy. Angew Chem Int Edit. 2017;56:14712–7.

70. Yang H, Zhang C, Yuan Z, et al. Synthesis and evaluation of a new macrocyclic actinium-225 chelator, quality control and in vivo evaluation of 225Ac-crownaMSH peptide. Chemistry. 2020;26:11435–40.

71. Roscher M, Bakos G, Benešová M. Atomic nanogenerators in targeted alpha therapies: Curie's legacy in modern cancer management. Pharmaceuticals. 2020;13:76. https://doi.org/10.3390/ph13040076.

72. Larsen RH, Borrebaek J, Dahle J, et al. Preparation of Th-227-labeled radioimmunoconjugates, assessment of serum stability and antigen binding ability. Cancer Biother Radiopharm. 2007;22:431–7.

The therapeutic approach of internally administered radiopharmaceuticals offers the potential to outmode the present approaches of conventional radiation therapy and chemotherapy because radiopharmaceuticals selectively irradiate target tissues internally often in only one radiation dose, noninvasively and nondramatically; also, the therapeutic use of radiopharmaceuticals has been followed by a lower incidence of leukemia, and other cancers, than have radiotherapy and chemotherapy. (William H. Beierwalters, M.D. *J Nucl Med* 22: 549–554, 1981)

19.1 Introduction

In 1890, antibodies were first described as a neutralizing substance found in blood, by Emil von Behring and Shibasabura Kitasato, who showed that the transfer of serum from animals immunized against diphtheria to animals suffering from it could cure the infected animals. Behring received the first Nobel Prize in medicine in 1901. In 1900, Paul Ehrlich was the first to propose a model for an antibody molecule in which the antibody was branched and consisted of multiple sites for binding to foreign material, known as antigen, and for the activation of the complement pathway [1]. This model agreed with the "lock and key" hypothesis for enzymes proposed by Emil Fischer. In 1908, Paul Ehrlich received the Nobel Prize in Medicine for his work on immunity.

In the 1950s, Frank Burnet and David Talmage developed the clonal selection theory, which states that a lymphocyte (specifically B cells) makes a single specific antibody molecule that is determined before it encounters an antigen [2]. In 1960, Frank Burnet received the Nobel Prize in Medicine for his work on acquired immunological tolerance. By 1959, Gerald Edelman and Rodney Porter independently published the molecular structure of antibodies [3, 4], for which they received the Nobel Prize in 1972. Polyclonal antibodies (pAbs) are a heterogeneous mixture produced by different B cell clones in the body that bind to many different epitopes of a single antigen. In contrast, mAbs are generated by identical B cells which are clones from a single parent cell. This means that the mAb binds to a single epitope and is monovalent. Georges Köhler and César Milstein invented the technology of producing mAbs and started the modern era of antibody-based pharmaceuticals. In 1986, Kohler and Milstein received the Nobel Prize in medicine for the discovery of hybridoma technique to produce mAbs [5].

In the 1990s, Tasuku Honjo discovered programmed death molecule-1 (PD-1) in apoptotic T cells, while James Allison discovered cytotoxic T lymphocyte-associated antigen-4 (CTLA-4) on T cells. Inhibition of these molecules by immune checkpoint inhibitors can successfully activate the immune system to fight cancer. Checkpoint inhibitors have brought about a breakthrough in

cancer immunotherapy. The 2018 Nobel Prize in Physiology or Medicine was awarded to Tasuku Honjo and James Allison for their discoveries in cancer immunology [6].

A century ago, Paul Ehrlich postulated the notion that a *magic bullet* could be developed to selectively target disease and he envisioned that an antibody could act as such [7]. The introduction of hybridoma technology for the mAb development turned this magic bullet concept into a reality. The first generations of mAbs were of murine origin and had limited clinical use; however, developments in recombinant DNA technology have resulted in the production of chimeric, humanized, and complete human mAbs.

In the pharmaceutical industry, biological products (biologics) represent one of the fastest growth sectors. Biologics include recombinant hormones and proteins, as well as cellular- and gene-based therapies. mAbs or antibody-drug conjugates (ADCs) represent the single most important branch of biologics. Around the world, more than 600 therapeutic mAbs have been studied in clinical trials, and more than 80 therapeutic mAbs have been approved by the United States Food and Drug Administration (US FDA) and European agencies, including 30 mAbs for the treatment of cancer (Table 19.1).

Table 19.1 Approved monoclonal antibodies in oncology[a]

No.	International non-proprietary name, US product identifier	Brand name	Target antigen	Format	Indication first approved or reviewed	First EU approval	First US approval
1	Rituximab	MabThera, Rituxan	CD20	Chimeric IgG1	Non-Hodgkin lymphoma	1998	1997
2	Trastuzumab	Herceptin	HER2	Humanized IgG1	Breast cancer	2000	1998
3	Ibritumomab tiuxetan	Zevalin	CD20	Murine IgG1	Non-Hodgkin lymphoma	2004	2002
4	Cetuximab	Erbitux	EGFR	Chimeric IgG1	Colorectal cancer	2004	2004
5	Bevacizumab	Avastin	VEGF	Humanized IgG1	Colorectal cancer	2005	2004
6	Panitumumab	Vectibix	EGFR	Human IgG2	Colorectal cancer	2007	2006
7	Ofatumumab	Arzerra	CD20	Human IgG1	Chronic lymphocytic leukemia	2010	2009
8	Ipilimumab	Yervoy	CTLA-4	Human IgG1	Metastatic melanoma	2011	2011
9	Pertuzumab	Perjeta	HER2	Humanized IgG1	Breast cancer	2013	2012
10	Obinutuzumab	Gazyva, Gazyvaro	CD20	Humanized IgG1 Glycoengineered	Chronic lymphocytic leukemia	2014	2013
11	Ramucirumab	Cyramza	VEGFR2	Human IgG1	Gastric cancer	2014	2014
12	Nivolumab	Opdivo	PD1	Human IgG4	Melanoma, non-small cell lung cancer	2015	2014
13	Pembrolizumab	Keytruda	PD1	Humanized IgG4	Melanoma	2015	2014
14	Blinatumomab	Blincyto	CD19, CD3	Murine bispecific tandem scFv	Acute lymphoblastic leukemia	2015	2014
15	Necitumumab	Portrazza	EGFR	Human IgG1	Non-small cell lung cancer	2015	2015
16	Dinutuximab	Qarziba; Unituxin	GD2	Chimeric IgG1	Neuroblastoma	2017; 2015#	2015
17	Daratumumab	Darzalex	CD38	Human IgG1	Multiple myeloma	2016	2015
18	Elotuzumab	Empliciti	SLAMF7	Humanized IgG1	Multiple myeloma	2016	2015
19	Atezolizumab	Tecentriq	PD-L1	Humanized IgG1	Bladder cancer	2017	2016
20	Avelumab	Bavencio	PD-L1	Human IgG1	Merkel cell carcinoma	2017	2017
21	Durvalumab	IMFINZI	PD-L1	Human IgG1	Bladder cancer	2018	2017
22	Cemiplimab, cemiplimab-rwlc	Libtayo	PD-1	Human mAb IgG4	Cutaneous squamous cell carcinoma	2019	2018

Table 19.1 (continued)

No.	International non-proprietary name, US product identifier	Brand name	Target antigen	Format	Indication first approved or reviewed	First EU approval	First US approval
23	Moxetumomab pasudotox, moxetumomab pasudotox-tdfk	Lumoxiti	CD22	Murine IgG1 dsFv immunotoxin	Hairy cell leukemia	**2021**	2018
24	Isatuximab, isatuximab-irfc	Sarclisa	CD38	Chimeric IgG1	Multiple myeloma	2020	2020
25	Tafasitamab, tafasitamab-cxix	Monjuvi, Minjuvi	CD19	Humanized IgG1	Diffuse large B-cell lymphoma	2021	2020
26	Naxitamab-gqgk	DANYELZA	GD2	Humanized IgG1	High-risk neuroblastoma and refractory osteomedullary disease	NA	2020
27	Margetuximab-cmkb	MARGENZA	HER2	Chimeric IgG1	HER2+ metastatic breast cancer	NA	2020
28	Tebentafusp, tebentafusp-tebn	KIMMTRAK®	gp100, CD3	Bispecific immunoconjugate	Metastatic uveal melanoma	In review	2022
29	Brentuximab vedotin	Adcetris	CD30	Chimeric IgG1; ADC	Hodgkin lymphoma, systemic anaplastic large cell lymphoma	2012	2011
30	Ado-trastuzumab emtansine	Kadcyla	HER2	Humanized IgG1; ADC	Breast cancer	2013	2012
Antibody drug conjugates (ADC)							
1	Inotuzumab ozogamicin	BESPONSA	CD22	Humanized IgG4; ADC	Acute lymphoblastic leukemia	2017	2017
2	Gemtuzumab ozogamicin	Mylotarg	CD33	Humanized IgG4; ADC	Acute myeloid leukemia	2018	2017; 2000[a]
3	Polatuzumab vedotin, polatuzumab vedotin-piiq	Polivy	CD79b	Humanized IgG1 ADC	Diffuse large B-cell lymphoma	2020	2019
4	Enfortumab vedotin, enfortumab vedotin-ejfv	Padcev	Nectin	Human IgG1 ADC	Urothelial cancer	Pending	2019
5	[fam-]trastuzumab deruxtecan, fam-trastuzumab deruxtecan-nxki	Enhertu	HER2	Humanized IgG1 ADC	HER2+ metastatic breast cancer	2021	2019
6	Belantamab mafodotin, belantamab mafodotin-blmf	BLENREP	B-cell maturation antigen	Humanized IgG1 ADC	Multiple myeloma	2020	2020
7	Sacituzumab govitecan; sacituzumab govitecan-hziy	TRODELVY	TROP-2	Humanized IgG1 ADC	Triple-neg. breast cancer	2021	2020
8	Loncastuximab tesirine, loncastuximab tesirine-lpyl	Zynlonta	CD19	Humanized IgG1 ADC	Diffuse large B-cell lymphoma	In review	2021
9	Tisotumab vedotin, tisotumab vedotin-tftv	TIVDAK	Tissue factor	Human IgG1 ADC	Cervical cancer	NA	2021

[a]Antibody therapeutics approved or under regulatory review in the EU or US—The Antibody Society

19.2   Antibody Structure and Function

Antibodies (Abs) are large glycoproteins that belong to the immunoglobulin (Ig) superfamily. The basic structure of Abs is composed of two heavy and two light chains in the shape of a Y (Fig. 19.1). At each tip of the Y lies the fragment antigen-binding (Fab) portion of the antibody which is responsible for recognition of the specific antigen. The fragment crystallizable (Fc) region located at the base of the Y structure is recognized by Fc receptors (FcRs) found on a wide range of immune cells. Based on the type of heavy chain, Abs can be separated into five distinct classes (*Isotypes*): IgA, IgD, IgE, IgG, and IgM, which can be further divided into one to four subclasses (such as IgG_1, IgG_2, IgG_3, and IgG_4). The IgG_1 isotype, however, is the most frequent form used in antibody therapy since IgGs interact with FCRs found on immune cells, such

as natural killer (NK) cells, as well as neutrophils, monocytes, dendritic cells, and eosinophils [9]. There is a significant difference between the IgG subclasses in terms of their half-lives in the blood (IgG_1, IgG_2, and IgG_4 approximately 21 days; IgG_3 approximately 7 days) and in terms of their capability to activate the classical complement pathway, and to bind Fc-receptors. The choice of an IgG subclass is a key factor in determining the efficacy of therapeutic mAbs. Most of the FDA approved mAbs belong to the IgG_1 subclass, which has a long half-life and triggers potent immune-effector functions, such as complement-dependent cytotoxicity (CDC), complement-dependent cell-mediated cytotoxicity (CDCC), and antibody-dependent cellular cytotoxicity (ADCC).

Antibodies are heavy proteins of about 10 nm in size with a molecular mass of ~150 kDa, arranged in three globular regions that roughly form a Y shape. Also, each IgG molecule con-

Fig. 19.1 (**a**) The fundamental structure of an intact, single immunoglobulin G (IgG) molecule has a pair of light chains and a pair of heavy chains. Light chains are composed of two separate regions [one variable region (V_L) and one constant region (C_L)], whereas heavy chains are composed of four regions (V_H, C_H1, C_H2 and C_H3). The complementarity-determining regions (CDRs) are found in the variable fragment (Fv) portion of the antigen-binding fragment (Fab). (**b**) Schematic overview of mAb humanization from murine antibodies (green domains) to fully human antibodies (blue domains) and associated suffixes. In the chimeric mAb, the variable regions are of murine origin, and the rest of the chains are of human origin. Humanized mAb only includes the hypervariable segments of murine origin. *CH:* domains of the constant region of the heavy chain; *CL:* constant domain of the light chain; *Fab and Fc* fragments resulting from proteolysis; *VH:* variable domain of the heavy chain; *VL:* variable domain of the light chain. [The figure on the right (**b**) was modified from [8]]

sists of four polypeptide chains; two identical *heavy chains* and two identical *light chains* connected by disulfide bonds. Each chain is made up of one to four domains; light chains consist of one variable domain V_L and one constant domain C_L, while heavy chains contain one variable domain V_H and three to four constant domains C_{H1}–CH_4. Each IgG has two Fabs, each containing one V_L, V_H, C_L, and C_{H1} domains, as well as the Fc fragment. The sub-region of each Fab fragment containing the variable regions (V_L and V_H) that binds to the antigen is referred to as F_V region and the existence of two identical antibody-binding sites (divalent) allows antibody molecules to bind strongly to multivalent antigen molecules.

The mouse hybridoma technology was initially used to produce murine monoclonal antibodies (Fig. 19.1b). These mouse-derived mAbs (*momab*) elicit an immune response resulting in the production of human-anti-mouse-antibodies (HAMAs) which interfere with therapeutic applications [10]. The antibody engineering technology identified regions that could be "humanized" without compromising the functionality of IgG molecule, resulting in chimeric antibodies (*ximab*) and "humanized" antibodies (*zumab*) and, finally, fully human antibody (*umab*) [11].

Chimeric mAbs are constructed with variable regions (V_L and V_H) derived from a murine source and constant regions derived from a human source. Humanized therapeutic mAbs are predominantly derived from a human source except for the complementarity-determining regions (CDRs), which are murine.

Antibodies are physically stable and experience a prolonged serum half-life resulting in an average half-life of several weeks, and accumulate in the liver, and kidney. Antibody engineering enabled the production of a wide variety of IgG derivatives (Fig. 19.2, Table 19.2) with significant differences in size (25–100 kDa) to improve pharmacokinetics, tumor localization, and antigen binding [12, 13]. Fab and Fab′ products are produced by enzymatic digestion of an IgG molecule, while the other derivatives are generated using genetic engineering of IgGs. Nanobodies are, specifically, engineered from a camelid antibody variant that contains only heavy chains. Single chains are formed by linking the variable light (V_L) and variable heavy (V_H) chains with an amino acid (AA) linker. Diabodies, triabodies, and even tetrabodies are formed spontaneously when smaller length AA chains are used to hold the V_H and V_L units together. Recombinant bispecific diabodies and
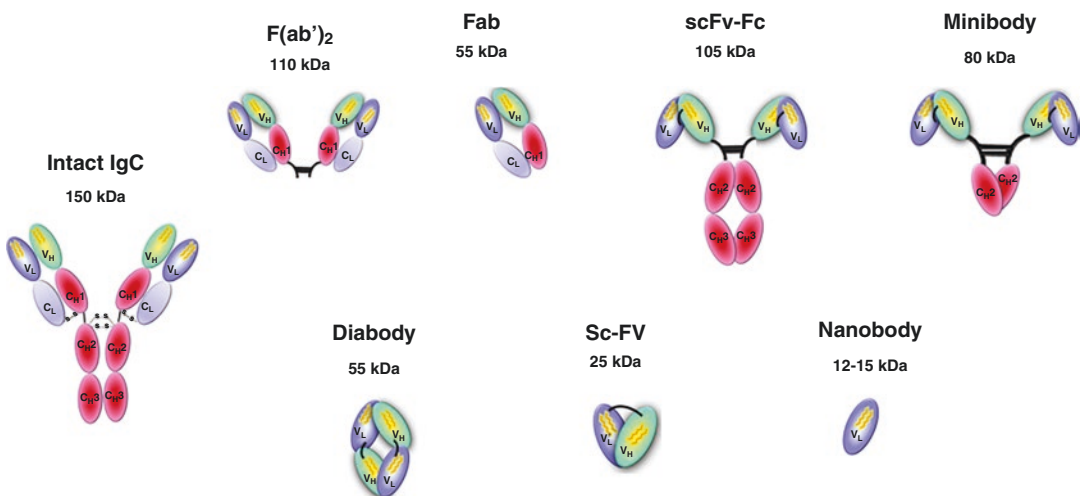
Fig. 19.2 Antibody fragments and derivatives of different sizes and molecular weights

other bispecific constructs can be prepared by pairing V_H and V_L of two antibodies with different specificities [13, 14].

19.2.1 Pharmacokinetics of Antibodies and Fragments

Intact mAbs have a long residence time in humans, ranging from a few days to weeks, which results in optimal tumor-to-nontumor ratios at 2–4 days post injection. In contrast, mAb fragments have a much faster blood clearance and, as a result, optimal tumor-to-nontumor ratios can be obtained at earlier time points; however, the absolute tumor uptake may be much lower compared to intact mAbs. The targeting properties of various antibody molecules of different sizes is compared in Table 19.2. In general, intact mAbs are preferable for therapy, while the optimal format for diagnosis is still under discussion.

Size is one factor that impacts the circulation time of Abs [15, 16]. A full IgG mAb is a large 150-kDa protein that can remain in circulation for 3–4 weeks while being metabolized slowly by the reticuloendothelial system. In contrast, a 25-kDa monovalent fragment (scFv) has a blood clearance time of <10 h with primarily renal excretion in 2–4 h. The Fv fragment, consisting only of the V_H and V_L domains, is the smallest immunoglobulin fragment available that carries the whole antigen-binding site. However, scFvs have never fared well in the clinic, despite their small size (25 kDa), because of their poor tumor retention. Molecules with molecular weights above >70 kDa (the glomerular filtration threshold) remain in circulation much longer than smaller more rapidly eliminated molecules. Recent protein engineering has been used to produce designer bispecific antibodies that are based on antibody Fv or scFv fragments as building blocks, rather than whole antibodies. One such fragment is the diabody, a dimer, each chain comprising two domains. Each chain consists of a V_H domain connected to a V_L domain using a linker too short to allow pairing between domains on the same chain [17]. Diabodies (55 kDa) are the smallest engineered fragments that are bivalent, retaining the chief advantage of whole antibodies, namely, avidity. Increased tumor uptake has been observed for intermediate-sized bivalent Ab formats, such as 75-kDa triabodies and 80-kDa

Table 19.2 Characteristics of antibodies and antibody fragments

Antibody/ fragment	Produced by	Mol. wt. (kDa)	Avidity	Clearance route	Tumor uptake	Clearance rate	Tumor penetration
Full-length (IgG)		150	Bivalent	Liver			
F(ab′)₂	IgG digestion with pepsin	110	Bivalent	Liver/kidney			
Minibody	Recombinant DNA technology	75	Bivalent	Liver			
Diabody	Recombinant DNA technology	55	Bivalent	Kidney			
Fab	IgG digestion with papain	50	Monovalent	Kidney			
Fab′	IgG digestion with pepsin + β-mercaptoethanol	55	Monovalent	Kidney			
scFv	Recombinant DNA technology	26	Monovalent	Kidney			
Nanobody	Recombinant DNA technology pf camelid Abs.	12	Monovalent	Kidney			
Affibody	Recombinant DNA technology of protein-A	6	N/A	Kidney			

minibodies (scFv-CH$_3$); however, slower blood clearance was evident. Larger bivalent antibody fragments, such as F(ab′)$_2$ fragments, have slower blood clearance than diabodies, resulting in optimal tumor-to-normal tissue ratios only at prolonged times (18–24 h) relative to those of diabodies (3–5 h).

The development of smaller, antigen binding antibody fragments, derived from conventional antibodies or produced recombinantly, has been growing at a fast pace. Antibody fragments can be used on their own or linked to other molecules to generate numerous possibilities for bispecific, multi-specific, multimeric, or multifunctional molecules, and to achieve a variety of biological effects. They offer several advantages over full-length monoclonal antibodies, particularly a lower cost, and because of their small size, they can penetrate tissues, access challenging epitopes, and have potentially reduced immunogenicity [18].

19.3 Hallmarks of Cancer

Cancer is a group of diseases involving abnormal cell growth with the potential to invade or spread to other parts of the body. Benign tumors do not spread. Metastasis is the spread of cancer to other locations in the body. Most cancer deaths are due to cancer that has metastasized.

The hallmarks of cancer, an idea coined by Douglas Hanahan and Robert Weinberg, are to identify different biological capabilities acquired during the multistep development of human tumors [19, 20]. Subsequently, a more organized and updated picture of cancer hallmarks was also proposed [21] and summarized as follows:

- Selective growth and proliferative advantage (self-sufficiency of growth signals turned on by activated oncogenes, while insensitivity to anti-growth signals by inactivation of tumor-suppressor genes).
- Altered stress responses favoring overall survival and propagation (such as increased DNA repair mechanisms, upregulate autophagy,

evading programmed cell death or apoptosis, and avoid senescence).
- Sustained angiogenesis and vascularization (by VEGF overexpression).
- Invasion and metastasis.
- Metabolic rewiring (deregulated metabolism).
- Immune modulation (evading the immune system).
- An abetting microenvironment.

The acquired capabilities described above refer mainly to the cellular and tissular hallmarks of cancer. Cancer is not just a lump of cells that divide, invade, and spread randomly but, rather a multilayered precisely tuned process that requires the participation of the whole organism. Geographically separated cancer tissues communicate between themselves, forming a system that interacts with the rest of the organism through cancer-induced systemic pathogenic networks. Based on this approach, Doru Paul recently introduced six systemic hallmarks of cancer that emerge because of these interactions [22]. The first systemic hallmark is the cancer system itself established through the connections between the primary tumor, the bone marrow, and the distal metastasis. The five other systemic hallmarks are the global inflammation, the immunity inhibition, the metabolic changes leading to cachexia, the propensity to thrombosis, and the neuro-endocrine changes.

Tumor development and survival is a chaotically governed process involving the interplay between cancer cells, normal stromal cells and host defense mechanisms. Generally, CD8+ cytotoxic T cells (CTL) and CD4+ helper T (Th)1 cells curb cancer development via mechanisms commonly involving their production of interferon (IFN)-γ and cytotoxins [20]. The immune system interacts intimately with tumors over the entire process of disease development and progression to metastasis. This complex cross talk between immunity and cancer cells can both inhibit, and enhance tumor growth, and is now classified as a hallmark of cancer. The immune system plays a critical role in maintaining an equilibrium between immune recognition and tumor development with a dual capacity to both

promote, and suppress tumor growth. Despite immune surveillance, tumors continue to develop with intact immune systems.

19.4 Cancer and Immunotherapy

There are many types of cancer treatment such as surgery, radiation therapy, chemotherapy, targeted therapy, immunotherapy, and radioimmunotherapy. Targeted therapy targets the changes in cancer cells that help them grow, divide, and spread. Immunotherapy is a kind of targeted therapy, specifically using the immune system to fight cancer. The discovery of targetable tumor-specific antigens fueled interest in designing immunotherapies [23]. Antibodies are extremely versatile as platforms for the development of novel therapeutics, which has resulted in a large diversity of approaches. Since the 1990s, various forms of mAb-derived treatments have been used clinically to capitalize on the potential of immunotherapy.

Antibody-based therapeutics for the treatment of cancer can be divided into two broad categories. The first category involves the direct use of the naked mAb, which can elicit cell death by different mechanisms. For antibodies in the second category, additional engineering is performed to enhance their therapeutic efficacy, such as antibody-drug conjugates (ADC) and therapeutic radiolabeled-antibody conjugates (RAC).

Most targeted naked antibodies are referred to as "passive" immunotherapies because they target tumor cells directly rather than immune cells; however, more recent innovations have produced variations of targeted antibodies that are considered "active" immunotherapies because they target immune cells. Bispecific antibodies are made by taking the antigen binding regions (Fv) of two different antibodies and combining them to create a product that can bind to different targets. For example, bispecific T Cell Engager (BiTE) antibodies that target a tumor antigen, such as CD19 and the activating receptor, CD3, on T cells. BiTEs combine direct targeting of tumor cells with recruitment of cytotoxic T cells into the tumor microenvironment [9]. Due to their ability to target immune cells directly, these BiTEs are considered "active" immunotherapies. Another approach to immunotherapy is to use antibody molecule as a carrier to transport a drug or a radionuclide to kill the cancer cells. ADCs are designed for a target specific antibody to carry anti-cancer drugs, so that when the antibody targets and binds to cancer cells, it also delivers a toxic drug that can kill the cancer cells. FDA-approved ADCs are listed in the Table 19.1. Radioimmunotherapy (RIT) with RACs exploits the ability of antibodies to target tumors in an antigen-specific manner for selective delivery of therapeutic radionuclide and localized release of cytotoxic ionizing but, non-penetrating radiations, such as α and β^- particles [24].

19.4.1 Mechanisms of Action of mAbs

Therapeutic mAbs induce anti-tumor effects via diverse mechanisms, which depend on the nature of the target antigen, target cell, and the nature of interactions between Fab, and Fc regions of mAbs with target antigen, and effector cells, respectively [9, 25].

- Functional neutralization of target antigen: Antibodies directly target antigens on tumor cells or the non-tumor cells in the tumor microenvironment (TME) and recognize, and:
  - Bind to growth factor receptors (such as EGFR, HER2, HER3) or their ligands and inhibit activation of downstream signaling pathways that promote growth, migration, and proliferation of tumor cells.
  - Bind to angiogenic receptors (such as VEGFR1 VEGFR2) present on tumor vasculature or their ligands VEGFA and inhibit endothelial cell proliferation, migration, vascular permeability, and angiogenesis.
  - Bind to immune checkpoint molecules such as inhibitory (CTLA4) and co-inhibitory receptors (PD-1) present on immune cells or their ligands (PD-L1) upregulated by tumor cells. The immune

check point blockade inhibits cell proliferation and survival.

- Engagement with effector cells: Antibodies crosslink tumor cells and effector arm of the immune system via their Fab and Fc domains, respectively, and elicit a range of effector functions, such as antibody-dependent cell cytotoxicity (ADCC) through neutrophils, and natural killer (NK) cells, antibody-dependent cell phagocytosis (ADCP) via macrophages, and complement-dependent cytotoxicity (CDC) by complement pathway of the immune system.
- ADCs bind to tumor cell antigens and, following internalization, release the cytotoxic drugs in the cytoplasm and prevent replication machinery or microtubule assembly, and subsequent cell death.
- Radioimmunotherapy (RIT) exploits the ability of RACs to target tumors in an antigen-specific manner for selective delivery of therapeutic radionuclide and localized release of cytotoxic ionizing radiations. The efficacy of RIT, however, depends on the type and size

of cancer tissue, and the choice of radionuclide, half-life, type of particle emission, kinetic energy, and range in tissue (Fig. 19.3).

19.5 Radiolabeled Antibodies

Almost 70 years ago, antibodies from a rabbit serum were labeled with ^{131}I and the biodistribution of antibodies in animals was determined using radioautographs [26]. The first use of radiolabeled antibody to treat cancer was performed in the 1950s by Dr. Beierwalters at the University of Michigan, USA, who used ^{131}I tagged antibodies made in rabbits against patient's own neoplastic tissue [27, 28].

Two decades later, the pioneering studies by Goldenberg and Mach in animal models [29, 30], and in human subjects demonstrated the feasibility of specific targeting with radioiodinated anti-CEA polyclonal antibodies [31, 32]. Following the discovery of mAb production based on hybridoma technology, the first clinical study of radiolabeled mAb was reported in 1981 by Mach

Fig. 19.3 Antibody effector mechanisms. *ADCC:* antibody-dependent cellular cytotoxicity, *CDC:* complement-dependent cytotoxicity, *ADCP:* antibody-dependent cellular phagocytosis, *ADC:* antibody drug conjugate, *ARC:* radiolabeled antibody conjugate. (Figure modified from [9])
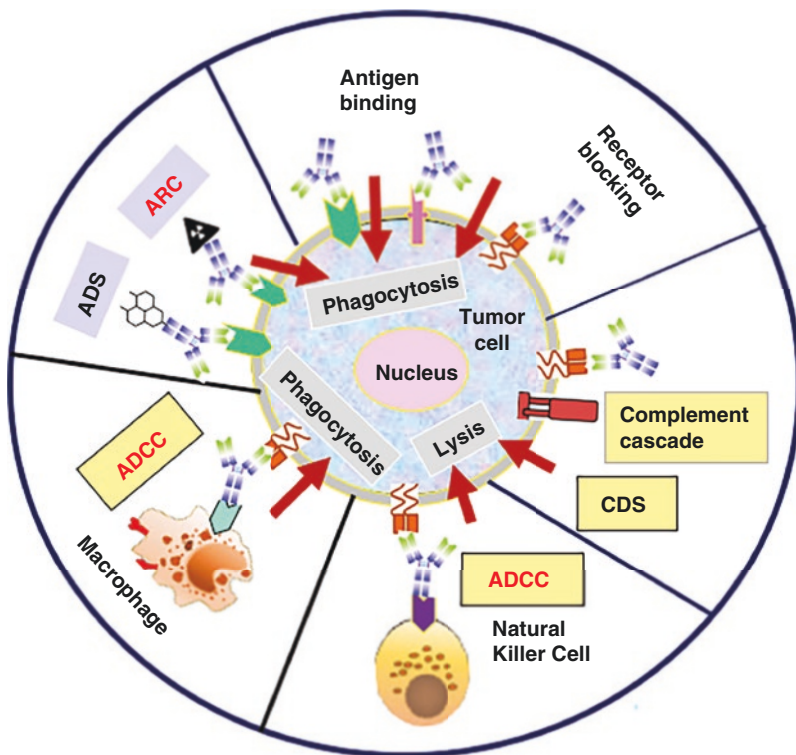
and associates, who used ^{131}I labeled anti-CEA antibodies in patients with CEA-bearing colon, and pancreatic carcinomas [33].

With the introduction of radiometals, such as ^{111}In, [67]Cu, and ^{90}Y, several chelating agents were developed to act as cross-linkers between the mAb molecule and the radiometal. Acyclic chelators were first developed in the 1970s [34, 35]. Subsequently, activated DTPA analogues via mixed anhydride or cyclic anhydride were developed in the 1970s to provide covalent attachment to the proteins [36, 37]. Although these acyclic agents form stable complexes with a variety of metal ions such as Fe, Co, In, their complexes with other metals, such as Cu and Y, they are labile with poor in vivo stability. To prepare stronger radiometal-mAb complexes with greater kinetic stability macrocyclic BFCs, such as DOTA and TETA were developed [38, 39].

19.5.1 FDA-Approved Radiolabeled Antibodies for Imaging and Therapy

After a couple of decades of intense investigation with radiolabeled antibodies, only six radiolabeled antibodies have gained FDA approval for use in clinical oncology; four immunodiagnostic agents and two targeted radioimmunotherapeutic agents (Table 19.3). In 1993, the FDA approved the first murine mAb, ^{111}In-Satumomab pendetide (OncoScint™) for the diagnosis of recurrent colorectal and ovarian cancer based on immune-SPECT imaging. Three other agents were quickly approved over the next 3 years: CEAScan™ for colorectal cancer, Veraluma™ for lung cancer and ProstaScint™ for prostate cancer. These first-generation diagnostic mAbs are mainly used for staging disease in patients suspected of recurrent or metastatic disease but, their overall clinical impact was not impressive due to suboptimal imaging characteristics and none of these approved diagnostic radiolabeled mAbs are in clinical use following the success of FDG-PET/CT studies in diagnostic oncology.

In the last 30 years, immunotherapy in oncology with engineered mAbs has become a major anticancer treatment modality. As of December 2021, more than 30 mAbs have been approved for the treatment of cancer (Table 19.1). Rituximab (or Rituxan) was the first therapeutic naked whole mAb approved by the FDA in 1997 for the treatment of cancer [40, 41]. Rituximab is a chimeric mAb directed against the cell surface marker CD20, which is expressed on B-lymphocytes and approved for the treatment of non-Hodgkin's lymphoma (NHL). While rituximab is effective in more than 50% of CD20-positive follicular NHL patients, it is less effective in other CD20-positive lymphoma subtypes, with activity in only 10–15% of CD20-expressing small lymphocytic lymphomas. When rituximab binds to CD20 protein, it triggers cell death or apoptosis. The Fc portion of rituximab mediates both ADCC and CDC [9].

Table 19.3 FDA-approved monoclonal antibodies for diagnosis and therapy in oncology

Year	Generic(Trade) name	Target	Type	Indication
1993	^{111}In-satumomab pendetide (OncoScint™) CYT-103	Tumor associated glycoprotein-72	Murine IgG	Ovarian and colorectal cancer
1996	^{99m}Tc-acritumomab (CEA-scan™)	Carcinoembryonic antigen (CEA)	Murine F(ab′)	Colorectal cancer
1996	^{99m}Tc-Nofetumomab Merpentan (Verluma™)	Epithelial cell adhesion molecule	Murine Fab	Small cell lung cancer
1996	^{111}In-capromab pendetide (ProstaScint™)	Prostate specific membrane antigen (PSMA)	Murine IgG$_1$	Prostate cancer
2002	^{90}Y-ibritumomab tiuxetan (Zevalin®)	CD20	Murine IgG$_1$	Non-Hodgkin's lymphoma
2003	^{131}I-Tositumomab (Bexxar®)	CD20	Murine IgG$_{2A}$	Non-Hodgkin's lymphoma

RIT with antibodies, however, was not clinically successful except in hematological malignancies. Combining mAbs with therapeutic radionuclides was first studied in hematologic malignancies based on the rationale that these cancers are more radiosensitive tumors than solid tumors [24]. The FDA approvals for two radiolabeled anti-CD20 mAbs, ^{90}Y-labeled Zevalin® (ibritumomab tiuxetan) in 2002 and ^{131}I-labeled Bexxar® in 2003 for the treatment of NHL were landmark events in the developmental history of TRT and RIT. Both these ^{90}Y and ^{131}I labeled anti-B1 mAbs produce overall response rates (ORR, 60–80%) and complete response rates (CRR, 15–40%) in relapsed NHL than the naked antibodies, such as rituximab [24].

Despite the safety and efficacy of RIT in lymphomas, the two FDA approved therapeutic radiolabeled antibodies are less frequently used compared to chemotherapy or naked antibodies. In fact, ^{131}I-tositumomab (Bexaar™) is no longer marketed.

The theranostic applications of radiolabeled mAbs in oncology, especially in the emerging field of personalized medicine, are becoming increasingly important since antibody theranostics can combine the diagnostic and therapeutic potential of an antibody, thereby selecting those patients who are most likely to benefit from antibody treatment. The past several decades yielded dramatic improvements in the commercial availability of several α and β^- emitting therapeutic radiometals. Also, new and improved BFCs have been created to optimize the radiolabeling and kinetic stability of radiometal labeled antibodies or antibody fragments. The multidisciplinary field of antibody theranostics is challenging and has yet to reach its full potential in both preclinical, and clinical domains.

19.5.2 Tumor Antigen Targets and Targeting Vehicles

Selection of the optimal receptor or an antigen on the cell surface or in the tumor microenvironment is critical to the success of a RIT program. An ideal target (receptor or antigen) for RIT is expressed at a high, uniform density in tumor tissue but, not expressed on normal cells, and not "shed" into the bloodstream. Antigenic targets (Tables 19.1 and 19.3) are usually tumor cell surface-expressed macromolecules easily accessible from the blood and extracellular fluid, and include

(a) Signal transduction molecules, such as epidermal growth factor receptor (EGFR), and human epidermal growth factor receptor 2 (HER2).
(b) Surface glycoproteins such as (e.g., mucins), enzymes, such as prostate-specific membrane antigen (PSMA) and carbonic anhydrase IX (CAIX), glycolipids, such as GD2, carbohydrates such, as Lewis antigen, and stromal components (e.g., fibroblast activation protein-α (FAPα).
(c) Components of blood vessels (e.g., integrins, vascular endothelial growth factor receptor (VEGFR), or the amino domain of fibronectin B).
(d) Hematopoietic cluster of differentiation ("CD") antigens, such as CD19, CD20, CD22, CD37, CD33 and CD45 that are expressed during hematopoietic maturation of distinct cell lineages.

19.5.2.1 Targeting Vectors: Antibody or Antibody Fragments

Following intravenous administration of radiolabeled antibodies or antibody fragments, the volume of distribution is very large (~15 L of extracellular space), and several factors play an important role in the biodistribution, catabolism, whole body clearance (via kidney, liver, and gut), and tumor localization of the radioimmunoconjugate [24]. In addition, apart from specific antigen binding at the target site in tumor, there may be competitive specific binding to antigen in other organs/tissues. The absolute tumor uptake and retention of the radioimmunoconjugate will also depend on the amount of antigen expression, saturation kinetics, and internalization of antibody-antigen complex.

The phenomenon known as "binding site barrier" suggests that high-affinity antibodies may accumulate around the vasculature and fail to dis-

tribute evenly throughout tumors. Tumor tissue may have increased vascular permeability but, also, have increased interstitial fluid pressure (IFP) due to poor drainage. While the phenomenon of enhanced permeability and retention (EPR) effect favors retention of macromolecules, IFP prevents diffusion of macromolecules into the tumor interstitium. Therefore, the selection of an appropriate antibody carrier molecule for a specific radionuclide is governed by several variables, including vascular permeability, diffusivity, affinity, valency, specificity, and tumor retention [42].

Full-length whole mAbs (IgG) are popular for RIT. A theoretical analysis also suggests that IgG-sized macromolecular constructs (~20 nm in diameter) exhibit the most favorable balance between systemic clearance and vascular extravasation, resulting in maximal tumor uptake [43]. However, full-length mAbs inherently have a longer blood circulating time, decreased vascular permeability, and lower diffusivity within solid tumors. The therapeutic index is also suboptimal due to higher bone marrow radiation dose. These challenges led to the exploration of mAb fragments as radionuclide vectors. Smaller antibody fragments have faster blood clearance kinetics and may have reduced absolute tumor uptake compared to whole mAbs but, smaller fragments (<55 kDa) may lead to more rapid tumor accumulation due to increased diffusion into the tumor. A compartmental model to quantitatively analyze the effect of size on tumor uptake, suggests that the absolute tumor uptake of different size antibody molecules is a trade-off between two opposing trends: systemic clearance and extravasation into the tumor tissue. The model predicts that the antibody fragments, such as scFvs, Fabs, diabodies, and the like ($\leq$55 kDa), essentially are too large for sufficiently rapid extravasation and, too small to escape renal clearance. As a result, the absolute tumor uptake will be much less compared to whole IgG [43].

In summary, the interplay of the above concepts is an imperative consideration of the antibody platform choice to produce beneficial results in a specific RIT program development. Ultimately, each antibody format and antibody-target pairing, requires proper characterization, and preclinical evaluation to determine the effective format, and the optimal dose as modifications on size affect uptake, therapeutic efficacy, and dose [42].

19.5.2.2 Bispecific and Poly-specific Antibodies (Bs-Ab and PsAb)

Monoclonal antibodies are bivalent but, naturally, are monospecific and both binding sites are directed against the same target antigen (epitope). In contrast, a bispecific antibody (BsAb) is an engineered antibody molecule composed of fragments of two different mAbs, which consequently binds to two different antigens. A tri-specific antibody (Ts-Ab) will bind to three different antigens on different cells. Blinatumomab (Blincyto) is FDA approved Bs-Ab for the treatment of acute B-cell acute lymphoblastic leukemia (ALL). Blinatumomab was created by the fusion of two single chain variable fragments (scFv) connected in a flexible manner through a peptide linker [44]. One part of blinatumomab is specific to the CD19, while the other part is specific to CD3 *T cells*. By binding to both antigens, this drug brings the cancer cells and immune cells together, which is thought to cause the immune system to attack the cancer cells since PsAbs are capable of binding two or more antigens/receptors at the same time or bringing two different targets together (Fig. 19.4). This character makes PsAbs as ideal targeting vehicles (vectors) in the development of radiopharmaceuticals for both radioimmunoimaging and targeted therapy.

19.5.3 Radionuclides for Antibody Therapy and Imaging

Antibodies and antibody-fragments can be efficiently labeled with a wide range of radionuclides. Several radionuclides useful for therapy and imaging studies are listed in Table 19.4. Antibody-related therapeutics represent a rapidly

Fig. 19.4 (**a**) Schematic showing different formats of mAbs, such as bispecific and trispecific antibody binding to the antigen on the tumor cell, and cells in the tumor microenvironment (Figure modified from [44]). (**b**) Blinatumomab (BLINCYT0®) is a bispecific antibody (Variable domains of two mABs fused to create a bispecific or dual-specific antibody) which targets malignant and benign B cells via the CD19 cell surface antigen while simultaneously engaging the patient's own T cells through the CD3 antigen. (Image from https://www. blincytohcp.com/)
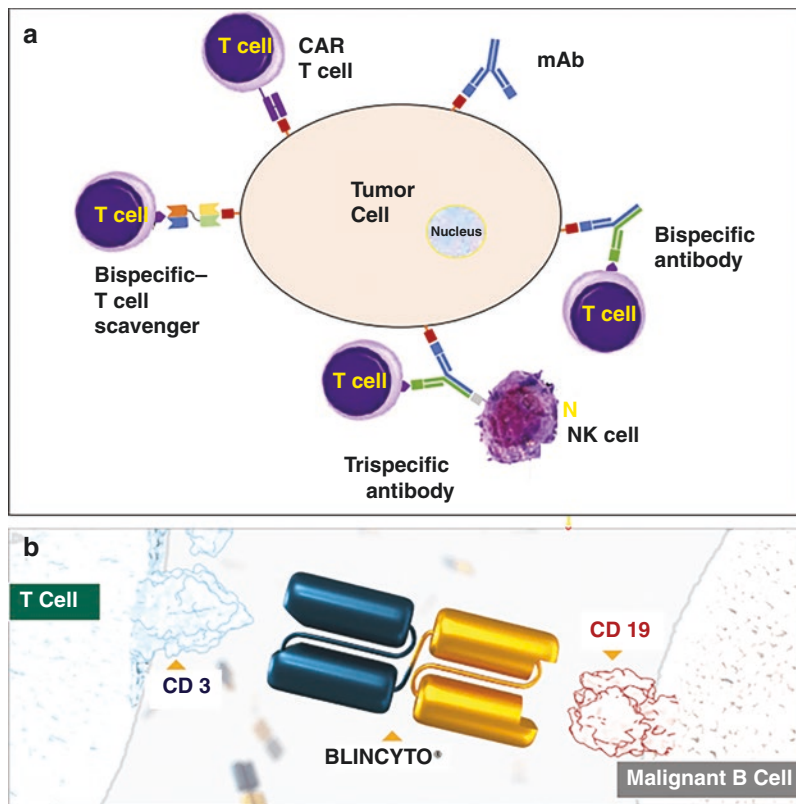
expanding group of cancer medicines. To develop companion diagnostics, several elements have isotopes for therapy, and for PET/SPECT imaging modalities. Selecting a suitable radionuclide generally depends on the following important consideration:

- Selection of the optimal antigen target on the cell surface or within the tumor tissue microenvironment.
- Selection of an appropriate antibody molecule (whole IgG or fragment) with high specificity and affinity for the antigen.
- The pharmacology of antigen-antibody complex is very important, especially the internalization of "antigen-antibody complex" following antibody binding to the antigen.
- The selection of the radionuclide for therapy or imaging starts by matching the serum half-life of the mAb or the fragment with the physical half-life of the radionuclide.

- The radiolabeling strategy, such as direct labeling or indirect labeling based on prosthetic groups or BFCs.

19.5.3.1 Therapeutic Radionuclides

Except for the radioisotopes of fluorine, iodine, and astatine, all other therapeutic radionuclides listed in Table 20.4 are metals. Therapeutic radionuclides (Table 20.4) emit particulate non-penetrating radiation (electrons and alpha particles) that deposit a significant amount of their kinetic energy within the tumor mass. The choice of an ideal radionuclide depends on several factors but, they are, generally, selected based on the decay mode, particle emission, half-life, particle energy, range in tissue (or the path length), and ease of radiolabeling. The decay schemes of beta emitting radionuclides (^{131}I and ^{177}Lu) are compared to that of an alpha emitter ^{225}Ac in Fig. 19.5.

Table 19.4 Radionuclides commonly used for the development of radiolabeled mAbs for therapy and molecular imaging

| Radionuclide | $T_{1/2}$ | Decay | | γ Energy | | Particle, E_{mean} | | |
		Mode	%	keV	%	keV	%	Imaging
^{99m}Tc	6 hours	IT	98	140				SPECT
^{123}I	13.22 days	EC	97	159	83.6			SPECT
^{111}In	2.8 days	EC	100	171.3	90.7			SPECT
				245.4	94.1			
^{18}F	109.8 min	β^+	96.73			250	96.73	PET
^{68}Ga	67.7 min	β^+	88.91			829	88.91	PET
^{44}Sc	3.97 hours	β^+	94.30			632	94.30	PET
^{64}Cu	12.7 hours	β^+	17.6			278	17.6	PET
		β^-	38.5					
		EC	44					
^{86}Y	14.74 hours	β^+	31.9	1076.5	82.5	662	31.9	PET
^{89}Zr	3.3 days	β^+	23	909	99	396	22.7	PET
		EC	77					
^{124}I	4.18 days	β^+	23	603	62.9	822	22.7	PET
		EC	77	723	10.4			
				1691	11.2			
^{131}I	8.025 days	β^-	100	364.5	81.5	181.9	100	Therapy
^{90}Y	2.66 days	β^-	100			932.3	100	Therapy
^{67}Cu	2.576 days	β^-	100	184.6	48.7	141	100	Therapy
^{177}Lu	6.647 days	β^-	100	113	6.23	133.6	100	Therapy
				208	10.4			
^{212}Pb	10.64 hours	β^-	100	238.6	43.6	101.3	100	Therapy
^{213}Bi	45.6 min	α	100	440.5	25.9	8440	100	Therapy
^{211}At	7.2 hours	α	41.8			5869	41.8	Therapy
^{225}Ac	9.92 days	α	100	218[a]	11.5	5830	100	Therapy
				440.5[a]	25.9			
^{227}Th	18.697 days	α	100	236	13.0	6000	100	Therapy

[a]Gamma photons from the daughters Fr-221 and Bi-213

Fig. 19.5 Decay schemes of ^{177}Lu and ^{225}Ac. ^{177}Lu decays by β^- emission and is converted to stable ^{177}Hf. In contrast, ^{225}Ac goes through a series decay (in vivo generator) with the emission of multiple α particles and β^- particles before it reaches stable ^{209}Bi

Alpha-emitting radionuclides release highly energetic $^4He^{2+}$ (5–9 MeV) nuclei with very short ranges (50–100 μm) in tissue. Also due to their high LET (50–230 keV/μm), they are highly cytotoxic, producing single or double strand breaks (SSBs/DSBs) in the DNA, which can't be easily repaired. While bismuth radionuclides (^{212}Bi and ^{213}Bi) have very short half-lives (~1 h), ^{225}Ac and ^{227}Th have relatively longer half-lives (10 and 18.7 days, respectively). Some of the α emitters, such as ^{225}Ac and ^{227}Th, act as in vivo generators and emit several α particles due to the short halves of daughter radionuclides. While this property may help deposit more radiation energy in the tumor, it may be challenging to identify a more appropriate chelator that can retain the parent and daughter nuclides within the tumor tissue. In general, radionuclides emitting α particles may be ideal for leukemias, small size tumors, and micrometastases but, they may be equally effective with large solid tumors.

Radionuclides that decay by the emission of intermediate energy electrons (β^- particles with 0.030–2.3 MeV) have low LET values (~0.2 keV/μm), have relatively longer range in tumor tissue (1–12 mm), and can reach up to 50 cell diameters [15]. As a result, the crossfire radiation may produce significant radiation induced damage in large tumors with heterogeneous expression of target-specific antigens. While the clinical utility of certain radionuclides (such as ^{131}I, ^{90}Y and ^{177}Lu) was well established, the availability of high specific activity radiometals (such as ^{67}Cu, ^{47}Sc, ^{188}Re and ^{212}Pb) may provide more flexibility in the design of therapeutic radionuclides. In recent years, the ^{212}Pb ($T\frac{1}{2}$, 10.6 h), a β^- emitter, has become a very popular radionuclide for TRT. It is widely used as an in situ generator of its α-emitting daughter isotope ^{212}Bi ($T\frac{1}{2}$, 60.6 m).

Radionuclides (such as ^{111}In and ^{67}Ga) that decay by electron capture loose a proton in the nucleus, and the decay product, an element that emits low energy orbital electrons (also known as "Auger electrons"), as an alternate to the emission of X-rays. The Auger electrons (AE) have medium LET (4–26 μm) and can deposit very high radiation energy to DNA due to their short range (<1 μm), only when the radionuclide is in close to the cellular DNA. While this concept has potential, AE emitters have not been used to develop radiolabeled antibodies for therapy, especially when several α-emitting radionuclides are commercially available for the development of therapeutic radioimmunoconjugates.

19.5.3.2 Radionuclides for Immuno-PET/SPECT

Since the 1980s, for diagnostic purposes, mAbs have been labeled with γ-emitting radionuclides (such as ^{99m}Tc, ^{123}I, ^{131}I, ^{186}Re and ^{111}In) and imaged with a single photon emission computerized tomography (SPECT) camera. In the 1990s, the FDA approved four radiolabeled antibodies or antibody fragments for imaging studies. Although these SPECT camera images were very informative and useful to determine the biodistribution of mAbs due to lack of quantitative information by SPECT, the development of radioimmnoconjugates based on gamma emitting radionuclides is not ideal. However, ^{111}In labeled mAbs have been used successfully as chemical and biological surrogates for ^{90}Y, ^{177}Lu, and other trivalent radiometal labeled therapeutic agents.

Compared to SPECT imaging, PET is more accurate in terms of in vivo activity quantification due to its superior spatial resolution, sensitivity, and specificity for tumor detection. Immuno-PET is a quantitative imaging procedure to investigate the biological effect and pharmacokinetics of radioimmunotherapy agents [45–47]. Several positron emitting radionuclides with different physical half-lives are available for developing radiolabeled antibodies and antibody fragments for Immuno-PET studies (Table 19.4). The positron emitter, however, should have appropriate decay characteristics for optimal resolution and quantitative accuracy, its production should be easy and cheap, and it should allow facile, efficient, and stable coupling to mAbs. Since the half-lives of ^{18}F and ^{68}Ga are very short (<2 h), these two radionuclides are only good to label antibody fragments with faster blood clearance rates or in pretargeting approaches. Interestingly, ^{44}Sc with a half-life of 4 h is a better alternative to

[18]F than [68]Ga. [124]I and [89]Zr are particularly suitable to label intact mAbs because their long half-lives (>3 days) allow imaging at late time points for obtaining maximum information. [124]I has several disadvantages, such as high positron energy resulting in poor resolution, several high energy γ photons degrading image quality, and in vivo dehalogenation. In contrast, [89]Zr has proven to be more suitable for Immuno-PET studies, especially for radiation dosimetry studies. In addition, as a radiometal, the in vivo stability of [89]Zr labeled mAb can be optimized using a BFC that can provide greater kinetic stability. Three other radionuclides with medium half-lives (12–14 h) [86]Y, [66]Ga and ^{64}Cu have also been used for immune-PET studies. Among these, ^{64}Cu is the most appropriate nuclide for immune-PET since it offers the best resolution, like that provided by ^{18}F-PET scans. A major advantage of radiometals is that when the radiometal-antibody complex gets internalized, the radiometals are trapped intracellularly unlike the radioiodide which can diffuse out of the cell. This phenomenon of residualization should be considered when selecting a positron emitter for immuno-PET applications [48].

19.5.4 Radiolabeling and Bioconjugation Strategies of Antibodies

There are several radiolabeling strategies available to incorporate a radionuclide into a protein and the choice of technique depends primarily on the radionuclide. The labeling of mAbs or antibody fragments involves direct substitution of halogens (such as ^{131}I and [124]I) on tyrosine residues or coupling to reactive sidechains of amino acids, such as lysine ε amino groups. The most common strategies for the radiolabeling of proteins are (a) Direct labeling, (b) Indirect labeling via complexation using a prosthetic group or a bifunctional chelating agent (BFC) [14, 42, 49]. The chemistry of radiolabeling techniques is discussed in greater detail in Chaps. 12, 18, and 20.

19.5.4.1 Direct Labeling of Proteins
The direct radioiodination of a protein is a key method for the synthesis of radioiodinated antibodies. The most straightforward approach is based on electrophilic substitution at tyrosine and histidine residues in the protein. The radioiodide is oxidized in situ creating the radioactive electrophile [131/124]I[+] using oxidizing agents like chloramine T, Iodogen® and N-halosuccinimides. The electrophile reacts with the tyrosine in the protein (Fig. 19.6) and substitution of radioiodine is performed at the tyrosine residue due to the electron donating hydroxyl group (on the tyrosine), which stabilizes the reaction. This reaction is performed under mild conditions. ^{131}I-Tositumomab (Bexaar®), the FDA-approved radioiodinated antibody was prepared using the direct labeling method using Iodogen® as the oxidizing agent. While this method of labeling is highly efficient, in vivo deiodination (or dehalogenation) may occur due to the action of the enzyme tyrosine deiodinase and free radioiodinated species will
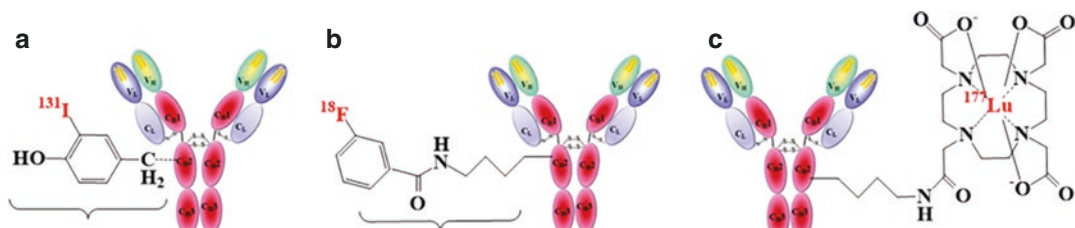
Fig. 19.6 Radiolabeling mAbs (or proteins) can be performed based on three approaches. Radioiodination can be performed by labeling tyrosine residue in the protein (**a**). Labeling with ^{18}F can be done using prosthetic groups attached to lysine residues in protein (**b**). Labeling proteins with radiometals can be done by conjugating BFC to the lysine residues in the protein (**c**)

escape from tumor tissue. In vivo stability of radioiodinated protein can be improved using indirect radioiodination technique which can be performed via conjugation using a prosthetic group such as N-succinimidyl 5-iodo-3-pyridinecarboxyl (SIPC) and N-succinimidyl-3-iodobenzoate (SIB) [50].

19.5.4.2 Indirect Labeling Using BFCs

Except for the isotopes of iodine, all other nuclides used for RIT or immune-PET/SPECT studies use isotopes of radiometals. BFCs are required to link the mAb and the radiometal. BFCs not only encapsulate the radiometal but also possess reactive functional groups for covalent binding to the mAb. Based on the chemistry of radiometal, an appropriate BFC can be selected which provides both thermodynamic stability and in vivo stability of radiometal-antibody complex.

Choice of BFC

In order to match the chemistry of a specific radiometal (whether it is soft or hard) with a corresponding soft or hard donor atoms of the chelator, several acyclic and macrocyclic BFCs (Figs. 19.7 and 19.8) have been evaluated in both

preclinical and clinical studies [42, 51]. The acyclic chelator DTPA and its derivative CHX-A"-DTPA can form an octadentate coordination radiometal complex with three tertiary amine nitrogen atoms and five oxygen atoms from the carboxylic acid arms. The macrocyclic DOTA also forms octadentate radiometal complex with four tertiary amine nitrogen donors and four oxygens from carboxylic acid groups. For all trivalent metals (such as ^{47}Sc, ^{90}Y, ^{111}In, ^{177}Lu, and ^{225}Ac), the most popular BFC is DOTA or DOTA derivative but, for actinides (^{225}Ac and ^{227}Th), Macropa, an 18-membered macrocyclic ligand, may be a better choice. Several chelating agents have been evaluated for different radiometals in order to match the most appropriate chelator to meet the demands of specific metal chemistry [51, 52].

Non-specific Conjugation

Lysine-based conjugation of BFCs to mAb is one of the most widely used non-specific conjugation strategies since it does not require any form of antibody engineering or modification and several BFCs can be conjugated to mAb to increase specific activity. A typical IgG1 mAb consists around 80 lysine amino acids out of which 30 are solvent
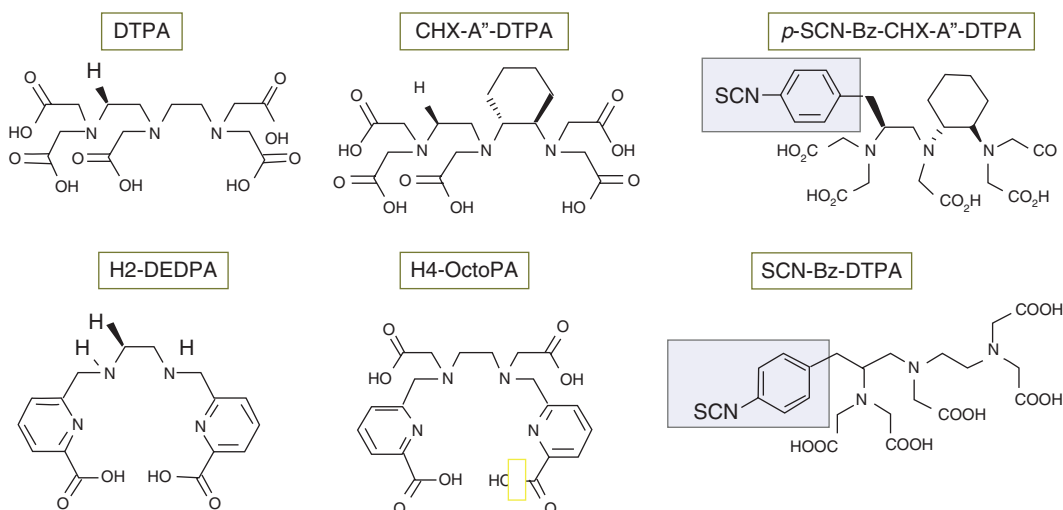
Fig. 19.7 Acyclic chelators for radiometal labeling of proteins. Blue shaded area shows functional groups in the BFC to facilitate conjugation to proteins
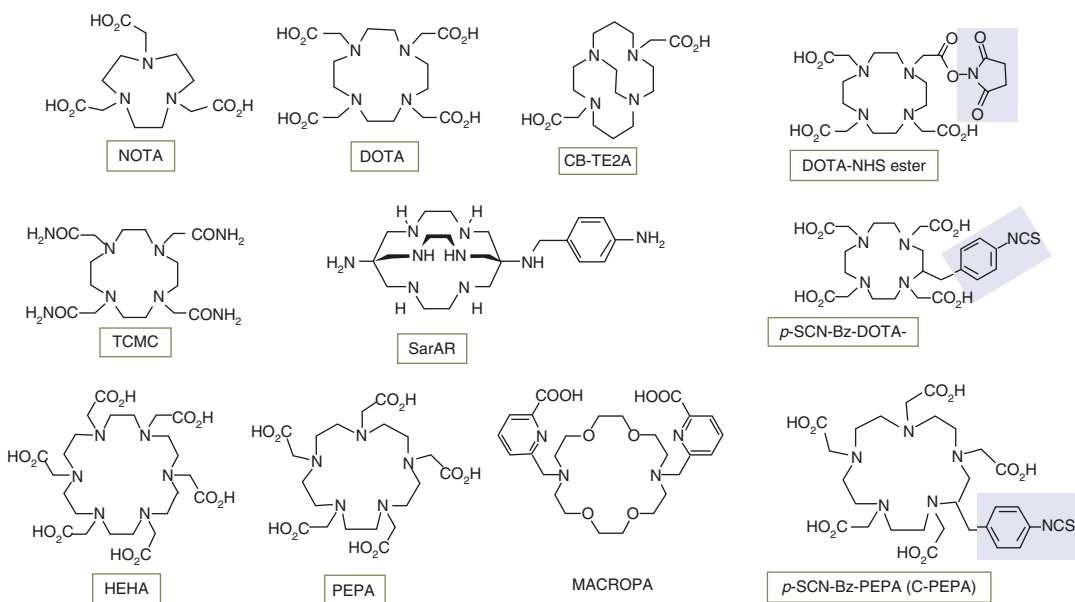
Fig. 19.8 Macrocyclic chelators for radiometal labeling of proteins. Blue shaded area shows functional groups in the BFC to facilitate conjugation to proteins

accessible (on both FC and Fab segments) and available for random conjugation to BFCs. After activation of the ε-amino groups of lysine residues at alkaline pH 9.0, lysine residues can be conjugated to BFCs containing reactive electrophilic groups such as activated esters (such as N-hydroxysuccinimide ester), anhydrides, isothiocyanate (SCN), and isocyanate [49].

Cysteine residues consist of highly reactive thiol side chains that form inter- or intramolecular disulfide bonds to enable correct protein folding. Thiol reactivity provides another strategy for non-specific conjugating of BFCs to antibodies. A full IgG molecule contains 16 cysteine pairs, forming 12 intra- and 4 inter-chain disulfide bonds. Only the four inter-chain disulfide bonds in the mAb hinge region are solvent exposed and available for conjugation. However, reduction of the disulfide bonds to generate reactive thiol groups is necessary for conjugation. Partial reduction with either dithiothreitol (DTT) or tris(2-carboxyethyl) phosphine (TCEP) results in the disruption of the heavy–light inter-chain disulfides to release free thiol groups for subsequent reaction with maleimide groups in the

BFCs. The major disadvantage of this strategy based on succinimidyl thioether linkage is that the in vivo stability of the radioimmunoconjugate is sub-optimal for RIT studies [42]. To improve the in vivo stability of cysteine conjugated antibodies, a new thiol reactive reagent phenyloxadiazolyl methylsulfone (PODS) was developed. Based on PODS, two BFCs were made synthesized; PODS-CHX-A''-DTPA (for ^{177}Lu labeling) and PODS-DFO (for [89]Zr labeling). Radioimmunoconjugates created using these novel bifunctional chelators displayed higher in vitro stability than their maleimide-derived cousins. More importantly, PET imaging in murine models of cancer revealed that [89]Zr-PODS-radioimmunoconjugate produced significantly lower uptake in non-target tissues than its analogous maleimide-based counterpart [53].

Site-Specific Conjugation

The main reason to use site-specific conjugation is to avoid conjugation of BFCs to the antigen binding region of the antibody, to produce uniform attachment of chelators across different batches of conjugations, and to prevent the loss

of immunoreactivity. Recent advances in bioconjugation technology have optimized the methods to prepare site-specific conjugation of BFCs to antibodies.

The cysteine amino acid residues can be engineered into mAbs or their fragments at specific sites (on the heavy chain of constant Fab) leaving the native sulfhydryl groups intact. This approach is potentially useful with antibody fragments which have less bioconjugation sites compared to whole mAb molecules.

Since the carbohydrate moiety (glycan) is located on an antibody molecule at the conserved N297 residue at the hinge region of the Fc domain, glycan conjugation could be an appropriate strategy for site-specific labeling with radiometals. This method, however, is not suitable for antibody fragments that do not have glycans or for whole IgG antibody for which FC receptor binding is essential for targeting. The FDA-approved ^{111}In-labeled antibody imaging agents, (OncoScint® and ProstaScint®) were based on glycan modification method.

Antibody glycans usually contain vicinal diol moieties that can be oxidatively cleaved to yield aldehydes using sodium periodate ($NaIO_4$) as an oxidation reagent. The reactive aldehyde groups can be subsequently conjugated with amines, hydrazines, hydroxylamines, or primary amine functionalized molecules [49]. The glycan oxidation conditions, however, can be harsh and may lead to inadvertent oxidation of methionine residues in the antibody and decrease the plasma clearance rate of labeled antibodies. An enzymatic modification of glycans is a better alternative to chemical modification of glycans [54]. The method uses two enzymes; first the terminal galactose residues are removed using β-1-4-galactosidase and then a modified galactose reactive group (such as azide) is inserted at this site using β-1,4-galactosyltransferase. ^{89}Zr-DFO-mAbs prepared based on glycan enzymatic modification method showed increased tumor uptake in preclinical studies compared to ^{89}Zr-DFO labeled antibodies prepared based on non-specific labeling methods [55–57].

19.6   Radioimmunotherapy (RIT)

RIT exploits the immune protein (mAb or antibody fragments) as a carrier for therapeutic radionuclides to its natural target or antigen-binding site on the tumor cell or within the tumor microenvironment. RIT represents a selective internal radiation-targeted therapy and, unlike external beam radiation therapy, RIT can attack not only the primary tumor but also micrometastatic lesions, residual tumor margins after surgical resection, tumors in the circulating blood, including hematologic malignancy, and malignancies that present as free-floating cells. The goal of RIT is to safely deliver a high-radiation dose to a tumor. Radiosensitive tumors such as lymphoma may have complete responses with radiation doses in the range of 1500–2000 cGy, while solid tumors typically require 3500–10,000 cGy for a meaningful response. Normal tissue radiosensitivity also varies from the bone marrow (typically >150 cGy) to the lung and kidney (1500–2000 cGy). The principle of targeted RIT is based on the selective and specific targeting of tumors relative to normal tissues, creating a therapeutic index (TI). Generally, the organs at risk for toxicity include the bone marrow, kidney, lungs, and colonic mucosa. The goal of the TI is to increase the ratio of the absorbed radiation dose to the tumor compared to normal tissue. Typically, the TI should be >10 for tumor/kidney and >50 for tumor/bone marrow [24].

The maximum tolerated activity/dose (The MTA or MTD) has also been described as the maximum administered dose, MBq or mCi/kg or m^2 of the RIT agent. MTD determination is critical to identify an optimum single dose to establish dosing schemes at or below the MTD threshold. It is important to note that it may be necessary to alter the PK of the RIT agent (by dose fractionation) to optimize the drug's efficacy, safety, and tolerability, and achieve the desired therapeutic effect while minimizing toxicities. Following the administration of radiolabeled mAb, clinically applicable parameters are monitored periodically. These tests include markers of liver function, kidney function, and extent of bone marrow suppression.

19.6.1 Direct and Indirect RIT Strategies

Although RIT has been investigated for the last 50 years, advances in the last decade in cancer biology, antibody engineering, and radiochemistry have enhanced the ability of RIT to play a major role in cancer-targeted immunotherapy. Two different strategies can be used in RIT. The "direct method" requires first the preparation of therapeutic radiopharmaceutical with optimal radiochemical purity and immunoreactivity prior to the administration into a patient. Subsequently, the direct method also requires a single-step administration of radioimmunoconjugate to patients. The therapeutic radiolabeled antibody is administered to the patients via different routes, i.e., intravenous injection, intra-peritoneally, or loco-regional (arterial or direct intra-tumoral) injection. Selection of an appropriate radionuclide and targeting vector are essential. The success of the direct method depends on achieving the optimal TI with minimal toxicity to normal organs and tissues. The two FDA approved RIT radiopharmaceuticals (Zevalin® and Bexaar®) and many of the ongoing clinical trials are based on this direct method.

In the "indirect method (also known as pretargeted RIT or PRIT)," directly radiolabeled mAbs are not used; that is, the antibody molecule and the radiolabeled effector molecule (therapeutic radiopharmaceutical) are administered separately, and they will be conjugated in vivo. This technique can achieve high TI and/or therapeutic efficacy. PRIT was developed in the 1980s to avoid the issues associated with the prolonged residence times of radiolabeled mAbs in the circulation.

19.7   RIT: Clinical Applications

Radiolabeled mAbs have been under clinical investigation as therapeutic radiopharmaceuticals for more than three decades. However, drugs for RIT of hematologic malignancy were only approved 20 years ago (Table 20.3). No other radiolabeled mAbs have been approved to treat solid tumors. A recent review of the literature on RIT provides a summary of the developments and 92 clinical trials conducted in the last 10 years [58]. The majority of the clinical studies (67%) concerned RIT of non-solid tumors. Radiolabeled antibodies under clinical development are summarized in the (Table 19.5).

19.7.1 Hematological Malignancies

Hematological malignancies are generally divided by whether the malignancy is mainly located in the blood (leukemia) or in lymph nodes (lymphomas), and these malignancies may derive from either of the two major blood lineages: myeloid and lymphoid cell lines. The myeloid cell line normally produces granulocytes, erythrocytes, thrombocytes, macrophages, and mast cells; the lymphoid cell line produces B, T, NK, and plasma cells. Lymphomas, lymphocytic leukemias, and myeloma are from the lymphoid line, while acute and chronic myelogenous leukemia (AML, CML), myelodysplastic syndromes and myeloproliferative diseases are myeloid in origin. Since the 1980s, hematological and lymphoid malignancies have dominated the development of radioimmunoconjugates for RIT studies for several reasons [24]:

- Leukemias and lymphomas are especially radiosensitive since the myeloid and lymphoid cells divide rapidly compared to cells of solid tumors.
- Several lineage-specific cell-surface differentiation antigens (such as CD20, CD22, CD33, CD37, CD38, CD45) that were not expressed on other tissues have been identified.
- Several mAbs against the CD antigens (such as Rituximab, Ofatumumab, Obinutuzumab, Ofatumumab, Gemtuzumab, Daratumumab) were also FDA approved for naked immunotherapy.
- Human anti-mouse antibodies (HAMAs) are less likely to form in patients following administration of murine mAbs.
- Widespread availability of hematopoietic cell transplantation makes myeloablative RIT an attractive option to increase radiation dose to malignant cells.

Table 19.5 Radiolabeled mAbs under clinical investigation for targeted therapy

Radiopharmaceutical	Target	Cancer type indicated	Route of administration	Clinical trial
[177]Lu-Lilotomab Satetraxetan (Betalutin)	CD37	Non-Hodgkin lymphoma (NHL), B-cell chronic lymphocytic leukemia (CLL), hairy-cell leukemia (HCL)	I.V.	Phase I/II
[227]Th-epratuzumab (BAY 1862864)	CD22	Relapsed/refractory NHL	I.V.	Phase I
[131]I-Apamistamab (BC8) (Iomab-B)	CD45	Advanced myeloid leukemia (AML)	I.V.	Phase III
[211]At-BC8-B10 mAb	CD45	Non-malignant diseases	I.V.	Phase I
[225]Ac-Lintuzumab	CD33	Advanced myeloid leukemia (AML)	I.V.	
[211]At-OKT10-B10 mAb	CD38	Multiple myeloma	I.V.	
[212]Pb-376.96	BH-H3	Ovarian cancer	Intra-peritoneal	Phase I
[131]I-3F8 or [131]I-8H9	GD2	Hi-risk and recurrent neuroblastoma	Intracerebro-ventricular injection	Phase II 62
[177]Lu-Omburtamab	B7-H3	Hi-risk and recurrent neuroblastoma	Intracerebro-ventricular injection	Phase I/II
[131]I-Omburtamab	B7-H3	Neuroblastoma CNS/leptomeningeal metastases	Intracerebro-ventricular injection	Phase II/III
^{177}Lu-DOTA-Panitumomab	EGFR	Solid tumors	I.V.	
[177]Lu-Certuximab	EGFR	Solid tumors	I.V.	
^{177}Lu-DTPA-2RS15D minibody)	HER2	Solid tumors	I.V.	
^{177}Lu-DTPA-Trastuzumomab	HER2	Breast cancer	I.V.	Phase I
[131]I-Metuximab (Licartin®)	Hab 18G/CD137	Unresectable hepatocellular carcinoma	Hepatic intra-arterial injection	Phase IV
[90]Y-cT84.66 mAb	CEA	Liver metastasis in patients with colorectal carcinoma	Hepatic intra-arterial infusion	Phase I/II
[211]At-MX35 (Fab)₂	NaPi2B	Ovarian cancer	I.V.	Phase I
			I.V.	
^{177}Lu-MVT1075 (5B1)	CA19-9	Pancreatic cancer	I.V.	Phase I
^{90}Y-DOTA-huJ591	PSMA	Metastatic castration resistant prostate cancer (mCRPC)	I.V.	
^{177}Lu-DOTA-huJ591	PSMA	mCRPC	I.V.	Phase I/II
[225]Ac-DOTA-huJ591		mCRPC	I.V.	
[177]Lu-huJ591 + docetaxel (dose-fractionation study)	PSMA	mCRPC	I.V.	Phase I
[177]Lu-huJ591 + ketoconazole + hydrocortisone	PSMA	mCRPC	I.V.	

Table 19.5 (continued)

Radiopharmaceutical	Target	Cancer type indicated	Route of administration	Clinical trial
^{177}Lu-DOTA-huJ591	PSMA	Non-prostate solid tumors	I.V.	Phase I
[177]Lu-Rosopatamab (TLX591)	PSMA	mCRPC	I.V.	Phase I/II
[227]Th-BAY 2315497	PSMA	mCRPC	I.V.	Phase I
[177]Lu-G250	Carbonic anhydrase	Advanced renal cancer	I.V.	Phase II
[177]Lu-Hu11B6	Kallekrein 2 (hK2)	Prostate cancer	I.V.	Phase I
[225]Ac-JNJ69086420	Kallekrein 2 (hK2)	Prostate cancer	I.V.	Phase I
^{90}Y-OSTA101	DFZ10	Relapsed or refractory synovial sarcoma	I.V.	Phase I
[227]Th-Anetumab (BAY2287411)	Mesothelin	Mesothelin positive cancer	I.V.	Phase I
[131]I-Anti-HER2 fragment CAM-H2	HER2	Advanced metastatic HER2 positive breast, gastric and GEJ cancer	I.V.	Phase I
[227]Th-BAY2701439	HER2	Advanced metastatic HER2+ breast, gastric and GEJ cancer	I.V.	Phase I
[225]Ac-FPI-1434	IGFR1	Advanced solid cancers	I.V.	Phase I
^{90}Y-FF-21101	p-cadherin	P-Cadherin positive tumors	I.V.	Phase I
[212]Pb-TCMC-Trastuzumomab	HER2	Ovarian cancer	Intra-peritoneal	Phase I
[177]Lu or [225]Ac Miltuximab	Glypican-1 (GPC-1)	Solid tumors expressing Glypican-1 (GPC-1)	I.V.	Phase I

19.7.1.1 Non-Hodgkin Lymphoma (NHL)

NHL is a group of blood cancers that includes all types of lymphomas in which the body produces too many lymphocytes. The specific characteristic of Hodgkin lymphoma (HL) is that multinucleated Reed-Sternberg cells (RS cells) are present in the patient's lymph nodes. Diffuse large B-cell lymphoma (DLBCL) is the most aggressive type of NHL. This fast-growing lymphoma comes from abnormal B cells in the blood.

The mAbs that target specific antigens on B cells include anti-CD20 antibodies (Zevalin® and Bexxar®), anti-CD22 antibodies (LL2), and anti-HLA-DR10β (LYM-1). While several clinical investigations were performed with all these antibodies, only Zevalin® and Bexxar® received FDA approval in 2002 and 2003 for the treatment of patients with CD20-positive, relapsed or refractory, low-grade, follicular, or transformed NHL, including patients with rituximab-refractory NHL.

[111]In- and ^{90}Y-Labeled Zevalin

Zevalin (ibritumomab tiuxetan) is the immunoconjugate resulting from a stable thiourea covalent bond between the mAb ibritumomab and the linker-chelator tiuxetan. The approximate molecular weight of ibritumomab tiuxetan is 148,000 Da. The antibody moiety of Zevalin is ibritumomab, a murine IgG$_I$ kappa mAb directed against the CD20 antigen. Each single-use vial includes 3.2 mg of ibritumomab tiuxetan in 2 mL of 0.9% Sodium Chloride.

Two separate and distinctly labeled kits are required for preparation of ^{111}In-Zevalin and

^{90}Y-Zevalin. To prepare ^{111}In-Zevalin, ^{111}In Chloride sterile solution (5.5 mCi/0.5 mL) is first mixed with 50 mM sodium acetate buffer (0.6 mL) and the mixture is then added to 1 mL of Zevalin (1.6 mg) solution in the reaction vial. Incubate the reaction mixture at RT for 30 min. At the end of incubation, add the formulation buffer to make the final volume to 10 mL. Similarly, to prepare ^{90}Y-Zevalin, ^{90}Y-chloride (40 mCi/0.5 mL) is first mixed with 50 mM sodium acetate buffer and then mixed with 1.3 mg of antibody (2.1 mg). At the end of 30 min incubation period, a formulation buffer is added to the incubation mixture to make the final volume of 10 mL. The radiochemical purity by TLC method ≥95%. The specific activity of ^{90}Y-Zevalin is around 20 mCi/mg of antibody.

^{131}I-Bexxar

The BEXXAR® therapeutic regimen is composed of the mAb tositumomab and the radiolabeled mAb ^{131}I-tositumomab. Tositumomab is a murine IgG$_{2a-\lambda}$ mAb directed against the CD20 antigen,

produced in mammalian cells. The approximate molecular weight of tositumomab is 150 kD.

Tositumomab is supplied as a sterile, pyrogen-free, clear to opalescent, colorless to slightly yellow, preservative-free solution that must be diluted before intravenous administration. The formulation contains 100 mg/mL maltose, 8.5 mg/mL sodium chloride, 1 mg/mL phosphate, 1 mg/mL potassium hydroxide, and water for injection, USP. The pH is approximately 7.2. Tositumomab is covalently linked to ^{131}I, and is supplied as a sterile, clear, preservative-free liquid. The drug product formulation contains 0.9–1.3 mg/mL ascorbic acid, 1–2 mg/mL maltose (dosimetric dose) or 9–15 mg/mL maltose (therapeutic dose), 4.4–6.6% (w/v) povidone, and 8.5–9.5 mg/mL sodium chloride. The pH of the drug product is approximately 7.0.

Clinical Studies

The protocols used for the administration of both Zevalin® and Bexxar® in eligible patients are summarized in Table 19.6. Both agents are

Table 19.6 Zevalin and Bexxar: recommended dose and administration

	Zevalin®	Bexxar®
mAb	Ibritumomab	Tositumomab
Radiolabeled mAb	^{111}In or ^{90}Y-Ibritumomab tiuxetan	^{131}I-Tositumomab
Biodistribution/ Dosimetric dose (Day 0)	Predosing: Rituximab, 250 mg/m^2 *Followed by*: ^{111}In-Zevalin: 185 MBq (5 mCi)	Predosing: Tositumomab 450 mg *Followed by*: ^{131}I-Tositumomab: 185 MBq (5 mCi)
	Imaging study: At 48–72 h	WB scan: At 1 h and days 3–4 and 6–7
Therapeutic dose	Only if the biodistribution is normal	Determine residence time (RT), and estimate patient specific therapy dose
	Predosing: Rituximab, 250 mg/m^2 *Followed by*: ^{90}Y-Zevalin: 1.184 MBq (32 mCi) *OR* 14.8 MBq (0.4 mCi)/kg	Predosing: Tositumomab 450 mg *Followed by*: ^{131}I-Tositumomab dose estimated based on RT and 75 or 65 cGy whole body radiation dose. Therapy dose may be between 1.85 and 5.55 GBq (50–150 mCi)
	Therapy dose on days 7–9	Therapy dose on days 8–14

administered in two steps; first a Biodistribution imaging study (with ^{111}In-Zevalin) or a dosimetry imaging study (with ^{131}I-Bexxar) is performed. Subsequently, the therapy dose is administered. It is important for both agents to have predosing with cold anti-B1 antibody to saturate the non-tumor cell CD20 antigen burden to achieve tumor-specific targeting of the antibody [59, 60]. Both Zevalin® and Bexxar® were FDA approved as a single-injection therapeutic agents for RIT of NHL in non-myeloablative regimens where the total therapeutic dose is administered in a single dose.

Many publications reported dramatic efficacy of both these agents in patients with indolent B-cell lymphomas with ORR of 95% and CR rates of 75% in the frontline setting as a single agent and ORR rates of 60–80% and CR rates of 20–40% in patients with relapsed or refractory indolent lymphomas. Many of these responses are durable with median remission durations exceeding 6 years after frontline therapy and with 15–20% of relapsed/refractory patients enjoying remissions exceeding 5 years [59, 60]. In addition, several phase II and phase III studies in newly diagnosed patients receiving frontline therapy, either alone or as consolidation following chemotherapy, have all demonstrated outstanding efficacy with ORR of 90–100% and CR rates of 60–100% [61, 62].

Despite the safety and proven efficacy of these two FDA-approved agents, RIT in NHL patients has not been widely accepted by the medical community. The marketing of Bexxar® was discontinued in 2014 but, Zevalin® remains available in the United States, however, sales are poor.

[177]Lu-Lilotomab Satetraxetan (Betalutin)

Lilotomab is a murine mAb HH1 against CD37, a glycoprotein which is expressed on the surface of mature human B cells [63, 64]. As of 2016, it was under development by the Norwegian company Nordic Nanovector ASA. In order to treat patients who received several cycles of rituximab, targeting CD37 antigen was considered an improved approach to treat lymphoma. During B-cell development, CD37 is expressed in cells progressing from pre-B to peripheral mature

B-cell stages and is absent on terminal differentiation to plasma cells. CD37 internalizes but, has modest shedding in transformed B-cells expressing the antigen. Therefore, CD37 represents a valuable therapeutic target for malignancies derived from peripheral mature B-cells, such as B-cell chronic lymphocytic leukemia (CLL), hairy-cell leukemia (HCL), and NHL [63, 65].

Lilotomab is conjugated to ^{177}Lu by means of a linker called satetraxetan, a derivative of DOTA. Preclinical studies demonstrated that ^{177}Lu-lilotomab has the potential to reverse rituximab resistance; it can increase rituximab binding and ADCC activity in vitro and can synergistically improve antitumor efficacy in vivo [65]. In 2016, a phase 1/2 clinical trial was performed in patients ($n = 74$) with indolent NHL, including patients with follicular lymphoma who failed initial anti-CD20–based immunochemotherapy or developed relapsed or refractory disease. To improve targeting of ^{177}Lu-lilotomab to tumor tissue and decrease hematologic toxicity, its administration was preceded by the rituximab and the "cold" anti-CD37 antibody lilotomab. Patients received a single dose of ^{177}Lu-Lilotomab (15–20 MBq/kg). With a single administration, the overall response rate was 61% (65% in patients with FL), including 30% complete responses. The overall median duration of response was 13.6 months (32.0 months for patients with a complete response). The study concluded that ^{177}Lu-lilotomab may provide a valuable alternative treatment approach in relapsed/refractory non-Hodgkin's lymphoma, particularly in patients with comorbidities unsuitable for more intensive approaches. In June of 2020, the FDA granted Fast Track designation to ^{177}Lu-lilotomab (Betalutin).

[227]Th-Epratuzumab mAb

[227]Th-Epratuzumab, anti-CD22-TTC mAb (Bayer) BAY 1862864 is an α-particle emitting [227]Th-labeled CD22-targeting antibody. CD22 belongs to the B cell-specific immunoglobulin superfamily and is expressed on the vast majority of R/R-NHL but, is absent on the surface of stem cells, B cell progenitors, and plasma cells [66].

The validity of the CD22-targeting approach has been shown previously in phase III studies of the recombinant anti-CD22 immunotoxin, moxetumomab pasudotox, in patients with CD22-positive hairy cell leukemia and ^{90}Y-epratuzumab (anti-CD22 antibody) tetraxetan in patients with NHL [67]. The [227]Th-epratuzumab conjugate is composed of an anti-CD22 humanized mAb (epratuzumab; Immunomedics, Inc., NJ) conjugated to the 3,2-HOPO chelator at a chelator-antibody ratio of 0.8 and then labeled with thorium-227 at a nearly 100% yield.

A first-in-human dose-escalation phase I study evaluated [227]Th-Epratuzumab in patients ($n = 21$) with CD22-positive relapsed/refractory B cell non-Hodgkin's lymphoma (R/R-NHL) [68]. The starting dose of 1.5 MBq (2 or 10 mg antibody) and the dose was then escalated in ~1.5 MBq increments (10 mg antibody) until the MTD was reported. However, MTD was not reached in this study but, two hematological-related DLTs at 4.5 MBq dose level were reported. The ORR was 25% including one complete and four partial responses. The ORR was 11% (1/9) and 30% (3/10) in patients with relapsed high- and low-grade lymphomas, respectively.

19.7.1.2   Leukemias

Acute myeloid leukemia (AML) is a hematologic malignancy characterized by an uncontrolled proliferation of abnormal myeloid blasts unable to differentiate into healthy mature cells. AML starts in the bone marrow but, most often, it quickly moves into the blood, as well. It may even spread to lymph nodes, liver, and spleen. The standard of care treatment in AML is chemotherapy, followed by bone marrow transplant (BMT), also referred to as a hematopoietic stem cell transplant (HSCT). Prior to BMT, the non-targeted intensive chemotherapy conditioning that is the current standard of care is not well tolerated by most older patients. Although allogeneic HCT can offer the best and sometimes the only, chance for cure, the conditioning regimen often fails to eradicate the target malignancy or is associated with fatal toxicities. It is therefore important to develop new approaches to improve control for diseases such as AML, acute lympho-blastic leukemia (ALL), and high-risk myelodysplastic syndrome (MDS) while limiting the toxicity of the conditioning regimen for patients undergoing HCT. Unlike normal cells, myeloid cells are characterized by the expression of CD45, a protein tyrosine phosphatase, and CD33 antigen, a sialic acid transmembrane receptor, both involved in modulation of immune cell functions [69]. Anti-CD45 mAb (BC8) and anti-CD33 mAb (M195), labeled with β- and α-emitting radionuclides, are being developed for RIT in order to deliver high doses of radiation directly to bone marrow, spleen, and other affected disease sites, while sparing other organs.

[131]I-Apamistamab (Iomab-B™)

Iomab-B is a radioimmunoconjugate consisting of anti-CD45 mAb BC8, a murine IgG$_1$ labeled with ^{131}I radionuclide. Iomab-B was first developed at the Fred Hutchinson Cancer Research Center, where it has been studied in several Phase I and II trials in almost 300 patients with leukemias and lymphomas [70]. Iomab-B has been granted Orphan Drug Designation for relapsed or refractory AML in patients 55 years and above by the US FDA and the European Medicines Agency.

Iomab-B in 2021 completed recruitment for the pivotal Phase 3 SIERRA (Study of Iomab-B in Relapsed or Refractory AML) trial, a randomized controlled clinical trial in 150 patients (≥55 years). The SIERRA trial is being conducted (by Actinium Pharmaceutical Inc.) in the USA with the primary endpoint of durable Complete Remission (dCR) at 6 months and a secondary endpoint of overall survival at 1 year. Each patient will have a dosimetric study with 185 MBq (5 mCi) of Iomab-B and followed by a therapeutic dose of (20–40 GBq) a week later. Upon approval, Iomab-B is intended to prepare and condition patients for a BMT. Based on safety data from 113 patients, representing 75% of patient enrollment on the SIERRA trial, it was recently reported that Iomab-B has enabled 100% of patients receiving a therapeutic dose (88/113) to proceed to BMT compared to 18% of patients receiving physician's choice of salvage therapy on the control arm [71].

[211]At-BC8-B10 mAb

[211]At, an α-emitter, is being investigated with anti-CD45 mAb as a lower-toxicity alternative to ^{131}I based anti-CD45 mAb RIT for bone marrow ablation in preparation for BMT. [211]At-BC8-B10 was developed for targeting CD45, a tyrosine phosphatase protein expressed at the surface of leukemia blast cell. A cGMP procedure and quality controls were developed for the preparation of astatinated anti-CD45 mAb for clinical trials [47]. Recruitment of patients is in progress for Phase I/II studies to determine potential side effects as well as the most efficient dose (NCT03128034). Another investigation of [211]At-BC8-B10 for the treatment of non-malignant diseases should start the recruiting phase soon (NCT04083183).

[225]Ac-Lintuzumab (Actimab-A)

Lintuzumab (or HuM195) is a humanized mAb for targeting CD33 with high affinity and without specific immunogenicity. Lintuzumab also induces antibody-dependent cell-mediated cytotoxicity and can fix human complement in vitro [72]. Historically, [213]Bi was the first α-emitter to reach clinical phase with [213]Bi-lintuzumab for treatment of AML. Phase I/II studies demonstrated the safety and potential clinical utility of targeted alpha therapy in AML [73]. A phase I/II complementary study demonstrated that sequential administration of cytarabine before treatment with [213]Bi-lintuzumab injected doses (18.5–46.25 MBq/kg) could induce complete remission in some patients. These results are attributed to the cytarabine that reduces tumor volume, improving the impact of radiations of [213]Bi-lintuzumab [72].

The dose-escalation studies with [225]Ac-Lintuzumab in patients with AML established that the MTD was 111 kBq/kg [74]. From these first results, investigations were pursued in a phase II trial in patients with untreated AML who were treated with two administrations of 55 or 74 kBq/kg [75]. A phase I dose-escalation study was also performed using fractionated doses of [225]Ac-lintuzumab in combination with low-dose cytarabine (a chemotherapy agent for inhibition of cell proliferation by interaction with DNA) [76] or associated with venetoclax, a BCL-2 inhibitor inducing cells apoptosis [77].

[211]At-OKT10-B10 mAb

The majority of patients with multiple myeloma (MM) ultimately die of progressive disease despite high rates of initial response to novel agents. While complete response (CR) is achievable in a significant subset of patients, most of these individuals relapse as a consequence of minimal residual disease (MRD) defined by occult foci of treatment insensitive tumor cells clones. High dose chemotherapy followed by autologous stem cell transplantation (ASCT) improves response but, relapse remains virtually inevitable. Daratumumab is an anti-CD38 directed monoclonal antibody approved for the treatment of multiple myeloma (MM) and functions primarily via Fc-mediated effector mechanisms, such as complement-dependent cytotoxicity (CDC), antibody-dependent cell cytotoxicity (ADCC), antibody-dependent cellular phagocytosis, and T-cell activation.

OKT10 is a mouse Anti-CD38 recombinant Antibody (clone OKT10). [211]At-OKT10-B10 is a radiolabeled immunoconjugate. Two phase I trials were reported for multiple myeloma. The clinical studies will be evaluated in combination with chemotherapeutic agents such as melphalan (NCT04466475) or cyclophosphamide/fludarabine (NCT04579523).

19.7.2 Solid Tumors

As previously mentioned, there are several antigenic targets for RIT of solid tumors. However, solid tumors are more resistant to radiation and less accessible to large molecules, such as antibodies. As a result, RIT of solid tumors has not provided the clinical impact observed with RIT in hematological malignancies [58]. Radiolabeled antibodies must overcome a number of barriers before they can effectively irradiate solid tumor targets [78]. They must extravasate and diffuse across an interstitial fluid space that is characterized by pressure gradients opposing macromolecular transport, and penetrate throughout

antigen-positive tumors, wherein a high antigen concentration itself presents a binding-site barrier. These barriers, along with the long circulation half-life of antibodies, lead to high bone marrow absorbed doses and insufficient dose delivery to tumors. Greater absorbed dose is required to effectively treat solid cancers. The hematological malignancies tend to be more radio-sensitive than solid tumors, with complete responses possible with radiation doses in the range of 1500–2000 cGy, as compared with the 3500–10,000 cGy required to demonstrate a clinical response in solid tumors [79].

Radiolabeled full-length antibodies remain in circulation for a longer time period (several days) compared to peptides. While the long half-life is beneficial in maintaining high serum concentrations of the radiolabeled antibody to allow maximum tumor targeting, it also exposes the bone marrow to prolonged exposure to the radioisotope. As a result, bone marrow suppression is almost exclusively the dose-limiting toxicity (DLT) for full-length antibodies in the treatment of solid tumors. Low therapeutic index remains a key problem for directly radiolabeled radioimmunoconjugates, especially in the treatment of macroscopic solid tumors. To reach significant antitumor efficacy, injected activities of radiolabeled antibodies must be close to toxic doses. However, some RIT approaches (such as dose-fractionation and pre-targeting) have shown promising results in specific clinical settings, especially for small-volume tumors disseminated to bone marrow or at an early minimal residual disease stage.

Table 19.5 shows radiolabeled mAbs under clinical investigation for RIT of hematological malignancies and solid tumors. In 2017, the FDA granted breakthrough designation to Omburtamab for metastatic neuroblastoma. The FDA approved [131]I-8H9 radioimmunoconjugate (anti-B7-H3; burtomab/omburtamab) for pediatric neuroblastoma patients with CNS metastasis and many other ongoing late-phase trials with this radioimmunoconjugate using the strategy of intracompartmental delivery of antibody [25]. Among the other solid tumors, TRT of prostate cancer is one of the most well-studied areas of investigation

following the discovery of prostate-specific membrane antigen (PSMA). Since many RIT clinical studies were performed with anti-PSMA mAbs in the last 20 years, a more detailed summary of clinical data is discussed below.

19.7.2.1 Prostate Cancer

In 1987, prostate-specific membrane antigen (PSMA) was discovered as a novel antigenic marker in prostate cancer cells and in the serum of prostate cancer patients [80]. PSMA, is also known as glutamate carboxypeptidase II (GCPII), N-acetyl-L-aspartyl-L-glutamate peptidase I (*NAALADase I*) or N-acetyl-aspartyl-glutamate (*NAAG*) *peptidase*, and is an enzyme that is encoded by the *folate hydrolase* (FOLH1) gene in humans [81]. PSMA/GCPII plays separate roles and in different tissues, such as the prostate, kidney, small intestine, central and peripheral nervous system and, thus, is recognized by different names. In the last two decades, PSMA has emerged as the pre-eminent prostate cancer target for developing both diagnostic and therapeutic agents in prostate cancer [82].

In 1997, Bander and his colleagues at Weill Cornell Medicine in New York reported the development of four mAbs (J591, J415, J533, and E99) to the extracellular domain of PSMA and demonstrated antibody induced internalization of PSMA (Chap. 22, Fig. 22.6) [83, 84]. Based on preclinical studies, J591 mAb was selected for the development of targeted radiopharmaceuticals for imaging and therapy [85–87]. Saturation-binding studies demonstrated that J591 mAb binds to PSMA with extremely high affinity ($K_d = 1.83 \pm 1.21$ nM). The bifunctional DOTA chelator was conjugated to humanized J591 mAb. The DOTA-J591 mAb (5–6 DOTAs/IgG) was labeled with ^{111}In or [89]Zr for imaging studies and ^{90}Y, ^{177}Lu, or [225]Ac for RIT.

RIT with ^{177}Lu-DOTA-huJ591 mAb

The clinical trials with ^{90}Y or ^{177}Lu labeled huJ591 mAbs started 20 years ago at Weill Cornell Medicine in New York. Two independent RIT phase I trials have been performed using ^{111}In/[90]Y- or ^{177}Lu-labeled DOTA-huJ591 in patients with mCRPC [88–91]. All patients

received a total of 20 mg of J591 mAb containing both, radiolabeled DOTA-J591 and naked J591 mAb. These trials defined the maximum tolerated dose (MTD), dosimetry, pharmacokinetics, and human anti-humanized antibody (HAHA) response, and demonstrated preliminary evidence of anti-tumor activity. With ^{90}Y, 0.647 GBq/m^2 the dose level was determined to be the MTD. With ^{177}Lu, 2.59 GBq/m^2 the dose level was determined to be the MTD. ^{177}Lu was chosen for further development based upon its physical properties, especially since the low energy beta particles deliver a lower radiation dose to bone marrow relative to the higher energy beta particles from ^{90}Y [92–94].

In a dual-center phase II study, two cohorts of patients (total $n = 47$) with progressive mCRP received one dose of ^{177}Lu-J591 (2.405 GBq/m^2, or 2.59 GBq/m^2). Sites of prostate cancer metastases were targeted in 94% of patients as determined by planar imaging. All patients experienced reversible hematologic toxicity with grade 4 thrombocytopenia occurring in 47% of patients. Patients ($n = 32$) who received a single dose of 2.59 GBq/m^2 had >30% PSA decline in 47% of patients and longer survival of 21.8 months [95, 96]. The safety and efficacy data of the phase II study are summarized in Table 19.7.

Dose-fractionation is a practical strategy to decrease the dose to bone marrow while increasing the cumulative radiation dose to the tumor at an optimal dose-rate [92–94]. In a phase I/II clinical study with a phase I dose-escalation component followed by phase IIa, dosing was performed using two dosing cohorts selected for exploration

(2.96 GBq and 3.33 GBq/m^2 total dose divided into two doses 2 weeks apart). As demonstrated before, there appeared to be a dose-dependent response for PSA decline and overall survival. At the highest cumulative dose (3.33 GBQ/m^2), 35% of patients had reversible grade 4 neutropenia, and 58.8% of patients had thrombocytopenia. This dose showed a greater PSA decline with a median survival of 3.5 years [97, 98]. The safety and efficacy data are given in Table 19.7. In addition, those with lower PSMA uptake on ^{177}Lu SPECT had a lower likelihood of significant PSA decline.

In order to evaluate the value of combination therapy, a phase 1 clinical study tested the therapeutic value of the combination of docetaxel chemotherapy with fractionated-dose ^{177}Lu-J591 mAb therapy [99]. In a pilot study, 15 patients with mCRPC received standard docetaxel (75 mg/m^2) in 21-day cycles, with cohorts of escalating fractionated doses of ^{177}Lu-J591 during cycle 3 (highest planned total dose 80 mCi/m^2). This study demonstrated safety of the combination with early evidence of activity, with 73% achieving >50% PSA decline. Toxicities were comparable to prior ^{177}Lu-J591 studies [99]. Although 2-dose fractionation appears attractive alone or with docetaxel, a pilot study explored the value of "hyper-fractionated" ^{177}Lu-J591, in which low dose ^{177}Lu-J591 (25 mCi/m^2) was administered every 2 weeks until greater than grade 2 toxicity emerged [100]. As designed, dosing was limited by myelosuppression (especially thrombocytopenia) but, the regimen did not appear more favorable than 2-dose fraction-

Table 19.7 RIT with ^{177}Lu-huJ591 safety and efficacy studies: PSA decline and toxicity

	Single dose		Cumulative dose given in two doses		
Response	2.405 GBq/m^2	2.59 GBq/m^2	1.48–2.59 GBq/m^2	2.96 GBq/m^2	3.33 GBq/m^2
Number of patients (n)	15	32	16	16	17
Any PSA decline (%)	46.7	65.6	37.5	50.0	87.5
>30% PSA decline (%)	13.3	46.9	12.5	25.0	58.8
>50% PSA decline (%)	6.7	12.5	6.3	12.5	29.4
Median survival (months)	*11.9*	*21.8*	*14.6*	*19.6*	*42.3*
Platelets Grade-4	27.0	56.3	20.0	43.8	58.8
Platelet transfusion	7.0	41.0	0.0	31.3	52.9
Neutropenia Grade-4	0.0	37.5	0.0	31.3	29.4
Febrile neutropenia	0.0	2.1	0.0	0.0	5.8

Fig. 19.9 ^{225}Ac-J591 mAb targeted therapy in a patient with mCRPC. The patient had prior treatment with two cycles of ^{177}Lu-PSMA-617 and when the disease was progressive received 4 MBq of ^{225}Ac-J591. ^{68}Ga-PSMA-PET scans before and after treatment show evidence of treatment response. The patient also had 86% decline in PSA level. (Images provided by Dr. Tagawa at Weill Cornell Medicine, NY)

ation and is also less convenient for patients. Therefore, this regimen is not being further explored.

RIT with ^{225}Ac-DOTA-huJ591 mAb

Twenty years ago, ^{213}Bi-J591 was proposed as a radiopharmaceutical for α-particle therapy of prostate cancer [101]. While ^{213}Bi demonstrated promising efficacy in the preclinical setting, it is not an appropriate radionuclide for whole IgG mAb with a longer circulation time. An alternative to ^{213}Bi was to utilize its parent nuclide, ^{225}Ac, which has a 10-day half-life and 5 net α-particles and 3 beta particles per decay. Also, as a trivalent metal, ^{225}Ac binds to the same DOTA chelator like ^{177}Lu.

Based on human biodistribution data and assuming RBE for alpha emitters is 5, the radiation dosimetry calculations suggested that administration of 6.06 MBq (164 μCi) of ^{225}Ac-J591 mAb may deliver ~2.0 Gy to the bone marrow. A phase I dose escalation study was designed to determine the dose-limiting toxicity (DLT) and the maximum tolerated dose (MTD) of ^{225}Ac-J591 in a single dose regimen [102, 103]. Patients received doses starting from 13.3 kBq/kg to a maximum of 93.3 kBq/kg (for an average person of 75 kg, the maximum dose administered is 7 MBq). Thirty-two patients with progressive

mCRPC were treated with ^{225}Ac-J591 in this protocol. In the dose-escalation phase of the study, there was one patient who had grade 4 thrombocytopenia and anemia. However, there was no MTD and the recommended phase 2 dose of the compound is 93.3 kBq/kg. Overall, 68.8% of patients had at least some level of PSA decline and 43.8% had a PSA decline of over 50%. The median biochemical progression-free survival in the entire population was 5.1 months and the median overall survival was 11.1 months. There were no cases of severe xerostomia. The study concluded that PSMA targeting with ^{225}Ac-J591 mAb is tolerable with early evidence of clinical activity (Fig. 19.9) in a pre-treated population with favorable patient-reported outcomes. Studies administering multiple or subsequent doses and/or combination therapy are underway.

19.8   Strategies to Increase the Therapeutic Efficacy of RIT

19.8.1   Dose Fractionation

The antitumor response of low dose rate radiotherapy is primarily due to induction of apoptosis by radiation [104, 105]. However, the degree of

antitumor response following the administration of radiolabeled mAbs depends on several variables, especially total (cumulative) radiation dose to the tumor, dose rate, and tumor radiosensitivity. Bone marrow is the dose-limiting organ in radioimmunotherapy in the absence of marrow reconstitution. Dose fractionation or multiple dosing is a practical strategy to decrease the dose to the bone marrow while increasing the cumulative radiation dose to the tumor at an optimal dose rate [106–108]. Preclinical data and clinical studies have shown that dose fractionation or multiple low dose treatments can decrease toxicity while increasing the efficacy [92–94, 109–111].

In Sect. 19.7.2.1, it was shown that a dose fractionation study was performed with ^{177}Lu-DOTA-huJ591 mAb using two dosing cohorts selected for exploration (2.96 GBq and 3.33 GBq/m^2 total dose divided into two doses 2 weeks apart). There was a dose-dependent response for PSA decline and overall survival. At the highest cumulative dose (3.33 GBQ/m^2), 35% of patients had reversible grade 4 neutropenia, and 58.8% of patients had thrombocytopenia. This dose showed a greater PSA decline with a median survival of 3.5 years [97, 98]. The cumulative radioactive dose with dose-fractionation strategy was ~20% higher compared to single dose RIT protocol.

19.8.2 Pretargeted RIT (PRIT)

As discussed earlier, PRIT is an indirect method and basically consists of three steps. In step 1, the targeting vector (antibody or antibody derivative) designed to bind both the target antigen and a radiolabeled small molecule is injected. In step 2A, the targeting vector is allowed to distribute for several days to achieve maximum tumor-specific binding and optimal clearance from circulation. Certain PRIT protocols may include an extra step (step 2B), in which a clearing agent is introduced to remove the unbound targeting vector from the circulation. In step 3, a complementary radiolabeled small molecule is administered, which will bind rapidly to the vector already bound to the tumor antigen. The

radioimmunoconjugate is formed in vivo at the tumor site and the free radiolabeled small molecule in blood will be excreted rapidly from the body. The PRIT method provides low background radioactivity and high TI and/or therapeutic efficacy. In the 1980s, it was originally postulated that Bs-mAb could be prepared with one arm binding selectively to a tumor, while the other arm would be derived from an anti-chelate antibody. Hapten is a small molecule that, when attached to a larger carrier protein, can elicit the production of antibodies that bind specifically to it. Originally, the indium-benzyl-EDTA complex was used as a hapten and Bs-Abs binding carcinoembryonic antigen (CEA), and the hapten were used for imaging tumors [112]. Biotin, which binds very tightly to avidin or streptavidin, was also proposed. The historical development of the PRIT method was extensively discussed in several reviews [113–116]. Several pretargeting methods developed in the last three decades have been described as follows:

(a) The streptavidin/avidin–biotin system is based on the strongest noncovalent biological interaction known between biotin (also known as vitamin B7) and avidin or streptavidin.

(b) Bs-Abs with one arm directed against the tumor antigen and one against a radiolabeled hapten (a small molecule that when attached to a larger carrier protein, can elicit the production of antibodies), such as indium-DTPA and histidine-succinyl-glycine (HSG) peptide).

(c) Enhanced affinity system: Bivalent hapten is used so that two Bs-Abs could be crosslinked at the cell surface resulting in enhanced affinity.

(d) Pretargeting method based on the hybridization of an oligonucleotide conjugated to an antibody and a radiolabeled complementary oligonucleotide. Since morpholine backbones are used, the method is also known as MORF/cMORF pretargeting).

(e) Bio-orthogonal click chemistry can also be an effective strategy because it exploits pairs of

functional groups that rapidly, selectively, and covalently bind in biological systems. One of the proposed click chemistry techniques is the inverse electron demand Diels–Alder (IEDDA) cycloaddition of trans-cyclooctene (TCO) and tetrazine (Tz) [72].

Preclinical studies have clearly documented the potential advantages of pretargeting strategies for both imaging studies and RIT. However, these methods require careful optimization, (a) for the design of the appropriate pretargeting reagents (such as Bs-Ab immunoconjugates specific tumor antigens, (b) the small molecules selected to carry the radioactivity, and (c) for the dosing and administration protocols to translate pretargeting methods into a clinical reality.

19.8.3 Combination RIT

RIT of metastatic cancers using a single-dose administration of a radioimmunoconjugate is not a practical approach because solid tumors are more resistant to radiation and less accessible to large proteins, such as intact whole IgG antibody molecules. Even though the potential of radiolabeled mAb as a stand-alone therapeutic strategy to act as a magic bullet is promising, the therapeutic clinical efficacy of radioimmunoconjugates remains limited in solid tumors. However, some RIT approaches have shown promising results in specific clinical settings, especially for small-volume tumors disseminated to bone marrow or at an early minimal residual disease stage [117]. Fractionation of injected activity or maximum tolerated dose (MTD), as a strategy to improve efficacy, has been shown to reduce hematologic toxicity as a consequence of faster and more efficient bone marrow repair than tumor cell repair. Consequently, bone marrow should withstand the injection of higher cumulative activity, resulting in higher tumor dose and improved efficacy. Fractionated administration of ^{177}Lu-DOTA-huJ591 allowed higher cumulative radiation dosing. The frequency and depth of PSA decreased, while overall survival, and toxicity (dose-limiting myelosuppression) increased with higher doses [97, 98].

Combination RIT is the approach where any substance, drug, and moiety that has the potential to either cause apoptosis, decrease interstitial pressure, degrade the extracellular matrix (ECM), overcome the junctional barrier, overcome immunosuppression, or act as a radiosensitizer is used, along with RIT, to enhance RIT delivery and to improve therapeutic efficacy [118]. Combination therapy has been the rule in chemotherapy for decades. Combination of RIT, especially fractionated RIT, with radio-sensitizing agents also represents an attractive option in poor prognostic metastatic solid tumors. The uptake of antibodies into the tumor area is highly intermittent due to elevated interstitial fluid pressure (IFP). Combination of RIT with high-intensity focused ultrasound (HIFU) showed higher penetration of mAb. The combination of RIT with paclitaxel also produced enhanced accumulation of mAb in tumor tissue. Tanexe induced apoptosis via disruption of the microtubular network associated with the reduction in interstitial pressure.

The immune system maintains immunity via immune surveillance and editing, where T cells continually patrol to find and kill antigens. Tumor tissue can proliferate in part because immune surveillance is blocked by regulatory immune cells, such as Tregs and tumor-associated macrophages. Antibodies such as pembrolizumab, nivolumab, and atezolizumab that target the key immune checkpoint receptors such as CTLA4 and PD-1, or its ligand PD-L1, relieve blockade of immune effector cells and show antitumor effects [6]. Ionizing radiation-(IR)induced tumor regression outside the radiation field is termed as abscopal effect [119]. It has been shown that external beam radiation therapy and brachytherapy could enhance or augment the anti-tumor immune response of checkpoint blockade by the antibodies [120, 121]. Thus, RIT, especially, fractionated RIT strategy and immune checkpoint inhibitors, could act synergistically in metastatic tumors, and improve therapeutic efficacy.

RIT, in combination with synergistic modalities can overcome various internal and external

barriers, and clear the pathway for mAb penetration into solid tumors, and, therefore, is highly promising and could contribute to substantial gains in overall survival for patients with solid tumors.

19.9 Immuno-PET and SPECT of Cancer

In the early 1980s, clinical nuclear imaging studies provided the proof of principle that tumor lesions could be imaged using radiolabeled mAbs. FDA approved four radiolabeled (with ^{111}In or ^{99m}Tc) mAbs for diagnostic imaging studies (Table 19.3). However, the diagnostic accuracy of these antibody-based scans was limited due to poor resolution of the Anger gamma cameras at that time. In addition, with the introduction of FDG-PET and PET/CT, antibody-based imaging for staging and restaging of cancer patients became obsolete [45]. With the availability of relatively long half-life positron emitters (^{124}I, $T_{1/2}$ = 4.2 days and ^{89}Zr, $T_{1/2}$ = 3.266 days), a revival of imaging with radiolabeled antibodies based on PET imaging has taken place. By combining the sensitivity of PET imaging and the specificity of antibodies, immuno-PET imaging has become a promising tool for monitoring the heterogeneity of specific gene expression and predicting the efficacy of RIT [123, 122]. ^{111}In-labeled mAbs are still useful for the initial development work based on SPECT imaging but, the lack of absolute quantitation with SPECT may not support clinical utility for dosimetry studies and to monitor response to RIT.

19.9.1 ^{89}Zr for ImmunoPET

The cyclotron production of ^{89}Zr was first reported in 1990 [124]. ^{89}Zr half-life is quite appropriate to study antibody biodistribution and is in the same range as the therapeutic radiometals such as ^{90}Y and ^{177}Lu. Several radiometals have been investigated for long-duration PET

studies, including ^{64}Cu, ^{86}Y, and ^{66}Ga, although ^{89}Zr best fulfills many of the desired properties with its 3.27-days half-life and 23% positron emission. In addition, other favorable physical properties include minimal contamination from the 909-keV prompt γ-photons within the 511-keV PET energy window, as well as superior spatial resolution compared with many other positron-emitting isotopes as a result of the relatively low excess decay energy (E_{mean} = 396 keV).

In 2003, ^{89}Zr-labeled antibodies were introduced as chemical and biological surrogates for immunoPET studies to assess the biodistribution of ^{90}Y- and ^{177}Lu-labeled antibodies [125, 126]. The first human study was published in 2006 with ^{89}Zr-labeled chimeric mAb U36 in patients with squamous head and neck cancers [127]. ^{89}Zr-PET imaging localized cervical lymph node metastasis with a high accuracy (93%). It has been shown that radiation doses of RIT with ^{90}Y-ibritumomab tiuxetan (Zevalin) can be predicted by immuno-PET with ^{89}Zr-ibritumomab tiuxetan [128] and other ^{90}Y- and ^{177}Lu-labeled mAbs [129]. In the last 15 years, a number of studies have been conducted to investigate the feasibility of ^{89}Zr immuno-PET imaging for predicting the efficacy of RIT and antibody therapies, imaging target expression, detecting target-expressing tumors, and the monitoring of anti-cancer chemotherapies. Many FDA-approved mAbs for immunotherapy (such as trastuzumab, bevacizumab, cetuximab, and rituximab) have been labeled with ^{89}Zr (Table 19.8) and were evaluated as radiopharmaceuticals for immunoPET [130, 131]. PET/CT scans of ^{89}Zr-rituximab and ^{89}Zr-trastuzumab are shown in Figs. 19.10 and 19.11. ^{111}In, ^{177}Lu-labeled huJ591 (anti-PSMA) mAb imaging studies showed excellent targeting of PSMA expression in mCRPC. However, the ^{89}Zr-IAB2M minibody (derived from J591 mAb) detected more lesions than bone scan and FDG-PET (Fig. 19.12). Immuno-PET using ^{89}Zr has the advantage of a high resolution and high specificity but, compared to ^{18}F-labeled radiotracers, patients generally receive higher radiation dose from ^{89}Zr-mAb PET (~20–40 mSv for 37–74 MBq) [130].

Table 19.8 Radiolabeled mAbs and fragments as molecular imaging probes for immuno-PET[a]

Radiolabeled antibody	Target	Targeting vector	Cancer types
89Zr-Df-cetuximab	EGFR	mAb	Solid tumors
89Zr-Panitumumab	EGFR	mAb	Colorectal cancer
89Zr-Df-trastuzumab	HER2	mAb	Breast cancer, esophagogastric adenocarcinoma (EGA)
64Cu-DOTA-trastuzumab	HER2	mAb	BC
89Zr-Df-Pertuzumab	HER2	mAb	BC
124I-trastuzumab	HER2	mAb	Gastric cancer, gastroesophageal cancer
64Cu-DOTA-Patritumab	HER3	mAb	Solid tumors
89Zr-GSK2849330	HER3	mAb	Solid tumors
89Zr-lumertuzumab	HER3	mAb	Solid tumors
89Zr-Df-bevacizumab	VEGF	mAb	Solid tumors
124I-huA33	A33	mAb	Colorectal cancer
89Zr-cmAb U36	CD44v6	mAb	Squamous cell carcinoma of the head and neck (HNSCC)
89Zr-RG7356	CD44	mAb	Solid tumors
89Zr-rituximab	CD20	mAb	Lymphoma
89Zr-DFO-5B1	CA19.9	mAb	Pancreatic cancer
89Zr-huJ591	PSMA	mAb	Prostate cancer
89Zr-girentuximab	CAIX	mAb	Renal cell carcinoma
124I-cG250	CAIX	mAb	Renal cell carcinoma
89Zr-DFO-MSTP2109A	STEAP1	mAb	Prostate cancer
89Zr-fresolimumab	TGF-β	mAb	Glioma
68Ga-ABY-025	HER2	Affibody	Breast cancer
68Ga-HER2-nanobody	HER2	Nanobody	Breast cancer
89Zr-IAB2M	PSMA	Minibody	Prostate cancer
68Ga-IMP288	CEA	BsAb	Medullary thyroid cancer
89Zr-AMG 211	CEA/CD3	BiTE	Gastrointestinal adenocarcinoma
89Zr-Df-IAB22M2C	CD8	Minibody	Solid tumors
89Zr-atezolizumab 111In-atezolizumab	PD-L1	mAb	Non-small cell lung cancer (NSCLC), bladder cancer, triple negative breast cancer (TNBC)
18F-BMS-986192	PD1	Adnectin (monobody)	Lung cancer
89Zr-Nivolumab	PD1	mAb	Lung cancer

[a] Table modified from Wei et al. [131]

19.9.2 124I for ImmunoPET

Based on the long half-life and physical properties of the positron-emitting isotope of iodine, 124I may be used for both imaging (positron) as well as for 131I dosimetry. The relatively low percentage of high-energy positrons (22.7%) and a high percentage of gamma photons compared to the conventional PET isotopes makes imaging with 124I technically challenging. However, optimizing image acquisition parameters and appropriate corrections within the image reconstruction process improve the image quality [135].

^{89}Zr-rituximab Immuno-PET/CT

Without preload
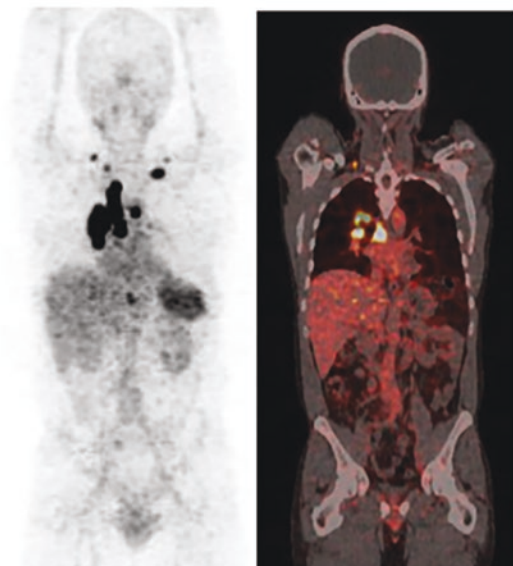
With preload
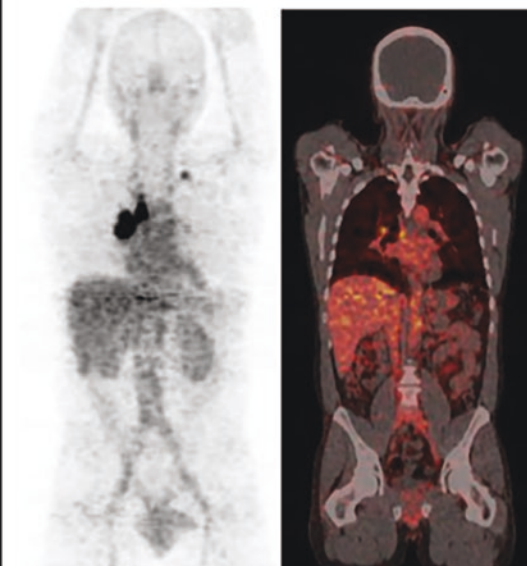
Fig. 19.10 ^{89}Zr-rituximab immuno-PET/CT images in a lymphoma patient (with CD20+ B-cell depletion) obtained 6 days after injection without and with a preload of unlabeled rituximab (250 mg/m^2) show consistently better tumor targeting without the preload. The uptake in the spleen, however, is significantly reduced with the preload. (Figure from [132])

I-124 is an attractive radionuclide for the development of mAbs for immunoPET. In 2007, ^{124}I-gerentuximab (anticarbonic anhydrase IX chimeric G250 mAb) PET clearly detected clear cell renal cancer [136]. This study indicated that immuno-PET/CT might be helpful in clinical decision making and might aid in the surgical management of small renal masses scheduled for partial nephrectomy. These promising results formed the basis for a multicenter phase III registration trial in 226 patients [137]. ^{124}I-huA33 mAb-PET images (Fig. 19.13) in a patient with colorectal cancer also showed excellent localization of lesions in the liver, 2 days post administration of the radiolabeled antibody (360 MBq/10 mg mAb) [138]. These early studies documented that immunoPET with ^{124}I can provide the tissue concentration and pharmacokinetics of radiolabeled antibodies. ^{124}I-labeled Trastuzumab, huA33, and cG250 have shown promise in human clinical trials but, there is no FDA-approved ^{124}I-labeled mAb. The major disadvantage is low resolution of PET images due to the high energy of positrons, in vivo dehalogenation of ^{124}I-labeled mAbs [135].

19.9.3 ImmunoPET: Applications

The concept of immunoPET originally meant to describe PET imaging of radiolabeled intact full-length mAbs. Now immunoPET includes radio-labeled antibody fragments or mimetics as targeting vectors. A variety of radionuclides and mAbs have been used to develop molecular imaging probes for immunoPET (Table 19.8).
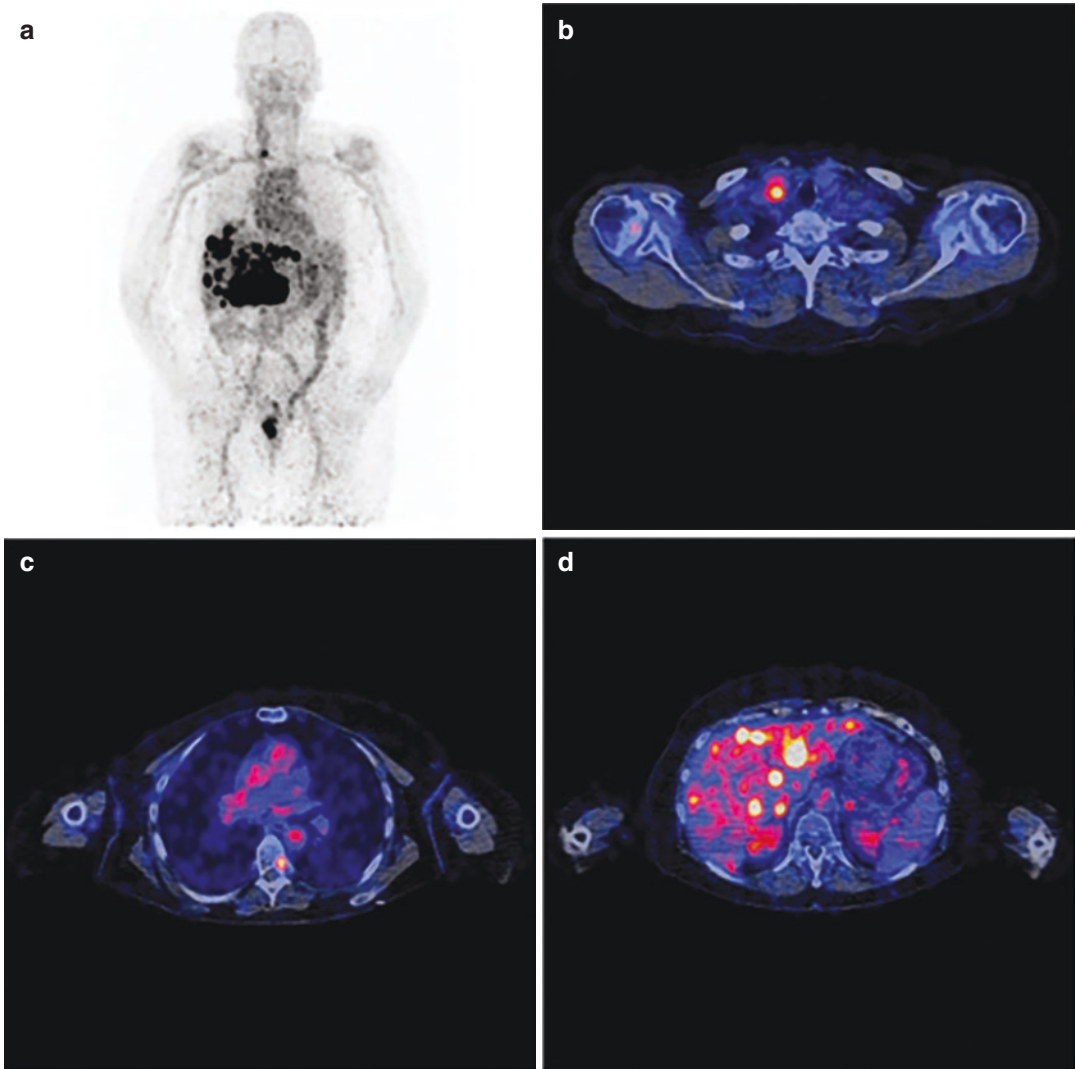
Fig. 19.11 ^{89}Zr-trastuzumab PET/CT scan in a patient with human epidermal growth factor receptor 2–positive metastatic breast cancer 4 days after injection of 89Zr-trastuzumab (37 MBq in 50 mg antibody). (**a**) The scan showing 89Zr activity in circulation, uptake in intrahepatic metastases, and intestinal excretion. (**b**) Transverse plane of fused PET/CT of chest showing tracer uptake in cervical lymph node. (**c**) Transverse plane showing tracer uptake in metastasis (left side) in T7. (**d**) Transverse plane showing tracer uptake in liver metastases. (Figure from [133])

^{99m}Tc-MDP   [^{18}F]FDG ^{89}Zr-IAB2M
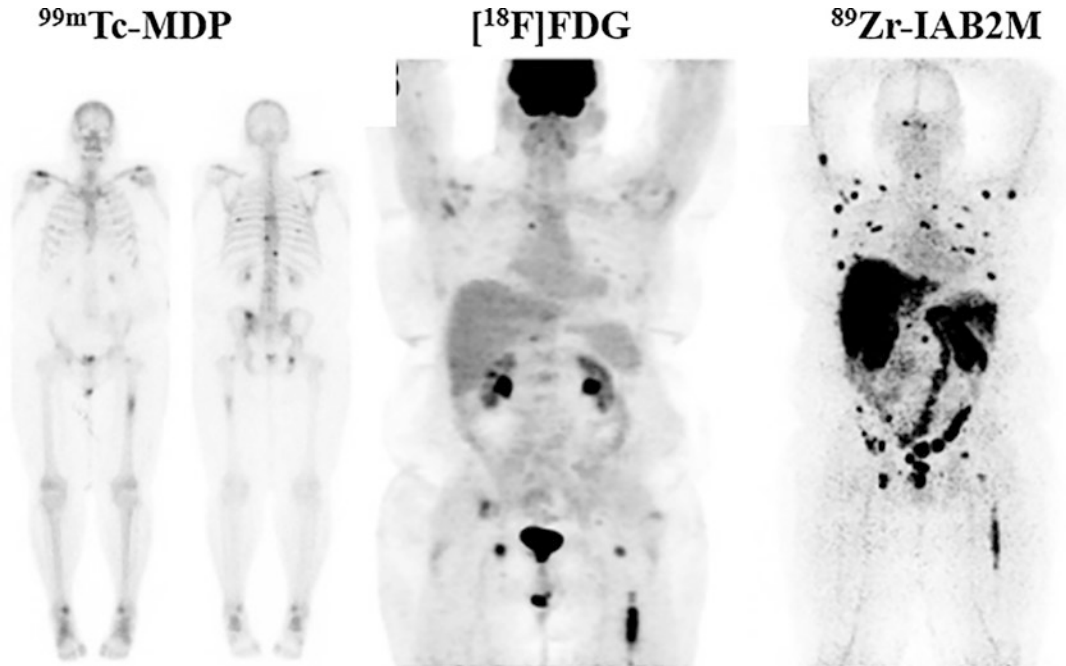
Fig. 19.12 ^{89}Zr-IAB2M-PET imaging in mCRPC. Targeting with IAB2M (minibody fragment from J591 mAb). Comparison with bone scan and FDG-PET. ^{89}Zr-IAB2M scan shows more lesions than bone scan or FDG-PET. (From [134])

^{124}I-huA33 mAb immunoPET

45 min   **2 d**   **7 d**
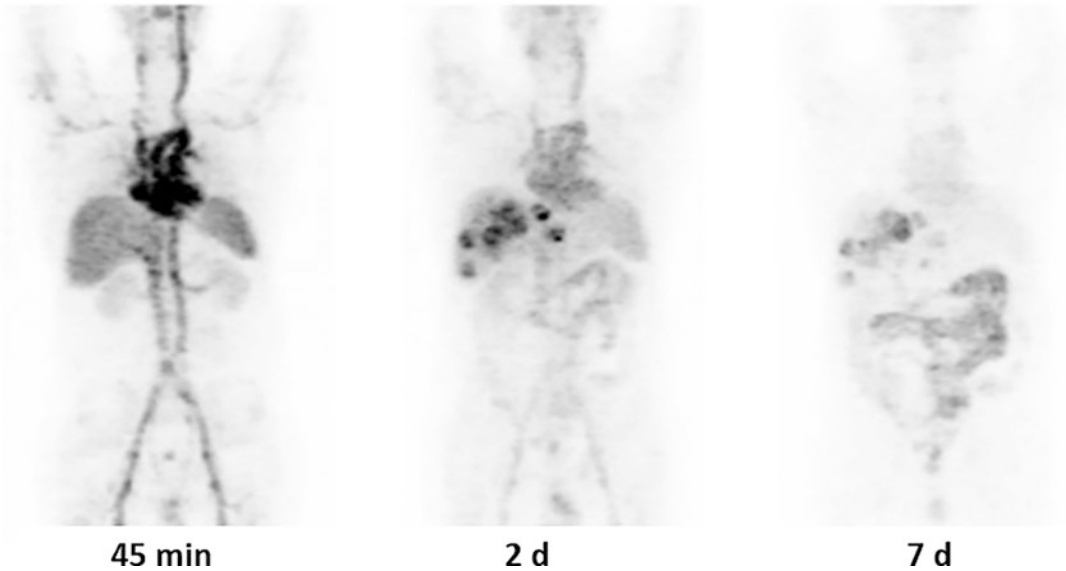
Fig. 19.13 ^{124}I-huA33 immuno-PET in a patient with colorectal cancer metastatic to liver after infusion of 361.4 MBq of ^{124}I-huA33 mAb. Initial image at 45 min shows predominant blood-pool activity. Two-day image shows excellent localization in liver lesions (SUV$_{max}$, 11.2) and some uptake in bowel. At 7 days, there is persistent uptake in liver lesions (SUV$_{max}$, 11.2), and prominent bowel uptake [138]

The clinical application of immunoPET imaging has increased our understanding of tumor heterogeneity and refined clinical disease management, and include the following applications [131, 139].

- To facilitate better management of cancer patients since it has the potential to provide excellent specificity and sensitivity in detecting primary tumors.
- To detect lymph node and distant metastases.
- Following immunoPET imaging, patients with positive findings can be selected for subsequent therapies (e.g., antibody therapy and antibody-based RIT), whereas patients with negative or heterogeneous findings may need multidisciplinary treatments.
- As a theranostic companion, immunoPET can provide radiation dosimetry prior to administering the therapeutic radiopharmaceuticals.
- ImmunoPET imaging is useful for improved triage during early disease stages and to facilitate image-guided surgery.
- The information provided by immunoPET will significantly enhance the existing diagnostic methods for better tumor characterization. One can envision that tumors may be classified not only according to their origins and mutation status but, also according to the expression of specific tumor antigens in the future.

19.9.4 Molecular Imaging for Cancer Immunotherapy

The recent success of cancer immunotherapy, especially with the checkpoint inhibitors, has renewed interest in the development of molecular imaging of immune system and tumor microenvironment. A variety of biomarkers that predict tumor response to immunotherapy have been evaluated, including the expression levels of the programmed cell death protein 1 (PD-1) or its ligand (PD-L1). The expression of these two immune markers is dynamic and depends on prior therapies [140].

The immune system maintains a delicate balance between eradicating infection/cancers and maintaining self-tolerance in part by the expression of immune checkpoints that control immune response. One major checkpoint inhibitor pathway is the PD-1 pathway. PD-1 is a negative costimulatory receptor expressed on the surface of activated T and B cells. PD-L1 is a surface glycoprotein ligand for PD-1 that facilitates immunosuppression on both antigen-presenting cells and human cancers. PD-L1 downregulates T-cell activation and cytokine secretion by binding to PD-1. Tumors exploit these checkpoint pathways by expressing coinhibitory proteins to evade antitumor immune responses. Elevated PD-L1 expression is correlated with poor prognosis in some cancers, which suggests that PD-L1 upregulation is a mechanism for tumor immune evasion. PET and SPECT imaging with radiolabeled probes targeting PD-1 and PD-L1 can provide in vivo, real-time, and non-invasive imaging of tumor biomarker expression, and immune responses to novel therapies, and, in addition, may also help to overcome some of the challenges of tumor biopsies. The FDA has approved several mAbs blocking the PD-1/PD-L1 interaction. These agents include PD-1 inhibitors nivolumab, pembrolizumab and cemiplimab, and PD-L1 inhibitors atezolizumab, avelumab, and durvalumab. Given the clinical success of PD-1 and PD-L1 inhibition for the treatment of advanced cancers, many radioligand imaging studies have targeted this receptor/ligand pair by radiolabeling PD-1 or PD-L1 antibodies.

19.9.4.1 [89]Zr-Atezolizumab

In patients with locally advanced or metastatic bladder cancer, NSCLC or triple-negative breast cancer, PET/CT imaging was performed with [89]Zr-atezolizumab prior to treatment with atezolizumab [141]. Uptake of the radiotracer was noted in the bone marrow, spleen, and tumors. Importantly, heterogeneity in uptake was observed intratumorally in large tumors as well as in different metastatic lesions in the same patient, supporting the notion of tumor biomarker heterogeneity and demonstrating the power of PET molecular imaging to visualize real-time

biomarker expression. Furthermore, on a per-lesion level, the baseline uptake on PD-L1 PET imaging was correlated with lesions demonstrating the best response to anti-PD-L1 immunotherapy. Compared with biopsy samples for PD-L1 IHC and RNA sequencing, [89]Zr-atezolizumab uptake was more strongly related to response, progression-free survival, and overall survival. These preliminary studies demonstrate the power of molecular immunoPET imaging to potentially personalize a patient's therapeutic regimen based on targeted biomarker expression [140, 141].

19.9.4.2 ^{18}F-BMS-986192 and [89]Zr-Nivolumab

In patients with advanced NSCLC, PET/CT imaging was performed with ^{18}F-BMS-986192 (adnectin, ~10 kDa and specific for PD L-1) and [89]Zr-Nivolumab (anti-PD-1 mAb) prior to treat-ment with nivolumab. Tracer uptake was heterogeneous both between patients, as well as within patients with different tumor lesions. ^{18}F-BMS-986192 identified more lesions and uptake in tumor lesions (SUV$_{peak}$), correlated with tumor PD-L1 expression, measured by IHC. [89]Zr-nivolumab uptake correlated with PD-1 positive tumor-infiltrating immune cells and demonstrated a correlation between tumor tracer uptake and response to nivolumab treatment for both tracers. These first in human studies suggest that ^{18}F-BMS-986192 and [89]Zr-nivolumab PET-CT may be useful imaging biomarkers to non-invasively evaluate PD-1 and PD-L1 expression [142, 143] (Fig. 19.14).

The clinical studies with radiolabeled antibodies and antibody fragments are very limited but, clearly demonstrated that immuno-PET provides high resolution images needed for diagno-
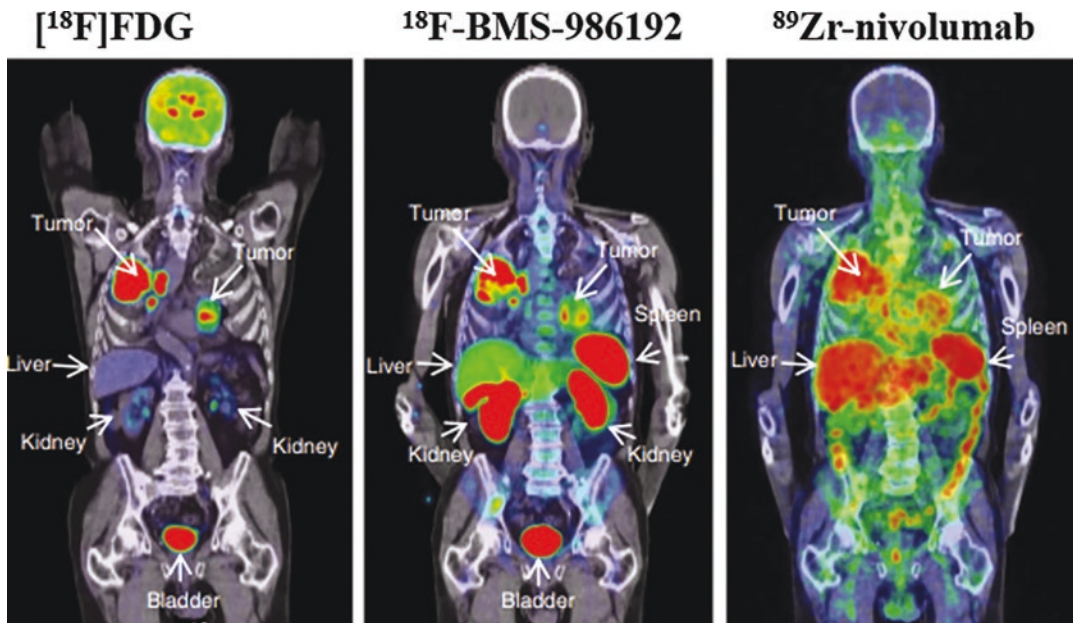
Fig. 19.14 FDG PET (225 MBq) scan demonstrates high glucose metabolism of tumors in both lungs and mediastinal lymph nodes. ^{18}F-BMS-986192 PET (146 MBq) scan at 1 h and [89]Zr-labeled Nivolumab PET (37.1 MBq) at 162 h post injection. Both immunoPET scans demonstrate heterogeneous tracer uptake within and between tumors. BMS-986192 is an adnectin, ~10 kDa, and specific for PD L-1 and nivolumab is an anti-PD-1 mAb). (Figure modified from [143])

sis and treatment assessment. More research and extensive imaging clinical trials are needed to refine immuno-PET for the diagnosis of cancers and assessment of response to therapy. ImmunoPET studies will be essential for the assessment of target antigen expression and identification of a right patient for a specific RIT clinical trial.

References

1. Davies DR, Chacko S. Antibody structure. Acc Chem Res. 1993;26:421–7.
2. Burnet FM. A modification of Jerne's theory of antibody production using the concept of clonal selection. Aust J Sci. 1957;20:67–9.
3. Edelman GM. Dissociation of γ-globulin. Am Chem Soc. 1959;81:3155–6.
4. Porter RR. The hydrolysis of rabbit y-globulin and antibodies with crystalline papain. Biochem J. 1959;73:119–26.
5. Köhler G, Milstein C. Continuous cultures of fused cells secreting antibody of predefined specificity. Nature. 1975;256:495–7.
6. Huang P-W, Chang JW-C. Immune checkpoint inhibitors win the 2018 Nobel prize. Biom J. 2019;42(5):299–306.
7. Himmelweit B, editor. The collected papers of Paul Ehrlich. Elmsford, NY: Pergamon; 1957.
8. Lu R-M, Hwang Y-C, Liu I-J, et al. Development of therapeutic antibodies for the treatment of diseases. J Biomed Sci. 2020;27:1–30.
9. Zahavi D, Weiner L. Monoclonal antibodies in cancer therapy. Antibodies. 2020;9:34. https://doi.org/10.3390/antib9030034.
10. Hwang WYK, Foote J. Immunogenicity of engineered antibodies. Methods. 2005;36:3–10.
11. Harding FA, Stickler MM, Razo J, DuBridge RB. The immunogenicity of humanized and fully human antibodies: residual immunogenicity resides in the CDR regions MAbs. 2010;2(3):256–65.
12. Holliger P, Hudson PJ. Engineered antibody fragments and the rise of single domains. Nat Biotechnol. 2005;23:1126–36.
13. Sharkey RM, Goldenberg DM. Perspectives on cancer therapy with radiolabeled monoclonal antibodies. J Nucl Med. 2005;46:115S–27S.
14. Dammes N, Peer D. Monoclonal antibody-based molecular imaging strategies and theranostic opportunities. Theranostics. 2020;10(2):938–55. https://doi.org/10.7150/thno.37443.
15. Boswell CA, Brechbiel MW. Development of radioimmunotherapeutic and diagnostic antibodies: an inside-out view. Nucl Med Biol. 2007;34:757–78.
16. Nelson AL. Antibody fragments-hope and hype. MAbs. 2010;2(1):77–83.
17. Holliger P, Winter G. Diabodies: small bispecific antibody fragments. Cancer Immunol Immunother. 1997;45:128–30.
18. Bates A, Power CA. David vs. Goliath: the structure, function, and clinical prospects of antibody fragments. Antibodies. 2019;8:28. https://doi.org/10.3390/antib802002.
19. Hanahan D, Weinberg RA. The hallmarks of cancer. Cell. 2000;100:57–70.
20. Hanahan D, Weinberg RA. Hallmarks of cancer: the next generation. Cell. 2011;144:646–74.
21. Fouad YA, Aanei C. Revisiting the hallmarks of cancer. Am J Cancer Res. 2017;7(5):1016–36.
22. Paul D. The systemic hallmarks of cancer. J Cancer Metastasis Treat. 2020;6:29.
23. Finn OJ. Human tumor antigens yesterday, today, and tomorrow. Cancer Immunol Res. 2017;5:347–54.
24. Larson SM, Carrasquillo JA, Cheung N-KV, Press OW. Radioimmunotherapy of human tumours. Nat Rev Cancer. 2015;15:347–60.
25. Shah A, Rauth S, Aithal A, et al. The current landscape of antibody-based therapies in malignancies. Theranostics. 2021;11(3):1493–512. https://doi.org/10.7150/thno.52614.
26. Pressman D. Tissue localizing antibodies. Ann N Y Acad Sci. 1955;59(3):376–80.
27. Beierwalters WH. Horizons in radionuclide therapy: 1985 update. J Nucl Med. 1981;26:421–6.
28. Vial AB, Callahan W. The effect of some ^{131}I tagged antibodies on human melanoblastoma: preliminary report. Univ Mich Med Bull. 1956;20:284–6.
29. Goldenberg DM, Preston DF, Primus FJ, Hansen HJ. Photoscan localization of GW-39 tumors in hamsters using radiolabeled anticarcinoembryonic antigen immunoglobulin G. Cancer Res. 1974;34(1):1–9.
30. Mach JP, Carrel S, Merenda C, Sordat B, Cerottini JC. In vivo localization of radiolabeled antibodies to carcinoembryonic antigen in human colon carcinoma grafted into nude mice. Nature. 1974;248(450):704–6.
31. Goldenberg DM, DeLand F, Kim E, et al. Use of radiolabeled antibodies to carcinoembryonic antigen for the detection and localization of diverse cancers by external photoscanning. N Engl J Med. 1978;298:1384–6.
32. Mach JP, Carrel S, Forni M, et al. Tumor localization of radiolabeled antibodies against carcinoembryonic antigen in patients with carcinoma: a critical evaluation. N Engl J Med. 1980;303:5–10.
33. Mach JP, Buchegger F, Forni M, et al. Use of radiolabeled monoclonal anticarcinoembryonic antigen anti-bodies for the detection of human carcinomas by external photoscanning and tomoscintigraphy. Immunol Today. 1981;2:239–49.
34. Sundberg MW, Meares CF, Goodwin DA, Diamanti CI. Chelating agents for the binding of metal ions to macromolecules. Nature. 1974;250:587–8.
35. Yen SM, Sherman DG, Meares CF. A new route to "bifunctional" chelating agents: conversion of amino

acids to analogs of ethylenedinitrilo-tetraacetic acid. Anal Biochem. 1979;700:152–9.

36. Hnatowich DJ, Layne WW, Childs RL, et al. Radioactive labeling of antibody: a simple and efficient method. Science. 1983;220:613–5.

37. Krejcarek GE, Tucker KL. Covalent attachment of chelating groups to macromolecules. Biochem Biophys Res Commun. 1976;77:581–5.

38. Meares CF, Goodwin DA. Linking radiometals to proteins with bifunctional chelating agents. J Protein Chem. 1984;3:215–28.

39. Moi MK, DeNardo SJ, Meares CF. Stable bifunctional chelates of metals used in radiotherapy. Cancer Res. 1990;50:789s–93s.

40. Knox SJ, Meredith RF. Clinical radioimmunotherapy. Semin Radiat Oncol. 2000;10(2):73–93.

41. Maloney DG, Grillo-López AJ, White CA, et al. IDEC-C2B8 (rituximab) anti-CD20 monoclonal antibody therapy in patients with relapsed low-grade non-Hodgkin's lymphoma. Blood. 1997;90:2188–95.

42. White JM, Escorcia FE, Viola NT. Perspectives on metals-based radioimmunotherapy (RIT): moving forward. Theranostics. 2021;11(13):6293–314.

43. Wittrup KD, Thurber GM, Schmidt MM, Rhoden JJ. Practical theoretic guidance for the design of tumor-targeting agents. Methods Enzymol. 2012;503:255–68.

44. Runcie K, Budman DR, John V, Seetharamu S. Bi-specific and tri-specific antibodies—the next big thing in solid tumor therapeutics. Mol Med. 2018;24:50. https://doi.org/10.1186/s10020-018-0051-4.

45. Boerman OC, Oyen WJ. Immuno-PET of cancer: a revival of antibody imaging. J Nucl Med. 2011;52:1171–2.

46. Liberini V, Laudicella R, Capozza M, et al. The future of cancer diagnosis, treatment and surveillance: a systemic review on immunotherapy and immuno-PET radiotracers. Molecules. 2021;26(8):2201.

47. Li Y, Hamlin DK, Chyan M-K, et al. cGMP production of astatine-211-labeled anti-CD45 antibodies for use in allogeneic hematopoietic cell transplantation for treatment of advanced hematopoietic malignancies. PLoS One. 2018;13(10):e0205135. https://doi.org/10.1371/journal.pone.0205135.

48. Van Dongen GAMS, Visser GWM, Hodge NL-D, et al. A navigator in monoclonal antibody development and applications. Oncologist. 2007;12:1379–89.

49. Dewulf J, Adhikari K, Vangestel C, et al. Development of antibody immuno PET/SPECT radiopharmaceuticals for imaging of oncological applications. Cancers. 2020;12:1868.

50. Oliveira MC, Correia JDG. Biomedical applications of radioiodinated peptides. Eur J Med Chem. 2019;179:56–77.

51. Price EW, Orvig C. Matching chelators to radiometals for radiopharmaceuticals. Chem Soc Rev. 2014;43:260.

52. Boros E, Packard AB. Radioactive transition metals for imaging and therapy. Chem Rev. 2019;119(2):870–901.

53. Adumeau P, Davydova M, Zeglis BM. Thiol-reactive bifunctional chelators for the creation of site-selectively modified radioimmunoconjugates with improved stability. Bioconjug Chem. 2018;29(4):1364–72.

54. Morais M, Ma MT. Site-specific chelator-antibody conjugation for PET and SPECT imaging with radiometals. Drug Discov Today Technol. 2018;30:91–104.

55. Kristensen LK, Christensen C, Jensen MM, et al. Site-specifically labeled [89]Zr-DFO-trastuzumab improves immuno-reactivity and tumor uptake for immuno-PET in a subcutaneous HER2-positive xenograft mouse model. Theranostics. 2019;9(15):4409–20.

56. Vivier D, Fung K, Sharma SK, Zeglis B. The influence of glycans-specific bioconjugation on the FcγRI binding and in vivo performance of [89]Zr-DFO-pertuzumab. Theranostics. 2020;10(4):1746–57.

57. Zeglis BM, Lewis JS. The bioconjugation and radiosynthesis of 89 Zr-DFO-labeled antibodies. J Vis Exp. 2015;96:e52521. https://doi.org/10.3791/52521.

58. Rondon A, Rouanet J, Degoul F. Radioimmunotherapy in oncology: overview of the last decade clinical trials. Cancers. 2021;13:5570.

59. Davies AJ. Radioimmunotherapy for B-cell lymphoma: Y90 ibritumomab tiuxetan and I-131 tositumomab. Oncogene. 2007;26:3614–28.

60. Goldsmith SJ. Radioimmunotherapy of lymphoma: Bexxar and Zevalin. Semin Nucl Med. 2010;40(2):122–3.

61. Larson SM, Carrasquillo JA, Cheung N-KV, Press OW (2015) Radioimmunotherapy of human tumours. Nature Reviews Cancer. 15: 347–360.

62. Green DJ, Press OW. Whither radioimmunotherapy: to be or not to be? Cancer Res. 2017;77(9):2191–6.

63. Repetto-Llamazares AHV, Larsen RH, Mollatt C, et al. Biodistribution and dosimetry of ^{177}Lu-Lilotomab, a new radioimmunoconjugate for treatment of non-Hodgkin lymphoma. Curr Radiopharma. 2013;6:20–7.

64. Kolstad A, Illidge T, Bolstad N, et al. Phase ½a study of ^{177}Lu-lilotomab satetraxetan in relapsed/refractory indolent non-Hodgkin lymphoma. Blood Adv. 2020;4(17):4091–101.

65. Malenge MM, Patzke S, Ree AH, et al. ^{177}Lu-Lilotomab satetraxetan has the potential to counteract resistance to rituximab in non-Hodgkin lymphoma. J Nucl Med. 2020;61(10):1468–75.

66. Shah NN, Sokol L. Targeting CD22 for the treatment of B-cell malignancies. Immunotargets Ther. 2021;2021(10):225–36.

67. Morschhauser F, Kraeber-Bodere F, Wegener WA, et al. High rates of durable responses with anti-CD22 fractionated radioimmunotherapy: results of a multicenter, phase I/II study in non-Hodgkin's lymphoma. J Clin Oncol. 2010;28:3709.

68. Linden O, Bates AT, Cunningham D, et al. Th labeled anti-CD22 antibody (BAY 1862864) in relapsed/refractory CD22-positive non-Hodgkin lymphoma: a first-in-human, phase I study. Cancer Biother Radiopharm. 2021;36(8):672–81. https://doi.org/10.1089/cbr.2020.4653.

69. Jurcic JG. Targeted alpha-particle therapy for hematologic malignancies. Semin Nucl Med. 2020;50:152–61.

70. Pagel JM, Gooley TA, Rajendran J, et al. Allogeneic hematopoietic cell transplantation after conditioning with ^{131}I–anti-CD45 antibody plus fludarabine and low-dose total body irradiation for elderly patients with advanced acute myeloid leukemia or high-risk myelodysplastic syndrome. Blood. 2009;114:5444–53.

71. Pandit-Paskar N, et al. Low incidence rates of mucositis, febrile neutropenia or sepsis in the prospective, randomized phase 3 Sierra trial for patients with relapsed or refractory acute myeloid leukemia with targeted delivery of anti-CD45 iodine (^{131}I) apamistamab (Iomab-B). J Nucl Med. 2021;62:1694.

72. Rosenblat TL, McDevitt MR, Mulford DA, et al. Sequential cytarabine and α-particle immunotherapy with bismuth-213–Lintuzumab (HuM195) for acute myeloid leukemia. Clin Cancer Res. 2010;16:5303–11.

73. Jurcic JG, Larson SM, Sgouros G, et al. Targeted α-particle immunotherapy for myeloid leukemia. Blood. 2002;100:1233–9.

74. Jurcic JG, Rosenblat TL, McDevitt MR, et al. Targeted alpha-particle nano-generator actinium-225 ([225]Ac)-lintuzumab (anti-CD33) in acute myeloid leukemia (AML). Clin Lymphoma Myeloma Leuk. 2013;13:S379–80.

75. Atallah E, Berger M, Jurcic J, et al. A phase 2 study of actinium-225 ([225]Ac)-lintuzumab in older patients with untreated acute myeloid leukemia (AML). J Med Imaging Radiat Sci. 2019;50:S37.

76. Jurcic JG, Levy MY, Park JH, et al. Phase I trial of targeted alpha-particle therapy with actinium-225 ([225]Ac)-lintuzumab and low-dose cytarabine (LDAC) in patients aged 60 or older with untreated acute myeloid leukemia (AML). Blood. 2016;128:4050.

77. Garg R, Allen KJH, Dawicki W, et al. [225]Ac-labeled CD33-targeting antibody reverses resistance against Bcl-2 inhibitor venetoclax in acute myeloid leukemia models. Cancer Med. 2021;10:1128–40.

78. Sgouros G, Bodei L, McDevitt MR, Nedrow JR. Radiopharmaceutical therapy in cancer: clinical advances and challenges. Nat Rev Drug Discov. 2020;9:589–608.

79. Sabanathan D, Lund ME, Campbell DH, et al. Radioimmunotherapy for solid tumors: spotlight on Glypican-1 as a radioimmunotherapy target. Ther Adv Med Oncol. 2021;13:1–21.

80. Horoszewicz JS, Kawinski E, Murphy GP. Monoclonal antibodies to a new antigenic marker in epithelial prostatic cells and serum of prostatic cancer patients. Anticancer Res. 1987;7:927–35.

81. O'Keefe DS, Su SL, Bacich DJ, et al. Mapping, genomic organization, and promoter analysis of the human prostate-specific membrane antigen gene. Biochim Biophys Acta. 1998;1443:113–27.

82. Evans JC, Malhotra M, Cryan JF, O'Driscoll CM. The therapeutic and diagnostic potential of the prostate specific membrane antigen/glutamate carboxypeptidase II(PSMA/GCPII) in cancer and neurological disease. Br J Pharmacol. 2016;2016:1733041–307.

83. Liu H, Moy P, Kim S, et al. Monoclonal antibodies to the extracellular domain of prostate-specific membrane antigen also react with tumor vascular endothelium. Cancer Res. 1997;57:3629–34.

84. Liu H, Rajasekaran AK, Moy P, et al. Constitutive and antibody-induced internalization of prostate-specific membrane antigen. Cancer Res. 1998;58:4055–60.

85. Smith-Jones PM, Vallabahajosula S, Goldsmith SJ, et al. In vitro characterization of radiolabeled monoclonal antibodies specific for the extracellular domain of prostate-specific membrane antigen. Cancer Res. 2000;60:5237–43.

86. Smith-Jones PM, Vallabhajosula S, St. Omer S, et al. ^{177}Lu-DOTA-HuJ591: a new radiolabeled monoclonal antibody (mAb) for targeted therapy of prostate cancer. J Label Compds Radiopharm. 2001;44:90–2.

87. Smith-Jones PM, Vallabhajosula S, Navarro V, et al. Radiolabeled monoclonal antibodies specific to the extracellular domain of prostate-specific membrane antigen: preclinical studies in nude mice bearing LNCaP human prostate tumor. J Nucl Med. 2003;44:610–7.

88. Bander NH, Trabulsi EJ, Kostakoglu L, Yao D, Vallabhajosula S, et al. Targeting metastatic prostate cancer with radiolabeled monoclonal antibody J591 to the extracellular domain of prostate specific membrane antigen. J Urol. 2003;170:171.

89. Bander NH, Milowsky MI, Nanus DM, Kostakoglu L, Vallabhajosula S, Goldsmith SJ. Phase I trial of [177]lutetium labeled J591, a monoclonal antibody to prostate-specific membrane antigen, in patients with androgen-independent prostate cancer. J Clin Oncol. 2005;23:4591–601.

90. Milowsky MI, Nanus DM, Kostakoglu L, Vallabhajosula S, Goldsmith SJ, Bander NH. Phase I trial of ^{90}Y-labeled anti-prostate specific membrane antigen monoclonal antibody J591 for androgen-independent prostate cancer. J Clin Oncol. 2004;22:2522–31.

91. Vallabhajosula S, Nikolopoulou A, Jhanwar YS, et al. Radioimmunotherapy of metastatic prostate cancer with ^{177}Lu-DOTA-huJ591 anti prostate specific membrane antigen specific monoclonal antibody. Curr Radiopharma. 2016;9:44–53.

92. Vallabhajosula S, Goldsmith SJ, Hamacher KA, et al. Prediction of myelotoxicity based on bone marrow radiation-absorbed dose: radioimmunotherapy studies using [90]Y- and ^{177}Lu-labeled J591 antibodies specific for prostate-specific membrane antigen. J Nucl Med. 2005;46:850–8.

93. Vallabhajosula S, Goldsmith SJ, Kostakoglu L, et al. Radioimmunotherapy of prostate cancer using ^{90}Y- and ^{177}Lu-labeled J591 monoclonal antibodies: effect of multiple treatments on myelotoxicity. Clin Cancer Res. 2005;11:7195s–200s.

94. Vallabhajosula S, Kuji I, Hamacher A, et al. Pharmacokinetics and biodistribution of ^{111}In- and ^{177}Lu-labeled J591 antibody specific for prostate-specific membrane antigen: prediction of ^{90}Y-J591 radiation dosimetry based on ^{111}In or ^{177}Lu? J Nucl Med. 2005;46:634–41.

95. Tagawa ST, Milowsky MI, Morris M, Vallabhajosula S, et al. Phase II study of lutetium-177-labeled anti-prostate-specific membrane antigen monoclonal antibody J591 for mCRPC. Clin Cancer Res. 2013;19:5182–91.

96. Tagawa ST, Akhtar NH, Nikolopoulou A, et al. Bone marrow recovery and subsequent chemotherapy following radiolabeled anti-prostate-specific membrane antigen monoclonal antibody J591 in men with mCRPC. Front Oncol. 2013;3:1–6.

97. Tagawa ST, Osborne JR, Hackett A, et al. Preliminary results of a phase I/II dose-escalation study of fractionated dose ^{177}Lu-PSMA-617 for progressive metastatic castration resistant prostate cancer (mCRPC). Ann Oncol. 2019;30(suppl_5):v325–55. https://doi.org/10.1093/annonc/mdz248.

98. Tagawa ST, Vallabhajosula S, Christos PJ, et al. Phase ½ study of fractionated dose lutetium-177-labeled anti-prostate-specific membrane antigen monoclonal antibody J591 (^{177}Lu-J591) for mCRPC. Cancer. 2019;125:2561–9.

99. Batra JS, Niaz MJ, Whang YE, et al. Phase I trial of docetaxel plus lutetium-177-labeled anti–prostate-specific membrane antigen monoclonal antibody J591 (^{177}Lu-J591) for metastatic castration-resistant prostate cancer. Urol Oncol. 2020;38(11):848.e9–848.e16.

100. Niaz MJ, Bastra JS, Walsh RD, Ramirez-Fort MK, Vallabhajosula S, et al. Pilot study of hyperfractionated dosing of lutetium-177 labeled antiprostate-specific membrane antigen monoclonal antibody J591 (^{177}Lu-J591) for metastatic castration-resistant prostate cancer. Oncologist. 2020;25(6):477–e895.

101. Li Y, Tian Z, Rizvi SM, Bander NH, Allen BJ. In vitro and preclinical targeted alpha therapy of human prostate cancer with bi-213 labeled J591 antibody against the prostate specific membrane antigen. Prostate Cancer Prostatic Dis. 2002;5:36–46.

102. Tagawa ST, Osborne J, Fernandez E, et al. Phase I dose-escalation study of PSMA-targeted alpha emitter ^{225}Ac-J591 in men with metastatic castration-resistant prostate cancer (mCRPC). J Clin Oncol. 2020;38(suppl 15):5560.

103. Tagawa ST, Sun M, Sartor AO, et al. Phase I study of ^{225}Ac-J591 for men with metastatic castration-resistant prostate cancer (mCRPC). J Clin Oncol. 2021;39(suppl 15):abstr 5015.

104. Meyn RE. Apoptosis and response to radiation: implications for radiation therapy. Oncology. 1997;11:349–56.

105. Mirzaie-Joniani H, Eriksson D, Sheikholvaezin A, et al. Apoptosis induced by low-dose and low-dose-rate radiation. Cancer. 2002;94:1210–4.

106. DeNardo GL, Schlom J, Buchsbaum DJ, et al. Rationales, evidence, and design considerations for fractionated radioimmuno-therapy. Cancer. 2002;94:1332–48.

107. O'Donoghue JA, Sgouros G, Divgi CR, Humm JL. Single-dose versus fractionated radioimmu-notherapy: model comparisons for uniform tumor dosimetry. J Nucl Med. 2000;41:538–47.

108. Shen S, Duan J, Meredith RF, et al. Model prediction of treatment planning for dose-fractionated radioimmunotherapy. Cancer. 2002;94:1264–9.

109. Buchsbaum DJ, Khazaeli MB, Liu TP, Bright S. Fractionated radioimmunotherapy of human colon carcinoma xenografts with I-131-labeled monoclonal antibody CC49. Cancer Res. 1995;55:5881–7.

110. Divgi CR, O'Donoghue JA, Welt S, et al. Phase I clinical trial with fractionated radioimmunotherapy using ^{131}I-labeled chimeric G250 in metastatic renal cancer. J Nucl Med. 2004;45:1412–21.

111. Vallabhajosula S, Smith-Jones PM, Navarro V, et al. Radioimmunotherapy of prostate cancer in human xenografts using monoclonal antibodies specific to prostate specific membrane antigen: studies in nude mice. Prostate. 2004;58:145–55.

112. Lollo C, Halpern S, Bartholomew R, David G, Hagan P. Non-covalent antibody-mediated drug delivery. Nucl Med Commun. 1994;15:483–91.

113. Bailly C, Bodet-Milin C, Rousseau C, et al. Pretargeting for imaging and therapy in oncological nuclear medicine. EJNMMI Radiopharm Chem. 2017;2:6. https://doi.org/10.1186/s41181-017-0026-8.

114. Patra M, Zarschler K, Pietzsch HJ, et al. New insights into the pretargeting approach to image and treat tumors. Chem Soc Rev. 2016;45:6415–31.

115. Stéen EJL, Edem PE, Nørregaard K, et al. Pretargeting in nuclear imaging and radionuclide therapy: Improving efficacy of theranostics and nanomedicines. Biomaterials. 2018;179:209–245.

116. Verhoeven M, Seimbille Y, Dalm SU. Therapeutic applications of pretargeting. Pharmaceutics. 2019;11:434. https://doi.org/10.3390/pharmaceutics1109043.

117. Kraeber-Bodere F, Barbet J, Chatal JF. Radioimmunotherapy: from current clinical success to future industrial breakthrough? J Nucl Med. 2016;57(3):329–31.

118. Zaheer J, Kim H, Lee Y-J, et al. Combination radioimmunotherapy strategies for solid tumors. Int J Mol Sci. 2019;20:5579.

119. Ashrafizadeh M, Farhood B, Musa AE, et al. Abscopal effect in radioimmunotherapy. Int Immunopharmacol. 2020;85:106663.

120. Fleischmann M, Glatzer M, Rödel C, Tselis N. Radioimmunotherapy: future prospects from the perspective of brachytherapy. J Contemp Brachytherapy. 2021;13(4):458–67.

121. Zhao X, Shao C. Radiotherapy-mediated immuno-modulation and anti-tumor abscopal effect combining immune checkpoint blockade. Cancers (Basel). 2020;12(10):2762.

122. Mayer AT, Gambhir SS. The immunoimaging toolbox. J Nucl Med. 2018;59:1174–82.

123. Liberani V, Laudicella R, Capozza M, et al. The future of cancer diagnosis, treatment and surveillance: a systemic review on immunotherapy and immuno-pet radiotracers. Molecules. 2021;26:2201.

124. Dejesus OT, Nickles RJ. Production and purification of ^{89}Zr, a potential PET antibody label. Appi Radial Isot. 1990;41:789–90.

125. Verel I, Visser GWM, Boellaard R, et al. Quantitative ^{89}Zr immuno-PET for in vivo scouting of ^{90}Y-labeled monoclonal antibodies in xenograft-bearing nude mice. J Nucl Med. 2003;44:1663–70.

126. Verel I, Visser GWM, Boellaard R, et al. ^{89}Zr Immuno-PET: comprehensive procedures for the production of ^{89}Zr-labeled monoclonal antibodies. J Nucl Med. 2003;44:1271–81.

127. Borjesson PK, Jauw YW, Boellaard R, et al. Performance of immuno-positron emission tomography with zirconium-89-labeled chimeric monoclonal antibody U36 in the detection of lymph node metastases in head and neck cancer patients. Clin Cancer Res. 2006;12:2133–40.

128. Perk LR, Visser OJ, Stigter-van, et al. Preparation and evaluation of ^{89}Zr-Zevalin for monitoring of ^{90}Y-Zevalin biodistribution with positron emission tomography. Eur J Nucl Med Mol Imaging. 2006;33:1337–45.

129. Perk LR, Visser GW, Vosjan MJ, et al. ^{89}Zr as a PET surrogate radioisotope for scouting biodistribution of the therapeutic radiometals ^{90}Y and ^{177}Lu in tumor-bearing nude mice after coupling to the internalizing antibody cetuximab. J Nucl Med. 2005;46:1898–1906.

130. Yoon J-K, Park B-N, Ryu E-K, et al. Current Perspectives on ^{89}Zr-PET Imaging Int J Mol Sci. 2020;21(12): 4309.

131. Wei W, Rosenkrans CT, Liu J. ImmunoPET: concept, design, and applications. Chem Rev. 2020;120(8):3787–851.

132. Muylle K, Flamen P, Vugts DJ. Tumour targeting and radiation dose of radioimmunotherapy with ^{90}Y-rituximab in CD20+ B-cell lymphoma as predicted by ^{89}Zr-rituximab immuno-PET: impact of preloading with unlabelled rituximab. Eur J Nucl Med Mol Imaging. 2015;42:1304–14.

133. Moek KL, Giesen D, Kok IC. Theranostics using antibodies and antibody-related therapeutics. J Nucl Med. 2017;58:83S–90S.

134. Pandit-Taskar N, O'Donoghue JA, Ruan S, et al. First-in-human imaging with ^{89}Zr-Df-IAB2M anti-PSMA minibody in patients with metastatic prostate cancer: pharmacokinetics, biodistribution, dosimetry, and lesion uptake. J Nucl Med. 2016;57(12):1858–64.

135. Kumar K, Ghosh A. Radiochemistry, production processes, labeling methods, and immunopet imaging pharmaceuticals of iodine-124. Molecules. 2021;26:414.

136. Divgi CR, Pandit-Taskar N, Jungbluth AA, et al. Preoperative characterisation of clear-cell renal carcinoma using iodine-124-labelled antibody chimeric G250 (^{124}I-cG250) and PET in patients with renal masses: a phase I trial. Lancet Oncol. 2007;8:304–10.

137. Divgi CR, Uzzo RG, Gatsonis C, et al. Positron emission tomography/computed tomography identification of clear cell renal cell carcinoma: results from the REDECT trial. J Clin Oncol. 2013;31:187–94.

138. Carrasquilo JA, Pandit-Taskar N, O'Donoghuye JA, et al. ^{124}I-huA33 antibody PET of colorectal cancer. J Nucl Med. 2011;52:1173–80.

139. Alauddin MM, Khawli LS. Advances in immuno-PET for the detection of cancer and assessment of response to therapy. Curr Med Chem. 2021;28(4):647–72.

140. Lim EA, Drake CG, Mintz A. Molecular imaging for cancer immunotherapy. Immunooncol Technol. 2020;5(3):10–21.

141. Bensch F, van der Veen EL, Lub-de Hooge MN, et al. (89)Zr-atezolizumab imaging as a non-invasive approach to assess clinical response to PD-L1 blockade in cancer. Nat Med. 2018;24:1852–8.

142. Donnelly DJ, Smith RA, Morin P, et al. Synthesis and biologic evaluation of a novel (18)F-labeled adnectin as a PET radioligand for imaging PD-L1 expression. J Nucl Med. 2018;59:529–35.

143. Niemeijer AN, Leung D, Huisman MC, et al. Whole body PD-1 and PD-L1 positron emission tomography in patients with non-small-cell lung cancer. Nat Commun. 2018;9:4664.

It is one of the more striking generalizations of bio-chemistry - which surprisingly is hardly ever mentioned in the biochemical textbooks - that the twenty amino acids and the four bases, are, with minor reservations, the same throughout Nature.
(Francis Crick)

20.1 Introduction

The first amino acid (AA or aa) was discovered in 1806 by two French chemists, Louis-Nicolas Vauquelin and Pierre Jean Robiquet. They isolated a compound from asparagus that was subsequently named asparagine. However, the first use of the term "amino acid" (AA) in the English language dates from 1898, while the German term, *Aminosäure*, was used earlier. In 1902, Emil Fischer and Franz Hofmeister independently proposed that proteins are formed from many AAs, whereby bonds are formed between the amino group of one AA with the carboxyl group of another, resulting in a linear structure that Fischer termed *peptide* (Fig. 20.1). A peptide bond is an amide type of covalent chemical bond linking two consecutive α-AAs. The amino acids that have been incorporated into peptides are termed "residues," since a water molecule is released when a peptide (amide) bond is formed. All peptides except cyclic peptides have an N-terminal (NH_2, amine group) and C-terminal (COOH, carboxyl group) residue at the end of the peptide.

Peptides are short chains of AAs containing less than 50 AAs. A peptide chain containing 10–15 AAs is called oligopeptide. A polypeptide is a longer, continuous, unbranched peptide chain, and a polypeptide that contains >50 AAs is known as a protein. A peptide is defined, however, by the FDA as a polymer composed of less than 40 amino acids (500–5000 Da) [1].

20.1.1 Proteinogenic and Non-proteinogenic AAs

Technically, any organic compound with an amine (-NH_2) and a carboxylic acid (-COOH) functional group is an AA. As of 2020, >500 naturally occurring AAs are known, although 20 appear in the genetic code and are considered as "standard" alpha AAs, (or proteinogenic AAs) because their generic structure (except for proline) includes a primary amino group (NH_2) and a carboxylic acid group (COOH) bonded to the same carbon, known as the α-carbon (C_α), as shown in Fig. 20.1. The standard α-AAs with their letter symbols are shown in Table 20.1. The chemical structures of the standard α-AAs are
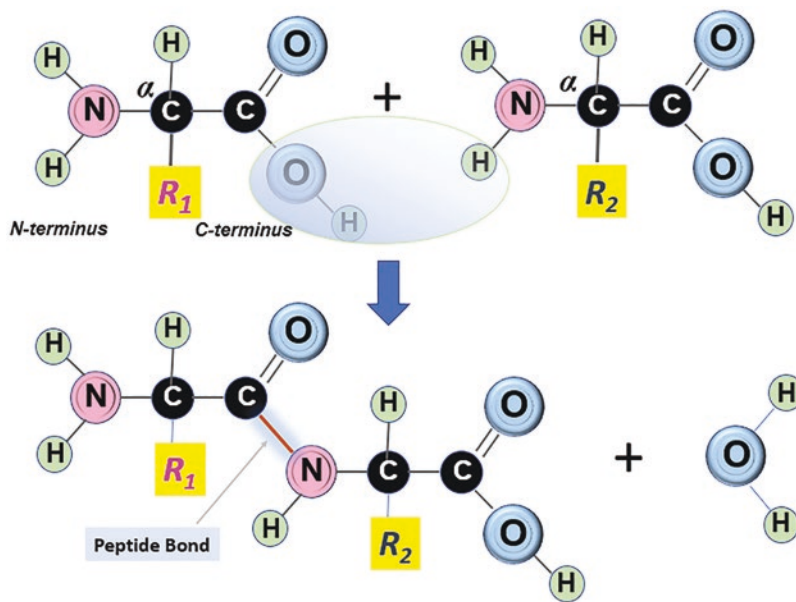
Fig. 20.1 The peptide bond is an amide type of covalent chemical bond formed between the amino group of one amino acid with the carboxyl group of another, linking two consecutive α-amino acids, resulting in a linear structure

Table 20.1 The standard proteinogenic alpha amino acids

No.	Amino acid	Letter code			Formula	Mol. wt.	Description
1	Alanine	ALA	Ala	A	$C_3H_7N_1O_2$	89.09	Aliphatic AAs with hydrophobic side chain
2	Isoleucine	ILE	Ile	I	$C_6H_{13}N_1O_2$	131.17	
3	Leucine	LEU	Leu	L	$C_6H_{13}N_1O_2$	131.17	
4	Valine	VAL	Val	V	$C_5H_{11}N_1O_2$	117.15	
5	Phenylalanine	PHE	Phe	F	$C_9H_{11}N_1O_2$	165.19	Aromatic AAs with hydrophobic side chain
6	Tryptophan	TRP	Trp	W	$C_{11}H_{12}N_2O_2$	204.23	
7	Tyrosine	TYR	Tyr	Y	$C_9H_{11}N_1O_3$	181.19	
8	Asparagine	ASN	Asn	N	$C_4H_8N_2O_3$	132.12	AAs with neutral side chain
9	Cysteine	CYS	Cys	C	$C_3H_7N_1O_2S_1$	121.16	
10	Glutamine	GLN	Gln	Q	$C_5H_{10}N_2O_3$	146.15	
11	Methionine	MET	Met	M	$C_5H_{11}N_1O_2S_1$	149.21	
12	Serine	SER	Ser	S	$C_3H_7N_1O_3$	105.09	
13	Threonine	THR	Thr	T	$C_4H_9N_1O_3$	119.12	
14	Arginine	ARG	Arg	R	$C_6H_{14}N_4O_2$	174.2	AAs with positive charged side chain
15	Histidine	HIS	His	H	$C_6H_9N_3O_2$	155.16	
16	Lysine	LYS	Lys	K	$C_6H_{14}N_2O_2$	146.19	
17	Aspartic acid	ASP	Asp	D	$C_4H_7N_1O_4$	133.1	AAs with negative charged side chain
18	Glutamic acid	GLU	Glu	E	$C_5H_9N_1O_4$	147.13	
19	Glycine	GLY	Gly	G	$C_2H_5N_1O_2$	75.07	Unique AAs
20	Proline	PRO	Pro	P	$C_5H_9N_1O_2$	115.18	

shown in the Fig. 20.2. There are two extra proteinogenic AAs: selenocysteine and pyrrolysine.

In AAs, the α-carbon atom is attached to four different groups; it is asymmetric and, therefore, exhibits optical isomerism. D-Amino acids involve the mirror image of the naturally occurring L-isomers. They are used for a range of applications, mostly to increase resistance against a range of degradation enzymes. Peptides containing D-amino acids are, therefore, significantly
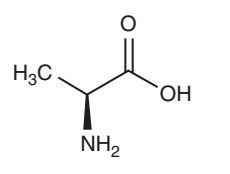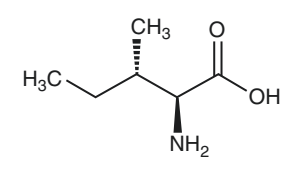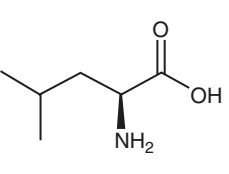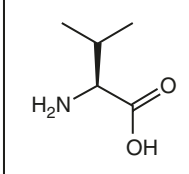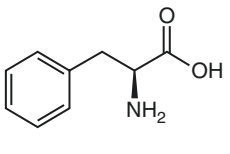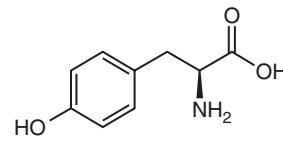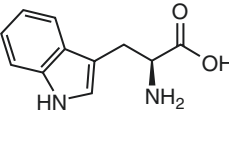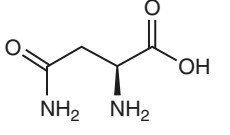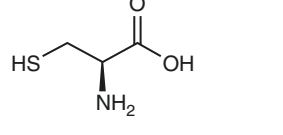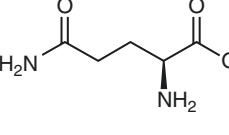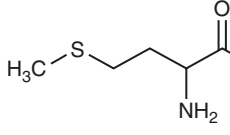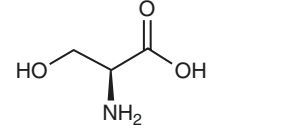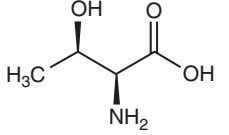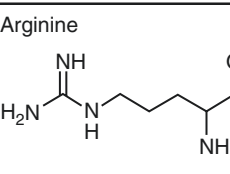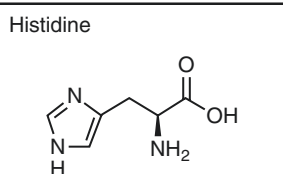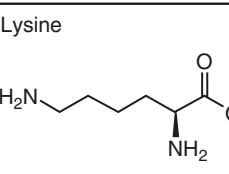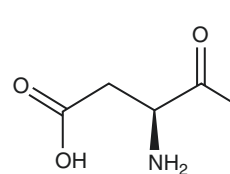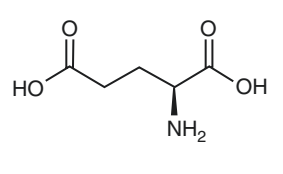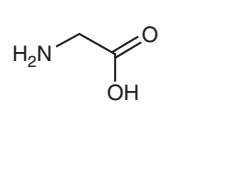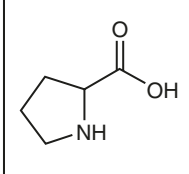
Fig. 20.2   The chemical structures of alpha amino acids
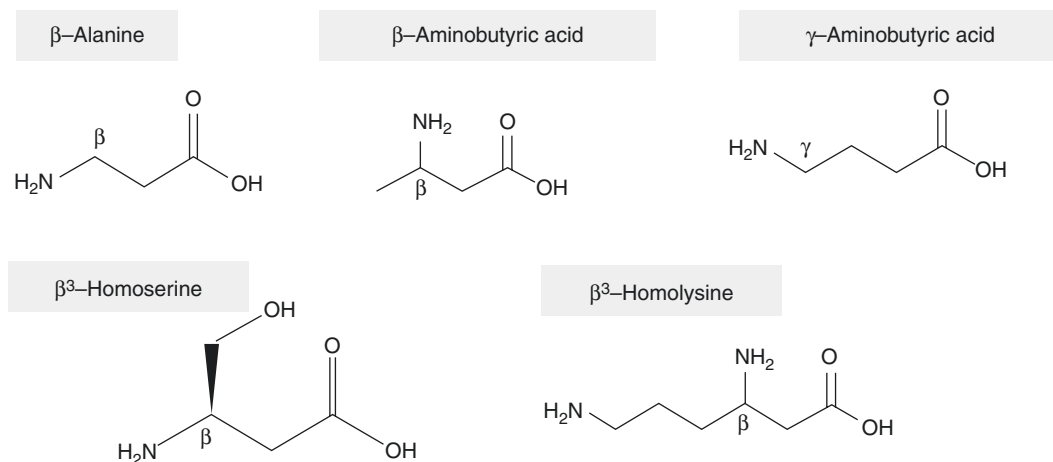
Fig. 20.3 Examples of non-natural amino acids

more stable than peptides containing only L-amino acids.

Most natural AAs are α-AAs in the *L* conformation but, some non-natural AAs (NNAAs) also exist in nature. In these AAs, the amine group and the carboxy groups are not attached to the same α-carbon atom. The most common examples are β-alanine and γ-aminobutyric acid (GABA), an inhibitory neurotransmitter in brain (Fig. 20.3).

20.1.2 Peptide Therapeutics

In 1902, Bayliss and Starling discovered the blood borne chemical messenger "secretin" and later coined the term "hormone" for the blood borne chemical messengers. Peptide hormones may contain three to several hundred AAs. For example, Somatostatin (SST), also known as growth hormone-inhibiting hormone (GHIH), is a peptide hormone made up of either 14 or 28 AAs, whereas human growth hormone (hGH) is a protein of 191 AAs. Peptide therapeutics have played a notable role in medical practice since the advent of "*insulin therapy*" in the 1920s. As of 2020, >70 peptide products have been approved and >100 commercial products are available in the global market. In addition, >160 therapeutic peptide products were reported in

Table 20.2 Approved radiolabeled peptide drug conjugates in clinical use

Radiotracer	Target	Year
[123]I-(Tyr[3]-octreotide)	SSTR-2	1989
^{111}In-DTPA-octreotide (OctreoScan(R*))	SSTR-2	1994
[99m]Tc-Apcitide (^{99m}Tc-P280, AcuTect)	GP II$_b$/III$_a$	1997
^{68}Ga-DOTA-TOC (^{68}Ga-endotreotide, Somakit)	SSTR-2	2016, 2020
[99m]Tc-Hynic-octreotide (Tektreotyd)	SSTR-2	2018
^{68}Ga-DOTA-TATE (NETSPOT®)	SSTR-2	2018
^{177}Lu-DOTA-TATE (LUTATHERA®)	SSTR-2	2018
[64]Cu-DOTA-TATE (DetectNet®)	SSTR-2	2020
^{68}Ga-PSMA-11	PSMA	2020
^{177}Lu-PSMA-617	PSMA	2022

active clinical trials and >200 were reported in the preclinical development [2].

Peptide drug conjugates (PDC) can offer a multifunctional approach for advancing targeted cancer therapeutics. In 1989, [123]I-204-090 (Tyr[3]-octreotide) was the first radiolabeled peptide used in humans for imaging studies but, the first radiolabeled PDC (RPDC) approved by US-FDA was ^{111}In-DTPA-octreotide (OctreoScan®) in 1994. Several approved radiolabeled PDCs (RPDCs) for imaging and therapy are summarized in Table 20.2.

In the design and development of RPDCs for theranostic applications, the pharmacokinetic (PK) properties, such as absorption, distribution, metabolism, and excretion (ADME) as well as pharmacodynamic (PD) properties need to be optimized to improve safety, reduce normal organ toxicities, and to enhance target specificity.

20.1.3 Advantages and Disadvantages of Peptides

The biological actions of the peptides are mediated upon binding with high affinity to specific receptors. Many of these regulatory peptide receptors are massively overexpressed in numerous cancers, compared to their relatively low density in physiological organs. Table 20.2 summarizes the expression of peptide receptors on different tumors and lists the peptides currently being studied for the development of receptor targeted PDCs.

Peptides have several advantages over small molecule, organic molecules, or large proteins and antibodies [3–6]:

- Peptides are naturally occurring biologics and, hence, safer than synthetic drugs and have a greater efficacy, selectivity, and specificity for the target receptor.
- In contrast to synthetic drugs, peptides are degraded into their component proteinogenic AAs without leading to toxic metabolites.
- Because of the short half-lives, peptide drugs are associated with less accumulation in the body, thereby reducing the risks that may arise from their degradation products.
- Compared with larger proteins and antibodies, peptides can penetrate and diffuse further into the tumor tissue because of their low molecular mass, and relatively small size.
- Due to high concentration in the tumor, rapid clearance from the blood and non-target tissues and high receptor affinity on tumor cells lead to optimal target-to-non-target ratios.
- Peptides are less immunogenic than recombinant proteins and antibodies. In addition,

they are associated with lower manufacturing costs, higher activity, and greater stability (they can be stored at room temperature).

- For diagnostic imaging, usually, tiny quantities of peptides (<10 μg) are sufficient. Even for therapeutic purposes, <500 μg is needed to deliver the therapeutic doses of radionuclides.
- Peptide molecules provide the flexibility for chemical modification and/or insertion of synthetic (non-natural) AAs in the sequence to optimize biodistribution, and enhance target binding.
- Peptide molecules provide the possibility of attaching a bifunctional chelator (BFC) at either the C- or N-terminus to facilitate easier labeling with radiometals. Peptides can tolerate the severe conditions (pH, temperature, organic solvent) associated with chemical modifications.
- Peptides can also be readily synthesized using conventional peptide synthesizers and, any desired modifications to the structure, can be easily engineered by making the appropriate changes to the peptide sequence during synthesis and/or by adding other structural modifications after synthesis.

The major disadvantages include short plasma-half-life, poor in vivo stability, and renal clearance.

- Natural peptides have a short half-life, due to their rapid degradation caused by many peptidases and proteases found in plasma.
- Short half-lives of peptides are also experienced due to rapid renal clearance. The glomeruli pores within the kidney have a size of ~8 nm. The circulating hydrophilic peptides that are <25 kDa are filtered through the glomeruli but, partly retained in the kidney due to reuptake by renal proximal tubules mediated by megalin receptors.
- Combination with a chelator and/or incorporation of a radionuclide may result in reduction of receptor-binding affinity compared to

the original peptide or chelate-conjugated peptide.

• The relatively high uptake and prolonged retention of radiolabeled peptides within the kidneys may lead to renal damage.

20.2 Design of Peptide Radiopharmaceuticals (PRP)

Except for radiohalogens (^{18}F, $^{123/124/131}$I), most PRPs for imaging and therapy are based on metallic radionuclides, such as ^{111}In, ^{64}Cu, ^{68}Ga, ^{90}Y, ^{177}Lu and ^{225}Ac. The chemical components of a target specific PRP may have four or five different individual components, such as targeting vehicle (peptide), spacer and/or linker, and finally, a bifunctional chelator (BFC) to complex the radiometal (Fig. 20.4). The significance of each of these components will be discussed in greater detail under different sections.

The development of a PRP for successful receptor targeting can be summarized in the following major steps [3]:

1. Identification of the molecular target (the peptide receptor) using receptor autoradiography or immunohistochemistry.

2. Synthesis of a peptide and/or its analogs based on the original natural peptide sequence. Modifications in the sequence may be needed to produce a metabolically stabilized peptide analog which preserves most of the biological activity of the original peptide molecule.

3. The peptide is covalently conjugated to a BFC via a spacer/linker for radiometal labeling.

4. The peptide may be chemically modified to have a prosthetic group for labeling to radiohalogens.

5. Optimization of a radiolabeling protocol.

6. Study the in vitro characteristics of PRP, such as labeling efficiency, radiochemical purity, specific activity, etc.

7. Determine the in vivo stability, specificity, and the diagnostic/or therapeutic potential based on preclinical studies.

8. Based on in vitro and in vivo studies in animal models, further optimizations of the PRP may be needed to improve the biological performance of the PRP.

The design and development of PRPs involve various strategies to improve the stability and PK (such as ADME) and PD characteristics of the final drug product. The PK of natural amino acid

Fig. 20.4 Schematic of a target specific peptide radiopharmaceutical showing different components, such as targeting vehicle (vector), spacer, linker, and chelating agent
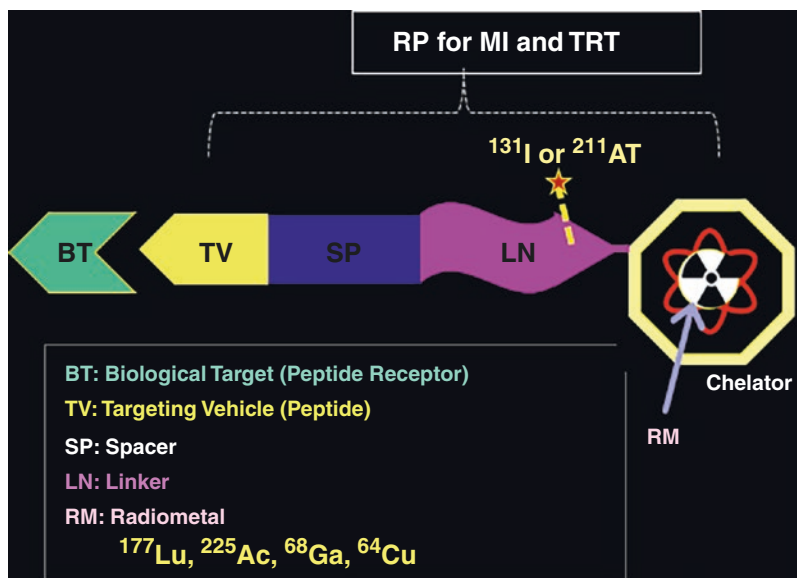
sequences can be optimized through the introduction of (a) conformational constraints (i.e., induced by cyclization, or insertion of non-natural amino acids in the peptide sequences) providing unfavorable changes in the binding entropy; and (b) conjugation with glycosylated moieties or polyether compounds at the N-terminus end of synthetic peptides. The stability of peptides can also be increased by the formation of dimers, tetramers, or heterodimers, which improve the stability and the affinity of synthetic peptide chains to their receptors [4, 6].

20.2.1 Peptide Modification and Insertion of Non-natural AAs

Cyclic peptide (CP) structures are mainly due to the formation of disulfide bonds between the thiol groups of two unprotected cysteines within the linear peptide. However, CPs can also be generated from lactam bridges between amino and carboxyl groups. Several cyclized peptides are currently used in nuclear medicine, such as somatostatin, RGD tripeptide, cholecystokinin, and minigastrin, as well as bombesin, and vasoactive intestinal peptide (VIP). Cyclization of peptides provides conformational and functional characteristics that are critical for their application as target-specific vectors to carry radionuclides. Cyclization also brings about conformational constraints that lead to stability against proteolytic degradation and improved receptor binding affinity.

20.2.1.1   Somatostatin (SST) Analogs
Various modifications in the AA sequence of somatostatin produced successful SST analogs for imaging and therapy (Fig. 20.5) [7]. Some of the important modifications are summarized here.

- SST-14 is a cyclic peptide with a disulfide bridge between Cys^3 and Cys^{14} and has a short half-life (<3 min) in circulation. Octreotide,

the 8 AA analog was synthesized by inserting the D-AAs such as D-Phe at N-terminus and the amino-alcohol Thr-ol at C-terminus, and preserving a disulfide bridge, between Cys^2 and Cys^7. Octreotide showed enhanced biological activity, reduced metabolic degradation with a half-life of about 2 h [3].

- Two octreotide analogs were developed by replacing Phe^3 at position-3 with Tyr^3. While Tyr^3-octreotide (TOC) has the amino-alcohol Thr-ol at C-terminus, octreotate (TATE) has a free carboxyl group at C-terminus. Octreotate showed higher affinity to SSTR-2 than octreotide and Tyr^3-Octreotide (Table 20.3).

- Replacing Phe^3 in octreotide with 1-naphthyl alanine $(1-Nal)^3$ produced an SST analog NOTATOC with higher affinity not only for SSTR-2 but, also for SSTR-3 and 5 (Table 20.3).

- Incorporation of stable AAs, such as β-DAP (β-(L-1,2-diamino propionic acid) and homo-cysteine (Hcy) in depreotide and (2-naphthyl)-D-alanine in lanreotide as well as the amidation of their C-terminus improved the tumor uptake in comparison to octreotide.

- The design of peptide antagonists required several chemical modifications, such as deletions or the introduction of NNAAs with different chirality. The fundamental differences in chirality between L- and D-AAs mean that peptides built on D-AAs are not recognized by many proteins, including proteases. The result of this lack of recognition is that while most L-peptides are vulnerable to enzymatic degradation in vivo, the analogous D-peptides are resistant to degradation and have low immunogenicity. In the octreotide scaffold, the inversion of chirality at positions 2 and 3 was shown to cause relevant structural modifications converting an SST agonist into an antagonist [8]. Several new SST antagonists (LM3, JR10, JR11) were developed (Fig. 20.6) by the introduction of D-4-aminocarbamoyl-Phenylalanine (D-Aph(Cbm)) in place of D-Trp, and 4-amino-L-hydroorotyl-phenylalanine (Aph(Hor)) in position Tyr to improve the receptor affinity [10].
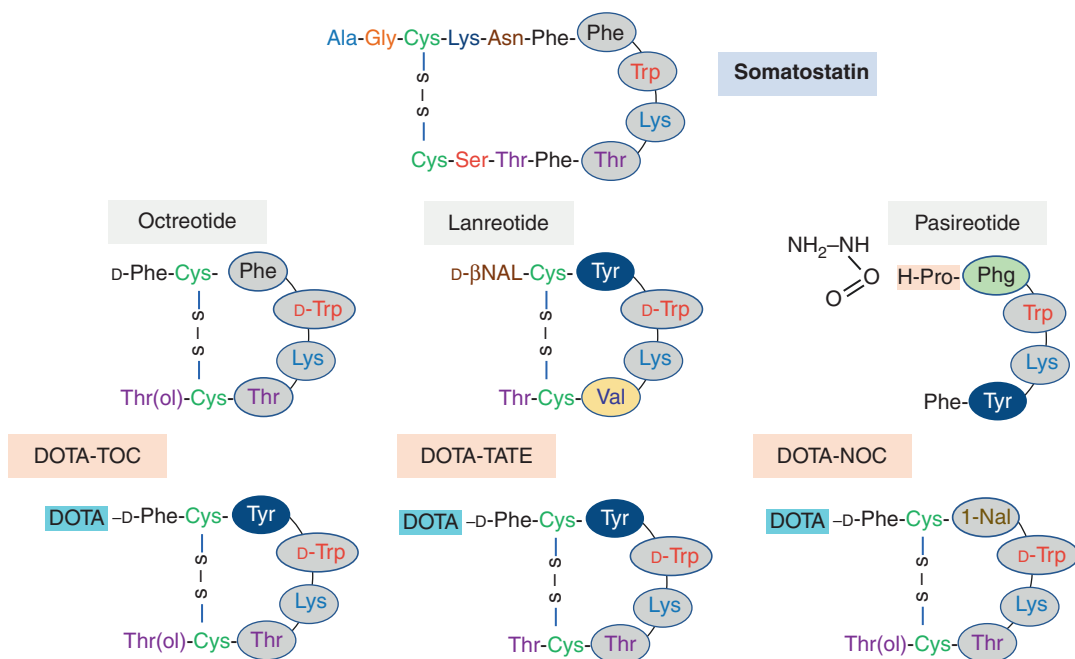
Fig. 20.5 Somatostatin analogs octreotide, lanreotide, and pasireotide are used as chemotherapeutic drugs to treat patients with neuroendocrine tumors. DOTA-conjugated octreotide analogs were developed to synthesize radiopharmaceuticals for molecular imaging and TRT

20.2.1.2 Cholecystokinin and Minigastrin (MG) Peptide

Cholecystokinin and minigastrin (MG) peptide hormones bind to the gastrin/CCK-2 receptor. Replacement of Met residues at positions 3 and 6 in CCK8 sequence with norleucine (NLe) residue produced CCK8(NLe) analog with higher affinity to the receptor. Similarly, replacement of Met residue at position 11 in MG sequence with NLe and also replacement of Phe residue at position 13 with naphthylalanine (NaI), generated two very important analogs (PP-F11N and MGS5) (Fig. 20.7) with higher affinity for the CCK-2 receptor and in vivo stability.

Bombesin (BN) is an amphibian 14-AA analog of the 27-AA human gastrin-releasing peptide (GRP). It has high binding affinity to the G protein-coupled gastrin-releasing peptide receptor (GRPR/BB2). The C-terminal 7–14 AA sequence (Fig. 20.7) is known to be critical for receptor binding and more stable in vivo than the full-length peptide molecule. Several chemical modifications have been introduced in the synthetic bombesin to stabilize the structure, to increase circulation time, to increase the binding affinity, and to potentiate agonist or antagonist properties. These analogs are usually modified by replacing Arg[3] by Lys, and at the C-terminus, Leu[13] and Met[14] by NNAAs such as statin (Sta) and NLe. Three important Bombesin analogs, AMBA, RM1, and RM2 (Fig. 20.7) were developed for theranostic studies.

20.2.2 Peptide Cyclization

Cyclic peptides (CPs) are generally generated from linear peptides by introducing disulfide bridges between sulfhydryl (thiol) groups of two peptidyl-cysteine residues. Cyclization of a linear peptide is usually achieved by linking the C-terminus to the N-terminus of the peptide backbone or by linking the C- or N-terminus to a side chain, or linking one side chain to another side chain. Peptide cyclization increases the pep-

Table 20.3 Affinity of SSTR peptides. Somatostatin analogs: affinity profiles IC_{50}[a] for the somatostatin receptor (SSTR) subtypes

Peptide	SSTR1	SSTR2	SSTR3	SSTR4	SSTR5
Somatostatin	5.2	2.7	7.7	5.6	4.0
Octreotide	>1000	0.4	4.4	>1000	5.6
Lanreotide	2129	0.75	98	1826	5.2
Pasireotide	9.3	1	1.5	>100	0.16
BFC-peptide conjugates					
DTPA-octreotide	>10,000	12	376	>1000	299
DOTA-TOC	>10,000	14	880	>1000	393
DOTA-TATE	>10,000	1.5	>1000	433	>1000
DOTA-NOC	>10,000	1.9	40	260	7.2
Metal-labeled chelate-peptide conjugates					
In-DTPA-octreotide	>10,000	22	182	>1000	237
In-DOTA-TOC	>10,000	4.6	120	230	130
Y-DOTA-TOC	>10,000	11	389	>1000	114
Ga-DOTA-TOC	>10,000	2.5	613	>1000	60
Ga-DOTA-TATE	>10,000	0.2	<1000	300	377
Lu-DOTA-TATE	>1000	2.0	162	>1000	1000
Ga-DOTA-NOC	>1000	1.9	40	260	7.2
Lu-DOTA-NOC	>1000	3.4	12.0	747	14.0
In-DOTA-BASS	>1000	9.4	>1000	380	>1000
In-DOTA-JR11	>1000	3.8	>1000	>1000	>1000
Ga-DOTA-JR11 (Ga-OPS201)	>1000	29	>1000	>1000	>1000
Lu-DOTA-JR11 (Lu-OPS201)	>1000	0.73	>1000	>1000	>1000
Ga-NODAGA-JR11 (Ga-OPS202)	>1000	1.2	>1000	>1000	>1000

[a]IC_{50} values expressed in nanomoles [9, 10]

Fig. 20.6 Amino acid sequences of somatostatin (or octreotide) analogs with specific binding to SSTR-2 receptors. Octreotide, Dotatoc, and Dotatate are agonists, while BASS, LM3, JR10, and JR11 are antagonists

CCK8:   D-Asp^1-Tyr^2-Met^3-Gly^4-Trp^5-Met^6-Asp^7-Phe^8-NH$_2$

sCCK8:   D-Asp^1-Tyr^2(OSO$_3$H)-Met^3-Gly^4-Trp^5-Met^6-Asp^7-Phe^8-NH$_2$

CCK8(Nle):   D-Asp^1-Tyr^2-Nle^3-Gly^4-Trp^5-Nle^6-Asp^7-Phe^8-NH$_2$

MG   Leu^1-(Glu)$_5$$^{2-6}$-Ala^7-Gly^9-Tyr^{10}-Met^{11}-Asp^{12}-Phe^{13}-NH$_2$

PP-F11N   (DGlu)$_6$-Ala^7-Tyr^8-Gly^9-Nle^{11}-Asp^{12}-Phe^{13}-NH$_2$

MGS5:   DGlu-Ala-Tyr-Gly-Trp-(N-Me)Nle-Asp-1-Nal-NH$_2$

Bombesin: Pyr^1-Gln^2-Arg^3-Leu^4-Gly^5-Asn^6-Gln^7-Trp^8-Ala^9-Val^{10}-Gly^{11}-His^{12}-Leu^{13}-Met^{14}-NH$_2$

AMBA: DO3A-CH$_2$-CO-Gly-4-aminobenzoyl-[Gln^7-Trp^8-Ala^9-Val^{10}-Gly^{11}-His^{12}-Leu^{13}-Met^{14}-NH$_2$]

RM1:   DOTA-Gly-aminobenzoyl-[D-Phe^6-Gln^7-Trp^8-Ala^9-Val^{10}-Gly^{11}-His^{12}-Sta^{13}-Leu^{14}-NH$_2$

RM2:   DOTA-4-amino-1-carboxymethyl-piperidine-[D-Phe^6-Gln^7-Trp^8-Ala^9-Val^{10}-Gly^{11}-His^{12}-Sta^{13}-Leu^{14}-NH$_2$]

Fig. 20.7 Cholecystokinin (CCK), Minigastrin (MG), and Bombesin analogs specific for Gastrin-Releasing Peptide Receptor (GRPR)

tides' structural rigidity and metabolic stability by locking the peptide into a conformation that is less susceptible toward proteolytic enzymes. It can also be used to increase biological activity by locking the peptide into a more biologically active conformation [10, 11].

The integrin family comprises numerous transmembrane receptors (such as $\alpha_v\beta_3$ and $\alpha_v\beta_5$) regulating cell adhesion and interaction with the extracellular matrix [12]. These receptors are recognized by several proteins and peptides containing the tripeptide L-arginine-glycine-L-aspartic acid (RGD) sequence. However, linear RGD peptides showed in general low binding affinity (IC$_{50}$ > 100 nmol/L), lack of specificity to $\alpha_v\beta_3$, and instability in the bloodstream due to the high degradation rate caused by the high susceptibility to proteases of the aspartic acid residue. Cyclization and incorporation of D-AA residues provided antagonists with increased stability and affinity by reducing structural flexibility as in the case of a cyclic pentapeptide, c(RGDfV). The methylated analog, c(RGDf(NMe)V) named cilengitide, with a half-life of ~2 h showed very high affinity for $\alpha_v\beta_3$ (0.61 nM) and $\alpha_v\beta_5$ (8.4 nM) integrins [6, 13]. Replacement of the Val^5 in c(RGDfV^5) by Lys or Glu generated c(RGDfK)

and c(RGDfE), respectively (Fig. 20.8), without altering the integrin $\alpha_v\beta_3$ binding affinity, and at the same time creating analogs which are useful for conjugating BFCs.

20.2.3 Insertion of β-Amino Acids

The incorporation of single or multiple β-AAs into peptides can decrease recognition by proteases and enhance in vivo metabolic stability and potency due to their different electronic environments, and backbone/side chain configurations compared to their α-amino acid analogs [11]. Incorporation of βAla–βAla linker, into bombesin peptide, however, did not improve in vivo stability. Bombesin analog modified with β^3-homoglutamic acid in the linker, with one single negative charge showed a significant increase in tumor uptake and tumor-to-tissue ratio but, did not necessarily increase the metabolic stability [11]. Also, the introduction of the *N*-methylated β-alanine linker in a statine-based GRPR-antagonist did not disrupt the binding affinity and presented a similar in vivo stability compared to the unmodified compound [14].
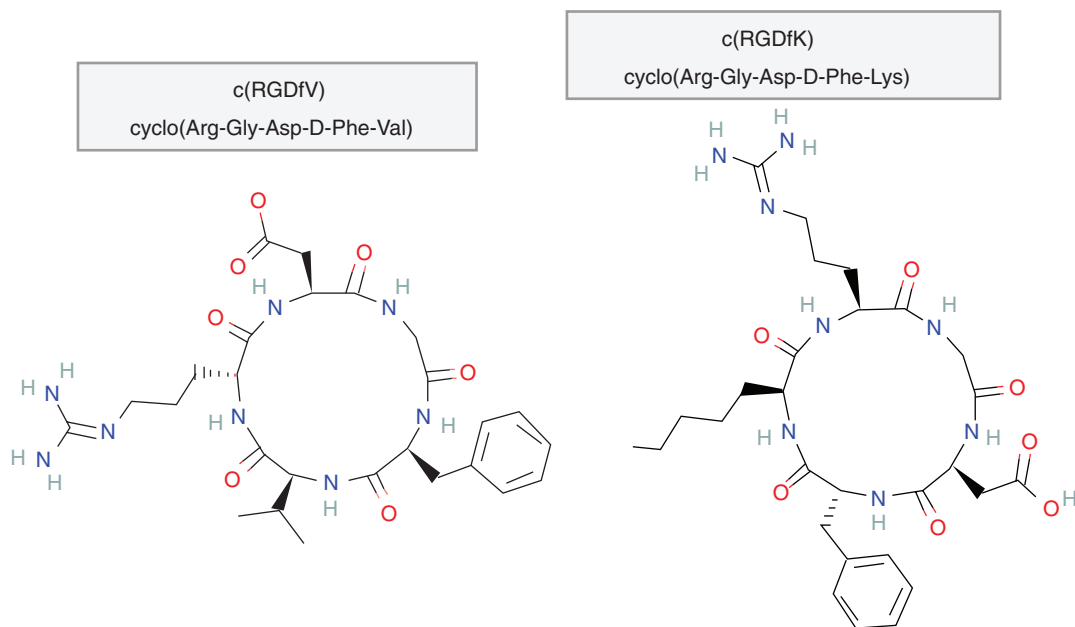
Fig. 20.8 Cyclic pentapeptide RGD analogs, c(RGDfV) and c(RGDfK) with high affinity for $\alpha_v\beta_3$ and $\alpha_v\beta_5$ integrins useful for developing radiopharmaceuticals for imaging

20.2.4   Substitution of Amides with Sulfonamides

Sulfonamides are amide analogs in which the carbonyl moiety is replaced with an isosteric SO_2 group. Sulfonamide groups contain a tetrahedral achiral sulfur atom bound to two electronegative oxygen atoms. To increase the metabolic stability of peptides-based radiopharmaceuticals, one or more amide groups in the backbone of a peptide can be substituted with relatively stable sulfonamide groups [11]. The most common method is to substitute the amide with the sulfonamide group at the cleavage site. However, it has also been found that the substitution of amides close to cleavage sites can also increase metabolic stability [11]. The potential benefits of substituting amide for sulfonamide bonds have not been fully explored in the design of radiopharmaceuticals.

20.2.5   N-Methylation (N-Alkylation)

Peptide modification through *N*-methylation constitutes substituting one or more NH groups in a peptide backbone with *N*-methyl (NCH₃) sub-

stituents. N-methylation has the potential to enhance resistance to proteases, increase membrane permeability, and biological activity. The *N*-methyl group will influence the conformational flexibility of both the peptide backbone and the side chains of the residues close to the N-CH₃ AAs [11].

N-methylation of the amide bond between the Ile[19] and Ile[20] residues in the endothelin peptide antagonist derivatives increased the half-life and receptor binding affinity compared to unmodified compound [15]. The mini-gastrin analog MGS5 (Fig. 20.7) shows several modifications in the C-terminal sequence of the peptide, namely, replacement of Met with Nle and of Phe with 1-naphtyl-alanine (1-Nal), as well as N-methylation of the peptide bond between Trp and Nle. Preclinical studies with radiolabeled DOTA-MGS5 demonstrated high and persistent tumor uptake and favorable tumor to-background activity ratios, including kidneys, suggesting that new radiopharmaceuticals based on DOTA-MGS5 will be powerful peptide probes in the localization and treatment of patients with CCK2R-expressing tumors [16].

20.2.6 PEGylation

The technique of chemical modification of the peptide using polyethylene glycol (PEG) polymer (Fig. 20.9) by covalent or non-covalent attachment is known as PEGylation. PEG possesses useful properties, including high solubility in water and many organic solvents, non-toxicity, and non-immunogenicity, and has been approved by the FDA for human use. PEGylation can improve both the physiochemical and PK performance of the peptides. The effects of PEGylation on peptide pharmacokinetics include avoidance of reticuloendothelial (RES) clearance, mitigation of immunogenicity, and reduction of enzymatic proteolysis and of losses by renal filtration, with potentially beneficial changes in biodistribution [11, 17]. These effects can dramatically increase the half-life of a peptide in circulation but, without adversely affecting binding and activity of the peptide ligand.

PEG's most common form is a linear or branched polyether with terminal hydroxyl groups. Monofunctional methoxy-PEG (mPEG) is the most common reagent used for PEGylation. PEG can also be derivatized with several linkage moieties yielding methoxyPEG-amines, -maleimides, or carboxylic acids (Fig. 20.9). The length and shape of PEGs (linear, branched, or dendritic) have been shown to influence the pharmacological properties of the PEGylated peptides and proteins, with branched PEG structures often most effective [11].

Many PEGylated peptide-based radiopharmaceuticals have been developed and shown to possess improved pharmacokinetic properties compared to their unmodified analogs, including increased receptor binding affinity, increased tumor uptake, and decreased kidney uptake [6, 11, 17]. Based on preclinical studies, radiolabeled DOTA-bombesin analogs with PEG chain as a linker between DOTA and the peptide showed superior PK properties and increase in half-life [18]. Incorporation of a mini-PEG (three ethylene oxide units) spacer into an RGD cyclic peptide was used to produce [^{18}F]-FB-mini-PEG-E[c(RGDyK)][2]. In preclinical studies, this agent showed greater radiolabeling yield, reduced renal clearance, and similar tumor uptake compared to the non-PEGylated analog [19].

20.2.7 Glycosylation

Glycosylation is a chemical reaction used to attach a carbohydrate (or glycan) to a hydroxyl or other functional group of another molecule. In N-linked glycosylation reactions, the glycans are attached to a nitrogen of asparagine or arginine side chain. In case of O-linked reactions, the glycans are attached to the hydroxyl oxygen of AA residues such as serine, threonine, and tyrosine. The introduction of carbohydrate moieties into a peptide changes the physiological properties of peptides, and may protect AA's side chain from oxidation, increase meta-
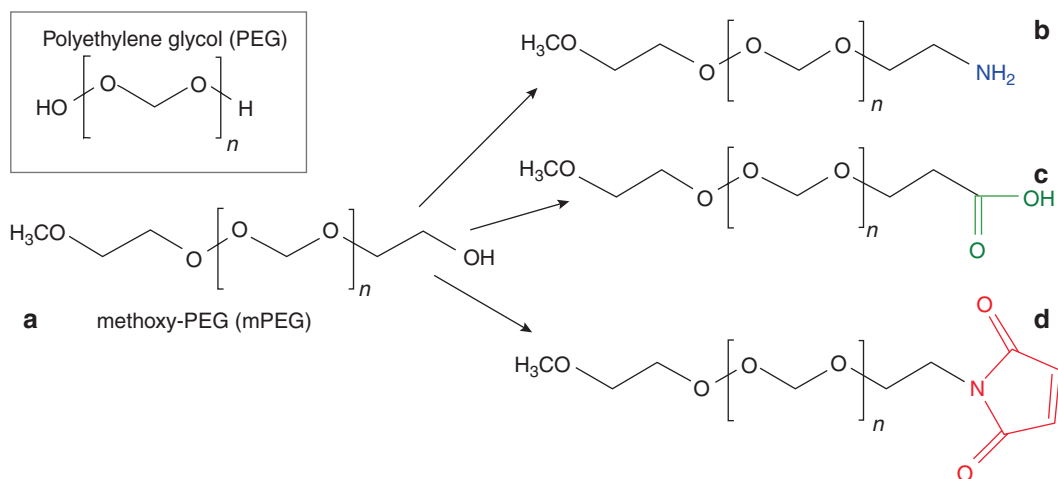
Fig. 20.9 Pegylation is a technique of chemical modification of the peptide using polyethylene glycol (PEG) polymer. Methoxy-PEG (mPEG) (**a**) is the most common reagent used for PEGylation. PEG can also be derivatized with several linkage moieties yielding methoxyPEG-amines (**b**), -carboxylic acids (**c**), or maleimides (**d**)

bolic stability, improve penetration through biological membranes, and even may facilitate active transport of the modified peptide by targeting glucose transporters on the cell membrane [20]. Conjugation of radiolabeled bombesin analogs with glucose moiety (through a triazole group) reduced abdominal accumulation and increased the uptake by tumors without affecting the cell internalization of the modified peptides [21]. Glycosylation of CCK analog, obtained by glucose binding to the Lys side chain at N-terminal region of the synthetic peptide, contributed to decrease its lipophilicity and to improve sensitivity, specificity, and pharmacokinetics in CCKR-expressing tumors [22]. Glycosylation and pegylation of modified cyclic RGD peptide have also shown to improve the pharmacokinetics. In particular, the F-Galacto-c(RGDfK) and c(RGDfK)-Peg-MPA) (MPA, mercapto propionic acid) showed IC_{50} of 100 nM and 8–15 nM, respectively [6]. Several examples (Fig. 20.10) for the application of ^{18}F-fluoroglycosylation as a strategy for the suc-
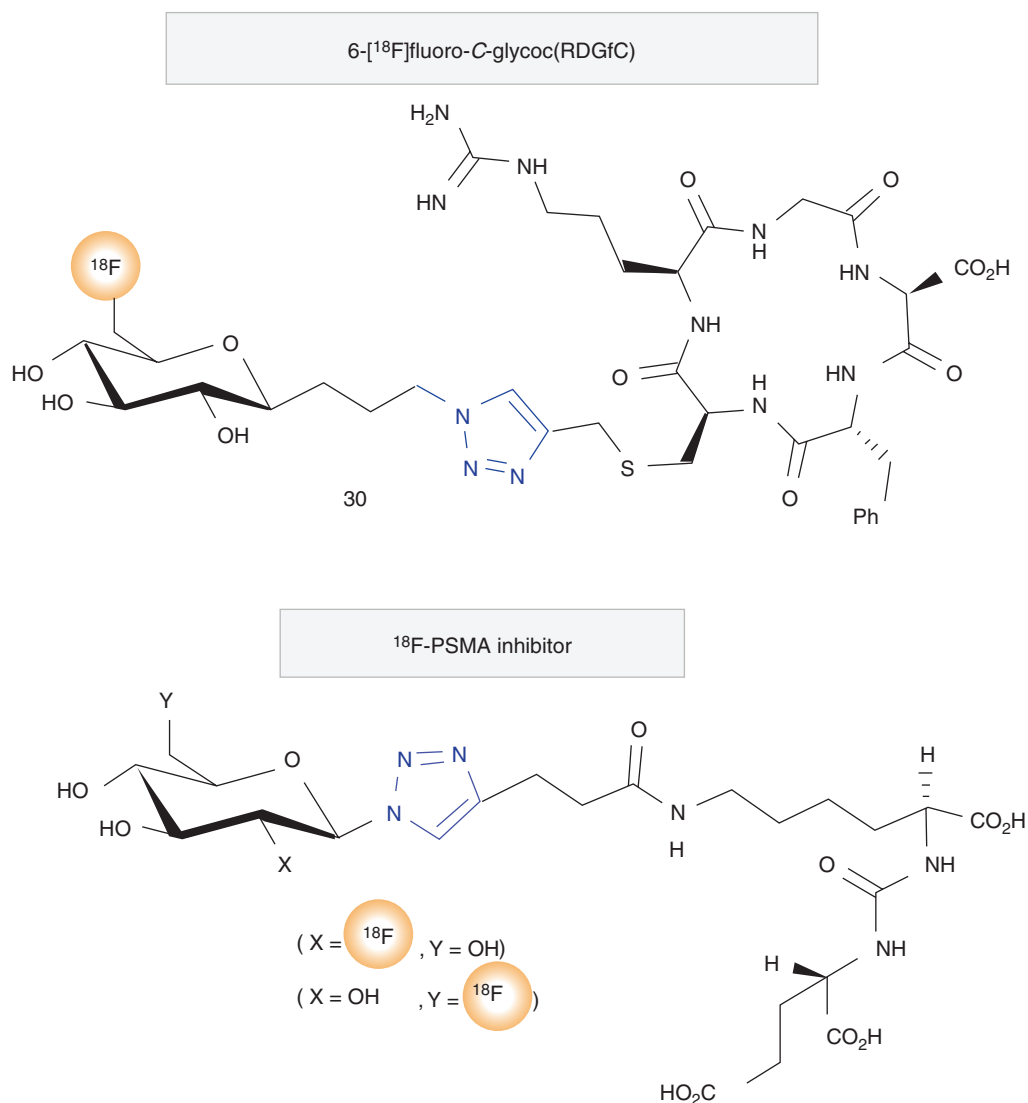
Fig. 20.10 Examples of ^{18}F labeled-RGD peptide and PSMA inhibitor synthesized based on click chemistry via Cu(I)-catalyzed Huisgen 1,3-cycloaddition reaction of an azide and an acyclic alkyne (CuAAC) using the ^{18}F-labeled prosthetic group 6-deoxy-6-[1^{8}F]fluoro-β-glucosyl azide. (From [23])
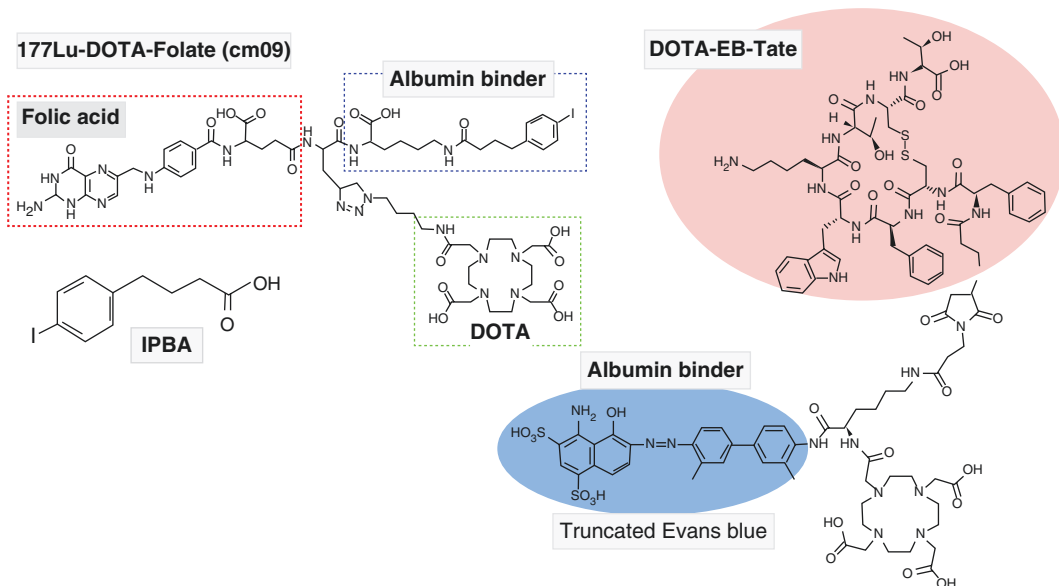
Fig. 20.11 Examples of ^{177}Lu labeled radiotracers with albumin binding molecule attached to the target specific vector. Folate analog was developed using 4-(p-iodophenyl)butyric acid (IPBA) as the albumin binder, while truncated Evans blue was used as the albumin binder to develop Dotatate analog. (Figures modified from Muller et al. [26] and Tian et al. [27])

cessful development of PET tracers has been recently reviewed [23].

20.2.8 Albumin Binding

The plasma protein, human serum albumin (HAS) has a long half-life of about 19 days, and because of its high molecular weight (67 kDa), it has low renal clearance making the protein a valuable candidate as a drug delivery system and a means to extend the half-life of peptides [4, 24, 25]. HSA is a widely recognized carrier for the passive targeting to solid tumors and has been frequently used to develop drug conjugates for longer plasma half-life. The covalent or non-covalent attachment of peptides to albumin can reduce the glomerular filtration rate and extend the half-life of peptides by increasing the size of peptide-based drugs. Albumin is also found to specifically target tumor regions because of its enhanced permeability and retention (EPR) effect as well as albumin receptor binding, which is a

unique advantage as the carrier for tumor-targeted drug delivery [25].

In addition to fatty acids, serum albumin can intrinsically bind a large diversity of small endogenous and exogenous organic molecules, shielding their hydrophobic character and strongly increasing their solubility in plasma [25]. Albumin binding ligands based on the lead structure 4-(p-iodophenyl)butyric acid (IPBA) (Fig. 20.11) have been identified by screening DNA-encoded chemical libraries [28]. The best derivative of IPBA known as Albutag was used to develop radiolabeled folate conjugates for imaging and therapy [26]. Albutag was also used to develop a novel class of trifunctional ligands, consisting of the high-affinity PSMA-binding domain, the Albutag, and the DOTA chelator, to facilitate the modification of the three moieties independently and ultimately enable the generation of spatial optimized conjugates PSMA conjugates for prostate cancer theranostics [29]. Preclinical studies demonstrated that the trifunctional ligands had high and persistent tumor

uptake with absorbed doses that were four times greater than those observed for a similar compound lacking the albumin-binding moiety. Albutag was also used to develop albumin-binding PSMA-targeting PET radioligands based on NODAGA chelator [30].

Amino acid analogs of IPBA (Lys-Glu-IPBA and Lys-Asp-IPBA) were used to investigate whether prolonging blood residence time of [177Lu]Lu-DOTATATE with albumin binders could increase tumor accumulation and tumor-to-kidney ratios for improved therapeutic efficacy. Preclinical studies demonstrated that addition of an albumin binder to DOTATATE increased blood residence time and tumor uptake of [177Lu]Lu-AspAB-DOTATATE; however, the increase in kidney uptake was proportionally higher, thus reducing the therapeutic index and clinical usefulness [31].

Evans blue (EB) is an azo dye that binds to serum albumin with low micromolar affinity, and each albumin molecule can bind up to 14 molecules of EB [32]. Several EB derivatives were developed to facilitate the development of radiolabeled peptides [32]. EB was used to increase the diagnostic and therapeutic efficacy of radiolabeled DOTATATE in patients with SSTR-2 positive neuroendocrine tumors. Preclinical studies in various animal tumor models demonstrated that the circulation half-life of radiolabeled EB-TATE was twice than that of DOTATATE and the tumor accumulation was much higher. Clinical studies with 177Lu-DOTA-EB-TATE in patients with metastatic NETs demonstrated higher blood retention, and achieved a 7.9-fold enhancement of tumor activity. However, the effective renal dose of 177Lu-DOTA-EB-TATE was significantly higher than that of 177Lu-DOTA-TATE [33].

20.2.9 Spacers/Linkers

Spacers are inert molecules used to increase the distance of peptides from chelators to prevent steric influence and loss of activity on the cell receptors upon functionalization [34]. In fact, the molecular size, lipophilicity, and the flexibility of the functional moiety can influence the binding of the bioactive peptide to its target [6]. Many spacers of different kinds, such as hydrocarbon chain, amino acid sequence, and PEG can be introduced to modify the pharmacokinetic properties of these biomolecules. Spacers with different charge and hydrophilicity affect the characteristics of the peptide conjugate. It has been shown that the complex with uncharged and hydrophobic spacers leads to increased liver uptake, while the composition with positively charged spacers results in high kidney retention. Therefore, the pharmacokinetics of radio complexes correlates to the structure and total charge of the conjugates [35]. In fact, the molecular size, lipophilicity, and the flexibility of the functional moiety can influence the binding of the bioactive radiolabeled peptide to its receptor [18, 36].

The influence of different spacers (PEG2, PEG4, N-acetyl glucosamine (GlcNAc), triglycine, β-alanine, aspartic acid, and lysine) between the chelator DOTA and the SST analog NOC were investigated. It was observed that in general, the spacers marginally influenced the binding affinities to the SSTR2 and SSTR5 receptor subtypes but, resulted an almost complete loss of SSTR3 affinity of the [111In-DOTA]-X-NOC peptides [3]. In preclinical studies, the influence of PEG spacers of different lengths on the biological profile of bombesin-based radiolabeled peptide antagonists were investigated. Among all the analogs studied, the PEG$_4$ and PEG$_6$ showed significantly better properties; very high tumor-to-non-target organ ratios, in particular, tumor-to-kidney ratios [18, 37].

20.2.10 Dimerization and Multimerization

Over the last years, many radiolabeled peptides were developed for diagnostic imaging and therapy, including peptides consisting of more than one copy of the targeting peptide. The radiolabeled peptides in routine clinical use (such as SST analogs), however, are primarily monovalent and composed of monomeric domain specific for one receptor. In contrast, multimeric

A. Homomultimers with the same copy of peptide:

Monomer:	c(RGDfK)	cyclo(-Arg-Gly-Asp-D-Phe-Lys)
Dimer:	E[c(RGDfK)]₂	Glu[cyclo(-Arg-Gly-Asp-D-Phe-Lys)]₂
Tetramer:	E{E[c(RGDy K)]₂}₂	Glu{Glu[cyclo(-Arg-Gly-Asp-D-Tyr-Lys)]₂}₂

B. Bispecific (Bivalent) Heterodimers

PEG₃-Glu-RGD-BN: -cyclo(-Arg-Gly-Asp-D-Tyr-Lys)-Glu-
(Aca-Gln[7]-Trp[8]-Ala[9]-Val[10]-Gly[11]-His[12]-Leu[13]-Met[14]-NH₂)
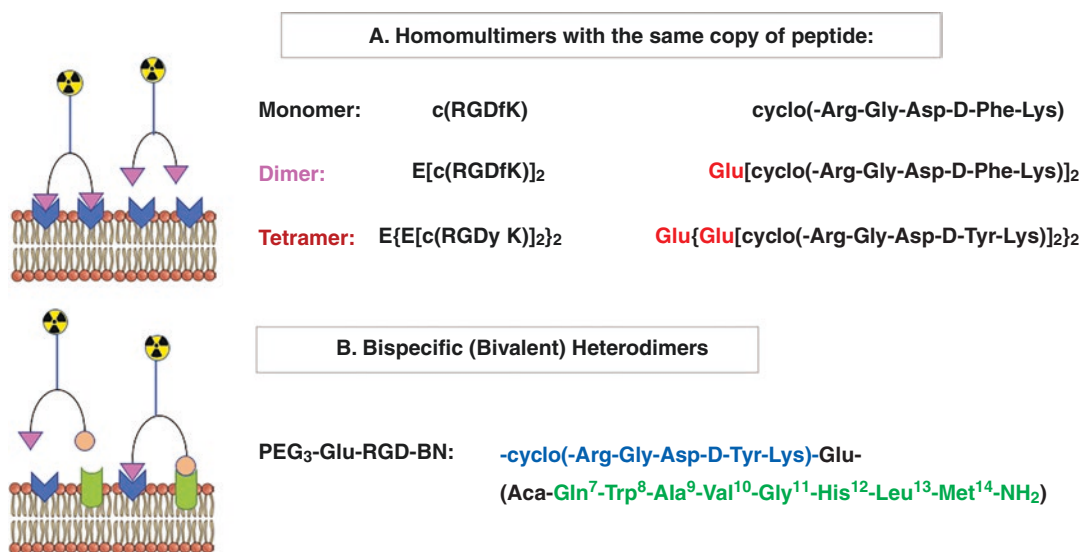
Fig. 20.12 Dimerization and multimerization of targeted peptide radiopharmaceuticals

ligands are composed of more than one monomeric domain attached to a backbone molecule so that the compound has the capability to bind to multiple binding sites on the same receptor or different receptors simultaneously (Fig. 20.12). Radiotracers being composed of two or more different target affine ligands designed to bind to several different receptors are known as heterobivalent ligands (or heteromultimers). If they bind to only one receptor by at least one allosteric interaction, such tracers are called bitopic ligands (or homomultimers).

In preclinical studies, ⁹⁹ᵐTc-HYNIC labeled dimeric RGD-peptide was compared with those of the monomeric analog [38]. Binding assays demonstrated a tenfold higher binding affinity to $\alpha_v\beta_3$ integrin for the dimeric analog compared with the monomeric (IC₅₀ values: 0.1 and 1.0 nM). The tumor uptake of both analogs was good but, was considerably greater for the dimeric RGD-peptide. In addition, the dimeric RGD-peptide showed greater kidney uptake and enhanced retention due to the difference in the molecular masses of the peptides. Similar studies with ⁶⁴Cu labeled tetrameric and octameric RGD peptides showed that ⁶⁴Cu-DOTA-octameric-RGD peptide had the greatest binding affinity, greater tumor uptake, and enhanced tumor retention compared with ⁶⁴Cu-DOTA-RGD tetramer [39].

Since several cancer cells express both integrin $\alpha_v\beta_3$ and GRP receptors, both RGD and BN radiopeptides have been widely used. ¹⁸F-labeled PEGylated-RGD-Bombesin heterodimer was developed and compared to the non-PEGylated analog, and the corresponding monomers. The receptor binding affinities of heterodimer were comparable to the corresponding monomers. Biodistribution and µPET imaging studies in nude mice with PC-3 cells confirmed that ¹⁸F-FB-PEG₃-Glu-RGD-BN displayed rapid and high tumor uptake with high tumor contrast and favorable PK with reduced liver accumulation [4, 40].

Radiolabeled heterobivalent peptidic ligands (HBPLs), being able to address different receptors, are highly interesting tumor imaging agents as they can offer multiple advantages over monovalent peptide receptor ligands. Furthermore, the application of a radiolabeled heterobivalent agent can solve the ubiquitous problem of limited tumor visualization sensitivity caused by differential receptor expression on different tumor lesions [4]. In the last 10 years, heterodimeric peptides for imaging and therapy were developed with several combinations of receptors, such as $\alpha_v\beta_3$ and GRPR, $\alpha_v\beta_3$ and PSMA and $\alpha_v\beta_3$ and STTR. In a pilot study, the safety, radiation dosimetry, and diagnostic performance of ⁶⁸Ga-BBN-RGD heterodimer peptide radiophar-

maceutical was studied in patients with breast cancer [32, 33, 41]. Both the primary cancer and metastases showed positive ^{68}Ga-B1/2BN-RGD accumulation.

tide labeling, and different methods of labeling of radionuclides to the peptides will be discussed briefly here. More detailed discussions of this topic are also presented in Chaps. 8 and 18.

20.3 Radiolabeling of Peptides

As described earlier, the first radiolabeled peptide used in 1989 for imaging studies was ^{123}I-Tyr^3-octreotide to detect SSTR-2 receptor positive NETs. In the last three decades, hundreds of radiolabeled peptides were developed and evaluated in preclinical studies to assess the potential for molecular imaging and TRT studies. Some of the most common radionuclides used in the development of radiolabeled peptides are shown in Table 20.4. Except for the radioisotopes of halogens (F, I, and At), all other radionuclides are metals.

The choice of the labeling approach is driven by the nature and the chemical properties of the radionuclide. The choice of radionuclide for pep-

20.3.1 Radionuclides

Radionuclides are useful for molecular imaging studies based on PET or SPECT decay either by positron (β^+) emission, electron capture (*EC*) or isomeric transition (IT). The radionuclides that are used for therapy decay by emitting either β^- particles or α particles.

The decay characteristics of some of the important radionuclides routinely used for imaging and therapy are listed in Table 20.4. Among the radionuclides listed in this table, radioisotopes of F, I, and At are non-metals and belong to the halogen (Group-7) family. All other radionuclides are metals differing in valency, oxidation state, and co-ordination chemistry. The γ-emissions of radionuclides decaying by IT or

Table 20.4 Radionuclides for imaging and therapy

Radionuclide	$T_{1/2}$	Decay Mode	%	γ Energy keV	%	Particle, E_{mean} keV	%	
^{99m}Tc	6 hours	IT	98	140				SPECT
^{123}I	13.22 days	EC	97	159	83.6			SPECT
^{111}In	2.8 days	EC	100	171.3 245.4	90.7 94.1			SPECT
^{18}F	109.8 min	β^+	96.73			250	96.73	PET
^{68}Ga	67.7 min	β^+	87	1077	3.22	830	99.9	PET
^{64}Cu	12.7 hours	β^+ β^- EC	17.6 38.5 44			278	17.6	PET
^{89}Zr	3.3 days	β^+ EC	23 77	909	99	396	22.7	PET
^{124}I	4.18 days	β^+ EC	23 77	603 723 1691	62.9 10.4 11.2	822	22.7	PET
^{131}I	8.025 days	β^-	100	364.5	81.5	181.9	100	Therapy
^{90}Y	2.66 days	β^-	100			932.3	100	Therapy
^{177}Lu	6.647 days	β^-	100	113 208	6.23 10.4	133.6	100	Therapy
^{213}Bi	45.6 min	α	100	440.5	25.9	8440	100	Therapy
^{211}At	7.2 hours	α	41.8			5869	41.8	Therapy
^{225}Ac	9.92 days	α	100	218[a] 440.5[a]	11.5 25.9	5830	100	Therapy

[a]Gamma photons from the daughters Fr-221 and Bi-213

EC are useful for planar and SPECT imaging studies, while PET is based on the annihilation radiation (511 keV photons) from radionuclides decaying by positron (β^+) emission.

The radionuclides that are used for therapy decay by emitting either β^- particles or α particles. The cytotoxic effects of therapy radionuclides are primarily due to irreversible DNA damage and cell death. Alpha particles with high LET deposit their high kinetic energy (5–8 MeV) over short distances (<100 μm) compared to low LET β^- particles (<15 mm). The decay mode and the kinetic energy of non-penetrating particle radiation will determine the particle range in the tissue the amount of energy absorbed (expressed in Grays) in the tissue.

It is also important to recognize that several radionuclides are also available as theranostic-pair, ideal for both imaging and therapy. Isotopes of the same element (such as ^{123}I, ^{124}I, and ^{131}I) have similar chemistry and the in vivo behavior of radiotracers labeled with isotopes of the same element will be identical. This contrasts with nonchemically identical matched pairs of isotopes (such as ^{111}In/^{90}Y and ^{68}Ga/^{177}Lu), which may have different biodistribution and PK. Therefore, ^{111}In or ^{68}Ga labeled diagnostic radiopharmaceuticals can only be regarded as chemical/biological surrogates for ^{90}Y, ^{177}Lu, ^{225}Ac, and other trivalent metal-labeled radiopharmaceuticals.

Radionuclidic purity and specific activity (SA) of radionuclides are very important quality control indicators, and provide quantitative information regarding the purity of the radionuclide, and the mass of radionuclide for a given amount of activity (MBq or mCi per mg or μmole). The radionuclide purity and SA, however, are very much dependent on the methods and nuclear reactions used to produce the radionuclides by cyclotrons and reactors. (please refer to Chap. 8, regarding the production of radionuclides).

20.3.2 Radiolabeling Methods

The labeling of peptides with radionuclides can be performed by direct labeling, with the addi-tion of a prosthetic group. Direct labeling is the method used to label peptides without using intermediates, such as BFCs. Direct labeling technique are generally used mostly for radio-iodination and in some cases labeling with Tc-99m. Prosthetic groups are small molecules able to bind with radionuclides in one site of the structure and, simultaneously, with a pep-tide at a second site. Prosthetic groups are bifunctional agents that consist of a suitable site for radioiodination or fluorination and functional groups to allow covalent attachment of the peptide. Radiometals specifically require bifunctional chelating agents (BFC or BFCA) to obtain the best conjugation of radiometal with peptides. The bifunctional nature of the chelators means that they have functional groups that can coordinate (form a complex) a metal ion and can also be covalently attached to the peptide.

20.3.3 Peptide Labeling with Radioiodine

Radioiodination of peptides can be performed either by electrophilic substitution (direct method) or via conjugation (indirect method) [3, 42, 43]. The reaction consists of the electrophilic substitution of an aromatic proton by electro-philic radioiodine and it takes place in an amino acid residue of the peptide which affords strong (but also weak) electron donating groups (e.g., -OH, -NH$_2$, -OR, -SR, -NHCOR) [3]. The tyro-sine (Tyr) or histidine (His) side chains in pep-tides offer the possibility of electrophilic aromatic substitution by electrophilic radioiodine with high efficiency under mild conditions. Since radioiodide is stable and chemically non-reactive, several oxidizing agents (such as chloramine T, Iodogen®, lactoperoxidase/H$_2$O$_2$) can be used for the generation of electrophilic iodine species ((HO*I, H$_2$O*I)). With Tyr residue, substitution of a hydrogen ion with the reactive iodonium ion occurs *ortho-* to the phenolic hydroxyl group, while with histidine, substitution occurs at the second position of the imidazole ring. Electrophilic substitutions can often be per-

formed fast on a nonderivatized substrate under mild reaction conditions.

In an indirect method, the incorporation of radioiodine can be performed by the utilization of radioiodinated prosthetic groups, which can be used for conjugation with specific functionalities introduced previously into the peptide precursors, such as amine, aminooxy or thiol groups [43]. Active esters, such as N-succinimidyl-4-iodobenzoate (PIB), N-succinimidyl-3-iodobenzoate (SIB), and N-succinimidyl-5-[*I]iodo-3-pyridine carboxylate (SIPC), have been developed. Aldehydes, such as 4-iodobenzaldehyde, have been used for the coupling of peptides to form stable radiolabeled oximes. This methodology has been proposed for radioiodination of multimeric cyclic RGD peptides [42]. Recently, the first bimodal fluorinated and iodinated prosthetic group, tetrafluorophenyl 4-fluoro-3-iodobenzoate (TFIB), was introduced as a suitable acylating agent for the labelling of a wide variety of primary amine-containing compounds. [^{125}I]/[^{18}F]TFIB was successfully used to tag tumor-targeting peptides, such as PEG3[c(RGDyK)]$_2$ and NDP-MSH, targeting αvβ3 integrin and MC1R receptors, respectively [43]. ^{125}I ($T_{1/2}$ = 59.4 days) labeled peptides are especially useful for all the preclinical development work to optimize the design of peptides for imaging and therapy (Fig. 20.13).

20.3.4 Peptide Labeling with Fluorine-18

^{18}F has the most ideal half-life and has a unique, and diverse chemistry for labeling of peptides. The most common method of cyclotron production is based on ^{18}O(p, n)^{18}F nuclear reaction, and ^{18}F-fluoride is produced in high amount of radioactivity (74–370 GBq), and SA (100 GBq/μmol) for use as a nucleophile. Fluorination of peptides may be conducted by direct methods or indirect methods. Direct methods are those in which the ^{18}F-fluoride is reacted directly with the peptide, which may have been previously modified to facilitate radiolabeling, and only subsequent purification is required to obtain the final product. Indirect methods require the prior radiosynthesis of a prosthetic group and subsequent bioconjugation to a peptide that has been modified for site specific reaction [3, 44–47].

Several successful attempts to introduce ^{18}F directly into small peptides have been reported in the literature. Direct substitution methods, how-

Fig. 20.13 Electrophilic and nucleophilic radioiodination
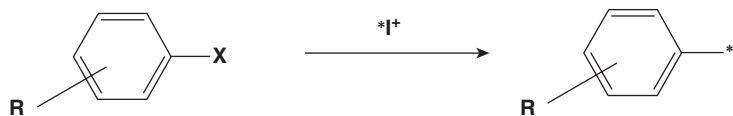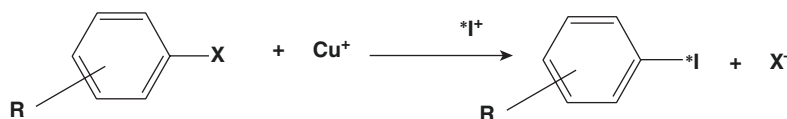
Fig. 20.14 Examples
of radiofluorination
techniques based on
substitution or addition
reactions commonly
used in the synthesis ^{18}F
labeled peptides. Isotope
exchange (**a**), click
chemistry (**b**), and
Fluorinate prosthetic
group (**c**)
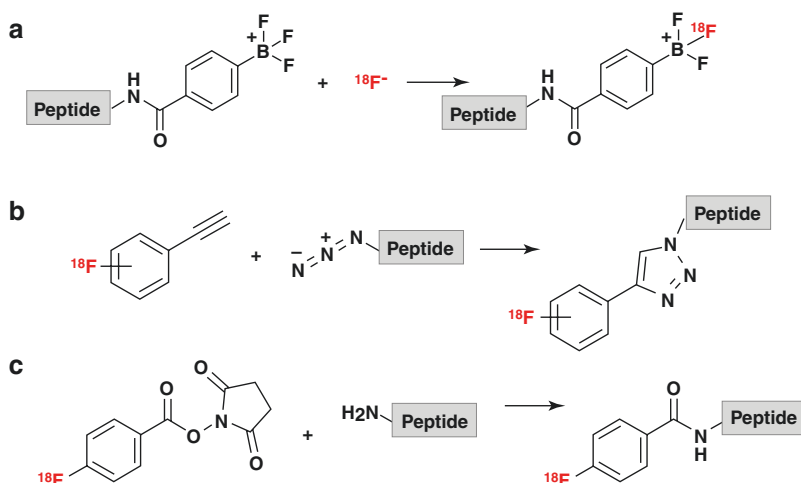
ever, usually require some non-physiological conditions of pH or temperature and most peptides do not tolerate such conditions, and may undergo hydrolysis. The use of prosthetic groups for the direct ^{18}F-labeling of peptides was first reported based on trimethylammonium-substituted modified peptides. This methodology has demonstrated usefulness toward direct ^{18}F-fuorination of peptides containing histidine, tryptophan, lysine, and arginine residues without the need of protecting groups [44]. Several new strategies for direct ^{18}F labeling have also been developed recently. An elegant site-selective C–H ^{18}F-fuorination of leucine residue within complex peptide using [^{18}F]-N-fluorobenzenesulfonimide ([^{18}F]NFSI) showed that a combination of photoactivated sodium decatungstate and ([^{18}F]NFSI effects site-selective ^{18}F-fluorination at the branched position in leucine residues in the unprotected and unaltered native peptides [48]. A method to introduce a 4-[^{18}F]fluorophenylalanine residue into peptide sequences by chemo-selective radiodeoxyfluorination of a tyrosine residue can label small peptides by formally replacing a single hydrogen, the para-hydrogen atom in Phenylalanine residue with [^{18}F]fluoride [49].

In the indirect labeling methods, the peptides are attached to the prosthetic groups mostly through amine- or thiol-reactive groups via acylation, alkylation, amidation, imidation, oxime, hydrazone formation, or using click chemistry [45]. Selected examples of prosthetic groups

include [^{18}F]SFB, [^{18}F]FBA, [^{18}F]FBAM, and [^{18}F]FBEM. The choice of prosthetic group, however, is critical for radiotracer development, as they may adversely alter the physical and physiological characteristics of the labeled molecule. Several examples of radiofluorination techniques based on substitution or addition reactions are shown in Fig. 20.14.

Since fluorine was known to bind and form stable complexes with many metals, a successful method was developed to form a stable NOTA Al-^{18}F complex of a peptide conjugated with macrocyclic chelators (such as NOTA) [50]. This labeling methodology has been used by several groups for the labeling of small molecules, peptides, and proteins using several acyclic and macrocyclic chelators (Fig. 20.15) [45, 52, 53]. The Al-[^{18}F]fluoride ([^{18}F]AlF) radiolabeling method combines the favorable decay characteristics of fluorine-18 with the convenience and familiarity of metal-based radiochemistry and has been used to parallel ^{68}Ga radiopharmaceutical developments. As such, the [^{18}F]AlF method is popular and widely implemented in the development of radiopharmaceuticals for the clinic [51].

20.3.5 Peptide Labeling with Trivalent Radiometals

Among the metals shown in Table 20.5, Tc-99 m is a unique transition metal exhibiting oxidation
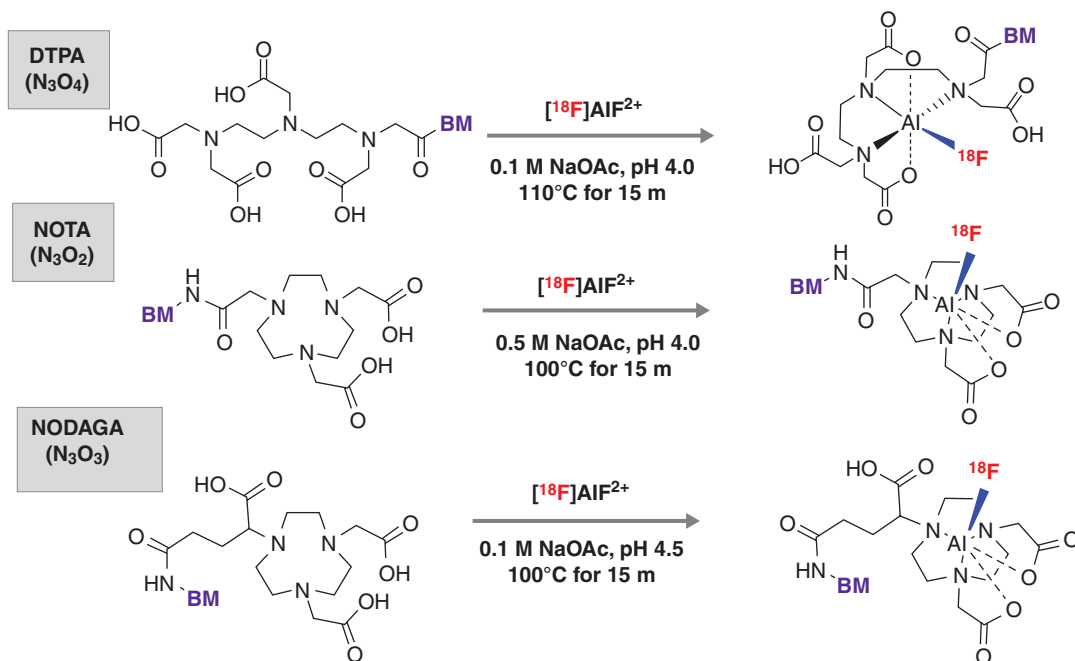
Fig. 20.15 ^{18}F labeling of peptides or biomolecules (BM) using aluminum-fluoride method [^{18}F]AlF. (Figure modified from Archibald and Allott [51])

Table 20.5 Physical and chemical characteristics of radiometals

Property	Transition metals			Post-transition metals				Lanthanides	Actinides	
	Cu	Y	Tc-99 m	Ga	In	Pb	Bi	Lu	Ac	Th
Atomic number	29	39	43	31	49	82	83	71	89	90
Group	11	3	7	13	13	14	15	3	n/a	n/a
Atomic radius (pm)	128	181	136	122	163	175	156	174		108–135
Ionic radius (pm)	80	90–108	51–78.5	47–62	62–92	79–143	96–117	86–103	112	105
Electron structure	[Ar] $3d^{10}$ $4s^1$	[Kr] $4d^1$ $5s^2$	[Kr] $4d^5$ $5s^2$	[Ar] $3d^{10}$ $4s^2$ $4p^1$	[Kr] $4d^{10}$ $5s^2$ $5p^1$	[Xe] $4f^{14}$ $5d^{10}$ $6s^2$ $6p^2$	[Xe] $4f^{14}$ $5d^{10}$ $6s^2$ $6p^3$	[Xe] $4f^{14}$ $5d^1$ $6s^2$	[Rn] $6d^1$ $7s^2$	[Rn] $6d^2$ $7s^{2X}$
Electronegativity	1.90	1.22	1.9	1.81	1.78	1.87 2.33	2.02	1.27	1.1	1.3
Oxidation state	+1, +2	+3	−3 to +7	+3	+3	+2, +3	+3	0 to +4	+3	+1 to +4
Coordination number	4	6–9	5–7	4–6	4–8	4–8	5–8	6–9	6–8	8

states from +7 to −1 and it can be stabilized using various ligands and coordination environments. Therefore, the chemistry of Tc-99 m will be discussed separately. All other metals (except copper) predominantly are hard Lewis acids and exist as trivalent cations (3+) and share similar chelation chemistry. Copper is an intermediate Lewis acid and prefers 2+ oxidation state. Hard metal ions prefer hard donating groups (e.g., carboxylic acids), which possess dense anionic character. Conversely,

soft metals have low charge density and polarizable electron shells, and form covalent bonds with softer, more electron-disperse donor groups.

20.3.5.1 Bifunctional Chelators (BFCs)

Chelation is a type of bonding of ions and molecules to metal ions. It involves the formation of two or more separate coordinate bonds between a polydentate ligand (known as chelators or chelating agents) and a single central metal atom. DTPA and DOTA are the two most frequently used chelators in nuclear medicine. The chelating agents have been modified to function as BFCs since they have a metal binding moiety function for the sequestration of the metallic radionuclide and also possess a chemically reactive functional group that can provide the requisite chemistry for covalent attachment to a targeting vector of interest, such as a small molecule peptide. The primary goal of radiometal complexation using BFCs is the formation of robust coordination complexes to prevent the release of free metals

in vivo. Based on the metal chemistry, it is important to identify the most appropriate BFC that provides both the thermodynamic stability in vitro, and kinetic stability in vivo (Table 20.6).

Polyaminocarboxylate ligands (containing nitrogen and oxygen donor atoms) have both acyclic, and macrocyclic options to encapsulate the metal ion. Initially, acyclic BFCs, such as EDTA, DTPA, and their derivatives were used to prepare ^{111}In and ^{90}Y labeled antibodies. To improve the in vivo stability of ^{90}Y labeled antibodies, full octadentate macrocyclic bifunctional DOTA derivatives have been developed for complexing trivalent radiometals, such as ^{111}In, ^{86}Y/^{90}Y, and ^{177}Lu [3, 6, 54, 55]. The most common chelators and BFCs used in the development of radiolabeled peptides are shown in the Figs. 20.16 and 20.17. Each of these chelating agents (Table 20.6) differ in size and offer different donor groups like carboxylic acids, alcohols, amines, thiols, and phosphonic acids.

Macrocyclic BFCs are generally more kinetically inert and require minimal physical manipu-

Table 20.6 Acyclic and macrocyclic ligands (or chelating agents) used for the labeling of peptides with radiometals

Chelator	Chemical name	Donor atoms	Coordination number (CN)	Metals
DTPA	Diethylenetriaminepentaacetic acid	N_3O_5	8	Ga, In
EDTA	Ethylenediaminetetraacetic acid	N_2O_4	6	Ga, In
HBED-CC	3-[3-[4-[5-(2-carboxyethyl)-2-hydroxyphenyl]-1,4-bis(carboxymethylamino)butyl]-4-hydroxyphenyl]propanoic acid	N_2O_6	8	Ga
NOTA	1,4,7-triazacyclononane-1,4,7-tri-acetic acid	N_4O_3	6	Ga
DOTA	1,4,7,10-tetraazacyclododecane-1,4,7,10-tetraacetic acid	N_4O_4	8	In, Ga, Y, Lu, Bi, Ac, Th, Cu
TCMC	1,4,7,10-tetrakis(carbamoylmethyl)-1,4,7,10-tetraazacyclododecane	N_4O^4	8	Pb
TETA	1,4,8,11-tetraazacyclotetradecane-1,4,8,11-tetraacetic acid	N_4O_4	8	Cu
CB-TE2A	4,11-bis-(carboxymethyl)-1,4,8,11-tetraazabicyclo[6.6.2]-hexadecane	N_4O_2	6	Cu
SarAr	1-N-(4-aminobenzyl)-3,6,10,13,16,19-hexaazabicyclo[6.6.6]eicosane-1,8-diamine (SarAr)	N_6	6	Cu
PCTA	3,6,9,15-Tetraazabicyclo[9.3.1]pentadeca-1(15),11,13-triene-3,6,9-triacetic acid	N_4O_3	7	Ga, Cu
PEPA	1,4,7,10,13-pentaazacyclopentadecane-N,N′,N″,N‴,N⁗-pentaacetic acid	N_5O_5	10	Ac
HEHA	1,4,7,10,13,16-hexaazacyclohexadecane-N,N′,N″,N‴,N⁗,N‴′-hexaacetic acid	N_6O_6	12	Ac

Fig. 20.16 Acyclic chelators used for the synthesis of radiometal-labeled peptide radiopharmaceuticals
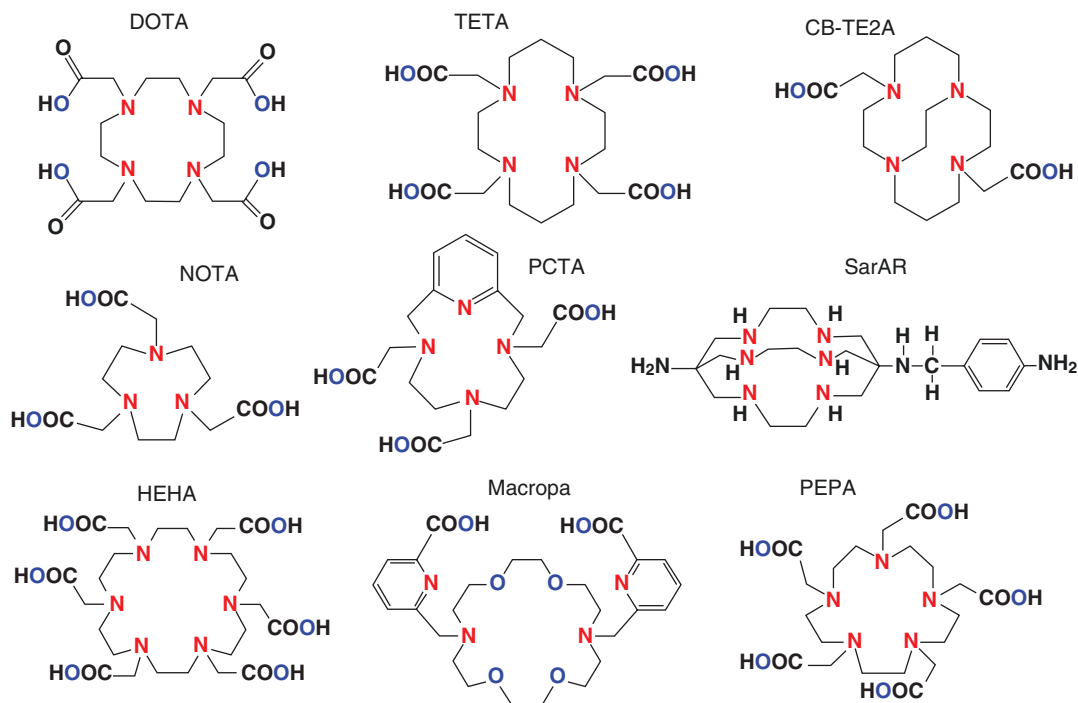
Fig. 20.17 Macrocyclic chelators used for the synthesis of radiometal-labeled peptide radiopharmaceuticals

lation during metal ion coordination, as they possess inherently constrained geometries and partially pre-organized metal binding sites. In contrast, acyclic chelators must undergo more drastic change in physical orientation and geometry in solution so as to enable the donor atoms to coordinate with metal ion. However, radiolabeling with acyclic chelators can happen at RT in a short time, whereas macrocycles may require higher temperatures and longer incubation times [55]. The stability of the metal–ligand complex is defined by the stability constant (K_S or K_{ML}) when the system reaches an equilibrium between interacting chemical species. The higher the value of K_{ML}, the greater the thermodynamic stability of the metal–ligand complex. The values of K_{ML} (such as 10^4 or 10^{30}) are normally represented as log K_{ML} values (such as 4 and 30). A more useful thermodynamic parameter is the *pM value* ($-\log[M]_{Free}$), and the pM values are linearly correlated with K_{ML} values, and express the extent to which a metal ion complex is formed in solution under physiologically relevant conditions [57]. The K_{ML} and pM values for different DOTA and DTPA with several metals is shown in Table 20.7.

20.3.5.2   Covalent Attachment of BFC to Peptide

BFCs are chelators (Fig. 20.18) with reactive functional groups that can be covalently coupled (or conjugated) to a primary amine (NH_2) or thiol (SH) group of the peptides. The bioconjugation techniques may utilize functional groups, such as carboxylic acids groups of the BFC, or BFC derivatives can be prepared with reactive groups that can facilitate the conjugation with peptides. Some common BFC derivatives are activated esters (*such as N*-hydroxysuccinimide NHS-ester) for amide couplings, isothiocyanates (NCS) for thiourea couplings, and maleimides for thiol couplings.

BFCs are often placed at the N- or C-terminus of the peptide. Often, additional spacers are used, which increases the molecular weight of whole structure, an adverse fact especially for small peptides. The labeling can influence charge or lipophilicity of the compound which, in turn, may change its biodistribution or excretion, particularly for small ligands. The right selection of labeling method is therefore crucial to obtain appropriate resolution of images, concentration in tumors cells, and excretion methods with efficient clearance.

20.3.5.3   Matching BFC to Radiometal
To identify the most appropriate chelator for a specific radiometal, the following factors are important:

- Fast radiolabeling kinetics at ambient temperature preferably, especially for heat sensitive peptides.
- The reaction time should be short (<10 min), especially for radionuclides with short half-life.
- The labeling yield and RCP should be high and preferably does not require HPLC purification of the drug product.
- The in vitro and in vivo stability (kinetic inertness) should be high to prevent the biodistri-

Table 20.7 Metal-Chelate complexes: coordination numbers (CN) and stability constants

	DOTA			DTPA		
	CN	Log K_{ML}	pM	CN	Log K_{ML}	pM
Ga^{3+}	N_4O_2	21.3–26.1	15.2, 18.5	N_3O_4	24.3, 25.5	20.2
Y^{3+}	N_4O_4	24.3–24.9	19.3, 19.8	N_3O_5	21.9, 22.5	17.6, 18.3
In^{3+}	N_4O_4	23.9	17.8, 18.8	N_3O_5	29.0, 29.5	24.4, 25.7
Lu^{3+}	N_4O_4	21.6, 23.5	17.1	N_4O_5	22.4, 22.6	19.1
Bi^{3+}	N_4O_4	30.3	27.0	N_4O_5	33.9, 35.2	
AC^{3+}						
Cu	N_4O_2	22.7, 22.7	17.6	N_3O_3	21.4	

Fig. 20.18 Bifunctional chelating (BFCs) BFCs have a metal binding moiety function for the sequestration of the metallic radionuclide, and also possess a chemically reactive functional group that can provide the requisite chemistry for covalent attachment to a targeting vector of interest, such as a peptide
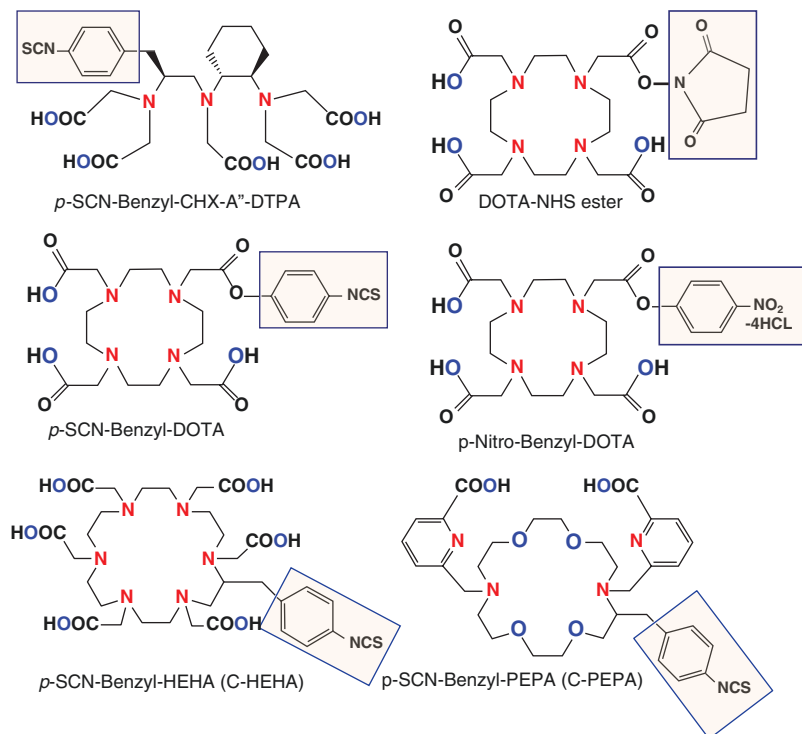
bution of free radiometal species to non-target organs. Kinetic inertness is the most important consideration for selecting the best chelator, especially for therapeutic radiometals.

The preference of various chelators for different radiometals is summarized in Table 20.6. Among the acyclic chelators, DTPA is acceptable for the chelation of ^{111}In, ^{90}Y, and ^{177}Lu but, CHX-A"-DTPA is the best acyclic chelator for these three metals. DOTA is one of the primary work-horse chelators for the development of radiolabeled peptides and one of the current "gold standards" for several radiometals including ^{111}In, ^{90}Y, ^{177}Lu, and ^{225}Ac. DOTA has also been used to complex metals, such as ^{64}Cu, ^{213}Bi, and ^{212}Pb, and clinical studies with radiolabeled peptides documented the potential safety of these peptides. DOTA has been extensively used with $^{67/68}$Ga but, it is widely accepted to be less stable than NOTA. ^{68}Ga-DOTATOC has been shown to exhibit superior in vivo properties to ^{111}In-DOTATOC (Octreoscan) despite non-optimal stability [55]. ^{68}Ga-DOTATATE, ^{177}Lu-DOTATATE, and

^{68}Ga-DOTATOC (Fig. 20.20) have received FDA approval for routine clinical studies (Fig. 20.19).

Although DOTA has been used, successfully with ^{212}Pb, but, its slow radiolabeling kinetics and stability properties were not ideal. The DOTA derivative TCMC is considered a good chelator for both ^{212}Pb and $^{212/213}$Bi [55].

The majority of Cu^{2+} chelator development in the last two decades has focused on tri- and tetraaza macrocycle-based polyamino carboxylates, such as NOTA and TETA. The best chelators to date are CB-TE2A, NOTA, and DiamSar. The clinical studies with ^{64}Cu-DOTATATE (DetectNet), however, showed adequate safety and efficacy to receive the FDA approval for the detection of SSTR-2 positive NETs.

A fundamental critical component of a radiometal-based radiopharmaceutical is the BFC, the ligand system that binds the radiometal ion in a tight stable coordination complex so that it can be properly directed to a desirable molecular target in vivo. The experimental methods by which chelators are assessed for their suitability with a variety of radiometal ions
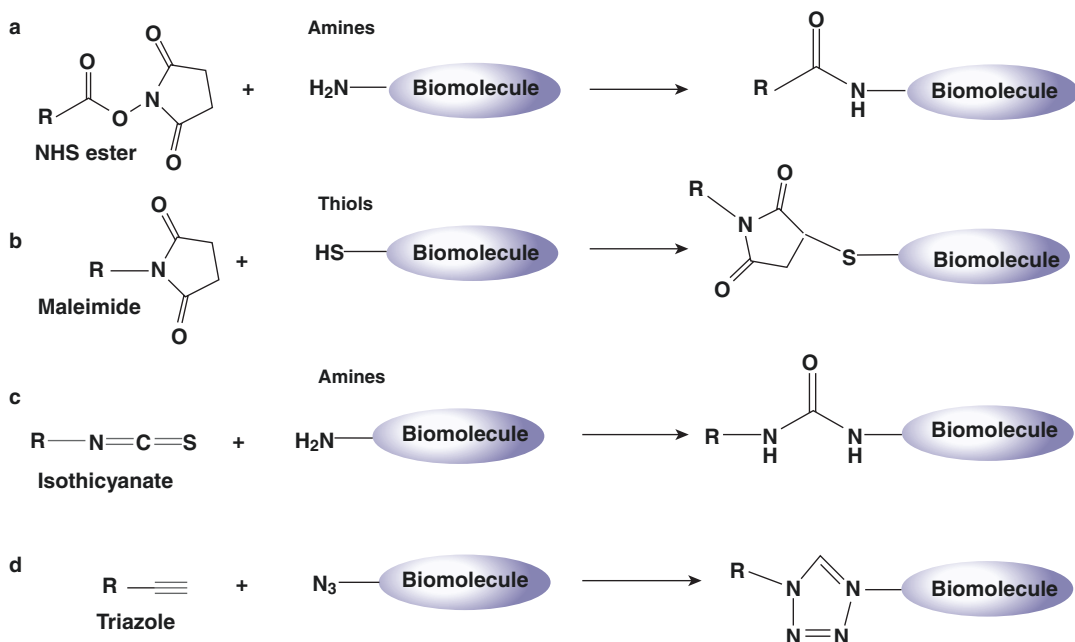
Fig. 20.19 Conjugation reactions commonly used for the covalent attachment of BFCA (R) to a targeting biomolecule with the formation of an amide (**a**), thioether (**b**), thiourea (**c**), and triazole bond (**d**)

was reviewed in several publications [3, 6, 54, 55] and also discussed in Chaps. 12 and 18.

20.3.6 Peptide Labeling with ^{99m}Tc

^{99m}Tc can be readily obtained from the ^{99}Mo → ^{99m}Tc generator as pertechnetate (^{99m}TcO$_4^-$) by elution of the generator with 0.9% saline solution. One of the characteristics of Tc is its diverse redox chemistry. The chemically stable pertechnetate ion (VII) must be reduced to lower oxidation states (I-V) to prepare ^{99m}Tc-labeled radiopharmaceuticals. During reduction by the stannous ion (Sn^{2+}), in an appropriate buffer and pH, the presence of a ligand stabilizes Tc in its lower oxidation state. In a specific Tc-complex, the oxidation state of Tc, however, depends on the chelate and pH. As a transition metal, Tc can adopt many coordination geometries, depending on the donor atoms and the type of the chelating agent. Several donor atoms, such as N, S, O and P, geometrically arranged in a che-

lating molecule, can form coordination complexes with technetium.

The radiopharmaceutical chemistry of Tc(V) is dominated by the [TcO]$^{3+}$ core, which is stabilized by a wide range of donor atoms (N, S, O) but, prefers thiolate, amido, and alkoxide ligands. Several tetra-ligand chelates designed to bind to Tc(V), typically form complexes (such as N$_2$S$_2$, N$_3$S, N$_3$O, and N$_4$) having square pyramidal geometries. The ^{99m}Tc complex of mercaptoacetyltriglycine (MAG3) forms a square pyramidal complex with Tc(V) with the basal plane consisting of three nitrogen atoms and one sulfur donor atom. A variety of BFCs, such as N$_2$S$_2$ diamidedithios, N$_3$S triamidethiols, N$_4$ tetraamines, or hydrazinonicotinic acid (HYNIC) have been evaluated upon conjugation to peptides to achieve labeling with ^{99m}Tc.

The direct method of ^{99m}Tc labeling to peptides uses a reducing agent to break a disulfide bridge of a peptide for binding of ^{99m}Tc to thiol groups in the peptide molecules. This method often suffers from lack of specificity and poor in vivo stability. In the indirect method, ^{99m}Tc is
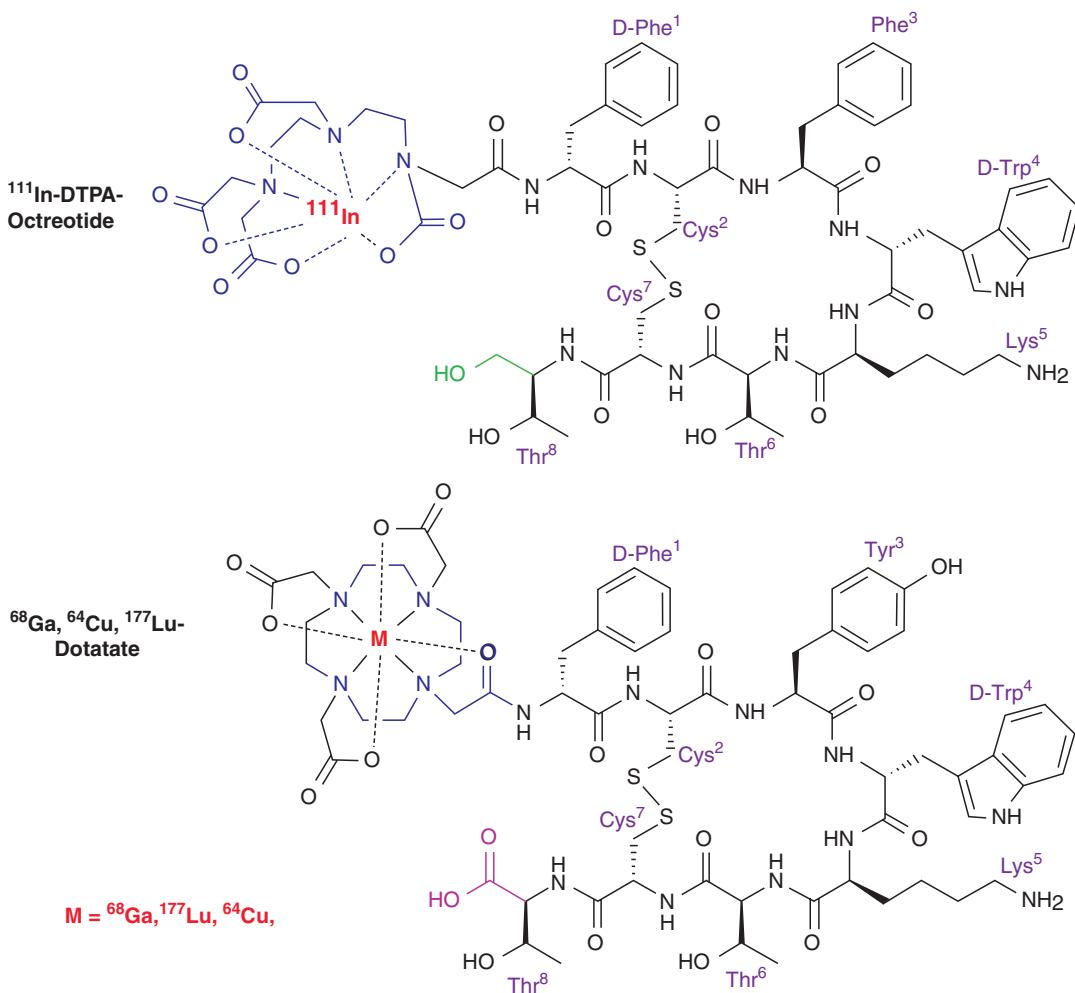
Fig. 20.20 Chemical structures of ^{111}In-DTPA-Octreotide (Octreoscan) and ^{68}Ga, ^{64}Cu, or ^{177}Lu-Dotatate (DOTA-Tyr[3]-octreotate)

bound to the peptide through a BFC, which can be conjugated to the peptide either before (post-labeling approach) or after labeling with [99m]Tc. In the 1990s, several approaches were developed to label peptides and proteins with [99m]Tc. Three important labeling methods [57, 58] have been developed based on three commonly used Tc-coordination environments (cores), as shown in Fig. 20.21.

- The MAG[3]-based bifunctional chelates (Tc(V) oxo core).
- The *N*-oxysuccinimidylhydrazino-nicotinamide system and (Tc(V)HYNIC core).
- The recently described single amino acid chelates for the Tc(I)-fac-tricabonyl core.

Mixed aminothiol-based chelators, such as N[2]S[2] ligand bisaminoethanethiol (BAT) and N3S ligand mercaptoacetyltriglycine (MAG[3]) were developed to label biomolecules based on Tc(V) O core. ^{99m}Tc-MAG3 (Mertiatide) was developed in 1986 as an anionic kidney functional imaging agent. The parent ligand is readily derivatized as the *S*-acetyl MAG[3]-ethyl ester, containing a *p*-isothiocyanatobenzyl substituent, or as the *S*-acetyl MAG3-hydroxysuccinimidyl ester for conjugation to biomolecules [59]. In the 1990s, MAG3 ligand was used to develop ^{99m}Tc-P829 peptide (Depreotide) for somatostatin receptor imaging. The original octreotide peptide was modified to eliminate the disulfide bridge to prevent reduction during the synthesis of ^{99m}Tc-P829
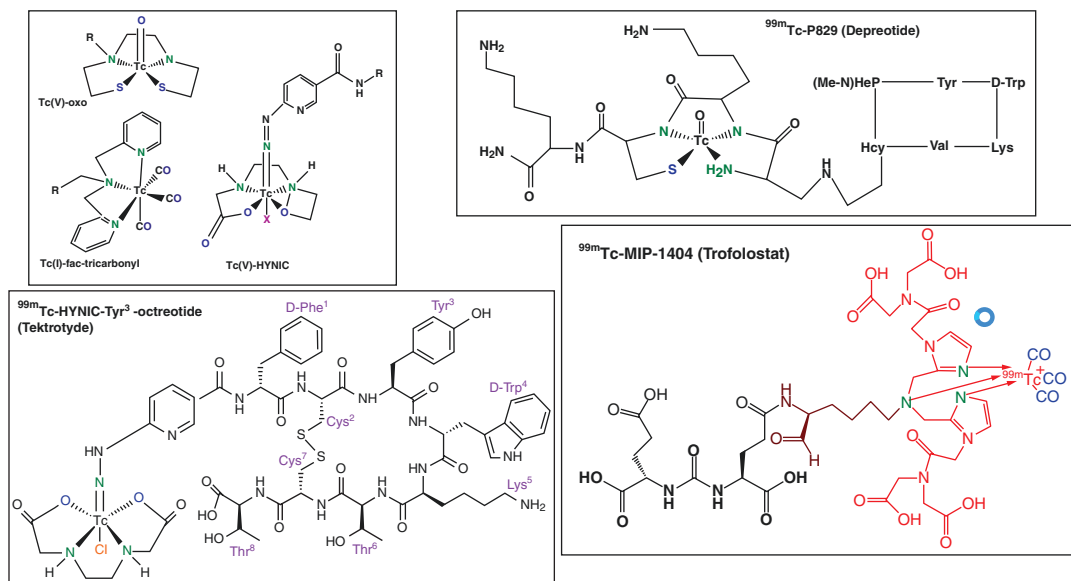
Fig. 20.21 Tc-coordination cores commonly used to develop radiometal labeled peptides

complex (Fig. 20.21). Tc-MAG3 core is robust and provides chemical versatility for the development of bifunctional tracers. There are, however, drawbacks, such as the use of stannous chloride as a reducing agent and the need for elevated pH condition, that may lead to aggregation of proteins, as well as nonquantitative radiolabeling yields [54].

An alternative pendant approach to ^{99m}Tc radiolabeling of biomolecules was provided by the introduction of hydrazinenicotinic acid (HYNIC) as a bifunctional chelator [60]. HYNIC with co-ligands like tricine and ethylenediamine diacetic acid (EDDA), in the presence of SnCl$_2$ performs fast and efficient labeling. Based on this Tc(V)HYNIC core, many small molecules, peptides, and proteins were labeled as imaging agents [5]. For example, Tyr^3-octreotide (TOC) was successfully labeled based on Tc-HYNIC core (Fig. 20.21). Since the HYNIC occupies only one or two coordination positions for ^{99m}Tc, co-ligands (such as tricine and EDDA) are needed to complete Tc's coordination positions. Changes in co-ligand number and type will have an effect on the in vivo behavior of the radiopharmaceutical. It has been understood that [HYNIC-^{99m}Tc(tricine)$_2$] complexes, usually, are not very

stable in solutions and could appear in different isomeric forms based on pH, temperature, and time [61].

20.3.6.1 Tc-Tricarbonyl Core [Tc(CO)$_3$]$^+$

A major advancement in Tc chemistry has been the discovery that a highly adaptable tricarbonyl Tc core makes it possible to prepare organometallic complexes in aqueous solution [61]. In an effort to develop new organometallic precursors, for the preparation of ^{99m}Tc-complexes, investigators have shown that, by treating pertechnetate (TcO_4^-) with sodium borohydride (NaBH$_4$) in the presence of carbon monoxide (CO) gas, one can produce the reactive Tc(I) species, [Tc(CO)$_3$(OH$_2$)$_3$]$^+$ [62, 63]. In this complex, the three facially oriented water molecules are sufficiently labile so that they can be readily displaced by a variety of mono-, bi- and tridentate ligands. Since it is difficult to work with CO gas, the technology is based on the use of a solid reagent, potassium boranocarbonate (K$_2$H$_3$BCO$_2$), which acts as both a reducing agent and a source of CO gas [64]. The kit is available from Mallinckrodt (Tyco) Medical under the trade name Isolink. Further, it has been shown that both, bidentate and tridentate chelates bind rapidly to the

[Tc(CO)$_3$]$^+$ core on a macroscopic scale and at the tracer level. ^{99m}Tc-tricarbonyl core is the favorite strategy for labeling of peptides because: (a) a high labeling yield is achieved; (b) purification is not needed after labeling protocol; and (c) attachment of ^{99m}Tc-tricarbonyl to peptide is easy and convenient [61]. Preclinical studies of several biomolecules labeled with Tc-tricarbonyl core revealed that these labeled compounds are biologically, kinetically, and thermodynamically stable for imaging studies.

Based on the chemistry of the organometallic fragment [^{99m}Tc][Tc(CO)$_3$(H$_2$O)$_3$]+, two radiopharmaceuticals, ^{99m}Tc-MIP-1404 and ^{99m}Tc-MIP-1405, were developed by Molecular Insight Pharmaceuticals (MIP). The preparation of these complexes was accomplished using a standard methodology and commercially available IsoLink kits (Covidien, Dublin, Ireland) and the imidazole chelator, which contains three nitrogen atoms suitable for binding to the ^{99m}Tc(I)-tricarbonyl-core (Fig. 20.21). The lead compound ^{99m}Tc-MIP-1404 (Trofolastat) completed phase III clinical trials as an imaging agent for the detection of prostate-specific membrane antigen (PSMA) positive prostate cancer [65, 66].

References

1. Cooper BM, Legre J, O'Donovan DH, et al. Peptides as a platform for targeted therapeutics for cancer: peptide–drug conjugates (PDCs). Chem Soc Rev. 2021;50:1480–94.
2. Zhang Y, Zhang H, Ghosh D, Williams RO. Just how prevalent are peptide therapeutic products? A critical review. Int J Pharma. 2020;587:119491.
3. Fani M, Maeske HR, Okavi SM. Radiolabeled peptides: valuable tools for the detection and treatment of cancer. Theranostics. 2012;2(5):481–501.
4. Gharibkandi NA, Conlon JM, Hosseinimehr SJ. Strategies for improving stability and pharmacokinetic characteristics of radiolabeled peptides for imaging and therapy. Peptides. 2020;133(12):170385.
5. Mikulová MB, Mikuš P. Advances in development of radiometal labeled amino acid-based compounds for cancer imaging and diagnostics. Pharmaceuticals. 2021;14:167.
6. Tornesello AL, Buonaguro L, Tornesello ML, Buonaguro FM. New insights in the design of bioactive peptides and chelating agents for imaging and therapy in oncology. Molecules. 2017;22(8):1282.
7. Maleki F, Farahani AM, Rezazedeh F, et al. Structural modifications of amino acid sequences of radiolabeled peptides for targeted tumor imaging. Bioorg Chem. 2020;99:103802.
8. Bass RT, Buckwalter BL, Patel BP, et al. (1996) Identification and characterization of novel somatostatin antagonists. Mol Pharmacol 50:709–715.
9. Günther T, Tulipano G, Dournaud P, et al. International Union of Basic and Clinical Pharmacology. CV. Somatostatin receptors: structure, function, ligands, and new nomenclature. Pharmacol Rev. 2018;70:763–835.
10. Fani M, Nicolas GP, Wild D. Somatostatin receptor antagonists for imaging and therapy. J Nucl Med. 2017;58:61S–6S.
11. Evans BJ, King AT, Katsifis A, et al. Methods to enhance the metabolic stability of peptide-based PET radiopharmaceuticals. Molecules. 2020;25:2314. https://doi.org/10.3390/molecules25102314.
12. Gai Y, Jiang Y, Long Y, et al. Evaluation of an integrin α(v)β(3) and aminopeptidase N dual-receptor targeting tracer for breast cancer imaging. Mol Pharm. 2020;17:349–58.
13. Kapp TG, Rechenmacher F, Neubauer S, et al. Comprehensive evaluation of the activity and selectivity profile of ligands for RGD-binding integrins. Sci Rep. 2017;7:39805.
14. Popp I, Pozzo D, Waser B, et al. Approaches to improve metabolic stability of a statine-based GRP receptor antagonist. Nucl Med Biol. 2017;45:22–9.
15. Cod WL, He JX, Reily MD, et al. Design of a potent combined pseudopeptide endothelin-A/endothelin-B receptor antagonist, Ac-d Bhg^{16}-Leu-Asp-Ile-[NMe] Ile-Trp^{21} (PD 156252): examination of its pharmacokinetic and spectral properties. J Med Chem. 1997;40:2228–40.
16. Klingler M, Summer D, Rangger C, et al. DOTA-MGS5, a new cholecystokinin-2 receptor-targeting peptide analog with an optimized targeting profile for theranostic use. J Nucl Med. 2019;60:1010–6.
17. Wu H, Huang J. PEGylated peptide-based imaging agents for targeted molecular imaging. Curr Protein Pept Sci. 2016;7(6):582–95.
18. Jamous M, Tamma ML, Gourni E, et al. PEG spacers of different length influence the biological profile of bombesin-based radiolabeled antagonists. Nucl Med Biol. 2014;41:464–70.
19. Wu Z, Li Z-B, Cai W, et al. ^{18}F-labeled mini-PEG spacered RGD dimer (^{18}F-FPRGD2): synthesis and microPET imaging of αvβ3 integrin expression. Eur J Nucl Med Mol Imaging. 2007;34:1823.
20. Moradi SV, Hussein WM, Varamini P, et al. Glycosylation, an effective synthetic strategy to improve the bioavailability of therapeutic peptides. Chem Sci. 2016;7:2492–500.
21. Schweinsberg C, Maes V, Brans L, et al. Novel glycated [^{99m}Tc(CO)$_3$]-labeled Bombesin analogues for improved targeting of gastrin-releasing pep-

tide receptor-positive tumors. Bioconjug Chem. 2008;19:2432–9.

22. Cho EH, Lim JC, Lee SY, Jung SH. An assessment tumor targeting ability of ^{177}Lu labeled cyclic CCK analogue peptide by binding with cholecystokinin receptor. J Pharmacol Sci. 2016;131:209–14.

23. Shinde SS, Maschauer S, Prante O. Sweetening pharmaceutical radiochemistry by ^{18}F-Fluoroglycosylation: recent progress and future prospects. Pharmaceuticals. 2021;14:1175. https://doi.org/10.3390/ph14111175.

24. Liu Z, Chen X. Simple bioconjugate chemistry serves great clinical advances: albumin as a versatile platform for diagnosis and precision therapy. Chem Soc Rev. 2016;45(5):1432–56.

25. Zorzi A, Linciano S, Angelini A. Non-covalent albumin-binding ligands for extending the circulating half-life of small biotherapeutics. Med Chem Commun. 2019;10:1068.

26. Muller C, Struthers H, Winiger C, et al. DOTA conjugate with an albumin-binding entity enables the first folic acid-targeted ^{177}Lu-radionuclide tumor therapy in mice. J Nucl Med. 2013;54(1):124–31.

27. Tian R, Jacobson O, Niu G. Evans blue attachment enhances somatostatin receptor Subtype-2 imaging and radiotherapy. Theranostics. 2018;8(3):735–45.

28. Dumelin CE, Trussel S, Buller F, et al. A portable albumin binder from a DNA encoded chemical library. Angew Chem Int Ed Engl. 2008;47:3196–201.

29. Kelly JM, Amor-Coarasa A, Ponnala S, et al. Albumin-binding PSMA ligands: implications for expanding the therapeutic window. J Nucl Med. 2019;60(5):656–63.

30. Umbricht CA, Benesova M, Hasler R, et al. Design and preclinical evaluation of an albumin-binding PSMA ligand for (64)Cu-based PET imaging. Mol Pharm. 2018;15(12):5556–64.

31. Rousseau E, Lau J, Zhang Z, et al. Effects of adding an albumin binder chain on [(177)Lu] LuDOTATATE. Nucl Med Biol. 2018;66:10–7.

32. Jacobson O, Kiesewetter DO, Chen X. Albumin-Binding Evans Blue Derivatives for Diagnostic Imaging and Production of Long-Acting Therapeutics Bioconjugate Chem. 2016;27(10):2239–47.

33. Zhang J, Wang H, Jacobson O, et al. Safety, pharmacokinetics, and dosimetry of a long-acting radiolabeled somatostatin analog (177)Lu-DOTA-EB-TATE in patients with advanced metastatic neuroendocrine tumors. J Nucl Med. 2018;59(11):1699–705.

34. Arezou FM, Fariba M, Nourollah S. The influence of different spacers on biological profile of peptide radiopharmaceuticals for diagnosis and therapy of human cancers. Anti Cancer Agents Med Chem. 2020;20(4):402–16.

35. Farahani AM, Maleki F, Sadeghzadeh N. The influence of different spacers on biological profile of peptide radiopharmaceuticals for diagnosis and therapy of human cancers. Anti Cancer Agents Med Chem. 2020;20(4):402–6.

36. Antunes P, Ginj M, Walter MA, et al. Influence of different spacers on the biological profile of a DOTA-somatostatin analogue. Bioconjug Chem. 2007;18:84–92.

37. Jia Y, Shi W, Zhou Z, et al. Evaluation of DOTA-chelated neurotensin analogs with spacer-enhanced biological performance for neurotensin-receptor-1-positive tumor targeting. Nucl Med Biol. 2015;42:816–23.

38. Janssen M, Oyen WJ, Massuger LF, et al. Comparison of a monomeric and dimeric radiolabeled RGD-peptide for tumor targeting. Cancer Biother Radiopharm. 2002;17(6):641–6.

39. Li ZB, Cai W, Cao Q, et al. (64)Cu-labeled tetrameric and octameric RGD peptides for small-animal PET of tumor alpha(v)beta(3) integrin expression. J Nucl Med. 2007;48(7):1162–71.

40. Liu Z, Yan Y, Chin FT, et al. Dual integrin and gastrin-releasing peptide receptor targeted tumor imaging using ^{18}F-labeled PEGylated RGD-bombesin heterodimer ^{18}F-FB-PEG3-Glu-RGD-BBN. J Med Chem. 2009;52(2):425–32.

41. Li H, Liu Z, Yuan L, et al. Radionuclide-based imaging of breast cancer: state of the art. Cancers (Basel). 2021;13(21):5459.

42. Jamous M, Haberkorn U, Mier W. Synthesis of peptide radiopharmaceuticals for the therapy and diagnosis of tumor diseases. Molecules. 2013;18:3379–409.

43. Oliveira MC, Correia JDG. Biomedical applications of radioiodinated peptides. Eur J Med Chem. 2019;179:56–77.

44. Ajenjo J, Destro G, Cornelissen B, Gouverneur V, et al. Closing the gap between ^{19}F and ^{18}F chemistry. EJNMMI Radiopharm Chem. 2021;6:33–70.

45. Jacobson O, Kiesewetter DO, Chen X. Fluorine-18 radiochemistry, labeling strategies and synthetic routes. Bioconjug Chem. 2015;26:1–18.

46. Richter S, Wuest F. ^{18}F-labeled peptides: the future is bright. Molecules. 2014;19:20536–56.

47. Halder R, Ritter T. ^{18}F-fluorination: challenge and opportunity for organic chemists. J Org Chem. 2021;86(20):13873–84.

48. Yuan Z, Nodwell MB, Yang H, et al. Site-selective, late-stage C−H ^{18}F-fuorination on unprotected peptides for positron emission tomography imaging. Angew Chemie Int Ed. 2018;57:12733–6.

49. Rickmeier J, Ritter T. Site-specific deoxyfluorination of small peptides with [^{18}F]fluoride. Angew Chem Int Ed. 2018;57:14207–11.

50. McBride WJ, Sharkey RM, Karacay H, et al. A novel method of ^{18}F radiolabeling for PET. J Nucl Med. 2009;50:991–8.

51. Archibald SJ, Allott L. The aluminum-[^{18}F]fluoride revolution: simple radiochemistry with a big impact for radiolabelled biomolecules EJNMMI. Radiopharm Chem. 2021;6:30.

52. Kumar K. ^{18}F-AlF-labeled biomolecule conjugates as imaging pharmaceuticals. J Nucl Med. 2018;59(8):1218–9.

53. Fersing C, Bouhlel A, Cantelli C, et al. A comprehensive review of non-covalent radiofluorination approaches using aluminum [^{18}F]fluoride: will [^{18}F]AlF replace ^{68}Ga for metal chelate labeling? Molecules. 2019;24(16):2866.

54. Boros E, Packard A. Radioactive transition metals for imaging and therapy. Chem Rev. 2019;119:870–90.

55. Price EW, Orvig C. Matching chelators to radiometals for radiopharmaceuticals. Chem Soc Rev. 2014;43:260.

56. Kostelnik TI, Orvig C. Radioactive main group and rare earth metals for imaging and therapy. Chem Rev. 2019;119(2):902–56.

57. Boschi A, Uccelli L, Martini P. A picture of modern Tc-99m radiopharmaceuticals: production, chemistry, and applications in molecular imaging. Appl Sci. 2019;9:2526.

58. Rezazadeh F, Sadeghzade N. Tumor targeting with ^{99m}Tc radiolabeled peptides: clinical application and recent development. Chem Biol Drug Des. 2019;93:205–21.

59. Ram S, Buchsbaum DJ. A peptide-based bifunctional chelating agent for ^{99m}Tc and ^{186}Re labeling of monoclonal antibodies. Cancer. 1994;73(s3):769–73.

60. Babich JW, Fischman AJ. Effect of co-ligand on the biodistribution of ^{99m}Tc labeled hydrazine nicotinic acid derivatized chemotactic peptides. Nucl Med Biol. 1995;22:25–30.

61. Piramoon M, Hosseinimehr SJ. The past, current studies and future of organometallic 99mTc(CO)3 labeled peptides and proteins. Curr Pharm Des. 2016;22:4854–67.

62. Alberto R, Schlibi R, Schubiger AP. First application of fac-[^{99m}Tc(OH$_2$)$_3$(CO)$_3$]$^+$ in bioorganometallic chemistry: design, structure, and in vitro affinity of a 5-HT1A receptor ligand labeled with ^{99m}Tc. J Am Chem Soc. 1999;121:6076–7.

63. Waibei R, Alberto R, Willude J, et al. Stable one-step technetium-99m labeling of His-tagged recombinant proteins with a novel Tc(I)-carbonyl complex. Nat Biotechnol. 1999;17:897–901.

64. Alberto R, Ortner K, Wheatley N, et al. Synthesis and properties of boranocarbonate: A convenient in situ CO source for the aqueous preparation of [^{99m}Tc(OH^2)^3(CO)^3]+. J Am Chem Soc. 2001;123:3135–136.

65. Schmidkonz C, Götz TI, Atzinger A, et al. ^{99m}Tc-MIP-1404 SPECT/CT for assessment of whole-body tumor burden and treatment response in patients with biochemical recurrence of prostate cancer. Clin Nucl Med. 2020;45(8):e349–57.

66. Vallabhajosula S, Nikolopoulou A, Babich JW (2014) ^{99m}Tc-labeled small-molecule inhibitors of prostate-specific membrane antigen: pharmacokinetics and biodistribution studies in healthy subjects and patients with metastatic prostate cancer. J Nucl Med 55(11):1791–1798.

Theranostics in Neuroendocrine Tumors

21

> *Scientific work must not be considered from the point of view of direct usefulness of it, it must be done for itself, for the beauty of science, and then there is always a chance that the scientific discovery may become like the radium a benefit for humanity* (Marie Curie)

21.1 Introduction

Neuroendocrine tumors (NETs) or neuroendocrine neoplasms (NENs) also previously referred to as APUDomas (amine precursor uptake and decarboxylation) represent a constellation of diverse neoplasms most commonly but, by no means exclusively, arising in the gastroenteropancreatic (GEP) system and lungs [1, 2]. NENs, however, can also arise from different anatomic sites, such as the sympathetic nervous system, adrenal gland, lung, pancreas, bladder, and prostate, and they display a wide range of clinical aggressiveness. The cell of origin of most neuroendocrine tumors is the neuroendocrine system, regardless of organ site, which is comprised of neuroendocrine cells that secrete bioactive substances and proteins (such as somatostatin, insulin, gastrin, serotonin, chromogranins, and synaptophysin) [3]. GI tract NETs are also called carcinoid tumors, while pancreas NETs were known as islet cell tumors.

NENs with an incidence of only 7/100,000 per year are rare, and account for 3% of all cancers

[1]. NENs are a heterogeneous group of epithelial neoplastic proliferations ranging from indolent well differentiated NETs to very aggressive poorly differentiated neuroendocrine carcinomas (NECs). NENs are classified according to their origin, extension, and histological differentiation, and grading is based on mitotic rate (MR/2 mm^2) and proliferation rate determined by *Ki-67* index—a nuclear protein marker. The World Health Organization (WHO) Classification [4] retains the dichotomy of most gastrointestinal NENs being considered either well-differentiated NETs or poorly differentiated NECs, with the latter being subtyped into small cell and large cell NECs (Table 21.1). The majority of NENs are slowly growing tumors with almost no symptoms and up to 50% are metastatic at diagnosis. Around 25% of NENs are the so-called functioning tumors secrete hormones that can lead to distinct symptoms [5]. The heterogeneity of NEN regarding the organ of origin, differentiation, and molecular subtypes makes the development of personalized therapy a challenge and needs more international and interdisciplinary collaborations and clinical trials allowing stratification according to biological subgroups [1].

Pheochromocytomas (PCCs) are rare sub-types of NETs with an annual incidence of 2–6 per 1 million population [6, 7]. Approximately 80–85% of these cancers arise from chromaffin cells residing in the adrenal medulla. The remaining 15–20%

Table 21.1 WHO Classification of gastrointestinal neuroendocrine neoplasms[a]

Histology	Grade	*Ki-67%*	MR/2 mm²	
Well-differentiated	NET G1 (low)	<3	0–1	Grow slowly
	NET G2 (intermediate)	3–20	2–20	Moderate growth rate
	NET G3 (high)	>20	>20	Grow quickly
Poorly differentiated	NEC (always high)	n/a >20	n/a >20	Highly proliferative

[a]From Gonzalez [4]

of these tumors are extra-adrenal. These extra-adrenal lesions which arise from the autonomic neural ganglia are termed paraganglioma (PGL) or sometimes called extra-adrenal PCC [8]. The clinical symptoms of the disease are common between the adrenal and extra-adrenal forms and are determined by excess secretion of catecholamines (norepinephrine, epinephrine, serotonin, and dopamine). Hypertension is a critical and often dramatic feature of PCC/PGL and its most prevalent reported symptom [8].

Neuroblastoma is the most common extracranial solid tumor of childhood and represents a neoplastic expansion of neural crest cells in the developing sympathetic nervous system. The primary tumor originates anywhere along the sympathetic chain but, most frequently, arises from the adrenal gland. The prognosis for neuroblastoma varies widely, from tumors that spontaneously regress and require no intervention to those that present widely metastatic and resistant to therapy with resulting high mortality [9]. Neuroblastoma tumor cells show varying degrees of differentiation that help predict patient prognosis. While neuroblastoma primarily contains immature cells, some have a component of fully mature ganglion cells that are typically found in a ganglioneuroma. A tumor with both elements of mature and immature cells is called a ganglioneuroblastoma [9].

21.1.1 Carcinoid Syndrome

The pathologist Oberndorfer is credited with the description of small bowel tumors, which he termed "karzinoide," meaning carcinoma-like. His publication in 1907, was the first to distinguish the slower growing tumors from true carcinomas [10]. Approximately 30–40% of patients

with well-differentiated neuroendocrine tumors present with carcinoid syndrome (CS), which is a paraneoplastic syndrome associated with the secretion of several humoral factors, such as polypeptides (such as somatostatin, gastrin, vasoactive intestinal peptide, neurotensin) vasoactive amines (such as serotonin, norepinephrine), and prostaglandins [10, 11]. The main symptoms of CS are episodic facial flushing that may be accompanied by hypotension and tachycardia, diarrhea, bronchoconstriction, venous telangiectasia, dyspnea, and ultimately fibrotic complications, such as mesenteric and retroperitoneal fibroses and carcinoid heart disease (CHD). CS is predominantly associated with NETs that arise from the midgut in the setting of extensive liver metastases but, may be present in patients with bronchial carcinoids and, more rarely, in patients with pancreatic NETs. Approximately 30–40% of patients with well-differentiated NETs present with carcinoid syndrome, which significantly and negatively affects patients' quality of life; increases costs compared with the costs of nonfunctioning NETs. For several decades, patients with NETs and carcinoid syndrome have been treated with ST analogues (octreotide and lanreotide) as the first-line treatment. While these agents provide significant relief from carcinoid syndrome symptoms, there is inevitable clinical progression, and new therapeutic interventions are needed [11].

The presence of carcinoid syndrome that results from the hypersecretion of amines and peptides often facilitates diagnosis of a NET. Confirmation of the diagnosis is based on the measurement of urinary 5-hydroxyindole acetic acid (5-HIAA), a serotonin metabolite (Fig 21.1), and serum chromogranin A (CgA), a glycoprotein that is secreted with serotonin [11]. Serum CgA is a more sensitive and broadly applicable marker and is preferred over 5-HIAA for
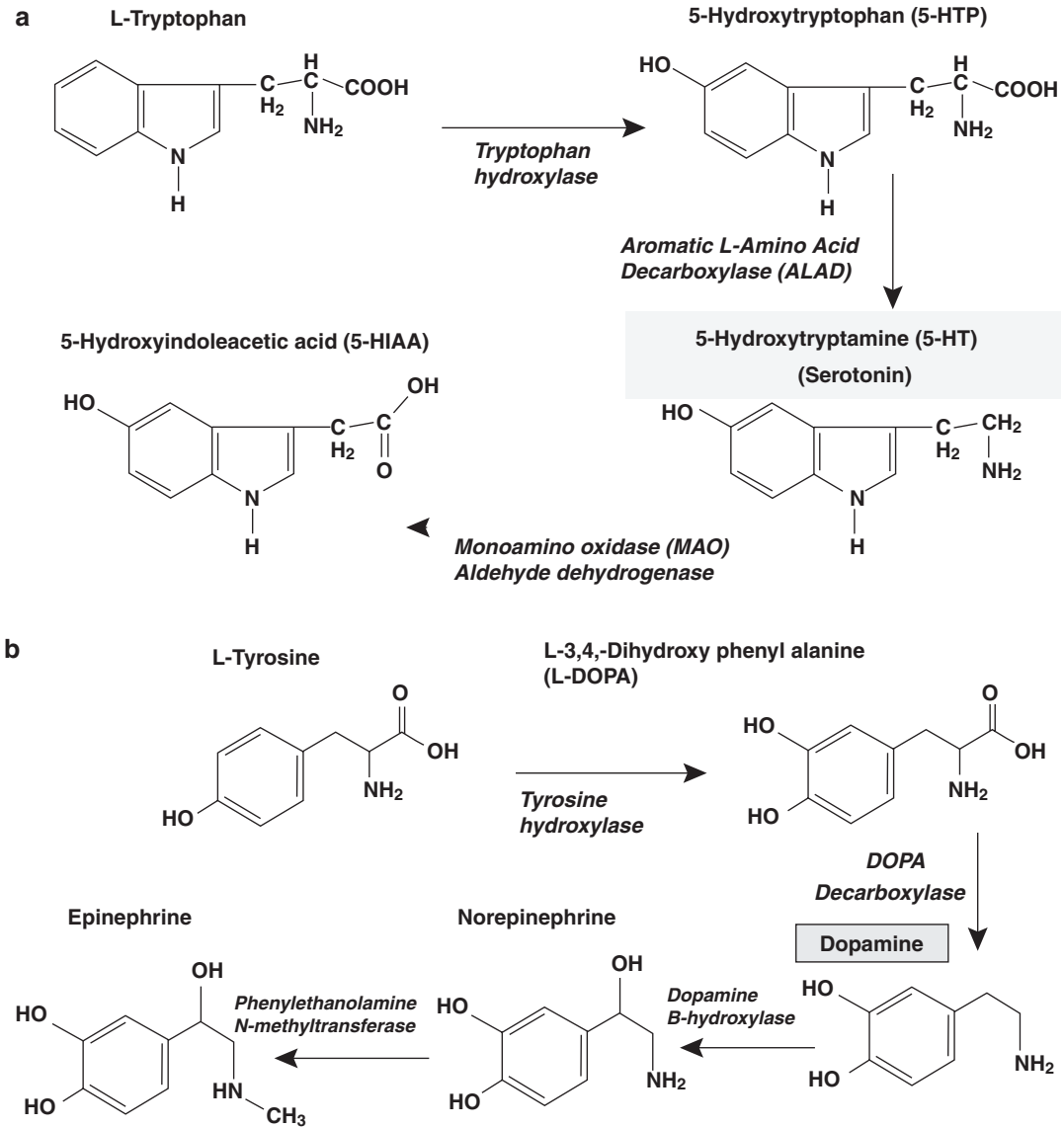
Fig. 21.1 Synthesis and metabolism of serotonin (**a**) and dopamine (**b**)

bronchial and rectal tumors, which do not generally secrete serotonin.

21.1.2 Therapeutic Modalities

Surgical extirpation or cytoreduction of NETs, if feasible, continues to be the treatment of choice and is associated with the best long-term overall survival and control of symptoms. Recurrence after resection is common and additional therapeutic modalities are therefore indispensable. Several therapeutic options exist for treating progressive metastatic/advanced NENs. The following schema (Fig. 21.2) represents a partial approach to the various therapeutic modalities [10].
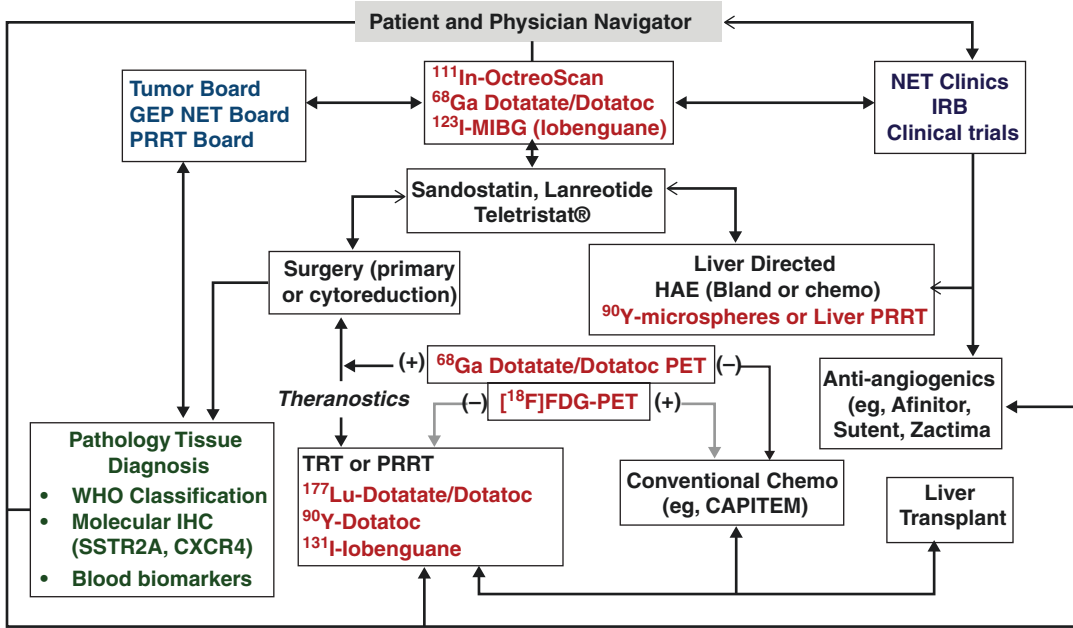
Fig. 21.2 Carcinoid and neuroendocrine tumors: cancer management and treatment options of care. (Figure modified from O'Dorisio et al. [10])

21.2   Theranostics in NETs

Molecular imaging and targeted radionuclide therapy (TRT) approaches have been utilized in the management of NETs since the 1980s, with promising results. The radio-theranostic concept of using a molecular marker (or the targeting vehicle) for both imaging and treatment has shown great promise in the personalized treatment of patients with NETs and serves as a model for developing targeted probes for several other cancers.

Theranostics refers to the pairing of diagnostic biomarkers with therapeutic agents that share a specific biological target in diseased cells or tissues. Therefore, theranostics describes a close connection between diagnostics and consequent therapy [5, 12–14] In nuclear medicine, the term theranostics is increasingly being used, specifically, for imaging and therapy with the same molecular marker (ligand or vector) but, labeled with different radionuclides appropriate for imaging and TRT, respectively. Diagnostic and therapeutic radiopharmaceuticals that access the same cellular structure and biologic process—

that is, that share the same biological target—are called theranostic pairs. Table 21.2 provides a list of both approved and investigational target-specific radiopharmaceuticals for imaging and TRT.

Since patients often present with nonspecific symptoms, it is very important to make the diagnosis of NET and identify the primary and metastatic sites. Sites of NETs can be small and can be difficult to characterize with conventional anatomic imaging (CT and MRI). Targeted molecular imaging techniques greatly improve the specificity for diagnosing and the PET/CT or PET/MRI imaging is very sensitive for detecting small NETs. Over the years, peptide receptor radionuclide therapy (PRRT) has evolved as an important modality in the therapeutic armamentarium of advanced, metastatic, or inoperable, progressive NENs. Selection of an appropriate therapeutic radionuclide is the key to the successful development of a therapeutic radiopharmaceutical. Figure 21.3 shows the schema of a theranostic radiopharmaceutical composed of a targeting molecule (peptide such as octreotate) that recognizes a targeted cell surface receptor

Table 21.2 Radiopharmaceuticals for molecular imaging and targeted therapy in neuroendocrine tumors

Biological target	Radiopharmaceutical	Trade name	Indication	FDA status
Somatostatin receptor	111In-DTPA-octreotide	Octreoscan	SPECT	Approved 1994
(SSTR-2) Agonist	68Ga-DOTA-TATE	NetSpot	PET	Approved 2016
	64Cu-DOTA-TATE	DetectNet	PET	Approved 2020
		Netmedix		
	177Lu-DOTA-TATE	Lutathera	TRT	Approved 2018
	177Lu-DOTA-EB-TATE		TRT	IND
	212Pb-DOTAM-TATE	AlphaMedix™	TRT	IND
	68Ga-DOTA-TOC		PET	Approved 2019
	177Lu-DOTA-TOC		TRT	Approved[a]
	90Y-DOTA-TOC		TRT	Approved[a]
	225Ac-DOTA-TOC		TRT	IND
	68Ga-DOTANOC		PET	IND
SSTR-2 antagonist	68Ga-NODAGA-JR11 (OPS202) or 68Ga-Satoreotide		PET	IND
	64Cu-NODAGA-JR11		PET	IND
	177Lu-DOTA-JR11 (OPS201)		TRT	IND
	177Lu-DOTA-LM3		TRT	IND
Norepinephrine transporter (NET)	123I-Iobenguane (MIBG)	Adreview	SPECT	Approved
	131I-Iobenguane (MIBG)	Azedra	TRT	Approved
	[18F]mFBG		PET	IND
	[11C]Hydroxyephedrine (HED)		PET	IND
B7-H3 antigen in neuroblastoma	131I-Omburtamab mAb		TRT	IND
Glucose transporter (Glut-1)	[18F]Fluorodeoxyglucose (FDG)		PET	Approved 2002
Dopamine precursor	[18F]FDOPA		PET	IND
Serotonin precursor	[11C]5-Hydroxytryptophan (5-HTP)		PET	IND
GLP-1 receptor	68Ga-Exendin-4		PET	IND
Cholecystokinin-2 receptor (CCK2R)	68Ga-MG48 minigastrin		PET	IND
	177Lu-PP-F11N		TRT	IND
Chemokine receptor-4 (CXCR-4)	68Ga-Pentixafor		PET	IND
	177Lu-Pentixafor		TRT	IND
Fibroblast activating protein (FAP)	68Ga-FAP inhibitor		PET	IND
Capillary blockade (embolization)	90Y-Glass Microspheres	TheraSphere™	Liver	Approved
	90Y-Resin Microspheres	SIR-Spheres®	Mets.	Approved

[a]Approved in Europe

(such as SSTR), a spacer/linker (e.g., aminohexa-noic acid [Ahx]) which links the peptide ligand to the chelator (e.g., DTPA, DOTA, etc.), which in turn is able to complex and stabilize the radionu-clide for imaging or therapy. This chapter will discuss various biological targets, radionuclides, radiolabeling techniques and clinical applications of targeted radiopharmaceuticals listed in Table 21.2.

21.2.1 Biological Targets

The most characteristic feature of NENs is the homogeneous overexpression of specific G-protein coupled peptide hormone receptors
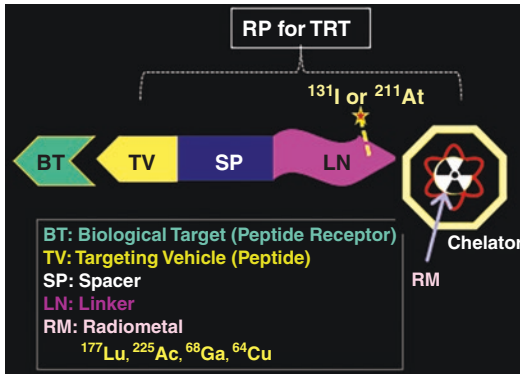
Fig. 21.3 The schema of a theranostic radiopharmaceutical for imaging and therapy

(PHRs) on the tumor cell surface [15, 16]. The PHRs control hormone secretion and cell proliferation in NENs and they represent molecular targets for the development of diagnostic and therapeutic radiopharmaceuticals. Somatostatin receptors (SSTRs) are the best-known and well-studied PHRs in NENs. The other promising receptors in NETs are glucagon-like peptide 1 (GLP-1) receptors, C-X-C motif chemokine receptor-4 (CXCR4), glucose-dependent insuli-notropic polypeptide receptor (GIPR), neuroten-sin receptors and cholecystokinin-2 (CCK2) receptors (Table 21.3).

In addition to PHRs, several other biological targets (such as glucose transporters and amino acid transporters) were also utilized in the development of targeted radiopharmaceuticals (Table 21.2). Since catecholamines play an important role in NETs, radiotracers based on norepinephrine (such as MIBG) were developed, which can be transported into the tumor cells via norepinephrine transporter (NET).

21.2.2 Radionuclides for Imaging and Therapy

The most common radionuclides used for PET/SPECT imaging and therapy of NETs are summarized in Table 21.4. The radionuclide preferred for SPECT imaging studies is ^{111}In, since it has

Table 21.3 Peptide hormone receptor (PHR) expression in human tumors

PHRs	Receptor sub-type	Natural peptide ligand	Human tumors
Somatostatin receptors	SSTR1–5	Somatostatin	NETs, GEP tumors, carcinoids, paragangliomas, non-Hodgkin's lymphoma (NHL), melanoma, breast, brain, small cell lung cancer (SCLC)
Cholecystokinin B/gastrin receptor	CCK2/CCK-B	Cholecystokinin, gastrin	Medullary thyroid cancer (MTC), SCLC, gastrointestinal stromal cancer, stromal ovarian cancer, astrocytomas
Glucagon-like peptide-1 receptor (GLP-1)	GLP-1	Exendin	Insulinomas, gastrinomas, phaeochromocytomas, paragangliomas and MTC
Neurotensin receptor	NTR-1	Neurotensin	Small cell lung cancer, colon, exocrine pancreatic cancer, Ewing's sarcoma, breast, prostate
Chemokine receptor 4 (CXCR4)		CXCR-4	Lymphatic system, lung, breast and prostate cancer

Modified from Fani and Mackae (2012)

Table 21.4 The most common radionuclides used for imaging and therapy of NETs

| Radionuclide | $T\frac{1}{2}$ | Decay mode | | E_{max} (keV) | Mean range (mm) | γ-Energy (keV) | Produced by |
		Mode	%				
^{99m}Tc	6.0 hours	IT	98			140	^{99}Mo generator
^{111}In	2.805 days	EC	100			171 and 245	Cyclotron
^{123}I	13.22 hours	EC	97			159	Cyclotron
^{11}C	20.4 min	β^+	100	0.960	1.2		Cyclotron
^{18}F	110 min	β^+	97	0.634	0.6		Cyclotron
^{124}I	4.2 days	β^+	23	2.138	0.9		Cyclotron
^{68}Ga	68 min	β^+	88.9	1.889	3.50		^{68}Ge generator, cyclotron
^{64}Cu	12.7 hours	β^+	17.9	0.653	0.7		Cyclotron
^{86}Y	14.7 hours	β^+	31.9	1.221			Cyclotron
^{131}I	8.02 days	β^-	100	0.606	0.91	364	^{235}U fission
^{90}Y	2.67 days	β^-	100	2.28	2.50		^{90}Sr generator
^{177}Lu	6.7 days	β^-	79	0.497	0.67	113 and 208.4	Reactor
^{212}Pb	10.6 hours	β^-	100	0.101			^{228}Th/^{224}Ra generator
^{211}At	7.2 hours	α	41.8	5.867α	0.06	77–92 X-rays	Cyclotron
^{225}Ac	10 days	α	100	5.800α	0.06	218 and 440	^{229}Th generator, accelerator

relatively longer half-life and high γ-photon abundance. Also, as a trivalent metal, ^{111}In is a chemical and biological surrogate for other trivalent metal labeled metals such as ^{90}Y, [177]u, and [225]Ac. Compared to SPECT imaging studies, PET scans provide higher resolution (4–5 mm), and quantitative information (such as SUV_{max} or SUV_{mean}) regarding the uptake of radiopharmaceutical in the target tumor lesions, and normal tissues. The most common PET radionuclides used for the development of PET radiopharmaceuticals are ^{18}F, ^{68}Ga, and [64]Cu.

For TRT, the particle kinetic energy (MeV) determines the amount of energy absorbed (Gy) in the target tissue. The quantity of linear energy transfer (LET) is the amount of energy deposited by the radiation per unit length of the path (KeV/μm). Low LET radiation (X-rays, γ-rays, electrons) deposits relatively a small quantity of energy, while high LET radiation (protons, neutrons, and α particles) deposits higher energy in the targeted areas. The higher the LET of a spe-

cific radionuclide, the greater is the relative biological effectiveness (RBE) [17]. The $β^-$ particles, Auger electrons, and conversion electrons have the same mass but, different kinetic energy and different ranges (0.1–3.0 mm) in tissue. All electrons have low LET values (0.2 keV/μm) and their RBE is unity. In contrast, α particles are 8000 times heavier and have very high LET values (40–100 keV/μm) and, therefore, the RBE values can be 5–10 depending on the tissue.

Radiation damage to the cell can be caused by the direct or indirect action on biological molecules [17]. In the direct action, the radiation hits the DNA molecule directly, causing single-stranded breaks (SSB) or double stranded breaks (DSB), disrupting the molecular structure (Fig. 21.4). Such structural change leads to cell damage or even cell death. This process becomes predominant with high-LET radiations, such as α-particles and neutrons, and high radiation doses. In the indirect action, the radiation hits the water molecules generating reactive oxygen spe-
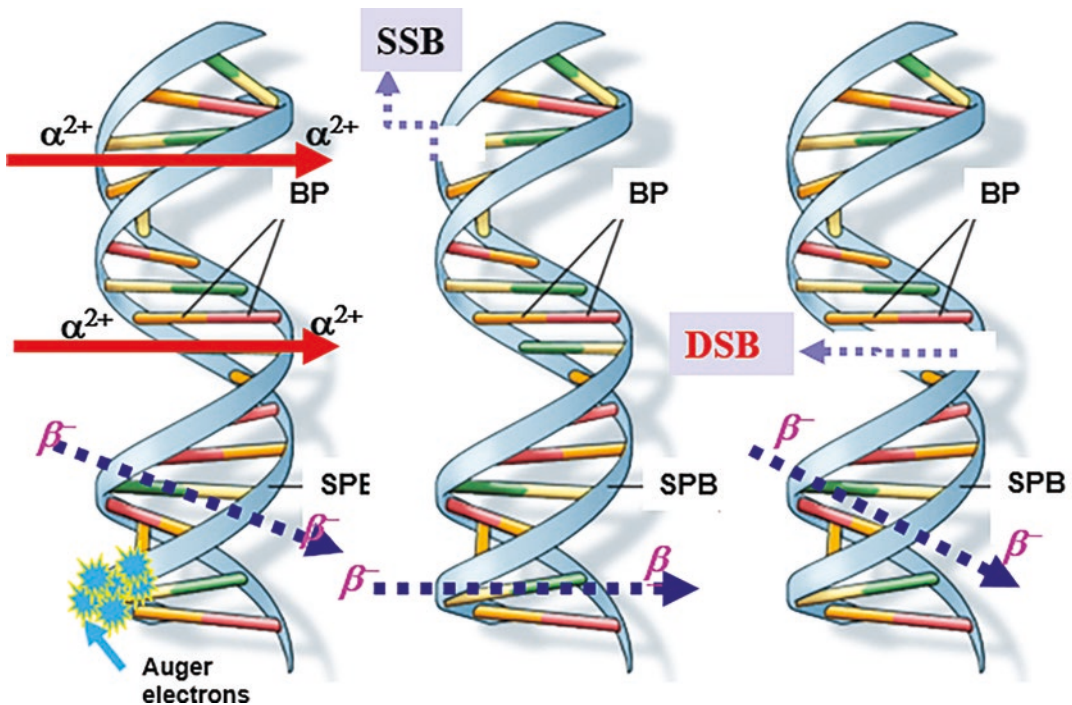
Fig. 21.4 Radiation damage to DNA. In the direct action, the radiation hits the DNA molecule directly, causing single-stranded breaks (SSB) or double stranded breaks (DSB), disrupting the molecular structure. Alpha (α) particles are more likely to induce DSBs compared to beta (β) particles

Fig. 21.5 Chelates used for metal conjugation
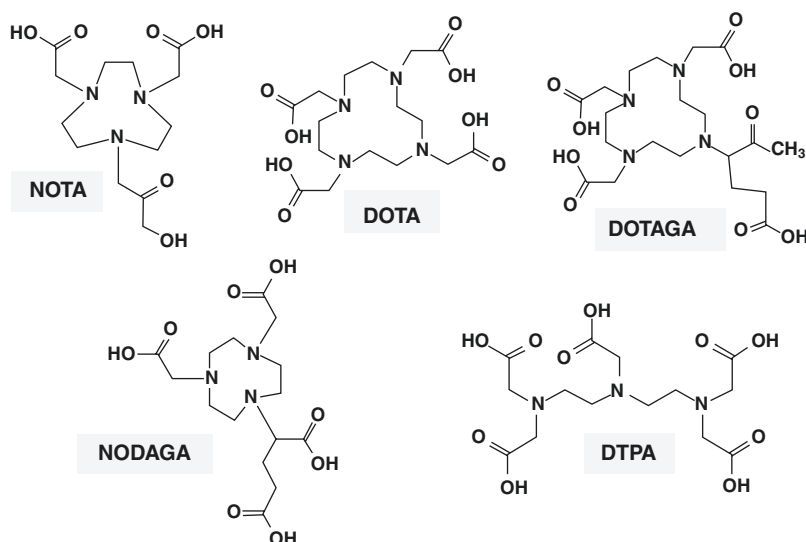
cies (ROS), such as hydrogen peroxide (H_2O_2) and free radicals (characterized by an unpaired electron), such as the hydroxyl (HO$^\bullet$) group. In addition, indirect effects of radiation may also involve reactive nitrogen species (RNS). All the reactive molecules are toxic and can have many effects, including the oxidation of biological macromolecules and activation of intracellular signaling pathways leading to apoptosis, necrosis, and cell death.

21.2.3 Radiolabeling Methods

Among the radionuclides listed in Table 21.4, ^{18}F and ^{211}At belong to the halogen family (Group 17 in the periodic table). ^{211}At, however, is also regarded as a metalloid since it also shares certain chemical properties with metals. All other radioisotopes listed in Table 21.4 are metals. The radionuclide production and the chemistry of halogens and radiometals are discussed in greater detail in Chaps. 8 and 18 of this book and in several review articles [18, 19].

The labeling of peptides with radionuclides can be performed by direct labeling, with the addition of a prosthetic group. Direct labeling is the method used to label peptides without using intermediates, such as BFCs. Direct labeling techniques are generally used for radioiodination

and, in some cases, labeling with Tc-99m. Prosthetic groups are small molecules able to bind with radionuclides in one site of the structure and, simultaneously, with a peptide at a second site. Prosthetic groups are bifunctional agents that consist of a suitable site for radioiodination or fluorination and functional groups to allow covalent attachment of the peptide. Radiometals specifically require bifunctional chelating agents (BFC or BFCA) to obtain the best conjugation of radiometal with peptides. The bifunctional nature of the chelators means that they can coordinate (form a complex) a metal ion and can, also, be attached to the peptide. The most common chelating agents used for the development of radiolabeled small molecules, peptides, and proteins are shown in Fig. 21.5. The design and development of radiolabeled peptides is discussed in greater detail in Chap. 20.

21.3 Somatostatin Receptors and SST Analogs

Most of the NETs are characterized by the expression of SSTRs on the cell membrane, and five different G-protein-coupled SSTR subtypes (SSTR 1–5) have been identified [20]. However, SSTR-2 is the most common receptor subtype expressed in approximately 90% of GEP-NENs.

SSTR-2 is the only receptor subtype which has two isoforms, SSTR-2a and SSTR-2b, produced by alternate splicing. The expression of SSTRs is less frequent and in lower density is more poorly differentiated than in well-differentiated subtypes. Lung NENs also express SST, with the subtypes 2, 3, and 5 being the most common. Lower expression of SSTRs has been shown in pheochromocytoma, medullary thyroid cancer (MTC), and benign insulinomas.

The natural ligand somatostatin (SST), a neuropeptide, also known as somatotropin release-inhibiting factor (SRIF), was originally discovered in 1973 as a hypothalamic neuropeptide based on its ability to inhibit growth hormone (GH) release from the anterior pituitary [21]. SST occurs in two forms, SST-14 (with 14 amino acids), and SST-28 (with 28 amino acids), with broad antisecretory activity on many hormones, including GH, insulin, glucagon, gastrin, cholecystokinin (CCK), and ghrelin. SST is secreted in the GI tract and the brain and regulates multiple physiological functions, such as neurotransmission, GI motility, hormone secretion, cell proliferation and apoptosis, and immune system modulation [20].

The clinical utility of native human SST-14 is limited by its short half-life (<3 min). Shortly after the discovery of SST, investigators at Sandoz (now Novartis) synthesized the first agonist analog octreotide (SMS 201-995, Sandostatin), a longer acting fragment of the eight amino acid ring of the native SST [22]. Subsequently, two other SRIF agonist analogs (lanreotide and pasireotide) with prolonged half-life were also developed for clinical use. The amino acid sequence of SST and its analogs is shown in Fig. 21.6. The amino acid, lysine, within the ringed portion is considered to be the primary peptide binding site of SST, octreotide, and lanreotide to the SSTR-2A, the most prevalent receptor of the five SSTR subtypes on neuroendocrine cells and their NETs. Also, to prevent enzyme degradation, the natural L-Trp amino acid in the ring was replaced with the D-Trp. These synthetic octapeptide SST analogs (SSAs) have a similar STTR binding profile, with high

SSTR2 and moderate SSTR5 affinity (Table 21.5). Pasireotide, a synthetic long-acting cyclic hexapeptide with SST-like activity, was also synthesized. Pasireotide activates a broad spectrum of SSTRs, exhibiting a much higher binding affinity for SSTR-1, 3, and 5 than octreotide in vitro, as well as a comparable binding affinity for SSTR-2. Both octreotide and lanreotide are very effective FDA-approved drugs for hormonal syndrome control in functioning tumors and exert an antiproliferative effect by inducing cell cycle arrest and apoptosis, and through immunomodulatory effects and angiogenesis inhibition [23]. The high-level expression of SSTRs 2 and 5 on the tumor cell surface in most neuroendocrine tumors (NETs) provides the basis not only for sensitive functional imaging but, also, for a tumor-targeted therapy with commonly "cold," as well as radio-isotope-labeled "hot" somatostatin analogs.

To develop radiopharmaceuticals for imaging and therapy, SST analogs (Fig. 21.6) were synthesized by introducing structural modifications in the octreotide (OC) molecule, and/or by the conjugation of chelating agents to facilitate radiometal labeling [25]. The goal was to develop SST analogs with nanomolar affinity to SSTR and appropriate pharmacokinetics suitable for clinical studies.

- The replacement of Phe[3] in octreotide by Tyr[3] leads to an analog, Tyr[3]-octreotide (TOC derivative) with improved SSTR-2 affinity, but the SSTR-3 and DDTR-5 affinity is reduced. The presence of tyrosine in the peptide sequence, however, facilitates radioiodination of the peptide molecule.
- The C-terminal introduction of Thr for Thr(ol) (TOC) results in a SSTR-2 selective ligand, [Tyr[3], Thr[8]]octreotide (TATE derivative) with a sevenfold improvement of SSTR-2 affinity (Table 21.5).
- Replacement of Tyr[3] in the TOC peptide with an unnatural amino acid, 1-Nal[3] (1-naphthyl alanine) results in an analog with affinity to SSTR-2, 3, and 5.
- Conjugation of acyclic chelator DTPA to the D-Phe[1] in the octreotide results in DTPA-
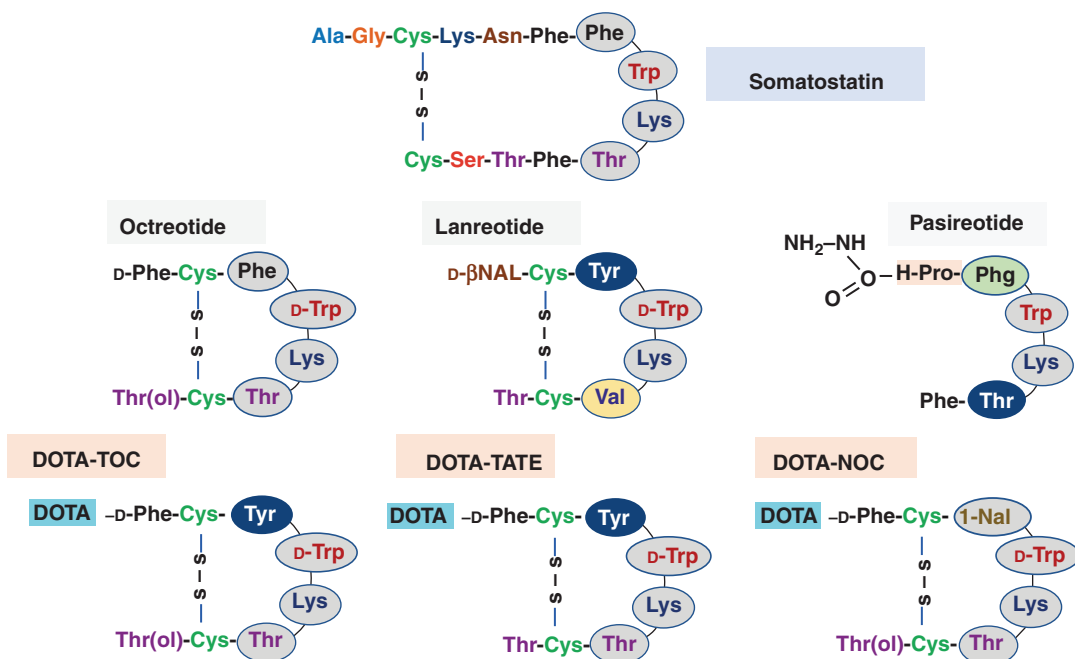
Fig. 21.6 The amino acid sequence of somatostatin (SST) and SST analogs

Table 21.5 Somatostatin analogs: affinity profiles (IC$_{50}$)[a] for the somatostatin receptor (SSTR) subtypes

Peptide	SSTR1	SSTR2	SSTR3	SSTR4	SSTR5
Somatostatin	5.2	2.7	7.7	5.6	4.0
Octreotide	>1000	0.4	4.4	>1000	5.6
Lanreotide	2129	0.75	98	1826	5.2
Pasireotide	9.3	1	1.5	>100	0.16
BFC-peptide conjugates					
DTPA-octreotide	>10,000	12	376	>1000	299
DOTA-TOC	>10,000	14	880	>1000	393
DOTA-TATE	>10,000	1.5	>1000	433	>1000
DOTA-NOC	>10,000	1.9	40	260	7.2
In-DTPA-octreotide	>10,000	22	182	>1000	237
In-DOTA-TOC	>10,000	4.6	120	230	130
Y-DOTA-TOC	>10,000	11	389	>1000	114
Ga-DOTA-TOC	>10,000	2.5	613	>1000	60
Ga-DOTA-TATE	>10,000	0.2	<1000	300	377
Lu-DOTA-TATE	>1000	2.0	162	>1000	1000
Ga-DOTA-NOC	>1000	1.9	40	260	7.2
Lu-DOTA-NOC	>1000	3.4	12.0	747	14.0
In-DOTA-BASS	>1000	9.4	>1000	380	>1000
In-DOTA-JR11	>1000	3.8	>1000	>1000	>1000
Ga-DOTA-JR11 (Ga-OPS201)	>1000	29	>1000	>1000	>1000
Lu-DOTA-JR11 (Lu-OPS201)	>1000	0.73	>1000	>1000	>1000
Ga-NODAGA-JR11 (Ga-OPS202)	>1000	1.2	>1000	>1000	>1000

[a]IC$_{50}$ values expressed in nanomoles [20, 24]

octreotide (pentetreotide), suitable for labeling with [111]In.

- For stable labeling with ^{90}Y and radiolanthanides, DTPA was replaced by macrocyclic chelator DOTA, which is a better choice as it forms thermodynamically and kinetically stable complexes with trivalent metals with 3+ charge.
- With DOTA chelator, three successful SST analogs, DOTA-TOC, DOTA-TATE, and DOTA-NOC were developed. Among these analogs, DOTA-TATE has the highest affinity for SSTR-2 (Table 21.5). However, all these SST agonist analogs trigger SSTR-2 internalization.
- Interestingly, radiometal complexation profoundly influence receptor affinity (Table 21.5), as all Ga-DOTA conjugates of these analogs have improved SSTR-2 affinity compared to the corresponding Y/Lu/In-DOTA conjugates.

21.3.1 Imaging SSTR-Positive NETs Radiolabeled SST Agonist Analogs for Imaging

Several NENs express SSTRs. The expression profile and coexpression of various SSTR subtypes, however, differ according to the NEN location, histological differentiation, and tumor grade. However, SSTR 2 expression predominance is generally found in more than 80% of the endocrine pancreatic and endocrine GI tract tumors [26]. It has been reported recently that G1 and G2 NETs were more common SSTR2-positive in comparison with G3 carcinomas [27]. Neuroendocrine carcinomas had significantly lower SSTR2 and SSTR5 expression compared with well-differentiated NETs. In addition, the SSTR2 expression in the early tumor stages was 100%, more often than in advanced stages (55.6%).

Following the discovery of octreotide in 1982 at the Sandoz Research Institute in Basel, Switzerland, Jean Claude Reubi and colleagues had demonstrated, for the first time, based on autoradiography, the presence of SSTR receptors on the surface of intestinal NET cells using ^{125}I-octreotide [28]. Subsequently, the investigators at the Erasmus University Medical Center (EUMC), Rotterdam in the Netherlands developed [^{123}I-Tyr[3]]octreotide as an imaging agent to localize NETs [29]. Due to biliary excretion and intestinal accumulation of I-123 activity, [^{123}I-Tyr[3]]octreotide was not ideal for the detection of lesions in the abdomen.

21.3.1.1 SSTR Agonists

Octreotide and other SST synthetic analogs are potent agonists and selectively bind to SSTR-2, and 5 receptor subtypes. The binding of agonists leads to receptor-mediated internalization and intracellular trapping of the radionuclide providing adequate time for imaging studies. In contrast, the SSTR antagonist is not internalized but, may offer the possibility to bind to more receptor sites and with a longer retention time [30]. The following SSTR agonist peptide radiopharmaceuticals are in clinical use.

^{111}In-DTPA-Octreotide (OctreoScan™)

Since ^{111}In is an ideal radiometal for imaging studies, the investigators at EUMC developed the DTPA conjugated derivative of octreotide (SDZ 215-811), as a precursor for ^{111}In labeling [31]. Dr. Krenning's team at EUMC performed planar and SPECT imaging studies with [^{111}In-DTPA-D-Phe[1]]octreotide (also known as ^{111}In-pentetreotide) in more than 1000 patients with NETs [32]. In 1994, the FDA approved ^{111}In-pentetreotide (OctreoScan, Mallinckrodt) as an agent for the scintigraphic localization of primary and metastatic neuroendocrine tumors bearing somatostatin receptors. The recommended dose for planar imaging is 111 MBq (3.0 mCi), and for SPECT imaging is 222 MBq (6.0 mCi).

OctreoScan was studied in nine unblinded clinical studies in a total of 365 patients. The most common tumors were carcinoids (132 of 309 evaluable patients). Scintigraphic results

were compared to results of conventional localization procedures (CT, ultrasound, MRI, angiography, surgery, and/or biopsy). OctreoScan results were consistent with the final diagnosis (success) in 86.4% of evaluable patients (OctreoScan, package insert, 12/2018). OctreoScan was the first peptide-based radiopharmaceutical ever approved for peptide receptor scintigraphy (PRS) for localization of primary and metastatic NETs bearing SSTRs.

OctreoScan™ is a kit for the preparation of indium ^{111}In-pentetreotide, consisting of two components:

(a) A 10-mL Octreoscan reaction vial which contains a lyophilized mixture of:
- 10 μg pentetreotide (octreotide-DTPA).
- 2.0 mg gentisic acid [2, 5-dihydroxybenzoic acid],
- 4.9 mg trisodium citrate, anhydrous,
- 0.37 mg citric acid, anhydrous, and
- 10.0 mg inositol.
(b) A 10-mL vial of ^{111}In chloride sterile solution, which contains:
- 1.1 mL of ^{111}In chloride (3.0 mCi/mL or 111 MBq/mL) in 0.02N HCl at time of calibration.
- The vial also contains ferric chloride at a concentration of 3.5 μg/mL.
  Procedure for the preparation of ^{111}In-pentetreotide is as follows:
- Transfer ^{111}In chloride sterile solution into the Octreoscan reaction vial.
  – Mix the contents well and incubate for 30 min at RT.
  – Determine the radiolabeling yield or radiochemical purity (RCP) using Sep-Pak cartridge as per the instructions in the package insert. RCP must be >90% for clinical use (Curium US LLC, 12/2018).

^{68}Ga-DOTA-TOC

In the late 1990s, several octreotide analogs conjugated with DOTA chelator were introduced in order to develop ^{90}Y-labeled SST analog for PRRT. Among these SST analogs, DOTATOC was shown to be suitable for labeling with either ^{90}Y or ^{67}Ga [33, 34]. DOTATOC exhibits high affinity (IC_{50}) for human SSTR-2 (14 ± 2.6 nM) with much lower binding affinity for all other human SSTRs (Table 21.5). A marked improvement of SSTR-2 affinity was found for Ga-DOTATOC (2.5 nM) compared with the Y-DOTATOC (11 nM) and OctreoScan (22 nM) [35]. In addition, it was also noted that changing the central atom in the chelator complex from In^{3+} to Ga^{3+} may induce an alteration of the complex conformation towards a lower hydrophobicity, with a resultant decrease in protein binding and increase in renal elimination. In 2001, it was reported that ^{68}Ga-DOTATOC-PET results in high tumor to non-tumor contrast and low kidney accumulation and yields higher detection rates (>30% more lesions) as compared with OctreoScan scintigraphy [36]. Since its introduction, ^{68}Ga-DOTATOC has been extensively used in Europe for the last two decades. A systematic review and meta-analysis concluded that ^{68}Ga-DOTATOC is useful for evaluating the presence and extent in disease for staging and restaging, and for assisting in the treatment decision-making for patients with NETs [37].

^{68}Ga-DOTA-TOC was approved in several European countries in 2016 (IASOtoc®), and in 2018 (TOCscan®). Also, in Europe, a kit preparation for ^{68}Ga-labeling of DOTA-TOC (SomaKit TOC®) was approved by the European Medicines Agency (EMA) in September 2016. Use of this kit along with an authorized ^{68}Ge/^{68}Ga-generator enables on-site preparation of ^{68}Ga-DOTA-TOC. In the United States, the FDA approved the ready-to-use ^{68}Ga-DOTA-TOC in August 2019. The holder of the NDA (New Drug Application) or marketing authorization is the UIHC–PET Imaging Center (University of Iowa Health Care [UIHC]), in Iowa, USA [38]. It is indicated for use with PET for the localization of SSTR-positive NETs in adult and pediatric patients. The recommended dose is 111–185 MBq (3–5 mCi).

The safety and efficacy of ^{68}Ga-DOTATOC Injection were established in two single-center, open-label studies in which 282 patients with known or suspected SSTR-positive NETs received a single dose. A total of 238 of the 282 patients (84%) had a history of neoplasm at the time of Ga-68 DOTATOC imaging.

Ga 68 DOTATOC Injection is supplied in a multiple-dose, capped 30 mL glass vial containing ^{68}Ga-DOTATOC at calibration time in approximately 14 mL. It is a sterile, pyrogen free, clear, colorless, buffered solution, with a pH between 4 and 8. It contains.

- 3.6 μg/mL (DOTA-0-Phe[1]-Tyr[3]) octreotide,
- 18.5–148 MBq/mL (0.5–4 mCi/mL) of ^{68}Ga-DOTATOC at calibration time,
- Ethanol (10% v/v) in sodium chloride (9 mg/mL) solution (~14 mL).

^{68}Ga-DOTATATE

DOTATATE is an SST analog and an SSTR agonist that closely simulates DOTATOC, in which the C-terminal threoninol (an amino alcohol) is replaced by threonine (Fig. 21.7). This chemical modification resulted in a nine-fold higher affinity (1.5 nM) for the SSTR-2 as compared with DOTA-TOC (14 nM). Also, the affinity of Ga-DOTATATE (0.2 nM) for SSTR-2 is 12 times higher compared to that of Ga-DOTATOC (2.5 nM) [35]. Preclinical studies in animal models demonstrated that DOTATATE may be a better SST analog for the development of radiotracers for imaging and targeted therapy compared to DOTATOC [39, 40]. No human data, however, was available at that time to support the preclinical observations.

A direct comparison of pharmacokinetics and dosimetry of ^{111}In-DOTATOC and ^{111}In-DOTATATE in patients with metastatic NETs indicated that the two peptides appear to be nearly equivalent, except with minor advantages for ^{111}In-DOTATOC [41]. Similarly, based on direct comparison of PET/CT studies with ^{68}Ga-DOTATOC and ^{68}Ga-DOTATATE, it was concluded that both these radiotracers possess a comparable diagnostic accuracy for the detection of NET lesions, with ^{68}GaDOTATOC having a potential advantage. The approximately ten-fold higher affinity for the SSTR-2 of ^{68}Ga-DOTATATE does not prove to be clinically relevant. Also, the study found that the SUV_{max} of ^{68}Ga-DOTATOC scans tended to be higher than their ^{68}Ga-DOTATATE counterparts [42].

In June 2016, the FDA approved ^{68}Ga-DOTATATE (NETSPOT™) (Fig. 21.7) for the localization of SSTR positive NETs in adult and pediatric patients. NETSPOT™ is the new

Fig. 21.7 The structure of radiometal (^{68}Ga, ^{64}Cu, or ^{177}Lu) labeled DOTA-TATE (DOTA-Tyr^3-octreotide) complex

Radiometal (^{68}Ga, ^{64}Cu or ^{177}Lu) Complex of DOTA-TATE
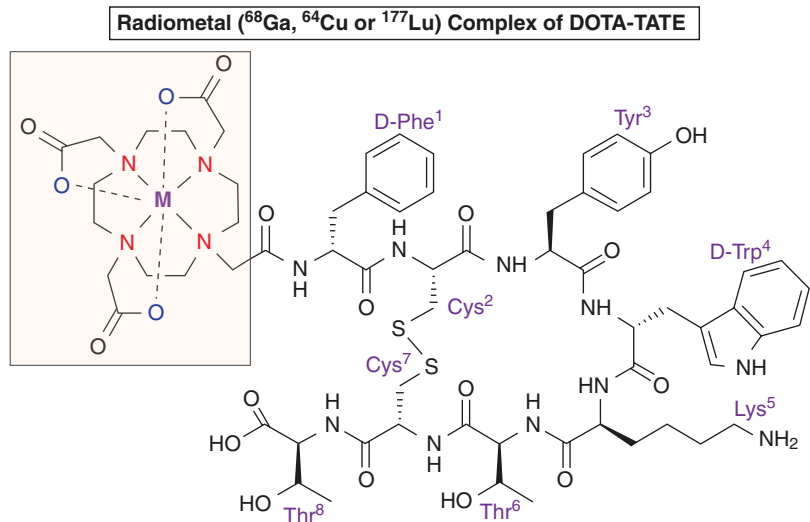
Table 21.6   Clinical studies to determine efficacy and safety of ^{68}Ga-DOTATATE

Study	n	Reference standard (RS)	^{68}Ga-DOTATATE	
		N	Positive (+ve)	Negative (−ve)
A	97	78, RS-scans[a]	48/50 RS-scan +ve	26/28 RS-scan −ve
			96%	93%
B	104	104, RS-HP	29/36 RS-HP +ve	61/68 RS-HP −ve
			81%	90%
C	63	63, RS-HP	22–23/29 RS-HP +ve	29–32/34 RS-HP −ve
			79%	94%

The data is from Octreoscan package insert (06/2016)

[a]RS-scans: CT, MRI, and Octreoscan; *RS-HP* Histopathology

market name for Somakit-TATE (a kit for the preparation of ^{68}Ga-dotatate injection using ^{68}Ga chloride from the GalliaPharm ^{68}Ga/^{68}Ga generator from Eckert & Ziegler). ^{68}Ga-dotatate received Orphan Drug Designation from both the FDA and the European Medicines Agency (EMA) in March of 2014. The efficacy of NETSPOT was established in three open label single center studies (Study A–C) in patients with known or suspected NETs (Table 21.6). NETSPOT is indicated for use with PET for the localization of SSTR-positive NETs in adult and pediatric patients. The recommended dose is 2 MBq/kg (0.054 mCi/kg) up to 200 MBq (5.4 mCi).

The NETSPOT is a kit for the preparation of ^{68}Ga-DOTATATE injection. The NETSPOT kit allows for direct preparation of ^{68}Ga-DOTATATE injection with the eluate from an Eckert & Ziegler GalliaPharm ^{68}Ge/^{68}Ga generator.

NETSPOT is supplied as a single dose kit containing.

- Vial 1 (reaction vial with lyophilized powder) containing 40 μg of Dotatate, 5 μg of 1,10 phenanthroline, 6 μg gentisic acid and 20 mg D-mannitol.
- Vial 2 (buffer vial) containing 1 mL of reaction buffer solution containing 60 mg formic acid, 56.5 mg sodium hydroxide.
- An accessory cartridge containing 660 mg porous silica.

Drug Preparation: Prepare the drug product under aseptic conditions according to the procedure described in the NETSPOT package insert.

- Use 5 mL of 0.1 N HCl solution (supplied by generator manufacturer) to elute the generator.
- To the reaction vial-1 with lyophilized powder, first add the reaction buffer solution (0.1–0.5 mL) from the buffer vial-2 based on the volume of ^{68}Ga chloride eluate from the generator to be used (1–5 mL).
- Add ^{68}Ga chloride solution (<50 mCi in 1–5 mL) via the conditioned accessory cartridge into the reaction vial-1 with the buffer.
- Incubate for 7–10 min at 95 °C and then cool it for 10 min.
- Assay the whole vial containing the ^{68}Ga-dotatate injection for total radioactivity concentration.
- Perform QC tests (such as visual inspection, pH, RCP by ITLC) in order to check compliance with the specifications. The drug product must be colorless and particulate free with a pH of 3.2–3.8. The RCP ≥ 92%, and Other Ga-68 species ≤5%.

^{68}Ga-DOTA-NOC

[DOTA^0,1-Nal^3]-octreotide (DOTA-NOC) is a peptide that has the potential to target a broader range of SSTR subtypes, including SSTR-2, 3, and 5 [43]. The affinity for SSTR-2, 3, and 5 are 1.9, 40, and 7.2 nM, respectively (Table 21.5). Direct comparison with ^{68}Ga-DOTA-TOC and ^{68}Ga-DOTA-TATE PET studies in patients with NETs indicated that ^{68}Ga-DOTA-NOC detects more metastases than do SSTR-2 specific tracers [44, 45]. Based on a retrospective study of patients with NETs

(n = 445) who underwent ^{68}Ga-DOTA-NOC PET/CT, it was concluded that ^{68}Ga-DOTA-NOC PET/CT is a highly sensitive and specific study for the diagnosis and follow-up of patients with NETs [46]. The sensitivity, specificity, negative-predictive value, and positive-predictive value of ^{68}Ga-DOTA-NOC were 87, 98, 80, 99%, respectively.

[64]Cu-DOTATATE (DetectNet)

The relatively longer half-life and low positron energy ($T\frac{1}{2}$ = 12.7 h; 0.653 β^+) of ^{64}Cu is appropriate for PET imaging. The initial studies with ^{64}Cu-TETA-octreotide showed high rate of lesion detection, sensitivity, and favorable dosimetry and pharmacokinetics [47]. Since ^{64}Cu forms a more stable complex with DOTA chelator, ^{64}Cu-DOTATATE has been studied as a potential PET radiotracer for SSTR-based imaging. The first human study clearly supports the clinical use of ^{64}Cu-DOTATATE for PET studies with excellent imaging quality, reduced radiation burden, and increased lesion detection rate when compared with OctreoScan [48, 49].

In a head-to-head comparison with ^{68}Ga-DOTATOC-PET in patients with NETs, ^{64}Cu-DOTATATE-PET scans detected more lesions although patient-based sensitivity was the same for both agents [50]. Recently, in a prospective trial in patients with Known or Suspected SSTR positive NETs, PET/CT scan with ^{64}Cu-DOTATATE was considered a safe imaging technique that provides high-quality and accurate images at a dose of 148 MBq (4.0 mCi) for the detection of SSTR expressing NETs [51]. The lower positron energy of ^{64}Cu compared to that of [68]Ga (0.65 vs. 1.90 MeV), which translates to lower positron range (0.56 vs. 3.5 mm), is thought to explain the anticipated improved spatial resolution and diagnostic performance of ^{64}Cu-DOTATATE (Fig. 21.8) Additionally, the longer physical half-life of [64]Cu (12.7 h) may

increase the shelf-life of ^{64}Cu-DOTATATE, and provide a more flexible scanning window, making it attractive for routine clinical imaging.

In September 2020, the FDA approved ^{64}Cu-DOTATATE injection (DetectNet) for the localization of SSTR–positive NETs. Two single-center, open-label studies confirmed the efficacy of the diagnostic agent. The results of the study-1 (n = 63) showed that the percent reader agreement for positive detection was 91% and negative detection was 80–95%. Study-2 was a retrospective analysis in which investigators examined published findings collected from 112 patients and the results demonstrated similar performance as study-1 (Detectnet, package insert 2020).

DetectNet is a sterile, clear, colorless to yellow solution for intravenous use. Each 10 mL single-dose vial contains 148 MBq (4 mCi) of copper Cu 64 dotatate at calibration date and time in 4 mL solution volume. Additionally, each mL of the solution contains 40 mg ascorbic acid, 0.05 mL of dehydrated alcohol, USP (ethanol) in sterile water for injection, USP. The pH is adjusted with sodium hydroxide, hydrochloric acid, and is between 5.5 and 7.5.

21.3.1.2   SSTR Antagonists

While the agonists activate SSTRs and internalize into tumor cells, the antagonists interact with SSTRs and block or reduce the physiological effect of an agonist [52]. It has been shown that potent SSTR antagonists, known to poorly internalize into tumor cells, may be as good as, or even superior to, agonists for developing radiopharmaceuticals for imaging and therapy, and some antagonist analogs show rapid blood clearance, poor kidney retention, and better accumulation in the tumor tissue [24, 30].

In 1996, it was reported that the inversion of chirality at positions 1 and 2 of the octapeptide (octreotide family) converted an agonist into a

^{111}In-DTPA-Octreotide ^{64}Cu-DOTATATE-PET
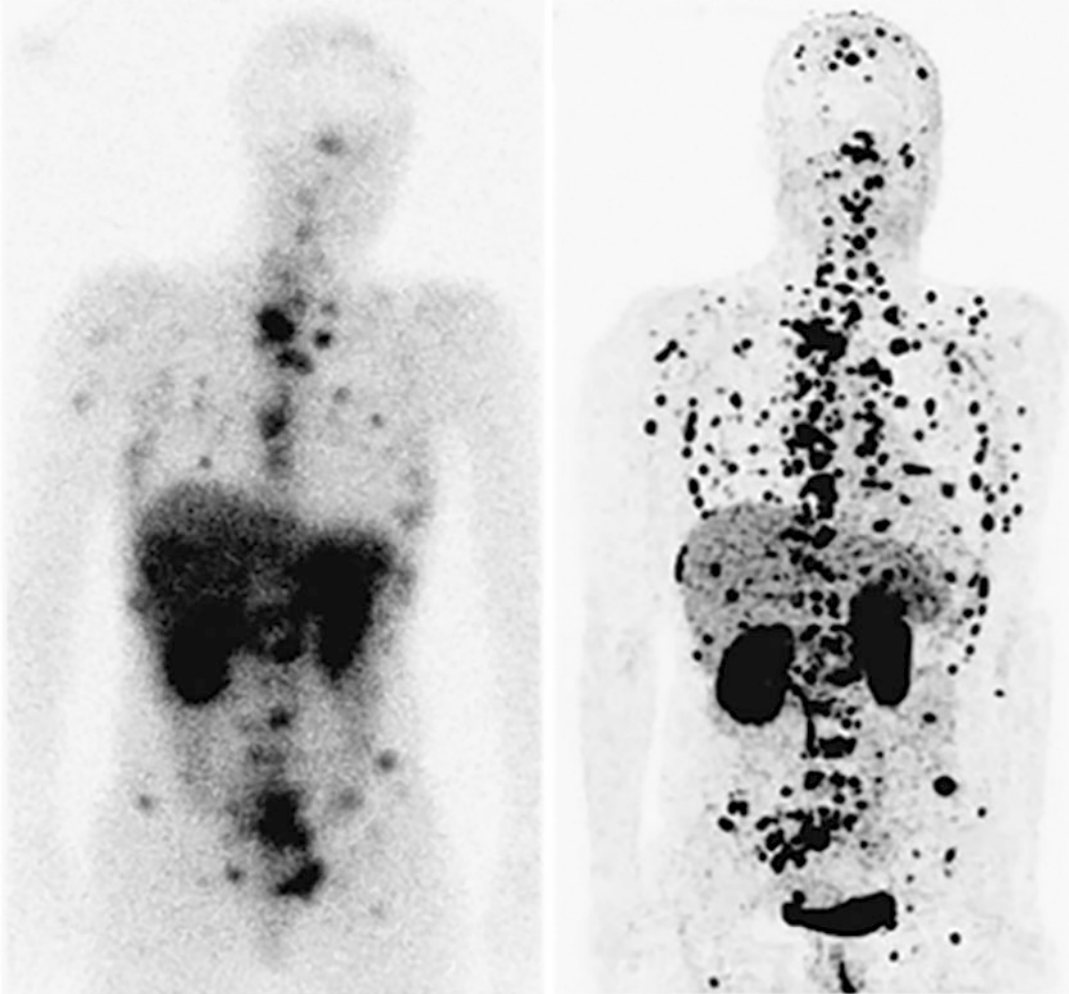
Fig. 21.8 Comparison of ^{64}Cu-DOTATE-PET and ^{111}In-DTPA-Octreotide (OctreoScan) in the same patient with NETs with multiple bone and soft tissue metastases. (From Pfeifer et al. [49])

potent antagonist [53]. The first radiolabeled SSTR antagonists were based on the SSTR-2-selective analog sst2-ANT or BASS [53]. The first proof of the concept clinical study with ^{111}In-DOTA-BASS demonstrated better accumulation of the tracer in the tumor and better visualization compared to that of OctreoScan® [45].

The second generation of antagonists include LM3, JR10, and JR11. The amino acid sequence of these antagonists is shown in Fig. 21.9. The chelate (DOTA, NODAGA) and the radiometal (In, Ga, Cu, Y, or Lu) make a significant difference in the affinity (Table 21.5) and pharmacokinetics of the radiolabeled SSTR-2 antagonists

SSTR Agonists

Octreotide: D-Phe^1-Cys^2-Phe^3-D-Trp^4-Lys^5-Thr^6-Cys^{7}Thr(ol)^8

DOTA-TOC   D-Phe^1-Cys^2-Tyr^3-D-Trp^4-Lys^5-Thr^6-Cys^{7}Thr(ol)^8

DOTA-TATE: D-Phe^1-Cys^2-Tyr^3-D-Trp^4-Lys^5-Thr^6-Cys^{7}Thr^8

SSTR Antagonists

SSTR-2-ANT (BASS):   p-NO$_2$-Phe^1-D-Cys^2-Tyr^3-D-Trp^4-Lys^5-Thr^6-Cys^7-D-Tyr^8-NH$_2$

LM3   p-Cl-Phe^1-D-Cys^2-Tyr^3-D-Aph^4(Cbm)-Lys^5-Thr^6-Cys^7-D-Tyr^8-NH$_2$

JR10   p-NO$_2$-Phe^1-D-Cys^2-Tyr^3-D-Aph^4(Cbm)-Lys^5-Thr^6-Cys^7-D-Tyr^8-NH$_2$

JR11 (Satoreotide)   p-Cl-Phe^1-D-Cys^2-Aph^3(Hor)-D-Aph^4(Cbm)-Lys^5-Thr^6-Cys^7-D-Tyr^8-NH$_2$

Fig. 21.9 The amino acid sequences in somatostatin receptor (SSTR) agonists and antagonists

[24]. The Ga-DOTA analogs had lower affinity for SSTR-2 than the respective Y, Lu, or In-DOTA counterparts. Interestingly, however, substitution of DOTA by the NODAGA chelator was able to substantially increase the binding affinity of the Ga-NODAGA analogs, compared with the Ga-DOTA analogs. Surprisingly, even a low-affinity antagonist was shown to be slightly superior to a high-affinity agonist, outweighing the affinity differences. More specifically, ^{68}Ga-DOTA-JR11, having a dramatically lower affinity for SSTR-2 (~150-fold) than ^{68}Ga-DOTATATE, showed a tumor uptake that was 1.3-fold higher, and ^{68}Ga-NODAGA-JR11, having a sixfold lower affinity than ^{68}Ga-DOTATATE, showed a tumor uptake that was up to 1.7-fold higher [54].

Among the radiolabeled SSTR-2 antagonists investigated, the analog JR11 performed the best in preclinical settings. PET/CT with ^{68}Ga-NODAGA-JR11 (or ^{68}Ga-OPS202) detected significantly more metastases with higher tumor-to-background ratios than the SSTR agonist ^{68}Ga-DOTATOC [55] (Fig. 21.10). Lu-DOTA-JR11 (Lu-OPS201, or

^{177}Lu-satoreotide tetraxetan) with affinity of only 0.73 nM demonstrated a favorable biodistribution profile and increased tumor dose compared with the agonist ^{177}Lu-DOTATATE [56]. A phase I study with ^{177}Lu-JR11 was performed in 20 patients with NETs (2 cycles, 3 months apart, 7.4 GBq/cycle). Preliminary data are promising and additional studies are on-going to determine optimal therapeutic dose/schedule [57].

Since the SSTR-2 affinity of ^{68}Ga-NODAGA-LM3 was tenfold higher than that of ^{68}Ga-DOTA-LM3, a phase 1 study compared the biodistribution of these two agents [58]. Both tracers showed favorable biodistribution, high tumor uptake, and good tumor retention, resulting in high image contrast, good tumor uptake, and retention. The first human studies of PRRT with ^{177}Lu-DOTA-LM3 were performed in 51 patients with metastatic NENs to assess safety, efficacy, and dosimetry. Patients received 2.8–7.1 GBq/cycle. Higher uptake and a longer effective half-life of ^{177}Lu-DOTA-LM3 was found for whole-body as well as kidneys, spleen, and metastases, resulting in higher mean absorbed organ and tumor doses as compared to
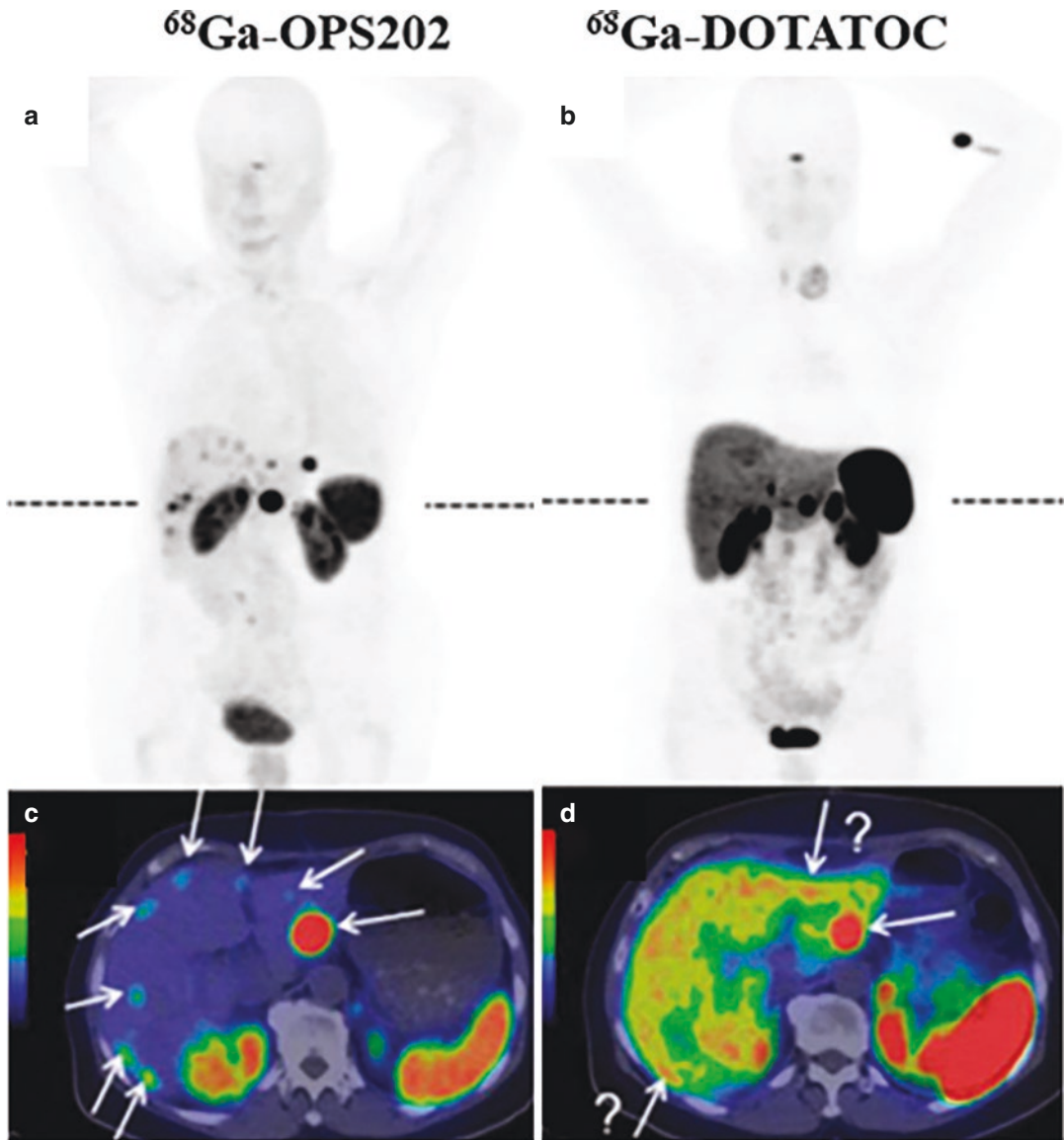
Fig. 21.10 [⁶⁸Ga]Ga-OPS202 PET/CT (**a**, **b**) and [⁶⁸Ga]Ga-DOTATOC PET/C.T (**c**, **d**) images of a patient with ileal neuroendocrine tumors, showing bilobar liver metastases (dashed lines indicate level of transaxial slices). Studies were performed on the same scanner within 2 months. With the antagonist, OPS-202, the background activity was lower in liver, intestine, and thyroid than with agonist DOTATOC, allowing better identification of the lesions in the liver which are confirmed by subsequent MRI. (Figure modified from Nicolas et al. [55])

the agonist ¹⁷⁷Lu-DOTA-TOC. The study concludes that ¹⁷⁷Lu-DOTA-LM3 appears to be very promising for PRRT, provides favorable biodistribution and higher tumor radiation doses than SSTR agonists [59].

21.3.2 Therapy of SSTR-2-Positive NETs

The acronyms PRS (peptide receptor scintigraphy) and PRRT (peptide receptor radionuclide therapy) were originally coined in the 1980s by the investigators at the Erasmus University

Medical Center, Rotterdam in the Netherlands. Since ^{111}In decays by electron capture (*EC*) and emits low energy Auger and conversion electrons, Dr. Krenning's group evaluated the potential of ^{111}In-pentetreotide for targeted therapy of SSTR positive NETs and introduced the concept of PRRT. A total of 50 patients received many cycles of ^{111}In-pentetreotide within about 5 years. Three of the six patients who received more than 100 GBq (2700 mCi) cumulatively developed myelodysplastic syndrome or leukemia at a mean bone marrow dose of about 3 Gy [60]. Further PRRT studies with ^{111}In-pentetreotide were discontinued since it became clear that radiometals decaying by β^- emission (such as ^{90}Y or ^{177}Lu) might be better suited for radionuclide therapy than ^{111}In, because the short tissue range of low energy Auger electrons resulted in relatively modest tumor shrinkage, as shown by CT/MRI imaging.

21.3.2.1   ^{90}Y-DOTA-TOC

Following the development of DOTA conjugated octreotide analogs in the early 1990s, a clinical study with ^{90}Y-DOTATOC was started in Basel in June 1996, but soon became a multi-center study. In 1998, the first results of ^{90}Y-DOTATOC in patients with SSTR-positive tumors were reported [61]. The results of a phase 2 study ($n = 41$) demonstrated an overall response rate of 24% and a significant reduction in carcinoid syndrome in 83% of the patients [62].

In 1997, Novartis launched a PRRT study with ^{90}Y-DOTATOC (edotreotide, or OctreoTher). A separate protocol was designed to study pharmacokinetics and biodistribution based on a PET imaging study with [86]Y-DOTATOC or a planar/SPECT study with ^{111}In-DOTATOC (as a chemical and biological surrogate for ^{90}Y-DOTATOC), to estimate maximum tolerated individual patient therapy doses of ^{90}Y-DOTATOC. The clinical experience of PRRT with ^{90}Y-DOTATOC treatment was published in two major reports. A study that included 1109 patients (treated with 3.7 GBq/m²; 1–10 cycles) demonstrated a morphologic response rate in 34% of patients but, 9.2% of patients had severe grade 4 or 5 permanent nephrotoxicity [63]. A second report showed 74.4% of

patients with metastatic carcinoid refractory to octreotide had stable disease following treatment with three cycles of 4.4 GBq (120 mCi) each, once every 6 weeks [64].

The primary observed disadvantage of PRRT with ^{90}Y-DOTATOC was renal toxicity. Renal failure was observed in patients when ^{90}Y-DOTATOC was administered without kidney protection, although some renal toxicity was still observed even with the administration of amino acids for kidney protection [65]. The investigators at EUMC started preclinical and clinical investigations to optimize kidney protection with the amino acids, lysine, and arginine during PRRT with somatostatin analogs. It was suggested that renal retention of radiometal labeled peptides is confined to proximal tubules in the kidney, in which megalin-(a multiligand scavenger receptor in renal proximal tubules)mediated endocytosis may play an important part [66]. The uptake of radiolabeled peptides can be inhibited by the administration of the positively charged amino acids lysine and arginine, which compete for negatively charged binding sites at the proximal tubule cell surface [67].

21.3.2.2   ^{177}Lu-DOTATOC

In order to decide which SST analog labeled with ^{177}Lu should be preferred for PRRT, the biodistribution and tissue distribution of ^{177}Lu-DOTATOC and ^{177}Lu-DOTATATE were compared in patients with SSRT-2 positive NETs [68]. The study concluded that octreotate was a better peptide for PRRT since ^{177}Lu-DOTATATE had a longer tumor residence time (τ) despite a longer residence time also in kidneys. A subsequent comparative clinical study [69] demonstrated that ^{177}Lu-DOTATOC delivers the lowest doses to healthy organs and has a more advantageous ratio—in terms of absorbed dose—between tumor and kidney (therapeutic index), compared to ^{177}Lu-DOTATATE and ^{177}Lu-DOTANOC (Table 21.7).

A phase 2 study evaluated the efficacy and safety profile of ^{177}Lu-DOTATOC in patients with advanced NETs who received various cycles (1–4) of ^{177}Lu-DOTATOC, with a median activity per cycle of 7.0 GBq and with intervals of 3

Table 21.7 Relative beneficial therapeutic index of ^{177}Lu-DOTATOC compared to ^{177}Lu-DOTATATE or ^{177}Lu-DOTANOC

| SST analog | Radiation dose (mGy/MBq) | | T/K ratio |
	Tumor (T)	Kidneys (K)	
^{177}Lu-DOTATOC	4.9 (0.3–39.7)	0.5 (0.3–1.6)	8.16
^{177}Lu-DOTATATE	5.2 (0.1–89.6)	0.8 (0.3–2.6)	6.50
^{177}Lu-DOTANOC	2.0 (0.5–31.7)	1.1 (0.6–1.5)	1.82

Table modified from Uccelli et al. [70]

months between one cycle and the next [71]. The results of this study confirmed that ^{177}Lu-DOTATOC treatment provides an objective response and survival times comparable to those obtained using ^{177}Lu-DOTATATE. The study results also showed an absence of significant side effects, especially affecting the renal parenchyma. Several clinical studies also showed a high percentage of objective responses and high survival times. Furthermore, the safety profile is also favorable, with bone marrow toxicity percentages comparable (and in some cases lower) to those reported in the PRRT studies with ^{177}Lu-DOTATATE [70].

Most of the clinical trials evaluating therapeutic radiopharmaceuticals showed that ^{90}Y radiopharmaceuticals are more effective on large lesions, while those with ^{177}Lu are more effective on smaller lesions. It may be appropriate to devise protocols in which patients with NETs could be treated with combined regimens of both [90]Y- and ^{177}Lu-labeled SST analogs. ^{90}Y-DOTATOC and ^{177}Lu-DOTATOC are designated as orphan drugs but, have not yet received marketing authorization and FDA approval. Several phase II and III clinical trials continue to evaluate the efficacy of ^{177}Lu-DOTATOC for TRT in patients with NETs.

21.3.2.3 ^{177}Lu-DOTATATE (LUTATHERA®)

Based on preclinical studies in animal models, investigators at ESMU, Rotterdam demonstrated that DOTTATE may be a better SST analog for the development of radiotracers for imaging and targeted therapy compared to DOTATOC [39]. The research group at Mallinckrodt Medical first reported that [^{177}Lu-DOTA[0]-Tyr[3]]octreotide (LuTate) was very successful as a therapeutic agent based on tumor regression and animal survival in a rat model [72]. Lu-DOTATATE has five-fold increase in affinity (2 nM) to SSTR-2 subtype compared to that of Y-DOTATOC (11 nM) (Table 21.5). In addition, with ^{177}Lu-DOTATATE, it is possible to perform dosimetry and therapy with the same compound while PET or SPECT scans with other radionuclides is not needed. The tissue penetration range of [177]Lu (~2 mm) is more favorable than that of [90]Y (~12 mm), especially for smaller tumors. The first clinical studies with ^{177}Lu-DOTATATE confirmed the relative advantage of ^{177}Lu-DOTATATE over ^{111}In-DTPA-Octreotide or ^{90}Y-DOTATOC [40].

Over the years, ESMU has performed PRRT in >1500 patients with ^{177}Lu-DOTA-TATE, even though the ^{177}Lu-DOTA-TATE has not yet been approved by regulatory authorities. After more than 15 years of experience with up to 29.6 GBq (800 mCi) of cumulative administered doses of ^{177}Lu-DOTA-TATE (usually in four treatment cycles with treatment intervals of 6–10 weeks), the safety, efficacy, and toxicity were well documented [73–76].

In 2001, BioSynthema Inc. was founded in St. Louis, Missouri to discover and develop pharmaceuticals targeting cell surface receptors overexpressed in cancer cells. In 2007, Covidien and BioSynthema Inc. signed exclusive agreements to develop cancer therapy with ^{177}Lu-DOTA-TATE. In 2010, BioSynthema Inc. was acquired by Advanced Accelerator Applications, S.A. (AAA), Saint-Genis-Pouilly, France. Subsequently, a regulatory pathway was negotiated with the FDA and the European Medicines Agency, and a pivotal multinational phase 3 study (NETTER-1) was conducted at 41 global sites [77]. By 2015, the NETTER-1 study had met its primary endpoint of assessing progression-free

survival, (PFS) demonstrating that LUTATHERA significantly improved PFS compared with octreotide acetate injection (Sandostatin LAR; Novartis; 60 mg) [78]. LUTATHERA® received regulatory registration for clinical use by the European Medical Association (EMA) in 2017 and the FDA approval in January 2018 [79].

A phase III randomized study (NETTER-1) evaluated 229 patients assigned to ^{177}Lu-DOTATATE or high-dose octreotide. Patients treated with PRRT showed significant improvement in PFS (28 vs. 8.4 months) with objective imaging response observed in 18% of patients [78]. A subsequent study including 610 patients with metastatic GEP and bronchial NETs showed PFS and overall survival for all patients of 29 months and 63 months, respectively [80]. LUTATHERA is indicated for the treatment of SSTR-positive GEP-NETs, including foregut, midgut, and hindgut NETs in adults. Important aspects of NETTER-1 study design were as follows:

- 229 patients with progressive SSTR-positive midgut carcinoid tumors were randomized (1:1) to receive either LUTATHERA injection intravenously (study drug) or high-dose long-acting octreotide 60 mg intramuscular injection every 4 weeks (control arm).
- Randomization was stratified by OctreoScan tumor uptake score (Grade 2, 3, or 4) and the length of time that patients had been on the most recent constant dose of octreotide prior to randomization (≤6 or >6 months).
- LUTATHERA 7.4 GBq (200 mCi) was administered every eight to 16 weeks concurrently with the recommended amino acid solution and with long-acting octreotide (30 mg administered by intramuscular injection within 24 h of each LUTATHERA dose) (n = 111).
- High-dose octreotide was administered every 4 weeks (n = 112).
- Among patients receiving LUTATHERA with octreotide, 79% received a cumulative dose >22.2 GBq (>600 mCi) and 76% of patients received all four planned doses.
- The median duration of follow-up was 24 months for patients receiving LUTATHERA

with octreotide and 20 months for patients receiving high-dose octreotide.

Dose and administration: Recommended doses are 7.4 GBq (200 mCi/) every 8 weeks for a total of four doses. Amino acid solution (described in the package insert) must be started 30 min before LUTATHERA infusion and continued for 3 h after LUTATHERA infusion. Also recommended is the administration of long-acting octreotide 30 mg intramuscularly 4–24 h after each LUTATHERA dose and short-acting octreotide for symptomatic management. Continue long-acting octreotide 30 mg intramuscularly every 4 weeks after completing LUTATHERA until disease progression or for up to 18 months following treatment initiation.

LUTATHERA Injection containing 370 MBq/mL (10 mCi/mL) of lutetium; Lu 177 dotatate is a sterile, preservative-free, and clear, colorless to slightly yellow solution (pH 4.5–6.0) supplied in a 30 mL single-dose vial containing 7.4 GBq (200 mCi) ± 10% at the time of injection. The solution volume in the vial is adjusted from 20.5 to 25 mL to provide a total of 7.4 GBq (200 mCi/~200 µg of dotatate peptide) (Fig. 21.11). Each single-dose vial contains:

- Acetic acid (0.48 mg/mL),
- Sodium acetate (0.66 mg/mL),
- Gentisic acid (0.63 mg/mL),
- Sodium hydroxide (0.65 mg/mL),
- Ascorbic acid (2.8 mg/mL),
- Diethylenetriamine pentaacetic acid (0.05 mg/mL),
- Sodium chloride (6.85 mg/mL), and
- Water for injection (ad 1 mL).

21.3.2.4　[177]Lu-DOTA-EB-TATE

Evans Blue (EB) dye binds reversibly to serum albumin with moderate affinity and has a relatively long half-life compared to small peptide molecules. Coupling of EB derivatives to small molecule peptide drug molecules would increase the peptide's residence time in blood, potentially allowing more therapeutic peptide to be absorbed into the target tissue during PRRT [82].
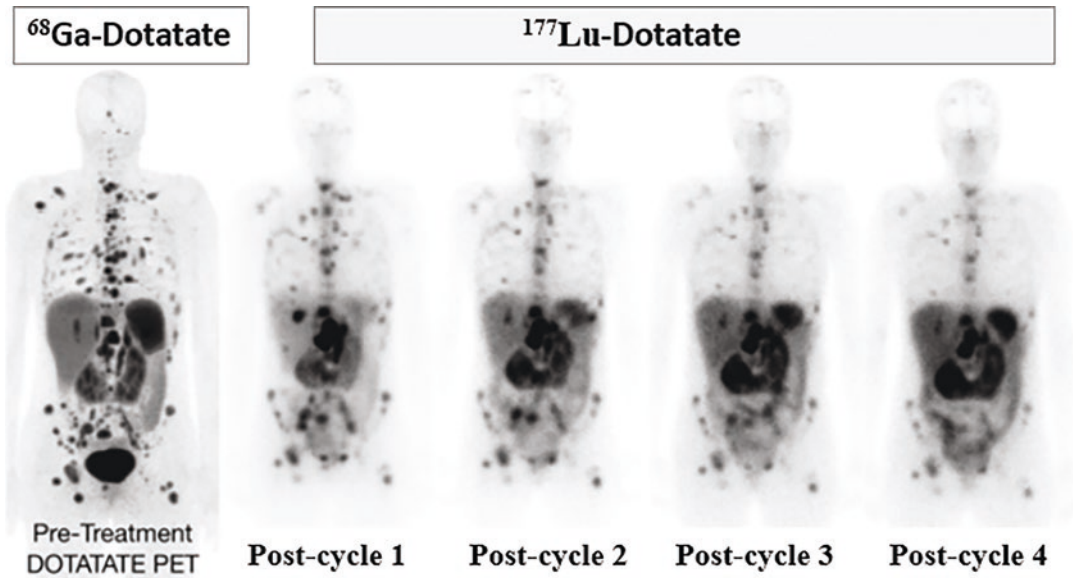
Fig. 21.11 ^{177}Lu-Dotatate (Lutathera) treatment of patients with NETs. Whole body ^{177}Lu images obtained after the administration of therapy dose at different treatment cycles. Pretreatment tumor burden was documented with ^{68}Ga-Dotatate-PET. (From Hope et al. [81]). Post treatment scans with ^{177}Lu-dotatate show partial response to therapy

In 2018, it was reported that EB modification of octreotate that uses endogenous albumin as a reversible carrier effectively extends the half-life in the blood and, substantially, increases accumulation, and retention of [86]Y/^{90}Y-DOTA-EB-TATE in the tumors, leading to highly effective eradication of SSTR2 positive tumors in multiple xenograft models [83, 84]. The first-in-human study showed remarkably higher tumor uptake and retention of ^{177}Lu-DOTA-EB-TATE over ^{177}Lu-DOTATATE [85].

A recent study aimed to evaluate the safety and efficacy of three cycles of ^{177}Lu-DOTA-EB-TATE therapy at escalating doses in neuroendocrine tumors NETs [86]. This preliminary study concluded that dose escalations of up to 3.97 GBq/cycle seem to be well tolerated for ^{177}Lu-DOTA-EB-TATE and doses of 1.89 and 3.97 GBq/cycle were effective in tumor control and more effective than 1.17 GBq/cycle. The maximum tolerated dose (MTD), however, has not been determined. A study designed to estimate dosimetry of ^{177}Lu-DOTA-EB-TATE showed remarkably higher uptake and retention in the tracer in tumor, as well as significantly

increased accumulation in the kidneys and red marrow. As a result, the radiation dose to kidneys and marrow was also increased (3.2 and 18.2-fold, respectively) in patients receiving ^{177}Lu-DOTA-EB-TATE compared with those receiving ^{177}Lu-DOTATATE [87]. Another study, with intra-individual comparison with ^{177}Lu-DOTATOC showed that tumor doses per administered activity were higher for ^{177}Lu-DOTA-EB-TATE in 4/5 patients but, the therapeutic index (tumor to critical organs absorbed dose ratios) was higher (or more favorable) after ^{177}Lu-DOTATOC in 4/5 patients [88]. Therefore, to determine the potential advantages of ^{177}Lu-DOTA-EB-TATE pharmacokinetics on the overall safety and efficacy, well designed clinical trials need to be performed.

21.3.2.5 Therapy with SSTR Antagonists

As mentioned in Sect. 21.3.1.2, among the radiolabeled SSTR-2 antagonists investigated, ^{68}Ga-NODAGA-JR11 targeted metastatic lesions in patients with NETs with higher tumor-to-background ratios. ^{177}Lu-DOTA-JR11

(Lu-OPS201, or ^{177}Lu-satoreotide tetraxetan) with an affinity of only 0.73 nM to SSTR-2 (Table 21.5) demonstrated a favorable biodistribution profile and increased tumor dose compared with the agonist ^{177}Lu-DOTATATE [56, 89]. A phase I study with ^{177}Lu-JR11 was performed in 20 patients with NETs (two cycles, 3 months apart, 7.4 GBq/cycle). Preliminary data are promising, and additional studies are on-going to determine optimal therapeutic dose/schedule [57].

Since the SSTR-2 affinity of ^{68}Ga-NODAGA-LM3 was tenfold higher than that of ^{68}Ga-DOTA-LM3, the first human studies of PRRT with ^{177}Lu-DOTA-LM3 were performed in 51 patients with metastatic NENs to assess safety, efficacy, and dosimetry (Fig. 21.12). Patients received 2.8–7.1 GBq/cycle. Higher uptake and a longer effective half-life of ^{177}Lu-DOTA-LM3 was found for whole-body, as well as kidneys, spleen, and metastases, resulting in higher mean absorbed organ and tumor doses as compared to the agonist ^{177}Lu-DOTA-TOC. The study concludes that ^{177}Lu-DOTA-LM3 appears to be very promising for PRRT, provides favorable biodistribution and higher tumor radiation doses than SSTR agonists [59].

21.3.3 Therapy with Alpha Particles

Alpha particles have much higher kinetic energy, higher LET, and cause more double strand DNA breaks than beta particles. Furthermore, the short range of alpha particles preserves the surrounding non-tumor tissue [90, 91]. Targeted alpha therapy can be applied to enhance the antitumor-effect and to overcome beta radiation resistance in SSTR-positive NETs after PRRT with ^{90}Y or ^{177}Lu radionuclides. Preliminary studies with [225]Ac-DOTA-TATE in relapsed NETs after beta PRRT revealed 63% objective
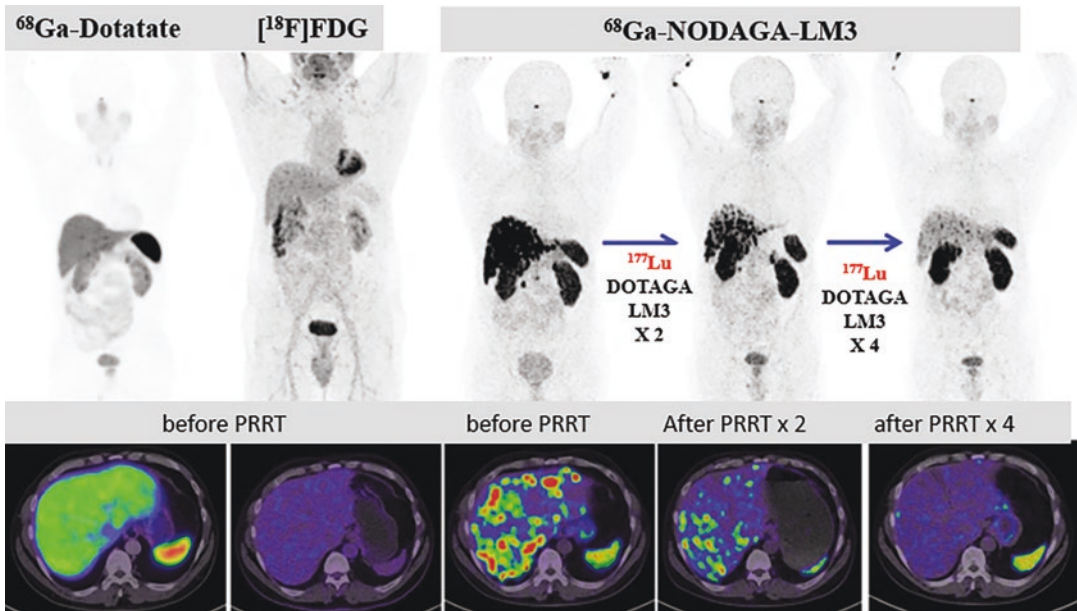
Fig. 21.12 ^{68}Ga-NODAGA-LM3-PET and ^{177}Lu-NODAGA-LM3 therapy in a patient with well-differentiated, non-functioning metastatic pancreatic NEN (Ki-67, 13%). Dotatate-PET showed very weak SSTR-avid small volume lesions in the liver and lymph nodes with extremely low uptake (left), which did not exhibit significant FDG uptake. ^{68}Ga-NODAGA-LM3 PET/CT then showed disseminated bilobar liver metastases, demonstrating very intense SSTR antagonist (LM3) uptake in the liver and lymph node metastases. Patient was treated with four cycles of ^{177}Lu-DOTA-LM3 PRRT (total 25.7 GBq). Restaging ^{68}Ga-NODAGA-LM3 PET/CT scans showed excellent response to PRRT with partial remission of the disease. (From Baum et al. [59])

response and 100% clinical benefit with no toxicity [92]. Alpha therapy was also reported with [255]Ac-DOTATOC [93].

[212]Pb decays ($T\frac{1}{2}$ = 10.6 h) by emitting low energy beta particles to [212]Bi, which decays ($T\frac{1}{2}$ = 60.6 m) by emitting alpha particles. [212]Pb-DOTAMTATE (AlphaMedix™) is in phase I/II clinical studies for the assessment of the safety and efficacy in PRRT-naïve patients with SSTR-positive NETs. In a phase I dose escalation trial, a cohort of ten subjects received at least three cycles of [212]Pb-DOTAMTATE at the highest dose level of 67.6 μCi/kg/cycle. Dramatic improvement in tumor burden and a positive impact on quality of life were seen in all of the PRRT naïve subjects at the highest dose tested.

21.4   Norepinephrine Transporter (NET): Imaging and Therapy Agents

Neuroblastoma and other cancers of sympathetic neuronal precursors express the norepinephrine (NE) transporter (NET), a 12 domain, transmembrane protein which functions to shuttle norepinephrine across the cell membrane. NET has very high affinity and specificity for norepinephrine and its analogs. NET actively transports NE primarily into adrenal chromaffin cells and presynaptic terminals by an ATP-dependent and specific process known as Uptake-1 [94, 95]. Uptake-1 transportation, however, is saturable and dependent upon serum sodium and chloride, temperature, pH, oxygen, and vascularity. Norepinephrine is also brought into cells by passive, nonspecific diffusion (a process known as Uptake-2) that is energy independent, unsaturable, and results in low-level norepinephrine accumulation in most tissues. Cells store norepinephrine within numerous neurosecretory vesicles via the vesicular monoamine transporter (VMAT) [95]. The expression NET in NENPs, specifically neuroblastoma, provides the basis and rationale for the use of radiolabeled NE analogs for targeted imaging and treatment of neuroblastoma.

21.4.1   MIBG Analogs for Imaging

In the 1980s, Dr. Wieland and his colleagues at the University of Michigan developed an analog of NE, known as [131]I-*meta*-iodobenzylguanidine (MIBG), a diagnostic tracer to allow imaging of the adrenal medulla [96, 97]. MIBG was developed by linking the benzyl portion of bretylium with the guanidine group of guanethidine (Fig. 21.13). Among the three isomers of iodobenzylguanidines, the meta isomer (MIBG) has less in vivo deiodination and liver uptake than the other two isomers. MIBG accumulates both in normal sympathetically innervated tissues, such
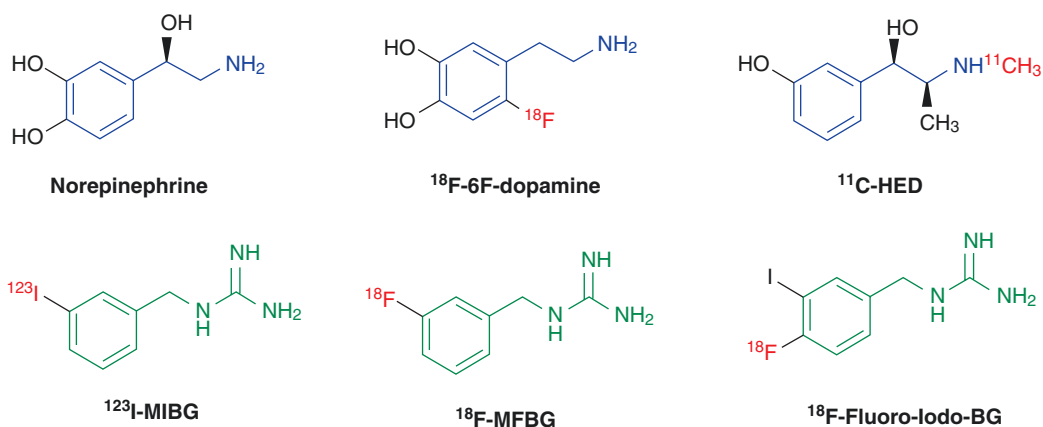
Fig. 21.13 MIBG, FMBG, and FIBG are analogs of norepinephrine and, are transported into the neuroendocrine tumor cell via norepinephrine transporter

as the heart and salivary glands but, also, in tumors that express NET, specifically those of neural crest and neuroendocrine origin. With MIBG the primary uptake in cancer cells is by active transport (Uptake-1), which is approximately 50 times more efficient than passive transport [95, 98]. NE analogs can inhibit Uptake-1 and any decrease in the activity of the Na/K-ATPase leads to reduced uptake, and increased outward transport of NR, and its analogs [95].

The potential use of MIBG to image pheochromocytoma and neuroblastoma was also reported in the early 1980s [99, 100]. In 1984, the first therapy with MIBG was described in patients with pheochromocytoma [101]. In the same period, the first reports appeared on the use of MIBG in patients with neuroblastoma [102] and neuroendocrine carcinomas [103]. In the last four decades, several studies in many countries demonstrated the clinical utility of $^{123/131}$I-MIBG imaging and targeted therapy in patients with neuroblastoma, pheochromocytoma and neuroendocrine tumors [95, 104].

In 1994, [^{131}I]MIBG also known as iobenguane sulfate I-131 intravenous (*low SA (LSA) formulation*), received FDA approval as an imaging agent for the localization of specific sites of pheochromocytomas and neuroblastomas [105]. In 2008, [^{123}I]MIBG or iobenguane I-123 injection was also approved by the FDA as a tumor imaging agent (Adreview; GE Healthcare). The commercial formulations of low specific activity [^{131}I]MIBG are prepared on the basis of radioiodide exchange reaction with unlabeled MIBG as a precursor and contain large mass amounts of unlabeled MIBG, or "cold carrier," molecules, which are not ideal for targeted radionuclide therapy with MIBG because the cold MIBG molecules competitively inhibit the uptake of radiolabeled MIBG molecules by adrenergic, and neuroendocrine cells expressing NET.

21.4.1.1   [^{18}F]MFBG and [^{18}F]FIBG
Although the MIBG is an established substrate for NET, [^{123}I/^{131}I]MIBG-SPECT/or planar imaging has several clinical limitations for diagnostic imaging. To develop derivatives of MIBG for PET studies, two methods have been used to introduce the ^{18}F

atom directly onto the benzylguanidine core structure: first, replace the iodine with fluorine directly to obtain ^{18}F-*meta-* and *para-*fluorobenzylguanidine, [^{18}F]MFBG and [^{18}F]PFBG [106] or add an additional fluorine to the MIBG structure to get ^{18}F-(4-fuoro-3-iodobenzyl)guanidine ([^{18}F]FIBG) [107]. Pre-clinical PET studies demonstrated higher [^{18}F]MFBG tumor uptake and tumor/normal ratios compared to [^{123}I]MIBG [108]. Based on an iodonium salt as a precursor for the electron-rich benzene ring, GMP manufacturing has been optimized for clinical studies. The first clinical study with [^{18}F]MFBG showed excellent in vivo stability and safety, as well as a favorable biodistribution with good targeting of lesions in patients with NETs. MFBG-PET/CT demonstrated high promise for imaging in patients, especially for children with neuroblastoma [109].

Preclinical studies with [^{18}F]FIBG demonstrated excellent tumor detectability and uptake comparable to MIBG. Moreover, [^{131}I]FIBG showed a greater therapeutic effect in malignant PCC than did [^{131}I]-MIBG [110]. These results support the potential usefulness of FIBG as a theranostic agent since both, ^{18}F and ^{131}I can be labeled to the same targeting molecule FIBG.

21.4.1.2   **Norepinephrine Analogs**

6-[^{18}F]Fluorodopamine (FDA)
FDA, a sympathoneural imaging agent developed at the National Institutes of Health (NIH), is an analog of dopamine and a metabolite of FDOPA. In catecholamine-synthesizing cells, FDA is transported actively and avidly by both, the plasma membrane NET and the intracellular vesicular monoamine transporter. It has also been shown that FDA (Fig. 21.13) is a better substrate for the cell membrane NET system when compared with most amines, including NE and MIBG [111]. In 2001, the first clinical results using FDA-PET scanning for the diagnostic localization of PCC were reported [112]. In patients with known disease, FDA-PET scanning localized PCC with high sensitivity. In patients for whom the diagnosis of PCC is considered but, excluded because of negative plasma metanephrine results, FDA-PET scans

were consistently negative. Also, FDA-PET was found to show more promising results when compared with [$^{123/131}$I]MIBG scintigraphy in the diagnostic localization of VHL-related adrenal PCC, with a 100% rate of localization [111]. In a head-to-head comparison between FDA and FDG, FDOPA, and MIBG scintigraphy, nonmetastatic paragangliomas (PGLs) were equally well localized by these techniques. For the detection of metastases seen on CT, however, FDA was superior to both FDOPA and MIBG scanning [113].

[^{11}C]Hydroxyephedrine (HED)

HED is a norepinephrine analog (Fig. 21.13) that binds to the NET and, from a structural point of view, HED is derived from metaraminol, which is biologically stable against MAO due to its ephedrine structure, where the α- and N-methyl groups can prevent/slow down the possible enzymatic oxidation/deamination [114]. HED-PET has shown high diagnostic potential in patients with PCC/PGL and neuroblastoma [115–117]. HED-PET can be used as an accurate tool for the diagnosis/ruling out of PCC and PGL in complex clinical scenarios, in contrast to CT/MRI characterization. In a major study, HED PET/CT was performed in a cohort of 102 patients, where 19 patients were correctly identified as having PCC, six with PGL, and 75 successfully excluded from having either [118]. Sensitivity, specificity, positive and negative predictive values of HED-PET/CT for PCC/PGL diagnosis was 96%, 99%, 96%, and 99%, respectively.

21.4.2 Therapy with MIBG (Azedra®)

In July 2018, the FDA approved a new high SA *(HSA) formulation* of iobenguane I-131 (AZEDRA®, Progenics Pharmaceuticals, Inc.).

The three FDA-approved MIBG formulations are compared in Table 21.8. No-carrier-added (n.c.a.) radioiodinated *HSA* MIBG preparations have been developed on the basis of electrophilic radioiodination reaction and solid-phase technology using dibutylstanyl benzylguanidine precursor linked to polymers [98].

With *LSA* [^{131}I]MIBG preparations, more than 99% of the MIBG molecules are not labeled with ^{131}I atoms, resulting in products with very *LSA* (3.3 mCi/mg; 123.3 MBq/mg). This, in turn, results in the administration of large doses of unlabeled cold MIBG, which compete for NET binding sites and disrupt the norepinephrine-reuptake mechanism. The resulting increase in circulating catecholamines can lead to life-threatening side effects, such as acute hypertensive crisis during or shortly after drug administration [119]. In contrast, *HSA* [^{131}I] MIBG (2500 mCi/mg; 92,500 MBq/mg) is a targeted therapeutic that consists almost entirely of I-131-labeled MIBG molecules [98, 120]. In clinical studies, no patients had drug-related acute hypertensive events during or after the administration of HSA [^{131}I]MIBG [120, 121].

The efficacy of AZEDRA was determined based on open-label, single-arm, multicenter clinical studies in patients with iobenguane scan-positive, unresectable, locally advanced, or metastatic PPGL who are at least 12 years of age and were ineligible for curative therapy. Other eligibility criteria required patients' tumors to have definitive iobenguane avidity; at least one tumor site identified by CT, MRI, or MIBG scan. Following dosimetry, 68 patients received at least one therapeutic dose and 50 patients received two therapeutic doses. After the final 12-month assessment, patients entered into long-term follow-up for up to four additional years. Among 64

Table 21.8 Comparison of FDA-approved MIBG radiopharmaceuticals

Components	[^{123}I]MIBG (Adreview)	[^{131}I]MIBG Sulfate (*LSA*)	[^{131}I]MIBG, (*HSA*) (AZEDRA®)
I-131 activity[a]	74 MBq/mL 2.0 mCi/mL	85.1 MBq/mL 2.3 mCi/mL	555 MBq/mL or 15 mCi/mL
Iobenguane sulfate	0.08 mg/mL	0.69 mg/mL	0.006 mg/mL (Iobenguane)
pH	5.0–6.5	–	5.4–5.5
Specific activity	~25 mCi/mg	~3.33 mCi/mg	~2500 mCi/mg

LSA low specific activity, *HSA* high specific activity
[a]At the time of calibration

patients with evaluable disease, 92% had a partial response or stable disease as the best objective response within 12 months. The median OS was 36.7 months. No patients had drug-related acute hypertensive events during or after the administration of AZEDRA® [121].

AZEDRA is indicated for the treatment of adult and pediatric patients 12 years and older with iobenguane scan positive, unresectable, locally advanced, or metastatic pheochromocytoma or paraganglioma who require systemic anticancer therapy (Fig. 21.14). The recommended dosimetric dose in patients >50 kg is 185–222 MBq (5 or 6 mCi), and in patients <50 kg is 3.7 MBq/kg (0.1 mCi/kg). AZEDRA therapeutic dose is based on body weight and reduced, if necessary, based on the dosimetry data. A total of two therapeutic doses (minimum of 90 days apart) must be administered. Therapeutic dose/cycle in patients weighing >62.5 kg is 18,500 MBq (500 mCi), and for patients weighing <62.5 kg is 296 MBq/kg (8 mCi/kg).

AZEDRA® (iobenguane I 131) injection supplied in dosimetric (30 mCi/2 mL) and therapeutic (337.7 mCi/22.5 mL) presentations at calibration time. Each milliliter of AZEDRA injection, contains:
- 555 MBq/mL (15 mCi/mL) of iobenguane I-131,
- 0.006 mg/mL of iobenguane,
- sodium ascorbate (58 mg/mL), and.
- sodium gentisate (23 mg/mL).

^{131}I-MIBG (Azedra)
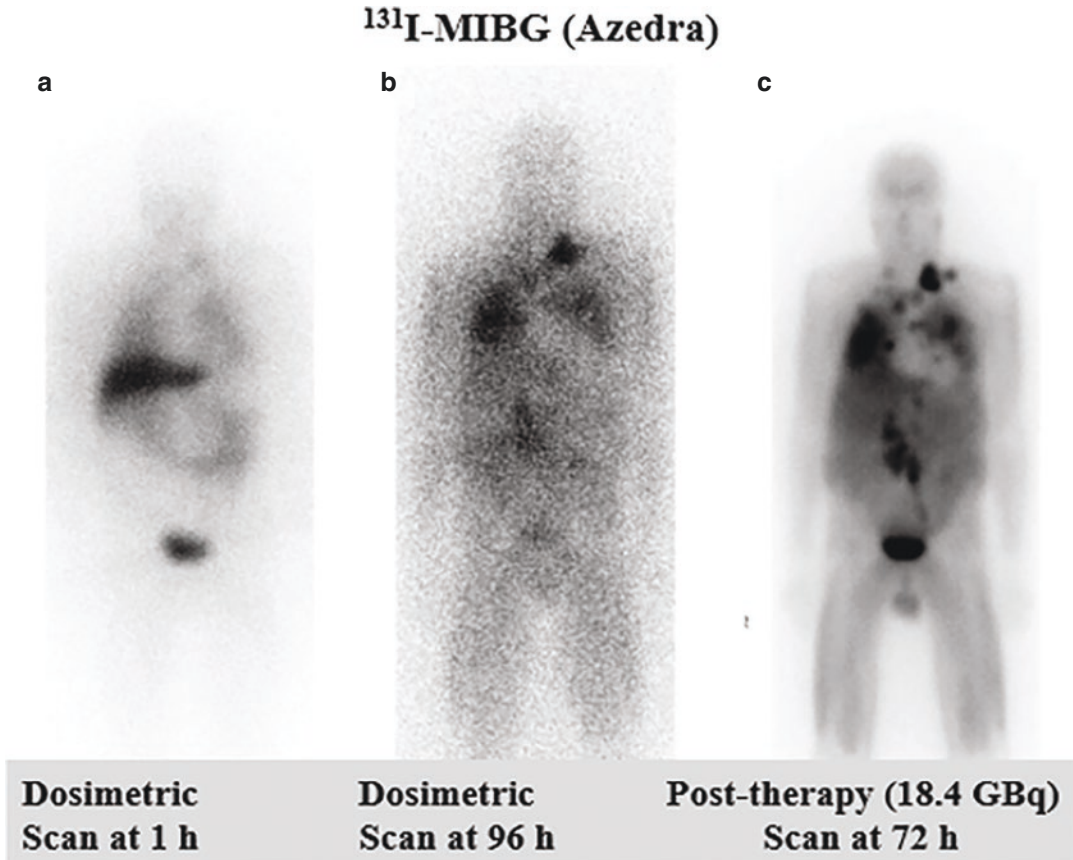
Fig. 21.14 ^{131}I-MIBG diagnostic scan in a patient with metastatic paraganglioma show multiple metastases (**a**) that increase in contrast over time (**b**). Three days after ^{131}I-MIBG therapy (**c**), imaging revealed robust retention in sites of disease, including some not visible on dosimetric images. (Figure modified from Carrasquillo et al. [122])

21.5 Glucose Transporters (GLUT)

The transport of glucose into cells is mainly through *facilitated diffusion*, also called *carrier-mediated diffusion* since the carrier facilitates the transport of glucose into the cell. Six isoforms of glucose transporters (GLUT) have been identified, which differ in kinetic properties, tissue location, etc. It has been shown that the overexpression of GLUT-1, GLUT-3, and GLUT-5 play a major role in the increased transport of glucose by tumor cells [123, 124]. In the cytosol, glucose is phosphorylated by the enzyme *hexokinase* to glucose 6-phosphate, which subsequently is metabolized to carbon dioxide and water. However, with FDG, FDG-6-phosphate does not undergo further metabolism and is trapped within the cell.

As discussed in Sect. 21.1, NENs form a heterogeneous group of tumors classified based on morphology (differentiation) and proliferation index (grade, and K_1 index). They include well-differentiated NETs (G1 and G2) with a low proliferation index, while poorly differentiated NETs show aggressive features, such as a high proliferation index (often of grade 3) or recurrence after resection and, in most cases, require chemotherapy-based treatments [125]. Increased FDG implies high glucose uptake, which is an indication of the glycolytic switch. It provides information about the pathologic differentiation and precise staging of tumors, predicts treatment response, and gives an indication of overall prognosis. A positive FDG PET/CT scan is a prognostic factor for poor outcome [126]. The flip-flop phenomenon of increasing FDG uptake with increasing tumor dedifferentiation and loss of SSTR expression is well described in NEMs, as shown in Fig. 21.15 [127]. FDG-PET imaging has been shown to be correlated with K1-67 and mitotic index, which reflect NENs aggressiveness. The presence of increased glucose in NENs highlights an increased propensity for invasion
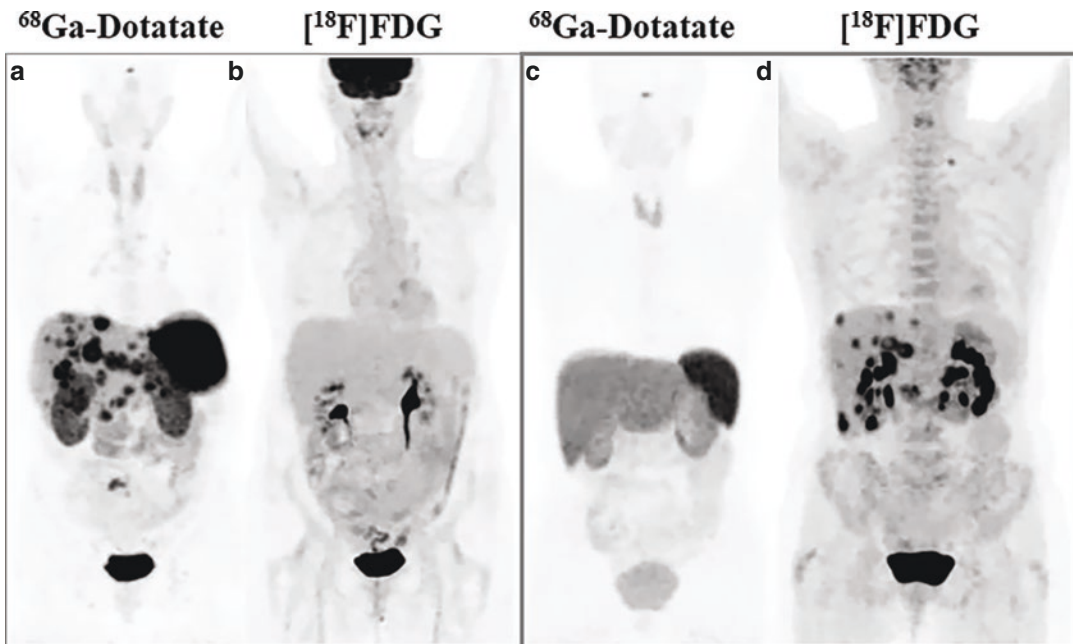
Fig. 21.15 Patterns of ^{68}Ga-Dotatate-PET and [^{18}F]FDG-PET in NETs. In the first patient (**a**, **b**) with grade 1 (Ki-67 < 1%) well differentiated NET, the scans demonstrate SSTR-positive and FDG-negative phenotype, while in the second patient (**c**, **d**) with a poorly differentiated grade 3 NET (Ki-67, 70%), the scans demonstrate SSTR-negative and FDG-positive phenotype. (From Pattison et al. [127])

and metastasis, and FDG-PET accordingly has higher sensitivity, especially in aggressive and high-grade tumors [127].

It was reported that FDG-PET/CT had no clinical impact on G1 NETs, and a moderate impact on G2 NETs. However, in poorly differentiated NETs, FDG-PET/CT plays a significant clinical role in combination with SSTR-PET/CT imaging. Recent reviews conclude that FDG-PET and SSTR-PET should be considered complementary in patients with NETs. They should be both performed in the initial staging and during follow-up, with a specific selection of patients and in a multidisciplinary vision [128, 129].

21.6 Amino Acid Transporters (AATs)

In cancer cells, AATs on the plasma membrane are upregulated since large numbers of amino acids are needed for rapid growth and continuous proliferation. System L is a major transport system providing cells with large neutral amino acids, including branched or aromatic amino acids [130]. The large amino acid transporter, LAT1 has been found in many malignant cells, while LAT2 functions in the epithelium of the kidney proximal tubules and digestive tract. LAT1 can transport large neutral amino acids, such as leucine, isoleucine, valine, phenylalanine, tyrosine, tryptophan, methionine, and histidine. Previous studies have reported that LAT1 can regulate multiple biological processes, including cell growth, invasion, and angiogenesis, that primarily characterize malignant tumors [130].

Carcinoids, together with the endocrine pancreatic tumors (EPTs), for example, gas-trinomas, insulinomas, and glucagonomas, have been regarded as APUDomas characterized by their capacity for amine precursor uptake and decarboxylation. Amine precursors, such as 5-hydroxy-

L-tryptophan (5-HTP) and L-dihydroxy-phenylalanine (L-dopa), are taken up by the tumor cells. Subsequently, through the action of *AADC*, these precursors become decarboxylated and converted to the corresponding amines, serotonin, and dopamine (Fig. 21.1). The resulting amines are then stored within the cell and, in response to stimuli, are released into the circulation through exocytosis. Based on the biochemical mechanism described above, ^{11}C-labeled amine precursors L-dopa and 5-HTP were first developed for PET imaging of NETs [131–133]. [18]F labeled L-DOPA (FDOPA), developed initially for imaging the dopamine metabolism in the brain, is also useful for imaging NETs [134, 135]. Following cellular uptake, decarboxylation of [11C]5-HTP and [18F]FDOPA, by the AADC leads to the formation of [11C]serotonin and [18F]dopamine, which are then stored subsequently in intracellular vesicles through vesicular transporters (VMATs).

Following intravenous administration, both [11C]5-HTP and [18F]FDOPA undergo extensive metabolism [136, 137]. [11C]5-HTP is rapidly decarboxylated to [11C]5-Hydroxytryptamine (serotonin) by the enzyme *aromatic amino acid decarboxylase* (AADC). Subsequently, [11C] serotonin is further metabolized to [11C]5-hydroxy indole acetic acid (HIAA) by the enzyme *monoamine oxidase* (MAO). Both of these C-11 metabolites are excreted into the urine.

[18F]FDOPA is converted to [18F] Fluorodopamine (FDA), which can be oxidized by the enzyme MAO to L-3,4-dihydroxy-6-[18F] fluorophenyl-acetic acid ([18F] FDOPAC), which subsequently is O-methylated by catechol *O*-methyl transferase (COMT) to 6-[18F]fluoro-homovanillic acid ([18F]FHVA). Both, *AAAD* and *COMT* are present in peripheral tissues, such as liver, kidneys, and lungs. Further, both the decarboxylation of the radiolabeled amino acid precursors and the release of radiometabolites into the blood can be reduced with carbidopa, a *decarbox-*

ylase inhibitor. Carbidopa pretreatment improves overall image quality, image interpretation, and may help detection of more lesions [138].

21.6.1 [¹¹C]-5-HTP

[¹¹C]-5-HTP was developed in Uppsala, Sweden, during the 1980s [131]. The multi-step enzyme synthesis of this tracer is difficult and only a few centers worldwide can produce this tracer. Although difficult to produce, this tracer has proven itself clinically useful for the detection of GEP NETs. Based on several clinical studies, it has been documented that [¹¹C]5-HTP-PET is clinically useful for the detection of NETs [139, 140]. The imaging technique is sensitive for imaging small NET-lesions, such as primary tumors, and in most cases, 5-HTP-PET scan image shows significantly more tumor lesions than somatostatin receptor imaging using OctreoScan or CT scans [141]. Pretreatment with carbidopa (200 mg) would significantly improve the image quality by reducing the urinary excretion of the tracer. 5-HTP-PET can also be helpful for evaluating the metabolic effects of treatment, which are not obtained with other imaging modalities. This functional approach to imaging, however, may yield false-negative results in detecting undifferentiated carcinoids. However, 5-HTP-PET can be universally applied in carcinoid and pancreatic islet-cell tumor patients, and also in patients without elevated 5-HIAA excretion in urine, as long as the tumor is not highly proliferating and/or dedifferentiating [141]. It has been recently reported that whole-body MRI, including DWI and dedicated liver-specific contrast agent-enhanced imaging, did not detect all NET lesions detected with whole-body 5-HTP PET/CT [142].

21.6.2 [¹⁸F]FDOPA

Since dopamine deficiency in the nigrostriatal system is a characteristic of Parkinson's disease, FDOPA was first developed in the 1980s to image basal ganglia in the human brain [143]. The ability of NETs to accumulate and decarboxylate L-DOPA is well known and increased activity of l-*DOPA decarboxylase* was found to be a hallmark of NETs [144]. Encouraging results with FDOPA-PET have been reported in NETs, medullary thyroid carcinomas, and phaeochromocytomas. In order to assess lung and liver involvement in patients with NETs, FDOPA-PET is regarded as being more accurate than conventional SSTR-SPECT based on OctreoScan [145, 146] (Fig. 21.16). Since different types of malignant and nonmalignant lesions may show variable expression of SSTRs, it may be helpful to use FDOPA as a tracer for catecholamine metabolic pathways when characterizing medullary thyroid cancer, midgut NENs, pheochromocytomas, neuroblastomas, and paragangliomas. The strength of the FDOPA-PET lies in its ability to detect well-differentiated and serotonin-secreting tumors in NENs [147, 148]. Based on intra-individual comparison of FDOPA and Ga-DOTA-TOC PET/CT studies, it has been suggested that [¹⁸F]FDOPA PET/CT seems not inferior to SSTR imaging for the delineation of metastatic spread of ileal NETs, and FDOPA-PET should be considered as a valid clinical diagnostic option for exhaustive metastatic assessment in patients with ileal NETs [149].

Based on results of a clinical trial (conducted by the Feinstein Institute for Medical Research, Long Island, NY) involving patients ($n = 56$) suspected of having a Parkinsonian syndrome, the FDA approved, in October 2019, Fluorodopa F18 (F-Dopa) for PET to help in
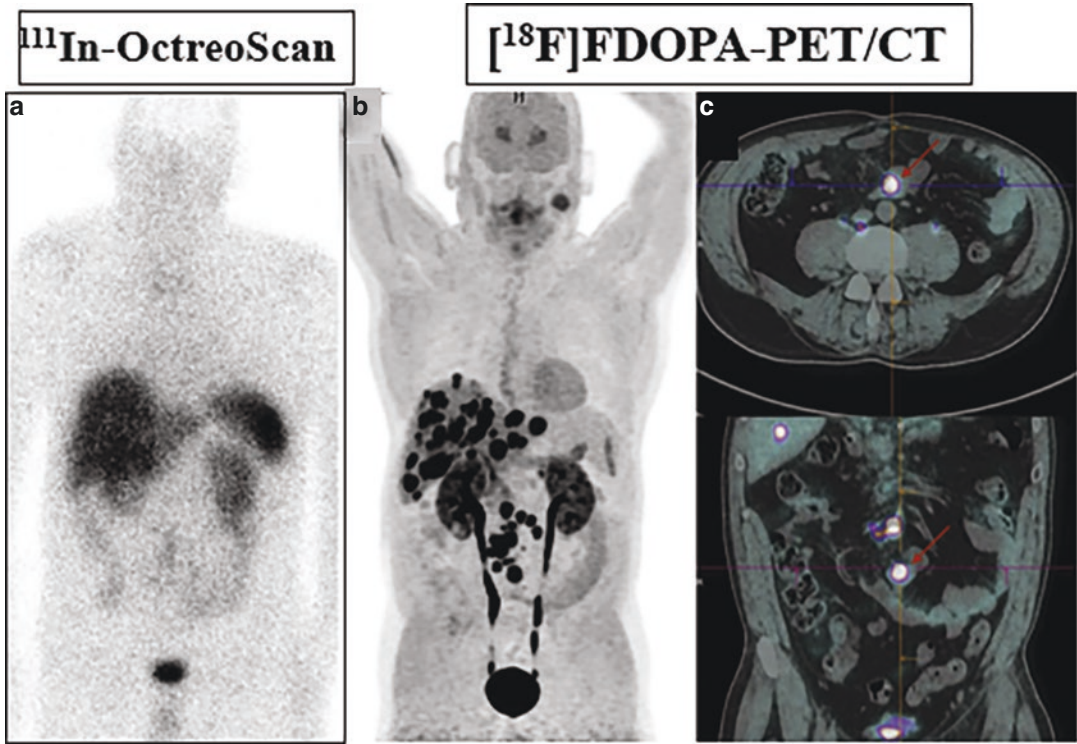
Fig. 21.16 Comparison of ^{111}In-Octreoscan (**a**) with [^{18}F] FDOPA (**b**, **c**) in a patient with carcinoid syndrome of a NET of unknown origin. FDOPA-PET/CT showed lymph nodes and liver metastases as well as a small bowel tumor (red arrow) corresponding to a low-grade well- differentiated grade-1 NET. The moderate left cervical focal ^{18}F-FDOPA uptake corresponds to an enlarged lymph node of the left parotid hilus. (From Lussey-Lepoutre et al. [135])

the diagnosis of PD and other Parkinsonian syndromes [150]. FDOPA-PET, however, was not approved for diagnostic studies in patients with NETs.

21.7   Glucagon-Like Peptide 1 Receptor (GLP-IR)

GLP-1 is a neuropeptide hormone composed of 36 AAs and stimulates insulin secretion from beta cells after nutrient intake through the GLP-1 receptor. The corresponding receptor (GLP-1R) is a member of the G protein-coupled receptor family and was found to be overexpressed in insulinoma, an unusually benign insulin-secreting NET of the pancreas. Gastrinomas, pheochromocytoma, PGL, and MT carcinomas also express GLP-1Rs but, with lower density and/or incidence. The native ligand GLP-1 has a short half-life ($\leq$2 min) in humans owing to rapid degradation by dipeptidyl-peptidase-4 (DPP4). However, GLP-1 stable analogs (containing 39 AAs) have been synthesized for the GLP-1R targeting, from which exendin-4 (agonist) and exendin-3 (antagonist) have been widely studied [151]. Exendin-4 (Fig. 21.17) has been radiolabeled with several radionuclides ([99m]Tc, [111]In, and [68]Ga) to develop radiopharmaceuticals for imaging insulinoma [152, 153]. The first exendin-4–based imaging tracer that was developed is the [Lys[40](Ahx-DTPA-[[111]In]In)NH$_2$]-exendin-4 [154].

Exendin-4

His-Gly-Glu-Gly-Thr-Phe-Thr-Ser-Asp-Leu-Ser-Lys-Gln-Met^{14}-Glu-Glu-Glu-Ala-Val-Arg-Leu-Phe-Ile-Glu-Trp-Leu-Lys-Asn-Gly-Gly-Pro-Ser-Ser-Gly-Ala-Pro-Pro-Pro-Ser-NH$_2$

^{68}Ga-DOTA-exendin-4

[Nle^{14},LyS^{40} (Ahx-DOTA-^{68}Ga)NH$_2$]exendin-4

(^{111}In-DOTA-exendin-4)

[Nle^{14},LyS^{40} (Ahx-DOTA-^{111}In)NH$_2$]exendin-4

Ahx = aminohexanoic acid

Fig. 21.17 Amino acid sequence of Exendin-4 and radiolabeled analogs

In a proof-of-principle study ^{68}Ga-DOTA-exendin-4 PET/CT showed better performance (Fig. 21.18) compared with ^{111}In-DOTA-exendin-4 SPECT/CT [155]. The diagnostic accuracy of ^{68}Ga-DOTA-exendin-4 PET/CT was evaluated in a prospective crossover imaging study in patients ($n =$ with occult insulinomas) [156]. In this prospective study the accuracy of ^{68}Ga-DOTA-exendin-4 PET/CT was 93.9%, which was significantly higher than for ^{111}In-DOTA-exendin SPECT/CT (67.5%) and MRI (67.6%). Another study with ^{68}Ga-NOTA-exendin-4 PET/CT reported an excellent sensitivity of more than 97% [157].
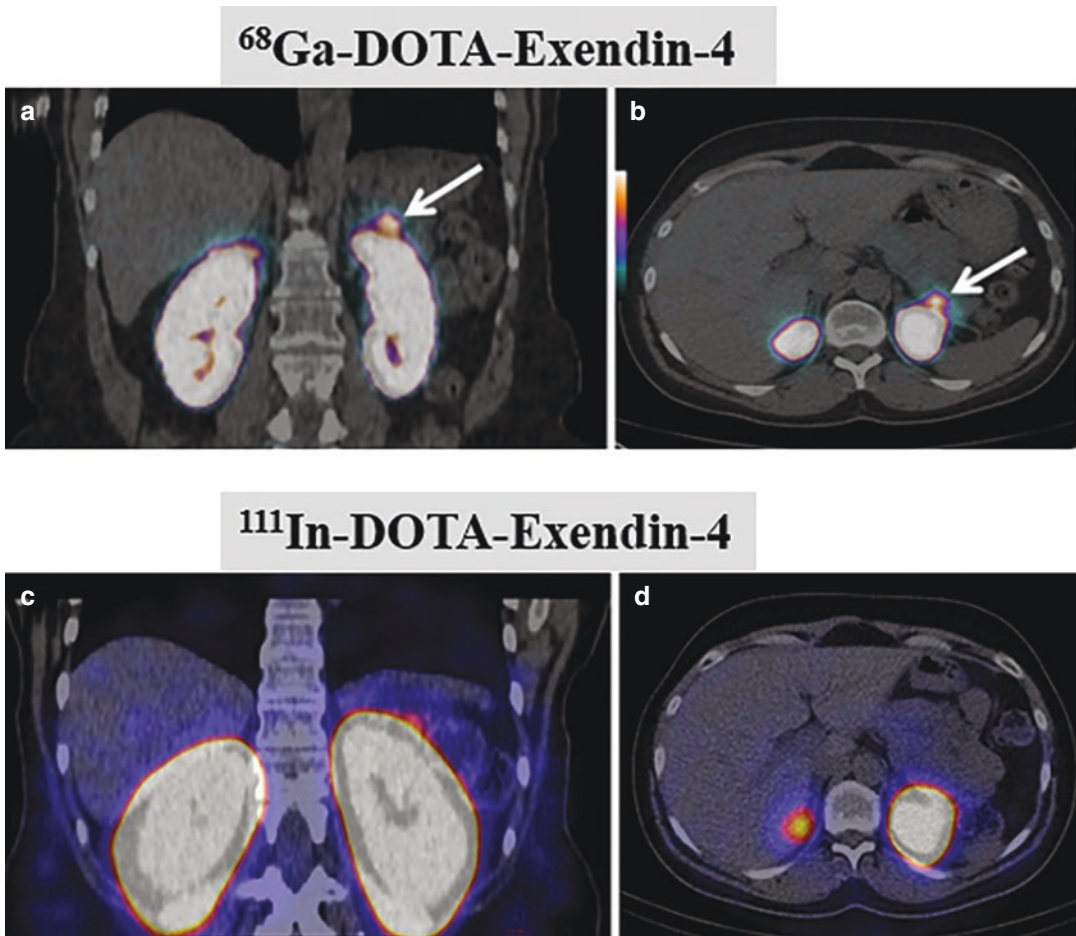
Fig. 21.18 ^{68}Ga-exendin PET (**a**, **b**) vs. ^{111}In-exendin SPECT (**c**, **d**). The arrows in PET/CT images (at 2.5 h) show focal uptake in distal pancreatic tail consistent with surgically removed insulinoma. SPECT/CT images (at 72 h) did not show the insulinoma. (Figure modified from Antwi et al. [155])

21.8 Cholecystokinin-2 Receptor (CCK2R)

Cholecystokinin receptor (CCK2R or CCKBR) is a biological target of high interest since MTC and SCLC have been reported to express the CCK2R with high incidence, and density [14]. The natural ligands for CCK2R are the hormones, cholecystokinin (CCK) and gastrin. The main functions of CCK in the GI tract are stimulation of bicarb secretion, gall bladder emptying, and inhibiting gut motility. Gastrin stimulates secretion of gastric acid (HCl) and aids in gastric motility. While CCK was shown to be present in more biologically active forms, the CCK octapeptide CCK8, and minigastrin (MG) are the two important molecules (Fig. 21.19) evaluated for CCK2 receptors [151]. In the C-terminal sequence, the amino acids, Trp-Met-Asp-Phe-NH$_2$, are known to be essential for receptor binding.

The first-generation MG-based radioligands showed higher affinity for the CCK2 receptor but, their clinical use has been hampered by the unfavorable high retention in the kidneys. After several modifications, several DOTA conjugated MG analogs were developed which have the C-terminal receptor-binding tetrapeptide sequence in common. Two of the most promising new compounds (Fig. 21.19) are DOTA-PP-F11N and DOTA-MGS5, which can be labeled with both ^{68}Ga and ^{177}Lu for theranostic studies [158, 159]. The first-in-humans results show that ^{177}Lu-PP-F11N has promising biodistribution, a low kidney uptake and accumulates specifically in MTC at a dose that is sufficient for a therapeutic approach.

21.9 Neurotensin Receptor 1 (NTR1)

The neurotensin (NT) is a 13 amino acid peptide hormone and neurotransmitter. Neurotensin receptors (NTRs) mediate the effects of the neuropeptide hormone neurotensin (NT), which acts as neuromodulator and peripherally as para- and endocrine factor in the gastrointestinal system. Physiologically, NTRs are mainly expressed in the central nervous as well as intestinal and hepatic system. Of the three known NTR subtypes, NTR1 is the primary mediator of NT signaling because of its sub nanomolar affinity to its natural ligand [160]. NTR1 is highly expressed in ductal pancreatic adenocarcinoma but, not in normal pancreatic tissue or chronic pancreatitis. Furthermore, the incidence of NTR1 expression and receptor density increases with higher malignancy of the pancreatic lesion, and hepatic metas-

Fig. 21.19 Cholecystokinin and minigastrin analogs

CCK-8:   Asp-Tyr-Met-Gly-Trp-Met-Asp-Phe-NH$_2$

Mini gastrin   Leu-(Glu)$_5$-Ala-Tyr-Gly-Trp-Met-Asp-Phe-NH$_2$

^{177}Lu-DOTA-PP-F11N

^{177}Lu-DOTA-(D-Glu)$_6$-Ala-Tyr-Gly-Trp-Nle-Asp-Phe-NH$_2$

^{177}Lu-DOTA-MG11

^{177}Lu-DOTA-D-Glu-Ala-Tyr-Gly-Trp-Met-Asp-Phe-NH$_2$

tases express NTR1 at an intensity like that of the primary tumor. The restricted expression in normal tissues (CNS and intestinal tract) makes NTR1 a promising target for the development of radiopharmaceuticals. A novel NT derivative, di-DOTA-α,ε-Lys-NT, a di-DOTA analog with three unnatural amino acids was synthesized. Preclinical studies demonstrate the potential theranostic potential when radiolabeled with ^{68}Ga and ^{225}Ac radionuclides [161].

SR-142948 is a non-peptide NTR antagonist that binds with high affinity. By attaching linker-chelator moieties to this known antagonist, novel diarylpyrazole-based NTR1 antag-

onists (3BP-227, 3BP228, 3BP-483) were synthesized [162]. Conjugation of DOTA chelator facilitated the development of precursors for complexation with trivalent radiometals. Among these, ^{177}Lu-3BP-227 (also known as ^{177}Lu-IPN01087) with favorable biodistribution has demonstrated anti-tumor activity in preclinical studies [163]. *The first clinical results in patients with confirmed ductal pancreatic adenocarcinoma who were treated wit.* In patients with confirmed ductal pancreatic adenocarcinoma, ^{177}Lu-3BP-227 (5.1–7.5 GBq) treatment showed clinical evidence of the feasibility of TRT (Fig. 21.20) [160].

Fig. 21.20 ^{177}Lu-3BP-227 planar/SPECT/CT scans of two patients with very advanced pancreatic adenocarcinoma with extensive metastases. Patient 1 (**a**, **b**) shows liver lesions and primary tumor. Patient 2 (**c**, **d**) shows large spinal lesion. (Figure modified from Baum et al. [160])

21.10 Chemokine Receptor-4 (CXCR-4)

Chemokines and their receptors were originally identified as mediators of inflammatory diseases and it has been increasingly recognized that they serve as critical communication bridges between tumor cells and stromal cells to create a favorable microenvironment for tumor growth, and metastasis [164]. Chemokine receptors with seven transmembrane domains are found on the surface of certain cells that interact with a type of cytokine called a chemokine. There have been 20 distinct chemokine receptors discovered in humans which are divided into four different families (C, CC, CXC, CX3C) [165]. Chemokine receptor 4 (CXCR4) is a member of G-protein coupled receptors which is involved in several physiological functions, such as cell migration, alteration of gene expression, and cell skeleton rearrangement via interaction with its ligand, CXCL12, also known as stromal cell-derived factor-1α (SDF-1α). The interactions between CXCL12 and CXCR4 comprise a biological axis that affects the growth, angiogenesis, and metastasis of cancer [166]. Overexpression of CXCR4 have been reported in a variety of malignancies. Therefore, CXCR4 is an ideal target for tumor imaging and therapy.

In the last decade, several radiolabeled peptides for targeting CXCR4 receptor have been developed. Among several antagonists evaluated, the cyclic pentapeptide analogue cyclo(D-Tyr[1]-D-[NMe]Orn[2](AMBS-[68Ga]DOTA)-Arg[3]-Nal[4]-Gly[5]) (68Ga-PentixaFor) (Fig. 21.21) showed high affinity and selectivity for human CXCR4, and rapid renal excretion

68Ga-PentixaFor
cyclo(D-Tyr[1]-D-[NMe]Orn[2](AMBS-[68Ga]DOTA)-Arg[3]-Nal[4] -Gly[5])
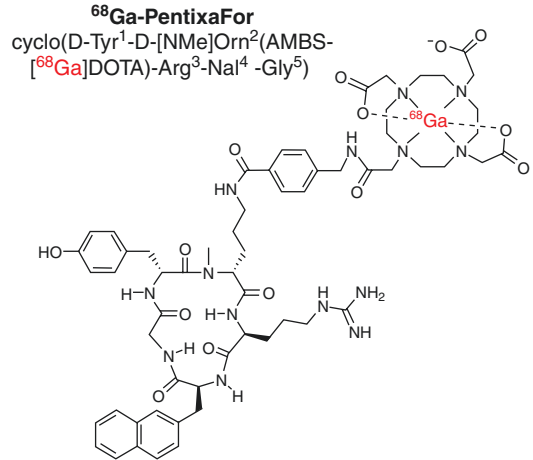
Fig. 21.21 68Ga-Pentixafor is an antagonist for molecular imaging of chemokine receptor (CXCR4)

[167]. In patients with small cell lung cancer (SCLC), 68Ga-Pentixafor was positive in 8/10 patients and revealed more lesions with significantly higher tumor-to-background ratios than SSTR-PET [168]. In a study involving 12 patients with GEP NENs, SSTR-PET was clearly superior compared to FDG-PET and 68Ga-Pentixafor, respectively. While CXCR4 was negative in all grade 1 patients, 50% of grade 2 patients and 80% of grade 3 patients showed 68Ga-Pentixafor-positive lesions [169]. In poorly differentiated neuroendocrine carcinomas, 68Ga-Pentixafor PET/CT was inferior to FDG-PET/CT [170]. Based on a closely related alternative peptide backbone, [177Lu] PentixaTher was also developed for targeted therapy [171]. 68Ga-pentixafor-PET is positive in a patient with SCLC compared to SSTR-PET with 68Ga-DOTATOC (Fig. 21.22) [168].
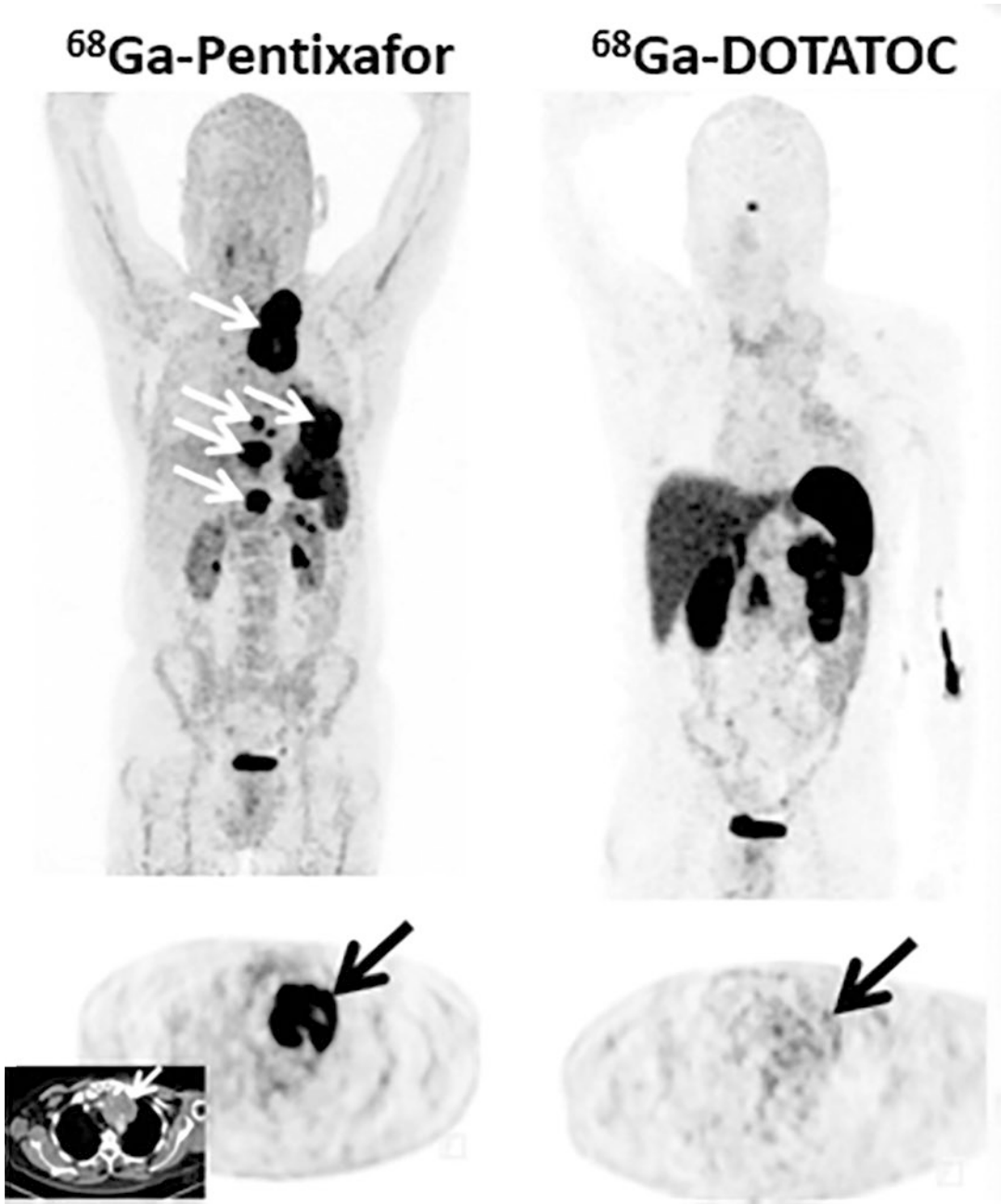
Fig. 21.22 ^{68}Ga-Pentixafor-PET is positive for chemokine receptors in a patient with recurrent small cell lung cancer (SCLC) compared to SSTR imaging. Pentixafor-PET demonstrates intense tracer retention in mediastinal lymph nodes, bone, and pleural lesions [168]

21.11 Tumor Antigens and RIT

Neuroblastoma (NB) is commonly diagnosed in the abdomen but, the incidence of metastatic disease to the CNS and of recurrence is increasing. Among the immune surface targets for NB, disialoganglioside GD2 is one of the most often studied clinically. It belongs to a unique class of carbohydrate antigens expressed at high density on all primary or metastatic tumors. Anti-GD2 IgG mAbs and anti-GD2 radioimmunoconjugates have shown successes in preclinical and clinical studies [172]. Compartmental RIT with antiGD2 [131]I-8H9 mAb has contributed to major survival improvements in patients with CNS relapsed NB [173].

B7-H3 (CD276) is a type I transmembrane glycoprotein molecule homogeneously expressed in both primary and metastatic NBs, and many pediatric, and adult solid cancers, including primary and metastatic brain cancers. The mAb 8H9 (omburtamab) is specific for 4Ig-B7-H3, the long and principal form of B7-H3 [172]. PET imaging with [124]I-omburtamab antibody administered intraventricularly shows specific uptake I the metastatic lesion (Fig. 21.23) and allows for noninvasive estimation of radiation dosimetry [174].
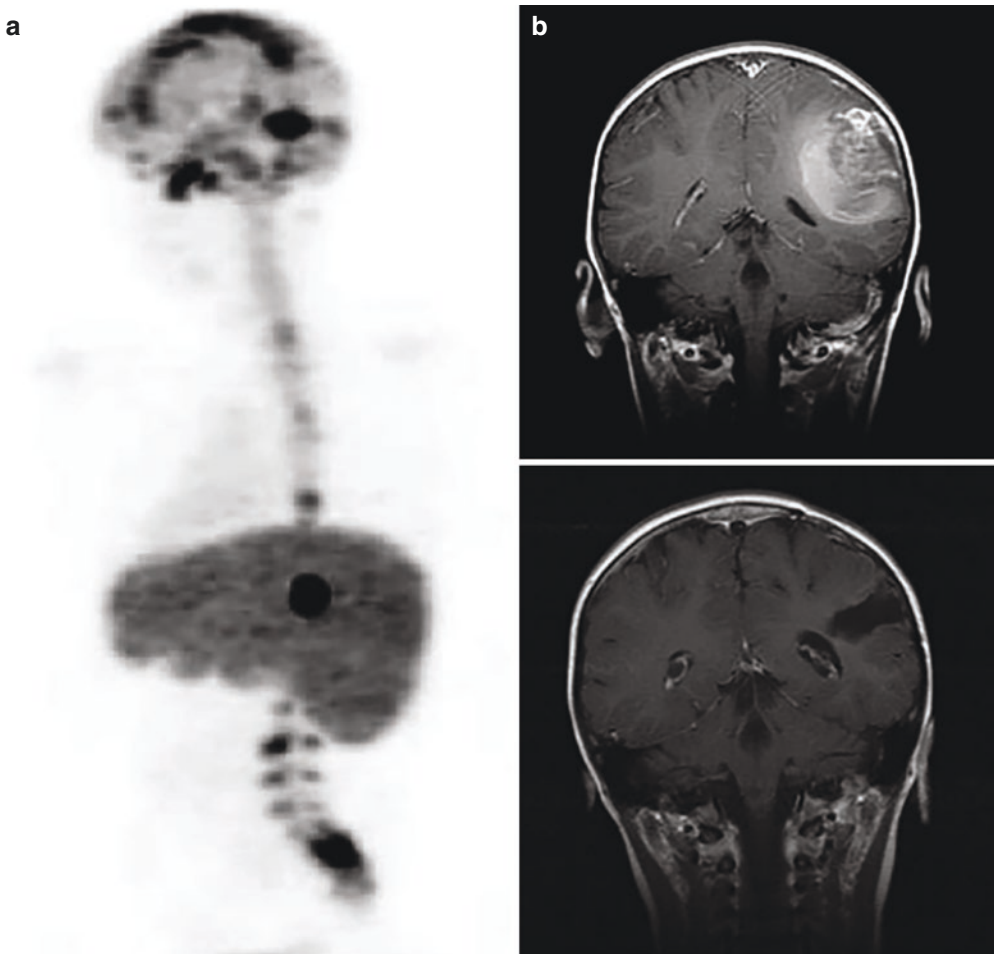
Fig. 21.23 Distribution of ^{131}I-B7-H3 antibody (omburtamab) after injection intraventricularly via Ommaya reservoir (**a**). Coronary MRI (**b**) of patient with recurrent leptomeningeal neuroblastoma before (top) and after (bottom) combined treatment with resection, external radiotherapy, and therapy with omburtamab. (Figure from Kramer et al. [173])

The safety and efficacy of omburtamab were evaluated in the Phase 1 study and the pivotal Phase 2/3 study [175]. In the Phase 1 study, a dose escalation scheme was used to find the maximally tolerated dose of intrathecal ^{131}I omburtamab (10–100 mCi). In 2019, it was reported that evaluable patients ($n = 107$) with CNS/leptomeningeal metastases from neuroblastoma received up to two doses of ^{131}I-omburtamab and study results showed that patients had a median survival of 50.8 months, with the final median survival not yet being reached. A multicenter phase 2/3 trial of the efficacy and safety of RIT using ^{131}I-omburtamab for neuroblastoma CNS/LM is in progress. Patients will receive up to two cycles of the study drug; each treatment cycle consists of 2 mCi dosimetric dose, followed by 50 mCi therapy dose [175].

21.12 Embolization Therapy with 90Y-Microspheres

It has been postulated that NETs with large SSTR-positive target lesions (>3 cm diameter) had significantly shorter PFS than patients with small lesions [176]. Also, most of the patients with large lesions had large liver lesions, and high liver burden is associated with worse prognoses. [177]Lu has a maximum tissue penetration of only 3 mm, which may be one reason for the worsened PFS of patients with large metastases. Such patients may need combined treatment with ^{90}Y-labeled SST analogs or liver-targeted treatment, such as radioembolization with [90]Y- or [166]Ho-labeled microspheres [177–179].

Two commercial preparations of ^{90}Y-labeled microspheres (20–60 μm), Theraspheres® and Sir-Spheres® are available for therapy.

TheraSphere® consists of insoluble glass microspheres where ^{90}Y is an integral constituent of the glass. The mean sphere diameter ranges from 20 to 30 μm. Each milligram contains between 22,000 and 73,000 microspheres. TheraSphere® is supplied in 0.6 mL of sterile, pyrogen-free water contained in a 1.0 mL vial secured within a clear acrylic vial shield.

TheraSphere® is available in six dose sizes, starting from 3 to 20 GBq (81–540 mCi).

SIR-Spheres® consist of biocompatible microspheres containing ^{90}Y with a size between 20 and 60 μm in diameter. SIR-Spheres microspheres are provided in a vial with water for injection. Each vial contains 3 GBq of Y-90 ± 10% (at the time of calibration) in a total of 5 cc water for injection. Each vial contains 40–80 million microspheres. SIR-Spheres® microspheres are a permanent implant.

The embolic resin (SIRspheres) or glass (THERAspheres) microspheres (~30–60 × 10⁶) are deposited by catheterization into the hepatic arterial system to preferentially target the NETs, as normal hepatic parenchyma receives the majority of its blood supply from the portal venous system. The target pathway in radioembolization, however, is not a specific molecular but, rather a mechanical pathway. Following release of the ^{90}Y-labeled microspheres in the hepatic artery via a microcatheter, the microspheres are permanently embedded in the terminal arterioles of the tumor. After the radio-embolization, the particles block the blood vessels and deliver the radiation dose locally. The ^{90}Y-labeled particles do not directly bind to cancer cells. Recent data showed that radioembolization of liver metastases is feasible in NET after initial PRRT. The objective responses after ^{90}Y and [166]Ho radioembolization were 16% and 43%, respectively [180, 181]. In the setting of multiple or innumerable hepatic metastasis and preserved hepatic function, radioembolization can be a viable option. It is important to note that these retrospective data are limited in patient number and need to be validated in larger series and prospective studies.

Since [99mTc]-MAA particles have physical characteristics similar to those of microspheres, [99mTc]-MAA scintigraphy (planar and SPECT) following administration into the hepatic arterial system will provide the necessary data of biodistribution and the extent of pulmonary embolization (if any!) of particles to help estimate the patient specific dosimetry of embolization therapy.

References

1. Bräutigam K, Rodriguez-Calero A, Kim-Fuchs C, et al. Update on histological reporting changes in neuroendocrine neoplasms. Curr Oncol Rep. 2021;23:65.
2. Harris AG, Vinik AI, O'Dorisio TM, O'Dorisio MS. Radioligand theranostics in the management of neuroendocrine tumors. Pancreas. 2020;49(5):599–603.
3. Rickman DS, Beltran H, Demichelis F, Rubin MA. Biology and evolution of poorly differentiated neuroendocrine tumors. Nat Med. 2017;23(6):664–73.
4. Gonzalez RS. Diagnosis and management of gastrointestinal neuroendocrine neoplasms. Surg Pathol. 2020;13:377–97.
5. Refardt J, Hofland J, Kwadwo A, et al. Theranostics in neuroendocrine tumors: an overview of current approaches and future challenges. Rev Endocr Metab Disord. 2020;22:581–94.
6. Taïeb D, Hicks RJ, Hindié E, et al. European association of nuclear medicine practice guideline/society of nuclear medicine and molecular imaging procedure standard 2019 for radionuclide imaging of phaeochromocytoma and paraganglioma. Eur J Nucl Med Mol Imaging. 2019;46:2112–37.
7. Taïeb D, Jha A, Treglia G, Pacak K. Molecular imaging and radionuclide therapy of pheochromocytoma and paraganglioma in the era of genomic characterization of disease subgroups. Endocr Relat Cancer. 2019;26:R627–52.
8. Tevosian SG, Ghayee HK. Pheochromocytomas and paragangliomas. Endocrinol Metab Clin N Am. 2019;48:727–50.
9. Van Arendonk KJ, Chung DH. Neuroblastoma: tumor biology and its implications for staging and treatment. Children. 2019;6:12. https://doi.org/10.3390/children6010012.
10. O'Dorisio TM, Harris AG, O'Dorisio MS. Evolution of neuroendocrine tumor therapy. Surg Oncol Clin N Am. 2020;29:145–63.
11. Ferrari AC, Glasberg J, Riechelmann RP. Carcinoid syndrome: update on the pathophysiology and treatment. Clinics. 2018;73(suppl 1):e490s.
12. Langbein T, Weber WA, Eiber M. Future of theranostics: an outlook on precision oncology in nuclear medicine. J Nucl Med. 2019;60:13S–9S.
13. Park S, Parihar AS, Bodei L, et al. Somatostatin receptor imaging and theranostics: current practice and future prospects. J Nucl Med. 2021;62:1323–9.
14. Werner RA, Weich A, Kircher M. The theranostic promise for neuroendocrine tumors in the late 2010s – where do we stand, where do we go? Theranostics. 2018;8(22):6088–100.
15. Basu S, Parghane RV, Kamaldeep CS. Peptide receptor radionuclide therapy of neuroendocrine tumors. Semin Nucl Med. 2020;50:447–64.
16. Bodei L, Schöder H, Baum RP, et al. Molecular profiling of neuroendocrine tumours to predict response and toxicity to peptide receptor radionuclide therapy. Lancet Oncol. 2020;21:e431–43.
17. Desouky O, Ding N, Zhou G. Targeted and non-targeted effects of ionizing radiation. J Radiat Res Appl Sci. 2015;2015:247–54.
18. Kostelnik TI, Orvig C. Radioactive main group and rare earth metals for imaging and therapy. Chem Rev. 2019;119(2):902–56.
19. Price EW, Orvig C. Matching chelators to radiometals for radiopharmaceuticals. Chem Soc Rev. 2014;43:260.
20. Günther T, Tulipano G, Dournaud P, et al. International Union of Basic and Clinical Pharmacology. CV. Somatostatin receptors: structure, function, ligands, and new nomenclature. Pharmacol Rev. 2018;70:763–835.
21. Brazeau P, Vale W, Burgus R, et al. Hypothalamic polypeptide that inhibits the secretion of immunoreactive pituitary growth hormone. Science. 1973;179:77–9.
22. Bauer W, Briner U, Doepfner W, et al. SMS 201-995: a very potent and selective octapeptide analogue of somatostatin with prolonged action. Life Sci. 1982;31(11):1133–40.
23. La Salvia A, Espinosa-Olarte P, Riesco-Martinez MDC, et al. Targeted cancer therapy: what's new in the field of neuroendocrine neoplasms? Cancer. 2021;13:1701. https://doi.org/10.3390/cancers13071701.
24. Fani M, Nicolas GP, Wild D. Somatostatin receptor antagonists for imaging and therapy. J Nucl Med. 2017;58:61S–6S.
25. Maecke HR, Reubi JC. Somatostatin receptors as targets for nuclear medicine imaging and radionuclide treatment. J Nucl Med. 2011;52:841–4.
26. Hankus J, Tomaszewska R. Neuroendocrine neoplasms and somatostatin receptor subtypes expression. Nucl Med Rev. 2016;19(2):111–7.
27. Popa O, Tabani SM, Pantea S, et al. The new WHO classification of gastrointestinal neuroendocrine tumors and immunohistochemical expression of somatostatin receptor 2 and 5. Exp Ther Med. 2021;22:1179.
28. Reubi JC, Hacki WH, Lamberts SW. Hormone-producing gastrointestinal tumors contain a high density of somatostatin receptors. J Clin Endocrinol Metab. 1987;65:1127–34.
29. Lamberts SW, Bakker WH, Reubi JC, Krenning EP. Somatostatin-receptor imaging in the localization of endocrine tumors. N Engl J Med. 1990;323:1246–9.
30. Ginj M, Zhang H, Waser B, et al. Radiolabeled somatostatin receptor antagonists are preferable to agonists for in vivo peptide receptor targeting of tumors. Proc Natl Acad Sci U S A. 2006;103:16436–41.
31. Bakker WH, Albert R, Bruns C, et al. ^{111}In-DTPA-D-Phe[1]-octreotide, a potential radiopharmaceutical for

imaging of somatostatin receptor-positive tumors: synthesis, radiolabeling and in vitro validation. Life Sci. 1991;49(22):1583–91.

32. Krenning EP, Kwekkeboom DJ, Bakker WH, et al. Somatostatin receptor scintigraphy with [^{111}In-DTPA-D-Phe^1]- and [^{123}I-Tyr^3]-octreotide: the Rotterdam experience with more than 1000 patients. Eur J Nucl Med. 1993;20:716–31.

33. De Jong M, Bakker WH, Krenning EP, et al. Yttrium-90 and indium-111 labelling, receptor binding and biodistribution of [DOTA^0,D-Phe^1,Tyr^3]octreotide, a promising somatostatin analogue for radionuclide therapy. Eur J Nucl Med. 1997;24:368–71.

34. Otte A, Jermann E, Behe M, et al. DOTATOC: a powerful new tool for receptor-mediated radionuclide therapy. Eur J Nucl Med. 1997;24:792–5.

35. Reubi JC, Schär J-C, Waser B, et al. Affinity profiles for human somatostatin receptor subtypes SST1–SST5 of somatostatin radiotracers selected for scintigraphic and radiotherapeutic use. Eur J Nucl Med. 2000;27:273–82.

36. Hofmann M, Maecke H, Börner AR, et al. Biokinetics and imaging with the somatostatin receptor PET radioligand Ga-68 DOTATOC preliminary data. Eur J Nucl Med. 2001;28:1751–7.

37. Graham MM, Gu X, Ginader T, et al. ^{68}Ga-DOTATOC imaging of neuroendocrine tumors: a systematic review and metaanalysis. J Nucl Med. 2017;58:1452–8.

38. Hennrich U, Benešová M. [^{68}Ga]Ga-DOTA-TOC: the first FDA-approved ^{68}Ga-radiopharmaceutical for PET imaging. Pharmaceuticals. 2020;13:38. https://doi.org/10.3390/ph13030038.

39. De Jong M, Breeman WAP, Bakker WH, et al. Comparison of ^{111}In-labeled somatostatin analogues for tumor scintigraphy and radionuclide therapy. Cancer Res. 1998;58:437–41.

40. Kwekkeboom DJ, Bakker WH, Kooji PPM, et al. [^{177}Lu-DOTA^0,Tyr^3]octreotate: comparison with [^{111}In-DTPA^o]octreotide in patients. Eur J Nucl Med. 2001;28:1319–25.

41. Forrer F, Uusijarvi H, Waldherr C, et al. A comparison of ^{111}In-DOTATOC and ^{111}In-DOTATATE: biodistribution and dosimetry in the same patients with metastatic neuroendocrine tumours. Eur J Nucl Med Mol Imaging. 2004;31:1257–62.

42. Poeppel TD, Binse I, Petersenn S, et al. ^{68}Ga-DOTATOC versus ^{68}Ga-DOTATATE PET/CT in functional imaging of neuroendocrine tumors. J Nucl Med. 2011;52:1864–70.

43. Wild D, Schmitt JS, Ginj M, et al. DOTA-NOC, a high-affinity ligand of somatostatin receptor subtypes 2, 3 and 5 for labelling with various radiometals. Eur J Nucl Med Mol Imaging. 2003;30:1338–47.

44. Kabasakal L, Demirci E, Ocak M, et al. Comparison of ^{68}Ga-DOTATATE and ^{68}Ga-DOTANOC PET/CT imaging in the same patient group with neuroendocrine tumours. Eur J Nucl Med Mol Imaging. 2012;39:1271–7.

45. Wild D, Fani M, Behe M, et al. First clinical evidence that imaging with somatostatin receptor antagonists is feasible. J Nucl Med. 2012;52:1412–7.

46. Mohamad H, Ali S, Emmanuel P, et al. The role of ^{68}Ga-DOTA-NOC PET/CT in evaluating neuroendocrine tumors. Nucl Med Commun. 2017;38(2):170–7.

47. Anderson CJ, Dehdashti F, Cutler PD, et al. ^{64}Cu-TETA-octreotide as a PET imaging agent for patients with neuroendocrine tumors. J Nucl Med. 2001;42:213–21.

48. Carlsen EA, Johnbeck CB, Binderup T, et al. ^{64}Cu-DOTATATE PET/CT and prediction of overall and progression-free survival in patients with neuroendocrine neoplasms. J Nucl Med. 2020;61:1491–7.

49. Pfeifer A, Knigge U, Mortensen J, et al. Clinical PET of neuroendocrine tumors using ^{64}Cu-DOTATATE: first-in-humans study. J Nucl Med. 2012;53:1207–15.

50. Johnbeck CB, Knigge U, Loft A, et al. Head-to-head comparison of ^{64}Cu-DOTATATE and ^{68}Ga-DOTATOC PET/CT: a prospective study of 59 patients with neuroendocrine tumors. J Nucl Med. 2017;58:451–7.

51. Delpassand ES, Ranganathan D, Wagh N, et al. ^{64}Cu-DOTATATE PET/CT for imaging patients with known or suspected somatostatin receptor–positive neuroendocrine tumors: results of the first U.S. prospective, reader-masked clinical trial. J Nucl Med. 2020;61:890–6.

52. Eychenne R, Bouvry C, Bourgeois M, et al. Overview of radiolabeled somatostatin analogs for cancer imaging and therapy. Molecules. 2020;25:4012. https://doi.org/10.3390/molecules25174012.

53. Bass RT, Buckwalter BL, Patel BP, et al. Identification and characterization of novel somatostatin antagonists. Mol Pharmacol. 1996;50:709–15.

54. Fani M, Braun F, Waser B, et al. Unexpected sensitivity of sst2 antagonists to N terminal radiometal modifications. J Nucl Med. 2012;53:1481–9.

55. Nicolas GP, Schreier N, Kaul F, et al. Sensitivity comparison of (68)Ga-OPS202 and (68)Ga DOTATOC PET/CT in patients with gastroenteropancreatic neuroendocrine tumors: a prospective phase II imaging study. J Nucl Med. 2018;59:915–21.

56. Wild D, Fani M, Fischer R, et al. Comparison of somatostatin receptor agonist and antagonist for peptide receptor radionuclide therapy: a pilot study. J Nucl Med. 2014;55:1248–52.

57. Reidy-Lagunes D, Pandit-Taskar N, O'Donoghue JA, et al. Phase I trial of well-differentiated neuroendocrine tumors (NETs) with radiolabeled somatostatin antagonist ^{177}Lu-satoreotide tetraxetan. Clin Cancer Res. 2019;25:6939–47.

58. Huo L, Zhu W, Cheng Y. A prospective randomized, double-blind study to evaluate the safety, biodistribution, and dosimetry of ^{68}Ga-NODAGA-LM3 and ^{68}Ga-DOTA-LM3 in patients with well-differentiated neuroendocrine tumors. J Nucl Med. 2021;62:1398–405.

59. Baum RP, Zhang J, Schuchardt C, et al. First-in-human study of novel SSTR antagonist ^{177}Lu-DOTA-LM3 for peptide receptor radionuclide therapy in patients with metastatic neuroendocrine neoplasms: dosimetry, safety and efficacy. J Nucl Med. 2021;62:1571–81.

60. Valkema R, De Jong M, Bakker WH, et al. Phase I study of peptide receptor radionuclide therapy with [In-DTPA]octreotide: the Rotterdam experience. Semin Nucl Med. 2002;32:110–122m.

61. Otte A, Mueller-Brand J, Dellas S, et al. Yttrium-90-labelled somatostatin-analogue for cancer treatment. Lancet. 1998;351:417–8.

62. Waldherr C, Pless M, Maecke HR. The clinical value of [^{90}Y-DOTA]-D-Phe^1-Tyr^3-octreotide (^{90}Y-DOTATOC) in the treatment of neuroendocrine tumours: a clinical phase II study. Ann Oncol. 2001;12:941–5.

63. Imhof A, Brunner P, Marincek N, et al. Response, survival, and long-term toxicity after therapy with the radiolabeled somatostatin analogue [^{90}Y-DOTA]-TOC in metastasized neuroendocrine cancers. J Clin Oncol. 2011;29:2416–23.

64. Bushnell D, O'Dorisio TM, O'Dorisio MS, et al. ^{90}Y-edotreotide for metastatic carcinoid refractory to octreotide. J Clin Oncol. 2010;28:1652–9.

65. Bodei L, Kidd M, Paganelli G, et al. Long-term tolerability of PRRT in 807 patients with neuroendocrine tumours: the value and limitations of clinical factors. Eur J Nucl Med Mol Imaging. 2015;42:5–19.

66. Melis M, Krenning EP, Bernard BF, et al. Localization and mechanism of renal retention of radiolabelled somatostatin analogues. Eur J Nucl Med Mol Imaging. 2005;32:1136–43.

67. Geenen L, Nonnekens J, Konijnenberg M, et al. Overcoming nephrotoxicity in peptide receptor radionuclide therapy using [^{177}Lu]Lu-DOTA-TATE for the treatment of neuroendocrine tumors. Nucl Med Biol. 2021;102–103:1–11.

68. Esser JP, Krenning EP, Teunissen JJM, et al. Comparison of [^{177}Lu-DOTA^0,Tyr^3]octreotate and [^{177}Lu-DOTA^0,Tyr^3]octreotide: which peptide is preferable for PRRT? Eur J Nucl Med Mol Imaging. 2006;33:1346–51.

69. Schuchardt C, Kulkarni HR, Prasad V, et al. The Bad Berka dose protocol: comparative results of dosimetry in peptide receptor radionuclide therapy using ^{177}Lu-DOTATATE, ^{177}Lu-DOTANOC, and ^{177}Lu-DOTATOC. Recent Results Cancer Res. 2013;194:519–36.

70. Uccelli L, Boschi A, Cittanti C, et al. ^{90}Y/^{177}Lu-DOTATOC: from preclinical studies to application in humans. Pharmaceutics. 2021;13:1463.

71. Baum RP, Kluge AW, Kulkarn H, et al. [^{177}Lu-DOTA]^0-D-Phe^1-Tyr^3-octreotide (^{177}Lu-DOTATOC) for peptide receptor radiotherapy in patients with advanced neuroendocrine tumours: a phase-II study. Theranostics. 2016;6:501–10.

72. Erion JL, Bugaj JE, Schmidt MA, et al. High radiotherapeutic efficacy of ^{177}Lu-DOTA-Y3-octreotate in a rat tumor model. [abstract]. J Nucl Med. 1999;40(Suppl):223.

73. Bergsma H, Konijnenberg MW, Kam BL, et al. Subacute haematotoxicity after PRRT with ^{177}Lu-DOTA-octreotate: prognostic factors, incidence, and course. Eur J Nucl Med Mol Imaging. 2016;43:453–63.

74. Bergsma H, Konijnenberg MW, van der Zwan WA, et al. Nephrotoxicity after PRRT with ^{177}Lu-DOTA-octreotate. Eur J Nucl Med Mol Imaging. 2016;43:1802–11.

75. Khan S, Krenning EP, van Essen M, et al. Quality of life in 265 patients with gastroenteropancreatic or bronchial neuroendocrine tumors treated with [^{177}Lu-DOTA^0,Tyr^3]octreotate. J Nucl Med. 2011;52:1361–8.

76. Kwekkeboom DJ, de Herder WW, Kam BL, et al. Treatment with the radiolabeled somatostatin analog [^{177}Lu-DOTA^0,Tyr^3]octreotate: toxicity, efficacy, and survival. J Clin Oncol. 2008;26:2124–30.

77. Levine R, Krenning EP. Clinical history of the theranostic radionuclide approach to neuroendocrine tumors and other types of cancer: historical review based on an interview of Eric P. Krenning by Rachel Levine. J Nucl Med. 2017;58:3S–9S.

78. Strosberg J, El-Haddad G, Wolin E, et al. Phase 3 trial of ^{177}Lu-dotatate for midgut neuroendocrine tumors. N Engl J Med. 2017;376(2):125–35.

79. Hennrich U, Kopka K. Lutathera®: the first FDA- and EMA-approved radiopharmaceutical for peptide receptor radionuclide therapy. Pharmaceuticals. 2019;12:114. https://doi.org/10.3390/ph12030114.

80. Brabander T, Zwan WA, Teunissen JJM, et al. Long-term efficacy, survival, and safety of [^{177}Lu-DOTA^0-Tyr^3]octreotate in patients with gastroentero-pancreatic and bronchial neuroendocrine tumors. Clin Cancer Res. 2017;23(16):4617–24.

81. Hope TA, Abbott A, Colucci K, et al. NANETS/SNMMI procedure standard for somatostatin receptor–based peptide receptor radionuclide therapy with ^{177}Lu-DOTATATE. J Nucl Med. 2019;60:937–43.

82. Jacobson O, Kiesewetter DO, Chen X. Albumin-binding Evans blue derivatives for diagnostic imaging and production of long-acting therapeutics. Bioconjug Chem. 2016;27(10):2239–47.

83. Bandara N, Jacobson O, Mpoy C, et al. Novel structural modification based on Evans blue dye to improve pharmacokinetics of a somatostatin-receptor-based theranostic agent. Bioconjug Chem. 2018;29:2448–54.

84. Tian R, Jacobson O, Niu G, et al. Evans blue attachment enhances somatostatin receptor subtype-2 imaging and radiotherapy. Theranostics. 2018;8(3):735–45.

85. Wang H, Cheng Y, Zhang J, et al. Response to single low-dose ^{177}Lu-DOTA-EB-TATE treatment in patients with advanced neuroendocrine neoplasm: a prospective pilot study. Theranostics. 2018;8(12):3308–16.

86. Liu Q, Zang J, Sui H, et al. Peptide receptor radionuclide therapy of late-stage neuroendocrine tumor patients with multiple cycles of ^{177}Lu-DOTA-EB-TATE. J Nucl Med. 2021;62:386–92.

87. Zhang J, Wang H, Jacobson Weiss O, et al. Safety, pharmacokinetics and dosimetry of a long-acting radiolabeled somatostatin analogue ^{177}Lu-DOTA-EBTATE in patients with advanced metastatic neuroendocrine tumors. J Nucl Med. 2018;59:1699–705.

88. Hänscheid H, Hartrampf PE, Schirbel A, et al. Intraindividual comparison of ^{177}Lu-DOTA-EB-TATE and ^{177}Lu-DOTA-TOC. Eur J Nucl Med Mol Imaging. 2021;48:2566–72.

89. Mansi R, Fani M. Design and development of the theranostic pair ^{177}Lu-OPS201/[68]GaOPS202 for targeting somatostatin receptor expressing tumors. J Labelled Comp Radiopharm. 2019;62:635–45.

90. Navalkissoor S, Grossman A. Targeted alpha particle therapy for neuroendocrine tumours: the next generation of peptide receptor radionuclide therapy. Neuroendocrinology. 2019;108:256–64.

91. Kunikowska J, Krolicki L. Targeted α-emitter therapy of neuroendocrine tumors. Semin Nucl Med. 2019;50:171–6.

92. Ballal S, Yadav MP, Bal C, et al. Broadening horizons with ([225])Ac-DOTATATE targeted alpha therapy for gastroenteropancreatic neuroendocrine tumor patients stable or refractory to ([177]) Lu-DOTATATE PRRT: first clinical experience on the efficacy and safety. Eur J Nucl Med Mol Imaging. 2020;47:934–46.

93. Zhang J, Kulkarni HR, Baum RP. Peptide receptor radionuclide therapy using [225]Ac-DOTATOC achieves partial remission in a patient with progressive neuroendocrine liver metastases after repeated β-emitter peptide receptor radionuclide therapy. Clin Nucl Med. 2020;45:241–3.

94. Bonisch H, Bruss M. The norepinephrine transporter in physiology and disease. Handb Exp Pharmacol. 2006;(175):485–524.

95. Streby KA, Shah N, Ranalli MA, Kunkler A, Cripe TP. Nothing but NET: a review of nor-epinephrine transporter expression and efficacy of ^{131}I-mIBG therapy. Pediatr Blood Cancer. 2015;62:5–11.

96. Wieland DM, Wu J, Brown LE, et al. Radiolabeled adrenergic neuronblocking agents: adrenomedullary imaging with [^{131}I]iodobenzylguanidine. J Nucl Med. 1980;21:349–53.

97. Wieland DM, Brown LE, Tobes MC, et al. Imaging the primate adrenal medulla with [^{123}I] and [^{131}I] meta-iodobenzylguanidine: concise communication. J Nucl Med. 1981;22:358–64.

98. Vallabhajosula S, Nikolopoulou A. Radioiodinated metaiodobenzylguanidine (MIBG): radiochemistry, biology, and pharmacology. Semin Nucl Med. 2011;41(5):324–33.

99. Hattner RS, Huberty JP, Engelstad BL, et al. Localization of m-iodo(^{131}I)benzylguanidine in neuroblastoma. AJR Am J Roentgenol. 1984;143(2):373–4.

100. Sisson JC, Frager MS, Valk TW, et al. Scintigraphic localization of pheochromocytoma. N Engl J Med. 1981;305(1):12–7.

101. Sisson JC, Shapiro B, Beierwaltes WH, et al. Radiopharmaceutical treatment of malignant pheochromocytoma. J Nucl Med. 1984;25:197–206.

102. Treuner J, Klingebiel T, Bruchelt G, et al. Treatment of neuroblastoma with metaiodobenzylguanidine: results and side effects. Med Pediatr Oncol. 1987;15:199–202.

103. Hoefnagel CA, Voûte PA, de Kraker J, Marcuse HR. Radionuclide diagnosis and therapy of neural crest tumors using I-131-meta-iodobenzylguanidine. J Nucl Med. 1987;28:308–14.

104. Pandit-Taskar N, Modak S. Norepinephrine transporter as a target for imaging and therapy. J Nucl Med. 2017;58:39S–53S.

105. Pharmacluence 2008 package insert: I-131 MIBG iobenguane sulfate I-131 injection diagnostic for intravenous use. Billerica: Pharmalucence; 2008.

106. Garg PK, Garg S, Zalutsky MR. Synthesis and preliminary evaluation of Para- and meta-[^{18}F]fuorobenzylguanidine. Nulc Med Biol. 1994;21(1):97–103.

107. Vaidyanathan G, Afeck DJ, Zalutsky MR. Validation of 4-[^{18}F] fuoro-3-iodobenzylguanidine as a positron-emitting analog of MIBG. J Nucl Med. 1995;36:644–50.

108. Zhang H, Huang R, Cheung NK, et al. Imaging the norepinephrine transporter in neuroblastoma: a comparison of [^{18}F]-MFBG and ^{123}I-MIBG. Clin Cancer Res. 2014;20(8):2182–91.

109. Pandit-Taskar N, Zanzonico P, Staton KD, et al. Biodistribution and dosimetry of ^{18}F-meta-fuorobenzylguanidine: a first-in human PET/CT imaging study of patients with neuroendocrine malignancies. J Nucl Med. 2018;59(1):147–53.

110. Yamaguchi A, Hanaoka H, Higuchi T, Tsushima Y. Radiolabeled (4-fuoro-3-iodobenzyl)guanidine improves imaging and targeted radionuclide therapy of norepinephrine transporter expressing tumors. J Nucl Med. 2018;59(5):815–21.

111. Kaji P, Carrasquillo JA, Linehan WM, et al. The role of 6-[^{18}F]fluorodopamine positron emission tomography in the localization of adrenal pheochromocytoma associated with von Hippel-Lindau syndrome. Eur J Endocrinol. 2007;156:483–7.

112. Pacak K, Eisenhofer G, Carrasquillo JA, et al. 6-[^{18}F] Fluorodopamine positron emission tomographic (PET) scanning for diagnostic localization of pheochromocytoma. Hypertension. 2001;38:6–8.

113. Timmers HJLM, Chen CC, Carrasquillo JA. Comparison of ^{18}F-Fluoro-L-DOPA, ^{18}F-fluorodeoxyglucose, and ^{18}F-fluorodopamine PET and ^{123}I-MIBG scintigraphy in the localization of pheochromocytoma and paraganglioma. J Clin Endocrinol Metab. 2009;94:4757–67.

114. Chen X, Kudo T, Lapa C, et al. Recent advances in radiotracers targeting norepinephrine transporter: structural development and radiolabeling improvements. J Neural Transm. 2020;127:851–73.

115. Shulkin BL, Wieland DM, Baro ME, et al. PET hydroxyephedrine imaging of neuroblastoma. J Nucl Med. 1996;37:16–21.

116. Shulkin BL, Wieland DM, Schwaiger M, et al. PET scanning with hydroxyephedrine: an approach to the localization of pheochromocytoma. J Nucl Med. 1992;33:1125–31.

117. Yamamoto S, Hellman P, Wassberg C, et al. ^{11}C-Hydroxyephedrine positron emission tomography imaging of pheochromocytoma: a single Center experience over 11 years. J Clin Endocrinol Metab. 2012;97:2423–32.

118. Vyakaranam AR, Crona J, Norlén O, et al. ^{11}C-hydroxy-ephedrine-PET/CT in the diagnosis of pheochromocytoma and paraganglioma. Cancers (Basel). 2019;11(6):pii:E847.

119. Gonias S, Goldsby R, Matthay KK, et al. Phase II study of high-dose [^{131}I] metaiodobenzylguanidine therapy for patients with metastatic pheochromocytoma and paraganglioma. J Clin Oncol. 2009;27:4162–8.

120. Azedra® (iobenguane I 131) injection for intravenous use [package insert]. New York: Progenics Pharmaceuticals, Inc.; 2018.

121. Pryma DA, Chin BB, Noto RB, et al. Efficacy and safety of high-specific-activity ^{131}I-MIBG therapy in patients with advanced pheochromocytoma or paraganglioma. J Nucl Med. 2019;60:623–30.

122. Carrasquillo JA, Chen CC, Jha A, et al. Systemic radiopharmaceutical therapy of pheochromocytoma and paraganglioma. J Nucl Med. 2021;62:1192–9.

123. Adekola K, Rosen ST, Shanmugama M. Glucose transporters in cancer metabolism. Curr Opin Oncol. 2012;24(6):650–4.

124. Macheda ML, Rogers S, Best JD. Molecular and cellular regulation of glucose transporter (GLUT) proteins in cancer. J Cell Physiol. 2005;202:654–62.

125. Basturk O, Yang Z, Tang LH, et al. The high-grade (WHO G3) pancreatic neuroendocrine tumor category is morphologically and biologically heterogenous and includes both well differentiated and poorly differentiated neoplasms. Am J Surg Pathol. 2015;39:683–90.

126. Bahri H, Laurence L, Edeline J, et al. High prognostic value of ^{18}F-FDG PET for metastatic gastroenteropancreatic neuroendocrine tumors: a long-term evaluation. J Nucl Med. 2014;55(11):1786–90.

127. Pattison DA, Hofman MS. Role of fluorodeoxyglucose PET/computed tomography in targeted radionuclide therapy for endocrine malignancies. PET Clin. 2015;10:461–47.

128. Alevroudis E, Spei M-E, Chatziioannou SN, et al. Clinical utility of ^{18}F-FDG PET in neuroendocrine tumors prior to peptide receptor radionuclide therapy: a systematic review and meta-analysis. Cancer. 2021;13:1813.

129. Evangelista L, Ravelli I, Bignotto A. Ga-68 DOTA-peptides and F-18 FDG PET/CT in patients with

130. Zhao Y, Wang L, Pan J. The role of L-type amino acid transporter 1 in human tumors. Intractable Rare Dis Res. 2015;4(4):165–9.

131. Bjurling P, Watanabe Y, Tokushige M, et al. Syntheses of β-^{11}C-labelled L-tryptophan and 5-hydroxy-L-tryptophan using a multi-enzymatic reaction route. J Chem Soc Perkin. 1989;1(7):1331–4.

132. Sundin A, Eriksson B, Bergstrom M, et al. Demonstration of (11C) 5-hydroxy-l-tryptophan uptake and decarboxylation in carcinoid tumors by specific positioning labeling in positron emission tomography. Nucl Med Biol. 2000;1:33–41.

133. Sundin A, Eriksson B, Bergstrom M, et al. PET in the diagnosis of neuroendocrine tumors. Ann N Y Acad Sci. 2004;1014:246–57.

134. Hoegerle S, Altehoefer C, Ghanem N, et al. Whole-body ^{18}F-DOPA PET for detection of gastrointestinal carcinoid tumors. Radiology. 2001;220:373–80.

135. Lussey-Lepoutre C, Hindié E, Montravers F, et al. The current role of ^{18}F-FDOPA PET for neuroendocrine tumor imaging. Médecine Nucléaire. 2016;40:20–30.

136. Bergstrom M, Lu L, Eriksson B, et al. Modulation of organ uptake of ^{11}C-labelled 5-hydroxytryptophan. Biog Amines. 1996;12:477–85.

137. Luxen A, Guillaume M, Melega WP, et al. Production of 6-[^{18}F]fluoro-L-dopa and its metabolism in vivo– a critical review. Int J Rad Appl Instrum B. 1992;19:149–58.

138. Orlefors H, Sundin A, Lu L, et al. Carbidopa pretreatment improves image interpretation and visualization of carcinoid tumours with ^{11}C-5-hydroxytryptophan positron emission tomography. Eur J Nucl Med Mol Imaging. 2006;33:60–5.

139. Oberg K. Diagnosis and treatment of carcinoid tumors. Expert Rev Anticancer Ther. 2003;3:863–77.

140. Orlefors H. Positron emission tomography in the management of neuroendocrine tumors. PhD Thesis, Uppsala University, Sweden; 2003.

141. Orlefors H, Sundin A, Garske U, et al. Whole-body ^{11}C-5-hydroxytrypto-phan positron emission tomography as a universal imaging technique for neuroendocrine tumors – comparison with somatostatin receptor scintigraphy and computed tomography. J Clin Endocrinol Metab. 2005;90:3392–400.

142. Carlbom L, Caballero-Corba J, Granberg D, et al. Whole-body MRI including diffusion-weighted MRI compared with 5-HTP PET/CT in the detection of neuroendocrine tumors. Ups J Med Sci. 2017;122(1):43–50.

143. Garnett ES, Firnau G, Nahmias C. Dopamine visualized in the basal ganglia of living man. Nature. 1983;305:137–8.

144. Gazdar AF, Helman LJ, Israel MA, et al. Expression of neuroendocrine cell markers L-dopa decarboxylase, chromogranin A, and dense core granules in

human tumors of endocrine and nonendocrine origin. Cancer Res. 1988;48:4078–82.

145. Becherer A, Szabo M, Karanikas G, et al. Imaging of advanced neuroendocrine tumors with ^{18}F-FDOPA PET. J Nucl Med. 2004;45:1161–7.

146. Rufini V, Calcagni ML, Baum RP. Imaging of neuroendocrine tumors. Semin Nucl Med. 2006;36:228–47.

147. Barachini O, Bernt R, Mirzaei S, et al. The impact of 18F-FDOPA-PET/MRI image fusion in detecting liver metastasis in patients with neuroendocrine tumors of the gastrointestinal tract. BMC Med Imaging. 2020;20:22–9.

148. Jager PL, Chirakal R, Marriott CJ, et al. 6-L-18F-fluorodihydroxyphenyl-alanine PET in neuroendocrine tumors: basic aspects and emerging clinical applications. J Nucl Med. 2008;49:573–86.

149. Ouvrard E, Chevalier E, Addeo P, et al. Intraindividual comparison of 18F-FDOPA and 68Ga-DOTATOC PET/CT detection rate for metastatic assessment in patients with ileal neuroendocrine tumours. Clin Endocrinol. 2021;94:66–73.

150. FDOPA-FDA 2019: drug trials snapshots: FLUORODOPA F18 | FDA

151. Mikulova MB, Mikus P. Advances in development of radiometal labeled amino acid-based compounds for cancer imaging and diagnostics. Pharmaceuticals. 2021;14:167–206.

152. Christ E, Antwi K, Fani M, Wild D. Innovative imaging of insulinoma: the end of sampling? A review. Endocr Relat Cancer. 2020;27:R79–92.

153. Jansen T, Van Lith S, Boss M, et al. Exendin-4 analogs in insulinoma theranostics. J Label Compd Radiopharm. 2019;62:656–72.

154. Wild D, Macke H, Christ E, Gloor B, Reubi JC. Glucagon-like peptide 1-receptor scans to localize occult insulinomas. N Engl J Med. 2008;359(7):766–8.

155. Antwi K, Fani M, Nicolas G, et al. Localization of hidden insulinomas with 68Ga-DOTA-Exendin-4 PET/CT: a pilot study. J Nucl Med. 2015;56:1075–8.

156. Antwi K, Fani M, Heye T, et al. Comparison of glucagon-like peptide-1 receptor (GLP-1R) PET/CT, SPECT/CT and 3T MRI for the localization of occult insulinomas: evaluation of diagnostic accuracy in a prospective crossover imaging study. Eur J Nucl Med Mol Imaging. 2018;45:2318–27.

157. Luo Y, Pan Q, Yao S, et al. Glucagon-like peptide-1 receptor PET/CT with 68Ga-NOTA-exendin-4 for detecting localized insulinoma: a prospective cohort study. J Nucl Med. 2016;57:715–20.

158. Rottenburger C, Nicolas GP, McDougall L, et al. Cholecystokinin 2 receptor agonist 177Lu-PP-F11N for radionuclide therapy of medullary thyroid carcinoma: results of the Lumed phase 0a study. J Nucl Med. 2020;61:520–6.

159. Sauter AW, Mansi R, Hassiepen U, et al. Targeting of the cholecystokinin-2 receptor with the minigastrin analog 177Lu-DOTA-PP-F11N: does the use of protease inhibitors further improve in vivo distribution? J Nucl Med. 2019;60:393–9.

160. Baum RP, Singh A, Schuchardt C, et al. 177Lu-3BP-227 for neurotensin receptor 1–targeted therapy of metastatic pancreatic adenocarcinoma: first clinical results. J Nucl Med. 2018;59:809–14.

161. Li D, Minnix M, Allen R, et al. Preclinical PET imaging of NTSR-1-positive tumors with 64Cu- and 68Ga-DOTA-neurotensin analogs and therapy with an 225Ac-DOTA-neurotensin analog. Cancer Biother Radiopharm. 2021;36(8):651.

162. Schulz J, Rohracker M, Stiebler M, et al. Comparative evaluation of the biodistribution profiles of a series of nonpeptidic neurotensin receptor-1 antagonists reveals a promising candidate for theranostic applications. J Nucl Med. 2016;57:1120–3.

163. Schulz J, Rohracker M, Stiebler M, et al. Proof of therapeutic efficacy of a 177Lu-labeled neurotensin receptor 1 antagonist in a colon carcinoma xenograft model. J Nucl Med. 2017;58:936–41.

164. Kircher M, Herhaus P, Schottelius M, et al. CXCR4-directed theranostics in oncology and inflammation. Ann Nucl Med. 2018;32:503–11.

165. Kakinuma T, Hwang ST. Chemokines, chemokine receptors, and cancer metastasis. J Leukoc Biol. 2006;79:639–51.

166. Guo F, Wang Y, Liu J. CXCL12/CXCR4: a symbiotic bridge linking cancer cells and their stromal neighbors in oncogenic communication networks. Oncogene. 2016;35:816–26.

167. Demmer O, Gourni E, Schumacher U, et al. PET imaging of CXCR4 receptors in cancer by a new optimized ligand. Chem Med Chem. 2011;6(10):1789–91.

168. Lapa C, Lückerath K, Rudelius M, et al. [68Ga]Pentixafor-PET/CT for imaging of chemokine receptor 4 expression in small cell lung cancer - initial experience. Oncotarget. 2016;7:9288. https://doi.org/10.18632/oncotarget.7063.

169. Werner RA, Weich A, Higuchi T, et al. Imaging of chemokine receptor 4 expression in neuroendocrine tumors - a triple tracer comparative approach. Theranostics. 2017;7:1489–98.

170. Weich A, Werner RA, Buck AK, et al. CXCR4-directed PET/CT in patients with newly diagnosed neuroendocrine carcinomas. Diagnostics. 2021;11(4):605. https://doi.org/10.3390/diagnostics11040605.

171. Osl T, Schmidt A, Schwaiger M, et al. A new class of PentixaFor- and PentixaTher-based theranostic agents with enhanced CXCR4-targeting efficiency. Theranostics. 2020;10:8264–80.

172. Park JA, Cheung N-KV. Targets and antibody formats for immunotherapy of neuroblastoma. J Clin Oncol. 2020;38:1836–48.

173. Kramer K, Kushner BH, Modak S, et al. Compartmental intrathecal radioimmunotherapy:

results for treatment for metastatic CNS neuroblastoma. J Neuro-Oncol. 2010;97:409–18.

174. Pandit-Taskar N, Zanzonico PB, Kramer K, et al. Biodistribution and dosimetry of intraventricularly administered [124]I-Omburtamab in patients with metastatic leptomeningeal tumors. J Nucl Med. 2019;60:1794–801.

175. Kaplona H, Reichert JM. Antibodies to watch in 2021. MAbs. 2021;13(1):e1860476, 34p

176. Strosberg J, Kunz PL, Hendifar A, et al. Impact of liver tumour burden, alkaline phosphatase elevation, and target lesion size on treatment outcomes with ^{177}Lu-dotatate: an analysis of the NETTER-1 study. Eur J Nucl Med Mol Imaging. 2020;47:2372–82.

177. Bozkurt MF, Salanci BV, Uğur O. Intra-arterial radionuclide therapies for liver tumors. Semin Nucl Med. 2016;46:324–39.

178. Chin R-I, Wu FS, Menda Y, Kim H. Radiopharmaceuticals for neuroendocrine tumors. Semin Radiat Oncol. 2020;31:60–70.

179. Yordanova A, Biersack H-J, Ahmadzadehfar H. Advances in molecular imaging and radionuclide therapy of neuroendocrine tumors. J Clin Med. 2020;9:3679. https://doi.org/10.3390/jcm9113679.

180. Braat AJAT, Ahmadzadehfar H, Kappadath SC, et al. Radioembolization with (90)Y resin microspheres of neuroendocrine liver metastases after initial peptide receptor radionuclide therapy. Cardiovasc Intervent Radiol. 2020;43:246–53.

181. Braat AJAT, Bruijnen RCG, Van Rooij R, et al. Additional holmium-166 radioembolization after lutetium-177-dotatate in patients with neuroendocrine tumor liver metastases (HEPAR PLuS): a single-center, single-arm, open-label, phase 2 study. Lancet Oncol. 2020;21:561–70.

I think it is the general rule that the originator of a new idea is not the most suitable person to develop it, because his fears of something going wrong are really too strong. (Paul Dirac)

22.1 Prostate Cancer

Prostate cancer, adenocarcinoma in the prostate gland, is the second most common cancer, and the fifth leading cause of cancer-related death among men worldwide. The American Cancer Society's estimated that the number of new cases of prostate cancer, in the Unites States, was 248,530 in 2021. and the estimated deaths were 34,130 [1]. For patients diagnosed with primary prostate cancer, 5-year survival rates exceed 90%. However, for patients with advanced prostate cancer with tumor cells present at distant sites outside of the prostate there are severe impacts on quality of life and a low (<30%) 5-year survival rate. Upon metastasis to the bone, the 5-year survival rate falls to a dismal 3–5%, making the disease essentially incurable [2, 3].

The androgen receptor (AR), an intracellular DNA-binding, hormone-responsive transcription factor, is the key molecular driver for male organ development and is the oncological driver of prostate cancer. Following binding of androgens, such as testosterone, in the cytoplasm, the AR is activated and then translocates to the nucleus and stimulates the expression of genes involved in differentiation and proliferation [4, 5].

22.1.1 Screening and Diagnosis

The initial screening in men of 45–50 years is based on the serum prostate-specific antigen (PSA) test and digital rectal examination (DRE). The disease progression (Fig. 22.1) from the primary disease in the prostate gland to the metastatic castrate-resistant prostate cancer (mCRPC) is monitored, generally, based on serum PSA levels. The diagnosis of prostate cancer is based on the microscopic evaluation of prostate tissue obtained via needle biopsy. If the PSA level is ≥3 ng/mL, a biopsy of the prostate, under the guidance of transrectal ultrasonography (TRUS), or MRI, is recommended to obtain 10–12 tissue samples in a grid-like pattern. A pathologist examines these samples and issues a primary *Gleason grade* for the predominant histological pattern and a secondary grade for the highest pattern, both on a scale of 1–5 based on the microscopic architecture, and appearance of the cells. As shown in Table 22.1, based on the sum of Gleason scores, PSA level, and clinical stage, the clinicians stratify the diagnosis of prostate cancer into low, intermediate, and high-risk categories [7].
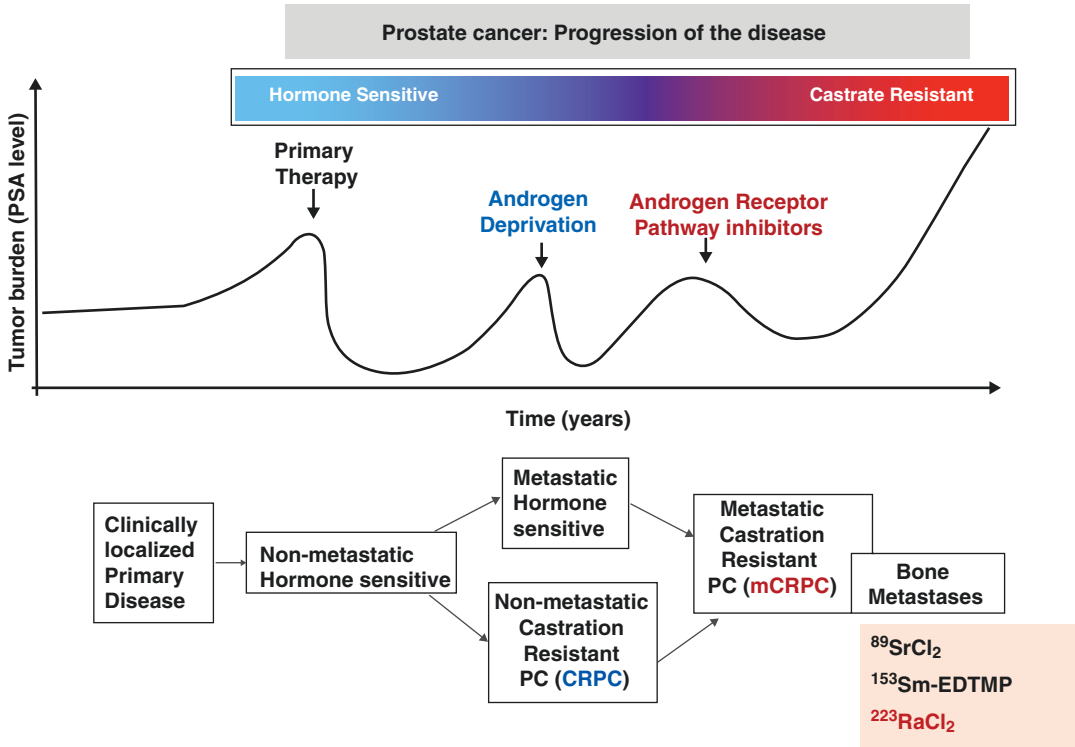
Fig. 22.1 A schematic showing the disease progression in patients with prostate cancer. At this time, the radiopharmaceuticals in clinical use are only for the treatment of bone pain palliation or alpha therapy of bone metastases in mCRPC. (The figure modified from Abou et al. [6])

Table 22.1 Prostate cancer risk stratification

Risk stratification[a]	Clinical status	PSA level (ng/mL)	Gleason score (GS)	Comment
Very low risk	T1c	<10	6 or less	With <3 biopsy cores with cancer
		0.15 ng/mL/g		Presence of 50% or less in each core
Low risk	T1–T2a	<10	6 or less	
Intermediate risk	T2b–T2c	10–20	7	
High risk	T3a	>20	8	
Very high risk	T3b–T4	>20	8–10	Primary Gleason pattern 5, or >4 biopsy cores with GS of 8–10

[a] National Comprehensive Cancer Network Risk Stratification from Litwin and Tan [7]

22.1.2 Treatment for Localized Prostate Cancer

For many low-risk patients with clinically localized primary disease, "watchful waiting" and "active surveillance" to monitor indolent disease by serial biopsy and prostate-specific antigen (PSA) measures is an appropriate option. If treatment is desired for primary prostate cancer, standards of care may involve surgical resection (radical prostatectomy), external beam or proton radiotherapy, and brachytherapy [6, 7]. These

treatment options are often curative. In the case of recurrent disease or advanced-stage prostate cancer, the main therapy is androgen ablation using luteinizing hormone releasing hormone (LHRH) agonists and antagonists and/or anti-AR drugs [8]. Although localized prostate cancer can be treated effectively by these therapies, almost all patients ultimately progress to mCRPC. Most patients with metastatic disease initially respond to androgen deprivation therapy, taxane-based chemotherapies, immunotherapy, or radium-223 but, each of these regimens provides only limited 2–4 months median survival benefit [9, 10]. The median survival for men with mCRPC ranges from 13 to 32 months with a 15%, 5-year survival rate. Most deaths from prostate cancer, however, are attributed to the incurable, late-stage cancer form [3, 11].

22.1.3 Role of Imaging in Prostate Cancer

Currently, imaging plays a key role in many aspects of prostate cancer but, its role is evolving to accurately answer key clinical questions at various phases of the disease in a cost-effective manner. The implementation of theranostic approaches to characterize and personalize patient management is beginning to be realized for prostate cancer patients. These clinical decision-making landmarks include:

- Accurate primary diagnosis,
- Characterization and staging of cancer at the time of initial presentation,
- Determination of local recurrence or distant disease at the time of biochemical recurrence of prostate cancer to select the most appropriate therapy,
- Accurate assessment of therapy response to various treatment regimen under the new practice paradigm,

- Prediction of patient outcomes such as time-to-event endpoints (for example, time to hormone refractoriness in castrate-sensitive disease, time to progression, and overall survival).

The imaging techniques in prostate cancer can be classified into two different methods: structural imaging and molecular imaging. The structural imaging (TRUS, CT, MRI, and multiparametric MRI) provides details about the anatomy and anatomical relations such as size, local invasions, tumor borders, and anatomical distortions. In contrast, molecular imaging shows molecular content, biochemistry, physiological dynamics, and the biology of the tumor tissue, noninvasively. To make medicine "personalized," the clinicians need to know both structural and molecular information about the tumor.

Theranostics refers to a combination of a predictive PET/SPECT biomarker with a therapeutic radiopharmaceutical with similar PK and biodistribution as that of imaging biomarker. The identification of potential biological targets in advanced prostate cancer and androgen-independent disease is critical for improving the detection of metastatic tumor burden based on PET, and SPECT molecular imaging studies, and for the development of targeted radionuclide therapy. Ideally these targets are exclusively expressed in normal prostate tissue but, which are highly expressed in metastatic disease. Several cell surface proteins, glycoproteins, receptors, enzymes, and peptides have been tested as targets for molecular imaging and targeted radionuclide therapy of prostate cancer. In recent years, significant advancements in the diagnostic molecular imaging studies and targeted radionuclide therapeutic modalities for metastatic prostate cancer have revolutionized its management in daily practice [6, 12]. As shown in Fig. 22.2, the role of molecular imaging may play a significant role in primary staging, secondary staging and, finally, in TRT.
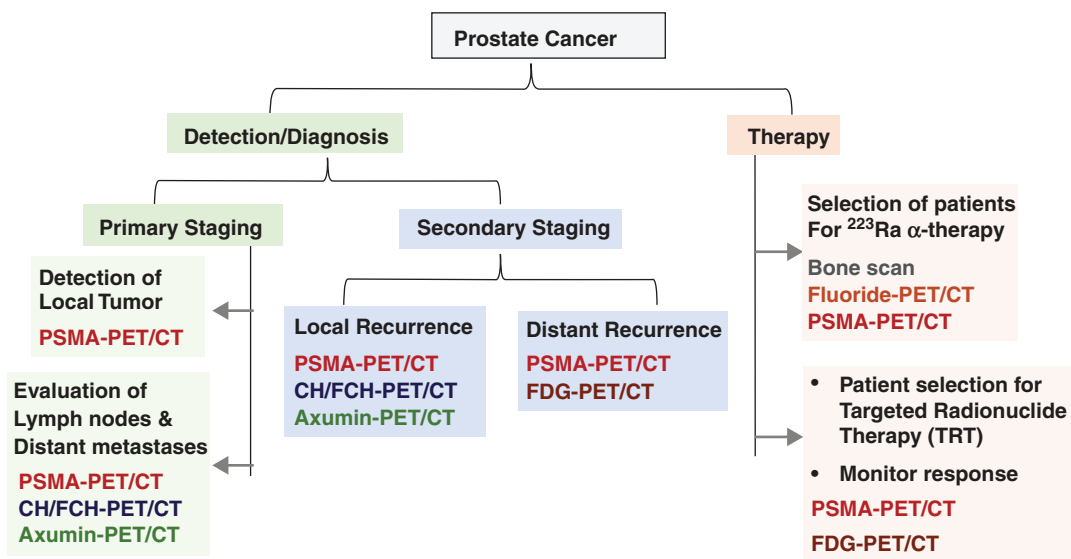
Fig. 22.2 Role of PET radiopharmaceuticals for molecular imaging studies in prostate cancer

22.2   Biological Targets in mCRPC

Prostate cancer starts as localized prostate cancer when it is only found in the prostate gland and surgery, or radiation can be used to treat the cancer. As it advances, there may be a biochemical recurrence, which means a rise in the PSA level. It might also progress to become nonmetastatic castration-resistant prostate cancer (mCRPC), a form of advanced prostate cancer when the localized prostate cancer no longer completely responds to treatments that lower testosterone. Metastatic hormone-sensitive prostate cancer (mHSPC) and metastatic castration-resistant prostate cancer (mCRPC) are advanced forms of the condition that do not respond to initial treatments and have started to spread beyond the prostate, such as the lymph nodes, bones, liver, or lungs. Both mHSPC and mCRPC refer to cases where the cancer cells have started to spread to other parts of the body. While mHSPC still responds to ADT, mCRPC does not respond to ADT and leads to very poor prognosis.

Several important biological targets (such as bone matrix, PSMA, and GRPR) have been identified to develop targeted radiopharmaceuticals for

molecular imaging and therapy of mCRPC. Tables 22.2 and 22.3 show both FDA-approved and investigational radiopharmaceuticals for imaging and therapy [13–18].

22.2.1 Bone Matrix

Bone is composed of three parts: compact bone, trabecular bone, and bone marrow. Compact bone is a hard, solid bone tissue and forms the outside layer of bone. Trabecular bone (or spongy bone) and bone marrow are found in the inside of bone. New bone is constantly being produced while old bone is broken down. The bone marrow is composed of two distinct stem cell lineages, cells of hematopoietic origin and those of mesenchymal origin. Hematopoietic stem cells (HSCs) give rise to all blood cell types, including macrophages that differentiate into osteoclasts, while mesenchymal stem cells (MSCs) are responsible for the generation of stromal cells, osteoblasts, and osteocytes. Bone is made up of an extracellular matrix (ECM) surrounding osteoclasts, osteoblasts, osteocytes, and bone marrow stromal cells (BMSC). The ECM contains both, an organic

Table 22.2 Radiopharmaceuticals for molecular imaging of prostate cancer

	Biochemical target/mechanism	Radiopharmaceutical	FDA
1	Bone matrix	^{99m}Tc-MDP and ^{99m}Tc-HDP	Approved
	Bisphosphonate analogs: Binding to hydroxyapatite	^{111}In-DOTA^{Zol}	IND
		^{68}Ga-DOTA^{Zol}	
	Bone matrix	^{18}F sodium fluoride	Approved 1972
2	Glucose metabolism	[^{18}F]Fluorodeoxyglucose (FDG)	Approved
	FDG is a substrate for the enzyme *hexokinase*		
3	Lipid metabolism	[^{11}C]Choline (CH)	Approved 2012
		[^{18}F]Fluorocholine (FCH)	IND
		[^{18}F]Fluoroethyl choline (FeCH)	IND
4	Amino acid transport	[^{18}F]FACBC ([^{18}F]Fluciclovine or Axumin®)	Approved 2016
5	Androgen receptor (AR)	[^{18}F]FDHT	IND
		[^{18}F]Enzalutamide (FEZT)	IND
6	Anti-PSMA (*prostate specific membrane antigen*) mAbs	^{111}In-capromab pendetide (ProstaScint™)	Approved 10/1996
		^{111}In-DOTA-J591 mAb	IND
		^{177}Lu-DOTA-J591 mAb	IND
		^{89}Zr-DFO-J591 mAb	IND
		^{89}Zr-DF-IAB2M (J591 minibody)	IND
7	PSMA: Small-molecule PSMA inhibitors	^{68}Ga-PSMA-HBED-CC (PSMA-11) (gozetotide)	Approved 12/2020
		[^{18}F]AlF-PSMA-11	IND
		^{18}F-DCFPyL (piflufolastat F 18) Pylarify®	Approved 5/2021
		[^{18}F]DCFBC	IND
		[^{18}F]PSMA-1007	IND
		[^{18}F]-rhPSMA-7.3	IND
		[^{18}F]JK-PSMA-7	IND
		[^{18}F]CTT1057	IND
		^{68}Ga-rhPSMA-7.3	IND
		^{68}Ga-PSMA-I&T	IND
		^{68}Ga-PSMA-617	IND
		^{152}Tb-PSMA-617	IND
		^{99m}Tc-MIP-1404 (Trofolastat™)	IND
		$^{123/124}$I-MIP-1095	IND
8	Gastrin-releasing Peptide receptor (GRPR) antagonists	^{68}Ga- BAY86-7548 (^{68}Ga-RM2)	IND
		^{68}Ga-SB3; ^{111}In/^{177}Lu-SB3	IND
		^{68}Ga-JMV4168; ^{177}Lu-JMV4168	IND
		^{68}Ga-NeoBOMB1; ^{177}Lu-NeoBOMB1	IND
		[^{66}Ga]Ga-NOTA-PEG2-RM26	IND
		^{64}Cu-CB-TE2A-AR06	IND
9	Poly (ADP-ribose) Polymerase-1 (PARP-1)	^{18}F-Olaparib	IND
		^{18}F-WC-DW-F	

component, formed by type I collagen, proteogly-cans and glycoproteins, and inorganic ions (calcium and phosphate) organized in hydroxyapatite crystals, a naturally occurring mineral form of calcium apatite, $Ca_5(PO_4)_3(OH)$.

In prostate cancer, bone is the most common and preferred site for metastatic involvement of cancer. The presence of bone metastases implies poorer prognosis, shortens survival, and is associated with a multitude of complications, including

Table 22.3 Radiopharmaceuticals for the targeted therapy of prostate cancer

	Biochemical target/mechanism	Radiopharmaceutical	Indication	FDA
1	Bone matrix *(binding to hydroxyapatite)*	^{89}Sr dichloride	Bone pain palliation	Approved 1993
		^{153}Sm-EDTMP (lexidronam)		Approved 1997
		^{177}Lu-EDTMP or DOTMP		
		^{166}Ho-DOTMP or EDTMP		
		^{177}Lu-DOTA^{Zol}		
2	Bone matrix *(binding to hydroxyapatite)*	^{223}Ra chloride	Therapy of mCRPC of bone	Approved 2013
3	Anti-PSMA *(prostate-specific membrane antigen)* mAbs	^{90}Y-DOTA-huJ591 mAb	Therapy of mCRPC	IND
		^{177}Lu-DOTA-huJ591 mAb		IND
		^{225}Ac-DOTA-huJ591 mAb		IND
		^{177}Lu-rosopatamab (TLX591, aka ^{177}Lu-J591)		IND
		^{227}Th-PSMA-TTC (BAY 2315497)		IND
4	Small-molecule PSMA inhibitors	^{177}Lu-PSMA-617 Vipivotide tetraxetan (Pluvicto)	Therapy of mCRPC	Approved 03/2022
		^{225}Ac-PSMA-617		IND
		^{149}Tb-PSMA-617		IND
		^{177}Lu-PSMA-I&T		IND
5	GRPR antagonists	^{177}Lu-RM2		IND

severe bone pain, pathological fracture, spinal cord compression, and hypercalcemia [19]. When tumor cells invade the bone, the cancer cells can stimulate osteoblasts and osteoclasts [20]. The activated osteoblasts stimulate bone formation, hardening the bone (osteoblastic or sclerotic process), while the activated osteoclasts then dissolve the bone, weakening the bone (osteolytic phenomenon). Bone metastases in prostate cancers are, typically characterized by an osteoblastic picture due to excess bone deposition [19]. Bisphosphonates inhibit osteoclast-mediated bone resorption by binding to bone mineral, interfering with osteoclast activation. These agents also promote repair by stimulating osteoblast differentiation and bone formation. Also, phosphate and diphosphonate molecules preferentially bind to calcium ions in the hydroxyapatite and accumulate to a high concentration only in bones. As a result, these agents play an increasing role in the treatment of painful bone metastases.

While Fluoride ion (^{18}F$^-$) can replace the hydroxy group (OH$^-$) in the hydroxyapatite, the divalent calcium analogs such as ^{89}Sr and ^{223}Ra substitute calcium or bind to hydroxyapatite in bones and deliver ionizing radiation to areas with increased osteoblastic activity [21]. Radiolabeled bisphosphonate analogs (Fig. 22.3) were developed for imaging studies to detect metastatic foci in bone and for the palliation of bone pain from osseous metastases.

22.2.2 Androgen Receptor (AR)

AR plays pivotal roles in prostate cancer, CRPC. The AR is the key driver of prostate differentiation and PC progression. AR is a steroid receptor transcriptional factor consisting of four main domains, an N-terminal domain (NTD), a DNA-binding domain (DBD), a hinge region (HR), and a ligand-binding domain (LBD) that binds androgens, including testosterone (T) and dihydrotestosterone (DHT) (Fig. 22.4). Upon steroid binding, the AR is activated and undergoes a conformational change and releases heat-shock proteins (hsps). The AR translocates to the nucleus where dimerization, DNA binding and the recruitment of coactivators occur. Target genes are transcribed (mRNA) and translated into proteins [22].

Fig. 22.3 Bisphosphonate analogs as radiopharmaceuticals for imaging and therapy of prostate cancer bone metastases

Fig. 22.4 PET radiopharmaceuticals for molecular imaging studies of androgen receptor (AR) in prostate cancer

Prostate cancer growth and progression is stimulated by androgens (testosterone), acting through the nuclear AR, which is a ligand-dependent transcription activator involved in cellular proliferation and differentiation, and is present in all histologic types of prostate tumors, in recurrent carcinoma, and in tumor metastases [4, 23].

The effectiveness of repressing or inhibiting this central AR signaling by androgen deprivation therapy (ADT) is the cornerstone of advanced PC treatment. In PCa, AR signaling is perturbed by excessive androgen synthesis, AR amplification, mutation, or the formation of AR alternatively spliced variants (AR-V) that lack the LBD. Current therapies for advanced PCa include androgen synthesis inhibitors that suppress T and/or DHT synthesis, and AR inhibitors that prevent ligand binding at the LBD. AR expression can be heterogeneous within and between lesions, and can change over time, either spontaneously or as a result of treatment; whole-body information about the AR status of all lesions in a patient would be advantageous for clinical management. Thus, imaging the expression levels of AR is a viable strategy to measure AR receptor density and the pharmacological response to antiandrogen therapies (such as abiraterone acetate and enzalutamide), designed to block the AR signaling axis [24]. [^{18}F]Fluoro-16β-5α-dihydrotestosterone ([^{18}F]FDHT), a ligand that targets the LBD of AR, was originally developed to assess AR occupancy [25–28]

22.2.3 Prostate-Specific Membrane Antigen (PSMA)

In 1987, PSMA was discovered as a novel antigenic marker in prostate cancer cells and in the serum of prostate cancer patients. PSMA, also known as glutamate carboxypeptidase II (GCPII), *N*-acetyl-L-aspartyl-L-glutamate peptidase I (*NAALADase I*) or *N*-acetyl-aspartyl-glutamate (*NAAG) peptidase*, is an enzyme that is encoded by the *folate hydrolase* (FOLH1) gene in humans [29]. PSMA/GCPII plays separate roles in different tissues, such as the prostate, kidney, small intestine, central and peripheral nervous system and, thus, is recognized by different names. In the last two decades, PSMA has emerged as the pre-eminent prostate cancer target for developing both diagnostic and therapeutic agents in prostate cancer [30].

PSMA/GCPII was first characterized by the murine mAb 7E11, derived from mice immunized with partially purified, cell membrane fractions, isolated from the human prostate adenocarcinoma (LNCap) cell line. Immunohistochemical analysis revealed high expression of PSMA/GCPII in the epithelial cells of the prostate with an intense overexpression in the cancer tissue, compared with normal or hyperplastic prostates. Other tissues have also shown to express lower amounts of PSMA/GCPII, for example epithelia of small bowel and the proximal tubules of the kidney [30].

PSMA is a class II transmembrane glycoprotein with a unique 3-part structure (Fig. 22.5a): a short N-terminal cytoplasmic tail of 1–18 AA, a single membrane-spanning helix of 19–43 AA, and an extracellular part, consisting of 44–750 AA with an approximate molecular weight of 84 kDa [30]. The bulk of PSMA protein is the extracellular part, which is further divided into three domains, namely, the protease (57–116 aa and 352–590 aa), apical (117–351 aa), and the C-terminal domain or the dimerization domain (591–750 aa) and collectively performs the substrate/ligand recognition role [31]. In PCa, the expression of PSMA/GCPII is negatively regulated by androgens [32]. PSMA expression on the cell surface increases with AR inhibition [33, 34] and is favored by other growth factors, such as basic fibroblast growth factor, TGF, and EGF. Also, the degree of PSMA/GCPII expression is positively correlated with the Gleason score and disease progression.

PSMA is considered to be the most well-established target antigen in prostate cancer, since it is highly and specifically expressed at all tumor stages on the surface of prostate tumor cells [35, 36]. PSMA switches from a cytosolically located protein in the normal prostate to a membrane-bound protein in prostatic carcinoma. The majority of PSMA expression appears to be restricted to the prostate and the level of PSMA expression is increased with increased tumor dedifferentiation, and in metastatic and hormone-
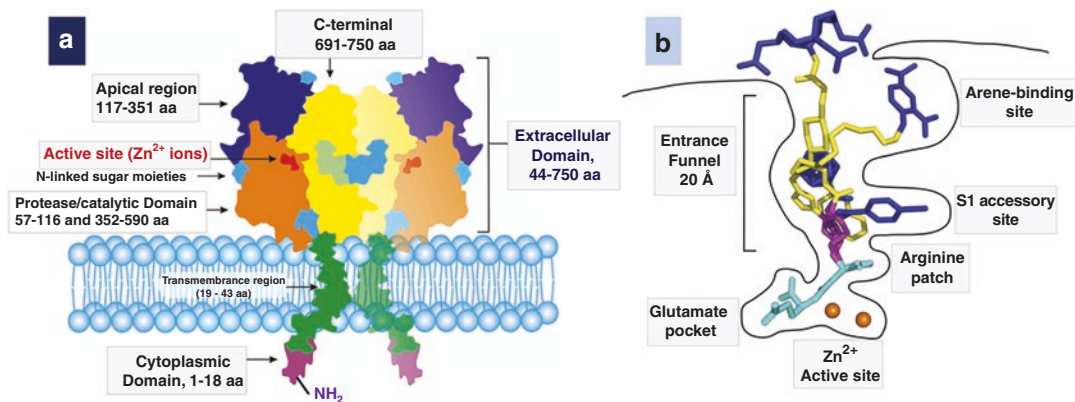
Fig. 22.5 Schematic representation of PSMA/GCPII (also termed as NAAG hydrolase) transmembrane protein homodimer (**a**) (From Evans et al. [30]). Schematic representation of the PSMA-binding cavity (**b**). Glu-Urea-based PSMA inhibitors should contain several structures for interaction between the ligand and the binding site. The pharmacophore (cyan) interacts with the arginine patch, glutamate pocket, and zinc active site, the linker (yellow) is positioned in the entrance funnel, the effector moiety (blue) interacts with the S1 accessory site and arene-binding site on the interior of the funnel. The orange spheres represent Zinc ions. (From Bařinka et al. [31])
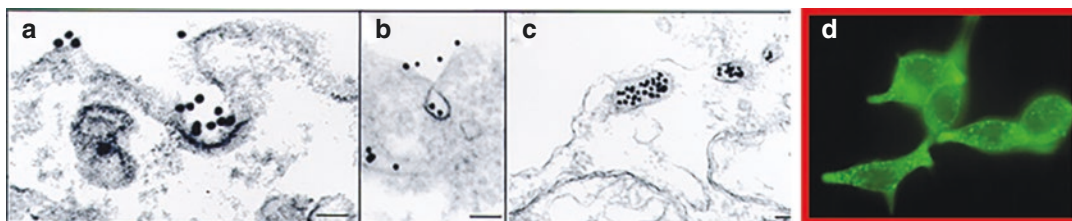
Fig. 22.6 Immunoelectron microscopy of internalized J591 mAb in LNCaP cells. Accumulation of gold particles in clathrin-coated vesicles (**a**, **b**), and in vesicles proximal to the plasma membrane (**c**). Confocal microscopy revealing internalization of J591 mAb (**d**). (From Lu et al. [40])

refractory cancers [37, 38]. In addition to expression by prostate cells, it can be expressed also by nonprostate tissues, such as small intestine, proximal renal tubules, and salivary glands albeit at levels 100- to 1000-fold less than in prostate tissue. PSMA expression was also found on the vascular endothelium of solid tumors and sarcomas but, not in normal tissues [30]. The rapid internalization and recycling of PSMA means that high concentrations of a targeted drug can be accumulated in PSMA/GCPII positive cells.

22.2.3.1   Anti-PSMA mAbs

As mentioned earlier, 7E11-C5.3 was the first anti-PSMA mAb originally developed in 1987. It recognizes and binds to an intracellular or cytoplasmic epitope of PSMA in the fixed cells and necrotic cells but, not the intact viable cells [39]. The 7E11-C5.3 antibody is of the IgG1, kappa subclass (IgG1κ) murine mAb. This antibody was radiolabeled with ^{111}In and was commercialized as an imaging agent, known as ^{111}In-capromab pendetide (ProstaScint™).

In 1997, Dr. Bander and his colleagues at Weill Cornell Medicine in New York reported the development of four mAbs (J591, J415, J533, and E99) to the extracellular domain of PSMA on viable tumor cells and demonstrated antibody induced internalization of PSMA (Fig. 22.6) [40, 41]. Based on preclinical studies, J591 mAb was selected for the development of targeted radiopharmaceuticals for imaging and therapy [42].

22.2.3.2   Small-Molecule PSMA Inhibitors

The two distinct enzyme activities of PSMA include *folate hydrolase* and *NAALADase 1*. The role of these two enzymes is to release the terminal glutamate residue from the substrate molecule. In the intestine, PSMA binds with folate(poly)gamma glutamate in the intestine and releases the glutamate and folic acid. In the brain, PSMA hydrolyzes the *N*-acetyl-L-aspartyl-L--glutamate (NAAG) substrate to yield aspartate and glutamate (Fig. 22.7). *NAALADase* enzyme activity of PSMA has been explored for the development of radiopharmaceuticals. Studies of the *NAALADase* enzyme structure have revealed an ~20 Å deep tunnel leading from the surface of the enzyme to the active site containing two zinc cations (Zn^{++}) participating in the NAAG binding, called the "*NAAG binding pocket*" (Fig. 22.5b), which is also the site for the binding of PSMA inhibitors [31].

PSMA or *NAALADase* enzyme inhibitors mimic the structure of the substrate (NAAG), bind to PSMA, and reduce the ability of the enzyme to convert the substrate NAAG into aspartate and glutamate. The enzyme inhibition capacity (IC_{50}) is expressed in nanomoles (nM). The lower the IC_{50} value is, the greater the ability of the inhibitor to block the enzyme reaction. Since the 1990s, three different families of PSMA inhibitors have been developed [13, 43]. The chemical structures of different families of small-molecule PSMA inhibitors are shown in Fig. 22.8.

(a) Phospho(i)nate and thiol-based analogs: Among these compounds, 2-Phosphonomethyl pentanedioic acid (2-PMPA) has the most potent enzymatic activity (EC_{50} = 0.3 nM).
(b) Glutamate-phosphoramidate analogs.
(c) Glutamate-Ureido-based inhibitors.

The clinical success of radiolabeled PSMA inhibitors is based on a small motif binding to the catalytic NAAG hydrolyzing site in the PSMA molecule. This 2-[3-(1,3-dicarboxypropyl)-ureido] pentanedioic acid (DUPA) motif was first described by Kozikowski et al. [44]. This class of inhibitors contain a urea bond (–NH–CO–NH–) formed by the conjugation of two amino acids (Glu and Asp). In 2002, Pomper et al. at John Hopkins School of Medicine in the USA reported the synthesis of the first radiolabeled PSMA inhibitor, [^{11}C]DCMC, one of the potent urea-based PSMA inhibitors synthesized (IC_{50} = 1.4 nM). Extensive structure–activity studies suggested that the L-glutamic acid must remain intact without structural modification to maintain the desired biological function. Hence, a variety of PSMA inhibitors have been synthesized based on DUPA motif (Fig. 22.8) and modification at the aspartate end by replacing aspartic acid with other amino acids, such as lysine, glutamic acid, or their derivatives [43].
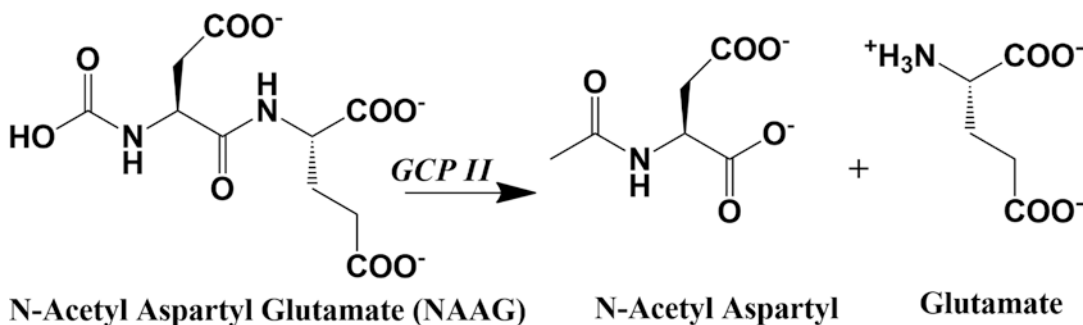
Fig. 22.7   In the brain, PSMA or the *NAALADase* enzyme converts the substrate NAAG into aspartate and glutamate
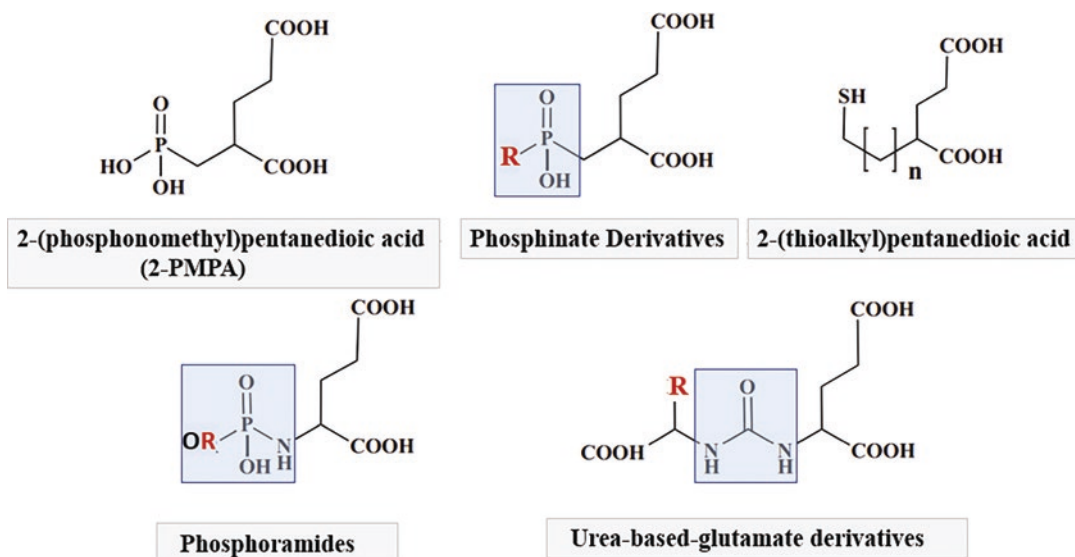
Fig. 22.8 Different families of small-molecule PSMA inhibitors. Phosphinate derivative 2-PMPA is one of the most potent PSMA inhibitors. Most of the radiolabeled PSMA inhibitors for imaging and therapy are urea-based glutamate derivatives containing two amino acids

22.2.4 Gastrin Releasing Peptide Receptor (GRPR)

GRPRs are G-protein coupled receptors of the bombesin family and are overexpressed in a majority of primary prostate cancers and more than 50% of lymph and bone metastases [45]. However, the expression of GRPR in prostate cancer is heterogeneous, dynamic, and dependent on the stage of the disease [46]. Overexpression of GRPR and GPRR-mediated signaling can stimulate the growth of both androgen-dependent, and androgen-independent prostate cancer cells [47], and indirectly promotes angiogenesis, and increase the invasive potential of prostate cancer [48]. Overexpression of the GRPR in prostate cancer but, not in the hyperplastic prostate, provides a promising target for staging and monitoring of prostate cancer.

Gastrin-releasing peptide (GRP), a neuropeptide, is a regulatory molecule that has been implicated in several physiological and pathophysiological processes. Bombesin (BBN) (Fig. 22.9) is a 14-amino acid analog (isolated from the European frog *Bombina bombina)* of the human GRP that binds to the GRPR (also known as BB2R). A variety of radiolabeled GRPR agonists and antagonists have been developed for targeting GRPR-positive tumors, and were evaluated in preclinical and clinical studies [49, 50]. Recent reports have shown that GRPR antagonists show properties superior to GRPR agonists, affording higher tumor uptake and lower accumulation in physiologic GRPR-positive nontarget tissues. GRPR agonists activate the receptor and induce side effects. GRPR antagonists, however, are expected to have no adverse effects [49].

Bombesin: Pyr-Gln-Arg-Leu-Gly-Asn-Gln-Trp-Ala-Val-Gly-His-Leu-Met-NH$_2$

^{68}Ga-RM2: ^{68}Ga-DOTA-4-amino-1-carboxymethylpiperidine-
   (BAY86-7548)   D-Phe-Gln-Trp- Ala-Val-Gly-His-Sta-Leu-NH$_2$

^{68}Ga-RM26: ^{68}Ga-1,4,7-triazacyclononane-N,N9,N\$-triacetic acid-
                        D-Phe-Gln-Trp-Ala-Val-Gly-His-Sta-Leu-NH$_2$

^{68}Ga-SB3: ^{68}Ga-DOTA-*p*-aminomethylaniline-diglycolic acid-
                        D-Phe-Gln-Trp-Ala-Val-Gly-His-Leu-NHEt

Fig. 22.9 Bombesin and radiolabeled analogs for theranostics of gastrin-releasing peptide receptor (GRPR) in prostate cancer

22.3 Radionuclides for Imaging and Therapy

Radionuclides useful for molecular imaging studies based on PET or SPECT decay either by positron (β^+) emission, electron capture (*EC*), or isomeric transition (IT). The radionuclides that are used for therapy decay by emitting either β^- particles or α particles. The decay characteristics of some of the important radionuclides routinely used for imaging and therapy are listed in Table 22.4. Among the radionuclides listed in this table, radioisotopes of fluorine, iodine, and astatine are nonmetals and belong to the halogen (Group-7) family. All other radionuclides are metals differing in valency, oxidation state, and coordination chemistry. The γ-emissions of radionuclides decaying by IT or EC are useful for planar and SPECT imaging studies, while PET is based on the annihilation radiation (511 keV photons) from radionuclides decaying by positron (β^+) emission.

It is also important to recognize that several radionuclides are also available as theranostic pair, ideal for both imaging and therapy. Isotopes of the same element (such as ^{123}I, ^{124}I, and ^{131}I) have similar chemistry, and the in vivo behavior of radiotracers labeled with isotopes of the same element will be identical. This contrasts with non-chemically identical matched pairs of isotopes (such as ^{111}In/^{90}Y and ^{68}Ga/^{177}Lu) which may have different biodistribution and PK. Therefore, ^{111}In or ^{68}Ga labeled diagnostic radiopharmaceuticals can only be regarded as chemical/biological surrogates for ^{90}Y, ^{177}Lu, ^{225}Ac, and other trivalent metal-labeled radiopharmaceuticals.

22.3.1 Beta vs. Alpha Dosimetry

Although numerous radionuclides have potential applications in radionuclide therapy, only a very few radionuclides possess favorable nuclear, physical, chemical, and biological characteristics which would identify them as practical for clinical use. The ideal radionuclides for developing TRT are those with an abundance of nonpenetrating radiations, such as charged particles (α^{2+}, β^-, *and Auger electrons*) and lack of penetrating radiations (γ or X-rays). While penetrating radiation is not essential for TRT, a small amount or abundance with an appropriate energy (100–400 keV) may be useful for imaging studies to demonstrate tumor localization or altered biodistribution. Most of the radionuclides in routine clinical use are β^- emitters (^{131}I, ^{90}Y, ^{177}Lu, ^{89}Sr, and ^{153}Sm) with a wide range of half-lives ranging from 1.95 to 59.5 days (Table 22.4). Depending on the kinetic energy, the average range of electrons in tissue can be between 0.1 and 5.0 mm. As a result, beta particles can pass through several cells (10–1000), a useful prop-

Table 22.4 The most common radionuclides used for imaging and therapy in prostate cancer

Radionuclide	$T\frac{1}{2}$	Decay mode Mode	%	E_{max} (MeV)	Mean range (mm)	γ-Energy (keV)	Produced by
^{99m}Tc	6.0 hours	IT	98			140	^{99}Mo generator
^{111}In	2.805 days	EC	100			171 and 245	Cyclotron
^{18}F	110 min	β^+	97	0.634	0.6		Cyclotron
^{68}Ga	68 min	β^+	88.9	1.889	3.50		^{68}Ge generator, Cyclotron
^{64}Cu	12.7 hours	β^+	17.9	0.653	0.7		Cyclotron
^{86}Y	14.7 hours	β^+	31.9	1.221	3.6		Cyclotron
^{89}Zr	3.27 days	β^+	22.8	0.902	1.1	908	Cyclotron
^{90}Y	2.67 days	β^-	100	2.28	2.50		^{90}Sr generator
^{177}Lu	6.7 days	β^-	79	0.497	0.67	113 and 208.4	Reactor
^{131}I	8.025 days	β^-	100	0.606	0.91	364.5	Fission or reactor
^{90}Sr	50.53 days	β^-	100	1.496	2.5		Fission
^{153}Sm	1.938 days	β^-	100	0.811	1.20	70 and 103	Reactor
^{166}Ho	1.12 days	β^-	100	1.85	3.2	80.6	Reactor
^{212}Pb	10.6 hours	β^-	100	0.101			^{228}Th/^{224}Ra generator
^{211}At	7.2 hours	α	41.8	5.867	0.06	77–92 X-rays	Cyclotron
^{213}Bi	45.6 min	α	100	5.9, 8.4	0.08	440	^{225}Ac generator
^{223}Ra	11.435 days	α	100	5.78	0.06	690	^{227}Th generator
^{225}Ac	10 days	α	100	5.80	0.06	218 and 440	^{229}Th generator, accelerator
^{227}Th	18.7 days	α	100	5.90	0.06	236	^{227}Ac generator

erty that has been termed "crossfire effect," which ensures sufficient dose delivery to each cell in a large tissue mass. Beta particles may also cause repairable DNA lesions by inducing single-stranded DNA breaks (SSDB). The biological effect, however, may be sublethal. It is important to match the range of the radionuclide with the anticipated size of the tumor target. Small tumors are more effectively treated by a short-range β^- emitter, while a higher cure rate could be obtained in larger tumors with a long-range β^- emitter [51].

Alpha (α) particles are naked helium (^{4}He)$^{2+}$ nuclei with two positive charges and consist of two protons and two neutrons, and are 7300 times heavier than electrons. Alpha particles are monoenergetic and have much higher kinetic energy (5–9 MeV) compared to beta particles.

The range (<100μm) of α particles in tissue is equivalent to only a few cell diameters and this short range is ideally suited for the treatment of small volume cancer tissue. Compared to β-particle emitters, α-particle emitters offer several important advantages for TRT. Alpha particles have higher LET in biological tissue. For example, ^{211}At has a mean LET of 97 keV/μm, compared to the LET (0.22 keV/μm) of high energy (2.2 MeV) beta particle of ^{90}Y. As a result of higher LET values, the probability of creating cytotoxic double-stranded breaks (DSBs) of DNA is much higher with α particles and the relative biological effect (RBE) is also significantly higher (3–5 times) compared to that of beta emitters [52]. In addition, cytotoxicity of alpha particles is nearly independent of dose rate and oxygenation status of the cells [53].

22.3.2 Radiolabeling Methods

The labeling of peptides and proteins with radionuclides can be performed by direct labeling, with the addition of prosthetic groups. Direct labeling is the method used to label peptides without using intermediates, such as BFCs. The direct labeling technique is, generally, used mostly for radioiodination and in some cases labeling with Tc-99m. Prosthetic groups are small molecules able to bind with radionuclides in one site of the structure and, simultaneously, with a peptide at a second site. Prosthetic groups are bifunctional agents that consist of a suitable site for radioiodination or fluorination and functional groups to allow covalent attachment of the peptide. Radiometals specifi-

cally require bifunctional chelating agents (BFC or BFCA) to obtain the best conjugation of radiometal with peptides. The bifunctional nature of the chelators means that they can coordinate (form a complex) a metal ion and can also be attached to the peptide. The most common acyclic and cyclic chelators used for radiometal labeling are shown in Figs. 22.10 and 22.11. The choice of a chelator depends on the valency and coordination requirements of the radiometal. For all trivalent metals (such as ^{111}In, ^{177}Lu, and ^{225}Ac), the macrocyclic chelator DOTA is, generally, used. One of the important requirements is the kinetic stability of the radiometal-chelate complex in vivo. The chemistry of radiolabeling methods is discussed in greater detail in Chaps. 9, 17, and 20.
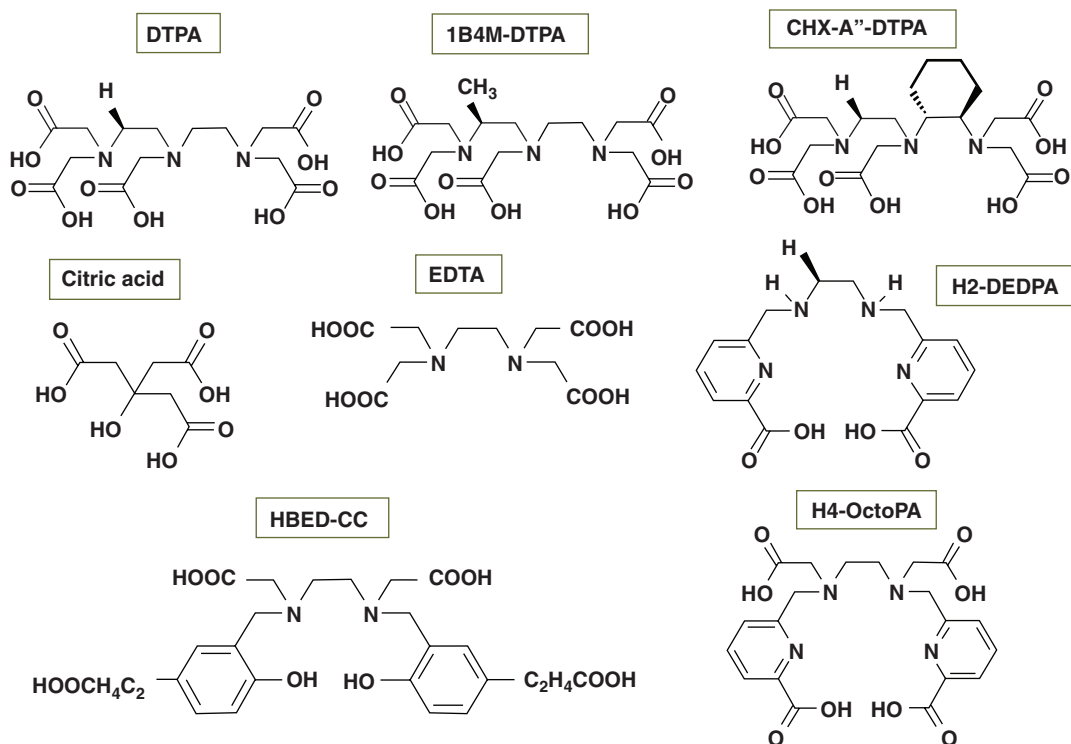
Fig. 22.10 Acyclic chelators used in the development of metal-based radiopharmaceuticals for imaging and therapy
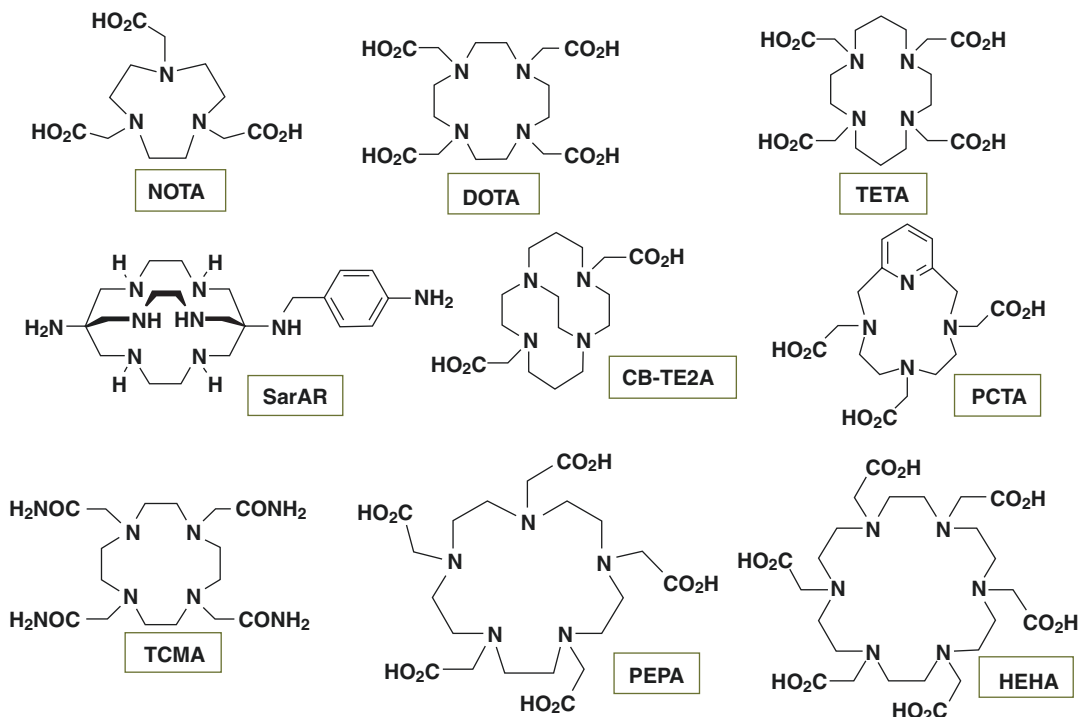
Fig. 22.11 Macrocyclic chelators used in the development of metal-based radiopharmaceuticals for imaging and therapy

22.4 Radiopharmaceuticals for SPECT and PET

The complex and heterogeneous biology of prostate cancer poses major challenges and opportunities for the development of radiopharmaceuticals for single photon emission computed tomography (SPECT) and positron emission tomography (PET). Molecular imaging based on SPECT/CT, PET/CT, and PET/MRI is the combined fusion imaging that can be obtained in a single imaging session. A summary of current, emerging, and future PET-based molecular imaging agents in development is discussed below. The mechanism(s) of tumor localization of several important radiopharmaceuticals, both FDA-approved, and investigational new drugs (IND) are summarized in Tables 22.2 and 22.3. In general, the radioisotope-based molecular imaging technology has the following unique advantages compared to structural imaging techniques:

- Provides information that is unattainable with other imaging technologies or that would require more invasive procedures such as biopsy or surgery.
- Identifies disease in its earliest stages and determines the exact location of a tumor, often before symptoms occur or abnormalities can be detected with other diagnostic tests.
- Determines the extent or severity of the disease, including whether it has spread elsewhere in the body.
- Assesses disease progression and identifies recurrence of disease.
- Selects the most effective TRT based on the unique biologic characteristics of the patient and the molecular properties of a tumor or other disease.
- Accurately assesses the effectiveness of a treatment regimen and determines a patient's response to specific drugs.

22.4.1 Bone Matrix

22.4.1.1   99mTc-MDP and 99mTc-HDP

Prostate cancer most frequently metastasizes to the bone with a predominantly osteoblastic (sclerotic) pathogenesis. Bone scan is the oldest and well-known imaging modality to investigate bone metastases in prostate cancer. 99mTc-labeled bisphosphonates (Fig. 22.3), such as methylene diphosphonate (MDP), hydroxyl diphosphonate (HDP), and hydroxyethylidene diphosphonate (EHDP), have been used to evaluate bone metastases since the 1980s [54]. The uptake mechanism of bone radiopharmaceuticals in metastatic sites depends on blood flow and osteoblastic activity [55]. The binding of radiotracer to bone is due to physicochemical adsorption (chemisorption) to the hydroxyapatite structure of bone tissue. Bone scan is used for initial staging of intermediate to high-risk disease and for restaging after PSA relapse. It has high sensitivity and the ability to survey the entire skeleton with a simple planar scan. However, it has limited specificity and is not sensitive enough to detect micrometastases. SPECT and SPECT/CT have been shown to improve the sensitivity and reduce the number of equivocal reports for detection of bone metastases in prostate cancer [56]. Besides metastatic lesions, infectious lesions, traumatic and degenerative changes also show increased uptake of bone agents. A quantitative parameter known as the Bone Scan Index (BSI) has been shown to be prognostic for survival and was proposed for stratifying patients entering tumor protocols to measure the extent of tumor involvement of bone and for the assessment of tumor response [57].

68Ga-DOTAZOL

Zoledronic acid, a last-generation bisphosphonate, has shown extremely high hydroxyapatite affinity and inhibition of the farnesyl diphosphate synthase. These properties render it an ideal candidate for theranostics, leading to the development of DOTA-zoledronic acid (DOTA-ZOL) (Fig. 22.3). Preclinical and first clinical evaluations revealed its high potential, and biodistribution and skeletal uptakes were found to be comparable to the 68Ga- or 177Lu-labeled compounds [58–60]. Thus, 68Ga/177Lu-DOTAZOL (or even 225Ac-DOTA-ZOL) provides a set of potential theranostic radiopharmaceuticals, enabling patient-individual dosimetry and pre- and post-therapeutic evaluation.

22.4.1.2   Sodium [18F]Fluoride (NaF)

NaF is one of the early skeletal scintigraphy agents that was approved by the US FDA in 1972, before the introduction of PET imaging technology; however, F-18 fluoride planar bone scan was displaced by the arrival of 99mTc-labeled diphosphonates, which provided better resolution. [18F] NaF is a marker of bone perfusion and turnover in which 18F fluoride (F^-) ions exchange with hydroxyl groups in the hydroxyapatite crystal of bone to form fluoroapatite with higher uptake in new bone, because of higher availability of binding sites [55, 61]. Na18F-PET/CT (Fig. 22.12) is a highly sensitive and specific modality for the detection of bone metastases in patients with high-risk prostate cancer. It is a more sensitive and specific imaging technique than planar and SPECT bone scan, and NaF-PET alone [61]. Dynamic bone scanning with 99mTc-MDP or 18F-NaF provides functional information sensitive for subtle changes in bone turnover and perfusion, which assists the clinical management of numerous osseous pathologies.

22.4.2 Glucose Metabolism

22.4.2.1   [18F]Fluoro-2-Deoxyglucose (FDG)

Malignancy-induced glucose hypermetabolism is due to the overexpression of cellular membrane glucose transporters (mainly GLUT-1) and enhanced hexokinase enzymatic activity in tumors [62, 63]. The phosphorylation of glucose, an initial and crucial step in cellular metabolism, is catalyzed by the enzyme *hexokinase* (*HK*), which converts glucose to glucose-6-phosphate, and helps to maintain the downhill gradient that results in the transport of glucose into cells through the facilitative glucose transporters. FDG, similar to glucose, enters the cells, converts to FDG-6-phosphate, and gets trapped in the cell.
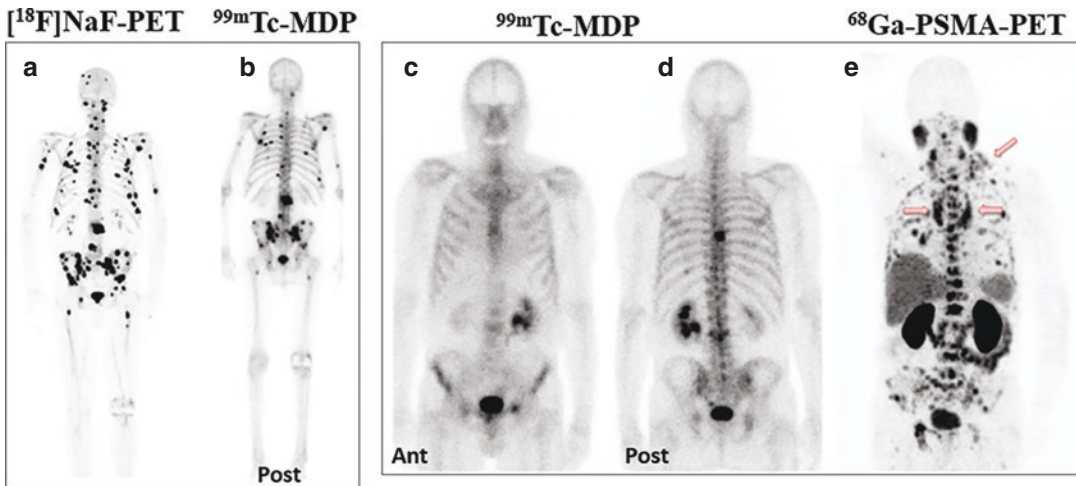
Fig 22.12 [^{18}F]NaF-PET (**a**) detects more bone metastatic lesions compared to ^{99m}Tc-MDP scan (**b**). In a different patient, ^{68}Ga-PSMA-PET (**e**) identifies more metastatic lesions than ^{99m}Tc-MDP. (**c, d**) show Fluoride PET Bone scan

In vitro studies have shown that GLUT1 expression is higher in the poorly differentiated prostate cancer cell lines than in the well-differentiated hormone-sensitive cell lines, suggesting that the level of GLUT1 expression increases with progression of malignancy grade. GLUT1 expression in prostate tumor is also correlated directly to the Gleason score (GS) and androgen level [64]. Therefore, FDG uptake is lower in well-differentiated, low GS and androgen-sensitive prostate cancer than poorly differentiated, high GS, and androgen-resistant tumors. It is well known that prostate cancer, especially, the more differentiated forms, do not exhibit a relevant Warburg effect, thus being characterized by absent or low [^{18}F]FDG avidity. Nevertheless, when progressing to the state of mCRPC, prostate tumors switch to glycolysis as a preferential pathway for producing energy. FDG may also show increased uptake in benign prostate hypertrophy or prostatitis.

FDG-PET/CT is not recommended in detecting primary focus of the cancer and staging of the patients with clinically organ-confined prostate cancer, because of its low sensitivity and specificity [65]. It also has relatively low uptake in the setting of biochemical recurrence or castrate-dependent disease. However, there is evidence that FDG-PET may be useful for restaging after PSA relapse and for assessment of treatment response in CRPC [66, 67]. In particular, FDG-PET is most useful for evaluating lymph node and bone metastases in patients with PSA >2.4 ng/mL and PSA velocity >1.3 ng/mL/year. In summary, FDG-PET/CT has an extremely limited diagnostic value in well-differentiated, androgen-sensitive and low GS prostate cancer. FDG-PET may be useful in the staging of those patients with aggressive primary tumors and can localize the site of disease in a small fraction of men with biochemical failure and negative conventional imaging studies. FDG-PET may be quite useful in treatment response assessment and prognostication of patients with castrate-resistant metastatic prostate cancer [68]. A recent review summarized that FDG-PET/CT has advantages in detecting local recurrence, visceral and lymph node metastases compared to ^{68}Ga-PSMA in partial progressive prostate cancer and castration-resistant prostate cancer patients and emphasized that FDG-PET/CT can compensate for the weakness of PSMA-PET/CT in progressive prostate cancer [69].

22.4.3 Lipid Metabolism

22.4.3.1 [11C]Choline (CH) and [18F] Fluorocholine (FCH)

Prostate cancer cells rely more on fatty acid metabolism than glycolysis with upregulation and increased activity of lipogenic enzymes, *choline kinase* and *fatty acid synthase* [70].

Choline is the fundamental precursor for the synthesis of phosphatidylcholine, which is the essential component of the cell membrane. Choline enters the cell via choline transporters and is used for the biosynthesis of phosphatidylcholine in the tumor cell membrane by *choline kinase*.

[11C]choline was initially developed in Japan for imaging brain tumors [71]. The short half-life of 11C limits the use of CH only to clinical centers with an on-site cyclotron. However, in 2012, the Mayo Clinic in the USA received FDA approval for [11C]Choline-PET to help detect recurrent prostate cancer. Two 18F-labeled choline derivatives, [18F]methyl-Fluorocholine (FCH) and [18F]ethyl-Fluorocholine (eFCH), are currently used in clinical practice. PET/CT with radiolabeled choline is a well-established diagnostic approach for the diagnosis of recurrent prostate cancer after surgery/radiotherapy [50]. Both, CH and FCH (Fig. 22.13) have rapid cancer cell uptake,

rapid blood clearance, relatively minimal excretion in the urine, and high diffuse liver uptake. FCH, however, shows more urinary excretion and intense bladder activity compared to CH.

The diagnostic potential of both, CH and FCH in detecting and staging or restaging of prostate cancer has been reviewed extensively [72, 73]. These two radiotracers are not ideal for initial staging due to false positives in prostatitis and BPH and false negatives in small (<5 mm) or necrotic tumors [74]. However, they have shown promise for restaging after PSA relapse, with high sensitivity for local recurrence, nodal metastases, and bone metastases. The current recommendation is to consider CH-PET/CT as the first-line diagnostic procedure in patients with biochemical relapse showing PSA levels greater than 1 ng/mL, PSA velocity higher than 1 ng/mL/year, or PSA doubling time <6 months [75, 76]. Overall, there is limited but, promising evidence for the use of choline PET/CT to stage patients with untreated, high-risk prostate cancer. Recent studies with 68Ga-PSMA-PET indicate that PSMA-PET is superior to Choline-PET (Fig. 22.14) in primary staging as well as in secondary staging [78]. FCH-PET, however, may be superior in some bone lesions and in a few hormone-resistant high-risk PC patients [77].

Fig. 22.13 PET radiopharmaceuticals used for molecular imaging in prostate cancer

[18F]Fluorodeoxyglucose (FDG)

[18F]Fluciclovine (Axumin(R))

[18F]Fluoromethylcholine (FCH)

[methyl-11C]Choline (CH)
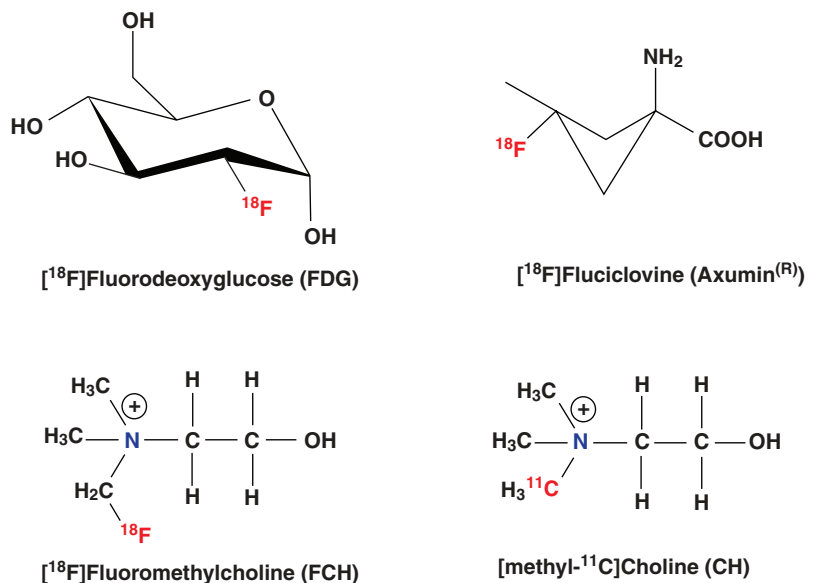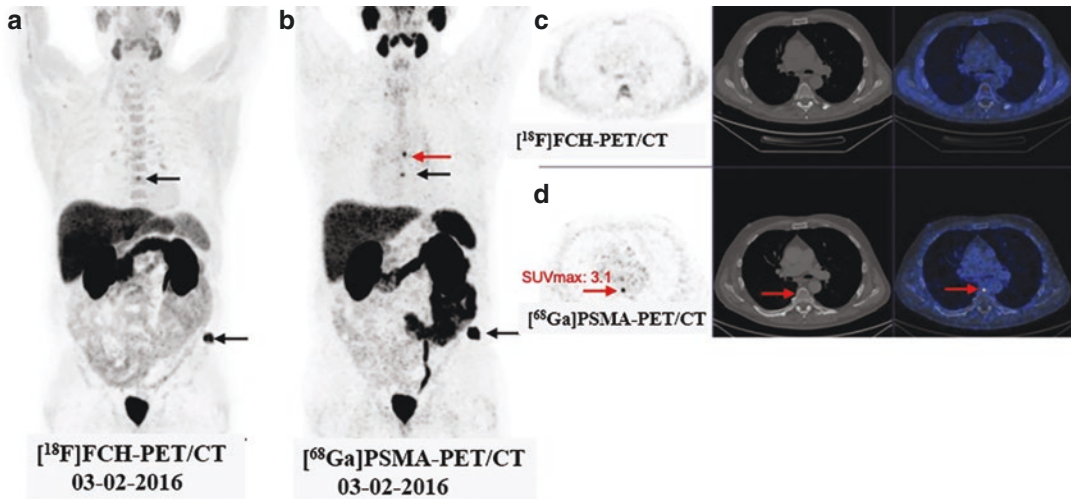
Fig. 22.14 Comparison of FCH-PET and Ga-PSMA-PET in prostate cancer recurrence: FCH-PET (**a**, **c**) revealed multiple bone metastases (arrows) in the left ilium and T10 vertebra corresponding with the sclerotic changes on CT. Ga-PSMA-PET (**b**, **d**) detected additional small bone metastasis on T9 vertebra (red arrows) without relevant morphological changes on CT. PSMA-PET detected small skeletal metastases (GS = 8, PSA: 0.7 ng/mL). (Figure from Paymani et al. [77])

22.4.4 Amino Acid (AA) Transport

Since amino acids are essential to cell metabolism and growth, AA transporter systems are overexpressed in prostate cancer, specifically, large neutral amino acid transporters (system L: LAT1, LAT3, and LAT4) and alanine-serine-cysteine transporters (system ASC: ASCT1 and ASCT2). Of these, LAT3, ASCT1, and ASCT2 are upregulated with androgen simulation and LAT1 and ASCT2 are associated with a more aggressive tumor phenotype [79, 80]. Prostate cancer may be imaged using both radiolabeled natural and synthetic amino acids. [11C]methionine has shown potential for initial evaluation of low- and high-grade primary prostate tumors [81]; however, it is not optimal because of the accumulation of metabolites in nontarget organs.

22.4.4.1   [18F]Fluciclovine (Axumin)

Fluciclovine (18F), also known as anti-1-amino-3-18F-fluorocyclobutane-1-carboxylic acid (anti-3[18F] FACBC) (Fig. 22.13), is a synthetic nonmetabolized, L-leucine analog that can accumulate in prostate cancer via overexpression of the ASC transporters [82]. Although it is transported by the AA transporter system, it does not undergo terminally incorporative metabolism within the body [83]. The distribution of the tracer in the body differs from choline and FDG, as kidney uptake of FACBC is negligible, and no activity is found in the urinary tract. There is low native brain uptake compared to FDG, which may enhance detection of brain metastases or primary brain tumors. The more intense native liver and pancreatic uptake seen with this agent would be expected to limit disease detection in those organs. FACBC-PET has shown early clinical success in imaging primary and recurrent disease in the prostate, pelvic lymph nodes, and bone, with relatively high tumor uptake with little urinary excretion, and improved sensitivity compared to ProstaScint™ imaging [84].

In 2016, [18F]fluciclovine was FDA approved for the localization of recurrent prostate cancer in patients with elevated PSA levels. Comprehensive clinical data demonstrate that 18F-fluciclovine is beneficial in the identification of the site of suspected recurrent disease. [18F] fluciclovine demonstrates improved accuracy when compared with conventional imaging modalities for whole-body staging. The detec-

tion of biochemical recurrence using [18F] Fluciclovine-PET was compared to 68Ga-PSMA-PET [85, 86]. These early reports indicate improved detection rates for PSMA-PET when compared with fluciclovine-PET in patients with recurrent PCa. Figure 22.15 shows comparison of Fluciclovine-PET to Ga-PSMA-PET. However, further studies are needed to compare [18F]fluciclovine-PET studies with PSMA radiotracers, and to characterize the patterns of bone uptake more completely, and also the uptake by other malignant tissues [79, 87].

22.4.5   Androgen Receptor

22.4.5.1   [18F]FDHT

Prostate cancer growth and progression is stimulated by androgens. Since the AR is the key driver of prostate differentiation and PC progression [22], inhibiting the central AR signaling by ADT it is the cornerstone of advanced PC treatment. [18F]Fluoro-16β-5α-dihydrotestosterone ([18F] FDHT) (Fig. 22.4), a ligand that targets the ligand-binding domain of AR, was originally developed to assess AR occupancy [25–27]. FDHT-PET can be used to evaluate the AR expression levels and
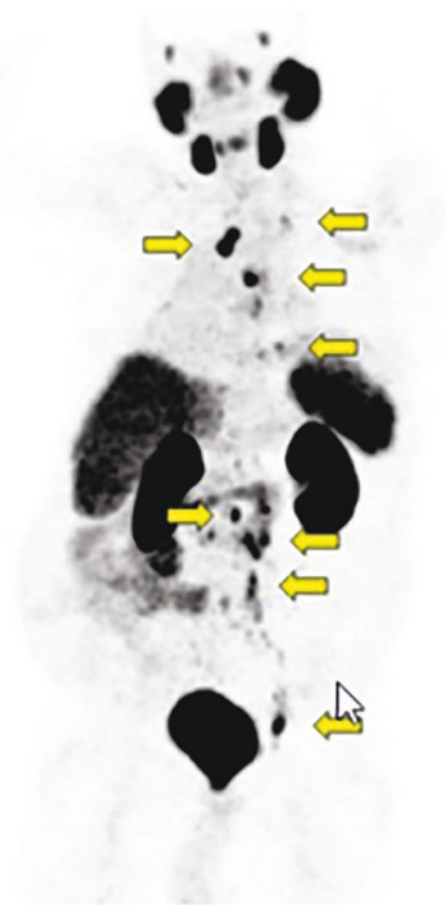
Fig. 22.15 In a patient with prostate cancer 68Ga-PSMA-11 PET indicates (arrows) intense uptake in pelvic, abdominal, thoracic, and supraclavicular lymph nodes (LNs). Corresponding LNs on 18F-fluciclovine-PET show no uptake [85]

receptor occupancy, and enables detection of AR-positive metastatic lesions as indicated by increased AR concentrations. Following treatment with AR antagonists, a decrease in FDHT uptake in the metastatic lesions is indicative of treatment response [88]. [18F]FDHT-PET scans in CRPC patients treated with MDV3100 (AR-mediated drug) found that tumors in nearly all patients showed a decrease in [18F]FDHT binding, indicating that MDV3100 can occupy the AR ligand-binding domain and preclude radiotracer binding. However, these [18F]FDHT-PET "responses" did not correlate with declines in serum PSA or tumor response [88, 89]. A recent study reported that baseline [18F]FDHT-PET/CT using SUV$_{peak}$ of all metastatic lesions predicts treatment response in patients with mCRPC treated with enzalutamide [90].

Direct comparison of FDHT-PET scans with FDG-PET studies has suggested that there may be diverse metabolic phenotypes (Fig. 22.16) of castrate-resistant cancers (androgen receptor predominant, glycolysis-predominant, or androgen receptor/glycolysis-concordant) and that 18F-FDHT is probably suited as a pharmacodynamic response marker, rather than a treatment response marker [91]. Therefore, PET studies to study AR expression (with FDHT) and glycolysis (with FDG) have the ability to determine heterogeneity of imaging phenotypes, which may be useful in distinguishing patients who will benefit from AR inhibitors from those who need alternative treatments [24].

Preclinical studies suggest that androgen blockade appears to increase expression of PSMA in both hormone-sensitive and castrate-resistant
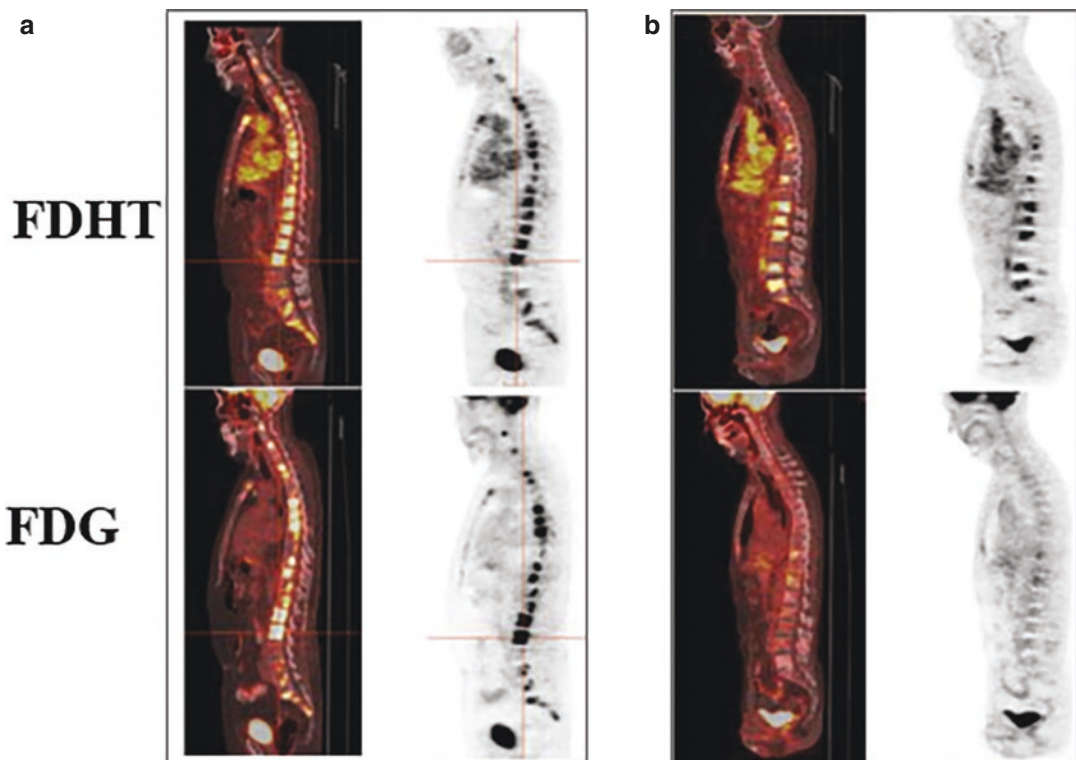
Fig. 22.16 [18F]FDHT vs. [18F]FDG phenotypes in CRPC patient with multiple osteoblastic metastases. The scans in (**a**) show uptake in bone lesions consistent with a "Glycolysis/AR Concordant" phenotype. While scans in (**b**) demonstrate intense FDHT uptake and relatively low level FDG uptake, consistent with an "AR Predominant" phenotype. (From Fox et al. [91])

xenotypes. Recently, Ga-PSMA-PET studies demonstrated higher tumor uptake suggesting enhanced PSMA expression following treatment with enzalutamide [92]. Since PSMA expression is influenced by AR signaling, further investigations should help to clarify the relative value of FDHT-PET vs. PSMA-PET imaging in guiding therapies for prostate cancer. It appears that the three molecular imaging modalities based on FDHT, FDG, and PSMA will have distinct and complementary roles to play in the management of patients with mCRPC.

22.4.5.2 [^{18}F]Enzalutamide (FEZT)

FDHT shows high specific binding to the AR but, is rapidly metabolized in humans [93]. The circulating radiolabeled metabolites show high background activity in blood and are cleared via the kidneys into the urine. Enzalutamide (Xtandi®) is a pure AR antagonist that possesses an AR affinity similar to that of dihydrotestosterone and is currently used in androgen therapy. Enzalutamide and its primary metabolite *N*-desmethylenzalutamide have an AR affinity comparable to that of FDHT but, are excreted mainly via the hepatic route [94]. It has been recently reported that FEZT (Fig. 22.4) may have more favorable properties for imaging of AR density with PET than FDHT [94]. Preclinical studies in AR-positive LnCaP xenograft model showed about three times higher tumor uptake for FEZT than for FDHT. Also, at 1 h after tracer injection, 93% of FEZT in plasma was still intact, compared with only 3% of FDHT.

22.4.6 Radiolabeled Antibodies

22.4.6.1 ^{111}In-Capromab Pendetide (ProstaScint™)

The mAb 7E11-C5.3 was the first anti-PSMA mAb originally developed with a type of prostate cancer cell line known as LNCaP cells [35]. This murine mAb was later conjugated to the linker-chelator, glycyl-tyrosyl-(*N*,ε-diethylenetriaminepentaacetic acid) lysine hydrochloride (GYK-DTPA-HCl), radiolabeled with ^{111}In and was commercialized as an imaging agent, known as ^{111}In capromab pendetide (ProstaScint™) [95]. Since it recognizes and binds to an intracellular epitope of PSMA, only the fixed cells and necrotic cells but not the intact viable cells, bind to the 7E11 mAb. The FDA in 1996, however, approved ProStacint™ as a staging agent indicated for the detection of recurrent prostate cancer in post-prostatectomy patients with a rising PSA and negative or equivocal standard metastatic evaluation, in whom there is high clinical suspicion of occult metastatic disease, and for newly diagnosed patients with biopsy-proven prostate cancer thought to be at high risk for lymph node metastasis. In patients with prostate carcinoma who are at high risk for metastatic disease, the sensitivity was 77% and the specificity was 86% [96]. Subsequent publications have revealed wide variance in the efficacy; such as sensitivity of 67% for disease detection in prostate bed, but a sensitivity of only 10% for extraprostatic disease detection. This agent repeatedly failed in the clinical setting, likely due to poor pharmacokinetics and failure to reach its target epitope on the intracellular portion of PSMA [97].

22.4.6.2 ^{177}In-huJ591 and ^{177}Lu-huJ591 mAb

J591 mAb targets the extracellular portion of PSMA and, therefore, binds to the viable tumor cells [41, 98]. The bifunctional DOTA chelator was conjugated to humanized J591 mAb. The DOTA-J591 mAb (5–6 DOTAs/IgG) was labeled with ^{111}In for imaging studies and ^{90}Y or ^{177}Lu for RIT [99]. Saturation binding studies demonstrated that J591 mAb binds to PSMA with extremely high affinity (K_d = 1.83 ± 1.21 nM). Based on ^{131}I-J591 mAb, it was estimated that LNCaP tumor cells express approximately a million PSMA-binding sites/cell [42].

Planar and SPECT imaging studies with ^{111}In and/or ^{177}Lu DOTA-huJ591 (Fig. 22.17) have shown accurate detection of prostate cancer bone and soft tissue metastases, as well as uptake in the tumor neovasculature of many solid tumors [100–104]. In a phase I study with 53 patients, ^{111}In-J591 accurately targeted bone and/or soft tissue lesions in 98% of the eligible patients. In a phase I dose escalation study with ^{177}Lu-J591, the planar/SPECT imaging detected almost 100% of the lesions identified by conventional imaging studies. These imaging studies indicated that
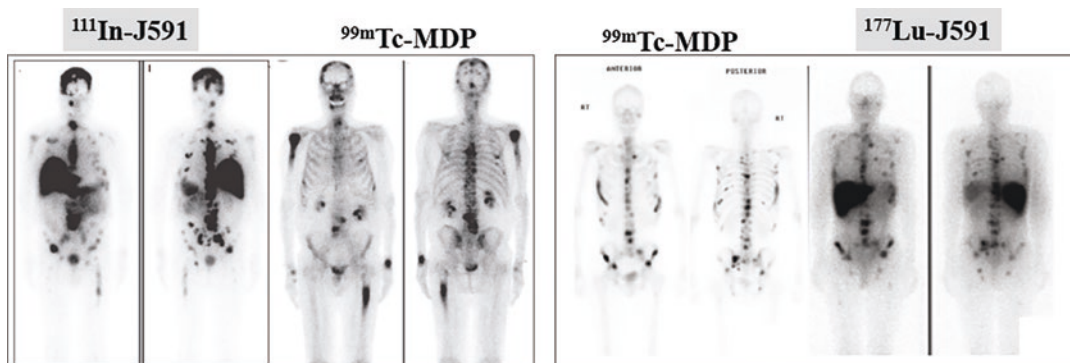
Fig. 22.17 J591 mAb targeting of PSMA in patients with prostate cancer. Panel on left shows comparison of ^{111}In-J591 with bone scan and panel on right shows comparison of ^{177}Lu-J591 with bone scan. (Images provided by Dr. Tagawa at Weill Cornell Medicine, NY)

J591 imaging of PSMA expression is a prognostic tool in patients with mCRPC.

22.4.6.3   [89]Zr-huJ591 mAb

[89]Zr decays in two ways (23% β^+ and 77% *EC*) with a half-life ($T\frac{1}{2}$ = 3.3 days) and ideal for PET/CT imaging with [89]Zr-labeled antibodies. Also, the [89]Zr has a relatively short positron range (shorter than ^{18}F) by emitting low energy β^+ particles (E_{mean} = 396 keV), which facilitates high-resolution PET imaging. Compared to [^{18}F]FDG and CT, patients generally receive higher radiation from [89]Zr-labeled mAb PET (~20–40 mSv for 37–74 MBq) [105].

[89]Zr-huJ591 mAb was used for PET imaging studies to detect PSMA-positive prostate cancer. Early studies have shown inconsistent results for the diagnostic performance of primary prostate cancers [106]. However, in patients with metastatic prostate cancers (n = 10), the sensitivity for detecting primary tumors increased to 100%. In patients (n = 50) with mCRPC [89]Zr-J591-PET had a higher sensitivity for bone metastasis than conventional imaging methods, while conventional imaging methods were more sensitive for soft tissue lesions [107, 108].

While imaging with radiolabeled whole IgG mAb approach is highly promising the optimal time for patient imaging after injection in terms of achieving adequate tumor to background ratios was 7 ± 1 days. Although radiolabeled antibodies offer the potential for tumor targeting, their effectiveness as diagnostic radiopharmaceutical is limited by a long plasma half-life, poor tumor penetrability, and the nonspecific localization exhibited with immunoglobulins.

22.4.6.4   [89]Zr-Df-IAB2M Minibody

IAB2M is an 80-kDa minibody genetically engineered from the parent J591 mAb. [89]Zr-IAB2M showed rapid accumulation in tumors and a fast clearance from the blood within 24 h in a prostate cancer model [109]. The [89]Zr-IAB2M uptake of bone and lymph node metastases was discernible in as little as 24 h and lasted up to 120 h in patients with prostate cancer [110]. The [89]Zr-IAB2M uptake correlated with PSMA expression [111]. With [89]Zr, the advantage of minibody is significant reduction of effective dose (0.41–0.68 mSv/MBq) compared to whole IgG. Figure 22.18 shows the [89]Zr-IAB2M PSMA targeting more metastatic prostate cancer lesions compared to bone scan, and FDG-PET [111].

22.4.6.5   [89]Zr-DFO-MSTP2109A, Anti-STEP-1 Antibody

The 6-transmembrane epithelial antigen of the prostate (STEAP) family is comprised of four novel cell surface markers (STEAP 1–4) highly expressed in prostate cancer [112]. It is also present in other cancers but, has little cross-reactivity with other normal tissues. STEAP1 is composed of 339 amino acid cell surface markers. Functionally, it appears to be an ion channel or transporter protein and may have roles in multiple biological processes, including cell adhesion, pro-
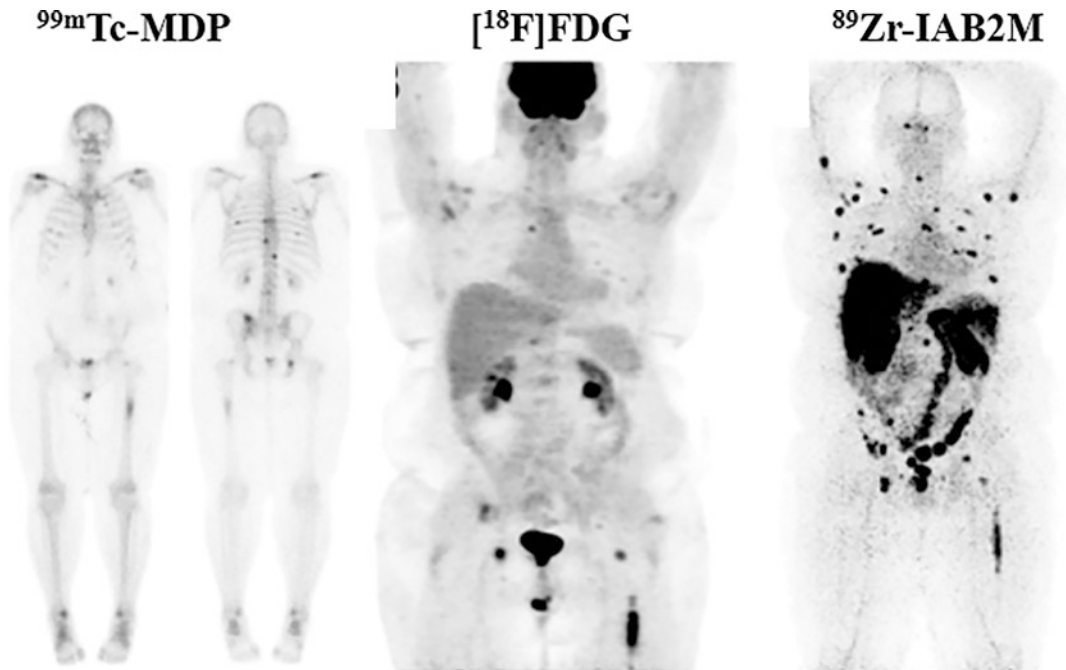
Fig. 22.18 ^{89}Zr-IAB2M-PET imaging in mCRPC. Targeting with IAB2M (minibody fragment from J591 mAb). Comparison with bone scan and FDG-PET.

^{89}Zr-IAB2M scan shows more   images   than bone scan or FDG-PET. (From Pandit-Taskar et al. [111])

liferation and invasiveness, intracellular communication, and tumor growth inhibition, and iron metabolism. STEAP1 overexpression in prostate cancer and its bone metastases has been very well documented, showing correlation between increased expression and tumor aggressiveness.

^{89}Zr-DFO-MSTP2109A mAb may have the potential to be used as a companion imaging agent for therapies that are being developed to target STEAP1. A phase 1 study evaluated the safety, biodistribution, and tumor targeting in patients with mCRPC [113]. There was no significant acute or subacute toxicity. Favorable biodistribution and enhanced lesion uptake (in both bone and soft tissue) were observed. The best lesion discrimination was seen around 6 days post administration.

22.4.7 Small-Molecule PSMA Inhibitors

Small molecules that interact specifically with PSMA and carry appropriate radionuclides for PET and SPECT provide an ideal molecular imaging option for prostate cancer. Smaller molecular weight compounds with higher permeability into solid tumors will likely have a definitive advantage in obtaining higher percent uptake per gram of tumor tissue and a high percentage of specific binding. Smaller molecules will likely also display improved blood clearance and tissue distribution in normal tissues compared to intact immunoglobulins making lesion detection more conspicuous.

Several groups have reported on the development of small-molecule inhibitors of PSMA based on the structural motifs of various NAALADASE inhibitors comprising two amino acids joined through their NH_2 groups by a urea linkage (glutamate urea heterodimers). Glutamate-ureido (Glu-ureido) based inhibitors are by far the most explored and clinically used class of PSMA agents. The urea-based PSMA-binding motifs are present in three forms: glutamate-urea-glutamate (*glu-urea-glu*) also known as DUPA motif, glutamate-urea-cysteine

(*glu-urea-cys*), or glutamate-urea-lysine (*glu-urea-lys*). Many of the current radiolabeled PSMA inhibitors used in the clinic for imaging and therapy (Tables 22.2 and 22.3) are based on the urea-based motif or pharmacophore.

22.4.7.1 DCFBC and DCFPyl

In 2002, Dr. Pomper's group at John Hopkins School of Medicine (JHSM) reported the synthesis of the first radiolabeled PSMA inhibitor, [11C]MeCys-C(O)-Glu ([11C]MCG or [11C]DCMC) (Fig. 22.19) which binds to PSMA with high potency (IC_{50} = 1.4 nM) [114]. Three years later, based on animal studies, [11C]DCMC was proposed for imaging prostate cancer and the authors stated that [11C]DCMC is not a substrate for PSMA, but is bound to the active site of the enzyme electrostatically so that PSMA is behaving like a receptor and not as an enzyme in this type of imaging studies [115].

[18F]DCFBC (Fig. 22.19) was the first 18F labeled PSMA inhibitor developed in 2008 at JHSM based on Cys-Urea-Glu pharmacophore and was successfully evaluated in several clinical studies [116]. The major drawback of this tracer was slow blood clearance and high background activity. As a result, early imaging studies did not provide optimal sensitivity.

In a prospective study in patients (n = 68) with documented biochemical recurrence after primary local therapy (prostatectomy and/or post radiation therapy) with negative conventional imaging, [18F]DCFBC-PET was able to identify recurrence with PSA >0.78 ng/mL in 60.3% of patients, which led clinicians to change the treatment strategy in 51% of patients [117].

[18F]DCFPyl (Pylarify™)

The next generation compound from JHSM is [18F]DCFPyl (Fig. 22.19), developed based on Lys-Urea-Glu motif, was hydrophilic, and showed faster renal excretion [118]. In patients with biochemical recurrence, direct comparison of [18F]DCFPyl with 68Ga-PSMA-11 indicated that [18F]
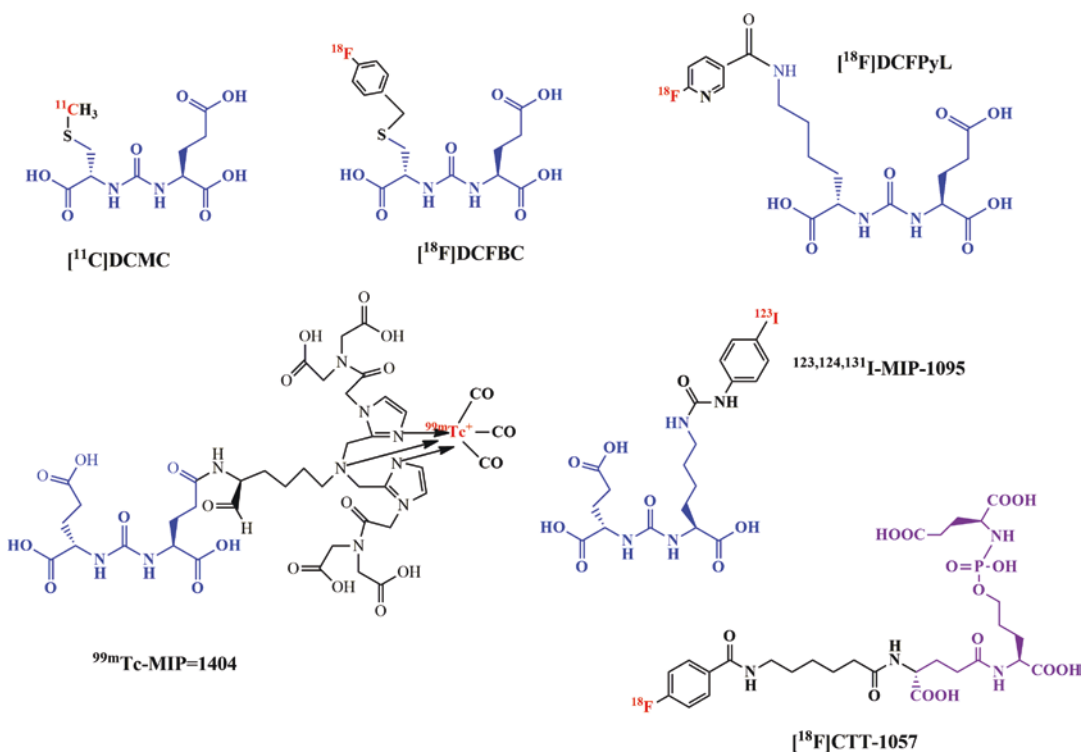
Fig. 22.19 Small-molecule PSMA inhibitors labeled with 18F, 99mTc, and 123/131I. Except for CTT-1057 ligand (phosphoramide derivative), all the other ligands share the urea-glutamate pharmacophore (shown in blue color)

DCFPyL is noninferior to ^{68}Ga-PSMA-11, and that imaging with [^{18}F]DCFPyL-PET may even exhibit improved sensitivity in localizing relapsed tumors after prostatectomy for moderately increased PSA levels [119]. A pilot study comparing [^{18}F]DCFPyl to [^{18}F]PSMA-1007 observed that excellent image quality was achieved with both agents, resulting in identical clinical findings. Nonurinary excretion of ^{18}F-PSMA-1007, however, might present some advantage with regard to delineation of local recurrence or pelvic lymph node metastasis in selected patients; the lower hepatic background might favor [^{18}F]DCFPyL in late stages, when rare cases of liver metastases can occur [120].

The FDA approval was based on data from two studies, the OSPREY and CONDOR trials, investigating the safety and diagnostic performance of ^{18}F-DCFPyL in prostate cancer. In the phase 2/3 OSPREY trial, improvements in the specificity (96–99%) and positive predictive value (78–91%) of the agent were observed when compared with conventional imaging for metastatic prostate cancer. Eligible patients in the OSPREY trial were divided into two cohorts, with cohort A including patients with high-risk, locally advanced prostate cancer, and cohort B including patients with metastatic or recurrent disease. In the phase 3 CONDOR study, a median PSA level of 0.8 ng/mL was observed among the 208 evaluable patients, with 68.8% having a PSA level of less than 2.0 ng/mL. The primary end point of correct localization rates (CLRs), identified by PyL–PET/CT and evaluated by 3 blinded independent central readers was observed at 85.6% (95% CI, 78.8–92.3%), 87.0% (95% CI, 80.4–93.6%), and 84.8% (95% CI, 77.8–91.9%) [121] (Fig. 22.20).
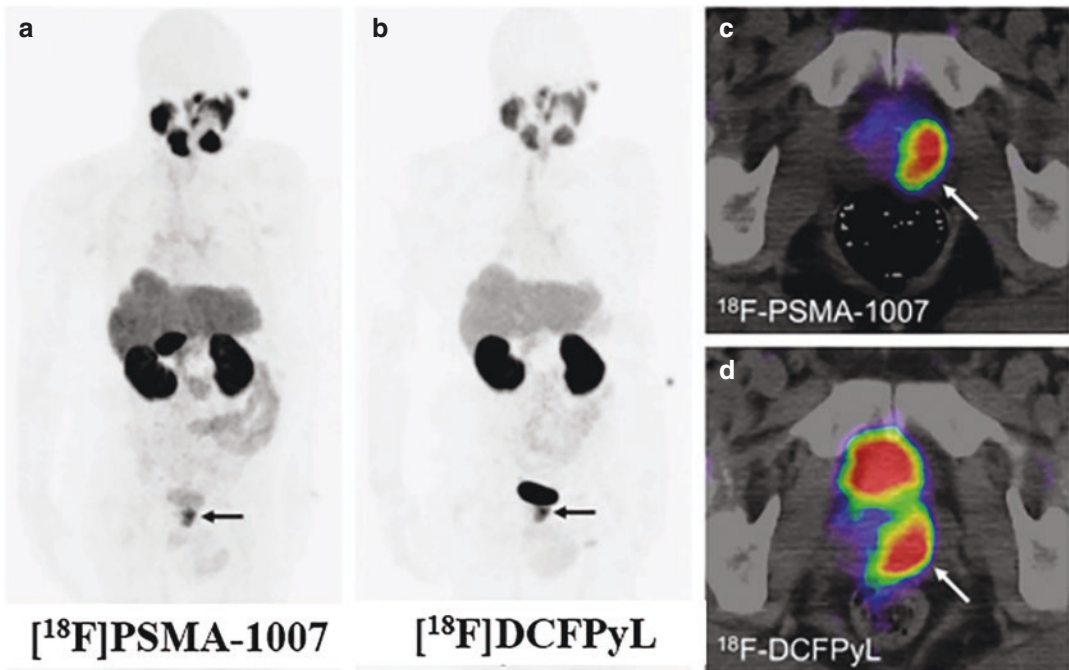
Fig. 22.20 [^{18}F]DCFPyl vs. ^{18}F-PSMA-1007 PET/CT in a patient with newly diagnosed prostate cancer with high PSA (95.43 ng/mL) and positive biopsy (GS = 8). DCFPyL (**b**, **d**) detects (SUV_{max} = 18.08) prostate cancer confined to prostate gland. PSMA-1007 (**a**, **c**) (SUVmax = 11.77) also provides the same diagnosis [120]

22.4.7.2 MIP-1095 and MIP-1404

In 2006, Dr. Babich's group at Molecular Insight Pharmaceuticals (MIP) company (later acquired by Progenics Pharmaceuticals Inc) started a program to design and synthesize a series of heterodimeric inhibitors of PSMA having Lys-urea-Glu pharmacophore that could be radiolabeled with different isotopes including halogens. They reported the development of two high-affinity radioiodinated PSMA inhibitors ^{123}I-PSMA-1072 ($Ki = 5$ nM) and ^{123}I-PSMA-1095 ($Ki = 0.3$ nM) for SPECT imaging studies [122]. The first human studies demonstrated that these tracers detect lesions in the prostate gland, soft tissue, lymph nodes, and distant metastases and clearly documented the potential utility of PSMA imaging at 4 h after injection based on planar and SPECT imaging studies [123]. Direct comparison with ProstaScint imaging clearly documented that ^{123}I-MIP-1072 identified several metastatic lesions in the pelvic lymph nodes not detected by anti-PSMA antibody, ProstaScint imaging. Based on these early clinical results, MIP-1095 (Fig. 22.19) was labeled with [131]I (a radionuclide that emits a beta particle) for targeted therapy of metastatic prostate cancer. [124/131]I-MIP-1095 was also developed for PET imaging studies and TRT of mCRPC [124].

^{99m}Tc-MIP-1404 (Trofolastat™)

Subsequently, in 2012, Dr. Babich's group also reported the development of two high-affinity ^{99m}Tc-labeled PSMA inhibitors, ^{99m}Tc-MIP-1404 (Fig. 22.19) and ^{99m}Tc-MIP-1405, based on Glu-Urea-Glu and Glu-Urea-Lys pharmacophores and tricarbonyl core chemistry [125]. The first human studies in patients with mCRPC showed both ^{99m}Tc tracers localized to lesions in bone and soft tissue that correlated with radiologic evidence of metastatic disease identified by the bone scan [126, 127]. In a 71-year-old patient who had prior prostatectomy and with a rising PSA (1.37–8.9 ng/mL over a period of 4 months), PSMA imaging with ^{99m}Tc-MIP-1404 (in March) detected more metastatic lesions earlier compared to the two bone scans performed either before (in January) or after (in June) the PSMA scan (Fig. 22.21). Based on these results a preliminary phase I study and a multicenter phase II study were conducted in high-risk prostate cancer patients scheduled for prostatectomy and extended pelvic node lymph node dissection. In all subjects with Gleason score > 7, [99m]Tc-
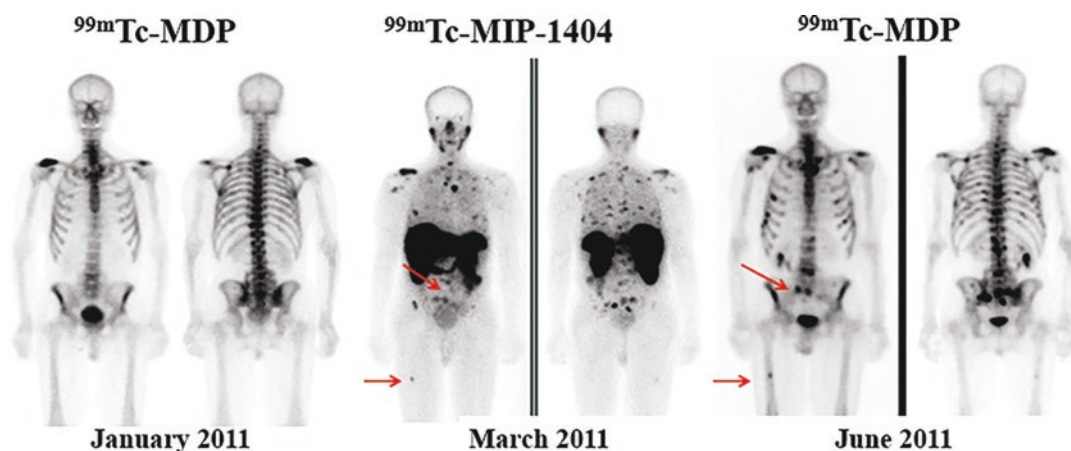
Fig. 22.21 ^{99m}Tc-MIP-1404 planar whole-body images in a patient who had prior prostatectomy and with a rising PSA (1.37–8.9 ng/mL over a period of 4 months), PSMA imaging with ^{99m}Tc-MIP-1404 (in March) detected more metastatic lesions earlier compared to the two bone scans performed either before (in January) or after (in June) the PSMA scan [126, 127]
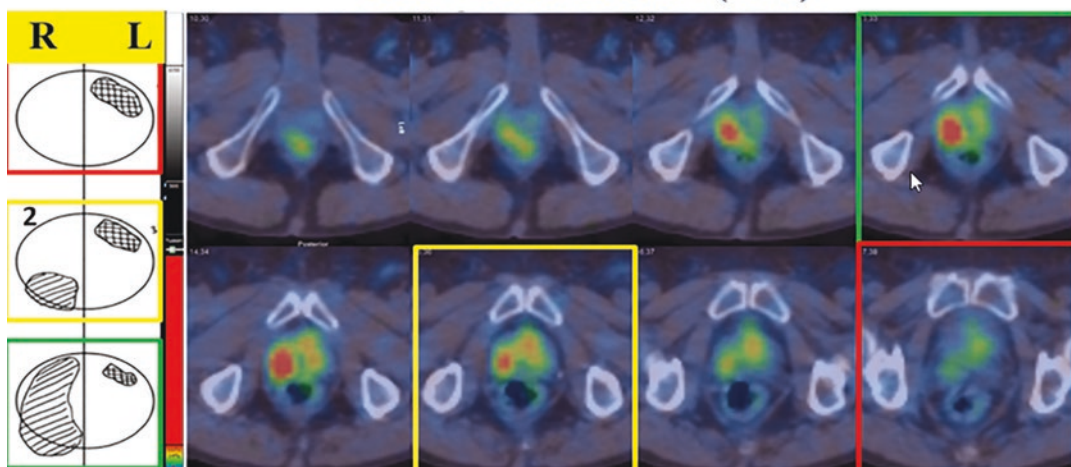
Fig. 22.22 99mTc-MIP-1404 images in a high-risk prostate cancer patient scheduled for prostatectomy and extended pelvic node lymph node dissection. 99mTc-MIP-1404 SPECT clearly identified the prostate cancer foci (Gleason score > 7) in the prostate gland, confirmed by histopathology (Vallabhajosula et al. Weill Cornell Medicine, NY)

MIP-1404 SPECT clearly identified the PCa foci in the prostate gland, confirmed by histopathology (Fig. 22.22), and PSMA staining [128]. Because 99mTc-MIP-1404 (Trofolastat™) showed minimal urinary excretion, it had a distinct advantage for detecting prostate cancer in the gland and pelvis at initial stages of the disease and was selected for phase II/III studies to determine sensitivity, and specificity to detect prostate cancer in high-risk patients. Trofolastat™ has been investigated in several clinical trials resulting as the first PSMA imaging agent to finalize phase 3 clinical trials [129]. It is therefore expected that 99mTc-MIP-1404 may be available as a "technetium instant kit" in the near future.

### 22.4.7.3	PSMA-11, PSMA-617, PSMA-1007, and PSMA-I&T

68Ga-PSMA-HBED-CC (or 68Ga-PSMA-11)
In 2012, the development of PSMA-HBED-CC (also known as PSMA-11 or DKFZ-PSMA-11) at the German Cancer Research Centre (GCRC) and the University Hospital at Heidelberg by Drs. Eder, Haberkorn, and Afshar-Oromieh should be regarded as a major milestone in the development of radiolabeled PSMA inhibitors for molecular imaging and targeted therapy.

PSMA-11 consists of a Glu-urea-Lys motif conjugated with the highly efficient and Ga-specific acyclic chelator HBED-CC (Fig. 22.10) via an aminohexanoic acid (Ahx) spacer [130]. The advantage of HBED-CC chelator is that it can form efficient 68Ga complex at room temperature with extremely high thermodynamic stability. In the first human studies, direct comparison to [18F] FCH, 68Ga-PSMA-targeted PET imaging was able to detect lesions much earlier in patients with low PSA values and showed reduced background activity in healthy tissue [131]. Subsequently, several clinical studies documented the clinical utility of 68Ga-PSMA-11 (Fig. 22.23) for molecular imaging of prostate cancer [132].

The FDA approval of 68Ga-PSMA-11 [133] was based on evidence from two clinical trials in patients with prostate cancer. The trials were conducted at two different sites in the USA (FDA package insert). Trial-1 enrolled patients who were recently diagnosed with prostate cancer and were awaiting surgery for the removal of the prostate and the nearby lymph nodes. Trial-2 enrolled
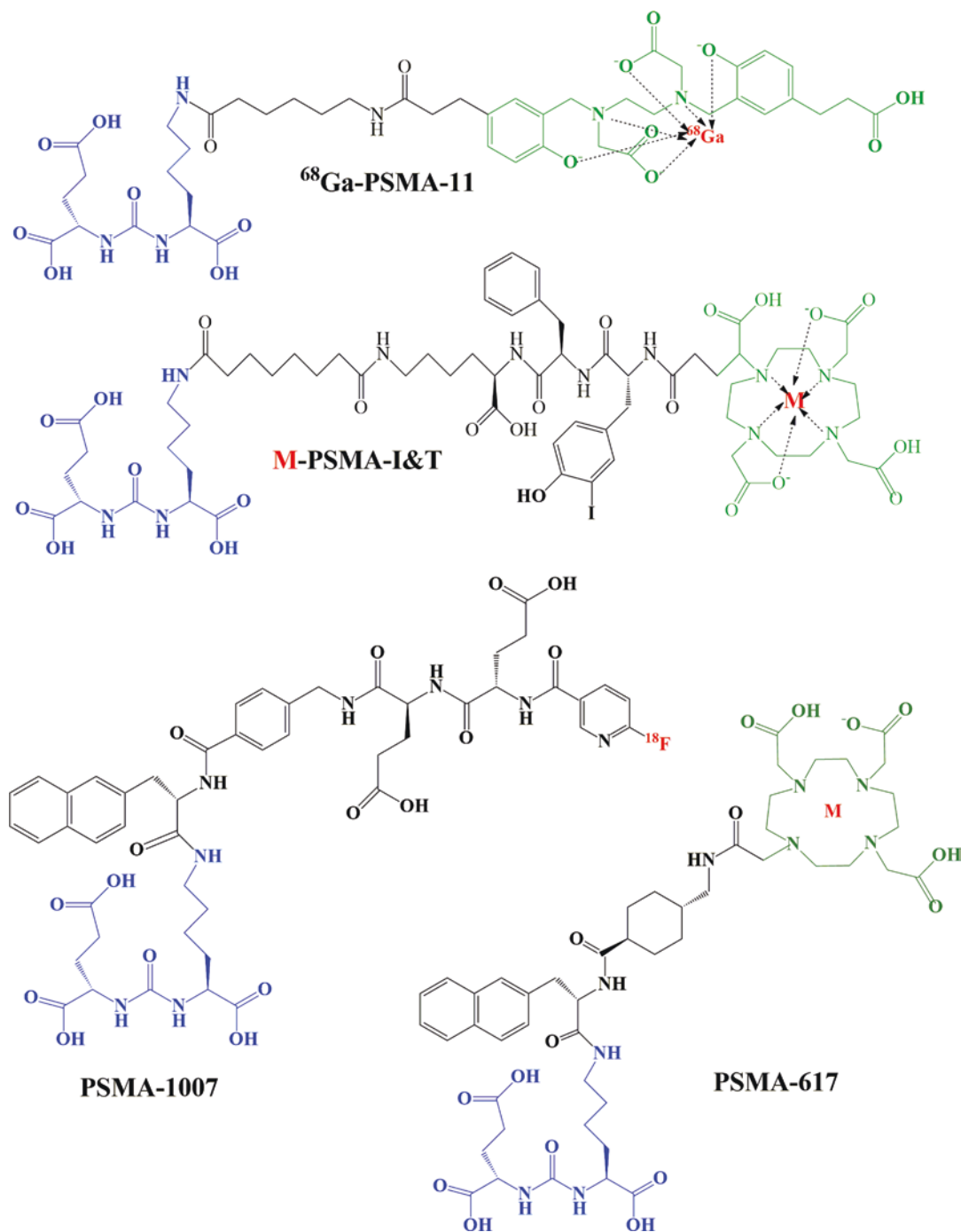
Fig. 22.23 Small-molecule PSMA inhibitors (PSMA-11, PSMA-617, and PSMA-I&T) were developed to complex trivalent metals, such as ^{68}Ga, ^{111}In, ^{177}Lu, and ^{225}Ac. PSMA-11 is based on HBED-CC chelator, while PSMA-617 and PSMA-I&T are based on DOTA chelator. All the ligands share the urea-glutamate pharmacophore (shown in blue color)

patients who were already treated for prostate cancer but, had rising PSA levels, suspicious for cancer spreading. In patients scheduled for radical prostatectomy, the positive predictive value was 61% and the negative predictive value was 84%. The sensitivity was 47% and specificity was 90%. In patients with biochemical recurrence, the likelihood of identifying a ^{68}Ga-PSMA-11 PET positive lesion generally increased with higher serum PSA level (36% at <0.5 ng/mL to 91% at >2.0 ng/mL).

PSMA-11, PSMA-617, PSMA-1007, and PSMA-I&T

In order to develop a theranostic PSMA inhibitor, the investigators at the GCRC in Heidelberg, conjugated the same Glu-Urea-Lys pharmacophore with DOTAGA chelator using a modified linker with D-amino acids and, thus, developed the first theranostic PSMA inhibitor, named PSMA-I&T, for imaging and therapy of prostate cancer [134, 135]. The targeting of PSMA with ^{177}Lu-PSMA-I&T was shown to be as good as that of ^{68}Ga-PSMA-11 (Fig. 22.24). Some clinical studies evaluated the potential of ^{68}Ga-PSMA I&T for the detection of primary prostate cancer before prostatectomy [43].

The HBED-CC chelator used for developing ^{68}Ga-PSMA-11 is not appropriate for labeling therapeutic radiometals such as ^{177}Lu, ^{90}Y, and [225]Ac. To overcome this restraint, the investigators at the GCRC developed two high-affinity PSMA inhibitors, PSMA-617 and PSMA-I&T, based on Glu-Urea-Lys pharmacophore and DOTA or DOTAGA chelators (Fig. 22.23). In addition, the choice of linker/spacer has a significant impact on tumor targeting, as well as on the pharmacokinetics. PSMA-617 was synthesized by conjugating DOTA chelator to the Glu-Urea-Lys motif by a naphthalic spacer [136]. PSMA-I&T was synthesized by DOTAGA chelator to the same Glu-Urea-Lys scaffold by a spacer con-
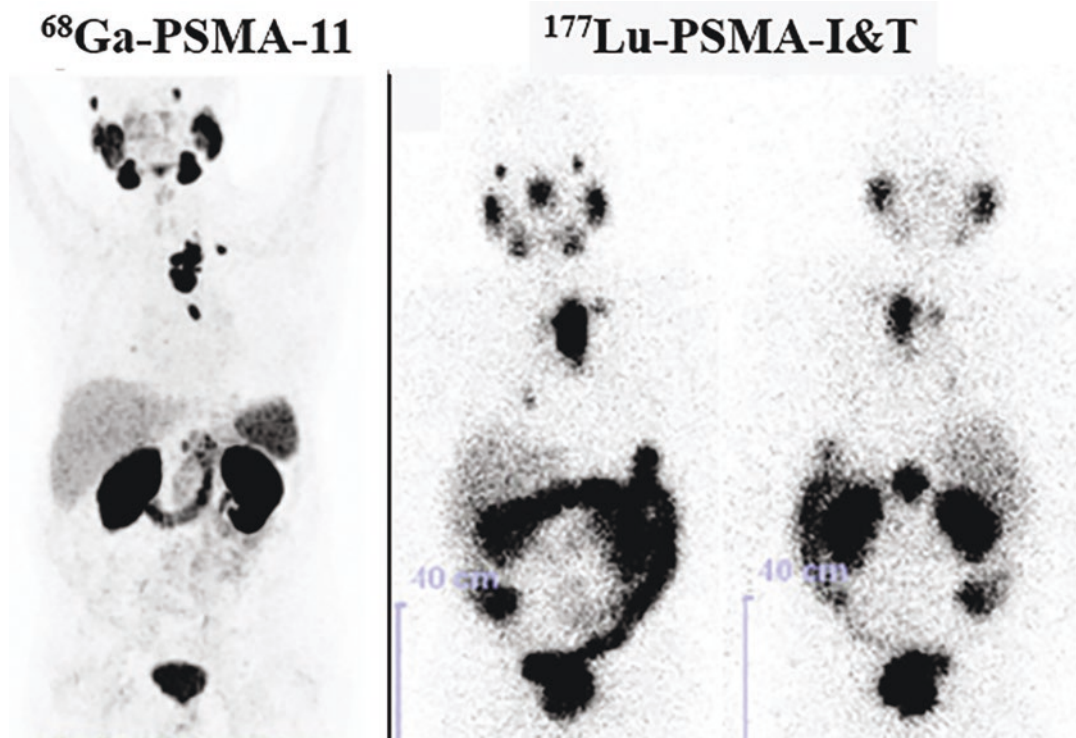
Fig. 22.24 PSMA targeting with ^{68}Ga and ^{177}Lu labeled small-molecule PSMA inhibitors. ^{68}Ga-PSMA-PET/CT showed intense tracer accumulation in mediastinal lymph node metastases. Correspondingly, these mediastinal lymph nodes demonstrated high ^{177}Lu-PSMA-I&T uptake 47 h after therapy with 5.7 GBq of ^{177}Lu-PSMA-I&T [134]

taining D-Phe-D-Phe-Lys amino acid residues. Further substitution of the D-Phenylalanine residues in the peptide linker by 3-iodo-D-tyrosine resulted in the final compound, DOTAGA-(I-y)-fk-(Sub-kuE), named PSMA-I&T (for imaging and therapy) since it can be used to label with either ^{68}Ga or [177]Lu [134].

^{177}Lu-PSMA-617 was quickly used as a therapeutic ligand because it has higher tumor uptake at later time points, lower spleen uptake, and highly efficient clearance from the kidneys [136]. Some studies, however, showed lower tumor uptake compared to PSMA-11 whereas the tissue distribution pattern and kinetics of PSMA-I&T are comparable to PSMA-11 [134].

The investigators at GCRC were also successful in developing a ^{18}F-labeled PSMA inhibitor [^{18}F]PSMA-1007. PSMA-1007 shares the same Glu-Urea-Lys motif and the naphthalene-based linker region as PSMA-617. The only difference is the ^{18}F radiolabeling moiety. The pharmacophore conjugated with NaI but, the linker is replaced by 4-carboxy-benzylamine residue followed by two glutamic acid residues and conjugated with 6-[^{18}F]fluronicotinic acid [137, 138]. In a pilot clinical study, [^{18}F]PSMA-1007 was directly compared to [^{18}F]DCFPyl in patients with newly diagnosed prostate cancer (Fig.

22.20). Excellent imaging quality was achieved with both tracers, resulting in identical clinical findings. With PSMA-1007, however, unlike the other PSMA inhibitors, excretion is mainly by hepatobiliary system and nonurinary excretion of [^{18}F]PSMA-1007 might present some advantage with regard to delineation of local recurrence or pelvic lymph node metastasis in selected patients [120].

22.4.7.4   rhPSMA-7.3

A unique and novel class of theranostic agents named radiohybrid (rh) PSMA inhibitors based on Glu-Urea-Lys pharmacophore were developed by Dr. Wester and colleagues at the Technical University of Munich, Garching, Germany (TUMG) [139, 140]. Radiohybrid concept represents a molecular species that offers two binding sites for radionuclides, a silicon-fluoride acceptor (SiFA) for ^{18}F and a chelator (such as DOTA) for radiometallation. One of these binding sites is radiolabeled, the other one labeled with a stable nuclide, thus is silent. These pairs of compounds (Fig. 22.25), either pure imaging pairs (A) or theranostic pairs (B), represent chemically identical species (monozygotic chemical twins) and thus exhibit identical in vivo characteristics (e.g., affinity, lipophilicity, pharmacokinetics). The lead compound [^{18}F]Ga-rhPSMA-7 with [nat]Ga-
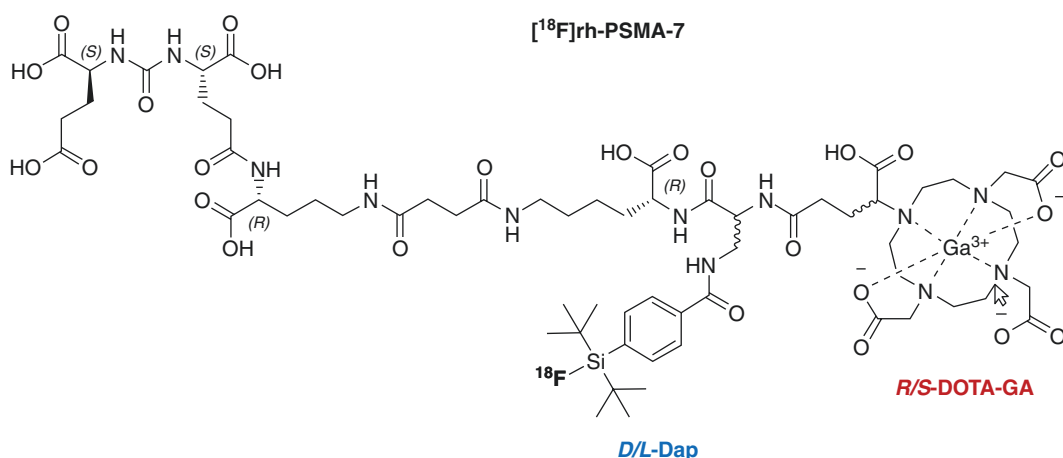
Fig. 22.25 Diastereomeric mixture [^{18}F,[nat]Ga]rhPSMA-7 is composed of the four isomers [^{18}F, [nat]Ga]rhPSMA-7.1 to 7.4, differing in the stereoconfiguration of diaminopropi-onic acid (D-/L-Dap) and DOTA-GA (R-/S-DOTAGA). The predominant species is [^{18}F,[nat]Ga]rhPSMA-7.3 [139, 140]

DOTAGA complex was evaluated in patients with biochemical recurrence [141]. The biodistribution was found to be similar to that of established PSMA ligands, and [^{18}F,^{nat}Ga]rhPSMA-7 PET/CT demonstrated high detection rates in early biochemical recurrence after radical prostatectomy, especially among patients with low PSA values. [^{18}F]Ga-rhPSMA-7, however, represents a mixture of four stereoisomers (7.1, 7.2, 7.3, 7.4), differing in the stereo-configuration of the diaminopropionic acid branching unit (D-Dap or L-Dap) and the glutamic acid pendant arm at the DOTA-GA-chelator (R-DOTA-GA or S-DOTA-GA) [139, 140]. Based on preclinical studies, [^{18}F,^{nat}Ga]rhPSMA-7.3 was identified as the preferred isomer since it showed high tumor accumulation, low uptake by the liver and kidney with low blood levels. [^{18}F]-rhPSMA-7.3 is currently in phase III trials (sponsored by BlueEarth Diagnostics) for prostate cancer (PCa) imaging. In order to assess the role in primary staging, [^{18}F]-rhPSMA-7.3 PET/CT studies in patients ($n = 279$) with primary prostate cancer were evaluated [142]. [^{18}F]-rhPSMA-7.3 offers superior diagnostic performance to morphological imaging for primary N-staging of newly diagnosed PCa, shows lower inter-reader variation, and offers good distinction between primary tumor and bladder background activity. In preclinical studies, the in vivo behavior of the therapeutic analog ^{177}Lu-rhPSMA-7.3 was compared to [^{177}Lu]PSMA-I&T [143]. Based on the results, ^{19}F/^{177}Lu-rhPSMA-7.3 can be considered a suitable candidate for clinical translation due to similar clearance kinetics and radiation dose to healthy organs but, superior tumor uptake and retention compared with ^{177}Lu-PSMA-I&T.

22.4.7.5 Albumin-Binding PSMA Inhibitors

The plasma protein human serum albumin (HAS) has a long half-life of about 19 days and, because of its high molecular weight (67 kDa), it has low renal clearance making the protein a valuable candidate as a drug delivery system and a means to extend the half-life of peptides [144–146]. HSA is a widely recognized carrier for the passive targeting to solid tumors and has been frequently used to develop drug conjugates for longer plasma half-life. The covalent or noncovalent attachment of peptides to albumin can reduce the glomerular filtration rate and extend the half-life of peptides by increasing the size of peptide-based drugs. Albumin is also found to specifically target tumor regions because of its enhanced permeability and retention (EPR) effect as well as albumin receptor binding, which is a unique advantage as the carrier for tumor-targeted drug delivery [145].

Albumin-binding ligands based on the lead structure 4-(*p*-iodophenyl)butyric acid (IPBA) have been identified by screening DNA-encoded chemical libraries [147]. The best derivative of IPBA, known as Albutag, was used to develop radiolabeled folate conjugates for imaging and therapy [148]. Albutag was also used to develop a novel class of trifunctional ligands, consisting of the high-affinity PSMA-binding domain, the Albutag, and the DOTA chelator, to facilitate the modification of the three moieties independently and ultimately enable the generation of spatial optimized conjugates PSMA conjugates for prostate cancer theranostics [149]. Preclinical studies demonstrated that the trifunctional ligands had high and persistent tumor uptake with absorbed doses that were four times greater than those observed for a similar compound lacking the albumin-binding moiety. It was also reported that the tumor uptake of the lead compound ^{177}Lu-RPS-077 continues to increase up to 24 h after injection and that the washout by 96 h was not significant. The tumor AUC and tumor-to-kidney ratio of ^{177}Lu-RPS-072 are significantly enhanced compared with any other small molecule investigated in a LNCaP xenograft model. Therefore ^{177}Lu-RPS-072 exhibits an increased therapeutic index, shows the potential to increase the dose delivered to tumors, and is a highly promising candidate for targeted radioligand therapy [149]. Albutag was also used to develop albumin-binding PSMA-targeting PET radioligands based on NODAGA chelator [150].

Recently, a new class of PSMA radioligands comprising ibuprofen as an albumin-binding entity was reported [151]. The isobutylphenyl propionic acid, known under the name "ibuprofen," is a nonsteroidal anti-inflammatory drug

(NSAID), which binds to plasma proteins. To develop radiometal-labeled PSMA inhibitors, several glutamate-urea-based PSMA ligands were synthesized with ibuprofen, conjugated via variable amino acid-based linker entities. The lead compound ^{177}Lu-Ibu-DAB-PSMA, in which ibuprofen was conjugated via a positively charged diaminobutyric acid (DAB) entity, showed distinguished tumor uptake and the most favorable tumor-to-blood and tumor-to-kidney ratios [151].

The benefit of an enhanced tumor uptake of long-circulating PSMA radioligands is, however, compromised by an increased retention of activity in healthy organs and tissues including the kidneys, and bone marrow, which may limit the number of therapy cycles that can be applied. Albumin-binding properties have, thus, to be carefully balanced to achieve an increased tumor uptake while keeping background activity as low as possible [152].

22.4.8   Bombesin and GRPR Analogs

A variety of radiolabeled GRPR agonists (such as ^{68}Ga/^{177}Lu-AMBA, ^{68}Ga/^{177}Lu-PESIN) have been developed for targeting GRPR-positive tumors and were evaluated in preclinical and clinical studies [49, 50, 153]. Several recent reports have shown that GRPR antagonists show properties superior to GRPR agonists, affording higher tumor uptake and lower accumulation in physiologic GRPR-positive nontarget tissues [154]. GRPR agonists activate the receptor and induce side effects. GRPR antagonists, however, are expected to have no adverse effects [49]. Several GRPR antagonists (such as ^{68}Ga-RM26, ^{68}Ga-RM2 (also referred to as ^{68}Ga-BAY86-7548), ^{64}Cu-CB-TE2A-AR06, ^{68}Ga-SB3) were evaluated in clinical studies to assess the potential clinical utility to detect primary prostate cancer lesions. The amino acid sequence of bombesin and analogs is shown in Fig. 22.9.

RM26 with high affinity was discovered by peptide backbone modification of bombesin analogs [155]. A pilot PET study with ^{68}Ga-NOTA-RM26 in 28 patients with newly diagnosed and post-therapy prostate cancer demonstrated that RM26 can detect both primary prostate cancer and metastases with high efficiency. There was a significant positive correlation between SUV derived from ^{68}Ga-RM26 PET and the expression level of GRPR [155]. Several pilot clinical studies with ^{68}Ga-RM2 (^{68}Ga-labeled DOTA-4-amino-1-carboxymethyl-piperidine-D-Phe-Gln-Trp-Ala-Val-Gly-His-Sta-Leu-NH_2) also showed GRPR-PET may have a potential clinical role in the molecular imaging and TRT of prostate cancer [156–158]. ^{68}Ga-RM2 has the highest physiologic uptake in the pancreas followed by moderate uptake of the tracer in the liver, spleen, and urinary excretion [159]. It has garnered interest as a target for prostate theranostics, especially, due to the lack of salivary gland uptake which is prominently seen in ^{68}Ga-PSMA-PET. A recent study examined the use of [^{68}Ga]RM2-PET/CT (GRPR antagonist) in patients with known biochemical recurrence of prostate cancer and negative or equivocal [^{18}F]fluoroethylcholine-PET/CT and demonstrated that [^{68}Ga] RM2-PET/CT was helpful in localizing the recurrence in such cases [157, 159]. Based on a direct comparison with [^{18}F]DCFPyl-PET (Fig. 22.26) it was concluded that ^{68}Ga-RM2 remains a valuable radiopharmaceutical even when compared with the more widely used ^{68}Ga-PSMA11/^{18}F-DCFPyL in the evaluation of biochemical recurrence of prostate cancer [160]. The first clinical data with ^{68}Ga-NeoBOMB1 in a group of prostate cancer patients highlighted its ability to visualize primary tumors, as well as liver metastases and bone lesions [161].

A recent review suggests that GRPR-targeted imaging may constitute a relevant addition for those patients with PSMA-negative tumors, or those with low-grade tumors that do not show on MRI nor PSMA-PET scans because retrospective studies have revealed that PSMA expression was inversely correlated with GRPR, underscoring the potential value of their combined use [153].
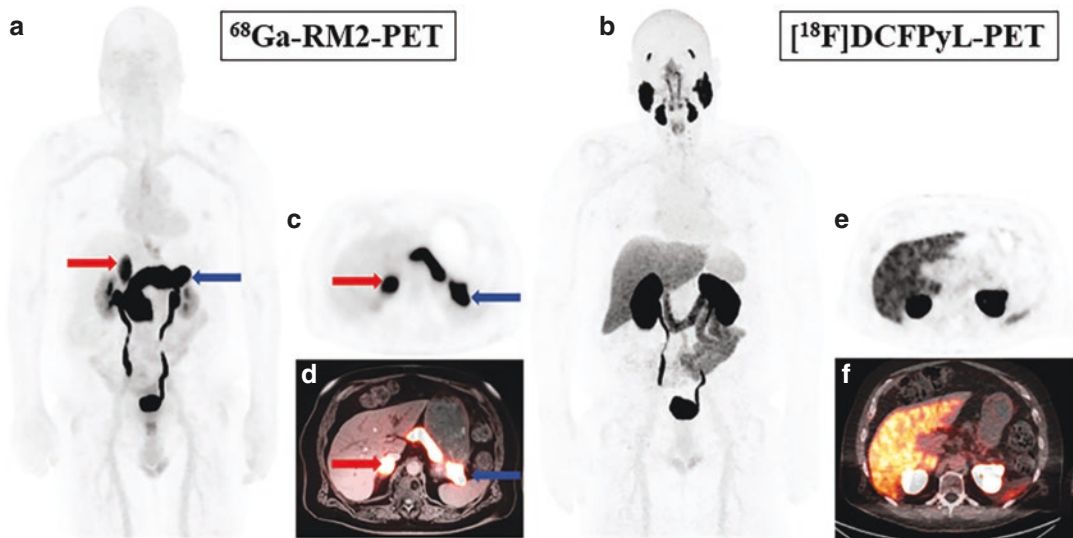
Fig. 22.26 Comparison of 68Ga-RM2-PET (bombesin analog for GRPR) with PSMA ligand, [18F]DCFPyL-PET in a patient presenting with prostate cancer biochemical recurrence (BCR) (PSA 11.6 ng/mL and PSA velocity 12.2 ng/mL/year). 68Ga-RM2 scans (**a**, **c**, **d**) compared to [18F]DCFPyL (**b**, **e**, **f**). Red arrows mark right adrenal lesion clearly seen on GRPR-PET but not prospectively identified on PSMA-PET given similar uptake in the adrenal gland and liver parenchyma. Blue arrows mark physiologic 68Ga-RM2 uptake in the pancreas [160]

22.5 Radiopharmaceuticals for Bone Pain Palliation

As discussed in Sect. 22.2.1, bone is the most common and preferred site for metastatic involvement in prostate cancer. The presence of bone metastases implies poorer prognosis, shortens survival, and is associated with a multitude of complications, including severe bone pain, pathological fracture, spinal cord compression, hypercalcemia, etc. [19]. Bone metastases in prostate cancers are typically characterized by an osteoblastic picture due to excess bone deposition [19].

Several radiopharmaceuticals were developed based on β^- emitting radionuclides, as shown in Table 22.3 [21, 162, 163]. Studies in radiobiology indicate that radiation doses delivered to bone metastases at higher dose rates would have a higher RBE. Therefore, the advantage of shorter-lived radionuclides at higher dose rates in comparison with longer lived radionuclides at lower dose rates will also depend on biokinetics of the radiopharmaceutical and how the dose rate in target tissue compares to the dose rate in critical organs [163]. These radiopharmaceuticals can broadly be classified into two categories based on the mechanism by which they get accumulated in the skeleton: Ca^{2+} analogs and diphosphonate complexes of radiometals due to the affinity of phosphonates towards calcium in the actively growing bone.

^{32}P as sodium orthophosphate administered orally (444 MBq) or intravenously (185 MBq) was used for the treatment of metastatic bone pain till the 1980s. ^{32}P is bound to hydroxyapatite of the inorganic bone matrix. In spite of its efficacious nature, the use of this agent declined owing due to the high energy β^- particle emission, which causes severe bone marrow toxicity including myelosuppression and pancytopenia [162]. Moreover, because of the radionuclide being a pure β^- particle emitter, simultaneous pharmacokinetic evaluation and dosimetric assessment cannot be done.

22.5.1 89Sr Dichloride (Metastron®)

The first use of ^{89}Sr for bone pain palliation was reported in 1942 [164]. Since it is a Ca^{2+} analog, $^{89}Sr^{2+}$ cation is internalized to the inorganic bone

matrix and the biochemical uptake is in proportion to local osteoblastic activity, which is tenfold higher in metastatic lesions. After localization, it still remains in the tumoral sites for 100 days. The excretion occurs predominantly from kidneys, limiting its use in the setting of renal failure. The recommended dose is 150 MBq. Based on the latest meta-analysis, an overall response rate of 70% has been reported, commencing typically within 14–28 days of administration and lasting up to 15 months [21]. The efficacy of ^{89}Sr chloride in bone pain palliation has been compared to other radiopharmaceuticals (such as [153]Sm-EDTMP and [186/188]Re-HEDP) revealing no significant difference. The hematological toxicity (myelosuppression) is the major side effect which is due to high energy β^- particles and like ^{32}P, it cannot be used for simultaneous pharmacokinetic evaluation and dosimetry studies.

22.5.2   Bisphosphonates: [153]Sm-EDTMP (Quadramet®)

The first clinical use of bone pain palliation with [153]Sm was reported in 1989 [165]. It is used with the chelator ethylenediamine tetramethylenephosphonate ([153]Sm-EDTMP), which is supplied as [153]Sm-lexidronam-pentasodium (Quadramet) (Fig. 22.3) with a recommended activity of 37 MBq/kg body weight. It is a well-known radiopharmaceutical for bone pain palliation and since it received FDA approval, it has been widely used in various osteoblastic metastatic lesions, especially in prostate and breast cancer. It has shown high uptake in the skeleton with $62 \pm 13\%$ at 24 h post-injection [163]. It rapidly binds to hydroxyapatite crystals, leading to less than 1% availability in the blood 5 h after injection. No specific uptake has been observed outside the skeleton, and excretion occurs mainly through the kidneys. The pharmacokinetics of [153]Sm-EDTMP is favored over [186]Re-HEDP with lower urinary excretion and potentially higher bone and lesion uptake [163]. Pain palliation is usually experienced within 1 week and frequently within 48 h of administration of [153]Sm-EDTMP. The pain reduction occurs as early as in the first week after injection, lasting for about 2–3 months [21]. Compared to ^{89}Sr, the moderate energy β^-emission reduces the possibility of bone marrow ablation and the adequate γ-emission of suitable energy of photons (103 keV) helps biodistribution and dosimetry studies. Overall, [153]Sm–EDTMP has been successfully used for pain control for three decades. One of the major drawbacks, however, is its relatively shorter half-life (46.3 h) which causes significant loss of activity due to radioactive decay in shipment.

22.5.2.1   Investigational Agents
Several other radiolabeled diphosphonates have been investigated in small clinical studies. [186/188]Re-HEDP complex behaves similar to ^{99m}Tc bone agents. Approximately 40% is localized in the skeleton at 24 h but, significantly less uptake compared to [153]Sm-EDTA. Repeated doses of [188]Re–HEDP, compared to a single administration, have shown improvement in PFS and OS, as well as a reduction of PSA levels in approximately half of the patients. The apparent antitumoral effect may be explained by higher β^- energy and tissue penetration, as well as a higher dose rate of [188]Re–HEDP administration due to very short physical half-life of 0.7 days [163]. I[188]Re-HEDP has not been approved in many countries for clinical use and the number of prospective trials with large populations is limited. The potential advantages include the availability of a long-lived on-site generator ([188]W→[188]Re), favorable pain control, the potential impact on OS, and cost-effectiveness.

^{177}Lu-EDTMP and ^{177}Lu-DOTAZOL
[177]Lu has been proposed as a possible radionuclide for bone pain palliation. It has the theoretical advantage of reduced bone marrow toxicity due to low energy beta particle energy and mean tissue range of 0.2 mm. ^{177}Lu–EDTMP has been studied as a safe and effective potential palliative therapy in painful bone metastases, due to rapid skeletal accumulation and minimal uptake in other organs. ^{177}Lu–DOTMP has also been investigated revealing rather similar characteristics to ^{177}Lu–EDTMP. Yet, the latter exhibits slightly higher skeletal uptake as well as retention in the liver and kidneys

[21]. ^{177}Lu-EDTMP has been compared to ^{153}Sm-EDTMP. Reportedly, they both have subjected bone metastases to similar radiation doses. Likewise, the response rate of approximately 75–80% has been noted for both radiopharmaceuticals. In addition, the cocktail of both these agents has shown safety in administration and pain relief/reduction in 24/25 patients [21]. ^{177}Lu labeled with zoledronic acid (^{177}Lu-DOTA^{ZOL}) (Fig. 22.3) is another investigational radiopharmaceutical with promising preliminary biodistribution and post-therapy dosimetry results. It also possesses a potential theragnostic application (using ^{68}Ga-DOTAZOL-PET) for the treatment of bone metastases [59, 60]. A recommended therapeutic activity was described with 45 MBq/kg for ^{177}Lu-EDTMP and higher activity of 5780 MBq for ^{177}Lu-DOTA^{ZOL}. A systematic review and meta-analysis conclude that ^{177}Lu-EDTMP seems to have a comparable efficacy and safety profile as that of the frequently administered radiopharmaceuticals for bone palliation [166].

22.6 Radiopharmaceuticals for Targeted Therapy

22.6.1 ^{223}Ra Dichloride (Xofigo)

^{223}Ra ($T_{1/2}$ = 11.4 days) decays to stable ^{207}Pb with five intermediate radionuclide progenies and a total of five α particles (Fig. 22.27). Currently, the clinical and commercial production of ^{223}RaCl$_2$ (Bayer Health Care Pharmaceuticals) involves ^{227}Ac and ^{227}Th isolation from a ^{231}Pa source (3.28 × 10^4 year) [167]. In 2013, [^{223}Ra]radium dichloride (Xofigo®; formerly alpharadin) became the first and only alpha-emitting radiopharmaceutical to receive FDA and EMEA approval for clinical use, with an intended purpose to treat patients with CRPC, symptomatic bone metastases, and no known visceral metastatic disease. ^{223}Ra^{2+} mimics calcium and forms complexes with the bone mineral hydroxyapatite at areas of increased bone turnover, such as bone metastases. The high LET (80 keV/μm) leads to a high frequency of DSDBs in adjacent cells, resulting in an antitumor effect on bone metastases. As shown in Table 22.5, the dose to metastatic lesions is around 25 Gy from one cycle of ^{223}Ra administration and is comparable to the dose from radiopharmaceuticals for bone pain palliation. The RBE effect, however, will be significantly higher compared to the beta emitters.

^{223}Ra dichloride injection is supplied as a single-use vial at a concentration of 1000 kBq/mL (27 microcurie/mL) at the reference date with a total radioactivity of 6000 kBq/vial (162 microcurie/vial) at the reference date. The recommended dose regimen of Xofigo is 50 kBq (1.35 microcurie) per kg body weight, given at 4-week intervals for six injections.

After intravenous injection, radium-223 is rapidly cleared from the blood and is distributed primarily into bone or is excreted into the intestine. At 4 h, about 4% of the injected radioactivity remained in blood, decreasing to <1% at 24 h after the injection. At 10 min post-injection, radioactivity was observed in bone and in the intestine. At 4 h, the bone uptake was 61% of the
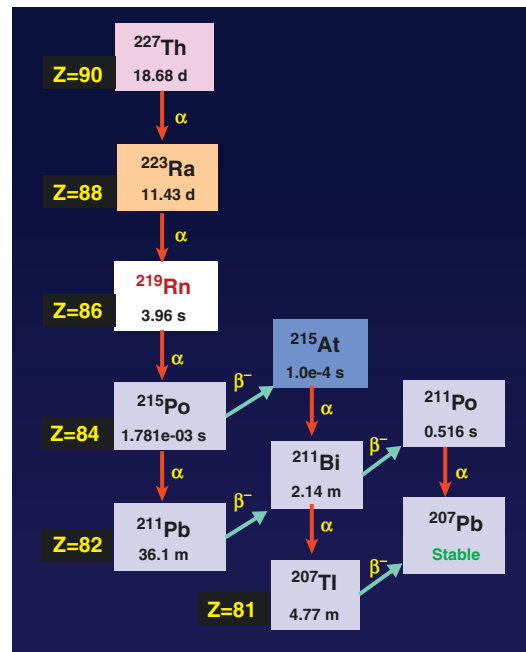
Fig. 22.27 Radium-223 is the daughter of Thorium-227. The decay scheme of Ra-223 shows both alpha and beta particle emissions before it reaches stable Pb-207

Table 22.5   Dosimetry[a] of radiopharmaceuticals for bone pain palliation

Radiopharmaceuticals	$T_{1/2}$ (Days)	B_{Emax} (MeV)	γ-Photons (keV)	Range (mm) Max	Range (mm) Mean	Dose (mMq)	Red marrow dose (mGy/MBq)	Bone Mets. (Gy)
[^{32}P]sodium orthophosphate	14.26	1.71		8.1	2.5	444	6.5	
^{89}Sr-dichloride	50.53	1.46	910 (0.01%)	6.6	1.9	150	19.0	0.03–50.0
^{153}Sm-EDTMP (*Quadramet*)	1.9292	0.81	103 (28%)	3.0	0.4	37/kg	0.89 ± 0.03	2.9–14.1
^{186}Re-HEDP	3.78	1.07	135 (9%)	4.5	0.8	1285	0.8	40.1
^{188}Re-HEDP	0.71	2.12	155 (15%)	10.45	2.8	~3000	0.61 ± 0.21	12.6 ± 6.6
^{177}Lu-EDTMP	6.71	0.49	113 (6%)	1.5	0.2	45/kg	0.80 ± 0.15	
^{177}Lu-DOTA^{ZOL}			208 (11%)			5780	0.36 ± 0.12	4.21 ± 2.4
^{223}Ra dichloride[b]	11.4	5–7.5 MeV α		<0.1 mm		0.05/kg	139.0	25.6

[a] Dosimetry values from Liepe et al. [163]

[b] The dosimetry data for ^{223}Ra is from Xofigo package insert

administered activity. Approximately 63% of the administered radioactivity was excreted from the body within 7 days after injection (after correcting for decay). Fecal excretion is the major route of elimination from the body (Xofigo-2013 PI).

The efficacy and safety of Xofigo were evaluated in a double-blind, randomized, placebo-controlled phase 3 clinical trial of patients with CRPC with symptomatic bone metastases. Patients receiving the treatment with ^{223}Ra exhibited a 3.6-month prolonged survival time (PST) over the placebo group and a 5.8 month improved timeframe before the occurrence of a systematic skeletal-related event with a reduction of occurrence of spinal compression [168, 169].

22.6.2 RIT with ^{177}Lu- or ^{225}Ac-Labeled J591 mAb

As discussed in Sect. 22.4.6.2, the clinical trials with ^{90}Y- or ^{177}Lu-labeled huJ591 mAbs started 20 years ago at Weill Cornell Medicine in New York. Two independent RIT phase I trials have been performed using ^{90}Y- or ^{177}Lu-labeled DOTA-huJ591 in patients with mCRPC [101, 170, 171]. All patients received a total of 20 mg of J591 mAb containing both radiolabeled DOTA-J591 and naked J591 mAb. These trials defined the maximum tolerated dose (MTD),

dosimetry, pharmacokinetics, and human anti-humanized antibody (HAHA) response, and demonstrated preliminary evidence of antitumor activity. With ^{90}Y, 0.647 GBq/m^2 dose level was determined to be the MTD. With ^{177}Lu, 2.59 GBq/m^2 dose level was determined to be the MTD. ^{177}Lu was chosen for further development based upon its physical properties, especially since the low energy beta particles deliver a lower radiation dose to bone marrow relative to the higher energy beta particles from ^{90}Y [102–104].

22.6.2.1 RIT with ^{177}Lu-DOTA-huJ591 mAb

In a dual-center phase II study, two cohorts of patients (total $n = 47$) with progressive mCRP received one dose of ^{177}Lu-J591 (2.405 GBq/m^2, or 2.59 GBq/m^2). Sites of prostate cancer metastases were targeted in 94% of patients as determined by planar imaging. All patients experienced reversible hematologic toxicity with grade 4 thrombocytopenia occurring in 47% of patients. In atients ($n = 32$) who received a single dose of 2.59 GBq/m^2, >30% PSA decline was observed in 47% of patients, and longer survival of 21.8 months [137, 138]. The safety and efficacy data of phase II study are summarized in Table 22.6.

Dose fractionation is a practical strategy to decrease the dose to bone marrow while increasing the cumulative radiation dose to the tumor at

an optimal dose rate [102–104, 174]. A phase I/II clinical study with a phase I dose escalation component followed by phase IIa dosing was performed using two dosing cohorts selected for exploration (2.96 GBq and 3.33 GBq/m^2 total dose divided into two doses 2 weeks apart). As demonstrated before, there appeared to be a dose-dependent response for PSA decline and overall survival. At the highest cumulative dose (3.33 GBQ/m^2), 35% of patients had reversible grade 4 neutropenia, and 58.8% of patients had thrombocytopenia. This dose showed a greater PSA decline with a median survival of 3.5 years [175, 176]. The safety and efficacy data are given in Table 22.6. In addition, those with lower PSMA uptake on ^{177}Lu SPECT had lower likelihood of significant PSA decline.

In order to evaluate the value of combination therapy, a phase 1 clinical study tested the therapeutic value of combination of docetaxel chemotherapy with fractionated dose ^{177}Lu-J591 mAb therapy [177]. In a pilot study 15 patients with mCRPC received standard docetaxel (75 mg/m^2) in 21-day cycles, with cohorts receiving escalating fractionated doses of ^{177}Lu-J591 during cycle 3 (highest planned total dose 80 mCi/m^2). This study demonstrated the safety of the combination with early evidence of activity, with 73% achieving >50% PSA decline. Toxicities were comparable to prior ^{177}Lu-J591 studies [177]. Although 2-dose fractionation appears attractive alone or with docetaxel a pilot study explored the value of "hyper-fractionated" ^{177}Lu-J591 in which low-dose ^{177}Lu-J591 (25 mCi/m^2) was administered every 2 weeks until greater than grade 2 toxicity

emerged [178]. As designed, dosing was limited by myelosuppression (especially thrombocytopenia) but, the regimen did not appear more favorable than 2-dose fractionation and is also less convenient for patients, so the regimen is not being further explored.

22.6.2.2 RIT with ^{225}Ac-DOTA-huJ591 mAb

Twenty years ago, ^{213}Bi-J591 was proposed as a radiopharmaceutical for α-particle therapy of prostate cancer [179]. While ^{213}Bi demonstrated promising efficacy in the preclinical setting, it is not an appropriate radionuclide for whole IgG mAb with a longer circulation time. An alternative to ^{213}Bi was to utilize its parent nuclide, ^{225}Ac, which has a 10-day half-life and 5 net α particles and 3 beta particles per decay (Fig. 22.28). Also, as a trivalent metal, ^{225}Ac binds to the same DOTA chelator like ^{177}Lu.

Based on human biodistribution data, and assuming RBE for alpha emitters is 5, the radiation dosimetry calculations suggested that administration of 6.06 MBq (164μCi) of ^{225}Ac-J591 mAb may deliver ~2.0 Gy to bone marrow. A phase I dose escalation study was designed to determine the dose-limiting toxicity (DLT) and the maximum tolerated dose (MTD) of ^{225}Ac-J591 in a single dose regimen [180, 181]. Patients received doses starting from 13.3 kBq/kg to a maximum of 93.3 kBq/kg (for an average person of 75 kg, the maximum dose administered is 7 MBq). Thirty-two patients with progressive mCRPC were treated with ^{225}Ac-J591 in this protocol. In the dose escalation phase of the study,

Table 22.6 Safety and Efficacy of RIT in mCRP with ^{177}Lu-huJ591: PSA decline and toxicity

Response	Single dose		Cumulative dose given in two doses		
	2.405 GBq/m^2	2.59 GBq/m^2	1.48–2.59 GBq/m^2	2.96 GBq/m^2	3.33 GBq/m^2
Number of patients (*n*)	15	32	16	16	17
Any PSA decline (%)	46.7	65.6	37.5	50.0	87.5
>30% PSA decline (%)	13.3	46.9	12.5	25.0	58.8
>50% PSA decline (%)	6.7	12.5	6.3	12.5	29.4
Median survival (months)	*11.9*	*21.8*	*14.6*	*19.6*	*42.3*
Platelets grade-4	27.0	56.3	20.0	43.8	58.8
Platelet transfusion	7.0	41.0	0.0	31.3	52.9
Neutropenia grade-4	0.0	37.5	0.0	31.3	29.4
Febrile neutropenia	0.0	2.1	0.0	0.0	5.8

there was one patient who had grade 4 thrombocytopenia and anemia. However, there was no MTD, and the recommended phase 2 dose of the compound is 93.3 kBq/kg. Overall, 68.8% of patients had at least some level of PSA decline

and 43.8% had a PSA decline of over 50%. The median biochemical progression-free survival in the entire population was 5.1 months and the median overall survival was 11.1 months. There were no cases of severe xerostomia. The study concluded that PSMA targeting with ^{225}Ac-J591 mAb is tolerable with early evidence of clinical activity (Fig. 22.29) in a pretreated population with favorable patient-reported outcomes. Studies administering multiple or subsequent doses and/or combination therapy are underway.
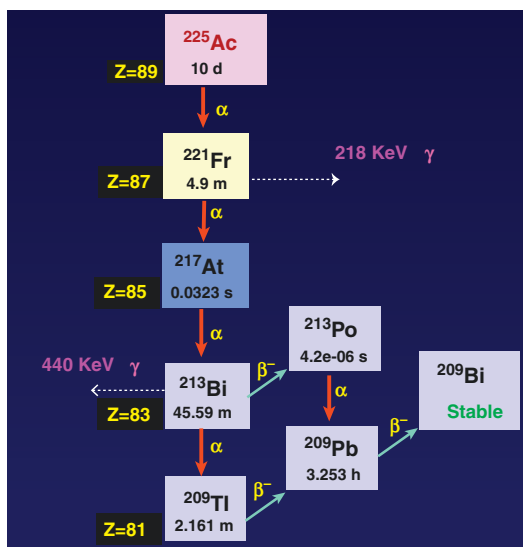
Fig. 22.28 The decay scheme of Ac-225 shows both alpha and beta particle emissions before it reaches stable Bi-209. The gamma photons for the daughters Fr-221 and Bi-213 are used to identify Ac-225 when the parent and daughters are in secular equilibrium

22.6.3 Small-Molecule PSMA Inhibitors

22.6.3.1 Lu 177 Vipivotide Tetraxetan (Pluvicto, ^{177}Lu-PSMA-617)

As discussed in Sect. 22.4.7.3, the design and synthesis of PSMA-617 was reported in 2015 by the Heidelberg group. Based on ^{68}Ga-PSMA-617 PET scan, they demonstrated the PSMA targeting potential of PSMA-617 [136]. The first clinical experience with ^{177}Lu-PSMA-617 targeted therapy in patients with advanced mCRPC resistant to or with contraindications to other conventional therapies and PSMA-positive tumor phenotypes demonstrated that ^{177}Lu-PSMA-617
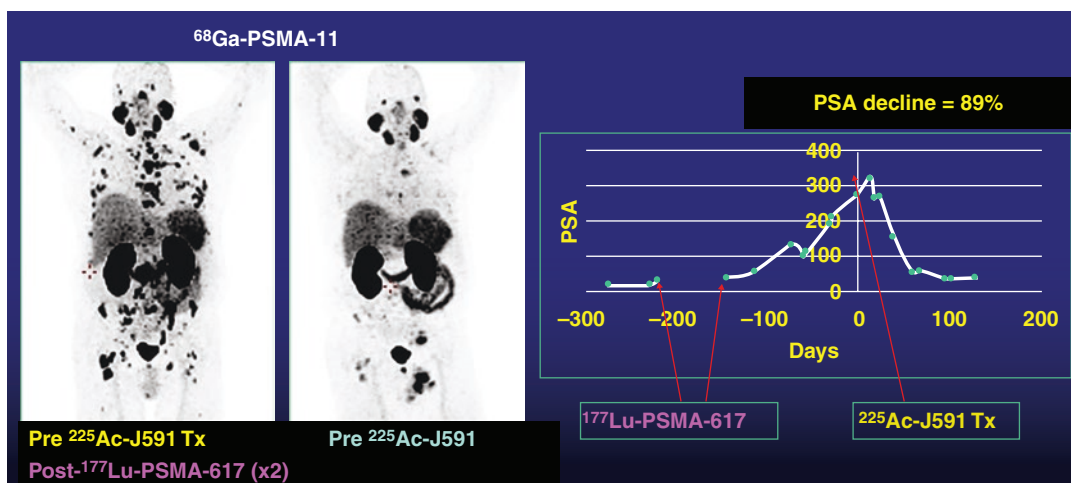
Fig. 22.29 ^{225}Ac-J591 mAb targeted therapy in a patient with mCRPC. The patient had prior treatment with 2 cycles of ^{177}Lu-PSMA-617 and when the disease was progressive received 4 MBq of 225Ac-J591. 68Ga-PSMA PET

scans before and after treatment show evidence of treatment response. The patient also had 86% decline in PSA level. (Images provided by Dr. Tagawa at Weill Cornell Medicine, NY)

^{68}Ga-PSMA	^{177}Lu-PSMA-617	^{177}Lu-PSMA-617	^{177}Lu-PSMA-617	^{99m}Tc-MIP-427
a	**b**	**c**	**d**	**e**
12/2014	12/2014	02/2015	04/2015	06/2015
PSA 387 ng/mL	PSA 387 ng/mL	PSA 9.24 ng/mL	PSA 1.98 ng/mL	PSA 1.08 ng/mL
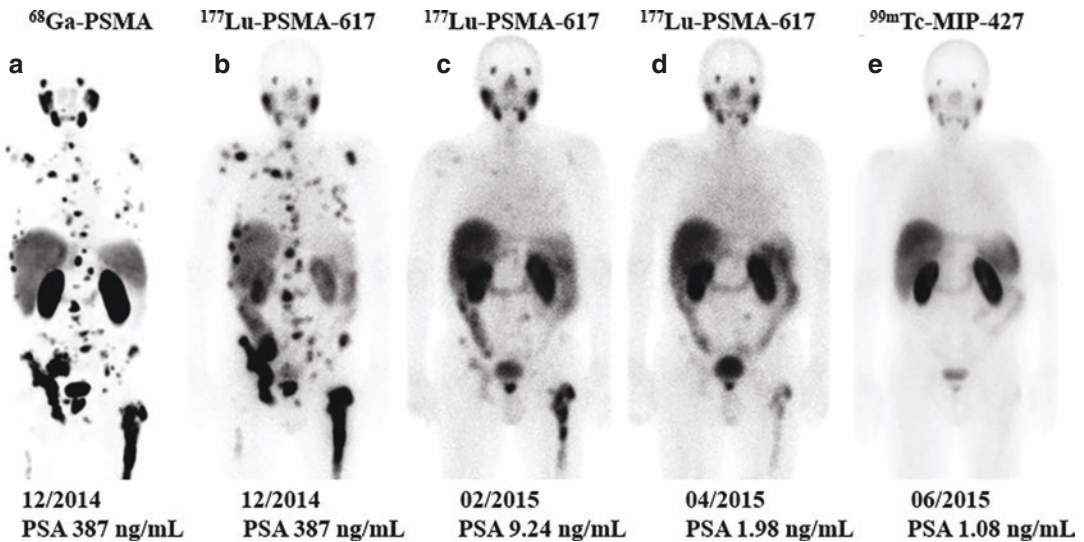
Fig. 22.30 ^{177}Lu-PSMA-617 therapy in a patient with PSMA-positive mCRPC (6 GBq/cycle, 3 cycles 2 months apart). Scan (**a**) represents 68Ga-PSMA-PET; scans (**b–d**) represent planar images after ^{177}Lu therapy dose. Scan (**e**) represents planar image with ^{99m}Tc-PSMA tracer. Scans (**c–e**) show good response to ^{177}Lu-PSMA-617 therapy [182, 183]

is a promising new option for therapy of mCRPC (Fig. 22.30) [182, 183]. Thirty patients received 1–3 cycles of ^{177}Lu-PSMA-617 (4 or 6 GBq/cycle). Dosimetry studies revealed kidney doses (~0.75 Gy/GBq), red marrow doses (0.03 Gy/GBq), and salivary gland doses (1.4 Gy/GBq), irrespective of tumor burden and consistent on subsequent cycles. Mean tumor-absorbed dose ranged from 6 to 22 Gy/GBq during the first cycle.

To assess the benefit of higher ^{177}Lu dose rate on the safety, a phase 1/II dose escalation study of fractionated dose of ^{177}Lu-PSMA-617 for progressive mCRPC was conducted at Weill Cornell Medicine in New York. Patients received two doses of ^{177}Lu-PSMA-617 in a cycle (cumulative dose of 7.4–22 GBq), 2 weeks apart. The study concluded that a single fractionated cycle of up to 22.2 GBq of ^{177}Lu-PSMA-617 is safe, with encouraging early efficacy signals, even without selection for PSMA expression by imaging. A trend for dose-response was observed [175, 176].

A single-arm, single-center phase 2 trial was performed in patients with mCRPC who progressed after standard treatments [184]. Fifty eligible patients received 7.5 GBq/cycle, 4 cycles at six weekly intervals. The study concluded that treatment with [^{177}Lu]-PSMA-617 has high response rates, low toxic effects, and reduction of pain in men with mCRPC who have progressed after conventional treatments. A randomized, multicenter open label phase 2 trial (TheraP trial) compared the efficacy of ^{177}Lu-PSMA-617 with cabazitaxel in patients with mCRPC [185]. The study results showed that ^{177}Lu-PSMA-617 treatment compared to cabazitaxel led to a higher PSA response and fewer grade 3 or 4 adverse events.

The VISION trial (Funded by Endocyte, a Novartis company) evaluated the advantages of ^{177}Lu-PSMA-617 over best supportive care in improving the overall survival (OS) and image-based progression-free survival (PFS) in patients with progressive mCRPC [186, 187]. Five hundred and fifty-one patients were allotted to the ^{177}Lu-PSMA-617 group (who received 7.4 GBq of ^{177}Lu-PSMA-617 every 6 weeks in 4–6 cycles), while 280 patients were in the standard of care (SOC) group. The results of the study report that the median PFS was significantly longer among patients in the ^{177}Lu-PSMA-617 arm at 8.7 months compared with 3.4 months in patients in the SOC-

alone arm. There was a significant improvement in the OS in the patients who received ^{177}Lu-PSMA-617 compared to standard care alone (15.3 months vs. 11.3 months). Around 46% (vs. 7.1% in control group) of the patients had >50% reduction and >33% (vs. 2% in control group) patients had >80% reduction in the PSA levels (SOC). The FDA granted priority review to NDA for ^{177}Lu-PSMA-617 to treat patients with metastatic castration-resistant prostate cancer (mCRPC) who have previously received androgen receptor pathway and taxane-based chemotherapy.

In March 2022, the US FDA approved Lu 177 vipivotide tetraxetan for the treatment of patients with metastatic castration-resistant prostate cancer in the post-androgen receptor pathway inhibition, post-taxane-based chemotherapy setting.

22.6.3.2 ^{177}Lu-PSMA-I&T

As discussed in Sect. 22.4.7.3, PSMA-I&T was developed using DOTAGA chelator to facilitate labeling with ^{68}Ga or [177]Lu. Compared to DOTA, the DOTAGA chelator has one extra carboxylic acid group which improves the stability of the radiometal complex. Several clinical studies quickly demonstrated the therapeutic potential of ^{177}Lu-PSMA-I&T [188–190]. Subsequently, ^{177}Lu-PSMA-I&T was evaluated in PSMA-positive patients with mCRPC under a compassionate use protocol [191]. One hundred patients received ^{177}Lu dose (7.4 GBq/cycle) every 6–8 weeks up to six cycles. PSA decline of ≥50% was achieved in 38 patients, median clinical PFS was 4.1 months, and median OS was 12.9 months.

A phase III, Open-Label, randomized study evaluating mCRPC treatment using ^{177}Lu-PSMA-I&T (also known as [Lu-177]-PNT2002) was performed after second-line hormonal treatment (SPLASH) (NCT04647526) (sponsored by Point Biopharma). The primary objective of the study is to determine the efficacy of ^{177}Lu therapy vs. abiraterone or enzalutamide in delaying radiographic progression in patients with mCRPC. PSMA-positive patients ($n = 390$) will be ran-

domized in a 2:1 ratio to receive either PNT2002 (Arm A), or enzalutamide or abiraterone (Arm B). All patients will be followed long-term for at least 5 years following the first therapeutic dose.

22.6.3.3 Dosimetry of ^{177}Lu-PSMA Ligands

Several studies reported radiation dosimetry results of ^{177}Lu-PSMA therapy with favorable outcomes [192]. Table 22.7 shows a summary of absorbed doses to several organs and tissues based on published data for both PSMA-617 and PSMA-I&T ligands. The studies used different dosimetry methods (whole body vs. SPECT/CT; MIRD (medical internal radiation dose) vs. voxel-based dosimetry) or molecules (PSMA-617 vs. I&T), which made the results heterogeneous. The usage of whole-body imaging for dosimetry could cause the overestimation of the absorbed organ doses, while studies based on SPECT/CT reported lower doses [192]. Based on the dosimetry data, the minimum and maximum organ doses from six cycles of [177]Lu (7.4 GBq/cycle) were estimated as shown in Table 22.7. Lacrimal glands may receive a minimum of 124 Gy and the general accepted limit is 40 Gy for lacrimal glands.

Table 22.7 Absorbed dose estimates for ^{177}Lu-labeled PSMA-617 and PSMA-I&T ligands

Organ/tissue	Absorbed radiation dose		Threshold dose[a] (Gy)
	Gy/GBq	Gy/44.4 GBQ[b]	
Lacrimal glands	2.80–3.8	124–167	34
Salivary glands	0.44–1.4	19–62	20
Kidney	0.39–0.99	17–44	23
Liver	0.10–0.36	4.4–16	32
Spleen	0.06–0.10	2.6–4.4	
Bone marrow	0.002–0.11	0.09–4.8	2.0
Tumor	3.2–13.1	141–576	

[a] Current thresholds of absorbed organ doses were defined based on external beam radiotherapy (EBRT) literature
[b] The absorbed doses to several organs is from Sanli et al. [192]

22.6.3.4 ^{225}Ac-PSMA-617 and ^{225}Ac-PSMA-I&T

In order to increase DNA damage, the investigators from Heidelberg introduced ^{225}Ac-PSMA-617 for α-particle therapy with substantial therapeutic efficacy which has the potential to overcome resistance to therapy based on β^- emitting nuclides [182, 183, 193–196]]. In a preliminary study, in which patients with mCRPC were treated with ~8 MBq (0.1 MBq/kg) every 2 months showed highly promising results (Fig. 22.31), with a PSA decline of at least 50% in 63% of patients and any PSA response in 87% of patients. The median duration of tumor control was 9.0 months and 5 patients (13%) had enduring responses of >2 year following complete remission of PSA. Some of the patients experienced hematological grade 3/4 toxicities, while all patients experienced at least grade 1–2 xerostomia [193] Another study in chemotherapy-naïve mCRPC patients (*n* = 17) reported an overall PSA decline of at least 50% in 88% of patients, while maintaining low toxicity [195].

The first clinical results for PSMA-targeted α-therapy using ^{225}Ac-PSMA-I&T in advanced mCRPC patients (*n* = 14) showed a promising antitumor effect, highly comparable to the data with ^{225}Ac-PSMA-617 therapy [197]. In 14 patients, ^{225}Ac-PSMA-I&T dose (6–8.5 MBq) was given in 1–5 cycles and a total of 34 cycles was given. PSA decline of >50% was observed in 50% of patients and any PSA decline was observed in 78% of patients.

The limited clinical data with ^{225}Ac-labeled PSMA inhibitors indicate that alpha therapy of mCRPC is promising and that several potential clinical situations in early- and end-stage disease could potentially benefit from ^{225}Ac therapy. Further evaluation and clinical study design strategies, however, need to be optimized to minimize toxicity and improve efficacy.

22.7   Combination Therapy

A combination therapy strategy employing two or more distinct therapeutic approaches in cancer management is aimed at circumventing tumor
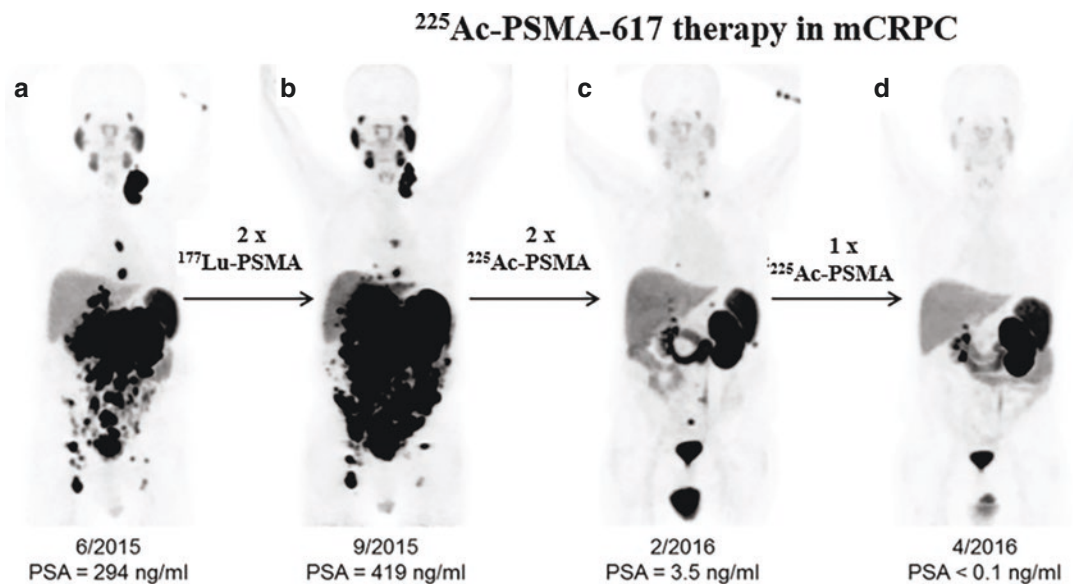
Fig. 22.31 ^{225}Ac-PSMA-617 therapy in a patient presented with peritoneal carcinomatosis and liver metastases that were progressive under ^{177}Lu-PSMA-617 therapy. The patient received 3 cycles of 6.4 MBq (100 kBq per kilogram of body weight) at bimonthly intervals. ^{68}Ga-PSMA-PET scans before (**a**, **b**) and after ^{225}Ac treatment (**c**, **d**) showed impressive response [182, 183]

resistance by simultaneously targeting compensatory signaling pathways or bypassing survival selection mutations acquired in response to individual monotherapies. Combination radionuclide therapy (CRT) is a newer application of the concept, utilizing a combination of radiolabeled molecular targeting agents with chemotherapy and beam radiation therapy for enhanced therapeutic index [198, 199].

The clinical studies based on PSMA-targeted radionuclide therapy based on both β^- and α emitting radionuclides have clearly documented that ~30% of patients, especially with bone metastasis, do not respond at all or develop resistance to TRT. The potential benefits of combining β^- and α emitting PSMA-targeted radiopharmaceuticals (also called tandem TRT) or combining targeted radiopharmaceuticals with chemotherapy or immunotherapy need to be explored to improve the efficacy of TRT and at the same time reducing the toxicity to normal organs.

The DLT with RIT is hematologic toxicity but, with small-molecule PSMA inhibitors, and the DLT is due to the absorbed dose to lacrimal glands and parotids. Combination of radiolabeled antibodies and peptides may be a practical strategy to enhance the tumor dose and reduce toxicity to normal organs. At Weill Cornell Medicine in New York, the combination of ^{225}Ac-J591 mAb with ^{177}Lu-PSMA-I&T is currently studied in a phase I/II protocol in patients with progressive mCRPC (NCT04886986). The two primary objectives of this trial are to determine the highest dose (MTD) of ^{225}Ac-J591 and ^{177}Lu-PSMA-I&T that can be administered together and to determine the effectiveness of the drug combination. The phase I component is a 3 + 3 dose escalation design, with maximum two cohorts. ^{177}Lu-PSMA-I&T will be given at a fixed dose of 6.8 GBq. ^{225}Ac-J591 will be given starting at 30 kBq/kg, with a subsequent dose escalation by an increment of 10–40 kBq/kg. The two drugs will be administered every 8 weeks, for two cycles. Once the maximum tolerated dose has been established, the phase II component of the trial will enroll up to 24 patients.

References

1. Siegel RL, Miller KD, Jemal A. Cancer statistics, 2021. CA Cancer J Clin. 2021;71:7–33.
2. Lilja H, Ulmert D, Vickers AJ. Prostate-specific antigen and prostate cancer: prediction, detection and monitoring. Nat Rev Cancer. 2008;8:268–78.
3. Logothetis C, Morris MJ, Den R, Coleman RE. Current perspectives on bone metastases in castrate-resistant prostate cancer. Cancer Metastasis Rev. 2018;37:189–96.
4. Augello MA, Den RB, Knudsen KE. AR function in promoting metastatic prostate cancer. Cancer Metastasis Rev. 2014;33:399–411.
5. Carver BS. Strategies for targeting the androgen receptor axis in prostate cancer. Drug Discov Today. 2014;19:1493–7.
6. Abou D, Benabdallah N, Jiang W, et al. Prostate cancer theranostics – an overview. Front Oncol. 2020;10:884.
7. Litwin MS, Tan H-J. The diagnosis and treatment of prostate cancer, a review. JAMA. 2017;317(24):2532–42.
8. Nuhn P, De Bono JS, Fizazi K, et al. Update on systemic prostate cancer therapies: management of metastatic castration-resistant prostate cancer in the era of precision oncology. Eur Urol. 2019;75:88–99.
9. Boettcher AN, Usman A, Morgans A, et al. Past, current, and future of immunotherapies for prostate cancer. Front Oncol. 2019;9:884.
10. Cattrini C, Castro E, Lozano R, et al. Current treatment options for metastatic hormone-sensitive prostate cancer. Cancers. 2019;11:1355.
11. Moreira DM, Howard LE, Sourbeer KN, et al. Predicting time from metastasis to overall survival in castration-resistant prostate cancer: results from SEARCH. Clin Genitourin Cancer. 2016;15:60–66.e2.
12. Czerwinska M, Bilewicz A, Kruszewski M, et al. Targeted radionuclide therapy of prostate cancer—from basic research to clinical perspectives. Molecules. 2020;25:1743–75.
13. Neels OC, Kopka K, Liolios C, Afshar-Oromieh A. Radiolabeled PSMA inhibitors. Cancers. 2021;2021(13):6255.
14. Piron S, Verhoeven J, Vanhove C, et al. Recent advancements in [^{18}F]F-labeled PSMA targeting PET radiopharmaceuticals. Nucl Med Biol. 2022;106–107:29–51.
15. Sandhu S, Guo C, Hofman MS. Radionuclide therapy in prostate cancer: from standalone to combination PSMA theranostics. J Nucl Med. 2021;62:1660.
16. Savit-Baruch B, Werner RA, Towe SP, Schuster DM. PET imaging for prostate cancer. Radiol Clin N Am. 2021;59(5):801–11.
17. Vallabhajosula S, Polack BD, Babich JW. Molecular imaging of prostate cancer: radiopharmaceuticals for positron emission tomography (PET) and single-

photon emission computed tomography (SPECT). In: Precision molecular pathology of prostate cancer. Berlin: Springer; 2018. p. 475–501.

18. Zhang H, Koumna S, Pouliot F, Beauregard JM, Kolinsky M. PSMA theranostics: current landscape and future outlook. Cancers. 2021;13:23.

19. Handkiewicz-Junak D, Poeppel TD, Bodei L, et al. EANM guidelines for radionuclide therapy of bone metastases with beta-emitting radionuclides. Eur J Nucl Med Mol Imaging. 2018;45:846–59.

20. Pandit-Taskar N, Batraki M, Divgi CR. Radiopharmaceutical therapy for palliation of bone pain from osseous metastases. J Nucl Med. 2004;45:1358–65.

21. Manafi-Farid R, Masoumi F, Divband G, et al. Targeted palliative radionuclide therapy for metastatic bone pain. J Clin Med. 2020;9:2622. https://doi.org/10.3390/jcm9082622.

22. Messner EA, Steele TM, Tsamouri MM, et al. The androgen receptor in prostate cancer: effect of structure, ligands and spliced variants on therapy. Biomedicine. 2020;8:422.

23. Shafi AA, Yen AE, Weigel NL. Androgen receptors in hormone-dependent and castration-resistant prostate cancer. Pharmacol Ther. 2013;140:223–38.

24. Fox JJ, Gavane SC, Blanc-Autran E, et al. Positron emission tomography/computed tomography–based assessments of androgen receptor expression and glycolytic activity as a prognostic biomarker for metastatic castration-resistant prostate cancer. JAMA Oncol. 2018;4(2):217–24.

25. Larimer BM, Dubois F, Bloch E, et al. Specific 18F-FDHT accumulation in human prostate cancer xenograft murine models is facilitated by prebinding to sex hormone-binding globulin. J Nucl Med. 2018;59:1538–43.

26. Larson SM, Morris M, Gunther I, et al. Tumor localization of 16beta-18F-fluoro-5alpha-dihydrotestosterone versus 18F-FDG in patients with progressive, metastatic prostate cancer. J Nucl Med. 2004;45(3):366–73.

27. Boers J, Venema CM, de Vries EFJ, et al. Serial [18F]-FDHT-PET to predict bicalutamide efficacy in patients with androgen receptor positive metastatic breast cancer. Eur J Cancer. 2021;144:151–61.

28. Katzenellenbogen JA. PET imaging agents (FES, FFNP, and FDHT) for estrogen, androgen, and progesterone receptors to improve management of breast and prostate cancers by functional imaging. Cancers. 2021;12:2020. https://doi.org/10.3390/cancers12082020.

29. O'Keefe DS, Su SL, Bacich DJ, et al. Mapping, genomic organization and promoter analysis of the human prostate-specific membrane antigen gene. Biochim Biophys Acta. 1998;1443:113–27.

30. Evans JC, Malhotra M, Cryan JF, O'Driscoll CM. The therapeutic and diagnostic potential of the prostate specific membrane antigen/glutamate carboxypep-

tidase II(PSMA/GCPII) in cancer and neurological disease. Br J Pharmacol. 2016;2016:1733041–307.

31. Bařinka C, Rojas C, Slusher B, Pomper M. Glutamate carboxypeptidase II in diagnosis and treatment of neurologic disorders and prostate cancer. Curr Med Chem. 2012;19:856.

32. Israeli RS, Powell CT, Fair WR, Heston WD. Molecular cloning of a complementary DNA encoding a prostate specific membrane antigen. Cancer Res. 1993;53:227–30.

33. Evans MJ, Smith-Jones PM, Wongvipat J, et al. Noninvasive measurement of androgen receptor signaling with a positron-emitting radiopharmaceutical that targets prostate-specific membrane antigen. Proc Natl Acad Sci U S A. 2011;108:9578–82.

34. Wright GL, Grob BM, Haley C, et al. Upregulation of prostate-specific membrane antigen after androgen-deprivation therapy. Urology. 1996;48:326–34.

35. Horoszewicz JS, Kawinski E, Murphy GP. Monoclonal antibodies to a new antigenic marker in epithelial prostatic cells and serum of prostatic cancer patients. Anticancer Res. 1987;7:927–35.

36. Israeli RS, Powell CT, Corr JG, Fair WR, Heston WD. Expression of the prostate-specific membrane antigen. Cancer Res. 1994;54:1807–11.

37. Wright GL Jr, Haley C, Beckett ML, Schellhammer PF. Expression of prostate-specific membrane antigen (PSMA) in normal, benign and malignant prostate tissues. Urol Oncol. 1995;1:18–28.

38. Wright GL, Grob B, Haley C, et al. Upregulation of prostate-specific membrane antigen after androgen-deprivation therapy. Urology. 1998;48:326–34.

39. Troyer JK, Beckett ML, Wright GL. Location of prostate-specific membrane antigen in the LNCaP prostate carcinoma cell line. Prostate. 1997;1997(30):232–42.

40. Liu H, Rajasekaran AK, Moy P, et al. Constitutive and antibody-induced internalization of prostate-specific membrane antigen. Cancer Res. 1998;58:4055–60.

41. Liu H, Moy P, Kim S, et al. Monoclonal antibodies to the extracellular domain of prostate-specific membrane antigen also react with tumor vascular endothelium. Cancer Res. 1997;57:3629–34.

42. Smith-Jones PM, Vallabahajosula S, Goldsmith SJ, et al. In vitro characterization of radiolabeled monoclonal antibodies specific for the extracellular domain of prostate-specific membrane antigen. Cancer Res. 2000;60:5237–43.

43. Pastorino S, Riondato M, Uccelli L, et al. Toward the discovery and development of PSMA targeted inhibitors for nuclear medicine applications. Curr Radiopharm. 2020;13:63–79.

44. Kozikowski AP, Nan F, Conti P, et al. Design of remarkably simple, yet potent urea-based inhibitors of glutamate carboxypeptidase II (NAALADase). J Med Chem. 2001;44:298–301.

45. Schroeder RPJ, van Weerden WM, Krenning EP, et al. Gastrin-releasing peptide receptor-based targeting

using bombesin analogues is superior to metabolism-based targeting using choline for in vivo imaging of human prostate cancer xenografts. Eur J Nucl Med Mol Imaging. 2011;38:1257–66.

46. Körner M, Waser B, Rehmann R, Reubi JC. Early over-expression of GRP receptors in prostatic carcinogenesis. Prostate. 2014;74:217–24.

47. Ischia J, Patel O, Bolton D, Shulkes A, Baldwin GS. Expression and function of gastrin-releasing peptide (GRP) in normal and cancerous urological tissues. BJU Int. 2014;113:40–7.

48. Aprikian AG, Tremblay L, Han K, Chevalier S. Bombesin stimulates the motility of human prostate-carcinoma cells through tyrosine phosphorylation of focal adhesion kinase and of integrin-associated proteins. Int J Cancer. 1997;72:498–504.

49. Baratto L, Jadvar H, Iagaru A. Prostate cancer theranostics targeting gastrin-releasing peptide receptors. Mol Imaging Biol. 2018;20:501–9.

50. Filippi L, Frantellizzi V, Chiaravalloti A, et al. Prognostic and theranostic applications of positron emission tomography for a personalized approach to metastatic castration-resistant prostate cancer. Int J Mol Sci. 2021;22:3036.

51. O'Donoghue JA, Bardiés M, Wheldon TE. Relationships between tumor size and curability for uniformly targeted therapy with beta-emitting radionuclides. J Nuci Med. 1995;36:1902–9.

52. Hall EJ. Radiation, the two-edged sword: cancer risks at high and low doses. Cancer J. 2000;6:343–50.

53. Hall EJ. Molecular biology in radiation therapy: the potential impact of recombinant technology on clinical practice. Int J Radiat Oncol Biol Phys. 1994;30:1019–28.

54. Subramanian G, McAfee JG, Thomas FD, et al. New diphosphonate compounds for skeletal imaging: comparison with methylene diphosphonate. Radiology. 1983;149(3):823–8.

55. Wong KK, Piert M. Dynamic bone imaging with ^{99m}Tc-labeled diphosphonates and ^{18}F-NaF: mechanisms and applications. J Nucl Med. 2013;54:590–9.

56. Helyar V, Mohan HK, Barwick T, et al. The added value of multi-slice SPECT/CT in patients with equivocal bony metastasis from carcinoma of the prostate. Eur J Nucl Med Mol Imaging. 2010;37(4):706–13.

57. Dennis ER, Jia X, Mezheritskiy IS, et al. Bone scan index: a quantitative treatment response biomarker for castration-resistant metastatic prostate cancer. J Clin Oncol. 2012;30(5):519–24.

58. Fernandez R, Eppard E, Lehnert W, et al. Evaluation of safety and dosimetry of ^{177}Lu-DOTA-ZOL for therapy of bone metastases. J Nucl Med. 2021;62:1126–32.

59. Khawar A, Eppard E, Roesch F, et al. Preliminary results of biodistribution and dosimetric analysis of [^{68}Ga]Ga-DOTAZOL: a new zoledronate-based bisphosphonate for PET/CT diagnosis of bone diseases. Ann Nucl Med. 2019;33:404–13.

60. Khawar A, Eppard E, Roesch F, et al. Biodistribution and post-therapy dosimetric analysis of [^{177}Lu]Lu-DOTA ZOL in patients with osteoblastic metastases: first results. EJNMMI Res. 2019;9:102.

61. Even-Sapir E, Metser U, Mishani E, et al. The detection of bone metastases in patients with high-risk prostate cancer: ^{99m}Tc-MDP planar bone scintigraphy, single- and multi-field-of-view SPECT, ^{18}F-fluoride PET, and ^{18}F-fluoride PET/CT. J Nucl Med. 2006;47(2):287–97.

62. Macheda ML, Rogers S, Bets JD. Molecular and cellular regulation of glucose transport (GLUT) proteins in cancer. J Cell Physiol. 2005;202:654–62.

63. Smith TA. Mammalian hexokinases and their abnormal expression in cancer. Br J Biomed Sci. 2000;57:170–8.

64. Stewardt GD, Gray K, Pennington CJ, et al. Analysis of hypoxia-associated gene expression in prostate cancer: lysyl oxidase and glucose transporter 1 expression correlate with Gleason score. Oncol Rep. 2008;20:1561.

65. Fox JJ, Schoder H, Larson SM. Molecular imaging of prostate cancer. Curr Opin Urol. 2012;22(4):320–7.

66. Meirelles GS, Schoder H, Ravizzini GC, et al. Prognostic value of baseline [^{18}F] fluorodeoxyglucose positron emission tomography and ^{99m}Tc-MDP bone scan in progressing metastatic prostate cancer. Clin Cancer. 2010;16(24):6093–9.

67. Schoder H, Herrmann K, Gonen M, et al. 2-[^{18}F]fluoro-2-deoxyglucose positron emission tomography for the detection of disease in patients with prostate-specific antigen relapse after radical prostatectomy. Clin Cancer Res. 2005;11(13):4761–9.

68. Jadvar H. Is there use for FDG-PET in prostate cancer? Semin Nucl Med. 2016;46(6):502–6.

69. Shen K, Liu B, Zhou X, et al. The evolving role of ^{18}F-FDG PET/CT in diagnosis and prognosis prediction in progressive prostate cancer. Front Oncol. 2021;11:683793. https://doi.org/10.3389/fonc.2021.683793.

70. Podo F. Tumor phospholipid metabolism. NMR Biomed. 1999;12:413–39.

71. Hara T, Kosaka N, Shinoura N, et al. PET imaging of brain tumor with [methyl-^{11}C] choline. J Nucl Med. 1997;38:842–7.

72. Umbehr MH, Muntener M, Hany T, et al. The role of ^{11}C-choline and ^{18}F-fluorocholine positron emission tomography (PET) and PET/CT in prostate cancer: a systematic review and meta-analysis. Eur Urol. 2013;64(1):106–17.

73. Evangelista L, Zattoni F, Guttilla A, et al. Choline PET or PET/CT and biochemical relapse of prostate cancer: a systematic review and meta-analysis. Clin Nucl Med. 2013;38(5):305–14.

74. Souvatzoglou M, Krause BJ, Purschel A, et al. Influence of [^{11}C]choline PET/CT on the treatment planning for salvage radiation therapy in patients

with biochemical recurrence of prostate cancer. Radiother Oncol. 2011;99(2):193–200.

75. Castellucci P, Picchio M. ^{11}C-Choline PET/CT and PSA kinetics. Eur J Nucl Med Mol Imaging. 2013;40(Suppl 1):S36–40.

76. Fanti S, Minozzi S, Castellucci P, et al. PET/CT with ^{11}C-choline for evaluation of prostate cancer patients with biochemical recurrence: meta-analysis and critical review of available data. Eur J Nucl Med Mol Imaging. 2016;43:55–69.

77. Paymani Z, Rohringer T, Vali R, et al. Diagnostic performance of [18F]Fluorocholine and [68Ga] Ga-PSMA PET/CT in prostate cancer: a comparative study. J Clin Med. 2020;9:2308. https://doi. org/10.3390/jcm9072308.

78. Virgolini I, Decristoforo C, Haug A, et al. Current status of theranostics in prostate cancer. Eur J Nucl Med Mol Imaging. 2018;45:471–95.

79. Parent EE, Schuster DM. Update on ^{18}F-fluciclovine PET for prostate cancer imaging. J Nucl Med. 2018;59:733–9.

80. Segawa A, Nagamori S, Kanai Y, et al. L-type amino acid transporter 1 expression is highly correlated with Gleason score in prostate cancer. Mol Clin Oncol. 2013;1:274–80.

81. Shiiba M, Ishihara K, Kimura G, et al. Evaluation of primary prostate cancer using ^{11}C-methionine-PET/CT and ^{18}F-FDG-PET/CT. Ann Nucl Med. 2012;26(2):138–45.

82. Okudaira H, Shikano N, Nishii R, et al. Putative transport mechanism and intracellular fate of trans-1-amino-3-^{18}F-fluorocyclobutanecarboxylic acid in human prostate cancer. J Nucl Med. 2011;52:822–9.

83. Schuster DM, Nanni C, Fanti S, et al. Anti-1-amino-3-^{18}F-fluorocyclobutane-1-carboxylic acid: physiologic uptake patterns, incidental findings, and variants that may simulate disease. J Nucl Med. 2014;55(12):1986–92.

84. Schuster DM, Votaw JR, Nieh PT, et al. Initial experience with the radiotracer anti-1-amino-3-[18F] fluorocyclobutane-1-carboxylic acid with PET/CT in prostate carcinoma. J Nucl Med. 2007;48(1):56–63.

85. Calais J, Czernin J, Cao M, et al. ^{68}Ga-PSMA-11 PET/CT mapping of prostate cancer biochemical recurrence after radical prostatectomy in 270 patients with a PSA level of less than 1.0 ng/mL: impact on salvage radiotherapy planning. J Nucl Med. 2018;59(2):230–7.

86. Tan N, Oyoyo U, Bavadian N, et al. PSMA-targeted radiotracers versus ^{18}F fluciclovine for the detection of prostate cancer biochemical recurrence after definitive therapy: a systematic review and meta-analysis. Radiology. 2020;296:44–55.

87. Bin X, Yong S, Kong Q-F, et al. Diagnostic performance of PET/CT using ^{18}F-FACBC in prostate cancer: a meta-analysis. Front Oncol. 2020;9:1438.

88. Scher HI, Beer TM, Higano CS, et al. Antitumour activity of MDV3100 in castration-resistant prostate cancer: a phase 1-2 study. Lancet. 2010;375(9724):1437–46.

89. Dehdashti F, Picus J, Michalski JM, et al. Positron tomographic assessment of androgen receptors in prostatic carcinoma. Eur J Nucl Med Mol Imaging. 2005;32(3):344–50.

90. Hoving H, Palthe S, Vallinga M, et al. Early ^{18}F-FDHT PET/CT as a predictor of treatment response in mCRPC treated with enzalutamide. J Clin Oncol. 2019;37(7s):232.

91. Fox JJ, Morris MJ, Larson SM, et al. Developing imaging strategies for castration resistant prostate cancer. Acta Oncol. 2011;50(Suppl 1):39–48.

92. Staniszewska M, Costa PF, Eiber M, et al. Enzalutamide enhances PSMA expression of PSMA-low prostate cancer. Int J Mol Sci. 2021;22:7431.

93. Beattie BJ, Smith-Jones PM, Jhanwar YS, et al. Pharmacokinetic assessment of the uptake of 16β-^{18}F-fluoro-5α-dihydrotestosterone (FDHT) in prostate tumors as measured by PET. J Nucl Med. 2010;51(2):183–92.

94. Antunes IF, Dost RJ, Hoving HD, et al. Synthesis and evaluation of ^{18}F-enzalutamide, a new radioligand for PET imaging of androgen receptors: a comparison with 16β-^{18}F-Fluoro-5α-dihydrotestosterone. J Nucl Med. 2021;62:1140–5.

95. Rosenthal SA, Haseman MK, Polascik TJ. Utility of capromab pendetide (ProstaScint) imaging in the management of prostate cancer. Tech Urol. 2001;7(1):27–37.

96. Hinkle GH, Burgers JK, Neal CE, et al. Multi center radioimmunoscintigraphic evaluation of patients with prostate carcinoma using indium-111 capromab pendetide. Cancer. 1998;83(4):739–47.

97. Wilkinson S, Chodak G. The role of [111]indium-capromab pendetide imaging for assessing biochemical failure after radical prostatectomy. J Urol. 2004;172(1):133–6.

98. Smith-Jones PM, Vallabhajosula S, Navarro V, et al. Radiolabeled monoclonal antibodies specific to the extracellular domain of prostate-specific membrane antigen: preclinical studies in nude mice bearing LNCaP human prostate tumor. J Nucl Med. 2003;44:610–7.

99. Smith-Jones PM, Vallabhajosula S, St. Omer S, et al. ^{177}Lu-DOTA-HuJ591: a new radiolabeled monoclonal antibody (mAb) for targeted therapy of prostate cancer. J Label Compds Radiopharm. 2001;44:90–2.

100. Bander NH, Trabulsi EJ, Kostakoglu L, Yao D, Vallabhajosula S, et al. Targeting metastatic prostate cancer with radiolabeled monoclonal antibody J591 to the extracellular domain of prostate specific membrane antigen. J Urol. 2003;170:171.

101. Bander NH, Milowsky MI, Nanus DM, Kostakoglu L, Vallabhajosula S, Goldsmith SJ. Phase I trial of [177]lutetium labeled J591, a monoclonal antibody to prostate-specific membrane antigen, in patients with androgen-independent prostate cancer. J Clin Oncol. 2005;23:4591–601.

102. Vallabhajosula S, Goldsmith SJ, Kostakoglu L, et al. Radioimmunotherapy of prostate cancer using [90]Y- and ^{177}Lu-labeled J591 monoclonal antibodies: effect

of multiple treatments on myelotoxicity. Clin Cancer Res. 2005;11:7195s–200s.

103. Vallabhajosula S, Goldsmith SJ, Hamacher KA, et al. Prediction of myelotoxicity based on bone marrow radiation-absorbed dose: radioimmunotherapy studies using [90]Y- and ^{177}Lu-labeled J591 antibodies specific for prostate-specific membrane antigen. J Nucl Med. 2005;46:850–8.

104. Vallabhajosula S, Kuji I, Hamacher A, et al. Pharmacokinetics and biodistribution of [111]In- and ^{177}Lu-labeled J591 antibody specific for prostate-specific membrane antigen: prediction of ^{90}Y-J591 radiation dosimetry based on ^{111}In or [177]Lu? J Nucl Med. 2005;46:634–41.

105. Yoon J-K, Park B-N, Ryu E-K, et al. Current perspectives on [89]Zr-PET imaging. Int J Mol Sci. 2020;21:4309. https://doi.org/10.3390/ijms21124309.

106. Osborne JR, Green DA, Spratt DE, et al. A prospective pilot study of [89]Zr-J591/prostate specific membrane antigen positron emission tomography in men with localized prostate cancer undergoing radical prostatectomy. J Urol. 2014;191:1439–45.

107. Pandit-Taskar N, O'Donoghue JA, Durack JC, et al. A phase I/II study for analytic validation of [89]Zr-J591 immunoPET as a molecular imaging agent for metastatic prostate cancer. Clin Cancer Res. 2015;21:5277–85.

108. Pandit-Taskar N, O'Donoghue JA, Beylergil V, et al. [89]Zr-huJ591 immuno-PET imaging in patients with advanced metastatic prostate cancer. Eur J Nucl Med Mol Imaging. 2014;41:2093–105.

109. Viola-Villegas NT, Sevak KK, Carlin, et al. Noninvasive imaging of PSMA in prostate tumors with (89)Zr-labeled huJ591 engineered antibody fragments: the faster alternatives. Mol Pharm. 2014;11:3965–73.

110. Joraku A, Hatano K, Kawai K, et al. Phase I/IIa PET imaging study with (89)zirconium labeled anti-PSMA minibody for urological malignancies. Ann Nucl Med. 2019;33:119–27.

111. Pandit-Taskar N, O'Donoghue JA, Ruan S, et al. First-in-human imaging with [89]Zr-Df-IAB2M anti-PSMA Minibody in patients with metastatic prostate cancer: pharmacokinetics, biodistribution, dosimetry, and lesion uptake. J Nucl Med. 2016;57:1858–64.

112. Gomes I, Maia C, Santos CRA. STEAP proteins: from structure to applications in cancer therapy. Mol Cancer Res. 2012;10:573–87.

113. O'Donoghue JA, Danila DC, Pandit-Taskar N, et al. Pharmacokinetics and biodistribution of [[89]Zr]Zr-DFO-MSTP2109A anti-STEAP1 antibody in metastatic castration resistant prostate cancer patients. Mol Pharm. 2019;16(7):3083–90.

114. Pomper MG, Musachio JL, Zhang J, et al. ^{11}C-MCG: synthesis, uptake selectivity, and primate PET of a probe for glutamate carboxypeptidase II (NAALADase), Mol Imaging. 2002;2:96–101.

115. Pillai MRA, Nanabala R, Joy A, et al. Radiolabeled enzyme inhibitors and binding agents targeting PSMA: effective theranostic tools for imaging and therapy of prostate cancer. Nucl Med Biol. 2016;43:692–720.

116. Mease RC, Dusich CL, Foss CA, et al. N-[N-[(S)-1,3-Dicarboxypropyl]Carbamoyl]-4-[^{18}F]fluorobenzyl-L-cysteine, [^{18}F]DCFBC: a new imaging probe for prostate cancer. Clin Cancer Res. 2008;14(10):3036–43.

117. Mena E, Lindenberg ML, Shih JH, et al. Clinical impact of PSMA-based ^{18}F-DCFBC PET/CT imaging in patients with biochemically recurrent prostate cancer after primary local therapy. Eur J Nucl Med Mol Imaging. 2018;45(1):4–11.

118. Chen Y, Pullambhatla M, Foss CA, et al. 2-(3-{1-carboxy-5-[(6-[^{18}F]fluoro-pyridine3-carbonyl)-amino]-pentyl}-ureido)-pentanedioic acid, [^{18}F]DCFPyL, a PSMA based PET imaging agent for prostate cancer. Clin Cancer Res. 2011;17:7645–53.

119. Dietlein F, Kobe C, Neubauer S, et al. PSA-stratified performance of [18]F- and ^{68}Ga-PSMA PET in patients with biochemical recurrence of prostate cancer. J Nucl Med. 2017;58:947–52.

120. Giesel FL, Will L, Lawal T, et al. Intraindividual comparison of ^{18}F-PSMA-1007 and [18]FDCFPyL PET/CT in the prospective evaluation of patients with newly diagnosed prostate carcinoma: a pilot study. J Nucl Med. 2018;59:1076–80.

121. Morris MJ, Rowe SP, Gorin MA, et al. Diagnostic performance of ^{18}F-DCFPyL-PET/CT in men with biochemically recurrent prostate cancer: results from the CONDOR phase III, multicenter study. Clin Cancer Res. 2021;27(13):3674–82.

122. Maresca KP, Hillier SM, Femia FJ, et al. A series of halogenated heterodimeric inhibitors of prostate-specific membrane antigen (PSMA) as radiolabeled probes for targeting prostate cancer. J Med Chem. 2009;52:347–57.

123. Barrett JA, Coleman RE, Goldsmith SJ, et al. First-in-man evaluation of two high-affinity PSMA-avid small molecules for imaging prostate cancer. J Nucl Med. 2013;54:1–8.

124. Zechmann CM, Afshar-Oromieh A, Armor T, et al. Radiation dosimetry and first therapy results with a [124]I/^{131}I-labeled small molecule (MIP-1095) targeting PSMA for prostate cancer therapy. Eur J Nucl Med Mol Imaging. 2014;41:1280–92.

125. Maresca KP, Hillier SM, Lu G, Marquis JC, Zimmerman CN, Eckelman WC, Joyal JL, Babich JW. Small molecule inhibitors of PSMA incorporating technetium-99m for imaging prostate cancer: effects of chelate design on pharmacokinetics. Inorganica Chimica Acta. 2012;389:168–75.

126. Vallabhajosula S, Smith-Jones PM, Navarro V, et al. Radioimmunotherapy of prostate cancer in human xenografts using monoclonal antibodies specific to prostate specific membrane antigen: studies in nude mice. Prostate. 2004;58:145–55.

127. Vallabhajosula S, Smith-Jones PM, Navarro V, Goldsmith SJ, Bander NH. Radioimmunotherapy of prostate cancer in human xenografts using

monoclonal antibodies specific to prostate specific membrane antigen: studies in nude mice. Prostate. 2004;58:145–55.

128. Vallabhajosula S, Polack JW, Babich JW. Molecular imaging of prostate cancer: radiopharmaceuticals for positron emission tomography (PET) and single-photon emission computed tomography (SPECT). In: Robinson B, Mosquera J, Ro J, Divatia M, editors. Precision molecular pathology of prostate cancer. Springer; 2017. p. 475–501.

129. Schmidkonz C, Gotz TI, Atzinger A, et al. 99mTc-MIP-1404 SPECT/CT for assessment of whole-body tumor burden and treatment response in patients with biochemical recurrence of prostate cancer. Clin Nucl Med. 2020;45(8):e349–57.

130. Eder M, Schäfer M, Bauder-Wust U, et al. 68Ga-complex lipophilicity and the targeting property of a urea-based PSMA inhibitor for PET imaging. Bioconjug Chem. 2012;23:688–97.

131. Afshar-Oromieh A, Haberkorn U, Eder M, et al. [68Ga]Gallium labelled PSMA ligand as superior PET tracer for the diagnosis of prostate cancer: comparison with 18F-FECH. Eur J Nucl Med Mol Imaging. 2012;39:1085–6.

132. Bois F, Noirot C, Dietemann S, et al. [68Ga]Ga-PSMA-11 in prostate cancer: a comprehensive review. Am J Nucl Med Mol Imaging. 2020;10(6):349–74.

133. Carlucci G, Ippisch R, Slavik R, et al. 68Ga-PSMA-11 NDA approval: a novel and successful academic partnership. J Nucl Med. 2021;62:149–55.

134. Weineisen M, Schottelius M, Simecek J, et al. 68Ga- and 177Lu-labeled PSMA I&T: optimization of a PSMA-targeted theranostic concept and first proof-of-concept human studies. J Nucl Med. 2015;56:1169–76.

135. Weineisen M, Simecek J, Schottelius M, et al. Synthesis and preclinical evaluation of DOTAGA-conjugated PSMA ligands for functional imaging and endoradiotherapy of prostate cancer. EJNMMI Res. 2014;4:63.

136. Benešová M, Schäfer M, Bauder-Wüst U, et al. Preclinical evaluation of a tailor-made DOTA-conjugated PSMA inhibitor with optimized linker moiety for imaging and endoradiotherapy of prostate cancer. J Nucl Med. 2015;56(6):914–20.

137. Giesel FL, Cardinale J, Schäfer M, et al. [18F]-Labelled PSMA-1007 shows similarity in structure, biodistribution and tumour uptake to the theragnostic compound PSMA-617. Eur J Nucl Med Mol Imaging. 2016;43:1929–30.

138. Cardinale J, Schäfer M, Benesova M, et al. Preclinical evaluation of 18F-PSMA-1007, a new prostate-specific membrane antigen ligand for prostate cancer imaging. J Nucl Med. 2017;58:425–31.

139. Wurzer A, Di Carlo D, Schmidt A, et al. Radiohybrid ligands: a novel tracer concept exemplified by 18F- or 68Ga-labeled rhPSMA inhibitors. J Nucl Med. 2020;61:735–42.

140. Wurzer A, Parzinger M, Konrad M. Preclinical comparison of four [(18)F, (nat)Ga]rhPSMA-7 isomers: influence of the stereo configuration on pharmacokinetics. EJNMMI Res. 2020;10(1):149.

141. Eiber M, Kroenke M, Wurzer A, Ulbrich L, Jooß L, Maurer T, et al. (18)F-rhPSMA-7 PET for the detection of biochemical recurrence of prostate cancer after radical prostatectomy. J Nucl Med. 2020;61(5):696–701.

142. Langbein T, Wang H, Rauscher I, et al. Utility of 18F-rhPSMA-7.3 positron emission tomography for imaging of primary prostate cancer and pre-operative efficacy in N-staging of unfavorable intermediate to very high-risk patients validated by histopathology. J Nucl Med. 2022;63:1334. https://doi.org/10.2967/jnumed.121.263440.

143. Yusufi N, Wurzer A, Herz M, et al. Comparative preclinical biodistribution, dosimetry and endoradiotherapy in mCRPC using 19F/177Lu-rhPSMA-7.3 and 177Lu-PSMA I&T. J Nucl Med. 2021;62:1106–11.

144. Liu Z, Chen X. Simple bioconjugate chemistry serves great clinical advances: albumin as a versatile platform for diagnosis and precision therapy. Chem Soc Rev. 2016;45:1432–56.

145. Zorzi A, Linciano S, Angelini A, et al. Non-covalent albumin-binding ligands for extending the circulating half-life of small biotherapeutics. Medchemcomm. 2019;10(7):1068–81.

146. Gharibkandi NA, Conlon JM, Hosseinimehr SJ. Strategies for improving stability and pharmacokinetic characteristics of radiolabeled peptides for imaging and therapy. Peptides. 2020;133(12):170385.

147. Dumelin CE, Trussel S, Buller F, et al. A portable albumin binder from a DNA-encoded chemical library. Angew Chem Int Ed Engl. 2008;47:3196–201.

148. Müller C, Struthers H, Winiger C, et al. DOTA conjugate with an albumin-binding entity enables the first folic acid–targeted 177Lu-radionuclide tumor therapy in mice. J Nucl Med. 2013;54:124–31.

149. Kelly JM, Amor-Coarasa A, Ponnala S, et al. Albumin-binding PSMA ligands: implications for expanding the therapeutic window. J Nucl Med. 2019;60(5):656–63.

150. Umbricht CA, Benešová M, Schibli R, Müller C. Preclinical development of novel PSMA-targeting radioligands: modulation of albumin-binding properties to improve prostate cancer therapy. Mol Pharm. 2018;15:2297–306.

151. Deberle LM, Benešová M, Umbricht CA, et al. Development of a new class of PSMA radioligands comprising ibuprofen as an albumin-binding entity. Theranostics. 2020;10(4):1678–93.

152. Kuo H-T, Lin K-S, Zhang Z, et al. 177Lu-labeled albumin-binder–conjugated PSMA-targeting agents with extremely high tumor uptake and enhanced tumor-to-kidney absorbed dose ratio. J Nucl Med. 2021;62:521–7.

153. Mansi R, Nock BA, Dalm SU, et al. Radiolabeled bombesin analogs. Cancers. 2021;13:5766.

154. Li X, Cai H, Wu X, et al. New frontiers in molecular imaging using peptide-based radiopharmaceuticals for prostate cancer. Front Chem. 2020;8:583309. https://doi.org/10.3389/fchem.2020.583309.

155. Zhang J, et al. PET using a GRPR antagonist ^{68}Ga-RM26 in healthy volunteers and prostate cancer patients. J Nucl Med. 2018;59:922.

156. Fassbender TF, Schiller F, Zamboglou C, et al. Voxel-based comparison of [^{68}Ga]Ga-RM2- PET/CT and [^{68}Ga]Ga-PSMA-11-PET/CT with histopathology for diagnosis of primary prostate cancer. EJNMMI Res. 2020;10:62.

157. Wieser G, Popp I, Christian Rischke H, et al. Diagnosis of recurrent prostate cancer with PET/CT imaging using the gastrin-releasing peptide receptor antagonist ^{68}Ga-RM2: preliminary results in patients with negative or inconclusive [^{18}F]fluoro-ethylcholine-PET/CT. Eur J Nucl Med Mol Imaging. 2017;44(9):1463–72.

158. Kurth J, Krause BJ, Schwarzenböck SM, et al. First-in-human dosimetry of gastrin releasing peptide receptor antagonist [^{177}Lu]Lu-RM2: a radiopharmaceutical for the treatment of metastatic castration-resistant prostate cancer. Eur J Nucl Med Mol Imaging. 2020;47:123–35.

159. Baratto L, Duan H, Laudicella R, et al. Physiological ^{68}Ga-RM2 uptake in patients with biochemically recurrent prostate cancer: an atlas of semi-quantitative measurements. Eur J Nucl Med Mol Imaging. 2020;47(1):115–22.

160. Baratto L, Song H, Duan H, et al. PSMA- and GRPR-targeted PET: results from 50 patients with biochemically recurrent prostate cancer. J Nucl Med. 2021;62(11):1545–9.

161. Nock BA, Kaloudi A, Lymperis E, et al. Theranostic perspectives in prostate cancer with the gastrin-releasing peptide receptor antagonist NeoBOMB1: preclinical and first clinical results. J Nucl Med. 2017;58:75–80.

162. Das T, Banerjee S. Radiopharmaceuticals for metastatic bone pain palliation: available options in the clinical domain and their comparisons. Clin Exp Metastasis. 2017;34(1):1–10.

163. Liepe K, Murray I, Flux G. Dosimetry of bone seeking beta emitters for bone pain palliation metastases. Semin Nucl Med. 2021;52:178.

164. Pecher C. Biological investigation with radioactive calcium and strontium: preliminary report on the use of radioactive strontium in treatment of metastatic bone cancer. Pharmacology. 1942;11:117–49.

165. Turner JH, Claringbold PG, Hetherington EL, et al. (1989) a phase I study of samarium-153 ethylenediaminetetra-methylene phosphonate therapy for disseminated skeletal metastases. J Clin Oncol. 1989;7:1926–31.

166. Askari E, Harsini S, Vahidfar N, et al. ^{177}Lu-EDTMP for metastatic bone pain palliation: a systematic review and meta-analysis. Cancer Biother Radiopharm. 2021;36(5):383–90.

167. Larsen RH, Henriksen G, Bruland O. Preparation and use of radium-223 to target calcified tissues for pain palliation, bone cancer therapy, and bone surface conditioning. Google Patents; 2003.

168. Parker C, Finkelstein SE, Michalski JM, et al. Efficacy and safety of radium-223 dichloride in symptomatic castration-resistant prostate cancer patients with or without baseline opioid use from the phase 3 ALSYMPCA trial. Eur Urol. 2016;70(5):875–83.

169. Sartor O, Coleman R, Nilsson S, et al. Effect of radium-223 dichloride on symptomatic skeletal events in patients with castration resistant prostate cancer and bone metastases: results from a phase 3, double-blind, randomised trial. Lancet Oncol. 2014;15:738–46.

170. Milowsky MI, Nanus DM, Kostakoglu L, Vallabhajosula S, Goldsmith SJ, Bander NH. Phase I trial of ^{90}Y-labeled anti-prostate specific membrane antigen monoclonal antibody J591 for androgen-independent prostate cancer. J Clin Oncol. 2004;22:2522–31.

171. Vallabhajosula S, Nikolopoulou A, Jhanwar YS, et al. Radioimmunotherapy of metastatic prostate cancer with ^{177}Lu-DOTA-huJ591 anti prostate specific membrane antigen specific monoclonal antibody. Curr Radiopharm. 2016;9:44–53.

172. Tagawa ST, Milowsky MI, Morris M, Vallabhajosula S, et al. Phase II study of lutetium-177-labeled anti-prostate-specific membrane antigen monoclonal antibody J591 for mCRPC. Clin Cancer Res. 2013;19:5182–91.

173. Tagawa ST, Akhtar NH, Nikolopoulou A, et al. Bone marrow recovery and subsequent chemotherapy following radiolabeled anti-prostate-specific membrane antigen monoclonal antibody J591 in men with mCRPC. Front Oncol. 2013;3:1–6.

174. O'Donoghue JA, Sgouros G, Divgi CR, Humm JL. Single-dose versus fractionated radioimmunotherapy: model comparisons for uniform tumor dosimetry. J Nucl Med. 2000;41:538–47.

175. Tagawa ST, Osborne JR, Hackett A, et al. Preliminary results of a phase I/II dose-escalation study of fractionated dose ^{177}Lu-PSMA-617 for progressive metastatic castration resistant prostate cancer (mCRPC). Ann Oncol. 2019;30(Suppl_5):v325–55. https://doi.org/10.1093/annonc/mdz248.

176. Tagawa ST, Vallabhajosula S, Christos PJ, et al. Phase 1/2 study of fractionated dose lutetium-177-labeled anti-prostate-specific membrane antigen monoclonal antibody J591 (^{177}Lu-J591) for mCRPC. Cancer. 2019;125:2561–9.

177. Batra JS, Niaz MJ, Whang YE, et al. Phase I trial of docetaxel plus lutetium-177-labeled anti–prostate-specific membrane antigen monoclonal antibody J591 (^{177}Lu-J591) for metastatic castration-resistant prostate cancer. Urol Oncol. 2020;38(11):848.e9–848.

178. Niaz MJ, Bastra JS, Walsh RD, Ramirez-Fort MK, Vallabhajosula S, et al. Pilot study of hyperfraction-

ated dosing of lutetium-177 labeled antiprostate-specific membrane antigen monoclonal antibody J591 (^{177}Lu-J591) for metastatic castration-resistant prostate cancer. Oncologist. 2020;25(6):477–e895.

179. Li Y, Tian Z, Rizvi SM, Bander NH, Allen BJ. In vitro and preclinical targeted alpha therapy of human prostate cancer with Bi-213 labeled J591 antibody against the prostate specific membrane antigen. Prostate Cancer Prostatic Dis. 2002;5:36–46.

180. Tagawa ST, Osborne J, Fernandez E, et al. Phase I dose-escalation study of PSMA-targeted alpha emitter [225]Ac-J591 in men with metastatic castration-resistant prostate cancer (mCRPC). J Clin Oncol. 2020;38(Suppl 15):5560.

181. Tagawa ST, Sun M, Sartor AO, et al. Phase I study of [225]Ac-J591 for men with metastatic castration-resistant prostate cancer (mCRPC). J Clin Oncol. 2021;39(Suppl 15):abstr 5015.

182. Kratochwil C, Bruchertseifer F, Giesel FL, et al. [225]Ac-PSMA-617 for PSMA-targeted alpha-radiation therapy of metastatic castration-resistant prostate cancer. J Nucl Med. 2016;57:1941–4.

183. Kratochwil C, Giesel FL, Stefanova M, et al. PSMA-targeted radionuclide therapy of metastatic castration-resistant prostate cancer with ^{177}Lu-labeled PSMA-617. J Nucl Med. 2016;57:1170–6.

184. Hofman MS, Violet J, Hicks RJ, et al. [^{177}Lu]-PSMA-617 radionuclide treatment in patients with metastatic castration-resistant prostate cancer (LuPSMA trial): a single-center, single-arm, phase 2 study. Lancet Oncol. 2018;19:825–33.

185. Hofman MS, Emmett L, Sandhu S, et al. [^{177}Lu]Lu-PSMA-617 versus cabazitaxel in patients with metastatic castration-resistant prostate cancer (TheraP): a randomized, open-label, phase 2 trial. Lancet. 2021;397(10276):797–804.

186. Sartor O, de Bono J, Chi KN, Fizazi K, Herrmann K, Rahbar K, et al. Lutetium-177-PSMA-617 for metastatic castration-resistant prostate cancer. N Engl J Med. 2021;385:1091–103.

187. Yadav MP, Ballal S, Bal C, Sahoo RK, et al. Efficacy and safety of ^{177}Lu-PSMA-617 radioligand therapy in metastatic castration-resistant prostate cancer patients. Clin Nucl Med. 2020;45:19–31.

188. Baum RP, Kulkarni HR, Schuchardt C, et al. ^{177}Lu-labeled prostate-specific membrane antigen radioligand therapy of metastatic castration-resistant

prostate cancer: safety and efficacy. J Nucl Med. 2016;57:1006–13.

189. Heck MM, Retz M, D'Alessandria C, et al. Systemic radioligand therapy with ^{177}Lu-PSMA-I&T in patients with metastatic castration-resistant prostate cancer. J Urol. 2016;196:382–91.

190. Okamoto S, Thieme A, Allmann J, et al. Radiation dosimetry for ^{177}Lu-PSMA I&T in metastatic castration-resistant prostate cancer: absorbed dose in Normal organs and tumor lesions. J Nucl Med. 2016;58:445–50.

191. Heck MM, Tauber R, Schwaiger S, et al. Treatment outcome, toxicity, and predictive factors for radioligand therapy with ^{177}Lu-PSMA-I&T in metastatic castration-resistant prostate cancer. Eur Urol. 2019;75(6):920–6.

192. Sanli YR, Simsek DH, Sanli O, et al. ^{177}Lu-PSMA therapy in metastatic castration-resistant prostate cancer. Biomedicine. 2021;9:430.

193. Kratochwil C, Bruchertseifer F, Rathke H, et al. Targeted alpha-therapy of metastatic castration-resistant prostate cancer with 225Ac-PSMA-617: swimmer-plot analysis suggests efficacy regarding duration of tumor control. J Nucl Med. 2018;59:795–802.

194. Kratochwil C, Haberkorn U, Giesel FL. (225)Ac-PSMA-617 for therapy of prostate cancer. Semin Nucl Med. 2020;50:133–40.

195. Sathekge M, Bruchertseifer F, Knoesen O, et al. 225Ac-PSMA-617 in chemotherapy-naive patients with advanced prostate cancer: a pilot study. Eur J Nucl Med Mol Imaging. 2019;46:129–38.

196. Yadav MP, Ballal S, Sahoo RK, et al. Efficacy and safety of (225)Ac-PSMA-617 targeted alpha therapy in metastatic castration-resistant prostate cancer patients. Theranostics. 2020;10:9364–77.

197. Zacherl MJ, Gildehaus FJ, Mittlmeier L, et al. First clinical results for PSMA-targeted a-therapy using 225Ac-PSMA-I&T in advanced-mCRPC patients. J Nucl Med. 2021;62:669–74.

198. Suman SK, Subramanian S, Mukherjee A. Combination radionuclide therapy: a new paradigm. Nucl Med Biol. 2021;98:40–58.

199. Khreish F, Ebert N, Ries M, et al. (225)AcPSMA-617/(177)Lu-PSMA-617 tandem therapy of metastatic castration-resistant prostate cancer: pilot experience. Eur J Nucl Med Mol Imaging. 2020;47:721–8.

Index

A

Active transport, 129–132, 187, 196, 204, 292, 297, 311, 321, 328, 333, 463, 485, 489, 589, 634

Affinity, 4, 13, 92, 102, 192–195, 200, 201, 204, 207, 267, 273–275, 278, 293–295, 298, 318, 331, 333, 336, 337, 339–341, 344, 346, 348, 351, 387, 396–398, 401, 402, 407, 412, 413, 444, 445, 451, 462, 479, 480, 488, 490, 492, 493, 520, 526, 543–545, 558, 559, 562, 581, 583–588, 590–592, 618–623, 625, 626, 629, 630, 632, 633, 642–644, 670, 676, 681, 684–688

Alkylation, 206, 231, 245, 247, 248, 250, 596

Alpha amino acids, 579

α decay, 53, 177

Alpha particles, 34, 52, 54, 56, 176, 470–474, 477, 479, 486, 501, 545, 594, 632–633, 667

Alpha therapy, 16, 529, 633, 656, 696

Aluminum-fluoride method [A^{18}F], 233, 597

Alzheimer's disease (AD), 11, 214, 222, 227, 249, 250, 382–386, 388–394, 396–403, 409, 411

Androgen receptor (AR), 192, 222, 346, 655, 659–662, 674–676, 695

Anger camera, 70–72, 77, 185

Antigen-antibody complex, 545

Apoptosis, 121, 142–145, 189, 192, 222, 305, 307–311, 329–332, 339, 383, 428, 478, 494, 539, 542, 558, 561, 563, 617, 618

Atherosclerosis, 425–429, 453–456

Atom, 21, 22, 32–34, 38, 40–42, 44–46, 58, 63–66, 70, 76, 87–94, 97, 100, 102–104, 107–110, 134, 149, 151, 152, 154, 155, 160, 165, 169, 170, 190, 192, 193, 196, 198, 201, 206, 217–219, 229, 230, 234–236, 247, 248, 263, 264, 275, 283, 312, 387, 392, 393, 397, 432, 470, 502, 509, 511, 515, 524, 578, 580, 587, 596, 598, 602, 621

Atomic emission, 46, 64

Atomic number (Z), 32, 33, 41, 42, 44, 45, 52, 54, 56, 63, 88, 100, 149, 150, 152, 153, 158, 169, 170, 214, 263, 266, 505, 509, 516, 517, 527, 597

Atomic theory, 23

Auger electrons, 15, 45, 46, 56, 66, 191, 464, 469, 474, 475, 479–481, 547, 616, 628, 666

B

β-amyloid, 7, 187, 192, 214, 222, 227, 250, 384, 385, 394, 396–398, 431, 449, 451

Beta decay, 52–54, 56, 58, 60, 464, 473

Beta particles, 30, 56, 76, 169, 464–470, 472, 473, 479, 486, 487, 560, 561, 632, 633, 666, 667, 681, 689–693

Bifunctional chelating agent (BFC), 107, 194, 206, 260, 263, 268–270, 284, 468, 483, 484, 515, 517, 520–522, 525, 526, 543, 545, 548–551, 586, 594, 598–601, 603, 617, 668

Binding potential, 294, 296, 401

Bone pain palliation, 14, 174, 175, 469, 470, 526, 527, 656, 660, 689–691

Bremsstrahlung, 28, 45, 64, 155, 173, 468

Bystander, 478

C

Cardiac amyloidosis (CA), 426, 430, 431, 448, 451

Cardiac sarcoidosis (CS), 426, 430, 446–449

Cell cycle, 122–124, 308, 315, 317, 318, 339, 481, 618

Cell differentiation, 125, 143

Cell structure and function, 117–122

Chemical bonds, 91–93, 100, 133, 208, 275, 470, 472, 475, 524, 526, 577, 578

Chemical elements, 22, 23, 30, 35, 39, 40, 43, 50, 52, 87, 147, 149, 169, 192, 193, 506, 527

Coincidence detection, 75–77

Combination therapy, 18, 560, 561, 692, 693, 696, 697

Compartmental modelling, 291

Computed tomography (CT) scanner, 8, 9, 15–17, 72, 80–82, 84, 259, 274, 277, 279, 280, 303, 304, 313–315, 319, 320, 322, 324, 325, 334, 340–343, 345, 346, 349–351, 354, 355, 358, 359, 363, 417, 436, 447, 448, 452, 455, 456, 564, 566, 567, 569, 570, 612, 622, 624, 626, 627, 632, 635, 637–641, 644, 669–672, 675, 677, 680, 684, 686, 687

Congestive heart failure (CHF), 425, 429, 440

A

Automated synthesis module (ASM), 194, 208, 209, 221, 223, 229, 232, 247, 273